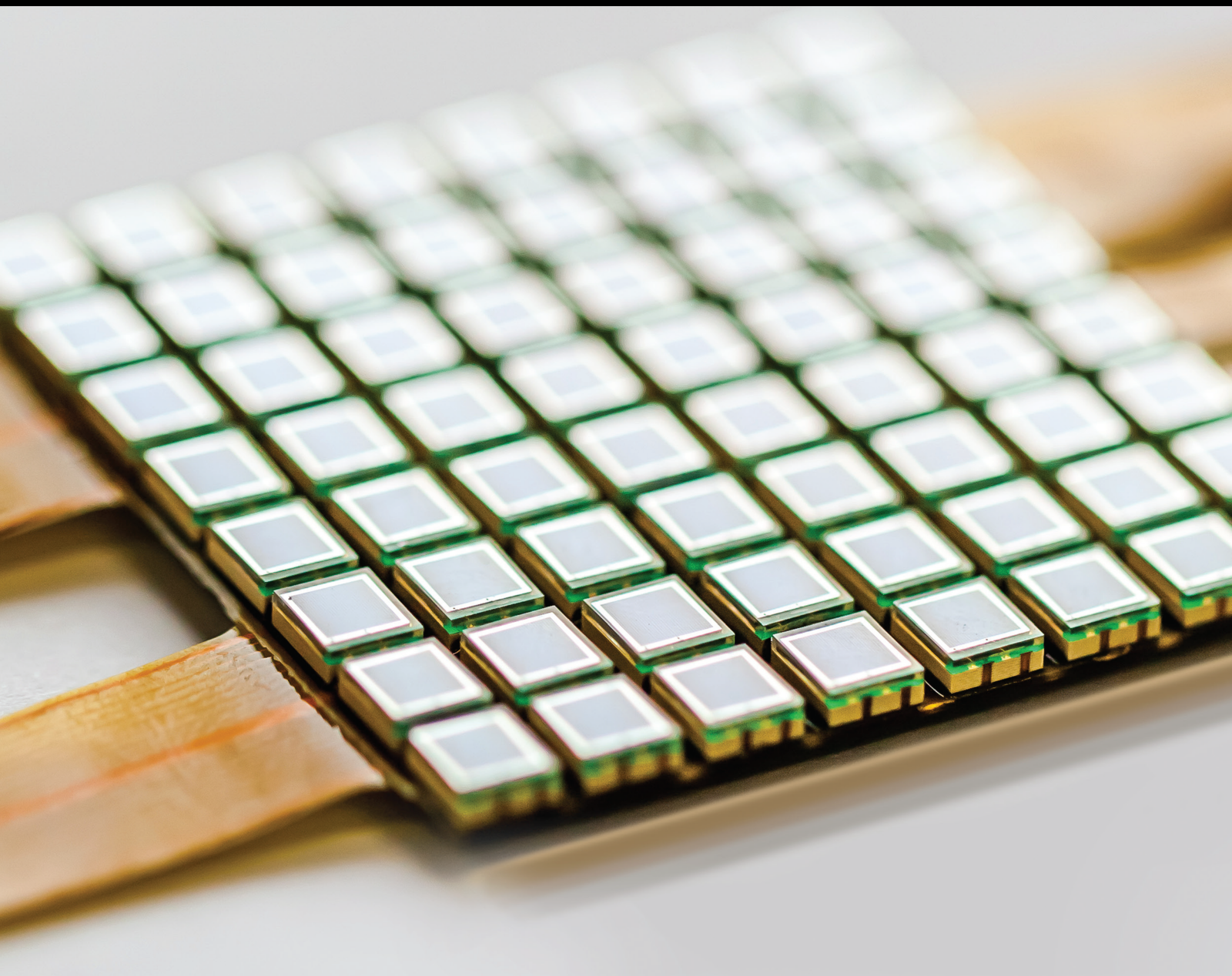# Intelligent Sensing, Monitoring, and Optimization of Advanced Manufacturing Systems

Lead Guest Editor: Min Xia
Guest Editors: Haidong Shao and Chao Wang

Intelligent Sensing, Monitoring, and Optimization of Advanced Manufacturing Systems

Intelligent Sensing, Monitoring, and Optimization of Advanced Manufacturing Systems

Lead Guest Editor: Min Xia
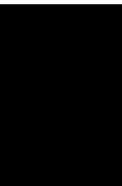Guest Editors: Haidong Shao and Chao Wang

Ehsan Namaziandost (iD), Iran
Heinz C. Neitzert (iD), Italy
Sing Kiong Nguang (iD), New Zealand
Calogero M. Oddo (iD), Italy
Tinghui Ouyang, Japan
SANDEEP KUMAR PALANISWAMY (iD),
India
Alberto J. Palma (iD), Spain
Davide Palumbo (iD), Italy
Abinash Panda (iD), India
Roberto Paolesse (iD), Italy
Akhilesh Pathak (iD), Thailand
Giovanni Pau (iD), Italy
Giorgio Pennazza (iD), Italy
Michele Penza (iD), Italy
Sivakumar Poruran, India
Stelios Potirakis (iD), Greece
Biswajeet Pradhan (iD), Malaysia
Giuseppe Quero (iD), Italy
Linesh Raja (iD), India
Maheswar Rajagopal (iD), India
Valerie Renaudin (iD), France
Armando Ricciardi (iD), Italy
Christos Riziotis (iD), Greece
Ruthber Rodriguez Serrezuela (iD), Colombia
Maria Luz Rodriguez-Mendez (iD), Spain
Jerome Rossignol (iD), France
Maheswaran S, India
Ylias Sabri (iD), Australia
Sourabh Sahu (iD), India
José P. Santos (iD), Spain
Sina Sareh, United Kingdom
Isabel Sayago (iD), Spain
Andreas Schütze (iD), Germany
Praveen K. Sekhar (iD), USA
Sandra Sendra, Spain
Sandeep Sharma , India
Sunil Kumar Singh Singh (iD), India
Yadvendra Singh (iD), USA
Afaque Manzoor Soomro (iD), Pakistan
Vincenzo Spagnolo, Italy
Kathiravan Srinivasan (iD), India
Sachin K. Srivastava (iD), India
Stefano Stassi (iD), Italy

Danfeng Sun, China
Ashok Sundramoorthy, India
Salvatore Surdo (iD), Italy
Roshan Thotagamuge (iD), Sri Lanka
Guiyun Tian (iD), United Kingdom
Sri Ramulu Torati (iD), USA
Abdellah Touhafi (iD), Belgium
Hoang Vinh Tran (iD), Vietnam
Aitor Urrutia (iD), Spain
Hana Vaisocherova - Lisalova (iD), Czech
Republic
Everardo Vargas-Rodriguez (iD), Mexico
Xavier Vilanova (iD), Spain
Stanislav Vítek (iD), Czech Republic
Luca Vollero (iD), Italy
Tomasz Wandowski (iD), Poland
Bohui Wang, China
Qihao Weng, USA
Penghai Wu (iD), China
Qiang Wu, United Kingdom
Yuedong Xie (iD), China
Chen Yang (iD), China
Jiachen Yang (iD), China
Nitesh Yelve (iD), India
Aijun Yin, China
Chouki Zerrouki (iD), France

Contents

Contents

Contents

Review Article

A Review on the Environment Perception and Control Technologies for the Hyperredundant Manipulators in Limited Space

Jiaxin Liu,[1] Aoshun Zhang [2,3] En Li [2,3] Rui Guo,[4] Shengchuan Li,[1] and Mingrui Luo [2,3]

[1]*State Grid Liaoning Electric Power Company Limited, Shenyang 110004, China*
[2]*School of Artificial Intelligence, University of Chinese Academy of Sciences, No. 19(A) Yuquan Road, Beijing 100049, China*
[3]*The State Key Laboratory of Management and Control for Complex Systems, Institute of Automation Chinese Academy of Sciences, Beijing 100190, China*
[4]*State Grid Shandong Electric Power Company, Jinan 250001, China*

Correspondence should be addressed to En Li; en.li@ia.ac.cn

As a typical kind of special robot with high flexibility and maneuverability, the hyperredundant manipulators (HRM) which can work in the narrow and complex space arose much related research work. Due to the particularity of the environment and the structural complexity of the manipulators, there are many problems for the HRM in specific applications. This paper summarizes some representative research works for HRM, including the mechanical design, environment perception, robotic navigation, and trajectory control. In order to make the design of the HRM systems more suitable for applications, the technical problems of current research are analyzed to address the key issues for the improvement. Finally, the prospect of spatial reachability, structural compactness, operation accuracy, and interaction friendliness of hyperredundant manipulators are presented.

1. Introduction

In the development of robotic technology, several kinds of robots have been used in many industrial fields to replace manual operation, reducing the labor intensity of workers and improving the quality of operation. However, in some complex and dangerous operating environments, especially those with narrow space and limited movement, it is difficult or even impossible for operators and traditional robots to enter the operating space. In addition, the operation mode using simple auxiliary tools cannot meet the requirements of operation scope and quality. Therefore, it is an important way to solve this kind of practical application problem to study the robot technology suitable for confined space operation.

Unstructured narrow working space is widely existed in lots of fields such as aerospace [1–4], nuclear power [5, 6], equipment manufacturing, and postdisaster rescue. Figure 1 lists some common usage scenarios of hyperredun-

dant manipulators. In the aviation manufacturing industry, the gluing, painting, riveting, grinding, maintenance, and other operations required for the assembly of narrow inner cavities such as wing box segment and inlet can only be realized manually at present. It is hard for the workers, and the quality of the product cannot be guaranteed which seriously compromises the safety of aircraft. In the equipment manufacturing industry, welding and maintenance of cabin cubicles, mining hydraulic supports, cathode busbars of electrolytic cells, and so on require workers to work continuously in high temperature, pollution, and narrow space. The environment is hard for workers, and it is difficult to ensure the quality of welding seams. In the nuclear power industry, nuclear power reactor body, fuel rod control pipeline, and other key equipment cross each other, creating a complex environment. There is no efficient maintenance means due to high temperature, strong radiation, and narrow space, which brings serious hidden danger to the safety

(a)

(b)

(c)

(d)

(e)

(f)
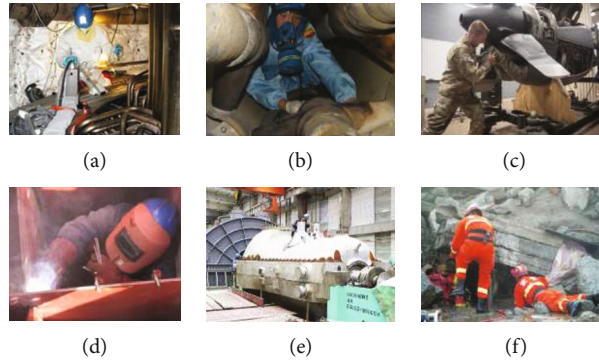
FIGURE 1: Typical complex and narrow operation scenario. Picture (a) is the repair of nuclear power pipeline, picture (b) is closed GIS equipment maintenance, picture (c) is aircraft inlet cleaning, picture (d) is cabin compartment welding, picture (e) is an internal inspection of closed tank, and picture (f) is a search and rescue after earthquake.

of nuclear power. In the power energy industry, when the complex and compact closed switchgear and integrated power distribution control cabinet in the substation need to be repaired due to an internal fault, usually, a large range of parts need to be disassembled to locate the fault, which greatly reduce the maintenance efficiency. In the task of postdisaster search and rescue, the narrow environment formed by collapsed buildings and equipment makes it difficult for search and rescue personnel to directly enter the rescue, to obtain information about trapping people and the surrounding environment, and to implement emergency treatment. After the above analysis, we need to analyze the scene characteristics and tasks in complex and narrow space and develop a robot system that can actively and flexibly avoid obstacles; thus, there is an actual demand in lots of fields.

Narrow and closed operation space, complex obstacle distribution, and insufficient light conditions, a special operating point that located inside the deep cavity, are the common characteristics of this kind of operation scene talked above. To solve the problem of narrow space operations, there is an urgent need to develop a robot system that can actively and flexibly avoid obstacles, which not only can precisely transport operating tools to the operating point, continuously move along the specified trajectory, but also it can adapt to the complex unstructured narrow environment. The robots in such robotic systems generally need to have a compact overall structure, which enables the robots to avoid different obstacles in space, thereby realizing flexible operations in small and confined spaces.

2. Summary of Related Research Work

As a kind of typical special application robot, robots that can work in narrow space have been widely concerned at home and abroad. A lot of researches had been carried out in the field of joint materials, mechanism design, control method, sensing technology, application system, and so on by research institutions in the United States, Germany, Britain, Japan, China, Norway, and other countries. And many fruitful theoretical methods and prototypes have been formed.

2.1. Manipulator Mechanism Design. Environmental adaptability and traversability in confined space are the key points of robot system design. However, in different narrow spaces, the operating conditions and working environments of robots are different. So robot mechanisms based on different operating modes have been developed for different operating scenarios at home and abroad. Figure 2 lists some common drive forms, structural forms, and propulsion methods of snake-shaped manipulators. Among them, the common driving forms and structural forms of the hyperredundant manipulator will be introduced in this section with specific research examples, and the propulsion device will be mainly introduced in the "Robotic Operating System" section.

Due to the limitation of the narrow space, the movement mechanism of the robot generally uses snake mechanism or soft machine. The kinematic joints of the robot mainly adopt rigid joints (with ball joints or hook joints), hollow bellows, and elastic ridge skeleton. As shown in Figure 2, the main driving modes of the robot are micromotor direct drive, wire rope drive, artificial muscle drive, gas drive, and so on. For example, the pneumatic flexible robot developed by the Tohoku University in Japan moves inside the pipe of the pressure vessel of nuclear power plant through the tension and drive of the pneumatic actuator [7]. Chuo University in Tokyo has developed an in-tube detection robot based on artificial muscles, which can achieve peristaltic crawling by stretching artificial muscles [8]. Carnegie Mellon University developed a snake-like robot composed of multiple modular electromechanical joints in series to realize operation control in narrow space [9]. HRM with different driving methods will have different characteristics and technical difficulties. In general, manipulator powered by micromotors provides limited driving force. Driving with gas requires more consideration of gas tightness and control accuracy and flexibility. At present, most high-redundancy manipulators prefer to use ropes for indirect control, which reduces the weight of the manipulator, but brings many control problems such as model solving and control decoupling. Chinese Shenyang Institute of Science and Technology, Beijing Institute of Technology, Shanghai Jiaotong University, National University of Defense Technology, Beijing University of Aeronautics and Astronautics, etc. have also made fruitful research achievements in this aspect [14–19]. For
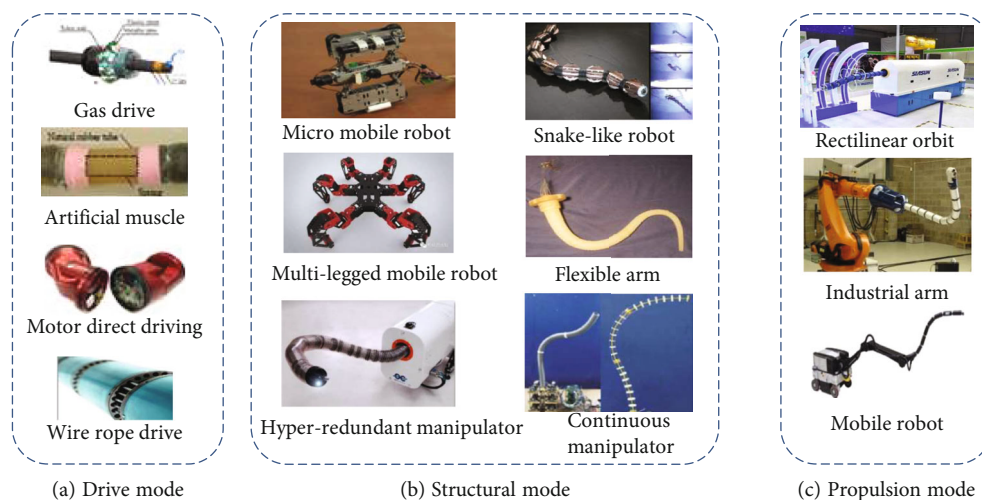
Figure 2: Typical robot operation mode in narrow space scenario. The three parts (a–c) introduce the driving mode, the structural mode, and the propulsion mode, respectively. The following is a detailed introduction and source of some images. The first picture in part (a) is a pneumatic drive structure published by the Tohoku University in Japan in 2017 [7]. The second image in part (a) is an artificial muscle actuation structure published by the Tokyo Chuo University in 2012 [8]. The third image in part (a) is a micromotor joint drive structure published by the Carnegie Mellon University in 2014 [9]. The forth image in part (a), the bottom left picture in part (b), and the second pictures in part (c) are snake-shaped manipulators made by OC-Robotic [1]. The first picture in part (c) is a snake-shaped manipulator developed by Siasun [10]. The middle right picture in part (b) is a soft robot arm made by silicone in the BioRobotics Institute, Scuola Superiore Sant Anna, Pisa [11]. The bottom right picture in part (b) is a hyperredundant manipulator for aircraft fuel tank inspection, which is designed by the China Civil Aviation University [12, 13].

example, a paper published by the Shenyang Institute of Automation of the Chinese Academy of Sciences in 2009 developed a three-dimensional snake-like robot model composed of modular universal units, which can achieve meandering motion, twisting motion, and twisting hill-climbing motion [15]. Later in 2012, they developed an amphibious snake-like robot [16]. The robot consists of 9 universal motion units with hermetic design. And the land and underwater mobility of the amphibious snake-like robot is verified by gait test. In 2008, the Institute of Robotics of Shanghai Jiao Tong University developed a climbing snake-like robot, which consists of many P-R modules (two joints connected in a pitch-roll manner as an execution unit) [17]. The different structural forms that HRM takes are often related to specific tasks. In some detection tasks that do not need to provide working force, a software mechanism can be used to achieve higher flexibility [11–13]. In some industrial scenarios, rigid joints are required to provide sufficient stability and work force [1]. High-redundancy robots with bionic form tend to pay more attention to the realization of shape and bionic motion.

Although snake-like robot and soft robot have better spatial adaptability and flexibility which can help pass through narrow pipes and spaces of different shapes, they can only carry out partial detection tasks and do not have the ability to perform actual operations due to their generally light weight and driving depends on adhesion to the tube wall.

In order to meet the needs of narrow space operation, scholars have carried out research on snake-like manipulator with slender structure. There is plenty of similarities between serpentine high-redundancy robot arm with snake-like robot and also differences. The former is a multijoint manip-

ulator with fixed foundation for operation, while the latter is a mobile bionic system developed to imitate the movement mechanism of snakes. For the operation in narrow space, the serpentine manipulator can avoid the interference of spatial obstacles to reach the operation target point and can provide enough acting force and positioning accuracy to meet the needs of the operation task.

Scholars have carried out a lot of exploratory research on typical snake-like manipulator, especially in the field of surgical robot, which has formed good technical achievements. In 2009, the CardioARM cardiac surgery robot developed by the Carnegie Mellon University is composed of 50 spherical joints. The internal and external tube structures realize the rigid and flexible alternation and relative movement under the control of ropes [20]. Imperial College London developed a TEMS colon surgery robot in 2017, which is connected in series with 7 joints in different directions, and can actively change the posture of the operating tool to achieve surgical operation in the slender and narrow colon [21]. IREP, an interventional operation robot developed by the Columbia University for single-hole entry surgery, is composed of two flexible arms and a parallel quadrilateral structure with 21 degrees of freedom. The hybrid mechanical structure improves the positioning accuracy of the flexible manipulator and achieves a larger working space [22]. The single-bore surgical robot developed by the Samsung Institute of Advanced Technology (SAIT) is mainly composed of a 6-DOF (degree of freedom) serpentine guiding arm, equipped with two tools and an auxiliary arm, and can reach different surgical sites in the abdominal cavity through incisions [23]. The Harbin Institute of Technology developed a colonoscopy surgical robot composed of a 5-segment continuum driven by steel wire, which can achieve

(a)

(b)

(c)

(d)
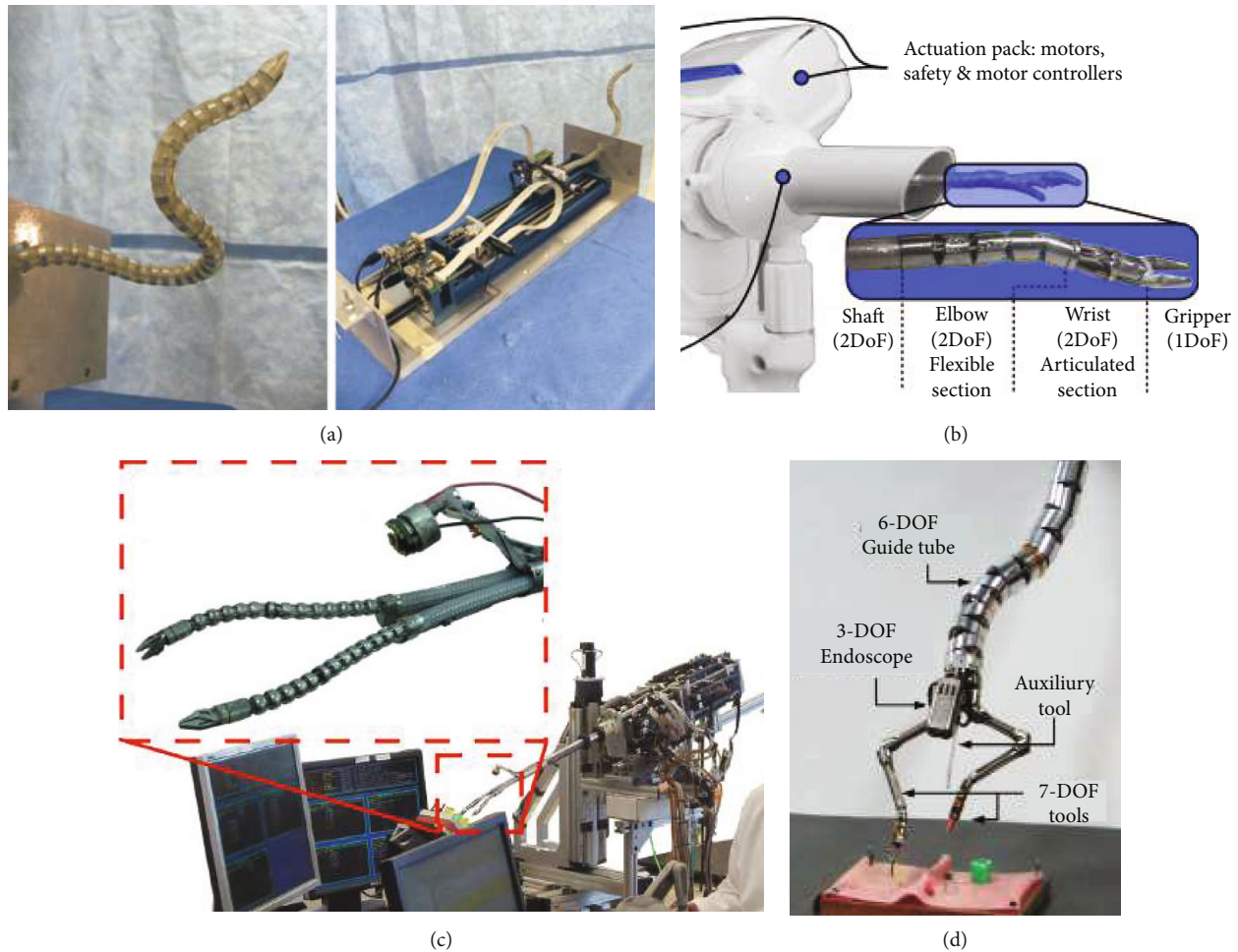
FIGURE 3: Typical flexible operating surgical robot. Picture (a) is a cardiac surgery robot named "CardioARM" developed by the Carnegie Mellon University [20], picture (b) is a colon surgery robot named "TEMS" developed by the Imperial College London [21], picture (c) is an interventional operation robot developed by the Columbia University [22], and picture (d) is a single-bore surgical robot developed by the Samsung Institute of Advanced Technology [23].

multidegree-of-freedom rotation and deformation [24]. Figure 3 shows a physical image of some of the hyperredundant manipulators mentioned above.

In the narrow space of industrial applications, different from the lightweight and dexterity requirements of medical robots, robots are required to have longer arm span, large load, high precision, space obstacle avoidance, and other characteristics, so as to be able to carry out tasks such as deep cavity detection and operation. At present, the most influential robot in the engineering of highly redundant robotic arms is the snake arm robot of OC-Robotics in the UK. They have carried out research for more than ten years and developed a variety of snake arm application systems in nuclear power equipment maintenance, aviation manufacturing, and other industries. These highly redundant serpentine robotic arms move through rigid joints driven by steel wire, which are connected in series by hook hinges [25]. In recent years, Chinese research institutions have also carried out research work on serpentine manipulator in narrow space applications. According to the requirements of aviation assembly, AVIC 625 Institute developed

a robot prototype consisting of 5 sections and 20 sections by referring to the structural characteristics of OC-Robotics [10]. Hit Shenzhen University of Technology developed a superredundant robot with steel wire traction composed of 10 joints, which has good bending characteristics and flexible space movement ability [26]. Tsinghua University designed a spatial redundancy manipulator composed of five segments, with six segments in each segment. The angle of each segment was basically the same through the connecting rope [27]. Researchers at the Beihang University have designed a snake-arm robot. The robot consists of three hollow slender segments consisting of a steel cable-driven spherical hinge. A cage-like structure was designed to drive the wire rope, and a special motor-driven control system was proposed to control the robot [28]. Jing and his team at the Shanghai Jiao Tong University proposed a serpentine arm based on an octahedral variable geometry truss [29–34]. The Shanghai Jiaotong University developed a rope-driven superredundant manipulator with 12 joints and 24 degrees of freedom, which can achieve a load capacity of 0.5 kg at the end through the drive control of 36
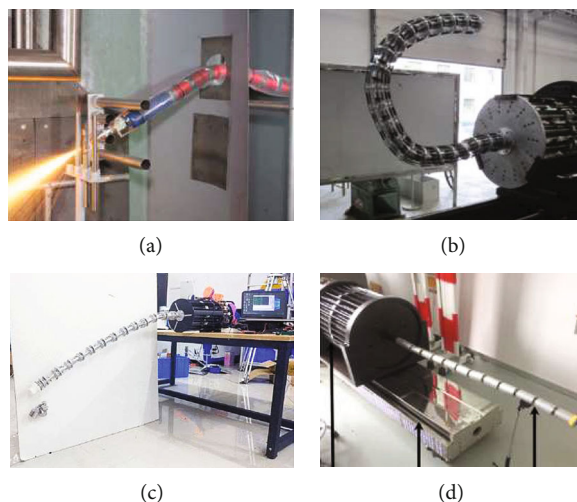
FIGURE 4: Typical snake-like robot. Picture (a) is a hyperredundant manipulator designed by OC-Robotics for welding [25], picture (b) is the hyperredundant manipulator developed by AVIC 625 for the needs of aviation assembly, referring to OC-Robotics [10], picture (c) is a hyperredundant manipulator composed of 10 joints developed by the Harbin Institute of Technology Shenzhen [26], and picture (d) is a rope-driven hyperredundant manipulator with 12 joints and 24 degrees of freedom developed by the Shanghai Jiaotong University [35].

motors [35, 36]. Figure 4 shows a physical image of some of the hyperredundant manipulators mentioned above.

In the above studies, in order to reduce the size of the manipulator and improve the deep cavity accessibility, steel wire is mostly used as the driving mode to meet the operation requirements of narrow space. For medical surgery, the robot has a small load capacity and limited operating range. It is often driven by an elastic skeleton and hollow threaded tube through a few steel wires, and the controlled freedom is far less than the inherent freedom of the mechanical arm. However, for industrial scenes such as cleaning and assembly of narrow space, the required arm span operation range is large, and the rigid requirements are high. Rigid joints are needed to meet the operation requirements. However, for industrial scenes such as cleaning and assembly in narrow space, the robot needs a large working range and high rigidity. Therefore, rigid joints are needed to meet the operating requirements. The high-redundancy manipulator composed of modular rigid joints or segmented joints with multijoint linkage needs to adjust the relative position of joints to adapt to the curvature changes of space. At the same time, the manipulator is required to have a long enough arm span to meet the spatial accessibility requirements. Therefore, the number of joints and the length of rigid joints directly affect the spatial obstacle avoidance capability of the manipulator. The number of independently controllable joints cannot be infinitely increased, so how to design a reasonable joint mechanism of the robot arm, so as to solve the contradiction between spatial obstacle avoidance ability and reachabilities through the limited number of controllable joints, is an important problem in the design of robot motion mechanism.

We summarized the characteristics of some typical hyperredundant manipulator and put the comparison results in Table 1. As shown in Table 1, we list some points such as the amount of DOF, the structural type of manipulators and in which field the manipulator is applied. Consid-

ering some manipulator is combined with other mechanical devices together to form a robotic system, we also give the total amount of DOF of the robotic system in the form of "$A + B$," which A represent the total DOF of HRM, and B is the total DOF of other mechanical devices.

2.2. Robotic Operating System. Although the robot arm with high redundancy can achieve strong obstacle avoidance ability by changing its configuration and posture, it must be pushed to the narrow working space by the corresponding propulsion mechanism to work in the narrow working space. Therefore, the manipulator and the propulsion mechanism together constitute a robot operating system that works in a narrow space. The mechanical arm with high redundancy is generally driven by steel wire, and the motor and other executive parts are installed on the base of the root, which makes the base have a large size and weight. A mobile platform is required to push the base and the mechanical arm outward to achieve corresponding movement. Common push platforms include linear guide rail, multidegree-of-freedom industrial robot, caterpillar robot, and so on. OC-Robotics adopts gantry structural beam as push mechanism, which forms a robot system with snake mechanical arm to carry out inspection and maintenance of nuclear facilities [24]. In the aviation manufacturing scene, industrial robots are used as the push platform of the manipulator [1]. The snake-like manipulator operating robot system developed by the Siasun And AVIC 625 Institute pushes the manipulator through the linear slide push mechanism. The whole machine size is larger than the manipulator itself, and it cannot adapt to the compact requirements of narrow space and peripheral sites [10]. The Hopkins University uses UR5 robot as the payload platform and carries wireline driven surgical robot to constitute the surgical robot system [37]. The Samsung Institute of Advanced Technology developed a surgical robot system composed of a 6-DOF serpentine guide arm and a 5-DOF

TABLE 1: Comparison between different HRMs.

Different HRMs	Amount of DOF	Structural type	Applying field
OC-Robotics [1]	20+7	Rigid joints connected by hook hinges	Aircraft assembly
Ringhals 1 [21]	20 are under control	Several discs connected by elastic objects	Nuclear
SAFIRE [25]	18	Rigid joints are connected by a rotation axis	Nuclear
CAUC [12]	6 are under control	Using discs as joints and the discs are connected by fiberglass rods	Aircraft fuel tank detection
CardioARM [20]	105 but only 2 are under control	50 rigid cylindrical links serially connected by three cables	Medical field
SAIT [23]	Guide tube with 6 DOF, two tools with 7 DOF, camera with 3DOF and slave arm with 5 DOF	Six equal-height saddle-shaped linkages (or rings) connected by wire ropes	Medical field
SJTU [36]	24	Rigid joints connected by hook hinges	Prototype for research

(a)

(b)

(c)
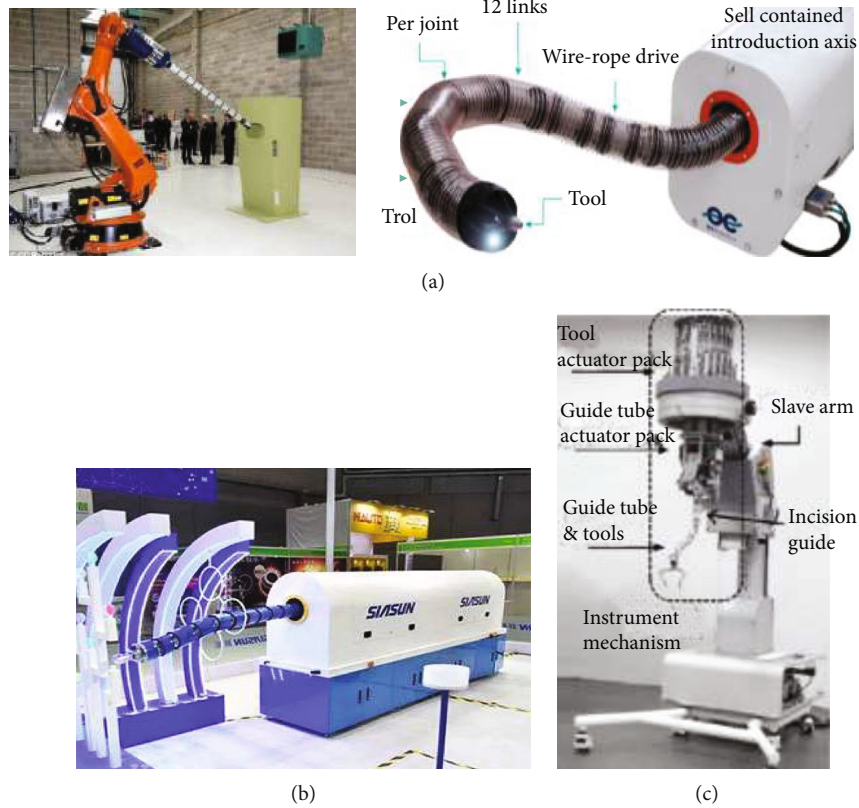
FIGURE 5: Robot operating system. Picture (a) is the hyperredundant manipulator designed by OC-Robotics [1], and picture (b) is the snake-shaped manipulator designed by SiaSum [10], a surgical robot system designed by the Samsung Institute of Advanced Technology [23].

auxiliary arm. The macroarm realized a wide range of propulsion motion, and the guide arm realized the attitude adjustment of the surgical arm [23]. Figure 5 shows a physical image of some of the hyperredundant manipulators mentioned above.

In the above studies, the robot system mainly uses a general or specially designed mobile platform to carry highly redundant robotic arms. Through the composite movement of the manipulator and the mobile platform to achieve movement and operation in the narrow space, this method is relatively easy to design and implement. The motion control of the push platform and the manipulator can be real-

ized through kinematic decomposition, so that the robot system can operate in a narrow space to a certain extent. However, because of the large movement range required by the push platform, a large installation site for the mobile platform is often required in actual use. For example, the size of the moving slide of the robot reaches 3.8 m × 0.8 m × 1.5 m, and its weight reaches 1.4 tons, which is difficult to be satisfied in many working environments (especially postdisaster search and rescue, nuclear power pipeline maintenance, etc.). As a result, although the ultraredundant manipulator itself has good flexibility and can realize the detection of narrow space, its application in practical scenes

is limited by the large size of the push platform and the weight of the whole machine. In addition, the push platform and the manipulator are designed separately, so the manipulator is usually in the extended state when it is not working, which not only occupies a large space but also is easy to be damaged. Therefore, the integration design of high-redundancy manipulator and push platform is an important issue to improve the practicability of robot operating system.

2.3. Planning and Control Methods.

Compared with conventional manipulators, high-redundancy manipulators have higher control requirements and greater difficulty because of the number of moving joints far more than the degree of freedom in the working space. Research in this area involves kinematics modeling, mechanical optimization, obstacle avoidance planning, positioning control, and other issues.

2.3.1. Kinematic Modeling and Inverse Kinematics Method.

In terms of kinematics modeling, for traditional manipulators, the DH [38] method or the POE [39] method can be used to establish the forward kinematics model. For a simple rigid multijoint hyperredundant manipulator, these two methods can also be used to establish a forward kinematics model. However, for hyperredundant manipulators with flexible or a large number of joints, other kinematic modeling methods need to be found. In 1994, Chirikjian and Burdick proposed an efficient hyperredundant manipulator kinematics modeling method that uses "backbone curves" to fit the macrogeometric features of the robot [40]. In 2012, Godage et al. of the Italian Institute of Technology established a kinematic model for a multijoint hyperredundant manipulator using the continuous modal function method [41]. Recently in 2022, Yang et al. established a kinematic model of a multisegment underwater manipulator based on the piecewise constant curvature (PCC) assumption [42]. The rope-driven hyperredundant manipulator has received extensive attention from researchers in recent years, and a lot of research results have been produced on the kinematic modeling of the rope-driven hyperredundant manipulator. Zhao and Gao of the Harbin Institute of Technology derived the relationship between the rope length and joint angle of the rope-pull redundant robot, established a kinematic model, and analyzed its motion space [43]. Zhang et al. analyzed the relationship between the length of the traction wire and the end pose in detail, studied the adjustment process of the PID parameters of the controller on the basis of the control model, and established a kinematic statics model to analyze the tension and stiffness [44]. In 2018, Xu et al. [45] analyzed the multilevel mapping relationship between motors, cables, joints, and end effectors. They established the corresponding rope-driven kinematics model using a combination of analytical and numerical methods and proposed a decoupling method to compensate for the coupled motion between the ropes.

Generally, the inverse kinematics methods of manipulators can be divided into the following categories: analytical methods, numerical methods, geometric methods, and intelligent algorithms. However, for the hyperredundant manipulator, the increase of degrees of freedom greatly increases the computational difficulty of the analytical method, so here we mainly introduce the last three methods: numerical method, geometric method, and intelligent algorithm. Numerical methods generally use the pseudoinverse of the Jacobian matrix to solve the differential kinematics equations [46]. However, for a hyperredundant manipulator, the result of the solution is likely to make the manipulator reach an odd isomerism, which makes the solution invalid. Using the damped least squares method [47] or the singular value decomposition method [48] can alleviate this problem, but it will lead to a decrease in the accuracy of the solution. For the geometric method, Chirikjian and Burdick [40] proposed the concept of "ridge line" function, through which the macroscopic structure of the hyperredundant manipulator is described. Based on this, they proposed the modulo function method [49], which divided the "ridge line" into segmented continuous curves and represented by a series of modal functions, and finally, used a fitting algorithm to obtain the joint angles. Mu et al. [50] used the piecewise geometry method to divide all the joint variables of the hyperredundant manipulator into three parts, shoulder, elbow, and wrist, and transformed the complex hyperredundancy problem into a low-redundancy problem. With the development of artificial intelligence algorithms, some new solutions are provided for the solution of inverse kinematics of hyperredundant manipulators. In 2014, Melingui et al. of Polytechnique Paris adopted qualitative modeling method based on RBF neural network to solve its linear and uncertain problems and selected specific inverse kinematics model from redundant manifold through remote supervised learning framework [51]. In 2021, Neng of Harbing University of Technology proposed an adaptive search space genetic algorithm [52], which can efficiently and accurately solve the inverse kinematics of a hyperredundant manipulator. In 2022, Yang et al. implemented the inverse kinematics solution of an underwater multijoint manipulator using a deep neural network (DNN) with six hidden layers [42].

2.3.2. Dynamic Modeling.

In terms of dynamic modeling, Chirikjian [49] proposed a continuum modeling method based on infinite degrees of freedom in an article published in 1993, and this method is called the continuous "Cosserat" method. In 2014, Renda et al. [11] established a dynamic model of a cable-driven continuous soft robotic arm based on a rigorous geometrically accurate method, which fully considered the dynamic interaction and tension coupling conditions of dense media. Later in 2018, Renda et al. [53] proposed a dynamic model of multisection soft manipulator based on discrete Cosserat method. Compared to the previous model, this model takes into account shear deformation and torsional deformation. Recently in 2021, Yang et al. propose a modular-based approach to modeling the dynamics of a cable-driven continuum robot that considers continuous deformations, including extension or contraction, bending, and torsion, and is validated by static and dynamic experiments [54]. Liu et al. proposed a real-time dynamic model of a cable-driven continuum robot, using the

covariant formula to describe the motion of the cable-driven continuum robot and using the virtual power principle to establish a dynamic model [55].

2.3.3. Positioning Control. In the aspect of positioning control, the wire traction mode has certain elastic deformation, and its control accuracy is lower than that of the rigid drive mode. Therefore, the deformation compensation of the wire should be considered to improve the control accuracy. Alambeigi et al. of Samsung Research Institute used model analysis and off-line measurement system to measure the clearance in order to reduce the error problem of the snake arm casing wire and realized the clearance compensation in the wire control process [37]. The backgap of wire traction mode is an important factor affecting the control accuracy of serpentine arm. Agrawal et al. of Purdue University specifically studied the system modeling of the actuator of wire traction for this problem and designed the backgap compensator of wire length control by using the smooth backgap inverse model as feedforward [56].

2.3.4. Obstacle Avoidance Planning. In the aspect of obstacle avoidance planning, it is generally divided into two steps, the first is to plan the obstacle avoidance path and then control the robot arm to move according to the planned path.

The first step in obstacle avoidance path planning is to find a collision-free path where the end of the manipulator moves from the starting point to the target operating point. In the field of robotics, a common approach is to rasterize the space and then use a suitable search algorithm such as the $A*$ algorithm and its improvements [57, 58] to find a suitable path. However, as far as the hyperredundant manipulator is concerned, some special path planning algorithms need to be designed for its high degree of freedom and continuum characteristics. In 2010, Marcos et al. [59] proposed a trajectory planning method that combined the closed-loop pseudoinverse method with a genetic algorithm and proposed an optimization criterion for repeatable control of a redundant manipulator, avoiding the problem of joint angle drift. Ananthanarayanan and Ordóñez [60] proposed a multipass sequential local search technique for hyperredundant manipulators in 2017. The method solves the dimensionality problem of the exhaustive search technique through multichannel sequential local search and solves the sensitivity problem of the greedy method to local minima through the backtracking technique. In 2021, Bulut and Conkur [61] proposed a simple, effective, and robust geometric method for real-time path planning of hyperredundant robots in a limited space full of obstacles.

The second step of obstacle avoidance path planning is to control the manipulator to move according to the planned path. The traditional method is to obtain the joint angles of a group of manipulators through some inverse kinematics methods according to the target path. The inverse kinematics solution method of the hyperredundant manipulator has been introduced in detail in the "Kinematic Modeling and Inverse Kinematics Method" section.

However, in practical applications, in most cases, the characteristics of the environment in a narrow space are unknown, so it is difficult to establish an accurate three-dimensional space model for robot motion planning. In most instances, the scene is gradually constructed in the process of robot moving. The follow-the-leader mode [62] is based on the head movement, and the subsequent joints follow the space running track of the head to move, which can ensure that the mechanical arm can avoid obstacles and reach the target point during the moving process, and there is no need to replan the posture of each joint during the movement. Conkur [63] proposed a hyperredundant manipulator path planning algorithm based on the follow-the-leader model in 2003. The algorithm decouples the coupling between the manipulator joints and uses numerical methods to establish the position of each joint relative to the curve. Finally, the motion of the highly redundant manipulator on the curve is realized.

However, in actual motion control, there is a big difference between the reachable space of other joints of the manipulator and the reachable space of the end joints, and there is a tension singularity problem of wire tension under different joint positions, which may lead to the situation that there is no solution for some joints, and thus, the obstacle avoidance function cannot be realized. At the same time, the task also has certain requirements on the stiffness and karma of the manipulator. Therefore, it is necessary to study reasonable obstacle avoidance planning and control strategy and solve the optimal pose suitable for the whole robot arm according to the obstacle model. At the same time, the stiffness of the manipulator is controlled according to the requirements of the task to achieve fixed-point operation tasks.

2.4. Environment Perception and Navigation Technology. Before robots operate in a narrow space, they often lack accurate prior models for the environment space. Therefore, it is necessary to use a variety of sensors to perceive the environment in a narrow space and to control the navigation process of the robot. The key of environment awareness technology is to extract effective feature information in the environment through algorithm and process and analyze it. Then, an environment reconstruction model that can be understood by the robot is formed to express the information of the robot's surrounding environment. The feature information in the environment is mainly spatial information, that is, the position and size of points, lines, and planes that constitute the environment space. In the unknown environment, the robot needs to know its precise position and then continuously correct its position by using the relative location of the environment features, so as to conduct localization and map construction (SLAM).

Different from the perception and navigation technology of mobile robots in conventional scenes, robots operating in narrow spaces are difficult to carry large size and multiple types of sensors to sense the environment due to the limitations of their own volume and load capacity. In the aspect of snake robot sensing technology, relevant research work has been carried out at home and abroad. Tanaka et al. of Tokyo University of electrical and communication realized the obstacle avoidance movement of the robot in limited space

through the small camera and laser ranging module installed on the head of the snake robot, combined with the infrared ranging sensor installed on each joint [64]. Tian et al. of Ritsumeikan University proposed a SLAM algorithm using single line lidar, which is fixed outside the robot head joint and can generate a two-dimensional environment map for navigation [65]. Chavan et al. used ultrasonic sensor and passive infrared sensor to create and navigate snake robot map and realized wireless control through ZigBee [66]. Morse and Choset of Carnegie Mellon University used rgb-d camera to build sparse attitude map and three-dimensional color point cloud map [67], but the quality of the map is closely related to the path quality, and the operator needs to reduce the robot speed in a specific gait to improve the image acquisition quality.

Sensors such as lidar and ultrasonic wave can measure environmental depth information, but they are not suitable for robot systems in narrow space because of their large volume and high energy consumption. Chinese and foreign scholars have carried out relevant research on compact sensor configuration and sensing technology. Ponte et al. of Carnegie Mellon University designed a triangulation sensor to adapt to the size and power constraints of snake robot using laser sensor and camera. When the robot raises its head, it scans the 3D point cloud of the environment in combination with the information of color camera [68]. Girerd of ubfc University in France and others carried out job navigation through a monocular camera fixed on the head of the tracheal surgery robot and proposed an automatic end guidance method based on dso-slam [69]. Sareh et al. of the University of London used optical fiber pressure elements to form tactile sensors to provide tactile feedback for flexible manipulators [70]. Figure 6 shows the block diagram of this tactile sensor. Beijing University of information technology uses cross laser combined with binocular stereo vision to form an environmental perception system for visual obstacle avoidance of snake manipulator in narrow space [71]. At present, the SLAM method of mobile robot is still used in the research of narrow space sensing technology. Some improvements have been made in sensor configuration and navigation methods. Therefore, it is necessary to carry out targeted research according to the characteristics of the scene. Table 2 summarizes and compares the performance of the environment perception and navigation methods in the above-mentioned papers.

The environment perception in narrow space scene has the following characteristics. First of all, light is often insufficient in narrow and closed scenes, so the contrast is low, and the target features are not obvious. Conventional visual processing methods are difficult to extract effective feature information from the collected images, which brings great difficulties to environment perception and target recognition. Secondly, due to the narrow cavity channel, conventional sensors are easy to enter their perceptual blind area and are blocked by obstacles, so the field of vision is severely limited, resulting in insufficient effective output information of sensors. Therefore, adaptive light filling and image enhancement are needed in narrow space. Then, the image data can be well recognized and resolved for the scene fea-

tures. In recent years, with the development of artificial intelligence and deep learning, many effective methods have been generated in image enhancement. In 2017, Ignatov et al. used the GAN model as the basic framework to propose a photoenhancement solution that can effectively convert ordinary smartphone cameras into high-quality DSLR cameras [72]. In 2018, Huang et al. proposed a scale-scaling global U-Net (Range Scaling Global U-Net, RSGU-Net) for image enhancement on mobile devices and won the ECCV-PIRM2018 (Perceptual Image Enhancement on Smartphones Challenge), the first place in the image enhancement task in the challenge [73]. Recently in 2020, Guo et al. proposed a Zero-Reference Deep Curve Estimation (Zero-DCE) method, using a lightweight deep network DCE-Net to estimate pixel-level and higher-order curves. This method achieves effect enhancement on low-brightness images [74]. At the same time, multisensor data with spatio-temporal continuity is used to deeply fuse the collected data in the scene and eliminate the wrong data caused by occlusion and other problems. Finally, the scene is constructed with offline map information to provide a basis for robot navigation control.

3. Key Technical Issues Analysis

Flexible manipulator with high redundancy is an effective technology to solve the problem of working in narrow space and has clear application requirements in many industries. It is of great practical significance to develop a highly redundant robot operating system adapted to the actual environment, to study the environment perception and navigation and positioning methods in complex scenes, and to propose a control method to improve the performance and efficiency of the robot operating in narrow space.

In the existing research work at home and abroad, the research focus is more on joint materials, mechanism design, environment perception, robot application system, and other aspects. Robot is mainly oriented to the detection task application, but the research on fine perception and precise positioning control oriented to the job task is less. In order to improve the kinematic flexibility and operational performance of robotic systems, the following key technical problems need to be solved:

3.1. Design of Mechanism with Both Smoothness Obstacle Avoidance and Operation Stiffness. The robot system based on highly redundant manipulator is most suitable for working in narrow space. Its outstanding feature lies in its good obstacle avoidance ability, because the number of independently controllable joints is a direct factor affecting the obstacle avoidance ability. In the design of wire driven manipulator, there is often a contradiction between the number of joints and the diameter of joints. Due to the limitation of the diameter of the manipulator, the number of joints can pass through the limited number of wires, and the number of joints directly affects the arm span and obstacle avoidance ability. In the existing studies, the basic design of each joint is 1-2 degrees of freedom of rotation. Each rotation angle range is limited due to the effect of wire traction
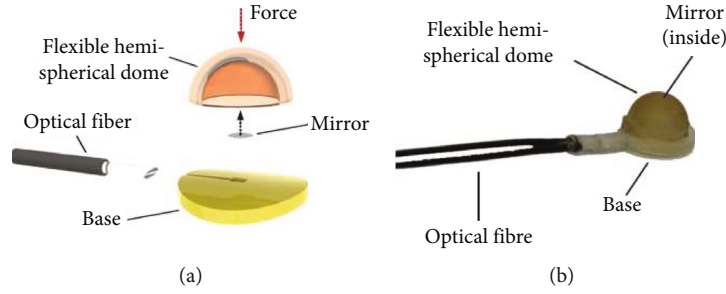
FIGURE 6: Tactile sensors developed by researchers at the University College London, (a) CAD drawing and (b) prototype of an assembled single tactile sensor [70].

TABLE 2: Comparison of different environment sensing and navigation techniques used by serpentine robots.

Reference	Sensors	Key technology	Performance
M. Tanaka [64]	Small camera, laser ranging sensor, infrared ranging sensor	Obstacle positions are estimated using the map data (obtained by Hector SLAM software) and the data from the range sensors in each link	Semiautonomous integral collision avoidance control system manually controlled by the operator
Morse [67]	RGB-D cameras	GraphSLAM, data filtering	Use filtered data to generate clearer and more accurate map images
Ponte [68]	Laser sensors and cameras	A structured light sensor composed of B/W teleoperated cameras, line laser sensors, etc. is designed to construct 3D environment maps	Adapt to snake robot size and power
S. Sareh [70]	Tactile sensor	Using digital optical fiber sensor as the main device, using ABS polymer as material, using the relationship between light reflection distance and intensity to make a tactile sensor	The developed sensor system can be loosely integrated on a soft arm, effectively works independently of the arm, and does not affect the movement of the arm when flexed or extended

efficiency. Therefore, there is a limit to the minimum bending radius of the manipulator, which makes it difficult to adapt to obstacles of different sizes. However, in nature, in addition to the serpentine movement of joint deflection, snakes also flexibly change the bending shape of their bodies through internode telescopic movement to better adapt to the characteristics of the environment.

Therefore, by referring to the movement characteristics of snakes and other animals in nature, it is a key problem to realize obstacle avoidance and operation of mechanical arm to design more flexible multidegree-of-freedom joints and robot mechanism under the condition of limited number of joints and traction wire through bionics principle.

3.2. Spatial Environment Perception Technology in Narrow and Closed Scenes. In the unstructured and unknown narrow application scenarios, the navigation control of the robot must be based on accurate environmental perception information. However, in the actual operation scenarios, not only the contrast is low, the target features are not obvious, but also there are problems such as insufficient lighting and reflection of the cavity wall, which bring great difficulties to the environmental perception. At the same time, because of the narrow cavity channel, the conventional sensor is easy to enter its perception blind area, the occlusion problem is serious, the field of vision is severely limited, resulting in the effective output information of the sensor is insufficient.

Therefore, in a narrow and closed unstructured environment, how to use a variety of measurement methods to build an environment perception system, integrate microsensors under the premise of limited space, and improve the accuracy of environment perception through the effective fusion of heterogeneous perception data are important prerequisites for robot operation. Figure 7 summarizes common approaches for environment perception and map building using multiple sensor data.

3.3. Obstacle Avoidance Planning of Drive Space under Multiple Constraints. The motion planning of the manipulator with high redundancy can adopt the ridge fitting method or the forward following method. The expected pose of each joint was planned from the perspective of kinematics, and then, the elongation of each wire was obtained by inverse kinematics analysis, to realize the motion control of the flexible arm. However, in the actual system, due to the effect of load and gravity of each joint, each wire not only needs to achieve the control of elongation but also needs to make the tension meet the safety threshold of the wire; only in this way can the desired operation accuracy be achieved.

Therefore, how to take wire tension limit as an important factor in the motion planning of high-redundancy manipulator, how to construct multiple constraints by combining three-dimensional space obstacles, operating target pose and interjoint pose relationship constraints, etc., and
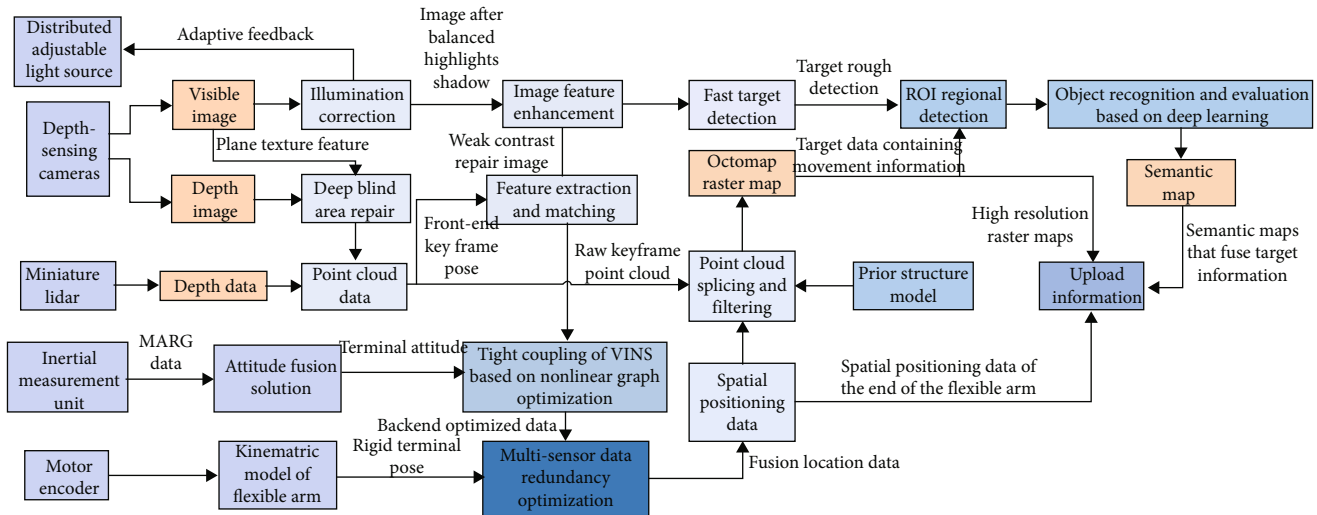
FIGURE 7: Environment perception and map construction in narrow space.

how to obtain joint space motion trajectory through trajectory interpolation and tension optimization are the problems that must be solved in the precise operation control of the manipulator. Figure 8 summarizes some key issues in obstacle avoidance planning for robotic arms, such as kinematic models, path planning methods, trajectory following methods, and some common constraints.

3.4. The End Precise Positioning Control Problem of Flexible Drive Mode. Wire traction is the main driving mode of high-redundancy manipulator. The attitude control of each joint can be realized by changing the length of each wire. But the tension state of the wire has a direct influence on the control accuracy, so the wire tension is usually maintained by connecting springs. However, the tension of steel wire varies greatly under different postures, and the elongation of spring also changes, which brings large control errors. At the same time, both the steel wire and the flexible arm have certain elastic deformation characteristics, which results in certain elastic shape variables in the whole system under different tension and different poses, affecting the control accuracy.

Therefore, we need to find out the factors affecting the tension and deformation errors of the mechanical arm movement, establish a dynamic deviation compensation model under different operating conditions, and eliminate or reduce the end positioning deviation through trajectory tracking compensation and synchronous control methods. These are important problems for precise operation control of highly redundant manipulators.

4. Prospect

In typical industrial application scenarios, all-round precision operation in complex and narrow space is the common feature. It is an inevitable trend for the development of robot technology to form a practical system to solve the problems of confined space operation through the integration of new materials, new configurations, new methods, and new technologies, closely combining with the requirements of practical application. The technological development of robots operating in narrow and confined space is mainly reflected in the following aspects.

4.1. Spatial Reachability. Working tasks in narrow space require the robot to be able to cross the narrow and long cavity channel, bypass the obstacles of different sizes in the cavity, and reach the operation point located in the deep space. However, many scenarios (such as GIS overhaul and inlet spraying) also require the robot to keep a certain safe distance between the whole body and the cavity wall and obstacles. Under these requirements, motion flexibility and high spatial accessibility are outstanding problems in practical applications. Therefore, hyperredundant robot based on new rigid-soft-soft coupling mechanism is an important development trend for solving complex tasks in confined space.

4.2. Structure Compactness. The overall size of the robot operating system is an important problem affecting its practicability, especially in postdisaster search and rescue, nuclear power pipeline maintenance, and other application scenarios. These scenarios are complex and space-constrained, requiring robotic systems to be able to push robotic arms into deep cavities in a compact structure. Therefore, the integrated systematic and comprehensive design of various parts such as mobile carrier platform, manipulator push platform, and high-redundancy manipulator is an important technical direction to meet the application requirements of confined space.

4.3. Operation Accuracy. At present, robots used in narrow space are mainly used for detection tasks, but few have operational capabilities. Compared with the detection task, the operation task has higher requirements for positioning accuracy, trajectory continuity, and real-time motion. Therefore, it is necessary to carry out research on terminal precise positioning control technology and job path tracking control technology of ultraredundant robots for specific application
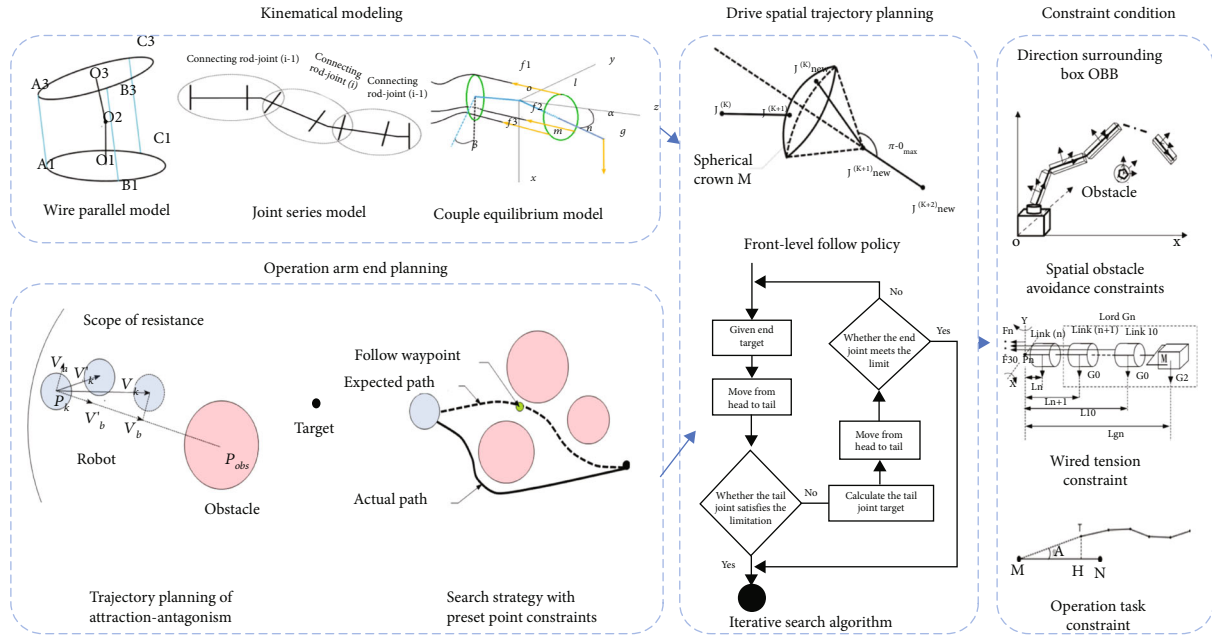
Figure 8: Obstacle avoidance path planning of drive space.

scenarios, to provide the precision of the operation process, which is the technical premise for the realization of confined space robot operation tasks.

4.4. Friendly Control. The operation process in complex scenes is difficult to rely on the robot system to complete fully autonomously and often requires the operator's tele-operation to help complete the operation. However, in some complex scenes, the light is often dim and there are many uncertain and peculiarly shaped obstacles. Content in visual images fed back by a single camera is generally difficult to identify and lack quantitative predictions. In this case, the control effect brought by the operator's remote control operation is difficult to meet the requirements. Therefore, it is necessary to enhance the presence of human-computer interaction process and improve the control efficiency of robot operation process. There are many technical problems in scene perception of closed and narrow space. Insufficient illumination, low contrast, and obscure features all bring great difficulties to detection and recognition. It is necessary to solve the problem of scene perception and reconstruction in a confined space by means of multisensor fusion and to build a human-computer interaction system with presence for narrow operation scenes. These are important technical approaches for solving the maneuverability of robots.

As a typical special operation robot, high-redundancy robot is an important technical approach to solve the requirements of confined space operation. In-depth study has a larger scope of operation, high control precision, strong flexibility, and high-redundancy and mechanical arm robot operating system and its key technologies, not only can solve the problem of the confined space of a specific homework but also can provide manufacturing tech-

nology and man-machine collaboration with a new solution, thus special task for many industries to provide important technical support.

Conflicts of Interest

No conflict of interest exists in the submission of this manuscript, and the manuscript is approved by all authors for publication.

Acknowledgments

References

[1] R. Buckingham, V. Chitrakaran, R. Conkie et al., *Snake-Arm Robots: A New Approach to Aircraft Assembly*, 2007, SAE Technical Paper.

[2] Y. A. Jinzhao, P. E. Haijun, J. Zhang, and W. U. Zhigang, "Dynamic modeling and beating phenomenon analysis of space robots with continuum manipulators," *Chinese Journal of Aeronautics*, vol. 35, no. 9, pp. 226–241, 2021.

[3] V. A. Sujan and S. Dubowsky, "Design of a lightweight hyper-redundant deployable binary manipulator," *Journal of Mechanical Design*, vol. 126, no. 1, pp. 29–39, 2004.

[4] J. Peng, W. Xu, T. Liu, H. Yuan, and B. Liang, "End-effector pose and arm-shape synchronous planning methods of a hyper-redundant manipulator for spacecraft repairing," *Mechanism and Machine Theory*, vol. 155, p. 104062, 2021.

[5] R. Buckingham and A. Graham, "Snaking around in a nuclear jungle," *Industrial Robot: An International Journal*, vol. 1, no. 6, pp. 254–259, 2005.

[6] R. Buckingham and A. Graham, "Nuclear snake-arm robots," *Industrial Robot: An International Journal*, vol. 39, no. 1, pp. 6–11, 2012.

[7] T. Yamamoto, M. Konyo, K. Tadakuma, and S. Tadokoroa, "A flexible in-pipe robot capable of moving in open spaces via a pneumatic rotary mechanism," *IFAC-Papers OnLine*, vol. 50, no. 1, pp. 1050–1055, 2017.

[8] M. Ikeuchi, T. Nakamura, and D. Matsubara, "Development of an in-pipe inspection robot for narrow pipes and elbows using pneumatic artificial muscles," in *2012 IEEE/RSJ International Conference on Intelligent Robots and Systems*, Vilamoura-Algarve, Portugal, 2012.

[9] D. Rollinson, Y. Bilgen, B. Brown, F. Enner, and S. Ford, "Design and architecture of a series elastic snake robot," in *2014 IEEE/RSJ International Conference on Intelligent Robots and Systems*, Chicago, IL, USA, 2014.

[10] Y. Yanbin, D. Zhaocai, and W. Zhiqiang, "Research on assembly system of serpentine arm robot," *Aeronautical Manufacturing Technology*, vol. 21, pp. 26–30, 2015, (In Chinese).

[11] F. Renda, M. Giorelli, M. Calisti, M. Cianchetti, and C. Laschi, "Dynamic model of a multibending soft robot arm driven by cables," *IEEE Transactions on Robotics*, vol. 30, no. 5, pp. 1109–1122, 2014.

[12] W. Wang, *Research on the Structure and Kinematics of the Aircraft Fuel Tank Inspection Robot*, Civil Aviation University of China, 2013, (In Chinese).

[13] Q. Gao, W. Wang, N. Guochen, L. Wang, and Z. Zheng, "Research on bionic structure and kinematics of aircraft fuel tank inspection robot," *Journal of Aeronautics and Astronautics*, vol. 34, no. 7, pp. 1748–1756, 2013, (In Chinese).

[14] S. Zhong, Z. Shuangbiao, and L. Xingcheng, "Review on research and development of snake-like robots," *China mechanical engineering*, vol. 26, no. 3, pp. 414–425, 2015, (In Chinese).

[15] C. Ye, S. Ma, B. Li, and Y. Wang, "Development of a three dimensional snake-like robot perambulator II," *Journal of Mechanical Engineering*, vol. 45, no. 5, pp. 128–133, 2009, (In Chinese).

[16] Y. Shumei, W. Minghui, M. Shugen, L. Bin, and W. Yuechao, "Development of an amphibious snake-like robot and its gaits on ground and in water," *Journal of Mechanical Engineering*, vol. 48, no. 9, pp. 18–25, 2012, (In Chinese).

[17] S. Hong, L. Lixiang, and P. Ma, "A new type climbing snake robot," *Drive system Technique*, vol. 22, no. 3, pp. 34–48, 2008.

[18] J. Aihong, D. Zhendong, and Z. Laishui, "Research development of bio-inspired robotics," *Robot*, vol. 27, no. 3, pp. 284–288, 2005.

[19] T. L. Liu, *Research on Super Redundant Manipulator Driven by Rope in Narrow Space [D]*, Harbin: Harbin University of technology, 2016, in Chinese.

[20] T. Ota, A. Degani, D. Schwartzman et al., "A highly articulated robotic surgical system for minimally invasive surgery," *Annals of Thoracic Surgery*, vol. 87, no. 4, pp. 1253–1256, 2009.

[21] K. Leibrandt, P. Wisanuvej, G. Gras et al., "Effective manipulation in confined spaces of highly articulated robotic instruments for single access surgery," *IEEE Robotics and Automation Letters*, vol. 2, no. 3, pp. 1704–1711, 2017.

[22] J. Ding, R. Goldman, K. Xu, P. Allen, D. L. Fowler, and N. Simaan, "Design and coordination kinematics of an insertable robotic effectors platform for single-port access surgery,"

[23] J. Lee, J. Kim, K. K. Lee et al., "Modeling and control of robotic surgical platform for single-port access surgery," in *2014 IEEE/RSJ International Conference on Intelligent Robots and Systems*, pp. 3489–3495, Chicago, IL, USA, 2014.

[24] H. Hu, P. Wang, B. Zhao, M. Li, and L. Sun, "Design of a novel snake-like robotic colonoscope," in *2009 IEEE International Conference on Robotics and Biomimetics (ROBIO)*, pp. 1957–1961, Guilin, China, 2009.

[25] R. Buckingham and A. Graham, "Dexterous manipulators for nuclear inspection and maintenance-case study," in *International Conference on Applied Robotics for the Power Industry*, Montreal, QC, Canada, 2010.

[26] T. Liu, W. Xu, T. Yang, and Y. Li, "A hybrid active and passive cable-driven segmented redundant manipulator: design, kinematics, and planning," *IEEE/ASME Transactions on Mechatronics*, vol. 26, no. 2, pp. 930–942, 2021.

[27] S. Ma, B. Liang, and T. Wang, "Dynamic analysis of a hyper-redundant space manipulator with a complex rope network," *Aerospace Science and Technology*, vol. 100, p. 105768, 2020.

[28] J. He, R. Liu, K. Wang, and H. Shen, "The mechanical design of snake-arm robot," in *IEEE International Conference on Industrial Informatics*, pp. 758–761, Beijing, China, 2012.

[29] L. H. Qian, *Kinematics and Dynamics Control of Variable Geometry Truss Manipulator*, Shanghai Jiao Tong University, Shanghai, 2016, in Chinese.

[30] X. Z. Wang, *Research on Camera Calibration and Super-Resolution Restoration of Vision System Based on spatial Flexible Robot*, Shanghai Jiao Tong University, Shanghai, 2018, in Chinese.

[31] D. D. Shen, *Fault Tolerance Planning and Experimental Research of Variable Geometry Truss Arm*, Shanghai Jiao Tong University, Shanghai, 2018, in Chinese.

[32] L. R. Jia, Y. B. Zhang, W. J. Chen, and B. Zhao, "Octahedral element variable geometry truss design and analysis," in *The 17th National Symposium on Modern Structural Engineering*, pp. 483–490, Industrial Architecture, Tianjin, 2017, in Chinese.

[33] Y. C. Zhao, S. Q. Hu, and Q. M. Xu, "Feedback passivity-based control of discrete nonlinear systems with time-delay for variable geometry truss manipulator," *Asian Journal of Control*, vol. 21, no. 4, pp. 1756–1767, 2019.

[34] Z. L. Jing, Q. M. Xu, S. Q. Hu, and Y. S. Yang, *A Model Positioning Method of Variable Geometry Truss, Patent Authorization: ZL201610406881.6 [P]*, 2016, (In Chinese).

[35] J. Wang and X. Zhu, *On Design and Motion Planning of a Cable-Driven Hyper-Redundant Manipulator*, Shanghai Jiaotong University, 2017, (In Chinese).

[36] L. Tang, J. Wang, Y. Zheng, G. Gu, L. Zhu, and X. Zhu, "Design of a cable-driven hyper-redundant robot with experimental validation," *International Journal of Advanced Robotic Systems*, vol. 14, no. 5, p. 172988141773445, 2017.

[37] F. Alambeigi, R. Murphy, E. Basafa, and R. Taylor, "Control of the coupled motion of a 6 DoF robotic arm and a continuum manipulator for the treatment of pelvis osteolysis," in *International Conference of the IEEE Engineering in Medicine and Biology Society*, pp. 6521–6525, Chicago, IL, USA, 2014.

[38] J. Denavit and R. S. Hartenberg, "A kinematic notation for lower-pair mechanisms based on matrices," *Journal of Applied Mechanics*, vol. 22, no. 2, pp. 215–221, 1955.

[39] R. W. Brockett, *Robotic Manipulators and the Product of Exponentials Formula [C]//Mathematical Theory of Networks and Systems*, Springer, Berlin, Heidelberg, 1984.

[40] G. S. Chirikjian and J. W. Burdick, "A modal approach to hyper-redundant manipulator kinematics," *IEEE Transactions on Robotics and Automation*, vol. 10, no. 3, pp. 343–354, 1994.

[41] I. S. Godage, D. T. Branson, E. Guglielmino, and D. G. Caldwell, "Path planning for multi-section continuum arms," in *IEEE International Conference on Mechatronics and Automation*, pp. 1208–1213, Chengdu, China, 2012.

[42] C. Yang, H. Xu, X. Li, and F. Yu, "Kinematic modeling and solution of rigid-flexible and variable-diameter underwater continuous manipulator with load," *Robotica*, vol. 40, no. 4, pp. 1020–1035, 2022.

[43] Q. Zhao and F. Gao, "Design and analysis of a new cable-driven hyper redundant manipulator," in *International Conference on Intelligent Computation and Automation*, Changsha, China, 2010.

[44] Z. Zhang, G. Yang, S. H. Yeo, W. B. Lim, and S. K. Mustafa, "Design optimization of a cable-driven two-DOF joint module with a flexible backbone," in *IEEE/ASME International Conference on Advanced Intelligent Mechatronics*, pp. 385–390, Montreal, QC, Canada, 2010.

[45] W. Xu, T. Liu, and Y. Li, "Kinematics, dynamics, and control of a cable-driven hyper-redundant manipulator," *IEEE/ASME Transactions on Mechatronics*, vol. 23, no. 4, pp. 1693–1704, 2018.

[46] S. R. Buss, "Introduction to inverse kinematics with Jacobian transpose, pseudoinverse and damped least squares methods," *IEEE Journal of Robotics and Automation*, vol. 17, no. 1-19, p. 16, 2004.

[47] Y. Nakamura and H. Hanafusa, "Inverse kinematic solutions with singularity robustness for robot manipulator control," *Journal of Dynamic Systems, Measurement, and Control*, vol. 108, no. 3, pp. 163–171, 1986.

[48] A. A. Maciejewski, "Dealing with the ill-conditioned equations of motion for articulated figures," *IEEE Computer Graphics and Applications*, vol. 10, no. 3, pp. 63–71, 1990.

[49] G. S. Chirikjian, "A continuum approach to hyper-redundant manipulator dynamics," in *Proceedings of 1993 IEEE/RSJ International Conference on Intelligent Robots and Systems (IROS '93)*, pp. 1059–1066, Yokohama, Japan, 1993.

[50] Z. Mu, H. Yuan, W. Xu, T. Liu, and B. Liang, "A segmented geometry method for kinematics and configuration planning of spatial hyper-redundant manipulators," *IEEE Transactions on Systems, Man, and Cybernetics: Systems*, vol. 50, no. 5, pp. 1746–1756, 2020.

[51] A. Melingui, R. Merzouki, J. B. Mbede, C. Escande, B. Daachi, and N. Benoudjit, "Qualitative approach for inverse kinematic modeling of a compact bionic handling assistant trunk," in *2014 International Joint Conference on Neural Networks (IJCNN)*, pp. 754–761, Beijing, China, 2014.

[52] L. Neng, *Research on Inverse Kinematics of Hyper-Redundant Manipulator Based on Adaptive Genetic Algorithm*, Harbin Institute of Technology, 2021, Chinese.

[53] F. Renda, F. Boyer, J. Dias, and L. Seneviratne, "Discrete cosserat approach for multisection soft manipulator dynamics," *IEEE Transactions on Robotics*, vol. 34, no. 6, pp. 1518–1533, 2018.

[54] J. Yang, H. Peng, W. Zhou, J. Zhang, and Z. Wu, "A modular approach for dynamic modeling of multisegment continuum robots," *Mechanism and Machine Theory*, vol. 165, p. 104429, 2021.

[55] Z. Liu, X. Zhang, Z. Cai, H. Peng, and Z. Wu, "Real-time dynamics of cable-driven continuum robots considering the cable constraint and friction effect," *IEEE Robotics and Automation Letters*, vol. 6, no. 4, pp. 6235–6242, 2021.

[56] V. Agrawal, W. Peine, and B. Yao, "Control of cable actuated devices using smooth backlash inverse," in *IEEE International Conference on Robotics and Automation*, pp. 1074–1079, Anchorage, AK, USA, 2010.

[57] P. E. Hart, N. J. Nilsson, and B. Raphael, "A formal basis for the heuristic determination of minimum cost paths," *IEEE transactions on Systems Science and Cybernetics*, vol. 4, no. 2, pp. 100–107, 1968.

[58] J. Yao, C. Lin, X. Xie, A. J. Wang, and C. C. Hung, "Path planning for virtual human motion using improved A∗ star algorithm," in *2010 seventh international conference on information technology: new generations*, pp. 1154–1158, Las Vegas, NV, USA, 2010.

[59] M. G. Marcos, J. A. Machado, and T. P. Azevedo-Perdicoúlis, "An evolutionary approach for the motion planning of redundant and hyper-redundant manipulators," *Nonlinear Dynamics*, vol. 60, no. 1-2, pp. 115–129, 2010.

[60] H. Ananthanarayanan and R. Ordóñez, "A fast converging optimal technique applied to path planning of hyper-redundant manipulators," *Mechanism and Machine Theory*, vol. 118, pp. 231–246, 2017.

[61] Y. Bulut and E. S. Conkur, "A real-time path-planning algorithm with extremely tight maneuvering capabilities for hyper-redundant manipulators," *Engineering Science and Technology, an International Journal*, vol. 24, no. 1, pp. 247–258, 2021.

[62] H. Choset and W. Henning, "A follow-the-leader approach to serpentine robot motion planning," *Journal of Aerospace Engineering*, vol. 12, no. 2, pp. 65–73, 1999.

[63] E. S. Conkur, "Path following algorithm for highly redundant manipulators," *Robotics and Autonomous Systems*, vol. 45, no. 1, pp. 1–22, 2003.

[64] M. Tanaka, K. Kon, and K. Tanaka, "Range-sensor-based semiautonomous whole-body collision avoidance of a snake robot," *IEEE Transactions on Control Systems Technology*, vol. 23, no. 5, pp. 1927–1934, 2015.

[65] Y. Tian, V. Gomez, and S. Ma, "Influence of two SLAM algorithms using serpentine locomotion in a featureless environment," in *IEEE International Conference on Robotics and Biomimetics (ROBIO)*, pp. 182–187, Zhuhai, China, 2016.

[66] P. Chavan, M. Murugan, E. V. Unnikkannan, A. Singh, and P. Phadatare, "Modular snake robot with mapping and navigation: urban search and rescue robot," in *2015 International Conference on Computing Communication Control and Automation*, Pune, India, 2015.

[67] B. H. Morse and H. Choset, "Adaptive data confidence using cyclical gaits on a modular snake robot," in *IEEE/RSJ International Conference on Intelligent Robots and Systems (IROS)*, pp. 4630–4636, 2014.

[68] H. Ponte, M. Queenan, C. Gong et al., "Visual sensing for developing autonomous behavior in snake robots," in *IEEE International Conference on Robotics and Automation (ICRA)*, pp. 2779–2784, Hong Kong, China, 2014.

[69] C. Girerd, A. V. Kudryavtsev, P. Rougeot, P. Renaud, K. Rabenorosoa, and B. Tamadazte, "Automatic tip-steering

of concentric tube robots in the trachea based on visual SLAM," *IEEE Transactions on Medical Robotics and Bionics*, vol. 2, no. 4, pp. 582–585, 2020.

[70] S. Sareh, A. Jiang, A. Faragasso et al., "Bio-inspired tactile sensor sleeve for surgical soft manipulators," in *IEEE International Conference on Robotics and Automation*, pp. 1454–1459, Hong Kong, China, 2014.

[71] C. De and L. Xiaoping, *Research on Visual Positioning and Navigation Technology of Serpentine Arm Robot*, Beijing Information Science and Technology University, 2013.

[72] A. Ignatov, N. Kobyshev, R. Timofte, K. Vanhoey, and L. Van Gool, "Dslr-quality photos on mobile devices with deep convolutional networks," in *Proceedings of the IEEE International Conference on Computer Vision*, pp. 3277–3285, 2017.

[73] J. Huang, P. Zhu, M. Geng et al., "Range scaling global u-net for perceptual image enhancement on mobile devices," in *Proceedings of the European conference on computer vision (ECCV) workshops*, 2018.

[74] C. Guo, C. Li, J. Guo et al., "Zero-reference deep curve estimation for low-light image enhancement," in *Proceedings of the IEEE/CVF Conference on Computer Vision and Pattern Recognition*, pp. 1780–1789, 2020.

Review Article

Digital Twin-Driven Machine Condition Monitoring: A Literature Review

He Liu [ID],[1] **Min Xia** [ID],[2] **Darren Williams,**[3] **Jianzhong Sun,**[1] **and Hongsheng Yan** [ID][1]

[1]*College of Civil Aviation, Nanjing University of Aeronautics and Astronautics, Nanjing 210016, China*
[2]*Department of Engineering, Lancaster University, Lancaster LA1 4YW, UK*
[3]*The Welding Institute, UK*

Correspondence should be addressed to Min Xia; m.xia3@lancaster.ac.uk

Digital twin (DT), aiming to characterise behaviors of physical entities by leveraging the virtual replica in real time, is an emerging technology and paradigm at the forefront of the Industry 4.0 revolution. The implementation of DT in predictive maintenance has facilitated its growth. As a major component of predictive maintenance, condition monitoring (CM) has great potential to combine with DT. To describe the state-of-the-art of DT-driven CM, this paper delivers a systematic review on the theoretical and practical development of DT in advancing CM. The evolution of concepts, main research areas, applied domains, and related key technologies are summarised. The driver of DT for CM is detailed in three aspects: data support, capability enhancement, and maintenance mode shift. The implementation process of DT-driven CM is introduced from the classification of DT modelling and the extension of monitoring algorithms. Finally, current challenges and opportunities for future research are discussed especially concerning the barriers and gaps in data management, high-fidelity modelling, behavior characterisation, framework standardisation, and uncertainty quantification.

1. Introduction

The fourth industrial revolution "Industry 4.0"demonstrates a new modernisation and digitisation trend of industrial machines driven by the advances of Internet of things (IoT), advanced computing, and artificial intelligence (AI) [1]. The industrial machines in this new trend are expected to be with higher efficiency, longer lifetime, and lower operating costs. Maintenance is crucial in achieving the requirements above. Therefore, a transformation from preventive maintenance to predictive maintenance is demanding in the era of Industry 4.0. Predictive maintenance can maximise machine in-service time by monitoring the condition and predicting the optimal schedule. Condition monitoring (CM) has played an increasingly significant role in supporting predictive maintenance by estimating the current and future condition of the monitored machine. Data-driven CM has achieved remarkable progress in the past decade with advances in sensors, information and communication technologies, and data mining. However, the pure data-driven approaches have faced fundamental chal-

lenges in providing interpretable, reliable, and practical solutions due to the limitation of data availability, black-box nature of machine learning, and diverse operational conditions.

With the development of smart sensors, digital modelling technology, and data science, a new concept and paradigm digital twin (DT) is developed, which mainly consists of physical space, virtual space, and the bidirectional connection. It corresponds one-to-one with a potential observation of a particular physical entity. The virtual mirror is the representation that implies capturing the real asset's essential physical manifestation in a digital format, such as CAD or engineering models with the associated metadata. DT can respond rapidly to stimuli (forces, temperatures, etc.) and describe the operating context, such as wind or waves, in which the assets exist or operate within. There has been continuous research towards building digital twins. DT was originally developed for air force vehicles by NASA and the US air force to enable the safety and reliability of equipment [2]. Since then, DT has gotten much interest from academics and industry, and many efforts have been made. Though the DT-related research is still

in the infant stage, a lot of definitions of DT have been proposed [3]. Current DT research mostly focuses on modelling methods and prototype frameworks depending on the usage scenario [1].

Due to the promising capabilities of DT, scientific research and practical applications of DT in CM have emerged in recent years. DT brings new solutions for CM in predictive maintenance, while the architecture, workflow, and related methods of DT-driven CM are not yet well defined and established. Besides, to the best of our knowledge, there are several papers [4–7] that reviewed the development of DT or predictive maintenance, but the advances of DT-driven CM have not been reported. A summary of the recent advances in CM facilitated by DT is needed. Therefore, this paper conducts a systematic review of the development on DT-driven CM.

This paper is organised as follows: Section 2 illustrates the background of CM and DT, providing the definitions, applications, and limitations; Section 3 describes the adopted methodology and materials for the literature review. Section 4 contains a descriptive and detailed analysis of the research results and a discussion of the faced challenges and opportunities. Finally, the conclusions of this study are provided in Section 5.

2. Background

This section aims to provide a brief overview of the principal concepts and applications of CM and DT.

2.1. Condition Monitoring. With the evolution from preventive maintenance to condition-based maintenance for machinery, the origins and concepts of condition monitoring have been defined as Table 1 shows. Conservatively, condition monitoring is a process of observing parameters that indicate the current status of the system [4]. It plays a significant role in the maintenance, management, and sustainable operations of various sectors, such as manufacturing industries [8], electronics [9], and transportation [10]. The execution of condition monitoring in these industries enables maintenance to be scheduled and actions to be taken to prevent consequential damages. It would bring many benefits, such as reducing machine downtime and costs and prolonging the machine's life.

The implementation of condition monitoring is spread in various applications, such as performance assessment [14], vibration modelling [15], thermal monitoring [16], and oil analysis [17]. Each implementation would include three basic steps: data acquisition, data processing, and decision-making process. Various sensors (e.g., electrical, electronic, and mechanical) have been installed in machinery to acquire kinds of data. These data then are processed to estimate the operating state of a machine by numerous techniques. Upon processing the data, the status information would be helpful for decision-making, such as in determining/predicting (i) health condition, (ii) remaining useful life, (iii) failure analysis, (iv) downtime reduction, and (v) performance improvement strategy.

The application of condition monitoring has increased the reliability of machinery, while there are still some limitations. Data unavailability or qualitative data makes it difficult to assess the equipment status. Failures and performance deterioration are not easy to trace and characterise without expertise and numerous samples.

2.2. Digital Twin. To have an overview of the digital twin concept, Table 2 provides some definitions in academic publications. The concepts are constantly being redefined, while most of them include three main elements: physical space, virtual space, and their connections of data and models. The features of DT can be drawn from these concepts as individualised, high-fidelity, real-time, and controllable [18]. By building an accurate one-to-one mapping and feedback link between real physical space and digital space, the digital twin can implement real-time data/information exchange, dynamic modelling, and update throughout its lifecycle.

The implementation of digital twins is based on several key technologies: (i) data management, (ii) high-fidelity modelling, and (iii) model-based simulation [18]. As the basis of a digital twin, data goes through the steps of collecting, processing, mapping, and calculating to drive DT. Both physical modelling and data-driven methods are used and integrated to characterise complex behavior of a physical object and make predictions/reactions rapidly in DT. Simulations enable a virtual model to predict the behaviors of physical entities in real-time, provide measures to locate failure parts, predict remaining life, and quantify uncertainties.

The research and practice of digital twin technology are inseparable from targeted systems and application scenarios. Numerous industries have been exploring its applicability, such as unmanned aerial vehicles [23], gas turbines [24], wind turbines [25], and manufacturing systems [26]. However, the connotation of the digital twin concept and technical framework has not yet formed a unified consensus in the operation and maintenance phase of these machines. Some bottleneck technologies, such as merging multidomain physical modelling and data-driven approaches, accurate mapping, and dynamic evolution of digital twins, are being investigated for breaking through.

3. Research Methodology

3.1. Research Objectives/Questions. Considering the faced challenges of CM and lots of opportunities arising from DT, this paper aims to analyse the combination ways between CM and DT, evaluating diverse views and benefits from the combination. In this review, we are attempting to answer the following research questions:

(i) Q1: why is digital twin technology suitable to facilitate machine condition monitoring?

(ii) Q2: how does digital twin technology drive machine condition monitoring?

Overall, the motivation of this paper is to research how condition monitoring is changing through digital twin technology, including reasons, measures, and gains. Meanwhile, critical challenges and future trends will be involved.

TABLE 1: Definitions of condition monitoring.

Author	Definitions of condition monitoring
Álvarez et al. (2013) [11]	"Assessing the current state and estimating the future state of a system by means of measurements and calculations."
Chaulya and Prasad (2016) [12]	A process of monitoring different parameters of condition in machinery in order to identify any significant change, which is indicative of a developing fault.
Correa and Guzman (2020) [13]	An evolution of predictive maintenance or proactive maintenance.
Ali and Abdelhadi (2022) [4]	A process of observing a set of parameters and/or variables that indicate the state of the system under investigation.

TABLE 2: Definitions of digital twin.

Author	Definition of digital twin
Glaessgen et al. (2012) [19]	An integrated multiphysics, multiscale, probabilistic simulation of a vehicle or system that uses the best available physical models, sensor updates, fleet history, etc., to mirror the life of its flying twin.
Chen (2017) [20]	A computerised model of a physical device or system that represents all functional features and links with the working elements.
Luo et al. (2019) [21]	A multidomain and ultrahigh fidelity digital model integrating different subjects such as mechanical, electrical, hydraulic, and control subjects.
Madni et al. (2019) [22]	A virtual instance of a physical system (twin) that is continually updated with the latter's performance, maintenance, and health status data throughout the physical system's life cycle.

3.2. Research Sources and Methods. A systematic literature review (SLR) is used to analyse and evaluate the existing status of research derived from the given questions. This method is different from the traditional review with advantages of avoiding biased introduction and lack of critical analyses. Referring to Zonta et al. [7] and Silvestri et al. [27], the implementation of this method includes five stages: (1) formulation of the research question, (2) collection of relevant literature in universal databases through specific keywords, (3) extraction of eligible papers which meet qualified criteria, (4) design of a database to assess and sort the extracted papers, and (5) description of the results and findings.

After determining the research questions, several common electronic databases are used to search related papers, including Google Scholar (http://scholar.google.com), IEEE (http://ieeexplore.ieee.org), Scopus (http://scopus.com), and Web of Science (http://webofscience.com). Considering that condition monitoring has multiple similar designations, search strings are derived from the research questions as follows:

(i) "Digital twin" AND ("real-time" OR "health" OR "condition") AND "monitoring"

(ii) "Digital twin" AND ("performance" OR "state") AND ("evaluation" OR "estimation")

A high volume of papers that match the scope of keywords were collected. Then, we selected the eligible papers by setting exclusion criteria listed in Table 3. 2017 was chosen as the start date of the search filter because DT in academia and industries was still in infancy before 2017. Digital twin technologies are applied across many areas, such as healthcare, smart cities, and machinery, where the meanings of condition monitoring

are different [3]. As shown in criteria 2, the implementation of both technologies in machines is the research object. Papers from professional conferences and journals are considered because of their concision and high quality.

We conducted a preliminary investigation on titles and abstracts to evaluate relevance. For better classification and analysis, the selected papers are categorised by article structure (concept, review, case study, etc.), research methods (data-driven, physical-based, hybrid, e.g.), research objects (gas turbines, wind turbines, manufacturing systems, etc.), and research purposes (health monitoring, structure damage assessment, performance evaluation, etc.). Meanwhile, the full text of selected articles was reviewed to extract features for research questions.

4. Results and Findings

Investigating results and findings based on research questions are presented in this section.

4.1. Descriptive Analysis of Research Results. We have collected 133 papers published from 2017 to 2022 in professional academic search databases. After removing duplicates, the final database contains 95 papers suitable for responding to the research objective. We chose one article to read the full text for papers that studied the same type of machines or used the same methods. Finally, 64 papers were explored fully, and others were read simply as shown in Table 4.

The article distribution by search databases and types is shown in Figure 1. Google Scholar and Web of Science are the main sources in this review. In the database, journal articles are obviously more than conference papers. According

TABLE 3: Quality evaluation criteria of papers.

Section	Description
Criteria 1	Set the published period from 2017 to now.
Criteria 2	Limit research object as machinery or equipment.
Criteria 3	Remove technical reports, dissertations, and theses.
Criteria 4	Remove documents less than 6 pages long.

TABLE 4: Summary of the systematic literature review search process.

	Identified articles	Articles post removing duplicates	Articles post abstract review	Articles post full text review
Total	133	38	31	64
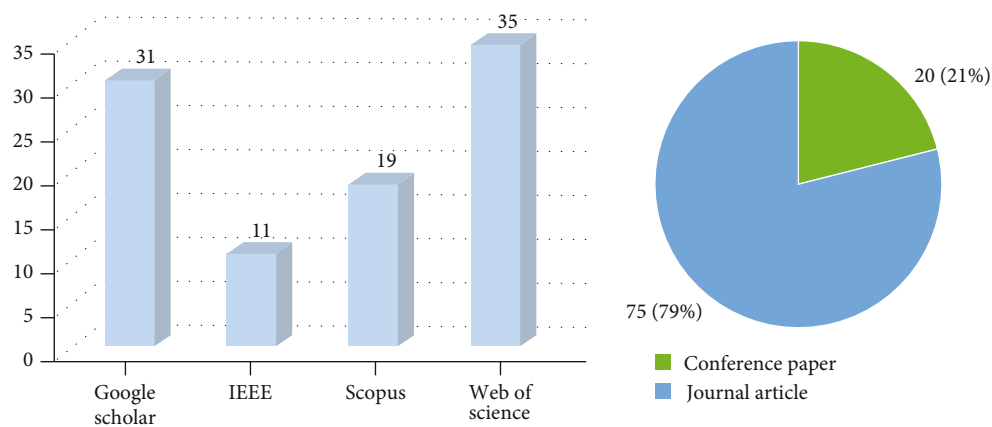
FIGURE 1: Distribution of publications by search engines and type.

to statistics, the main journals and conferences that presented more than one occurrence were IEEE Access, International Journal of Advanced Manufacturing Technology, Robotics and Computer-Integrated Manufacturing, Journal of Manufacturing Systems, ASME Turbo Expo, and IEEE international conference.

Since 2015, the number of publications has generally increased yearly, as shown in Figure 2. Most of the literature is dominated by case studies (74.7%), which were divided into three categories: (i) theoretical simulation (17.9%): theories were proposed and compared by simulation; (ii) experimentation (31.6%): methods and models were verified by virtual-real interaction under ideal experimental conditions; (iii) prototype (25.3%): methodology was proved with real monitoring data or applied in in-service machines. The rising trend of papers with experimentation and prototype means that the study of DT-driven CM is shifting from theories to implementation. Meanwhile, this shifting situation facilitated discussions about related technologies and challenges, which caused an increase in the review literature.

To demonstrate the applied area and cases of DT-driven CM, we present some representative papers listed by date in Table 5. Each paper's research area, objects, and related parameters were extracted for analysis. Digital twins bring more connotations and extensions to condition monitoring, as shown in the column of specific areas, such as structural load monitoring,

remote online cluster monitoring, and prediction of remaining useful life (RUL). The experiments and applications have been spread in numerous domains, including energy (steam turbines and wind turbines), transportation (vehicle braking systems and vessels), aeronautics (aircraft and aero-engines), astronautics (satellites), manufacturing (lathes and 3D printers), and electronic (converters and batteries). In these scenes, most monitoring variables are inaccessible, unpredictable, or changing obviously with operating conditions, which are unable or difficult to monitor and estimate only by traditional sensors and data processing technologies.

To find all terms directly related to the combination between condition monitoring and digital twins, we generated a relation map of keywords, occurrences of which are more than twice, from the literature database and categorised them into four groups, as presented in Figure 3 and Table 6. "Digital twin" is the most frequently occurring word, which builds the links among developing backgrounds and subjects, emerging technologies and approaches, as well as innovations in implementations. Modern technologies (digital twin, cyber-physical systems, Internet of things, etc.) enable traditional condition monitoring to be incorporated with various novel methods, i.e., artificial intelligence, cloud computing, and virtual sensing.

According to keyword analysis, DT-driven CM is presently used mostly in two fields: manufacturing processes (represented by smart manufacturing [62]) and operation and

	2017	2018	2019	2020	2021	2022
Theoretical simulation	2	2	3	3	3	4
Experimentation	0	1	7	8	7	7
Prototype	1	1	4	4	6	8
Review	1	1	2	5	5	6
Concept	0	1	1	0	1	1
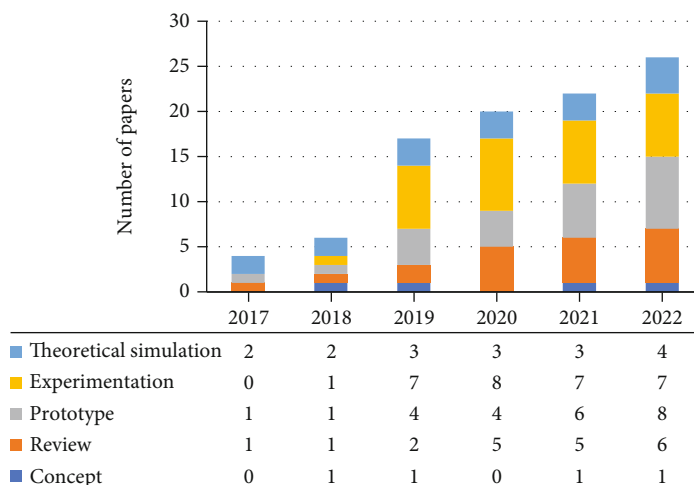
Figure 2: Content type of DT-driven CM literature.

maintenance processes (represented by predictive maintenance [63]). Some studies take a modelling-oriented approach, digital twin, based on technical engineering challenges, with the goal of characterising precise physical behaviors. Others take an information management-oriented approach, such as IoT, emphasising semantic relationships and seamless information flow. Both approaches are derived from artificial intelligence, cloud computing, and other methods, all of which are in the early stages of development. The above advances provide possibilities for the application of condition monitoring in multiple fields, such as RUL prediction components, rapid failure diagnosis of complex systems, and structural health monitoring.

4.2. Content Analysis of Digital Twin Driven Condition Monitoring. This section presented the results and discussions based on the previously elaborated questions.

4.2.1. Q1: Why Is DT Suitable to Facilitate Machine Condition Monitoring? Currently, there are still obstacles to traditional condition monitoring, including (i) data inaccessibility due to harsh environments or insufficient sensing, (ii) lack of interpretability and transparency due to the use of black-box models, and (iii) weak ability to support prediction and comprehensive decision-making. DT-driven CM is a customised, high-fidelity, real-time, controllable process to assess the current status and simulate predictable scenarios. DT provides a high-fidelity accurate model to characterise and predict the state of a physical entity in virtual space. The physical entity and virtual model links can provide real-time information on machine performance and operating feedback [3]. The real-time interaction lays the foundation for condition monitoring development. Therefore, DT-driven CM can overcome the limitations of existing approaches and provide additional benefits, such as the following:

(i) Availability of a multilevel, multidomain database

DT belongs to an integrated database, which stores holistic and hierarchical data covering the whole life cycle. This data-

base is built with design-manufacturing-operating-maintenance data and records from machine layer to part layer. The new monitorable variables (stress, strain, etc.) are available for condition monitoring and make it possible to assess RUL of new failure modes. Li et al. built a versatile probabilistic model to realise the digital twin vision and predict the aircraft wing fatigue crack growth [28]. Magargle et al. presented a digital twin-driven approach to support heat monitoring and accumulated wear prediction of an automotive braking system [30]. Xie et al. proposed an attitude monitoring method for hydraulic supports based on the digital twin theory [36].

Furthermore, a new concept, "virtual sensor," has been proposed by Nguyen et al. as a novel analytical solution for a process variable that can be used in place of a sensor [59]. They used virtual sensors based on DT to construct performance prediction models for a feedwater heater. Virtual sensors driven by digital twin have also been applied in vertical transportation systems [47] and dredgers [53] to monitor guide alignment and defined residual warning values.

Condition monitoring and diagnostics have become more practical as the type and volume of available data have grown. However, multilevel database-related literature was few proposed because the scale of digital twin research subjects mainly focuses on small structures. Meanwhile, the above-referred approaches for obtaining novel variables mostly rely on numerical simulations or equilibrium equations, which inevitably exist errors and nonconvergence conditions. The output of virtual sensors is affected by the physical entity, environments, and usage history, which are rarely considered in existing research.

(ii) Enhanced ability of fault tracing and degradation prediction:

Condition monitoring based on data-driven methods with monitoring data as input can trigger early warnings accurately while identifying the root cause of faults is a challenge for such approaches due to lacking connections with failure mechanism and physical structure. Conversely, the virtual mirror of DT is

Table 5: Types, areas, and objects presentation of case studies.

Authors	Specific area	Case	Variable
Li et al. (2017) [28]	Structural health monitoring	Steam turbine	Stress, strain, fatigue crack length
Zakrajsek and Mall (2017) [29]	Structural health monitoring	Aircraft tire	Sink rate, tire profile, wear state
Magargle et al. (2017) [30]	Predictive maintenance	Automotive braking system	Speed, force, accumulated wear
Tao et al. (2018) [31]	DT-driven PHM	Gearbox of wind turbines	Vibration, stress
Zaccaria et al. (2018) [32]	Fleet monitoring	Aircraft engine	Component performance parameters
Gholami Mayani et al. (2018) [33]	Operating condition monitoring	Drilling	Temperature, pressure, etc.
Tygesen et al. (2018) [34]	Structural health monitoring	Offshore platform	Stress, fatigue damage
Johansen and Nejad (2019) [35]	RUL prediction	Drivetrains in marine	Displacements
Xie et al. (2019) [36]	State monitoring	Hydraulic support	Tilt angles, hydraulic-support height
Venkatesan et al. (2019) [37]	ML-based condition monitoring	Permanent magnet synchronous motor	Distance, operating time, RUL
Qamsane et al. (2019) [38]	Machine failure prediction	Numerical control lathe	Spindle current
Revetria et al. (2019) [39]	Load real-time monitoring	Metal shelving	Strain, stress
Balta et al. (2019) [40]	Performance monitoring	Off-the-shelf 3D printer	Heater input and output signal
Zheng et al. (2019) [41]	Remote, real-time, visual monitoring	Welding production line	Geometric, physical parameters
Peng et al. (2019) [42]	Condition monitoring	Dc-dc converter	Inductor current, output voltage
Moi et al. (2020) [43]	Structural load monitoring	Knuckle boom crane	Strain, stress
Yu et al. (2020) [44]	Online performance monitoring	Steam turbine	Mass flow, pressure, temperature
Shangguan et al. (2020) [45]	Health monitoring	Satellite power system	Current, voltage, health index
Ye et al. (2020) [46]	Structure health monitoring	Spaceship's bearing beam	Vibration, stress, fatigue crack growth
Gonzalez et al. (2020) [47]	State/parameter estimation	Vertical transportation system	Speed, forces, guide alignment
Li et al. (2020) [48]	Health state estimation	Battery system	Current voltage, remaining capacity
Moutis and Alizadeh-Mousavi (2021) [49]	Real-time monitoring	Distribution power transformer	Voltage, current
Panov and Cruz-Manzo (2021) [50]	Performance evaluation	Industrial small gas turbine	Performance parameters
Wang et al. (2021) [51]	Real-time monitoring	Die-cutting machine	Speed, pressure, position of the cutting plate
Yu et al. (2021) [52]	Health monitoring	Electro-optical system	Transfer function of phase, modulation, optical
Zhuang et al. (2021) [53]	Tool Wear monitoring	Cutting tool	Temperature, vibration, lubricant
Wu and Li (2021) [54]	Health management	Aircraft engine	Performance parameters
Li et al. (2021) [55]	Pre-warning	Trailing suction hopper dredger	Torsional vibrations, residual warning value
Toothman et al. (2021) [56]	Health state estimation	Industrial pump system	Flow rate and pressure, health index
Moghadam and Nejad (2022) [57]	RUL prediction	Main shaft of wind turbines	Torque, stress, RUL
Abbate et al. (2022) [58]	Health monitoring	Electric motor	Signal and energy of vibration
Nguyen et al. (2022) [59]	Fault detection	Thermal–hydraulic system	Flowrate, temperature
VanDerHorn et al. (2022) [60]	Fatigue damage monitoring	Containership	Wave condition, fatigue damage
Bonilla et al. (2022) [61]	State estimation	Pump	Operating speed, pressure, flow rate
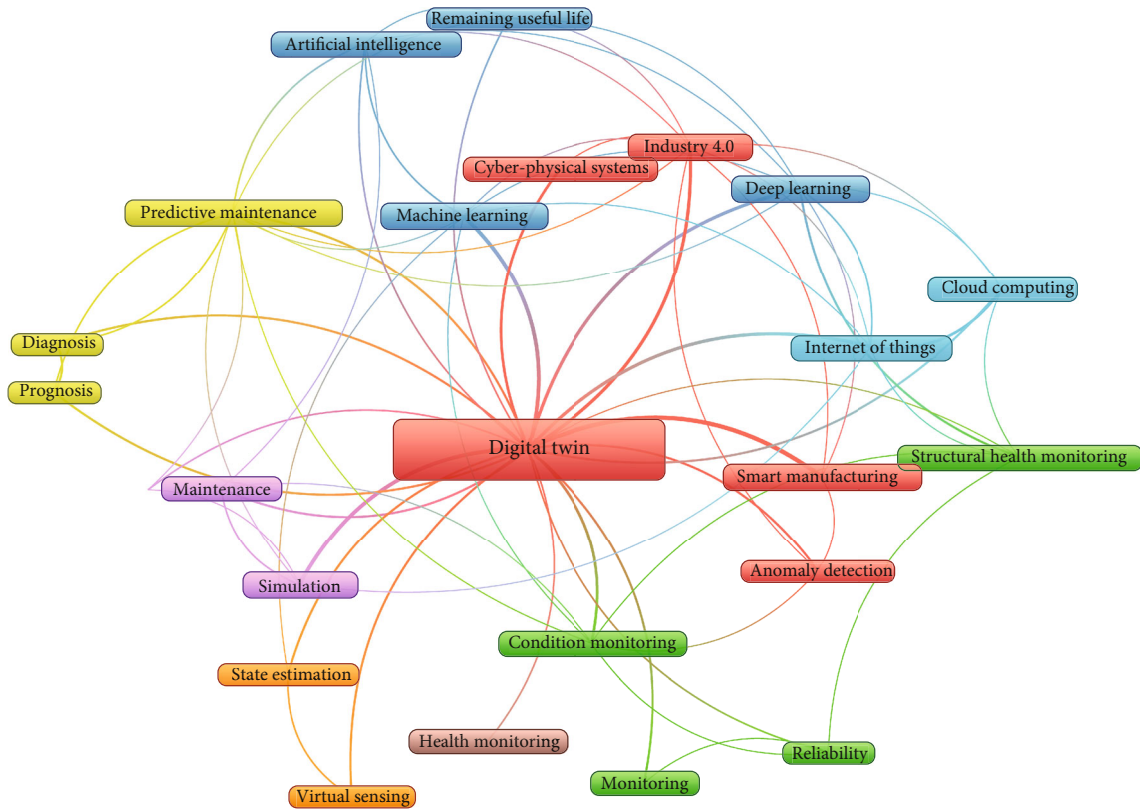
FIGURE 3: Mapping of keywords in related publications.

TABLE 6: Keyword classification.

	Key terms
Backgrounds	Industry 4.0, smart manufacturing, and predictive maintenance
Technologies	Digital twin, cyber-physical systems, and Internet of things
Methods	Artificial intelligence, machine/deep learning, cloud computing, virtual sensing, and simulation
Implementations	Condition monitoring, anomaly detection, structural health monitoring, state estimation, and RUL prediction

an intergradation of multiphysics, multiscale, and multidomain models, which can characterise the dynamic behavior of the physical entity. Therefore, components or systems that cause failures are located directly by the output and inner interactions of the virtual mirror. Tao et al. proposed a DT-driven PHM method to identify and estimate gearbox failure, and the DT model had much better performance in detecting the fault cause (e.g., tooth wear, fatigue, and breakage) than the signal diagnostic method [31]. The DT-based method proposed in this paper covers physical entity, virtual equipment, service, data, and connection, which is suitable for improving the accuracy of prognosis. However, balancing the costs and benefits of the DT and processing a large amount of DT data would impact the application. Zaccaria et al. built a framework for monitoring, diagnostics, and health management of an aircraft engine fleet based on a digital twin [32]. By this framework, different degrees of coupling failures were identified and isolated accurately. However, this framework is far too simplistic to suit the needs of digital twins as it is based solely on an engine performance model and Monte Carlo simulations.

For machines with a long service lifetime, the impacts of performance degradation and structural deterioration must be considered when conducting condition monitoring. Digital twins can characterise these features not only from monitoring data analytics but also from the perspective of part deviations. Craft et al. built a multilevel digital twin of aero engines. They characterised the degradation of whole engine performance and key module characteristics with damaged images of components, e.g., the erosion of high-pressure compressor blades [64]. Dawes et al. proposed an automated morph-mesh-solve workflow to update the geometry model of high-pressure-turbine blades to predict the performance of a gas turbine digital twin with consideration of the blade corrosion [65]. Although these technologies have much practical value, relevant data and samples are difficult to obtain and gather for each DT physical entity.

TABLE 7: Classification of modelling methods.

Methods type	Methods
Physical-based	Principle-based modelling [59]; finite element analysis [60]; computational fluid dynamics [68]; equivalent modelling [48]
Data-driven	Machine learning [53]; neural network [61]; deep learning [69]
Hybrid	Reduced-order modelling [30]; surrogate modelling [23]

(iii) Requirements for maintenance mode revolution

Condition monitoring has already been applied in operation and maintenance of high-value assets. However, this measure driven by solely monitoring data can only provide reference information rather than final decisions for maintenance plans in most cases because the trained model is not reliable and interpretable enough to locate failure and predict serviceability. Thus, maintenance intervals are fixed for most machines, leading to high costs and low utilisation. Predictive maintenance is a method that produces updated information allowing the prediction of future behavior to maximise the part's service life [13]. It aims to minimise maintenance costs while ensuring the safety and reliability of machines. Currently, the application of DT in predictive maintenance is the most related topic both in academic research and industry practice [18].

It is necessary to promote the combination between DT and monitoring methods to achieve predictive maintenance. Ding et al. proposed a predictive maintenance method for shearer key parts to predive the RUL and support decision-making based on high-fidelity modelling and hyperrealistic behavior simulations, both of which are the key technologies of digital twin modelling [66]. Moghadam and Nejad proposed an innovative drivetrain RUL monitoring approach based on digital twin modelling to perform predictive maintenance of the turbine main shaft [57]. Both papers only explore predictive maintenance in a narrow sense, and future research should include more failure models and decision considerations. Mi et al. proposed a cooperative awareness and decision-making framework integrated with data, knowledge, and DT to support fault diagnosis and maintenance planning and an actual engineering case, prediction maintenance decision-making for bearings in grinding rolls of the large vertical mill, is analysed to illustrate the accuracy and applicability of this framework [67]. In general, the framework is broad and advanced, taking into account all critical elements such as multilevel data, self-adaptive models, uncertainties, and operating conditions.

4.3. Q2: How Does Digital Twin Drive Condition Monitoring? DT is a physical-digital replica with high-fidelity and individualised models, as well as a bidirectional and real-time data transmission process. The advanced modelling methods enable the digital model to characterise its entity's operating conditions and provide additional data on loads, damage, and faults. The physical-to-digital connection means that the conditional data of the physical entity is transmitted into the virtual environment in real-time. Then, the digital model updates itself to match its counterpart, and conditional data are utilised for fault diagnosis and prognosis. The foundation of DT-driven CM is advanced

modelling methods. Then, new condition monitoring and fault diagnosis algorithms have been developed based on DT's remarkable features. The progression of modelling and algorithm development is summarised as follows:

(i) DT modelling to characterise machine behaviors

Numerous modelling methods have been developed to make accurate and bidirectional mapping between the physical entity and the virtual model. They can be divided into physical-based, data-driven, and hybrid methods, as shown in Table 7. Physical-based methods are applied to keep virtual models with high fidelity, including principle-based modelling for mechanical systems, numerical simulation for structure, and equivalent modelling for electronic devices. Data-driven methods build the specific link between machine operating conditions and the variables of interest. Hybrid methods combined with physical-informed and data-driven methods are commonly employed to integrate physical or system principle knowledge. Rapid response scan be generated by reducing the model degree of freedom using hybrid methods. Models built by hybrid methods have required features for standard DT, such as high-fidelity, quick-update, and rapid-response abilities.

According to the literature investigation, most of the current prototype studies are aimed at simple systems or structures. The physical-based modelling is qualified to support digital twin modelling in this situation. Shangguan et al. presented a new physical-virtual convergence approach for a satellite system by Modelica-based modelling [45]. Moi et al. built a digital twin of a small-scale knuckle boom crane by finite element modelling and verified the results by strain gauges [43]. Some studies use data-driven approaches to build data links in digital twins. Li compared the accuracy of digital twin-driven virtual sensors built by different models, such as long-short term memory network, extreme gradient boosting, support vector regression, and deep belief network [55]. Stoumpos and Theotokatos employ a neural networks data-driven method into digital twin as virtual sensors of marine dual-fuel engines [70]. Booyse et al. proposed a new form of DT, deep digital twin [71]. It is constructed from deep generative models which learn the distribution of healthy data directly from operational data at the beginning of an asset's life-cycle [71]. However, the parameter mapping performed by the black box model has yet to meet the requirements of DT-driven CM, due to a lack of interpretability and physical knowledge.

Recently, hybrid approaches combining physical-based and data-driven models have been investigated in academics to reduce the computing and mapping time of a high-order virtual model. Bonilla et al. used graph convolutional neural network theory and a hydraulic modelling method to generate a digital twin of the water system [61]. Magargle et al. built a

multilevel model for an automotive braking system with 3-D finite element analysis, 0-D multidomain circuit simulation, and reduced-order modelling [30]. Vasilyev et al. propose a coupling modelling method that can be efficiently utilised to estimate gas-turbine-engine blades' residual life with thermal-solid integrated analysis and ensemble machine learning [72]. Hybrid-method-based DT can swiftly calculate and predict the outcomes of multilevel or complex machines. However, the calculating errors derived from quick mapping as well as the time and resource costs resulting from physical modelling must be optimised in the application of hybrid methods.

(ii) Development of model-based diagnosis and prediction

Sensors set in machines are commonly limited, and the available sensor data are often not rich to support the training of robust data-driven condition monitoring algorithms [52]. With the increase of monitorable variables in DT, many diagnosis and prediction methods have been proposed, and the area of monitoring has been broadened. In these methods, performance evaluation is mainly carried out in the whole machine layer; fault detection and health status assessment are often conducted in the system or subsystem layer; RUL prediction mainly focuses on the part and component layer. The details are as follows:

(a) Performance evaluation

The in-service performance of machines, which determines the profitability of operators, is a critical factor triggering repair in predictive maintenance, especially for rotating machinery. In previous studies, the performance degradation trend is usually evaluated with the historical data by statistic methods, which can only reflect the average level. As for now, the individual performance condition can be traced and assessed by digital twin, which considers the operating environments and load usages of the specific machine. Unlike the simple baseline fitting method, Panov and Cruz-Manzo built a performance digital twin platform of gas turbines to track performance degradation with the novel gas path component capacity index [50]. A distributed control system network was built in Panov's work, but each module of individual engines was based on a one-dimensional model, which is not conducive to obtaining high-precision prediction results. Johansen and Nejad proposed a fuel consumption evaluation method in vessels through motion data generated by the DT [35]. The results show that the lower fidelity model was more accurate than the higher fidelity model. The higher dimensionality and fidelity of virtual models indicate that more data is needed as input and optimisation.

(b) Anomaly detection

The related variables of inaccessible locations and harsh environments can be monitored based on the digital twin modelling. Thus, the anomaly can be directly identified and detected with these parameters. Balta et al. built a DT architecture with appropriate mathematical modelling formalisms and the deviation of defined variables shows the anomaly of the 3D printer occurring in additive manufacturing processes [40]. Zaccaria et al. proposed an automated signature-based algorithm for anomaly detection and fault isolation of aero-engine components based on the gas flow parameters generated by a digital twin platform [32]. High-value assets with complex structures would benefit from the anomaly detection supported by DT, which could monitor related parameters from hard-to-assess locations.

(c) Health monitoring

Health monitoring is a critical part of predictive maintenance in complex systems. The health status indicates whether the equipment meets the operating conditions. The real-time monitoring parameters of a digital twin can be used to be a health indicator and update the health status of the machine rapidly. Yu et al. proposed a digital twin-based method to evaluate the health state of an electro-optical system with an optical transfer function as the indicator [52]. Peng et al. concluded specific health indicators in different levels of power converters and applied particle swarm optimisation to estimate the circuit parameters based on the incoming data from both the digital twin and the physical prototype [42]. Compared with the traditional data-driven method, the DT model estimation results are more accurate, and it can update and self-learn in real time, demonstrating that the digital twin methodology has good performance and broad applicability in health monitoring.

(d) RUL prediction

The amount of papers related to RUL prediction based on DT dominates the literature database. On the one hand, the remaining life of key components has a significant impact on the safety of the whole machine and the maintenance schedule. On the other hand, it can acquire real-time load of components and calculate the accumulative damage based on digital twin. Upon getting the load, the RUL can be obtained by using a damage estimation model of the specific failure mode, such as accumulated wear of a braking system [30], fatigue crack length of aircraft wings [46], thermal mechanic fatigue of turbine blisks [73], and creep damage of turbine blades [72]. These methods are based on reduced order modelling to build a quick mapping model from performance monitoring parameters to thermal or structural loads of key components. DT provides the potential for predicting the RUL of these critical parts, of which life is always affected by loads and temperatures. However, collection of data such as geometric, material, and historical failure data has made algorithm development and validation complex.

4.4. Challenges and Future Directions. Though effects have been made for improving condition monitoring through digital twin technologies, some barriers and restrictions still exist. Simultaneously, the application of digital twins on condition monitoring in this paper proves that there are many chances and new directions for further research in this field. Hence, the challenges and future directions were discussed in this section.

4.4.1. Current Challenges

(1) Data Collection and Management. Multisource, multi-modal, multitemporal scale data (e.g., geometry, material, monitoring data, environments, usage, and maintenance records) will be involved in building a digital twin, which can accurately reflect the operating condition. They cover the whole life cycle of a machine, including designing, manufacturing, operation, and maintenance phases. Collecting the above data with high quality and completeness is an essential but difficult challenge. After data collection, managing these data into a complete and standard order, which supports condition monitoring, is one more critical issue.

The amount of data generated by a cluster of individual digital twins is far too large to be stored on standard storage devices. Meanwhile, these data should be easily accessible online to conduct remote real-time condition monitoring without delay. Wang et al. proposed the big data-driven control mechanism and IoT-cloud technologies to build CPS-Digital-twin for the multi-life-cycle remanufacturing process [74]. Although cyber-physical systems and the IoTs are fast evolving, implementing online storage and access will be costly and time-consuming.

(2) Modelling and Method Development. Digital twin modelling for machines needs a good trade-off between fidelity and efficiency, with the consideration of the requirements for rapid response and the available computational resources. Physical-based modelling is a time-consuming computing process. The data-driven methods are efficient but lack interpretability and transparency. Though the integration of both methods is a solution for DT-driven CM, the error and uncertainty that occurred in the model-coupling process is a derived problem that is being explored in academia.

DT-driven CM is currently in its early stages. How to develop new methods based on the new variables generated by the digital twin for monitoring new states still needs in-depth research and innovation.

(3) Validation of Accuracy of Behavior Characterisation. The operation condition of a large system is dynamically changing. Time and operational environments affect the performance degradation and part damage. Incorporating these changing characteristics of a physical entity into the updating process of the virtual model is a challenge. Then, the accuracy of the updated digital twin remains to be verified after each replacement. However, few digital twins can enable real-time updates based on input data. Hence, condition monitoring cannot rely entirely on this kind of digital twins.

4.4.2. Future Directions

(1) Multicomponent, Multilevel Model Development in DT-Driven CM. Most research objects of DT are single-component models in the reviewed papers. It may be a part of multicomponent, multilevel machinery in the industry. Single-component DT is hard to satisfy the needs of performance evaluation and fault isolation for the complex system. In addition, each system element might be simulated and modelled by different software due to adaptability. Coupling all elements into an integrated system is one concerning part that needs to be designed and organised effectively. The integrated system should ensure that existing submodels can be reused, replaced, or modified without corrupting the entire system simulation. Therefore, this is deemed a promising direction for DT-driven CM research.

(2) Framework Standardisation for DT-Driven CM. The concept and connotation of digital twins have been fully developed in the decade since DT was proposed. However, the implementation of DT-driven CM comes into many forms. No standardisation is slowing the progress of in-depth development and leading readers unable to find appropriate solutions for machines. An effective way is to propose the standard DT framework for condition monitoring, including system architecture, workflow, modelling methods, and evaluation indices.

(3) Uncertainty Quantification for DT-Driven CM. Numerous sources of uncertainty cause decision-makers to have reservations about the accuracy and reliability of monitoring performance. The three major sources include input data uncertainty, such as geometry, operating conditions, and the uncertainty of model forms, which are only an approximation to a real condition and are limited by computational budgets, as well as numerical uncertainty induced by iterative error, discretization error. To effectively manage uncertainties, uncertain quantification should be incorporated into DT-driven CM, containing uncertainty identification, propagation, analysis, and optimisation stages.

5. Conclusion

The development of DT creates new opportunities and difficulties for CM. This review focuses on solving two questions, why and how DT is utilised to drive CM. We conducted a systematic literature review on 95 papers collected from common electronic databases to provide an overview of DT-driven CM. We analysed the studies regarding the causes, methods, and applications that corresponded with the notion of DT-driven CM. Through in-depth analysis, conclusions can be drawn that the reasons include:

(i) Many new monitorable variables provided by DT extend the monitoring scope.

(ii) DT's real-time response and behavior characterisation enhance the monitoring ability.

(iii) Predictive maintenance based on DT provides novel monitoring paradigms.

The details of the modelling methods of DT towards CM (e.g., physical-based, data-driven, and hybrid methods) and the novel monitoring paradigms (performance evaluation, anomaly detection, health monitoring, RUL prediction, etc.) were discussed to provide insights for building DT-driven CM. This work investigates more the support

supplied by DT for CM and details less how CM is really applied based on DT, as influenced by the gathered literature. In the future, more emphasis should be placed on the superiority and usability of digital twin-driven condition monitoring over traditional condition monitoring.

Overall, various frameworks and methodologies for DT-driven CM have been presented, but only a few have gained industry consensus. The majority of present research focused on individual component modelling and one-way physical to digital communication, which has not yet proven to be a powerful driver of condition monitoring from a technical engineering view. Meanwhile, there is no unifying standard for DT-driven CM, making the research more dispersed and difficult to refer to by other scholars, which may cause repeated research. It is critical that researchers work together to create a systematic framework for DT and DT-driven CM further.

Conflicts of Interest

The authors declare that they have no known competing financial interests or personal relationships that could have appeared to influence the work reported in this paper.

Acknowledgments

References

[1] Y. You, C. Chen, F. Hu, Y. Liu, and Z. Ji, "Advances of digital twins for predictive maintenance," *Procedia Computer Science*, vol. 200, pp. 1471–1480, 2022.

[2] E. Glaessgen and D. Stargel, "The digital twin paradigm for future NASA and U.S," *Air Force Vehicles*, 2012.

[3] A. Fuller, Z. Fan, C. Day, and C. Barlow, "Digital twin: enabling technologies, challenges and open research," *IEEE Access*, vol. 8, pp. 108952–108971, 2020.

[4] A. Ali and A. Abdelhadi, "Condition-based monitoring and maintenance: state of the art review," *Applied Sciences*, vol. 12, no. 2, p. 688, 2022.

[5] D. M. Botín-Sanabria, S. Mihaita, R. E. Peimbert-García, M. A. Ramírez-Moreno, R. A. Ramírez-Mendoza, and J. J. Lozoya-Santos, "Digital twin technology challenges and applications: a comprehensive review," *Remote Sensing*, vol. 14, no. 6, 2022.

[6] M. Perno, L. Hvam, and A. Haug, "Implementation of digital twins in the process industry: a systematic literature review of enablers and barriers," *Computers in Industry*, vol. 134, article 103558, 2022.

[7] T. Zonta, C. A. da Costa, R. da Rosa Righi, M. J. de Lima, E. S. da Trindade, and G. P. Li, "Predictive maintenance in the industry 4.0: a systematic literature review," *Computers & Industrial Engineering*, vol. 150, article 106889, 2020.

[8] H. Shao, M. Xia, J. Wan, and C. W. de Silva, "Modified stacked autoencoder using adaptive Morlet wavelet for intelligent fault diagnosis of rotating machinery," *IEEE/ASME Transactions on Mechatronics*, vol. 27, no. 1, pp. 24–33, 2022.

[9] M. Xia, H. Shao, X. Ma, and C. W. de Silva, "A stacked GRU-RNN-based approach for predicting renewable energy and electricity load for smart grid operation," *IEEE Transactions on Industrial Informatics*, vol. 17, no. 10, pp. 7050–7059, 2021.

[10] H. Liu, J. Sun, S. Lei, and S. Ning, "In-service aircraft engines turbine blades life prediction based on multi-modal operation and maintenance data," *Propulsion and Power Research*, vol. 10, no. 4, pp. 360–373, 2021.

[11] T. Álvarez Tejedor, R. Singh, and P. Pilidis, "Advanced gas turbine asset and performance management," in *Modern Gas Turbine Systems*, P. Jansohn, Ed., pp. 515–564, Woodhead Publishing, 2013.

[12] S. K. Chaulya and G. M. Prasad, "Formation of digital mine using the internet of things," in *Sensing and Monitoring Technologies for Mines and Hazardous Areas*, pp. 279–350, Elsevier, 2016.

[13] J. C. J. Correa and A. L. Guzman, *Mechanical Vibrations and Condition Monitoring*, Elsevier, Cambridge, 2020.

[14] Y. G. Li, "Gas turbine performance and health status estimation using adaptive gas path analysis," *Journal of Engineering for Gas Turbines and Power*, vol. 132, no. 4, article 041701, 2010.

[15] J. Zhu, C. Wang, Z. Hu, F. Kong, and X. Liu, "Adaptive variational mode decomposition based on artificial fish swarm algorithm for fault diagnosis of rolling bearings," *Proceedings of the Institution of Mechanical Engineers, Part C: Journal of Mechanical Engineering Science*, vol. 231, 2017.

[16] B. Rodriguez, E. Sanjurjo, M. Tranchero, C. Romano, and F. Gonzalez, "Thermal parameter and state estimation for digital twins of E-powertrain components," *IEEE Access*, vol. 9, pp. 97384–97400, 2021.

[17] H. Yan, J. Sun, and H. Zuo, "Anomaly detection based on multivariate data for the aircraft hydraulic system," *Proceedings of the Institution of Mechanical Engineers Part I Journal of Systems and Control Engineering*, vol. 235, no. 5, pp. 593–605, 2021.

[18] M. Liu, S. Fang, H. Dong, and C. Xu, "Review of digital twin about concepts, technologies, and industrial applications," *Journal of Manufacturing Systems*, vol. 58, pp. 346–361, 2021.

[19] E. H. Glaessgen and D. S. Stargel, "The digital twin paradigm for future NASA and U.S. Air Force vehicles," in *Presented at the 53rd AIAA/ASME/ASCE/AHS/ASC Structures, Structural Dynamics and Materials Conference - Special Session on the Digital Twin*, Honolulu, HI, 2012.

[20] Y. Chen, "Integrated and intelligent manufacturing: perspectives and enablers," *Engineering*, vol. 3, no. 5, pp. 588–595, 2017.

[21] W. Luo, T. Hu, C. Zhang, and Y. Wei, "Digital twin for CNC machine tool: modeling and using strategy," *Journal of Ambient Intelligence and Humanized Computing*, vol. 10, no. 3, pp. 1129–1140, 2019.

[22] A. Madni, C. Madni, and S. Lucero, "Leveraging digital twin technology in model-based systems engineering," *Systems*, vol. 7, no. 1, p. 7, 2019.

[23] M. G. Kapteyn, D. J. Knezevic, and K. Willcox, "Toward predictive digital twins via component-based reduced-order models and interpretable machine learning," in *Presented at the AIAA Scitech 2020 Forum*, Orlando, FL, 2020.

[24] M. Xiong, H. Wang, Q. Fu, and Y. Xu, "Digital twin–driven aero-engine intelligent predictive maintenance," *The International Journal of Advanced Manufacturing Technology*, vol. 114, no. 11–12, pp. 3751–3761, 2021.

[25] M. Fahim, V. Sharma, T.-V. Cao, B. Canberk, and T. Q. Duong, "Machine learning-based digital twin for predictive modeling in wind turbines," *IEEE Access*, vol. 10, pp. 14184–14194, 2022.

[26] J. Wan, M. Xia, J. Hong, Z. Pang, B. Jayaraman, and F. Shen, "IEEE access special section editorial: key technologies for smart factory of industry 4.0," *IEEE Access*, vol. 7, pp. 17969–17974, 2019.

[27] L. Silvestri, A. Forcina, V. Introna, A. Santolamazza, and V. Cesarotti, "Maintenance transformation through industry 4.0 technologies: a systematic literature review," *Computers in Industry*, vol. 123, article 103335, 2020.

[28] C. Li, S. Mahadevan, Y. Ling, S. Choze, and L. Wang, "Dynamic Bayesian network for aircraft wing health monitoring digital twin," *AIAA Journal*, vol. 55, no. 3, pp. 930–941, 2017.

[29] A. J. Zakrajsek and S. Mall, *The Development and Use of a Digital Twin Model for Tire Touchdown Health Monitoring*, 2017.

[30] R. Magargle, L. Johnson, P. Mandloi et al., "A simulation-based digital twin for model-driven health monitoring and predictive maintenance of an automotive braking system," in *Proceedings of the 12th International Modelica Conference*, Prague, Czech Republic, 2017.

[31] F. Tao, M. Zhang, Y. Liu, and A. Y. C. Nee, "Digital twin driven prognostics and health management for complex equipment," *CIRP Annals*, vol. 67, no. 1, pp. 169–172, 2018.

[32] V. Zaccaria, M. Stenfelt, I. Aslanidou, and K. G. Kyprianidis, "Fleet monitoring and diagnostics framework based on digital twin of aero-engines," *Turbo Expo: Power for Land, Sea, and Air*, vol. 51128, 2018.

[33] M. Gholami Mayani, R. Rommetveit, S. I. Oedegaard, and M. Svendsen, "Drilling automated realtime monitoring using digital twin," in *Abu Dhabi International Petroleum Exhibition & Conference*, Abu Dhabi, United Arab Emirates, 2018.

[34] U. T. Tygesen, M. S. Jepsen, J. Vestermark, N. Dollerup, and A. Pedersen, "The true digital twin concept for fatigue re-assessment of marine structures," in *International Conference on Offshore Mechanics and Arctic Engineering*, vol. 51203, Madrid, Spain, 2018.

[35] S. S. Johansen and A. R. Nejad, "On digital twin condition monitoring approach for drivetrains in marine applications," in *International Conference on Offshore Mechanics and Arctic Engineering*, vol. 58899, Glasgow, Scotland, UK, 2019.

[36] J. Xie, X. Wang, Z. Yang, and S. Hao, "Virtual monitoring method for hydraulic supports based on digital twin theory," *Mining Technology*, vol. 128, no. 2, pp. 77–87, 2019.

[37] S. Venkatesan, K. Manickavasagam, N. Tengenkai, and N. Vijayalakshmi, "Health monitoring and prognosis of electric vehicle motor using intelligent- digital twin," *IET Electric Power Applications*, vol. 13, no. 9, pp. 1328–1335, 2019.

[38] Y. Qamsane, C.-Y. Chen, E. C. Balta et al., "A unified digital twin framework for real-time monitoring and evaluation of smart manufacturing systems," in *2019 IEEE 15th international conference on automation science and engineering (CASE)*, Vancouver, BC, Canada, 2019.

[39] R. Revetria, F. Tonelli, L. Damiani, M. Demartini, F. Bisio, and N. Peruzzo, "A real-time mechanical structures monitoring system based on digital twin," in *2019 Spring Simulation Conference (SpringSim)*, Tucson, AZ, USA, 2019.

[40] E. C. Balta, D. M. Tilbury, and K. Barton, "A digital twin framework for performance monitoring and anomaly detection in fused deposition modeling," in *2019 IEEE 15th International Conference on Automation Science and Engineering (CASE)*, Vancouver, BC, Canada, 2019.

[41] Y. Zheng, S. Yang, and H. Cheng, "An application framework of digital twin and its case study," *Journal of Ambient Intelligence and Humanized Computing*, vol. 10, no. 3, pp. 1141–1153, 2019.

[42] Y. Peng, S. Zhao, and H. Wang, "A digital twin based estimation method for health indicators of DC–DC converters," *IEEE Transactions on Power Electronics*, vol. 36, no. 2, pp. 2105–2118, 2021.

[43] T. Moi, A. Cibicik, and T. Rølvåg, "Digital twin based condition monitoring of a knuckle boom crane: an experimental study," *Engineering Failure Analysis*, vol. 112, article 104517, 2020.

[44] J. Yu, P. Liu, and Z. Li, "Hybrid modelling and digital twin development of a steam turbine control stage for online performance monitoring," *Renewable and Sustainable Energy Reviews*, vol. 133, article 110077, 2020.

[45] D. Shangguan, L. Chen, and J. Ding, "A digital twin-based approach for the fault diagnosis and health monitoring of a complex satellite system," *Symmetry*, vol. 12, no. 8, p. 1307, 2020.

[46] Y. Ye, Q. Yang, F. Yang, Y. Huo, and S. Meng, "Digital twin for the structural health management of reusable spacecraft: a case study," *Engineering Fracture Mechanics*, vol. 234, article 107076, 2020.

[47] M. Gonzalez, O. Salgado, J. Croes, B. Pluymers, and W. Desmet, "A digital twin for operational evaluation of vertical transportation systems," *IEEE Access*, vol. 8, pp. 114389–114400, 2020.

[48] W. Li, M. Rentemeister, J. Badeda, D. Jöst, D. Schulte, and D. U. Sauer, "Digital twin for battery systems: cloud battery management system with online state-of-charge and state-of-health estimation," *Journal of Energy Storage*, vol. 30, article 101557, 2020.

[49] P. Moutis and O. Alizadeh-Mousavi, "Digital twin of distribution power transformer for real-time monitoring of medium voltage from low voltage measurements," *IEEE Transactions on Power Delivery*, vol. 36, no. 4, pp. 1952–1963, 2021.

[50] V. Panov and S. Cruz-Manzo, "Gas turbine performance digital twin for real-time embedded systems," in *Presented at the ASME Turbo Expo 2020: Turbomachinery Technical Conference and Exposition*, 2021.

[51] K.-J. Wang, Y.-H. Lee, and S. Angelica, "Digital twin design for real-time monitoring - a case study of die cutting machine," *International Journal of Production Research*, vol. 59, no. 21, pp. 6471–6485, 2021.

[52] J. Yu, Y. Song, D. Tang, and J. Dai, "A digital twin approach based on nonparametric Bayesian network for complex system health monitoring," *Journal of Manufacturing Systems*, vol. 58, pp. 293–304, 2021.

[53] K. Zhuang, Z. Shi, Y. Sun, Z. Gao, and L. Wang, "Digital twin-driven tool wear monitoring and predicting method for the turning process," *Symmetry*, vol. 13, no. 8, p. 1438, 2021.

[54] Z. Wu and J. Li, "A framework of dynamic data driven digital twin for complex engineering products: the example of aircraft engine health management," *Procedia Manufacturing*, vol. 55, pp. 139–146, 2021.

[55] M. Li, Q. Lu, S. Bai, M. Zhang, H. Tian, and L. Qin, "Digital twin-driven virtual sensor approach for safe construction operations of trailing suction hopper dredger," *Automation in Construction*, vol. 132, article 103961, 2021.

[56] M. Toothman, B. Braun, S. J. Bury et al., "A digital twin framework for mechanical system health state estimation," *IFAC-Papers OnLine*, vol. 54, no. 20, pp. 1–7, 2021.

[57] F. K. Moghadam and A. R. Nejad, "Online condition monitoring of floating wind turbines drivetrain by means of digital twin," *Mechanical Systems and Signal Processing*, vol. 162, article 108087, 2022.

[58] R. Abbate, M. Caterino, M. Fera, and F. Caputo, "Maintenance digital twin using vibration data," *Procedia Computer Science*, vol. 200, pp. 546–555, 2022.

[59] T. N. Nguyen, R. Ponciroli, P. Bruck, T. C. Esselman, J. A. Rigatti, and R. B. Vilim, "A digital twin approach to system-level fault detection and diagnosis for improved equipment health monitoring," *Annals of Nuclear Energy*, vol. 170, article 109002, 2022.

[60] E. VanDerHorn, Z. Wang, and S. Mahadevan, "Towards a digital twin approach for vessel-specific fatigue damage monitoring and prognosis," *Reliability Engineering & System Safety*, vol. 219, article 108222, 2022.

[61] C. A. Bonilla, A. Zanfei, B. Brentan, I. Montalvo, and J. Izquierdo, "A digital twin of a water distribution system by using graph convolutional networks for pump speed-based state estimation," *Water*, vol. 14, no. 4, p. 514, 2022.

[62] Y. Lu, C. Liu, K. I.-K. Wang, H. Huang, and X. Xu, "Digital twin-driven smart manufacturing: connotation, reference model, applications and research issues," *Robotics and Computer-Integrated Manufacturing*, vol. 61, article 101837, 2020.

[63] N. G. Kuftinova, A. V. Ostroukh, O. I. Maksimychev, Y. E. Vasil'ev, and M. G. Pletnev, "Predictive diagnostics and maintenance of industrial equipment," *Russian Engineering Research*, vol. 42, no. 2, pp. 158–161, 2022.

[64] J. Kraft and S. Kuntzagk, "Engine fleet-management: the use of digital twins from a MRO perspective," in *Presented at the ASME Turbo Expo 2017: Turbomachinery Technical Conference and Exposition*, Charlotte, North Carolina, USA, 2017.

[65] W. N. Dawes, N. Meah, A. Kudryavtsev, R. Evans, M. Hunt, and P. D. Tiller, "Geometry to support a gas turbine digital twin," in *Presented at the AIAA Scitech 2019 Forum*, San Diego, California, 2019.

[66] H. Ding, L. Yang, and Z. Yang, "A predictive maintenance method for shearer key parts based on qualitative and quantitative analysis of monitoring data," *IEEE Access*, vol. 7, pp. 108684–108702, 2019.

[67] S. Mi, Y. Feng, H. Zheng, Y. Wang, Y. Gao, and J. Tan, "Prediction maintenance integrated decision-making approach supported by digital twin-driven cooperative awareness and interconnection framework," *Journal of Manufacturing Systems*, vol. 58, pp. 329–345, 2021.

[68] C. Klein, F. Wolters, S. Reitenbach, and D. Schönweitz, "Integration of 3D-CFD component simulation into overall engine performance analysis for engine condition monitoring purposes," in *Presented at the ASME Turbo Expo 2018: Turbomachinery Technical Conference and Exposition*, Oslo, Norway, 2018.

[69] M. Candon, M. Esposito, H. Fayek et al., "Advanced multi-input system identification for next generation aircraft loads monitoring using linear regression, neural networks and deep learning," *Mechanical Systems and Signal Processing*, vol. 171, p. 108809, 2022.

[70] S. Stoumpos and G. Theotokatos, "A novel methodology for marine dual fuel engines sensors diagnostics and health management," *International Journal of Engine Research*, vol. 23, no. 6, pp. 974–994, 2022.

[71] W. Booyse, D. N. Wilke, and S. Heyns, "Deep digital twins for detection, diagnostics and prognostics," *Mechanical Systems and Signal Processing*, vol. 140, article 106612, 2020.

[72] B. Vasilyev, S. Nikolaev, M. Raevskiy, S. Belov, and I. Uzhinsky, "Residual life prediction of gas-engine turbine blades based on damage surrogate-assisted modeling," *Applied Sciences*, vol. 10, no. 23, p. 8541, 2020.

[73] L.-K. Song, G.-C. Bai, C.-W. Fei, and J. Wen, "Reliability-based fatigue life prediction for complex structure with time- varying surrogate modeling," *Advances in Materials Science and Engineering*, vol. 2018, 16 pages, 2018.

[74] Y. Wang, S. Wang, B. Yang, L. Zhu, and F. Liu, "Big data driven hierarchical digital twin predictive remanufacturing paradigm: architecture, control mechanism, application scenario and benefits," *Journal of Cleaner Production*, vol. 248, article 119299, 2020.

Research Article

Rotating Machinery Fault Identification via Adaptive Convolutional Neural Network

Luke Zhang [ID],[1] Jia Liu [ID],[1] Shu Su [ID],[1] Tong Lu [ID],[1] Chunrong Xue [ID],[2] Yinjun Wang [ID],[3] Xiaoxi Ding [ID],[4] and Yimin Shao [ID][4]

[1]*Science and Technology on Reactor System Design Technology Laboratory, Nuclear Power Institute of China, Chengdu 610213, China*
[2]*Chongqing Research Institute, China Coal Technology Engineering Group, Chongqing 400039, China*
[3]*School of Mechanical Engineering, Chongqing Technology and Business University, 400067, China*
[4]*State Key Laboratory of Mechanical Transmission, Chongqing University, Chongqing 400044, China*

Correspondence should be addressed to Xiaoxi Ding; dxxu@cqu.edu.cn

Rotating machinery plays an important role in transportation, petrochemical industry, industrial production, national defence equipment, and other fields. With the development of artificial intelligence, the equipment condition monitoring especially needs an intelligent fault identification method to solve the problem of high false alarm rate under complex working conditions. At present, intelligent recognition models mostly increase the complexity of the network to achieve the purpose of high recognition rate. This method often needs better hardware support and increases the operation time. Therefore, this paper proposes an adaptive convolutional neural network (ACNN) by combining ensemble learning and simple convolutional neural network (CNN). ACNN model consists of input layer, subnetwork unit, fusion unit, and output layer. The input of the model is one-dimensional (1D) vibration signal sample, and the subnetwork unit consists of several simple CNNs, and the fusion unit weights the output of the subnetwork units through the weight matrix. ACNN recognizes the self-adaptive of weight factors through the fusion unit. The adaptive performance and robustness of ACNN for sample recognition under variable working conditions are verified by gear and bearing experiments.

1. Introduction

As a key component of mechanical transmission system, rotating machineries have been widely used in the transmission system of automobiles [1], ships [2], wind turbine [3], machine tools, etc. However, in the actual industrial scene, they are easy to be broken down due to the harsh service environment and variable speed and load [4, 5]. So, it is vulnerable to catastrophic accidents if health state of equipment is not considered in a timely manner. Therefore, the research on intelligent and efficient recognition model is of great significance to ensure the healthy operation of equipment [6–8].

At present, the common monitoring technology can be divided into three groups: index-based trend forecast methods, spectrum signal-based analysis methods [9], and data-driven deep learning (DL) methods [10, 11]. The former two rely heavily on expert experience and require more labour input. In the past decade years, benefiting from the rapid development of computer systems and intelligent sensing technologies, deep learning methods have been attached to too much attention. As an end-to-end fault diagnosis technology, deep learning aims to build a learning model and mine the inherent complex mapping between feature space and fault types by learning massive labeled data, to predict and judge diagnosis of unknown samples. Existing

favourable deep learning methods include deep belief network (DBN), Auto-Encoder (AE) [12], and convolutional neural network (CNN) that present significant advantages in solving varieties of classification problems. Wang proposes a deep interpolation neural network (DICN) [13], which improves the fault recognition rate of neural network under time-varying conditions. Eren et al. [14] used compact 1D-CNN to extract recognition features from the original fault data, and the classification time is less than 1 msec, which is very suitable for the fact monitoring and diagnosis of mechanical equipment. Zhang et al. [15] proposed a deep convolutional neural network with wide first-layer kernels (WDCNN) which used the wide kernels in the first convolutional layer for extracting features and suppressing high-frequency noise. Liu et al. [16] proposed a multiscale kernel-based residual CNN (MK-ResCNN) which overcomes the problem that the gradient of deep network disappears, and used multiscale nuclear energy to extract fault features more accurately. Du et al. [17] proposed a convolution sparse learning model for deconvolution of complex modulation of transmission path, and successfully detecting the transient fault impulses of gearbox vibration signal. Huang et al. [18] used minimax concave penalty function to construct an objective function and constraint the sparsity coefficients. As a result, the repetitive transient's information is effectively extracted. Li et al. [19] proposed a power spectral entropy based variational mode decomposition method and introduced it into deep neural networks, and achieve a promising fault recognition rate. Li et al. [20] proposed a named WaveletKernelNet framework where the first layer of a standard CNN is replaced with continuous wavelet transform, achieving an interpretable feature map with clear physical meaning. Sun et al. [21] combined sparse autoencoder SAE with DNN and presented a SAE-based CNN to learn more differentiated features of unlabeled data, and experimentally verified its effectiveness. Guo et al. [22] established a named hierarchical learning rate adaptive deep convolution neural network where the two-dimensional (2D) CNN hierarchical framework with an adaptive learning rate is adopted to recognize bearing fault categories and sizes. Cheng et al. [23] proposed a hybrid time-frequency analysis method, which was successfully used for railway bearing fault identification, which could effectively recover fault information from raw signals contaminated by strong noise and other interferences.

With the research and development of intelligent recognition methods, the scale of the model is becoming larger and larger in order to pursue high recognition rate, which obviously does not correspond to a good direction of fault diagnosis. The large scale of intelligent recognition model needs better hardware support and increases the recognition operation time, which is obviously unfavourable to the industrial application of intelligent recognition methods. Therefore, this paper proposes an adaptive convolutional neural network (ACNN) by combining ensemble learning and simple convolutional neural network (CNN). ACNN model consists of input layer, subnetwork unit, fusion unit, and output layer. The input of the model is one-

dimensional (1D) vibration signal sample, and the subnetwork unit consists of several simple CNNs, and the fusion unit weights the output of the subnetwork units by the weight matrix. The weight matrix can adjust the proportion of each subnetwork output, increase the influence of identifying the correct subnetwork unit output, and weaken the influence of identifying the wrong subnetwork output. ACNN realizes the integrated learning of the model by adaptively adjusting the simple CNN as the output of the basic classifier, which can improve the recognition rate of the model without significantly increasing the network parameters. The adaptive performance and robustness of ACNN for sample recognition under variable working conditions are verified by gear and bearing experiments.

The main innovations and contributions of this paper are summarized as follows.

(1) ACNN is proposed by combining ensemble learning with simple 1D-CNN, which can accurately identify rotating machinery faults under unknown working conditions. It provides a new idea and method for intelligent fault diagnosis

(2) ACNN replaces the combination strategy in traditional bagging ensemble learning with optimized weight parameters. The combination strategy is optimized by continuously optimizing the weight parameters

(3) The proposed ACNN is generalizable, and it can also be applied to other machine learning algorithms. Besides, it can be also found that the proposed ACNN not only has a good identification performance for multiple load conditions but also shows a strong ability to unknown information representation for samples under variational working conditions, including speed, load, and oil

The rest of this paper is organized as follows. Section 2 presents theoretical background. In Section 3, the architecture of ACNN is proposed and the training strategy of model is introduced. In Section 4, compared with other network architectures, the fault diagnosis results of the ACNN are discussed on the gearbox dataset and bearing dataset, and the validity of the model is verified. Section 5 concludes this paper.

2. Theoretical Background

The model proposed in this paper is based on one-dimensional (1D) CNN theory and reference learning. The 1D-CNN is essentially a multilayer perceptron, which adopts the method of local receptive fields and shared weights. On the one hand, this method reduces the number of weights and makes the network easy to optimize; on the other hand, it reduces the risk of overfitting. The 1D-CNN is generally composed of input layer, 1D convolution layer, activation function, pooling layer, and full connection layer, as shown in Figure 1.

The calculation formula of 1D convolution is defined as follows.
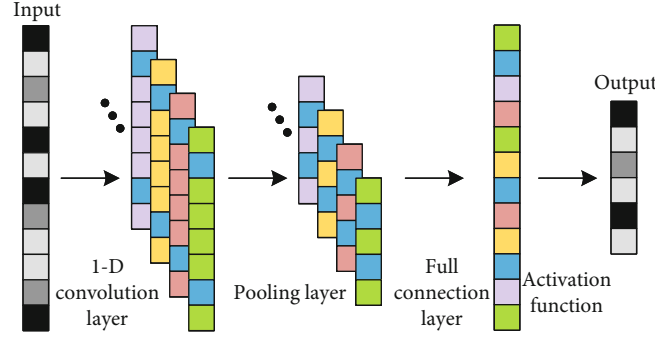
FIGURE 1: The structure of 1D-CNN.

$$\text{if } \frac{l-k}{s} \in N^*, y_i = \sum_{j=1}^{k} w_j \cdot x_{(i-1)s+j} + b_i, i \in [1, (l-k)/s + 1],$$

$$\text{if } \frac{l-k}{s} \notin N^*, \begin{cases} y_i = \sum_{j=1}^{k} w_j \cdot x_{(i-1)s+j} + b_i, i \in [1, \lfloor(l-k)/s\rfloor] \\ y_i = \sum_{j=1}^{l-i\times s} w_j \cdot x_{i\times s+j} + b_i, i \in \lceil(l-k)/s\rceil \end{cases},$$

$$(1)$$

where l is the length of 1D input x, k is the length of convolution kernel w, and s is the convolution stride. $N*$ is the set of positive integers. $\lfloor \cdot \rfloor$ and $\lceil \cdot \rceil$ represent rounding down and up, respectively. y_i is the i-th element in the output of convolution layer. x is the 1D original vibration signal. w and b are the kernel and bias, respectively. The convolution formula is abbreviated as:

$$y = w \otimes x + b. \quad (2)$$

where $\otimes$ denotes convolution operation and w and b are the kernel and bias, respectively. To reduce network parameters and retain effective signal characteristics, a max-pooling function is processed after each small convolution layer as follows.

$$y_i^l = \max\left(y_{(i-1)\times s}^{l-1}, y_{(i-1)\times s+1}^{l-1}, \cdots, y_{i\times s}^{l-1}\right), i \in \left[1, \left\lceil len\left(y^{l-1}\right)/s\right\rceil\right] \text{ and } i \in N^*,$$

$$(3)$$

where y_i^l is the i-th data of the l layer, y_{l-1} is the output of the l-1 layer, s is the stride of the pooling, $len(\cdot)$ is the length of the vector, $\lceil \cdot \rceil$ is the up rounding, and the padding type is set to same. The rectified linear unit (ReLU) is used to activation function after each convolution operation. ReLU is defined as:

$$\text{ReLU} = \begin{cases} 0, x \leq 0 \\ x, x > 0 \end{cases}. \quad (4)$$

The high-dimensional spatial feature map obtained after the input data that is subjected to the convolution

operation will be inputted to the pooling layer for subsampled processing. The most commonly used pooling operation is the max-pooling operation. The max-pooling operation will divide the feature map into several nonoverlapping regions according to the relevant parameters and step size of the pooling region, and then extract the maximum value in each region as the representative value of this region, and discard other values of this region. The maximum values of different regions are sequentially combined into a new feature map as the output of the pooling layer.

3. Adaptive Convolutional Neural Network

3.1. Motivation. The ensemble learning refers to a machine learning method that integrates multiple basic classifiers with certain criteria or strategies in order to obtain a strong learner to achieve the target task. For a complex problem, multiple experts have given different opinions and solutions. If you can discuss these different opinions and methods, and get a comprehensive opinion and solution, it is often more comprehensive and better than any one of them. Ensemble learning is based on this idea to complete the learning task. Its concept can be summarized as follows: For a specific target task, use sample data to train to obtain a few base learners with certain training criteria and strategies and then use appropriate fusion criteria or algorithm, which integrates multiple basic classifiers to obtain a strong classifier with excellent performance to complete the target task. Figure 2 shows the general structure of ensemble learning. The traditional bagging is an algorithm that optimizes the output of weak learners by combining strategies. The bagging algorithm not only improves its accuracy and stability but also avoids overfitting by reducing the variance of the results. The voting average method is a common combination strategy. However, the traditional combination strategy cannot be updated. We use the network weight parameters to replace the traditional combination strategy, and continuously adjust the output weight of each weak classifier through the network parameter update iteration. Combining the idea of bagging algorithm with CNN, an ACNN framework is proposed.

3.2. ACNN Architecture. The ACNN model is mainly composed of the following four parts: input layer, subnetwork unit, fusion unit, and output layer. The input layer is used
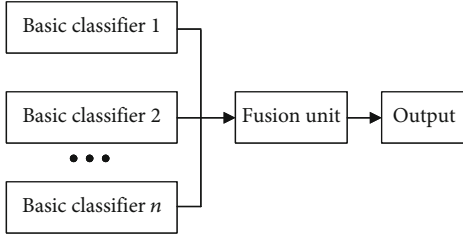
Figure 2: Schematic diagram of ensemble learning.

to receive the time-domain signal and input it to the subnetwork unit, which architecture is shown in Figure 3. The subnetwork unit is composed of 1D-CNN fault identification subnetworks. The number of subnetworks is consistent with the number of working conditions (speeds or loads) of samples in the training dataset. Each subnetwork has the same structure and corresponds to different working conditions, respectively. ACNN can accurately extract the fault-sensitive information of rotating machinery under variable working conditions and accurately identify the fault type. The fusion unit stores the weight matrix obtained through supervised training, which is used to assign different weights to the output results of the subnetwork, then performs fusion learning and outputs the final recognition results.

The processing process of the input data by the subnetwork unit is shown in Figure 3. During fault identification, a fault sample to be identified is input into the ACNN; the input layer receives the sample and inputs it into the subnetwork unit. Each subnetwork receives the sample and is activated, and uses the stored fault type information and sample feature distribution information to learn and identify the sample.

Among them, the subnetwork corresponding to the input sample speed condition will output the original fault identification results with high accuracy, and other subnetworks will show inconsistent responses. Therefore, the construction of subnetwork unit realizes the transformation of fault identification problem under multiple working conditions into fault identification problem under single working condition, that is, for each known working condition fault sample to be identified, there is a subnetwork identification module with high identification accuracy corresponding to its working condition. After the subnetwork unit completes the processing of the input data and obtains the original recognition results O^1, O^2, ..., O^N, it inputs the original recognition results O^1, O^2, ..., O^N to the fusion output layer for the next step. When the multi subnetwork unit completes the processing of input data and obtains the original identification results O^1, O^2, ..., O^N, we input the result to the fusion output layer for weighted information fusion learning, as shown fusion unit in Figure 3. The original identification results O^1, O^2, ..., O^N are output by different CNN fault identification subnetworks. The identification subnetworks consistent with the working conditions of the input samples will output high-accuracy fault identification results, while other identification subnetworks will output low-accuracy fault identification

results. In other words, after the fusion output layer performing weighted fusion learning on the input original identification results O^1, O^2, ..., O^N, high-accuracy fault identification results occupy a large proportion in the final identification results, and the results with low accuracy are suppressed, so that the accuracy of the final identification results is guaranteed.

The fusion layer uses the weight matrix W obtained through supervised training to perform fixed weight fusion learning on the original recognition results O^1, O^2, ..., O^N; the weight matrix W and output of N-th subnetwork are defined as follows:

$$W = \begin{bmatrix} \omega_{11} & \omega_{21} & \cdots & \omega_{N1} \\ \omega_{12} & \omega_{22} & \cdots & \omega_{N1} \\ \cdots & \cdots & \omega_{nl} & \cdots \\ \omega_{1L} & \omega_{2L} & \cdots & \omega_{NL} \end{bmatrix}, \quad (5)$$

$$O^N = \left[O_1^N, O_2^N, \cdots, O_L^N \right], \quad (6)$$

where ω_{nl} indicates the probability value of the input fault sample at fault type l at speed n. O^N is the original recognition result vector. O_L^N represents the probability value of the input fault sample with fault type L in the condition V_N. L is the number of nodes in the subnet, and equal to the number of fault types. The original identification results O^1, O^2, ..., O^N of the multi subnetworks are used as intermediate input of the fusion unit. The original identification results O^1, O^2, ..., O^N are given different weights by the weight matrix W, and then the output results of the same fault type in different original identification results are accumulated, as shown in the following formula: (take fault type 1 as an example).

$$O_1 = O_1^1 \omega_{11} + O_1^2 \omega_{21} + \cdots + O_1^N \omega_{N1}. \quad (7)$$

The final identification result O is as follows:

$$O = [O_1, O_2, \cdots, O_L], \quad (8)$$

where O_L represents the probability that the input fault sample belongs to fault type L. The fault types corresponding to the maximum probability are output through maximum function, and that is the final fault identification result. The maximum function $\mathrm{Max}\,(O)$ sets the largest element in the final identification result $O = [O_1, O_2, \cdots, O_L]$ to 1 and the remaining other elements to 0. Therefore, the prediction result of the ACNN network model for the input sample is the fault type corresponding to element 1 in the final fault identification result. The maximum function is as follows:

$$\mathrm{Max}(O) = [\mathrm{Max}(O_1), \mathrm{Max}(O_2), \cdots, \mathrm{Max}(O_L),] \quad (9)$$
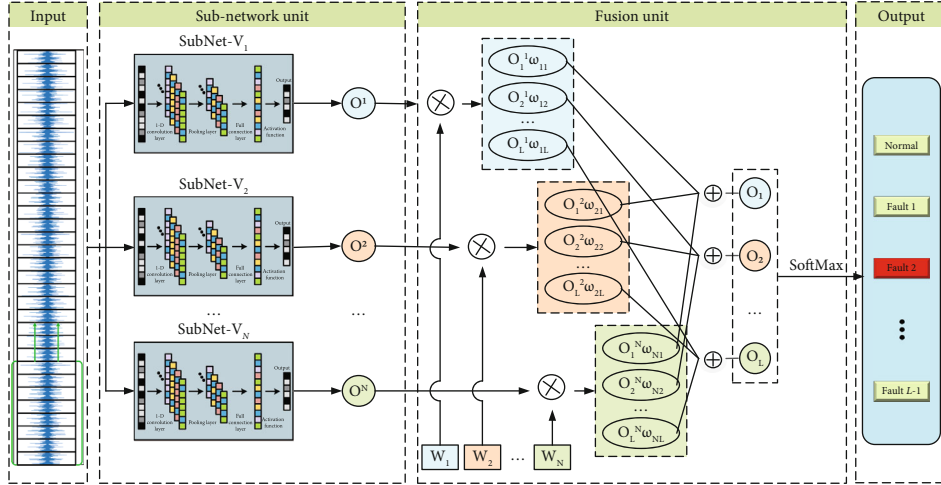
FIGURE 3: Illustration of the proposed MLDTN architecture.

where

$$
\text{Max}(O_l) = \begin{cases} 1 & O_l = \text{Max}(O) \\ 0 & O_l \neq \text{Max}(O) \end{cases}. \tag{10}
$$

The weighted fusion output result can be obtained from (5) to (8), and its expression is as follows:

$$
\begin{aligned}
O &= W\left[O^1, O^2, \cdots, O^N\right] \\
&= \begin{bmatrix} \omega_{11} & \omega_{21} & \cdots & \omega_{N1} \\ \omega_{12} & \omega_{22} & \cdots & \omega_{N1} \\ \cdots & \cdots & \omega_{nl} & \cdots \\ \omega_{1L} & \omega_{2L} & \cdots & \omega_{NL} \end{bmatrix} \begin{bmatrix} O_{11} & \omega_{21} & \cdots & O_{N1} \\ O_{12} & \omega_{22} & \cdots & O_{N1} \\ \cdots & \cdots & O_{nl} & \cdots \\ O_{1L} & O_{2L} & \cdots & O_{NL} \end{bmatrix} \\
&= [O_1, O_2, \cdots, O_L]^{\text{T}}.
\end{aligned} \tag{11}
$$

The weight matrix W of the fusion output layer is obtained through supervised training. According to the error between the final recognition result of the fusion output layer and the real label of the input sample, the classical gradient descent algorithm is used to optimize the network parameters, and the back propagation algorithm is used to transfer the error layer by layer in the training process. The initialization of network parameters adopts the random mode of normal distribution, and the value of the initial value of parameters ranges from (-1,1). When the model parameters reach an optimal value after continuous updating iteration, the model training is completed. Assuming that the real label of a fault sample set is T and the final fault identification result is O, the error between the final identification result output by the fusion output layer and the real label of the input sample can be calculated as follows:

$$
ep = \frac{1}{2} \sum_{p=1}^{P} \left(O^P - T^P\right)^2, \tag{12}
$$

where O^P and O^T, respectively, represent the final fault identification result output by the model and the real label of the fault sample set, and p is the number of training samples. In the process of weight matrix W training, the weight matrix W is optimized by minimizing the error ep. Given that the final recognition result is obtained after the process of maximum function, the influence of the maximum function $\text{Max}(O)$ on the back propagation process of training error should be considered first in the training process of weight matrix W. According to the classical chain derivation algorithm in the back propagation and the definition of the maximum function $\text{Max}(O)$, the partial derivative of $\text{Max}(O)$ with respect to its input variable O_l is calculated as follows:

$$
\frac{\partial \text{Max}(O_l)}{\partial O_l} = \lim_{\Delta \longrightarrow 0} \frac{\text{Max}(O_l + \Delta) - \text{Max}(O_l)}{\Delta}, \tag{13}
$$

where O_l is the l-th element in the final recognition result $O = [O_1, O_2, \cdots, O_L]$. Δ is an infinitesimal quantity. In line with the definition of the maximum function:

$$
\begin{aligned}
\frac{\partial \text{Max}(O_l)}{\partial O_l} &= \lim_{\Delta \longrightarrow 0} \frac{\text{Max}(O_l + \Delta) - \text{Max}(O_l)}{\Delta} \\
&= \lim_{\Delta \longrightarrow 0} \frac{O_l + \Delta - O_l}{\Delta} = \lim_{\Delta \longrightarrow 0} \frac{\Delta}{\Delta} = 1.
\end{aligned} \tag{14}
$$

The partial derivative of the maximum function for any input is 1, and the maximum function has no effect on the error back propagation and chain derivation process. Hence, there is no need to consider the influence of the maximum function in the training process of the weight matrix W. According to the output function of the fusion unit and the classical chain derivation in the back propagation algorithm, the partial derivative of the final recognition result O to the weight matrix W is as follows:

$$\frac{\partial O}{\partial W} = O_l^n. \qquad (15)$$

Considering the case of a single training sample, the training error, that is, the partial derivative of the error function ep to the weight matrix W, is as follows:

$$\delta_W = \frac{\partial 1/2 \sum_{p=1}^{P} (O^P - T^P)^2}{\partial W} = \frac{\partial O}{\partial W}(O - T) = \sum_{l=1}^{L} O_l^n (O_l - T_l), \qquad (16)$$

where O_l^n is the output value of the original identification result that belongs to the l-th node of the n-th identification model. O_l is the output value of the l-th node in the final identification result, and T_l is the l-th node value of the real label of the input sample. Based on classical gradient descent algorithm, the optimization formula for the weight matrix W is as follows:

$$\omega_{nl} = \omega_{nl} + \Delta\omega_{nl},$$
$$\Delta\omega_{nl} = -\eta \sum_{l=1}^{L} O_l^n (O_l - T_l), \qquad (17)$$

where η is the learning rate in the training process of weight matrix W.

3.3. ACNN Training. The fault feature mapping information under variable conditions is extracted and saved into different conditions identification subnetworks by the model training process, and the analysis results of the subnetworks are fused through the weighted information fusion learning algorithm to obtain the final fault identification results. The flowchart of ACNN fault identification method is shown in Figure 4. The training and testing steps are as follows:

(1) Extracting the time-domain signals of fault vibration at different conditions in the actual industrial scene, construct the fault sample set under all conditions

(2) Divide the fault sample set into sample sets under different conditions, and then train the subnetworks and weight matrix of ACNN model

(3) Put the fault sample under a certain condition in the same scene into the trained ACNN network model to obtain the fault type corresponding to this sample

4. Experimental Verification and Analysis

The performance of ACNN is verified on gear dataset and bearing dataset. The gear dataset [24] came from Chongqing University, and the bearing dataset came from Case Western Reserve University (CWRU) [25].

4.1. Case I: Gear Dataset

(1) Test platform and dataset description
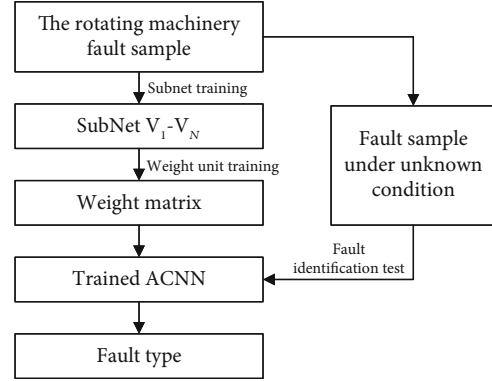
FIGURE 4: The training and fault identification of ACNN.
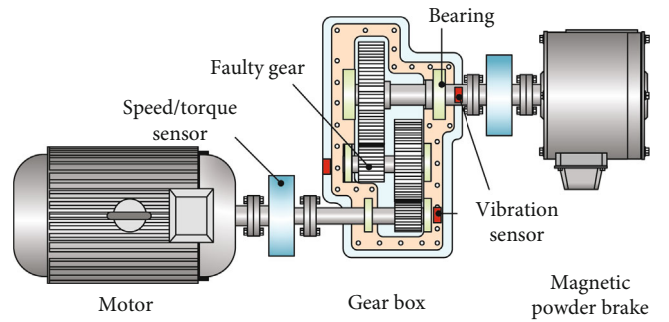
FIGURE 5: Test platform for acquiring vibration signals.

TABLE 1: Structure parameters of experimental gearbox.

Number of high-speed gear teeth	Number of low-speed gear teeth	Transmission ratio	Center distance
23	25	1.696	93 mm
39	53	2.12	117 mm

The schematic diagram of the structure of the gear test bench is shown in Figure 5. It consists of five parts: the drive motor, the two-stage spur gear reducer, the speed sensor, the magnetic powder brake, and the control cabinet. The speed of the drive motor and the load of the magnetic powder brake are controlled by the control cabinet, which enable the gearbox to run stably under various speeds and loads. The transmission ratio of the two-stage spur gear reducer is 3.59, the gear ratio of the first transmission stage is 23/39, and the gear ratio of the second transmission stage is 25/53. The motor is a DC motor of YVFF-112M-4, with rated power of 4 kw, rated voltage of 380 V, and maximum speed of 1200 rpm. The magnetic particle brake model is CZ10, rated voltage is 380 V, rated current is 1.2A, and can provide controllable stable torque load for the experimental system within 0 to 500 N.

The structural parameters of the gearbox are shown in Table 1. The fault gear is the intermediate transmission gear with 25 teeth. The gear faults include tooth surface spalling, root crack, tooth surface pitting, and tooth fracture, which
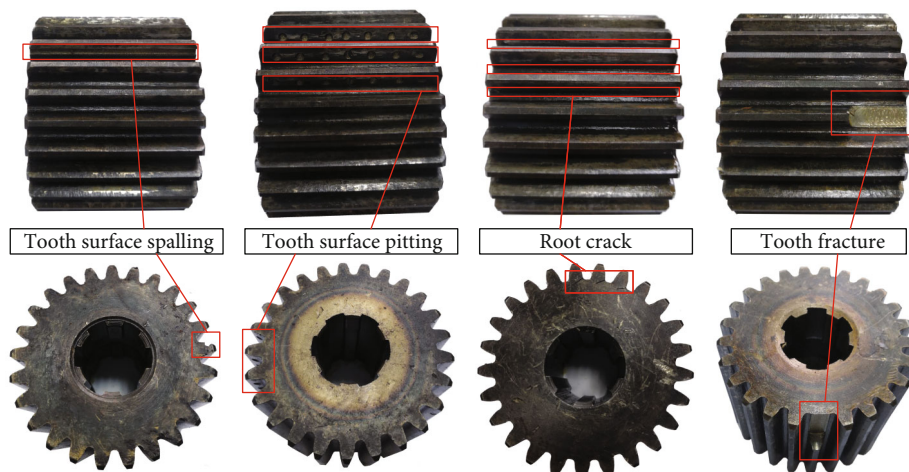
FIGURE 6: Four gears with different fault conditions.

TABLE 2: Gear fault experiment conditions and experiment parameter setting.

Fault type	Fault size (mm)	Input speed (rpm)	Sampling frequency (Hz)	Sampling time (s)
Healthy	None			
Tooth surface spalling	$60 \times 3 \times 0.5$			
Root crack	60×3	700, 750, 800, 850,900, 950, 1000, 1050, 1100	20480	15
Tooth surface pitting	2 mm			
Broken tooth	30% tooth width (18 mm)			

are shown in Figure 6. The vibration sensor is set in the vertical direction of three transmission shafts. The training and test data are obtained from the vibration signal of the middle drive shaft position sensor.

The gear fault and vibration acquisition settings are shown in Table 2.

The vibration was measured at a sampling frequency of 20.48 kHz with an input torque of 200 Nm, and the acquisition time is 15 seconds. In the gear fault simulation experiment, 13 speed conditions are set evenly in the speed range of 500 to 1100 rpm, and the interval between two adjacent speeds is 50 rpm. In this experiment, each sample contains 2048 data points. The 1000 samples were gotten by 2048 steps for sliding sampling under each speed and fault type. In order to verify the performance of the proposed network, the training sets and the test sets use samples with different speeds; 4 different training sets are set up. The settings of the training sets and the test sets are shown in Table 3. Each training set and testing set contain five gearbox states: health, tooth surface spalling, tooth root crack, tooth surface pitting, and broken tooth. The rotation speed of the training set is different, and the rotation speed of the test set is from 500 to 1100 rpm. The number of subnetworks included in ACNN is consistent with the number of working conditions. In this experiment, ACNN contains two subnetworks on training sets A and B. ACNN contains three subnetworks on training sets C and D.

TABLE 3: Training sets and test sets of models.

Datasets	Train sets	Test sets	Number of training/ testing samples
A	600, 900 rpm		10000/65000
B	800, 1100 rpm	500 to 1100 rpm	10000/65000
C	500, 700, 900 rpm		15000/65000
D	550, 750 950 rpm		15000/65000

(2) Classification comparison and analysis

In order to verify the advantage of ACNN, CNN [14], residual networks (ResNet) [26], wide first-layer kernels (WDCNN) [15], and multiscale kernel-based ResCNN (MK-ResCNN) [16] are used as comparison networks. The comparison models and ACNN are built based on Python 3.7 and Pytorch 1.7.1. The main configurations of the computer are as follows: CPU-i9-9900k, RAM-128GB, GPU-RTX 2080Ti. The five methods (ACNN, DCNN, ResNet, WDCNN, and MK-ResCNN) are trained and tested by the datasets in Table 3; the classification results are shown in Figure 7.
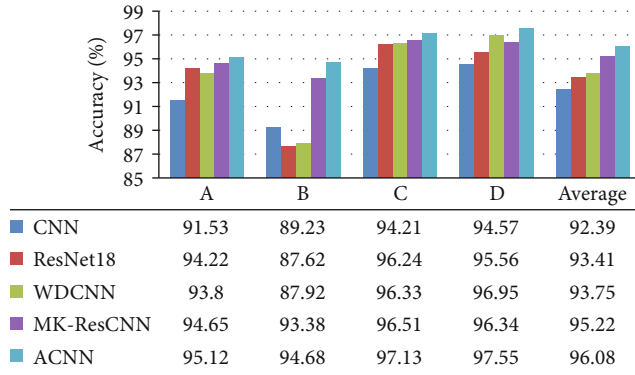
FIGURE 7: Classification performance by different methods on CU gear datasets.

	A	B	C	D	Average
CNN	91.53	89.23	94.21	94.57	92.39
ResNet18	94.22	87.62	96.24	95.56	93.41
WDCNN	93.8	87.92	96.33	96.95	93.75
MK-ResCNN	94.65	93.38	96.51	96.34	95.22
ACNN	95.12	94.68	97.13	97.55	96.08

There is no cross sample between the training set and the test set. This verification method is also called fixed dataset verification. It can better verify the recognition ability of the recognition model to unknown working condition samples and improve the robustness. The recognition rates of CNN, ResNet, WDCNN, MK-ResCNN, and ACNN are 91.53%, 94.22%, 93.8%, 94.65%, and 95.12% on dataset A, respectively. The recognition accuracy of ACNN model is higher than that of the other four comparison models. The sample recognition rate of ACNN model is also higher than that of other models on datasets B, C, and D. The average recognition rate of ACNN is 3.69%, 2.67%, 2.33%, and 0.86% higher than that of CNN, ResNet, WDCNN, and MK-ResCNN, respectively. Although the recognition rate of MK-ResCNN model is close that of ACNN model, the network parameter number of MK-ResCNN is more than three times that of ACNN model, and its training time is longer. The experimental results show that ACNN has high recognition rate and strong robustness. The recognition accuracy of datasets C and D samples is higher than that of datasets A and B, because the training set of datasets C and D contains more speed samples, which is also reasonable. The confusion matrix of the identification result on dataset D is shown in Figure 8.

It can be found that the recognition accuracy of healthy samples is the highest by the confusion matrix of the recognition results. There are 75 samples of tooth surface spalling fault incorrectly classified as tooth surface pitting corrosion. The number of tooth surface pitting fault samples incorrectly identified as tooth surface spalling is 60. This shows that the fault characteristics of tooth surface spalling and tooth surface pitting are similar. The number of tooth root crack fault samples incorrectly identified as tooth surface spalling and tooth fracture is 21 and 45, respectively. The parameters and calculation time of the comparison model on dataset A are shown in Table 4. It can be found that the parameters of ACNN network are less than those of the comparison model, and the training and testing time are the least.

4.2. CWRU Bearing Data

(1) Test platform and data description

FIGURE 8: Confusion matrix of ACNN model on gear dataset D.

TABLE 4: Training sets and test sets of models.

Models	Training time (s)	Testing time (s)	Model parameter quantity
CNN	0.501	0.304	211672
ResNet18	1.015	0.156	661508
WDCNN	0.241	0.162	99270
MK-ResNet	3.395	1.261	835274
ACNN	0.116	0.128	54076
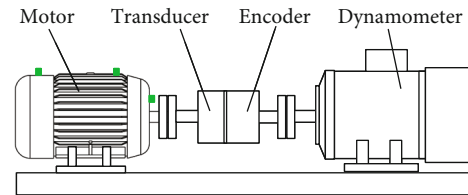
FIGURE 9: Test stand for acquiring vibration signals.

The experimental data are collected from the accelerometer of the motor-driven mechanical system (Figure 9) at a sampling frequency of 12 kHz. There are four kinds of bearing faults, that are normal, inner ring fault, ball fault, and outer ring fault. The fault dimensions of the three fault kinds are divided into 0.007 inch, 0.014 inch, and 0.021 inch. Therefore, there are 10 kinds of bearing states that need to be classified. The failure frequency of bearing fault types (inner ring fault, outer ring fault, and ball fault) is different, so we use this data to verify the performance of ACNN.

In this experiment, to verify the recognition performance of the model for samples with unknown loads, those datasets are divided into training/testing dataset according to the load of the samples. The input sample is the original vibration signal with the length of 2048, where 400 samples are

TABLE 5: Training sets and test sets of models.

Datasets	Train datasets	Test datasets	Number of training/testing samples
A	0, 1 hp	2, 3 hp	8000/8000
B	0, 2 hp	1, 3 hp	8000/8000
C	0, 3 hp	1, 2 hp	8000/8000
D	1, 2 hp	0, 3 hp	8000/8000
E	1, 3 hp	0, 2 hp	8000/8000
F	2, 3 hp	0, 1 hp	8000/8000
G	1, 2, 3 hp	0 hp	12000/4000
H	0, 2, 3 hp	1 hp	12000/4000
I	0, 1, 3 hp	2 hp	12000/4000
J	0, 1, 2 hp	3 hp	12000/4000

	A	B	C	D	E	F	G	H	I	J	Average
CNN	89.49	88.63	88.95	83.21	85.69	85.98	85.53	88.61	92.86	94.3	88.33
ResNet	89.7	93.11	83.08	87.64	88.04	87.2	91.35	93.15	97.11	87.47	89.79
WDCNN	88.48	85.41	81.23	83.16	84.39	88.19	83.27	92.18	95.55	93.15	87.50
MK-ResCNN	88.48	88.48	88.48	88.48	88.48	88.48	88.48	88.48	88.48	88.48	88.48
ACNN	95.49	93.12	91.20	93.25	90.97	91.69	92.32	94.87	98.52	99.19	94.06
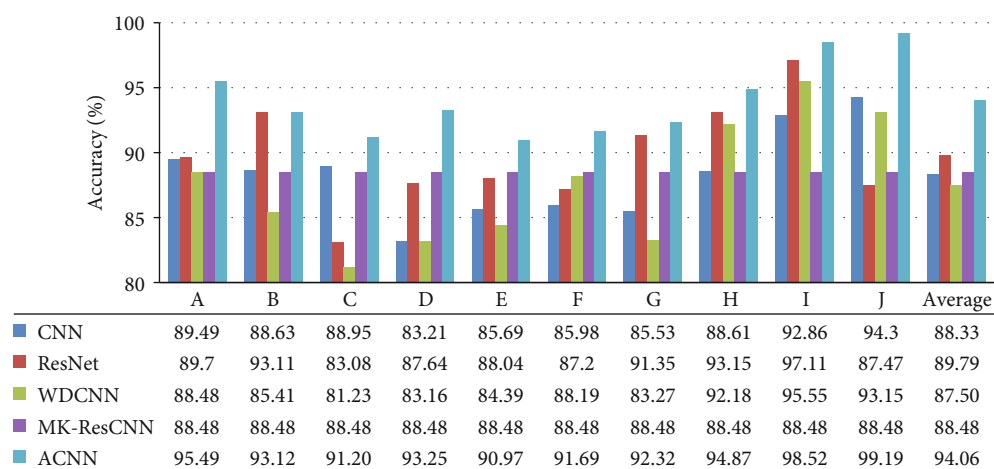
FIGURE 10: Classification performance by different methods on CWRU bearing datasets.

obtained by 200 steps via sliding sampling on one load and one fault state, so samples with the size of 400×10 were obtained under each load. The samples of any two or three loads are selected as the training datasets, and the remaining samples are used as the testing datasets. The information of training datasets and testing datasets is shown in Table 5. It can be found that there is no intersection between the training datasets and the test datasets. The performance of the ACNN model to identify the health state of the samples under unknown load is further verified.

(2) Classification comparison and analysis

In order to verify the advantage of ACNN, CNN [14], residual networks (ResNet) [26], wide first-layer kernels (WDCNN) [15], and multiscale kernel-based ResCNN (MK-ResCNN) [16] are used as comparison networks. The five methods (ACNN, DCNN, ResNet, WDCNN, and MK-ResCNN) are trained and tested by the datasets in Table 5; the classification results are shown in Figure 10. The recognition accuracy of ACNN is 95.49%, which is 6%, 5.79%, 7.01%, and 13.24% higher than CNN, ResNet, WDCNN, and MK-ResCNN on bearing dataset A, respectively. The recognition accuracy of ACNN

is 93.12%, which is 4.49%, 0.01%, 7.11%, and 10.84% higher than CNN, ResNet, WDCNN, and MK-ResCNN on bearing dataset B, respectively. The average recognition rates of ACNN, CNN, ResNet, WDCNN, and MK-ResCNN models on bearing datasets are 94.06%, 88.33%, 8.79%, 87.50%, and 86.06%, respectively. The average accuracy of ACNN is more than 4.28% higher than that of other comparison models, which proves that ACNN has strong recognition performance and adaptability to samples under variable load conditions. In order to explore the identification details of samples by ACNN model, the confusion matrix of the output results of dataset A is shown, which is shown in Figure 11.

In the confusion matrix, it can be found that all health status samples are correctly classified, and the number of 0.014 inch inner ring fault samples incorrectly identified as ball faults is 124. The number of ball fault samples incorrectly identified as outer ring fault is 81. This shows that there are similarities between inner ring fault characteristics and ball fault characteristics. The parameters and calculation time of the comparison model on dataset A are shown in Table 6. It can be found that the parameters of ACNN network are less than those of the comparison model, and the training and testing time are the least.

FIGURE 11: Confusion matrix of ACNN model on bearing dataset A. Health, IF7, IF14, IF21, B7, B14, B21, OF7, OF14, and OF21 represent health status, 0.007 inch inner ring fault, 0.014 inch inner ring fault, 0.021 inch inner ring fault, 0.007 inch ball fault, 0.014 inch ball fault, 0.021 inch ball fault, 0.007 inch outer ring fault, 0.014 inch outer ring fault, and 0.021 inch fault, respectively.

TABLE 6: Training sets and test sets of models.

Models	Training time (s)	Testing time (s)	Model parameter quantity
CNN	0.401	0.043	211672
ResNet18	0.812	0.022	661508
WDCNN	0.193	0.023	99270
MK-ResNet	2.716	0.180	835274
ACNN	0.093	0.018	54076

5. Conclusions

This paper proposes an adaptive convolutional neural network by combining ensemble learning and simple convolutional neural network. ACNN model consists of input layer, subnetwork unit, fusion unit, and output layer. The input of the model is one-dimensional (1D) vibration signal sample, and the subnetwork unit consists of several simple CNNs, and the fusion unit weights the output of the subnetwork units by the weight matrix. In gear and bearing experiments, the performance and robustness of ACNN model are verified by comparing with CNN, ResNet, WDCNN, and MK-ResCNN models.

Data Availability

Data available on request.

Conflicts of Interest

The authors declare that they have no conflicts of interest.

Acknowledgments

References

[1] S. Xiang, Y. Qin, J. Luo, and H. Pu, "Spatiotemporally multi-differential processing deep neural network and its application to equipment remaining useful life prediction," *IEEE Transactions on Industrial Informatics*.

[2] Z. Wang, G. Li, L. Yao, X. Qi, and J. Zhang, "Data-driven fault diagnosis for wind turbines using modified multiscale fluctuation dispersion entropy and cosine pairwise-constrained supervised manifold mapping," *Knowledge-Based Systems*, vol. 228, p. 107276, 2021.

[3] M. Zhang, K. Wang, and Y. Li, "Motion periods of planet gear fault meshing behavior," *Sensors*, vol. 18, no. 11, p. 3802, 2018.

[4] X. Ding and Q. He, "Energy-fluctuated multiscale feature learning with deep ConvNet for intelligent spindle bearing fault diagnosis," *IEEE Transactions on Instrumentation and Measurement*, vol. 66, no. 8, pp. 1926–1935, 2017.

[5] Z. Wan, R. Yang, and M. Huang, "Deep transfer learning-based fault diagnosis for gearbox under complex working

conditions," *Shock and Vibration*, vol. 2020, Article ID 8884179, 13 pages, 2020.

[6] Q. Li, X. Ding, Q. He, W. Huang, and Y. Shao, "Manifold sensing-based convolution sparse self-learning for defective bearing morphological feature extraction," *IEEE Transactions on Industrial Informatics*, vol. 17, no. 5, pp. 3069–3078, 2021.

[7] H. Zhiyi, S. Haidong, D. Ziyang, J. Hongkai, and C. Junsheng, "Modified deep autoencoder driven by multisource parameters for fault transfer prognosis of aeroengine," *IEEE Transactions on Industrial Electronics*, vol. 69, no. 1, pp. 845–855, 2022.

[8] X. Ding, Q. He, Y. Shao, and W. Huang, "Transient feature extraction based on time–frequency manifold image synthesis for machinery fault diagnosis," *IEEE Transactions on Instrumentation and Measurement*, vol. 68, no. 11, pp. 4242–4252, 2019.

[9] X. Ding, Q. Li, L. Lin, Q. He, and Y. Shao, "Fast time-frequency manifold learning and its reconstruction for transient feature extraction in rotating machinery fault diagnosis," *Measurement*, vol. 141, pp. 380–395, 2019.

[10] Z. Chen, K. Gryllias, and W. Li, "Intelligent fault diagnosis for rotary machinery using transferable convolutional neural network," *IEEE Transactions on Industrial Informatics*, vol. 16, no. 1, pp. 339–349, 2020.

[11] Y. Wang, L. Zeng, L. Wang, Y. Shao, Y. Zhang, and X. Ding, "An efficient incremental learning of bearing fault imbalanced data set via filter StyleGAN," *IEEE Transactions on Instrumentation and Measurement*, vol. 70, pp. 1–10, 2021.

[12] S. Haidong, X. Min, W. Jiafu, and C. W. de Silva, "Modified stacked auto-encoder using adaptive morlet wavelet for intelligent fault diagnosis of rotating machinery," *IEEE/ASME Transactions on Mechatronics*, vol. 27, no. 1, pp. 24–33, 2022.

[13] Y. Wang, X. Ding, R. Liu, and Y. Shao, "ConditionSenseNet: a deep interpolatory ConvNet for bearing intelligent diagnosis under variational working conditions," *IEEE Transactions on Industrial Informatics*1.

[14] L. Eren, I. Turker, and K. Serkan, "A generic intelligent bearing fault diagnosis system using compact adaptive 1D CNN classifier," *Journal of Signal Processing Systems*, vol. 91, no. 2, pp. 179–189, 2019.

[15] W. Zhang, G. Peng, C. Li, Y. Chen, and Z. Zhang, "A new deep learning model for fault diagnosis with good anti-noise and domain adaptation ability on raw vibration signals," *Sensors*, vol. 17, no. 425, 2017.

[16] R. Liu, F. Wang, B. Yang, and S. J. Qin, "Multiscale kernel based residual convolutional neural network for motor fault diagnosis under nonstationary conditions," *IEEE Transactions on Industrial Informatics*, vol. 16, no. 6, pp. 3797–3806, 2020.

[17] Z. Du, X. Chen, and H. Zhang, "Convolutional sparse learning for blind deconvolution and application on impulsive feature detection," *IEEE Transactions on Instrumentation and Measurement*, vol. 67, no. 2, pp. 338–349, 2018.

[18] W. Huang, S. Li, X. Fu, C. Zhang, J. Shi, and Z. Zhu, "Transient extraction based on minimax concave regularized sparse representation for gear fault diagnosis," *Measurement*, vol. 151, p. 107273, 2020.

[19] Y. Li, G. Cheng, C. Liu, and X. Chen, "Study on planetary gear fault diagnosis based on variational mode decomposition and deep neural networks," *Measurement*, vol. 130, pp. 94–104, 2018.

[20] T. Li, Z. Zhao, C. Sun et al., "WaveletKernelNet: an interpretable deep neural network for industrial intelligent diagnosis," *IEEE Transactions on Systems, Man, and Cybernetics: Systems*, vol. 52, pp. 1–11, 2021.

[21] W. Sun, S. Shao, R. Zhao, R. Yan, X. Zhang, and X. Chen, "A sparse auto-encoder-based deep neural network approach for induction motor faults classification," *Measurement*, vol. 89, pp. 171–178, 2016.

[22] X. Guo, L. Chen, and C. Shen, "Hierarchical adaptive deep convolution neural network and its application to bearing fault diagnosis," *Measurement*, vol. 93, pp. 490–502, 2016.

[23] Y. Cheng, D. Zou, W. Zhang, and Z. Wang, "A hybrid time-frequency analysis method for railway rolling-element bearing fault diagnosis," *Journal of Sensors*, vol. 2019, 12 pages, 2019.

[24] X. Ding, L. Lin, D. He, L. Wang, W. Huang, and Y. Shao, "A weight multinet architecture for bearing fault classification under complex speed conditions," *IEEE Transactions on Instrumentation and Measurement*, vol. 70, pp. 1–11, 2021.

[25] Bearing Data Center, 2017, http://csegroups.case.edu/bearingdatacenter/pages/download-data-file.

[26] K. He, X. Zhang, S. Ren, and J. Sun, "Deep residual learning for image recognition," in *IEEE Conference on Computer Vision and Pattern Recognition (CVPR)*, pp. 770–778, Las Vegas, NV, USA, 2016.

Research Article

Reliability Analysis of the High-Voltage Power Battery System Based on the Polymorphic Fuzzy Fault Tree

Haonan Jiang [ID],[1] Changbo Lin [ID],[2] Gaoshan Feng,[2] Enyong Xu,[2] and Weiguang Zheng [ID][1,2,3]

[1]*School of Mechanical and Electrical Engineering, Guilin University of Electronic Technology, Guilin 541004, China*
[2]*Commercial Vehicle Technology Center, Dong Feng Liuzhou Automobile Co., Ltd., Liuzhou 545005, China*
[3]*School of Mechanical and Automotive Engineering, Guangxi University of Science and Technology, Liuzhou 545616, China*

Correspondence should be addressed to Changbo Lin; lcb_dflzm@163.com

Accidents caused by the failure of high-voltage power battery systems are rising with the increase of pure electric commercial vehicles. The fault tree analysis method based on traditional reliability is no longer suitable for quantitative evaluation of polymorphic systems. In this paper, the polymorphic fuzzy fault tree of the high-voltage power battery system for pure electric commercial vehicles is established and analyzed qualitatively and quantitatively based on a combined theory of the polymorphic theory, fuzzy mathematical theory, group decision theory, and fault tree analysis theory. The results showed that the multistate reliability-analysis method of the fuzzy fault tree could describe the various fault states of the high-voltage power battery system. Through quantitative evaluation of the reliability of system, the low-temperature environment and CAN high and low reverse connection were the weakest links of the system, and the problem of the occurrence probability of each state of the unknown polymorphic bottom event in the sub-fault tree of the deteriorated-state mode was solved quickly using group decision-making to deal with fuzzy probability. It provides theoretical reference for system design and detection process, which has important practical significance for the improvement of high-voltage power battery system.

1. Introduction

The problems of energy and environmental protection are becoming more and more serious with the increased number of automobiles. At present, BYD, Dongfeng LiuQi, BAIC, and other major vehicle enterprises have focused on pure electric commercial vehicles with energy conservation, environmental protection, and large cargo capacity. With promoted pure electric commercial vehicles, the accidents on the reliability of the high-voltage power battery system also increase year by year. According to the statistics of the GGII (Gao Gong Industrial Research Institute), there were 34 fire accidents caused by battery problems in domestic electric vehicles from January to May 2021, involving up to 38 vehicles. Each accident is a severe challenge to the reliability of the high-voltage power battery system. The system produces hundreds of amperes of charge and discharge currents in the working process, which seriously threatens the safety of vehicles and drivers.

Reliability analysis methods have been widely used in engineering fields in continuous development. Huang et al. [1] proposed the fault tree analysis (FTA) and applied it to the design of the militia missile launch control system to predict the failure probability of missile launch in the 1960s. Subsequently, Dhillon et al. [2] of Boeing Company developed a program of the fault tree analysis method, which reduces the workload of data processing in the reliability research at the early stage of aircraft design and promotes fault-tree analysis algorithms. Rahman et al. [3] of MIT applied the fault tree analysis method in the risk assessment of nuclear power plants and listed all the causes of nuclear power plant failures in 1974. Yang et al. [4] proposed a diagnosis method that combined the fault tree analysis with an expert system to develop a fault diagnosis expert system to meet the fault diagnosis function of the DC charging pile. Lanza et al. [5] analyzed the reliability of feedback fault information to establish the machine-tool fault diagnosis and prediction system. Besides, the reliability guarantee

system is built in the designing, manufacturing, and assembly process of NC machine tools. The reliability analysis method is also applied to the field of fault diagnosis, and the fault diagnosis method proposed by Xin et al. [6–8] can effectively solved the problem of mechanical reliability. The fuzzy fault tree analysis method is proposed to solve fuzzy probability in practical engineering.

The fuzzy fault tree analysis was first proposed by Tanaka et al. [9]. Fuzzy probability is used to replace accurate probability to solve the uncertain probability in the fault tree analysis. Singer [10] used L-R-type fuzzy numbers to represent the occurrence probability of bottom events and further developed the fuzzy fault tree analysis method. Yuhua and Datao [11] combined expert heuristics with the fuzzy set theory to solve the fuzziness of failure probability of some bottom events in oil and gas transmission pipelines. Liu et al. [12] proposed a reliability analysis method based on the Bayesian network and T-S (Takagi-Sugeno) fault tree. The nodes in the Bayesian network are represented by the fuzzy probability, and the fault degree of the system is represented by fuzzy variables. This technology is applied to the reliability analysis of the injection system of the chemotherapy robot. Yin et al. [13] proposed a safety evaluation method for natural gas storage tanks based on the fuzzy fault-tree analysis method of similarity aggregation.

The theory of the multistate system (MSS) provides a new way for the reliability analysis of complex systems. Satyanarayana and Prabhakar [14] studied the reliability of networked systems to propose the idea of solving the reliability of a system by simply computing the sum of the probabilities of acyclic subgraphs in the 1970s. Iscioglu [15] proposed a new method to evaluate the MRL (mean residual lifetime) function of a one-unit, three-state system using the conditional residual function. Borges et al. [16] proposed the Monte Carlo parallel reliability analysis method, which has high efficiency in testing the actual power system model and can evaluate the reliability of a large-scale power grid. Mahadevan et al. [17] used the Bayesian network to compare with the traditional reliability analysis methods of series and parallel systems, with its effectiveness verified. Considering the impact of component degradation and different maintenance strategies, Mohammadhasani [18] used the Markov maintenance model to quantify the effectiveness of maintenance activities. These models are coupled with the fault tree method, providing a more practical and accurate fault tree analysis tool. Research on the smoothness of commercial vehicles has expanded the application of reliability in engineering [19, 20].

Among the numerous causes of the functional failure of the high-voltage power battery system, the occurrence probability of power battery system failure caused by insulation failure is assumed to be between 0.02 and 0.03. Namely, the accurate occurrence probability is a fuzzy number. Among the reasons for the degradation of the high-voltage power battery system, the oxidation and reduction of battery electrolyte is a dynamic process, that is, a multistate event. Therefore, after considering the limitation of the traditional fault tree analysis method on the fuzziness and polymorphism of the high-voltage power battery system of pure elec-

tric commercial vehicles, the multistate fuzzy fault tree analysis method is used to analyze its reliability.

The work took a high-voltage power battery system of pure electric commercial vehicles as an example and applied theories such as the multistate theory and fuzzy mathematics to establish a multistate fuzzy fault tree for the high-voltage power battery system. Minimum reliability was 0.4607, and maximum reliability was 0.5370 for the high-voltage power battery system. Furthermore, low-reliability events directly affecting the reliability of the system were identified.

The following items have been accomplished: (1) A complete multistate fuzzy fault tree for high-voltage power battery systems of pure electric commercial vehicles was established to solve the functional-failure mode, deteriorated-state mode, and subfault tree models to analyze the reliability of high-voltage power battery systems. (2) Qualitative and quantitative analyses were performed on all bottom events of the subfault tree causing the functional failure mode. The weak links causing the system failure were identified by the fuzzy-probability importance of each bottom event. (3) For the problem of unknown probability of multistate bottom events in each state, group decision-making was used to deal with fuzzy probabilities, thus solving the subfault trees in the state deterioration mode.

The remainder of the work is organized as follows. Section 2 introduces the basic theory of the polymorphic fuzzy fault tree analysis method. The polymorphic fuzzy fault tree of the high-voltage power battery system of pure electric commercial vehicles is established and analyzed in Section 3. Section 4 solves the fuzzy-probability importance of each bottom event of the subfault tree in the functional failure mode. Finally, the conclusions are summarized in Section 5.

2. Basic Theory of the Polymorphic Fuzzy Fault Tree Analysis Method

2.1. Fault Tree Analysis. The fault tree analysis (FTA) [21] can analyze all the possible causes of system failure in the system design process. A "tree" logic block diagram is drawn to identify the basic events causing system failure. Qualitative analysis is used to solve the probability of system failure and the importance of the bottom event.

2.1.1. Qualitative FTA

(1) Cut Set and Minimum Cut Set. The set composed of the bottom events causing the occurrence of the top event of the fault tree is called the cut set. The set consisting of the minimum number of bottom events causing the occurrence of the top event of the fault tree is called the minimum cut set.

(2) Method of Solving the Minimum Cut Set. There are two methods of solving for the minimum cut set, the downward method (Fussell-Vesely) and the upward method (Semanderes) [22]. The downward method starts from the top event layer by layer down and lists "OR" gate events and top events into different lines. Besides, "AND" gate events and

top events are listed in the same line. The non-minimum cut set is eliminated to obtain the minimum cut set until the basic events can no longer be decomposed. The upward method, i.e., proceeding from the bottom to the top, replaces the corresponding logic gate symbols with set symbols and expresses the fault tree structure-function in terms of event symbols and set operators. Finally, the expressions for the top event are listed to find the minimum cut set.

2.1.2. Quantitative FTA

(1) Calculation of the Occurrence Probability of Top Events. In the quantitative analysis of the fault tree, the probability of the top event can be calculated according to the occurrence probability of the bottom event and structural function. The probability of the occurrence of base event $X_i (i = 1, 2, \cdots, n)$ is assumed to be $P(X_i)(i = 1, 2, \cdots, n)$. When the logic gate is "OR" and "AND," and the occurrence of the base event is independent of each other, the calculation method of the probability of the top event is as follows:

(1) When the fault-tree logic gates are logical "OR" gates, the probability of at least one bottom event occurring is

$$P_{\cup} = 1 - [1 - P(X_1)] \times [1 - P(X_2)] \times \cdots \times [1 - P(X_n)]$$
$$= 1 - \prod_{i=1}^{n} [1 - P(X_i)]$$
$$(1)$$

(2) When the fault-tree logic gates are logical "AND" gates, the probability of n bottom events occurring simultaneously is

$$P_{\cap} = P(X_1) \times P(X_2) \times \cdots \times P(X_n) = \prod_{i=1}^{n} P(X_i) \quad (2)$$

(2) Calculation of probability's Importance of the Bottom Event. Importance is the magnitude of the contribution of the minimum cut set or bottom event to the occurrence of the top event, and the importance of the bottom event to the top event is positively related to its probability importance. If the probability's importance of a bottom event is close to 1, then the system must fail once that bottom event occurs.

Probability's importance is defined as

$$I_i(t) = \frac{\partial g(Q(t))}{\partial Q_i(t)}, \quad (3)$$

where Q is the unreliability of the system.

(3) Calculation of Subsystem Reliability. According to the traditional reliability theory, the general expression of the function between reliability and failure probability is

$$R(t) = e^{-\int_0^t \lambda(t)dt}, \quad (4)$$

where $\lambda(t)$ is the failure probability.

When $\lambda(t)$ is a constant, i.e., $\lambda(t) = \lambda$. Then, the reliability of the system is

$$R(t) = e^{-\lambda}. \quad (5)$$

According to the relationship between reliability and unreliability, the relationship between unreliability and failure probability is

$$F(t) = 1 - R(t) = 1 - e^{-\lambda}. \quad (6)$$

2.2. Fuzzy Fault Tree Analysis

2.2.1. L-R Fuzzy Number. The occurrence probability of the bottom event of the high-voltage power battery system of pure electric commercial vehicles is fuzzy. A fuzzy number is used to analyze the fault tree.

Generally, fuzzy numbers are described by reference functions. Let L and R be the reference functions of fuzzy numbers, if

$$\mu_{\tilde{A}}(x) = \begin{cases} L\left(\dfrac{m-x}{\alpha}\right), x \le m, \alpha > 0, \\ R\left(\dfrac{x-m}{\beta}\right), x \ge m, \beta > 0. \end{cases} \quad (7)$$

Then, the fuzzy number $\tilde{A}$ in Equation (7) is defined as $L\text{-}R$ fuzzy number. It is recorded as $\tilde{A} = (m, \alpha, \beta)_{LR}$, where m is the mean value of fuzzy number $\tilde{A}$, α and β are the upper and lower confidence limits of fuzzy number $\tilde{A}$, and $\mu_{\tilde{A}}(x)$ is the membership function of $\tilde{A}$. When α and β are equal to 0, $\tilde{A}$ is no longer a fuzzy number but a regular clear number. Moreover, larger α and β indicate more ambiguous $\tilde{A}$ [22]. α and β are generally taken as 10 to 20% of fuzzy mean m [23]. The commonly used membership functions of $L\text{-}R$ fuzzy numbers are triangular and normal.

(1) Triangular. The triangular membership function can be expressed as

$$\mu_{\tilde{A}}(x) = \begin{cases} 0, & x < m - \alpha, \\ 1 - \dfrac{m-x}{\alpha}, & m - \alpha \le x \le m, \\ 1 - \dfrac{x-m}{\beta}, & m < x \le m + \beta, \\ 0, & x > m + \beta. \end{cases} \quad (8)$$

Figure 1 shows the triangular membership function.
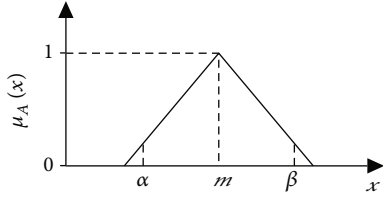
FIGURE 1: Triangular membership function

The λ-cut set interval of triangular fuzzy number $\tilde{A} = [(m-\alpha), m, (m+\beta)]$ is

$$\tilde{A}_\lambda = [(m-\alpha) + \alpha \bullet \lambda, (m+\beta) - \beta \bullet \lambda]. \tag{9}$$

If there are two triangular fuzzy numbers $\tilde{A}$ and $\tilde{B}$, there are four algorithms for expansion according to the classical extension principle [24] for any λ in interval $[0, 1]$.

(1) Fuzzy-number addition:

$$\tilde{A}_\lambda + \tilde{B}_\lambda = \left[L_A^\lambda, R_A^\lambda\right] + \left[L_B^\lambda, R_B^\lambda\right] = \left[L_A^\lambda + L_B^\lambda, R_A^\lambda + R_B^\lambda\right]. \tag{10}$$

(2) Fuzzy-number subtraction:

$$\tilde{A}_\lambda - \tilde{B}_\lambda = \left[L_A^\lambda, R_A^\lambda\right] - \left[L_B^\lambda, R_B^\lambda\right] = \left[L_A^\lambda - L_B^\lambda, R_A^\lambda - R_B^\lambda\right]. \tag{11}$$

(3) Fuzzy-number multiplication:

$$\tilde{A}_\lambda \times \tilde{B}_\lambda = \left[L_A^\lambda, R_A^\lambda\right] \times \left[L_B^\lambda, R_B^\lambda\right] = \left[L_A^\lambda \times L_B^\lambda, R_A^\lambda \times R_B^\lambda\right]. \tag{12}$$

(4) Fuzzy-number division:

$$\tilde{A}_\lambda / \tilde{B}_\lambda = \left[L_A^\lambda, R_A^\lambda\right] / \left[L_B^\lambda, R_B^\lambda\right] = \left[\frac{L_A^\lambda}{L_B^\lambda}, \frac{R_A^\lambda}{R_B^\lambda}\right]. \tag{13}$$

(2) Normal. The normal membership function can be expressed as

$$\mu_{\tilde{B}}(x) = \begin{cases} \left(\dfrac{m-x}{\alpha}\right)^2, & x \in \left[m - \alpha\sqrt{-ln\lambda}, m\right), \\ R(x) = e^{-((x-m)/\beta)^2}, & x \in \left(m, m + \beta\sqrt{-ln\lambda}\right], \\ 1, & x = m, \\ 0, & \text{others}. \end{cases} \tag{14}$$

The interval of the λ-cut set of normal type membership function $\tilde{B}$ can be obtained as

$$\tilde{B}_\lambda = \left[m - \alpha\sqrt{-ln\lambda}, m + \beta\sqrt{-ln\lambda}\right]. \tag{15}$$

Figure 2 shows the normal membership function.

2.2.2. Fuzzy Operator of the Fault Tree Analysis. The logic gate operator is used to calculate the probability of the basic bottom event, thus obtaining the probability of the top event of the traditional fault tree [25]. The system's occurrence probability of the top event, namely, the failure probability of the top event, can be accurately obtained by the bottom-event occurrence probability and structure function. Besides, system reliability can be obtained. Fuzzy number $\tilde{F}_i$ is introduced to represent the occurrence probability of the basic bottom event in the process of analyzing the fuzzy fault tree, and the fuzzy logic gate operator is used to replace the traditional one, which can obtain the fuzzy number of the occurrence of the top event [26].

Probability $\tilde{F}_i$ of the bottom event represented by a triangular fuzzy number that λ-cut set is

$$\begin{aligned} \tilde{F}_{1\lambda} &= [(m_1 - \alpha_1) + \lambda\alpha_1, (m_1 + \beta_1) - \lambda\beta_1], \\ \tilde{F}_{2\lambda} &= [(m_2 - \alpha_2) + \lambda\alpha_2, (m_2 + \beta_2) - \lambda\beta_2], \\ &\vdots, \\ \tilde{F}_{i\lambda} &= [(m_i - \alpha_i) + \lambda\alpha_i, (m_i + \beta_i) - \lambda\beta_i], \\ &\vdots, \\ \tilde{F}_{n\lambda} &= [(m_n - \alpha_n) + \lambda\alpha_n, (m_n + \beta_n) - \lambda\beta_n]. \end{aligned} \tag{16}$$

According to the characteristics of fault-tree logic "AND" and "OR" gates, the fuzzy operators of a triangular fuzzy number "AND" and "OR" gates are as follows.

(1) Logic "AND" gate:

$$\begin{aligned} \tilde{F}_{S\cap} &= \prod_{i=1}^n \tilde{F}_{i\lambda} = \tilde{F}_{i\lambda} \bullet \tilde{F}_{2\lambda} \bullet \tilde{F}_{3\lambda} \bullet \cdots \bullet \tilde{F}_{(n-1)\lambda} \bullet \tilde{F}_{n\lambda} \\ &= \left[\prod_{i=1}^n [(m_i - \alpha_i) + \lambda\alpha_i], \prod_{i=1}^n [(m_i + \beta_i) + \lambda\beta_i]\right]. \end{aligned} \tag{17}$$

(2) Logic "OR" gate:

$$\begin{aligned} \tilde{F}_{S\cup} &= 1 - \prod_{i=1}^n \left(1 - \tilde{F}_{i\lambda}\right) \\ &= \left[1 - \prod_{i=1}^n [1 - (m_i - \alpha_i) - \lambda\alpha_i], 1 - \prod_{i=1}^n \right. \\ &\quad \left. \cdot [1 - (m_i + \beta_i) + \lambda\beta_i]\right]. \end{aligned} \tag{18}$$
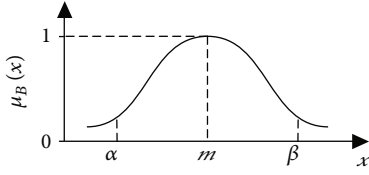
FIGURE 2: Normal membership function.

Probability $\tilde{F}_i$ of the bottom event represented by a normal fuzzy number that λ-cut sets is

$$
\begin{aligned}
\tilde{F}_{1\lambda} &= \left[m_1 - \alpha_1 \sqrt{-\ln \lambda}, \, m_1 + \beta_1 \sqrt{-\ln \lambda} \right], \\
\tilde{F}_{2\lambda} &= \left[m_2 - \alpha_2 \sqrt{-\ln \lambda}, \, m_2 + \beta_2 \sqrt{-\ln \lambda} \right], \\
&\qquad\qquad \vdots \, , \\
\tilde{F}_{i\lambda} &= \left[m_i - \alpha_i \sqrt{-\ln \lambda}, \, m_i + \beta_i \sqrt{-\ln \lambda} \right], \\
&\qquad\qquad \vdots \, , \\
\tilde{F}_{n\lambda} &= \left[m_n - \alpha_n \sqrt{-\ln \lambda}, \, m_n + \beta_n \sqrt{-\ln \lambda} \right].
\end{aligned}
\tag{19}
$$

Similarly, the fuzzy operators of "AND" and "OR" gates of normal fuzzy numbers are as follows.

(1) Logic "AND" gate:

$$
\begin{aligned}
\tilde{F}_{S\cap} &= \prod_{i=1}^{n} \tilde{F}_{i\lambda} = \tilde{F}_{i\lambda} \bullet \tilde{F}_{2\lambda} \bullet \tilde{F}_{3\lambda} \bullet \cdots \bullet \tilde{F}_{(n-1)\lambda} \bullet \tilde{F}_{n\lambda} \\
&= \left[\prod_{i=1}^{n} \left(m_i - \alpha_i \sqrt{-\ln \lambda} \right), \prod_{i=1}^{n} \left(m_i + \beta_i \sqrt{-\ln \lambda} \right) \right].
\end{aligned}
\tag{20}
$$

(2) Logic "OR" gate:

$$
\begin{aligned}
\tilde{F}_{S\cup} &= 1 - \prod_{i=1}^{n} \left(1 - \tilde{F}_{i\lambda} \right) \\
&= \left[1 - \prod_{i=1}^{n} \left[1 - \left(m_i - \alpha_i \sqrt{-\ln \lambda} \right) \right], 1 - \prod_{i=1}^{n} \right. \\
&\quad \left. \cdot \left[1 - \left(m_i + \beta_i \sqrt{-\ln \lambda} \right) \right] \right].
\end{aligned}
\tag{21}
$$

2.3. Polymorphic Fuzzy Fault-Tree Analysis

2.3.1. Multistate Fault Gate. When the input event of the system top event contains one or more multistate events, this logic gate is called a polymorphic fault gate. Supposing there are n polymorphic input events $X_i (i = 1, 2, \cdots, n)$ in the fault gate, i.e., the state of the input event meets $S_{X_i} \in$ $\{0, 0.5, 1\}$, $S_{X_i} \in \{normal, degradation, failure\}$. Then the state of top event U satisfies the following equation:

$$
S_U = \begin{cases}
0, & \sum_{i=1}^{n} S_{X_i} = 0, \\
0.5, & S_{X_i} \leq 0.5 \text{ and } \sum_{i=1}^{n} S_{X_i} \neq 0, \\
1, & \text{others.}
\end{cases}
\tag{22}
$$

Equation (22) shows that when the states of input polymorphic events are all 0, that is, all input polymorphic events are normal, and the state of output events is also normally 0. When the state of the input polymorphic event is 0.5 or a combination of 0 and 0.5, namely, the input polymorphic event is in a degraded state or a combination of the degraded state and normal state, and the state of the output event is also degraded. When at least one of the input polymorphic events is in state 1, that is, the state of at least one input event is in a failure state, and the output of the whole system is in a failure state.

2.3.2. Analysis of the Deteriorated-State Mode. Aiming at the problem to determine the exact probability of polymorphic bottom events in different states in the deteriorated-state mode, the work used group decision-making, expert experience, and fuzzy numbers. The probability of polymorphic bottom events in each state was obtained by averaging, defuzzifying, and normalizing the obtained fuzzy probability.

(1) Fuzzy Probability Obtained according to the Language Variables. Seven linguistic variables are introduced to combine fuzzy probability with linguistic variables [27]. Table 1 shows the relationship between language variables and the fuzzy probability.

The last column of Table 1 represents the triangular fuzzy number corresponding to the language variable, and this method can convert the expert experience into a fuzzy probability expressed in triangular fuzzy numbers (see Table 1). Namely, it is a constant under the membership function, and its value corresponds to the fuzzy probability and solved the problem of probability unknown.

If q experts are participating in the decision-making that the language variable of the bottom event X_i given by the k-th decision-maker in the $j (j = 1, 2, \text{and } 3)$, state is transformed into the fuzzy probability as $\tilde{P}_{ij}^k = (\alpha_{ij}^k, m_{ij}^k, \beta_{ij}^k) \, k = 1, 2, \cdots, q.$

(2) Fuzzy-Probability Averaging. The obtained fuzzy probability is mathematically averaged. Then, the fuzzy probability of bottom event X_i in state j is

$$
\tilde{P}_{ij}^{'} = \frac{\tilde{P}_{ij}^1 + \tilde{P}_{ij}^2 + \cdots + \tilde{P}_{ij}^q}{q}.
\tag{23}
$$

Table 1: Correspondence between language variables and the fuzzy probability.

Serial number	Fuzzy language	Semantic symbols	Triangular fuzzy number
1	Very high	VH	(0.9, 1.0, 1.0)
2	High	H	(0.7, 0.9, 1.0)
3	Generally high	GH	(0.5, 0.7, 0.9)
4	Medium	M	(0.3, 0.5, 0.7)
5	Generally low	GL	(0.1, 0.3, 0.5)
6	Low	L	(0, 0.1, 0.3)
7	Very low	VL	(0, 0, 0.1)

(3) *Defuzzification*. After the fuzzy probability is processed by the mean area method, the accurate probability of each bottom event X_i in state j is obtained as follows:

$$P'_{ij} = \frac{\tilde{P}'_{ij}(1) + 2\tilde{P}'_{ij}(2) + \tilde{P}'_{ij}(3)}{4}. \quad (24)$$

(4) *Normalization*. The accurate probability of the bottom event in each state is normalized to ensure that the sum of the probabilities of the bottom event in each state is 1. After processing, the accurate probability of each bottom event X_i in state j is obtained as

$$P_{ij} = \frac{P'_{ij}}{\sum_{j=1}^{3} P'_{ij}}. \quad (25)$$

3. Fault-Tree Analysis of the High-Voltage Power Battery System

3.1. Working Principle of the High-Voltage Power Battery System. The high-voltage power battery pack provides electricity for pure electric commercial vehicles. Its high-voltage DC output flows the high-voltage power equipment such as the steering power motor, brake air pump motor, and DC/DC motor inverter. The high-voltage current flowing through the motor inverter is converted into a three-phase alternating current and flows into the high-voltage drive motor and electric air conditioner motor through the high-voltage wiring harness. Figure 3 shows the working principle of the high-voltage power battery system.

3.2. Establishment of the Fault Tree for the High-Voltage Power Battery System. The fault types of the high-voltage power battery system of pure electric commercial vehicles mainly include the battery-module fault and battery-management-system fault. Battery module faults are mainly single-cell and battery-pack ones. Single-cell faults are manifested by electrolyte decomposition, active substance shedding, and the internal short circuit of the battery. Battery pack faults are manifested by single-cell inconsistency, and charging faults and battery-management-system faults are manifested by no communication, electromagnetic interference, and low drive voltage.

For the high-voltage power battery system, the power battery system fault was selected as the top event, and two intermediate events were established—the functional failure mode and state deterioration mode. The functional-failure mode was divided into battery module failure and battery management system failure to analyze the bottom event, and these two events were regarded as intermediate ones of a lower level. Then, the battery module fault and battery management system fault were analyzed until they were decomposed into events that could not be decomposed, i.e., the bottom event of the subfault tree of the functional failure mode. Meanwhile, the subfault tree of the deteriorated-state mode was decomposed and analyzed. Besides, the events of the established polymorphic fuzzy fault tree of the high-voltage power battery system were coded. The fault of the power battery system was recorded as T, and Table 2 shows the event definition and code.

According to Table 2, the polymorphic fault tree of the high-voltage power battery system of pure electric commercial vehicles is simplified as shown in Figure 4.

3.3. Qualitative Analysis of the Fault Tree. When the minimum cut set of the polymorphic fault tree is calculated, only the qualitative analysis of the subfault tree of functional failure mode is carried out due to polymorphic events and polymorphic fault gates in the subfault tree of the deteriorated-state mode. The fault tree established in the work uses the downward method according to the principle of multiplication of the "AND" gate and the addition of the "OR" gate.

$$
\begin{aligned}
U_1 &= E_5 + V_1 + V_2, \\
V_1 &= W_1 + W_2, \\
V_2 &= W_3 + W_4 + W_5, \\
W_1 &= S_1 + S_2 + S_3, \\
W_2 &= S_4 + S_5, \\
W_3 &= E_{21} + E_{22} + E_{23}, \\
W_4 &= E_{24} + E_{25} + E_{26} + E_{27} + E_{28}, \\
W_5 &= S_6 + S_7, \\
S_1 &= E_6 + E_7 + E_8, \\
S_2 &= E_9 + E_{10}, \\
S_3 &= E_{11} + E_{12}, \\
S_4 &= E_{13} + E_{14}, \\
S_5 &= E_{15} + K_1 + K_2, \\
S_6 &= E_{29} + E_{30}, \\
S_7 &= E_{31} + E_{32}, \\
K_1 &= E_{16} + E_{17}, \\
K_2 &= E_{18} + E_{19} + E_{20}.
\end{aligned}
\quad (26)
$$
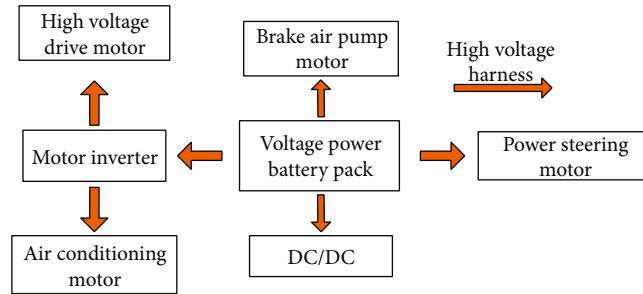
FIGURE 3: Working principle of the high-voltage power battery system.

TABLE 2: Event definitions and codes.

Event name	Event code	Event name	Event code
Functional-failure mode	U_1	Deteriorated-state mode	U_2
Battery module failure	V_1	Management system failure	V_2
Battery unit failure	W_1	Battery pack failure	W_2
No CAN communication	W_3	Inaccurate signal	W_4
No execution	W_5	Overtemperature	S_1
Short circuit	S_2	Low voltage	S_3
Monomer inconsistency	S_4	Charging fault	S_5
Fan failure	S_6	Main relay fault	S_7
Cannot be charged	K_1	High charge voltage	K_2
Electrolyte redox	E_1	Positive material phase change	E_2
Negative electrode material aging	E_3	Aging of diaphragms and increased porosity	E_4
Insulation failure	E_5	Fan not ON	E_6
Loose connection	E_7	Increased internal resistance of the battery	E_8
Plate damage	E_9	Short circuit	E_{10}
Low SOC	E_{11}	Capacity attenuation	E_{12}
Inconsistent voltage	E_{13}	Inconsistent temperature	E_{14}
Charger fault	E_{15}	Shedding of active substances	E_{16}
Battery deformation	E_{17}	Low-temperature environment	E_{18}
Late life	E_{19}	High SOC	E_{20}
No external internal resistance	E_{21}	CAN high and low reverse connection	E_{22}
Software bug	E_{23}	Impact fault	E_{24}
Bias fault	E_{25}	Electromagnetic interference	E_{26}
Sampling circuit fault	E_{27}	Connection line failure	E_{28}
Line damage	E_{29}	Damaged cooling fan	E_{30}
No working power supply	E_{31}	Low driving voltage	E_{32}

Then,

$$U_1 = E_5 + E_6 + E_7 + E_8 + \cdots + E_{30} + E_{31} + E_{32}. \qquad (27)$$

Therefore, the minimum cut set of the functional failure mode's subfault tree of the power battery system is $\{E_5\}$, $\{E_6\}, \{E_7\}, \{E_8\}, \cdots, \{E_{31}\}, \{E_{32}\}$, where the minimum cut set contains 28 basic base events.

3.4. Quantitative Analysis of Fault Tree. Two intermediate events of the functional failure mode and deteriorated-state mode are selected for analysis to more accurately reflect the failure mode of the high-voltage power battery system. The subfault tree of functional failure mode is solved by the fuzzy fault tree analysis, and the subfault tree of deteriorated-state mode is solved by group decision-making and fuzzy probability.
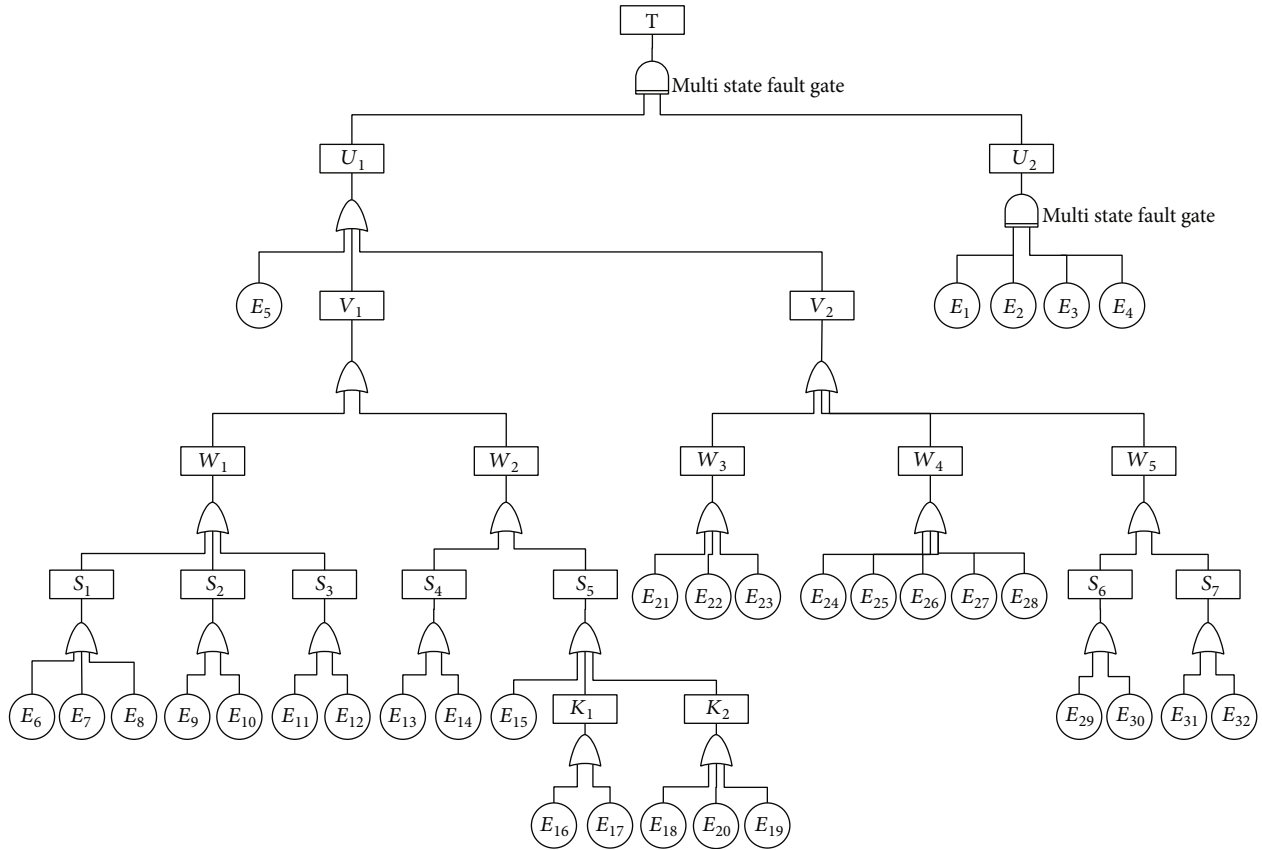
Figure 4: Multistate fault tree of the high-voltage power battery system.

3.4.1. Quantitative Analysis of the Subfault Tree of the Functional Failure Mode. According to the data and relevant experience and the probability of subfault tree bottom event of the functional failure mode (see Table 3).

In Table 3, m represents the mean of the fuzzy number, which is a dimensionless number, indicating the size of the fuzzy probability of the occurrence of the bottom event. The larger the mean of m, the greater the fuzzy probability of the occurrence of the bottom event, and the smaller of m, the smaller the fuzzy probability of the bottom event occurring. According to the reference of [23], the upper and lower limits of α and β take 10 to 20% of the fuzzy mean m, considered the harshness of the actual working environment of the high-voltage power battery system and the ambiguity of the probability of causing system failure, and according to Figure 1, the larger the value of α and β, the larger the fuzzy probability interval, and the reverse is the opposite, when α and β take 10% of the mean of m, and the probability interval is contained in the 20% probability interval of α and β taking m, so in order to make the probability interval better represent the fuzzy probability of the event occur and then selected α and β as 20% of m in combination with the data.

The interval of each bottom event can be obtained using Table 3, Equation (16), and the triangular membership function.

Since top event $U_1 = E_5 + E_6 + E_7 + E_8 + \cdots + E_{30} + E_{31} + E_{32}$, Equation (18) is used to select the triangular member-

ship function. The probability section of top event U_1 varies with λ (see Figure 5 for the scattering curve).

The interval of each bottom event can be obtained from Table 3, Equation (19), and the normal membership function.

Similarly, when the normal membership function is selected, the probability of top event U_1 varies with λ (see Figure 6 for the scattering curve).

By comparing Figures 5 and 6, it can be seen that whether triangular membership function or normal membership function is selected, the probability interval of the top event becomes smaller and smaller with increased λ. When λ is equal to 1, the interval is an accurate number, consistent with the theory. However, for the normal membership function, when λ tends to 0, the fuzzy operator of the top event tends to infinity. The closer it is to 0, the greater the fuzzy probability interval of the top event. When $\lambda \in (0, 1]$, the whole probability interval about the change of λ is nonlinear, and the absolute value of the slope of the upper and lower bounds of the top-event probability curve decreases as λ increases. That is, the closer it is to 0, the greater the changing trend of the curve; the closer it is to 1, the more gentle the change of the curve.

When λ takes the special value of 0.01, Equation (21) is used to obtain that the probability interval of top-event occurrence is [0.4230, 0.7644] and the corresponding reliability interval of the top event is [0.4656, 0.6551]. Compared with the triangular fuzzy operator, the interval is too

TABLE 3: Probability of the bottom event of the functional failure mode.

Event code	m	α	β
E_5	0.026	0.0052	0.0052
E_6	0.046	0.0092	0.0092
E_7	0.016	0.0032	0.0032
E_8	0.016	0.0032	0.0032
E_9	0.026	0.0052	0.0052
E_{10}	0.018	0.0036	0.0036
E_{11}	0.1	0.02	0.02
E_{12}	0.05	0.01	0.01
E_{13}	0.016	0.0032	0.0032
E_{14}	0.016	0.0032	0.0032
E_{15}	0.01	0.002	0.002
E_{16}	0.01	0.002	0.002
E_{17}	0.06	0.012	0.012
E_{18}	0.12	0.024	0.024
E_{19}	0.016	0.0032	0.0032
E_{20}	0.05	0.01	0.01
E_{21}	0.028	0.0056	0.0056
E_{22}	0.14	0.028	0.028
E_{23}	0.02	0.004	0.004
E_{24}	0.014	0.0028	0.0028
E_{25}	0.025	0.005	0.005
E_{26}	0.016	0.0032	0.0032
E_{27}	0.026	0.0052	0.0052
E_{28}	0.02	0.004	0.004
E_{29}	0.018	0.0036	0.0036
E_{30}	0.016	0.0032	0.0032
E_{31}	0.014	0.0028	0.0028
E_{32}	0.012	0.0024	0.0024

FIGURE 5: Probability interval distribution of top events changing with λ under the triangular membership function.
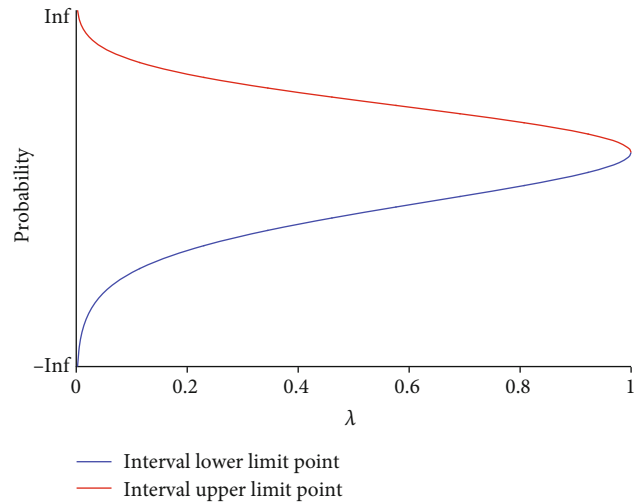
FIGURE 6: Probability interval distribution of top events changing with λ under the normal membership function.

fuzzy and has no practical significance. Therefore, considering the fuzziness of the occurrence probability of the bottom event and the rationality of operation, the triangular fuzzy operator is selected to calculate the fuzzy probability interval of the top event.

Figure 5 shows that the upper and lower limits of the probability of top-event occurrence are approximately linear. Hence, the least square linear fitting and the intercept interval for the occurrence of the top event of the functional failure mode are used to obtain

$$\tilde{F}_{U_1} = [0.0838\lambda + 0.5415, -0.0694\lambda + 0.6947]. \quad (28)$$

Therefore, please see as follows:

(1) When $\lambda = 1$, the probability of the bottom event of the functional failure mode is a certain value, and

that of the functional failure U_1 of the high-voltage power battery system of the top event is

$$\tilde{F}_{U_1, \lambda=1} = 0.6253 \quad (29)$$

When $\lambda = 1$, the reliability of functional failure mode U_1 of the high-voltage power battery system of the top event can be obtained from Equation (5).

$$R_{U_1, \lambda=1} = 0.5351. \quad (30)$$

(2) When $\lambda = 0$, the probability of the bottom event of the functional-failure mode is a fuzzy number and $\tilde{F}_{U_1}$ is an interval range, i.e., the probability interval

of function-failure U_1 of the high-voltage power battery system of the top event is

$$\tilde{F}_{U_1,\lambda=0} = [0.5415, 0.6947] \qquad (31)$$

That is, the minimum probability of top event U_1 is 0.5415, and the maximum is 0.6947.

When $\lambda = 0$, the reliability interval of functional failure mode U_1 of the high-voltage power battery system of the top event can be obtained from Equation (5).

$$R_{U_1,\lambda=0} = [0.4992, 0.5819]. \qquad (32)$$

3.4.2. Quantitative Analysis of the Subfault Tree in the Deteriorated State.
According to the definition of a polymorphic fault gate, when U_1 does not occur and U_2 is in a degraded state, the power battery system is in a degraded state and is not recognized as failure. At this time, the high-voltage power battery system of pure electric commercial vehicles does not need immediate maintenance, consistent with the actual operation condition. When U_1 occurs or U_2 is in a failure state, the high-voltage power battery system is in a failure state and needs to be overhauled.

The decision information of the decision-maker is collected by group decision-making because the probability of each bottom event in each state of the subfault tree of the deteriorated-state mode cannot be accurately obtained. According to the conclusion of the relationship between group size and decision-making, when the number of group decision-makers is 2-5, consensus can be obtained; moreover, 5-11 people are the most effective to draw more correct conclusions.

Consequently, the work collected the probability of four polymorphic bottom events in each state from five experts and combined the language variables of expert opinions with the corresponding triangular fuzzy numbers (see Table 4).

(1) Averaging of Fuzzy Probability. According to the corresponding relationship between language variables and fuzzy probability in Table 1 and Equation (23), the mean value of the fuzzy probability of each polymorphic bottom event in each state is determined as follows:

$$\tilde{P}'_{1-0} = (0.82, 0.96, 1.0), \tilde{P}'_{1-0.5} = (0.1, 0.22, 0.38), \tilde{P}'_{1-1} = (0, 0, 0.1),$$
$$\tilde{P}'_{2-0} = (0.82, 0.96, 1.0), \tilde{P}'_{2-0.5} = (0.1, 0.26, 0.46), \tilde{P}'_{2-1} = (0, 0, 0.1),$$
$$\tilde{P}'_{3-0} = (0.82, 0.96, 1.0), \tilde{P}'_{3-0.5} = (0.08, 0.2, 0.38), \tilde{P}'_{3-1} = (0, 0, 0.1),$$
$$\tilde{P}'_{4-0} = (0.86, 0.98, 1.0), \tilde{P}'_{4-0.5} = (0.1, 0.24, 0.42), \tilde{P}'_{4-1} = (0, 0, 0.1).$$
$$\qquad (33)$$

(2) Defuzzification of the Fuzzy Probability. The fuzzy probability is defuzzified according to Equation (24) to convert the obtained fuzzy probability into accurate probability, that is,

$$P'_{1-0} = 0.935, P'_{1-0.5} = 0.230, P'_{1-1} = 0.025,$$
$$P'_{2-0} = 0.935, P'_{2-0.5} = 0.270, P'_{2-1} = 0.025,$$
$$P'_{3-0} = 0.935, P'_{3-0.5} = 0.215, P'_{3-1} = 0.025,$$
$$P'_{4-0} = 0.955, P'_{4-0.5} = 0.250, P'_{4-1} = 0.025.$$
$$\qquad (34)$$

(3) Normalization of exact probability. According to Equation (25), the accurate probability of polymorphic bottom events occurring in each state is normalized to obtain

$$P_{1-0} = 0.7857, P_{1-0.5} = 0.1933, P_{1-1} = 0.0210,$$
$$P_{2-0} = 0.7602, P_{2-0.5} = 0.2195, P_{2-1} = 0.0203,$$
$$P_{3-0} = 0.7957, P_{3-0.5} = 0.1830, P_{3-1} = 0.0213,$$
$$P_{4-0} = 0.7764, P_{4-0.5} = 0.2033, P_{4-1} = 0.0203.$$
$$\qquad (35)$$

According to the structural characteristics of a multistate fault gate, when at least one bottom event state is 1, the system's top-event output is in the failure state. According to the calculated occurrence probability of each state of the polymorphic bottom event, the probability of each polymorphic bottom event in state 1 is substituted into Equation (1). The occurrence probability of the sub-fault tree of the top event in the deteriorated-state mode is

$$P_{U2} = 1 - (1 - P_{1-1}) \times (1 - P_{2-1}) \times (1 - P_{3-1}) \times (1 - P_{4-1})$$
$$= 0.0804.$$
$$\qquad (36)$$

According to Equation (5), the subfault tree reliability in the deteriorated mode can be obtained.

$$R_{U_2} = 0.9228. \qquad (37)$$

(1) $R_{U1,\lambda=1} = 0.5351$ when $\lambda = 1$. The reliability of the high-voltage power battery system of pure electric commercial vehicles is

$$R_T = 0.4938 \qquad (38)$$

(2) $R_{U1,\lambda=0} = [0.4992, 0.5819]$ when $\lambda = 0$. The reliability of the high-voltage power battery system of pure electric commercial vehicles is

$$R_T = [0.4607, 0.5370] \qquad (39)$$

TABLE 4: Expert opinion and fuzzy probability of the bottom event in each state.

| Bottom event | E_1 | | | E_2 | | | E_3 | | | E_4 | | |
State	0	0.5	1	0	0.5	1	0	0.5	1	0	0.5	1
Expert 1	VH	GL	VL	H	L	VL	VH	GL	VL	H	VL	VL
Expert 2	VH	GL	VL	VH	GL	VL	VH	L	VL	VH	L	VL
Expert 3	H	VL	VL	VH	GL	VL	H	VL	VL	VH	GL	VL
Expert 4	H	VL	VL	H	L	VL	H	L	VL	VH	M	VL
Expert 5	VH	M	VL	VH	M	VL	VH	M	VL	VH	GL	VL

4. Fuzzy Probability Importance of the Bottom Event

Similar to the probability's importance of the bottom event of the traditional fault tree, the fuzzy probability's importance of the bottom event also refers to the degree to which the probability of the top event is affected when the probability of the bottom event changes. According to the definition of Equation (3), the fuzzy probability's importance is

$$I_h(j) = \frac{\partial h(p)}{\partial p_j}, j = 1, 2, 3, \cdots, n, \tag{40}$$

where $h(p) = h(p_1, p_2, p_3, \cdots, p_n)$ is the unreliability function of the top event; p_j the fuzzy probability of the occurrence of the jth bottom event. Triangular fuzzy numbers were selected to analyze the probability of bottom events of the subfault tree of the functional failure mode in the work. Besides, the logic gates of the subtree of the established functional failure mode are "OR" gates, so we can obtain

$$h(p) = 1 - \prod_{i=1}^{n}\left(1 - \tilde{F}_{i\lambda}\right)\left[1 - \prod_{i=1}^{n}[1 - (m_i - \alpha_i) - \lambda\alpha_i], 1 - \prod_{i=1}^{n} \right.$$
$$\left. \cdot [1 - (m_i + \beta_i) + \lambda\beta_i]\right], \tag{41}$$

$$p_j = [(m_i - \alpha_i) + \lambda\alpha_i, (m_i + \beta_i) - \lambda\beta_i]. \tag{42}$$

Equations (40), (41), and (42) are used to obtain

$$I_h(j) = \frac{\partial h(p)}{\partial p_j}$$
$$= \prod_{i=1,i \neq j}^{n}\{[1 - (m_i - \alpha_i) - \lambda\alpha_i], [1 - (m_i + \beta_i) + \lambda\beta_i]\}. \tag{43}$$

It can be seen from the previous chapters that in the high-voltage power battery system of pure electric commercial vehicles, although the probability of each fault of the bottom event is low, the reliability of the whole system is only 0.4938. Therefore, the probability's importance of each bottom event is vital for the prevention and improvement of top events. The bottom event of the subfault tree of the func-

TABLE 5: Interval of probability's importance of the bottom event.

Code	Probability interval	Code	Probability interval
E_5	[0.3163, 0.4695]	E_6	[0.3243, 0.4773]
E_7	[0.3124, 0.4657]	E_8	[0.3124, 0.4657]
E_9	[0.3163, 0.4695]	E_{10}	[0.3132, 0.4665]
E_{11}	[0.3482, 0.4998]	E_{12}	[0.3260, 0.4789]
E_{13}	[0.3124, 0.4657]	E_{14}	[0.3124, 0.4657]
E_{15}	[0.3102, 0.4635]	E_{16}	[0.3102, 0.4635]
E_{17}	[0.3302, 0.4830]	E_{18}	[0.3580, 0.5086]
E_{19}	[0.3124, 0.4657]	E_{20}	[0.3260, 0.4789]
E_{21}	[0.3171, 0.4703]	E_{22}	[0.3683, 0.5178]
E_{23}	[0.3140, 0.4673]	E_{24}	[0.3117, 0.4650]
E_{25}	[0.3159, 0.4692]	E_{26}	[0.3124, 0.4657]
E_{27}	[0.3163, 0.4695]	E_{28}	[0.3140, 0.4673]
E_{29}	[0.3132, 0.4665]	E_{30}	[0.3124, 0.4657]
E_{31}	[0.3116, 0.4650]	E_{32}	[0.3109, 0.4642]

tional failure mode is taken as the research object. According to Equation (43), $\lambda = 0$ is introduced to obtain the interval of probability's importance of each bottom event of the subfault tree in the functional failure mode (see Table 5). Figure 7 shows the broken line of the interval of probability's importance.

According to Table 5, the fuzzy importance ranking of the bottom event can be obtained as follows.

$$I_h(22) > I_h(18) > I_h(11) > I_h(17) > \cdots > I_h(16) = I_h(15). \tag{44}$$

In terms of the event definition and code in Table 2, the maximum importance interval of CAN high and low reverse connection probability is [0.3683, 0.5178], and the minimum is [0.3102, 0.4635]. The relationship between the importance of each probability is as follows: CAN high and low reverse connection > low-temperature environment > low SOC > battery deformation > $\cdots$ >shedding of active substances = charger fault.

In the light of the previous section, the higher the probability's importance of the bottom event, the greater the impact on the high-voltage power battery system of pure electric commercial vehicles. Figure 7 shows that
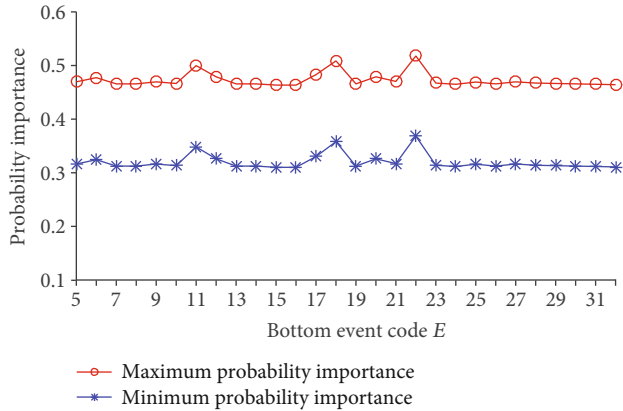
FIGURE 7: Broken lines of importance interval of bottom event's probability of the high-voltage battery system.

the probability's importance of the bottom event coded as E_{11}, E_{17}, E_{18}, and E_{22} is higher than that of other bottom events. The corresponding bottom events are low SOC, battery deformation, low-temperature environment, CAN high, and low reverse connection. Compared with the four bottom events, the fluctuation of the probability's importance interval of the other bottom events is relatively small, and the changing trend of the broken line chart of the corresponding probability's importance interval is relatively flat. Therefore, these four bottom events with probability's high importance are the weak links of the high-voltage power battery system. We should focus on the optimization and timing detection of these four bottom events.

During designing, testing, and optimizing the high-voltage power battery system of pure electric commercial vehicles, the bottom event with a high probability of importance is selected according to the probability's importance interval curve of the high-voltage battery system, which can improve the tests of the whole system to a certain extent and reduce the occurrence of serious failures.

5. Conclusions

Taking a pure electric commercial vehicle as an example, the work analyzed the reliability of the high-voltage power battery system. The basic theory of polymorphic fuzzy fault-tree analysis, the working principle of the high-voltage power battery system and fault type, and the polymorphic fuzzy fault tree of the high-voltage power battery system were introduced to divide the fault tree into two sub-fault trees (functional failure and deteriorated-state modes) for qualitative and quantitative analysis.

The triangular membership function was selected as the fuzzy operator for the bottom event of the subfault tree in the functional failure mode by comparing the influences between the triangular membership function and the normal membership function on the probability interval of the top event. It could solve the subfault tree in a functional failure mode with better effect and obtain its reliability. For the subfault tree in the deteriorated-state mode, the expert expe-

rience and triangular fuzzy numbers were combined by the group decision theory, with the fuzzy probability averaged, defuzzified, and normalized. Accurate probability was obtained to solve the subfault tree in the deteriorated-state mode and the reliability of the high-voltage power battery system.

Finally, the fuzzy probability's importance analysis of bottom events of the functional failure mode showed that the key weak links of the system were low SOC, Battery deformation, low-temperature environment, CAN high, and low reverse connection. In system design and fault detection, checking according to the importance of probability can improve system's fault detection. The calculation results showed that although the state deterioration mode did not play a decisive role in system failure, it is still a potential safety hazard to system failure from the reliability of the whole high-voltage power battery system as well as an indispensable detection link in the process of fault detection.

Data Availability

The dataset and codes of the work for the simulation are available from the corresponding author if requested.

Conflicts of Interest

The authors declare that there is no conflict of interest regarding the publication of this paper.

Acknowledgments

References

[1] H. Huang, X. Tong, and M. J. Zuo, "Posbist fault tree analysis of coherent systems," *Reliability Engineering & System Safety*, vol. 84, no. 2, pp. 141–148, 2004.

[2] B. S. Dhillon, *Design reliability: fundamentals and applications*, CRC press, 1999.

[3] F. A. Rahman, A. Varuttamaseni, M. Kintner-Meyer, and J. C. Lee, "Application of fault tree analysis for customer reliability assessment of a distribution power system," *Reliability Engineering & System Safety*, vol. 111, pp. 76–85, 2013.

[4] S. Yang, H. Li, Y. Yue, J. Hao, W. Luo, and M. Zhao, "Summary on reliability analysis of distributed power access on distribution network," *AIP Conference Proceedings. AIP Publishing LLC*, vol. 1955, no. 1, article 040016, 2018.

[5] G. Lanza, P. Werner, D. Appel, and B. Behmann, "Increased trustability of reliability prognoses for machine tools," in *Glocalized Solutions for Sustainability in Manufacturing*, J. Hesselbach and C. Herrmann, Eds., pp. 225–228, Springer, Berlin, Heidelberg, 2011.

[6] X. Li, H. Shao, S. Lu, J. Xiang, and B. Cai, "Highly-efficient fault diagnosis of rotating machinery under time-varying speeds using LSISMM and small infrared thermal images," *IEEE Transactions on Systems, Man, and Cybernetics: Systems*, 2022.

[7] H. Cao, H. Shao, X. Zhong, Q. Deng, X. Yang, and J. Xuan, "Unsupervised domain-share CNN for machine fault transfer diagnosis from steady speeds to time-varying speeds," *Journal of Manufacturing Systems*, vol. 62, pp. 186–198, 2022.

[8] L. Xin, S. Haidong, J. Hongkai, and X. Jiawei, "Modified Gaussian convolutional deep belief network and infrared thermal imaging for intelligent fault diagnosis of rotor-bearing system under time-varying speeds," *Structural Health Monitoring*, vol. 21, no. 2, pp. 339–353, 2022.

[9] H. Tanaka, L. T. Fan, F. S. Lai, and K. Toguchi, "Fault-tree analysis by fuzzy probability," *IEEE Transactions on Reliability*, vol. 32, no. 5, pp. 453–457, 1983.

[10] D. Singer, "A fuzzy set approach to fault tree and reliability analysis," *Fuzzy Sets Systems*, vol. 34, no. 2, pp. 145–155, 1990.

[11] D. Yuhua and Y. Datao, "Estimation of failure probability of oil and gas transmission pipelines by fuzzy fault tree analysis," *Journal of Loss Prevention in the Process Industries*, vol. 18, no. 2, pp. 83–88, 2005.

[12] Y. Liu, Z. Zhang, and M. Zhong, "Reliability analysis on the injection system by mapping TS fault trees into Bayesian networks," in *3rd International Conference on Mechatronics, Robotics, and Automation*, pp. 1134–1139, Shanghai, China, 2015.

[13] H. Yin, C. Liu, W. Wei, K. Song, D. Liu, and Y. Dan, "Safety assessment of natural gas storage tank using similarity aggregation method based fuzzy fault tree analysis (SAM-FFTA) approach," *Journal of Loss Prevention in the Process Industries*, vol. 66, article 104159, 2020.

[14] A. Satyanarayana and A. Prabhakar, "New topological formula and rapid algorithm for reliability analysis of complex networks," *IEEE Transactions on Reliability*, vol. R-27, no. 2, pp. 82–100, 1978.

[15] F. Iscioglu, "A new approach in the mean residual lifetime evaluation of a multi-state system," *Proceedings of the Institution of Mechanical Engineers, Part O: Journal of Risk and Reliability*, vol. 235, no. 4, pp. 700–710, 2021.

[16] C. L. Borges, D. M. Falcao, J. C. Mello, and A. C. Melo, "Composite reliability evaluation by sequential Monte Carlo simulation on parallel and distributed processing environments," *IEEE Transactions on Power Systems*, vol. 16, no. 2, pp. 203–209, 2001.

[17] S. Mahadevan, R. Zhang, and N. Smith, "Bayesian networks for system reliability reassessment," *Structural Safety*, vol. 23, no. 3, pp. 231–251, 2001.

[18] F. Mohammadhasani and A. Pirouzmand, "Multi-state unavailability analysis of safety system redundant components with aging effect under surveillance testing," *Progress in Nuclear Energy*, vol. 126, no. 1, article 103415, 2020.

[19] K. Chen, S. He, E. Xu, R. Tang, and Y. Wang, "Research on ride comfort analysis and hierarchical optimization of heavy vehicles with coupled nonlinear dynamics of suspension," *Measurement*, vol. 165, article 108142, 2020.

[20] S. He, T. Tang, M. Ye, E. Xu, J. Deng, and R. Tang, "A domain association hierarchical decomposition optimization method for cab vibration control of commercial vehicles," *Measurement*, vol. 138, pp. 497–513, 2019.

[21] P. O'Connor and A. Kleyner, *Practical reliability engineering*, John Wiley & Sons, 2012.

[22] J. P. Sawyer, "Fault tree analysis of mechanical systems," *Microelectron and Reliability*, vol. 54, no. 4, pp. 653–667, 1994.

[23] J. Zhang, "Reliability analysis of high voltage electric system of pure electric passenger car based on polymorphic fuzzy fault tree," *Journal of Intelligent & Fuzzy Systems*, vol. 38, no. 4, pp. 3747–3754, 2020.

[24] H. O. Wang and K. Tanaka, *Fuzzy control systems design and analysis: a linear matrix inequality approach*, John Wiley & Sons, 2004.

[25] H.-Z. Huang, Z.-J. Liu, Y. Yanfeng Li, and L. H. Liu, "A warranty cost model with intermittent and heterogeneous usage," *Maintenance and Reliability*, vol. 4, pp. 9–15, 2008.

[26] R. Kenarangui, "Event-tree analysis by fuzzy probability," *IEEE Transactions on Reliability*, vol. 40, no. 1, pp. 120–124, 1991.

[27] C. D. Wickens, W. S. Helton, J. G. Hollands, and S. Banbury, *Engineering Psychology and Human Performance*, Routledge Publishers, 5th edition, 2021.

Research Article

Robot Path Planning Based on an Improved Salp Swarm Algorithm

Xianbao Cheng,[1] Liucun Zhu [iD],[2] Huihui Lu,[1] Jinzhan Wei,[2] and Ning Wu [iD][2]

[1]*School of Electronics and Information Engineering, Beibu Gulf University, No. 12, Binhai Avenue, Qinzhou, Guangxi, China*
[2]*Advanced Science and Technology Research Institute, Beibu Gulf University, No. 12, Binhai Avenue, Qinzhou, Guangxi, China*

Correspondence should be addressed to Liucun Zhu; lczhu@bbgu.edu.cn and Ning Wu; n.wu@bbgu.edu.cn

This paper demonstrates an improved version of the Salp Swarm Algorithm (SSA) to solve the problems of slow convergence and local minima of the original version. In the population initialization of this scheme, ten chaotic searches with dynamic inertia coefficients are introduced to increase the diversity so that the probability of being trapped in local minima is reduced. Genetic algorithms are then applied to improve the global search ability and convergence speed. The experiments with 12 test functions show that the improved version achieves better accuracy and convergence speed over the original SSA. In the test with robot path planning problem, the proposed algorithm shows improved performance in the average number of iterations, path length, and average number of turns by 69.2%, 19.1%, and 43%, respectively, compared with the original SSA.

1. Introduction

Traditional mathematical methods are effective to solve linear and differentiable optimization problems, but for more complicated problems like nondifferentiable functions, more intelligent algorithms are needed. Intelligent algorithms solve optimization problems by imitating natural phenomena, for example, Particle Swarm Optimization (PSO) [1] simulates bird foraging behavior, Gray Wolf Algorithm (GWA) [2] focuses on wolf predation behavior, and artificial bee colony algorithm (ABC) [3] simulates bee foraging behavior.

The Salp Swarm Algorithm (SSA) [4] is a relatively new swarm intelligence algorithm to simulate the foraging behavior of the sea swarm slap. As a new heuristic optimization algorithm, the SSA has the advantages of less parameter requirements and effectiveness for both continuous and discrete problems.

Salp is one kind of Salpidae with a transparent barrel-shaped body similar to jellyfishes with a length of about 1~10 cm. Salps do not behave active locomotion, and the movement is performed by pumping water through the body as propulsion to go forward. The individual salp does

not forage very well, and they live in groups to get more feeding. When salps prey in groups, multiple of them are lined up to form a chain structure (salp chain). The first salp in the chain is called the leader, and the rest is called the follower. The leader guides the whole chain, and the followers are mobile following each other [4]. The leader leads the followers to move towards the food source for global search, while the followers go accordingly for a local search. In the SSA, the position update of each follower will only be affected by the position of the previous follower, and the leader's position update is only affected by the food source position. The hierarchical system of the SSA makes the followers cooperate closely with each other to increase the optimization efficiency and reduce the chance of being trapped in a local optimum. The SSA has been widely used in many industrial applications such as variable speed wind turbine [5], industrial design [6], extreme learning machine [7], feature selection [8], neural network [9], image segmentation [10], and biomedicine [11–13].

Path planning is a key topic for the mobility of the robot to navigate the robot automatically from one position to another [14, 15]. Robots often face uncertain and complex

operating environment, and in the meantime time, an efficient path connecting one position to another in this environment is required to be found quickly and accurately [16, 17]. Depending on the operation task of the robot, the optimal path of an environment is generally evaluated based on the shortest distance or time, the minimum energy consumption, or the highest safety rate. The path planning algorithm with superior performance can plan the most efficient path in the uncertain and complex environment, to increase the working efficiency of the robot and reduce the wear and tear of robot. Since one of the key technologies of mobile robot is to look for the optimal path solution for a task, path planning algorithm has become a research hotspot in recent years [18].

Traditional algorithms to solve the path planning problem in known environments include artificial potential field method [19–21], A∗ algorithm [22–24], Dijkstra algorithm [25–27], and rapidly-exploring random tree (RRT) [28–30]. However, the exploration performance of these algorithms is generally poor, and it is difficult for them to find the optimal path in an unknown environment. For this reason, a swarm intelligence algorithm was introduced to make use of the exploration and optimization performance to find the optimal path, such as the Particle Swarm Optimization (PSO) [31], the ant colony (AC) [32], the whale algorithm for UAV path planning [33], and the water wave algorithm for the path planning of underwater vehicles [34]. However, the performance of the SSA for robot path planning has rarely been reported in the literature.

This paper focuses on demonstrating an improved version of the SSA and its application to path planning. The problems with the original SSA such as the locomotion and slow convergence will be overcome. The initialization of the population of the SSA will be improved, and a set of dynamic inertia weight coefficients are defined to maintain the diversity of population. Genetic algorithm (GA) is then used to assist with the globalization of search. In the experiment, the improved SSA method will be tested on the 12 most popular test functions and compared with five other evolution methods. The optimization of robot path planning problem will also be tested with the proposed method, and the comparison with other methods will be shown. This paper is organized in six sections. The second section reviews the related works for SSA and path planning. The third section demonstrates the theory of the proposed algorithm, and the fourth section tests the performance of the improved SSA. The fifth section gives examples of the application of the improved SSA to path planning, and a conclusion is made in Section 6.

2. Related Works

2.1. The Original Salp Swarm Algorithm (SSA). Similar to other swarm intelligence algorithms, the SSA initializes the population in an n-dimensional search space, and the fitness function is regarded as the food source. The salp chain is always trying to approach the food source and finally reach the valuable food source in the search area, which is hopefully the global optimum. The procedure of the SSA can be given as follows:

(1) Initialize the population according to the upper and lower limits of each of the n dimensions, and it can be written as

$$x_m^i = lb(m) + \text{rand}\,(N, D) * (ub(m) - lb(m)), \qquad (1)$$

where X_m^i represents the ith salp of m-dimensional space, $i = 1, 2, \cdots, N\,m = 1, 2, \cdots, D$, N is the total number of salps in the chain, and D is the dimension of the objective function. rand (N, D) represents a random number matrix of N rows and D columns with elements evenly distributed between 0 and 1. $lb(m)$ represents the lower limit, and $ub(m)$ represents the upper limit. The initialization according to Equation (1) will generate an x_D^N matrix such that

$$X = \begin{bmatrix} x_1^1 & x_2^1 & \cdots & x_D^1 \\ x_1^2 & x_2^2 & \cdots & x_D^2 \\ \vdots & \vdots & \cdots & \vdots \\ x_1^N & x_2^N & \cdots & x_D^N \end{bmatrix} \qquad (2)$$

(2) The fitness value of each individual is calculated based on the fitness function

(3) Determine the initial location of the selected food source according to the salp with the best fitness value

(4) Identify the leader and followers: the first scalp in the chain is the leader, and the rest are followers

(5) Update the position of the leader according to Equation (3) such that

$$x_i^1 = \begin{cases} F_i + c_1((ub_i - lb_i)c_2 + lb_i), c_3 \geq 0.5, \\ F_i - c_1((ub_i - lb_i)c_2 + lb_i), c_3 \geq 0.5, \end{cases} \qquad (3)$$

where x_i^1 is the ith component of the leader and F_i represents ith element of the food source. c_2 and c_3 are random numbers generated in the interval of [0, 1], which represent the length and direction of the movement, respectively. c_1 is a coefficient for adjusting the exploration and exploitation of the salp chain and can be written as $c_1 = 2e^{-(4t/T_{\max})^2}$, where t is the current iteration and $T_{\max}$ is the maximum number of iteration

(6) Update the position of the followers:

Since the salp chain moves in the direction of the food source during foraging, the update of followers depends on the initial speed, iteration, and acceleration like the Newton's law of motion [4], such that

$$x_j^i(t) = \frac{1}{2}\left[x_j^i(t-1) + x_j^{i-1}(t-1)\right], \qquad (4)$$

TABLE 1: The test functions used in this experiment.

No.	Test functions	Dimension	Search range	Minimum value
1	$f_1(x) = \sum_{i=1}^{n} x_i^2$	50	[-100, 100]	0
2	$f_2(x) = \sum_{i=1}^{n} \lvert x_i \rvert + \prod_{i=1}^{n} \lvert x_i \rvert$	50	[-10, 10]	0
3	$f_3(x) = \sum_{i=1}^{n} \left(\sum_{j=1}^{i} x_j \right)^2$	50	[-100, 100]	0
4	$f_4(x) = \max \left\{ \lvert x_i \rvert : 1 \le i \le n \right\}$	50	[-100, 100]	0
5	$f_5(x) = \sum_{i=1}^{n-1} \left[100 \left(x_{i+1} - x_i^2 \right)^2 + (x_i - 1)^2 \right]$	50	[-100, 100]	0
6	$f_6(x) = \sum_{i=1}^{n} \left(\lvert x_i + 0.5 \rvert \right)^2$	50	[-100, 100]	0
7	$f_7(x) = \sum_{i=1}^{n} i x_i^4$	50	[-1.28, 1.28]	0
8	$f_8(x) = \sum_{i=1}^{n} \left(-x_i \sin \left(\sqrt{\lvert x_i \rvert} \right) \right)$	50	[-500, 500]	0
9	$f_9(x) = \sum_{i=1}^{n} \left[x_i^2 - 10 \cos \left(2\pi x_i \right) + 10 \right]^2$	50	[-5.12, 5.12]	0
10	$f_{10}(x) = -20 \exp \left(-0.2 \sqrt{\dfrac{1}{n} \sum_{i=1}^{n} x_i^2} \right) - \exp \left(\dfrac{1}{n} \sum_{i=1}^{n} \cos(2\pi x_i) \right) + e + 20$	50	[-32, 32]	0
11	$f_{11}(x) = \dfrac{1}{4000} \sum_{i=1}^{n} (x_i^2) - \prod_{i=1}^{n} \cos \left(\dfrac{x_i}{\sqrt{i}} \right) + 1$	50	[-600, 600]	0
12	$f_{12}(x) = 0.1 \left\{ \sin^2(3\pi x_1) + \sum_{i=1}^{n} (x_i - 1)^2 \left[1 + \sin^2(3\pi x_i + 1) \right] + (x_n - 1)^2 \left[1 + \sin^2(2\pi x_n) \right] \right\} + \sum_{i=1}^{n} \mu(x_i, 5,100,4)$	50	[-50, 50]	0

TABLE 2: Test results for the 12 functions listed in Table 1.

Test function	Value types	SSA	WOA	PSO	ABC	CSSA	Proposed SSA
f_1	Minimum	7.27e-29	9.27e-34	8.23e-24	2.39e-17	4.26e-34	**7.23e-38**
	Average	9.45e-29	4.26e-34	7.92e-23	8.93e-17	1.28e-34	**1.58e-38**
	Standard variance	4.66e-29	2.78e-34	1.25e-23	2.45e-17	7.21e-34	7.23e-38
f_2	Minimum	4.98e-38	5.44e-38	7.21e-12	3.63e-2	1.77e-99	**2.63e-148**
	Average	8.64e-38	9.48e-38	6.74e-12	5.67e-2	7.62e-99	**9.33e-148**
	Standard variance	7.58e-38	6.55e-38	7.25e-12	4.23e-2	5.38e-99	8.47e-148
f_3	Minimum	4.29e-23	5.11e-68	9.27e-21	3.47e-10	9.26-70	**2.46e-115**
	Average	3.24e-23	1.27e-68	1.31e-21	6.26e-10	1.86e-70	**8.77e-115**
	Standard variance	9.26e-23	6.67e-68	7.25e-21	3.77e-10	4.61e-70	6.55e-115
f_4	Minimum	4.21e-25	5.58e-168	4.25e-149	1.70e-13	1.41e-140	**9.25e-169**
	Average	9.93e-25	6.45e-168	4.33e-149	8.67e-18	8.92e-140	**2.80e-169**
	Standard variance	8.45e-25	7.22e-168	9.75e-149	5.49e-18	7.20e-140	5.39e-169
f_5	Minimum	6.72e-26	9.76e-68	2.43e-25	5.12e-12	5.80e-70	**9.24e-112**
	Average	7.28e-26	2.73e-67	1.73e-24	7.48e-11	2.62e-69	**1.50e-111**
	Standard variance	9.30e-26	7.77e-67	5.76e-25	2.66e-12	6.67e-70	6.90e-111
f_6	Minimum	4.37e-07	1.57e-08	4.96e-08	3.24e-07	1.46e-08	**8.24e-11**
	Average	7.61e-06	8.26e-08	6.44e-07	5.67e-06	8.43e-08	**2.10e-10**
	Standard variance	2.78e-08	3.21e-08	8.33e-07	3.22e-06	3.49e-08	3.94e-10
f_7	Minimum	7.22e-04	4.37e-09	8.66e-07	4.33e-03	8.25e-13	**2.43e-18**
	Average	5.46e-03	8.26e-08	1.45e-06	5.55e-02	2.82e-12	**9.44e-13**
	Standard variance	6.28e-04	3.15e-08	7.34e-06	3.36e-02	7.88e-14	7.10e-19
f_8	Minimum	4.52e-02	2.76e-03	6.99e-02	5.44e-01	**1.22e-05**	3.77e-05
	Average	6.25e-02	9.74e-03	3.22e-02	6.12e-01	**2.64e-05**	8.94e-04
	Standard variance	1.13e-04	3.44e-04	4.54e-02	5.33e-01	6.74e-05	6.60e-05
f_9	Minimum	9.95e-02	9.33e+01	7.26e-15	5.66e-12	6.53e+01	**2.73e-15**
	Average	7.24e-01	9.66e+01	5.31e-14	7.81e-11	8.98e+01	**1.54e-14**
	Standard variance	6.58e-02	5.43e-02	5.76e-14	6.54e-11	7.11e-02	9.12e-15
f_{10}	Minimum	1.56e-11	3.28e-07	2.46e-13	2.69e-11	8.93e-13	**1.19e-15**
	Average	4.21e-11	8.26e-06	7.11e-13	4.33e-10	1.22e-08	**8.74e-14**
	Standard variance	8.72e-11	4.33e-06	2.36e-13	5.36e-10	5.69e-11	4.63e-12
f_{11}	Minimum	5.46e-07	5.74e-05	1.93e-11	5.43e-07	4.44e-02	**9.56e-34**
	Average	8.23e-07	8.73e-05	5.86e-10	6.72e-07	2.44e-01	**1.72e-30**
	Standard variance	9.42e-07	7.74e-05	7.42e-10	5.64e-06	6.93e-03	6.72e-32
f_{12}	Minimum	2.96e-04	3.66e-02	4.08e-08	6.45e-08	5.35e+01	**3.54e-10**
	Average	3.37e-04	2.98e-01	2.76e-07	9.45e-07	8.70e+01	**8.25e-10**
	Standard variance	4.29e-04	2.16e-02	5.45e-08	7.73e-08	4.24e-01	4.77e-11

where $x_j^i(t)$ is the value of the jth component of the ith salp in the chain at iteration t

(7) If an updated component moves over the boundary, set the position of the boundary, and then, the food source location is updated according to the optimal salp

(8) If the result meets the accuracy requirements or if the number of iterations is reached, output the cur-

rent position; otherwise, turn to step 4 for further evolution

2.2. Robot Path Planning. The optimal path designed for a robot is usually calculated considering the constraints like time, distance, and energy consumption. The current most commonly used path planning optimization method is based on artificial intelligence algorithms. Deep learning has also been introduced to path planning, but the adaptability to environmental changes is relatively poor [35].
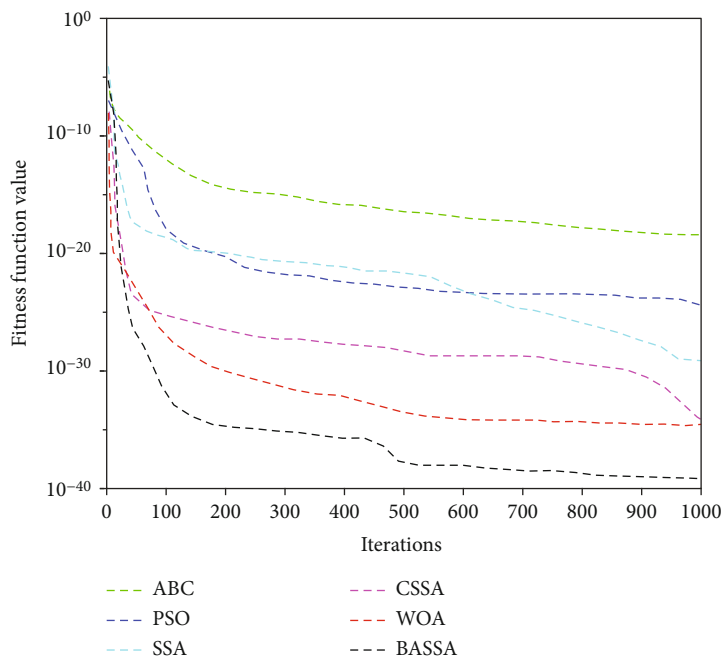
FIGURE 1: Comparison of the convergence curves of average fitness value for f_1.
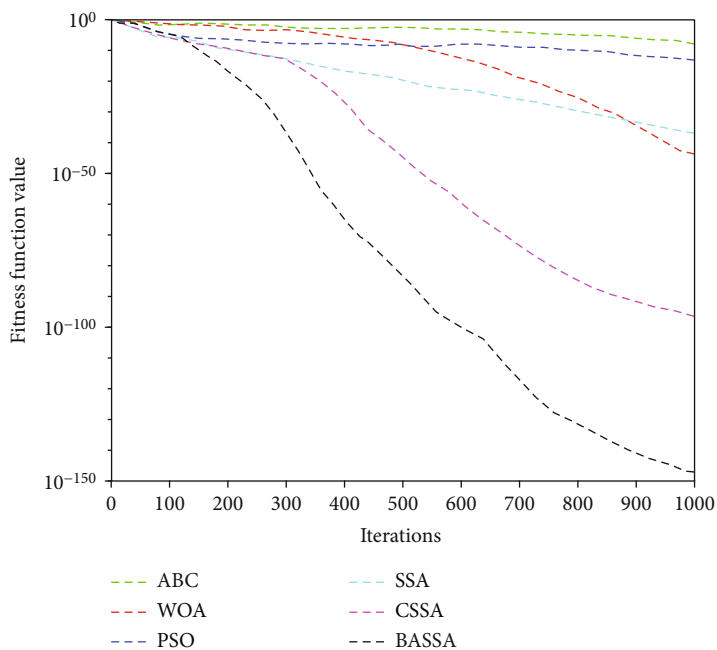
FIGURE 2: Comparison of the convergence curves of average fitness value for f_2.

To find the optimal path in the obstacle environment for a robot, the model of the mobile environment is required to register. There are currently two types of methods for environment modeling, one is the road sign method and the other is the grid method. The road sign method is to line up the feasible path map by connecting the labeled points and the boundaries of obstacles, while the grid method abstracts the mobile environment of the robot into a grid space and marks all grids that belong to the path. Grid method is more convenient to use and easier to implement, and therefore, it is more popular than the road sign method [36]. In this paper, an optimized grid modeling method is calculated for robot path planning.

In the grid modeling of three-dimensional (3D) mobile environment, a two-dimensional (2D) is marked with grids of equal size to represent the 3D space, and each grid is labeled with 0 or 1 representing without or with an obstacle [37].
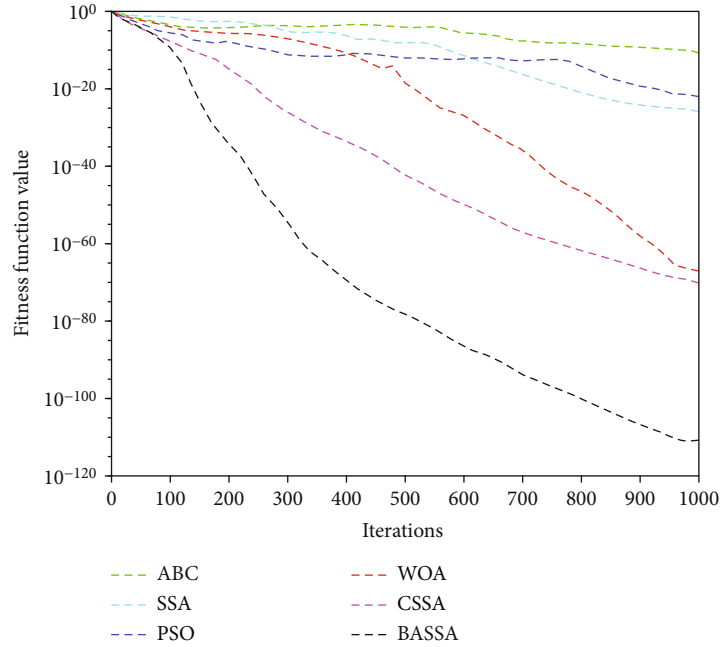
FIGURE 3: Comparison of the convergence curves of average fitness value for f_3.
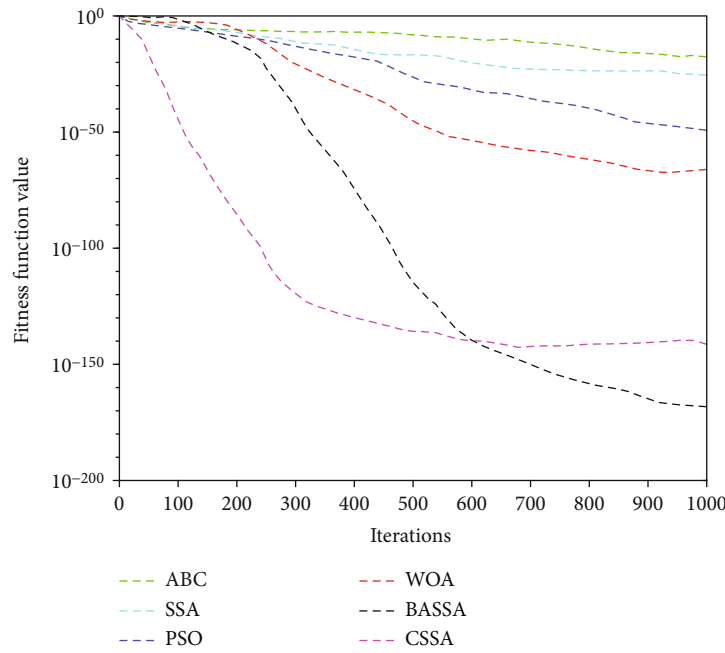
FIGURE 4: Comparison of the convergence curves of average fitness value for f_4.

The grid modeling is usually used to simulate a limited area, and a coordinate system xOy is established with the lower left corner as the origin and the horizontal and vertical orientations are x axis and y axis, respectively. The step length (l) of the robot represents the length of a single grid in the x or y axis; therefore, the number of grids in each x axis and y axis are $n_x = x_{max}/l$ and $n_y = y_{max}/l$, respectively. It is defined that each of the grids in the area is marked with a label starting from the upper left corner in the way of from left to right and from top to bottom, such that $A = \{1, 2, \cdots, N\}$. Then, the relationship between the coordinates and the label number can be given as:

$$x_i = ((i-1) \bmod n_x) + 1,$$
$$y_i = n_y - \text{ceil}\left(\frac{i}{n_x}\right) + 1, \tag{5}$$
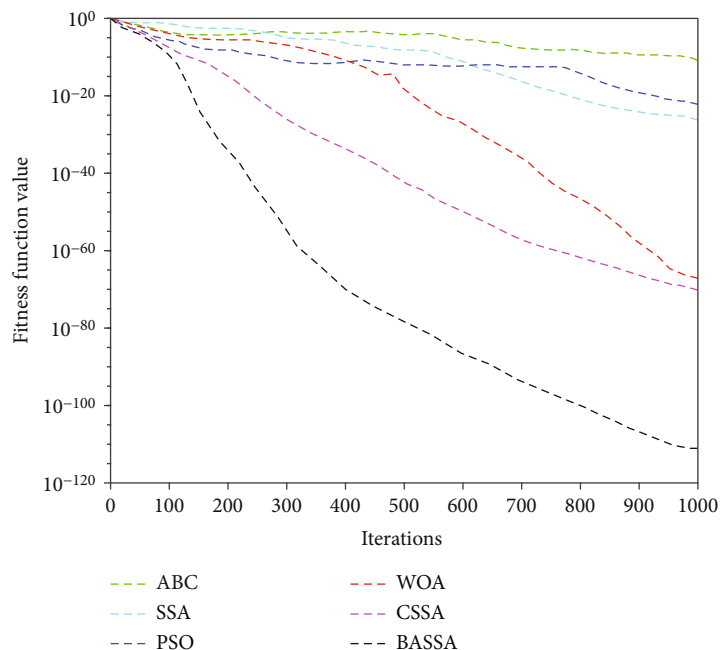
FIGURE 5: Comparison of the convergence curves of average fitness value for f_5.
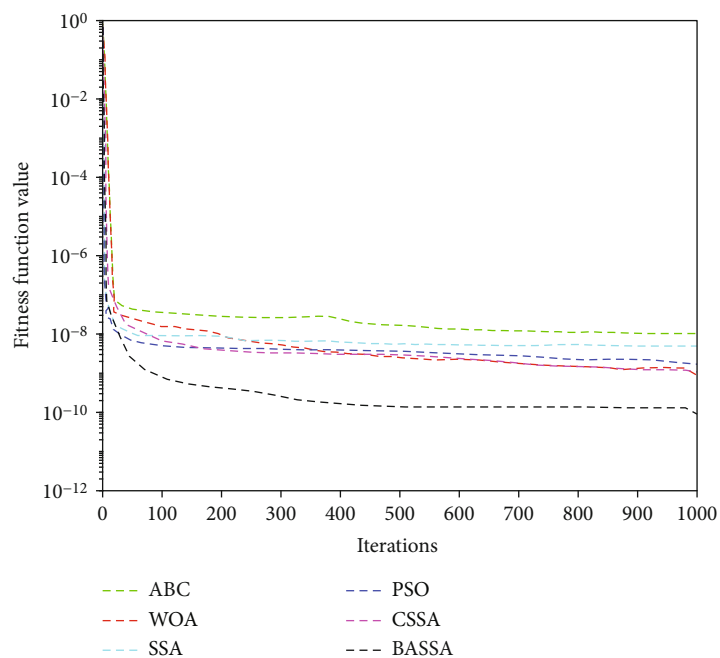
FIGURE 6: Comparison of the convergence curves of average fitness value for f_6.

where i represents the ith label number, mod is the remainder operation, ceil means rounding operation, n_x, n_y represent the number of grids per row and column, respectively, and x_i, y_i denote the ordinate of the grid center of the ith grid. In this optimization task, it is expected to find the shortest Euclidean distance between the current position (x_1, y_1) and the target position (x_2, y_2), which is regarded as the fitness vale, such that $h(x) = \sqrt{(x_1 - x_2)^2 + (y_1 - y_2)^2}$ [38].

3. The Improved SSA

In SSA, the leader is designed to make global exploration while the follower makes a full local search, and in this way, the chance of falling in a local optimum is greatly reduced. Since the SSA requires fewer parameters than other evolution optimization methods and therefore it is easier to implement, however, like most swarm intelligence
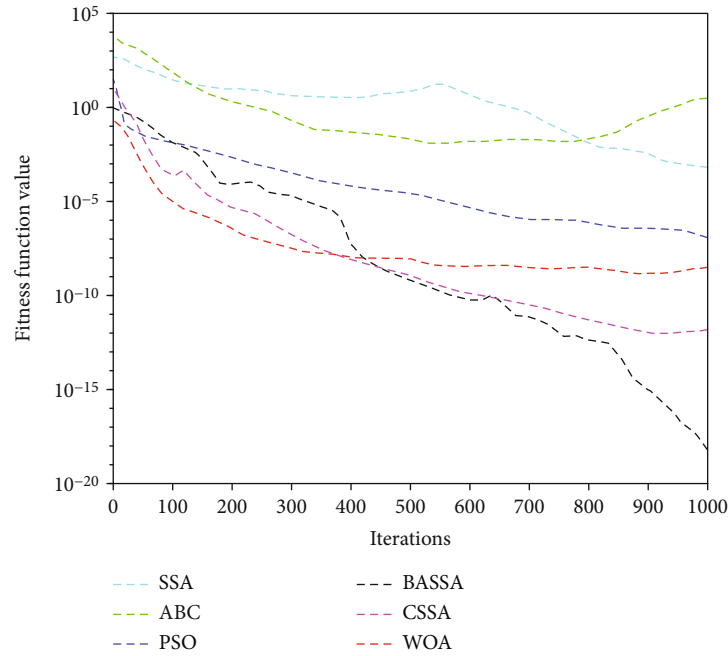
FIGURE 7: Comparison of the convergence curves of average fitness value for f_7.
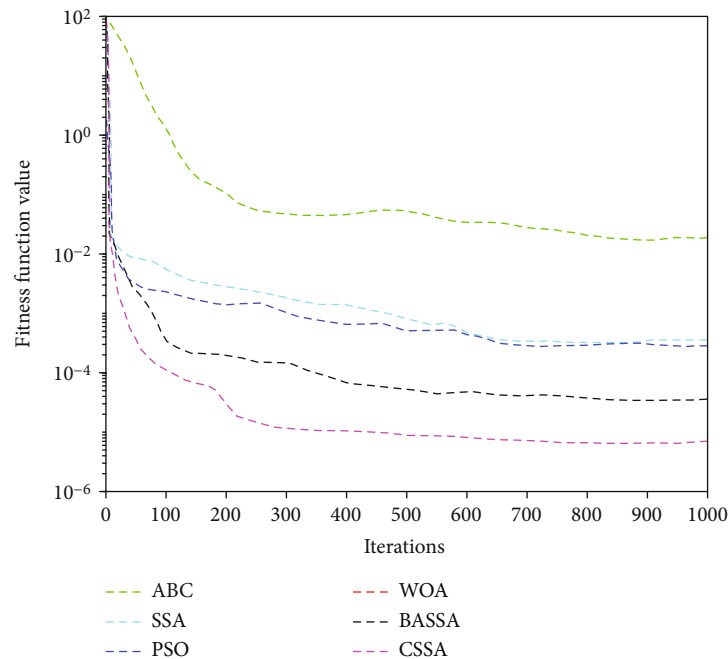
FIGURE 8: Comparison of the convergence curves of average fitness value for f_8.

algorithms, it is difficult for the SSA to converge at the later stage of optimization.

In the optimization using SSA, the initialization of the population is given within a certain range such that $x_m^i = lb(m) + rand(N, D) * (ub(m) - lb(m))$. Therefore, if the initial positions of the population are too concentrated, there will be a lack of diversity, resulting in the convergence to a local minimum. While if the initial positions are too scattered, the convergence process will be greatly slowed down. Besides, in the salp chain, the position of the individual is updated from one to the next along the chain; in some special cases, the value cannot be passed on, or in some cases,
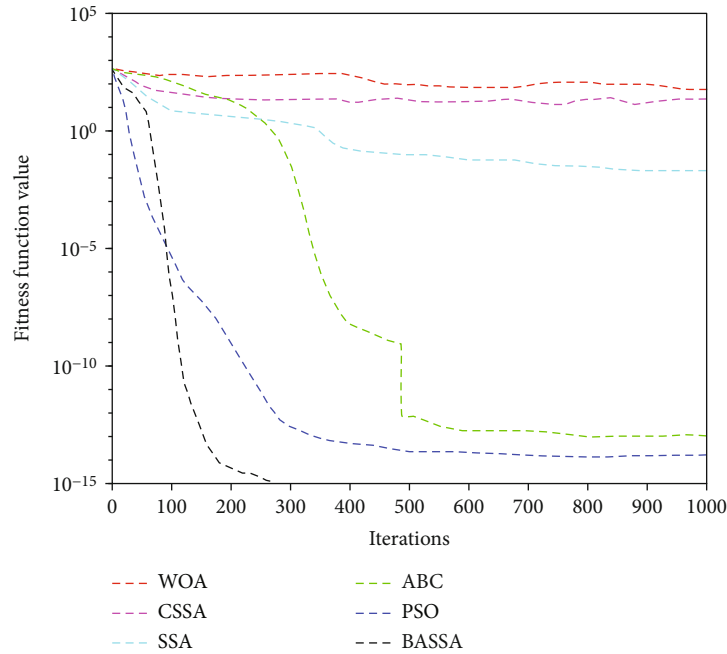
FIGURE 9: Comparison of the convergence curves of average fitness value for f_9.
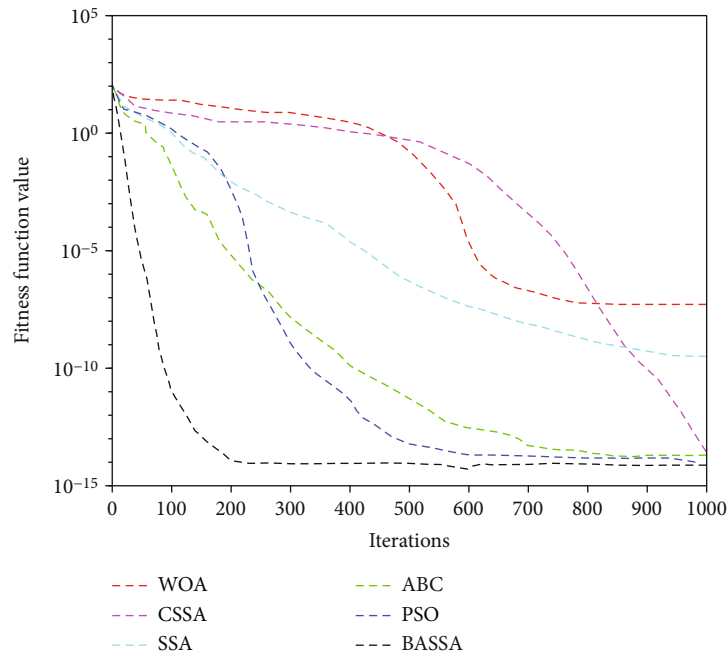
FIGURE 10: Comparison of the convergence curves of average fitness value for f_{10}.

some of the salp individuals may pass on inaccurate position values, and then, the optimization will fall into a local trap. To overcome these problems, a modified version of the SSA is required.

Since the convergence of the SSA is strongly influenced by the initial population at a later stage of iteration, and the random distribution of the initial population cannot guarantee the diversity, the tent chaotic sequence can be used to increase the randomness, diversity, and aperiodicity of the initial population [39], such that

$$z_{k+1} = \begin{cases} 2z_k & 0 \le z_k < 0.5, \\ 2(1 - z_k) & 0.5 \le z_k \le 1, \end{cases} \quad k = 0, 1, 2 \cdots. \tag{6}$$

In Equation (6), the initial value of z_k can be randomly
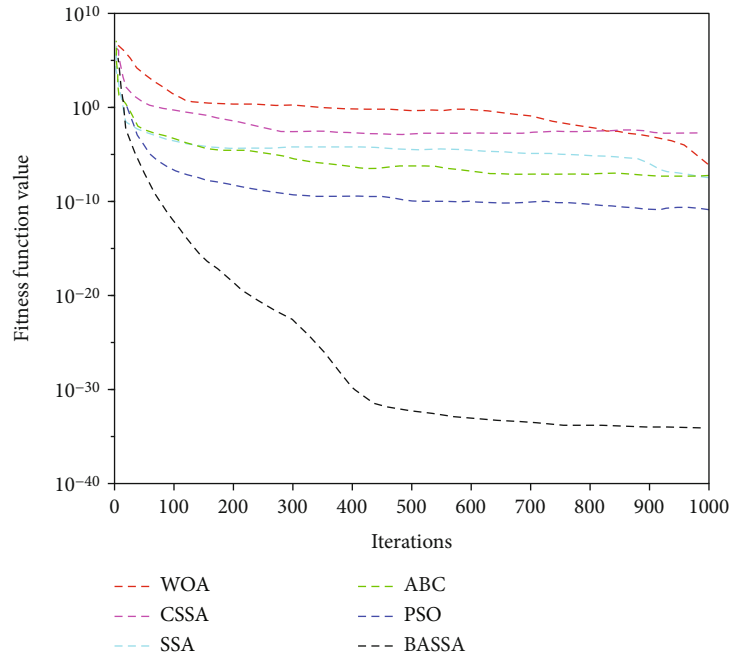
Figure 11: Comparison of the convergence curves of average fitness value for f_{11}.
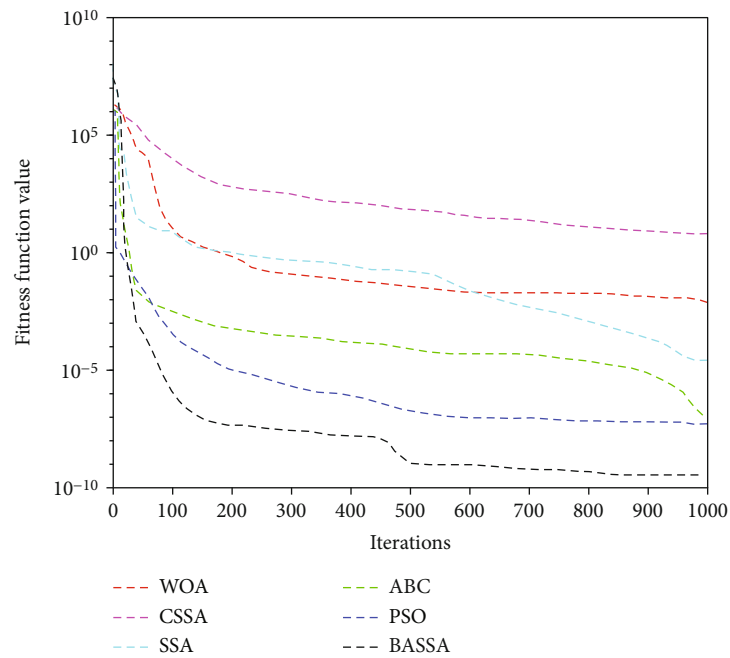
Figure 12: Comparison of the convergence curves of average fitness value for f_{12}.

generated within the value range, and it can be converted into the SSA variables such as

$$x_m^i = lb(m) + \text{rand}\,(N, D) * (ub(m) - lb(m)) * z_k \, k = 0, 1, 2 \cdots .$$

$$(7)$$

In this way, the procedure for initializing using tent chaotic mapping can be given as,

Step 1. According to the number of variables in the target function n, the initial value of z_k in Equation (6) is assigned with z_0

Step 2. Generate chaotic sequence variables $\{z_{i,k}\, i = 1, 2, \cdots n\}$ according to Equation (7)
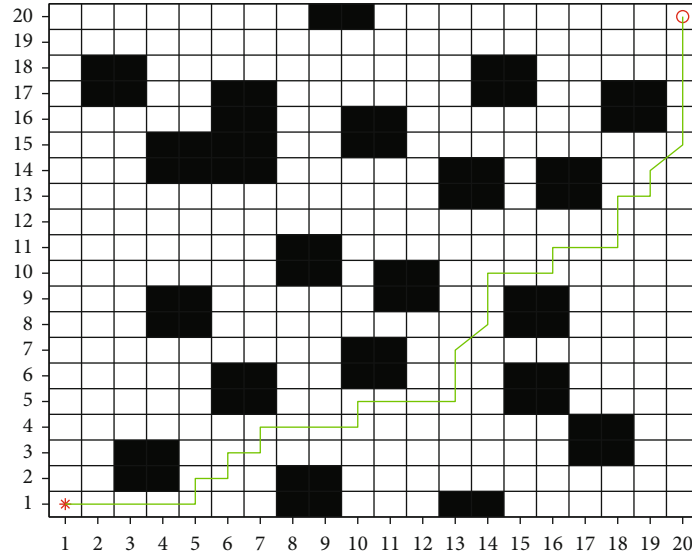
FIGURE 13: The simulation of path planning with the ABC method.
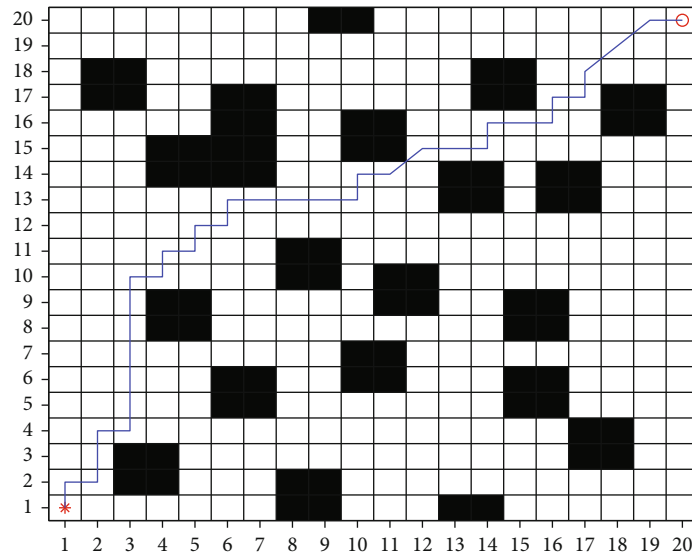
FIGURE 14: The simulation of path planning with the PSO method.

Step 3. Use Equation (7) to map the chaotic variable z_{ik} to the population solution space to complete the initialization

According to the update rule for the followers, if the jth salp passes on incorrect information to the next, the movement of all subsequent individual will be affected, especially when it finds a local minimum, it will not be likely to move out of this hole, and the whole chain will stay there forever. To solve this problem, an inertia weight strategy is introduced in the position update of the SSA [40], such that

$$\omega_t = (\omega_{max} - \omega_{min}) \left(\frac{T_{max} - t}{T_{max}} \right) + \omega_{min} \times Z_{k+1}, \quad (8)$$

where ω_{max} and ω_{min} are the initial and final values of the weights, T_{max} is the maximum number of iterations, t is

the current number of iterations, and Z_{k+1} is the chaotic mapping coefficient [39]. However, the mobile performance of this linearly decreasing inertia adjustment strategy is not satisfactory in the global search. Since the weighting factor is decreasing, in the initial stage of search, the algorithm tends to search globally. However, this duration is too short, the global search performance cannot be fully exploited before the weight factor becomes too small, and the whole chain may have already been trapped in a local optimum. In addition, when the values of $\omega_{max}, \omega_{min}$, and t are fixed, the amplitude of ω is also fixed, resulting in a deterioration in the performance of solving complex and nonlinear optimization problems. Therefore, it is required that a large weight is maintained to enhance the global search at the initial stage of optimization, while at the later stage, a small
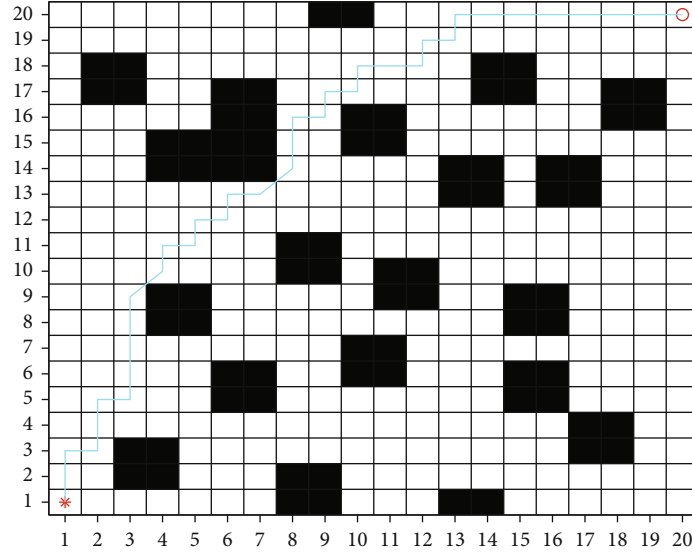
FIGURE 15: The simulation of path planning with the SSA method.
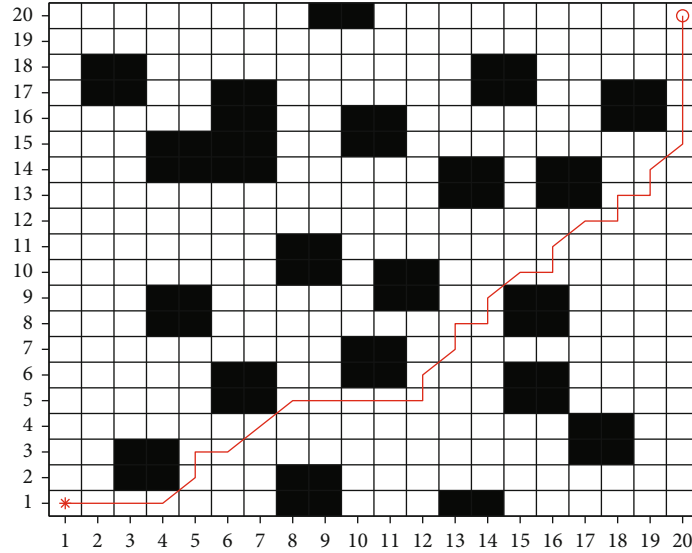
FIGURE 16: The simulation of path planning with the WOA method.

weight helps to focus on the local search. Inspired by deep learning methods, this nonlinear mapping process can be modeled with a Sigmoid function such that

$$\omega = \omega_{\max} - (\omega_{\max} - \omega_{\min}) \left(\frac{1}{1 + e^{-(T_{\max} - t)/T_{\max}}} \right)^3. \quad (9)$$

It can be seen that the output of Sigmoid function has a large initial value, which can ensure the global search capability of the algorithm, and the output value will be reduced gradually to the balance between the global and local search strategy.

To increase the possibility of achieving a global optimum, GA can be introduced in the later stage of the optimization by assigning a big mutation probability such as 0.1 in this paper.

In this way, the optimization process with the improved SSA can be divided into three stages, the first stage is when $t < (T_{\max}/2)$, the improved SSA without the GA is used; at the second stage, when $(T_{\max}/2) < t \le (2/3)T_{\max}$, if the global output value does not change for 10 consecutive times, the GA operation is used. When $t > (2/3)T_{\max}$, many experiments show that it is very likely to fall into a local optimum at this stage; therefore, a GA process is needed to help with the global search.

4. Experiments and Analysis

To test the effectiveness and performance of the improved algorithm, this paper compares the performance of the proposed algorithm with the original SSA [4], the Chaotic Salp Swarm Algorithm (CSSA) [41], and other intelligent algorithms such as the WOA [39], PSO, and ABC.
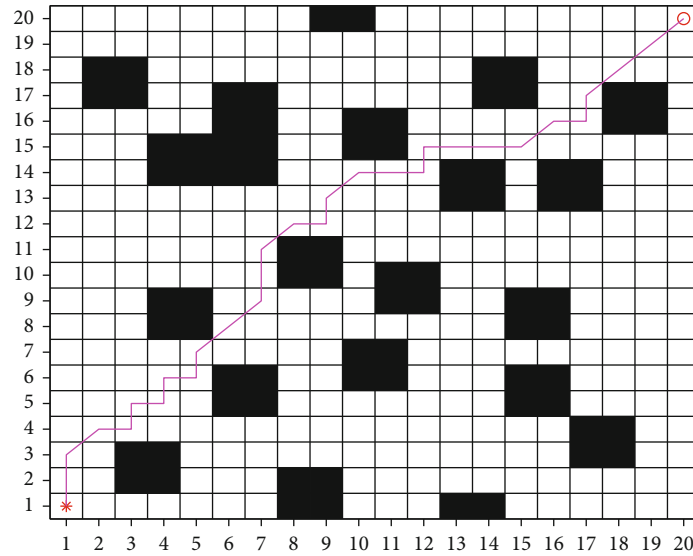
FIGURE 17: The simulation of path planning with the CSSA method.
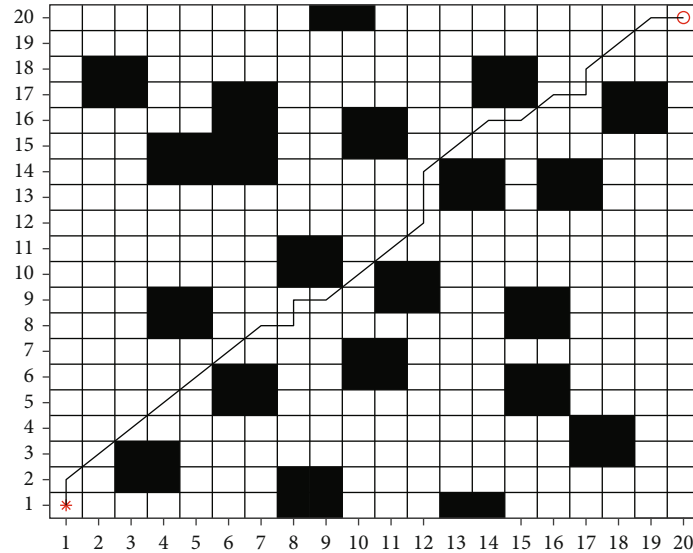
FIGURE 18: The simulation of path planning with the BASSA method.

In the experiment, there are 12 functions to be tested, among which $f_1 \sim f_7$ are unimodal functions for convergence speed testing, and $f_8 \sim f_{12}$ are multimodal functions for global search testing. The test functions are listed in Table 1.

The tests are carried out on the platform of Matlab 2018a on a PC with 16 G RAM. To confirm the result, each testing is independently run for 50 times to take the average. The dimension of the test function is set to 50, and the number of iterations is 2000. The parameter settings of other algorithms are consistent with the corresponding references. The test results are shown in Table 2.

From the experimental data, it can be seen that in the unimodal function $(f_1 \sim f_7)$, the proposed algorithm achieves the best optimal value as well as the average value. This test shows that the proposed algorithm has better opti-

mization stability and the optimal values achieved are at least several orders of magnitude better than that of other algorithms. For f_2 function, the optimal value of the proposed algorithm is nearly 110 orders of magnitude smaller that of the original SSA. In the test with f_2 function, the optimal value of the proposed algorithm is about 144 orders of magnitude less than that of the original SSA and 20 orders of magnitude less than that of the second best PSO algorithm. In the test with functions of f_1, f_3, f_5, f_6, and f_7, the improved SSA has also achieved the minimum values among several algorithms. It shows that the optimization accuracy of the improved SSA has obvious advantage than other algorithms for unimodal functions.

Among the five multimodal functions $(f_8 \sim f_{12})$ tested, the results of the proposed method are significantly better than other algorithms, except for the average value of f_8 in

Table 3: The comparison of simulation results for the six methods in robot path planning.

Methods	The optimal length	Average number of iterations	Average number of turnings
ABC	36.8324	93.3	22.4
PSO	36.2426	92.2	24.6
SSA	36.8284	86.4	25.1
WOA	33.8995	64.7	23.7
CSSA	32.7279	58.5	21.6
Proposed	29.7990	26.6	14.3

which case the CSSA algorithm has achieved the best but very close to the proposed method. In the test with function f_9, it was found that the WOA and the CSSA have been trapped in local minima under the same number of iterations as the proposed algorithm. In the test with functions $f_{10} \sim f_{12}$, the improved algorithm has achieved all the minimum values, which shows better exploration ability in multimodal function to avoid local optima.

Figures 1–12 show the convergence curves of average fitness value for $f_1 \sim f_{12}$, respectively, and it can be seen that the proposed method has the advantages of convergence rate and optimization accuracy over all other algorithms. In the test with the functions of f_2, f_3, f_5, f_7, and f_{11}, the proposed method can jump out of the local optimal solution at an earlier stage than others. Among the 12 functions tested, only the result for the function f_{10} is not optimal for the proposed method, but it is very close to the optimal result. It is clear from these experimental results that the proposed algorithm has better performance in optimization accuracy and convergence speed compared to the original SSA, as well as the CSSA, WOA, PSO, and ABC. The global search performance of the proposed method benefits from the increased diversity of the population and the mobility at the later convergence stage with the GA.

5. The Application in Robot Path Planning

This paper applies the proposed algorithm to the optimization of path planning for robots, and for better evaluation, the above methods are also tested and compared. In this experiment, a 20 ∗ 20-grid map is used to simulate the robot mobile environment, and the parameter settings of each algorithm are listed as follows:

(1) ABC: the number of artificial bees is $M = 50$, and the maximum number of attempts limit = 15

(2) PSO: the number of particles, $M = 50$, the constant of inertia $\omega_{max}=0.8, \omega_{min}=0.3$, $c_1=0.5$, and $c_2=0.5$

(3) SSA: the number of salps is $M = 50$, and the individual dimension is $d = 28$

(4) WOA: the position dimension: 20, population size: 50, spiral coefficient $b = 1$, and selection probability $P = 0.5$

(5) CSSA: the settings are consistent with those in the literature [42]

(6) The proposed algorithm: the same as the SSA

For all methods, the total iteration number is 300.

In the test, a 20 ∗ 20-grid map is randomly generated, and the simulated routes of all methods for robot path planning are shown in Figures 13–18, and the related results are listed in Table 3.

From the simulation results, it can be seen that the improved SSA achieves the shortest path length and is 23.6% shorter than ABC algorithm with the longest path length and 9.83% shorter than the CSSA. The average number of iterations achieved by the proposed method is less than half of that of the CSSA. This is due to the high optimization accuracy and better convergence rate of the proposed method. The average number of turnings for the proposed method is 43% less than the original SSA and 33.8% less than the CSSA. This shows that the proposed algorithm travels more straight in the current simulation environment, effectively avoiding unnecessary turns. From the comparison data, it can be seen that the improved SSA is a more efficient way to solve the robot path planning problem.

6. Conclusion

This paper proposed an improved SSA to solve the problems of locomotion and slow convergence of the original SSA. A tent chaotic mapping procedure is introduced to the initialization of the population, which effectively increases the diversity. During the optimization, dynamic inertia weight coefficients are used to maintain the diversity of population and the balance between the global and local search. At a later stage of optimization, GA is implemented to strengthen the global search ability of the algorithm. The proposed method is tested on the 12 most popular test functions and compared with five other evolution methods. The results show that the improved algorithm has better performance in convergence speed and optimization accuracy. Finally, the proposed algorithm is applied to the optimization of robot path planning and compared with the above methods. The experimental data shows that the proposed method finds the optimal path faster than other intelligent algorithms in the same environment with a better route and less iterations.

References

[1] R. Eberhart and J. Kennedy, "Particle swarm optimization," *Proceedings of the IEEE International Conference on Neural Networks*, vol. 4, pp. 1942–1948, 1995.

[2] S. Mirjalili, S. M. Mirjalili, and A. Lewis, "Grey wolf optimizer," *Advances in Engineering Software*, vol. 69, pp. 46–61, 2014.

[3] D. Karaboga and B. Akay, "A comparative study of artificial bee colony algorithm," *Applied Mathematics and Computation*, vol. 214, no. 1, pp. 108–132, 2009.

[4] S. Mirjalili, A. H. Gandomi, S. Z. Mirjalili, S. Saremi, H. Faris, and S. M. Mirjalili, "Salp swarm algorithm: a bio-inspired optimizer for engineering design problems," *Advances in Engineering Software*, vol. 114, no. 6, pp. 163–191, 2017.

[5] M. H. Qais, H. M. Hasanien, and S. Alghuwainem, "Enhanced salp swarm algorithm: application to variable speed wind generators," *Engineering Applications of Artificial Intelligence*, vol. 80, pp. 82–96, 2019.

[6] L. Abualigah, M. Shehab, A. Diabat, and A. Abraham, "Selection scheme sensitivity for a hybrid salp swarm algorithm: analysis and applications," *Engineering with Computers*, vol. 38, pp. 1149–1175, 2020.

[7] H. Faris, S. Mirjalili, I. Aljarah, M. Mafarja, and A. A. Heidari, "Salp swarm algorithm: theory, literature review, and application in extreme learning machines," in *Nature-Inspired Optimizers. Studies in Computational Intelligence, vol 811*, S. Mirjalili, J. Song Dong, and A. Lewis, Eds., vol. 811, pp. 185–199, Springer, Cham, 2020.

[8] S. Ahmed, M. Mafarja, H. Faris, and I. Aljarah, "Feature selection using salp swarm algorithm with chaos," in *Proceedings of the 2nd international conference on intelligent systems, metaheuristics & swarm intelligence*, pp. 65–69, New York, 2018.

[9] A. A. Abusnaina, S. Ahmad, R. Jarrar, and M. Mafarja, "Training neural networks using salp swarm algorithm for pattern classification," in *Proceedings of the 2nd international conference on future networks and distributed systems*, pp. 1–6, New York, 2018.

[10] A. Ibrahim, A. Ahmed, S. Hussein, and A. E. Hassanien, "Fish image segmentation using salp swarm algorithm," in *International Conference on advanced machine learning technologies and applications*, pp. 42–51, Springer, Cham, 2018.

[11] H. T. Ibrahim, W. J. Mazher, O. N. Uçan, and O. Bayat, "Feature selection using salp swarm algorithm for real biomedical datasets," *International Journal of Computer Science and Network Security*, vol. 17, no. 12, pp. 13–20, 2017.

[12] A. Ibrahim, S. Mohammed, H. A. Ali, and S. E. Hussein, "Breast cancer segmentation from thermal images based on chaotic salp swarm algorithm," *IEEE Access*, vol. 8, pp. 122121–122134, 2020.

[13] W. He, Y. Xie, H. Lu, M. Wang, and H. Chen, "Predicting coronary atherosclerotic heart disease: an extreme learning machine with improved salp swarm algorithm," *Symmetry*, vol. 12, no. 10, p. 1651, 2020.

[14] J. Gao, W. Ye, J. Guo, and Z. Li, "Deep reinforcement learning for indoor mobile robot path planning," *Sensors*, vol. 20, no. 19, p. 5493, 2020.

[15] A. Stentz, "Optimal and efficient path planning for partially known environments," in *Intelligent Unmanned Ground Vehicles*, pp. 203–220, Springer, Boston, MA, 1997.

[16] M. A. Contreras-Cruz, V. Ayala-Ramirez, and U. H. Hernandez-Belmonte, "Mobile robot path planning using artificial bee colony and evolutionary programming," *Applied Soft Computing Journal*, vol. 30, pp. 319–328, 2015.

[17] F. H. Ajeil, I. K. Ibraheem, A. T. Azar, and A. J. Humaidi, "Grid-based mobile robot path planning using aging-based ant colony optimization algorithm in static and dynamic environments," *Sensors*, vol. 20, no. 7, p. 1880, 2020.

[18] H. Zhang, W. Lin, and A. Chen, "Path planning for the mobile robot: a review," *Symmetry*, vol. 10, no. 10, p. 450, 2018.

[19] Y. Chen, G. Luo, Y. Mei, J. Q. Yu, and X. L. Su, "UAV path planning using artificial potential field method updated by optimal control theory," *International Journal of Systems Science*, vol. 47, no. 6, pp. 1407–1420, 2016.

[20] P. Vadakkepat, K. C. Tan, and W. Ming-Liang, "Evolutionary artificial potential fields and their application in real time robot path planning," in *Proceedings of the 2000 congress on evolutionary computation. CEC00 (Cat. No. 00TH8512)*, pp. 256–263, IEEE, La Jolla, CA, USA, 2000.

[21] Q. Zhang, D. Chen, and T. Chen, "An obstacle avoidance method of soccer robot based on evolutionary artificial potential field," *Energy Procedia*, vol. 16, pp. 1792–1798, 2012.

[22] F. Duchoň, A. Babinec, M. Kajan et al., "Path planning with modified a star algorithm for a mobile robot," *Procedia Engineering*, vol. 96, pp. 59–69, 2014.

[23] X. Liu and D. Gong, "A comparative study of A-star algorithms for search and rescue in perfect maze," in *2011 International Conference on Electric Information and Control Engineering*, pp. 24–27, IEEE, Wuhan, 2011.

[24] C. Wang, L. Wang, J. Qin et al., "Path planning of automated guided vehicles based on improved A-star algorithm," in *2015 IEEE International Conference on Information and Automation*, pp. 2071–2076, IEEE, Lijiang, China, 2015.

[25] Y. Deng, Y. Chen, Y. Zhang, and S. Mahadevan, "Fuzzy Dijkstra algorithm for shortest path problem under uncertain environment," *Applied Soft Computing*, vol. 12, no. 3, pp. 1231–1237, 2012.

[26] Y. Chen, S. Shen, T. Chen, and R. Yang, "Path optimization study for vehicles evacuation based on Dijkstra algorithm," *Procedia Engineering*, vol. 71, pp. 159–165, 2014.

[27] A. Sedeno-Noda and M. Colebrook, "A biobjective Dijkstra algorithm," *European Journal of Operational Research*, vol. 276, no. 1, pp. 106–118, 2019.

[28] S. M. LaValle, "Rapidly-Exploring Random Trees: A New Tool for Path Planning," *The Annual Research Report*, p. 98, 1998.

[29] J. Zhu, S. Zhao, and R. Zhao, "Path planning for autonomous underwater vehicle based on artificial potential field and modified RRT," in *2021 International Conference on Computer, Control and Robotics (ICCCR)*, pp. 21–25, IEEE, Shanghai, China, 2021.

[30] R. Mashayekhi, M. Y. I. Idris, M. H. Anisi, I. Ahmedy, and I. Ali, "Informed RRT*-connect: an asymptotically optimal single-query path planning method," *IEEE Access*, vol. 8, pp. 19842–19852, 2020.

[31] B. Song, Z. Wang, and L. Zou, "An improved PSO algorithm for smooth path planning of mobile robots using continuous high-degree Bezier curve," *Applied Soft Computing*, vol. 100, article 106960, 2021.

[32] Z. Masoumi, J. Van Genderen, and N. A. Sadeghi, "An improved ant colony optimization-based algorithm for user-centric multi-objective path planning for ubiquitous environments," *Geocarto International*, vol. 36, no. 2, pp. 137–154, 2021.

[33] K. Liu, C. Xv, D. Huang, and X. Ye, "UAV path planning based on improved whale optimization algorithm," in *2021 IEEE International Conference on Consumer Electronics and Computer Engineering (ICCECE)*, pp. 569–573, IEEE, Guangzhou, China, 2021.

[34] Z. Yan, J. Zhang, J. Zeng, and J. Tang, "Water wave optimization algorithm for autonomous underwater vehicle path planning problem," *Journal of Intelligent & Fuzzy Systems*, vol. 40, no. 5, pp. 9127–9141, 2021.

[35] M. A. Hossain and I. Ferdous, "Autonomous robot path planning in dynamic environment using a new optimization technique inspired by bacterial foraging technique," *Robotics and Autonomous Systems*, vol. 64, pp. 137–141, 2015.

[36] M. B. Metea, "Route planning for intelligent autonomous land vehicles using hierarchical terrain representation," *Proceedings. 1987 IEEE International Conference on Robotics and Automation*, vol. 4, pp. 1947–1952, 1987.

[37] A. Botea, M. Muller, and R. J. Schaeffe, "Near optimal hierarchical path-finding," *Journal of Game Development*, vol. 1, no. 1, pp. 7–28, 2004.

[38] G. Liu, T. Li, Y. Peng, and X. Hou, "The ant algorithm for solving robot path planning problem," *Proceedings of the Third International Conference on Information Technology and Applications. (ICITA'05)*, vol. 2, 2005.

[39] M. Qinghua, Y. Lin, and W. Yanliang, "Grey wolf algorithm based on improved tent chaos and simulated annealing," *Mathematics Practice and Cognition*, vol. 51, no. 5, pp. 147–161, 2021.

[40] M. A. Arasomwan and A. O. Adewumi, "On the performance of linear decreasing inertia weight particle swarm optimization for global optimization," *The Scientific World Journal*, vol. 2013, Article ID 860289, 12 pages, 2013.

[41] S. Mirjalili and A. Lewis, "The whale optimization algorithm," *Advances in Engineering Software*, vol. 95, pp. 51–67, 2016.

[42] G. I. Sayed, G. Khoriba, and M. H. Haggag, "A novel chaotic salp swarm algorithm for global optimization and feature selection," *Applied Intelligence*, vol. 48, no. 10, pp. 3462–3481, 2018.

Research Article

Research on Cavitation Flow Dynamics and Entropy Generation Analysis in an Axial Flow Pump

Simin Shen [ID],[1,2,3] **Bensheng Huang** [ID],[1] **Si Huang** [ID],[3] **Shun Xu** [ID],[4] and **Shufeng Liu** [ID][1]

[1]*Guangdong Research Institute of Water Resources and Hydropower, Guangzhou 510610, China*
[2]*School of Water Resources and Hydropower Engineering, Wuhan University, Wuhan 430072, China*
[3]*School of Mechanical and Automotive Engineering, South China University of Technology, Guangzhou 510641, China*
[4]*School of Aerospace Engineering, Huazhong University of Science and Technology, Wuhan 430074, China*

Correspondence should be addressed to Simin Shen; emilyfluent@126.com

The entropy generation theory is introduced to investigate the effects of different NPSH and tip clearance size on the cavitation flow dynamics and mechanical energy dissipation intuitively and quantitatively within an axial flow pump through numerical simulations. The results indicate that main mechanical energy dissipation of the pump gathers in part impeller and diffuser, and most are turbulent dissipation. Meanwhile, the impeller is the largest place of mechanical energy dissipation of the pump under cavitation conditions, accounting for more than 50%. NPSH has significant effects on the cavitation pattern, which reflects on the field that the areas of attached sheet cavitation and tip leakage vortex cavitation around blades increase obviously with NPSH reducing under the tip clearance of 0.1% span. With NPSH decreasing, high regions of turbulent dissipation in the impeller mainly expands along blades and move downstream, with span S0.98 near the shroud having larger turbulent dissipation. Besides, high regions of turbulent dissipation are mainly distributed at the rear part of the cavity for every corresponding span of the impeller, which indicates that the turbulent dissipation has a strong relation with the cavitation pattern. In the impeller, the unstable flows cause cavity shedding at the rear of the cavity and wake flows near the blade trail induce higher turbulent kinetic energy, finally resulting in higher turbulent dissipation there. Under the same NPSH, areas of tip leakage vortex cavitation and areas of tip clearance cavitation around the tip both expand with the tip clearance increasing from 0.1% span to 0.8% span. And high areas of turbulent dissipation also are distributed at the rear of the cavity and moving downstream along the blade suction side, especially at span S0.98. Therefore, the tip clearance width mainly affects the cavitation development and turbulent dissipation distribution near the impeller's shroud under same NPSH.

1. Introduction

It is well known that axial-flow pumps are widely used in hydraulic engineering projects like agricultural irrigation, water supply, and drainage. The cavitation in hydraulic machinery is an important phenomenon of complex phase change, which often occurs where local pressure is lower than liquid vaporization pressure. Due to the existence of radial clearance between blades and the shroud for the impeller, tip leakage flows would occur inevitably and cause the tip leakage vortex cavitation cloud under the cavitation conditions, which finally makes the cavitation process more complicated. When the cavitation is severe, it can influence

the flow structure and energy loss characteristic, then finally result in vibration, noise, and the deterioration of hydraulic machinery performance [1–4].

Currently, the two common methods to study the cavitation dynamics in hydraulic machinery are through experiments and numerical simulations. As for the study on the cavitation inside axial-flow pumps, several scholars investigate the cavitation combined the experiment with the numerical simulation. Saito [5] investigated the flow pattern under cavitation conditions within an axial-flow impeller and found that the change of pump performance has a close relation with cavitation growth around blades. Due to the cavitation, the flow pattern at the impeller outlet changed

remarkably. Zhang and Chen [6] investigated the inner flows in a slanted axial pump with different cavitation conditions by numerical simulations. The research introduced boundary vorticity flux to diagnose the cavitation flow and found the decrease of cavitation performance had a relation with unstable cavitation flows on the suction sides of blades. Hosono et al. [7] studied the internal flow and the influence of the cavitation within an axial pump by measurements through the high-speed camera and numerical simulations. Shi et al. [8] studied effects of different blade tip geometries on the cavitation and leakage vortex for an axial pump. Zhang et al. [9, 10] investigated the internal flow by CFD method to investigate the tip flow cavitation patterns of a pump. They found the phenomenon that tip leakage vortex- (TLV-) induced periodically collapse of perpendicular vortices is universal for axial flow pumps. Tan et al. [11] applied high-speed imaging to investigate some forms of cavitation patterns like sheet cavitation and tip clearance cavitation under varying discharge for a pump. Feng et al. [12] investigated impacts of inlet guide vane on the cavitation dynamics and pump performance with varying discharge. They found a variable called the total vapor fraction to predict critical net positive suction head. Also, many scholars [13–22] carried out the research on the tip leakage vortex, pressure pulsation, and cavitation mechanism fields in hydraulic machinery and obtained a certain number of achievements, while for studies on energy loss characteristics in hydraulic machinery, an increasing number of scholars use the entropy production method to investigate the loss characteristic accompany with the numerical simulation. Comparing with traditional energy evaluation method, entropy generation analysis method can intuitively and quantitatively determine the position of mechanical energy dissipation in hydraulic machinery; thus, this method is currently applied by some researchers. Gong et al. [23] investigated energy dissipation of a hydroturbine by entropy generation analysis, and they found the runner and guide vane were mainly locations of energy loss. Li et al. [24, 25] investigated hysteresis characteristics using entropy generation analysis of a pump-turbine model by simulations. Through analysis, they found that the hump characteristic was induced by the energy dissipation of the runner. Hou et al. [26] introduced the entropy production theory to investigate energy dissipation in pumps. Pei et al. [27] conducted the research of energy dissipation applying entropy generation analysis in a pump with varying distance between the guide vane and impeller. Chang et al. [28] applied the entropy generation method to investigate effects of the blade thickness distribution on losses in novel self-priming pump and obtained optimal blade. Li et al. [29] introduced entropy generation theory to investigate about the cavitation and loss characteristic in a centrifugal pump. From their simulation results, they found the decrease of pump head is related to the change of overall entropy production rate of part impeller. Wang et al. [30] applied entropy production diagnostic model (EPDM) to study energy dissipation under cavitation conditions in a pump, and they proved that the EPDM can predict the inception and development of the cavitation. Some studies [31–34] investigated the inner flow and energy

dissipation based on entropy generation theory in hydraulic machinery and get some results. These above studies about energy loss characteristics in hydraulic machinery prove the entropy generation method is effective to assess mechanical energy dissipation due to its intuitive and quantitative advantages.

The above studies are about cavitation dynamics or about loss characteristics of hydraulic machines using entropy generation method, while there is still few studies on the relations between the cavitation dynamics and entropy production for axial-flow pumps, especially with different NPSH and tip clearance. The main focus of this research is to investigate cavitation dynamics and entropy generation analysis of an axial-flow pump with different NPSH and tip clearance width and found the relations between the cavitation and entropy production. Therefore, four NPSH with the same tip clearance of 0.1% span are selected to investigate effects of NPSH on cavitation flows and energy dissipation, while four tip clearance widths with the same cavitation condition are selected to investigate impacts of the tip clearance on cavitation patterns and energy dissipation. That is how this research organized. Then, we summarize some conclusions about cavitation dynamics and mechanical energy dissipation for an axial-flow pump. This research can finally provide some theoretical guidance to the cavitation and energy dissipation in hydraulic machinery and give reference for designing highly reliable pumps.

2. Experimental Apparatus and Parameters

As shown in Figure 1, the closed experimental loop is installed at the Laboratory of Pump Station in Wuhan University, Wuhan, China [14]. The experimental apparatus mainly consists of three parts: the axial-flow pump facility, the cavitation generating facility, and the data acquisition system. The test pump loop includes water tanks, a flowmeter, valves, an axial flow pump, and other related equipment displayed in Figure 2. Specific parameters for the experimental model are given in Table 1. The cavitation generating facility mainly contains a vacuum pump, a pressure tank, and a regulating valve. During the experiment, the inlet pressure of test pump is maintained by a vacuum pump through adjusting the regulating valve to different required degrees of vacuum. The data acquisition system consists of pressure sensors, the electromagnetic flowmeter, and speed torque meter. The electromagnetic valve controls the mass flow rate. And the KROHNE electromagnetic flowmeter measures the mass flow (accuracy 0.3%). While a frequency converter controls the pump rotation speed and torque. And the WDH300Z speed torque meter measures these parameters (accuracy 0.2%). The WDHYL101 pressure sensors measure the inlet and outlet pressure of test pump (accuracy 0.2%). To avoid accidental errors, repeated measurements are performed for every working condition. Comparing the results of 3, 5, and 10 times, it was found that the average values of five measurements were enough for this test. During the measurements, the uncertainties of mass flow rate, head,

Figure 1: Experimental pump station installed in the Wuhan University.
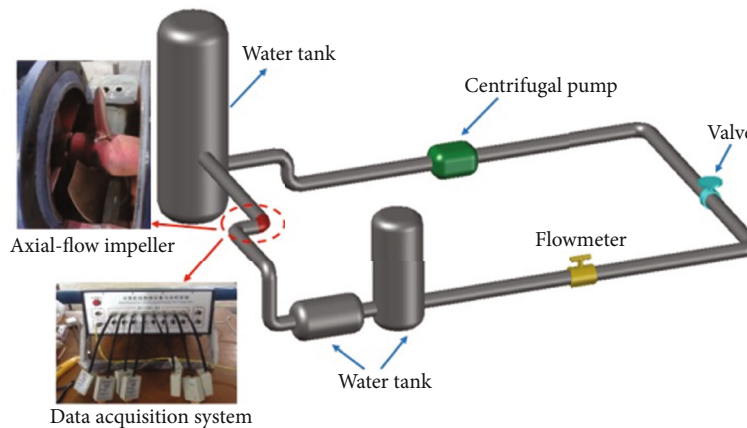
Figure 2: Schematic of test pump.

input power, and efficiency were less than 0.84%, 0.58%, 0.75%, and 1.01%, respectively.

3. Physical Modelling and Numerical Methodology

3.1. Governing Equations, Turbulence Model, and Cavitation Model. For the cavitation flow under isothermal conditions, a homogeneous mixture model has been applied in a wide range of numerical calculations. The homogeneous mixing model assumes the velocity and pressure between the liquid phase and gas phase are continuous. Governing equations for cavitation flows accompany with the homogeneous mixture model include continuity and momentum equations, which can be expressed as:

$$\frac{\partial \rho_m}{\partial t} + \frac{\partial (\rho_m u_i)}{\partial x_i} = 0, \tag{1}$$

$$\begin{aligned}\frac{\partial (\rho_m u_i)}{\partial t} &+ \frac{\partial (\rho_m u_i u_j)}{\partial x_j} \\ &= -\frac{\partial p}{\partial x_i} + \frac{\partial}{\partial x_j}[(\mu_{0+}\mu_m)]\left(\frac{\partial u_i}{\partial x_j} + \frac{\partial u_j}{\partial x_i}\right),\end{aligned} \tag{2}$$

where p is the pressure; u is the velocity; ρ_m denotes mixture phase density and can be defined by Equation (3); μ_0 represents mixture laminar viscosity, which can be calculated by Equation (4); and μ_m denotes mixture turbulent viscosity

Table 1: Specific parameters of test pump.

Parameters	Value
Impeller diameter D (mm)	300
Number of diffuser blades	5
Number of impeller blades	3
Design rotational speed n (r/min)	1450
Design head H_d (m)	3.3
Design flow rate Q_d (kg/s)	330
Tip clearance (mm)	0.15

and can be acquired by adopting turbulence model. Because the SST k-ω turbulence model can effectively predict flow separation and vortexes with adverse pressure gradients in hydraulic machinery, the governing equations are solved by SST k-ω turbulence model in current study.

$$\rho_m = \alpha_v \rho_v + (1 - \alpha_v)\rho_1, \tag{3}$$

$$\mu_0 = \alpha_v \mu_v + (1 - \alpha_v)\mu_1, \tag{4}$$

$$\alpha_v + \alpha_1 = 1, \tag{5}$$

where α_v is volume fraction of vapor; subscripts m, l, and v represent mixing, liquid, and vapor phases, respectively. The vapor transport equation can solve the volume fraction of water vapor, the equation is:

$$\frac{\partial(\rho_v \alpha_v)}{\partial t} + \frac{\partial(\rho_v \alpha_v u_j)}{\partial x_j} = \dot{m}^+ + \dot{m}^-, \qquad (6)$$

where $\dot{m}^+$ is the evaporation source term; $\dot{m}^-$ is condensation source term. This study adopts Zwart-Gerber-Belamri cavitation model to express mass exchange of interphase; thus, $\dot{m}^+$ and $\dot{m}^-$ can be defined as:

$$\dot{m}^+ = F_{va} \frac{3\alpha_c(1-\alpha_v)\rho_v}{R_b} \sqrt{\frac{2|p_v - p|}{3\rho_1}}, \qquad (7)$$

$$\dot{m}^- = F_{co} \frac{3\alpha_v \rho_v}{R_b} \sqrt{\frac{2|p_v - p|}{3\rho_1}}, \qquad (8)$$

where F_{va} and F_{co} represent the empirical coefficient of evaporation and condensation, respectively; p_v denotes saturated vapor pressure; R_b stands for the bubble radius; and α_c represents nucleation site volume fraction. The recommended values for parameters are $F_{va} = 50$, $F_{co} = 0.01$, $R_b = 1 \times 10^{-6}$ m, and $\alpha_c = 5 \times 10^{-4}$.

3.2. Entropy Generation Calculation Equations. In current research, the entropy generation analysis is used to assess mechanical energy dissipation within an axial flow pump. According to the second law of thermodynamics, entropy generation refers to irreversible energy losses in the energy conversion process. Regarding the internal fluid of a pump as an incompressible and adiabatic process, entropy generation created by heat transfer could be ignored. Therefore, mechanical energy dissipation within the flow passage of a pump mainly is viscous and turbulent dissipation. And local entropy generation rate caused by dissipation for cavitation flows is written as $\bar{\Phi}/T$, which can be defined directly as:

$$\frac{\bar{\Phi}}{T} = \ddot{S}_{\bar{D}}'' + \dot{S}_{D'}'', \qquad (9)$$

where $\ddot{S}_{\bar{D}}''$ and $\dot{S}_{D'}''$ represent the entropy generation rate caused by time-averaged movements and velocity fluctuations, respectively. Thus, $\ddot{S}_{\bar{D}}''$ and $\dot{S}_{D'}''$ represent viscous and turbulent dissipation, respectively. The two terms can be expressed by:

$$\ddot{S}_{\bar{D}}'' = \frac{2\mu}{T} \left[\left(\frac{\partial \bar{u}}{\partial x}\right)^2 + \left(\frac{\partial \bar{v}}{\partial y}\right)^2 + \left(\frac{\partial \bar{w}}{\partial z}\right)^2 \right]$$
$$+ \frac{\mu}{T} \left[\left(\frac{\partial \bar{u}}{\partial y} + \frac{\partial \bar{v}}{\partial x}\right)^2 + \left(\frac{\partial \bar{u}}{\partial z} + \frac{\partial \bar{w}}{\partial x}\right)^2 \right. \qquad (10)$$
$$\left. + \left(\frac{\partial \bar{v}}{\partial z} + \frac{\partial \bar{w}}{\partial x}\right)^2 \right],$$

$$\dot{S}_{D'}'' = \frac{2\mu_{ef}}{T} \left[\left(\frac{\partial u'}{\partial x}\right)^2 + \left(\frac{\partial v'}{\partial y}\right)^2 + \left(\frac{\partial w'}{\partial z}\right)^2 \right]$$
$$+ \frac{\mu_{ef}}{T} \left[\left(\frac{\partial u'}{\partial y} + \frac{\partial v'}{\partial x}\right)^2 + \left(\frac{\partial u'}{\partial z} + \frac{\partial w'}{\partial x}\right)^2 \right. \qquad (11)$$
$$\left. + \left(\frac{\partial v'}{\partial z} + \frac{\partial w'}{\partial x}\right)^2 \right],$$

where $\bar{u}, \bar{v}, \bar{w}$ and u', v', w' represent the mean and fluctuating velocity quantities along x, y, z direction, respectively. μ_{ef} denotes effective viscosity and can be defined as:

$$\mu_{ef} = \mu + u_t, \qquad (12)$$

where μ and μ_t represent molecular and turbulent viscosity, respectively. Through the postprocessing of CFD POST, the term $\ddot{S}_{\bar{D}}''$ can be calculated directly by Equation (10). But we cannot obtain the term $\dot{S}_{D'}''$ directly, and the reason is that fluctuating velocities are not available during simulations. Refer to studies of Kock et al. [35, 36], when using SST k-ω turbulence model, $\dot{S}_{D'}''$ can be expressed by:

$$\dot{S}_{D'}'' = \alpha \frac{\rho \omega k}{T}, \qquad (13)$$

where $\alpha = 0.09$, ω is characteristic frequency, and k is turbulence kinetic energy. Besides, the overall entropy generation rate of a region is calculated by the volume integration of specific entropy generation rate:

$$\dot{S}_{\bar{D}} = \int_V \ddot{S}_{\bar{D}}'' dV, \qquad (14)$$

$$\dot{S}_{D'} = \int_V \dot{S}_{D'}'' dV, \qquad (15)$$

$$\dot{S}_D = \dot{S}_{\bar{D}} + \dot{S}_{D'}, \qquad (16)$$

where $\dot{S}_{\bar{D}}$ and $\dot{S}_{D'}$ represent the overall entropy generation rates caused by time-averaged movements and velocity fluctuations, respectively. $\dot{S}_D$ denotes the entropy generation rate of the domain, as the sum of $\dot{S}_{\bar{D}}$ and $\dot{S}_{D'}$. Then, parameters about entropy generation can be calculated for cavitation flows in the pump. With the help of entropy generation method, we can have the quantitative analysis of mechanical energy dissipation.

3.3. Calculation Domain and Meshing Technique. The calculation domain is the whole flow passage, which consists of the impeller, diffuser, and other parts, as seen from Figure 3. The lengths of the inlet and outlet pipe are set as 10 times of pipe diameter. Only part impeller is the rotating component while others are stationary. The sliding interfaces are set at split planes of part impeller, as shown in the following figure.
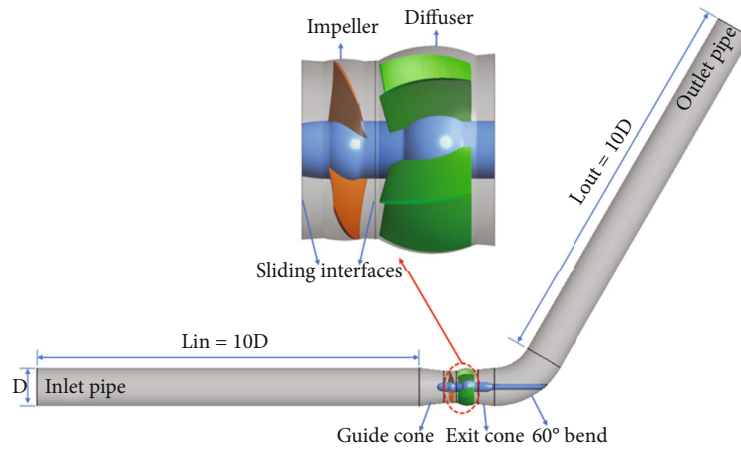
FIGURE 3: 3D view of calculation domain.
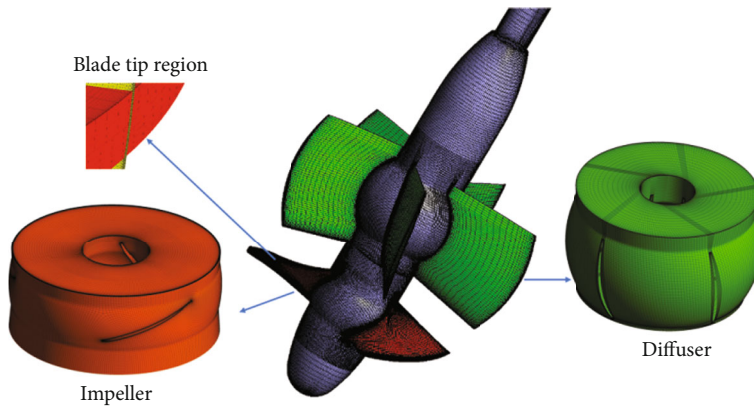
FIGURE 4: Mesh of main parts for the pump.

TABLE 2: Grid independence verification.

Mesh nodes	Q (kg/s)	NPSH (m)	Convergence criterion	Numerical simulation head (m)	Relative error between simulations and experiments
3004495	302.917	9.280	10^{-5}	3.885	5.937%
4047425	302.917	9.280	10^{-5}	3.981	3.668%
5136088	302.917	9.280	10^{-5}	4.008	3.024%
6036526	302.917	9.280	10^{-5}	4.014	2.864%

In order to have better convergence, structured hexahedral meshing scheme is applied for all components in the calculation domain. Most meshes are created by software ANSYS ICEM except the mesh of part Impeller. Considering the highly distorted shape of impeller's blades and small radial clearance between blades and the shroud, the mesh of part impeller is created by the software ANSYS TURBOGRID, especially for the O-Grid around blades. In order to simulate the tip region accurately, the tip clearance with a size of 1.2 mm is placed 80-layer mesh grids at the tip. For other tip clearances, the simulation model uses a uniform tip gap with a size of 1.2 mm. To generalize the results and discussions, we should convert the tip clearance size to a fraction of span. Then, 0.15, 0.45, 0.9, and 1.2 mm can be changed to 0.1%, 0.3%, 0.6%, and 0.8% span through divid-

TABLE 3: Comparison between simulations and tests.

NPSH (m)	Simulation head (m)	Experimental head (m)	Relative error between simulations and tests
11.531	3.915	4.027	2.786%
9.280	4.008	4.133	3.024%
7.456	3.996	4.058	1.537%

ing by the impeller diameter in the following. The obtained mesh of main parts for the pump is displayed in Figure 4.

For the whole calculation domain, four sets of mesh are created, and the verification of grid independence is conducted under specific flow rate and cavitation condition
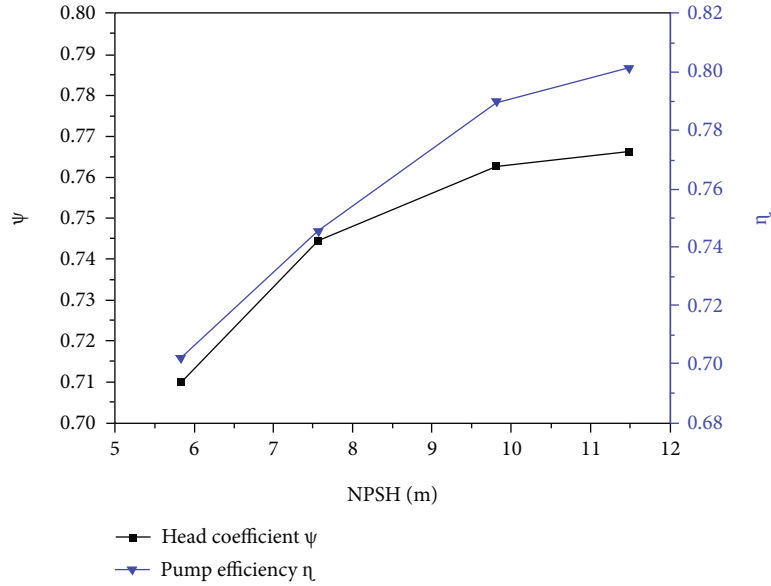
FIGURE 5: Pump performance with varying NPSH under the tip clearance of 0.1% span.
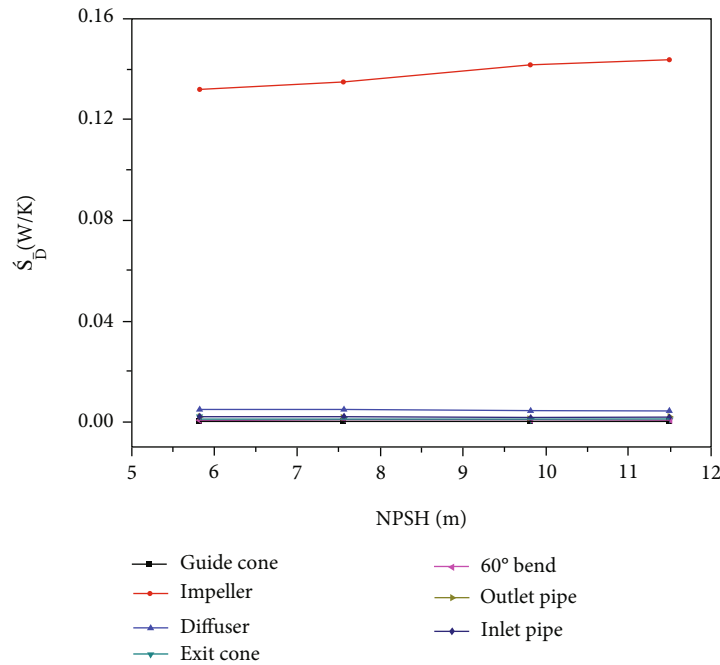
FIGURE 6: Overall entropy generation rate caused by time-averaged movements $\dot{S}_{\bar{D}}$ for different components.

according to the experiment as displayed in Table 2. The NPSH is an important physical parameter that describes the pump cavitation condition, which can be calculated by:

$$\text{NPSH} = \frac{p_s}{\rho g} + \frac{v_s^2}{2g} - \frac{p_v}{\rho g}, \tag{17}$$

where p_s denotes the absolute pressure, v_s represents the average velocity at the pump inlet, and p_v represents the vapour pressure. SST k–ω turbulence model is taken into consideration for the grid independence study. Through grid

independence verification displayed in Table 2, we consider that the number of 5,136,088 nodes is sufficient to simulate cavitation flows in this pump.

3.4. Numerical Setup. In this research, 3D transient calculations of the internal flow for different cavitation conditions within an axial-flow pump were conducted applying software ANSYS CFX accompany with the RANS equation. In the calculation, SST k-ω turbulence model and ZGB cavitation model were used. The finite volume method was adopted to discretize govern equations. The second-order upwind scheme was applied for space discretization. For
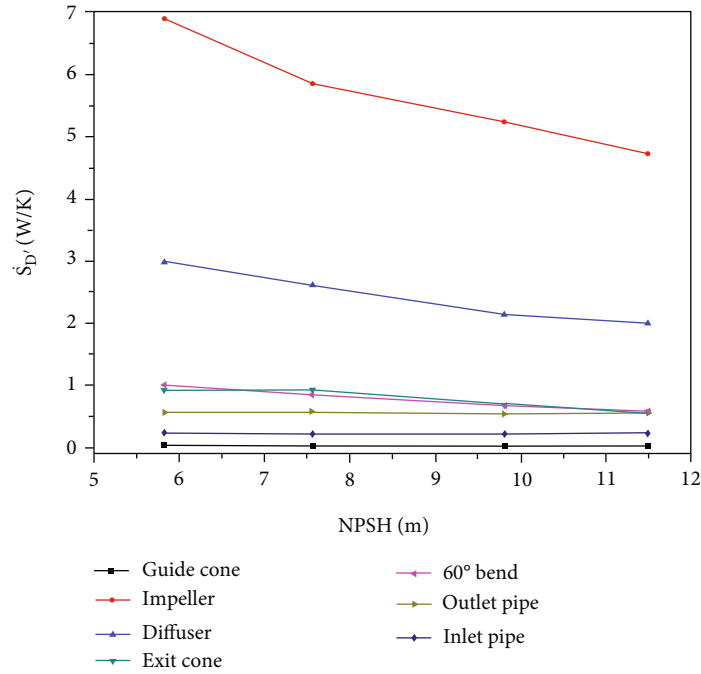
FIGURE 7: Overall entropy generation rate caused by velocity fluctuations $\dot{S}_{D'}$ for different components.
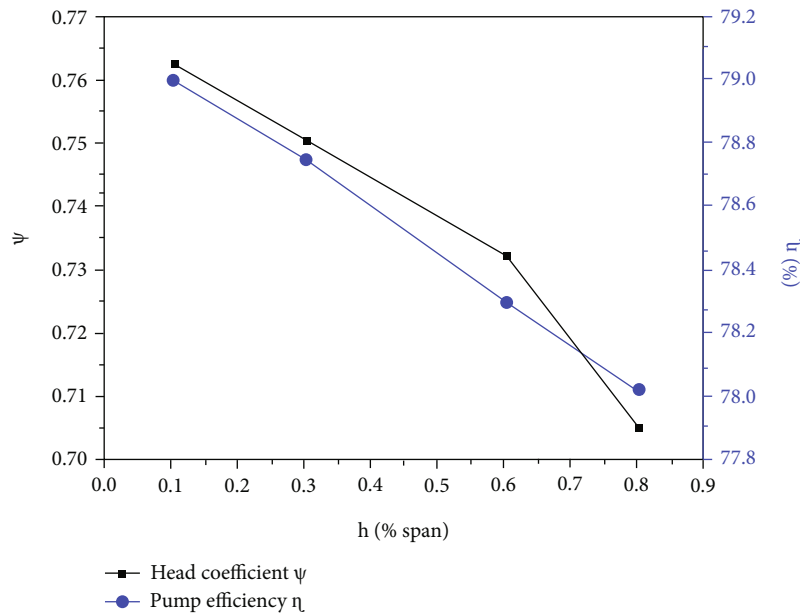
FIGURE 8: Pump performance for varying tip clearance under NPSH = 9.816 m.

advection terms, the high-resolution scheme with second order backward Euler algorithm was applied. The inlet boundary condition was set as the total pressure inlet; the outlet boundary condition was set as the mass flow rate outlet according to the test data. The wall boundary was assumed for no-slip wall. The calculated media were liquid and vapor at 25°C, and the volume fraction of liquid and vapor was set as 1 and 0 at the pump inlet. The transient rotor stator was employed for the rotor stator interaction. For simulations, steady calculations of noncavitation were first performed, and then, we applied these noncavitation flow results as the initial value to calculate unsteady simulations under cavitation conditions. The convergence criterion was set as 10^{-5}. For unsteady calculations, the time step was set to 0.0003448276 s, which is equivalent to 1/120 of the design rotational period. During every time step, the maximum number of iterations was assumed as 20 that can generally help the result reach stable periodicity. The total calculation time for unsteady calculations was set to 20 rotating cycles. For analysis, we select the last four periods as our time sample. All results that we used for analysing are based on this average result of the time sample.
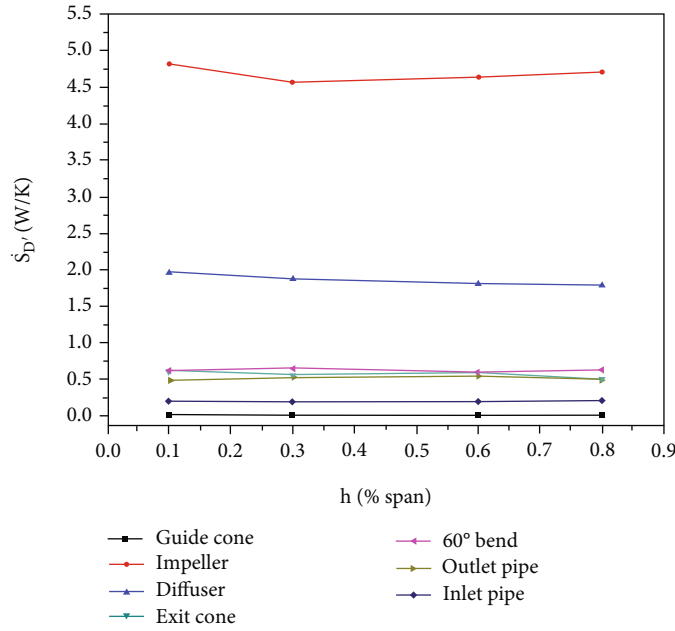
FIGURE 9: Overall turbulent entropy generation rate $\dot{S}_{D'}$ of different components for varying tip clearance under NPSH = 9.816 m.

(a)

(b)

(c)

(d)
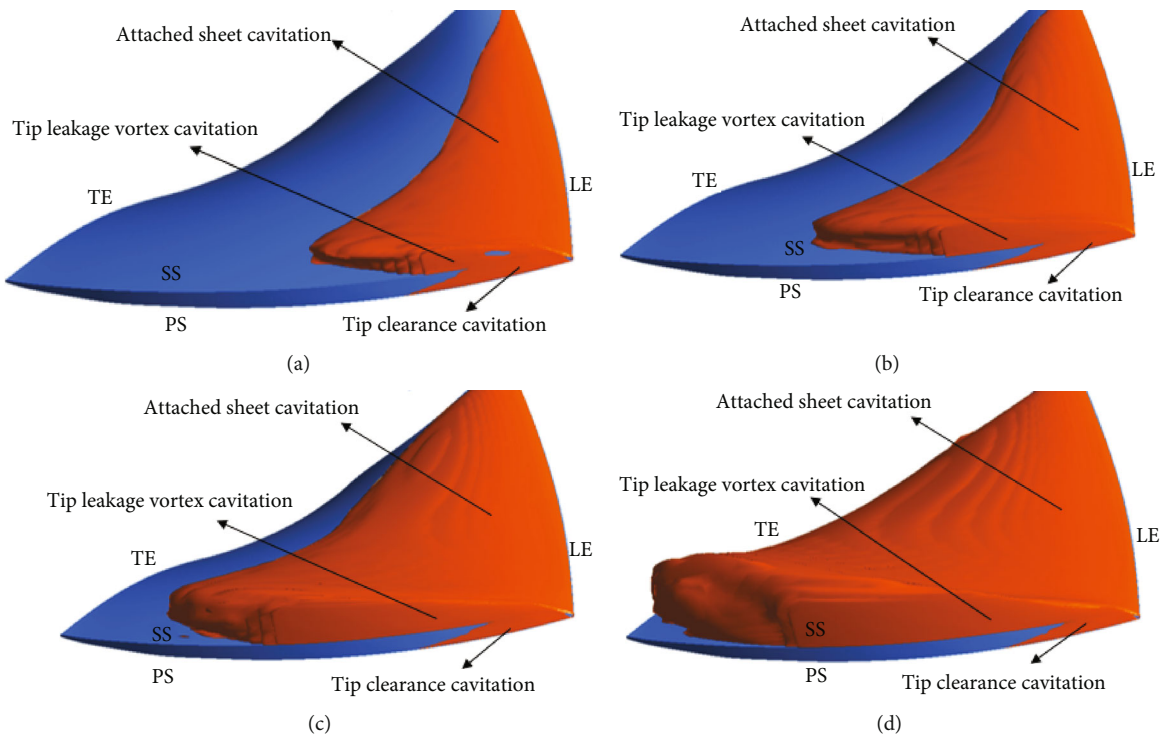
FIGURE 10: Cavitation patterns with varying NPSH under the tip clearance of 0.1% span. Iso-surface of vapor volume fraction ($\alpha_v = 0.1$) ((a) NPSH = 11.492 m; (b) NPSH = 9.816 m; (c) NPSH = 7.562 m; (d) NPSH = 5.830 m).

3.5. Validation of Numerical Simulations. Table 3 shows the comparison of the pump head between experiments and numerical simulations. As displayed in Table 3, the simulation data under three different NPSH are in good agreement with the test data. And the relative error between them is below 5%. Thus, we believe that the model, grid, and calculation method adopted in this research are reasonable and

reliable. And we consider the results of simulations can be used for the following analysis.

4. Results and Discussion

4.1. Analysis of Pump Performance and Entropy Generation with Varying NPSH. During the experiment, it is difficult
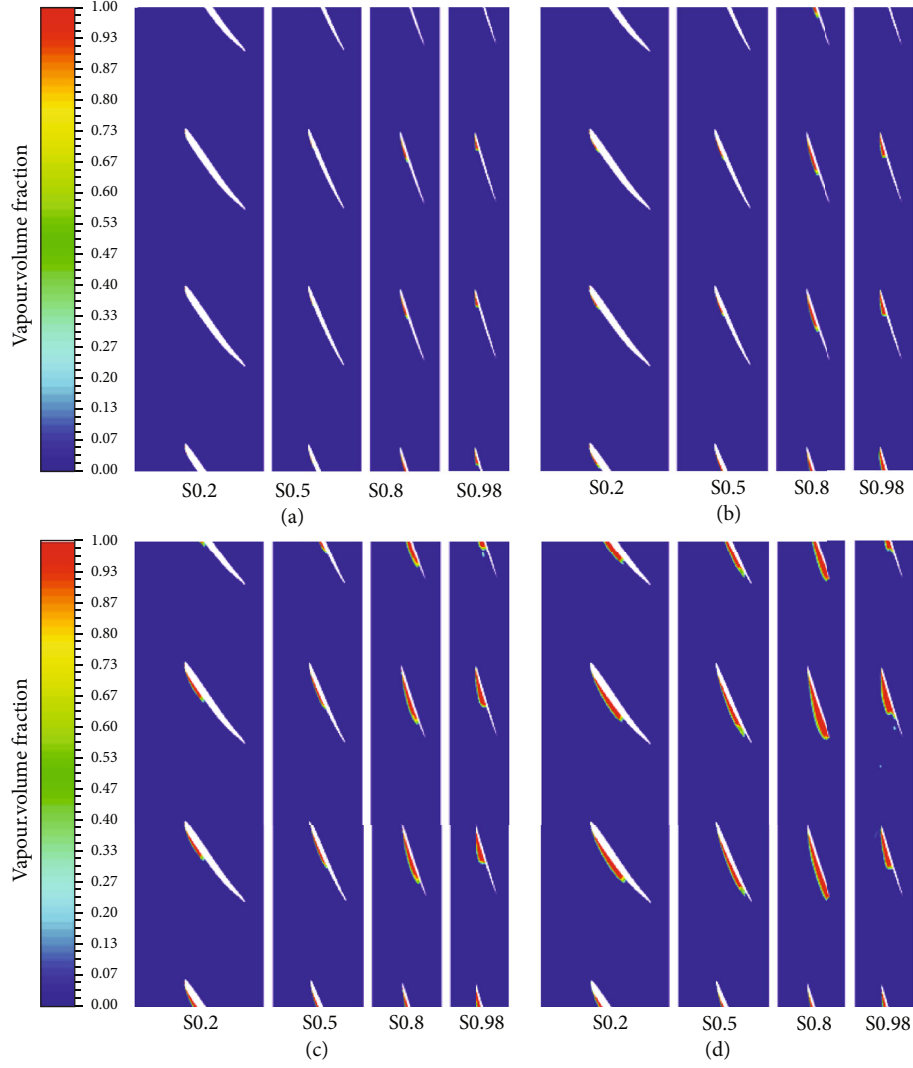
FIGURE 11: The vapor volume fraction at different spans of part impeller with varying NPSH under the tip clearance of 0.1% span ((a) NPSH = 11.492 m; (b) NPSH = 9.816 m; (c) NPSH = 7.562 m; (d) NPSH = 5.830 m).

to keep the flow rate unchanged when we change the pressure of pump inlet by the vacuum pump; thus, the above simulation results according to the experimental data just adopted for verifying the reliability of simulations. For the following analysis, we use the same conditions except for the analysis variable. To investigate the pump performance and entropy generation with varying NPSH, we select four cavitation points that are similar to the experiment cavitation conditions A (NPSH = 11.492 m), B (NPSH = 9.816 m), C (NPSH = 7.562 m), and D (NPSH = 5.830 m) under the same flow rate ($Q = 302.917$ kg/s) and the tip clearance of 0.1% span for detailed analysis. The calculated pump performance is shown in Figure 5. The nondimensional parameters are calculated by:

$$\text{head coefficient}: \psi = \frac{gH}{(\Omega/2\pi)^2 D^2}, \tag{18}$$

$$\text{pump coefficient}: \eta = \frac{gQH}{3600 M\Omega}. \tag{19}$$

As seen from Figure 5, the pump head and efficiency both reduce with the NPSH reducing, which indicates that there will be more energy loss when the cavitation becomes more severe. To better understand the energy dissipation distribution under different NPSH in the axial-flow pump, we calculate the overall entropy generation rate caused by time-averaged movements and velocity fluctuations of different components for analysis, as displayed in Figures 6 and 7. From Figure 6, the entropy generation rates caused by time-averaged movements $\dot{S}_{\bar{D}}$ of different components are very small and change not evidently with varying NPSH. From Figure 7, it is obviously seen that the overall entropy generation rate $\dot{S}_{D'}$ for different components grows from part guide cone, inlet pipe, outlet pipe, 60° bend, exit cone, diffuser, to part impeller. With the NPSH decreasing, the overall entropy generation rate $\dot{S}_{D'}$ of part impeller and diffuser increase obviously while the values for other components remain stable and small. And the overall turbulent entropy generation rate for 60° bend and exit cone increase slowly with the NPSH reducing. Comparing
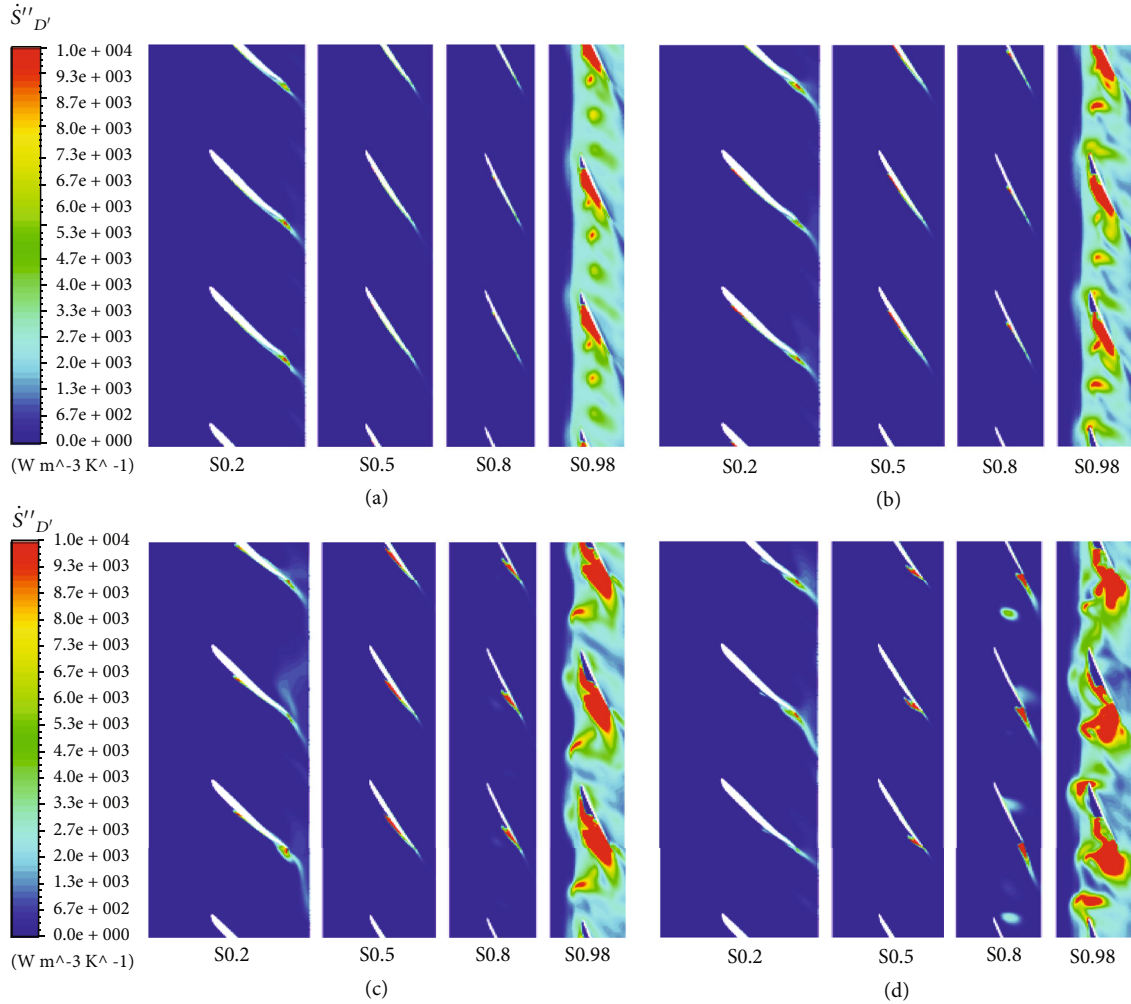
FIGURE 12: Distributions of turbulent entropy generation rate $\dot{S}_{D'}''$ at different spans of part impeller with varying NPSH under the tip clearance of 0.1% span ((a) NPSH = 11.492 m; (b) NPSH = 9.816 m; (c) NPSH = 7.562 m; (d) NPSH = 5.830 m).

the values in Figures 6 and 7, we found that most of the irreversible energy loss are turbulent dissipation; thus, we would focus on the analysis of turbulent dissipation behind. As seen from Figure 7, we found that part impeller and diffuser are main places where the irreversible energy loss occurs, and energy dissipation of part impeller is more than double of the energy dissipation of part diffuser. In a pump, the dissipation of part impeller accounts more than 50% and become bigger with the cavitation being worse. Therefore, the NPSH has significant effects on the turbulent dissipation for part impeller.

4.2. Analysis of Pump Performance and Entropy Generation with Varying Tip.

When pumps operate, tip clearance between the blade and the impeller's shroud is inevitable. To study impacts of tip clearance width on the pump performance and entropy generation, we select four tip clearance width with the same cavitation (NPSH = 9.816 m) for the following analysis. Figure 8 displays pump performance with four tip clearances under the same cavitation condition, and we can observe that pump head and pump efficiency both

reduce as the tip increasing from 0.1% span to 0.8% span. Meanwhile, the difference between the maximum and minimum head is less than 6%, and the difference between the maximum and minimum pump efficiency is about 1%. This indicates that as the tip grows from 0.1% span to 0.8% span under same cavitation condition (NPSH = 9.816 m), the pump performance decreases slightly.

Through the above analysis in Section 4.1, we know most of energy dissipation is turbulent dissipation, thus here mainly analyze the turbulent entropy generation within this pump. Figure 9 displays overall turbulent entropy generation rate $\dot{S}_{D'}$ of different components with varying tip under the same cavitation condition (NPSH = 9.816 m). From Figure 9, it is obviously observed that $\dot{S}_{D'}$ for different components grows from part guide cone, inlet pipe, outlet pipe, 60° bend, exit cone, diffuser, to part impeller. As the tip increases, the overall turbulent entropy generation rates of part impeller first decreases a little then increase slowly, and the changing of the value is not big. While overall entropy generation rate of part diffuser reduces very slowly when the tip increases. And the turbulent entropy generation rate of other components
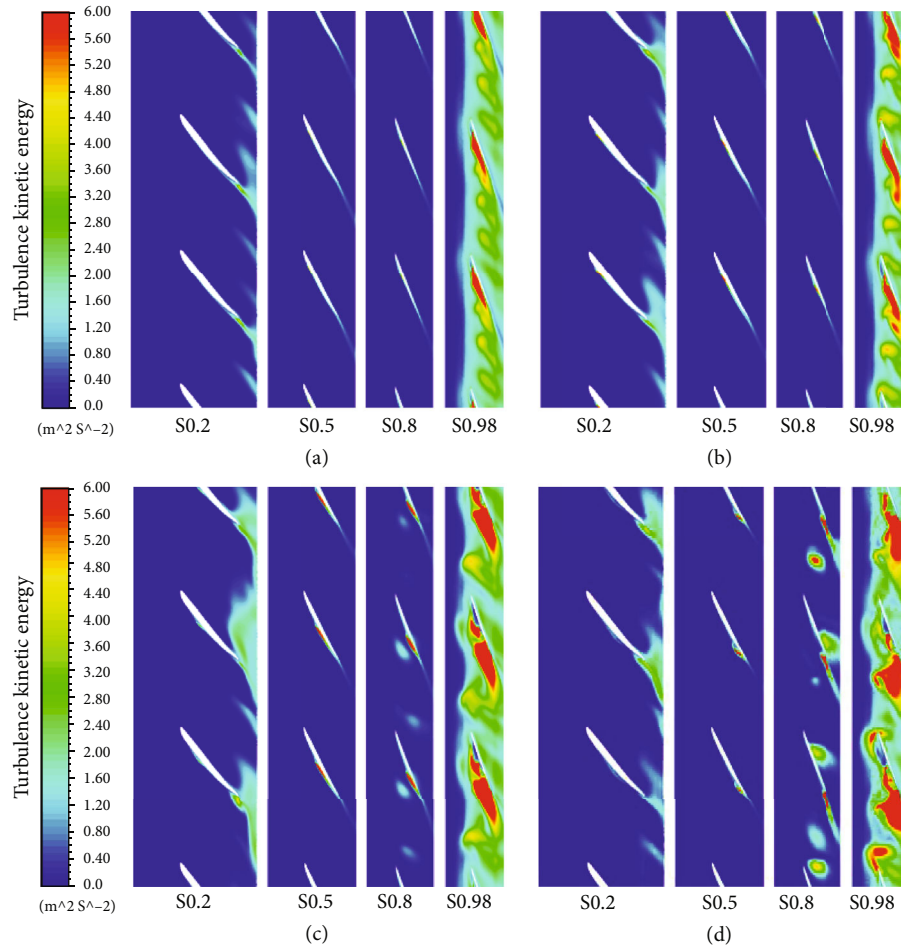
FIGURE 13: Distributions of turbulence kinetic energy at different spans of part impeller with varying NPSH under the tip clearance of 0.1% span ((a) NPSH = 11.492 m; (b) NPSH = 9.816 m; (c) NPSH = 7.562 m; (d) NPSH = 5.830 m).

remains small and fluctuates in a very small range as the tip increases. From Figure 9, we found that part impeller and diffuser are still main location that irreversible energy loss happens, and the turbulent dissipation of part impeller is more than double of the dissipation of part diffuser. Therefore, the impeller is still the largest place that irreversible energy loss occurs with varying tip. And the tip clearance has a little impact on turbulent dissipation of part impeller.

4.3. Cavitation Patterns and Entropy Generation Distributions with Varying NPSH. When axial-flow pumps operate under cavitation conditions, lower pressure generally is located at leading edges of blades' suction sides near part impeller's shroud; thus, the cavitation generally occurs around blade suction surfaces of the impeller. Meanwhile, the impeller has the largest energy dissipation for this axial-flow pump, and most are turbulent dissipation based on the above analysis. Therefore, we here mainly study the cavitation patterns and detailed turbulent entropy generation rate distributions for part impeller. To study the impacts of NPSH on cavitation patterns and entropy generation distributions, we fix the flow rate to 302.917 kg/s and the tip clearance to 0.1% span. Figure 10 shows the cavitation pattern, with iso-surface of vapor volume fraction

($\alpha_v = 0.1$) with varying NPSH for the impeller. Displayed in Figure 10, the cavitation mainly consists of the attached sheet cavitation, tip leakage vortex cavitation, and tip clearance cavitation. Among them, attached cavitation on blades' suction sides and tip leakage vortex cavitation are caused due to pressure difference between pressure and suction sides of blades, and tip clearance cavitation is caused by tip corner vortex on the tip. These types of cavitation also have been validated applying the PIV experiment and simulations [18]. For severe cavitation conditions, different types of cavitation can merge into a large-scale cavitation cloud and block the flow passage in part impeller, then finally decreasing the pump performance. As seen from Figure 10, the red regions of attached sheet cavitation and tip leakage vortex cavitation both increase greatly as NPSH decreases from 11.492 m to 5.83 m. While the red areas of tip clearance cavitation attached on the blade tip surface has no significant changes, this may be due to the smallest tip clearance of 0.1% span. With the NPSH reducing displayed in Figure 10, the attached sheet cavitation extends from first covering less than half of the blade's suction surface in Figure 10(a) to almost covering the entire blade suction tip side in Figure 10(d). Meanwhile, attached sheet cavitation region develops thicker and induces the blockage for the
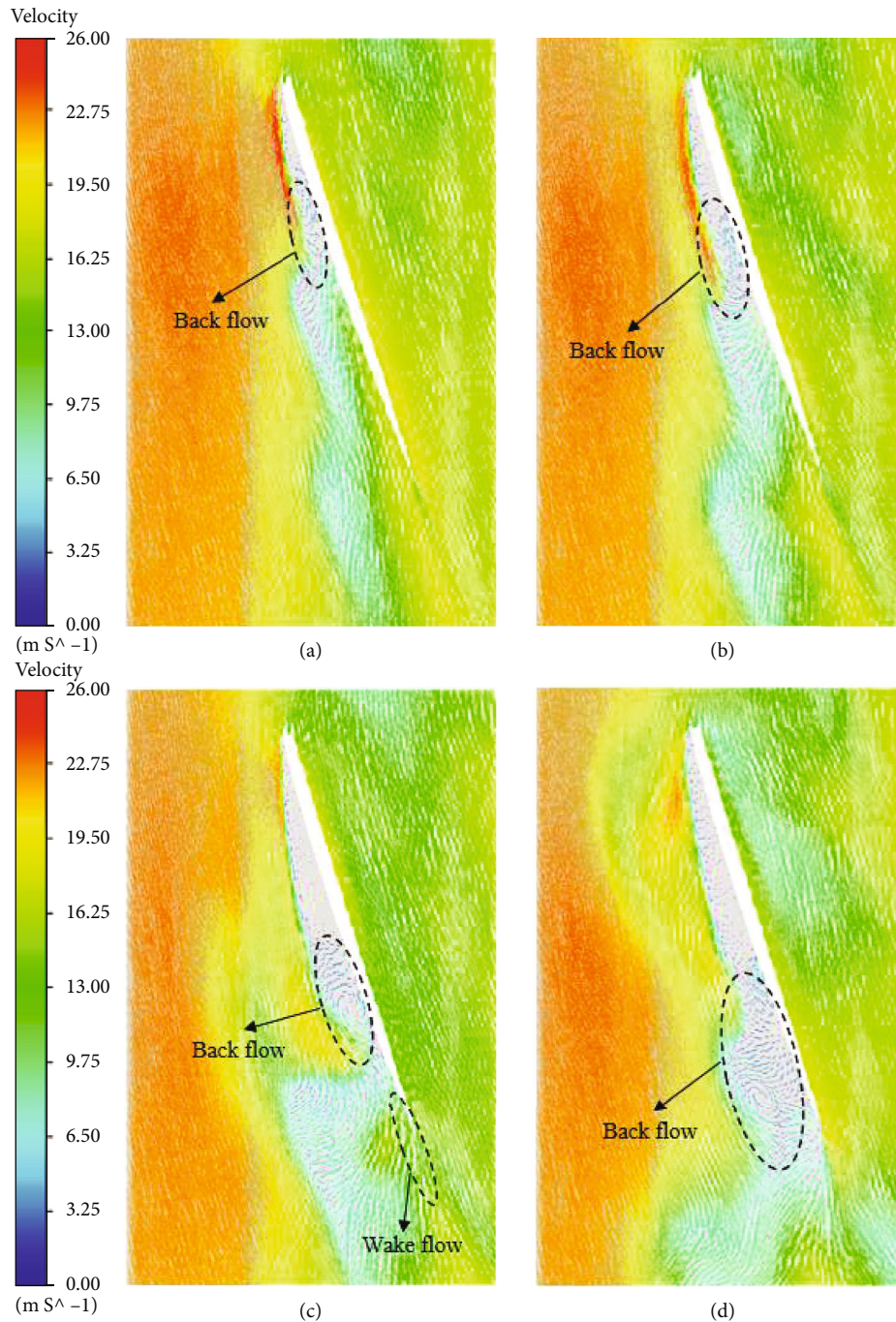
Figure 14: Velocity vector at S0.98 of part impeller with varying NPSH under the tip clearance of 0.1% span ((a) NPSH = 11.492 m; (b) NPSH = 9.816 m; (c) NPSH = 7.562 m; (d) NPSH = 5.830 m).

impeller's channel with the NPSH reducing. From the Figure 10, the tip leakage vortex cavitation connects with attached cavitation, the location at which leakage vortex cavitation leaves from the blade near the shroud moves downstream. Thus, the NPSH has significant effects on the cavitation patterns of the impeller.

To study the relations between the cavitation development and energy dissipation in part impeller with varying NPSH, we here draw the contours of vapor volume fraction at different spans of part impeller as shown in Figure 11 and

its corresponding contours of turbulent entropy generation distributions at different spans as shown in Figure 12 to conduct the analysis. The span from hub to shroud is set as 0~1, and S0.98 is close to the shroud. Figure 11 displays vapor volume fraction at varying span (S0.2, S0.5, S0.8, and S0.98) of part impeller under varying NPSH. As seen from Figure 11(a), the areas of cavity mainly emerge near blades' suction sides, with S0.8 and S0.98 having large cavity areas. When the NPSH reduces to 9.816 m as shown in Figure 11(b), the cavity areas extend larger along the blade
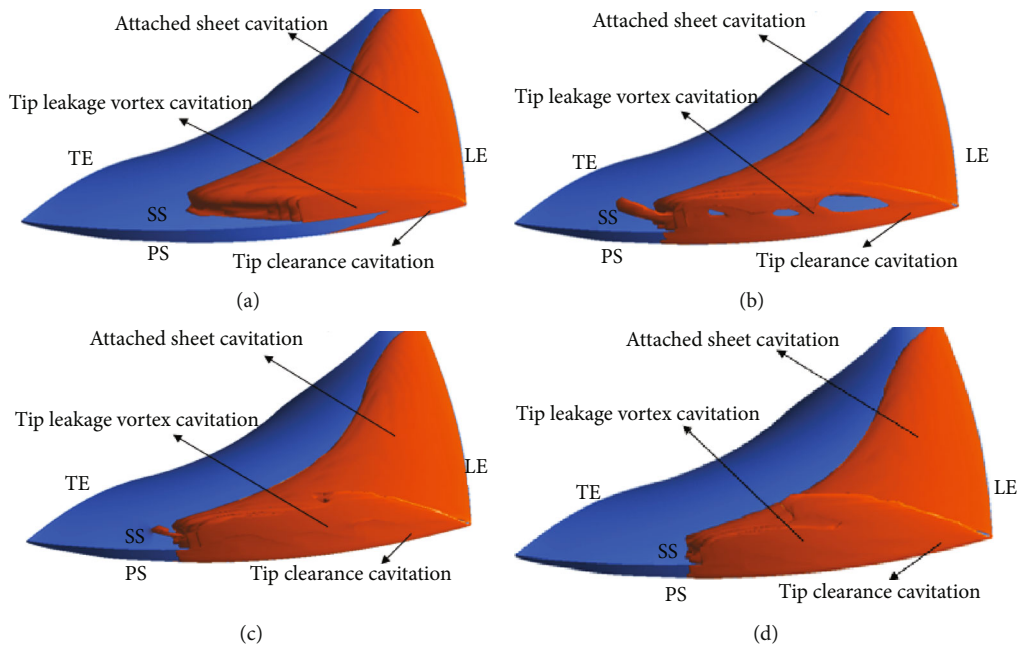
FIGURE 15: Cavitation patterns with varying tip clearance under NPSH = 9.816 m. Iso-surface of vapor volume fraction ($\alpha_v = 0.1$) ((a) h = 0.1% span; (b) h = 0.3% span; (c) h = 0.6% span; (d) h = 0.8% span).

suction side than that shown in Figure 11(a) for each corresponding span especially for span S0.8 and S0.98. When the NPSH further drops from 9.816 m to 5.83 m that changing from Figure 11(b) to Figure 11(d), the cavity areas increase obviously for every corresponding span, which is similar with the variation trend in Figure 10. Thus, the cavity areas of the impeller extend larger along the blade's suction side with NPSH decreasing.

Figure 12 displays distributions of turbulent entropy generation rate $\dot{S}_{D'}''$ in part impeller at varying span (S0.2, S0.5, S0.8, and S0.98) under varying NPSH. Detailed turbulent entropy generation rate distributions can help us determine the locations and magnitude of energy dissipation intuitively and quantitatively. As seen from Figure 12(a), the high regions of $\dot{S}_{D'}''$ most happen near suction surfaces of blades, with S0.98 having largest turbulent dissipation. Through comparing Figure 11 with Figure 12, we observe that the cavitation development has a strong relation with turbulent entropy generation distributions of part impeller. The relation reflects on the field that the high regions of turbulent entropy generation are generally concentrated on the rear part of the cavity for every corresponding span of the impeller. When the NPSH decreases to 9.816 m displayed in Figure 12(b), the distributions of turbulent generation rate are similar with the phenomena displayed in Figure 12(a), but the high areas of $\dot{S}_{D'}''$ at span S0.98 extend larger than that displayed in Figure 12(a). As the NPSH further decreases to 7.562 m displayed in Figure 12(c), the large regions of $\dot{S}_{D'}''$ expand larger along the blade's suction side for each corresponding span especially for S0.98 than that displayed in Figure 12(b). As the NPSH drops to 5.83 m displayed in Figure 12(d), the high areas of $\dot{S}_{D'}''$ extend farther along the blade suction side for S0.98 and other corresponding span. The distribution of large turbulent dissipation at

S0.98 shown in Figure 12(d) becomes more disorder and moves more downstream of the impeller than that displayed in Figure 12(c). From the analysis above, we can conclude that the turbulent entropy generation rate of part impeller is mainly located at rear part of the cavity and expand along suction surfaces of blades, with S0.98 having higher turbulent dissipation under these cavitation conditions. And the high areas of turbulent dissipation in part impeller expand larger and move downstream along the blade suction side especially for S0.98 with NPSH reducing. For the cavitation development, the cavity areas increase along the blade suction side especially for the span S0.8 and S0.98 with the NPSH decreasing. As for the relation between the cavitation patterns and turbulent dissipation, the cavity areas and high areas of turbulent dissipation both increase especially for the spans near the shroud with the decrease of the NPSH. Besides, the regions of high turbulent dissipation are mainly occurred at the rear part of cavity and trail of the blade for every corresponding span of the impeller, which indicates that the energy dissipation is concentrated on the rear part of the cavity and the tail of the blade. To study the reason why the high turbulent dissipation gathers in these places, we draw their corresponding contours of turbulence kinetic energy at varying span (S0.2, S0.5, S0.8, and S0.98) of part impeller displayed in Figure 13 to analyze. Through the comparison between the turbulence kinetic energy distributions in Figure 13 and distributions of turbulent entropy generation in Figure 12, we can observe that the regions of large turbulence kinetic energy also have high turbulent entropy generation rate. To deeply investigate the reason for large turbulence kinetic energy near the shroud, here, draw velocity vector on S0.98 under different NPSH with a tip clearance of 0.1% span shown in Figure 14 to analyze. In Figure 14, there is a backflow area at the rear part of the
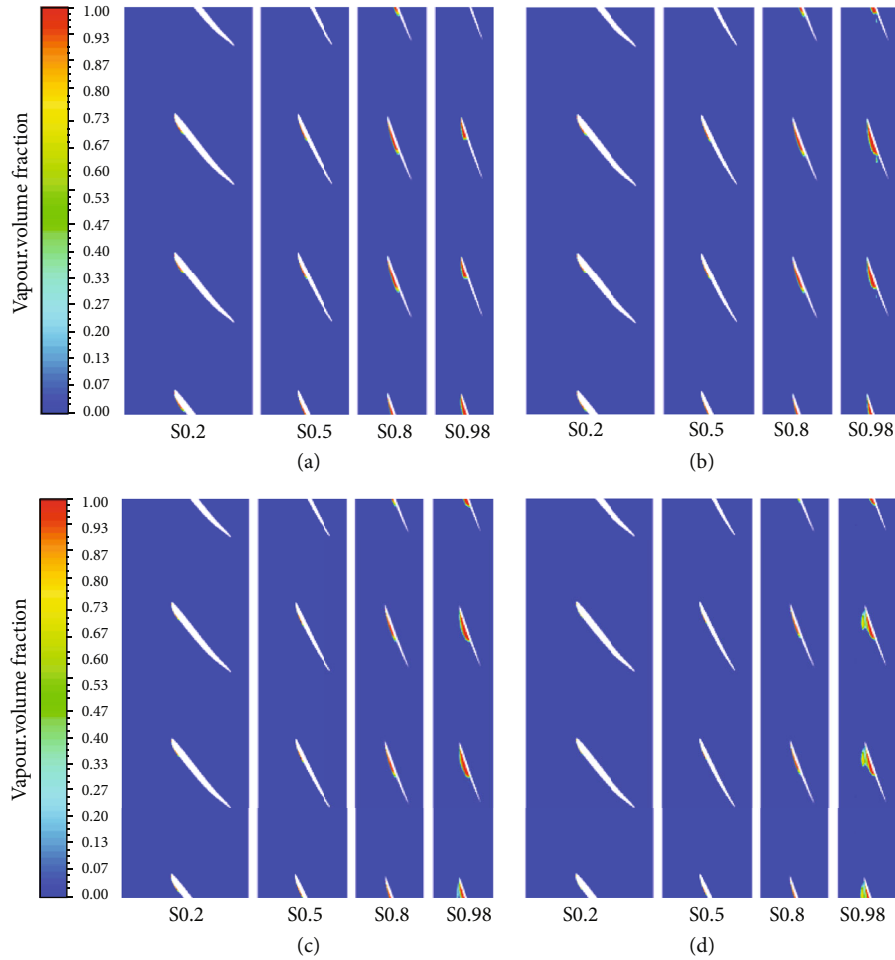
Figure 16: The vapor volume fraction at different spans in part impeller for varying tip clearance under NPSH = 9.816 m ((a) $h = 0.1\%$ span; (b) $h = 0.3\%$ span; (c) $h = 0.6\%$ span; (d) $h = 0.8\%$ span).

cavity and a wake area at the tail of blade, and the backflow area moves downstream and expands along blades' suction sides with the NPSH declining. When the thickness of the backflow area gets close to the thickness of the rear of the cavity, the cavity trail would no longer attach to the blade suction side. When large scale of tail part of the cavity shed from blades, the unsteadiness of the flow increases and high turbulence kinetic energy are generated there. Thus, the unstable flows caused by the rear of the cavity shedding and wake flows are generated at the rear part of the cavity and tail part of the blade, then gathering high turbulence kinetic energy of these areas and finally resulting in large turbulent dissipation there. Therefore, the turbulent dissipation has a close relationship with the cavitation pattern for part impeller. And NPSH has significant impacts on the cavitation development and turbulent dissipation especially the span near part impeller's shroud.

4.4. Cavitation Patterns and Entropy Generation Distributions with Varying Tip Clearance. To study impacts of tip clearance on cavitation patterns and entropy generation distributions for the impeller, we fix the NPSH to 9.816 m and flow rate to 302.917 kg/s. Similar to the above

analysis, the cavitation patterns by iso-surface of vapor volume fraction ($\alpha_v = 0.1$) with varying tip clearance for the impeller are shown in Figure 15. Also from Figure 15, the cavitation mainly includes the attached sheet cavitation, tip leakage vortex cavitation, and tip clearance cavitation. With the tip increasing from 0.1% span to 0.3% span from Figure 15(a) to Figure 15(b), the red areas of tip leakage vortex cavitation and tip clearance cavitation attached on the blade tip increase obviously under the same NPSH = 9.816 m, while the areas of attached sheet cavitation on blade suction surface change less obviously with the tip increasing from 0.1% span to 0.3% span. Meanwhile, the tip leakage vortex cavitation connects with attached cavitation, the location at which leakage vortex cavitation leaves from blade suction side near the shroud moving downstream as the tip growing from 0.1% span to 0.3% span. With the tip increasing further from 0.3% span to 0.6% span, regions of tip leakage vortex cavitation change from a cavity with holes in Figure 15(b) to a solid and larger cavity that thickens nearer the impeller's inlet in Figure 15(c). Meanwhile, the location at which tip leakage vortex cavitation detaches from the blade suction surface near the shroud changes not evidently with tip clearance growing from 0.3% span to 0.6%
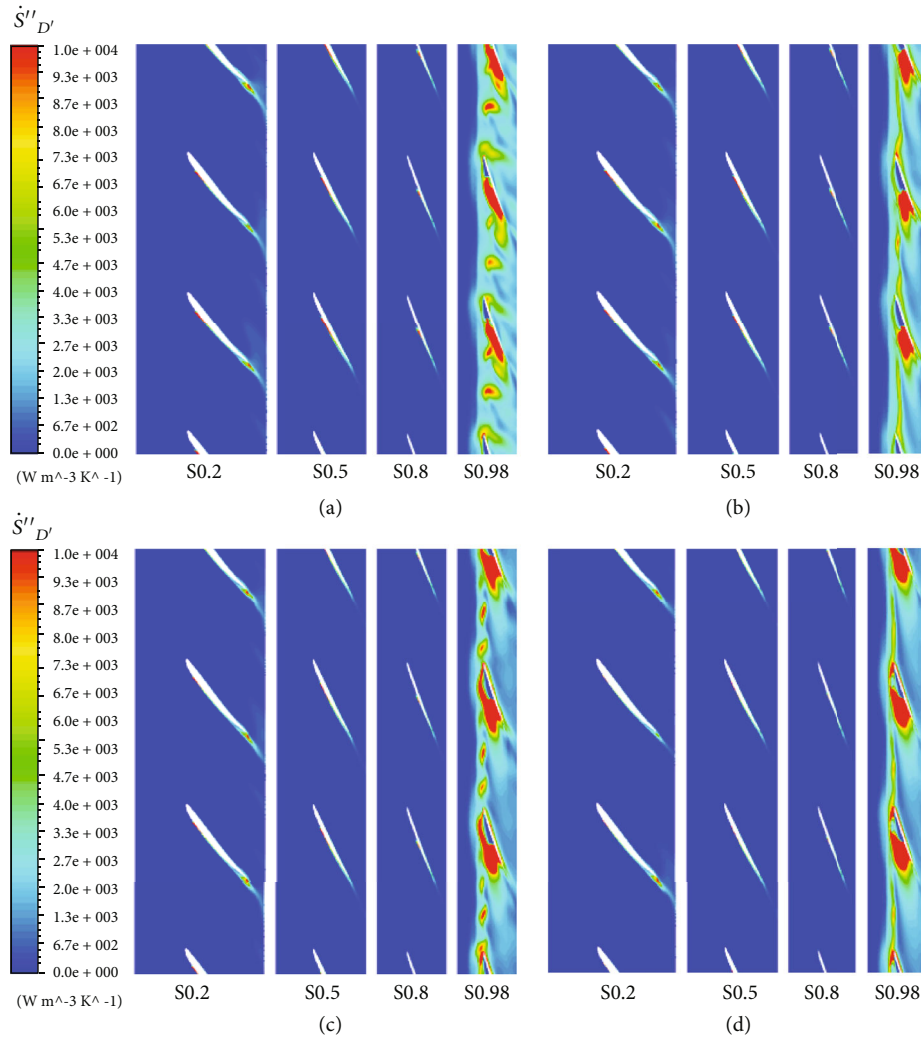
FIGURE 17: Distributions of turbulent entropy generation rate $\dot{S}''_{D'}$ at different spans in part impeller for varying tip clearance under NPSH = 9.816 m ((a) h = 0.1% span; (b) h = 0.3% span; (c) h = 0.6% span; (d) h = 0.8% span).

span. And areas of tip clearance cavitation that attached on blade tip surface have not evident changes with the growth of the tip from 0.3% span to 0.6% span. As the tip gets to 0.8% span, regions of tip leakage vortex cavitation expand larger, moving more toward the impeller inlet as shown in Figure 15(d) than that as shown in Figure 15(c). Also, the location at which tip leakage vortex cavitation detaches from blades and areas of tip clearance cavitation have not evident changes as the tip growing from 0.6% span to 0.8% span. All in all, we can conclude that the tip gap alters the pattern of tip leakage vortex cavitation and clearance cavitation under this same NPSH. This indicates that tip clearance mainly effects on cavitation patterns near the shroud for the impeller under the same NPSH = 9.816 m.

Like the analysis above, we here draw the contours of vapor volume fraction and turbulent entropy generation at different spans in part impeller as shown in Figures 16 and 17 to investigate impacts of tip width on the cavitation development and energy dissipation for the impeller. Figure 16 shows the vapor volume fraction at different spans

(S0.2, S0.5, S0.8, and S0.98) of the impeller with varying tip clearance under the same NPSH = 9.816 m. Figure 16(a) is the same with Figure 11(b), and the areas of cavity mainly occur near the blades' suction surfaces especially for the span S0.8 and S0.98. When the tip increases to 0.3% span displayed in Figure 16(b), regions of the cavity at span S0.98 extend larger along the blade suction side than that displayed in Figure 16(a). As the tip further increases from 0.3% span to 0.8% span that changes from Figure 16(b) to Figure 16(d), the cavity areas mainly change at span S0.98, and the cavity moves more towards the impeller inlet, which is consistent with variation phenomenon in Figure 15. Thus, the increase of tip clearance mainly changes the cavity areas at S0.98 of part impeller. Figure 17 displays the distributions of turbulent entropy generation rate $\dot{S}''_{D'}$ in part impeller at different spans (S0.2, S0.5, S0.8, and S0.98) with varying tip under NPSH = 9.816 m. Figure 17(a) is the same with Figure 12(b), and high regions of $\dot{S}''_{D'}$ are located near the suction surfaces of blades, with S0.98 having larger turbulent dissipation. Through comparing Figure 16 with Figure 17,

we also found that high regions of turbulent entropy generation rate are generally located at the rear part of cavity for every corresponding span of part impeller. As the tip increases from 0.1% span to 0.3% span with same NPSH, high areas of turbulent entropy generation rate at span S0.98 move farther downstream along the blade suction side that seen changing from Figure 17(a) to Figure 17(b). When the tip clearance further increases to 0.6% span displayed in Figure 17(c), the large regions of $\dot{S}_{D'}''$ at span S0.98 extend and move towards the impeller inlet comparing with Figure 17(b). As the tip clearance grows to 0.8% span displayed in Figure 17(d), the areas of high $\dot{S}_{D'}''$ have small changes towards the impeller inlet comparing the high regions of $\dot{S}_{D'}''$ displayed in Figure 17(c). Also, the unstable flows caused by cavity shedding at the rear of the cavity and wake flows at the trail of the blade induce large turbulent dissipation at S0.98 in part impeller. In our current research for the cavitation flows, we conclude that the tip clearance mainly influences the cavitation development and turbulent dissipation distribution around part impeller's shroud under the same NPSH. Meanwhile, the turbulent dissipation has a strong relation with the cavitation pattern for different tip within part impeller, which reflects on the field that high turbulent dissipation is generally located at the rear part of cavity for every corresponding span.

5. Conclusions

In the current research, the impacts of different NPSH and tip clearance width on cavitation patterns and energy dissipation in an axial pump are investigated applying numerical simulations with entropy generation method. Through calculating overall entropy generation rate of different parts and analyzing the cavitation patterns and entropy generation distributions for the impeller under varying conditions, we can summarize the following conclusions.

(1) The calculated results indicate that pump performance declines greatly as NPSH reducing with same tip size of 0.1% span, which shows that there are more energy losses when the cavitation becomes more severe. With the tip growing from 0.1% span to 0.8% span under the same cavitation condition (NPSH = 9.816 m), the pump performance decreases slightly. Meanwhile, part impeller and diffuser are mainly places of entropy generation for different NPSH and tip width; part impeller is the component with more than 50% of the dissipation for the entire pump. And most are turbulent dissipation.

(2) As the NPSH decreases from 11.492 m to 5.83 m under the tip clearance of 0.1% span, the regions of attached sheet cavitation and tip leakage vortex cavitation near blades both increase greatly as displayed in Figure 10, while the areas of tip clearance cavitation attached on the blade tip surface have no significant changes. The cavity areas of the impeller extend larger along blade suction side especially for the span S0.8 and S0.98 with the decrease of the

NPSH. With the NPSH decreasing, the high regions of dissipation in part impeller expand along the blades and move downstream, with S0.98 having larger turbulent dissipation under the same tip clearance of 0.1% span. Besides, the areas of large turbulent dissipation are mainly located at the rear part of cavity for every corresponding span of the impeller, which indicates that the turbulent dissipation has a relationship with cavitation pattern of part impeller. The unstable flows caused by cavity shedding at the rear of the cavity and wake flows near the blade trail induce high turbulent dissipation of part impeller. Therefore, the change of NPSH has significant impacts on the cavitation development and turbulent dissipation especially for the span near the impeller's shroud.

(3) With the tip growing from 0.1% span to 0.8% span under the same NPSH displayed in Figure 15, the areas of tip leakage vortex cavitation and tip clearance cavitation near the shroud expand along blade suction surface. This indicates that tip clearance mainly effects on cavitation patterns near the shroud for the impeller under the same NPSH. With the tip clearance growing, high regions of turbulent dissipation are mainly distributed along the blade suction sides and move downstream, with the span S0.98 having larger turbulent dissipation. Also, the regions of high turbulent dissipation are mainly occurred at the rear part of cavity for every corresponding span in part impeller. Thus, the tip clearance width mainly influences the cavitation development and turbulent dissipation distributions around part impeller's shroud under the same NPSH.

Nomenclature

Q:	Mass flow rate (kg/s)
D:	Impeller diameter (mm)
H:	Head (m)
n:	Rotational speed (r/min)
H_d:	Design head (m)
Q_d:	Design flow rate (kg/s)
M:	Torque ($N * m$)
Ω:	Rotor angular velocity (rad/s)
p:	Pressure (Pa)
g:	Gravity acceleration (m/s^2)
p_v:	Vapor pressure (Pa)
h:	Tip clearance width (mm)
ρ:	Density (kg/m^3)
α_v:	Volume fraction of vapor
φ:	Flow coefficient
ψ:	Head coefficient
η:	Pump efficiency (%)
ω:	Characteristic frequency
μ:	Molecular viscosity
μ_t:	Turbulent viscosity
k:	Turbulence kinetic energy (m^2/s^2)
NPSH:	net positive suction head (m)

Subscripts l, m, v: Liquid, mixture, vapor

u, v, w: Velocity component along x, y, z direction (m/s)

$(\,)$:   Mean component

$(\,)'$:   Fluctuating component

LE: Leading edge

TE: Trailing edge

PS: Pressure side

SS: Suction side

$\dot{S}_D''$:   Entropy generation rate caused by time-averaged movements (Wm^{-3}K^{-1})

$\dot{S}_{D'}''$:   Entropy generation rate caused by velocity fluctuations (Wm^{-3}K^{-1})

$\dot{S}_{\bar{D}}$:   Overall entropy generation rate caused by time-averaged movements of a region (W/K)

$\dot{S}_D{}'$:   Overall entropy rate caused by velocity fluctuations of a region (W/K)

$\dot{S}_D$:   Overall entropy generation rate of a region (W/K).

Data Availability

All data generated or analyzed during this study are included in this article.

Conflicts of Interest

The authors declare that they have no conflicts of interest.

Authors' Contributions

Simin Shen (first author and corresponding author) is responsible for conceptualization, resources, software, methodology, formal analysis, investigation, writing—original draft, and writing—review and editing; Bensheng Huang (second author) for supervision; Si Huang (third author) for supervision and validation; and Shun Xu (fourth author) and Shufeng Liu (fifth author) for funding acquisition.

Acknowledgments

References

[1] S. Gopalan, J. Katz, and H. L. Liu, "Effect of gap size on tip leakage cavitation inception, associated noise and flow structure," *Journal of Fluids Engineering*, vol. 124, no. 4, pp. 994–1004, 2002.

[2] S. Christopher and S. Kumaraswamy, "Identification of critical net positive suction head from noise and vibration in a radial flow pump for different leading edge profiles of the vane," *Journal of Fluids Engineering*, vol. 135, no. 12, 2013.

[3] C. Haosheng, L. Jiang, and L. Shihan, "Thermal effect at the incipient stage of cavitation erosion on a stainless steel in ultrasonic vibration cavitation," *Journal of Fluids Engineering*, vol. 131, no. 2, 2009.

[4] B. Pouffary, R. F. Patella, J. L. Reboud, and P. A. Lambert, "Numerical simulation of 3D cavitating flows: analysis of cavitation head drop in turbomachinery," *Journal of Fluids Engineering*, vol. 130, no. 6, 2008.

[5] S. Saito, "Cavitation aspect and flow pattern in an axial-flow impeller," *Transactions of The Japan Society of Mechanical Engineers*, vol. 53, no. 492, pp. 2483–2491, 1987.

[6] R. Zhang and H. Chen, "Numerical analysis of cavitation within slanted axial-flow pump," *Journal of Hydrodynamics*, vol. 25, no. 5, pp. 663–672, 2013.

[7] K. Hosono, Y. Kajie, S. Saito, and K. Miyagawa, "Study on cavitation influence for pump head in an axial flow pump," *Journal of Physics*, vol. 656, no. 1, p. 012062, 2015.

[8] L. Shi, D. S. Zhang, R. J. Zhao, W. D. Shi, and Y. X. Jin, "Effect of blade tip geometry on tip leakage vortex dynamics and cavitation pattern in axial-flow pump," *Science China Technological Sciences*, vol. 60, no. 10, pp. 1480–1493, 2017.

[9] D. Zhang, L. Shi, W. Shi, R. Zhao, H. Wang, and B. P. M. (Bart) van Esch, "Numerical analysis of unsteady tip leakage vortex cavitation cloud and unstable suction-side-perpendicular cavitating vortices in an axial flow pump," *International Journal of Multiphase Flow*, vol. 77, pp. 244–259, 2015.

[10] D. Zhang, W. Shi, D. Pan, and M. Dubuisson, "Numerical and experimental investigation of tip leakage vortex cavitation patterns and mechanisms in an axial flow pump," *Journal of Fluids Engineering*, vol. 137, no. 12, 2015.

[11] D. Y. Tan, R. L. Miorini, J. Keller, and J. Katz, "Flow visualization using cavitation within blade passage of an axial waterjet pump rotor," *Fluids Engineering Division Summer Meeting*, vol. 44755, pp. 395–404, 2012.

[12] W. Feng, Q. Cheng, Z. Guo, and Z. Qian, "Simulation of cavitation performance of an axial flow pump with inlet guide vanes," *Advances in Mechanical Engineering*, vol. 8, no. 6, 2016.

[13] Z. Qian, F. Wang, Z. Guo, and J. Lu, "Performance evaluation of an axial-flow pump with adjustable guide vanes in turbine mode," *Renewable Energy*, vol. 99, pp. 1146–1152, 2016.

[14] S. Shen, Z. Qian, B. Ji, and R. K. Agarwal, "Numerical investigation of tip flow dynamics and main flow characteristics with varying tip clearance widths for an axial-flow pump," *Proceedings of the Institution of Mechanical Engineers, Part A: Journal of Power and Energy*, vol. 233, no. 4, pp. 476–488, 2019.

[15] Z. Guo, J. Pan, Z. Qian, and B. Ji, "Experimental and numerical analysis of the unsteady influence of the inlet guide vanes on cavitation performance of an axial pump," *Proceedings of the Institution of Mechanical Engineers, Part C: Journal of Mechanical Engineering Science*, vol. 233, no. 11, pp. 3816–3826, 2019.

[16] D. Zhang, W. Shi, B. B. Van Esch, L. Shi, and M. Dubuisson, "Numerical and experimental investigation of tip leakage vortex trajectory and dynamics in an axial flow pump," *Computers & Fluids*, vol. 112, pp. 61–71, 2015.

[17] Y. Liu, L. Tan, Y. Hao, and Y. Xu, "Energy performance and flow patterns of a mixed-flow pump with different tip clearance sizes," *Energies*, vol. 10, no. 2, p. 191, 2017.

[18] H. Wu, R. L. Miorini, and J. Katz, "Measurements of the tip leakage vortex structures and turbulence in the meridional plane of an axial water-jet pump," *Experiments in Fluids*, vol. 50, no. 4, pp. 989–1003, 2011.

[19] Y. Hao and L. Tan, "Symmetrical and unsymmetrical tip clearances on cavitation performance and radial force of a mixed

flow pump as turbine at pump mode," *Renewable Energy*, vol. 127, pp. 368–376, 2018.

[20] L. Shi, D. Zhang, R. Zhao, W. Shi, and B. V. Bpm, "Visualized observations of trajectory and dynamics of unsteady tip cloud cavitating vortices in axial flow pump," *Journal of Fluid Science and Technology*, vol. 12, no. 1, p. JFST0007, 2017.

[21] Y. Liu and L. Tan, "Tip clearance on pressure fluctuation intensity and vortex characteristic of a mixed flow pump as turbine at pump mode," *Renewable Energy*, vol. 129, pp. 606–615, 2018.

[22] D. Li, Z. Ren, R. Fan, Y. Chai, R. Gong, and H. Wang, "Influence of axial clearance on the performance characteristics of a turbo pump," *Journal of Mechanical Science and Technology*, vol. 35, no. 10, pp. 4543–4555, 2021.

[23] R. Z. Gong, H. J. Wang, L. X. Chen, D. Y. Li, H. C. Zhang, and X. Z. Wei, "Application of entropy production theory to hydro-turbine hydraulic analysis," *Science China Technological Sciences*, vol. 56, no. 7, pp. 1636–1643, 2013.

[24] D. Li, H. Wang, Y. Qin, L. Han, X. Wei, and D. Qin, "Entropy production analysis of hysteresis characteristic of a pump-turbine model," *Energy Conversion and Management*, vol. 149, pp. 175–191, 2017.

[25] D. Li, H. Wang, Y. Qin, X. Wei, and D. Qin, "Numerical simulation of hysteresis characteristic in the hump region of a pump-turbine model," *Renewable Energy*, vol. 115, pp. 433–447, 2018.

[26] H. Hou, Y. Zhang, Z. Li, T. Jiang, J. Zhang, and C. Xu, "Numerical analysis of entropy production on a LNG cryogenic submerged pump," *Journal of Natural Gas Science and Engineering*, vol. 36, pp. 87–96, 2016.

[27] J. Pei, F. Meng, Y. Li, S. Yuan, and J. Chen, "Effects of distance between impeller and guide vane on losses in a low head pump by entropy production analysis," *Advances in Mechanical Engineering*, vol. 8, no. 11, 2016.

[28] H. Chang, W. Shi, W. Li, and J. Liu, "Energy loss analysis of novel self-priming pump based on the entropy production theory," *Journal of Thermal Science*, vol. 28, no. 2, pp. 306–318, 2019.

[29] X. Li, Z. Jiang, Z. Zhu, Q. Si, and Y. Li, "Entropy generation analysis for the cavitating head-drop characteristic of a centrifugal pump," *Proceedings of the Institution of Mechanical Engineers, Part C: Journal of Mechanical Engineering Science*, vol. 232, no. 24, pp. 4637–4646, 2018.

[30] C. Wang, Y. Zhang, H. Hou, J. Zhang, and C. Xu, "Entropy production diagnostic analysis of energy consumption for cavitation flow in a two-stage LNG cryogenic submerged pump," *International Journal of Heat and Mass Transfer*, vol. 129, pp. 342–356, 2019.

[31] S. Shen, Z. Qian, and B. Ji, "Numerical analysis of mechanical energy dissipation for an axial-flow pump based on entropy generation theory," *Energies*, vol. 12, no. 21, p. 4162, 2019.

[32] A. Yu, Q. Tang, H. Chen, and D. Zhou, "Investigations of the thermodynamic entropy evaluation in a hydraulic turbine under various operating conditions," *Renewable Energy*, vol. 180, pp. 1026–1043, 2021.

[33] L. Ji, W. Li, W. Shi, H. Chang, and Z. Yang, "Energy characteristics of mixed-flow pump under different tip clearances based on entropy production analysis," *Energy*, vol. 199, p. 117447, 2020.

[34] T. Lin, X. Li, Z. Zhu, J. Xie, Y. Li, and H. Yang, "Application of enstrophy dissipation to analyze energy loss in a centrifugal pump as turbine," *Renewable Energy*, vol. 163, pp. 41–55, 2021.

[35] F. Kock and H. Herwig, "Local entropy production in turbulent shear flows: a high-Reynolds number model with wall functions," *International Journal of Heat and Mass Transfer*, vol. 47, no. 10-11, pp. 2205–2215, 2004.

[36] J. Mathieu and J. Scott, *An Introduction to Turbulent Flow*, Cambridge University Press, 2018.

Research Article

The Time-Dependent Reliability Analysis of Brake Piston Special-Shaped Seal of the Caliper Disc Brake

Meng Sun [iD],[1] **Liqun Lu** [iD],[1] **Xin Bai,**[1] **Huiting Ni,**[1] **and Leilei Shi**[2]

[1]*School of Transportation and Vehicle Engineering, Shandong University of Technology, Zibo 255000, China*
[2]*Department of Automotive Engineering, Shandong Labor Vocational and Technical College, Jinan 250300, China*

Correspondence should be addressed to Liqun Lu; luliqun@sdut.edu.cn

To solve the brake caliper disc brake piston sealing ring in the high temperature, pressure, and changeful, complex working environments, such as vibration failure cause brake short service life, low reliability, in the original brake piston O seal ring and cross section, the research, based on the standard of sealing ring, such as special-shaped seal structure is put forward in order to improve the reliability of the caliper disc brake piston sealing performance. Based on the basic concept of time-varying reliability and the theoretical basis of stress-strength interference model, the time-varying reliability model of the plum blossom seal ring of the brake piston under shear stress failure and leakage failure modes was established. The reliability of the plum blossom seal ring under single failure mode and multiple failure modes is obtained. The results show that under the same conditions, the reliability of the plum blossom seal ring is greater than that of the O seal ring, and its sealing performance is better than that of the O seal ring.

1. Introduction

With the progress of vehicle technology and the improvement of vehicle speed, higher requirements are put forward for the quality of vehicle braking system. The caliper disc brake is widely used in automobile braking systems because of its excellent characteristics such as stable braking, good heat dissipation, high safety, and convenient installation and maintenance [1, 2]. The sensitivity and reliability of the caliper disc brakes have a great relationship with the rationality of the sealing structure of the brake piston. The function of the sealing structure is to ensure that the brake fluid cannot leak through the sealing ring during the braking process and provide sufficient reset force for the brake piston at the end of the braking process. At present, the brake piston seal structure adopts the form of O-shaped or rectangular section seal ring. Although the traditional standard O-shaped or rectangular section seal form is widely used because of its simple structure, low cost, compact design structure, and easy installation, the brake piston seal is under time-dependent and complex working conditions such as

high temperature, variable pressure and vibration, leakage, wear, insufficient elasticity, and other phenomena are easy to occur, to reduce the braking efficiency and even brake failure, affecting the driving safety. On the premise of ensuring the braking efficiency of caliper disc brake, research and explore new structural forms which can meet the special-shaped seal of high-efficiency brake piston, to improve the reliability of the sealing performance of caliper disc brake piston.

Based on the caliper disc brake piston special-shaped seal structure plum flower ring as the research object, the brake piston stress of the plum flower ring is seen as a random process, to have the maximum stress as equivalent stress, equivalent stress analysis how the probability distribution of changes over by stress; according to the stress-strength interference theory model, the whole working time was divided into n periods to calculate the reliability, and the time-varying failure reliability model of the quincunx seal ring of the brake piston was established. At the same time, the failure of the brake piston seal ring was divided into shear stress failure and leakage failure by using the total

probability formula and stress-strength interference model, and the time-varying failure reliability of the brake piston ququin-shaped seal ring and O-shaped seal ring under single failure mode and multiple failure modes was analyzed and calculated.

2. Time-Dependent Reliability Calculation of Brake Piston Seal of Caliper Disc Brake

Reliability design is regarded as a leap of safety design concept. In the process of reliability analysis, load, strength, and other design parameters are treated as random variables, so it can describe load properties and material properties objectively and scientifically. At the same time, the goal of reliability design is to ensure that the strength is greater than the load, and the safety degree of the design can be expressed quantitatively. As shown in Figure 1, when the brake piston works under random load, the contact force of the seal ring changes with the passage of time. If reliability and failure rate are taken as its performance indicators, the reliability model of the seal ring can be expressed as a function of reliability over time [3]. Real-time variable reliability analysis is to analyze the probability distribution of the performance function of the brake piston seal ring when the input is random variable.

2.1. The Calculation Method of Time-Dependent Reliability. Structural reliability can be expressed as the ability of a system to accomplish the specified task under a certain times and conditions or the probability that the product can work normally at the specified time in the normal service environment. Generally, the limit state function for the reliability of time-invariant structures is a random variable model.

$$Z = g(X) = g(X_1, X_2, \cdots, X_n), \qquad (1)$$

When analyzing the reliability, variables $X_1, X_2, \cdots, X_n$ are generally used to replace the factors affecting the structure. It can be seen from the above formula that the traditional study of reliability does not take into account the change of pressure over time and the influence of other factors. During the working period, the brake piston of clamp disc brake will be affected by time-varying factors such as abrasion of sealing structure materials and variable pressure, and its sealing performance will be reduced, resulting in the decrease of contact stress with the increase of working time. The ability of the piston seal ring to complete the sealing function under the given conditions will be reduced, that is, the working reliability of the piston seal structure will be reduced [4, 5].

In order to accurately calculate the brake piston seal reliability, based on the definition of reliability, considering the time factor, the two scholars of domestic Li Yi and Yan Yun through research suggests that for most of the system model structure, its load effect and structural resistance are changes over time, and changes in the reliability of the stochastic process is a dynamic process. At the same time, the two scholars obtained the relationship expression of the time-varying reliability function of the system structure:

$$Z(t) = g[R(t), S(t)] = R(t) - S(t). \qquad (2)$$

In Equation (2), $S_{(t)}$ is the loading effect, namely, the random application process of the medium pressure load, $R_{(t)}$ is the random process of the system structure resistance, that is, the contact stress of the sealing ring, and $Z_{(t)}$ is the function of the sealing ring in a certain limit state. The random process is a linear or nonlinear function. Then, the reliability probability of the piston sealing ring in the period T can be expressed as:

$$P(T) = P\{Z(t) > 0, t \in [0, T]\} = P\{R(t) - S(t) > 0, t \in [0, T]\}. \qquad (3)$$

The contact stress of the brake piston quin-shaped seal ring is greater than the pressure of the brake fluid at every moment t_i during the working period. In this case, the brake piston seal ring can be in a reliable normal working state. According to the complementary theorem of probability, the failure probability of the piston seal ring within the service period T can be expressed as:

$$P_f = 1 - P_s(T) = P\{R(t_i) < S(t_i), t_i \in [0, T]\}. \qquad (4)$$

Formula (4) shows that in the working process of the brake piston quin-shaped seal ring, as long as there is a moment when the contact stress of t_i sealing structure is less than the medium pressure, the sealing failure phenomenon will occur. The reliability probability and failure probability expressed by Equation (3) and Equation (4) are both related to the factor of time T, which is called time-dependent reliability analysis.

2.2. Stress-Strength Interference Model. The stress-strength interference model is the basic model for calculating the reliability of components. In the process of calculating the reliability, the basic idea of interference analysis with random variables can be expressed as follows: as shown in Figure 2, the probability density function curves of stress and strength are drawn in the same coordinate system. Generally, an interference phenomenon happens when the two curves intersect. It will appear failure where the stress is larger than the strength [6]. The stress and strength in the definition are both generalized, and the stress can be the external factors leading to the failure of the sealing ring or sealing system, such as the pressure, friction, and wear of the brake fluid. Strength is the resistance of the sealing ring or sealing system corresponding to various stresses, such as static strength, fatigue static strength, and contact stress. When the probability density function of strength S is $f_S(S)$ and the probability density function of stress s is $f_s(s)$, the probability density function of the reliability R can be expressed as
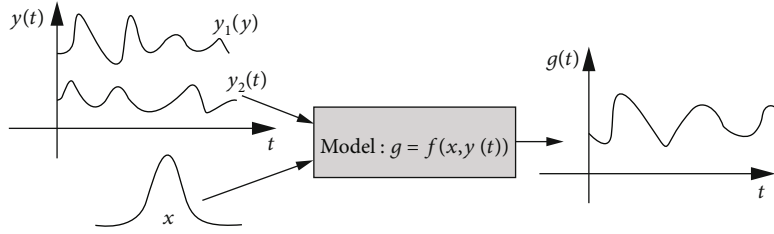
FIGURE 1: Input and output of time-varying reliability.
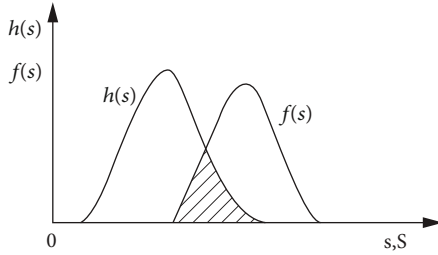
FIGURE 2: Stress-strength interference (SSI) model.

follows:

$$R = P(S > s) = \int_{-\infty}^{+\infty} f_s(s) \int_{s}^{+\infty} f_s(S)dSds = \int_{-\infty}^{+\infty} f_s(S) \int_{-\infty}^{\delta} f_s(s)dsdS.$$

(5)

Then, the failure probability F is expressed as follows:

$$F = 1 - R = \int_{-\infty}^{+\infty} f_s(s) \int_{s}^{+\infty} f_s(S)dSds = \int_{-\infty}^{+\infty} f_s(S) \int_{S}^{-\infty} f_s(s)dsdS.$$

(6)

When the stress distribution overlaps with the strength distribution due to some external or internal reason, the stress strength interference phenomenon occurs. The shaded part in Figure 2 is the "stress-strength interference area". The larger the area of the stress strength interference area, that is, the larger the shadow part in the figure, the greater the probability that the stress is greater than the strength, and the greater the failure possibility of the structure.

When the brake piston seal ring is subjected to a single load in the working process, the probability density function of strength S is expressed as $f_S(S)$, and the probability density function of load L is expressed as $f_L(L)$. As the stress-strength interference theory shows, the reliability of the seal ring can be expressed as follows:

$$R = \int_{-\infty}^{+\infty} f_L(L) \int_{s(L)}^{+\infty} f_S(S)dSdL.$$

(7)

Equation (7) is suitable for calculating the reliability of seal rings under a single load or under a single failure mode. In practice, seal rings are often affected by different failure modes which are independent of each other. When there are multiple failure modes in the working process of the sealing ring, every failure mode will cause the sealing ring to fail.

As is shown in Figure 3, the reliability calculation of the brake piston seal ring can be equivalent to the reliability of the series system constituting its failure mode [7, 8].

When the working load of the sealing ring is a definite value L, there is an independent relationship among the failure modes. The reliability of the sealing ring can be equivalent to the reliability of the series system under independent failure. The reliability R_L can be expressed as follows:

$$R_L = P(S_1 > s_1 \cap S_2 > s_2 > \cdots S_n)$$
$$= P(S_1 > s_{1(L)}) P(S_2 > s_{2(L)}) \cdots P(S_n > s_{n(L)}).$$

(8)

In formula (8), when the load is determined value L, if the applied load obeys the random variable of the density function $f_L(L)$, the relationship expression of the reliability R of the sealing ring can be obtained according to the stress strength interference theory and the calculation formula of full probability, as shown in

$$R = \int_{-\infty}^{+\infty} P(S_1 > s_1 \cap S_2 > s_2 > \cdots S_n > s_n) f_L(L)dL$$
$$= \int_{-\infty}^{+\infty} f_L(L) \int_{s_1(L)}^{+\infty} f_{S_1}(S_1)dS_1 \int_{s_2(L)}^{+\infty} f_{S_2}(S_2)dS_2 \cdots$$
$$\cdot \int_{s_n(L)}^{+\infty} f_{S_n}(S_n)dS_ndL$$
$$= \int_{s_n(L)}^{+\infty} f_L(L) \left\{ \prod_{i=1}^{n} \int_{s_i(L)}^{+\infty} f_{S_i}(S_i)dS_i \right\} dL,$$

(9)

where S_i is the strength in failure mode i, $i = 1, 2, \cdots n$, $S_i(L)$ is the stress generated by load L in failure mode i, and n is the number of failure modes. If the value of n is 1, it becomes the reliability of components under a single failure mode, which is a general stress-strength interference theoretical model.

3. Force Model of Brake Piston of Caliper Disc Brake

The friction force produced by the contact surface between the brake piston seal ring and the brake piston can make the seal ring produce a certain contact stress, which is used to resist the pressure of the brake fluid acting on its surface. When the contact stress is greater than the pressure of brake fluid, Von·Mises stress will make the seal ring leak in the direction of pressure. As a result, it will
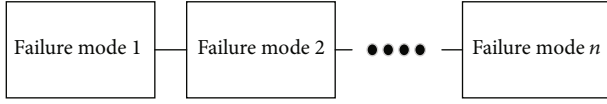
FIGURE 3: Reliability block diagram of series system.
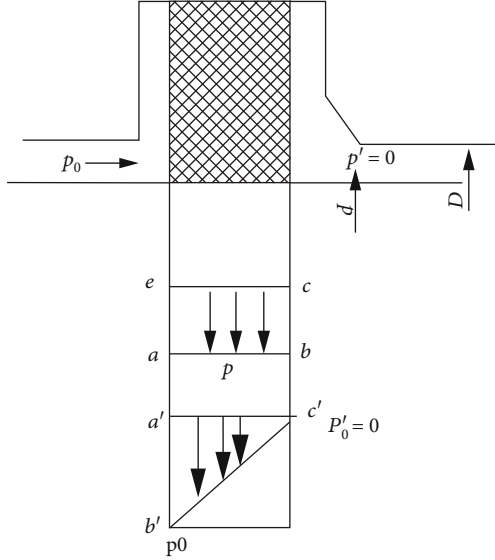
FIGURE 4: Pressure stress of the piston by the deformation of the seal ring.

destroy the original contact state and reduce the sealing performance.

Assuming that the seal structure of the brake piston is a rectangular sealing ring, the deformation diagram of the rectangular sealing ring in the working process is shown in Figure 4. When the brake fluid pressure is p_0, the sealing ring and the piston will only have a relatively sliding contact without force deformation, and what remains unchanged is the width of the contact, that is, the pressure of the deformed rectangular sealing ring on the piston is distributed in a rectangular shape, which can be expressed by a rectangular $abce$. At the same time, to keep the rectangular seal ring well sealed in the contact width, in the pressure direction of the brake fluid, the pressure drops from p_0 to $p_0' = 0$, so that the pressure distribution generated by the oil pressure can be represented by a triangle ε_{min}. The sealing condition of the rectangular seal is that the contact stress is greater than the brake fluid pressure. The contact pressure can be expressed by the area A_1 of rectangular $abce$, and the medium pressure can be expressed by the area A_2 of triangle ε_{min}. Then, the condition of sealing structure is that the area A_1 of rectangular.

$abce$ is larger than the area A_2 of triangle ε_{min}. The average stress produced by sealing ring to piston is $p_0/2$ [9].

The hold force F of the sealing ring to the piston is:

$$F = \pi \cdot d \cdot b_0 \cdot \frac{p_0}{2}, \tag{10}$$

where d is the inner diameter of the piston sleeve of brake

caliper in mm, b_0 is the diameter of the sealing ring in mm, and p_0 is the braking pressure of hydraulic oil in MPa.

Assuming that the friction coefficient between the seal ring and the piston sleeve of the brake caliper is expressed as μ, the friction resistance F_0 required to ensure good sealing performance can be expressed as follows:

$$F_0 = \mu N = \mu \pi \cdot d \cdot b_0 \cdot \frac{p_0}{2}. \tag{11}$$

The friction provided by the seal ring is expressed as F_ε. The radial deformation ε of the seal ring is the main cause of friction F_ε.

$$\varepsilon = \frac{(h_0 - h)}{h_0} \times 100\%, \tag{12}$$

$$F_\varepsilon = \mu \cdot \sigma \cdot S = \mu \cdot \sigma \cdot \pi \cdot d \cdot b_0, \tag{13}$$

where μ is the friction coefficient of rubber material, h is the thickness of the compressed seal ring in mm, h_0 is the thickness of the seal ring without pressure in mm, S is the contact area between the seal ring and the piston sleeve of brake pliers in mm^2, and σ is the compressive stress in MPa. The number of σ is determined by the function of the deformation of the seal ring and the parameters of the rubber material. The material parameters will change with the change of temperature because the rubber is a hyperelastic body. Therefore, the relationship between stress and strain is not linear throughout the working period.

In order to ensure good sealing performance, the sealing rings need to be satisfied: σ_{xy}. From Equation (11) and Equation (13), we can come to the conclusion that $\sigma_{min} = p_0/2$.

$$\frac{2}{3}E\left(1 + 2\mu \cdot \frac{b_0}{2h_0}\right)\left(\frac{1}{\sqrt{1 - \varepsilon_{min}}} + \varepsilon_{min} - 1\right) = \frac{p_0}{2}. \tag{14}$$

In Equation (14), ε_{min} is the minimum deformation of the sealing ring in the sealing process.

When the brake pressure disappears, the brake piston returns to the original position which is the starting position of the brake under the reset force of the seal ring. The reset force and the internal pressure are equal.

$$F_{fw} = F_0 = \pi \cdot \mu \cdot \pi \cdot d \cdot b_0 \cdot \frac{p_0}{2}. \tag{15}$$

The relationship between the maximum contact stress of the sealing ring and the hydraulic pressure is approximately linear, which conforms to the self-tight sealing mechanism [10].

$$P_z = P_0 + kp, \tag{16}$$

where P_z is the maximum contact stress on the sealing ring, P_0 is the maximum contact pressure on the sealing ring during installation, the P on behalf of the pressure of brake fluid, and k is the fluid pressure transfer coefficient and can be

taken as 1 for O-ring. As for other types of sealing ring, it depends on the type of sealing ring [11–13].

4. Time-Dependent Reliability Analysis of Special-Shaped Seal Ring of Brake Piston

As a key component of caliper disc brakes, the brake piston sealing ring will not only reduce the braking performance but also greatly reduce the safety of driving. Therefore, the reliability of the sealing ring can affect the efficient braking performance of the vehicle. In this paper, time-dependent reliability analysis of special-shaped seal ring of the brake piston takes plum-shaped seal ring as an example (as shown in Figure 5). There are four sealing contact planes designed at the contact between the quincunx seal ring and the groove of the brake piston and the brake caliper piston, to achieve good self-sealing function; at the same time, grooves are designed on the four seal contact planes to store lubricating oil, so as to improve the lubrication capacity of the special-shaped seal ring and reduce the wear in the reciprocating process and effectively reduce the leakage. Because the cross section of the special-shaped seal ring is similar to plum blossom, it is called plum blossom seal ring.

The failure modes of the seal ring can be divided into shear failure and leakage failure. The maximum shear stress of the plum ring is σ_{xy}, and the shear resistant strength is τ_0. Plum blossom seal ring will fail due to shear failure when the maximum shear stress of the sealing ring is greater than its shear resistant strength. The shear failure function of plum blossom seal ring is assumed to be as follows:

$$g(x) = [\tau_b] - \sigma_{xy}, \tag{17}$$

where σ_{xy} is the maximum shear stress of the plum-shaped seal ring which can be calculated in the finite element software ANSYS Workbench, $[\tau_0]$ is the allowable shear strength of rubber, p is the pressure of brake fluid, and $(\sigma_x)_{\max}$ is expressed by the maximum contact stress of plum-blossom seal ring. Therefore, the leakage failure function can be described in

$$g(x) = (\sigma_x)_{\max} - p. \tag{18}$$

4.1. Determination of Maximum Shear Stress Distribution.
The maximum shear stress of the plum-shaped seal ring of the brake piston is related to the parameters of compression, medium pressure, and friction coefficient. Because each parameter has the characteristics of randomness, the stress σ_{xy} also belongs to random variables and has certain distribution characteristics. The uncertainty of the load means that the load applied to the brake piston is a random quantity subject to a certain distribution. The load value for calculating the reliability is not fixed. Its load value fluctuates around the average load, and the fluctuation range is expressed by the coefficient of variation [14, 15].

Friction coefficient, medium pressure, and compression are selected as the main factors affecting the two failure
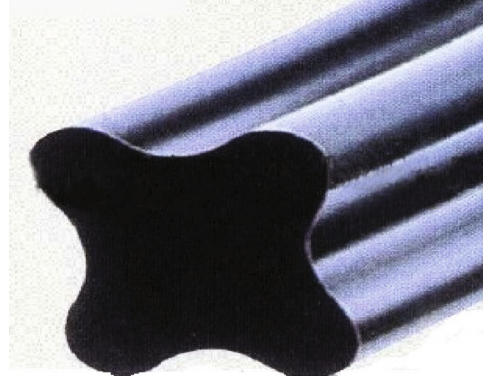
FIGURE 5: Plum blossom seal ring.

modes of quincunx seal ring. Set the above three factors as random variables and assume that the three random variables obey a normal distribution. The mean value and variation coefficient of each random variable are shown in Table 1.

In order to ensure that the quincunx seal ring meets the strength requirements during operation, the maximum stress is generally taken as its maximum value during operation. In the process of time-dependent reliability analysis of plum-blossom seal failure, the whole working time is divided into n time periods to calculate the reliability. Therefore, the maximum shear force is selected from the simulated data of each time period to represent the shear force of that period. From the knowledge of probability and mathematical statistics, we can know that [16] a random variable X obeys a normal distribution, and the n samples $X_1, X_2 \cdots X_n$ of X, the maximum values taken from these samples form the sequence $X_m = \max (X_1, X_2, \cdots, X_n)$, the distribution function of X_m is represented by $F_m(x)$, and the density function is represented by $f_m(x)$, then its expression is:

$$F_m(x) = [F(x)]^n, \tag{19}$$

$$f_m(x) = n[F(x)]^{n-1}f(x), \tag{20}$$

where $F(x)$ represents the distribution function of a single sample and $f(x)$ represents the density function of a single sample. At a certain time, the probability distribution $F(x)$ of shear stress X obeys the normal distribution with a mean value of μ and standard deviation of σ. When the sample size increases infinitely, the limit distribution of statistics is similar to that of sampling. Therefore, the maximum order statistics X_n of random variables $(X_1, X_2, \cdots, X_n)$ obey the extreme value I distribution. The distribution function is:

$$F_m(x) = \exp \{-\exp [-a_n(x - u_n)]\}. \tag{21}$$

TABLE 1: The mean values and variation coefficients of the random variables.

Program	Compression	Medium pressure	Coefficient of friction
Mean values	0.55 mm	5 MPa	0.15
Variation coefficients	0.1	0.1	0.1

The mean and variance are expressed as:

$$E(X_n) = \frac{0.5772}{a_w} + u_w,$$

$$\text{Var}(X_n) = \frac{\pi^2}{6a_n^2}, \tag{22}$$

where

$$u_n = \sigma \sqrt{2 \ln n} - \sigma \frac{\ln(\ln n) + \ln 4\pi}{2\sqrt{2 \ln n}} + \mu,$$

$$a_n = \frac{\sqrt{2 \ln n}}{\sigma}. \tag{23}$$

The distribution function of the equivalent shear stress of the maximum shear stress $X_{(n)}$ in each period is obtained by Equation (21). Taking the plum-blossom seal ring as an example, the test shows that at the significant level ($\alpha = 0.05$), the maximum shear stress obeys the normal distribution ($\mu_\sigma = 2.8069 \times 10^6, \sigma_\sigma = 2.5095 \times 10^5$), the cumulative distribution function of the equivalent shear stress in n time periods is expressed as follows:

$$F_m(m) = \left\{ \int_{-\infty}^{x} \frac{1}{0.2509\sqrt{2\pi}} e^{-1/2(X-2.8069/0.2509)^2} dX \right\}^n. \tag{24}$$

By deriving the cumulative distribution function Equation (24), the expression of the probability density function $f_m(x)$ of the equivalent shear stress can be obtained.

$$f_m(m) = n \left\{ \int_{-\infty}^{x} \frac{1}{0.2509\sqrt{2\pi}} e^{-1/2(X-2.8069/0.2509)^2} dX \right\}^{n-1}$$
$$\cdot \frac{1}{0.2509\sqrt{2\pi}} e^{-1/2(X-2.8069/0.2509)^2}. \tag{25}$$

4.2. Determination of Maximum Shear Resistance Stress Distribution.
According to the actual situation of the shear stress on the plum-shaped seal ring, the time-dependent effect of the stress should be taken into account when calculating the time-dependent reliability of the failure of the plum-shaped seal ring. Therefore, on the basis of the shear stress and shear strength of the plum-shaped seal ring, the influence of the random process of stress is considered,

and the function can be expressed as follows:

$$g(X, t) = \delta(t) - s\left(Y', t\right), \tag{26}$$

where $\delta(t)$ is a random variable of shear strength of rubber sealing ring, $s(Y', t)$ is a random process of shear stress, and Y' is a related random variable. The time-dependent reliability index corresponding to the function can be expressed as follows:

$$\beta(t) = \frac{\mu_{g(t)}}{\sigma_{g(t)}} = \frac{E[g(X, t)]}{\text{Var}[g(X, t)]}, \tag{27}$$

where $\mu_{g(t)}$ is the mean of the function and $\sigma_{g(t)}$ is the standard deviation of the function. The expression of time-dependent reliability corresponding to the function can be expressed as

$$R = \varphi(\beta(t)) = P\left\{ \delta(t) > s\left(Y', t\right) \right\}, \tag{28}$$

where $t \in [0, T]$ and R represents the working reliability of the sealing ring. To ensure the sealing performance of the sealing ring, the shear stress of the sealing ring must be less than its shear strength within each time t in the working process.

Generally speaking, the sampling data of shear strength of sealing rings can be obtained mainly through experiments, and then, the correlation distribution and digitally characteristics can be obtained by statistical calculation. Assuming that the shear strength of plum-shaped rubber seal obeys the normal distribution ($\mu_r = 4.46, \sigma_r = 0.29$), the shear strength of O-shaped rubber seal obeys the normal distribution ($\mu_r = 4.6, \sigma_r = 0.32$) [17, 18]. The same method can be used to calculate the failure time-depending reliability of plum-shaped seal ring and O-shaped seal ring under leakage and the failure time-depended reliability of standard seal structure.

4.3. Time-Dependent Reliability Distribution of Seal Ring under Single Failure Mode.
The action time history of random loads is not considered in the calculation of static reliability model. The calculation of static reliability model directly uses the stress strength interference theory to solve the problem, which can express the reliability of the corresponding load within the action time. Based on the actual working condition of plum-shaped seal ring of brake piston of forceps disc brake, and taking the action time of the shear force as the measurement index of the working life, this paper establishes the time-varying reliability model of the failure of the plum blossom seal ring.

Assuming that the probability density function of the maximum shear resistant stress δ_H of the plum blossom seal ring is expressed by $f_{\delta_H}(\delta_H)$, the cumulative distribution function of contact stress s_H is expressed by $F_{s_H}(s_H)$, and the probability density function is expressed by $f_{s_H}(s_H)$. When calculating the reliability of the plum-blossom seal
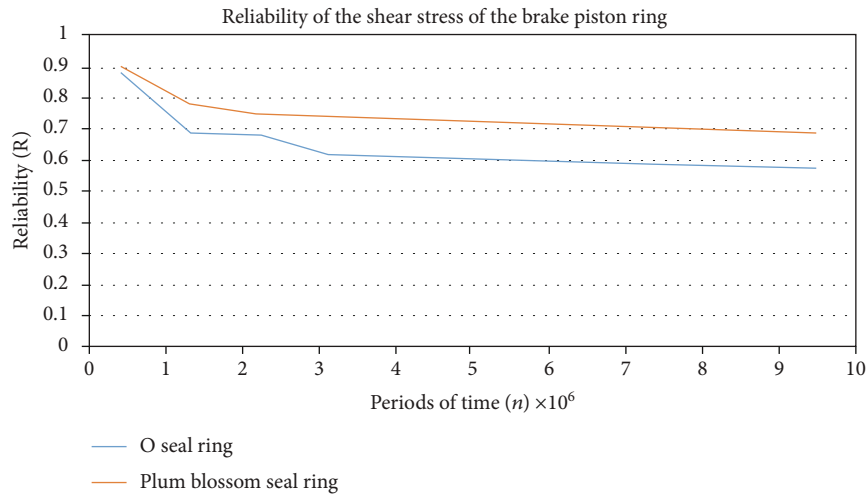
FIGURE 6: Reliability of the shear stress of the brake piston ring.

ring, according to the stress-strength interference theory, the reliability of the seal ring in a period of time can be expressed as follows:

$$R = \int_{-\infty}^{+\infty} f_{\delta_H}(\delta) \int_{-\infty}^{\delta_H} f_{s_H}(s_H) ds_H = \int_{-\infty}^{+\infty} f_{\delta_H}(\delta_H) F_{s_H}(\delta_H) d\delta_H. \tag{29}$$

In n time periods, as Equation (19) and Equation (20) show, when the shear strength of plum blossom seal rings does not change or deteriorate, the cumulative distribution function $F_m(s)$ and probability density function $f_m(s)$ of the equivalent shear stress can be expressed as follows:

$$F_m(s_H) = \left[F_{s_H}(s_H)\right]^n, \tag{30}$$

$$f_m(s_H) = n\left[F_{s_H}(s_H)\right]^{n-1} f_{s_H}(s_H). \tag{31}$$

By substituting Equation (30) and Equation (31) into Equation (29), the time-dependent reliability of plum-blossom seal rings in n time periods can be calculated as follows:

$$\begin{aligned} R(n) &= \int_{-\infty}^{+\infty} f_{\delta_H}(\delta) \int_{-\infty}^{\delta_H} n\left[F_{s_H}(s_H)\right]^{n-1} f_{s_H}(s_H) ds_H d\delta_H \\ &= \int_{-\infty}^{+\infty} f_{\delta_H}(\delta_H)\left[F_{s_H}(\delta_H)\right]^n d\delta_H \\ &= \int_{-\infty}^{+\infty} n\left[f_{s_H}(s_H)\right]^{n-1} f_{s_H}\left[1 - F_{\delta_H}(s_H)\right] ds_H. \end{aligned} \tag{32}$$

When the plum blossom seal ring passes through working n period, the relationship between its failure rate and reliability is shown in Equation (33) [18]. Therefore, the expression of the failure rate of plum blossom seal ring

is:

$$\begin{aligned} h(n) &= \frac{R(n) - R(n-1)}{R(n)} = \frac{\int_0^{+\infty} f_{\delta_H}(\delta_H)\left[1 - F_{s_H}(\delta_H)\right]^n d\delta_H}{\int_0^{+\infty} f_{\delta_H}(\delta_H)\left[F_{s_H}(\delta_H)\right]^n d\delta_H} \\ &= \frac{\int_0^{+\infty} \left[n - (n+1)F_{s_H}(s_H)\right]\left[f_{s_H}(s_H)\right]^{n-1} f_{s_H}(s_H)\left[1 - F_{\delta_H}(S_H)\right] ds_H}{\int_0^{+\infty} n\left[f_{s_H}(s_H)\right]^{n-1} f_{s_H}(s_H)\left[1 - F_{\delta_H}(s_H)\right] ds_H}. \end{aligned} \tag{33}$$

According to the relationship between the reliability of the plum blossom seal ring of the brake piston under the shear stress failure mode and the stress action time and the shear stress and antishear stress distribution and parameters introduced earlier, the reliability of plum blossom seal ring and O seal ring in shear stress failure mode can be obtained, as shown in Figure 6. As can be seen from the figure, under the same conditions, the reliability of the shaped seal ring is greater than that of the traditional O seal ring.

4.4. Time-Dependent Reliability Distribution of Seal Ring under Multiple Failure Mode. Based on the two failure modes of leakage failure and shear failure of quincunx seal ring, the time-varying failure reliability model of seal ring is established in this paper. It can be seen from Equation (9) that under the assumption that each failure mode is not related to each other, the reliability of the sealing ring can be obtained according to the logical relationship of the series system.

$$R = \prod_{i=1}^{m} R_i = \prod_{i=1}^{m} \int_{-\infty}^{+\infty} f_{s_i}^{+\infty}(\delta_i) d\delta_i ds_i. \tag{34}$$

The above formula is based on the assumption that the failure modes are independent of each other, but in practice, most of the failure modes have a certain failure correlation. In this case, Equation (34) needs to be revised, and the reliability results [19–21] can be revised according to the experimental data or practical experience. However, the reliability

Time-dependent failure reliability of a brake piston ring
in a variety of failure modes
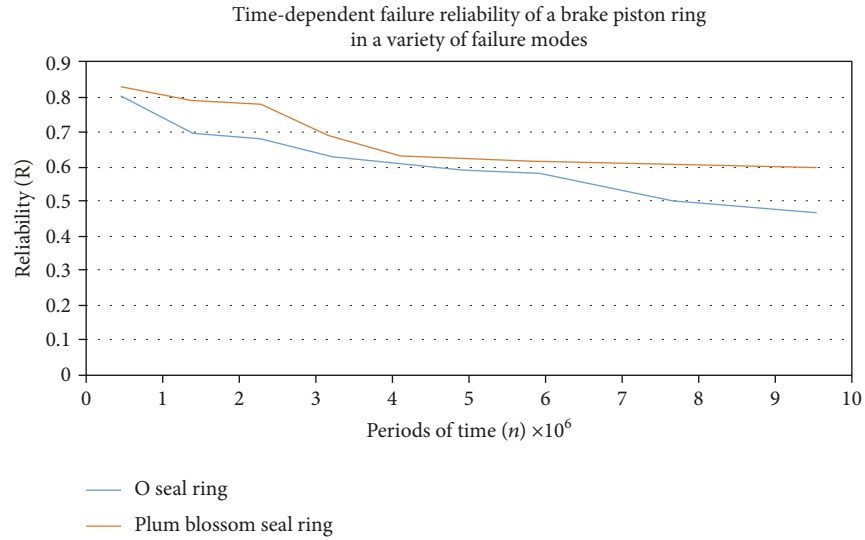
FIGURE 7: Time-dependent failure reliability of a brake piston ring in a variety of failure modes.

obtained by this method is not very accurate, and there is a big error between the calculated reliability and the practical reliability.

In the actual work of the seal ring, due to the influence of various uncertain factors, few failure modes are completely independent of each other. Therefore, it is of great engineering significance to establish a multimode reliability model considering common cause failure. It has been said that in the working process of the sealing ring, due to the influence of external environmental factors and their own factors, two failure forms of shear failure and leakage failure will occur. According to the stress strength interference theory and considering various failure modes of the sealing ring, a time-dependent failure reliability model is established.

When the shear force on the seal ring is equivalent to force in n time periods, the failure between the two failure modes is independent. The reliability of the seal ring under multiple failure modes can be expressed by Equation (8) and Equation (9):

$$R(n) = \int_{-\infty}^{+\infty} \left[\prod_{i=1}^{m} 1 - F_i(L_i) \right] n[F_L(L)]^{n-1} f_L(L) dL. \quad (35)$$

According to the load distribution function obtained above, the time-dependent failure reliability of seal rings under various failure modes can be obtained by substituting Equation (35) as shown in Figure 7. It can be seen from the figure that the reliability of the sealing ring decreases with the increase of time, and the reliability under the multieffect failure mode is smaller than that under the failure mode, respectively.

5. Conclusions

(1) Based on time-varying reliability of the basic concepts and theoretical basis of stress-strength interference model, based on the service life of brake piston

plum blossom seal ring measures, established the brake piston reciprocating motion situation many times the load equivalent model of sealing ring, and the brake piston seal in the shear failure and leakage failure of reliability model under two kinds of failure modes

(2) Based on the force model of the brake piston of the caliper disc brake, the calipering force and friction resistance of the seal ring before and after the braking power disappeared are analyzed

(3) For sealing ring shear failure and leakage failure of the existence of the two failure modes, respectively, set up special seal structure of the plum blossom seal ring under single load and failure mode of the stress-strength interference model, calculate the reliability under two kinds of failure modes; under the same conditions, the reliability of the plum blossom seal ring is greater than the reliability of the O ring

Data Availability

The (data type) data used to support the findings of this study are included within the article.

Conflicts of Interest

The authors declare that they have no conflicts of interest.

Authors' Contributions

Xin Bai and Huiting Ni are responsible for relevant investigation; Liqun Lu for conceptualization; Leilei Shi for computing method; Meng Sun, Xin Bai, and Leilei Shi for model establishment; Liqun Lu, Meng Sun, and Leilei Shi for reliability study; Liqun Lu and Huiting Ni for verification; Liqun Lu for resources; and Liqun Lu and Meng Sun for writing the manuscript.

Acknowledgments

References

[1] Z. Guiying, "The research of the automobile brake pliers sealing technology test," *Hydraulics and Pneumatics*, vol. 2, pp. 3-4, 2012.

[2] T. Juan, G. Zhongnan, and Z. Xiaodong, "Matching design of car brake caliper assembly of cylinder bore and piston clearance," *Automobile spare parts*, vol. 7, pp. 84-85, 2013.

[3] Nifan, *Time-Varying Reliability Analysis and Design for Multiple Failure Mode of the Filtering Reducer*, University of Electronic Science and Technology of China, Master's thesis, Wuhan, 2016.

[4] H. Sarper, "Reliability analysis of descent systems of planetary vehicles using bivariate exponential distribution," *In: Proceeding of Annual Reliability and Maintainability Symposium*, vol. 1, pp. 165–169, 2005.

[5] W. Wang, *Time-Varying Reliability Assessment Prestressed Strand Anchor System of Suspension Bridge [D]*, Southwest Jiaotong University, Master's thesis, Chengdu, 2016.

[6] L. Yuchen, *Research on Analytical Method of Time-Dependent Reliability of Open Type Wharf on Piles [D]*, Tianjin University, Master's thesis, Tianjin, 2015.

[7] T. Togawa, T. Tachibana, Y. Tanaka, and J. Peng, "Hydro-disk-type of electrorheological brakes for small mobile robots," *International Journal of Hydromechatronics*, vol. 4, no. 2, pp. 99–115, 2021.

[8] W. Zheng, X. Liyang, and L. Bing, "R reliability model of mechanical components considering the common cause failure," *Mechanical design*, vol. 24, no. 1, pp. 67–69, 2007.

[9] Y. Wu, *Analysis and Application of Time-Varying Reliability for Reinforced Concrete Simply Supported Beam Based on Numerical Simulation*, Jilin University, Master's thesis, Changchun, 2012.

[10] S. Y. Woo, Y. J. Lee, I. M. Choi, and B. S. Kim, "How to reduce non-linearity in effective area caused by the O-ring seal in a high-pressure balance," *Metro*, vol. 39, no. 6, pp. 537–541, 2002.

[11] M. Shaojie, Y. Juntang, and D. Xuehua, "Hard disk cover-integrated gasket," *Lubrication and Sealing*, vol. 3, no. 11, pp. 10–12, 2002.

[12] H. Zhang, Y. Xia, C. Luo, L. Zeng, and H. Yu, "Static performance of DAS composition seal ring for automobile crane leg cylinder," *Lubrication Engineering*, vol. 2016, no. 3, pp. 12-13, 2016.

[13] Y. Minjia, "Some overview of research on reciprocating motion flexible seals," *Special rubber products*, vol. 2, pp. 50–67, 1983.

[14] K. L. Martins, R. B. D. Silva, G. M. Silvestre et al., "Constructal design applied to geometrical analysis of a triangular arrangement of H-Darrieus wind turbines," *International Journal of Hydromechatronics*, vol. 3, no. 2, pp. 155–166, 2020.

[15] Y. Runsheng and Y. Xiuping, "Finite element analysis and optimization design of Yx shape hydraulic sealing ring," *Lubrication and Sealing*, vol. 36, no. 7, pp. 66–74, 2011.

[16] G. Wenjin, *Research on Sealing Performance of the Pneumatic Solenoid Valve*, South China University of Technology, Master's Thesis, Guangzhou, 2013.

[17] Z. Wang, Z. Wang, Sheryang et al., "Failure rate model of mechanical parts based on load-strength intervention," *Papers Collection of the 2010 National Mechanical Industry Reliability Technology Symposium and the 2nd General Committee of the 4th Reliability Engineering Branch*, vol. 5, pp. 132–136, 2010.

[18] L. X. L. X. H. Le, "Finite element analysis of the structure of W-shaped lip oil seal," *Lubrication and Sealing*, vol. 38, no. 7, pp. 113–116, 2013.

[19] Y. Song Yuehang and W. H. Tianxiang, "Reliability analysis of O-ring considering temperature effect," *Lubrication and sealing*, vol. 39, no. 12, pp. 63–66, 2014.

[20] V. T. Pinto, M. L. Cunha, K. L. Martins et al., "Geometric evaluation of steel plates subjected to uniform transverse load with rectangular or trapezoidal stiffeners by means constructal design method," *International Journal of Hydromechatronics*, vol. 3, no. 2, pp. 190–198, 2020.

[21] A. O. Bernard, J. S. Hawong, D. C. Shin, and H. S. Lim, "Internal stress distribution of X-ring using photoelastic experimental hybrid method," *Journal of Mechanical Science and Technology*, vol. 28, no. 5, pp. 1697–1708, 2014.

Research Article

A Deep Domain-Adversarial Transfer Fault Diagnosis Method for Rolling Bearing Based on Ensemble Empirical Mode Decomposition

Xiao Yu [ID],[1,2,3] Bing Xia,[1,2,3] Shuxin Yang,[3,4] Hongshen Yin,[1,2,3] Yajie Wang,[1,2,3] and Xiaowen Liu [ID] [3,4]

[1]*IOT Perception Mine Research Center, China University of Mining and Technology, Xuzhou 221000, China*
[2]*School of Information and Control Engineering, China University of Mining and Technology, Xuzhou 221000, China*
[3]*The National Joint Engineering Laboratory of Internet Applied Technology of Mines, China University of Mining and Technology, Xuzhou 221008, China*
[4]*School of Electrical and Power Engineering, China University of Mining and Technology, Xuzhou 221000, China*

Correspondence should be addressed to Xiaowen Liu; xwliucumt@126.com

Received 27 December 2021; Revised 24 March 2022; Accepted 11 April 2022; Published 18 May 2022

Academic Editor: Min Xia

In recent years, the deep learning-based fault diagnosis methods for rotating mechanical equipment have attracted great concern. However, because the data feature distributions present differences in applications with varying working conditions, the deep learning models cannot provide satisfactory performance of fault prediction in such scenarios. To address this problem, this paper proposes a domain adversarial-based rolling bearing fault transfer diagnosis model EMBRNDNMD. First of all, an EEMD-based time-frequency feature graph (EEMD-TFFG) construction method is proposed, and the time-frequency information of nonlinear nonstationary vibration signal is extracted; secondly, a multi-branch ResNet (MBRN) structure is designed, which is used to extract deep features representing the bearing state from EEMD-TFFG; finally, to solve the model domain adaptation transfer problem under varying working conditions, the adversarial network module and MK-MMD distribution difference evaluation method are introduced to optimize MBRN, so as to reduce the probability distribution difference between the deep features of source domain and target domain, and to improve the accuracy of EMBRNDNMD in state diagnosis of target domain. The results of experiments carried out on two bearing fault test platforms prove that EMBRNDNMD can maintain an average accuracy above 97% in fault transfer diagnosis tasks, and this method also has high stability and strong ability of scene adaptation.

1. Introduction

The rotating mechanical equipment has broad applications in various fields, such as related industries, military, and for civil use. As an important component of rotating mechanical equipment, the rolling bearing directly affects the operating efficiency and working conditions of mechanical equipment. However, due to long-term exposure to harsh working conditions of high load, the parts of rolling bearing tend to suffer from damages. Minor damage may reduce the operating efficiency of mechanical equipment, while serious damage might lead to shutdown of equipment, which may even cause casualties. Therefore, study on the state detection and fault diagnosis of rolling bearing has important theoretical significance and engineering value for improving productivity and ensuring production safety.

In researches on fault diagnosis based on signal processing, good results have has been achieved by combining traditional feature extraction and machine learning classification [1–4]. Especially the signal processing method represented by ensemble empirical mode decomposition (EEMD), the bearing fault mechanism information can be obtained by analyzing the intrinsic mode functions (IMFs) of vibration signal. Han et al. [5] put forward a method for rolling

bearing fault diagnosis based on EEMD permutation entropy and fuzzy clustering. Wang et al. [6] proposed an improved EEMD algorithm, in which the sifting and ensemble number are self-adaptive. Yang et al. [7] and Hu et al. [8] proposed a fault detection and diagnosis method based on EEMD and support vector machine (SVM). Besides, Shao et al. [9] put forward a method called deep wavelet auto-encoder with extreme learning machine (ELM) for intelligent fault diagnosis of rolling bearing. Li et al. [10] proposed a density-based clustering method with principal component analysis (PCA) to improve the performance of variable load diagnosis in fault diagnosis. In the above researches, appropriate signal processing methods need to be selected to extract effective features according to the characteristics of data, such as EEMD, wavelet transform (WT), and PCA. However, these methods are too empirical, as a result of which, the selection of features will directly affect the diagnosis results. In order to reduce the influence of human experiences, a better method is to enable the model to automatically extract features [11, 12].

In recent years, with the rapid development of deep learning in computer vision, many scholars have applied deep learning methods to the field of fault diagnosis. Compared with machine learning, deep learning can adaptively extract deep features from signals, which has solved the difficulty to extract fault features [13]. Zhou and Yao et al. [14, 15] developed a convolutional neural network (CNN) based fault diagnosis method for rolling rearing by using the waveform of vibration as the 2-D image input of CNN. Fan et al. [16] advanced a method about the convolutional neural network and transfer learning based fault diagnosis method, aiming at the vibration image samples of rolling bearing affected by strong noise.

However, with the increase of network layers, the traditional deep learning methods suffer from the problems of gradient disappearance and gradient explosion, and as a result the weight of the model cannot be updated effectively [17, 18]. In order to solve this problem, HE et al. [19] proposed a deep residual network (ResNet) in 2015, which uses shortcuts to directly transmit the data of the front layer to the back layer of the network and completes the feature fusion through addition. Wei et al. [20] presented a novel framework that combines a residual network as a backbone and an extreme learning machine as a classifier to diagnose the faults of rotating machinery. Wang and Wen et al. [21, 22] constructed a multi-scale deep intra-class adaptation network, which uses the modified ResNet-50 to extract low-level features, and the experimental results show that the model outperforms both other deep learning models and the conventional methods. How to effectively extract features in the bearing intelligent diagnosis model is a problem worthy of study. This article proposes a method based on the EEMD and improved multi-branch ResNet to extract deep features of bearing faults from the time domain and frequency domain. However, the success of deep learning methods in fault diagnosis largely depends to sufficient and labelled training samples, but it is difficult to meet these requirements in practical works.

Transfer learning method can effectively solve the problem of data scarcity, because it is able to apply the knowledge learned in the source domain into the target domain, which can help improve the prediction accuracy of unlabelled data [23–26]. In the field of fault diagnosis, the transfer learning methods can be divided into model-based methods, such as maximum mean discrepancy (MMD), and domain distribution-based methods, such as domain adversarial training of neural networks (DANN) [27–29]. Li and Yang et al. [30, 31] presented a feature representation enhancement method based on MMD and domain confrontation training. Che et al. [32] put forward a domain-based adaptive method, which can calculate the multi-core maximum mean difference (MK-MMD) of the selected hidden layer and add it to the loss function, so as to improve the generalization ability of the deep neural network. Tang et al. [33] integrated the MK-MMD loss into the traditional fine-tuning convolutional neural network (CNN) transfer learning framework and proposed a new semi-supervised transfer learning (STL) method. Mao and Cai et al. [34, 35] advanced a novel adversarial DA method called the adversarial residual transformation network (ARTN), which directly transforms the source features into the target feature space to improve the generalization capability. Li et al. [36] came up with a novel weighted adversarial transfer network (WATN) for fault diagnosis in certain domains and achieved satisfactory performance. Both MMD and DANN have achieved good performances in fault diagnosis, but in some situations of variable working conditions, a single transfer method often performs poorly. Therefore, this paper proposes a multiple transfer fault diagnosis method combining MMD and DANN to address degradation of model diagnosis performance in scenarios with transfer of working conditions.

The deep learning technique has the advantage of adaptively extracting deep features of data, which can be used to build an end-to-end diagnosis mechanism. A lot of researches have been carried out on intelligent diagnosis models for rotating mechanical equipment based on deep learning. However, various problems are also encountered in current studies, such as vibration signals susceptible to interference of noises, insufficient samples of equipment faults, and the difference in distributions between target data and source data caused by change of equipment working conditions. Solving these problems should be the focus of deep learning-based fault diagnosis model in future studies.

In our paper, the EEMD method is adopted to preprocess the rolling bearing vibration signal, and we propose obtaining the time-frequency information of vibration signal by building EEMD-TFFG. To address the problem of degraded model diagnosis ability under transfer of working conditions, DANN and MK-MMD are introduced to optimize the multi-branch ResNet (MBRN), so as to reduce the differences in probability distributions of deep features between source domain and target domain and to improve the state diagnosis accuracy of target domain. The main contributions of this paper are as follows:

(1) We propose an EEMD-based vibration signal construction method—EEMD-TFFG, so as to achieve

time-frequency analysis and feature extraction of vibration signals

(2) A multi-branch feature extraction network MBRN based on ResNet is designed, which can extract deep features reflecting the fault state from EEMD-TFFG

(3) DANN and MK-MMD are introduced to optimize MBRN, reduce the probability distribution difference of data deep features between source domain and target domain, and improve the diagnosis ability of EMBRNDNMD under transfer of working conditions. The experimental analysis results show that EMBRNDNMD can achieve a high diagnosis accuracy for target domain states under various transfer modes, which has a strong ability to adapt to varying working conditions

Section 2 introduces the principles of various methods, including EEMD, ResNet, DANN, and MK-MMD; Section 3 presents the design idea and the structure of EMBRNDNMD model; in Section 4, experiments are carried out on the two datasets of CWRU and MFS-RDS by using EMBRNDNMD, and related analysis is conducted; Section 5 draws conclusions of our work. Furthermore, we present some acronyms in Table 1.

2. Preliminaries

2.1. Ensemble Empirical Mode Decomposition (EEMD). Hilbert-Huang transform (HHT) is one of the time-frequency analysis methods with broadest applications. First, HHT carries out empirical mode decomposition (EMD) of signal to obtain a series of intrinsic mode functions (IMFs) of different scales; then, instant frequency information with physical significance is obtained through Hilbert transform of various IMF components. However, EMD still has some problems, such as end effect and mode confusion [37], which may reduce the accuracy of fault classification. To address the mode confusion problem of EMD, Zhaohua et al. [38] proposed the ensemble empirical mode decomposition (EEMD) method based on EMD. EEMD adds white Gaussian noise on the basis of original signal, which makes the signal smooth, effectively inhibits mode confusion, and improves the precision of signal decomposition. The decomposition process of EEMD is as shown in Figure 1.

The specific decomposition procedure of EEMD consists of following steps:

(1) For the given original signal $x(t)$, initialize variable $i = 1$, and set the mean times of EEMD set as M

(2) For the original signal, add a group of white noises $n_i(t)$, and obtain signal $x_i(t)$.

$$x_i(t) = x(t) + n_i(t), \tag{1}$$

where $x_i(t)$ is the i-th decomposed signal of additive white noise, and $n_i(t)$ is the i-th additive white noise ($i = 1, 2, 3, \ldots, M$).

(3) Carry out EMD of $x_i(t)$, and obtain various IMF components and residual components as

$$x_i(t) = \sum_{j=1}^{J} c_{ij}(t) + r_{ij}(t), \tag{2}$$

where $c_{ij}(t)$ is the j-th IMF component obtained in the i-th decomposition, and $r_{ij}(t)$ is the residual component of the i-th decomposition.

(4) Obtain the sum and average value of corresponding IMF components got in M decompositions to offset the noise, and obtain the final IMF components

$$c_j(t) = \frac{1}{M} \sum_{i=1}^{M} c_{ij}(t), \tag{3}$$

where $c_j(t)$ ($j = 1,2,3, \ldots, J$) is the final j-th IMF component obtained from EEMD.

(5) Through EEMD, signal $x(t)$ is finally decomposed to:

$$x(t) = \sum_{j} c_j(t) + r(t), \tag{4}$$

where $r(t)$ is the final residual component obtained after EEMD of signal.

2.2. Residual Network (ResNet). Convolutional neural network (CNN) is a network structure commonly used in deep learning, which has achieved broad applications in the field of fault diagnosis. CNN mainly consists of the input layer, output layer, and hidden layer, while the hidden layer can also be further divided into the convolutional layer, down-sampling layer, and fully connected layer. In the traditional CNN, the expression ability will be enhanced with the increase of depth, and more complicated features can be extracted. However, if the network layers are too deep, it may also cause gradient attenuation, gradient explosion, and other problems, leading to declined accuracy of prediction.

To solve the problem of model degradation caused by convolutional network being too deep, in 2015, Kaiming He et al. [19] from Microsoft Research proposed the residual network (ResNet). Utilizing shortcut, ResNet directly transfers data from previous layers to following layers of network and uses addition to achieve feature fusion, as shown in Figure 2.

Addition connects input x and $F(x)$ obtained after stacking weight layers cross layer, and obtains output $H(x) = F(x) + x$. Here, $F(x) = H(x) - x$, which is the residual. Because the residual network has integrated such skip structure, even if the network depth is increased, the learning network is only added with the load of identity function

TABLE 1: A list of acronyms used in this paper.

Acronym	Full form	Acronym	Full form
EMBRNDNMD	Domain adversarial-based rolling bearing fault transfer diagnosis model	TL	Transfer learning
EMD	Empirical mode decomposition	CNN	Convolutional neural networks
EEMD	Ensemble empirical mode decomposition	ResNet	Residual network
EEMD-TFFG	Time-frequency feature graph	MMD	Maximum mean discrepancy
MBRN	Multi-branch ResNet	MK-MMD	Multi-core maximum mean difference
RNB	ResNet module	GAN	Generative adversarial network
IMF	Intrinsic mode function	DANN	Domain-adversarial neural network
IMFs	Intrinsic mode functions	GRL	Gradient reversal layer
HHT	Hilbert-Huang transform	t-SNE	t-Distributed stochastic neighbor embedding
HES	Hilbert envelope Spectrum	TCA	Transfer component analysis
SVM	Support vector machine	JDA	Joint distribution adaptation
PCA	Principal component analysis	CWRU	Case Western Reserve University
ELM	Extreme learning machine	MFS-RDS	Mechanical fault diagnosis experiment platform
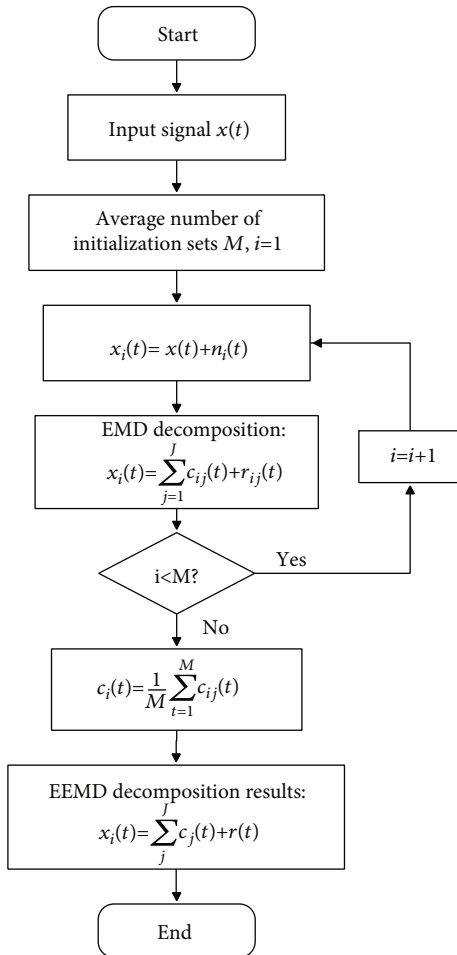
FIGURE 1: Decomposition flow chart of EEMD.

computation, and the data utilization efficiency will not be reduced. As a result, more data information can be transferred to deeper network, so as to prevent model degradation caused by convolutional network being too deep.

2.3. Domain-Adversarial Neural Network (DANN). The conventional machine learning methods not only require massive labelled data for training but also need similar probability distributions between the source domain and target domain. If the source domain and target domain present significant difference in data distribution, the generalization performance of model will degrade in the target domain. The domain adaptive transfer learning mechanism is an effective approach to solve this problem.

In recent years, with the application of generative adversarial network (GAN) in image processing, the ideal of generative adversarial has been broadly used in adaptive transfer learning applications in various fields. A classic example is the domain-adversarial neural network (DANN) proposed by Ganin Y [29] in 2016. DANN utilizes the feature extractor and domain discriminator for adversarial training, and the Nash equilibrium can be finally reached, making the domain classifier unable to determine which domain the data comes from. In this way, data from the source domain and target domain with different distributions can be mapped to the same feature space, and the classifier trained in the source domain can be used to directly classify data from target domain. The structure of DANN is as shown in Figure 3 [29].

Specifically speaking, DANN consists of the three parts of feature extractor, label predictor, and domain classifier. The feature extractor is used to (1) confuse data from the source domain and target domain to trick the domain classifier; (2) extract features required by subsequent network from the mixed data. The feature extractor and label predictor form a feed-forward neural network to achieve
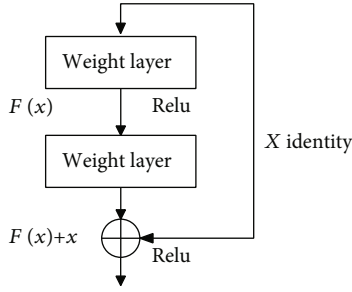
FIGURE 2: Residual module of ResNet.

adversarial training between different fields. DANN adds a domain classifier after the feature extractor, which is connected by a gradient reversal layer (GRL). With the addition of GRL, the gradient direction will be automatically flipped during back propagation in the training process of model, and identical transformation can be achieved during forward propagation.

Assuming X represents the input space, $Y = \{0, \cdots, L-1\}$ represents L labels, S is the labelled source sample and T is the unlabelled target sample. There are two different distributions of source domain D_S and target domain D_T, then the sample functions of source domain and target domain can be expressed as:

$$S = \{(x_i, y_i)\}_{i=1}^n \sim (D_S)^n \,;\, T = \{(x_i)\}_{i=n+1}^N \sim \left(D_T^X\right)^{n'}, \quad (5)$$

where $N = n + n'$, which represents the total number of samples.

According to the source domain sample (x_i, y_i), the classification loss of label predictor can be represented by the negative logarithmic probability of correct label:

$$L_y\left(G_y\left(G_f(x_i)\right), y_i\right) = \log \frac{1}{G_y\left(G_f(x)\right)_{y_i}}, \quad (6)$$

where G_f represents feature extraction network of X; $G_y(G_f(x))$ represents the conditional probability of network mapping X to Y.

Similarly, the loss function of domain classifier can be represented as:

$$L_d\left(G_d\left(G_f(x_i)\right), d_i\right) = d_i \log \frac{1}{G_d\left(G_f(x_i)\right)} + (1 - d_i) \log \frac{1}{1 - G_d\left(G_f(x_i)\right)}, \quad (7)$$

where d_i is a binary variable representing the domain class. If $d_i = 0$, it means $X_i \sim D_S^X$; if $d_i = 1$, $X_i \sim D_T^X$. G_d represents the domain classifier.

The total loss L_{DANN} of model consists of the two parts of source label prediction loss L_y and domain classifier loss L_d:

$$L_{DANN}(\theta_f, \theta_y, \theta_d) = \frac{1}{n_S} \sum_{x_i \in D_S} L_y\left(G_y\left(G_f(x_i)\right), y_i\right) - \frac{\lambda}{n} \sum_{x_i \in (D_S \cup D_T)} L_d\left(G_d\left(G_f(x_i)\right), d_i\right). \quad (8)$$

During the training process, the feature extractor learns parameter θ_f by maximizing the loss function L_d of domain classifier, and the domain classifier adjusts its parameter θ_d by minimizing the loss function L_d.

2.4. Multi-Kernel Maximum Mean Discrepancy (MK-MMD). Maximum mean discrepancy (MMD) was proposed for double-sample test, which is used to determine the distribution difference between two types of data, and it is a common loss function in transfer learning. In MMD, the most critical step is to choose kernel parameters, and unsuitable kernel parameters will not only affect the final performance of mapping but also cause deviation in distance measurement. To prevent selecting unsuitable kernel of MMD, the MK-MMD method proposed by Gretton [39] is employed in our paper. In MK-MMD, it is assumed that the optimal kernel is obtained via linear combination of multiple kernels, which can prevent choosing unsuitable kernel parameters when only one kernel is used. Assuming the source domain dataset $X^s = \{x_i^s\}_{i=1,\cdots n}$ satisfies P distribution and the target domain dataset $X^t = \{x_j^t\}_{j=1,\cdots n}$ satisfies Q distribution, the Euclidean distance between X^s and X^t in MK-MMD is defined as:

$$d_k^2(P, Q) \triangleq \left\| E_P[\phi(X^s)] - E_Q\left[\phi(X^t)\right] \right\|_{\mathcal{H}_k}^2, \quad (9)$$

where E represents the mathematical expectation; ϕ stands for the mapping of reproducing Hilbert space; $\mathcal{H}_k$ refers to the reproducing kernel Hilbert space with feature kernel k.

The feature kernel often chooses the convex optimization combination of m kernels $\{k_u\}$ associated with features to provide effective mapping. The feature kernel is defined as follows:

$$\mathcal{K} \triangleq \left\{ k = \sum_{u=1}^m \partial_u k_u : \sum_{u=1}^m \partial_u = 1, \partial_u \geq 0, \forall_u \right\}, \quad (10)$$

where ∂_u is the weighted parameter of different kernels, and the characteristic of multi-kernel k is guaranteed via constraint of ∂_u.

3. Proposed Method and System Framework

By combining EEMD and MK-MMD, this paper proposes a deep residual adversarial transfer bearing fault analysis method EMBRNDNMD. In our paper, first, EEMD is utilized to adaptively decompose the vibration signal into empirical mode components IMFs of different scales, and IMFs and corresponding Hilbert envelope spectrum (HES) form the EEMD time-frequency feature graph (EEMD-TFFG) of time-frequency features. Then, the multi-branch ResNet structure is used to extract deep features of EEMD-TFFG, the domain adversarial mechanism is introduced to ensure consistent low-dimensional expressions of the deep features of data between source domain and target domain, and in the meantime, MK-MMD is utilized to constrain the distribution difference between them in high-dimensional
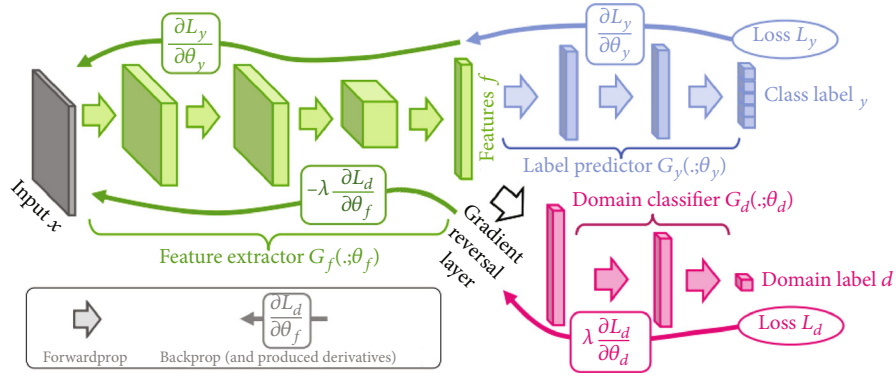
FIGURE 3: Schematic diagram of DANN model structure.

space. Finally, the back propagation of ResNet is optimized according to the fault state classification loss of source domain data, the discriminant loss between source domain and target domain, and the distribution difference loss of MK-MMD, so as to improve the state classification ability and domain adaptation ability of deep features, and to solve the transfer problem of state diagnosis model under different working conditions.

3.1. Construction of EEMD Time-Frequency Graph. After EEMD of vibration signal, a group of linear stable empirical mode components IMFs are obtained, and IMFs are automatically distributed from high frequency to low frequency. Considering that not every IMF can effectively represent the time-frequency characteristic or the information of original signal, Equation (11) is utilized to calculate the correlation coefficient between each IMF component and the original signal $x(t)$, so as to eliminate illusive components in IMF component.

$$\rho_{(c_i(t), x(t))} = \frac{E[(c_i(t) \cdot x(t)] - E[c_i(t)] \cdot E[x(t)])]}{\sqrt{D(c_i(t))} \cdot \sqrt{D(s(t))}}, \quad (11)$$

where $c_i(t)$ represents the i-th IMF component, $E[\cdot]$ represents the expected value of signal, and $D(\cdot)$ represents the mean square value of signal.

The bigger the correlation coefficient is, the more closely related is the IMF component to the original signal, and the richer time-frequency information it contains. Then, the Hilbert envelope spectrum (HES) used to select the IMF component is calculated. Here, the selected IMF components and its envelope spectrum are rearranged into a matrix in the order that IMF is the first and HES is the last, so as to improve the correlation of the features and obtain a group of time-frequency feature graphs, which are denoted as EEMD-TFFG, and this step aims to facilitate subsequent extraction of their deep features using 2D convolution kernel.

The construction process of EEMD-TFFG includes the following steps:

(1) After EEMD of the vibration signal, a group of empirical mode components IMFs are obtained
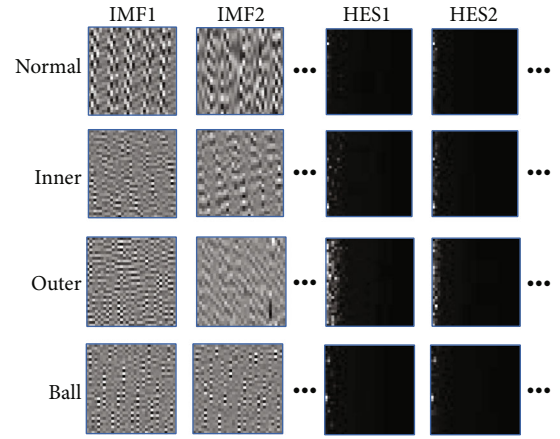
FIGURE 4: EEMD-TFFG of bearing vibration signals.

(2) The correlation coefficient between each IMF component and the original signal is calculated, and the IMF components with correlation coefficients higher than the threshold value are selected for subsequent analysis

(3) Corresponding HES of IMF components selected in Step (2) is calculated

(4) The selected IMF components and HES sequences are rearranged into a matrix, and saved as a gray-scale image

3.2. Design of Network Model Structure

3.2.1. Design of Deep Feature Extraction Network. Figure 4 shows the EEMD-TFFG of a group of vibration signals under different bearing states, and each vibration signal sample includes 1024 sampling points. We can see that EEMD-TFFG has the following two characteristics:

(1) Each gray-scale image has the size of 32∗32, which is small

(2) For the same signal, the features between the gray-scale images of different IMF components are relatively independent
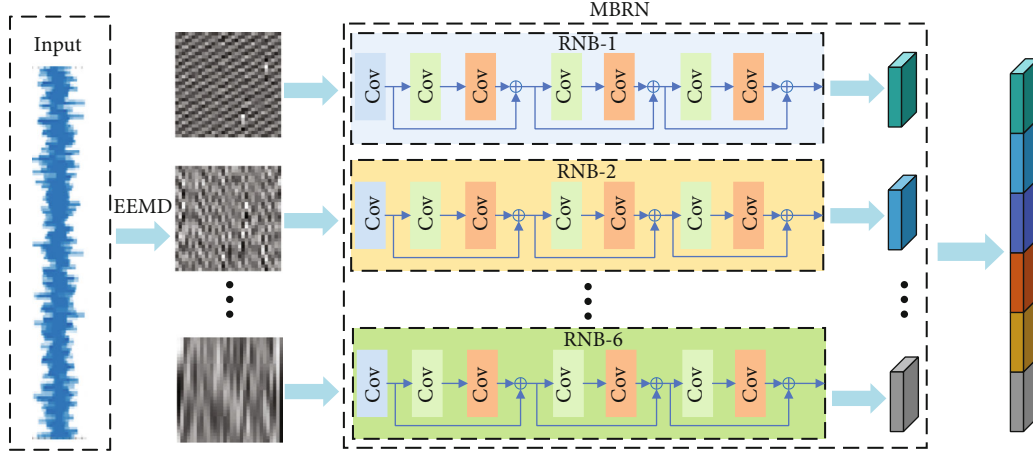
FIGURE 5: Multi-branch parallel ResNet structure.

TABLE 2: Specific parameters of RNB.

Type	Layer	Kernel/stride/channels	Input size	Output size
Input		/	(32,32,1)	(32,32,1)
Conv1	Conv2d	(3,3)/1/16	(32,32,1)	(32,32,16)
	InstanceNorm2d	/	(32,32,16)	(32,32,16)
	ReLU	/	(32,32,16)	(32,32,16)
Block1	Conv2d	(3,3)/1/16	(32,32,16)	(32,32,16)
	InstanceNorm2d	/	(32,32,16)	(32,32,16)
	ReLU	/	(32,32,16)	(32,32,16)
	Conv2d	(3,3)/1/16	(32,32,16)	(32,32,16)
	InstanceNorm2d	/	(32,32,16)	(32,32,16)
Block2	Conv2d	(3,3)/1/32	(32,32,16)	(32,32,32)
	InstanceNorm2d	/	(32,32,32)	(32,32,32)
	ReLU	/	(32,32,32)	(32,32,32)
	Conv2d	(3,3)/2/32	(32,32,32)	(16,16,32)
	InstanceNorm2d	/	(16,16,32)	(16,16,32)
	Conv2d	(3,3)/1/32	(16,16,32)	(16,16,32)
	InstanceNorm2d	/	(16,16,32)	(16,16,32)
Block3	ReLU	/	(16,16,32)	(16,16,32)
	Conv2d	(3,3)/2/32	(16,16,32)	(8,8,32)
	InstanceNorm2d	/	(8,8,32)	(8,8,32)
Pooling	AvgPool	/	(8,8,32)	(1,1,32)

Based on these two characteristics of EEMD-TFFG, we designed a multi-branch parallel ResNet structure as shown in Figure 5, which is denoted as MBRN. In Figure 5, we assume that 3 IMF components of vibration signal after EEMD and corresponding HES are selected. The parameters of each convolution layer of MBRN are shown in Table 2, in which the normalization and *relu* layers are not represented.

According to characteristic (1) of EEMD-TFFG, if the network layers are too deep, it will affect the extraction of features of small-size image, so a single ResNet module (RNB) is set with 1 convolutional layer and 3 basic residual modules, and there are 7 convolutional layers in total, and this setting can restrict the network depth. In RNB, various convolutional fea-

ture extraction layers have all used a $3*3$ convolution kernel, a small receptive field is utilized for network stacking, and the step size is set as 1. Besides, because the main redundant information has been filtered through the EEMD time-frequency figures, it will not cause information redundancy even if there is no pooling layer. So we cancel the pooling layer of the model to reduce the computational load.

According to characteristic (2) of EEMD-TFFG, a multi-branch parallel network structure MBRN is built. RNB, which has the same structure and independent parameters, is used to extract the gray-scale image features for different IMF and HES, and the deep features from the final output layers of various RNBs are combined and used as the output feature F of MBRN.

3.2.2. Loss Calculation and Back Propagation Network. The structural design of EMBRNDNMD model is as shown in Figure 6. In addition to the deep feature extraction network G_{MBRN}, the model also includes the state classification network G_y and domain discriminant network G_d. Here, G_y is a two-layer fully connected linear network, and G_d is a three-layer fully connected linear network. Three loss functions are used to optimize the network model via back propagation, and they are the bearing state classification loss L_y, the discriminant loss L_d between source domain and target domain, and the MK-MMD distribution difference loss L_{MK-MMD} between deep features of source domain and target domain, respectively. The deep feature set of source domain is denoted as $F^s = \{f_i^s\}_{i=1,..n}$, the sample label of source domain data is denoted as Y^s, and the deep feature set of target domain is denoted as $F^t = \{f_j^t\}_{j=1,..n}$.

The bearing state classification loss L_y is used to optimize G_{MBRN} and G_y. L_y is defined as:

$$L_y = \sum_{i=1}^{n} \log \frac{1}{G_y(f_i^s)_{y_i^s}}. \tag{12}$$

L_d involves two back propagation stages, which are for optimizations of G_{MBRN} and G_d, respectively. The two stages

FIGURE 6: Bearing fault transfer diagnosis model EMBRNDNMD.

FIGURE 7: CWRU bearing fault diagnosis and experiment platform.

of back propagation are connected by the gradient reverse layer (GRL), and the reverse mechanism of GRL is utilized to form an adversarial relation between G_{MBRN} and G_d. Back propagation optimization aims to reach Nash equilibrium between G_{MBRN} and G_d. The equation of L_d is:

$$L_d = \sum_{i=1}^{n} \log \frac{1}{G_d(f_i^s)} + \sum_{i=1}^{n} \log \frac{1}{1 - G_d(f_i^t)}. \quad (13)$$

L_{MK-MMD} represents the MK-MMD distribution difference loss, which is used to optimize G_{MBRN}. L_{MK-MMD} is defined as:

$$L_{MK-MMD} = \|E[\phi(F_s)] - E[\phi(F_t)]\|_{H_k}^2, \quad (14)$$

where E represents the mathematical expectation; ϕ stands for the mapping of reproducing Hilbert space; and H_k refers to the kernel k used by reproducing the kernel Hilbert space.

The total loss of G_{MBRN} can be expressed as:

$$L_{MBRN} = L_y - \lambda_1 L_d + \lambda_2 L_{MK-MMD}. \quad (15)$$

3.3. Procedure of Diagnosis Model. The procedure of transfer diagnosis using the EMBRNDNMD model is as follows:

(1) Collect rolling bearing vibration signals under different working conditions, assign data into the source domain or target domain, the source domain consists of labelled data, and the target domain is composed of unlabeled data

(2) Use the EEMD method to calculate the IMF and HES of vibration signal samples from the source domain and target domain, and build corresponding EEMD-TFFG

(3) Input the EEMD-TFFG of source domain and target domain into MBRN, and extract deep features F_s and F_t of EEMD-TFFG

(4) Calculate the state classification loss L_y of source domain data, and optimize G_y via back propagation

(5) Calculate the MK-MMD distribution difference between the deep features of source domain and target domain, and obtain L_{MK-MMD}

(6) Calculate the domain classifier loss L_d, and optimize G_d via back propagation

TABLE 3: Experiment datasets of bearing.

	Power	Normal	Inner race				Outer race			Rolling ball			
Damage (mm)	—	—	0.007	0.014	0.021	0.028	0.007	0.014	0.021	0.007	0.014	0.021	0.028
Label	—	0	1	2	3	4	5	6	7	8	9	10	11
Dataset A	0HP	50	50	50	50	50	50	50	50	50	50	50	50
Dataset B	1HP	50	50	50	50	50	50	50	50	50	50	50	50
Dataset C	2HP	50	50	50	50	50	50	50	50	50	50	50	50
Dataset D	3HP	50	50	50	50	50	50	50	50	50	50	50	50
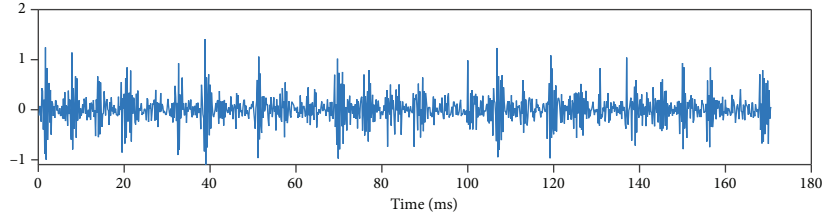
(a) Vibration signal
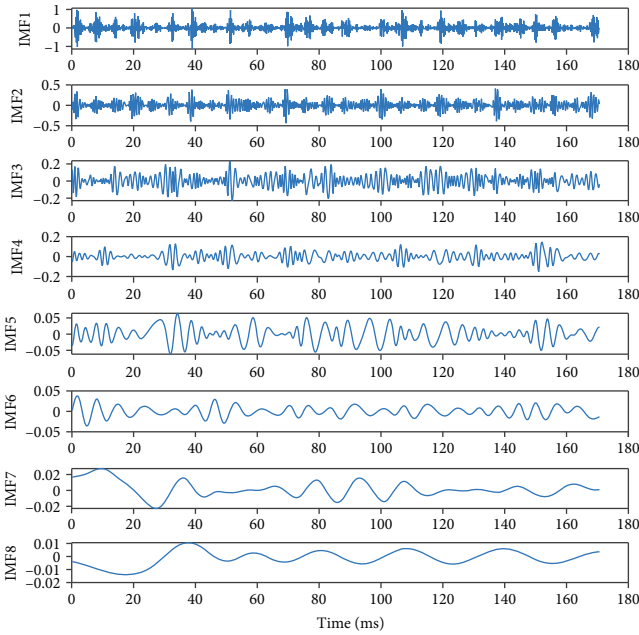
(b) IMF components
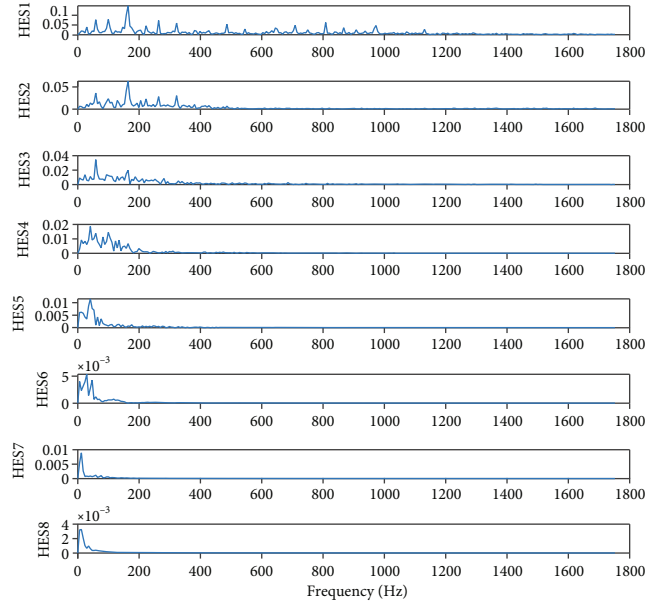
(c) Hilbert envelope spectrum

FIGURE 8: Vibration signal and its time-frequency components.

(7) Calculate the total loss L_{MBRN}, and optimize G_{MBRN} via back propagation

(8) Iterate steps (3)-(7) until L_{MBRN} is smaller than the set value or iterations have reached the target requirement, and obtain G_{MBRN} and G_y after training

(9) The trained G_{MBRN} is utilized to calculate the deep feature F_t of sample EEMD-TFFG from the source domain, and input F_t into the trained G_y to obtain the label of test samples

4. Experimental Verification

4.1. Experimental Analysis on the CWRU Bearing Dataset

4.1.1. Introduction of the CWRU Bearing Dataset. In our experiment, the CWRU bearing fault simulation and experiment platform developed by Case Western Reserve University was used, and the rolling bearing vibration signals under various states were collected to verify the performances of algorithm and model proposed in this paper. The experiment platform is presented in Figure 7, which mainly consists of the parts of motor, rolling bearing, axis of rotation, torque sensor/decoder, acceleration sensor, and signal acquisition instrument.

In the experiment, the Reliance Electric motor of 2 HP was used. Electrical discharge machining was used to create different types of faults for motor bearings, the locations included inner race, outer race, and rolling ball, and the

damage diameters were 0.007 inch, 0.014 inch, 0.021 inch, and 0.028 inch, respectively. As shown in Table 3, there are 12 types of faults and 50 samples in each type.

In this paper, the vibration signals at motor drive end with sampling frequency of 12 kHz are chosen for analysis. In the experiment, four different motor powers of 0HP, 1HP, 2HP, and 3HP were set as 4 different working conditions, and 12 transfer modes were obtained (A->B, A->C, A->D, B->A, B->C, B->D, C->A, C->B, C->D, D->A, D->B, D->C). Among them, A->B means that we set the dataset A as source domain and dataset B as target domain.

4.1.2. EEMD Analysis. First of all, we obtain the IMF components of vibration signal sample by EEMD; then, we perform Hilbert transform and spectral analysis of IMF components, and calculate the envelope spectra of IMF components. With fault at the inner race of bearing as example, the waveform of original vibration signal and the IMF components after EEMD are as shown in Figure 8.

The correlation calculation method described in Section 3.1 is used to select the IMF components. Under normal conditions and fault conditions such as inner race fault (IR), outer race fault (OR), and ball fault (BF), the correlation coefficients between the IMF components of bearing vibration signal at various order and the original signal are shown in Figure 9. According to Figure 9, with the increase of order, the correlation coefficient between the IMF component and the original signal gradually declines. The IMF components and the original signal only maintain a high correlation at the first four orders, so the IMF components of first four orders after EEMD and corresponding HES are chosen for subsequent extraction of deep features in this paper.

4.1.3. Validation of IMFs Selection. To verify that the first 4-order IMFs selected by the correlation calculation of bearing vibration signals can effectively characterize the bearing fault features, the first 3-, 5-, and 6-order IMFs (ET3, ET5, and ET6, respectively) are selected as comparative groups, and their performances are compared with the first 4-order IMFs (ET4) used in this paper in the input signal experiment. Finally, it is tested on the CWRU dataset, and the results are shown in Table 4.

It can be seen from the table that the diagnostic accuracy when using ET4 as input signal is basically higher than that of other groups, because ET3 lacks IMF4 component's fault features, resulting in incomplete expression of fault features. On the other hand, ET5 and ET6 add higher-order IMF on the basis of ET4, resulting in high redundancy in the signal, which interferes with the final results. The experimental results verify the validity of the conclusion reached in EEMD Analysis, which indicates that using the first 4-order IMF component as the input signal can effectively improve the accuracy of bearing fault diagnosis.

4.1.4. Analysis of Diagnosis Results. In this section, we test the transfer diagnosis performance of EMBRNDNMD model under four different working conditions of 0HP, 1HP, 2HP, and 3HP. To verify the theoretic analysis in Sec-
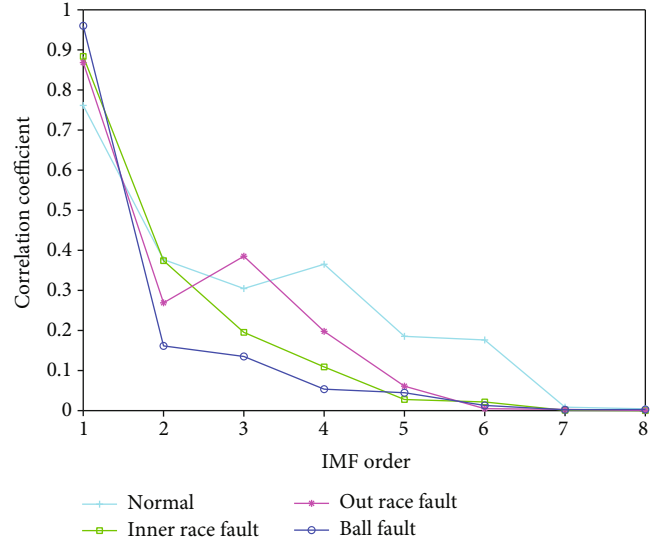
FIGURE 9: Correlation coefficient between the IMF and the original vibration signal.

TABLE 4: Test results of different IMFs input signals.

Working condition	IMF1-IMF3	IMF1-IMF5	IMF1-IMF6	IMF1-IMF4
A->B	94.17%	96.67%	97.83%	97.83%
A->C	93.50%	95.33%	96.50%	97.33%
A->D	94.00%	96.83%	97.33%	96.50%
B->A	92.83%	94.83%	95.83%	96.67%
B->C	95.83%	98.33%	99.33%	100%
B->D	94.67%	97.83%	97.50%	97.17%
C->A	92.33%	94.33%	94.83%	96.50%
C->B	92.83%	98.83%	97.33%	97.33%
C->D	94.83%	97.17%	98.67%	99.50%
D->A	93.17%	95.83%	96.33%	97.17%
D->B	94.50%	96.17%	98.00%	97.33%
D->C	95.17%	96.67%	98.83%	99.83%
Average	93.99%	96.18%	97.36%	98.17%

tion 3 and to evaluate the performance of EMBRNDNMD model, we designed some models for comparative analysis, and the specific designs include:

(1) EMBRN model: Compared to the EMBRNDNMD model, this model also uses MBRN to extract deep features of EEMD-TFFG and inputs deep features into the state classification network, but it does not involve the MK-MMD loss or the domain adversarial network

(2) EMBRNDN model: On the basis of the EMBRN model, it integrates a domain adversarial network to optimize MBRN

(3) EMBRNMD network: On the basis of the EMBRN model, it combines the MK-MMD loss to optimize MBRN via back propagation
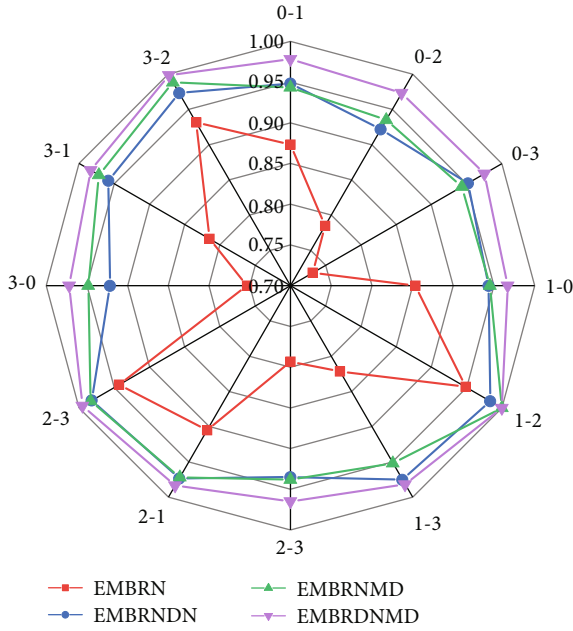
FIGURE 10: Accuracy distributions of various models.

TABLE 5: Fault classification results using various network models.

Working condition	EMBRN	EMBRNDN	EMBRNMD	EMBRNDNMD
A->B	87.33%	94.83%	94.33%	97.83%
A->C	78.50%	92.17%	93.50%	97.33%
A->D	73.17%	95.17%	94.33%	97.50%
B->A	85.33%	94.33%	94.50%	96.67%
B->C	94.83%	98.33%	100%	100%
B->D	82.17%	97.50%	95.17%	98.17%
C->A	79.33%	93.50%	93.83%	96.50%
C->B	90.50%	97.33%	97.17%	98.33%
C->D	94.33%	98.17%	98.33%	99.50%
D->A	75.32%	92.17%	94.83%	97.17%
D->B	81.50%	95.83%	97.17%	98.33%
D->C	93.17%	97.33%	98.83%	99.83%
Average	84.50%	95.67%	95.83%	98.17%

Table 5 lists the state identification accuracies of every diagnosis model, and Figure 10 shows the radar comparison maps of the identification accuracies of these models. According to Table 5 and Figure 10, we can draw the following conclusions:

(1) The diagnosis accuracy of EMBRN is significantly lower than that of the other three models, which indicates that the deep features of data present distribution differences under different working conditions, and the domain adversarial network and MK-MMD domain adaptation method can well solve this problem

(2) EMBRNDNMD has higher diagnosis accuracy than EMBRNDN and EMBRNMD, which is consistent with the theoretic analysis in Section 3.2. The reason is that the EMBRNDNMD model has not only considered the consistency of deep feature distribution in high-dimensional kernel space (MK-MMD loss) but also increased the distribution similarity in low-dimensional space (domain classification loss).

(3) EMBRNDN and EMBRNMD have poor performances under partial transfer modes, but EMBRNDNMD can maintain a high accuracy under all transfer modes, and it also has better stability than the other models for comparison, which proves the effectiveness and reliability of EMBRNDNMD model

Figure 11 shows how the diagnosis accuracies of various models change with iterations on various transfer modes. According to Figure 11, in all transfer modes, every model

can converge after 2000 iterations and become stable after 1000 iterations. Compared to the other three models, EMBRNDNMD has the fastest convergence speed, and its accuracy curve is the most stable. The analysis results show that under various transfer modes, EMBRNDNMD can not only provide high diagnosis accuracies but also has higher stability.

Figure 12 shows the t-SNE diagrams of deep features under the transfer mode of A->B by using different models, and the high-dimensional features are mapped to the two-dimensional space. According to Figure 12, compared to EMBRN, by integrating the domain transfer method, the deep features of models EMBRNMD and EMBRNDN have a bigger between-class distance and a smaller within-class distance, and the confusion problem among features under various states is significantly alleviated. By combining the MK-MMD loss and DANN, the separability of deep features of the EMBRNDNMD model is further improved, and the between-class confusion is also further reduced. The t-SNE analysis proves that compared to the other three models, the deep features extracted using EMBRNDNMD have better cross-domain invariance, and it also has stronger adaptation ability to working condition transfer.

4.1.5. The Influence of Hyperparameters on the Model. Four kinds of optimizers—Ada Delta, RMS Prop, SGD, and Adam—are selected for the test. The learning rates range from 0.001 to 0.2, and the results are listed in Table 6. It can be seen that when the learning rates are less than 0.1, the accuracy remains at a higher level. However, when the learning rates are higher than 0.1, it will make the network difficult to converge and obtain satisfactory training results. The Adam optimizer has the highest accuracy when the learning rate is 0.001, reaching 99.79%, so we ultimately choose the Adam optimizer to optimize the network parameters.

4.1.6. Comparison with Other Diagnosis Methods. To verify the effectiveness of the EMBRNDNMD model proposed in this paper under transfer of working conditions, we choose

(a) A->B

(b) A->C

(c) A->D

(d) B->A

(e) B->C

(f) B->D

(g) C->A

(h) C->B

FIGURE 11: Continued.

(i) C->D

(j) D->A

(k) D->B

(l) D->C
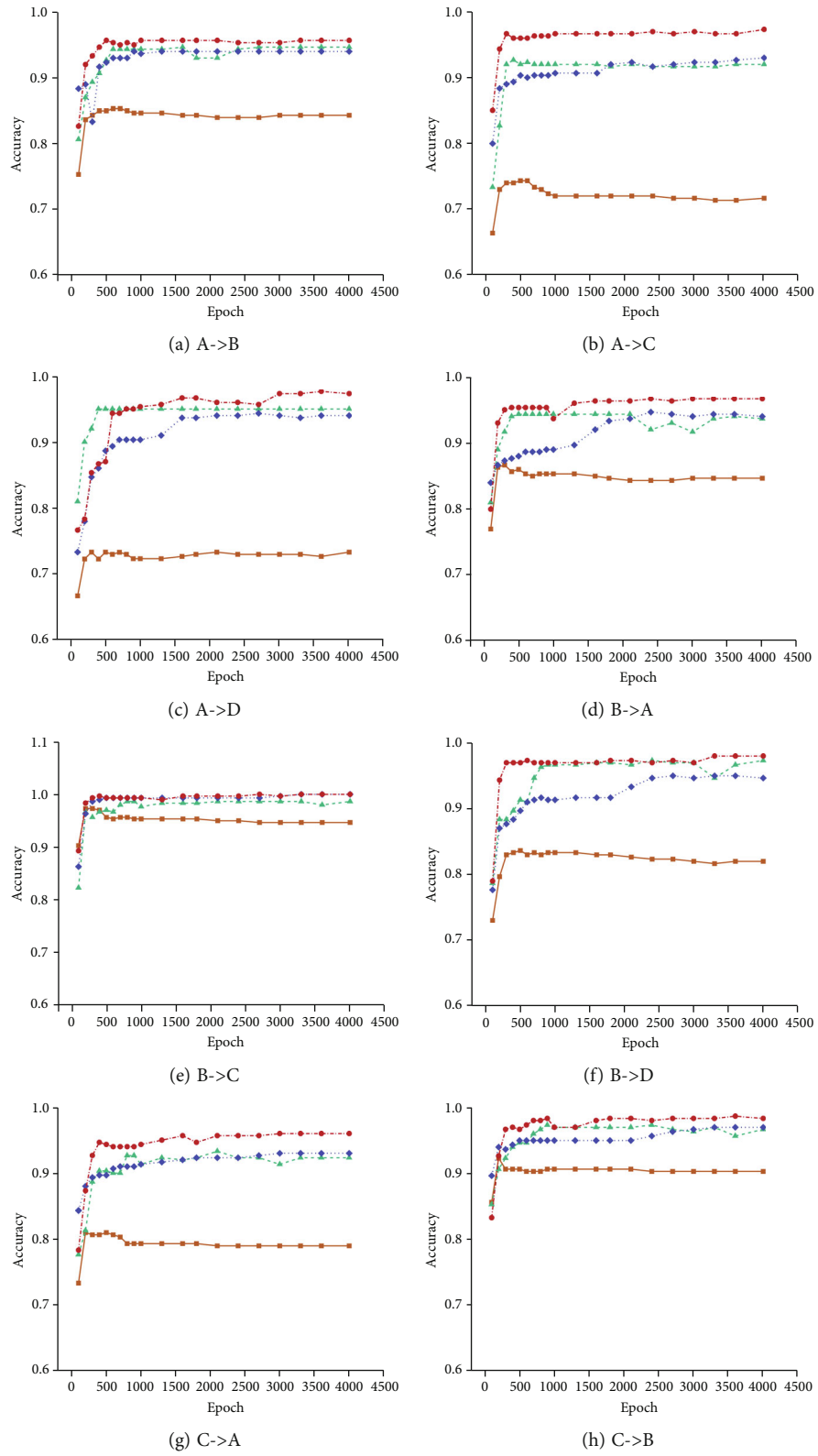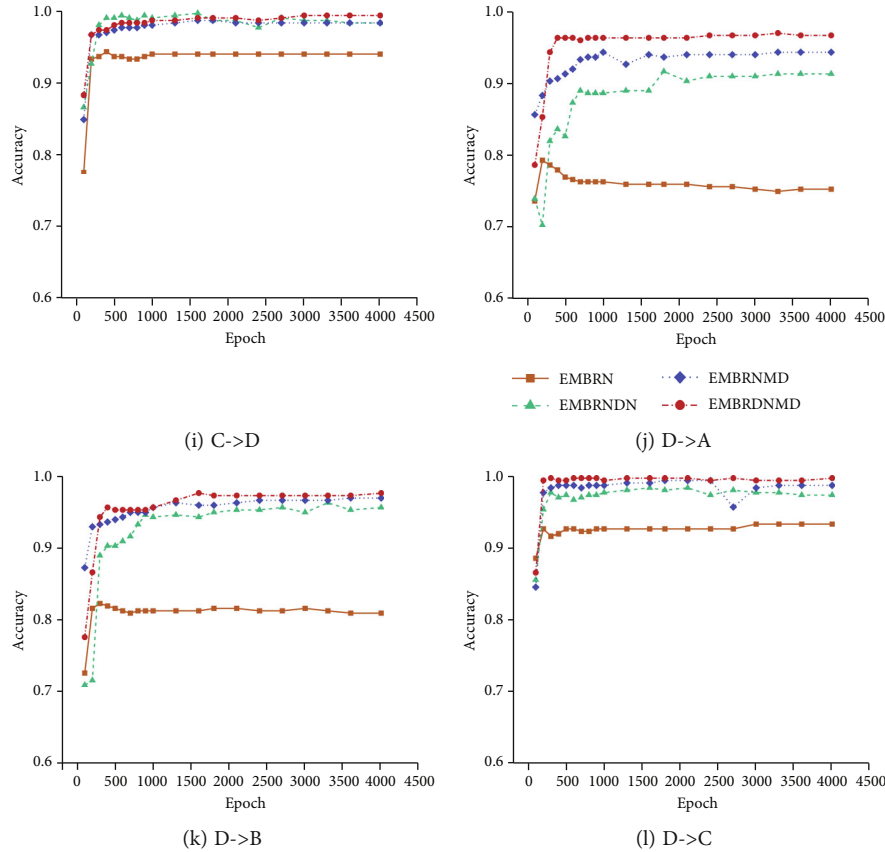
FIGURE 11: Comparison of model accuracy-iterations.

TABLE 6: Hyperparameters experimental results.

Learning rates	Ada delta	RMS prop	SGD	Adam
0.001	99.25%	98.29%	99.46%	99.79%
0.05	99.17%	98.12%	99.21%	99.42%
0.01	98.67%	97.95%	99.16%	99.29%
0.1	94.21%	92.86%	95.37%	96.25%
0.2	93.63%	90.28%	93.71%	93.33%

some classic diagnosis models based on machine learning and deep learning to test on the CWRU dataset, including SVM, CNN, TCA, and JDA, and their diagnosis accuracies under 12 transfer modes are obtained. The results are listed in Table 7. According to comparison and analysis results, we can find:

(1) Under varying working conditions, EMBRNDNMD can provide higher diagnosis accuracies than the methods of SVM, CNN, TCA, and JDA

(2) JDA has the closest diagnosis accuracies to EMBRNDNMD, and its accuracies are even higher than 90% under some transfer modes. However, it also has poor performance under some other transfer modes, and its overall performances are not as stable as EMBRNDNMD

(3) Compared with the conventional models, EMBRNDNMD is more advantageous in solving the problem of working condition transfer, which also proves the effectiveness of the design of EMBRNDNMD model

4.2. Tests on the MFS-RDS Experiment Platform and Related Analysis

4.2.1. Introduction of MFS-RDS Experiment Platform.
To verify the generalization ability of the proposed EMBRNDNMD model, the mechanical fault diagnosis experiment platform (MFS-RDS) was used to further evaluate the model performance. The MFS-RDS platform mainly consists of a three-phase motor, AC variable frequency drive (VFD) and tachometer. The sound and vibration data recorder WebDAQ-504 (MCC, US) was used for data collection. The vibration acceleration sensor was installed above the bearing seat. The experiment platform is as shown in Figure 13. In the experiments, bearings under the four states of normal condition, damage of 0.1 mm inner ball, damage of 0.1 mm outer ball, and damage of 0.1 mm rolling ball were used.

In the experiment, the vibration signals with sampling frequency of 8 kHz under the three speeds of 900 r/min, 1200 r/min, and 1800 r/min were collected, corresponding to the three working conditions of E, F, and G. With the vibration signal of 1024 continuous sampling points as a

(a) EMBRN model

(b) EMBRNDN model

(c) EMBRNMD model
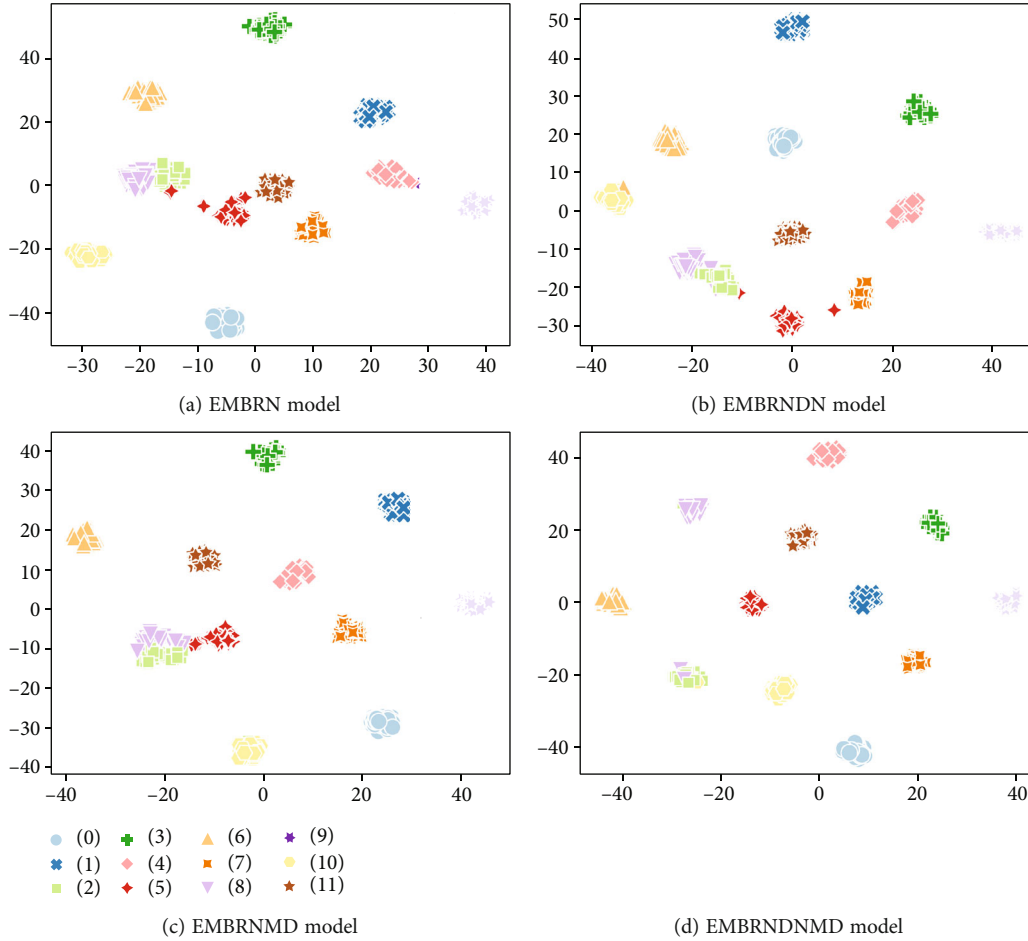
(d) EMBRNDNMD model

FIGURE 12: t-SNE diagrams of all models under the transfer learning task A->B.

TABLE 7: Comparison of different models in diagnosis accuracy.

Working condition	SVM	CNN	TCA	JDA	EMBRNDNMD
A->B	67.25%	78.33%	80.38%	91.75%	97.83%
A->C	67.42%	79.33%	75.67%	84.58%	97.33%
A->D	67.37%	78.17%	76.25%	85.31%	97.50%
B->A	75.13%	80.53%	91.75%	93.28%	96.67%
B->C	62.38%	78.87%	74.63%	91.27%	100%
B->D	67.56%	80.05%	82.18%	93.83%	98.17%
C->A	65.37%	71.08%	84.37%	91.08%	96.50%
C->B	61.22%	69.50%	84.53%	87.58%	98.33%
C->D	67.51%	79.33%	82.75%	91.32%	99.50%
D->A	62.34%	78.00%	80.52%	92.64%	97.17%
D->B	64%	78.83%	86.78%	91.16%	98.33%
D->C	67.36%	74.17%	86.43%	90.93%	99.83%
Average	66.24%	77.14%	82.34%	90.39%	98.17%

sample, 120 vibration signal samples were collected under each bearing state, as listed in Table 8. Three working conditions correspond to 6 transfer modes (E->F, E->G, F->E, F->G, G->E, G->F).

4.2.2. Experimental Results and Analysis. On the MFS-RDS bearing dataset, the diagnosis results of different methods under various transfer modes are presented in Table 9 and Figure 14. According to analysis of the experimental results, we can come up to the following conclusions:

(1) Under various transfer modes, the average diagnosis accuracy of EMBRN model reaches 85.39%; after introducing the domain adversarial module, the average accuracy of EMBRNDN is 93.51%; after introducing the MK-MMD loss, the average accuracy of EMBRNMD is 96.01%. This further proves that the domain adaptation mechanism can effectively improve the fault diagnosis accuracy under varying working conditions of bearing

(2) EMBRNDNMD maintains a high accuracy under all transfer modes and also shows great stability. Its average accuracy reaches 98.54%, which proves that the distribution consistency between deep features
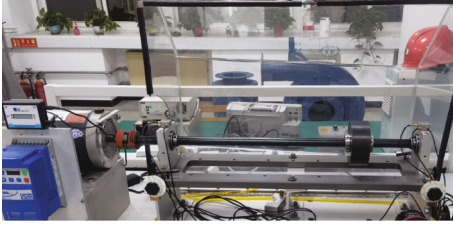
FIGURE 13: Mechanical fault diagnosis and rotor dynamic simulation and experiment platform.

TABLE 8: Introduction of MFS-RDS bearing dataset.

	Speed (r/min)	Normal	Inner race	Outer race	Rolling ball
Damage (mm)	—	—	0.1	0.1	0.1
Label	—	0	1	2	3
Dataset E	900	120	120	120	120
Dataset F	1200	120	120	120	120
Dataset G	1800	120	120	120	120

FIGURE 14: Transfer results statistics on the MFS-RDS bearing dataset.

TABLE 9: Results of various network models on the MFS-RDS bearing dataset.

	EMBRN	EMBRNDN	EMBRNMD	EMBRNDNMD
E->F	86.04%	94.38%	97.71%	99.79%
E->G	85.63%	92.92%	96.04%	98.96%
F->E	83.96%	92.08%	94.37%	98.33%
F->G	85.21%	93.95%	97.79%	97.51%
G->E	86.46%	94.79%	96.86%	98.12%
G->F	85.02%	92.92%	92.63%	98.54%
Average	85.39%	93.51%	96.01%	98.54%

TABLE 10: Comparison of different models in diagnosis accuracy.

Working condition	SVM	CNN	TCA	JDA	EMBRNDNMD
E->F	72.92%	81.67%	88.33%	94.17%	99.79%
E->G	69.17%	84.17%	86.67%	92.71%	98.96%
F->E	68.33%	80.62%	81.04%	91.04%	98.33%
F->G	66.46%	79.79%	79.79%	87.29%	97.51%
G->E	69.38%	74.79%	83.33%	93.33%	98.12%
G->F	69.58%	80.83%	86.67%	92.29%	98.54%
Average	69.31%	80.31%	84.31%	91.81%	98.54%

from source domain and target domain can be effectively improved by combining the MK-MMD loss and domain adversarial module

To further prove the above conclusions, we use the confusion matrix of the test dataset sample labels and prediction labels of various models to analyze the diagnosis precision, and use the t-SNE diagrams to carry out visual analysis of the deep features extracted by every model. Figure 15 shows the confusion matrices and t-SNE diagrams of every model under transfer mode G->E. According to the confusion matrices, we can see that EMBRNDNMD designed in this paper has the best performance. With the introduction of MK-MMD loss and domain adversarial module, the types and number of false classifications by both EMBRNDN and EMBRNMD show remarkable decline. Moreover, by combing the MK-MMD loss and domain adversarial mechanism, the number of false classifications by EMBRNDNMD is further reduced. In the meantime, the t-SNE diagrams show that compared to other models, the deep features extracted by EMBRNDNMD present bet-

ter class separability, which proves that EMBRNDNMD has better adaptability to various scenes.

4.2.3. Comparison with Other Diagnosis Methods. To verify the generalization ability of the EMBRNDNMD model, the same comparative experiment as in Section 4.1.6 is set and carried out on the MFS-RDS dataset. The experimental results are shown in Table 10.

From the table, it can be seen that the experimental results of EMBRNDNMD on MFS-RDS datasets are basically consistent with the results in Section 4.1. The diagnostic accuracies of EMBRNDNMD under varying working conditions are higher than the other groups, and the accuracies are all above 97%. This shows that the EMBRNDNMD model still performs well in cross-platform device diagnostics. It also has excellent stability when running on the MFS-RDS datasets, which can effectively improve the fault diagnosis accuracy under varying working conditions of bearing.
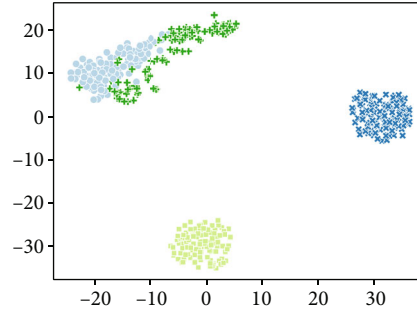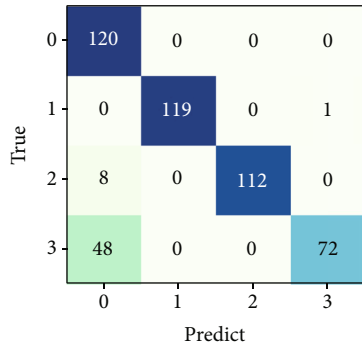
(a) EMBRN
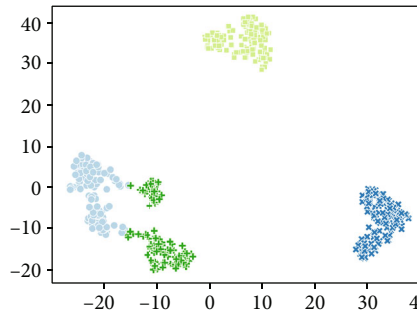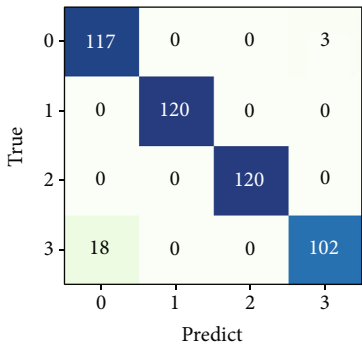
(b) EMBRNDN
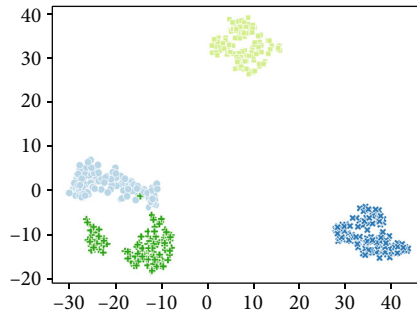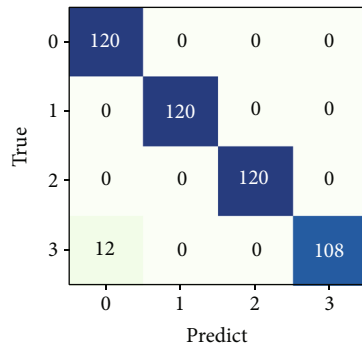
(c) EMBRNMD
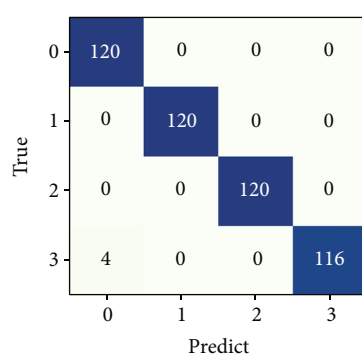
(d) EMBRNDNMD
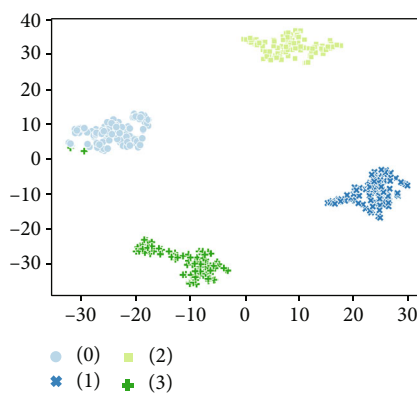
Figure 15: Compare the confusion matrices and t-SNE diagrams of different models.

5. Conclusions

This paper proposes a transfer diagnosis method EMBRNDNMD for rolling bearing faults. In this method, the EEMD method is used to extract the time-frequency information of the vibration signal, and the time-frequency feature graph EEMD-TFFG is constructed; then, the feature extraction network MBRN is designed according to the characteristics of EEMD-TFFG to extract deep features of EEMD-TFFG fault status; finally, the MBRN is optimized by combining DANN and MK-MMD, which improve the diagnosis ability of EMBRNDNMD under transfer of working conditions. According to theoretical derivation and experimental verification, we can draw the following conclusions:

(1) Using the EEMD method to perform time-frequency analysis of vibration signals, a construction method of EEMD-TFFG is proposed, which can provide time-frequency feature information reflecting the state of rolling bearings for subsequent deep learning networks

(2) MBRN is designed according to the characteristics of EEMD-TFFG. The multi-branch network structure and residual stacking mechanism can solve various problems of EEMD-TFFG, such as small size, scattered features, and independent time-frequency features of different scale information

(3) A joint domain transfer mechanism is designed based on DANN and MK-MMD, which can effectively improve the consistency of data deep features between the source domain and target domain, and reduce the distribution differences of deep features in high-dimensional kernel space between the source domain and target domain. It can effectively improve the diagnosis ability of EMBRNDNMD under transfer of working conditions. The results of experiments carried out on two bearing fault test platforms show that the EMBRNDNMD model can achieve high diagnostic accuracy in various working condition transfer modes

Data Availability

The data used to support the findings of this study are available from the corresponding author upon request.

Conflicts of Interest

The authors declare that there is no conflict of interest regarding the publication of this paper.

Acknowledgments

References

[1] W. Fu, K. Shao, J. Tan, and K. Wang, "Fault diagnosis for rolling bearings based on composite multiscale fine-sorted dispersion entropy and SVM with hybrid mutation SCA-HHO algorithm optimization," *Access*, vol. 8, pp. 13086–13104, 2020.

[2] Z. Wang, L. Yao, Y. Cai, and J. Zhang, "Mahalanobis semi-supervised mapping and beetle antennae search based support vector machine for wind turbine rolling bearings fault diagnosis," *Renewable Energy*, vol. 155, pp. 1312–1327, 2020.

[3] W. Gong, H. Chen, Z. Zhang et al., "A novel deep learning method for intelligent fault diagnosis of rotating machinery based on improved CNN-SVM and multichannel data fusion," *Sensors*, vol. 19, no. 7, p. 1693, 2019.

[4] Z. Huo, Y. Zhang, L. Shu, and M. Gallimore, "A new bearing fault diagnosis method based on fine-to-coarse multiscale permutation entropy, Laplacian score and SVM," *IEEE Access*, vol. 7, pp. 17050–17066, 2019.

[5] L. Han, C. Li, L. Zhan, and X. Li, "Rolling bearing fault diagnosis method based on EEMD permutation entropy and fuzzy clustering," in *Fifth International Conference on Instrumentation and Measurement, Computer, Communication and Control (IMCCC)*, Qinhuangdao, China, 2016.

[6] C. S. Wang, C. Y. Sha, M. Su, and Y. K. Hu, "An algorithm to remove noise from locomotive bearing vibration signal based on self-adaptive EEMD filter," *Journal of Central South University*, vol. 24, no. 2, pp. 478–488, 2017.

[7] S. Yang and J. Yue, "Fault diagnosis of EMU rolling bearing based on EEMD and SVM," in *International Conference on Computer-aided Design*, Marrakech, Morocco, May 2018.

[8] C. Z. Hu, M. Y. Huang, Q. Yang, and W. J. Yan, "On the use of EEMD and SVM based approach for bearing fault diagnosis of wind turbine gearbox," in *2016 Chinese Control and Decision Conference (CCDC)*, Yinchuan, China, 2016.

[9] S. Haidong, J. Hongkai, L. Xingqiu, and W. Shuaipeng, "Intelligent fault diagnosis of rolling bearing using deep wavelet auto-encoder with extreme learning machine," *Knowledge-Based Systems*, vol. 140, pp. 1–14, 2018.

[10] G. Li and Y. Hu, "Improved sensor fault detection, diagnosis and estimation for screw chillers using density-based clustering and principal component analysis," *Energy & Buildings*, vol. 173, pp. 502–515, 2018.

[11] Q. Qian, Y. Qin, Y. Wang, and F. Liu, "A new deep transfer learning network based on convolutional auto-encoder for mechanical fault diagnosis," *Measurement*, vol. 178, article 109352, 2021.

[12] S. Guo, T. Yang, W. Gao, C. Zhang, and Y. Zhang, "An intelligent fault diagnosis method for bearings with variable rotating speed based on pythagorean spatial pyramid pooling CNN," *Sensors*, vol. 18, no. 11, p. 3857, 2018.

[13] S. Tang, S. Yuan, and Y. Zhu, "Data preprocessing techniques in convolutional neural network based on fault diagnosis towards rotating machinery," *Access*, vol. 8, pp. 149487–149496, 2020.

[14] F. Zhou, W. Zhou, D. Chen, and C. Wen, "Rolling bearing real time fault diagnosis using convolutional neural network," in

2019 Chinese Control And Decision Conference (CCDC),, vol. 12, Nanchang, China, 2019.

[15] Y. Yao, S. Zhang, S. Yang, and G. Gui, "Learning attention representation with a multi-scale CNN for gear fault diagnosis under different working conditions," *Sensors*, vol. 20, no. 4, p. 1233, 2020.

[16] H. Fan, C. Xue, X. Zhang, X. Cao, S. Gao, and S. Shao, "Vibration images-driven fault diagnosis based on CNN and transfer learning of rolling bearing under strong noise," *Shock and Vibration*, vol. 2021, no. 2, pp. 1–16, 2021.

[17] K. Zhang, B. Tang, L. Deng, and X. Liu, "A hybrid attention improved ResNet based fault diagnosis method of wind turbines gearbox," *Measurement*, vol. 179, no. 10, article 109491, 2021.

[18] C. Wang, Y. Xie, and D. Zhang, "Deep learning for bearing fault diagnosis under different working loads and non-fault location point," *Journal of Low Frequency Noise Vibration and Active Control*, vol. 40, no. 1, 2019.

[19] K. He, X. Zhang, S. Ren, and J. Sun, "Deep residual learning for image recognition," in *IEEE Conference on Computer Vision and Pattern Recognition (CVPR)*, pp. 770–778, Las Vegas, USA, 2016.

[20] W. Hao, Q. Zhang, M. Shang, and Y. Gu, "Extreme learning Machine-based classifier for fault diagnosis of rotating Machinery using a residual network and continuous wavelet transform," *Measurement*, vol. 183, article 109864, 2021.

[21] X. Wang, C. Shen, M. Xia, D. Wang, J. Zhu, and Z. Zhu, "Multi-scale deep intra-class transfer learning for bearing fault diagnosis," *Reliability Engineering, System Safety*, vol. 202, p. 107050, 2020.

[22] L. Wen, X. Li, and L. Gao, "A transfer convolutional neural network for fault diagnosis based on ResNet-50," *Neural Computing and Applications*, vol. 32, no. 10, pp. 6111–6124, 2020.

[23] J. Lu, V. Behbood, P. Hao, H. Zuo, S. Xue, and G. Zhang, "Transfer learning using computational intelligence: a survey," *Knowledge-Based Systems*, vol. 80, pp. 14–23, 2015.

[24] F. Zhuang, Z. Qi, K. Duan et al., "A comprehensive survey on transfer learning," *Proceedings of the IEEE*, vol. 109, no. 1, pp. 43–76, 2020.

[25] A. Mohammed and B. Carlos, "Domain adversarial for acoustic emotion recognition," *IEEE/ACM Transactions on Audio Speech & Language Processing*, vol. 26, no. 12, pp. 2423–2435, 2018.

[26] X. Li, W. Zhang, H. Ma, Z. Luo, and X. Li, "Deep learning-based adversarial multi-classifier optimization for cross-domain machinery fault diagnostics," *Journal of Manufacturing Systems*, vol. 55, pp. 334–347, 2020.

[27] W. Lu, B. Liang, Y. Cheng, D. Meng, J. Yang, and T. Zhang, "Deep model based domain adaptation for fault diagnosis," *IEEE Transactions on Industrial Electronics*, vol. 64, no. 3, pp. 2296–2305, 2017.

[28] I. Goodfellow, J. Pouget-Abadie, M. Mirza et al., "Generative adversarial networks," *Advances in Neural Information Processing Systems*, vol. 3, pp. 2672–2680, 2014.

[29] Y. Ganin, E. Ustinova, H. Ajakan et al., "Domain-adversarial training of neural networks," *Journal of Machine Learning Research*, vol. 17, no. 1, p. 2096, 2017.

[30] Y. Li, Y. Song, L. Jia, S. Gao, Q. Li, and M. Qiu, "Intelligent fault diagnosis by fusing domain adversarial training and maximum mean discrepancy via ensemble learning," *IEEE Transactions on Industrial Informatics*, vol. 17, no. 4, pp. 2833–2841, 2021.

[31] B. Yang, Y. Lei, F. Jia, N. Li, and Z. Du, "A polynomial kernel induced distance metric to improve deep transfer learning for fault diagnosis of machines," *IEEE Transactions on Industrial Electronics*, vol. 67, no. 11, pp. 9747–9757, 2020.

[32] C. Che, H. Wang, X. Ni, and Q. Fu, "Domain adaptive deep belief network for rolling bearing fault diagnosis," *Computers & Industrial Engineering*, vol. 143, p. 106427, 2020.

[33] Y. Tang, B. Wu, L. Peng, and C. Liu, "Semi-supervised transfer learning for convolutional neural network based Chinese character recognition," in *2017 14th IAPR International Conference on Document Analysis and Recognition (ICDAR),*, Kyoto, Japan, 2018.

[34] W. Mao, Y. Liu, L. Ding, A. Safian, and X. Liang, "A new structured domain adversarial neural network for transfer fault diagnosis of rolling bearings under different working conditions," *IEEE Transactions on Instrumentation and Measurement.*, vol. 70, pp. 1–3, 2020.

[35] G. Cai, Y. Wang, L. He, and M. Zhou, "Unsupervised domain adaptation with adversarial residual transform networks," *IEEE Transactions on Neural Networks and Learning Systems*, vol. 31, no. 8, pp. 3073–3086, 2019.

[36] W. Li, Z. Chen, and G. He, "A novel weighted adversarial transfer network for partial domain fault diagnosis of machinery," *IEEE Transactions on Industrial Informatics*, vol. 17, no. 3, pp. 1753–1762, 2020.

[37] J. Dybala and R. Zimroz, "Rolling bearing diagnosing method based on Empirical Mode Decomposition of machine vibration signal," *Applied Acoustics*, vol. 77, pp. 195–203, 2014.

[38] W. U. Zhaohua and N. E. Huang, "Ensemble empirical mode decomposition: a noise-assisted data analysis method," *Advances in Adaptive Data Analysis*, vol. 1, no. 1, pp. 1–41, 2009.

[39] A. Gretton, D. Sejdinovic, H. Strathmann et al., "Optimal kernel choice for large-scale two-sample tests," in *Advances in Neural Information Processing Systems 25 (NIPS 2012)*, California, USA, 2012.

Research Article

LETR: An End-to-End Detector of Reconstruction Area in Blades Adaptive Machining with Transformer

Zikai Yin,[1] **Yongshou Liang** [ID],[1] **Junxue Ren,**[1] **Jungang An,**[2] **and Famei He**[3]

[1]*Key Laboratory of High-Performance Manufacturing for Aero Engines, School of Mechanical Engineering,*
 Northwestern Polytechnical University, 127 West Youyi Road, Beilin District, Xi'an 710072, China
[2]*Haimo Research Institution, 22 Technology of Fifth Road, High Technology District, Xi'an 710000, China*
[3]*Beijing Institute of Technology, No. 5, South Street, Zhongguancun, Haidian District, Beijing 100000, China*

Correspondence should be addressed to Yongshou Liang; liangyongshou@nwpu.edu.cn

In the leading/trailing edge's adaptive machining of the near-net-shaped blade, a small portion of the theoretical part, called the reconstruction area, is retained for securing aerodynamic performance by manual work. The next work is to recognize the reconstruction area of the reconstructed leading/trailing edge's image. To accelerate this process, an anchor-free neural network model based on Transformer was proposed, named Leading/trailing Edge Transformer (LETR). LETR extracts image features from an aspect of mixed frequency and channel domain. We also integrated LETR with the newest meta-Acon activation function. We tested our model on the self-made dataset LDEG2021 on a single GPU and got an mAP of 91.9%, which surpassed our baseline model, Deformable DETR, by 1.1%. Furthermore, we modified LETR's convolution layer and named the new model after Ghost Leading/trailing Edge Transformer (GLETR) as a lightweight model for real-time detection. It is proved that GLETR has fewer weight parameters and converges faster than LETR with an acceptable decrease in mAP (0.1%) by test results. The proposed models provide the basis for subsequent parameter extraction work in the reconstruction area.

1. Introduction

The near-net-shaped blades are applied to the blades of the aero-engine as it fits the modern aero-engine performance better. The blank material and typical structure of the near-net-shaped blade are shown in Figures 1(a) and 1(b), respectively. A section curve of the blade is presented in Figure 2. The geometric parameters of the near-net-shaped blade's suction/pressure surface have met the designing requirement after being forged, which means that it needs no further machining, while the leading/trailing edge cannot be forged precisely due to the sharply changing curvature. On the other hand, although blank material is forged within the design tolerances, complex deformation still occurs [1]. That means we cannot plan the tool path according to the designed model. Hence, we need to reconstruct the theoret-

ical leading/trailing edge. In this case, adaptive machining [2] is imported to the machining process of near-net-shaped blades. Adaptive machining technology aims to modify manufacturing data on the basis of changed conditions. In our previous manual work, we retained a part of the theoretical leading/trailing edge and bridged it with blank material considering the design intent and aerodynamic performance. The reconstructed blade's section curves are shown in Figure 3. This process, however, is time-consuming and depends on the human experience. Deep learning has a cutting-edge advantage in improving efficiency and avoiding human error, based on which we proposed a model reconstruction framework in [3].

Unlike traditional reconstruction methods based on geometric prediction, we reconstructed models based on the accomplished reconstruction stored in images. Our method

(a) The blank to be formed

(b) The near-net-shaped blade
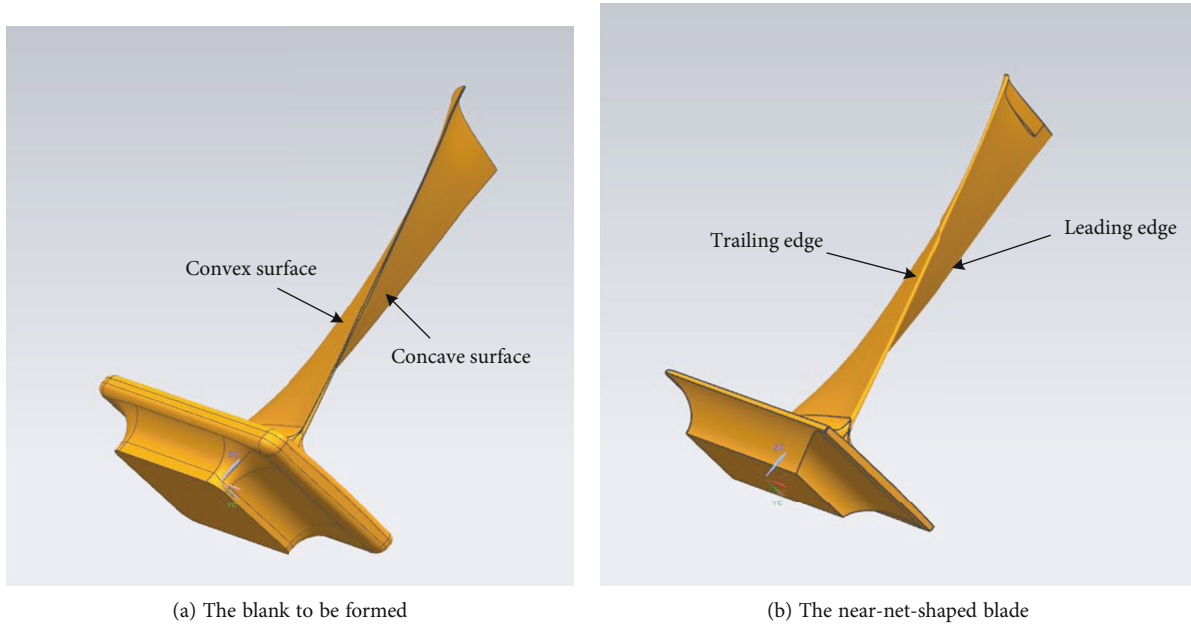
FIGURE 1: The typical structure of near-net-shaped blade.
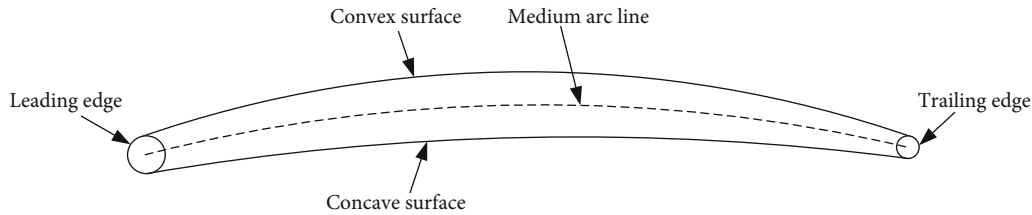
FIGURE 2: A section line of the near-net-shaped blade.

can be described in the following steps. In the first stage, we use Generative Adversarial Networks (GAN) [4] to classify optimal reconstructed leading/trailing edge's images based on our previous manual works [3]. However, the reconstructed curves in images cannot be adopted in computer-aided design (CAD) software for model reconstruction directly. So, we need to detect the retained part and bridged curves of these reconstructed curves on the next step. Thirdly, we will extract parameter information from them. As long as these parameters are obtained, we can utilize CAD software to adjust the theoretical leading/trailing edge and reconstruct it automatically to realize the adaptive machining of the near-net-shaped blade. This paper's main focus is to detect the retained part of the theoretical leading/trailing edge, and we use the item "reconstruction area" to represent it.

A small object usually contains a small quantity of semantic information due to its small size. As shown in Figure 3, in comparison with the general object detection task, there is no complex feature in the leading/trailing edge's image. Moreover, the leading/trailing edge's image contains less semantic information, and the background is relatively simple. For this reason, the leading/trailing edge's reconstruction area detection is defined as a small object

detection task in this paper, and the reconstruction area is approximated by the area of the bounding box.

The performance of object detection has improved significantly with the help of convolutional neural networks (CNNs) [5], which detect objects by extracting features from considerable data. Generally speaking, object detection algorithms employing CNNs are divided into two-stage methods and one-stage methods according to their processing stages. A typical method of two-stage is the Regions with CNN features (R-CNN) series [6–8], which imports the selective search algorithm to predict the region of interest. Unlike two-stage methods, one-stage methods predict bounding boxes and classes in a single neural network. Symptomatic one-stage methods include You Only Look Once (YOLO) series [9–12] and Single-Shot Multibox Detector (SSD) [13].

The methods mentioned above have three points to be further ameliorated. First, the anchor box size needs to be manually designed for different detection tasks, which takes a great amount of time. Furthermore, the sizes of ground-truth bounding boxes of small objects are relatively small, which may lead to the class imbalance problem [14]. Moreover, the nonmaximum suppression (NMS) algorithm is not sensitive to small objects which contain less semantic

(a) Leading edge's reconstruction area

(b) Trailing edge's reconstruction area
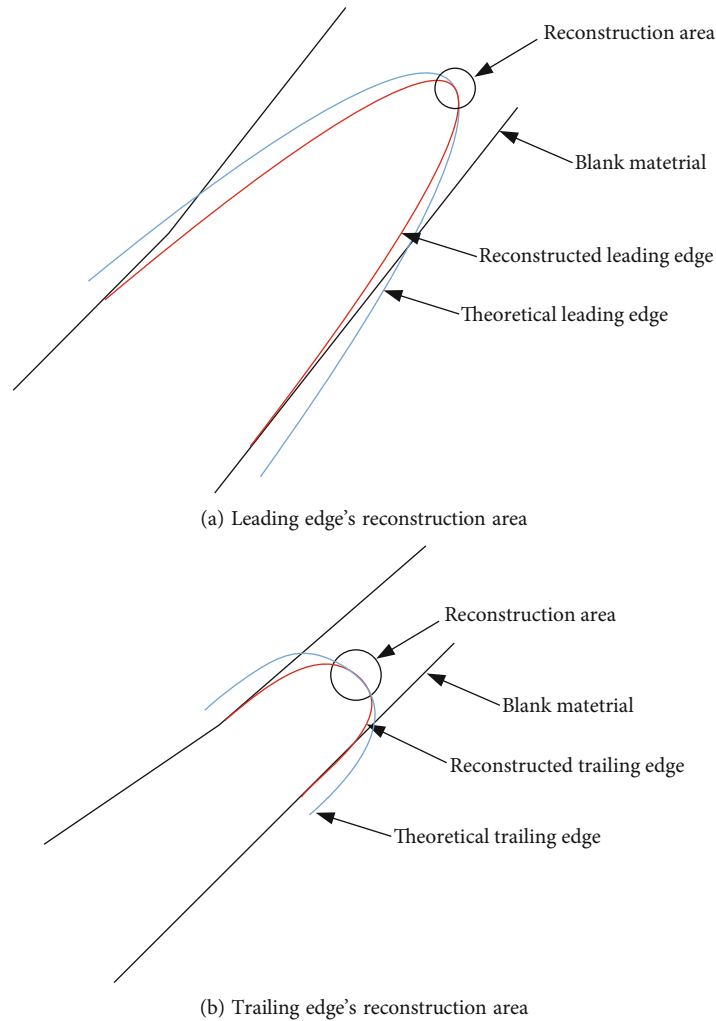
FIGURE 3: The reconstruction area of a blade.

information. The number of the network's predictions is much larger than that of the actual objects' number, and NMS is employed here to remove superfluous predicted bounding boxes. The NMS algorithm sets a threshold value and deletes all bounding boxes higher than the threshold value and keeps the bounding box with the highest score. The postprocess of NMS during the small object detection is often obstructed by background, and small targets are easily covered by objects of medium and large sizes.

Considering the variable shape of the leading/trailing edge, we decided to take an anchor-free model as our leading/trailing edge detector, which abandons anchors and the postprocessing of the NMS algorithm. In recent years, Transformer has shown its superiority in the object detection field due to its capacity for spatial relation modeling of targets. The model that works best now with Transformer is Deformable DETR (Deformable Detection Transformer) [15]. Nevertheless, Deformable DETR has its issues. Firstly, Deformable DETR extracts features from input images based on the spatial attention mechanism. That means some valuable information is abandoned during this process. Its accuracy, therefore, remains a huge space to be promoted. Then,

despite that Deformable DETR has achieved prominent results, it still needs to be further compressed to meet the requirement of real-time detection. Focusing on these two abovementioned problems, the main works of this study are summarized below:

(1) We proposed an anchor-free model named Leading/ trailing Edge Detection Transformer (LETR). LETR extracts features of reconstruction areas from the frequency-channel mixed domain. Besides, LETR activates nonlinear units dynamically in view of the simplex background of our dataset

(2) To balance model weight and performance, we introduced a lightweight model by modifying LETR for real-time detection. Technically, the specific convolutional layers of LETR are replaced by lightweight modules. The model is called Ghost Leading/trailing Edge Detection Transformer (GLETR).

(3) We tested LETR and GLETR on the self-made dataset LDEG2021. It is proved that LETR has state-of-the-art performance on detecting reconstruction

areas. Moreover, GELTR has significantly fewer parameters and converges faster than LETR in the training process

The rest of this paper is structured as follows. Section 2 illustrates the recent works on the reconstruction of edge shape in adaptive machining and object detection. Section 3 reviews the attention mechanism in computer vision. Our proposed models are presented in Section 4. Section 5 reports the experimental results on the self-made dataset. Section 6 gives the conclusions and future works. The code will be available at https://github.com/andrewsilver1997/LETR.

2. Related Works

Our research is the combination of adaptive machining and computer vision algorithms. In this section, we will discuss the related works from the aspects of edge shape reconstruction, small object detection, self-attention mechanism, activation function, and efficient networks.

2.1. Reconstruction of Edge Shape.
The prevalent model reconstruction methods can be concluded in three aspects: by fitting curves of measured data, predicting the deformation of the blade's surface, and predicting design intent. Our reconstruction work is mainly based on design intent and deformation of blank material. A model similar to the original counterpart is constructed according to the existing data in the reconstruction of the edge shape procedure. Some representative research is illustrated as follows. Yun et al. [16] imported parameterization design to Free-Form Deformation (FFD) and realized the model reconstruction based on measure data. Zhao et al. [17] improved the accuracy of reconstruction by inserting knots. Feng et al. [2] predicted the desired spline curves considering the deformation and thickness of the blank material while preserving the design intent. Yu et al. [18] established the relationship between measured points and the velocity field of the blade's section. Further, they calculated the curves in the area without measuring data. Zhang et al. [19] considered the constraints of the chord length, angle of attack, and radius during the reconstruction process. Wu et al. [20] proposed a novel reconstruction algorithm by removing bad measure points and optimizing the iterative closest point (ICP) algorithm. Nevertheless, the current research on the modeling of large curvature inexact forming regions mainly focuses on simple geometric element fitting but does not fully consider the relationship between the design intention of the blade, the similarity relationship between the actual blade surface and theoretical surface, and the complex deformation of blank materials. Our previous manual works addressed the aforementioned issue to a certain extent [3]. For this article, we further proposed an algorithm based on deep learning to accelerate this process and reduce errors caused by human experiences.

2.2. Small Object Detection.
It is usually a small part of the theoretical model and has less semantic information in an image. Hence, the detection of the reconstruction area can be seen as a small object detection task. Some models based on the two-stage method were proposed to detect small objects. Based on Faster R-CNN [7], Singh and Davis [21] proposed Scale Normalization for Image Pyramids (SNIP) for small object detection. Furtherly, they modified SNIP and proposed SNIPER [22] for efficient and fast detection. Zhang et al. [23] utilized a multiscale feature fusion layer (MFL), and a certain extent of improvement was obtained. On the other hand, a typical one-stage detector is RetinaNet [14], which uses focal loss and feature pyramid maps [24] to detect small objects. Based on YOLO v2, the work of Liu et al. [25] can detect arbitrary-oriented targets of small sizes.

Some researchers proposed anchor-free methods. The representative works include CornerNet [26], ExtremeNet [27], and CenterNets [28, 29]. These models detect objects by implementing keypoint estimation. Some novel works aiming to solve the problems of the traditional NMS algorithms were published. Dong et al. [30] integrated transfer learning with faster RCNN for annotation and improved accuracy. Cai and Vasconcelos [31] proposed cascade RCNN. Cascade RCNN connects a sequence of detectors and adapts threshold in NMS processing to avoid the mismatch between predicted bounding boxes and ground-truth objects. Our models discard anchor boxes and NMS postprocessing. Experiments verified that our models dominate in existed models without the help of the anchor box and NMS algorithm.

2.3. The Self-Attention Mechanism in Computer Vision.
In recent years, the progress of natural language processing [32] (NLP) has led researchers to investigate its application in computer vision. Vaswani et al. [33] introduced Transformer in NLP for the first time. The Transformer achieves impressive results on sequence prediction. Carion et al. [34] modified the Transformer and named their model as Detection Transformer (DETR). The DETR model abandons anchor boxes and NMS's implementation. However, DETR has a low speed of convergence and does not perform well on small object detection tasks. Sun et al. [35] argued the cross-attention module of DETR is not necessary and proposed two models named Transformer-based Set Prediction with FCOS [36] (TSP-FCOS) and Transformer-based Set Prediction with R-CNN (TSP-RCNN), respectively. Zhu et al. [15] imported deformable convolution [37] to DETR and proposed Deformable DETR. Deformable DETR deals with input feature maps from the spatial domain. In this study, we tried to extract features from a different aspect, that is, the mixed domain of frequency and channel.

2.4. Activation Functions.
Some researchers attempted to modify the activation function in networks and gained improvements to a certain extent. The most-used activation function is Rectified Linear Unit (ReLU) [38] which activates the neurons linearly when the input is bigger than zero. Its variant, Leaky ReLU [39], activates the neurons when the input is nonzero. The ReLU-based activation functions are too simple to be implemented on complicated visual tasks as some features may be missed. Sigmoid-

weighted Linear Unit (SiLU) [40] combines ReLU and sigmoid function together. Compared with ReLU, it is smooth and nonmonotonic. [41] applied automatic search to a variety of activation functions and found a better function named Swish. But it also brings huge computation resource consumption. [42] imported spatial context to the activation function and gained state-of-the-art performance on dense visual tasks. A recent work is called Dynamic Rectified Linear Unit (DY-ReLU) [43] adapts the parameters dynamically by a hyperfunction. When implemented on deep neuron networks, however, the abovementioned activation functions' effects become weaker. Unlike previous activation functions, Activate or Not functions (Acon) [44] learn whether to activate the specific neurons and convert models into dynamic networks, which brings better performance as networks go deeper.

2.5. Efficient Networks. For deploying object detection models on mobile devices, some operations for lightweighting are inevitable to save computational cost and memory. There are two types of strategies for efficient networks. One is to compress the model by pruning redundant connections [45] and channels [46], quantization [47], and knowledge distillation [48]. Such model compression methods usually require well-designed architecture and pretrained models. The other strategy is to design a lightweight model directly [49]. Some typical lightweight models are proposed by researchers. Xception [50] introduced depthwise separable convolution modules and realized better performance with fewer model parameters. MobileNet series [51–53], for example, are based on depth-wise and pointwise separable convolutions as well as automated machine learning (AutoML) technologies [54]. Other famous lightweighted models are ShuffleNet [55, 56] series, which exchange their inner channel information to reduce computational cost. The redundancy of feature maps has not been solved well. GhostNet [49], on the contrary, utilizes these redundant feature maps and has more excellent performance compared with previous lightweight models. We integrated our LETR with GhostNet and presented GLETR. More details of GLETR are seen in Section 4.

3. Revisiting Deformable Attention

3.1. Self-Attention Mechanism. DETR is a successful object detection model using the self-attention mechanism, achieving outstanding performance on the COCO dataset [57]. In this part, we briefly reviewed the inner mechanism of DETR.

3.1.1. Multihead Attention. In the natural language processing field, the self-attention mechanism was adopted in the Transformer model. By computing the values of Query, Key and Value of input images, the Transformer modulates the compatibility of every pixel. In the multihead attention mechanism, the outputs of several attention heads are aggregated linearly with learnable weight parameters. Given the Value's input feature z_q and the Query and Key's input feature $x \in HW \times C$, where H, W, and C are the heights, widths, and channels of input images, the formulation of multihead attention is shown as:

$$\text{MultiHeadAttn}(z_q, x) = \sum_{m=1}^{M} W_m \left[\sum_{k \in \Omega_k} A_{mqk} \cdot W'_m x_k \right]. \quad (1)$$

In Equation (1), $q \in \Omega_q$ and $k \in \Omega_k$ are elements of Query and Key set, m is the number of attention heads, $A_{mqk} \propto \exp\{z_q^T U_m^T V_m^T x_k / \sqrt{C_v}\}$ is attention weight, where U_m and V_m are the transformation matrices of Query, Key, respectively, and $C_v = C/M$. W_m and W'_m are transformation matrices of Value. Please note that U_m, V_m, W_m, and W'_m's parameters are all learnable.

3.1.2. Position Embedding. DETR adopts position embedding to our extracted features. This is owing to that the Transformer demands information about the relative or absolute position of pixels in feature maps. In DETR, sine and cosine functions are used to represent the positions of different pixels. The position embedding equations are written as:

$$PE(\text{pos}, 2i) = \sin\left(\frac{\text{pos}}{10000^{2i/d_{\text{model}}}}\right),$$
$$PE(\text{pos}, 2i + 1) = \cos\left(\frac{\text{pos}}{10000^{2i/d_{\text{model}}}}\right), \quad (2)$$

where pos denotes the position and i is the dimension index; d_{model} represents the channel dimension of the input features.

3.1.3. Match Loss. Unlike previous object detection models using NMS, DETR outputs fixed N predictions and N is much larger than the number of objects in an image. DETR needs to allocate predictions to objects in images, and match loss is introduced to evaluate this process. Assuming that y_i is the set of ground-truth bounding boxes, $y_{\sigma(i)}$ is a set of predicted bounding boxes with index $\sigma_{(i)}$, the optimal permutation σ is written as:

$$\sigma = \arg \min_{\sigma \in P_N} \sum_{i}^{N} L_{\text{match}}\left(y_i, y_{\sigma(i)}\right), \quad (3)$$

where σ stands for a permutation of predicted objects. Finally, the match loss L_{match} is defined as:

$$L_{\text{match}} = \sum_{i=1}^{N} \left[-\log P_{\sigma(i)} + L_{\text{box}}\left(b_i, \hat{b}_i\right)\right]. \quad (4)$$

Albeit the fact that DETR has achieved state-of-the-art performance, it costs massive computational resources, and its convergence speed is relatively low. Furthermore, the performance of DETR on small target datasets is
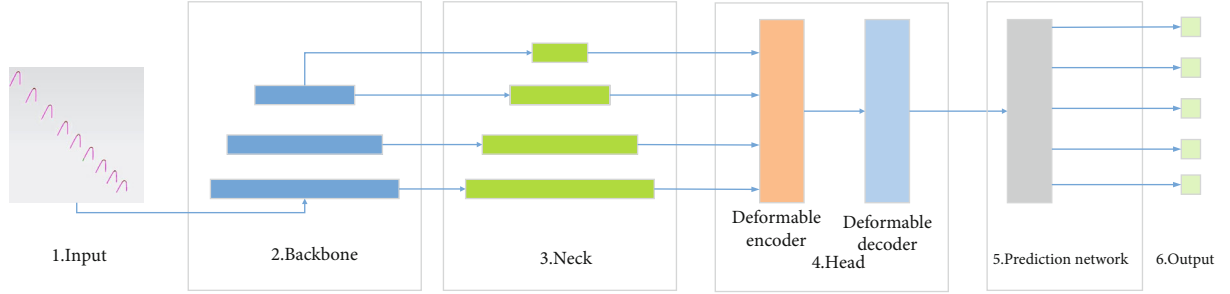
FIGURE 4: Overview of LETR.
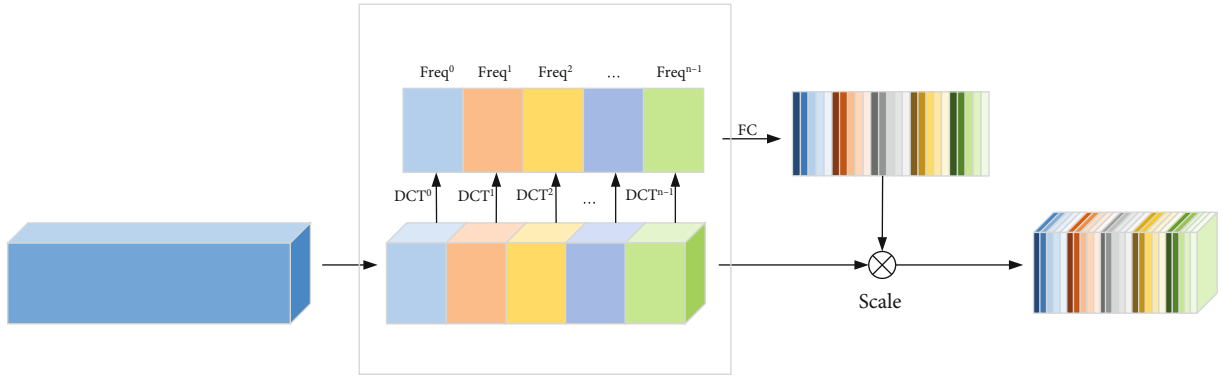
FIGURE 5: The feature extraction process of the multispectral channel attention module.

disappointing. Besides, the test results of DETR present no outstanding performance on our detection task. Hence, it is proved that DETR is not suitable for our detection task.

3.2. Deformable Attention. DETR did not perform well on small target detection tasks, owing to its inner mechanism. Zhu et al. [15] combined DETR with deformable convolution and named their model Deformable DETR, by which self-attention is generated to image deformable attention in the image domain. The feature of the deformable attention is computed by:

$$\mathrm{DeformAttn}\left(z_q, p_q, x\right) = \sum_{m=1}^{M} W_m \left[\sum_{k=1}^{K} A_{mqk} \cdot W'_m x\left(p_q + \Delta p_{mqk}\right)\right]. \tag{5}$$

k indicates the sampled keys, and K means the number of sampled keys. p_q denotes the reference point, and Δp_{mqk} is sampling offset.

In small object detection tasks, the sizes of objects vary from small size to large size. To adapt the multiscale size of input features, the deformable attention generates to multiscale deformable attention and can be calculated by:

$$\mathrm{MSDeformAttn}\left(z_q, \widehat{p}_q, x^l\Big|_{l=1}^{L}\right) = \sum_{m=1}^{M} W_m \left[\sum_{l=1}^{L}\sum_{k=1}^{K} A_{mlpk} \cdot W'_m x^l\left(\left(\phi_q\right) + \Delta p_{mlqk}\right)\right], \tag{6}$$

where $\widehat{p}_q$ is the coordinates of sampled points being normalized, l indexes the level of input feature maps. A_{mlqk} and Δp_{mlqk} represent the attention weight and offset of sampling for the lth input feature map, respectively. $\phi_l(p_q)$ function rescales p_q according to the lth input feature map.

Deformable DETR speeds up its convergence and makes progress on small targets datasets. For our leading/trailing edge's reconstruction area detection task, however, Deformable DETR's performance can be further improved compared with previous detectors using anchor box and NMS.

4. LETR and GLETR

4.1. Overview of LETR. As shown in Figure 4, our model adopted state-of-the-art methods implemented in small object detection. A frequency-channel mixed backbone (we named it after FcaAconNet) extracts features using a pyramid neck. And then the pyramid-shaped feature maps are sent to the Deformable Transformer head for encoding and decoding. A feed-forward network is configured to output the predicted classes and locations. We adapted the configurations of the deformable encoder, deformable decoder, and prediction network in [15].

4.2. Feature Extraction. Technically, the backbone is responsible for extracting feature maps over input images. Previous

(a) The convolution operation

(b) The processing of ghost module

(c) The inner connection of the ghost module
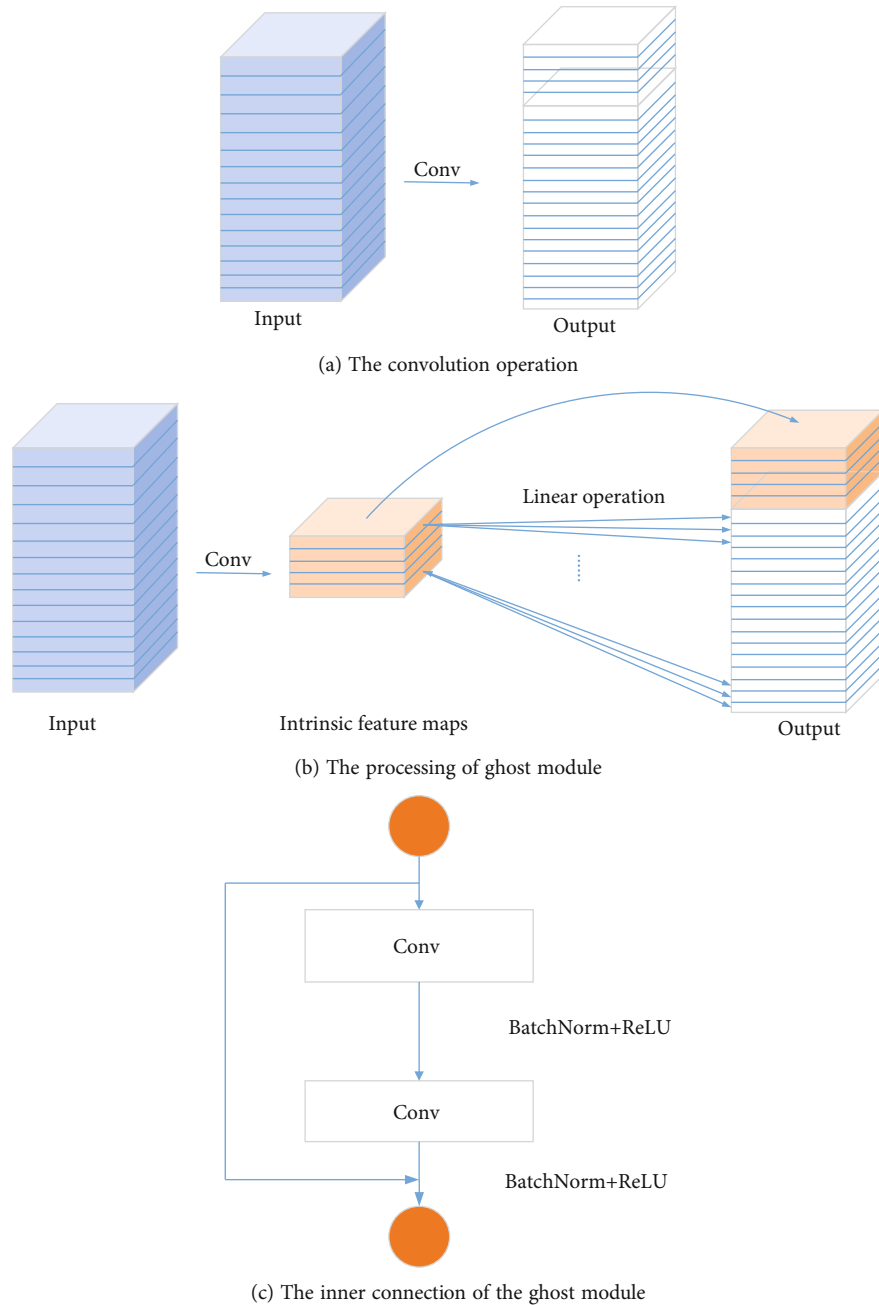
FIGURE 6: The ghost module in Ghost-FcaAconNet.

neural network models output a single-scale feature map. However, the reconstruction areas in our dataset vary in different sizes. Hence, we adopted the pyramid architecture in Deformable DETR for multiscale object detection. Furthermore, inspired by FcaNet [58], we imported the multispectral channel attention module of FcaNet to the feature extraction process of the model's backbone. The details of the utilized module are demonstrated in Figure 5.

Assuming that the dimension of the input feature is $C \times H \times W$, the multispectral channel attention module transforms input features into frequency domain with the help of 2-dimensional discrete cosine transformation (2D DCT). 2D DCT is formulated by Equation (7):

$$2\text{DDCT}\left(x^{2d}\right) = \sum_{i=0}^{H-1} \sum_{j=0}^{W-1} x^{2d}_{i,j} \cos\left(\frac{\pi h}{H}\left(i+\frac{1}{2}\right)\right) \cos\left(\frac{\pi w}{W}\left(j+\frac{1}{2}\right)\right),$$

(7)

where x^{2d} is the input image, and $h \in [0, 1, \cdots, H-1]$, $w \in [0, 1, \cdots, W-1]$.

(a) Leading edge

(b) Trailing edge
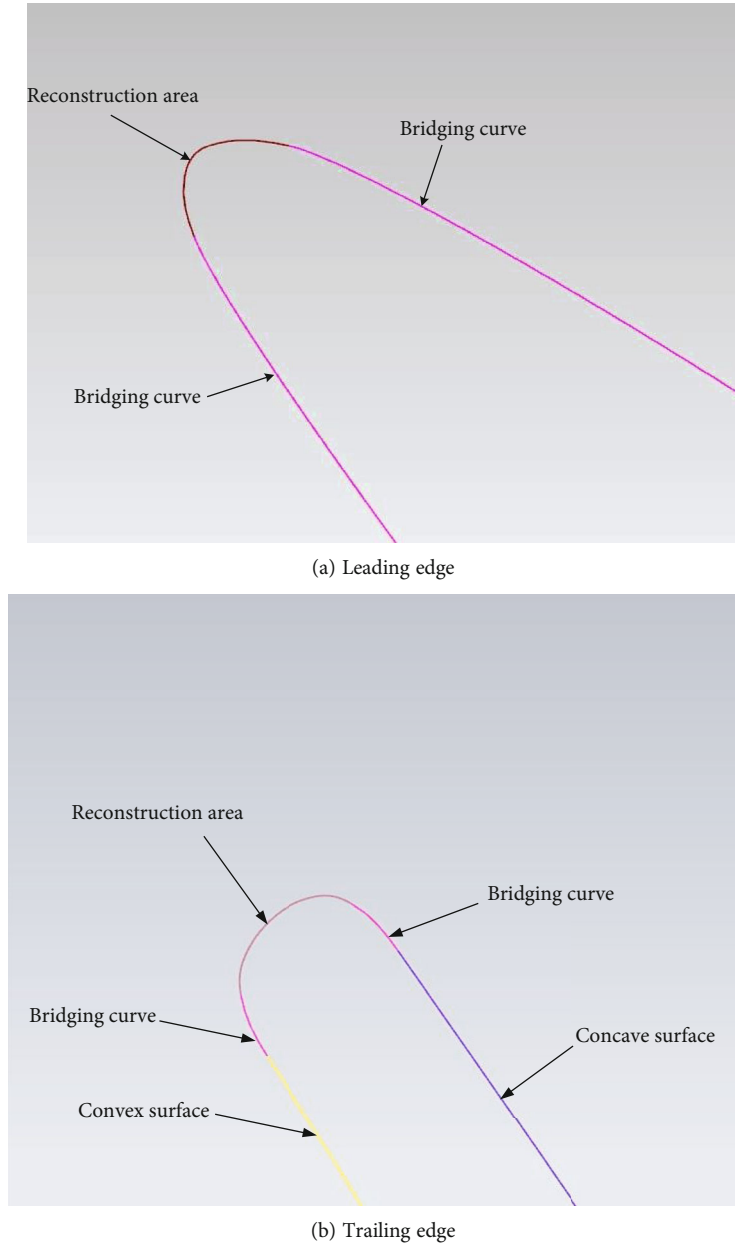
Figure 7: Selected samples in LDEG2021.

In FcaAconNet, the feature extraction procedure is illustrated as follows. First, input features X are split into n parts according to the channel. This process can be denoted as:

$$X = \left[X^0, X^1, \cdots, X^{n-1} \right]. \tag{8}$$

Next, the ith frequency feature of a given input X^i is computed by the following formulation. $2DDCT$ is represented for 2D DCT operation.

$$\text{Freq}^i = 2\text{DDCT}\left(X^i \right). \tag{9}$$

Thus, by concatenating all Freq^i, we have the final frequency feature Freq of the input feature:

$$\text{Freq} = \text{cat}\left(\left[\text{Freq}^0, \text{Freq}^1, \cdots, \text{Freq}^{n-1} \right] \right). \tag{10}$$

And finally, the attention of the mixed frequency-channel domain is computed by the following formulation:

$$\text{MSAttn} = \text{sigmoid}(\text{fc}(\text{Freq})), \tag{11}$$

where sigmoid is sigmoid function and $fc(\cdot)$ is a fully connected layer. By rescaling X with $MSAttn$, the output of

(a)

(b)

(c)

(d)

(e)

(f)
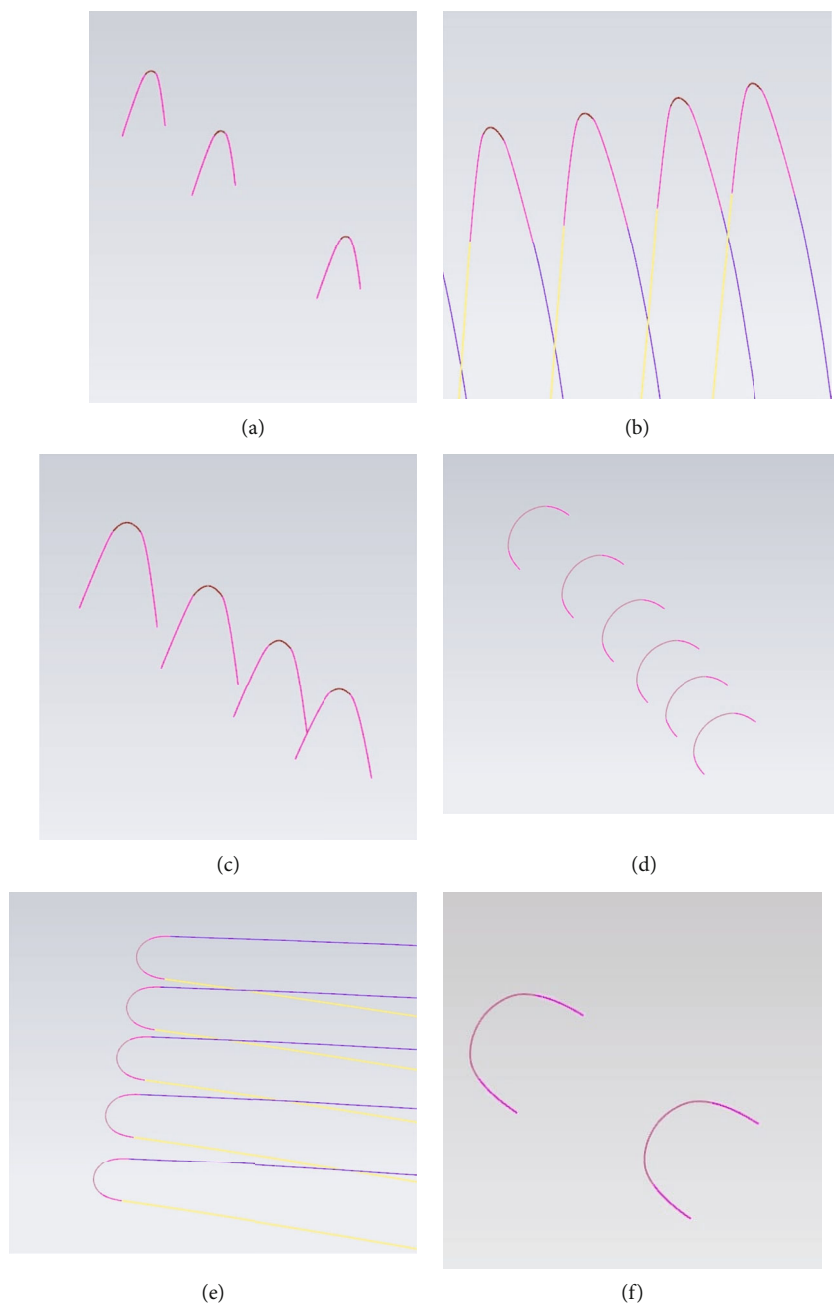
FIGURE 8: Examples of LDEG2021 dataset.

multispectral channel attention module, denoted as $\tilde{X}$, is computed as:

$$\tilde{X} = F_{\text{scale}}(X, \text{MSAttn}) = \text{MSAttn} \times X. \qquad (12)$$

The mixed frequency and channel weights are applied to the input feature maps after the multispectral channel attention module. In this method, adequate frequency and channel information is utilized by our backbone, and the accuracy is enhanced gradually in deep neural networks.

4.3. Activation Function. In the neural network's architecture, the activation function plays a key role in importing

TABLE 1: Confusion matrix.

Ground-truth	Prediction	
	Positive	Negative
Positive	TP	FN
Negative	FP	TN

nonlinearity to improve the model's classification capability. Considering the big difference between the foreground and background of our task, we employed Acon functions because of their excellent ability to control the extent of

(a) Comparisons of PRCs on leading edges

——— Deformable DETR-ResNet50   ——— LETR
——— Deformable DETR-ResNet101   ——— GLETR

(b) Comparisons of PRCs on trailing edges
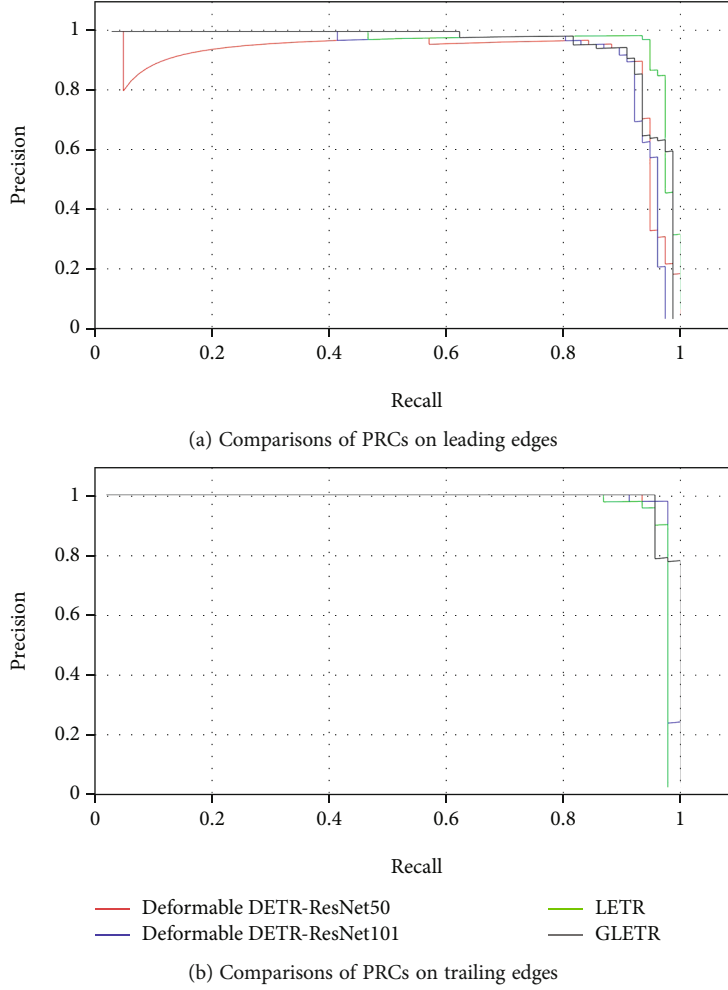
FIGURE 9: Comparison of PRCs.

nonlinear activation. In other words, by learning whether to activate and to what extent the input is activated, the model filters some disturbing information. More concretely, Acon functions are divided into three types: Acon-A, Acon-B, and Acon-C. Acon-A and Acon-B can be seen as special cases of Acon-C. According to Ma et al. [44], meta-Acon, the variant of Acon-C, showed the best performance in the test. Therefore, we adopted it as our activation function. Here, we gave the definition of Acon-C and meta-Acon.

Firstly, we use a function s_β to approximate the general maximum function $\max(x_1, x_2, \cdots, x_n)$:

$$s_\beta(x_1, x_2, \cdots, x_n) = \frac{\sum_{i=1}^{n} x_i e^{\beta x_i}}{\sum_{i=1}^{n} e^{\beta x_i}}, \tag{13}$$

where β is the switching factor. Next, we consider the situation where $s_\beta(x_1, x_2, \cdots, x_n)$ is in neural networks. In this case, $s_\beta(x_1, x_2, \cdots, x_n)$ degenerizes to the following format:

$$s_\beta(\eta_a(x), \eta_b(x)) = (\eta_a(x) - \eta_b(x)) \cdot \sigma[\beta \eta_a(x) - \eta_b(x)] + \eta_b(x). \tag{14}$$

σ is the sigmoid function, $\eta_a(x)$ and $\eta_b(x)$ represent linear functions. Considering a more general situation where $\eta_a(x) = p_1 x$ and $\eta_b(x) = p_2 x$, Acon-C is written as:

$$\text{Acon} - C(x) = s_\beta(p_1 x, p_2 x) = (p_1 - p_2)x \cdot \sigma[\beta(p_1 - p_2)x] + p_2 x. \tag{15}$$

And furthermore, we see β as a learnable network $G(x)$ and $Acon - C(x)$ can be generated to $\text{meta} - \text{Acon}(x)$, which is computed as:

$$\text{meta} - \text{Acon}(x) = (p_1 - p_2)x \cdot \sigma[G(x)(p_1 - p_2)] + p_2 x. \tag{16}$$

We replaced the first two ReLU functions with meta-Acon in each bottleneck of the original FcaNet to avoid overfitting and proposed FcaAconNet. Relative experiments are seen in Section 4.

As Figure 6(a) shows, convolution operation generates a great amount of output feature maps which contains a certain extent of redundancy. Han et al. proved that some similar feature maps exist in this redundancy and argued that these superfluous feature maps are the ghost of intrinsic
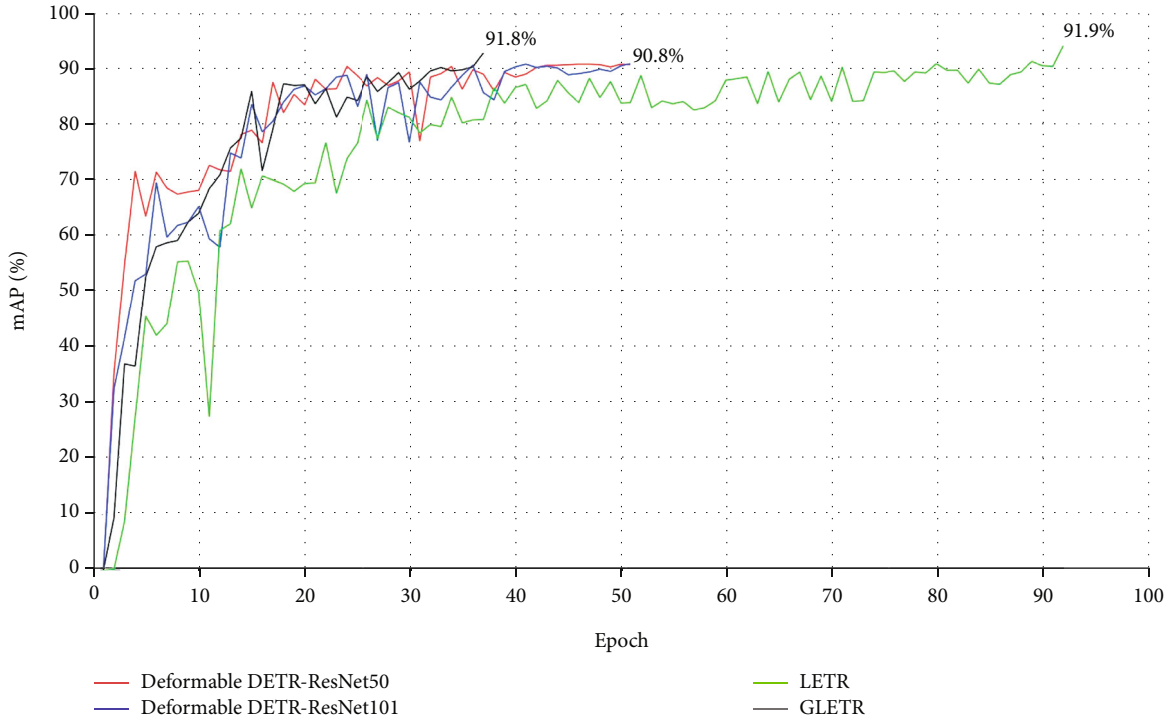
FIGURE 10: Convergence curves of three models on LDEG2021.

TABLE 2: Comparison of LETR and GLETR with Deformable DETR on the LDEG2021 test set.

Detector	Backbone	mAP	Model weight	Training hours
Deformable DETR	ResNet-50	90.6%	491.2 MB	3.5
	ResNet-101	90.8%	718.9 MB	3.5
LETR	FcaAconNet	91.9%	545.6 MB	8.5
GLETR	Ghost-FcaAconNet	91.8%	424.4 MB	3.5

feature maps. Thus, they generated intrinsic feature maps by a primary convolution and obtains ghost features through a linear operation, by which the complexity of the model is reduced. The whole procedure is described as follows.

4.4. Ghost Module. If we use X to represent the input feature map, the output Y after general convolution is defined by:

$$Y = X * f + b, \qquad (17)$$

where $*$ and b denote the convolution operation and bias, respectively, and f is the convolution operator. In ghost module's first stage, however, f is replaced by a new operator f' and bias is canceled for lower model complexity. Thus, the output Y' of the ghost module's first stage is denoted as:

$$Y' = X * f'. \qquad (18)$$

In the second stage, the ghost module implements a series of linear operations to output Y' to match the dimen-

sion of the channel of the original output Y. The linear operations in the ghost module are written as:

$$y_{i,j} = \phi_{i,j}\left(y_i'\right), \qquad (19)$$

where y_i' is the ith intrinsic feature map, $\Phi_{i,j}$ represents the ith linear operation, and $y_{i,j}$ is the generated ghost feature map.

The details of the ghost module are depicted in Figure 6(b). Some intrinsic feature maps are output by the previous convolution layer in the first stage. Next, by linear operation, we mentioned above, a large number of ghost feature maps are produced. Finally, the intrinsic feature maps and their corresponding "ghost" are concatenated according to the channel dimension. In practice, the inner connection of the ghost module is shown in Figure 6(c). The linear operation is carried out by a convolution layer. Technically, we replaced all convolution layers with ghost modules in FcaAconNet's bottleneck, and we called the FcaAconNet backbone with ghost module Ghost-FcaAconNet.

(a) PRCs of the models with different components on the leading edges

(b) PRCs of the models with different components on the trailing edges
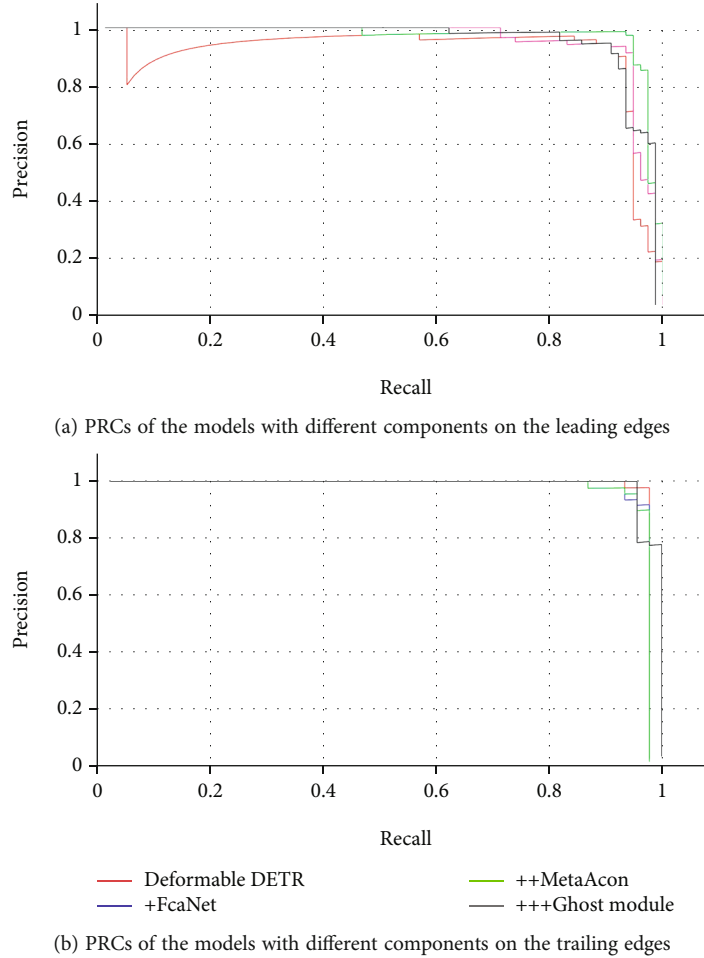
Figure 11: PRCs of the models with different components.

5. Experiments

5.1. Dataset. We made LDEG2021 to detect the reconstruction area of the leading and trailing edge. The whole images of LDEG2021 are the multiple sizes of section curves of different reconstruction areas of the leading and trailing edges of the different blades' different heights. These images are acquired from the screenshots of Unigraphics NX 7.5 (UG) software. LDEG2021 has 397 images annotated with two classes: leading edge and trailing edge. Two selected samples and their corresponding captions in LDEG2021 are shown in Figure 7. We used different colors to distinguish different curves. The magenta curves in Figures 7(a) and 7(b) are the bridge curves of reconstructed leading/trailing edges. And the crimson curves indicate the reconstruction areas of leading edges. On the other hand, the plum curves are the reconstruction areas of trailing edges. The section lines of convex and concave faces are presented in purple and yellow.

The reconstruction areas vary in different sizes. So, we applied scaling and rotation to the models of reconstruction areas. In this way, some screenshots of reconstruction areas are no longer in actual sizes. We need to notice that this process is to train the ability to detect shape-varied

reconstruction areas. In Figure 8, we also gave other examples of the LDEG2021 dataset. Figures 8(a)–8(c) present the images of reconstructed leading edges. Figures 8(d)–8(f) are the images of reconstructed trailing edges. In this article, we aim to train a high-performance model which can detect a certain number of reconstruction areas at the same time. That explains why there are more than one leading/trailing edge in an image. It is also worth noting that some overlapping phenomena occurred in Figures 8(b) and 8(e). This is due to the fact that these images are obtained from different perspectives in UG. The LDEG2021 dataset will be open-sourced on https://github.com/andrewsilver1997/LDEG2021.

5.2. Data Augmentation. Generally, a neural network model gets better performance when the dataset's scale gets larger. The number of images in LDED2021, nevertheless, is limited. The data augmentation methods we applied include random flipping, random cropping, and resizing. The training procedure was carried out on a CPU of Intel Xeon E5-2678 V3 and a single GPU of Nvidia RTX 2080Ti. We used MMDetection object detection toolbox [59] with Pytorch 1.5.1, cuDNN 7.6.1, and CUDA 10.1 for implementation.
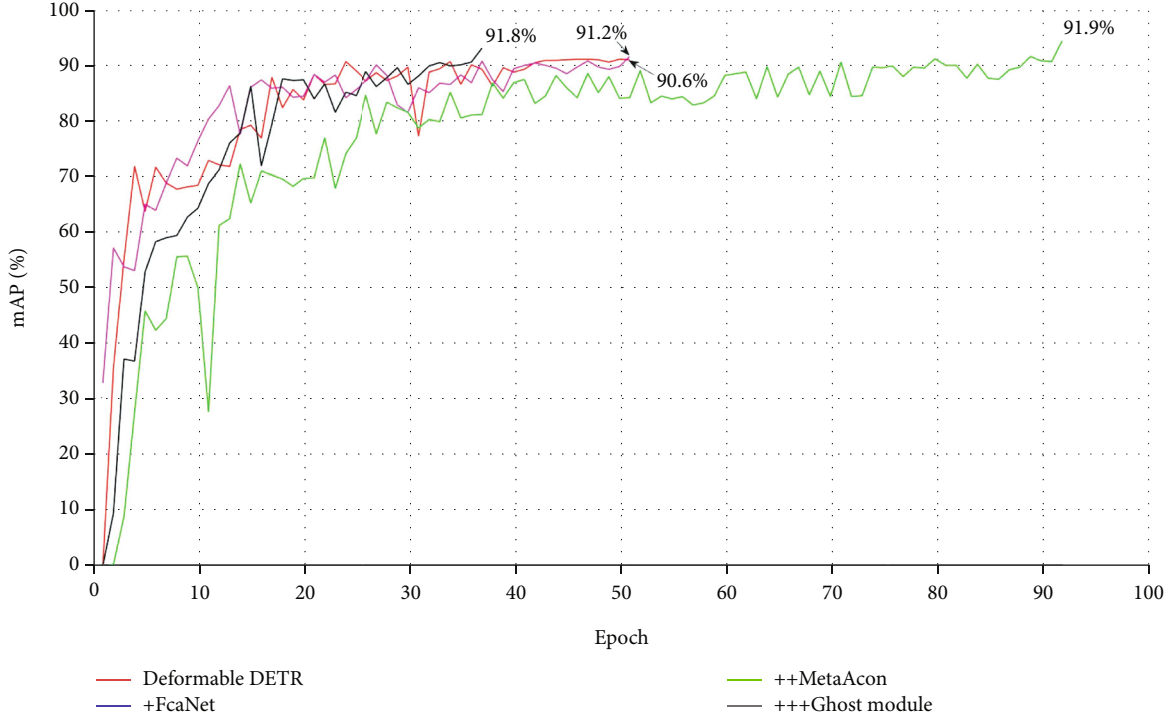
FIGURE 12: Convergence curves of the models with different components.

TABLE 3: Ablation studies for FcaNet, meta-Acon, and ghost module.

ResNet	FcaNet	Meta-Acon	Ghost module	mAP	Model weight	Training hour
✓				90.6%	491.2 MB	3.5
	✓			91.2%	543 MB	3.5
	✓	✓		91.9%	545.6 MB	8.5
	✓	✓	✓	91.8%	424.4 MB	3.5

The batch size and learning rate were set to 2 and 2×10^{-4} at first, respectively. The learning rate was decreased to 2×10^{-5} after 40 training epochs. Moreover, we chose adamW as our optimizer.

5.3. Results and Discussions

5.3.1. Evaluation Metrics. True positive (TP), false positive (FP), false negative (FN), and true negative (TN) are usually needed in the evaluation of a model's performance. Table 1 shows their definition by giving a confusion matrix.

We utilized the precision-recall curve (PRC) and mAP (mean average precision) to evaluate the proposed approach's performance. Firstly, we give the definition of precision and recall:

$$\text{Precision} = \frac{\text{TP}}{\text{TP} + \text{FP}},$$
$$\text{Recall} = \frac{\text{TP}}{\text{TP} + \text{FN}}. \tag{20}$$

Generally speaking, a good object detection model is supposed to raise its precision and keep the recall at a relatively high level.

AP (average precision) represents the performance that the model detects a specific class of all objects. AP is defined in

$$AP = \int_0^1 p(r)sdr, \tag{21}$$

where p and r are short for precision and recall. mAP (mean average precision) is defined as the average of all classes' AP. It is calculated by

$$m\text{AP} = \frac{\sum_{i=1}^{N} \text{AP}_i}{N}, \tag{22}$$

where AP_i is the AP value of the ith class and N indicates the total number of all classes. mAP measures the overall performance of the model. In other words, the higher the mAP is, the higher accuracy our models have. The other metrics we implemented are model weight and training hour, which measure the number of weight parameters and convergence speed.

5.3.2. Results on LDEG2021 Dataset. Figures 9(a) and 9(b) show the PRC curves of Deformable DETRs with ResNet50 and ResNet101 backbone, LETR, and GLETR. The performances of the Deformable DETRs with ResNet50 and ResNet101 were nearly the same when detecting the reconstruction areas of the leading edge. Maintaining the same

(a) Raw image

(b) Detection results of Deformable DETR

(c) Detection results of LETR

(d) Detection results of GLETR
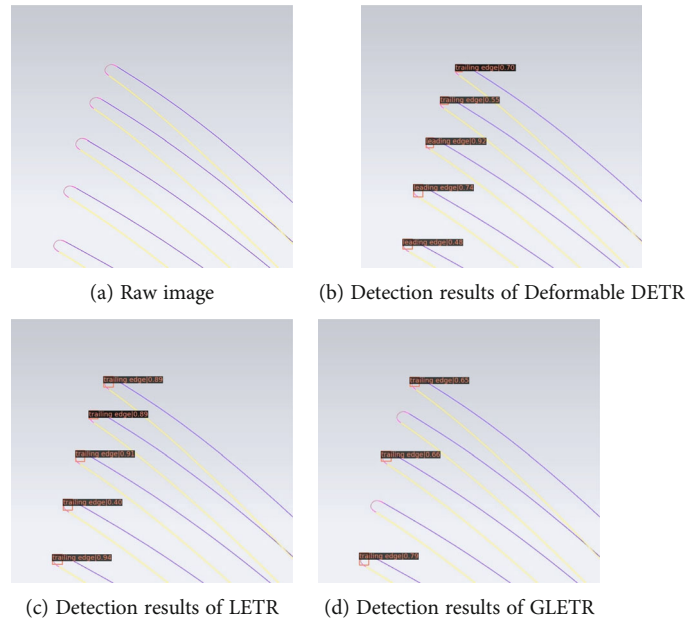
FIGURE 13: Selected examples from the detection results on trailing edges.

(a) Raw image

(b) Detection results of Deformable DETR

(c) Detection results of LETR

(d) Detection results of GLETR
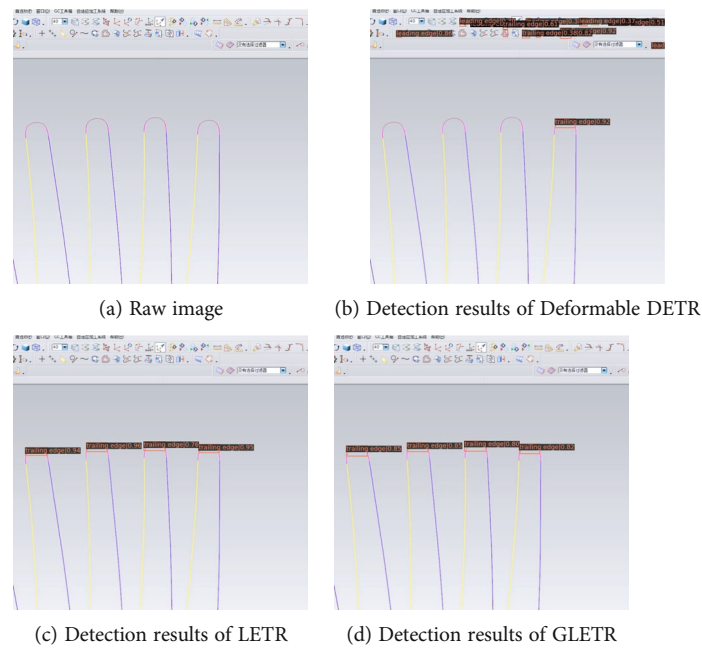
FIGURE 14: Another examples from the detection results on trailing edges.

recall, the precision values of LETR and GLETR were higher than Deformable DETRs. The enhancement of the performance when detecting the trailing edge' reconstruction area was unobvious as shown in Figure 9(b). It is worth noting that the shapes of trailing edge's reconstruction areas have no such big differences as leading edge's reconstruction areas do. Besides, the retained theoretical parts of the trailing edge's reconstruction areas are relatively larger than that of the leading edge's reconstruction areas. That explains why the improvement in Figure 9(b) is not obvious. But even though the improvement in Figure 9(b) is not distinct, LETR

and GLETR still show their comparable performance. We will give a more detailed illustration in the following discussions of detection results. The convergence curves of the three models are presented in Figure 10. Deformable DETR with ResNet50 backbone took 50 epochs to converge and the mAP was 90.6%. The Deformable DETR with ResNet101 backbone did not show significant differences compared with the Deformable DETR with ResNet50. On the other hand, LETR, achieved a higher mAP even though its training time was longer. GLETR had the fastest convergence speed (less than 40 epochs) and the mAP was 91.8%.

(a) Raw image

(b) Detection results of Deformable DETR

(c) Detection results of LETR

(d) Detection results of GLETR
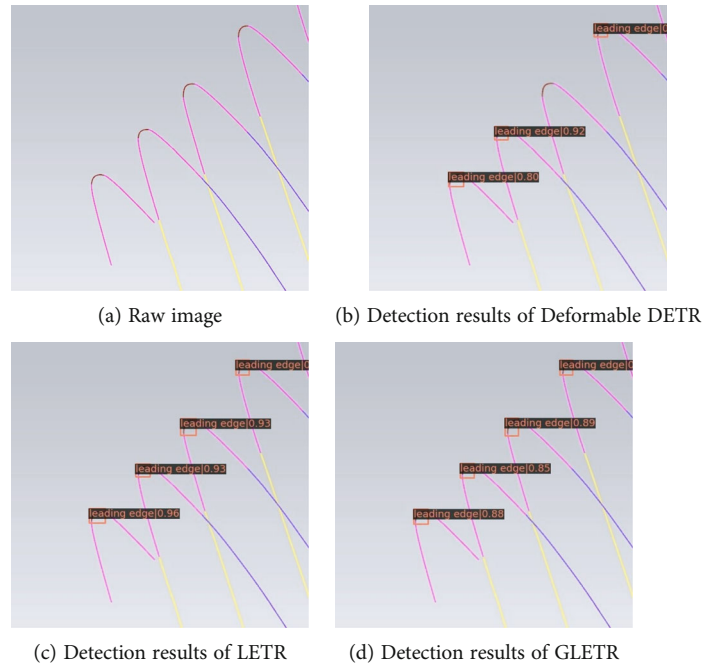
FIGURE 15: Comparison of detection results of the top area.

(a) Raw image

(b) Detection results of Deformable DETR

(c) Detection results of LETR

(d) Detection results of GLETR
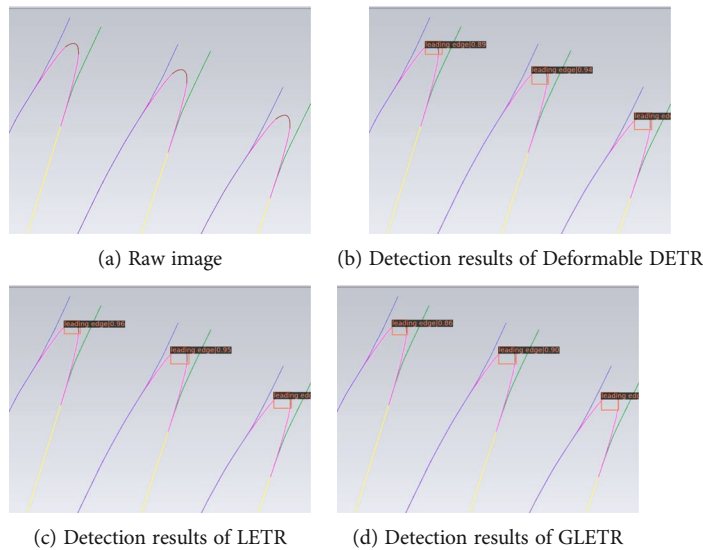
FIGURE 16: Comparison of detection results of the middle area.

Table 2 illustrates the results of the test. Compared with Deformable DETR, LETR achieves better performance with a 1.1% improvement of mAP. On the other hand, GLETR decreased model weight by 121.2 MB with a slight decrease of mAP (0.1%). It is worth noting that the results were obtained on a single GPU. We believe the improvement in the performance of our models will be more pronounced on multiple GPUs with higher computational accuracy and speed.

Figures 11(a) and 11(b) show the effects of different components on PRC curves. The symbol "+" indicates the number of design components the model has. As Figure 11(a) illustrates, the performances of models when detecting the leading edge's reconstruction areas were enhanced by introducing the FcaNet and MetaAcon. The imported components' effects on detecting the reconstruction area of the trailing edge were unremarkable. Figure 12 is the convergence curves of the models with different components. The training epochs of the Deformable DETR whose backbone was replaced by FcaNet were the same as Deformable DETR with ResNet with an increase of mAP. After importing the MetaAcon function, the training epochs

(a) Raw image

(b) Detection results of Deformable DETR

(c) Detection results of LETR

(d) Detection results of GLETR
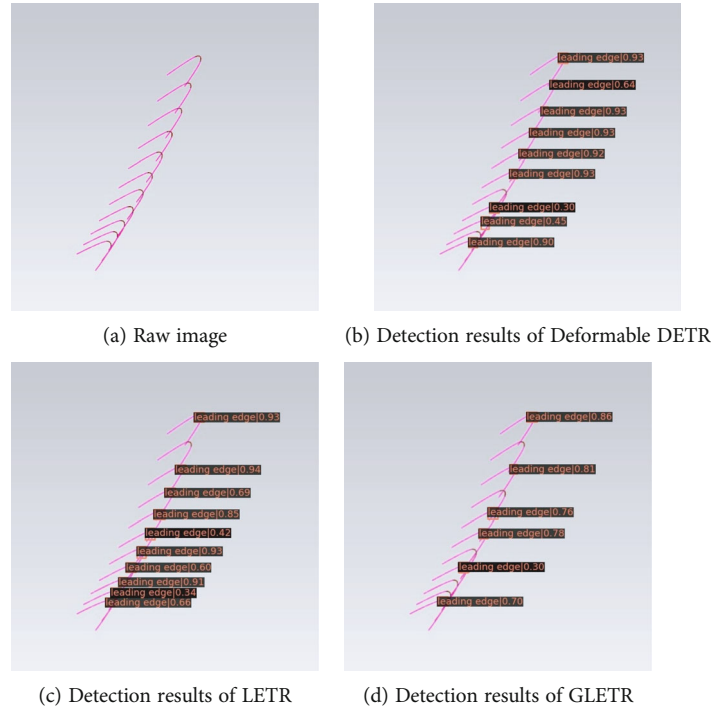
Figure 17: Comparison of detection results of the bottom area.

went to 92. The ghost modules lowered the training epochs significantly to less than 40 and the decrease in mAP was tolerable.

Table 3 presents ablations for three design components of LETR. If we use ResNet as the backbone, LETR degenerates to Deformable DETR, and the mAP is 90.6%. Using FcaNet instead of ResNet improves mAP by 0.6%. Next, replacing ReLU with the meta-Acon activation function can effectively improve mAP by 0.7%. By importing the ghost module, the weight of LETR dropped to 424.4 MB, and the mAP of GLETR is 91.8%, which was lower than that of LETR. This decrease is acceptable. More importantly, the training hour is lowered by the ghost module from 8.5 hours to 3.5 hours. Therefore, it is proved that GLETR performs as good as LETR on the LDEG2021 dataset with fewer parameters and a faster speed of convergence, even though there was a tiny decrease in mAP.

We need to point out that the edge shapes of reconstructed leading/trailing edges are different. Moreover, the reconstructed leading edges' shapes vary from the bottom to the top of the blade. In the rest part of this section, we will discuss the performance of LETR and GLETR when detecting the reconstruction areas of leading/trailing edges and the reconstruction areas of leading edges from different heights of the blade.

The detection results on different reconstructed trailing edges are demonstrated in Figures 13 and 14. In Figure 13, the baseline model, Deformable DETR, detected all targets while some detected objects were misclassified. On the contrary, LETR detected all reconstruction areas of trailing edges without any misclassification as shown in Figure 13(c). How-

ever, GLETR missed two targets even though the detected targets were correctly recognized.

We also showed an example in Figure 14 where Deformable DETR failed to detect all reconstruction areas of trailing edges and recognized the wrong targets. By comparing Figures 14(a) and 14(b), we knew that only one target was detected successfully. It was unexpected that Deformable DETR classified some interferences in the background as reconstruction areas of trailing edges. Figures 14(c) and 14(d) give the detection results of LETR and GLETR on reconstructed trailing edges.

To test LETR and GLETR's performance in detecting the reconstruction areas of leading edges of the near-net-shaped blades, we picked raw images from the bottom, middle, and top areas of the blade in LDEG2021 and tested three models on them. The detection results on the top area's images of the blade are shown in Figure 14. The reconstructed curves of the blade's top area usually contain limited reconstruction areas. That is, the targets are relatively smaller. Figure 15(a) is the raw image of this area's reconstructed curves. As Figures 15(b)–15(d) show, Deformable DETR did not perform well while LETR and GLETR recognized these small reconstruction areas with high probability. LETR and GLETR detected all four targets with no mistakes.

As for the middle area of the blade, the reconstructed curves of this area retained more reconstruction areas, as shown in Figure 16(a). The detection results of the middle area of the blade are given in Figures 16(b)–16(d). All three models performed well with no reconstruction area missed.

The detection results of the bottom area of the blade are seen in Figure 17. Figure 17(a) indicates that the cross

sections to be further machined in this area are quite dense, which means that the reconstruction areas may be obscured by each other. The test results in Figures 17(b) and 17(c) illustrate that Deformable DETR missed two targets whilst LETR missed only one target. However, GLETR did not behave well, which disregarded five small reconstruction areas in this area.

From Figures 13–17, it also can be summarized that the classification probability of LETR is higher than that of Deformable DETR in most cases. On the anther hand, the classification probability of GLETR is lower than that of LETR and Deformable DETR as a result of importing ghost modules.

The experiment results on the reconstruction areas of leading and trailing edges demonstrate that LETR and GLETR have superior performance. Nonetheless, GLETR's performance in detecting dense and small targets still needs to be improved, which is one of the focuses of our future works.

To test the performance of LETR and GLETR on general small objects detection tasks, we also conducted experiments on two remote sensing datasets: RSOD [60] and NWPU VHR-10 [61]. However, the results on these two remote sensing datasets were not ideal. Due to the imbalanced numbers of different classes' images, we encountered the long-tail effect. We plan to address this problem by applying more data augmentation methods, not just random flipping, cropping, and resizing.

We also want to mention that this paper still has some subsequent works to be accomplished. The reconstruction areas' sizes in images are quite different from their actual sizes. Hence, the correspondence between the actual sizes and the sizes in an image is of great essence. In this article, we did not give such correspondence. So, it is worth exploring how to transfer the detected positions of reconstruction areas in images into real-world models.

6. Conclusions

Aiming to detect the reconstruction area of the near-net-shaped blade, this paper proposed two end-to-end and anchor-free models based on Deformable DETR. Experiment results show that the proposed models have higher accuracy and less weight, respectively. They also offer strong support to our following works. The main contributions of this article are concluded as follows:

(1) We optimized the architecture of Deformable DETR from the aspect of feature extraction and activation function. The new model was named after LETR. LETR extracts features from a frequency-channel mixed domain and activates nonlinear units dynamically. The test results on the self-made dataset LDEG2021 surpassed the baseline model by mAP of 1.3% on a single GPU

(2) On the other hand, we imported the ghost module to LETR and presented a lightweight model, GLETR. Compared with LETR, GLETR achieved a faster con- vergence speed and less model weight with a tiny decrease in accuracy on LDEG2021. It is proved that GLETR has the potential to be applied to real-time detection

(3) We are capable of obtaining the position and area of the reconstruction area with high efficiency and no errors caused by human experience by applying LETR and GLETR to our task. With the position and area, we can know the geometric parameters of the reconstructed curves by exploring parameter extraction algorithms

LETR and GLETR are two successful attempts combining object detection and adaptive machining. However, there are some issues remained in this paper and can be investigated in the future:

(1) GLETR has its disadvantages when detecting the targets in the bottom area of the blade. That is due to the fact that the objects cover each other and some features are ignored by the ghost module. One potential solution to this problem is to feed the network with images of larger sizes during the training process, by which the position and semantic information is enhanced

(2) The test results of LETR and GLETR on remote sensing datasets were unsatisfactory due to the long-tail effect. Here, we suggest adopting more data augmentation algorithms to keep the number of objects' classes balanced. A promising way is to stitch the images, especially for the objects which have fewer images

(3) We need to extract the geometric parameters in images in the future. In detail, the next step is to find the relationship between the coordinates of the reconstruction area's each pixel and its corresponding geometric parameters, like curvature and chord length

Data Availability

The data of this article is within the paper. The code and dataset will be available after acceptance.

Conflicts of Interest

The authors declare that there is no conflict of interest regarding the publication of this article.

Acknowledgments

References

[1] J. E. Makem, O. Hengan, and C. G. Armstrong, "A virtual inspection framework for precision manufacturing of aerofoil components," *Computer-Aided Design*, vol. 44, no. 9, pp. 858–874, 2012.

[2] Y. Feng, J. Ren, and Y. Liang, "Prediction and reconstruction of edge shape in adaptive machining of precision forged blade," *International Journal of Advanced Manufacturing Technology*, vol. 96, no. 5-8, pp. 2355–2366, 2018.

[3] Z. Yin, J. Ren, and Y. Liang, "Classification of blade's leading edge based on neural networks in adaptive machining of near-net-shaped blade," *International Journal of Precision Engineering and Manufacturing*, vol. 22, no. 11, pp. 1817–1828, 2021.

[4] I. Goodfellow, J. Pouget-Abadie, M. Mirza et al., "Generative adversarial nets," *Advances in Neural Information Processing Systems*, vol. 27, p. 16, 2014.

[5] L. Liu, W. Ouyang, X. Wang et al., "Deep learning for generic object detection: a survey," *International Journal of Computer Vision*, vol. 128, no. 2, pp. 261–318, 2020.

[6] R. Girshick, J. Donahue, T. Darrell, and J. Malik, "Rich feature hierarchies for accurate object detection and semantic segmentation," in *2014 IEEE Conference on Computer Vision and Pattern Recognition*, pp. 580–587, Columbus, Ohio, USA, 2014.

[7] R. Girshick, "Fast R-CNN," in *2015 IEEE International Conference on Computer Vision*, pp. 1440–1448, 2015.

[8] S. Ren, K. He, R. Girshick, and J. Sun, "Faster R-CNN: towards real-time object detection with region proposal networks," *IEEE Transactions on Pattern Analysis and Machine Intelligence*, vol. 39, no. 6, pp. 1137–1149, 2017.

[9] J. Redmon, S. Divvala, R. Girshick, and A. Farhadi, "You only look once: unified, real-time object detection," in *2016 IEEE Conference on Computer Vision and Pattern Recognition*, pp. 779–788, 2016.

[10] J. Redmon and A. Farhadi, "YOLO9000: better, faster, stronger," in *2017 IEEE Conference on Computer Vision and Pattern Recognition*, pp. 6517–6525, 2017.

[11] J. Redmon and A. Farhadi, "YOLOv3: an incremental improvement," 2018, http://arxiv.org/abs/1804.02767v1.

[12] A. Bochkovskiy, C. Y. Wang, and H. Liao, "YOLOv4: optimal speed and accuracy of object detection," 2020, http://arxiv.org/abs/2004.10934v1.

[13] W. Liu, D. Anguelov, D. Erhan et al., "SSD: single shot multibox detector," in *European Conference on Computer Vision*, vol. 9905, 2016.

[14] T.-Y. Lin, P. Goyal, R. Girshick, K. He, and P. Dollar, "Focal loss for dense object detection," *IEEE Transactions on Pattern Analysis and Machine Intelligence*, vol. 42, no. 2, pp. 318–327, 2020.

[15] X. Zhu, W. Su, L. Lu, B. Li, X. Wang, and J. Dai, "Deformable DETR: deformable transformers for end-to-end object detection," 2020, http://arxiv.org/abs/2010.04159v2.

[16] Z. Yun, C. Zhi-Tong, and N. Tao, "Reverse modeling strategy of aero-engine blade based on design intent," *The International Journal of Advanced Manufacturing Technology*, vol. 81, no. 9-12, pp. 1781–1796, 2015.

[17] Z. Zhao, Y. Fu, X. Liu, J. Xu, J. Wang, and S. Mao, "Measurement-based geometric reconstruction for milling turbine blade using free-form deformation," *Measurement*, vol. 101, pp. 19–27, 2017.

[18] H. Yu, L. Xuegeng, and P. Liu, "Stream surface reconstruction of aero engine blade based on limited measured points," *Advances in Engineering Software*, vol. 131, pp. 90–101, 2019.

[19] Y. Zhang, Z. Chen, and Z. Zhu, "Adaptive machining framework for the leading/trailing edge of near-net-shape integrated impeller," *International Journal of Advanced Manufacturing Technology*, vol. 107, no. 9-10, pp. 4221–4229, 2020.

[20] D. Wu, H. Wang, K. Zhang, B. Zhao, and X. Lin, "Research on adaptive CNC machining arithmetic and process for near-net-shaped jet engine blade," *Journal of Intelligent Manufacturing*, vol. 31, no. 3, pp. 717–744, 2020.

[21] B. Singh and L. S. Davis, "An analysis of scale invariance in object detection - SNIP," in *2018 IEEE/CVF Conference on Computer Vision and Pattern Recognition*, pp. 3578–3587, 2018.

[22] B. Singh, M. Najibi, and L. S. Davis, "SNIPER: efficient multi-scale training," *Advances in Neural Information Processing Systems*, vol. 31, 2018.

[23] W. Zhang, L. Jiao, X. Liu, and J. Liu, "Multi-scale feature fusion network for object detection in VHR optical remote sensing images," in *IGARSS 2019 - 2019 IEEE International Geoscience and Remote Sensing Symposium*, pp. 330–333, 2019.

[24] T.-Y. Lin, P. Dollár, R. Girshick, K. He, B. Hariharan, and S. Belongie, "Feature pyramid networks for object detection," in *2017 IEEE Conference on Computer Vision and Pattern Recognition*, pp. 936–944, 2017.

[25] W. Liu, L. Ma, and C. He, "Arbitrary-oriented ship detection framework in optical remote-sensing images," *IEEE Geoscience and Remote Sensing Letters*, vol. 15, no. 6, pp. 937–941, 2018.

[26] H. Law and J. Deng, "CornerNet: detecting objects as paired keypoints," *International Journal of Computer Vision*, vol. 128, no. 3, pp. 642–656, 2018.

[27] X. Zhou, J. Zhuo, and P. Krähenbühl, "Bottom-up object detection by grouping extreme and center points," in *2019 IEEE/CVF Conference on Computer Vision and Pattern Recognition*, pp. 850–859, 2019.

[28] X. Zhou, D. Wang, and P. Krhenbühl, "Objects as points," 2019, http://arxiv.org/abs/1904.07850v2.

[29] X. Zhou, V. Koltun, and P. Krhenbühl, "Probabilistic two-stage detection," 2021, http://arxiv.org/abs/2103.07461v1.

[30] R. Dong, D. Xu, J. Zhao, L. Jiao, and J. An, "Sig-NMS-based faster R-CNN combining transfer learning for small target detection in VHR optical remote sensing imagery," *IEEE Transactions on Geoscience and Remote Sensing*, vol. 57, no. 11, pp. 8534–8545, 2019.

[31] Z. Cai and N. Vasconcelos, "Cascade R-CNN: delving into high quality object detection," in *2018 IEEE/CVF Conference on Computer Vision and Pattern Recognition*, pp. 6154–6162, 2018.

[32] T. Young, D. Hazarika, S. Poria, and E. Cambria, "Recent trends in deep learning based natural language processing [review article]," *IEEE Computational Intelligence Magazine*, vol. 13, no. 3, pp. 55–75, 2018.

[33] A. Vaswani, N. Shazeer, N. Parmar et al., "Attention is all you need," *Advances in Neural Information Processing Systems*, vol. 30, 2017.

[34] N. Carion, F. Massa, G. Synnaeve, N. Usunier, A. Kirillov, and S. Zagoruyko, "End-to-end object detection with transformers," in *European Conference on Computer Vision*, pp. 213–229, 2020.

[35] Z. Sun, S. Cao, Y. Yang, and K. M. Kitani, "Rethinking transformer-based set prediction for object detection," 2020, http://arxiv.org/abs/2011.10881v1.

[36] Z. Tian, C. Shen, H. Chen, and T. He, "Fcos: fully convolutional one-stage object detection," in *Proceedings of the IEEE/CVF international conference on computer vision*, pp. 9627–9636, 2019.

[37] J. Dai, H. Qi, Y. Xiong et al., "Deformable convolutional networks," in *2017 IEEE International Conference on Computer Vision*, pp. 764–773, 2017.

[38] R. Hahnloser, R. Sarpeshkar, M. A. Mahowald, R. J. Douglas, and H. S. Seung, "Digital selection and analogue amplification coexist in a cortex-inspired silicon circuit," *Nature*, vol. 405, no. 6789, pp. 947–951, 2000.

[39] I. J. Goodfellow, D. Warde-Farley, M. Mirza, A. Courville, and Y. Bengio, "Maxout networks," 2013, http://arxiv.org/abs/1302.4389v1.

[40] S. Elfwing, E. Uchibe, and K. Doya, "Sigmoid-weighted linear units for neural network function approximation in reinforcement learning," *Neural Networks*, vol. 107, pp. 3–11, 2018.

[41] P. Ramachandran, B. Zoph, and Q. V. Le, "Searching for activation functions," 2017, http://arxiv.org/abs/1710.05941.

[42] N. Ma, X. Zhang, and J. Sun, "Funnel activation for visual recognition," in *European Conference on Computer Vision*, pp. 351–368, 2020.

[43] Y. Chen, X. Dai, M. Liu, D. Chen, L. Yuan, and Z. Liu, "Dynamic relu," in *European Conference on Computer Vision*, pp. 351–367, 2020.

[44] N. Ma, X. Zhang, and J. Sun, "Activate or not: learning customized activation," 2020, http://arxiv.org/abs/2009.04759v2.

[45] Y. Wang, C. Xu, S. You, D. Tao, and C. Xu, "Cnnpack: packing convolutional neural networks in the frequency domain," *Advances in Neural Information Processing Systems*, vol. 29, 2016.

[46] C. Liu, Y. Wang, K. Han, C. Xu, and C. Xu, "Learning instance-wise sparsity for accelerating deep models," in *Proceedings of the 28th International Joint Conference on Artificial Intelligence*, pp. 3001–3007, 2019.

[47] B. Jacob, S. Kligys, B. Chen et al., "Quantization and training of neural networks for efficient integer-arithmetic-only inference," in *Proceedings of the IEEE conference on computer vision and pattern recognition*, pp. 2704–2713, 2018.

[48] H. Chen, Y. Wang, C. Xu et al., "Data-free learning of student networks," in *Proceedings of the IEEE/CVF International Conference on Computer Vision*, pp. 3514–3522, 2019.

[49] K. Han, Y. Wang, Q. Tian, J. Guo, C. Xu, and C. Xu, "Ghost-Net: more features from cheap operations," in *2020 IEEE/CVF Conference on Computer Vision and Pattern Recognition*, pp. 1577–1586, 2020.

[50] F. Chollet, "Xception: deep learning with depthwise separable convolutions," in *Proceedings of the IEEE conference on computer vision and pattern recognition*, pp. 1251–1258, 2017.

[51] A. G. Howard, M. Zhu, B. Chen et al., "MobileNets: efficient convolutional neural networks for mobile vision applications," 2017, http://arxiv.org/abs/1704.04861v1.

[52] M. Sandler, A. Howard, M. Zhu, A. Zhmoginov, and L. C. Chen, "MobileNetV2: inverted residuals and linear bottlenecks," in *2018 IEEE/CVF Conference on Computer Vision and Pattern Recognition*, pp. 4510–4520, 2018.

[53] A. Howard, M. Sandler, G. Chu et al., "Searching for Mobile-NetV3," in *2019 IEEE/CVF International Conference on Computer Vision*, pp. 1314–1324, 2019.

[54] B. Zoph, V. Vasudevan, J. Shlens, and Q. V. Le, "Learning transferable architectures for scalable image recognition," in *Proceedings of the IEEE conference on computer vision and pattern recognition*, pp. 8697–8710, 2018.

[55] X. Zhang, X. Zhou, M. Lin, and J. Sun, "ShuffleNet: an extremely efficient convolutional neural network for mobile devices," in *2018 IEEE/CVF Conference on Computer Vision and Pattern Recognition*, pp. 6848–6856, 2018.

[56] N. Ma, X. Zhang, H.-T. Zheng, and J. Sun, "ShuffleNet V2: practical guidelines for efficient CNN architecture design," in *European Conference on Computer Vision*, pp. 122–138, 2018.

[57] T.-Y. Lin, M. Maire, S. Belongie et al., "Microsoft COCO: common objects in context," in *European Conference on Computer Vision*, pp. 740–755, 2014.

[58] Z. Qin, P. Zhang, F. Wu, and X. Li, "FcaNet: frequency channel attention networks," 2020, http://arxiv.org/abs/2012.11879.

[59] K. Chen, J. Wang, J. Pang et al., "MMDetection: open MMLab detection toolbox and benchmark," 2019, http://arxiv.org/abs/1906.07155.

[60] Y. Long, Y. Gong, Z. Xiao, and Q. Liu, "Accurate object localization in remote sensing images based on convolutional neural networks," *IEEE Transactions on Geoscience and Remote Sensing*, vol. 55, no. 5, pp. 2486–2498, 2017.

[61] C. Gong, P. Zhou, and J. Han, "Learning rotation-invariant convolutional neural networks for object detection in VHR optical remote sensing images," *IEEE Transactions on Geoscience and Remote Sensing*, vol. 54, no. 12, pp. 7405–7415, 2016.

[62] Z. Yin, Y. Liang, J. Ren, J. An, and F. He, "LETR: an end-to-end detector of reconstruction area in blade's adaptive machining with transformer," 2022, Preprints: 2021090332.

Research Article

Camera Calibration for Long-Distance Photogrammetry Using Unmanned Aerial Vehicles

Yang Zhang,[1] **Jun Yang** ⓘ**,**[1] **Guoliang Li,**[1] **Tianqing Zhao,**[1] **Xiaokai Song,**[2] **Suoqi Zhang,**[1] **Ang Li,**[1] **Hui Bian,**[1] **Jin Li,**[1] **and Min Zhang**[1]

[1]*Northwest Institute of Nuclear Technology, Xi'an 710024, China*
[2]*School of Automation, Wuhan University of Technology, Wuhan 430070, China*

Correspondence should be addressed to Jun Yang; yangj85@mail.ustc.edu.cn

The traditional target-dependent camera calibration method has been widely used in close-distance and small field of view scenes. However, in view of the field coordinate measurement in the large-scale monitoring area under the complex field environment, the standard target can hardly meet the requirements of covering most of the camera's field of view. In view of the above problem, a stereo camera calibration method is studied, using the unmanned aerial vehicles (UAV) as feature points, combined with the high-precision position information measured by the real-time kinematic (RTK) positioning system it carries. The measured UAV coordinates are unified in World Geodetic System 1984 (WGS-84). Therefore, through several preset points, the measurement reference coordinate system which is the new world coordinate system we need can be established in any monitoring area, which greatly improves the flexibility of measurement. The experimental results show that the measurement accuracy of the proposed method can reach 0.5% in the monitoring area with a diameter of 100 m. The calibration method has a wide range of application and does not need the traditional standard target, and the measurement reference coordinate system can be established according to the actual needs. It is suitable for field spatial coordinate measurement in long-distance and complex terrain environment.

1. Introduction

Binocular stereo vision simulates human eye vision to realize the mapping from two-dimensional (2D) images to three-dimensional (3D) space and realizes the use of 3D information. At present, this method has been widely used in autonomous driving, robot navigation, virtual reality, and industrial production [1–6]. The process of solving this mapping relationship is called camera calibration, which involves some parameters, including both intrinsic and extrinsic parameters. Intrinsic parameters consist of principal points, focal lengths, and lens distortion. Extrinsic parameters include a rotation matrix and a translation vector between the two cameras.

Various effective calibration methods have been proposed, including traditional calibration methods, self-calibration methods, and camera calibration based on active

vision. In the traditional calibration method, the intrinsic and extrinsic parameters of the camera are obtained by mathematical transformation of 3D coordinates and 2D image coordinates by presetting some targets. Faig [7] proposed an imaging model based on the optimization algorithm, which has a complex solution process and high initial value requirements. Abdel-Aziz and Karara [8] proposed the direct linear transformation (DLT) method, which ignored the effects of distortion and obtained unknown parameters of the equation by solving the linear equations. Tsai [9] proposed a two-step method based on radial constraint by combining optimization algorithm and direct linear transformation method on the basis of only considering radial distortion. Zhang [10] is best known for his flexible calibration method, in which he provided a good method for estimating the initial parameters of the camera by using the constraints of the homography between planes. The

premise of the application of the above methods is to manufacture specific targets, such as checkerboard or circular targets, which is difficult to achieve in the field with a large field of view due to the size limitation. In response to the above problems, Faugeras et al. [11] and Maybank and Faugeras [12, 13] proposed a camera self-calibration method, which calibrated the camera by taking multiple images with distinct features and relative motion. However, this method had great limitations in sky, desert, sea, and other environments, and its robustness was poor and data reliability was insufficient. Similarly, Ma and Zhang [14–17] proposed a calibration method based on active vision, which required the camera to make specific movement and was not suitable for the occasion when the camera was fixed in the field with a large field of view. Besides, many scholars have proposed camera calibration methods in large field of view environment. For example, Kong et al. [18] proposed a method of camera calibration based on the Global Positioning System (GPS), which directly took the GPS instrument as the feature points, which limited the flexibility of the method in practical use. Xiao et al. [19] proposed a binocular 3D measurement system that uses a cross target with ring coded points. Shang et al. [20] proposed a large field of view calibration method in which the optical center and control point of the camera are close to the coplanar, which has many limitations. Sun et al. [21] proposed a baseline-based camera calibration method in which the calibration target must be randomly placed in the field of view several times. Wang et al. [22–24] proposed a stereo calibration method for out-of-focus cameras when acquiring images for long- and short-distance photogrammetry, which has high robustness and high accuracy. None of these methods enable precise and fast camera calibration at large field of view.

In this paper, a calibration method using the UAV with RTK as a high-precision mobile calibration target is proposed. This method does not need to manufacture large-scale calibration target, which reduces the requirement of calibration conditions, and is suitable for large scene field environment. In addition, by using the WGS-84 earth coordinate system as the intermediary, the measurement reference coordinate system can be flexibly converted to any desired position through several preset coordinate points, even if the position cannot be observed by the binocular cameras simultaneously, which is very suitable for some complex field scenes where the view is partially obscured by trees or hills. Experimental results show that the proposed method performs well in the monitoring area with a diameter of 50-100 m at the distance of 500-1000 m from the cameras.

The subsequent compositions of this article are as follows: Section 2 introduces the basic principles, Section 3 introduces the calibration process and experimental results, and Section 4 summarizes this article.

2. Calibration Theory

2.1. Camera Imaging Model.
This paper focuses on where the camera is 500 m-1000 m away from the center of the monitoring area; therefore, the telephoto lens is used. Considering that the telephoto lens of the camera has very little distortion, the ideal pinhole imaging mode [25] is chosen to describe the mapping relationship between the object space and the image space, as is shown in Figure 1.

According to the pinhole imaging model, the coordinates from the world coordinate system, camera coordinate system, camera physical coordinate system and image pixel coordinate system have undergone three parts of rigid body transformation, projection transformation, and rigid body transformation, respectively. One point in the camera coordinate system is expressed as (X_c, Y_c, Z_c) and in the world coordinate system is expressed as (X_w, Y_w, Z_w), which are named (x, y) and (u, v), respectively, in the camera physical and image pixel coordinate systems. According to the relationship between each coordinate system, the linear transformation relationship between the world coordinate system (X_w, Y_w, Z_w) and the pixel coordinate system (u, v) is established by the following equation.

$$
Z_c \begin{bmatrix} u \\ v \\ 1 \end{bmatrix} = \begin{bmatrix} \dfrac{1}{dx} & 0 & u_0 \\ 0 & \dfrac{1}{dy} & v_0 \\ 0 & 0 & 1 \end{bmatrix} \begin{bmatrix} f & 0 & 0 & 0 \\ 0 & f & 0 & 0 \\ 0 & 0 & 1 & 0 \end{bmatrix} \begin{bmatrix} \mathbf{R} & \mathbf{T} \\ 0 & 1 \end{bmatrix} \begin{bmatrix} X_w \\ Y_w \\ Z_w \\ 1 \end{bmatrix},
\tag{1}
$$

where $\mathbf{R}$ and $\mathbf{T}$ are the rotation matrix and translation vector between the world coordinate system and the camera coordinate system. f is the focal length of the lens. dx and dy are the physical size of the pixel. u_0 and v_0 are the camera principal points. Camera calibration requires the solution of these parameters.

2.2. Coordinate System Conversion.
As can be seen from Section 2.1, obtaining the correspondence between the pixel coordinates and the world coordinates of the feature point is the key to estimating the camera parameters. With the help of the UAV working in RTK mode, we can obtain the UAV's current GPS navigation coordinates $\mathbf{P}_G(B, L, H)$, which can be converted into earth rectangular coordinates $\mathbf{P}_E(X_E, Y_E, Z_E)$ [18]:

$$
\begin{cases} X_E = (N + H) \cos B \cos L, \\ Y_E = (N + H) \cos B \sin L, \\ Z_E = \left(N\left(1 - E^2\right) + H \right) \sin B, \end{cases}
\tag{2}
$$

where N is the radius of curvature of the ellipsoid and E is the first eccentricity of the ellipsoid. Let a, b be the long and short semiaxes of the Earth, respectively, and χ be the ellipsoidal flattening rate of the Earth. Without losing generality [26],

$$
\begin{cases} a = 6378137, \\ \chi = \dfrac{1}{298.257223563}, \\ b = a \times (1 - \chi). \end{cases}
\tag{3}
$$
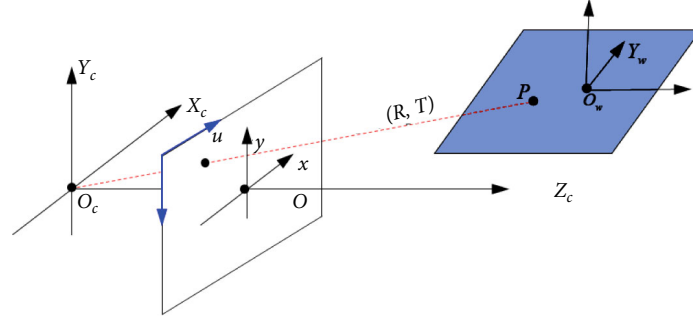
FIGURE 1: Camera pinhole imaging mode.

Also, we know

$$
\begin{cases}
E = \dfrac{\sqrt{a^2 + b^2}}{a}, \\[2mm]
N = \dfrac{a}{\sqrt{1 - E^2 \sin^2 B}}.
\end{cases}
\tag{4}
$$

By combining equations (2)–(4), the representation of P_G in the WGS-84 earth rectangular coordinate system, P_E, can be obtained. However, the coordinates obtained by the above steps are based on the Earth's center of mass, which has two disadvantages: first, the scale of the obtained coordinates is too large to estimate the camera parameters; second, the origin and direction of the current coordinate axes have been fixed, which is not conducive to further measurement. Therefore, we need to set the origin and direction of the world coordinate system according to our own needs and complete the camera calibration in this coordinate system which is also called the preset coordinate system. Since coordinates of all measuring points are in the WGS-84 earth rectangular coordinate system, this transformation is not difficult. According to different application scenarios, the preset coordinate systems can be established by the following two ways.

(1) Establishment of the preset coordinate system for a rectangular region of interest

As is shown in Figure 2, the latitude and longitude of A, B, C, and D four points are measured at the four corners of a rectangle and converted to the earth rectangular coordinate system by the above steps. Take the coordinates of the intersection of lines AC and BD as the origin of the preset coordinate system O_w, and the vector between O_w and the midpoint of CD is the direction vector X of the X-axis. Then, the direction vector of the Z-axis can be expressed as $\overrightarrow{O_w D} \times \overrightarrow{O_w C}$, and the direction vector of the Y-axis can be represented as $Z \times X$.

(2) Establishment of the preset coordinate system for a region of interest with a center point

Measure the latitude and longitude of a point as the origin O_w of the preset coordinates and convert the coordinate to the earth rectangular coordinate system under WGS-84.

Without loss of generality, in the wild, due north is usually used as the Y-direction vector, due east is the X-direction vector, and the Z direction is perpendicular to them.

The preset coordinate system can be established by the above rules, as is shown in Figure 3. And the transformation vector between the preset coordinate system and the earth rectangular coordinate system is obtained as $T_E = O_w$.

Normalize the three orthogonal direction vectors:

$$
I = \left[\frac{X}{|X|}, \frac{Y}{|Y|}, \frac{Z}{|Z|} \right],
\tag{5}
$$

where $| \;|$ represents the modular arithmetic. Then, we can obtain the rotation matrix R_E between the preset coordinate system and the earth rectangular coordinate system:

$$
R_E = I^{-1}.
\tag{6}
$$

Thus, all space coordinates P_{EUAV} of UAV in the earth rectangular coordinate system can be converted to the preset coordinate system (new world coordinate system):

$$
P = R_E \cdot (P_{EUAV} - T_E).
\tag{7}
$$

2.3. Single-Camera Calibration. The basic condition of parameter estimation is to find the matching relationship between image coordinates and 3D coordinates. In this paper, the centroid of the UAV is designated as the feature points in the left and right cameras, as shown in Figure 4.

First, the initial values of intrinsic parameters are given based on the theoretical values:

$$
\begin{cases}
f_x = \dfrac{f}{dx}, \\[2mm]
f_y = \dfrac{f}{dy}, \\[2mm]
u_0 = \dfrac{u_{\max}}{2}, \\[2mm]
v_0 = \dfrac{v_{\max}}{2},
\end{cases}
\tag{8}
$$

where f is the theoretical focal length and f_x and f_y are the focal lengths (in pixels). dx and dy represent the physical size of pixels in the x and y directions, respectively, and
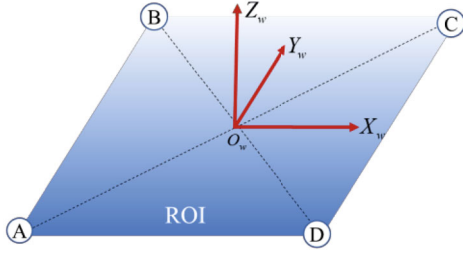
FIGURE 2: Establishment of the preset coordinate system for a rectangular region of interest.
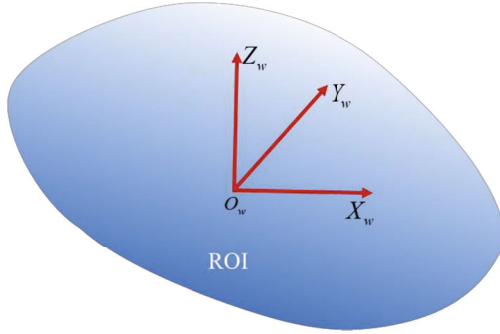
FIGURE 3: Establishment of the preset coordinate system for a region of interest with a center point.

$u_{\max}$ and $v_{\max}$ represent the resolution of the image in the x and y directions, respectively. Subsequently, initial solutions for other parameters (such as extrinsic parameters) can be obtained by DLT [8]. Finally, the constrained adjustment method is used to minimize the reprojection errors:

$$\arg\min \sum_{n=1}^{N} \left\| \mathbf{m}_n - \widehat{\mathbf{m}} \left[f_x, f_y, u_0, v_0, \mathbf{R}, \mathbf{T}, \mathbf{M_n} \right] \right\|^2, \quad (9)$$

where $\mathbf{m}_n$ represents the image coordinate of the n-th point, $\mathbf{M_n}$ denotes its corresponding spatial coordinate, $\widehat{\mathbf{m}}$ is the projection of point $\mathbf{M_n}$ in image n according to equation (1), and $\mathbf{R}$ and $\mathbf{T}$ represent the rotation matrix and translation vector, respectively. It is worth noting that the principal points u_0 and v_0 are set to constant values and do not participate in the iterative process because their values are an order of magnitude smaller than the other parameters. Otherwise, although small reprojection errors can be obtained, these values have no physical significance and cause instability of other parameters. It has been experimentally proven in Reference [27] that the fixation of the principal points has little effect on the final reconstruction accuracy.

2.4. Binocular Calibration. According to Section 2.2, we can convert the GPS navigation coordinates of UAV to the required preset coordinate system. Suppose $\mathbf{P}$ is the coordinates of a point in the preset coordinate system and $\mathbf{P}_L$ and $\mathbf{P}_R$ are its corresponding coordinates in the left and right camera coordinate system, as is shown in Figure 5, their rela-

tionship can be described as

$$\begin{cases} \mathbf{P}_L = \mathbf{R}_L \mathbf{P} + \mathbf{T}_L, \\ \mathbf{P}_R = \mathbf{R}_R \mathbf{P} + \mathbf{T}_R, \end{cases} \quad (10)$$

where $[\mathbf{R}_L, \mathbf{T}_L]$ and $[\mathbf{R}_R, \mathbf{T}_R]$ describe the extrinsic parameters of the left and right cameras, respectively. Obviously, it is easy to obtain the extrinsic parameters between the left and right cameras as

$$\begin{aligned} \mathbf{R}_w &= \mathbf{R}_R \mathbf{R}_L^{-1}, \\ \mathbf{T}_w &= \mathbf{T}_R - \mathbf{R}_R \mathbf{R}_L^{-1} \mathbf{T}_L. \end{aligned} \quad (11)$$

In this way, the binocular camera can be calibrated. The advantage of establishing the preset world coordinate system is that we can quickly convert the coordinates $\mathbf{P}_L$ (generally in the left camera coordinate system) reconstructed by the binocular camera to the preset coordinate system:

$$\mathbf{P} = \mathbf{R}_L^{-1} (\mathbf{P}_L - \mathbf{T}_L). \quad (12)$$

3. Experiments and Analysis

To verify the effectiveness of the proposed method, we set up a series of experiments. Five groups of camera-lens pairs were calibrated independently. Details of the camera-lens pairs are shown in Table 1.

In each group, identical camera-lens pairs were used to form a stereo camera, with the two cameras placed vertically, while monitoring an area 500-1000 meters away. The area covered by the cameras varies in diameter from 50 m to 100 m, depending on the focal lengths.

In the experiment, the UAV (DJI M300) with RTK (DJI RTK-2) was used as the high-precision mobile calibration target. The RTK master station was arranged on the ground, and the fuselage was equipped with the RTK slave station. In the range of 10 km, the measuring accuracy of the slave station can reach the order of centimeters [28], which is a satisfactory accuracy compared with the camera monitoring diameter of tens of meters.

Control the UAV navigate over the monitoring area, and confirm that the UAV is in the field of view of the cameras. At 8 m, 16 m, 24 m, 32 m, and 40 m above the plane X-O-Y in the preset coordinate system, 10 points were suspended to record the GPS navigation coordinates and corresponding image coordinates of the UAV. Figure 6 illustrates the UAV images taken by two cameras. Convert the GPS coordinates to the preset coordinate system, and the position distribution of the UAV is shown in Figure 7.

3.1. Influence of the Feature Point Number on Calibration Results. As we know, the camera parameters can be correctly estimated only if there are at least six sets of 2D and 3D coordinates corresponding to each other. Adding a feature point means that the UAV needs to fly one more time, which will undoubtedly increase our workload. Therefore, it is meaningful to explore the appropriate number of feature points to reduce the work. Five independent experiments

FIGURE 4: UAV in a single camera.

TABLE 1: Details of the camera-lens pairs.

Group	Camera resolution	Camera model	Lens model	Pixel size (μm)	Focal length (mm)
1	1920 × 1080	Phantom V341	Nikon 70-200 mm	10	100
2	1024 × 1024	Photron Nova s12	Nikon 70-200 mm	20	130
3	1280 × 800	Phantom VEO 310	Nikon 200-500 mm	20	350
4	1280 × 800	Phantom VEO 310	Nikon 200-500 mm	20	350
5	1920 × 1080	Phantom VEO 440	Nikon 70-200 mm	10	170
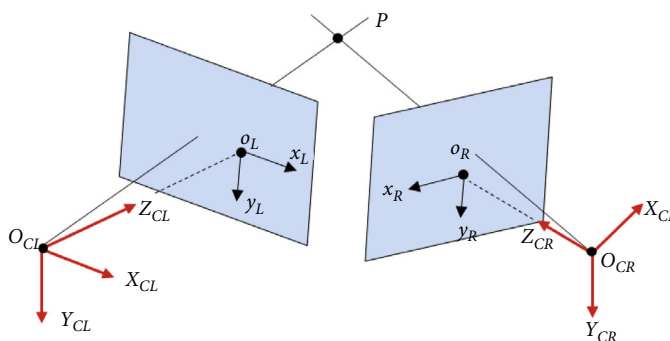
FIGURE 5: Binocular vision model [27].

FIGURE 6: UAV in camera images.

were carried out for the five camera-lens pairs described in Table 1.

In each experiment, 6, 10, and 40 UAV images (one image corresponds to a feature point position) were used to calibrate the stereo cameras. Then, the calibration results were used to reconstruct the space positions of another 10 UAVs. It is worth noting that the navigation coordinates measured by the GPS on the fuselage were used as the real
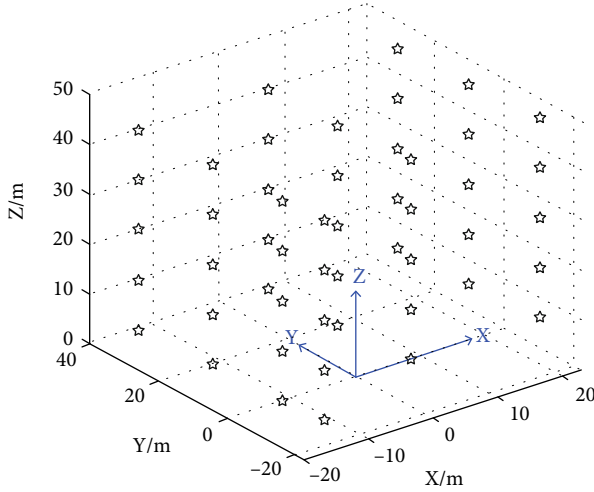
FIGURE 7: Position distribution of UAV in the preset coordinate system.

TABLE 2: Errors between reconstructed positions and ideal positions (unit: m).

Point number	Group 1	Group 2	Group 3	Group 4	Group 5
6	12.69	0.39	8.36	8.68	3.2
10	1.44	0.31	3.32	0.35	0.21
12	0.16	0.32	0.11	0.36	0.19
15	0.13	0.30	0.09	0.28	0.21
20	0.12	0.28	0.09	0.22	0.16
25	0.12	0.28	0.09	0.17	0.17
30	0.11	0.26	0.08	0.15	0.15
35	0.11	0.25	0.08	0.14	0.16
40	0.10	0.22	0.08	0.13	0.15

TABLE 3: Distance errors of the two marks (unit: m).

Group number	Measured length	Reconstruction length	Absolute errors	Relative errors
1	24.25	24.36	0.11	0.45%
2	32.83	32.77	0.06	0.18%
3	46.60	46.48	0.12	0.26%
4	46.60	46.50	0.10	0.21%
5	30.00	29.95	0.05	0.17%

FIGURE 8: Relationship between errors and the number of feature points.

slightly. Therefore, 15~30 points are a good choice to balance efficiency and accuracy in practical applications.

3.2. Reconstruction Accuracy. The actual measurement accuracy is an important criterion to evaluate the calibration accuracy. Two markers were placed in the monitoring area of the cameras, and the actual distance between them can be measured by RTK. The same steps were used to calibrate the two cameras, and the coordinates of the two markers were reconstructed according to the calibration results, and then, the distance between them was calculated. Experiments were carried out on the five groups of camera-lens configurations, and the reconstruction errors are shown in Table 3.

It can be seen that the reconstruction results are stable in accuracy, the maximum absolute error is less than 0.12 m, and the relative error is less than 0.5%. This is satisfactory when the monitoring diameter ranges from 50 m to 100 m. The results show that the proposed method is accurate and flexible in calibrating cameras with large field of view in the wild.

4. Conclusion

In this paper, a camera calibration method for long-distance photogrammetry using unmanned aerial vehicles is studied. Instead of traditional targets, the GPS carried by UAV is used to obtain the spatial coordinate information, so as to complete camera calibration. This method overcomes the problem that standard target cannot cover most of the camera's field of view and enhances the environmental adaptability. In addition, by using the WGS-84 coordinate system as the intermediary, the preset coordinate system can be established in any area of interest, improving the

space position of the UAV positions. Table 2 reveals the influence of different numbers of feature points on calibration results, in which the mean Euclidean distances of the reconstructed space positions and ideal ones of UAV are used to evaluate the accuracy of the results.

As is shown in Figure 8, the results of five experiments show that when the number of feature points is less than 12, the reconstruction errors decrease rapidly with the increase in the number of feature points. However, when the number of feature points is greater than 12, the impact of the number of feature points on the accuracy becomes smaller and the reconstruction accuracy only improves

flexibility of measurement. Experimental results show that the absolute measurement error of the proposed method is less than 0.5% in the monitoring area with a diameter of 50-100 m and at the distance of 500-1000 m from the cameras.

Data Availability

The data used to support the findings of this study are available from the corresponding author upon request.

Conflicts of Interest

The authors declare that there is no conflict of interest regarding the publication of this paper.

References

[1] X. P. Zhu and Y. Fu, "A camera calibration based on traffic video," *Electronic Design Engineering*, vol. 20, no. 9, pp. 48–52, 2012.

[2] L. A. Souto, A. Castro, L. M. Gonçalves, and T. P. Nascimento, "Stairs and doors recognition as natural landmarks based on clouds of 3D edge-points from RGB-D sensors for mobile robot localization," *Sensors*, vol. 17, no. 1824, pp. 1–16, 2017.

[3] H. J. Zhao and B. Wu, "Three-dimensional face modeling technology based on 5G virtual reality binocular stereo vision," *Communication Systems*, vol. 35, no. 5, 2022.

[4] M. Xia, H. D. Shao, D. Williams, S. Lu, L. Shu, and C. W. de Silva, "Intelligent fault diagnosis of machinery using digital twin-assisted deep transfer learning," *Reliability Engineering & System Safety*, vol. 215, p. 107938, 2021.

[5] H. D. Shao, M. Xia, J. F. Wan, and C. W. de Silva, "Modified stacked autoencoder using adaptive morlet wavelet for intelligent fault diagnosis of rotating machinery," *IEEE/ASME Transactions on Mechatronics*, vol. 27, no. 1, pp. 24–33, 2022.

[6] M. Xia, H. D. Shao, X. D. Ma, and C. W. de Silva, "A stacked GRU-RNN-based approach for predicting renewable energy and electricity load for smart grid operation," *IEEE Transactions on Industrial Informatics*, vol. 17, no. 10, pp. 7050–7059, 2021.

[7] W. Faig, "Calibration of close-range photogrammetric systems: mathematical formulation," *Photogrammetric Engineering and Remote Sensing*, vol. 41, no. 12, pp. 1479–1486, 1975.

[8] Y. I. Abdel-Aziz and H. M. Karara, "Direct linear transformation from comparator coordinates in close-range photogrammetry," *Proceedings American society of photogrammetry symposium on close-range photogrammetry*, pp. 1–18, 1971.

[9] R. Y. Tsai, "A versatile camera calibration technique for high-accuracy 3D machine vision metrology using off-the-shelf tv cameras and lenses," *IEEE Journal on Robotics and Automation*, vol. 3, no. 4, pp. 323–344, 1987.

[10] Z. Y. Zhang, "Flexible camera calibration by viewing a plane from unknown orientations," in *The Seventh IEEE International Conference on Computer Vision*, Kerkyra, Greece, 1999.

[11] O. D. Faugeras, Q. T. Luong, and S. J. Maybank, "Camera self-calibration: theory and experiments," *European Conference on Computer Vision*, pp. 321–334, 1992.

[12] S. J. Maybank and O. D. Faugeras, "A theory of self-calibration of a moving camera," *The International Journal of Computer Vision*, vol. 8, no. 2, pp. 123–151, 1992.

[13] X. H. Li, G. Y. Wang, and J. G. Liu, "Automatic camera calibration method based on dashed lines," in *MIPPR 2013: remote sensing image processing, geographic information systems, and other applications*, pp. 892112-1–892112-8, SPIE, 2013.

[14] S. D. Ma and Z. Y. Zhang, *Computer Vision*, Beijing Science Press, 1998.

[15] L. G. Zhao, C. K. Wu, and J. F. Ning, "A camera calibration method based on two orthogonal vanishing points," *Concurrency and Computation: Practice and Experiment*, vol. 26, no. 5, pp. 1185–1199, 2014.

[16] D. M. Sang, "A self-calibration technique for active vision systems," *IEEE Transactions on Robotics and Automation*, vol. 12, no. 1, pp. 114–120, 1996.

[17] Z. Y. Hu and F. C. Wu, "A review on some active vision based camera calibration techniques," *Chinese Journal of Computers*, vol. 25, no. 11, pp. 1149–1156, 2002.

[18] X. F. Kong, Q. Chen, G. H. Gu, W. X. Qian, K. Ren, and J. J. Wang, "A GPS-based camera calibration method," *China Ordnance Society*, vol. 37, no. 12, pp. 2301–2307, 2016.

[19] Z. Xiao, L. Jin, D. Yu, and Z. Tang, "A cross-target-based accurate calibration method of binocular stereo systems with large-scale field-of-view," *Measurement*, vol. 43, no. 6, pp. 747–754, 2010.

[20] Y. Shang, X. Sun, X. Yang, X. Wang, and Q. Yu, "A camera calibration method for large field optical measurement," *Optik*, vol. 124, no. 24, pp. 6553–6558, 2013.

[21] J. H. Sun, Z. Wu, Q. Liu, and G. Zhang, "Field calibration of stereo vision sensor with large FOV," *Optical Precision Engineering*, vol. 17, no. 3, pp. 633–640, 2009.

[22] Y. W. Wang, X. C. Chen, J. Y. Tao, K. Wang, and M. Ma, "Accurate feature detection for out-of-focus camera calibration," *Applied Optics*, vol. 55, no. 28, pp. 7964–7971, 2016.

[23] Y. W. Wang, Y. J. Wang, L. Liu, and X. Chen, "Defocused camera calibration with a conventional periodic target based on Fourier transform," *Optics Letters*, vol. 44, no. 13, pp. 3254–3257, 2019.

[24] Y. W. Wang, L. Liu, B. L. Cai et al., "Stereo calibration with absolute phase target," *Optics Express*, vol. 27, no. 16, pp. 22254–22267, 2019.

[25] R. Hartley and A. Zisserman, *Multiple View Geometry in Computer Vision*, Cambridge University Press, 2004.

[26] X. Y. Kong and J. M. Guo, *Control Surveying*, Wuhan university press, 2015.

[27] H. J. Zhao, Z. Wang, H. Z. Jiang, Y. Xu, and C. Dong, "Calibration for stereo vision system based on phase matching and bundle adjustment algorithm," *Optics and Lasers in Engineering*, vol. 68, pp. 203–213, 2015.

[28] Z. G. Yan, Z. L. Zhang, and X. H. Zhao, "The principle of GPS RTK pattern and the practical technology in its application," *Surveying and Mapping of Sichuan*, vol. 24, no. 2, pp. 66–69, 2001.

Research Article

A Novel Niche Quantum Ant Colony-Based Clustering Optimization Approach for Wireless Auto Meter Reading Network

Jingyun Li [ID],[1,2] **Hu Qin** [ID],[3] **Yang Liu** [ID],[3] **Jie Zhou** [ID],[3,4] **and Yao Zhang** [ID][5]

[1]*School of Economics and Management, University of Chinese Academy of Sciences, Beijing 100190, China*
[2]*Xinjiang Tianfu Jinyang New Energy Co., Ltd, Xinjiang 832000, China*
[3]*College of Information Science and Technology, Shihezi University, Shihezi 832000, China*
[4]*Xinjiang Tianfu Information Technology Co., Ltd, China*
[5]*University of the Cordilleras, Baguio City 2600, Philippines*

Correspondence should be addressed to Yao Zhang; y-z7247@students.uc-bcf.edu.ph

Since the low cost and high flexibility, wireless automatic meter reading network (WAMRN) is widely used by utility companies to realize automatic collection and transmission of remote energy consumption information. Considering that WAMRN is composed of several wireless communication nodes, the lifetime of the network will be affected by factors such as the changeable deployment environment and the limited energy of nodes. Thus, a novel niche quantum ant colony-based WAMRN clustering optimization method is proposed in this paper to address the problem of how to make full use of the limited energy to extend network lifetime and improve data transmission efficiency. In the proposed approach, a clustering model of WAMRN is defined; moreover, an improved Niche Quantum Ant Colony Optimization (NQACO) is proposed to optimize the model therefore to obtain an optimal clustering scheme, which can help WAMRN reduce unnecessary energy loss to achieve the purpose of extending the lifetime of the entire network. To verify the performance of the proposed method, NQACO is compared with some popular clustering methods, i.e., GA and SA, under different scenarios. The results show that under the premise of ensuring network communication, NQACO is superior to the other two methods in reducing the total energy consumption and prolonging the network lifetime.

1. Introduction

In the age of production automation, the realization of automatic meter reading (AMR) for water, electricity, and gas supplies has become an urgent problem for energy companies, for a reason that accurate and timely replication of water and electricity data will directly affect business decisions and economic benefits [1, 2]. By leveraging electronic, communication, computer, and network technologies to identify, read, process, and transmit meter data automatically, it enables the problems of single function, low accuracy, and undesirable real-time performance of traditional meter reading to be solved. Especially, the adoption of automatic meter reading technology not only improves the economic efficiency of enterprises but also enhances the degree of informatization [3]. Hence, there appears an inevitable trend of the application of automatic meter reading technology for water, electricity, and gas data reading.

At present, the technology of automatic meter reading consists of wired automatic meter reading and wireless automatic meter reading according to the mode of data transmission. Specifically, the former mainly makes use of power line networks, telephone line networks, RS-485 bus networks, etc. One disadvantage of the existing wired meter reading method lies in that it cannot be applied in a large scale and reliable way in the home meter reading system. It is because of its high cost, complex wiring,

difficulty in commissioning and maintenance, susceptibility to the power grid, poor security, and poor scalability [4]. With the appearance of wireless automatic meter reading, it makes up for the deficiency of the wired automatic meter reading. The technologies used for wireless meter reading include GSM/GPRS, Bluetooth technology, and short-range wireless radio frequency transmission technology. Compared with traditional meter reading methods as well as wired methods, wireless meter reading can save labor costs, reduce wiring costs, and simplify the management to find problems and take corresponding measures promptly. To this end, WAMR has become a leading research direction of AMR.

In WAMRN, each energy meter node is powered by a battery with limited energy. In this way, to prolong the network lifetime as much as possible with energy limitation, researchers have conducted a lot of research on ways which can effectively enhance the energy utilization. Finding that the design of network topology and the selection of routing have a significant impact on the energy dissipation of nodes [5–7], researchers improve the energy utilization in WAMRN by designing a reasonable clustering model and using efficient optimization algorithm [8, 9]. Therefore, the focus of this paper is on the optimization of network clustering to effectively extend the lifetime of WAMRN.

In this paper, the most desirable nodes in the WAMRN are selected as cluster head nodes for clustering, such that the whole network is divided into several connected regions. In addition, the noncluster head nodes in each region are named member nodes, and the cluster head nodes manage the surrounding member nodes. In [10], the authors have shown that the optimal cluster head selection problem is an NP-hard problem. Therefore, we propose a Niche Quantum Ant Colony Optimization (NQACO) which combines the optimization mechanism of quantum evolutionary algorithms with the ant colony optimization. By using this approach, it can significantly enhance the search traversal and convergence speed when the problem size is large, while NQACO uses the niche technique to ensure the species diversity of the whole large ant colony. The existence of stable individual differences in the colony aids NQACO in overcoming the premature problem exhibited by other algorithms and allows for more desirable local search capabilities. In a nutshell, the proposed clustering approach can efficiently search for optimal routing clusters from the solution space, thus effectively decreasing the energy loss in WAMRN and thus extending the network lifecycle.

The structure of this thesis is just as below. In Section 2, the research work related to the clustering of sensor networks is introduced. Section 3 describes the entire network structure of WAMRN. Meanwhile, the corresponding mathematical model is designed and established. Section 4 proposes a new optimization algorithm to optimize the problem of clustering of WAMRN in Section 3. Section 5 shows the optimization performance of NQACO on the cluster routing model by comparing it with GA and SA. Finally, the whole work of this paper is summarized in Section 6.

2. Related Work

At present, there exist many kinds of AMR communication technologies. For instance, paper [11] applying radio frequency technology to AMR systems, which can help energy companies effectively reduce data collection costs and quickly collect key information to provide insights for decision-makers. Paper [12] realizes a wireless power monitoring system based on ZigBee technology monitoring power quality and remotely control power services. In addition, paper [13] uses the single-chip microcomputer STM32 to manage energy data and uses ZigBee for communicating between the electric energy meter and the data center. Afterwards, paper [14] designed a GPRS-based remote automatic meter reading wireless communication system hardware, which supports UDP communication protocol and can carry out remote data transmission through message transmission and network communication.

A lot of research results show that WSN is considered to be the key technology for building a new generation of smart grid AMR systems in the future [15–18]. However, since the energy supply of sensor nodes in WSN is battery-powered, the energy of the nodes has a certain limitation, and the energy of wireless sensor network nodes cannot be replenished at work. Therefore, considering extending the lifetime of the entire network as much as possible, it is an important design principle to improve the energy utilization rate and reduce the energy loss of the wireless sensor node in the construction of WSN. In paper [19], the researchers use the water meter as a node to form a wireless sensor network. That research focuses on making the energy consumption as small as possible by avoiding packets whose lengths exceed the length limit. The paper [20] points out that sensor nodes in WSN send their data to the central cluster head, which forwards the data to the desired receiver. Moreover, clustering can realize bandwidth reuse, thereby increasing system capacity.

To make up for the sustainability of QoS and bridge the gap between suboptimal solutions, the paper [21] proposed a quality-of-service routing algorithm based on genetic algorithm. That work solves the imbalance characteristic schematic diagram of QoS optimization in the ad hoc network and the previous convergence problem. However, the genetic algorithm used in this study has a specific dependence on selecting the initial population. In addition, the algorithm is prone to premature problems when solving large-scale computing problems.

In paper [22], the author proposed a lightweight dynamic TRUST model and bee mating algorithm for clustering. More specifically, to prevent malicious nodes from becoming cluster head nodes, they proposed a gradually reasonable priority scheme in the trust measurement. Nevertheless, since the amount of crossover operation information is small and the similarity of the bee colony is high in the process of optimizing the problem with the bee mating algorithm, it is prone to fall into the local optimum and seriously affect the performance of the algorithm.

Paper [23] proposes a modified clustering method based on LEACH (Low Energy Adaptive Clustering Hierarchy),

which uses the Particle Swarm Optimization (PSO) algorithm to optimize the network clustering and determines cluster heads by considering factors such as energy, communication overhead, and load balance. Although the particle swarm algorithm used in the research has the characteristics of simple structure and fast search speed compared with other algorithms, it has some inescapable disadvantages such as low accuracy, easy divergence, and easy falling into local optimum. These shortcomings are in the process of clustering optimization, making the clustering undesirable.

In other perspectives, paper [24] proposes a clustering routing algorithm on the basis of chaotic binary ant colony optimization (CBACO) for wireless sensor networks. The algorithm calculates the energy consumption of the cluster head based on the remaining energy, the number of neighbors, and the distance to the base station (BS). In that paper, the routing process is divided into two steps, where the first step is to process the data transmission from the cluster head to the cluster head and the second one is to apply the biologically inspired optimization technology ant colony algorithm (ACO) to optimize the path finding process from the cluster head to the BS. Although the information interaction of ant colony algorithm is realized by pheromone, the convergence to the optimal solution is the process of information positive feedback. Positive feedback is designed to enhance the quality of the solution and achieve better performance. However, this algorithm will have the problem of evolutionary stagnation.

3. System Model

3.1. WAMRN Network Model. The structure of the WAMRN network model is shown in Figure 1. After the terminal collection node obtains the meter data, it transmits the data to the remote BS through the wireless communication node in WAMRN. To save energy, each wireless communication device can select an optimal path according to the actual situation and then transmit the data to the cluster head node through the optimal path for data integration. Without considering other factors, all wireless communication nodes have the same initial energy. Since each wireless communication device has the same data communication capability, the energy loss in the process of data transmission, fusion, and transmission is also the same. In WAMRN, the energy of the BS is not limited, and the BS is always in a normal working state. However, the wireless communication equipment in the network is restricted by its energy. If the energy is exhausted, the node will no longer work.

In common cases, the installation location of data collection and transmission wireless equipment depends on the actual situation. Therefore, the distribution of various meters is irregular. This situation can be understood as that each sensor device in WAMRN is randomly distributed.

3.2. Energy Loss Model of Wireless Communication Nodes. The wireless meter reading device in WAMRN belongs to one kind of the wireless communication device, so the energy consumption of the WAMRN can be calculated by using the energy consumption model of the wireless communication device. In fact, there is a lot of research work on the energy consumption of wireless terminals. Papers [25–27] put forward the theoretical explanation of content radio transmission and microcontroller processing. And in paper [28], the author proposes a first-order radio model, which models that the energy consumption of wireless terminals can widely describe the energy consumption in wireless terminals; it is used to calculate the energy consumption in many related research works. Therefore, this energy model is adopted in our research work.

The energy consumption of wireless communication nodes in WAMRN mainly includes three parts: sensing energy consumption, data communication energy consumption, and microprocessor energy consumption. Many current research results show that the energy consumption of wireless communication nodes in data communication accounts for more than 50% of the total energy consumption of WAMRN. Besides, the sensing energy consumption and microprocessor energy consumption are comparative fixed, so it is hard to reduce them through optimization. Therefore, this paper primarily analyzes the energy loss of each wireless communication node in WAMRN and studies a reasonable clustering method for achieving low energy consumption in the network.

As shown in Figure 2, if the sensor node transmits k bit packets to adjacent nodes with a distance of d meters, the energy consumption generated by the transmitting node is $E_{tx}(k, d)$, which mainly contains $E_{TX-\text{elec}}(k)$ and $E_{TX-\text{amp}}(k, d)$, where $E_{TX-\text{elec}}(k)$ represents the energy loss generated when the signal transmitting circuit unit transmits data information. And $E_{TX-\text{amp}}(k, d)$ denotes the energy consumption generated when the signal power amplifier circuit unit amplifies the transmission power. Equations (1), (2), and (3) are the calculation of the above three types of energy consumption, respectively.

$$E_{Tx}(k, d) = E_{Tx-\text{elec}}(k) + E_{Tx-\text{amp}}(k, d), \tag{1}$$

$$E_{Tx-\text{elec}}(k) = k \cdot E_{\text{elec}}, \tag{2}$$

$$E_{Tx-\text{amp}}(k, d) = \begin{cases} k \cdot \varepsilon_{fs} \cdot d^2, & d < d_0 \\ k \cdot \varepsilon_{mp} \cdot d^4, & d \geq d_0 \end{cases}. \tag{3}$$

In formula (3), the $E_{Tx-\text{amp}}(k, d)$ adopts two different calculation methods according to the value of the communication distance d between nodes. If $d < d_0$, it can be assumed that the signal is in the ideal state of no attenuation, no blocking, and no multipath mode during the propagation process, so that the parameter used for signal power amplification is ε_{fs}, and then, the calculation method of a is $E_{Tx-\text{amp}}(k, d) = k \cdot \varepsilon_{fs} \cdot d^2$. If $d > d_0$, the signal attenuation caused by the increase in communication distance needs to be considered. At this time, the signal power amplification parameter is ε_{mp}, and $E_{Tx-\text{amp}}(k, d) = k \cdot \varepsilon_{mp} \cdot d^4$. The d_0 is
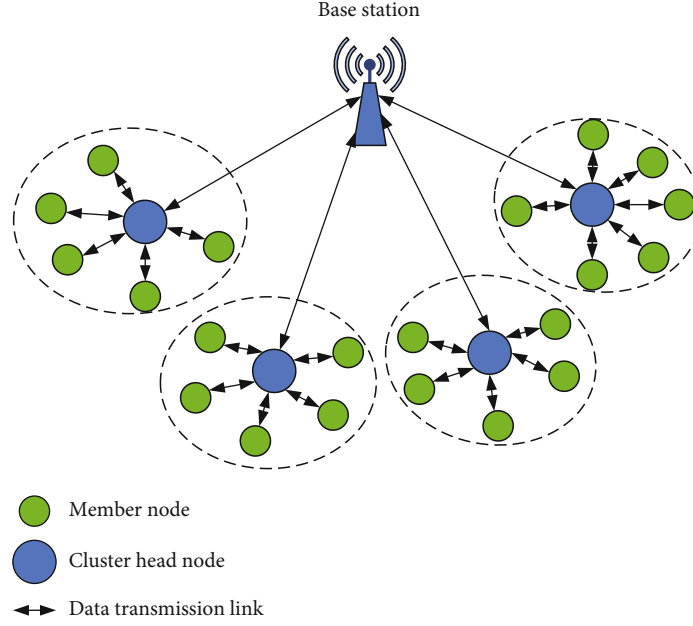
FIGURE 1: WAMRN network model diagram.
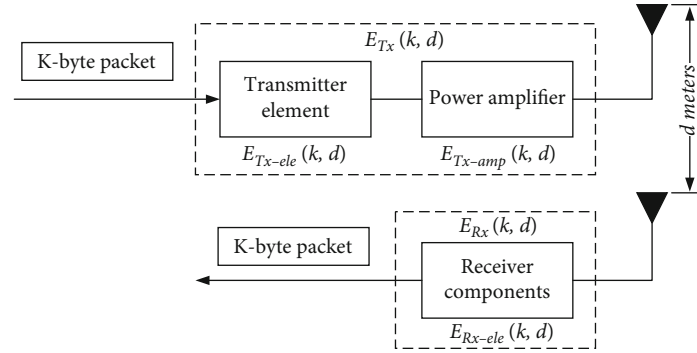
FIGURE 2: Energy loss model of wireless communication.

the distance threshold calculated as follows:

$$d_0 = \sqrt{\frac{\varepsilon_{fs}}{\varepsilon_{emp}}}. \tag{4}$$

When receiving k bit packets, the energy consumption of nodes is calculated by as follows:

$$E_{Rx-ele} = k \cdot E_{ele} = E_{Rx-ele}(k). \tag{5}$$

Additionally, to decrease the amount of communication data and decrease the sending of redundant data, the cluster head will perform data fusion on the data from each member node, and there will be a small amount of energy consumption in this process. In this article, E_{Fs} is used to represent the energy consumption during data fusion, assuming that the fusion of 1 bit data requires energy consumption E_{Df}; then, the energy consumption of k-bit data fusion can be

defined by as follows:

$$E_{Fs} = k \cdot E_{Df}. \tag{6}$$

4. NQACO for Clustering Optimization in WAMRN

The proposed NQACO, based on quantum evolution and niche technology, is an improvement and upgrade of the traditional ant colony algorithm. It introduces the concept and theory of quantum computing, uses qubit coding to store information, and completes the update of quantum coding through quantum rotation gate. Meanwhile, the quantum evolution ensures that the performance of the algorithm will not be affected, and it can even significantly improve the convergence speed of the algorithm. Besides, to find an optimal solution in the whole solution space, NQACO use the niche mechanism to divide the ant colony into several niches. Due to the relative isolation between multiple niches,

there is less gene exchange between different species, so there are some differences in species genes between these niches, which provides the species diversity of the whole ant colony. On the level of swarm intelligence optimization algorithm, stable individual differences facilitate NQACO to overcome the premature problem shown by other algorithms and can enhance the ability of local search.

The detailed procedures of using NQACO to solve the clustering optimization problem in WAMRN are as follows.

Step 1. Initialize NQACO with various parameters, including population size, the maximum number of iterations, pheromone trajectory strength, visibility parameters, pheromone volatility factor, number of wireless communication nodes in the network, and crowding factor.

Step 2. Quantum coding for ant colony according to Equation (7) and Equation (8) and initialization by chaotic mapping according to Equation (10) and Equation (11).

Step 3. Measure the qubit state according to Equation (9).

Step 4. Calculate the fitness value of each ant individual according to Equation (12)–Equation (16), and record the ant individual with the largest fitness value.

Step 5. Update pheromones according to pheromone strength and visibility using Equation (17) and Equation (18), and then, move the ants according to the transition probability calculated by formula Equation (19).

Step 6. Recalculate the fitness value of each individual ant, and record the individual with most significant fitness value.

Step 7. Use the optimal solution to update the direction of the quantum revolving gate, and then, update the quantum encoding ant through the quantum revolving gate by Equation (20).

Step 8. Randomly select ant individuals from the current population as crowded individuals. Then, calculate the correlation between other individuals in the ant colony according to Equation (21) and the excluded individual. Suppose the correlation between the excluded individual and another ant individual is greater than the average correlation between all individuals. Based on the exclusion mechanism, the individual with the lower fitness value of the two ants will be replaced by the individual with the higher fitness value.

Step 9. Judge whether the termination condition is reached, and output the optimal individual if it is reached, and use the binary code corresponding to this individual as the optimal clustering scheme for WAMRN. Otherwise, the algorithm will continue from Step 3 to the next iteration.

Figure 3 is the flow chart of NQACO.

4.1. Quantum Coding and State Measurement.
In NQACO, the algorithm introduces quantum coding and state measurement to solve the WAMRN clustering problem. Typically, information is stored in the form of binary bits, and the state of the binary bits can only be 0 or 1. But in quantum computing, information is stored in the form of qubits, which are a one-dimensional complex vector space. However, in quantum computing, information units are stored in qubits. A linear combination of two superposition components $|0\rangle$ and $|1\rangle$ can be used to represent any state of a qubit. In this paper, $|\psi\rangle$ is used to represent the state of the qubit, and its calculation method is as follows:

$$|\psi\rangle = \alpha|0\rangle + \beta|1\rangle, \tag{7}$$

where α and β represent the probability magnitudes of the two superposition vectors $|0\rangle$ and $|1\rangle$, respectively, while $|\alpha|^2$ and $|\beta|^2$ denote the probability of the quantum bits being at 0 and 1, respectively, and $|\alpha|^2 + |\beta|^2 = 1$.

In NQACO, the information carried by the ants in the ant colony is represented by a group of qubits. In the clustering optimization problem, the code composed of this group of qubits is actually a clustering scheme. Assume that there are n wireless communication nodes in the WAMRN, where c wireless communication nodes are selected as cluster heads and the remaining $n - c$ wireless communication nodes are member nodes. Thus, the length of the encoding carried by a single ant in the encoding process is n. The following mathematical expression (8) can represent the encoding of the information carried by an individual ant.

$$p_i = \begin{pmatrix} \alpha_1^t & \alpha_2^t & \cdots & \alpha_n^t \\ \beta_1^t & \beta_2^t & \cdots & \beta_n^t \end{pmatrix}. \tag{8}$$

Each column in p_i is the probability of the appearance of two superimposed vectors constituting the state of the corresponding qubit. However, this coding method cannot obtain the clustering scheme directly, so converting quantum coding to binary coding is necessary. Thus, this paper uses the method of measuring the qubit's state to realize the conversion process. In the measurement process, the n wireless communication nodes in the network are numbered from 1 to n; then, the state of the corresponding quantum bit count can be used to determine whether the wireless communication node is a cluster head or not. In this paper, the state of the ith qubit is calculated by Equation (9). If the state measurement value of the ith qubit in a code is 0, the wireless communication node numbered i is a member node. Otherwise, the wireless communication node numbered i is a cluster head.

$$z_i = \begin{cases} 0 & \text{random}[0, 1] > |\alpha_i|^2 \\ 1 & \text{random}[0, 1] \leq |\alpha_i|^2 \end{cases}. \tag{9}$$

4.2. Initialization of Ant Population.
Individuals of NQACO carry a feasible clustering scheme. Before the first generation of population evolution, the population with size popSize
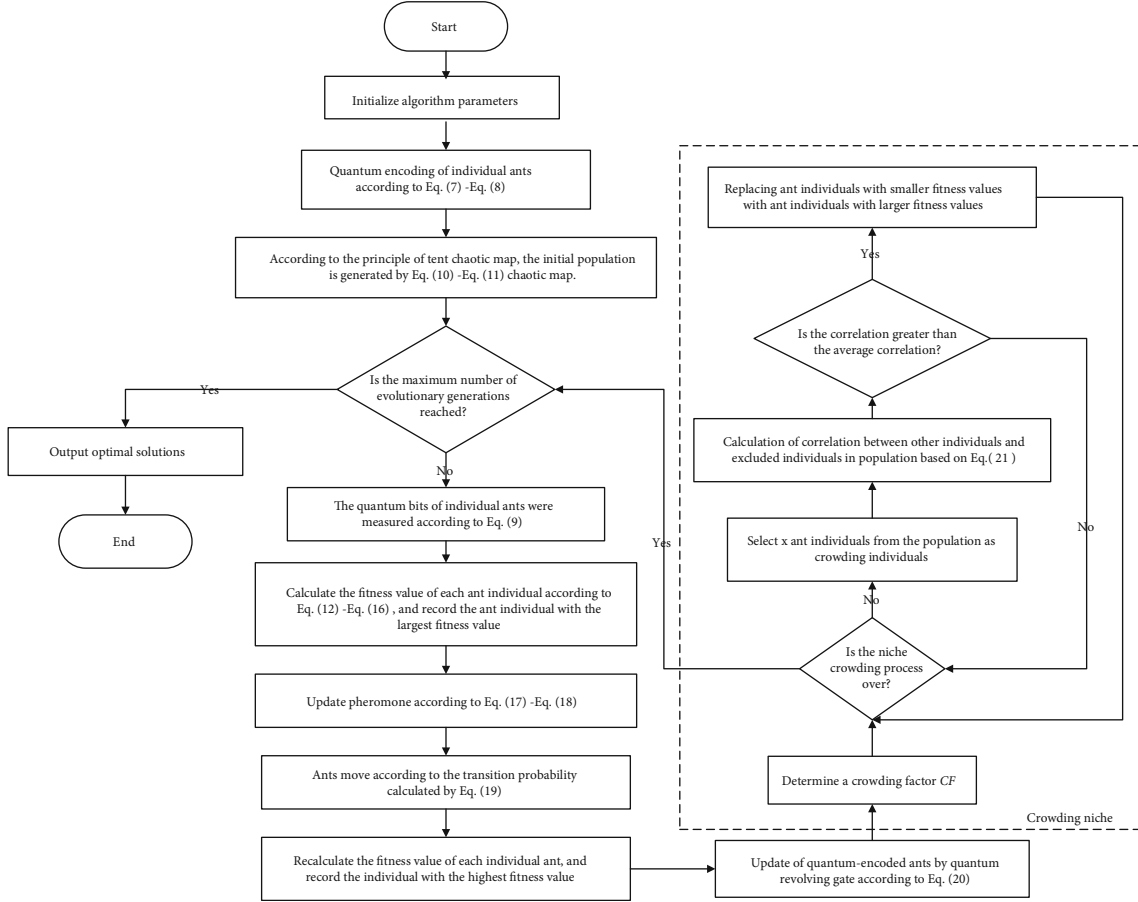
FIGURE 3: Algorithm flowchart of NQACO.

TABLE 1: Rotation angle strategy.

z_l	$z_{\text{best}}^{\text{old}}$	fitness$(z_l) >$ fitness$\left(z_{\text{best}}^{\text{old}}\right)$	$\Delta\theta_l$	$S(\alpha_l\beta_l)$			
				$\alpha_l\beta_l > 0$	$\alpha_l\beta_l < 0$	$\beta_l = 0$	$\alpha_l = 0$
1	0	F	0.001π	-1	+1	0	±1
0	0	F	0	0	0	0	0
1	0	T	0.025π	+1	-1	±1	0
0	0	T	0	0	0	0	0
1	1	F	0.005π	+1	-1	±1	0
0	1	F	0.05π	+1	-1	±1	0
1	1	T	0.025π	+1	-1	±1	0
0	1	T	0.005π	-1	+1	0	±1

needs to be initialized. In this article, NQACO uses a tent map to generate the initial information code carried by each ant in the ant colony. Compared with the commonly used logistic mapping, the chaotic sequence generated by the tent mapping in the interval [0,1] is more evenly distributed and faster iteration speed. The calculation method of the tent mapping function is as follows:

$$x_{i+1} = \begin{cases} 2x & 0 \le x_i \le 1/2 \\ 2(1-x_i) & 1/2 \le x_i \le 1 \end{cases}. \quad (10)$$

In the formula, x is a random number with a value range of [0,1]. The formula can also be expressed in the following form.

$$x_{i+1} = (2x_i) \bmod (1). \quad (11)$$

In the process of population initialization, a random number x_0 with a value range of [0,1] is given first. On this basis, tent mapping is used to generate n chaotic variables. Let the individual ants encode $\alpha_n = \sin(2\pi x_n)$ and $\beta_n = \cos(2\pi x_n)$ in p_i, so that the probability amplitude of each qubit

TABLE 2: Network environment parameters.

Parameter	Value
k	1000 bits
E_{elec}	50 nJ/bit
ε_{amp}	100 pJ/bit/m^2
ε_{fs}	0.0013 pJ/(bit×m^4)
E_{Df}	5 nJ/bit

TABLE 3: Initial parameters of NQACO.

Parameter	Value
Number of individuals	80
Pheromone track intensity	2
Visibility parameter	2
Pheromone volatilization coefficient	0.9

TABLE 4: Initial parameters of GA.

Parameter	Value
Number of individuals	80
Crossover probability	0.7
Mutation probability	0.05
Computing era	0.9

TABLE 5: Initial parameters of SA.

Parameter	Value
Starting temperature	300
Cooling factor	0.95
Maximum number of iterations	100

in the information encoding carried by the initial ant will be evenly distributed in the solution space. By repeating the above operation popSize times, an initial population $P = \{p_1, p_2, p_3, \cdots, p_{popSize}\}$ with a population size of popSize can be obtained.

4.3. Construction of the Fitness Function. In this paper, the overall goal of optimizing the entire WAMRN is to minimize the entire network's energy dissipation during data transmission to extend the network's life as much as possible. Therefore, in the optimization process, the wireless communication nodes with higher residual energy, smaller communication distance within the cluster, and closer to the BS are more suitable to be selected as cluster heads.

In the process of heuristic optimization algorithm to find the optimal cluster head selection scheme, the fitness function plays a very important role, because the fitness function can be used to measure the efficiency of the algorithm when searching for the optimal cluster head selection scheme. Suppose the expected number of cluster heads in WAMR is c, n_j represents the quantity of member nodes in j^{th} net-

work cluster, $D(CH_j, BS)$ and $D(MEM_i, CH_j)$, respectively, represent the distance from j^{th} cluster head to the BS and the distance from i^{th} member node to j^{th} cluster head node. Thus, the fitness function in NQACO is defined as follows:

$$\text{fitness} = f_{CH} + f_{MEM}, \quad (12)$$

where $f_{CH} = \sum_{j=1}^{c} f_{CH}^j$, f_{CH} is the energy consumption of the jth cluster head in the process of one information transmission, and it can be calculated with the help of the following:

$$f_{CH}^j = E_{Tx}(k, d_{toBS}) + n_j E_{Rx-ele}(k) + n_j E_{Fs}(k), \quad (13)$$

$$d_{toBS} = \frac{1}{c}\left(\sum_{i=1}^{c} D(CH_i, BS)\right). \quad (14)$$

In formula (12), $f_{MEM} = \sum_{j=1}^{c} f_{MEM}^j$, it represents the energy consumption of member nodes. The calculation process of f_{MEM}^j is as follows:

$$f_{MEM}^j = n_j E_{Tx}(k, d_{toCH}), \quad (15)$$

$$d_{toCH} = \frac{1}{n_j}\sum_{i=1}^{n_j} D(MEM_i, CH_j). \quad (16)$$

4.4. Mobile Strategy and Positivity Update. To solve the clustering problem of WAMRN, before adjusting the position of individual ants in NQACO, the pheromone on the path needs to be updated. The corresponding update formulas are as follows:

$$\tau_{i,0}(t+1) = \rho \cdot \tau_{i,0}(t) + \Delta\tau, \quad (17)$$

$$\tau_{i,1}(t+1) = \rho \cdot \tau_{i,1}(t) + \Delta\tau, \quad (18)$$

where ρ is the pheromone volatilization coefficient, and its value range is $[0, 1]$, where $\Delta\tau = 1/\text{fitness}(x_{best})$, fitness($x_{best}$) represents the network energy consumption corresponding to the optimal clustering scheme for each generation.

After the pheromone update is completed, it is necessary to adjust the movement of the ant by calculating the transition probability P_{ij} of the ant. The calculation method of transition probability P_{ij} is as follows:

$$p_{ij}(t) = \frac{\tau_{ij}^{\lambda}(t)\eta_{ij}^{\mu}(t)}{\tau_{i0}^{\lambda}(t)\eta_{i0}^{\mu}(t) + \tau_{i1}^{\lambda}(t)\eta_{i1}^{\mu}(t)}, \quad (19)$$

where τ_{ij} and η_{ij}, respectively, represent the pheromone track intensity and visibility parameters. Variable t represents the iteration times of the algorithm, i represents the quantity of steps the ant has taken, and $j \in \{0, 1\}$ represents the two positions that an individual ant may choose during the ith step.
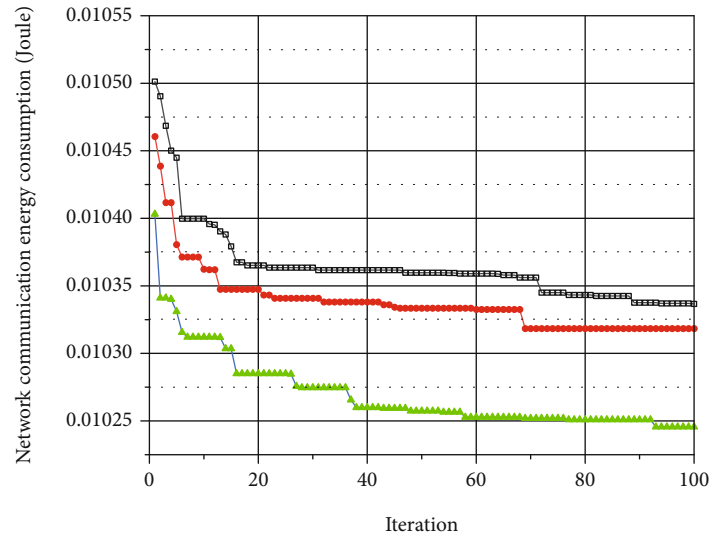
(a)
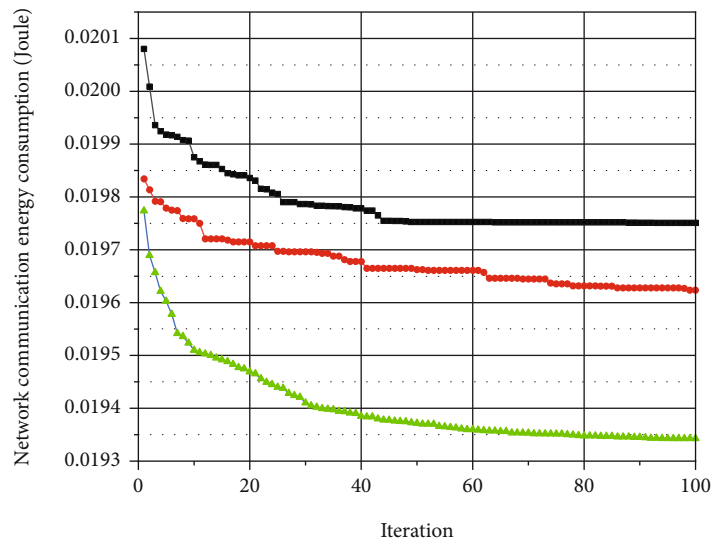
(b)
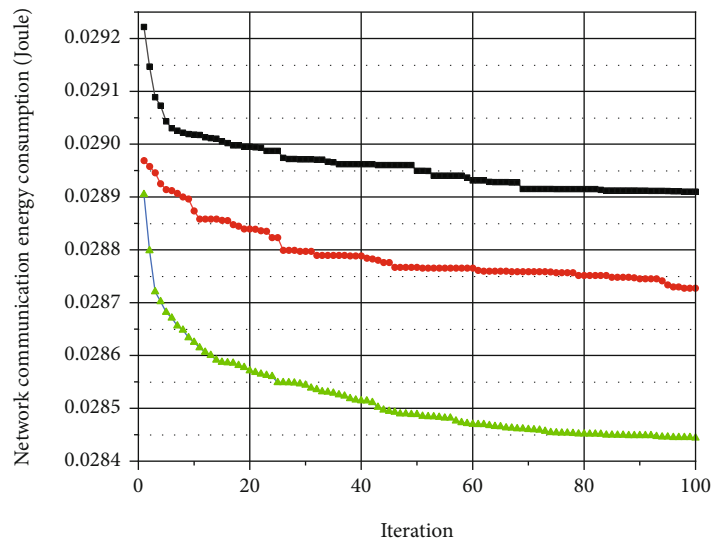
(c)

Figure 4: Continued.
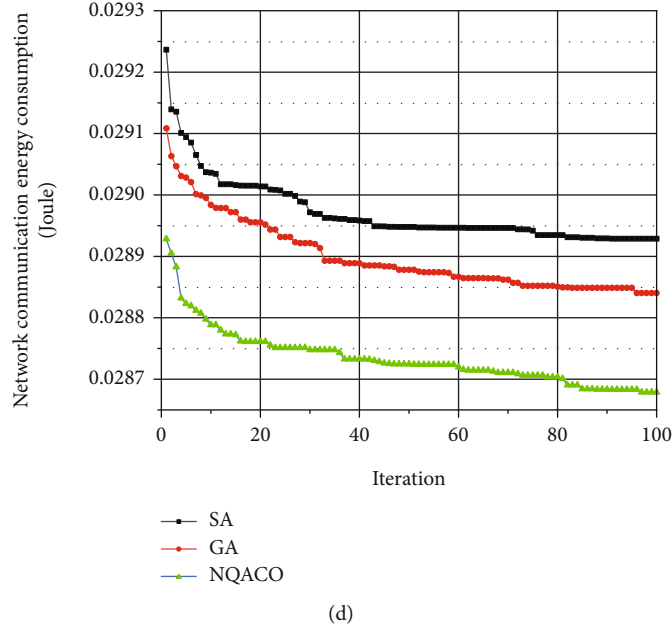
(d)

FIGURE 4: Variation of energy consumption with different number of wireless communication nodes: (a) 100 nodes; (b) 200 nodes; (c) 300 nodes; (d) 400 nodes.

4.5. Variation of Quantum Bits. The quantum bits act as a guide for the individuals in NQACO to move in a globally optimal direction. After each individual in the ant colony change its positions, all the qubit on an ant is required to be updated base on the optimization scheme in the previous iteration. The update process is indicated as follows:

$$
\begin{bmatrix} \alpha_l^{\text{new}} \\ \beta_l^{\text{new}} \end{bmatrix} = \begin{bmatrix} \cos\theta & -\sin\theta \\ \sin\theta & \cos\theta \end{bmatrix} \begin{bmatrix} \alpha_l \\ \beta_l \end{bmatrix}, \tag{20}
$$

where α_l^{new} and β_l^{new} are the probability amplitudes of qubit's corresponding state after the update. α_l and β_l are the probability amplitudes before the update. The size and direction of the rotation angle $\theta_l = S(\alpha_l\beta_l)\Delta\theta_l$ are obtained from Table 1.

In Table 1, $z_{\text{best}}^{\text{old}}$ represents the optimal cluster routing scheme generated by the previous generation, and T and F represent true and false in Boolean algebra, respectively.

4.6. Niche Based on Exclusion Mechanism. This paper mainly uses niche technology based on the crowding mechanism to classify the individuals in the ant colony for obtaining a desirable scheme of clustering. The basic idea stems from the fact that in a limited living environment, in order to survive, various creatures must compete with each other for various limited living resources. Specifically, it is first necessary to determine a crowding factor CF and then randomly select 1/CF ant individuals from the ant colony as crowding individuals and then calculate the correlation between other unselected ant individuals and the crowding individuals. Since the code carried by an individual ant is a quantum code, it can be regarded as a matrix. Therefore, the correlation between two individuals in an ant population can be

obtained by calculating the correlation between the encoding matrices representing the two individuals. The calculation method of interindividual correlation is shown as follows:

$$
R(A, B) = \frac{C(A, B)}{\sqrt{V[A] \times V[B]}}, \tag{21}
$$

where A is the crowding individuals, B is other individuals, $C(A, B)$ is the covariance of A and B, and $V(A)$ and $V(B)$ are the variances of A and B, respectively.

Assuming that the correlation between two individuals is higher than the average value of the correlation between individuals in the colony, based on the exclusion mechanism, the individual with the lower fitness value of the two ants will be replaced by the individual with the higher fitness value.

4.7. Termination Condition. If NQACO runs to the set maximum number of iterations, the clustering scheme carried by the individual with the best fitness value will be output. Otherwise, the iterative optimization is continued.

5. Simulation

To verify the optimization effectiveness of NQACO for the clustered routing problem in WAMRN, this paper compares NQACO with GA; SA under different conditions and through MATLAB simulations, total energy consumption generated during data transmission in the network is used as the evaluation metric. The WAMRN scenario simulated in this paper is static, and the concrete environmental parameters are shown in Table 2.

In the following simulation, the maximum number of iterations MAXGEN of the four algorithms for comparison

(a)

(b)

(c)

(d)
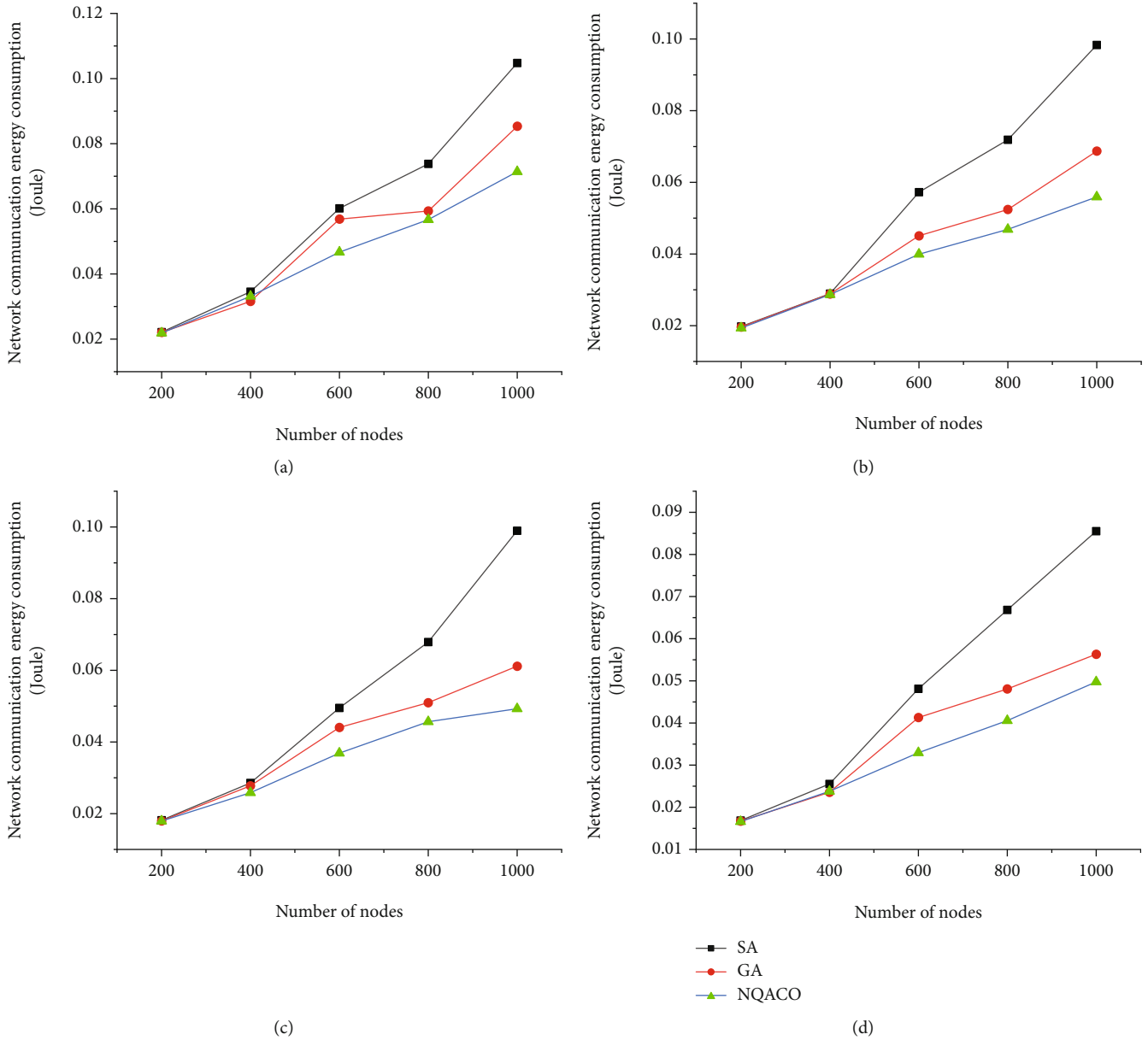
FIGURE 5: Variation of total network energy consumption with different cluster head ratios: (a) 5% cluster heads; (b) 10% cluster heads; (c) 15% cluster heads; (d) 20% cluster heads.

is set to 100 rounds. Noting that different algorithms have different initial parameters, to ensure that these four algorithms can be in their respective optimal optimization states, the specific initial parameter settings of each algorithm are shown in Tables 3–5.

In the simulation experiment of Figure 4, each algorithmic optimization process was repeated 50 times. The corresponding value in the line chart was the average value of 50 simulations.

Figure 4 shows the optimization effect of these four algorithms on the total energy consumed of WAMRN when the network contains 100, 200, 300, and 400 wireless communication nodes, and the proportion of cluster heads in each final clustering scheme is 10%. From the trend of the curves in Figures 4(a)–4(d), although the total energy consumption

of the three algorithms varies significantly during the first 60 iterations, the network optimized by NQACO is always lower than the GA and SA in terms of total energy consumption. In addition, the advantage of NQACO over the other two algorithms becomes more and more evident as the number of iterations increases.

Figure 5 shows the comparison between NQACO and the other two algorithms regarding the optimization of the network energy consumption for four cases of 5%, 10%, 15%, and 20% of the quantity of cluster heads in WAMRN with various wireless sensor sizes. In the simulations, each algorithm was run 100 times, and all calculation results were averaged over 50 Monte Carlo runs. From figure (a), it is clear that the total network energy consumption of the WAMRN optimized by NQACO is always less than that of
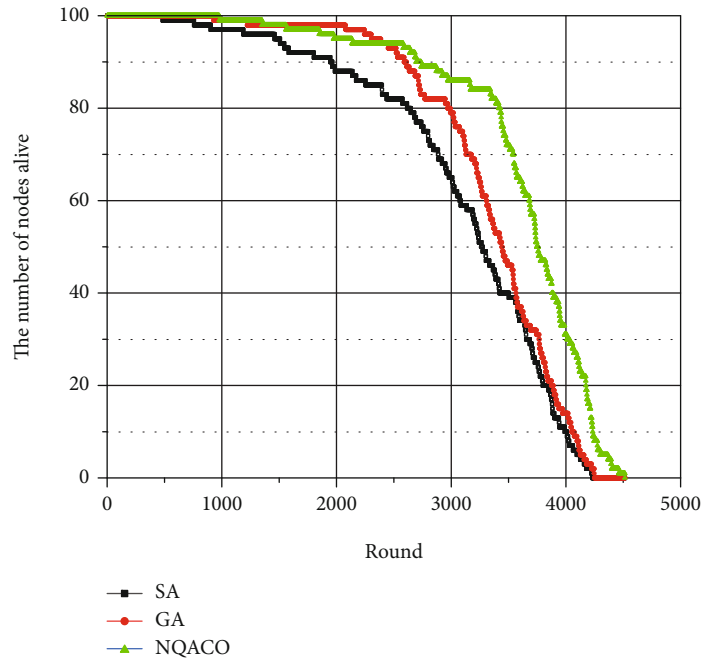
FIGURE 6: The relationship between the quantity of alive nodes and the round.
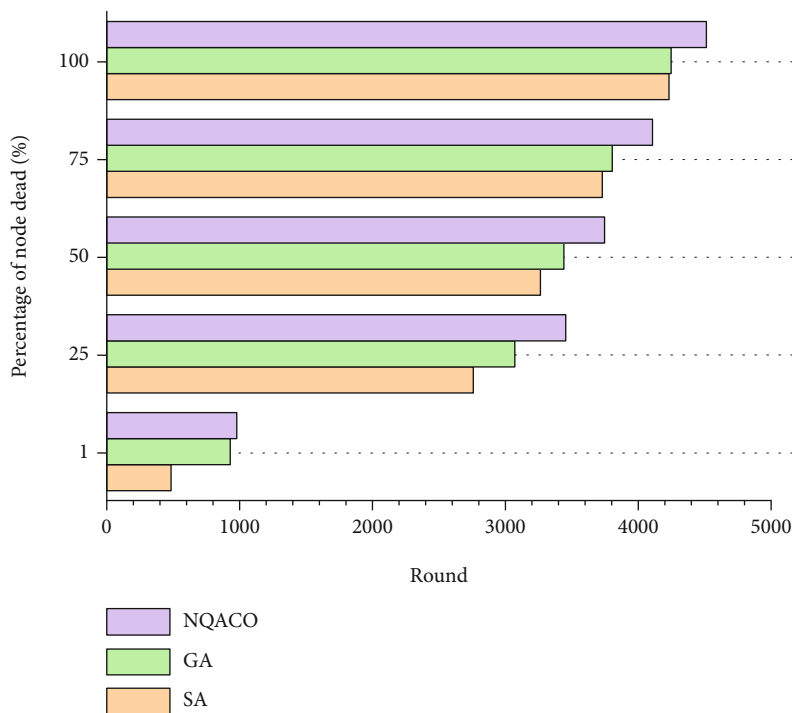
FIGURE 7: The relationship between the death node proportion and the round.

SA and GA for different sizes of wireless sensor numbers. Meanwhile, when the number of wireless communication nodes in WAMRN increases, the overall network energy consumption also increases. The same conclusion can be easily drawn from figures (b), (c), and (d).

Figures 6 and 7 illustrate the relationship between surviving nodes' quantity and round. During the experiment, the WAMRN contains 100 wireless communication nodes,

and the initial energy of each wireless communication node is set to 0.5 J, and then, we record the number of surviving nodes in each round of data transmission and the remaining energy of each node. When a node runs out of energy, we remove it from the network so that the node cannot send or receive messages. Network lifetime is a key indicator of how well balanced the network's energy consumption is. The longer the network lifecycle, the more balanced the

network energy consumption, and the better the performance of the routing protocol is proven. Otherwise, the network energy consumption is unbalanced. From Figures 6 and 7, it can be seen that the WAMRN after SA and GA optimization starts to have wireless communication nodes die at rounds 484 and 929, respectively; however, NQACO effectively delays the death of the first node of the network until round 978. Moreover, after round 2388, it can be seen that after NQACO optimization, the number of surviving wireless communication nodes in WAMRN is always more than the other two algorithms. When all 100 nodes die due to energy exhaustion, the network after NQACO optimization has more data transmission rounds than GA and SA with more than 6.3% and 6.7%, respectively.

Through the comparative analysis of the above simulation experiments, it can be seen that NQACO introduces the chaos operator, which makes use of the randomness and convenience of chaotic variables so that the individuals in the ant colony can be evenly distributed in the solution space, which significantly enhances the algorithm's optimality finding ability and prevents NQACO from falling into local optimum prematurely like GA and SA. Meanwhile, the ants in NQACO adopt quantum bit-based coding, which introduces the quantum state vector into the coding of the ant colony algorithm to avoid the phenomenon of premature convergence. Overall, the NQACO proposed in this paper always has better performance in reducing the network's total energy consumption than GA and SA for the different number of wireless communication nodes.

6. Conclusions

In this paper, a clustering model is proposed to reduce energy consumption and prolong the network lifetime in WAMRN by selecting optimal cluster heads for efficient use of energy. The optimization problem of this model has been shown to be NP-hard, so we propose a new NQACO algorithm to optimize it. Through simulation experiments, the effectiveness and efficiency of the NQACO algorithm in optimizing and reducing the total network energy consumption are verified. The simulation results indicate that our proposed NQACO scheme has lower communication energy consumption than the traditional GA and SA schemes and has more advantages in extending the lifetime of WAMRN.

Data Availability

The datasets generated and analyzed during the current study are available from the corresponding author on reasonable request.

Additional Points

Additional Information. Correspondence and requests for materials should be addressed to Y.Z.

Conflicts of Interest

The authors declare no competing interests.

Authors' Contributions

J.L. and Y.Z. conceived and designed the study. J.L. and H.Q. performed the experiments. J.L. and H.Q. wrote the paper. J.L., Y.L., and J.Z. reviewed and edited the manuscript. All authors read and approved the manuscript.

Acknowledgments

References

[1] Y. Liu, J. Liu, and Y. Ke, "A detection and recognition system of pointer meters in substations based on computer vision," *Measurement*, vol. 152, article 107333, 2020.

[2] E. Kochneva and A. Sukalo, "Comparison of estimates calculated on the energy flow problem basis and using testing equations method," *MATEC Web of Conferences*, vol. 208, 2018.

[3] X. Wu, X. Shi, Y. Jiang, and J. Gong, "A high-precision automatic pointer meter reading system in low-light environment," *Sensors*, vol. 21, no. 14, 2021.

[4] A. I. Kawoosa and D. Prashar, "A review of cyber securities in smart grid technology," in *2021 2nd International Conference on Computation, Automation and Knowledge Management (ICCAKM)*, pp. 151–156, Dubai, United Arab Emirates, 2021.

[5] Y. Yu, B. Xue, Z. Chen, and Z. Qian, "Cluster tree topology construction method based on PSO algorithm to prolong the lifetime of ZigBee wireless sensor networks," *EURASIP Journal on Wireless Communications and Networking*, vol. 1, 2019.

[6] F. Sales, Y. Marante, A. Vieira, and E. Silva, "Energy consumption evaluation of a routing protocol for low-power and lossy networks in mesh scenarios for precision agriculture," *Sensors*, vol. 20, no. 14, p. 3814, 2020.

[7] M. A. Alharbi, M. Kolberg, and M. Zeeshan, "Towards improved clustering and routing protocol for wireless sensor networks," *EURASIP Journal on Wireless Communications and Networking*, vol. 1, 2021.

[8] A. Lipare, D. R. Edla, and R. Dharavath, "Energy efficient fuzzy clustering and routing using BAT algorithm," *Wireless Networks*, vol. 27, no. 4, pp. 2813–2828, 2021.

[9] D. Karaboga, S. Okdem, and C. Ozturk, "Cluster based wireless sensor network routing using artificial bee colony algorithm," *Wireless Networks*, vol. 18, no. 7, pp. 847–860, 2012.

[10] S. Augustine and J. P. Ananth, "Taylor kernel fuzzy C-means clustering algorithm for trust and energy-aware cluster head selection in wireless sensor networks," *Wireless Networks*, vol. 26, no. 7, pp. 5113–5132, 2020.

[11] G. van de Kaa, T. Fens, J. Rezaei, D. Kaynak, Z. Hatun, and A. Tsilimeni-Archangelidi, "Realizing smart meter connectivity: analyzing the competing technologies power line communication, mobile telephony, and radio frequency using the best worst method," *Renewable and Sustainable Energy Reviews*, vol. 103, pp. 320–327, 2019.

[12] H. Chen and L. Chang, "Design and implementation of a ZigBee-based wireless automatic meter reading system," *Przegląd Elektrotechniczny (Electrical Review)*, vol. 88, no. 1B, pp. 64–68, 2012.

[13] L. Zhao, S. Qu, and W. Zhang, "Design of multi-channel data collector for highway tunnel lighting based on STM32 and Modbus protocol," *Optik*, vol. 213, article 164388, 2020.

[14] J. Sun, Q. Wu, F. Han, Y. Liang, B. Sun, and Y. Wang, "Design and implementation of remote intelligent meter reading system," in *2017 Chinese Automation Congress (CAC)*, pp. 3511–3516, Jinan, China, 2017.

[15] A. Viswanathan, N. B. Sai Shibu, S. N. Rao, and M. V. Ramesh, "Security challenges in the integration of IoT with WSN for smart grid applications," in *2017 IEEE International Conference on Computational Intelligence and Computing Research (ICCIC)*, pp. 1–4, Coimbatore, India, 2017.

[16] L. Hou and H. Qu, "Automatic recognition system of pointer meters based on lightweight CNN and WSNs with on-sensor image processing," *Measurement*, vol. 183, article 109819, 2021.

[17] N.-Q. Nhan, M.-T. Vo, T.-D. Nguyen, and H.-T. Huynh, "Improving the performance of mobile data collecting systems for electricity meter reading using wireless sensor network," in *The 2012 International Conference on Advanced Technologies for Communications*, pp. 241–246, Hanoi, 2012.

[18] J. Liu, Z. Zhao, J. Ji, and M. Hu, "Research and application of wireless sensor network technology in power transmission and distribution system," *Intelligent and Converged Networks*, vol. 1, no. 2, pp. 199–220, 2020.

[19] S. Lineykin, M. Sitbon, and A. Kuperman, "Design and optimization of low-temperature gradient thermoelectric harvester for wireless sensor network node on water pipelines," *Applied Energy*, vol. 283, article 116240, 2021.

[20] H. Singh and D. Singh, "Hierarchical clustering and routing protocol to ensure scalability and reliability in large-scale wireless sensor networks," *The Journal of Supercomputing*, vol. 77, no. 9, pp. 10165–10183, 2021.

[21] M. Radhika and P. Sivakumar, "Energy optimized micro genetic algorithm based LEACH protocol for WSN," *Wireless Networks*, vol. 27, no. 1, pp. 27–40, 2021.

[22] R. R. Sahoo, A. R. Sardar, M. Singh, S. Ray, and S. K. Sarkar, "A bio inspired and trust based approach for clustering in WSN," *Natural Computing*, vol. 15, no. 3, pp. 423–434, 2016.

[23] W. Kiran, S. Smys, and V. Bindhu, "Clustering of WSN based on PSO with fault tolerance and efficient multidirectional routing," *Wireless Personal Communications*, vol. 121, no. 1, pp. 31–47, 2021.

[24] A. Rajasekaran and V. Nagarajan, "Cluster-based wireless sensor networks using ant colony optimization," in *International Conference on Intelligent Data Communication Technologies and Internet of Things (ICICI)*, pp. 42–55, Cham, 2018.

[25] M. N. Halgamuge, M. Zukerman, K. Ramamohanarao, and H. L. Vu, "An estimation of sensor energy consumption," *Progress in Electromagnetics Research B*, vol. 12, pp. 259–295, 2009.

[26] P. K. Batra and K. Kant, "LEACH-MAC: a new cluster head selection algorithm for wireless sensor networks," *Wireless Networks*, vol. 22, no. 1, pp. 49–60, 2016.

[27] C. Li, Y. Liu, J. Xiao, and J. Zhou, "MCEAACO-QSRP: a novel QoS secure routing protocol for Industrial Internet of Things," *IEEE Internet of Things Journal*, 2022.

[28] W. R. Heinzelman, A. Chandrakasan, and H. Balakrishnan, "Energy-efficient communication protocol for wireless microsensor networks," in *Proceedings of the 33rd Hawaii International Conference on System Sciences*, p. 10, Maui, HI, USA, 2000.

Research Article

Prognostics and Predictive Maintenance Optimization Based on Combination BP-RBF-GRNN Neural Network Model and Proportional Hazard Model

Guoqiang Tong,[1,2] **Xinbo Qian** [1,3] **and Yilai Liu**[2,3]

¹Key Laboratory of Metallurgical Equipment and Control Technology, Ministry of Education, Wuhan University of Science and Technology, Wuhan 430081, China
²Hubei Key Laboratory of Mechanical Transmission and Manufacturing Engineering, Wuhan University of Science and Technology, Wuhan 430081, China
³Precision Manufacturing Institute, Wuhan University of Science and Technology, Wuhan 430081, China

Correspondence should be addressed to Xinbo Qian; xinboqian@wust.edu.cn

Owning to the advantage of keeping the operating environment safe, high reliability, and low production cost, predictive maintenance has been widely used in industry and academia. Predictive maintenance based on degeneration state mainly studies the degeneration prediction. However, on account of the error of the sensor and human, condition monitoring data may not directly reflect the true degeneration. The degeneration model with dynamic explanatory covariates which is named as proportional hazard model is proposed to deal with the semi-observed monitoring condition. And the degeneration prediction mainly adopts a single prediction model, which leads to low prediction accuracy. A combination forecasting model can effectively solve the above problem. Compared to the traditional prediction method, the neural network model can use the "black box" characteristic to indirectly construct the degeneration model without complex mathematical derivation. Therefore, we propose a combination BP-RBF-GRNN neural network model which is applied to improve the degeneration prediction with dynamic covariate. Based on the above two aspects, a predictive maintenance optimization framework based on the proportional hazard model and BP-RBF-GRNN neural network model is proposed to improve maintenance efficiency and reduce maintenance costs. The simulation results of thrust ball bearing show that the proposed method can effectively improve the degeneration prediction accuracy and reduce the maintenance cost rate to a certain extent.

1. Introduction

It can improve the reliability of equipment, greatly reduce the maintenance cost, and improve production quality, predictive maintenance (PdM) has been widely used in industry and academia [1, 2]. Engineers and researchers use condition-based monitoring data, mathematical models, and simulation to predict the degeneration process of equipment [3]. Common mathematical models or methods include artificial neural network, Bayesian network, decision tree, linear regression, principal component analysis, and random forest [4]. The data-driven method mines monitor-

ing data to predict potential failure, which can reduce maintenance costs and improve reliability [5]. Machine learning (ML) has currently become an effective tool for PdM applications [4]. It is normally difficult to describe the physical degeneration process accurately by modeling. The neural network model can establish the mapping relationship between input and output without complex mathematical derivation. These neural networks try to replicate the way the neurons in any intelligent organism (like human neurons) are coded to take inputs. And neural networks have been used extensively for classification problems, detection problems, pattern recognition, nonlinear regression, feature

selection, time series prediction, and data normalization. In solar sunshine intensity, the BP neural network model is used to predict solar sunshine intensity [6]. In the water quality, BP neural network can be used to predict the water quality of Yuqiao Reservoir in Tianjin, and the simulation shows that the neural network has a good prediction performance on reservoir water quality [7]. In the ethanol fuel, generalized regression neural network can be used to predict the emission characteristics of ethanol fuel HCCI engine, and the results show that the error of parameter forecasting is controlled within 2% [8]. In water evaporation capacity, GRNN neural network and RBF neural network are used to estimate water evaporation capacity, respectively [9].

The core idea of PdM is to optimize maintenance policy according to some criteria, such as risk, cost, reliability, and availability. The effectiveness of this maintenance strategy is determined by the age at which PdM takes place. "Under-maintenance" will result in a high maintenance cost per unit time. "Over-maintenance" will result in a higher probability of failure and maintenance costs. The common optimization problems include the optimization of the structure, the optimization of maintenance costs, and the optimization of reliability. As for the optimization of the structure, the generalized perturbation-based Stochastic Finite Element Method can be used to optimize the structure of the truss-type [10]. As for the optimization of maintenance costs, a methodology can be proposed to minimize the life cycle maintenance costs and maximize the life cycle quality level of the track-bed [11]. As for the optimization of reliability, the mission reliability model of unmanned aerial vehicles and the measuring method can be used to support mission planning and the design of the structure [12]. The co-optimization of economy and reliability as a new target can be used to improve the reliability of energy supply [13]. A deducing-based reliability optimization method for electrical equipment can be proposed to enhance the reliability of electrical equipment [14]. The traditional method of maintenance reliability analysis includes qualitative failure mode, tree, and hazard analysis. And the common method of reliability assessment is the Bayesian approaches, reliability-based design optimization tools, multivariate analyses, and fuzzy set theory [15]. The optimization object normally includes reliability, failure rate, remaining useful life, and expected cost per unit. The expected cost per unit can normally be used as the optimization object to take maintenance activity [16].

This paper proposes a predictive maintenance optimization framework based on the proportional hazard model and BP-RBF-GRNN neural network model to improve the maintenance efficiency and reduce the maintenance cost. Owing to the accuracy of the sensor or complicated monitoring environment, the condition monitoring data may not directly reflect the degree of degeneration. Life data and condition monitoring values must be considered comprehensively. To solve the above problem, we adopt the degeneration modeling with dynamic explanatory covariates, that is, proportional hazard model (PHM), to consider both life data and condition monitoring values to

evaluate the failure rate of mechanical equipment. Compared with the traditional conditional variable or basic reliability model, PHM can reflect the statistical characteristics of the whole sample to reduce the error of failure rate evaluation. In addition, the single prediction model can easily lead to low accuracy, and we adopt the combination BP-RBF-GRNN neural network model to improve the prediction performance. The reason for the choice of sub-prediction model is as follows. The BP neural network model has high prediction accuracy, but it easily falls down the local minimum and has a slow convergence speed. RBF neural network model can solve the problem of local minimum caused by BP, but it has a low prediction accuracy when there are few data samples. The GRNN neural network model has good generalization ability and is good at dealing with prediction under small samples. Therefore, this paper uses a combination forecasting model which contains BP, RBF, and GRNN neural network to predict the degeneration process.

The structure of this paper is as follows. Section 2 is the degeneration model with dynamic covariates. Section 3 is the degeneration prognostics based on covariates prediction via combination BP-RBF-GRNN neural network model. Section 4 is predictive maintenance optimization based on degeneration prognosis. Section 5 is the simulation case study. Section 6 is the conclusion.

2. Degeneration Modeling with Dynamic Covariates

In industrial applications, the risk factor which is called covariate affects the lifetime of the mechanical equipment, and it may influence or indicate the failure time. The covariates can be classified into external and internal variables [17]. The external covariate changes over time, but it is not affected by previous failure. The internal covariate is the measurement of the individual, and it is affected by survival state. As for the research of prognostics and life prediction, probabilistic model using covariates that contains the diagnostic factors and operating environment factors has become one of the indispensable methods [18]. The proportional hazard model is one of the basic theories of the covariate model, which uses the historical failure data to build the baseline hazard function and uses covariate data to build the covariate function.

The hazard rate of WPHM contains the baseline failure rate function and an exponential function including the effect of the monitoring variable, as shown in Equation (1).

$$h(t) = h_0(t) \exp(\gamma_i Z_i), \qquad (1)$$

where the baseline hazard rate $h_0(t)$ is related to the historical lifetime, and the covariate Z_i is a row vector of the monitoring variable at the time t. The covariance coefficient γ_i is a column vector corresponding to the i_{th} monitoring variable.

The baseline failure rate function is shown in Equation (2).

$$h_0(t) = \frac{\beta}{\eta} \left(\frac{t}{\eta} \right)^{\beta-1},\tag{2}$$

where β is the shape parameter and η is the scale parameter.

According to the principle of reliability analysis, the reliability and failure probability density function can be obtained by Equation (3).

$$R(t) = \exp \left[-\int_0^t h(t)dt \right].\tag{3}$$

The maximum likelihood method is constructed to estimate the unknown parameters of WPHM. As shown in Equation (4), the likelihood function is as follows.

$$L(\beta, \eta, \gamma) = \prod_{i=1}^n f(t_i) \prod_{j=1}^m R(t_i),\tag{4}$$

where n is the number of failure samples and m is the number of suspension samples.

The optimal solution of the parameters can be obtained by solving the partial derivatives of Equation (5).

$$L(\beta, \eta, \gamma) = \prod_{i=1}^n \frac{\beta}{\eta} \left(\frac{t_i}{\eta} \right)^{\beta-1} \exp \left(\gamma Z_{t_i} \right) \prod_{j=1}^{n+m} \exp \left[-\left(\frac{t_j}{\eta} \right)^{\beta} \exp \left(\gamma Z_{t_j} \right) dt \right].\tag{5}$$

Since the condition monitoring data measured by the various sensors can partially reflect the actual degeneration state, the monitoring data can be regarded as dynamic covariates to build a degeneration model. The degeneration model based on monitoring data is as follows [19]. We assume that $Z_i(t_{ij})$ can be the observed condition monitoring measurements for the unit i at the time t_{ij}, where $i = 1, \cdots, n$, $j = 1, \cdots, m$, n is the number of units, and m is the number of measurement points for unit i. $Z_i(t) = [Z_{i1}(t), \cdots, Z_{ik}(t)]$ is a vector of dynamic covariate observation, where $k = 1, \cdots, p$, and p is the number of the dynamic covariate. Therefore, $Z_i(t) = \{Z_i(T), 0 \le T \le t\}$ represents the history of dynamic covariate process for unit i at time t. In conclusion, $Z(t) = \{Z_1(t), \cdots, Z_n(t)\}$ is the history of the dynamic covariate process from time 0 to time t for all units n.

3. Degeneration Prognostics Based on Covariates Prediction via Combination BP-RBF-GRNN Neural Network Model

3.1. Prediction Sub-Model

3.1.1. BP Neural Network. As shown in Figure 1, the back-propagation (BP) neural network is a feed-forward neural network, which is one of the common neural networks and has good learning ability. The learning rule is to constantly adjust the weight and threshold of network connection by the steepest descent method [20]. But the method of obtaining the optimal parameters with the gradient descent can easily fall into local minimum [21].

The training process of BP neural network is as follows [22, 23].

Step 1. Initialize parameters of BP network.

It is needed to confirm the weight, the threshold, and the number of neurons in each layer.

Step 2. Calculate the j_{th} neuron of output H in the hidden layer.

$$H_j = f \left(\sum_{i=1}^n w_{ij} X_i - a_j \right),\tag{6}$$

where $X = [X_1, \cdots, X_i, \cdots, X_n]'$ is a input matrix, $i = 1, 2, 3, \cdots, n$, n is the length of time series for the covariate, and it is also the number of input layer neurons. $X_i = [x_1, \cdots, x_{s_1}]$ represents the monitoring value of covariate at time i for all samples s_1. $j = 1, 2, \cdots, g$, g is the number of neurons in the hidden layer. $O = [O_1, \cdots, O_k, \cdots, O_m]'$ is an output matrix, $k = 1, 2, 3, \cdots, m$, m is the length of time series for the covariate, and it is also the number of output layer neurons. $O_k = [o_1, \cdots, o_{s_2}]$ represents the predicted value of covariate at time k for all samples s_2.

Step 3. Calculate the k_{th} neuron of output O in the output layer.

$$O_k = f \left(\sum_{j=1}^l H_j w_{jk} - b_k \right).\tag{7}$$

Step 4. Calculate the error E.

$$E = \frac{1}{2} \sum_{k=1}^m (Y_k - O_k)^2,\tag{8}$$

where O_k is the predictive result and Y_k is the expected output.

Step 5. Update the weight w.

The weight and threshold of the network should be modified along the negative gradient direction with the fastest function decline.

The weight w_{jk} is updated by Equation (9).

$$w_{jk} = w_{jk} + \eta H_j e_k,\tag{9}$$

where η is the learning rate.

The weight w_{ij} is updated by Equation (10).

$$w_{ij} = w_{ij} + \eta' \left(1 - H_j^2 \right) X(i) \sum_{k=1}^m w_{jk} e_k,\tag{10}$$

where η' is the learning rate.

Step 6. Update the threshold values a and b.
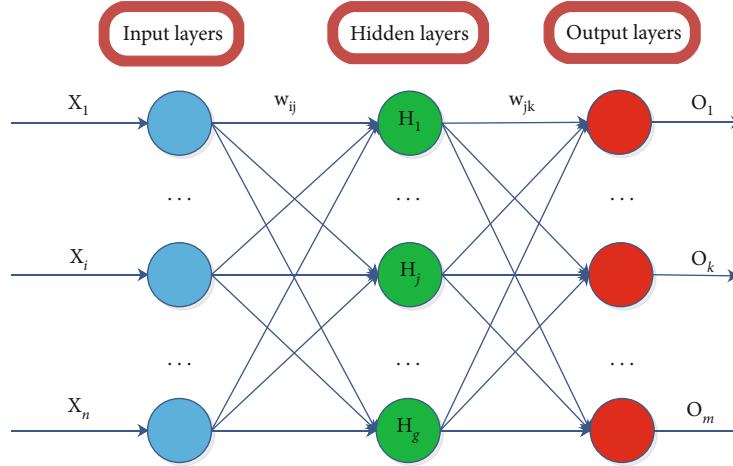
FIGURE 1: The architecture of BP neural network.

The process of updating the threshold is similar to the process of updating weight. The process of updating the threshold values a and b is as follows.

$$b_k = b_k + \eta e_k, \tag{11}$$

$$a_j = a_j + \eta' \left(1 - H_j^2\right) \sum_{k=1}^{m} w_{jk} e_k. \tag{12}$$

Step 7. Determine the requirement of iteration.

If the iteration requirement is not met, it should repeat the process from Step 2 to Step 6. Otherwise, trained neural network parameters can be outputted.

3.1.2. RBF Neural Network. As shown in Figure 2, the radial basis function (RBF) is a two-layer feed-forward network with a single hidden layer [24], which can approximate the nonlinear function with arbitrary precision and realize the global optimization in theory [25]. It is a direct mapping from the input layer to the hidden layer. Therefore, the training time of parameters is shorter than BP neural network. The hidden layer and output layer are connected by the linear weight.

As shown in Equation (13), the radial basis function is used as the node transfer function of the hidden layer.

$$R_j = \exp \left[\frac{\left(X - c_j\right)^T \left(X - c_j\right)}{2\sigma_j^2} \right], \tag{13}$$

where $X = [X_1, \cdots, X_i, \cdots, X_n]'$ is a input matrix, $i = 1, 2, 3, \cdots, n$, n is the length of time series for the covariate, and it is also the number of input layer neurons. $X_i = [x_1, \cdots, x_{s_1}]$ represents the monitoring value of covariate at time i for all samples s_1. R_j is the output of the j_{th} hidden node, c_j is the center of the Gaussian function in the j_{th} hidden node, σ_j is the output standardized variance of the j_{th} hidden node, $j = 1, 2, \cdots, g$, and g is the number of neurons in the hidden layer. $O = [O_1, \cdots, O_k, \cdots, O_m]'$ is an output matrix, $k = 1, 2, 3, \cdots, m$, m is the length of time series for the covariate, and

it is also the number of output layer neurons. $O_k = [o_1, \cdots, o_{s_2}]$ represents the predicted value of covariate at time k for all samples s_2.

The k_{th} neuron output O_k in the output layer is shown in Equation (14).

$$O_k = \sum_{j=1}^{l} w_{jk} \bullet R_j, \tag{14}$$

where l is the number of neurons in the hidden layer, $k = 1, 2, 3, \cdots, m$, and m is the number of neurons.

3.1.3. GRNN Neural Network. As shown in Figure 3, generalized regression neural network (GRNN) has four layers. GRNN is also a kind of radial basis function neural network [26], which is used to solve the regression problem. It has more advantages than RBF neural network in approximation ability and learning speed. Especially, it has a good effect in prediction under small samples.

Data transmission from the input layer to the pattern layer is direct transmission. In the pattern layer, the transfer function is the radial basis function, as shown in Equation (15).

$$P_i = \exp \left[-\frac{\left(X - X_i\right)^T \left(X - X_i\right)}{2\sigma^2} \right], \tag{15}$$

where $X = [X_1, \cdots, X_i, \cdots, X_n]'$ is a input matrix, $i = 1, 2, 3, \cdots, n$, n is the length of time- series for the covariate, and it is also the number of input layer neurons. $X_i = [x_1, \cdots, x_{s_1}]$ represents the monitoring value of covariate at time i for all samples s_1. P_i is the output of the i_{th} hidden node; σ denotes the smoothing parameter. S_D is the first type of the summation; S_N is the second type of the summation. $O = [O_1, \cdots, O_k, \cdots, O_m]'$ is an output matrix, $k = 1, 2, 3, \cdots, m$, m is the length of time series for the covariate, and it is also the number of output layer neurons. $O_k = [o_1, \cdots, o_{s_2}]$
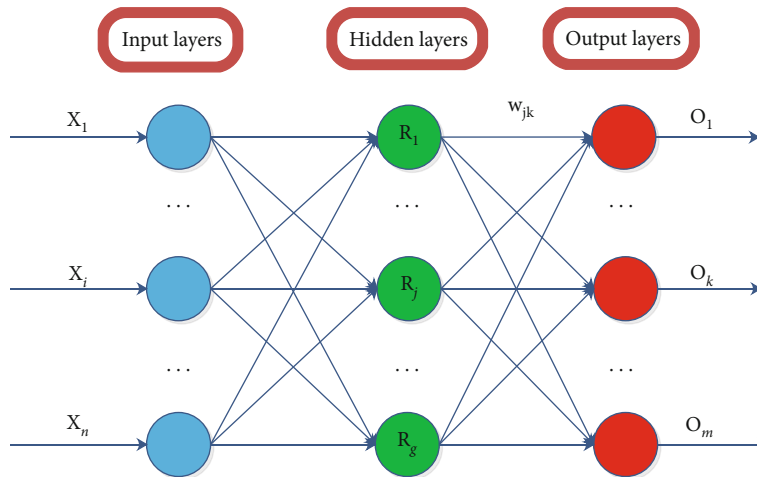
FIGURE 2: The architecture of RBF neural network.
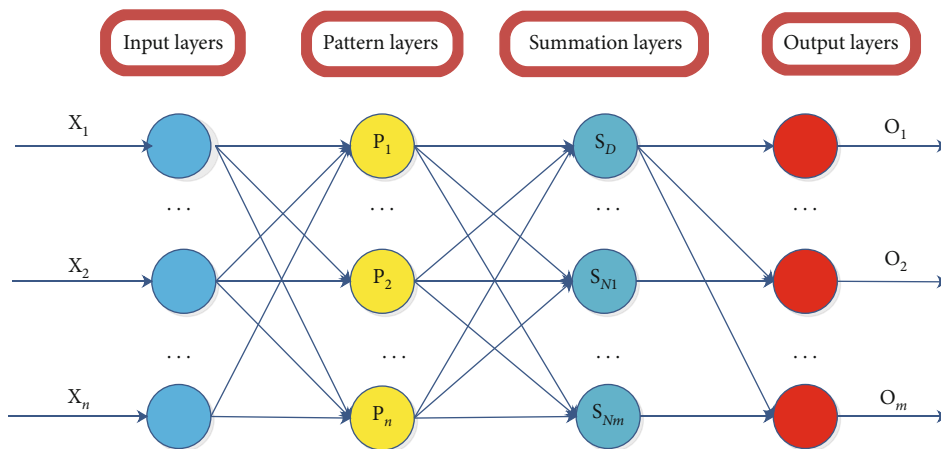
FIGURE 3: The architecture of GRNN neural network.
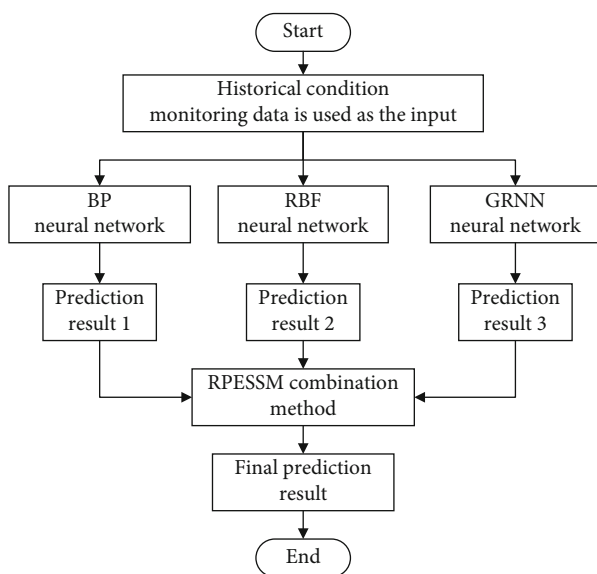
FIGURE 4: Flow chart of the combination forecasting method.

represents the predicted value of covariate at time k for all samples s_2.

There are two summations in the summation layer [27], namely, S_D and S_{NK}.

The first type of summation is shown in Equation (16).

$$S_D = \sum_{i=1}^{n} P_i. \tag{16}$$

The second type of summation is shown in Equation (17).

$$S_{Nk} = \sum_{i=1}^{n} w_{ik} P_i. \tag{17}$$

The output layer can be calculated as shown in Equation (21).

$$O_k = \frac{S_{Nk}}{S_D}. \tag{18}$$
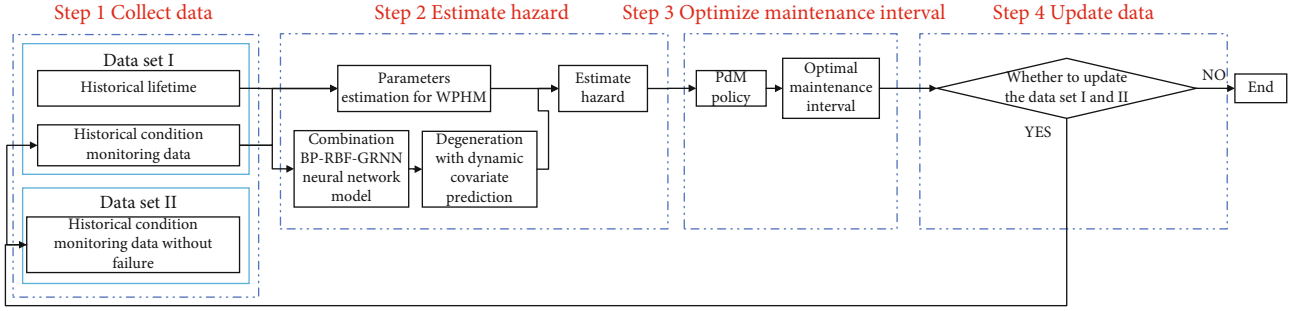
FIGURE 5: Flow chart of the PdM model framework based on combination BP-RBF-GRNN neural network model and proportional hazard model.

TABLE 1: Parameter distribution of covariate model.

Symbol	Normal distribution	Numerical value
μ_0	Mean	-6.031
σ_0^2	Variance	0.346
μ_1	Mean	8.061×10^{-3}
σ_1^2	Variance	1.034×10^{-5}
μ	Mean	0
σ^2	Variance	7.3×10^{-3}

3.2. Combination Method. As shown in Figure 4, three prediction sub-models, respectively, use historical monitoring data to predict the degeneration process, and the final prediction result will be output by the combination method. The combination forecasting model makes use of the characteristics of different sub-models to comprehensively improve the prediction performance. Reciprocal prediction error sum of squares method (RPESSM) can be used as the combination method to predict degeneration process [28, 29]. A small RPESSM value indicates the high performance of the prediction sub-model.

Therefore, y_{1t}, y_{2t}, and y_{3t} show the prediction result of the BP, RBF, and GRNN neural network at the time t, respectively. And e_{1t}, e_{2t}, and e_{3t} are the prediction errors correspondingly. As shown in Equation (19), y_t is the prediction result of the combination BP-RBF-GRNN neural network model at the time t, respectively. As shown in Equations (20) to (22), w_{1t}, w_{2t}, and w_{3t} are the weight coefficients at the time t.

$$\begin{cases} y_t = w_{1t} \bullet y_{1t} + w_{1t} \bullet y_{1t} + w_{1t} \bullet y_{1t} \\ w_{1t} + w_{2t} + w_{3t} = 1 \end{cases}, \quad (19)$$

$$w_{1t} = \frac{e_{1t}^2}{e_{1t}^2 + e_{2t}^2 + e_{3t}^2}, \quad (20)$$

$$w_{2t} = \frac{e_{2t}^2}{e_{1t}^2 + e_{2t}^2 + e_{3t}^2}, \quad (21)$$

$$w_{3t} = \frac{e_{3t}^2}{e_{1t}^2 + e_{2t}^2 + e_{3t}^2}. \quad (22)$$

The role of the weight coefficient allocation is to make prediction sub-model with the highest prediction accuracy play a decisive role in the final prediction result, thus reducing the negative influence of other prediction sub-models. Therefore, the combination forecasting model can overcome the low prediction accuracy of the single prediction sub-model.

4. Predictive Maintenance Optimization Based on Degeneration Prognosis

4.1. The Framework of Predictive Maintenance Optimization. As shown in Figure 5, a PdM optimization framework based on the combination BP-RBF-GRNN neural network model and proportional hazard model is proposed in this section. The first step is to collect historical lifetime and condition monitoring data, which can be divided into two types. Data set I containing historical lifetime and historical condition monitoring data is used as the input of the WPHM and combination BP-RBF-GRNN neural network model for parameter estimation. Data set II containing historical condition monitoring data without failure is used for the performance evaluation of condition forecasting. In the second step, the hazard can be predicted based on both condition forecasting and WPHM. In the third step, the optimal preventive maintenance interval is updated by the PdM policy. At the last step, the optimal maintenance interval will be updated with the updated condition monitoring data and events.

4.2. Predictive Maintenance Optimization Policy Based on Proportional Hazard Model. As shown in Equation (23), a quantitative function of the average cost in a maintenance period for PdM optimization policy is established, which is named as the cost rate function. The PdM policy for the optimal age replacement can be divided into two types [30]. One is to reach the replacement life T under the condition of preventive maintenance, and the other is to reach the actual lifetime τ under the condition of repairing upon failure. Therefore, the cost types can be divided into two categories correspondingly. C_{PM} denotes the cost of preventive maintenance at the maintenance life T and C_{ER} denotes
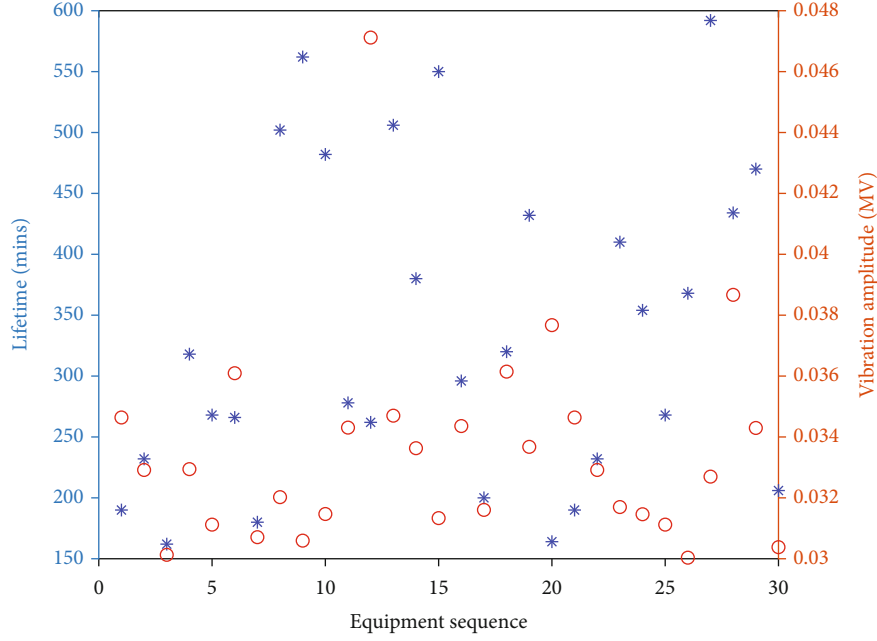
Figure 6: Lifetime data and vibration amplitude of thrust ball bearings.

Table 2: Combination scheme of training set and test set.

Training set	Test set
#2, #3, #4, #5, ⋯, #30	#1
#1, #3, #4, #5, ⋯, #30	#2
#1, #2, #4, #5, ⋯, #30	#3
#1, #2, #3, #5, ⋯, #30	#4
...	...
#1, #2, #3, #4, ⋯, #29	#30

the cost of corrective maintenance at the maintenance life τ. In general, C_{ER} is greater than C_{PM}.

$$\eta_{\text{age}}(T) = \min_{T} \frac{F(T)C_{ER} + (1 - F(T))C_{PM}}{\int_0^T (1 - F(X))dx}, \qquad (23)$$

where the denominator is the average maintenance age, and the numerator is the average maintenance cost in a period. $F(t)$ is the unreliability function which can be obtained by the Weibull distribution proportional hazard model. Owning to the difficult explicit expression by the form of the mathematical formula, it is hard to solve the optimal solution. Therefore, an approximate solution method, namely, the trapezoidal numerical integration method, is used to solve the calculation problem.

5. Simulation Case Study

5.1. Prediction Performance Criteria.
The evaluation index of prediction performance adopts root mean square percentage error (RMSPE) and root mean square error (RMSE) [31].

$$\text{RMSPE} = \sqrt{\frac{1}{N}\sum_{i=1}^{N}\left(\frac{y_i - \widehat{y}_i}{y_i}\right)^2} \times 100\%, \qquad (24)$$

$$\text{RMSE} = \sqrt{\frac{1}{N}\sum_{i=1}^{N}(y_i - \widehat{y}_i)^2}, \qquad (25)$$

where y_i is the actual value, $\widehat{y}_i$ is the prediction, and N is the length of time series. RMSPE is a relative error-index, which shows the deviation between the prediction and the actual value. RMSE reflects the dispersion and concentration of error size and distribution.

5.2. Maintenance Performance Criteria.
To measure the maintenance performance between combination BP-RBF-GRNN neural network model and the traditional prediction model (Bayesian parameter updating prediction model) in PdM policy, we establish the evaluation index, as shown in Equations (26) and (27) [32].

$$R_{T\text{opt}}^i = \left(\frac{T\text{opt}_C^i}{T\text{opt}_P^i} - 1\right) \times 100\%, \qquad (26)$$

where T_{opt} is the optimal maintenance interval. And the letters subscript of "P" indicates the prediction model to be compared, and the letters subscript of "C" indicates the combination BP-RBF-GRNN neural network model. $R_{T\text{opt}}^i$

TABLE 3: Model parameters of BP neural network.

The parameter name	Value or option
P	Input matrix. $(tk/2) \times 29$
T	Output matrix. $(tend - tk/2) \times 1$
Hidden layer nodes (S)	18
Hidden layer nodes transfer function type (TF)	tansig
Output layer neuron transfer function type (TF)	logsig
Training function type (BTF)	traingd
Learning function type (BLF)	learngdm
The max iteration number	7000
Network training goal error	0.01

TABLE 4: Model parameters of RBF neural network.

The parameter name	Value or option
P	Input matrix. $(tk/2) \times 29$
T	Output matrix. $(tend - tk/2) \times 1$
Network training goal error	0.001
Spread of radial basis function	0.01
Maximum number of neurons (MN)	400
Number of neurons to add between displays (DF)	5

TABLE 5: Model parameters of GRNN neural network.

The parameter name	Value or option
P	Input matrix. $(tk/2) \times 29$
T	Output matrix. $(tend - tk/2) \times 1$
Spread of radial basis function	0.01

represents the relative error percentage in maintenance interval under the i_{th} training-test set scheme.

$$R_\eta^i = \left(\frac{\eta_C^i \left(Topt_P^i \right)}{\eta_C^i \left(Topt_C^i \right)} - 1 \right) \times 100\%, \quad (27)$$

where η is the minimum cost rate under the optimal maintenance age. And R_η^i represents the relative error percentage in cost rate the i_{th} training-test set scheme.

5.3. Case Study

5.3.1. Data Sources. As shown in Equation (28) [33], we use the popular covariate model of vibration degeneration by the MATLAB software for the simulation [34]. Equation (29) can be obtained by the logarithm of Equation (36). Table 1 shows the probability distributions of model parameters in Equation (29) [35].

$$S(t) = \varnothing + \theta \exp \left(\beta t + \varepsilon(t) - \frac{\sigma^2}{2} t \right), \quad (28)$$

$$L(t) = \ln \left(S(t) - \varnothing \right) = \theta' + \beta' + \varepsilon(t), \quad (29)$$

where $\theta' \sim N(\mu_0, \sigma_0^2)$, $\beta' \sim N(\mu_1', \sigma_1^2)$, and $\varepsilon(t_i) - \varepsilon(t_{i-1}) \sim N(\mu, \sigma^2)$. $\varepsilon(t)$ follows winner process, and it can be generated by the method of pseudo-random number. Simulation failure threshold is $D = 0.03$ MV [33], simulation length is 600 minutes, and simulation interval is 2 minutes. And we generate 30 group thrust ball bearing vibration signals for the simulation case study. The double ordination of the simulation lifetime data and simulation vibration amplitude is shown in Figure 6.

5.3.2. Experiment Design. As shown in Table 2, to avoid the problem of overfitting, we designed the experiment by the method of leave-one-out cross-validation, and chose 1 group as the test set and another 29 groups as the training set. Therefore, there are 30 training-test set schemes.

We focus on five prediction point values of t_{ki}, $t_{ki} \in \{ 0.1T_{Aj}, 0.3T_{Aj}, 0.5T_{Aj}, 0.7T_{Aj}, 0.9T_{Aj} \}$, which represent the early-stage, early-to-mid stage, mid-stage, mid-to-late stage, and late-stage for each component j, respectively. T_{Aj} is the actual life of component j. As shown in Equations (30)–(32), we use the modified newff MATLAB toolbox to construct the structure of the BP neural network, use the newrb MATLAB toolbox to construct the structure of the RBF neural network, and use the newgrnn MATLAB toolbox to construct the structure of GRNN neural network. And the detailed parameters are determined as shown in Tables 3–5.

$$net = newff (P, T, S, TF, BTF, BLF), \quad (30)$$
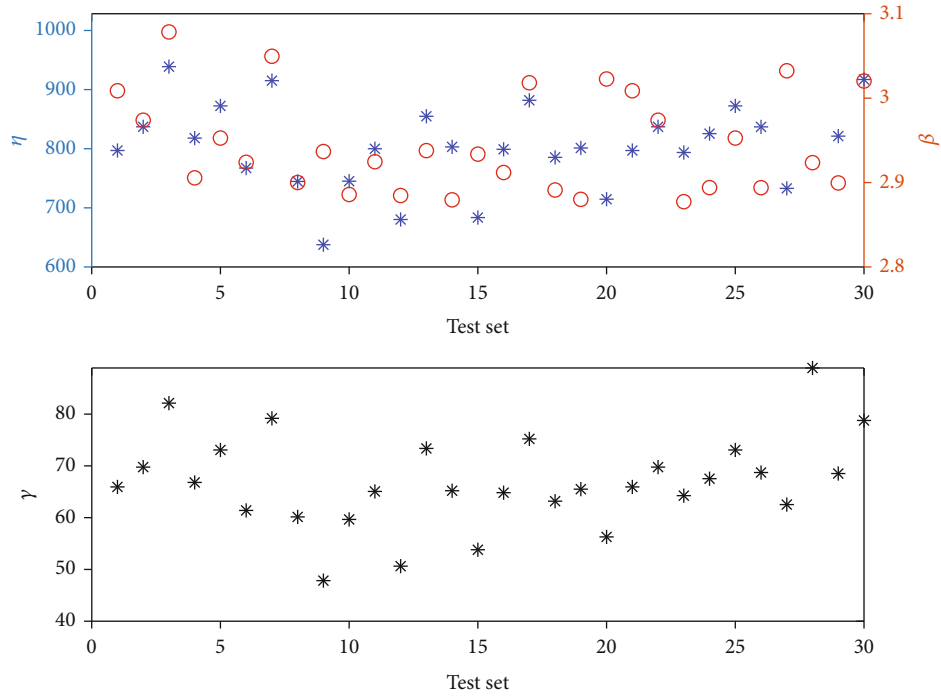
Figure 7: WPHM parameters.

(a)

(b)
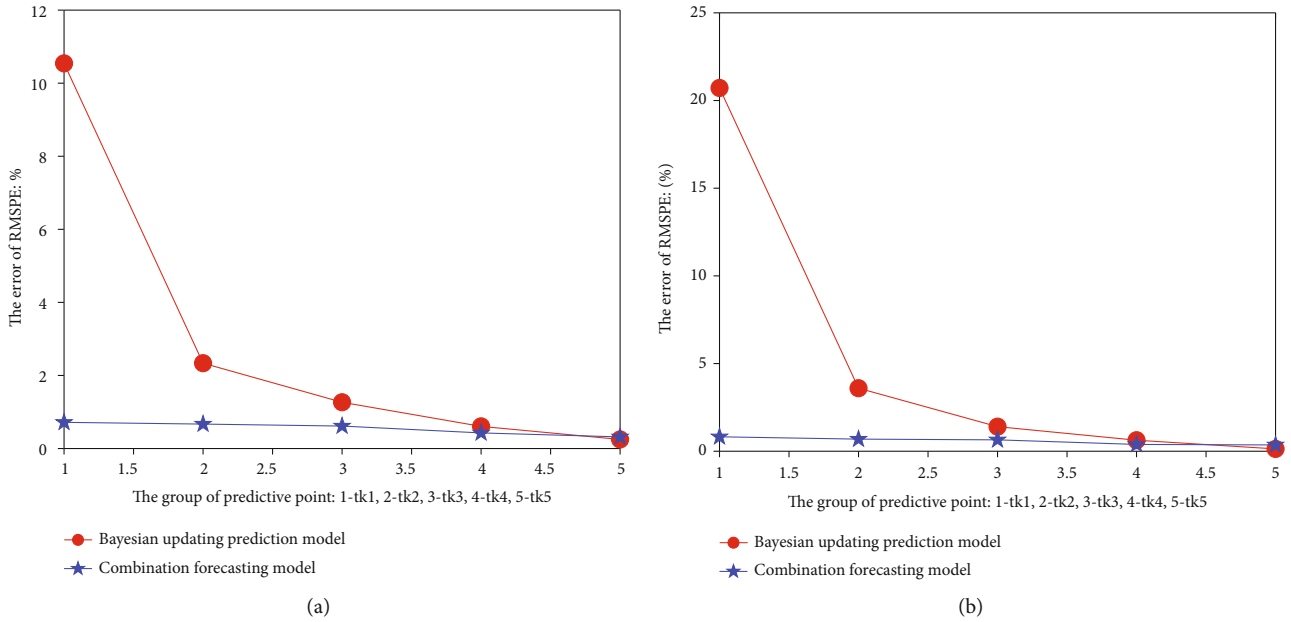
Figure 8: The error of RMSPE. (a) RMSPE mean; (b) RMSPE standard deviation.

$$net = newrb(P, T, goal, spread, MN, DF), \quad (31)$$

$$net = newgrnn(P, T, spread). \quad (32)$$

Where t_k is the prediction start point, t_{end} is the prediction end point, and sample interval is 2 minutes. We take 29 samples of $[0, t_k]$ time series monitoring data as the input vector and 1 sample of $[t_k, t_{end}]$ time series monitoring data as the output vector. Where tansig means hyperbolic tangent

sigmoid transfer function, logsig means log-sigmoid transfer function, traingd means gradient descent backpropagation, learngdm means gradient descent with momentum weight and bias learning function.

5.3.3. Result Analysis. The main WPHM parameters under 30 training-test set schemes, i.e., the covariance coefficient γ, the shape parameter β, and the scale parameter η, are shown in Figure 7.
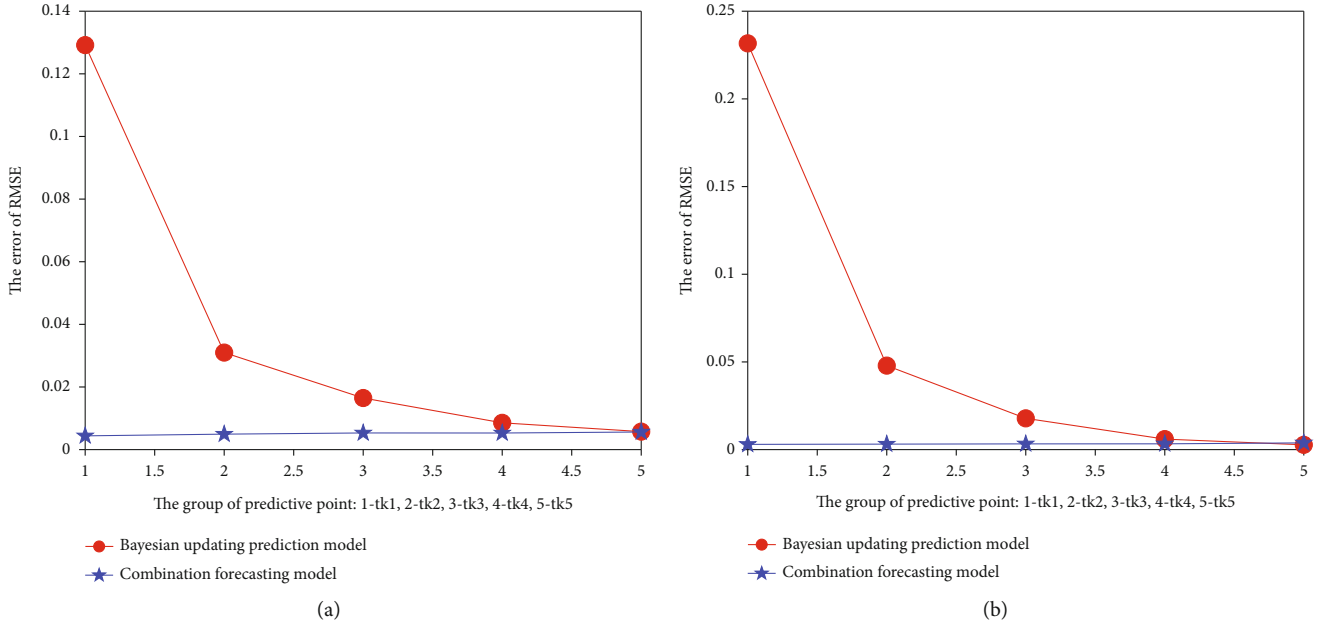
FIGURE 9: The error of RMSE. (a) RMSE mean; (b) RMSE standard deviation.

Figure 8 shows the mean and standard deviation of RMSPE under 30 training-test set schemes, respectively. Figure 9 shows the mean and standard deviation of the RMSE under 30 training-test set schemes, respectively. We can draw two conclusions. One is that the prediction accuracy of the Bayesian parameter updating prediction model and combination BP-RBF-GRNN neural network model can be improved when the prediction point shifts right. The other is that the prediction accuracy of the combination BP-RBF-GRNN neural network model is higher than that of the Bayesian parameter updating prediction model from the early-stage to mid-stage. But the prediction accuracy of two prediction models is nearly equivalent from mid-to-late stage to late-stage.

Figure 10 shows the box diagram of the cost ratio percentage when $C_{PM}/C_{ER} = 0.3$, $C_{PM}/C_{ER} = 0.2$, and $C_{PM}/C_{ER} = 0.1$. Figure 11 shows the box diagram of the maintenance interval percentage when $C_{PM}/C_{ER} = 0.3$, $C_{PM}/C_{ER} = 0.2$, and $C_{PM}/C_{ER} = 0.1$. Figure 12(a) shows the average cost rate percentage with three maintenance ratios under 30 training-test set schemes. Figure 12(b) shows the average maintenance interval percentage with three maintenance ratios under 30 training-test set schemes. Figure 12 shows that the maintenance ratio has a great influence on the average cost percentage and the average maintenance interval percentage from the early-stage to mid-stage. With the increasement of maintenance cost ratio (C_{PM}/C_{ER}), the combination BP-RBF-GRNN neural network model has more advantages than the Bayesian parameter updating prediction model in cost rate percentage and maintenance interval percentage from the early-stage to mid-stage.

To validate the effectiveness of the combination BP-RBF-GRNN neural network model, we have compared the combination BP-RBF-GRNN neural network model to other three single deep learning models which are named the BP, RBF, and GRNN neural network models in prediction performance and maintenance performance. The leave-one-out cross-validation is used as the validation method. The model parameters of the combination BP-RBF-GRNN neural network model are shown in Tables 3–5. RMSE is used as the prediction performance criteria.

Tables 6–8, respectively, show the maintenance performance comparison of cost rate percentage between the single deep learning model and combination BP-RBF-GRNN neural network model. As shown in (27), the cost rate percentage of Tables 6–8 uses the cost of BP, RBF, and GRNN neural network model to be divided by that of the combination BP-RBF-GRNN neural network model, respectively. The value of cost rate percentage in Tables 6–8 is greater than 0, which means that the cost of other three single deep learning models is higher than that of the combination BP-RBF-GRNN neural network model. And if the value of the cost rate percentage is high, the cost of the combination BP-RBF-GRNN neural network model will be low. Tables 9–11, respectively, show the maintenance performance comparison of maintenance interval percentage between the single deep learning model and combination BP-RBF-GRNN neural network model. As shown in (26), the maintenance interval percentage of Tables 9–11 uses the maintenance interval of the combination BP-RBF-GRNN neural network model to be divided by that of the BP, RBF, and GRNN neural network model, respectively. The value of maintenance interval percentage in Tables 9–11 is greater than 0, which means that the maintenance performance of the combination BP-RBF-GRNN neural network model is higher than that of other three single deep

(a)

(b)

(c)
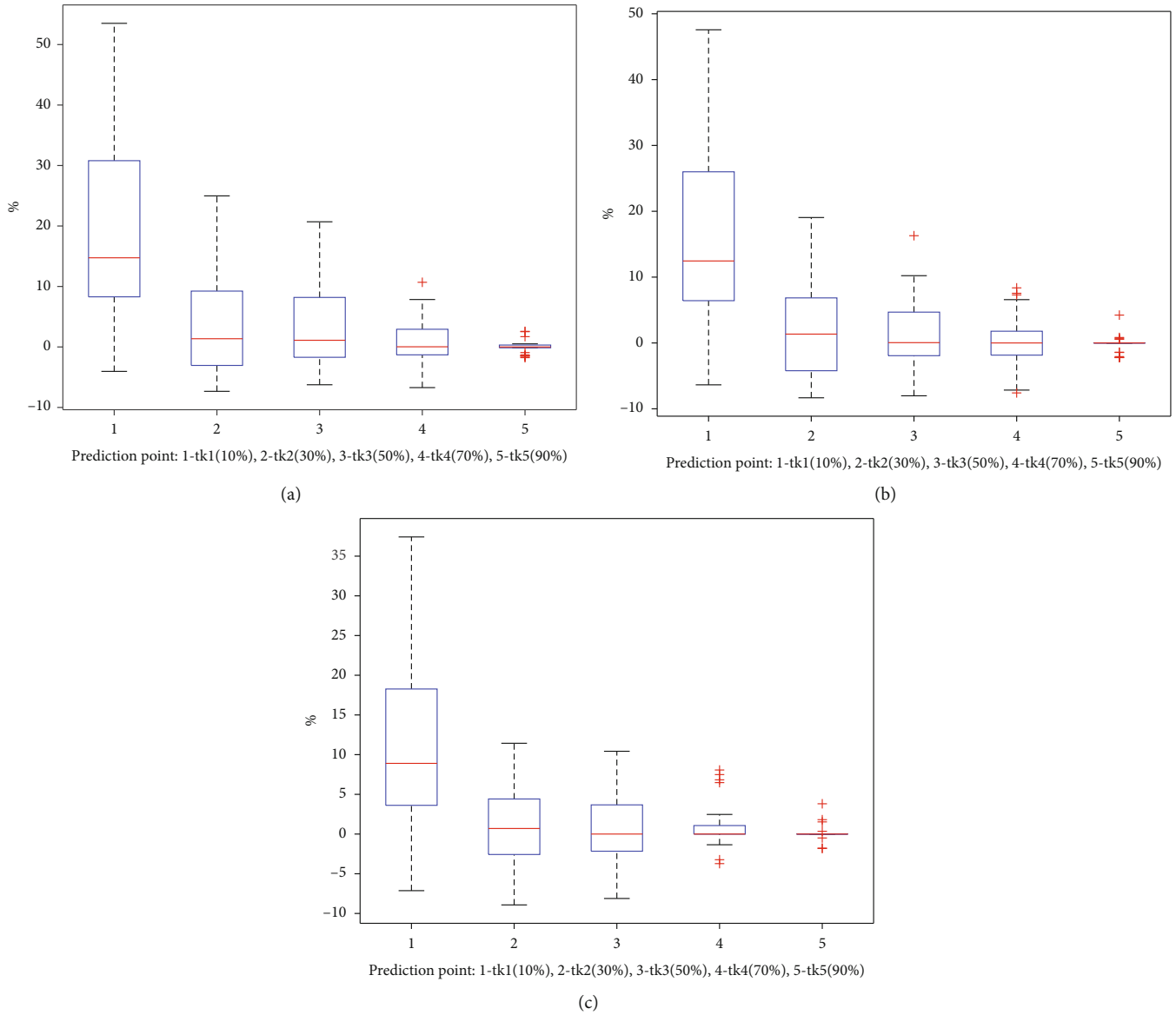
Figure 10: Box diagram of cost rate percentage. (a) Box diagram of cost rate percentage when $C_{PM}/C_{ER} = 0.3$. (b) Box diagram of cost rate percentage when $C_{PM}/C_{ER} = 0.2$. (c) Box diagram of cost rate percentage when $C_{PM}/C_{ER} = 0.1$.

learning models. And if the value of the maintenance interval percentage is high, the maintenance performance of the combination BP-RBF-GRNN neural network model will be good. Table 12 shows the prediction performance comparison of the BP, RBF, GRNN, and combination BP-RBF-GRNN neural network model. Tables 6 and 9 indicate that the cost rate percentage and maintenance interval percentage of the combination BP-RBF-GRNN neural network model from the early-stage to the mid-stage are more advantageous than that of BP. And with the increasement of maintenance cost ratio, the combination BP-RBF-GRNN neural network model has advantages over the BP in cost rate percentage and maintenance interval percentage. Table 7 indicates that the cost rate percentage of the combination BP-RBF-GRNN neural network model is basically equivalent to that of RBF. Table 10 indicates that the maintenance

interval percentage of the combination BP-RBF-GRNN neural network model from the early-stage to the mid-to-late stage is more advantageous than that of RBF. And with the increasement of maintenance cost ratio, the combination BP-RBF-GRNN neural network model has advantages over the RBF in cost rate percentage and maintenance interval percentage. Tables 8 and 11 indicate that the cost rate percentage and maintenance interval percentage of the combination BP-RBF-GRNN neural network model from the early-stage to the mid-stage are more advantageous than those of GRNN. And with the increasement of maintenance rate, the combination BP-RBF-GRNN neural network model is basically equivalent to the GRNN in cost rate percentage and maintenance interval percentage. Table 12 indicates that the prediction accuracy of BP and GRNN can be improved with the predicted point moving right. And RBF

(a)

(b)

(c)
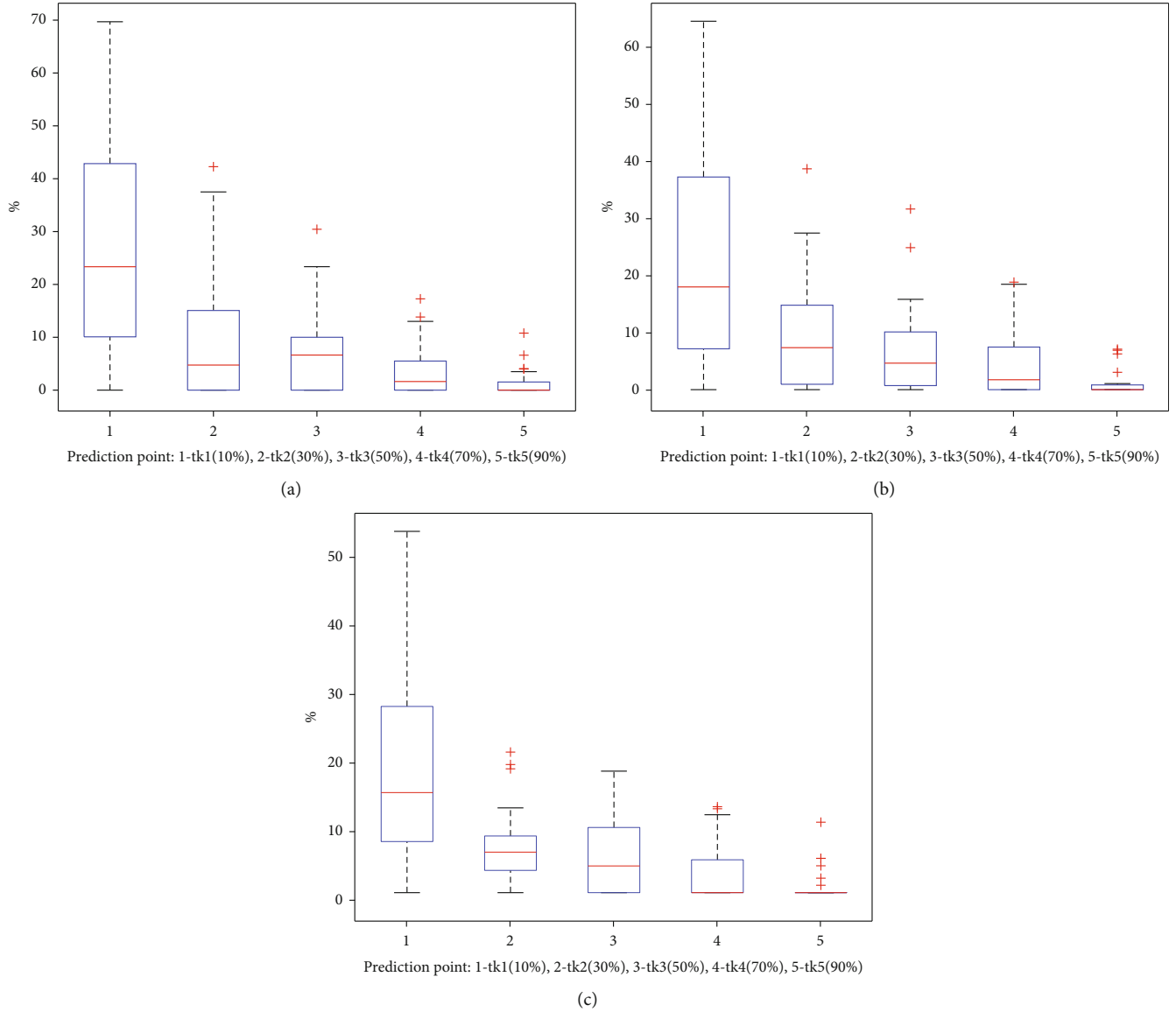
FIGURE 11: Box diagram of maintenance interval percentage. (a) Box diagram of maintenance interval percentage when $C_{PM}/C_{ER} = 0.3$. (b) Box diagram of maintenance interval percentage when $C_{PM}/C_{ER} = 0.2$. (c) Box diagram of maintenance interval percentage when $C_{PM}/C_{ER} = 0.1$.

can control the prediction error at a relatively stable range. It is obvious to find that the prediction accuracy of combination BP-RBF-GRNN neural network model is higher than that of the BP, RBF, and GRNN under five prediction points.

To justify the validity of the proposed method, we will change the covariate simulation parameters to simulate the other degeneration scenarios, and verify the proposed method. The covariate model parameters of θ' and β' are the original property of thrust ball bearing vibration, and the covariate model is mainly affected by the error term $\varepsilon(t$) which represents the noise in the operation environment or the measurement error caused by the human. Moreover, the high value of the error term $\varepsilon(t)$ will increase the degen-

eration degree of thrust ball bearing, and lead to the decline of lifetime. Therefore, as shown in Table 13, we designed three simulation experiments by changing the normal distribution of error term $\varepsilon(t)$ to randomly simulate the different degeneration scenarios, and test the prediction performance and maintenance performance of the combination BP-RBF-GRNN neural network model. Each simulation experiment will generate 30 group thrust ball bearing vibration signals to be used as data sources. And we focus on five prediction point values of t_{ki}, $t_{ki} \in \{0.1T_{Aj}, 0.3T_{Aj}, 0.5T_{Aj}, 0.7T_{Aj}, 0.9T_{Aj}\}$, which represent the early-stage, early-to-mid stage, mid-stage, mid-to-late stage, and late-stage for each component j, respectively. T_{Aj} is the actual life of component j.

(a)

(b)
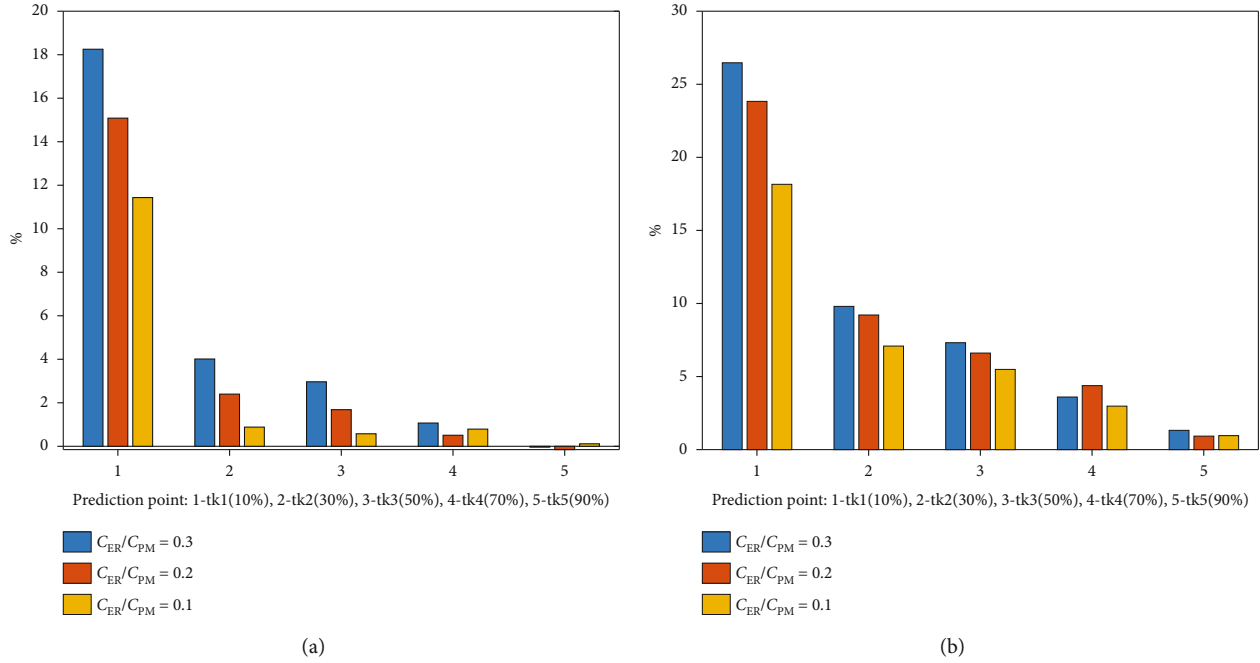
FIGURE 12: Maintenance evaluation index. (a) Average cost rate percentage with three maintenance ratios under 30 training-test set schemes. (b) Average maintenance interval percentage with three maintenance ratios under 30 training-test set schemes.

TABLE 6: The maintenance performance comparison of cost rate percentage R_η (%) between the BP and the combination BP-RBF-GRNN neural network model under three different maintenance cost ratios (C_{PM}/C_{ER}).

C_{PM}/C_{ER}	t_{k1}	t_{k2}	t_{k3}	t_{k4}	t_{k5}
0.5	15.92	17.14	15.28	7.42	1.86
0.4	14.31	15.62	12.28	5.73	1.35
0.3	12.61	14.40	9.34	3.80	0.91

TABLE 7: The maintenance performance comparison of cost rate percentage R_η (%) between the RBF and the combination BP-RBF-GRNN neural network model under three different maintenance cost ratios (C_{PM}/C_{ER}).

C_{PM}/C_{ER}	t_{k1}	t_{k2}	t_{k3}	t_{k4}	t_{k5}
0.5	0.26	0.24	0.27	0.20	0.17
0.4	0.14	0.20	0.17	0.18	0.12
0.3	0.09	0.10	0.10	0.10	0.12

TABLE 8: The maintenance performance comparison of cost rate percentage R_η (%) between the GRNN and the combination BP-RBF-GRNN neural network model under three different maintenance cost ratios (C_{PM}/C_{ER}).

C_{PM}/C_{ER}	t_{k1}	t_{k2}	t_{k3}	t_{k4}	t_{k5}
0.5	4.18	2.00	0.55	0.29	0.17
0.4	3.81	1.46	0.73	0.35	0.24
0.3	3.51	1.56	1.05	0.36	0.01

TABLE 9: The maintenance performance comparison of maintenance interval percentage R_{Topt} (%) between the BP and the combination BP-RBF-GRNN neural network model under three different maintenance cost ratios (C_{PM}/C_{ER}).

C_{PM}/C_{ER}	t_{k1}	t_{k2}	t_{k3}	t_{k4}	t_{k5}
0.5	31.05	32.85	29.62	15.96	4.11
0.4	30.45	32.09	26.72	15.14	3.73
0.3	29.84	32.75	23.91	11.64	3.49

TABLE 10: The maintenance performance comparison of maintenance interval percentage R_{Topt} (%) between the RBF and the combination BP-RBF-GRNN neural network model under three different maintenance cost ratios (C_{PM}/C_{ER}).

C_{PM}/C_{ER}	t_{k1}	t_{k2}	t_{k3}	t_{k4}	t_{k5}
0.5	1.57	2.08	2.22	1.47	0.64
0.4	1.32	1.78	1.31	1.39	0.50
0.3	1.00	1.22	1.23	1.65	0.38

TABLE 11: The maintenance performance comparison of maintenance interval percentage R_{Topt} (%) between the GRNN and the combination BP-RBF-GRNN neural network model under three different maintenance cost ratios (C_{PM}/C_{ER}).

C_{PM}/C_{ER}	t_{k1}	t_{k2}	t_{k3}	t_{k4}	t_{k5}
0.5	9.47	5.72	2.38	1.86	0.90
0.4	9.99	5.54	3.11	1.46	1.21
0.3	9.89	5.75	4.77	1.83	0.51

TABLE 12: The prediction performance comparison of the BP, RBF, GRNN, and combination method.

Method	t_{k1}	t_{k2}	t_{k3}	t_{k4}	t_{k5}
BP	0.3101	0.3092	0.3139	0.2141	0.1907
RBF	0.0167	0.0175	0.0182	0.0177	0.0183
GRNN	0.1821	0.0358	0.0238	0.0165	0.0159
Combination BP-RBF-GRNN neural network model	0.0045	0.0049	0.0055	0.0055	0.0056

TABLE 13: The introduction of the experimental design scheme.

Experimental design scheme	Covariate simulation parameter
1st degeneration scenario	$\theta' \sim N(\mu_0, \sigma_0^2), \beta' \sim N\left(\mu_1', \sigma_1'\right), \varepsilon(t_i) - \varepsilon(t_{i-1}) \sim N\left(0.5 \times \mu_0, 0.5 \times \sigma^2\right)$
2nd degeneration scenario	$\theta' \sim N(\mu_0, \sigma_0^2), \beta' \sim N\left(\mu_1', \sigma_1'\right), \varepsilon(t_i) - \varepsilon(t_{i-1}) \sim N\left(1 \times \mu_0, 1 \times \sigma^2\right)$
3rd degeneration scenario	$\theta' \sim N(\mu_0, \sigma_0^2), \beta' \sim N\left(\mu_1', \sigma_1'\right), \varepsilon(t_i) - \varepsilon(t_{i-1}) \sim N\left(2 \times \mu_0, 2 \times \sigma^2\right)$

Table 14 is the prediction performance of the Bayesian parameter updating prediction model and combination BP-RBF-GRNN neural network model in RMSPE under three different degeneration scenarios. The result in Table 14 can be calculated by using the prediction error minuses that of the combination BP-RBF-GRNN neural network model, and the high value of RMSPE means the low prediction performance. As shown in Table 14, we can draw the conclusion that in every degeneration scenario, the prediction performance of the combination BP-RBF-GRNN neural network model from the early-stage to the mid-stage is more advantageous than those of the Bayesian parameter updating forecasting model.

Tables 15 and 16 are the maintenance performance of the Bayesian parameter updating prediction model and combination BP-RBF-GRNN neural network model in cost rate and maintenance under three different degeneration scenarios when $C_{PM}/C_{ER} = 0.3$, respectively. Table 15 represents the cost rate percentage, which uses the cost rate of the Bayesian parameter updating prediction model to be divided by that of the combination BP-RBF-GRNN neural network model. The value of the cost rate percentage is greater than 0, which means that the cost of the Bayesian parameter updating prediction model is higher than that of the combination BP-RBF-GRNN neural network model. And if the value of the cost rate percentage is high, the cost of the combination BP-RBF-GRNN neural network model will be low. As shown in Equation (26), Table 16 represents the maintenance interval percentage, which uses the maintenance interval of the combination BP-RBF-GRNN neural network model to be divided by that of the Bayesian parameter updating prediction model. The value of the maintenance interval percentage is greater than 0, which means that the maintenance performance of the combination BP-RBF-GRNN neural network model is higher than that of the Bayesian parameter updating prediction model. And if the value of the maintenance interval percentage is high, the maintenance performance of the combination BP-RBF-GRNN neural network model will be good. The high value

TABLE 14: The prediction performance difference of RMSPE (%) between the combination BP-RBF-GRNN neural network model and Bayesian parameter updating prediction model under different degeneration scenarios.

Experimental design scheme	t_{k1}	t_{k2}	t_{k3}	t_{k4}	t_{k5}
1st degeneration scenario	1.98	1.78	1.14	0.06	-0.06
2nd degeneration scenario	9.83	5.67	3.65	0.08	-0.07
3rd degeneration scenario	6.78	3.51	1.63	-0.09	-0.04

TABLE 15: The maintenance performance comparison of cost rate percentage R_η (%) between the combination BP-RBF-GRNN neural network model and Bayesian parameter updating prediction model when $C_{PM}/C_{ER} = 0.3$ under different degeneration scenarios.

Experimental design scheme	t_{k1}	t_{k2}	t_{k3}	t_{k4}	t_{k5}
1st degeneration scenario	16.45	8.43	3.39	0.54	0.22
2nd degeneration scenario	18.25	4.01	2.96	1.07	-0.04
3rd degeneration scenario	20.70	14.56	9.02	2.92	1.31

TABLE 16: The maintenance performance comparison of maintenance interval percentage R_{Topt} (%) between the combination BP-RBF-GRNN neural network model and Bayesian parameter updating prediction model when $C_{PM}/C_{ER} = 0.3$ under different degeneration scenarios.

Experimental design scheme	t_{k1}	t_{k2}	t_{k3}	t_{k4}	t_{k5}
1st degeneration scenario	20.22	11.66	7.95	4.38	2.07
2nd degeneration scenario	26.47	9.80	7.32	3.60	1.32
3rd degeneration scenario	21.05	15.02	8.49	3.18	2.19

TABLE 17: Computational cost (second).

Bayesian parameter updating prediction model	Combination BP-RBF-GRNN neural network model
201.39	334.16

in Tables 15 and 16 means that the combination BP-RBF-GRNN neural network model has a better maintenance performance than that of the Bayesian parameter updating prediction model. As shown in Tables 15 and 16, we can draw the conclusion that in every degeneration scenario, the cost rate percentage and maintenance interval percentage of the combination BP-RBF-GRNN neural network model from the early-stage to the mid-stage are more advantageous than those of Bayesian parameter updating prediction model. The conclusion from Table 14 and Tables 15 and 16 can illustrate the fact that the improvement of accuracy will improve the maintenance efficiency.

5.3.4. Computational Cost. We use a laptop computer as a baseline device. Its specifications include an Intel Core i7-9750H processor with a base frequency of 2.60 GHz, equipped with 16 GB of RAM. The comparison of computational cost between the combination BP-RBF-GRNN neural network model and the Bayesian parameter updating prediction model is shown in Table 17. We calculated the cost of the first experiment (Figures 8–12), which includes the cost from five predicted points for two prediction models under 30 training-test set schemes. It can be clearly found that the computational cost of the combination BP-RBF-GRNN neural network model is not much higher than that of the Bayesian parameter updating prediction model. But the combination BP-RBF-GRNN neural network model has a better performance than the Bayesian parameter updating prediction model in degeneration prediction and maintenance. The explanation for the above result is as follows. The Bayesian parameter updating prediction model uses the prior distributions of model parameters to obtain that of the posterior distributions, and the Monte Carlo Simulation is used to simulate N degeneration scenarios to predict the degeneration process. However, the high degeneration scenario will lead to the high computational cost of the Bayesian parameter updating prediction model. In order to improve the accuracy of the degradation process, we simulated 10000 degradation scenarios at each predicted point under 30 training-test set schemes, which resulted in high computational cost. The combination BP-RBF-GRNN neural network model contains three prediction sub-models, namely, BP, RBF, and GRNN neural network. The BP and RBF neural networks adopt one hidden layer. One hidden layer normally does not cause high computational cost. Although the GRNN neural network uses two hidden layers, the weight of the whole neural network is equal to 1, which indicates that two adjacent layers can be connected without updating the weight, thus reducing the computational cost.

6. Conclusion

This paper puts forward a predictive maintenance optimization framework based on the proportional hazard model and BP-RBF-GRNN neural network model to improve the accuracy of degeneration prediction and reduce the maintenance cost to a certain extent. The main contribution can be illustrated in two aspects. Firstly, the combination forecasting method based on deep learning is rarely applied in degeneration prediction, which can improve the accuracy of degeneration. Therefore, the combination BP-RBF-GRNN neural network model based on deep learning is used to predict the degeneration prediction. Secondly, condition monitoring data may not directly reflect the degree of degeneration, life data and condition monitoring values must be considered comprehensively. Therefore, WPHM which considers both life data and condition monitoring values can be used to evaluate the hazard rate. We design two experiments to illustrate the advantage of combination BP-RBF-GRNN neural network model. For the first experiment, we compared the combination BP-RBF-GRNN neural network model to the Bayesian parameter updating prediction model in prediction performance and maintenance performance. The simulation results show that the combination BP-RBF-GRNN neural network model can effectively improve the accuracy of the thrust ball bearings degeneration process and reduce the maintenance cost percentage from early-stage to mid-stage than that of the Bayesian parameter updating prediction model. For the second experiment, we compared the combination BP-RBF-GRNN neural network model to other three single deep learning models in prediction performance and maintenance performance. The simulation results show that the combination BP-RBF-GRNN neural network model has advantages over other three single prediction sub-models in cost rate percentage and maintenance interval percentage from the early-stage to the mid-stage.

Data Availability

The data used to support the findings of this study are available from the corresponding author upon request.

Conflicts of Interest

The authors declare no conflict of interest.

Acknowledgments

References

[1] A. Patwardhan, A. K. Verma, and U. Kumar, "A survey on predictive maintenance through big data," in *Current Trends in Reliability, Availability, Maintainability and Safety*, pp. 437–445, Springer, 2016.

[2] L. Spendla, M. Kebisek, P. Tanuska, and L. Hrcka, "Concept of predictive maintenance of production systems in accordance with industry 4.0," in *2017 IEEE 15th International Symposium*

on *Applied Machine Intelligence and Informatics (SAMI)*, Herl'any, Slovakia, 2017.

[3] N. Sakib and T. Wuest, "Challenges and opportunities of condition-based predictive maintenance: a review," *Procedia CIRP*, vol. 78, pp. 267–272, 2018.

[4] T. P. Carvalho, F. A. A. M. N. Soares, R. Vita, R. . P. Francisco, J. P. Basto, and S. G. S. Alcalá, "A systematic literature review of machine learning methods applied to predictive maintenance," *Computers & Industrial Engineering*, vol. 137, article 106024, 2019.

[5] H. D. Faria, J. Costa, and J. Olivas, "A review of monitoring methods for predictive maintenance of electric power transformers based on dissolved gas analysis," *Renewable and Sustainable Energy Reviews*, vol. 46, pp. 201–209, 2015.

[6] W. Zhe, W. Fei, and S. Shi, "Solar irradiance short-term prediction model based on BP neural network," *Energy Procedia*, vol. 12, pp. 488–494, 2011.

[7] Y. Zhao, J. Nan, F. Y. Cui, and L. Guo, "Water quality forecast through application of BP neural network at Yuqiao reservoir," *Journal of Zhejiang University-SCIENCE A*, vol. 8, no. 9, pp. 1482–1487, 2007.

[8] H. Bendu, B. B. V. Deepak, and S. Murugan, "Application of GRNN for the prediction of performance and exhaust emissions in HCCI engine using ethanol," *Energy Conversion and Management*, vol. 122, pp. 165–173, 2016.

[9] I. Ladlani, L. Houichi, L. Djemili, S. Heddam, and K. Belouz, "Modeling daily reference evapotranspiration (ET0) in the north of Algeria using generalized regression neural networks (GRNN) and radial basis function neural networks (RBFNN): a comparative study," *Meteorology and Atmospheric Physics*, vol. 118, no. 3-4, pp. 163–178, 2012.

[10] M. Kamiński and M. Solecka, "Optimization of the truss-type structures using the generalized perturbation- based Stochastic Finite Element Method," *Finite Elements in Analysis and Design*, vol. 63, pp. 69–79, 2013.

[11] S. Bressi, J. Santos, and M. Losa, "Optimization of maintenance strategies for railway track-bed considering probabilistic degradation models and different reliability levels," *Reliability Engineering & System Safety*, vol. 207, article 107359, 2021.

[12] H. Dui, C. Zhang, G. Bai, and L. Chen, "Mission reliability modeling of UAV swarm and its structure optimization based on importance measure," *Reliability Engineering & System Safety*, vol. 215, article 107879, 2021.

[13] B. Yin, Y. Li, S. Miao, Y. Lin, and H. Zhao, "An economy and reliability co-optimization planning method of adiabatic compressed air energy storage for urban integrated energy system," *Journal of Energy Storage*, vol. 40, article 102691, 2021.

[14] Z. Han, L. Tian, and L. Cheng, "A deducing-based reliability optimization for electrical equipment with constant failure rate components duration their mission profile," *Reliability Engineering & System Safety*, vol. 212, no. 2, article 107575, 2021.

[15] M. Leimeister and A. Kolios, "A review of reliability-based methods for risk analysis and their application in the offshore wind industry," *Renewable and Sustainable Energy Reviews*, vol. 91, pp. 1065–1076, 2018.

[16] S. Wu, N. Gebraeel, M. Lawley, and Y. Yih, "A neural network integrated decision support system for condition-based optimal predictive maintenance policy," *IEEE Transactions on Systems, Man, and Cybernetics - Part A. Systems and Humans*, vol. 37, no. 2, pp. 226–236, 2007.

[17] A. C. Mendes and N. Fard, "Accelerated failure time models comparison to the proportional hazard model for time-dependent covariates with recurring events," *International Journal of Reliability, Quality and Safety Engineering*, vol. 21, no. 2, article 1450010, 2014.

[18] N. Gorjian, L. Ma, M. Mittinty, P. Yarlagadda, and Y. Sun, "A review on reliability models with covariates," in *Engineering Asset Lifecycle Management*, pp. 385–397, Springer, 2010.

[19] Z. Xu, "Statistical modeling and predictions based on field data and," *Dynamic Covariates*, 2 3, 2014.

[20] N. G. Wang, X. W. Zhu, and J. Zhang, "License plate segmentation and recognition of Chinese vehicle based on BPNN," in *2016 12th International Conference on Computational Intelligence and Security (CIS)*, Wuxi, China, 2016.

[21] Y. Dai, J. Guo, L. Yang, and W. You, "A new approach of intelligent physical health evaluation based on GRNN and BPNN by using a wearable smart bracelet system," *Procedia Computer Science*, vol. 147, pp. 519–527, 2019.

[22] J. Li, J.-h. Cheng, J.-y. Shi, and F. Huang, "Brief introduction of back propagation (BP) neural network algorithm and its improvement," in *Advances in Computer Science and Information Engineering*, pp. 553–558, Springer, 2012.

[23] B. Wang, X. Gu, L. Ma, and S. Yan, "Temperature error correction based on BP neural network in meteorological wireless sensor network," *International Conference on Cloud Computing & Security*, vol. 23, no. 4, p. 265, 2017.

[24] M. Maarouf, A. Sosa, B. Galván et al., "The role of artificial neural networks in evolutionary optimisation. A review," in *Advances in Evolutionary and Deterministic Methods for Design, Optimization and Control in Engineering and Sciences*, vol. 36, pp. 59–76, Springer International Publishing, 2015.

[25] T. K. Leong, P. Saratchandran, and N. Sundararajan, "Real-time performance evaluation of the minimal radial basis function network for identification of time varying nonlinear systems," *Computers and Electrical Engineering*, vol. 28, no. 2, pp. 103–117, 2002.

[26] D. F. Specht, "A general regression neural network," *IEEE Transactions on Neural Networks*, vol. 2, no. 6, pp. 568–576, 1991.

[27] W. Li, X. Yang, H. Li, X. Yang, H. Li, and L. Su, "Hybrid forecasting approach based on GRNN neural network and SVR machine for electricity demand forecasting," *Energies*, vol. 10, no. 1, p. 44, 2017.

[28] S. Yin, L. Liu, and J. Hou, "A multivariate statistical combination forecasting method for product quality evaluation," *Information Sciences*, vol. 355-356, pp. 229–236, 2016.

[29] A. R. Aladro-Gonzalvo, G. A. Araya-Vargas, M. Machado-Díaz, and W. Salazar-Rojas, "Pilates-based exercise for persistent, non-specific low back pain and associated functional disability: A meta-analysis with meta-regression," *Journal of Bodywork and Movement Therapies*, vol. 17, no. 1, pp. 125–136, 2013.

[30] Q. Zhang, C. Hua, and G. Xu, "A mixture Weibull proportional hazard model for mechanical system failure prediction utilising lifetime and monitoring data," *Mechanical Systems and Signal Processing*, vol. 43, no. 1-2, pp. 103–112, 2014.

[31] H. K. Ghritlahre and R. K. Prasad, "Investigation of thermal performance of unidirectional flow porous bed solar air heater using MLP, GRNN, and RBF models of ANN technique," *Thermal Science and Engineering Progress*, vol. 6, pp. 226–235, 2018.

[32] B. De Jonge, W. Klingenberg, and R. Teunter, "Optimum maintenance strategy under uncertainty in the lifetime distribution," *Reliability Engineering & System Safety*, vol. 133, pp. 59–67, 2015.

[33] N. Z. Gebraeel, M. A. Lawley, R. Li, and J. K. Ryan, "Residual-life distributions from component degradation signals: a Bayesian approach," *IIE Transactions*, vol. 37, no. 6, pp. 543–557, 2005.

[34] G. Q. Tong and X. B. Qian, "An extended predictive maintenance model under covariate distribution parameters with uncertainty," in *Proceedings of the RICAI 2020.2020 2nd International Conference on Robotics, Intelligent Control and Artificial Intelligence*, Shanghai, China, 2020.

[35] A. H. Elwany, N. Gebraeel, and L. M. Maillart, "Structured replacement policies for components with complex degradation processes and dedicated sensors," *Operations Research*, vol. 59, no. 3, pp. 684–695, 2011.

Research Article

Effects of High-Concentration CO$_2$ on Ignition Delay Time of 70% n-Heptane/30% Toluene Mixtures

Shengzhuo Yao,[1] **Yuewei Zhang,**[1] **Yongfeng Liu** ⬢,[1] **Guijun Bi** ⬢,[2] **Lu Zhang,**[1] **Ping Wei,**[3] **Jinou Song,**[4] **and Hua Sun**[5]

[1]*Beijing Engineering Research Center of Monitoring for Construction Safety, Beijing University of Civil Engineering and Architecture, Beijing 100044, China*
[2]*Singapore Institute of Manufacturing Technology (SIMTech), 73 Nanyang Drive, Singapore 637662*
[3]*School of Civil Engineering and Survey, Beijing Polytechnic College, Beijing 100042, China*
[4]*State Key Laboratory of Engines, Tianjin University, Tianjin 300072, China*
[5]*School of Humanities, Beijing University of Civil Engineering and Architecture, Beijing 100044, China*

Correspondence should be addressed to Yongfeng Liu; liuyongfeng@bucea.edu.cn and Guijun Bi; biguijun@hotmail.com

In order to research the high-concentration CO$_2$ effects on ignition delay time (IDT) of diesel surrogate fuel (70% n-heptane/ 30% toluene), a carbon dioxide effect (CDE) model is established, which considers fuel and ambient gas concentration, density, and temperature influence on autoignition under CO$_2$/O$_2$ atmosphere. Firstly, a chemical model of n-heptane/ toluene is established, and the coupling, reduction, and simulation processes are carried out in chemical kinetic software with the IDT as the target parameter. Secondly, a constant volume combustion chamber (CVCC) visualization platform is built by incorporating a high-speed camera system and different working conditions are set in the CO$_2$ volume fraction range (40%-70%) at 3.0 MPa and 850 K for an autoignition experiment. Thirdly, experiment and simulation results are discussed in air, 60% CO$_2$/40% O$_2$, 50% CO$_2$/50% O$_2$, and 40% CO$_2$/60% O$_2$ atmospheres, including the IDT, CO$_2$ effects, temperature sensitivity, and OH radical rate of production (ROP). The results show that the CDE model well predicts the 70% n-heptane/30% toluene IDT under the CO$_2$/O$_2$ atmosphere and the average error in 60% CO$_2$/40% O$_2$ atmosphere is 5.29%. Besides, when the CO$_2$ volume fraction increases from 40% to 60%, the CO$_2$ thermal effect plays a leading role in the IDT prolongation and the OH radical ROP peak of R4 (O+H$_2$O⟶2OH) decreases by 180%.

1. Introduction

Diesel engines play an indispensable role in industrial development, but the CO$_2$ emission poses a great threat to the lives of workers in such as underground, underwater, and other closed environments [1]. When the CO$_2$ concentration reaches 5% in a closed environment, it causes severe damage to body functions, loss of consciousness, and even death [2, 3]. In order to solve the CO$_2$ emission problem in closed environments, Pei and Liu [4] proposed a closed cycle diesel engine (CCDE) system with liquid oxygen car-bon sequestration whose working principle is that diesel burns in the "artificial atmosphere" (only O$_2$ and CO$_2$). In addition, the combustion process takes advantage of the CO$_2$ high specific heat and the flame retardant properties to avoid diesel excessive combustion in the oxygen-rich atmosphere, and the CO$_2$ in the diesel exhaust is cooled and collected by using the physical properties of liquid oxygen vaporization heat absorption. The vaporized O$_2$ and the remaining unsolidified CO$_2$ are sent to the cylinder for the next combustion cycle through exhaust gas recirculation. The unique advantage of the closed cycle system is

that the emission of pollutants such as nitrogen oxides and soot is almost "zero" during the working process. Unfortunately, the CCDE has the problem of unstable combustion and unpredictable autoignition in practice [5], so in-depth research on diesel IDT under the CO_2/O_2 atmosphere is necessary.

Diesel is a complex mixture composing hundreds of different components, which is not feasible to consider the oxidation chemistry of all the compounds [6, 7]. Encouragingly, n-heptane is commonly adopted as DSF due to it having a similar cetane number to diesel and the oxidation reaction is well known [8–11]. Additionally, the aromatic compounds in diesel account to about 30% [12], and the most representative substance with a simple structure is toluene. In general, binary mixed fuel can potentially provide a better representation of autoignition delay properties than those on the basis of a single fuel. In order to simulate the diesel C/H ratio and the physical and chemical properties in the actual autoignition process as accurately as possible, binary mixed fuel becomes a hot topic in diesel IDT research [13–19], especially toluene reference fuels (TRFs) [20–23]. Therefore, the IDT of 70% n-heptane/30% toluene under the CO_2/O_2 atmosphere needs to be further investigated to provide a reference for the optimized design of future diesel engines.

Researchers made extensive studies on the IDT of n-heptane/toluene mixtures in air. Herzler et al. [24] studied the n-heptane/toluene mixtures IDT by using a high-pressure shock tube (HPST), which laid a foundation for developing and improving the DSF autoignition kinetic model. Later, Hartmann et al. [25] employed the HPST experiment to prove the toluene inhibitory effect on autoignition in a low-temperature environment by adding toluene to n-heptane, and they explained the nonlinear effects on the IDT of n-heptane/toluene mixtures. In addition, Di Sante [26] obtained the n-heptane chemical properties that dominated the toluene/n-heptane mixture when the toluene content was low through a rapid compression machine (RCM) experiment, while the effect of toluene content change on IDT was not significant when the temperature was higher than 800 K. Malliotakis et al. [27] combined HPST and RCM experiments to study the variation of n-heptane/toluene mixtures IDT with toluene content at different pressures and equivalence ratios using reaction paths and sensitivity analysis (SA) methods, and they also described the key aspects of toluene oxidation and explained its characteristics as reaction inhibition. Besides, Hernandez et al. [28] adopted 50% n-heptane/50% toluene as DSF to conduct an autoignition experiment in a single-cylinder engine and proved that toluene eliminated numerous active groups through the dehydrogenation reaction of OH radical at low temperatures, which remarkably prolonged the IDT. Subsequently, Hellier et al. [29] further researched the interaction between toluene and n-heptane during the compression autoignition process by changing the toluene content, which caused the changes in IDT. The result proved that a distinct two-stage autoignition process appeared with the increase of toluene content, and the toluene content exceeded 50% without spontaneous combustion. Further, Zhang et al. [30] selected n-heptane and toluene (6 : 4 by mass) as DSF using a numerical simulation to study the diesel autoignition in different oxygen concentrations, and the oxidation process of the mechanism was verified by the CVCC experiment.

In recent years, many studies have been reported on ignition and combustion under the CO_2/O_2 atmosphere. Zhou et al. [31] investigated the ignition characteristics of single-particle slime in a tube furnace at initial temperatures of 923-1173 K and O_2 volume fractions of 5%-80% and showed that the IDT and ignition temperature decreased significantly with increasing ambient temperature and oxygen concentration. But Liu et al. [32] studied the ethane IDT variation with the change of equivalence ratio and pressure through a shock tube experiment. Hu and Wei [33] further investigated the CO_2 effects on the propane laminar flow flame speed by Bunsen burner experiment, and the results concluded that the CO_2 thermal effect is the determining factor, followed by the chemical effect and finally the radiation effect. Additionally, Chen et al. [34] studied the diesel combustion process through optical engine experiments, and the results showed that the engine power loss was minimized and the IDT was shortened obviously in the 50% CO_2/50% O_2 atmosphere. Peng et al. [35] compared the autoignition delay of butane in CO_2/O_2 and air atmosphere by HPST experiment and analyzed the equivalence ratio and CO_2 effect on the IDT. Subsequently, Zhao et al. [36] studied the ignition characteristics of n-heptane by the visualization platform experiment of CVCC, and the results showed that the IDT in 35% CO_2/65% O_2 atmosphere was significantly shortened by 50% than that in air. Moreover, Liu et al. [37] studied the effects of CO_2 concentration on the combustion characteristics of diesel in different CO_2/O_2 atmosphere through the CVCC experiment.

Although researchers extensively studied the n-heptane/toluene mixtures auto-ignition characteristics in air, few reports under CO_2/O_2 atmosphere, especially in a high-concentration CO_2 environment. Thus, the goal of the present work is to propose a model that is appropriate for calculating the diesel IDT under the CO_2/O_2 atmosphere. Firstly, the CDE model of 70% n-heptane/30% toluene is established in the CO_2/O_2 atmosphere. Then, the n-heptane and toluene chemical models are coupled and reduced. Finally, the CVCC visualization experiment platform is built to verify the CDE model, and the important factors affecting the IDT are specifically analyzed and discussed. The discussion focuses on the autoignition process, the flame natural luminosity, calculation and validation of IDT, CO_2 effect, temperature sensitivity, and OH radical ROP.

2. Simulation

2.1. CDE Model. The CDE model is used to calculate the diesel IDT from the Arrhenius formula [38] as shown in Equation (1). Later, Ryan and Callahan [39] creatively converted the pressure effect into the gas concentration and ambient density effects on IDT on the basis of Equation (1). Besides, the influence of fuel concentration, oxygen concentration, and ambient temperature and density on IDT is considered as shown in Equation (2).

$$\tau_{id} = Ap^{-n} \exp\left(\frac{E_a}{\tilde{R}T}\right), \quad (1)$$

where A and n are calibration coefficients, which vary with fuel type, test method, and test condition; p and T are the gas average pressure and temperature before fuel spontaneous combustion, Pa, K; $\tilde{R}$ is the universal gas constant, J/(mol·K); and E_a is the global activation energy, kJ/mol.

$$\tau_{id} = b_0 C_{O_2}^{b_1} C_{fuel}^{b_2} \rho^{b_3} \exp\left(\frac{b_4}{T}\right), \quad (2)$$

where b_0, b_1, b_2, and b_3 are regression coefficients; b_4 is global activation energy over $\tilde{R}$ (universal gas constant); C_{O_2} and C_{fuel} are the oxygen concentration and the fuel concentration before fuel spontaneous combustion, moles/m^3; ρ is the average gas density before fuel spontaneous combustion, kg/m^3; and T is the average gas temperature before fuel autoignition, K.

However, Equation (2) describes the IDT in air without considering the special CO_2/O_2 atmosphere, where the CO_2 concentration is much higher than that in air and CO_2 has a higher specific heat capacity compared to N_2. Additionally, in a high-temperature environment, CO_2 cracks and directly participates in the reaction, which affects the oxidation process. Thus, the CDE model is established as shown in Equation (3), which considers the CO_2 retardant effect on autoignition.

$$\tau_{CDE} = b_0 C_{O_2}^{b_1} C_{fuel}^{b_2} \rho^{b_3} \exp\left(\frac{b_4}{T}\right) C_{CO_2}^{b5}, \quad (3)$$

where τ_{CDE} is the ignition delay time, s; C_{CO_2} is the carbon dioxide concentration at the ignition moment; and b_5 is the regression coefficient.

The CDE model considers the coupled effects of gas temperature and density and the ratio of oxygen to fuel on IDT. Furthermore, the CO_2 volume fraction is divided into multiple group working conditions from 40% to 70%, and the multiple linear regression analysis methods are adopted to correlate the species data with the IDT. The final function converges by iterative calculation, and the goodness-of-fit (R^2) of the CDE model is 0.9482 with the coefficients shown in

$$\tau_{CDE} = 0.221 C_{O_2}^{-1.127} C_{fuel}^{0.050} \rho^{-4.512} \exp\left(\frac{5914}{T}\right) C_{CO_2}^{1.762} \quad (4)$$

The coefficients in Equation (4) are expressed as follows. The τ_{CDE} decreases with increasing O_2 concentration in the mixture but increases with increasing CO_2 concentration, and they both influence each other coupling. The ignition delay time is inversely proportional to the mixture temperature, and the nature of this relationship can be expressed by the Arrhenius formula. The effect of density is more significant at higher fuel flow rates, as the spray may hit the wall at lower densities. The effect of fuel flow on ignition delay is relatively small but significant, with evaporation at higher fuel flow (richer mixture) causing pressure reduction and resulting in longer ignition delay.

The actual diesel engine has a different CO_2 concentration before and after autoignition as the working conditions change. More importantly, owing to the rapid and intense working process of the diesel engine, the in-cylinder temperature has strong transient characteristics, which affect the reactions of CO_2 and DSF. The CDE model has the advantage of better linking experimental data to actual diesel engines to quickly and accurately predict the IDT under CO_2/O_2 atmosphere, and the autoignition parameters of actual engines are further optimized to achieve the purpose of stable combustion. In addition, the density effect depends on the amount of fuel injected.

2.2. Chemical Model. The chemical model includes the n-heptane and toluene mechanisms from Lawrence Livermore National Laboratory. The adopted n-heptane mechanism is version 3.1 of the detailed chemical kinetics model developed by Mehl et al. [40], which is prominent in numerical research experiments in a wide temperature range and well characterizes the ignition. Besides, the adopted chemical kinetic model of toluene is developed by Nakamura et al. [41] to simulate a single aromatic hydrocarbon, which has outstanding performance in pioneering studies of reaction pathways and reaction rates. In addition, when the chemical reaction rate of the system reaches a high level, a large number of active molecules are clustered together at the autoignition moment, which accompanies by intense luminescence and heating. Among them, the OH radical determines the reaction activity in a low-temperature environment, so the autoignition moment is defined as the OH radical reaching the maximum [42], as shown in Figure 1.

2.3. Coupling and Reduction Processes of Mechanism. The n-heptane and toluene mechanisms need to be coupled and reduced by a directed relation graph with error propagation (DRGEP) [43] and SA [44] methods to reduce calculation time and cost. Firstly, according to the weight value, the larger elementary reactions are retained when the mechanisms are coupled. Secondly, the elementary reactions with fewer correlations with the coupling mechanism are eliminated according to the target parameter. Thirdly, the DRGEP method eliminates the error propagation caused by species reduction and further reduces the retained species through the SA method. Finally, the reduction process is controlled by setting the target parameters and error range to obtain the skeleton mechanism with different accuracy. However, if the target parameters are less and the error is large, the final obtained mechanism is simplified and if the error is small enough, the reduced mechanism converges to the detailed mechanism. The n-heptane/toluene mechanism with 273 components and 1544 elementary reactions is obtained by setting the IDT as the target parameter and the relative error is 10%. The reduced mechanism well simulates the diesel autoignition process thanks to the calculation errors of the simplified and detailed mechanism are
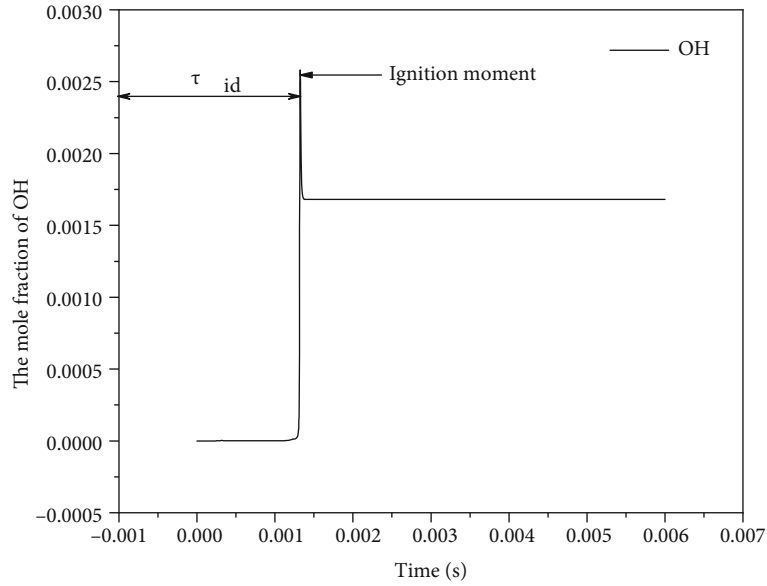
Figure 1: Autoignition criterion.
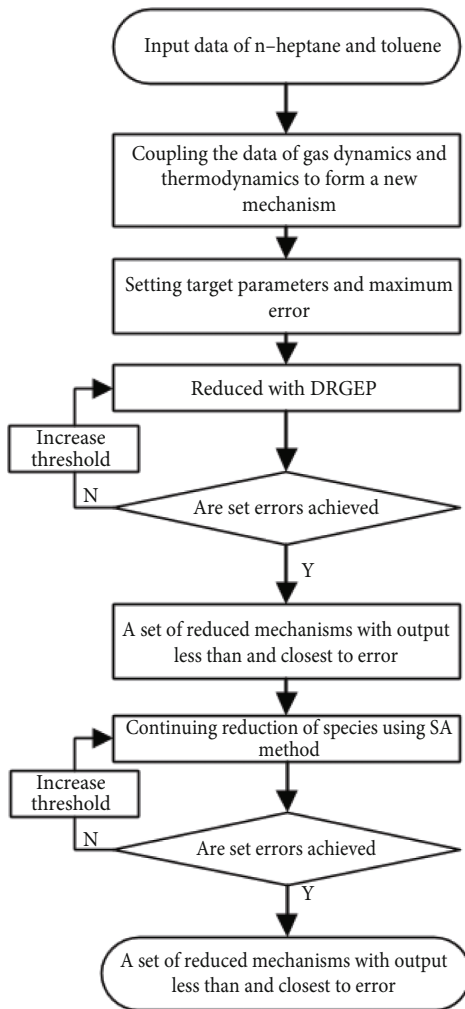
Figure 2: Mechanism coupling and reduction flow diagram.

within 5%, and the mechanism coupling and reduction process are shown in Figure 2.

3. Experiment

In the experiment, the CVCC visualization platform is built to analyze the auto-ignition process of 70% n-heptane/30% toluene under the CO_2/O_2 atmosphere. As shown in Figure 3, the experiment platform divides into six parts, which are the CVCC device, cooling circulation system, intake and exhaust system, high-pressure fuel injection system, high-speed camera system, and electronic control unit (ECU), and the experimental parameters are shown in Table 1.

The shape of the CVCC device (product number: Y1403, produced by Beijing Institute of Technology) is similar to a cylinder with four fused quartz windows that are evenly distributed as shown in Figure 4. The CVCC device simulates the working environment of the actual diesel engine top dead center with an interior radius of 150 mm and an interior height of 560 mm. The electric heating wires maximum power is 11 kW, regulating the CVCC temperature by thermal convection, and its internal maximum temperature reaches 900 K, which meets the actual engine top dead center autoignition temperature. The quartz window diameter is 120 mm, and its effective observation diameter is 100 mm, which can achieve the high-speed camera to get the entire autoignition process. In addition, the cooling circulation system is composed of a condition control cabinet, a water tank, a water pump, temperature sensors, and cooling water channels. The CVCC outer wall is covered with cooling water channels that are monitored in real time by temperature sensors to regulate dynamically the temperature and avoid danger. The intake and exhaust system consists of the condition control cabinet, high-pressure gas cylinders, pressure regulator valves, pressure sensors and intake, and
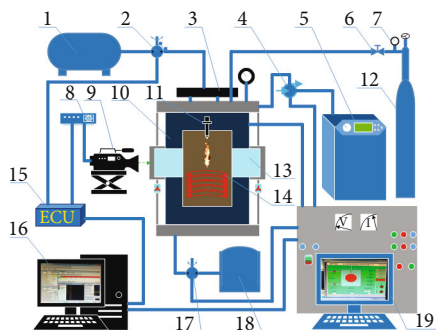
FIGURE 3: Schematic diagram of CVCC visualization platform. (1) Oil tank. (2) Oil pump and motor. (3) High pressure oil rail. (4) Water pump and motor. (5) Water tank. (6) Pressure regulator valve. (7) Pressure gauge. (8) Digital delay generator. (9) High-speed camera. (10) Constant volume combustion chamber. (11) Injector. (12) Gas cylinder. (13) Visual window. (14) Electric heating wire. (15) Electronic control unit. (16) Control computer. (17) Vacuum pump. (18) Gas collecting tank. (19) Condition control cabinet.

TABLE 1: Experimental parameters.

Parameters	Value	Units
Initial pressure	3.0	MPa
Initial temperature	850	K
Fuel temperature	300	K
Fuel injection pressure	120	MPa
Fuel injection pulse width	2.0	ms
Injection quantity (per time)	18.4	mg
Taken speed rate	10000	FPS
Time of exposure	20	μs
Image resolution	$896 * 848$	px
Diaphragm	2.8	—

FIGURE 4: Constant volume combustion chamber.

exhaust pipelines. During the intake process, the pressure regulator valve needs to be manually adjusted to feed evenly the mixture gas with a 0.02 MPa intake gradient. At the same time, the heating wires are cooperatively heated to ensure a steady rise in pressure and temperature in the CVCC until the initial values for the experiment are reached. When the first exhaust is completed, a certain amount of mixture gas needs to be charged again before continuing the exhaust to eliminate the disturbance of the previous cycle of combustion. Additionally, the high-pressure fuel injection system consists of the ECU, oil tank, oil pump and motor, battery, high-pressure oil rail, and injector (0.14 mm single-hole injector from BOSCH). The high-pressure oil pump driven by a variable-frequency motor enables the fuel to reach a maximum injection pressure of 175 MPa. The pressure is increased in 10 MPa gradients from 0 to 100 MPa and in 5 MPa gradient above 100 MPa to achieve precise regulation and protection of the high-pressure oil rail. A single-hole injector with a diameter of 0.12 mm is used for the experi-

ment. The high-speed camera system is composed of a control computer, high-speed camera (FASTCAM SA5, Photron), digital delay generator (DG535), and the ECU. The maximum shooting speed is 10000 frames per second (FPS) of the high-speed camera, which is triggered by the digital delay generator. The digital delay generator is employed to adjust the time relationship between the fuel injection and the high-speed camera. At the same time, the autoignition process is recorded in real time by using the acquisition software matching with the high-speed camera.

The testing procedure of the CVCC visualization experiment platform is mainly divided into 4 steps. (a) Before the experiment starts, the high-speed camera needs to complete the focus and image size calibration, as shown in Figure 5. (b) The CVCC is charged with a specific ratio of CO_2/O_2 mixture gas at a certain gradient pressure while the electric heating wires are adjusted to heat until reaching the initial temperature and pressure of the experiment. (c) When the high-pressure fuel injection system reaches the experimental injection pressure with a certain gradient, the control computer sends an electrical signal to the digital delay generator while the high-speed camera is triggered to work. (d) The first 60 images are sent back to the control computer for storage as a set of data since the combustion process is finished at 6 ms.

4. Results and Discussion

4.1. Ignition Delay Time. Figure 6(a) shows the key frames of the actual 70% n-heptane/30% toluene autoignition
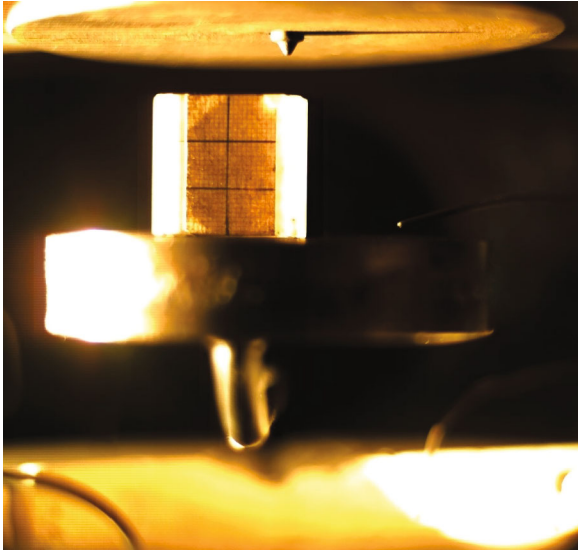
Figure 5: Image calibration of the high-speed camera.

processes from the high-speed camera in four different conditions. The images are processed with pseudocolor to better highlight the autoignition moment and the flame shape as shown in Figure 6(b). Thus, the IDT obtained using the space integrated natural luminosity (SINL) [45, 46] method are 2.3 ms, 1.7 ms, 1.4 ms, and 1.1 ms in the four working conditions (air, 60% CO_2/40% O_2, 50% CO_2/50% O_2, and 40% CO_2/60% O_2). The IDT is reduced obviously by 52.17% in 40% CO_2/60% O_2 atmosphere than that in air. Besides, the flame front has an "umbrella" shape in air, while the flame is thinner and longer under CO_2/O_2 atmospheres. Due to the oxygen concentration increases, the collision chance between oxygen and fuel molecules becomes greater, resulting in shorter IDT and more complete combustion than that in air. Comparing the autoignition processes in the different CO_2/O_2 atmospheres, the IDTs in 40% CO_2/60% O_2 and 60% CO_2/40% O_2 atmospheres are 27.27% longer and 21.43% shorter than those in 50% CO_2/50% O_2 atmosphere, respectively. The result shows that the same O_2 and CO_2 volume fractions of change have different promotion and inhibition degrees of autoignition because the two have a coupling effect. Liu et al. [36] studied the effects of different CO_2 concentrations on the diesel combustion characteristics in the CVCC experiment at an initial temperature and pressure of 850 K and 3.0 MPa, respectively. The result shows that with the increase of CO_2 concentration, the flame length decreases and the IDT increases in the CO_2/O_2 atmosphere, and similar conclusions are drawn in the current experimental conditions.

The flame natural luminosity change processes of 70% n-heptane/30% toluene in the four working conditions are shown in Figure 7. The flame natural luminosity is obtained by converting the red (R), green (G), and blue (B) values of each pixel point on the image into the corresponding gray values and then superimposing them [47]. As shown in Figure 7, the flame natural luminosity in air is much smaller

than that in the CO_2/O_2 atmospheres. On the one hand, the phenomenon is caused by a large amount of inert gas (N_2) in air as well as the low oxygen concentration, which leads to insufficient combustion. On the other hand, N_2 does not participate in the fuel oxidation reaction, while CO_2 is involved in the reaction in localized high-temperature conditions [48]. In the 50% CO_2/50% O_2 atmosphere, the area enclosed by the flame natural luminosity curve and the time axis are the largest, indicating that the combustion is sufficient and lasts for a long time. However, the flame natural luminosity curves fluctuate strongly and even show flame breakage in the flame images in the different CO_2/O_2 atmospheres. What may explain the phenomenon is that CO_2 is a triatomic gas, and its higher specific heat capacity and lower polytropic index disrupt the oxygen-rich conditions in CVCC, causing unstable combustion [49, 50]. Moreover, the diffusive combustion of gas entrained fuel during the fuel injection combustion process forms turbulence, which further leads to combustion fluctuations. The time from the beginning to the first slope of the flame natural luminosity curve also reflects the trend that the IDT gradually prolongs with increasing the CO_2 volume fraction.

Figure 8 shows the simulation and experiment IDT in air and the three different CO_2/O_2 atmospheres and the CDE model reproduces negative temperature dependence. At the initial temperature and pressure of 700 K and 3.0 MPa, the IDT in air is much longer than that in CO_2/O_2 atmospheres, which all decrease gradually as the initial temperature increases from 700 K to 850 K. On the contrary, with the increase of the initial temperature from 850 K to 950 K, the IDT is prolonged, especially in air and 50% CO_2/50% O_2 atmospheres. The phenomenon shows that the oxidation of toluene in air and 50% CO_2/50% O_2 atmospheres consume a large amount of OH radical and the reaction heat release is much less than the heat loss, which eventually leads to a decrease in the system reactivity and a longer IDT. Overall, this is similar to the conclusion reached by Fu and Aggarwal [51], who explained the phenomenon of negative temperature coefficients for n-heptane/methane mixtures, where the reactions generating HO_2 radical are preferred over those generating OH radical in this temperature interval, resulting in a smaller heat release than heat loss for low-temperature reactions. Subsequently, with increasing the initial temperature from 950 K to 1200 K, the IDT in the four atmospheres gradually shortens to zero. Because the higher initial temperature determines the progress of the reaction, the fuel spontaneously ignites immediately as soon as it is injected. The reasons for the error mainly include the simplification of the model and the experimental error, and the maximum error between the simulation and experiment is 16.96% in air. Moreover, the errors between the simulation and experiment IDT of 60% CO_2/40% O_2, 50% CO_2/50% O_2, and 40% CO_2/60% O_2 are 5.29%, 5.71%, and 8.18%, respectively, which verifies the CDE model applicability to predict the IDT in the O_2/CO_2 atmosphere.

4.2. The CO_2 Effects. Figure 9 shows the correspondence between the IDT and temperature for different CO_2 volume fraction working conditions at the initial temperature of
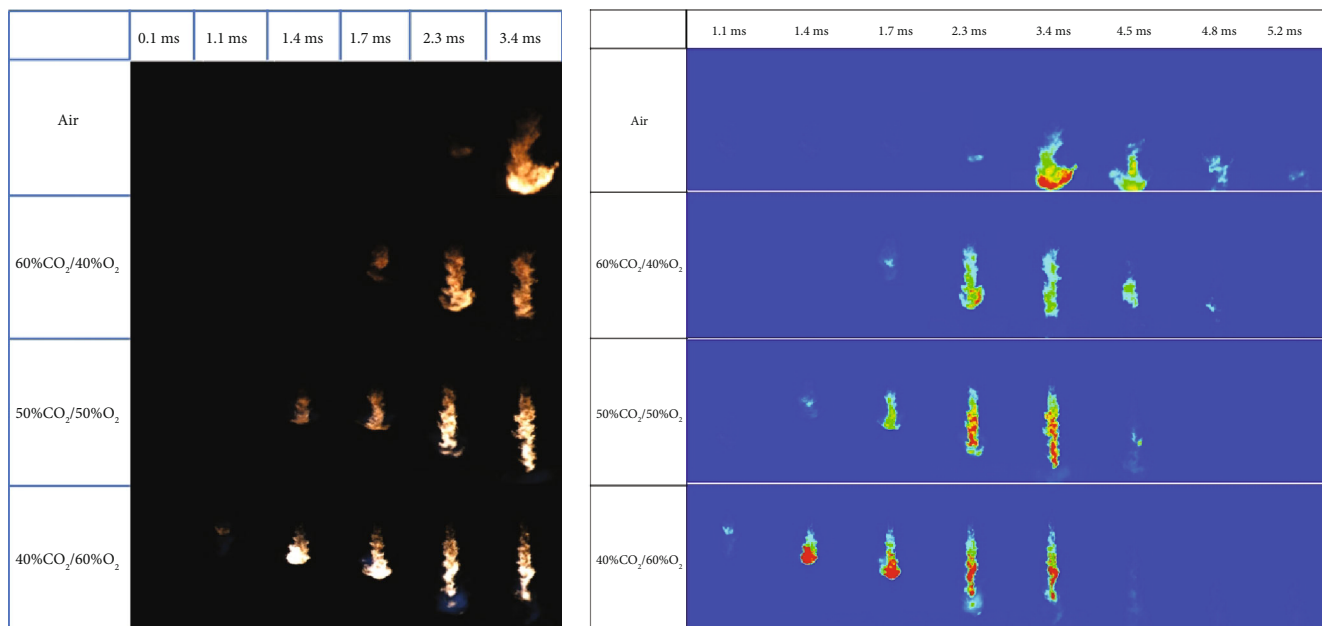
(a) Actual flame images

(b) Pseudocolor flame images

FIGURE 6: Autoignition processes in four working conditions.
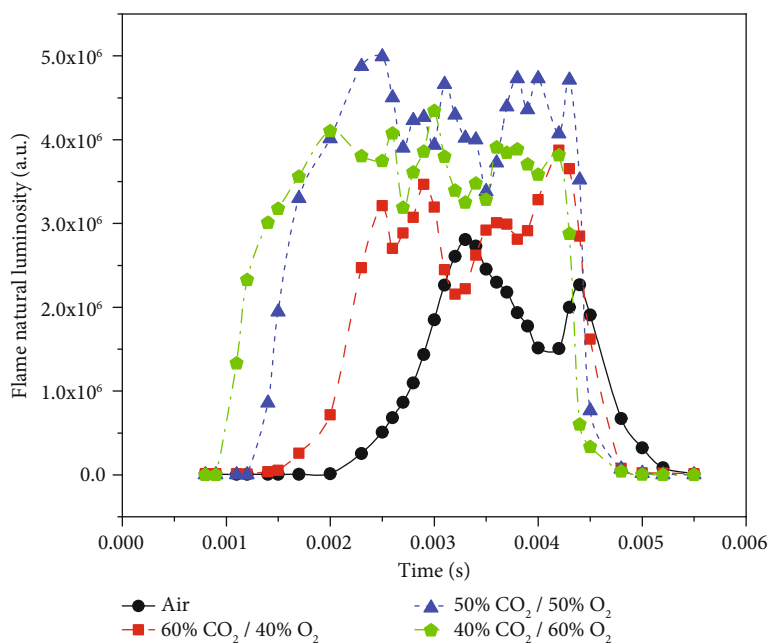
FIGURE 7: Flame natural luminosity change processes in four working conditions.

850 K and the pressure of 3.0 MPa. Under CO_2/O_2 atmosphere, the IDT prolongs with the increases of CO_2 volume fraction and the corresponding autoignition temperature gradually decreases, and the three effects of CO_2 show distinct changes. Then, when the CO_2 volume fraction changes from 40% to 60%, the IDT growth rate gradually increases, reaching a maximum of 18.75% between 55% and 60%. However, when the CO_2 volume fraction continues to increase, the growth rate drops instead, and the growth rate drops to 10.53% between 60% and 70%. Thus, the change in growth rate indicates that the way of CO_2 inhibiting autoignition has changed. The CO_2 thermal effect gradually increases and causes a significant decrease in temperature with increasing the CO_2 volume fraction from 40% to 60%, which is the
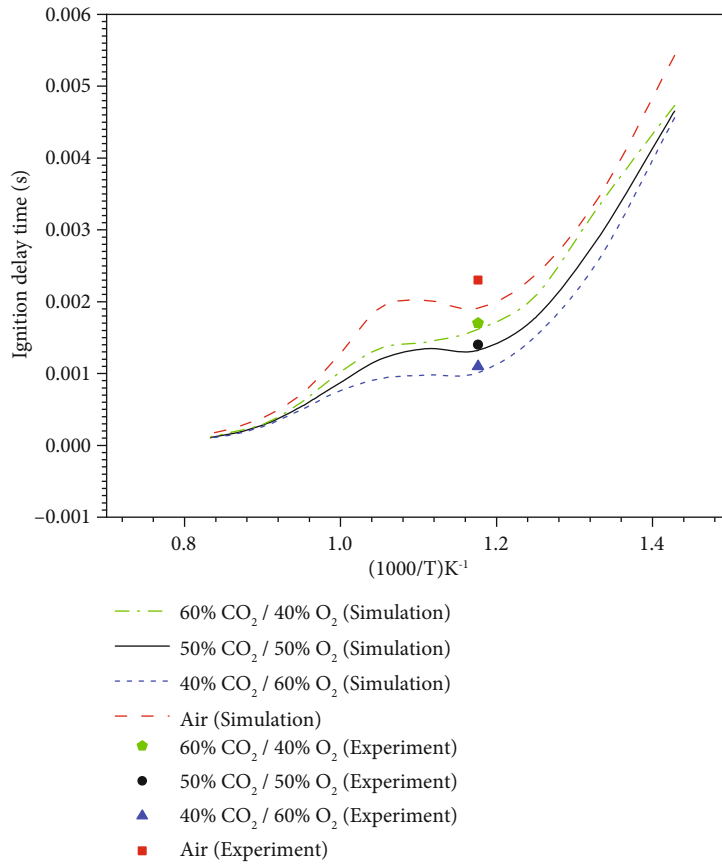
Figure 8: The IDT of simulation and experiment.
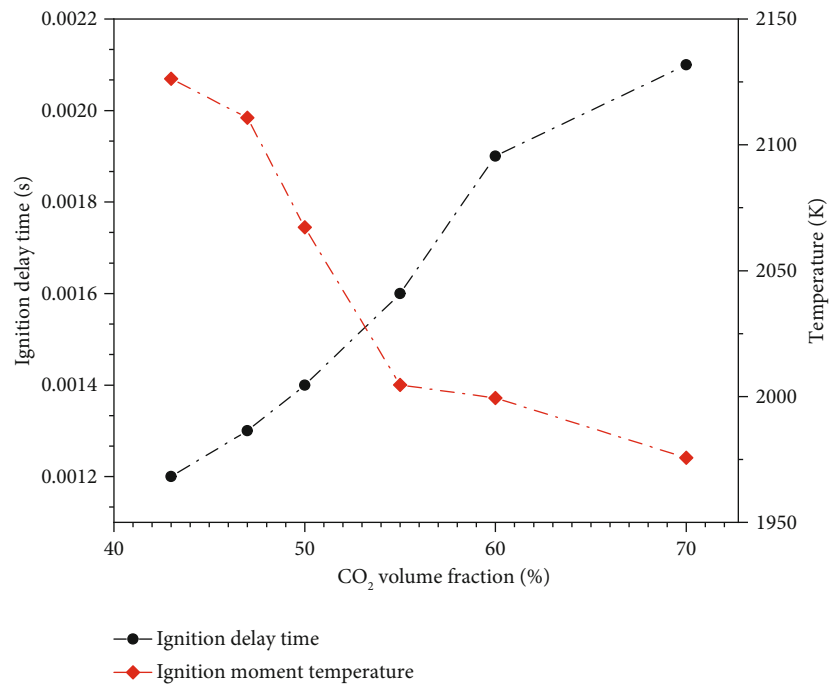
Figure 9: The IDT and temperature in the different working conditions.

main reason for the increase in the IDT growth rate. However, when the volume fraction of CO_2 reaches over 60%, the CO_2 third body collision efficiency is improved obviously, which promotes the occurrence of autoignition and reduces the IDT growth rate. Zhang et al. [10] and Sabia et al. [52] studied the autoignition process of n-heptane and propane. To study a certain CO_2 effect separately, virtual species were introduced to replace the thermal CO_2 effect, the CO_2 third body collision effect, and the CO_2 chemical effect through numerical simulation. The research results under a low-temperature environment are consistent with this paper that the CO_2 thermal effect is the most important factor affecting the IDT. Furthermore, when the CO_2 volume fraction reaches 60%, the third body effect of CO_2 is significantly enhanced.

4.3. Sensitivity Analysis. The oxidation process of the mechanism strongly depends on temperature, so it is important to identify the elementary reactions that are sensitive to the temperature for studying the autoignition. The temperature sensitivity of the n-heptane/toluene coupling mechanism is analyzed by the SA module in the kinetic software CHEMKIN-PRO [53] to determine the important elementary reactions affecting IDT, as shown in Figure 10. The initial ambient temperature and pressure for conducting SA are 850 K and 3.0 MPa, respectively, which are consistent with the CVCC experiment. Besides, Table 2 lists the ten most important elementary reactions affecting the IDT, including dehydrogenation of nC_7H_{16}, chain branching, isomerization of $C_7H_{15}OO$ radical, and chain termination reaction.

The sensitivity coefficients of R13 and R43 are negative for all four working conditions, implying the decrease in the system temperature and inhibition of auto-ignition with increasing the reaction rates, as shown in Figure 10. In addition, the R670, R852, R856, R861, and R864 are isomerization reactions of $C_7H_{15}OO$ radical to form isomeric peroxyalkyl and the sensitivity coefficients are positive. The sensitivity coefficients increase with increasing the oxygen concentration, indicating that by increasing the reaction rate, the system temperature is increased and the autoignition is promoted. The elementary reaction R15 has the negative sensitivity coefficients in air and high CO_2 volume fraction ambient. However, the sensitivity coefficient of R15 is positive when the CO_2 volume fraction is reduced to 40%. On the one hand, it shows that the R15 is the H_2O_2 dehydrogenation reaction in high CO_2 volume fraction ambient, which absorbs a large amount of heat. On the other hand, when the oxygen concentration is high, the sensitivity coefficient is positive, which is explained by the Le Chatelier principle.

The elementary reaction R16 has the negative sensitivity coefficient in the 40% CO_2/60% O_2 atmosphere. Hence, when the oxygen concentration is high, the R15 takes precedence over the R16, resulting in an obvious decrease in the H_2O_2 concentration. However, the R16 sensitivity coefficients are positive in the other three working conditions because the reaction of H_2O_2 decomposition into two OH radical releases a lot of heat, which is often adopted as an autoignition sign. Also, the sensitivity coefficients are much

higher in 60% CO_2/40% O_2 and 50% CO_2/50% O_2 atmospheres than in air under these three conditions. In fact, the high concentration of CO_2 enhances the CO_2 third body collision effect and increases the energy transfer efficiency, resulting in a faster reaction process. Moreover, among the ten elementary reactions with the greatest impact on IDT in Table 2, the CO_2 does not show a significant chemical effect in the experimental conditions. Zhang et al. [10] studied the CO_2 effects on the autoignition process of n-heptane by separating the CO_2 thermal effect and third body effect and got similar results that the thermal effect of CO_2 is the main reason for the autoignition delay.

According to Figure 10 and Table 2, R16 (H_2O_2 (+M)⟶2OH (+M)) is sensitive to temperature also an important reaction that affects the IDT. Also, R16 is the major source of OH radical and the reaction most affected by the CO_2 third body collision effect [54]. With the progress of the elementary reaction, the reaction activity and temperature of the system are increased markedly. The R43 and R670 are dehydrogenation reactions through OH radical, while R120 is the chain termination reaction, and they all consume a certain number of OH radical. Besides, R15 ($H_2O_2+O_2⟶2HO_2$) is dehydrogenated by O_2 to generate the HO_2 radical, and then, HO_2 radical is consumed by R13 ($HO_2+OH⟶H_2O+O_2$). Except in the 40% CO_2/60% O_2 atmosphere, R15 consumes a large number of radicals in the other three working conditions and significantly reduces the reaction activity and temperature of the system. Additionally, the reactions R852, R856, R861, and R864 are isomerization reactions of C7H15OO radical, which release large amounts of heat and promote the autoignition occurrence. The above reactions are consistent with Wu et al. [55] using a zero-dimensional model to study the reaction of O_2 content to the low-temperature oxidation process of n-heptane.

The SA of temperature shows that H_2O_2, HO_2, and OH radicals have strong correlations with the autoignition of n-heptane/toluene mixtures. Therefore, it is necessary to analyze the total production of H_2O_2, HO_2, and OH radicals in four different CO_2 volume fractions, as shown in Figure 11. Comparing Figures 11(a)–11(d), we conclude that the production peaks of H_2O_2, HO_2, and OH radicals under the CO_2/O_2 atmosphere are obviously higher than those in air, and the time to reach the peaks is shorter obviously. Comparing Figures 11(a) and 11(b), the biggest difference is that the time required for H_2O_2 to reach the peak in Figure 11(b) is 16.67% shorter than Figure 11(a), but the peaks reached by both are almost the same. However, the HO_2 radical all first increase, then decrease, and finally reach their peak at the same time as the OH radical in all four working conditions. The first peak of the HO_2 radical is mainly produced by the n-heptane dehydrogenation reaction through oxygen in the low-temperature reaction stage, and the second peak is caused by the oxidation of hydrogen peroxide. Additionally, with the increase of the CO_2 volume fraction, the OH mole fraction change remarkably, reduced by 18.6%, and the time to reach the peak of the OH mole fraction is prolonged by 17.78%. The results show that the CO_2 high-concentration atmosphere prolongs
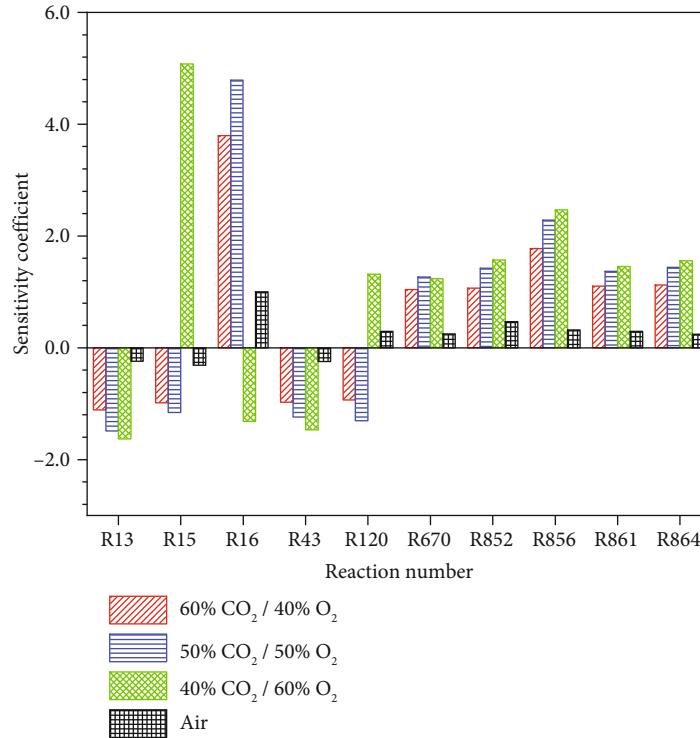
FIGURE 10: Sensitivity coefficient to temperature in four working conditions.

TABLE 2: The most important ten elementary reactions affecting IDT.

Reaction number	Reaction	Reaction number	Reaction
R13	$HO_2 + OH \longrightarrow H_2O + O_2$	R670	$nC_7H_{16} + OH \longrightarrow C_7H_{15\text{-}2} + H_2O$
R15	$H_2O_2 + O_2 \longrightarrow 2HO_2$	R852	$C_7H_{15}O_{2\text{-}1} \longrightarrow C_7H_{14}OOH_{1\text{-}3}$
R16	$H_2O_2\,(+M) \longrightarrow 2OH\,(+M)$	R856	$C_7H_{15}O_{2\text{-}2} \longrightarrow C_7H_{14}OOH_{2\text{-}4}$
R43	$CH_2O + OH \longrightarrow HCO + H_2O$	R861	$C_7H_{15}O_{2\text{-}3} \longrightarrow C_7H_{14}OOH_{3\text{-}5}$
R120	$CH_3O_2 + OH \longrightarrow CH_3OH + O_2$	R864	$C_7H_{15}O_{2\text{-}4} \longrightarrow C_7H_{14}OOH_{4\text{-}2}$

obviously the IDT, but the increase of the CO_2 volume fraction does not affect the formation of H_2O_2 and HO_2 radicals.

4.4. Rate of Production Analysis. OH radical has a strong relationship with IDT [56, 57], so further research on the ROP of OH radical is essential for autoignition. The four elementary reaction processes with the greatest influence on the OH radical ROP under the initial temperature of 850 K and pressure of 3.0 MPa in four working conditions are shown in Figure 12. What is most intuitive in Figure 12 are the rapid change processes of the R4 ($O + H_2O \longrightarrow 2OH$) and R1 ($H + O_2 \longrightarrow O + OH$), while the peaks of R12 ($HO_2 + O \longrightarrow OH + O_2$) and R16 ($H_2O_2\,(+M) \longrightarrow 2OH\,(+M)$) have lower peaks. In addition, two peaks appear during the R16 reaction, which drops immediately after reaching the second peak and shows negative values under the CO_2/O_2 atmosphere. Due to the rapid increase in temperature at the moment of autoignition, the reaction R16 proceeds towards heat absorption.

Next, the change processes of OH radical ROP under four different working conditions are specifically analyzed. From Figures 12(a) and 12(b), the OH radical maximum ROP of reactions R4 and R16 increase by 138% and 94.2%, respectively. The results show that the increase of oxygen concentration significantly boosts the OH radical ROP, which is consistent with the conclusions drawn from the above analysis of OH production. Buras et al. [57] used convolutional neural networks to investigate the relationship between the onset time scale of spontaneous oxidation and the IDT of first-stage under stoichiometric engine-related conditions and concluded that a strong relationship between the ROP peak of radicals such as OH and IDT was derived. From Figures 12(b) and 12(c), the OH radical maximum ROP peaks of reactions R4 and R16 increase by 36.8% and 23.8%, respectively. Then, from Figures 12(c) and 12(d), the OH radical maximum ROP peaks of reactions R4 and R16 increase by 105% and 80%, respectively. Comparing the changes of R4 and R16 in Figures 12(b)–12(d), we obtain
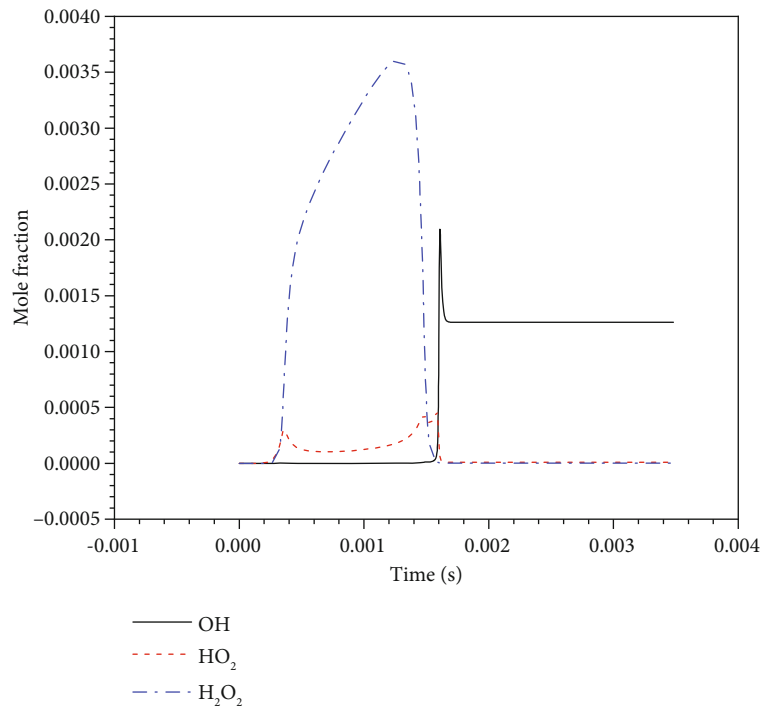
(a) $60\%CO_2/40\%O_2$
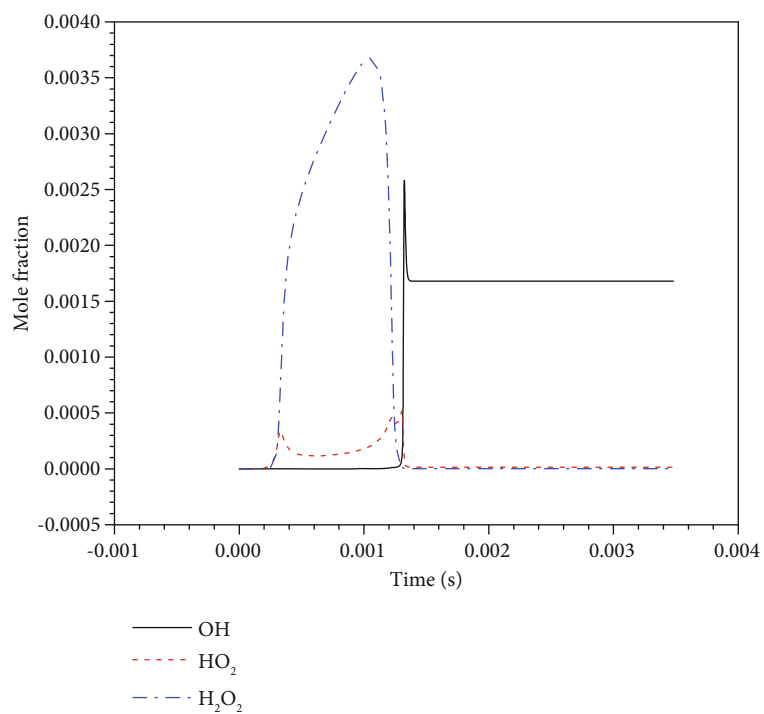
(b) $50\%CO_2/50\%O_2$

FIGURE 11: Continued.

(c) 40%CO_2/60%O_2

(d) Air
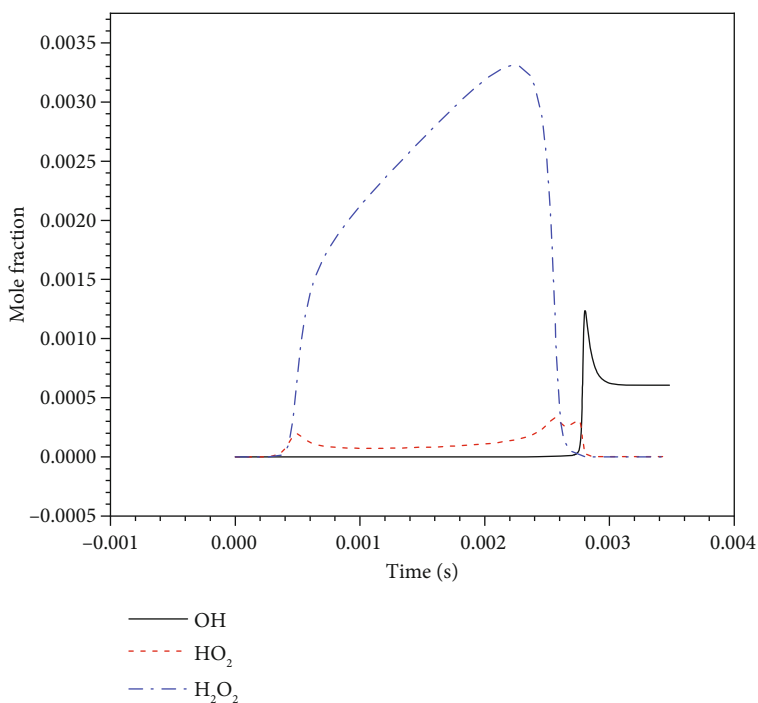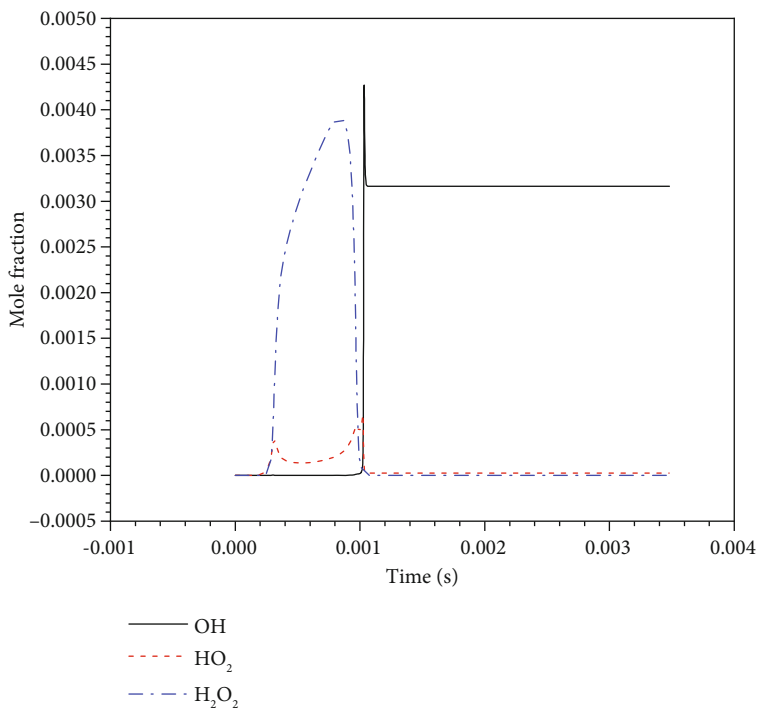
FIGURE 11: Mole fraction of OH, HO_2, and H_2O_2 in four working conditions.

that the ROP peaks of OH radical decrease significantly with an equal proportional increase of the CO_2 volume fraction and do not show a regular linear change. Hence, the result also indicates a change in the way CO_2 affects the ROP of OH radical as increasing the CO_2 volume frac-

tion. In addition, with the increase of CO_2 volume fraction, the OH radical ROP peak shows a trend of rapid decline first and then slowly decline. When the CO_2 volume fraction is changed from 60% to 40%, the reaction R4 and R16 OH radical ROP peaks increase by 180%
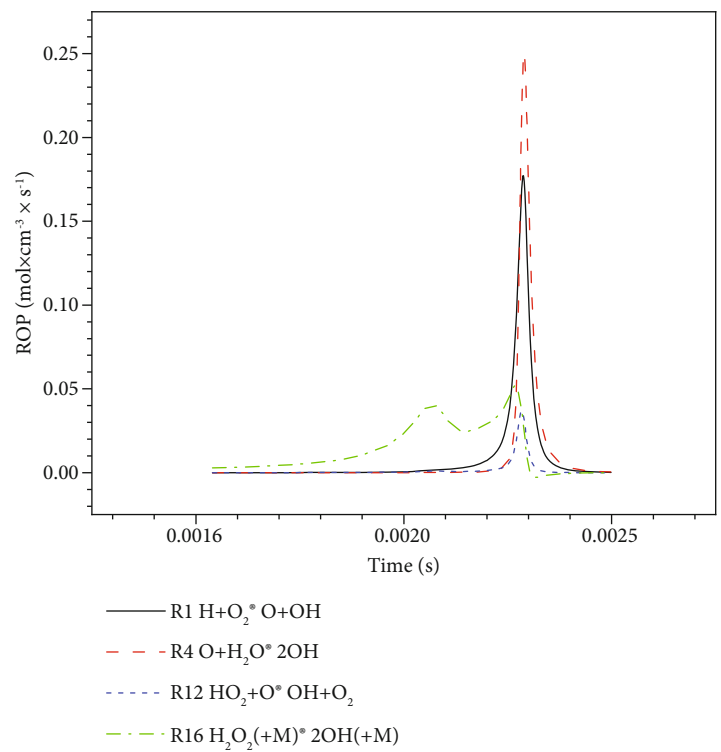
(a) Air
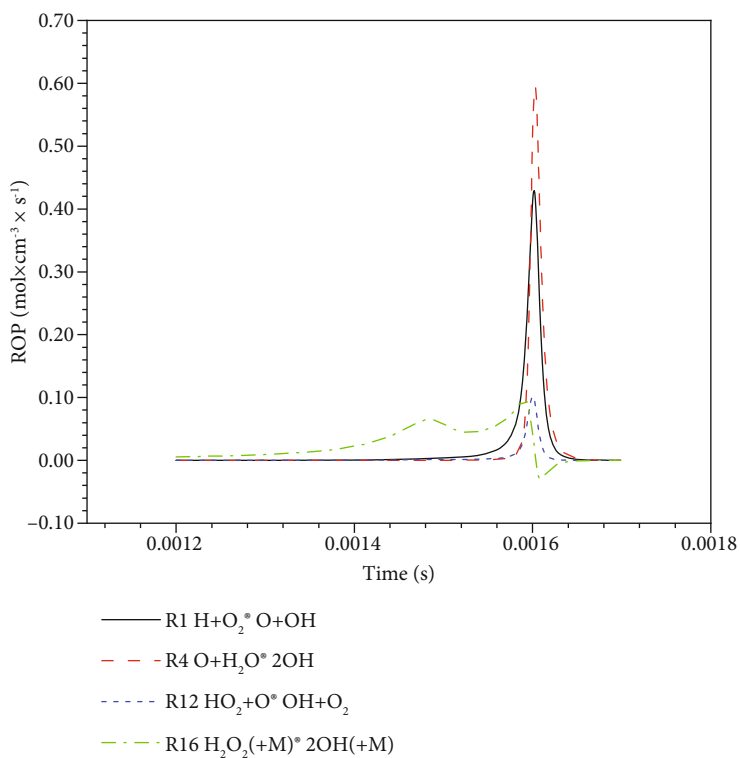
(b) 60% CO_2/40% O_2

FIGURE 12: Continued.

(c) 50% CO_2/50% O_2

(d) 40% CO_2/60% O_2
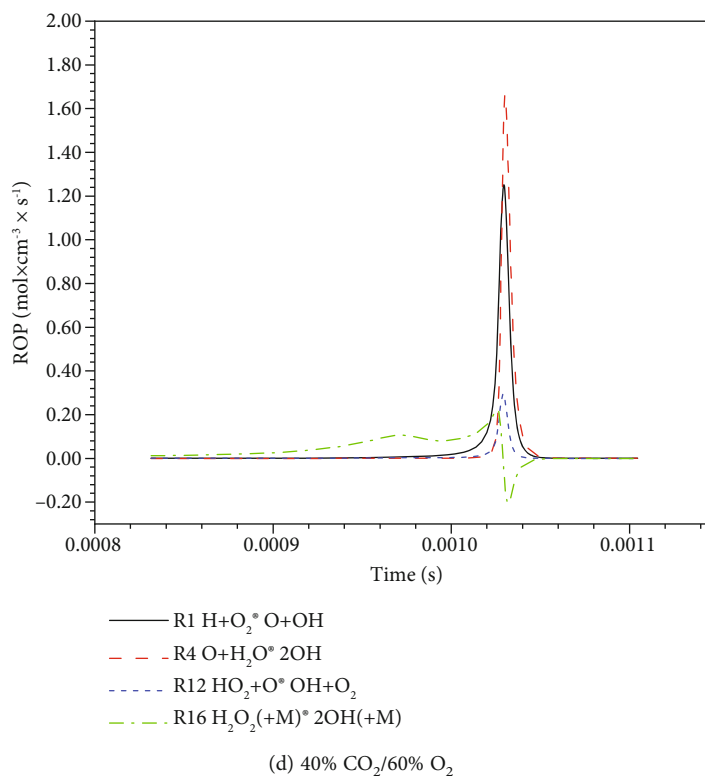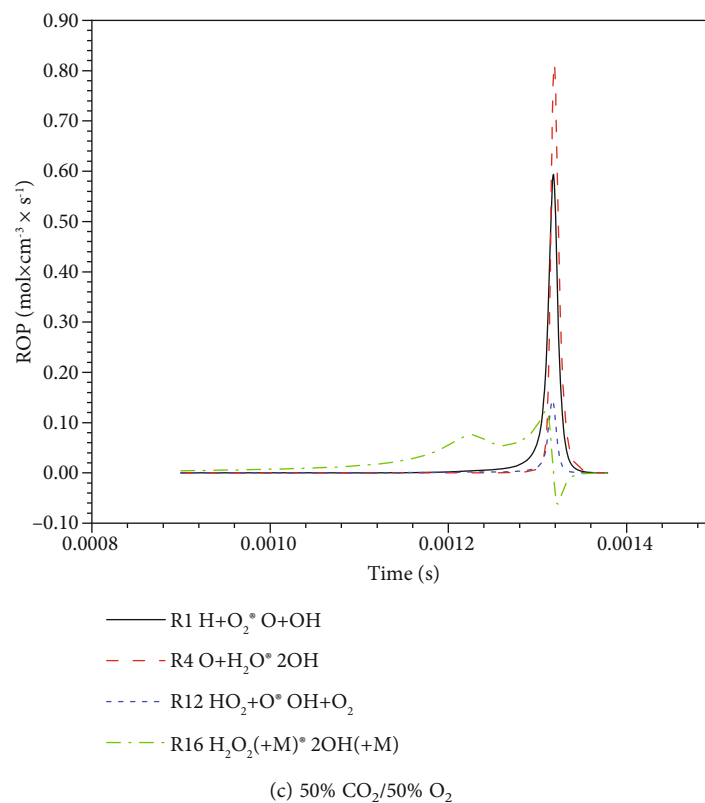
FIGURE 12: The rate of production of OH radical in four working conditions.

and 124%, respectively. The result shows that R16 has a greater contribution to the generation of OH radical in a high-concentration CO_2 atmosphere, while the R16 is an important reaction affecting IDT.

5. Conclusions

This work studies the IDT of 70% n-heptane/30% toluene in a high-concentration CO_2/O_2 atmosphere and establishes

the CDE model. Then, the CDE model is verified through experiment, and the relevant factors affecting the IDT are discussed. In summary, we draw the following conclusions:

(1) The CDE model is employed to predict well the IDT of 70% n-heptane/30% toluene under the CO_2/O_2 atmosphere, and the IDT average errors in 60% CO_2/40% O_2, 50% CO_2/50% O_2, and 40% CO_2/60% O_2 atmospheres are 5.29%, 5.71%, and 8.18%, respectively

(2) With increasing the CO_2 volume fraction from 40% to 60%, the CO_2 thermal effect is the main reason for the prolongation of IDT, while the chemical effect has little effect. However, when the CO_2 volume fraction exceeds 60%, the CO_2 third body effect is significantly enhanced, reducing the growth rate of IDT

(3) The CO_2 content significantly affected the OH radical ROP, and the OH radical ROP peak of R4 ($O+H_2O \longrightarrow 2OH$) decreases by 180% when the CO_2 volume fraction increases from 40% to 60%

Limited by time and experimental conditions, there is still room for further research in this paper in the future: (1) The initial conditions of the constant volume combustion chamber test in this paper are relatively simple, only 850 K and 3 MPa. In future research, tests can be carried out for n-heptane ignition at different temperatures and pressures to verify the CDE model. (2) In this paper, the high-speed camera direct shooting method is used to photograph the ignition process of the flame. This test method cannot obtain the content and distribution of free radicals in the flame. Laser-induced fluorescence testing can be added in future research. (3) The inclusion of quantum chemical calculations in the n-heptane/toluene mechanistic study to explore new reaction pathways and the impact of new pathways on ignition characteristics.

Data Availability

No data were used that are available upon request or included within the article.

Conflicts of Interest

There is no conflict of interest between all authors, and it does not influence the publication of this article.

Authors' Contributions

Yongfeng Liu and Guijun Bi proposed the idea of a visualization experiment combined with the simulation experiment. Yuewei Zhang and Jinou Song designed the experiments. Ping Wei and Hua Sun performed the experiments and analyzed the data. Yuewei Zhang accomplished the numerical simulation. Shengzhuo Yao and Yuewei Zhang wrote the paper. Yongfeng Liu and Lu Zhang revised the paper.

References

[1] M. Fritz, P. Plötz, and S. A. Funke, "The impact of ambitious fuel economy standards on the market uptake of electric vehicles and specific CO_2 emissions," *Energy Policy*, vol. 135, no. 443, p. 111006, 2019.

[2] T. A. Jacobson, J. S. Kler, M. T. Hernke, R. K. Braun, K. C. Meyer, and W. E. Funk, "Direct human health risks of increased atmospheric carbon dioxide," *Nature Sustainability*, vol. 2, no. 8, pp. 691–701, 2019.

[3] A. Franco and F. Leccese, "Measurement of CO_2 concentration for occupancy estimation in educational buildings with energy efficiency purposes," *Journal of Building Engineering*, vol. 32, article 101714, 2020.

[4] P. C. Pei and Y. F. Liu, "Internal combustion engine using liquid oxygen to fixed carbon without emissions China," CN201826979U, 2011.

[5] S. V. Khandal, N. R. Banapurmath, and V. N. Gaitonde, "Performance studies on homogeneous charge compression ignition (HCCI) engine powered with alternative fuels," *Renewable Energy*, vol. 132, pp. 683–693, 2019.

[6] H. An, W. M. Yang, J. Li, and D. Z. Zhou, "Modeling study of oxygenated fuels on diesel combustion: effects of oxygen concentration, cetane number and C/H ratio," *Energy Conversion and Management*, vol. 90, pp. 261–271, 2015.

[7] P. G. Szymkowicz and J. Benajes, "Development of a diesel surrogate fuel library," *Fuel*, vol. 222, pp. 21–34, 2018.

[8] Z. Gao, E. Hu, Z. Xu, G. Yin, and Z. Huang, "Effect of 2, 5-dimethylfuran addition on ignition delay times of n-heptane at high temperatures," *Frontiers in Energy*, vol. 13, no. 3, pp. 464–473, 2019.

[9] L. Ruwe, L. Cai, J. Wullenkord et al., "Low- and high-temperature study of n -heptane combustion chemistry," *Proceedings of the Combustion Institute*, vol. 38, pp. 405–413, 2021.

[10] D. Zhang, Y. Wang, C. Zhang, P. Li, and X. Li, "Experimental and numerical investigation of vitiation effects on the auto-ignition of _n_ -heptane at high temperatures," *Energy*, vol. 174, pp. 922–931, 2019.

[11] W. Liu, J. Zhang, Z. Huang, and D. Han, "Applicability of high dimensional model representation correlations for ignition delay times of n-heptane/air mixtures," *Frontiers in Energy*, vol. 13, no. 2, pp. 367–376, 2019.

[12] J. Gustavsson, V. I. Golovitchev, and A. Helmantel, *3-D modelling of conventional and HCCI combustion diesel engines. SAE technical paper*, SAE International, 2004.

[13] A. S. AlRamadan, M. B. Houidi, J. Sotton, M. Bellenoue, B. Johansson, and S. M. Sarathy, "Three-stage auto-ignition of n-heptane and methyl-cyclohexane mixtures at lean conditions in a flat piston rapid compression machine," *Proceedings of the Combustion Institute*, vol. 38, pp. 5539–5548, 2021.

[14] L. Lu, C. Zou, Q. Lin, Y. Liu, and H. Jing, "Experimental and simulated study on the ignition delay time of dimethyl ether/ n-heptane/oxygen/argon mixtures," *Fuel*, vol. 264, 2020.

[15] C. Yang, W. Wang, Y. Li, and X. Cheng, "Quantitative study on chemical effects of actual/simulated recirculated exhaust gases on ignition delay times of n-heptane /ethanol fuel blends at elevated temperature," *Fuel*, vol. 263, article 116327, 2020.

[16] D. Kang, D. Kim, K. H. Yoo, A. Violi, and A. Boehman, "The effect of molecular structures of alkylbenzenes on ignition characteristics of binary n-heptane blends," *Proceedings of the Combustion Institute*, vol. 37, no. 4, pp. 4681–4689, 2019.

[17] S. Lee and S. Song, "Rapid compression machine studies on ignition delay changes in a methyl butanoate/ n -heptane mixture by hydrogen addition," *International Journal of Hydrogen Energy*, vol. 41, no. 42, pp. 19207–19217, 2016.

[18] J. Liang, Z. Zhang, G. Li, Q. Wan, L. Xu, and S. Fan, "Experimental and kinetic studies of ignition processes of the methane- n -heptane mixtures," *Fuel*, vol. 235, no. 1178, pp. 522–529, 2019.

[19] E. Hu, Z. Gao, Y. Liu, G. Yin, and Z. Huang, "Experimental and modeling study on ignition delay times of dimethoxy methane/ n -heptane blends," *Fuel*, vol. 189, pp. 350–357, 2017.

[20] T. Javed, C. Lee, M. AlAbbad et al., "Ignition studies of n -heptane/ iso -octane/toluene blends," *Combustion and Flame*, vol. 171, pp. 223–233, 2016.

[21] D. Kim, C. K. Westbrook, and A. Violi, "Two-stage ignition behavior and octane sensitivity of toluene reference fuels as gasoline surrogate," *Combustion and Flame*, vol. 210, pp. 100–113, 2019.

[22] H. Feng, X. Wang, and J. Zhang, "Study on the effects of intake conditions on the exergy destruction of low temperature combustion engine for a toluene reference fuel," *Energy Conversion and Management*, vol. 188, pp. 241–249, 2019.

[23] G. Coskun, Y. Delil, and U. Demir, "Analysis of an HCCI engine combustion using toluene reference fuel for different equivalence ratios - comparison of experimental results with CFD and SRM simulations," *Fuel*, vol. 247, pp. 217–227, 2019.

[24] J. Herzler, M. Fikri, K. Hitzbleck et al., "Shock-tube study of the autoignition of _n_ -heptane/toluene/air mixtures at intermediate temperatures and high pressures," *Combustion and Flame*, vol. 149, no. 1–2, pp. 25–31, 2007.

[25] M. Hartmann, I. Gushterova, M. Fikri, C. Schulz, R. Schießl, and U. Maas, "Auto-ignition of toluene-doped n -heptane and iso-octane/air mixtures: high- pressure shock-tube experiments and kinetics modeling," *Combustion and Flame*, vol. 158, no. 1, pp. 172–178, 2011.

[26] R. Di Sante, "Measurements of the auto-ignition of _n_ -heptane/toluene mixtures using a rapid compression machine," *Combustion and Flame*, vol. 159, no. 1, pp. 55–63, 2012.

[27] Z. Malliotakis, C. Banyon, K. Zhang et al., "Testing the validity of a mechanism describing the oxidation of binary n -heptane/ toluene mixtures at engine operating conditions," *Combustion and Flame*, vol. 199, pp. 241–248, 2019.

[28] J. J. Hernandez, J. Sanz-Argent, J. Benajes, and S. Molina, "Selection of a diesel fuel surrogate for the prediction of auto-ignition under HCCI engine conditions," *Fuel*, vol. 87, no. 6, pp. 655–665, 2008.

[29] P. Hellier, N. Ladommatos, R. Allan, and J. Rogerson, "Combustion and emissions characteristics of toluene/n-heptane and 1-octene/n-octane binary mixtures in a direct injection compression ignition engine," *Combustion and Flame*, vol. 160, no. 10, pp. 2141–2158, 2013.

[30] K. Zhang, Q. Xin, Z. Mu, Z. Niu, and Z. Wang, "Numerical simulation of diesel combustion based on *n* -heptane and toluene," *Propulsion and Power Research*, vol. 8, no. 2, pp. 121–127, 2019.

[31] K. Zhou, Q. Lin, H. Hu et al., "Ignition and combustion behaviors of single coal slime particles in CO_2/O_2 atmosphere," *Combustion and Flame*, vol. 194, pp. 250–263, 2018.

[32] Y. Liu, J. Cheng, C. Zou, L. Lu, and H. Jing, "Ignition delay times of ethane under O_2/CO_2 atmosphere at different pressures by shock tube and simulation methods," *Combustion and Flame*, vol. 204, pp. 380–390, 2019.

[33] X. Hu and H. Wei, "Experimental investigation of laminar flame speeds of propane in O_2/CO_2 atmosphere and kinetic simulation," *Fuel*, vol. 268, 2020.

[34] H. Chen, H. Shen, T. Wu, and C. Zuo, "Numerical simulation and experimental research on combustion characteristics of compression-ignition engine under an O_2/CO_2 atmosphere," *HKIE Transactions Hong Kong Institution of Engineers*, vol. 24, no. 3, pp. 121–132, 2017.

[35] C. Peng, C. Zou, W. Xia et al., "Ignition delay times of n-butane and i-butane under O_2/CO_2 atmospheres: shock tube experiments and kinetic model," *Combustion and Flame*, vol. 234, article 111646, 2021.

[36] Y. Liu, T. Zhao, Z. Li et al., "Auto-ignition characteristics of diesel fuel in an O_2-CO_2 mixture," *Transactions of the Canadian Society for Mechanical Engineering*, vol. 43, no. 1, pp. 1–12, 2019.

[37] Y. Liu, Q. Xiang, P. Wei et al., "Effects of carbon dioxide addition on diesel spray flame characteristics in oxygen-carbon dioxide atmospheres," *Fuel*, vol. 276, 2020.

[38] L. J. Spadaccini and J. A. Tevelde, "Autoignition characteristics of aircraft-type fuels," *Combustion and Flame*, vol. 46, pp. 283–300, 1982.

[39] T. W. Ryan and T. J. Callahan, "Engine and constant volume bomb studies of diesel ignition and combustion," *SAE Trans J Fuels Lubrificant*, vol. 97, pp. 756–764, 1988.

[40] M. Mehl, W. J. Pitz, C. K. Westbrook, and H. J. Curran, "Kinetic modeling of gasoline surrogate components and mixtures under engine conditions," *Proceedings of the Combustion Institute*, vol. 33, no. 1, pp. 193–200, 2011.

[41] H. Nakamura, D. Darcy, M. Mehl et al., "An experimental and modeling study of shock tube and rapid compression machine ignition of _n_ -butylbenzene/air mixtures," *Combustion and Flame*, vol. 161, no. 1, pp. 49–64, 2014.

[42] F. E. Corcione, M. Costa, B. M. Vaglieco, and A. De Maio, "The role of radical species in diesel engine auto-ignition detection," *SAE Technical Papers*, vol. 2001, no. 724, 2001.

[43] P. Pepiot-Desjardins and H. Pitsch, "An efficient error-propagation-based reduction method for large chemical kinetic mechanisms," *Combustion and Flame*, vol. 154, no. 1–2, pp. 67–81, 2008.

[44] Y. T. Hwang, "On the proper usage of sensitivities of chemical kinetics models to the uncertainties in rate coefficients," *Proceedings of the National Science Council B. ROC*, vol. 6, pp. 270–278, 1982.

[45] R. Zang, C. Yao, Z. Yin, P. Geng, J. Hu, and T. Wu, "Mechanistic study of ignition characteristics of diesel/methanol and diesel/methane dual fuel engine," *Energy and Fuels*, vol. 30, no. 10, pp. 8630–8637, 2016.

[46] H. Shao, W. Li, M. Xia et al., "Fault diagnosis of a rotor-bearing system under variable rotating speeds using two-stage parameter transfer and infrared thermal images," *IEEE Transactions on Instrumentation and Measurement*, vol. 70, pp. 1–11, 2021.

[47] Z. He, H. Shao, Z. Ding, H. Jiang, and J. Cheng, "Modified deep autoencoder driven by multisource parameters for fault transfer prognosis of aeroengine," *IEEE Transactions on Industrial Electronics*, vol. 69, no. 1, pp. 845–855, 2022.

[48] W. Xia, C. Peng, C. Zou et al., "Shock tube and modeling study of ignition delay times of propane under $O_2/CO_2/Ar$ atmosphere," *Combustion and Flame*, vol. 220, pp. 34–48, 2020.

[49] S. Verma, L. M. Das, S. C. Kaushik, and S. S. Bhatti, "The effects of compression ratio and EGR on the performance and emission characteristics of diesel-biogas dual fuel engine," *Applied Thermal Engineering*, vol. 150, pp. 1090–1103, 2019.

[50] Z. He, H. Shao, X. Zhong, and X. Zhao, "Ensemble transfer CNNs driven by multi-channel signals for fault diagnosis of rotating machinery cross working conditions," *Knowledge-Based Systems*, vol. 207, article 106396, 2020.

[51] X. Fu and S. K. Aggarwal, "Two-stage ignition and NTC phenomenon in diesel engines," *Fuel*, vol. 144, pp. 188–196, 2015.

[52] P. Sabia, M. Lubrano Lavadera, P. Giudicianni, G. Sorrentino, R. Ragucci, and M. de Joannon, "CO_2 and H_2O effect on propane auto-ignition delay times under mild combustion operative conditions," *Combustion and Flame*, vol. 162, no. 3, pp. 533–543, 2015.

[53] "Chemkin overview," http://www.reactiondesign.com/products/chemkin.

[54] A. Alfazazi, O. A. Kuti, N. Naser, S. H. Chung, and S. M. Sarathy, "Two-stage Lagrangian modeling of ignition processes in ignition quality tester and constant volume combustion chambers," *Fuel*, vol. 185, pp. 589–598, 2016.

[55] Z. Wu, Z. Kang, J. Deng, Z. Hu, and L. Li, "Effect of oxygen content on n-heptane auto-ignition characteristics in a HCCI engine," *Applied Energy*, vol. 184, pp. 594–604, 2016.

[56] J. Zádor, C. A. Taatjes, and R. X. Fernandes, "Kinetics of elementary reactions in low-temperature autoignition chemistry," *Progress in Energy and Combustion Science*, vol. 37, no. 4, pp. 371–421, 2011.

[57] Z. J. Buras, C. Safta, J. Zádor, and L. Sheps, "Simulated production of OH, HO_2, CH_2O, and CO_2 during dilute fuel oxidation can predict 1st-stage ignition delays," *Combustion and Flame*, vol. 216, pp. 472–484, 2020.

Research Article

Intelligent Diagnosis Model of Traction Seat of Urban Rail Vehicle Based on Harris Hawks Optimization

Qi Chang,[1] Minglei Zheng,[1] Jiaxin Luo,[1] Lin Li,[2] Junfeng Man,[1] Yiping Shen [3], and Yi Liu [1,2,4]

[1]*School of Computer Science, Hunan University of Technology, Zhuzhou, 412000 Hunan, China*
[2]*National Rail Transit Advanced Equipment Innovation Center, Zhuzhou, Hunan 412000, China*
[3]*School of Mechanical Engineering, Hunan University of Science and Technology, Xiangtan 412000, China*
[4]*CRRC Zhuzhou Electric Locomotive Co., LTD., Zhuzhou, 412000 Hunan, China*

Correspondence should be addressed to Yi Liu; liuyi_hust@163.com

Traction seat is an important connecting part of urban rail vehicle, which plays an important role in maintaining smooth running and power transmission of the vehicle body. Timely diagnosis of early failure of traction seat is the key to ensure the safe operation of urban rail vehicles. In order to realize the intelligent diagnosis of traction seat, a multialgorithm fusion scheme based on the Harris Hawk algorithm (HHO) is proposed to realize the fault diagnosis of traction seat. Firstly, the early mechanism of traction seat was studied, and the simulation experiment platform of urban rail vehicle traction seat was built to obtain the vibration data of the early crack traction seat model, so as to facilitate the simulation experiment research. Then, the vibration data of the traction seat were processed by HHO optimized variational mode decomposition (HVMD) to obtain several intrinsic mode functions (IMFs). Secondly, the multiscale permutation entropy (MPE) of each IMF is quantified and its average value is used to construct the energy characteristic vector. Finally, feature vectors are input into the HHO optimized support vector machine (HSVM) model to train a pattern recognizer. Through Python simulation verification, the results show that the model can accurately extract the characteristic information of traction seat and accurately identify the fault type, and the recognition rate reaches 100%.

1. Introduction

As an economical and practical urban public transport system, urban rail transit has the advantages of large capacity, energy saving, and environmental protection and has become the main force of urban transport development in the world. With the support of the state, urban rail transit is constantly improving and perfecting. At present, under the promotion of the state, the urban rail network is expanding, the number of urban rail vehicles is increasing, the maintenance services are also increasing, and the quality demand for operation and maintenance is also increasing. Under the current situation, the fault diagnosis of urban rail vehicles mainly relies on manual troubleshooting and processing but has not realized real-time status monitoring, and the troubleshooting process needs to spend a lot of manpower, material resources, and financial resources to do offline detection, diagnosis, and maintenance. In this environment, the importance of intelligent perception and operation and maintenance technology of urban rail vehicles is self-evident. For the rapid development of transportation, it is imperative to study the fault diagnosis of urban rail vehicles. The safe operation and condition monitoring of urban rail vehicles is an important research focus in the field of modern urban rail transit, which bears the responsibility of passengers' safety and social stability.

In urban rail vehicles, traction seat is an important part connecting the car body and bogie. The traction seat not only plays the role of power transmission but also plays the role of traction and braking. At the same time, it can also ensure the smooth running of urban rail vehicle by avoiding the interference of bogie and car body when driving in complex sections. Traction seat load is a complicated and intense vibration environment for a long time, this makes the traction seat easy to produce slight early cracks in a weld, The early crack detection is very difficult to the operation and maintenance of the vehicle. If the crack of the traction seat is not found in time, once the crack expands, it will bring safety hazards to the safe operation of the vehicle. Crack fault is a common defect in mechanical structure and is also one of the common factors causing the failure of mechanical equipment. In recent years, mechanical equipment is often accompanied by cracks in the operation of the occurrence of disasters and accidents, prompting many experts and scholars to begin to study mechanical cracks. In the field of urban rail transit, the state of traction seat affects the effectiveness and reliability of urban rail vehicles, and the traditional traction seat fault detection method has disadvantages of poor real-time performance and low efficiency. Therefore, the establishment of an intelligent traction seat fault detection system can prevent the further expansion of early cracks in time to solve the occurrence of accidents.

At present, the crack detection of mechanical equipment is mainly divided into two aspects [1–10]: one is the nondamage detection method: the integration of modern technology with physical or chemical technology to create equipment that can detect the thermal, acoustic, optical, electrical, magnetic, and other reaction changes within the material, to detect the crack defects of mechanical equipment; the second is the intelligent diagnosis method: analyze the vibration signals of the mechanical equipment collected, extract the sensitive characteristics of the equipment, and then, use the pattern recognition method to identify the crack state. Traditional nondamage detection technologies (such as ultrasonic detection, X-ray detection, eddy current detection, and magnetic particle detection) can detect cracks in mechanical equipment without damaging or affecting the performance of the test object, which has been widely used in engineering [1–6]. When the traditional nondamage detection technology cannot meet the requirements, many scholars adopt intelligent diagnosis methods to diagnose crack faults and adapt to more engineering applications, among which the vibration diagnosis method is the most widely studied [7–10]. Literature [7] analyzes gear cracks based on vibration signals and proposes a re-weighted singular value decomposition (RSVD) method for periodic pulse extraction, which has achieved good results in fault detection and severity assessment. Literature [8] proposed a numerical fault detection model based on dynamic transmission error (DTE). The experimental results show that with the increase of crack level, the meshing stiffness of gear decreases, which provides a scheme to solve the crack fault in gear operation. In Reference [9], the Jensen-Shannon Divergence (JSD) algorithm was proposed, which had high sensitivity in measuring small changes between probability distributions and

could detect small cracks (0.01 mm~0.04 mm) that could not be detected in baseline impedance signal measurement. In literature [10], the gear meshing stiffness under different crack sizes was calculated by using the analytical tooth crack model. Then, considering the nonlinearity of backlash and bearing clearance, a 3-dof spur gear pair model was established. Based on the multiple statistical indicators obtained from the nonlinear frequency response of the gear system, to assess the vibration characteristics of the gear system and fault condition, the experiment results show that the built model can predict the meshing stiffness of the gear system and vibration behavior of crack, and the corresponding vibration analysis, for researchers and engineers to provide the reference for tooth crack detection. It can be seen from the above research that the crack method based on vibration diagnosis has a solid theoretical foundation and has been fully studied, on the basis of the previous research results, according to the data source, data processing method, and fault identification model of traction seat fault diagnosis. Therefore, based on the data and the characteristics of the traction seat data collected, an intelligent fault diagnosis model based on HHO_VMD and HHO_MPE_SVM is proposed based on the vibration diagnosis method (i.e., the framework of "signal acquisition + feature extraction + pattern recognition"). The model puts forward novel improvement measures in feature extraction and pattern recognition.

Fault diagnosis is affected by mechanical equipment signals, signal analysis methods, and signal features. In the aspect of signal feature extraction, the commonly used signal analysis methods are classical statistical analysis, time-domain, frequency-domain, and time-frequency domain combined methods. The signal analysis method is developed from classical Fourier transform, short-time Fourier transform, wavelet transform, empirical mode decomposition, empirical mode decomposition, empirical wavelet transform, and variational mode decomposition. Because of the complexity of the mechanical system, these methods are not always feasible, many experts and scholars try to on the basis of the signal analysis methods was improved, and the existing research mostly stays in the experimental validation phase. The feature extraction method has some limitations in practical application, and domestic and foreign researchers put forward various solutions for feature extraction algorithm. Jardine et al. studied statistical indicators in time domain and frequency domain to diagnose the advantages and disadvantages of bearing faults [11]. Ahrabian et al. extended the synchronous compression transformation method from one-dimensional to parallel multidimensional in time-frequency analysis, which improved the antinoise performance of the algorithm [12]. Wu et al., considering the superior performance of variational modal decomposition (VMD) in signal processing, proposed an algorithm based on EMD-VMD asymptotic reconstruction and quadratic decomposition to solve the difficulty in accuracy of bearing fault diagnosis [13]. Zhang et al. analyzed wind force sequence based on VMD and built a prediction model, proving that VMD has a better prediction effect compared with other decomposition methods [14]. Sun et al. used VMD to decompose the signal into multiple IMFs to improve the

signal-to-noise ratio, laying a foundation for the visual detection of laser ultrasonic track surface defects [15]. Xu et al. developed a variable mode decomposition method to optimize management parameters, a particle swarm optimization algorithm, and a method based on maximum entropy, which can accurately detect the existence of leakage in the pipeline [16]. Jiang et al. proposed an improved VMD strategy in view of the fact that VMD can be used to reveal weak transient pulses in complex vibration signals, but its reasonable modal number is difficult to be set in advance. This method combines the advantages of traditional VMD and empirical mode decomposition (EMD) and adaptively selects sensitive intrinsic mode function (IMF) components for fault component analysis using the proposed index values to solve this difficulty [17]. Glowacz and other scholars based on the current gear fault diagnosis mainly based on vibration signals; acoustic signal analysis research is less. A gear fault diagnosis method based on deep learning based on acoustic signal analysis was proposed. Time-domain and frequency-domain signals are input to the model as original signals, without feature engineering [18]. Zhang et al. proposed a VMD optimization method based on the grasshopper optimization algorithm (GOA) to analyze vibration signals of rotating machinery, which can estimate the optimal modal number and modal frequency bandwidth control parameters matching the analyzed vibration signals [19]. Many studies have demonstrated the obvious advantages of VMD in signal decomposition. In order to further quantify the characteristics of fault signals extracted from vibration signals, some scholars use nonlinear parameter estimation (entropy theory). According to literature [20], multiscale permutation entropy can describe the complexity and randomness of signals. Reference [19] mentioned that MPE has stronger robustness compared with sample entropy, approximate entropy, and permutation entropy and can study information changes of time series at multiple scales, so as to extract fault features more comprehensively. The different crack types of the traction seat of the bogie will lead to the characteristics of nonlinear and nonstationary vibration signals collected. Since the complexity is difficult to analyze, this experiment uses VMD, an adaptive signal processing tool, to reveal the complex vibration signals of the traction seat. In addition, in order to study traction on the output time series of complex systems, which contains abundant characteristic information, this paper decides to adopt MPE calculation of the traction characteristic information and can dig the hidden more abundant characteristic information in time series, which accurately reflects the change of system, scale for more than the original single state.

An important link in fault diagnosis is the selection of pattern recognition methods. At present, an artificial neural network (ANN) is a commonly used pattern recognition method, which has the advantages of strong adaptability, strong robustness, and good fault tolerance. Through sufficient data training, the mapping relationship of nonlinear input and output can be obtained [21]. However, ANN has the disadvantages of overfitting, slow convergence speed, and easy to fall into local extremum, which makes the diagnostic accuracy of ANN not high enough. Support vector machine (SVM) is a new computational learning method developed by Vapnik on the basis of statistical learning theory, which can successfully solve the problems of overfitting, local optimal solutions, and slow convergence in ANN [22]. SVM has been successfully applied in many fields [23–27]. For example, in the intelligent intrusion detection system, the SVM intrusion detection algorithm has been widely used to quickly and accurately identify intrusions [23]; in the field of healthcare, the application of SVM to accurately diagnose Alzheimer's disease (AD) and its early mild cognitive impairment (MCI) is crucial to provide early treatment for patients [24]; in text detection, SVM has high-dimensional spatial learning ability and adopts SVM as a texture classifier. Compared with the text detection method of the neural network, the SVM classifier proves the superiority of this method [25]; in the field of image recognition, SVM technology is currently a research hotspot in the field of pattern recognition. Their combination not only effectively solves the problem but also improves the accuracy of classification and prediction [26, 27]. In this paper, SVM is selected to classify the state of traction seat according to the typical characteristics of traction seat samples.

Based on the above analysis of fault diagnosis results of vibration diagnosis methods, VMD, MPE, and SVM were selected as the theoretical basis for the study of crack fault identification of traction seat of urban rail vehicles in this experiment. Considering that selecting appropriate parameter values is crucial to the accuracy of fault identification, parameter selection combined with an intelligent optimization algorithm can directly affect the effectiveness of feature extraction and the accuracy of state classification and then directly affect the fault diagnosis results [28–30]. In recent years, a large number of optimization algorithms have been applied to solve complex optimization problems in various fields, among which HHO is a new optimization algorithm whose potential in practical problems has not been extensively studied [31]. Compared with the existing metaheuristic algorithms and traditional methods, HHO's global search capability can better select the parameters of VMD, MPE, and SVM.

The main contributions of this paper are as follows:

(i) According to the difficulty of the lack of traction seat data, the operating force of the traction seat under the actual working condition was simulated, the appropriate experimental instruments were selected, reasonable parameters were set, and vibration data were collected

(ii) According to the characteristics of traction seat vibration signal, a reasonable signal processing method is selected to extract the feature set which can better represent the traction seat operation state. The pattern recognition algorithm suitable for the state characteristics of the traction seat is selected to identify the uneven crack state of the traction seat

(iii) According to the importance of determining reasonable parameters, the key parameters of VMD and SVM were optimized adaptively by the intelligent optimization algorithm HHO

(iv) The hybrid model based on VMD, MPE, and SVM algorithms has accurate diagnostic performance. The model can be used to accurately diagnose different crack conditions of traction seat

In this paper, based on the data acquisition of traction seat, VMD, MPE, and SVM algorithms are used to diagnose the fault state of traction seat of urban rail vehicles, in which HHO is used for parameter optimization of multiple algorithms. The validity of HVMD and HMSVM fault diagnosis models is verified by experiments. This method provides a new guarantee for the safe operation of urban rail vehicles and has practical engineering application value.

2. Theory and Method

In the operation of urban rail vehicles, bogies bear high frequency and random variation of load, and there is a large probability of structural failure, leading to the decline of vehicle running quality, and even leading to derailment and overturn. In order to ensure the safe operation of urban rail vehicles, we must pay attention to the frequent cracks of traction seat. A fault diagnosis model of HVMD_HMSVM is proposed to detect the early crack fault of traction seat and to prevent irreparable loss caused by further crack propagation. At present, there are several difficulties in the fault diagnosis research of urban rail vehicle bogie traction seat as follows:

(1) Acquisition of traction seat data set: at the present stage, the fault diagnosis of traction seat crack is mainly through data analysis and mining, while urban rail vehicle data is extremely scarce. Therefore, the acquisition of traction seat data is a difficulty in current research. In order to solve the difficulty that there is no test data at present, the simulation experiment platform of bogie traction seat is built in this experiment

(2) Feature extraction of traction seat signals: at present, there are two problems of "redundancy" and "sparsity" in signal feature analysis, which cannot be comprehensively analyzed. In order to solve the problem of feature extraction, an information processing method of HHO_VMD_MPE was proposed to extract the feature information contained in the traction seat signal comprehensively

(3) Pattern recognition of traction seat fault: in the process of crack fault identification of traction seat, the selection of a classifier will affect the diagnosis accuracy. In order to solve the errors existing in the current pattern recognition, the HHO_MPE_SVM algorithm is proposed, and the feature set is input into the classifier of HHO_SVM to accurately identify the fault types

In view of the technical difficulties existing in the traction seat at the present stage, the bogie traction seat was taken as the research object, the simulation experiment platform was completed, and the traction seat diagnostic model based on HVMD_HMSVM was constructed. The general framework of the research method is shown in Figure 1, which can be described as six steps, as follows:

(1) Data samples of traction seat vibration signals were obtained on the simulation experimental platform

(2) Use HHO to optimize VMD parameters, using the optimized HHO_VMD signal decomposition, to obtain an IMFs

(3) Calculate the MPE values of each modal component and construct feature vectors to describe the state characteristics of traction seat

(4) The traction seat sample data obtained in Step 3 were divided into two groups according to a certain proportion for training samples and test samples, respectively

(5) HHO was used to optimize SVM to obtain the HHO_SVM diagnostic model

(6) Input the training samples into HHO_SVM for training to obtain the HHO_SVM classifier, and then input the test samples into the trained HHO_SVM classifier to identify the traction seat fault type through the classifier

2.1. Experimental Platform Construction and Traction Seat Data Acquisition. The traction seat of urban rail vehicles is affected by complex factors in vehicle operation. On the one hand, it is affected by the environment, such as temperature difference, strong and weak light, and bad weather, and on the other hand, it is affected by complex forces, such as the vertical and transverse force of the route, bend impact force, and heavy load. Under the influence of many factors, traction seat is prone to wear, corrosion, deformation, etc., which eventually leads to early slight cracks in traction seat, and cracks usually appear at the weld. It is difficult to obtain the operating state data of traction seat of urban rail vehicle under actual working conditions, and it is impossible to fully analyze the data for fault diagnosis, resulting in low diagnostic accuracy. In order to prevent the irretrievable loss caused by the bad evolution of the early crack, the detection method of the traction seat early crack was studied. Therefore, the vibration data of the traction seat model of the early crack was firstly provided in the experiment, so as to facilitate the study of the detection of the early crack failure state of the traction seat.

According to the maintenance standard of the bogie of the urban rail train in China, it can be known that when there are scratches and cracks on the surface of the parts and parts, their depth is less than or equal to 10% of the steel plate thickness, and they need to be polished to eliminate them. Welding is required when the defect depth is greater than 10% of the plate thickness and cracks can be visually detected. According to the above criteria, the different widths and depths of the traction seat cracks of urban rail vehicles were used as the quantitative representation indexes for different crack failure states. Namely, the traction seat
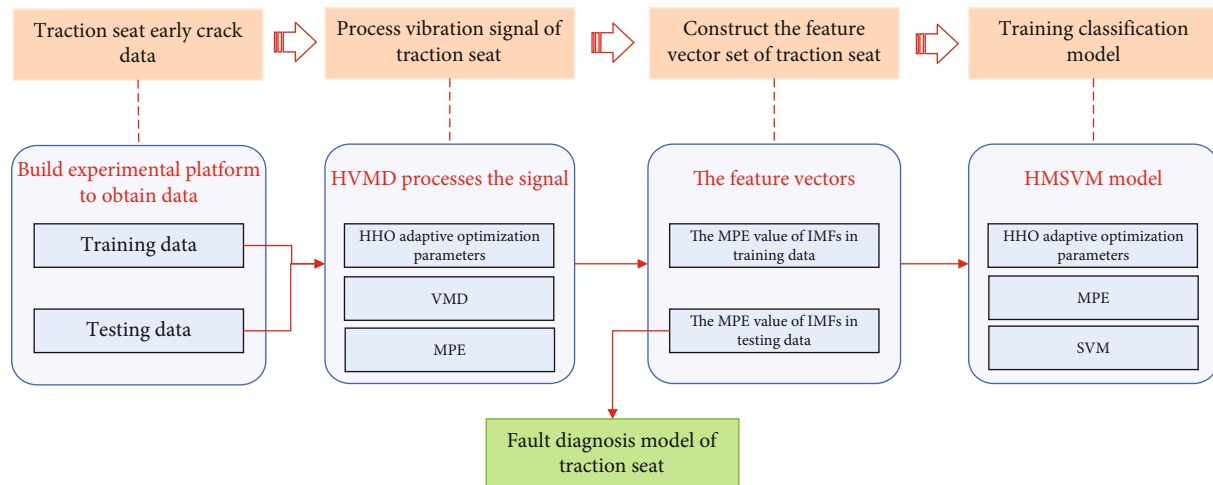
FIGURE 1: General research block diagram of traction seat intelligent diagnosis model. Establishment of the traction seat fault diagnosis model.

crack fault state is divided into no crack state (normal state), small crack state, and large crack state. That is, when there is a crack on the traction seat surface whose width is less than or equal to 10% of the thickness of the vertical plate, it is a small crack state and needs to be polished to eliminate it. When the crack width is greater than 10% of the thickness of the vertical plate, it is a big crack state and must be repaired by welding. In the normal state, no operation is required. Experimental design traction seat model size: roof and bottom plate is 30 cm long, 20 cm wide, the height between the roof and bottom plate is 20 cm, the middle support plate is a trapezoidal plate, the upper bottom is 21 cm long, the lower bottom is 26 cm long, and the distance between the two support plates is 15 cm. The vertical plate thickness is 1.3 cm. Due to the crack fault that happens in traction seat welding place, therefore making fault model, not the side of the base plate and support plate welds welded completely, set aside a weld as the crack fault, the simulation of traction seat produced two different degree of crack model and a normal traction model, respectively, set the model for the degree of crack corresponding cracks (normal status is not set). The traction seat without crack was quantified as the normal model. The early crack width and depth of 1 mm × 3 mm was the small crack model, and 2 mm × 8 mm was the large crack model (Table 1, Figure 2).

According to the common failure states of the traction seat (Table 1), the simulation experiment platform of urban rail vehicle bogie was built, including the real model and simulation model of the traction seat (Figure 2). In the dynamic response experiment, the measured signal is generally the structural excitation vibration response signal. In this experiment, the method of acceleration is selected for the detection of vibration signal. Since the early crack signal is difficult to detect, the dynamic performance, frequency response bandwidth, and sensitivity of the sensor need to be considered. A piezoelectric accelerometer is widely used in vibration signal detection due to its advantages of convenient use, good reliability, fast dynamic response speed, wide frequency band, and so on. The CAYD051V piezoelectric

acceleration sensor is selected to be installed on the experimental object. The sensitivity of the sensor is up to 100 mV/g, and weak traction seat signal can be detected. The host computer and wireless transmission technology were used to obtain the original, true, and reliable data source of the traction seat (Figure 3). Experimental environment: Inter(R) Core (TM) I7-7700HQ CPU @ 2.80 GHz, 16 GB RAM, Python3.7.

In the process of train running, the vibration of traction seat will change with the change of speed, even if the train is in a uniform speed state, the vibration of traction seat will change with the change of road conditions, so the experimental signal must be dynamic change, here choose to provide vibration signal source with frequency sweep instrument; the output end of the sweep is connected to the input port of the power amplifier through the signal line; the signal output end of the power amplifier is connected to the excitation source input port of the shaker; the shaker is connected to the side plane of the crack traction seat through the magnetic excitation top rod. The top rod must be perpendicular to the side plane; otherwise, the shaker will be damaged during the excitation. In order to reduce the interference of data acquisition, the traction seat must be suspended by elastic rope; in order to weaken the interference of the impact of the excitation top rod and avoid the sensor falling off due to too intense vibration, the acceleration sensor is installed on the traction seat bottom plate and installed through the magnetic head adsorption; the signal line of the acceleration sensor is connected with the acceleration sensor to the YE6213 data acquisition card; the YE6213 data acquisition card is connected to the PC through USB, and the data acquisition system matching the data acquisition card is installed on the PC to collect and store vibration data. After the control and sensing devices are installed, the entire system needs to be checked (Figure 3 shows the device connection diagram). According to the actual operating conditions and relevant theoretical basis, determine the experimental excitation frequency range of 100 Hz to 2500 Hz; the excitation output mode of frequency sweep is set as fixed

TABLE 1: Classification of traction seat status.

State	Normal	Small crack	Big crack
Judging basis: crack width and depth	No set fault	1 mm × 3 mm	2 mm × 8 mm

(a) Real model-traction seat

(b) Experimental model-traction seat

(c) Experimental model-small crack

(d) Experimental model-big crack
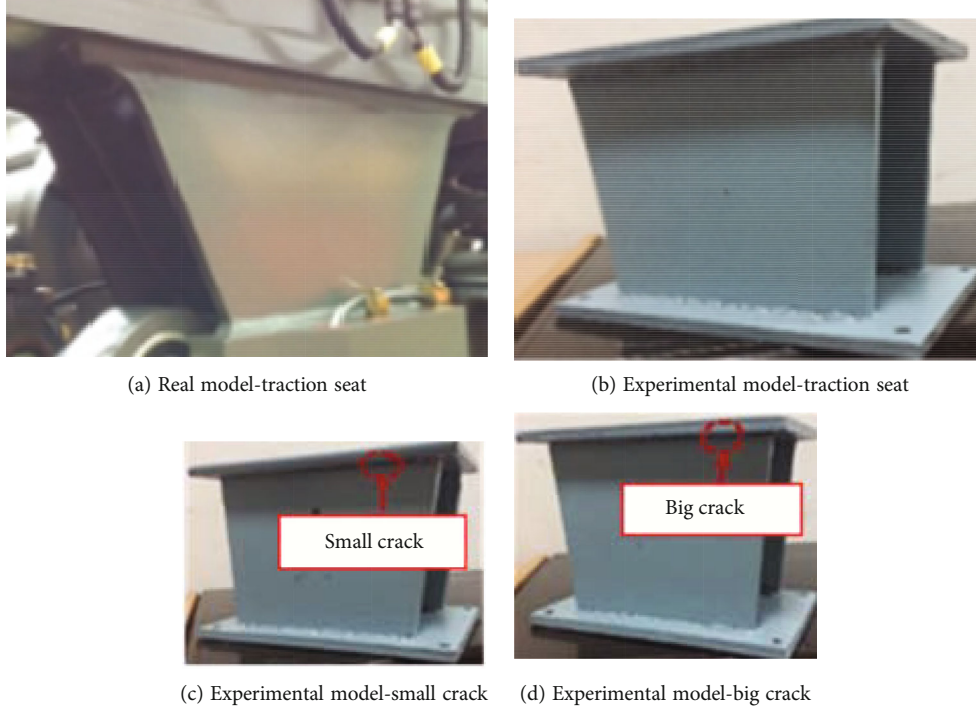
FIGURE 2: Real model and simulation model of traction seat.

frequency output, and the output signal is a steady sinusoidal signal. Frequency sweep output frequency from 100 Hz to 2500 Hz fixed output excitation signal; sampling frequency was set as Fs = 12 KHz; sampling time $t = 5$ s; the sampling interval is $T = 1$ h, and 6,000 samples and 30 sets of data are collected in each state. After the completion of experimental data collection, the data of the three states were selected. Finally, according to the specific experimental situation, 600 groups of data were selected for the experiment, including 200 groups of samples in the normal state, large crack state, and small crack state. According to the experimental situation, 75% were randomly selected as the training set. Take 25% as the test set. The details are shown in Table 2.

2.2. Traction Seat Feature Extraction Based on HMVMD

2.2.1. Harris Hawks Optimization.
Harris Hawks Optimization (HHO) is a novel crowd-based algorithm proposed by Heidari et al. in 2019, inspired by the smartest birds around: Harris eagle (chestnut-winged eagle) developed a corresponding stochastic mathematical model by simulating its behavior when hunting rabbits. The HHO algorithm has been used to solve several optimization problems, including manufacturing, feature selection, classification, and engineering design. Because the structure is good, it can flexibly improve the optimization performance, and the selection of

parameters determined by HHO is the most appropriate choice at present. The HHO algorithm mainly includes three stages: exploration stage, transition stage from exploration to development, and development stage, which are briefly introduced as follows:

Stage 1 (exploration stage): escape energy $|E| \geq 1$, or the location of the Harris Hawks according to the location of the rabbit and with the center position of the entire group vector difference, such as type (1) shown in the following:

$$X(t+1) = \begin{cases} X_{\text{rand}}(t) - r_1|X_{\text{rand}}(t) - 2r_2 X(t)|, & q \geq 0.5, \\ (X_{\text{rabbit}}(t) - X_m(t)) - r_3(\text{LB} + r_4(\text{UB} - \text{LB})), & q < 0.5, \end{cases}$$
(1)

where $X(t+1)$ and $X(t)$ represent the position of the eagle in the $t+1$ and t iterations, respectively. $X_{\text{rand}}(t)$ represents the position of the random eagle in the t iteration, and r and q are uniformly distributed random numbers in the interval [0,1]. $X_{\text{rabbit}}(t)$ and $X_m(t)$ represent the rabbit position (the optimal value of the current iteration) and the center position of the eagle flock. LB and UB represent the upper and lower bounds of the value range, as shown in the following:

$$X_m(t) = \frac{1}{N}\sum_{i=1}^{N} X_i(t),$$
(2)
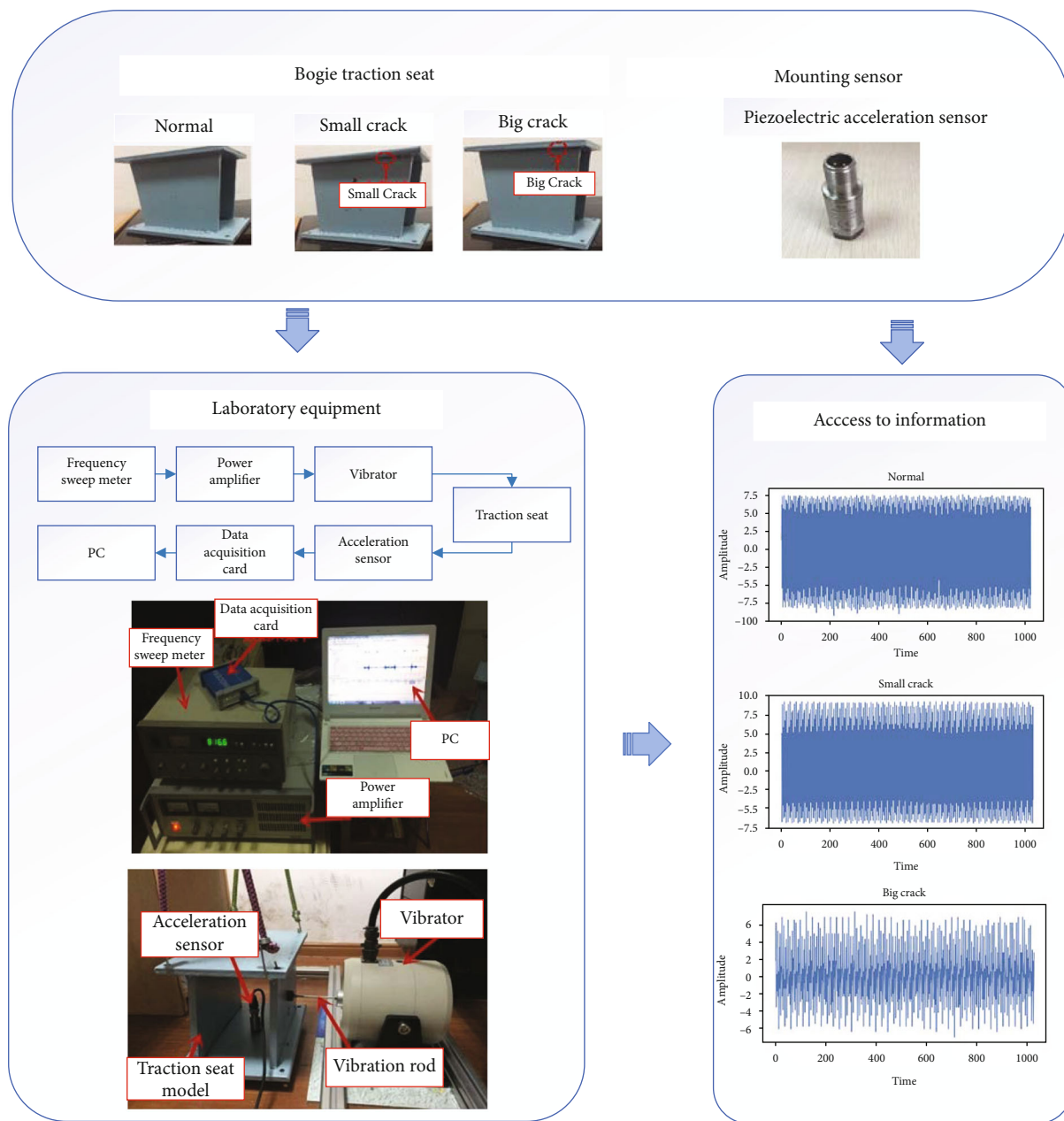
FIGURE 3: Shows the installation of experimental acquisition equipment, excitation equipment, and sensing equipment.

TABLE 2: Experimental test data.

Model state	The normal state	Small crack	Big crack
Tag name	0	1	2
Points in a single sample	60000	60000	60000
The training sample	90 group	90 group	90 group
The test sample	30 group	30 group	30 group
Number of sets of sample	12 group	12 group	120 group

where $X_i(t)$ represents the position of each eagle at iteration t and N represents the total number of eagles.

Stage 2 (transition stage): when the $|E| > 1$, one is exploratory behavior. After the exploration phase, there is a transition phase before entering the mining phase. In this transient stage, the rabbit energy needs to be modeled according to

$$E = 2E_0 \left(1 - \frac{t}{T} \right), \tag{3}$$

where E is the escape energy of the rabbit, T is the maximum number of iterations, and E_0 is the initial energy value of the rabbit. According to the physical condition of the victim, the random number $[-1, 1]$ is uniformly distributed. As E_0 moves towards −1, it means the victim is losing energy, and vice versa.

According to rabbit behavior, rabbit energy is inversely proportional to time. That means as long as t goes up, E goes down. According to Harris, when $|E| \geq 1|$, the eagle decided either to search different areas, to detect the location of rabbit, or move forward into the development phase.

Stage 3 (development stage): when the $|E| < 1$, indicating that the eagle has discovered the direction of the rabbit and needs to model two behaviors. According to the energy of the rabbit absolute value $|E|$ compared with 0.5 percentage and escape r judgment, it can be divided into two kinds of behavior, four kinds of strategy.

(1) Soft siege. If $|E| \geq 0.5$, $|r| \geq 0.5$, then the rabbit escape has high energy; at the same time, the probability of successful escape is higher than 50%. This means that the eagle will carry out a soft siege and update its position according to

$$X(t + 1) = \Delta X(t) - E|J X_{\text{rabbit}}(t) - X(t)|, \qquad (4)$$

where $\Delta X(t)$ is the position difference between rabbit and eagle, and the calculation method is as follows:

$$\Delta X(t) = X_{\text{rabbit}}(t) - X(t). \qquad (5)$$

J is a random number, representing the jump intensity that can be obtained, as shown in the following:

$$J = 2(1 - r_5), \qquad (6)$$

where r_5 is a random number that varies between 0 and 1

(2) Fast dive soft siege. If $|E| \geq 0.5$, $r < 0.5$, it indicates that rabbits have higher energy. However, the chances of a successful escape are not great. In this case, the eagle will engage in a soft siege but will gradually dive quickly. The eagle's next move will be based on the following:

$$Y = X_{\text{rabbit}}(t) - E|J X_{\text{rabbit}}(t) - X(t)|. \qquad (7)$$

The eagle will compare the current position to the previous dive to evaluate which is better. If the previous dive was better, the eagle would take advantage of it. If not, the eagle will make a new dive using the LF formula, as shown in LF formula (8). Harris eagle will then evaluate the Y and Z positions and reupdate the positions according to formulas (9), (10), and (11).

$$\text{LF}(x) = 0.01 \left(\frac{u \bullet \sigma}{|v|^{1/\beta}} \right), \qquad (8)$$

$$Z = Y + S \bullet \text{LF}(D), \qquad (9)$$

where D is the problem dimension and S is a random vector with a size of $1 \times D$. The LF function can be calculated from equation (8), where u and σ are random numbers that vary between 0 and 1. β is a constant value of 1.5. The formula for calculating σ is shown in (10).

$$\sigma = \left(\frac{(1 + \beta) \sin (\pi\beta/2)}{((1 + \beta)/2) \bullet \beta \bullet 2^{(\beta-1)/2}} \right)^{1/\beta}, \qquad (10)$$

$$X(t + 1) = \begin{cases} Y, & F(Y) < F(X(t)), \\ Z, & F(Z) < F(X(t)) \end{cases} \qquad (11)$$

(3) A siege. If the $|E| < 0.5$, $r \geq 0.5$, which means the rabbit has a relatively low energy, but it has a medium chance of making a successful escape. In this case, the eagle will carry out a difficult siege and update its equations according to

$$X(t + 1) = X_{\text{rabbit}}(t) - E|\Delta X(t)| \qquad (12)$$

(4) Fast dive hard siege. If the $|E| < 0.5$, $r < 0.5$, it means the victim has low energy and a low chance of escape. In this case, the eagle will also perform a difficult encirclement, but with a gradual rapid dive, the eagle's next position will be updated using equation (11). Z is calculated by equation (9) and Y by equation (13), as shown in the following:

$$Y = X_{\text{rabbit}}(t) - E|J X_{\text{rabbit}}(t) - X_m(t)| \qquad (13)$$

2.2.2. Variational Modal Decomposition. The VMD algorithm is an adaptive, quasiorthogonal, and completely nonrecursive decomposition method, which can be divided into two processes of constructing variational problem and solving variational problem: (1) constructing variational problem (equation (14)): the original input signal $x(t)$ was decomposed into K IMF components $u(t)$, each component $u(t)$ was demodulated by Hilbert transform to obtain its envelope signal and then mixed with the estimated center frequency ω_k. Under the constraint that the sum of all $u(t)$ components was equal to the original signal $x(t)$, the construction of the variational problem is shown in equation (14). (2) To solve the variational problem (equation (15)): the constrained variational problem is transformed into an unconstrained variational problem by adding Lagrange multiplication to calculate $\lambda(t)$ and quadratic penalty factor α, as shown in equation (15). Alternate Direction Method of
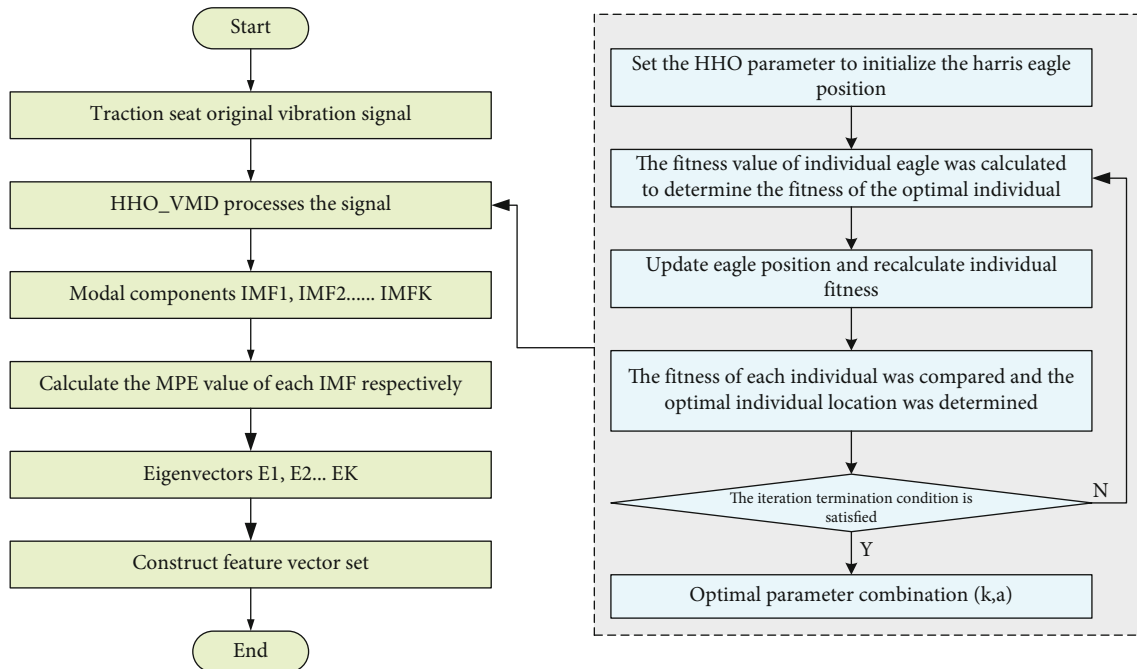
FIGURE 4: Feature extraction of traction seat vibration signals based on HVMD_MPE.
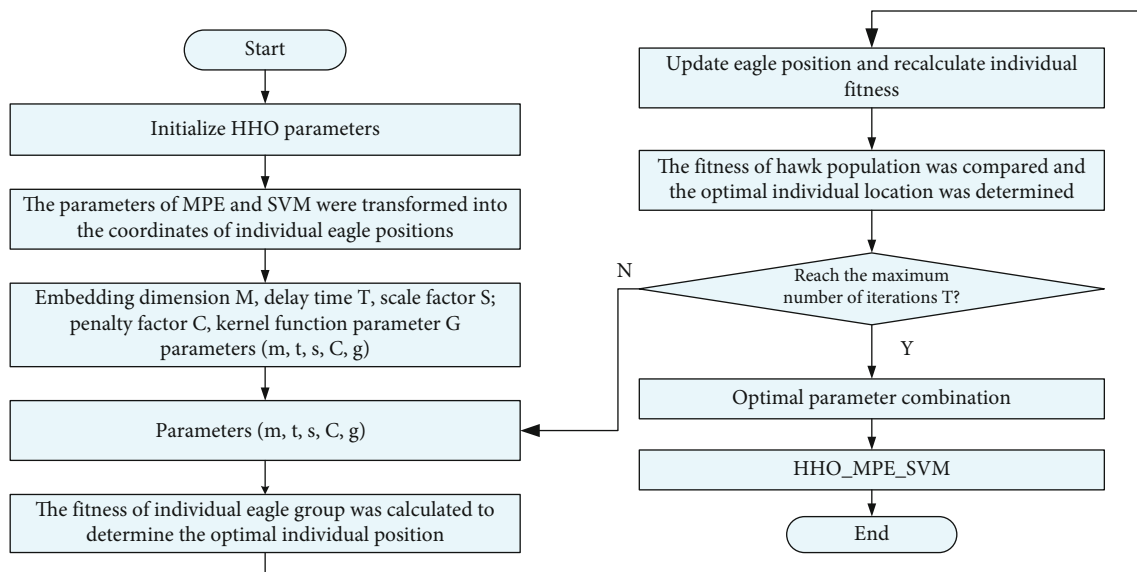
FIGURE 5: Fault diagnosis flow chart based on HMVM.

Multiplier (ADMM) is used to obtain the saddle point in equation (15), that is, the optimal solution of

where ∂_t is the partial derivative of t; $\delta(t)$ is the shock function.

$$
\begin{cases}
\min_{\{u_k\} \cdot \{\omega_k\}} \left\{ \sum_{k=1}^{K} \left\| \partial_t \left[\left(\delta(t) + \frac{j}{\pi t} \right) * u_k(t) \right] e^{-j\omega_k t} \right\|_2^2 \right\} \\
\text{s.t.} \sum_{k=1}^{K} u_k = x(t),
\end{cases}
\tag{14}
$$

$$
\begin{aligned}
L(\{u_k\}, \{\omega_k\}, \lambda) = {} & \alpha \sum_k \left\| \partial_i \left[\left(\delta(t) + \frac{j}{\pi t} \right) * u_k(t) \right] e^{-j\omega_k t} \right\|_2^2 \\
& + \left\| x(t) - \sum_{k=1}^{K} u_k(t) \right\|_2^2 \\
& + \left\langle \lambda(t), x(t) - \sum_{k=1}^{K} u_k(t) \right\rangle.
\end{aligned}
\tag{15}
$$

Normal

(a) Time-domain diagram of normal state

Small crack

(b) Time-domain diagram of small cracks

Big crack

(c) Time-domain diagram of the big crack
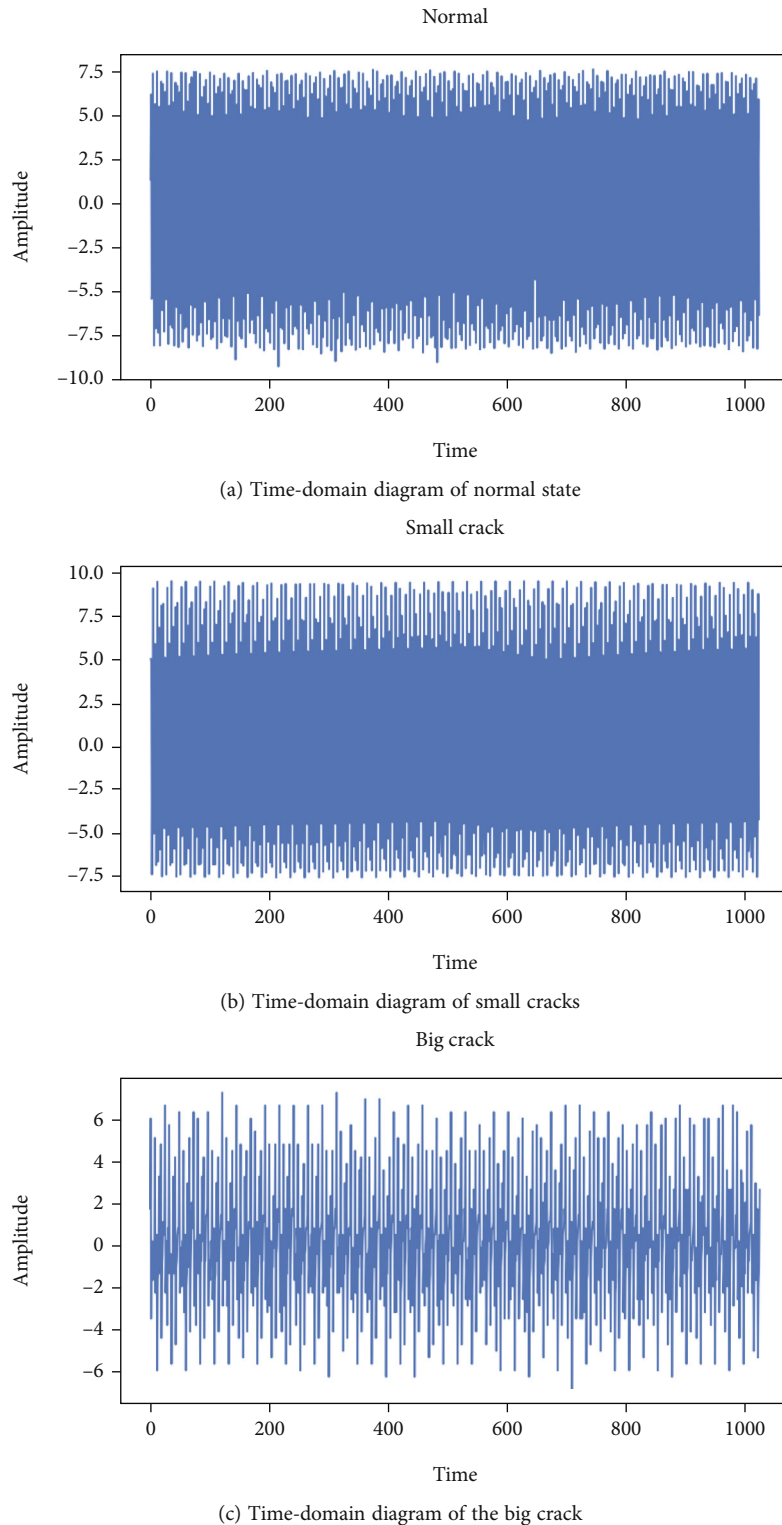
FIGURE 6: Time-domain diagram of traction seat in three states.

The data of traction seat has the characteristics of nonlinearity, nonstationarity, randomness, and noise. In order to better describe these characteristics, the vibration signal of traction seat needs to be decomposed into multiple components. There are some defects in wavelet transform, empirical mode decomposition, and ensemble empirical mode decomposition, which are not suitable for the analysis of traction seat vibration signal. VMD not only ensures the integrity of the characteristics but also improves the computational efficiency of the algorithm. Compared with other common time-frequency domain processing methods, VMD can better solve the problems

Normal

(a) Frequency-domain diagram of the normal state

Small crack

(b) Frequency-domain diagram of small cracks

Big crack

(c) Frequency-domain diagram of large cracks
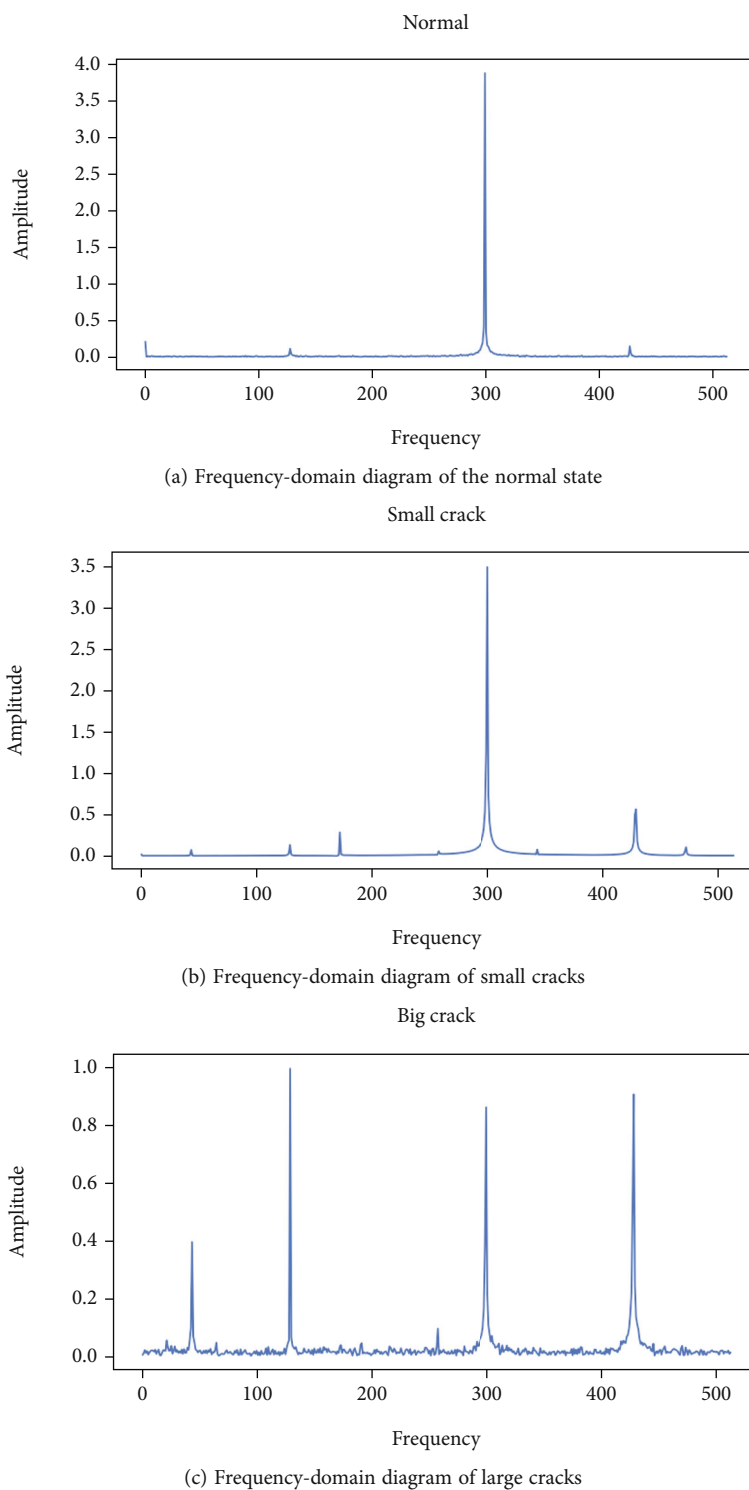
FIGURE 7: Frequency-domain diagram of traction seat in three states.

of modal aliasing and boundary effect of signal decomposition and has good robustness to noise; this paper introduces the VMD algorithm. VMD was used to decompose the original vibration signal of the traction seat into K intrinsic mode functions (IMF) under limited bandwidth, and the corresponding IMF central frequency was extracted, so that the mode u_k fluctuated around the central frequency K.

2.2.3. Multiscale Permutation Entropy. Mechanical equipment usually contains rich feature information at multiple scales. In order to study the complexity change of time series at multiple scales, MPE can mine more rich feature information hidden in time series, so as to accurately reflect the change of the system and obtain more state quantity than the original single scale. MPE can be summarized as follows:
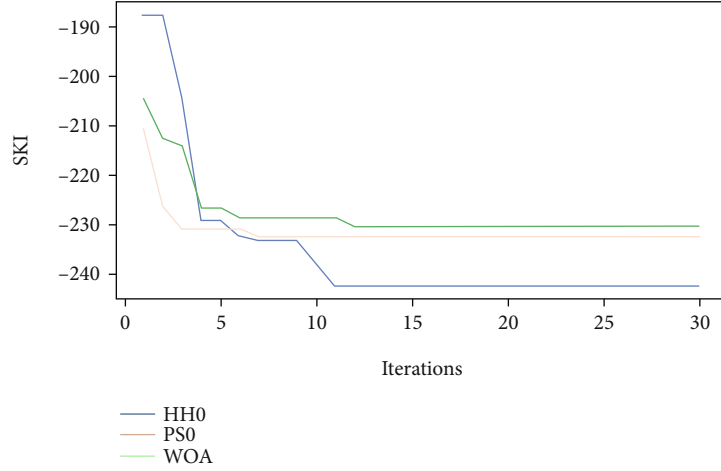
FIGURE 8: Results of HHO optimizing VMD parameters.

calculate a group of permutation entropy values in time series of different scales, combine coarse-grained process with permutation entropy, and calculate results in different time scales by calculating the entropy of coarse-grained time series. The MPE algorithm includes two steps:(1) using coarse-grained process to obtain multiscale time series from original time series; (2) calculate the PE value of each coarse-grained time series.

The detailed process is as follows:

(1) For a given time series $x(k)$, $k = 1, 2, \cdots, N$, the coarse-grained sequence is obtained after coarse-grained processing, as shown in

$$y_j^\tau = \frac{1}{\tau} \sum_{i=(j-1)\tau+1}^{j\tau} x_i \quad 1 \le j \le \left\lfloor \frac{N}{\tau} \right\rfloor, \tag{16}$$

where τ is the scale factor and is a positive integer. $\lfloor a \rfloor$ is an integer less than or equal to a

(2) Multiscale permutation entropy MPE can be obtained by calculating the permutation entropy PE value of coarse-grained time series, as shown in

$$\mathrm{MPE}(x, \tau, m, \delta) = \mathrm{PE}\left(y_j^\tau, m, \delta\right), \tag{17}$$

where m is the embedding dimension; δ is the delay parameter

PE is a method to analyze mechanical equipment under one-dimensional time series, but it cannot analyze all the characteristic information of mechanical equipment comprehensively. In order to analyze the characteristics of traction seat vibration signal in detail and study the characteristics of equipment under multiscale time series, more states hidden in the time series can be excavated, so as to reflect the traction seat fault state more accurately.

2.2.4. *HMVMD.* At present, there are "redundancy" and "sparsity" in signal characteristic analysis, which can not achieve effective and comprehensive signal analysis. An information processing method based on HHO_VMD_ MPE is proposed to extract feature information comprehensively. Due to its good structure and high optimization performance, HHO is used to solve several optimization problems (such as manufacturing, feature selection, classification, and engineering design). In view of the advantages of HHO in optimization, selecting HHO to determine parameter values is a more appropriate scheme at present. In this section, when feature extraction of traction seat vibration signal is carried out, VMD is used to process vibration signal of traction seat, and HHO is used to adaptively select the optimal parameter combination of VMD $[k, a]$.

In the process of HVMD, the fitness function is designed to achieve the best searching effect. Kurtosis index (KI) and Spearman correlation coefficient are two common indexes in mechanical equipment damage. If KI is used as the optimization target to optimize VMD parameters for fault feature extraction, some influences with large vibration amplitude but dispersed distribution can be omitted. The correlation coefficient can represent the similarity of two signals but is easily affected by noise, in view of their own shortcomings and complementary elimination. Therefore, this paper constructed the kurtosis index (SKI) integrating the Spearman correlation coefficient as the objective function of VMD parameter optimization. SKI is defined as follows:

$$\mathrm{KI} = \frac{(1/N)\sum_{i=1}^{N}(x_i - \bar{x})^4}{\left((1/N)\sum_{i=1}^{N}(x_i - \bar{x})^2\right)^2}, \tag{18}$$

$$S_{x,y} = \frac{E(XY) - E(X)E(Y)}{\sqrt{E(X^2) - E^2(X)}\sqrt{E(Y) - E^2(Y)}}, \tag{19}$$

$$\mathrm{SKI} = |S| \times |K|, \quad |S| \le 1. \tag{20}$$

Spielman kurtosis index, the calculation formula of signal sequence kurtosis index is shown in formulas (18),
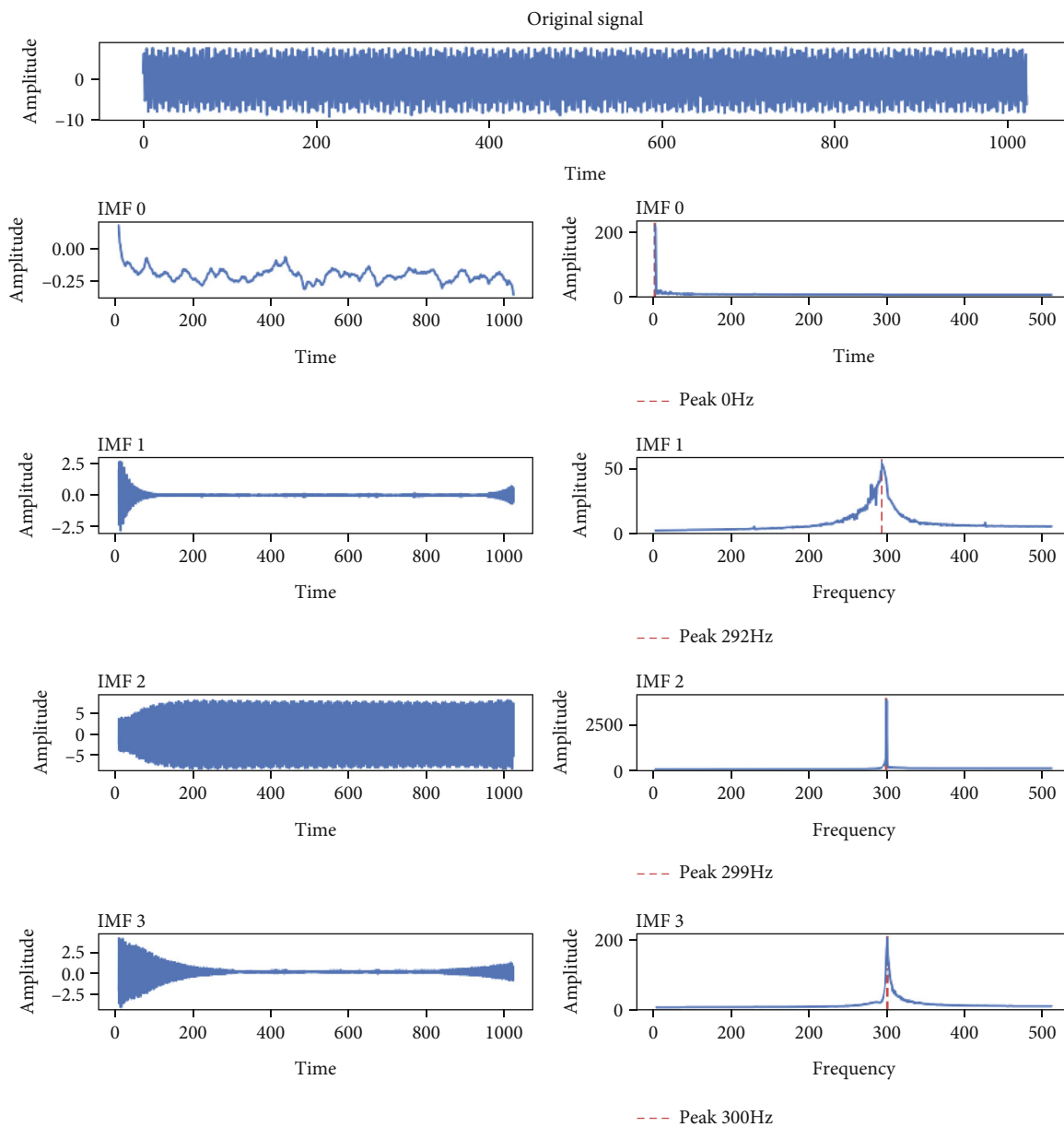
(a) The traction seat is decomposed by HVMD in normal state

FIGURE 9: Continued.
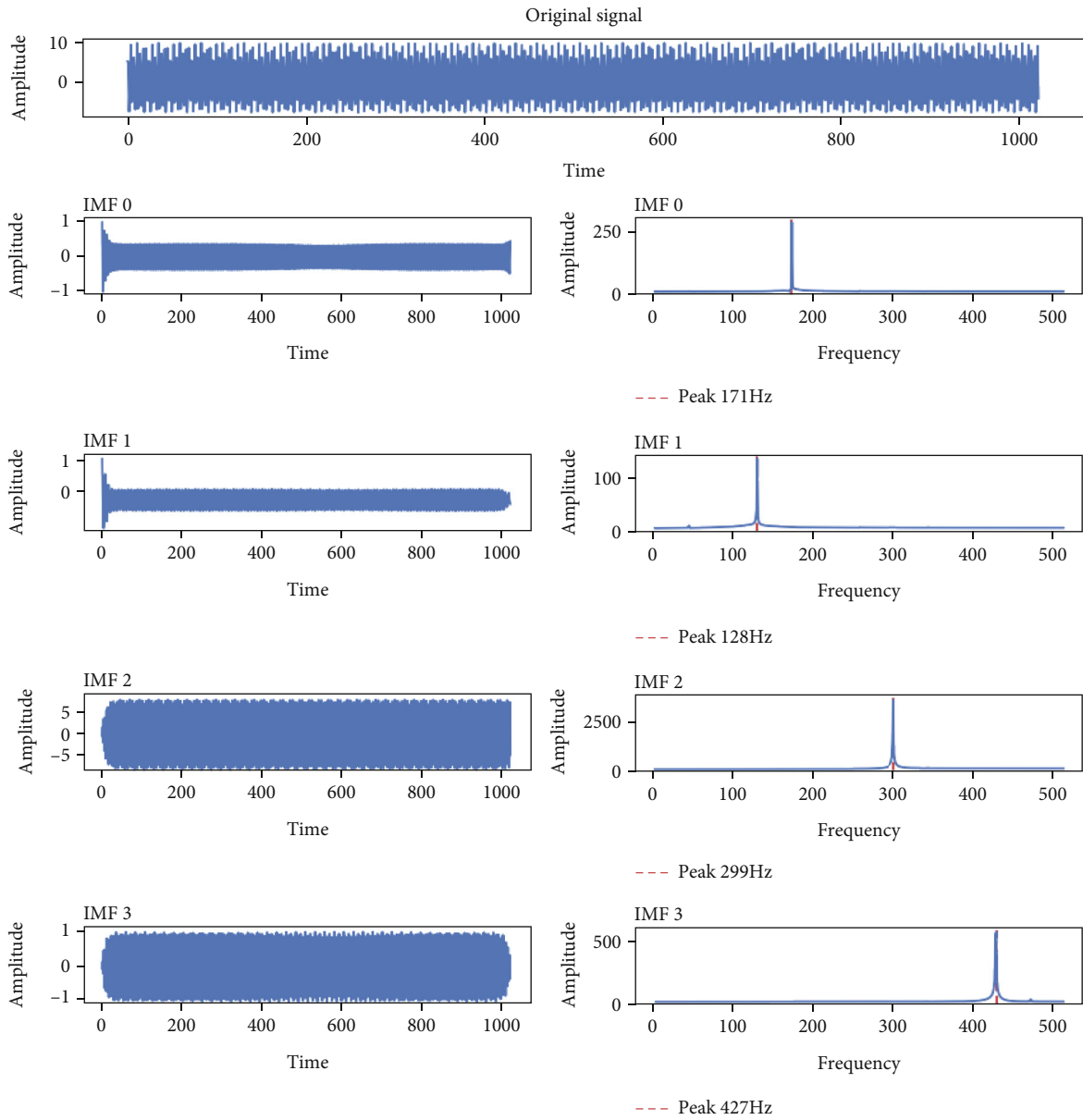
(b) HVMD decomposition spectrum of traction seat under small crack state

Figure 9: Continued.
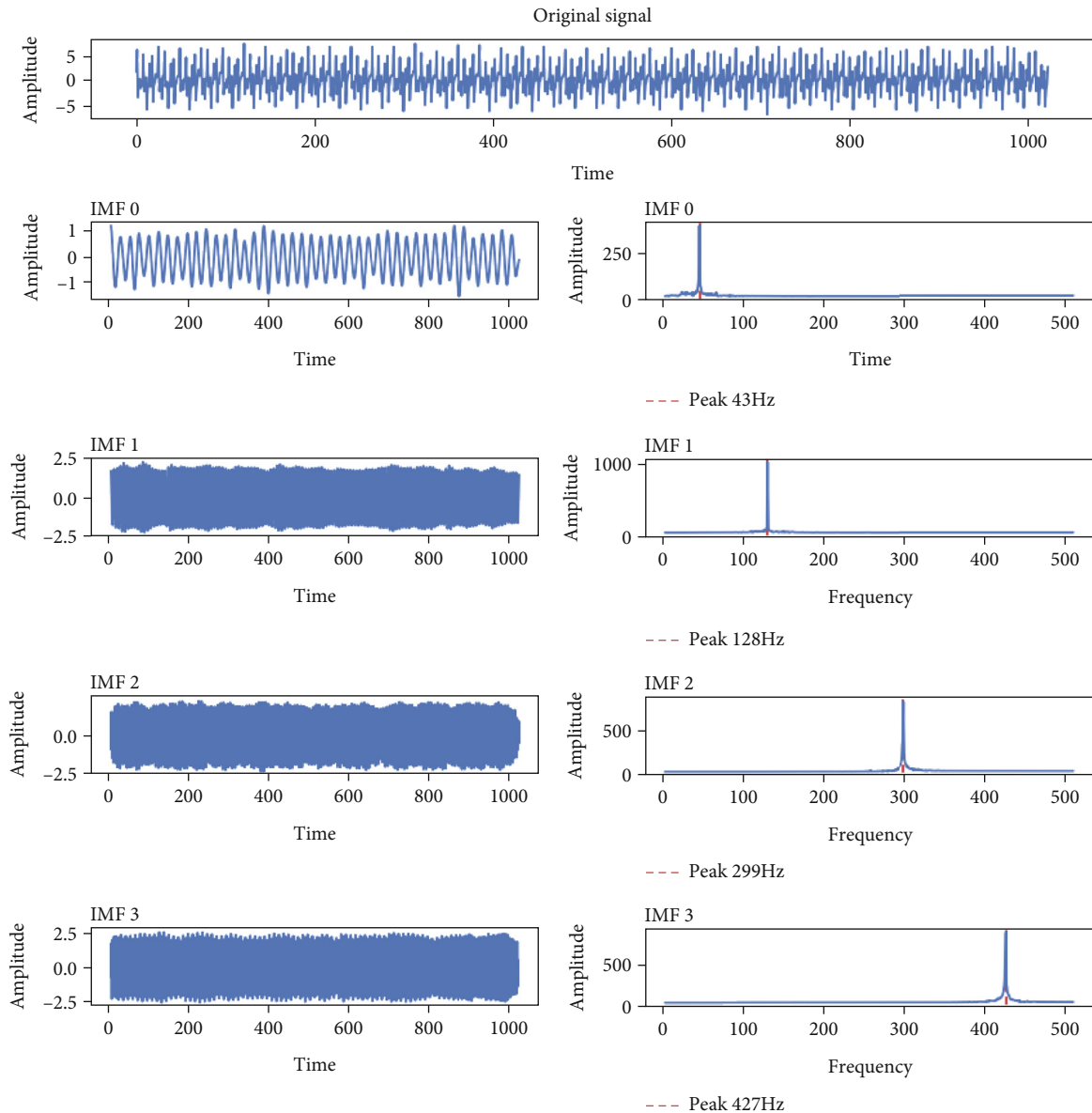
(c) HVMD decomposition spectrum of traction pedestal under large crack state

FIGURE 9: Spectrum of three states of traction seat decomposed by HVMD.

(19), and (20). N is the signal length; S is the correlation coefficient between signals X and Y.

The extraction process of traction seat features is shown in Figure 4. Firstly, the position vector of the eagle group was initialized, SKI was used as a fitness function, and the fitness of each eagle was calculated. Then, the iterative formula was selected to update iteratively by judging the size of the convergence factor until the termination condition was satisfied, and the optimal VMD parameter combination was output. In order to more accurately reflect the characteristic information of the traction seat fault state, as the common permutation entropy (PE) is far from enough to only study the one-dimensional time series, MPE is used to conduct multiscale analysis of the vibration signals of the traction seat under the time series to study the complexity changes

of the time series under the multiscale. You can get more states hidden in time series.

2.3. Traction Seat Pattern Recognition Based on HSVM

2.3.1. Support Vector Machine.
SVM is proposed based on statistical learning theory and based on the VC dimension theory and the minimum structural risk theory of statistical learning theory. It obtains the best-expected value from limited sample information through learning. It is widely used in mechanical equipment fault diagnosis and pattern recognition. SVM is a machine learning method based on small sample data processing. By mapping low-dimensional sample space to high-dimensional space, the nonlinear problems in sample space are transformed into linear problems in
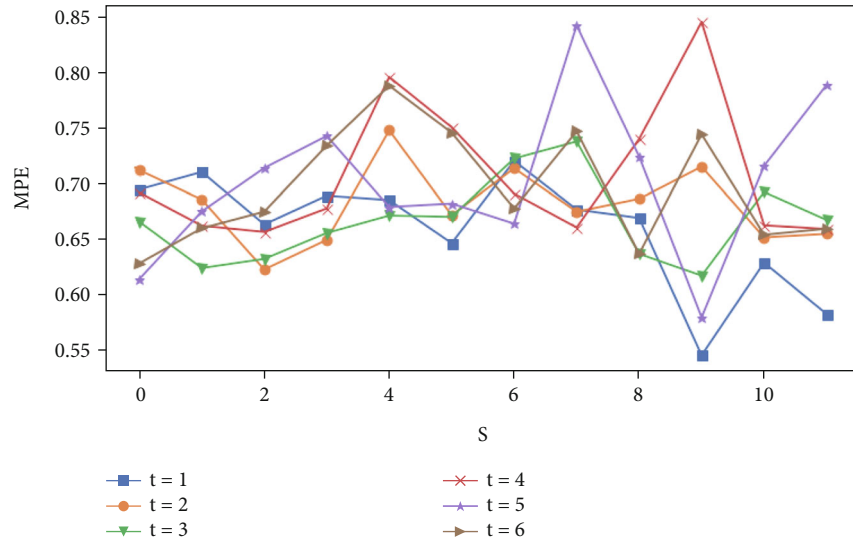
(a) Embedding dimension $m = 4$
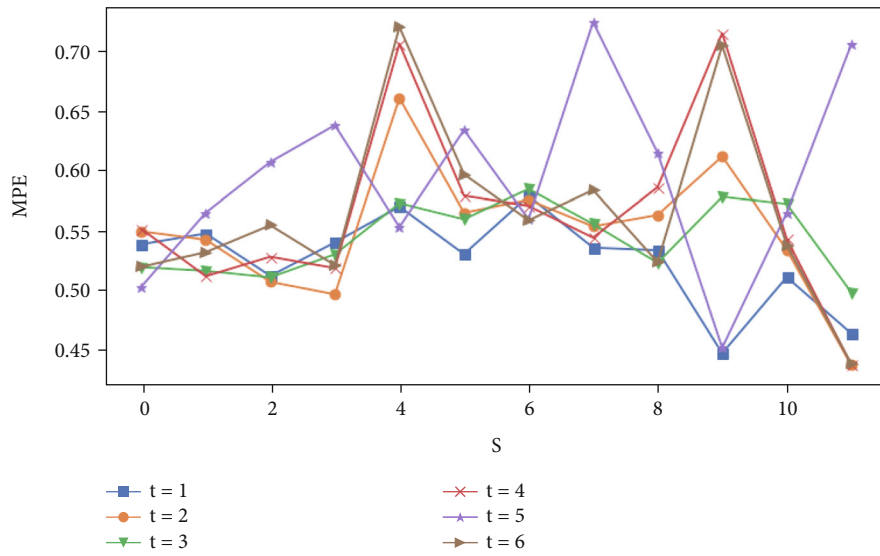
(b) Embedding dimension $m = 5$

Figure 10: Continued.
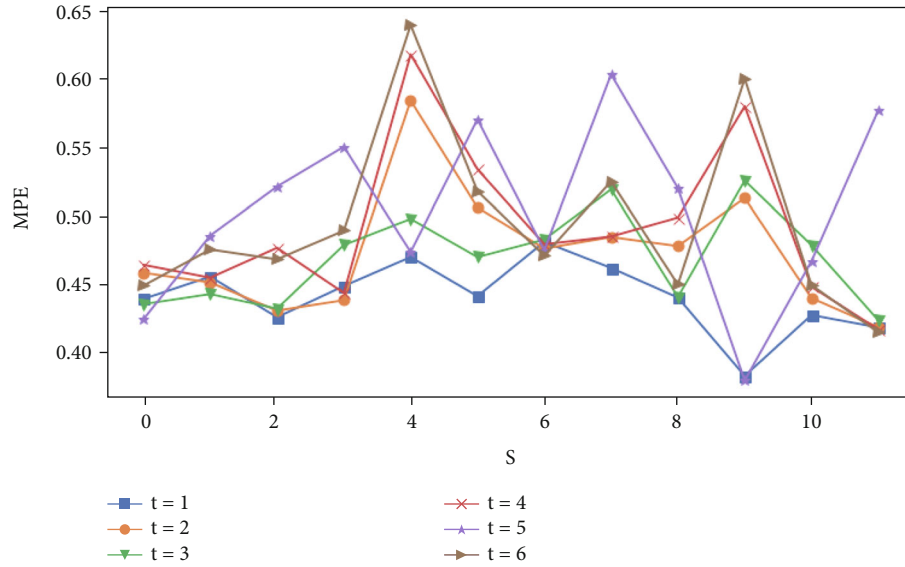
(c) Embedding dimension $m = 6$
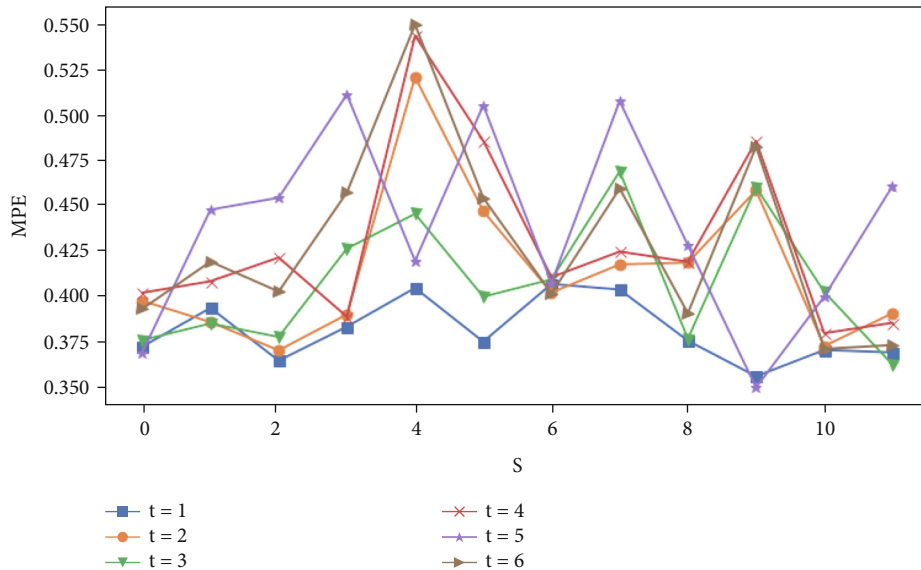
(d) Embedding dimension $m = 7$

Figure 10: MPE diagram of the delay time t of small crack in traction seat under different embedding dimensions.

high-dimensional space to solve nonlinear classification problems. Through this method, the optimal solution of the problem can be obtained well, so as to avoid the problem of trapping local optimal.

The essence of SVM: for a nonlinear problem that is difficult to deal with in the original low-dimensional space, it can be transformed into a linearly separable problem in higher dimensional feature space under the action of kernel function. A hyperplane is found to divide samples in a high-dimensional space, so that the distance between the nearest sample objects of the two kinds of samples distributed on both sides of the hyperplane is the largest. For the training sample $M = \{(x_1, y_1), (x_2, y_2), \cdots, (x_m, y_m)\}$, the classification function constructed based on the principle of structural risk minimization is shown in formula (18):

$$F(x) = \mathrm{sign}\left(\sum_{i=1}^{m} a_j y_i k\left(x_i, y_j\right) + d\right) 0 < a_j < C, \qquad (21)$$

where x_i and x_j are input feature vectors; y_i is the output vector; m is the total number of training samples; a_j is the Lagrange multiplier; $k(x_i, y_j)$ is the kernel function; C is the penalty factor; d is the threshold.

State identification is the last and most important step in fault diagnosis. The final result of fault diagnosis depends on the selection of an appropriate pattern recognition classifier. In practice, the sample size of crack fault characteristic of traction seat of locomotive bogie is small, so it is required that pattern recognition classifier can be trained by small
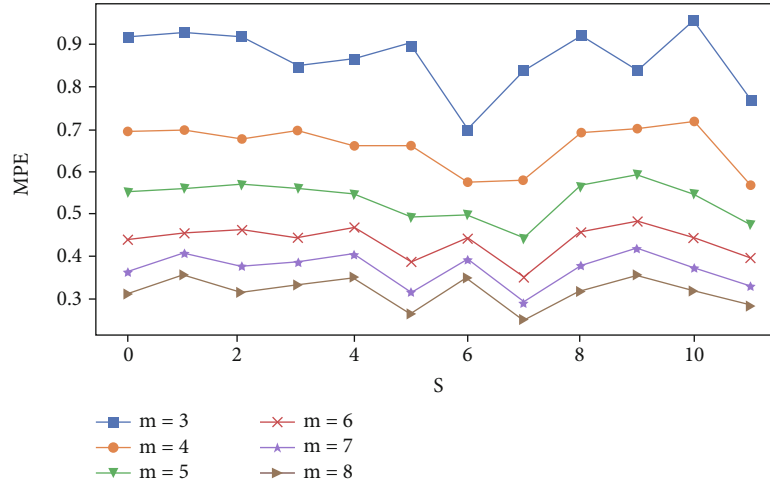
FIGURE 11: MPE diagram of small cracks in traction seat under different embedding dimensions.
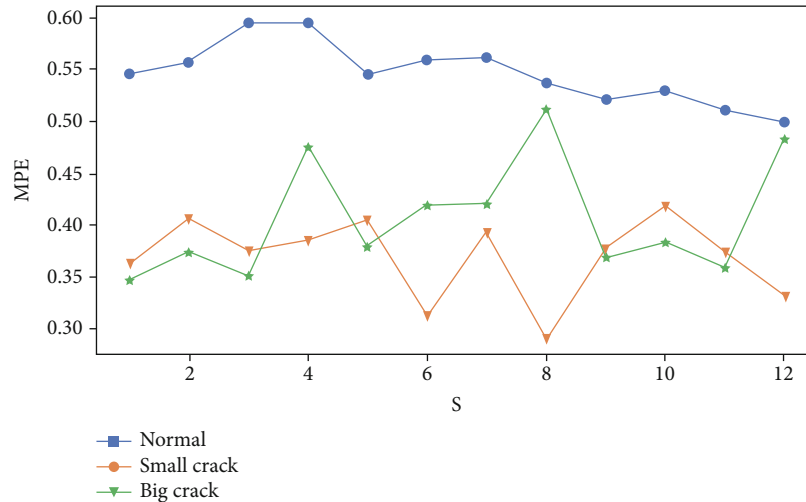
FIGURE 12: Under different scales, the three health states of traction seat are MPE diagram.

sample, and then identify the crack state of traction seat with high accuracy.

2.3.2. HSVM. The HHO_MPE_SVM (HSVM) algorithm is proposed to reduce the diagnosis error and identify the fault type accurately. In the process of traction seat diagnosis, the selection of parameters is worth considering. The scale factor s, embedding dimension m, sequence length N, delay time t, penalty coefficient C, and kernel function parameter g of MPE and SVM will affect the accuracy of fault diagnosis. With the classification accuracy as the evaluation index, HHO is used to optimize the parameters of MPE and SVM simultaneously, which is a beneficial attempt for traction seat fault diagnosis. Fault diagnosis process based on HMSVM is shown in Figure 5. The specific construction process is described as follows:

(1) The training set and test set are constructed and normalized

(2) HHO parameter initialization. Set the sum of random values, set the sum of upper and lower bounds, the maximum number of iterations, set the value range of parameter combination $[m, t, S, C, g]$, select the Gaussian kernel function, and randomly initialize the initial position of the Harris eagle group

(3) Using the classification accuracy of SVM as fitness function, the fitness of each individual eagle group was calculated to find and preserve the best habitat position of the individual eagle group in the current population

(4) The HHO algorithm is used to optimize the habitat position of individual eagles

(5) The fitness function was used to recalculate the fitness of each optimized eagle group and update and save the current optimal eagle group individual position

(a) $m = 6$, $t = 1$, $s = 13$

(b) $m = 4$, $t = 6$, $s = 9$
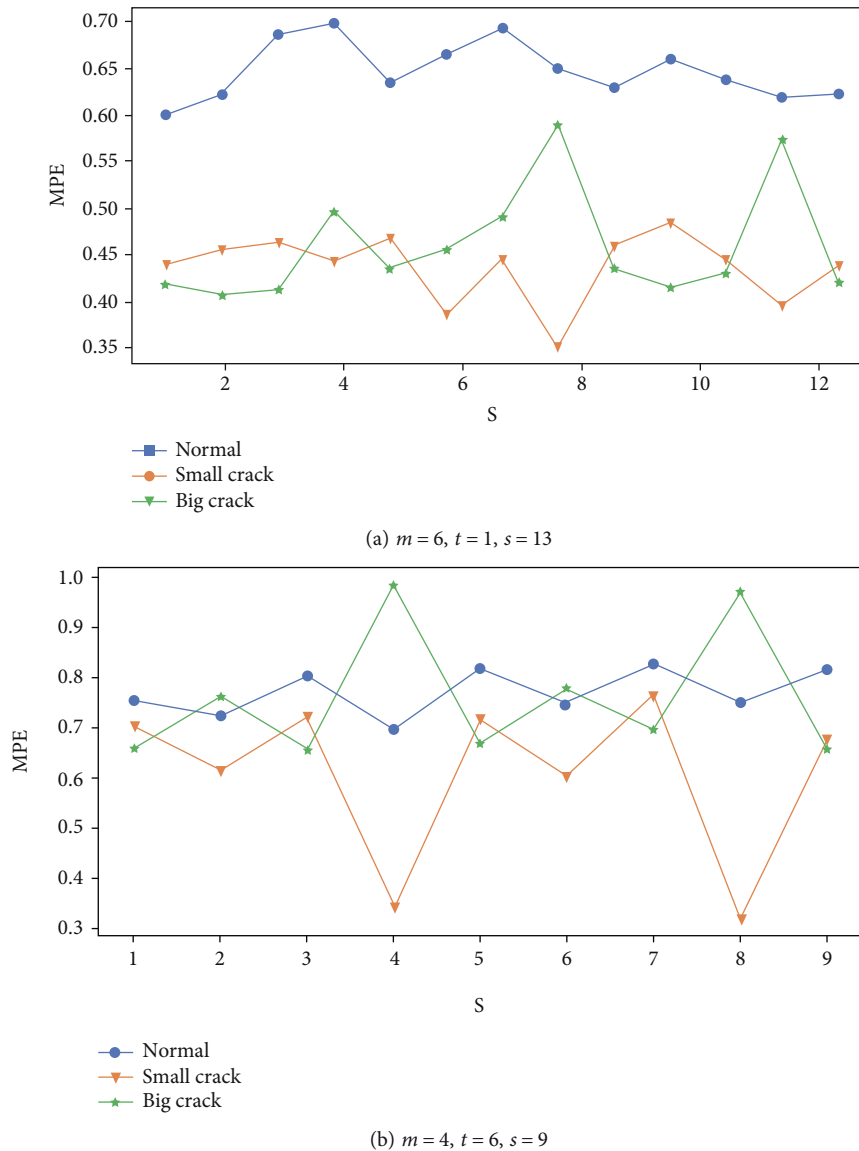
FIGURE 13: Select different parameters, traction seat three states of MPE changes.

(6) Determine whether the iteration termination conditions are met. If so, end the optimization; otherwise, continue the cycle

(7) Output the spatial position corresponding to the fitness value of the best eagle group, that is, the optimal parameter combination $[m, t, s, C, g]$

3. Experimental Verification

3.1. Signal Analysis Based on HHO_VMD. The vibration signals of the traction seat in three states were collected through the experimental platform, and the vibration signals of each state were 6000×20, 6000×60 in total. In order to ensure the accuracy of data and the prediction speed of the experiment, the number of sampling points N was set to 1024 as the experimental data set. Figures 6 and 7, respectively, show the time-domain and frequency-domain analysis of a group

of original vibration signals in three states of the traction seat when $N = 1024$.

Figures 6 and 7 show that the time-domain and frequency-domain waveforms of the three states of the traction seat show different changes, indicating that the method based on vibration signals can realize the identification of the traction seat state, but there is uncertainty. In order to identify the fault state of traction seat more accurately, VMD is used to decompose the vibration signal of traction seat.

Taking the large crack fault of traction seat as an example, in the experiment, the number of modes of the VMD algorithm $K \in [2, 10]$ is an integer, and the penalty parameter $a \in [200, 4000]$ is taken as an integer. The change of the SKI value of the VMD parameter with the number of Harris update iterations after HHO optimization is shown in Figure 8. Figure 8 shows that SKI is -241.75, corresponding to the optimal position, namely, the optimal parameter combination [4, 2383]. After the optimization parameters are
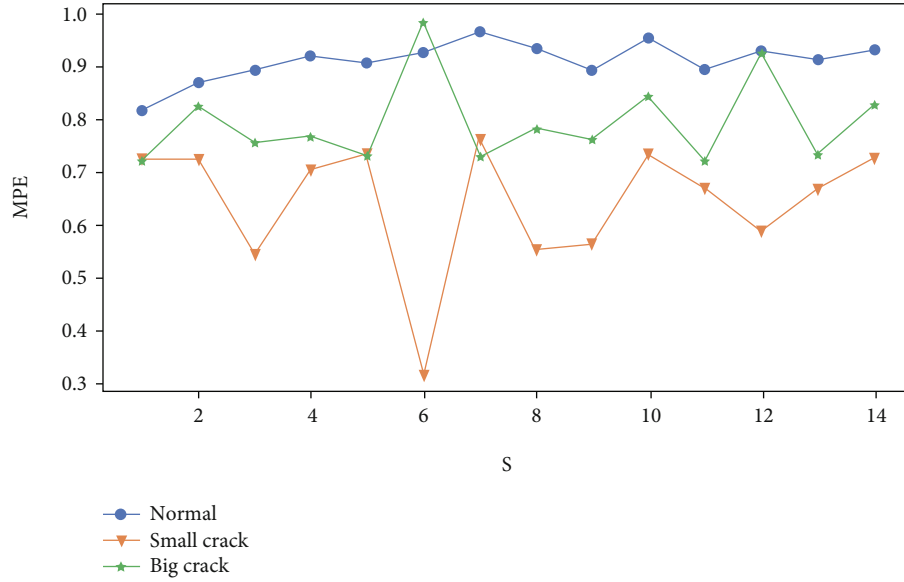
FIGURE 14: Three state diagrams of traction seat based on HHO_MPE.

TABLE 3: Multiscale permutation entropy values of the three health states of the traction seat (only part is shown due to limited space).

State	Sample	MPE1	MPE2	MPE3	MPE4
Normal (0)	0	0.816852	0.868982	0.892605	0.918061
	1	0.708248	0.844968	0.781680	0.897962
	2	0.847388	0.886976	0.910367	0.911917
	3	0.860285	0.883452	0.914914	0.941772
	4	0.844852	0.896652	0.931031	0.929070
Small crack (1)	0	0.727376	0.729275	0.551191	0.707729
	1	0.792196	0.650526	0.565574	0.645749
	2	0.746012	0.640071	0.619615	0.567530
	3	0.756012	0.645144	0.623558	0.603248
	4	0.748917	0.647531	0.597829	0.618770
Big crack (2)	0	0.724450	0.825055	0.758960	0.770725
	1	0.703779	0.844347	0.742504	0.782242
	2	0.725932	0.841112	0.767185	0.767448
	3	0.706949	0.823326	0.750810	0.831523
	4	0.709567	0.840849	0.749813	0.794277

obtained, VMD decomposition is performed on the vibration signal of the traction seat, and the IMF component is obtained by the decomposition, as shown in Figure 9. It can be seen from Figure 9 that each IMF central frequency is independent from each other, which can effectively avoid the mode aliasing problem. Using this method, relatively pure modal components can be obtained quickly.

3.2. Experimental Verification Based on HHO_MPE. From the above analysis, it can be seen that there are obvious differences between the signals of the traction seat in the normal state and the two fault states. Next, according to the characteristics of traction seat vibration signal under the actual working condition, the MPE was used to analyze the

experiment. Set the time series to $N = 1024$. The delay time is generally set as 1-6, and the scale factor $s = 12$ is set in the experiment. Figure 10 shows the change of MPE value of small crack state under different embedding dimensions (due to the limited space, a failure state of traction seat is taken as an example). It can be concluded that the delay time $t = 1$ is more appropriate. The embedding dimension is generally 3-8. Figure 11 shows the MPE values of small crack states under different embedding dimensions (delay time $t = 1$, scale factor $s = 12$). By comparison, it can be concluded that embedding dimension $m = 4$ is more appropriate. Figure 12 shows (delay time $t = 1$, embedding dimension $m = 4$) the MPE values of the traction seat in three states under different scale factors S. The comparison shows that

TABLE 4: Experimental comparative analysis of traction seat fault diagnosis.

SVM model	Parameter C	Kernel function g	Accuracy (%)	Time (s)
SVM	48.92	135.00	95.56	8.78
PSO_SVM	78.23	175.04	97.78	107.92
WOA_SVM	91.11	111.82	98.89	102.18
HHO_SVM	57.13	73.03	100.00	188.42
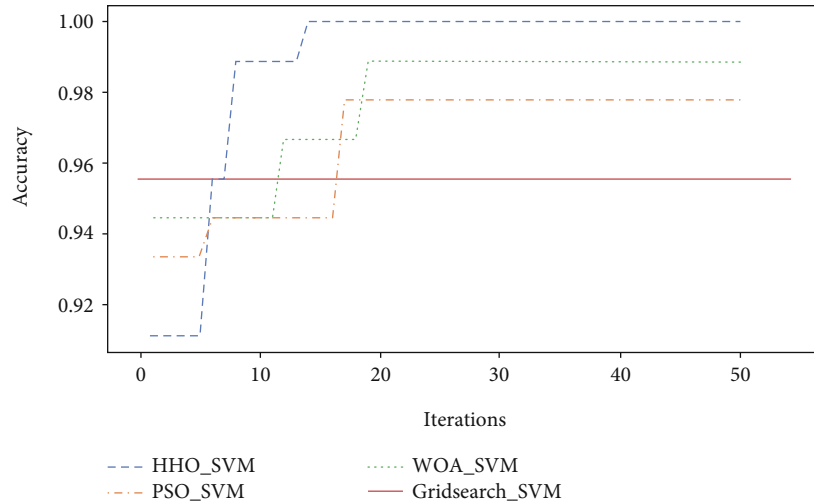
FIGURE 15: Accuracy of different models.

the scale factor $s = 6$ is more appropriate. To sum up, it can be concluded from observation and comparison that it is appropriate to select $m = 4$, $t = 1$, and $s = 6$ as MPE parameters, respectively. Figure 12 shows that the normal state and fault state of the traction seat can be distinguished by manually selected parameters, but the fault type cannot be further distinguished.

In order to further illustrate the MPE values the importance of reasonable selection, Figure 13 shows the different parameter selection, pulling the MPE values under different conditions, it is not hard to find: the MPE parameters selection, traction is mixed overlapping between different states, and distinguishing between each other is not obvious, which is not conducive to further accurate judgment of the traction state type. According to the manually selected MPE parameters, it is impossible to distinguish the three states of the traction seat accurately. In order to avoid the inaccuracy of selected parameters, HHO was used in this experiment to optimize MPE parameters, and the optimization results were as follows: $m = 4$, $t = 4$, and $s = 14$. Figure 14 shows the three-state diagrams of traction seat of HHO_MPE. It is not difficult to find that the three states of the traction seat can be accurately separated at different scales. At the high scale, the MPE of the different states of the traction seat has no overlap and is clearly distinguished from each other, which is conducive to further accurate judgment of the state type of the traction seat.

When the traction seat fails, different modal components will contain different impact components. In order to check the fault information contained in each modal component, the MPE of each IMF component was calculated and the feature vector was formed, which was used as the input data for fault diagnosis. 90 sets of vibration signals of the traction seat in three states were processed in the experiment, with a total of 3×90 sets of data for feature analysis. That is, for the 4 IMF of each group of data, the MPE of each IMFs is calculated for quantitative processing, respectively, and the average value of the MPE of each IMF is taken to construct the energy feature $Y = [\text{MPE1}, \text{MPE2}, \text{MPE3} \cdots \text{MPE} 14]$, as shown in Table 3 (due to space limitation, 5 groups of each state of the traction seat are displayed; MPE only selects the first 4 dimensions for display).

As can be seen from Table 3, the normal state and fault state of traction seat can be clearly identified. There are also obvious differences between MPE values of large crack and small crack in fault state. From the analysis, it can be concluded that the IMF of each IMF component is calculated, and the average value of MPE of each IMF is taken to construct feature vectors, which are used as input data for fault diagnosis to further identify the type of traction seat state.

3.3. Pattern Recognition Based on HHO_SVM. After the above experiments, after the feature vector containing the traction seat feature information is extracted, an effective pattern recognition algorithm is needed for fault diagnosis. In this experiment, HSVM was selected for traction seat fault diagnosis. In order to verify that the diagnosis model of HSVM has better fault diagnosis ability, the same traction

seat feature vectors were used as input data to HHO_SVM, WOA_SVM, PSO_SVM, and SVM models, respectively, for fault identification. The population parameters of the first 3 models are all 30, and the maximum iteration times are 200. Among them, the optimization range of SVM penalty parameter C is [0.01,200], the optimization range of kernel function parameter G is [0.01,200], the training data is 270 groups, and the test data is 90 groups. Finally, the classification results of the four models are compared and analyzed as shown in Table 4. The accuracy of different models is shown in Figure 15.

It can be seen from Table 4 that the accuracy of all the four classification models can reach more than 95%, indicating that the feature extraction method of HVMD_MPE adopted in this experiment is feasible and contains relatively complete feature information of traction seat. Figure 15 illustrates the following: HHO effect compared with other algorithms at the beginning of the number of iterations is poorer, attributed to HHO, WOA, and the population initialization in a different way of PSO, HHO to avoid falling into local optimum, as much as possible for a wide range of global search; finally, on the whole, achieve HSVM least number of iterations and identify fault has the highest accuracy.

4. Conclusion

In this paper, a bogie traction seat fault diagnosis model based on HVMD and HMSVM is constructed. HHO was used to optimize the parameters to determine the best parameter combination of VMD, MPE, and SVM. The VMD with optimized parameters was used to decompose the traction seat vibration signal. The calculated MPE values of each IMF were quantified, and the average MPE values of each IMF were taken to form feature vectors, which were used as input data for fault diagnosis. Finally, the effective feature vectors are extracted and input into the classifier HSVM to automatically identify the fault types. Finally, the accuracy of fault identification reaches 100% by using the vibration data set of traction seat, which proves the effectiveness and generalization of the proposed method.

Data Availability

The data and the Python programs used to support the findings of this study are available from the corresponding author upon request.

Conflicts of Interest

The authors declared no potential conflicts of interest with respect to the research, authorship, and/or publication of this article.

Authors' Contributions

The author's contributions are as follows: Qi Chang helped in the conceptualization, methodology, data curation, software, validation, investigation, and original draft. Minglei Zheng performed the investigation, review, and editing.

Jiaxin Luo and Junfeng Man reviewed and edited the manuscript. Lin Li provided test guidance and reviewed the manuscript. Yiping Shen performed criticism and correction. Yi Liu helped in guiding conceptualization and methodology and providing test guidance, criticism, and correction.

References

[1] M. Naeimi, Z. Li, Z. Qian et al., "Reconstruction of the rolling contact fatigue cracks in rails using X-ray computed tomography," *NDT and E International*, vol. 92, pp. 199–212, 2017.

[2] J. Chakraborty, A. Katunin, P. Klikowicz, and M. Salamak, "Early crack detection of reinforced concrete structure using embedded sensors," *Sensors*, vol. 19, no. 18, p. 3879, 2019.

[3] P. Liu, J. Jang, S. Yang, and H. Sohn, "Fatigue crack detection using dual laser induced nonlinear ultrasonic modulation," *Optics and Lasers in Engineering*, vol. 110, pp. 420–430, 2018.

[4] K. Tsukada, M. Hayashi, Y. Nakamura, K. Sakai, and T. Kiwa, "Small eddy current testing sensor probe using a tunneling magnetoresistance sensor to detect cracks in steel structures," *IEEE Transactions on Magnetics*, vol. 54, no. 11, pp. 1–5, 2018.

[5] A. Zolfaghari, A. Zolfaghari, and F. Kolahan, "Reliability and sensitivity of magnetic particle nondestructive testing in detecting the surface cracks of welded components," *Nondestructive Testing and Evaluation*, vol. 33, no. 3, pp. 290–300, 2018.

[6] A. Tsukamoto, T. Hato, S. Adachi, Y. Oshikubo, K. Tsukada, and K. Tanabe, "Development of eddy current testing system using HTS-SQUID on a hand cart for detection of fatigue cracks of steel plate used in expressways," *IEEE Transactions on Applied Superconductivity*, vol. 28, no. 4, pp. 1–5, 2018.

[7] Y. Chen, X. Liang, and M. J. Zuo, "An improved singular value decomposition-based method for gear tooth crack detection and severity assessment," *Journal of Sound and Vibration*, vol. 468, article 115068, 2020.

[8] O. Doğan and F. Karpat, "Crack detection for spur gears with asymmetric teeth based on the dynamic transmission error," *Mechanism and Machine Theory*, vol. 133, pp. 417–431, 2019.

[9] X. Zhang, C. Delpha, and D. Diallo, "Incipient fault detection and estimation based on Jensen-Shannon divergence in a data-driven approach," *Signal Processing*, vol. 169, article 107410, 2020.

[10] Y. Yang, W. Xia, J. Han, Y. Song, J. Wang, and Y. Dai, "Vibration analysis for tooth crack detection in a spur gear system with clearance nonlinearity," *International Journal of Mechanical Sciences*, vol. 157-158, pp. 648–661, 2019.

[11] A. K. S. Jardine, D. Lin, and D. Banjevic, "A review on machinery diagnostics and prognostics implementing condition-based

maintenance," *Mechanical Systems and Signal Processing*, vol. 20, no. 7, pp. 1483–1510, 2006.

[12] A. Ahrabian, D. Looney, L. Stanković, and D. P. Mandic, "Synchrosqueezing-based time-frequency analysis of multivariate data," *Signal Processing*, vol. 106, pp. 331–341, 2015.

[13] Z. Wu, J. Fan, S. Xi, and J. Feng, "Bearing fault diagnosis method based on EMD-VMD adjacent reconstruction and secondary decomposition," in *2021 33rd Chinese control and decision conference (CCDC)*, pp. 6785–6790, Kunming, China, 2021.

[14] G. Zhang, H. Liu, J. Zhang et al., "Wind power prediction based on variational mode decomposition multi-frequency combinations," *Journal of Modern Power Systems and Clean Energy*, vol. 7, no. 2, pp. 281–288, 2019.

[15] Z. Sun, S. Zhao, and J. Zhang, "Short-term wind power forecasting on multiple scales using VMD decomposition, K-means clustering and LSTM principal computing," *IEEE Access*, vol. 7, pp. 166917–166929, 2019.

[16] X. Diao, J. Jiang, G. Shen et al., "An improved variational mode decomposition method based on particle swarm optimization for leak detection of liquid pipelines," *Mechanical Systems and Signal Processing*, vol. 143, article 106787, 2020.

[17] F. Jiang, Z. Zhu, and W. Li, "An improved VMD with empirical mode decomposition and its application in incipient fault detection of rolling bearing," *IEEE Access*, vol. 6, pp. 44483–44493, 2018.

[18] A. Glowacz, W. Glowacz, J. Kozik et al., "Detection of deterioration of three-phase induction motor using vibration signals," *Measurement Science Review*, vol. 19, no. 6, pp. 241–249, 2019.

[19] X. Zhang, Q. Miao, H. Zhang, and L. Wang, "A parameter-adaptive VMD method based on grasshopper optimization algorithm to analyze vibration signals from rotating machinery," *Mechanical Systems and Signal Processing*, vol. 108, pp. 58–72, 2018.

[20] Y. Wang, L. Hongru, and Y. Peng, "Fault identification of hydraulic pump based on multi-scale perarray entropy," *China Mechanical Engineering*, vol. 26, no. 4, pp. 518–523, 2015.

[21] H. Xue, S. Wang, L. Yi, R. Zhu, B. Cai, and S. L. Sun, "Tool life prediction based on particle swarm optimization–back-propagation neural network," *Proceedings of the Institution of Mechanical Engineers, Part B: Journal of Engineering Manufacture*, vol. 229, no. 10, pp. 1742–1752, 2015.

[22] X. Zhu, J. Xiong, and Q. Liang, "Fault diagnosis of rotation machinery based on support vector machine optimized by quantum genetic algorithm," *IEEE Access*, vol. 6, pp. 33583–33588, 2018.

[23] P. Tao, Z. Sun, and Z. Sun, "An improved intrusion detection algorithm based on GA and SVM," *IEEE Access*, vol. 6, pp. 13624–13631, 2018.

[24] N. Zeng, H. Qiu, Z. Wang, W. Liu, H. Zhang, and Y. Li, "A new switching-delayed-PSO-based optimized SVM algorithm for diagnosis of Alzheimer's disease," *Neurocomputing*, vol. 320, pp. 195–202, 2018.

[25] C. S. Shin, K. I. Kim, M. H. Park, and H. J. Kim, "Support vector machine-based text detection in digital video," in *Neural Networks for Signal Processing X. Proceedings of the 2000 IEEE Signal Processing Society Workshop (Cat. No.00TH8501)*, vol. 2, pp. 634–641, Sydney, NSW, Australia, 2000.

[26] Y. Chen, W. Xu, J. Zuo, and K. Yang, "The fire recognition algorithm using dynamic feature fusion and IV-SVM classifier," *Cluster Computing*, vol. 22, Supplement 3, pp. 7665–7675, 2019.

[27] F. Jiang, Y. Lu, Y. Chen, D. Cai, and G. Li, "Image recognition of four rice leaf diseases based on deep learning and support vector machine," *Computers and Electronics in Agriculture*, vol. 179, article 105824, 2020.

[28] M. Mohammadi, T. A. Rashid, S. H. T. Karim et al., "A comprehensive survey and taxonomy of the SVM-based intrusion detection systems," *Journal of Network and Computer Applications*, vol. 178, article 102983, 2021.

[29] X. Yan and M. Jia, "A novel optimized SVM classification algorithm with multi-domain feature and its application to fault diagnosis of rolling bearing," *Neurocomputing*, vol. 313, pp. 47–64, 2018.

[30] D. Kong, Y. Chen, N. Li, C. Duan, L. Lu, and D. Chen, "Tool wear estimation in end milling of titanium alloy using NPE and a novel WOA-SVM model," *IEEE Transactions on Instrumentation and Measurement*, vol. 69, no. 7, pp. 5219–5232, 2020.

[31] A. A. Heidari, S. Mirjalili, H. Faris, I. Aljarah, M. Mafarja, and H. Chen, "Harris hawks optimization: algorithm and applications," *Future Generation Computer Systems*, vol. 97, pp. 849–872, 2019.

Hindawi

Research Article

Fault Diagnosis Method of Rotating Machinery Based on Collaborative Hybrid Metaheuristic Algorithm to Optimize VMD

Zhou Guifan [ID]

School of Data Science and Technology, North University of China, Taiyuan, Shanxi, China 030051

Correspondence should be addressed to Zhou Guifan; 1907040628@st.nuc.edu.cn

With the improvement of the complexity and reliability of mechanical equipment, it has been difficult for the commonly used variational modal decomposition method of vibration signal of rotating machinery to meet the current practical engineering requirements. In order to further improve the adaptability, processing efficiency, and robustness of rotating machinery fault diagnosis methods, a collaborative hybrid element heuristic to multiobjective optimization algorithm is introduced in this paper. Combined with variational modal decomposition (VMD) method, the fault diagnosis method of rolling bearing under complex working conditions is studied. This paper mainly uses a collaborative hybrid metaheuristic algorithm to improve the nondominated sorting genetic algorithm II (NSGA II) and multiobjective particle swarm optimization (MOPSO), which improves the convergence efficiency of multiobjective optimization method and solves the problem of uneven distribution of optimal solutions. Then, the improved multiobjective optimization algorithm is combined with VMD to solve the problem of parameter selection of the VMD method under complex working conditions of rotating machinery. At the same time, the variation relationship between various signal features and VMD decomposition results is compared and studied, and the features with good effect are taken as the objective function of the optimization algorithm; the ability of denoising and feature extraction of VMD in rotating machinery fault diagnosis is improved. In this paper, the proposed method is explored by using analog signals and experimental data of rolling bearings. Through comparison, the improvement of adaptive ability, operation speed, and robustness of the proposed method in rotating machinery fault diagnosis is verified.

1. Introduction

With the mass production and operation of various modern mechanical equipment, the safety and reliability requirements of modern industry for mechanical equipment are also increasing [1]. As the most widely used rotating mechanical component in various mechanical equipment, rolling bearing plays an important supporting role in the mechanical system. Because it undertakes most of the load of mechanical equipment, the failure rate of various mechanical components is also high [2]. If the fault of rolling bearing is light, it will reduce the operation efficiency of equipment. If it is serious, it may lead to complete failure of mechanical equipment and even serious engineering accidents. According to statistics, in various mechanical equipment failure cases in recent years, more than 70% are caused by rotating mechanical parts such as rolling bearing

and gear failure [3]. Therefore, the research on rolling bearing fault method is of great significance [4].

At present, the most commonly used fault diagnosis method for rotating parts of mechanical equipment is through vibration signal analysis of mechanical equipment [5]. The time-frequency characteristic of vibration signal is the key to solve the problem of rotating machinery fault diagnosis [6]. The classical methods and theories include wavelet transform (WT), empirical mode decomposition (EMD), and variational mode decomposition (VMD) [7]. In recent years, relevant scholars have also optimized and improved these classical methods to make them more in line with the current engineering safety and reliability requirements. For example, Chen et al. proposed an improved VMD method based on fractional Fourier transform (FRFT), which makes VMD more sensitive to periodic pulses, so that the early fault features of rolling bearings

can be extracted [8]. Zhu et al. improved the WT method by using the double evaluation multiscale template matching algorithm, which greatly improved the operation speed and performance of the WT method [9]. Chen et al. combined EMD with deep neural network (DNN) and proposed an EMD-DNN method for acceleration signal noise reduction, which achieved better results in acceleration data baseline correction [10]. Therefore, the classical signal time-frequency domain analysis methods can still be further optimized to solve various practical engineering problems. This paper will start with VMD [11], which is the most commonly used fault diagnosis of rolling bearing, and proposes a fault state detection method which can adaptively distinguish the actual working conditions of rolling bearing, so as to improve the safety and reliability of rotating machinery equipment [12].

Although the VMD method can efficiently complete the modal decomposition of vibration signals, the eigenmode functions (IMFs) obtained by the decomposition often have modal aliasing or underfitting [13]. Through the research and exploration of scholars, it is found that the unsatisfactory result of the VMD method is mainly due to the number of parameter modes K and the quadratic penalty term α. Due to improper selection, when K is less than the actual number of modes, it will lead to the decomposition result of multimodal aliasing. When K is greater than the actual number of modes, it will lead to overdecomposition. The noise component is decomposed as one of the IMFs, resulting in analysis errors; α will affect the division criteria of frequency band in the decomposition process, affect the decomposition between adjacent modes, and also cause mode aliasing [14]. Therefore, to obtain the optimal VMD parameters, it is necessary to optimize the parameter selection method of VMD [15]. At present, there are many studies on VMD parameter optimization methods. For example, Li et al. proposed a PSO optimization method for VMD parameter selection, combined with VMD and LSSVM classification methods to complete the early fault diagnosis of rolling bearing signals [16]. Kumar et al. extracted the instantaneous frequency feature of rolling bearing signal through Fourier compression transform (FSST) and took the feature as the objective function of genetic algorithm (GA), so as to select the optimal parameters of VMD [17]. Wang et al. proposed a method of spatial scale, which adaptively obtains the optimal parameters of VMD by extracting signal features and has been verified on the gearbox fault data set [18]. Xu and Hu took the minimum average mutual information (GWOMI) as the objective function of gray wolf optimization algorithm (GWO), optimized the parameters of VMD, and achieved good vibration signal analysis results [19].

Through the research of the above scholars, it can be found that the best VMD parameter results can be obtained through the multiobjective optimization algorithm. In this paper, a more efficient multiobjective optimization algorithm—the cooperative optimization algorithm of nondominated genetic and multiobjective particle swarm optimization (NSGA II MOPSO)— is used to optimize the two parameters of VMD; as a collaborative hybrid meta-heuristic optimization algorithm, this optimization method can combine the advantages of the two optimization algorithms. The performance of the NSGA II MOPSO method used in this paper in multiparameter optimization has also been verified [20]. By combining the generation by generation optimization scheme of NSGA II with the rapid optimization ability of MOPSO, this method can realize the rapid and accurate optimization of multiobjective parameters [21]. At present, it has been applied to multiparameter optimization problems in some projects [22]. In addition, in order to obtain the optimal parameters in rolling bearing fault diagnosis, it is also necessary to provide a reasonable objective function for the multiobjective optimization algorithm [23]. Through the vibration signal, we can obtain a variety of signal time-frequency domain characteristic parameters, such as vibration signal extraction method based on spectrum index [24], time-frequency spectrum extraction method [25], information extraction method of multifeature fusion, and the extraction method of signal entropy [26]. Combined with the decomposition results of the VMD method, this paper will also study the change relationship between eigenmode function and relevant features, so as to select dominant features, combine them to form new feature indexes, and improve the VMD processing method for rolling bearing vibration signal [27]. Starting from the optimization of variational modal decomposition parameters, this paper proposes a new time-frequency characteristic index to reflect the fault state of rolling bearing and completes the selection of variational modal decomposition parameters of rolling bearing vibration signal by the NSGA II MOPSO method. The multiobjective optimization method used in this paper has stronger adaptability and also ensures the efficiency of the method, the accuracy of the results, and robustness.

In this paper, the research process is complete from theoretical research to method verification, as well as improved methods and experimental verification. In the second part, the basic theories and methods of this paper are introduced in detail, such as VMD and the principle of multiobjective optimization algorithm. Then, starting from the theoretical research, the proposed method assumptions are introduced in detail in the third part of the article, and the method is verified and improved through the analog signal, forming a complete feasible scheme. In the fourth part, the method is verified by using the actually collected vibration signals of rolling bearing, and the method is compared with ergodic method, nondominated sorting genetic algorithm, and multiobjective particle swarm optimization method to verify the efficiency and robustness of the proposed method. Finally, the content of the article is summarized.

2. Involving Methods

2.1. Variational Modal Decomposition (VMD).
VMD is a common signal mode decomposition method. The VMD method can iteratively decompose complex multimodal signals into eigenmodes (IMF) with different spectral components [28]. In mechanical fault diagnosis, the IMFs can be obtained by VMD of the vibration signal generated by the

mechanical system. The specific components of the mechanical system can be known by analyzing the obtained IMFs, so as to judge the specific state of the mechanical system [29].

In the VMD method, the IMF obtained by initial signal decomposition can be expressed as

$$Y = \sum_K u_k(t) + \text{residual}. \tag{1}$$

The kth IMF obtained by decomposition can be expressed as

$$u_k(t) = A_k(t) \cos(\phi_k(t)), \tag{2}$$

where $A_k(t)$ represents the amplitude of the kth IMF at time t, $\phi_k(t)$ represents the nonattenuation function of the kth IMF at time t, and the derivative of $\phi_k(t)$ represents the instantaneous frequency at time t.

The VMD method is essentially a solution method of a constrained variational problem. In the process of processing vibration signals, the constrained variational problem required by this method can be expressed as

$$\min_{\{u_k\},\{\omega_k\}} \left\{ \sum \left\| \partial_t \left[\left(\delta(t) + \frac{j}{\pi t} \right) * u_k(t) \right] e^{-j\omega_k t} \right\|_2^2 \right\}, \tag{3}$$

where $\delta(t)$ represents the Dirac function at time t, ∂_t represents the gradient function obeyed by t, and $e^{-j\omega_k t}$ is the complex exponent. In order to solve the constrained variational problem, the quadratic penalty term and Lagrange multiplier are added on the basis of equation (3), and the unconstrained variational solution function is obtained:

$$\ell(\{u_k\}, \{\omega_k\}, \lambda) = \alpha \sum_k \left\| \partial_t \left[\left(\delta(t) + \frac{j}{\pi t} \right) \cdot u_k(t) \right] e^{-j\omega_k t} \right\|_2^2 \\ + \left\| f(t) - \sum_k u_k(t) \right\|_2^2 + \left\langle \lambda(t), y(t) - \sum_k u_k(t) \right\rangle, \tag{4}$$

where $\{u_k\}$ and $\{\omega_k\}$ represent each IMF and its center frequency, respectively. The extracted IMF and its center frequency can be updated and obtained iteratively through equations (5) and (6).

$$\widehat{U}_k^{n+1}(\omega) \longleftarrow \frac{\widehat{Y}(\omega) \sum_{i<k} \widehat{U}_k^{n+1}(\omega) - \sum_{i<k} \widehat{U}_k^n(\omega) + \left(\widehat{\Lambda}^n(\omega)/2 \right)}{1 + 2\alpha(\omega - \omega_k^n)^2}, \tag{5}$$

$$\omega_k^{n+1} \longleftarrow \frac{\int_0^\infty \omega \left| \widehat{U}_k^{n+1}(\omega) \right|^2 d\omega}{\int_0^\infty \left| \widehat{U}_k^{n+1}(\omega) \right|^2 d\omega}. \tag{6}$$

In the above formula, $\widehat{U}_k^{n+1}(\omega)$ represents the Fourier transform frequency domain of the kth IMF obtained by decomposition; $\widehat{Y}(\omega)$ and $\widehat{\Lambda}^n(\omega)$ represent the Fourier

transform forms of $y(t)$ and $\widehat{\lambda}^n(t)$, respectively. Based on the above conditions, the Fourier transform update formula of the Lagrange operator is

$$\widehat{\Lambda}^{n+1}(\omega) \longleftarrow \widehat{\Lambda}^n(\omega) + \tau \left(\widehat{Y}(\omega) - \sum_k \widehat{U}_k^{n+1}(\omega) \right). \tag{7}$$

τ in the formula represents the constraint strength. The iteration termination condition of VMD can be expressed by equation (8), where ε represents the minimum accuracy value and $\varepsilon = 10^{-7}$ is usually selected empirically.

$$\sum_k \frac{\left\| \widehat{u}_k^{n+1} - \widehat{u}_k^n \right\|_2^2}{\left\| \widehat{u}_k^n \right\|_2^2} < \varepsilon. \tag{8}$$

2.2. Nondominated Sorting Genetic Algorithm II (NSGA II). NSGA II is an improved multiobjective optimization method based on genetic algorithm. The NSGA II algorithm introduces the concepts of crowding degree and crowding distance operator on the basis of traditional sorting genetic algorithm. In the optimization process, samples are further selected through crowding degree to form a new parent population. Therefore, NSGA II can solve the problem of finding the optimal solution of various multiobjective functions. It has strong adaptability and high computing performance [30]. The basic flow of the NSGA II algorithm is shown in Figure 1.

The optimal solution group of multiobjective optimization can be obtained through the NSGA II method. This method has the characteristics of simple use and high efficiency, and its disadvantage is that it is unable to obtain a more accurate optimal solution vector. Based on the characteristics of the NSGA II method, this paper intends to use this method to screen the optimal solution set and quickly and effectively reduce the selection range of multiobjective optimal solution.

2.3. Multiobjective Particle Swarm Optimization Algorithm (MOPSO). The multiobjective particle swarm optimization algorithm introduces Pareto advantage into particle swarm optimization (PSO), so that PSO has the ability to optimize multiobjective function. The biggest advantage of this method is the use of mutation operator, which improves the global exploration ability of the algorithm [31]. The algorithm steps of MOPSO are shown in Table 1.

The MOPSO method can obtain the multiobjective optimal solution with ideal effect under the condition of reasonable parameters. This paper will effectively use the global parameter search ability of MOPSO to quickly obtain the optimal parameter vector within the optimal solution with limited range.

2.4. Signal Time-Frequency Domain Characteristics. In order to judge the decomposition effect of VMD, it is necessary to extract the signal features related to eigenmode groups (IMFs) to judge the decomposition effect. In order to verify the best signal feature indexes, this paper selects some features commonly used to evaluate the signal and uses $X(t)$
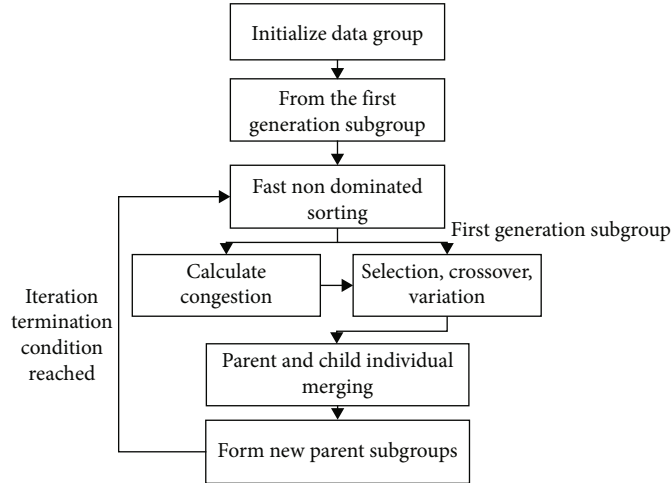
FIGURE 1: Basic flow of the NSGA II algorithm.

TABLE 1: Algorithm steps of MOPSO.

Step 1	Initialize the population and storage space set, assign initial values to the parameters, generate the initial population P_1, and copy the noninferior solution in P_1 to the storage space to obtain A_1. Let the current evolutionary algebra be t, and proceed to steps 2~4 when t is less than the total evolutionary algebra.
Step 2	Evolution produces the next generation of population: Let the current evolving particle j complete the contents of (a)–(c) when j is smaller than the population size. (a) Calculate the density information of particles in the storage space (b) Select the optimal particle $g_{j,t}$ in A_t for particle $P_{j,t}$ in the population; the quality of $g_{j,t}$ particles determines the convergence performance of MOPSO algorithm and the diversity of noninferior solution sets. Its selection is based on the density information of particles in the storage space (c) Update the position and velocity of particles in the population, and search the optimal solution in the particle swarm under the guidance of $g_{j,t}$
Step 3	Update storage set.
Step 4	Truncate storage space set: When the number of particles in the storage space set exceeds the specified size, redundant individuals need to be deleted to maintain a stable storage space set size. For mesh k with more than one particle number, calculate the number of particles P_N to be deleted in the mesh and then delete P_N particles randomly in mesh k.
Step 5	Output particle information in the storage space set.

to represent the time series of the signal. Table 2 shows the commonly used feature indexes [32].

The characteristic index can be used to evaluate the fluctuation of vibration signal and the characteristics of time-frequency domain, so as to determine the specific components in the signal. The signal categories can be classified by extracting the characteristic indexes of different signals. At the same time, it also provides a method for further analyzing the signal components. By studying the correlation between different characteristic indexes and signal categories, signal processing can be used and methods to solve many practical engineering problems [33].

3. NSGA II-MOPSO VMD

3.1. Proposed Method. In order to realize the parameter optimization of VMD, this paper proposes a collaborative hybrid heuristic optimization algorithm—multiobjective particle

swarm optimization algorithm with nondominated sorting (NSGA II-MOPSO). Firstly, the optimization target population is nondominated sorted to obtain the particle population with good and bad sorting, and then, the multiobjective particle swarm optimization algorithm is used to further find the optimal solution. This method combines the fast optimization of nondominated genetic algorithm and the high-precision optimization of particle swarm optimization algorithm, solves the problems of low optimization accuracy of nondominated genetic algorithm and low efficiency of particle optimization, and forms an efficient, adaptive, and robust algorithm combined with VMD optimization. The proposed algorithm flow is shown in Figure 2.

Figure 2 shows the specific process of optimizing VMD parameters by using the NSGA II-MOPSO method. First, determine the parameter selection range of the VMD method according to the actual situation, find the optimal

TABLE 2: Some signal characteristics involved in this paper.

Time domain characteristics	Average value	$\mu_x(t) = \lim\limits_{N \longrightarrow \infty} (1/N)x_i(t)$
	Variance	$\psi_x^2(t) = \lim\limits_{N \longrightarrow \infty} 1/N \sum_{i=1}^{N} x_i^2(t)$
	Root mean square	$X_{\text{rms}} = \sqrt{\sum_{i=1}^{N} X_i^2(t)/N}$
	Standard deviation	$X_{\text{std}} = \sqrt{(1/N) \cdot \sum_{i=1}^{N} (X_i - \mu_x)^2}$
Waveform characteristics	Peak coefficient	$C_f = X_{\text{rms}}/X_{\max} - X_{\min}$
	Waveform coefficient	$C_s = X_{\text{rms}}/(1/N) \cdot \sum_{i=1}^{N} |X(t)|$
	Kurtosis	$C_k = 1/N \sum_{i=1}^{N} X(t)^4$
	Kurtosis factor	$C_{\text{kf}} = C_k/X_{\text{rms}}^4$

NSGA II-MOPSO-VMD

VMD
- Input signal initialize input parameters set value range of K and α
- Traverse the input parameters according to the value range and VMD process the signal
- Construct the processed feature data set

NSGA II — Initialize input parameters of NSGA II
- Fast non dominated sorting of data form a new dataset

MOPSO — Initialize input parameters of MOPSO
- Multi-objective particle swarm optimization

Varitation of output characteristics and optimal results

FIGURE 2: NSGA II-MOPSO optimizing VMD parameter process.

parameter vector within the value range, and decompose the fault components of the signal; first, obtain the dominant group of the optimal solution through NSGA II and reduce the global range of the MOPSO method, which can improve the accuracy of the optimal solution search efficiency, while further global search also ensures the accuracy of the method.

3.2. Method Validation. In order to verify the feasibility of the method, a group of analog signals are used to simulate the actual rolling bearing fault vibration signal to verify the effectiveness of the method. The analog signal function is shown in the following equation:

$$x(t) = \sum_i A_i S(t - T_i) + n(t), \qquad (9)$$

where $S(t - T_i)$ represents the waveform generated by the ith pulse at time T_i and $n(t)$ represents the random noise generated during vibration. In this paper, a group of signals with four vibration frequency components are simulated by using periodic pulse signal, and the formed simulation signal is shown in Figure 3.

The four vibration frequencies of the set simulation signal are, respectively, $fn1 = 800$, $fn2 = 1600$, $fn3 = 2200$, and $fn4 = 4000$. In addition, noise with a signal-to-noise ratio of -8 is added to the mixed signal to simulate external conditions.

The obtained simulation signals are used to verify the VMD method, and different K and α are verified, respectively, the peak factor, waveform coefficient, kurtosis, and the change of kurtosis factor. When the number of decomposed modes is 4, the signal characteristic index curve obtained is shown in Figure 4.

(a)

(b)
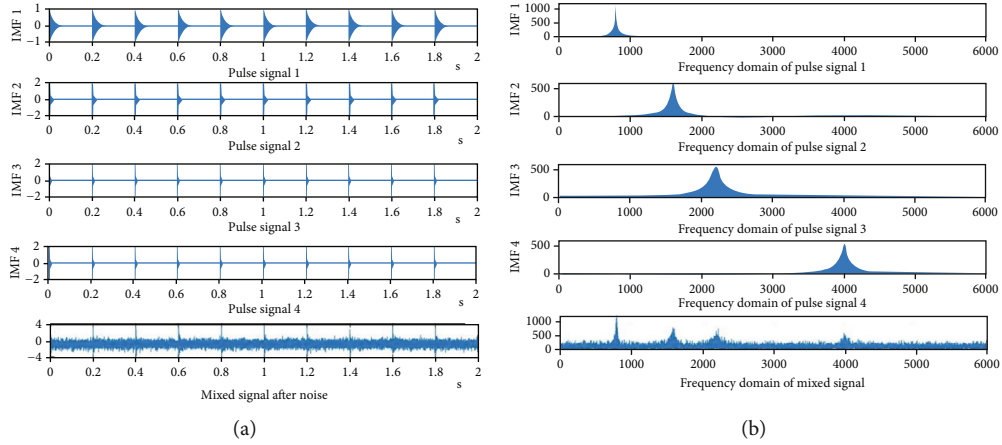
FIGURE 3: Simulation signal. (a) Time domain diagram of simulation signal. (b) Frequency domain diagram of simulation signal.
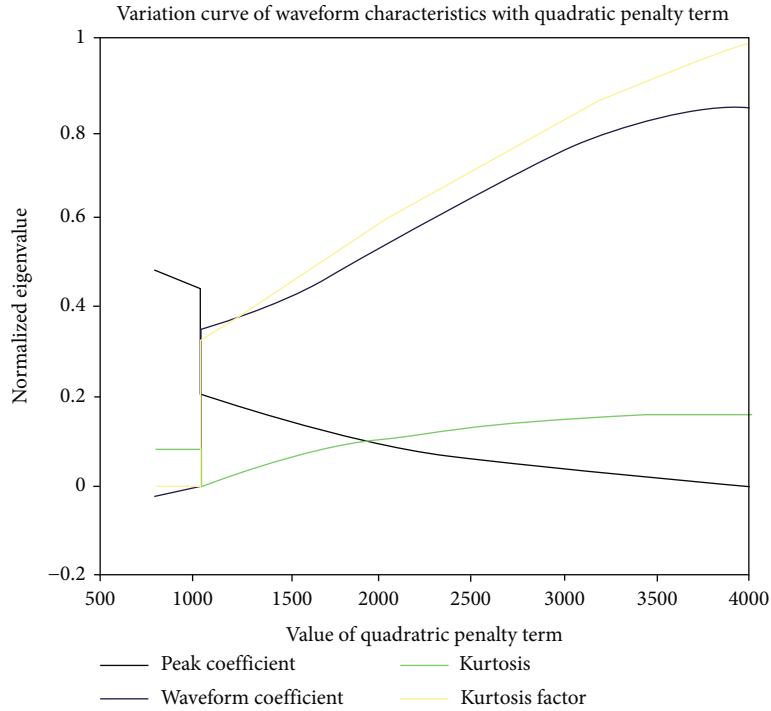
FIGURE 4: Curve of signal correlation characteristics with quadratic penalty term α when K takes 4.

Figure 4 shows that the characteristics change regularly with the penalty term α; as the value increases, kurtosis, peak factor, waveform coefficient, and kurtosis factor tend to be stable, so it can be studied according to its variation law α, the range of the best value method. In the characteristic curve, the characteristic curve at $\alpha = 1100$ has mutation. Take $\alpha = 800$ and $\alpha = 1700$ to test the mutation, respectively. The comparison diagram of the decomposition results before and after is shown in Figure 5.

Through the comparison of Figure 5, it can be found that in case $\alpha < 1100$, the VMD method cannot correctly divide the center frequency of the signal, and its decomposition result is unreliable, while in case $\alpha > 1100$, the decomposition result of VMD is basically consistent with the simulation actual frequency. Therefore, it also shows

that among the above four eigenvalues, the peak factor, waveform coefficient, and kurtosis factor other than kurtosis can determine the parameters within the correct range. It can be seen from Figure 5 that the characteristic parameters with strong correlation with α value are peak factor and waveform coefficient. Therefore, this paper proposes characteristic mutation factor C_m and accuracy index C_a as the objective function of optimizing VMD parameters, respectively. The two characteristic expressions proposed are

$$C_m = \frac{N \sum_{t=1}^{N} X(t)^4}{(X_{\max} - X_{\min}) \cdot \left(\sum_{t=1}^{N} X(t)\right)^2},$$
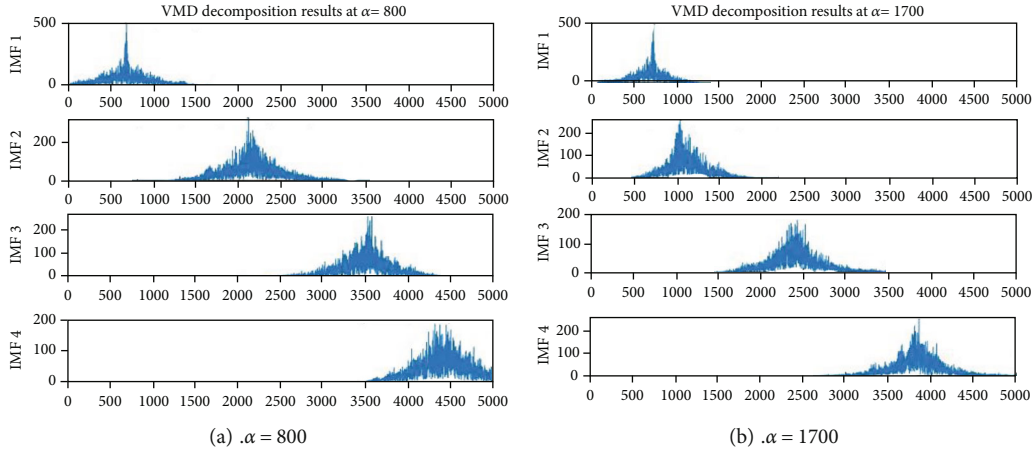
FIGURE 5: VMD decomposition results of simulation signals obtained with different α values.
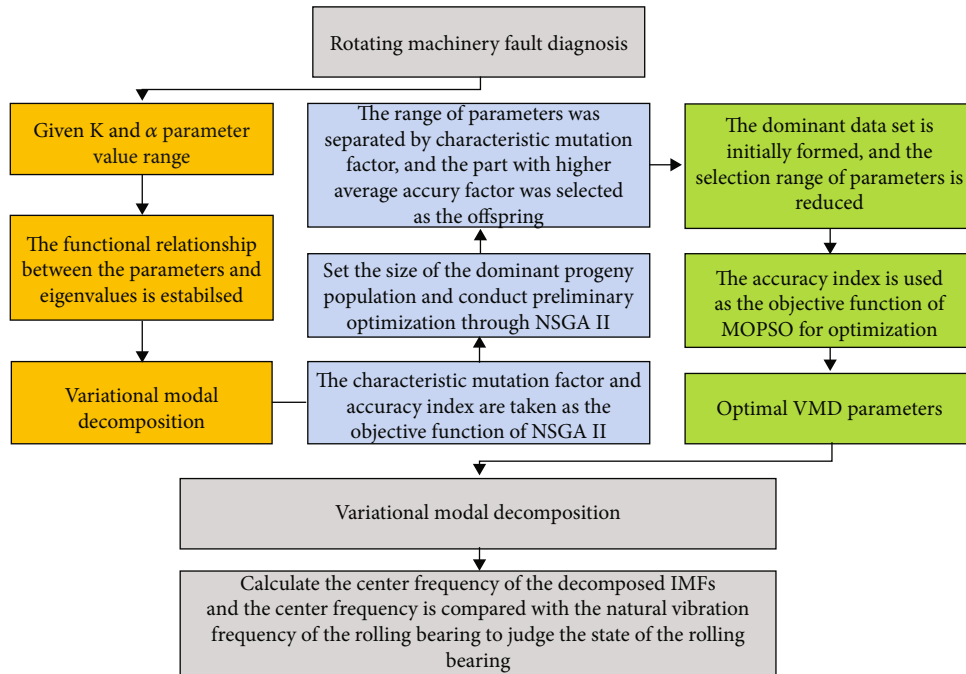
FIGURE 6: Flow chart of the improvement method.

$$C_{a} = \frac{\sum_{t=1}^{N}X(t)}{N(X_{\max} - X_{\min})}. \tag{10}$$

The proposed characteristic mutation factor and accuracy index comprehensively consider the change trend of relevant indexes in Figure 4. When the parameter value is gradually close to the optimal solution, the value of the two eigenvalues will be stable at a certain level. Whether the optimal result is obtained in the optimization process can be judged by detecting whether the two groups of eigenvalues tend to be stable.

Therefore, the two characteristic parameters proposed in this paper will be used as the objective function of the NSGA II-MOPSO method, so as to realize the parameter optimization of VMD.
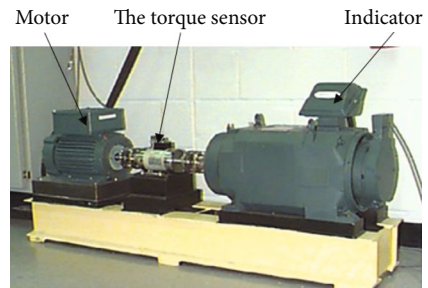
FIGURE 7: Rolling bearing sampling test bed.

3.3. Overall Improvement Method and Process. Firstly, the bearing signal is collected by the acceleration vibration sensor, the selection range of VMD parameters is set, and the characteristic mutation factor and accuracy index are taken
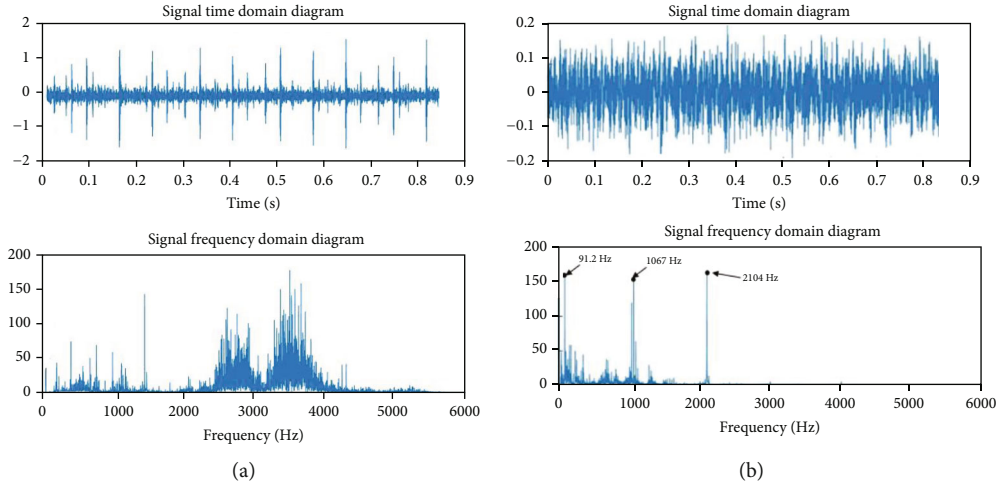
FIGURE 8: Time-frequency diagram of actual collected signal.

TABLE 3: Setting of parameter value in optimization algorithm.

Number of modes	Quadratic penalty term coefficient	Primary population size of NSGA II	Target population size of NSGA II	Initial population number of MOPSO	Number of optimization targets
$K = [3, 8]$	$\alpha = [400, 5000]$	$N_1 = 5 \times 1000$	$N_n = 3 \times 200$	$P_1 = N_n$	$P_n = 1$

as the objective function of the nondominated sorting genetic algorithm. Then, the parameter set is optimized by the nondominated sorting genetic algorithm. In this step, the nondominated sorting genetic algorithm can optimize the range of parameters, the disadvantage of this method is that it cannot quickly obtain the optimal data set, and its accuracy needs to be improved by multiple iterations, which greatly affects the optimization efficiency. The disadvantage of MOPSO is that if the parameter selection interval is too large and the number of particle swarm optimization and the number of iterations are limited, the optimization results are not reliable. Therefore, taking the preliminary screening data set of nondominated sorting genetic algorithm as the optimization interval of MOPSO can not only improve the optimization efficiency but also ensure the reliability of the results. The collaborative hybrid metaheuristic algorithm for VMD parameter optimization formed by combining the two advantages is shown in Figure 6.

4. Experiment

In order to verify the effectiveness of the proposed method, the actual data of the bearing data center of Case Western Reserve University in the United States are used to verify the method [34]. The experimental device and rolling bearing are shown in Figure 7.

The acquisition frequency of vibration signal is fs = 12 kHz, the motor speed is set to rpm = 1750, the bearing model adopted is SKF6205, the fault type is 0.014 inch wide and 0.011 inch deep artificial pit inner ring fault, and a group of fault free experimental data is used as the control experimental group. The signal segment and its time-
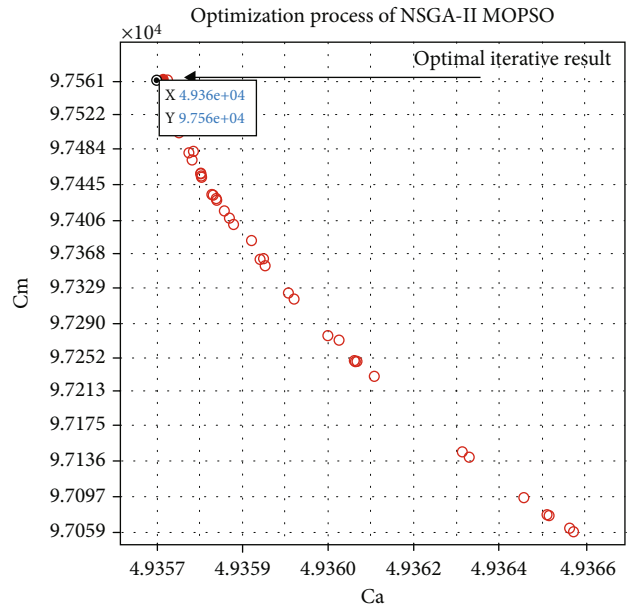
FIGURE 9: Optimization results obtained with C_m and C_a as objective functions.

frequency domain used in the experiment are shown in Figure 8.

Take the selected signal as the input to verify the optimization performance of the NSGA II-MOPSO method on VMD parameters. According to the proposed method, the relevant parameters of the algorithm are shown in Table 3.

In Table 3, the value of K represents the value of the number of modes, which is based on the number of modes that can be generated by the rolling bearing experimental

equipment. When the rolling bearing has no fault and no external noise, K can be taken as 3. When the rolling bearing has compound fault and environmental noise interference, K may be taken as 8. Therefore, the range of K value is [3, 8]. The selection of quadratic penalty term coefficient α is based on the possible modal frequency range in the signal. By referring to the basic parameters of the experimental bearing, the value α is set within the range of [400, 5000]. N_1 represents the number of initial parameter groups, K and α represent the initial population number of vector combinations, and N_n represents the size of the dominant data set processed by the NSGA II method. The initial population of the MOPSO method is the same as the dominant set obtained by NSGA II. Finally, a group of optimal parameter vectors are selected from the dominant set by the MOPSO method. There is only one optimal solution obtained by this method, so there is no problem of uneven distribution of the optimal solution. The experimental results also verify the reliability of the obtained optimal solution.

The parameter optimization results of this method are shown in Figure 9

The values of K and α corresponding to the best point are $K = 5$ and $\alpha = 2832$. The decomposition results as shown in Figure 10 can be obtained by substituting the optimal parameter values into VMD. The inner ring fault frequency of the experimental bearing is calculated through equation (11) and compared with the obtained results to verify the actual effect of this parameter.

$$\text{BPFI} = \frac{N}{2} n \left[1 + \left(\frac{\cos \alpha}{D} \right) \right]. \tag{11}$$

The inner ring fault frequency of the rolling bearing is $f_{\text{inner}} = 157.94$, which is basically close to the second modal center frequency $f_{\text{IMF2}} = 158.4$ of the decomposition result, so the improved method is effective.

In order to verify the effectiveness of the optimization parameter methods, this paper compares the ergodic method, nondominated sorting genetic optimization, and multiobjective particle swarm optimization methods, respectively. The results of the comparison are shown in Table 4. The performance of different methods in optimizing VMD is shown by comparing the time required for parameter optimization and the differences between the optimal parameter results.

The optimal parameters obtained by different algorithms are substituted into VMD to obtain the decomposition results. The difference between the calculated fault frequency and the theoretically calculated frequency value is calculated and expressed in the form of thousandth ratio on the frequency scale to express the reliability of the decomposition results. By comparing the experimental results, it can be found that the traversal method needs to involve all the parameter vector combinations, so the calculation efficiency is very slow, while the defect of NSGA II lies in the low efficiency of the iterative dominant group and the fast iteration
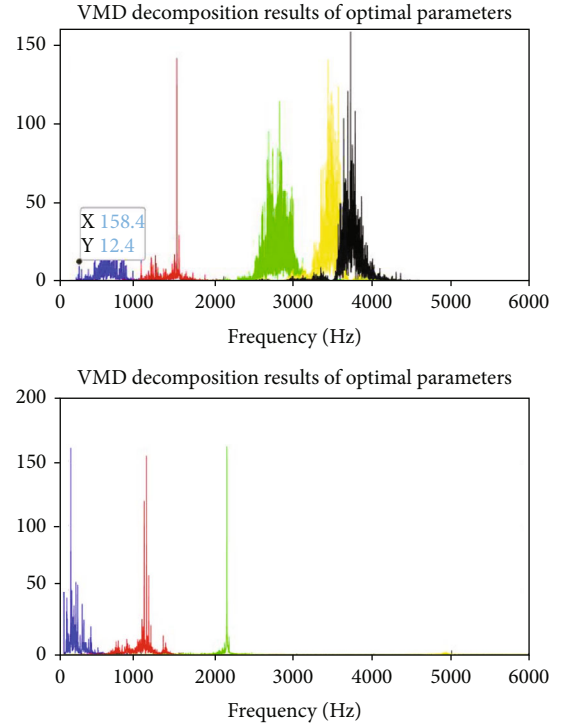
FIGURE 10: VMD results of two sets of optimal parameters.

TABLE 4: Performance comparison of different optimization methods.

Methods	Running time	Difference between parameter selection result and theoretical real value (difference ratio on frequency axis, unit: ‰)
Ergodic method	$T_{\text{Ergodic}} \gg T_{\text{NSGA II MOPSO}}$	0.08 (158.4)
MOEA	$T_{\text{MOEA}} < T_{\text{NSGA II MOPSO}}$	9.44 (214.6)
NSGA II	$T_{\text{NSGA II}} > T_{\text{NSGA II MOPSO}}$	0.28 (159.6)
MOPSO	$T_{\text{MOPSO}} < T_{\text{NSGA II MOPSO}}$	5.08 (188.4)
NSGA II MOPSO	$T_{\text{NSGA II MOPSO}}$	0.08 (158.4)

speed of MOPSO, but the optimization result is poor due to the rapid selection of the best. The NSGA II MOPSO method used in this paper is relatively fast in speed and can ensure reliable operation results, so the method proposed in this paper is feasible.

5. Conclusion

This paper mainly optimizes the parameter selection method of VMD and completes the VMD parameter optimization of rolling bearing vibration signal by using the NSGA II MOPSO multiobjective optimization algorithm. In addition, by analyzing the change of signal waveform characteristics, the characteristic mutation factor and accuracy index are proposed, and the new index is used as the objective

function to optimize the parameter selection. The effectiveness and the advanced nature of the method are verified by comparison. The main contributions of this paper are as follows:

(1) The practical performance of the cooperative hybrid metaheuristic algorithm is studied. The NSGA II and MOPSO are combined to optimize the VMD of rolling bearing signals, which proves the advanced nature of the cooperative hybrid metaheuristic algorithm

(2) The relationship between the waveform characteristics of signal modal decomposition results and VMD parameters is studied, and two characteristics of characteristic mutation factor and accuracy index are proposed to be used in parameter optimization. The performance of characteristics in VMD optimization is verified by experiments

(3) A complete process of optimizing VMD parameter selection using NSGA II MOPSO is proposed. This method is compared with other parameter optimization methods to verify the improvement of the proposed method in adaptive ability, operation speed, and robustness

Data Availability

The data is not publicly available and therefore cannot be provided.

Conflicts of Interest

The author declares no conflicts of interest.

Authors' Contributions

Zhou Guifan wrote the paper and processed the data.

References

[1] Z. He, H. Shao, X. Zhong, and X. Zhao, "Ensemble transfer CNNs driven by multi-channel signals for fault diagnosis of rotating machinery cross working conditions," *Knowledge-Based Systems*, vol. 207, article 106396, 2020.

[2] Z. J. Wang, J. Zhou, W. H. Du, Y. G. Lei, and J. Y. Wang, "Bearing fault diagnosis method based on adaptive maximum cyclostationarity blind deconvolution," *Mech Syst Signal Pr*, vol. 162, p. 108018, 2022.

[3] F. Y. Deng, H. Ding, S. P. Yang, and R. J. Hao, "An improved deep residual network with multiscale feature fusion for rotating machinery fault diagnosis," *Measurement Science and Technology*, vol. 32, no. 2, p. 024002, 2021.

[4] Z. J. Wang, X. X. He, B. Yang, and N. Li, "Subdomain adaptation transfer learning network for fault diagnosis of roller bearings," *IEEE Transactions on Industrial Electronics*, vol. 69, no. 8, pp. 8430–8439, 2022.

[5] Z. J. Wang, W. L. Zhao, W. H. Du, N. P. Li, and J. Y. Wang, "Data-driven fault diagnosis method based on the conversion of erosion operation signals into images and convolutional neural network," *Process Saf Environ*, vol. 149, pp. 591–601, 2021.

[6] X. X. He, Z. J. Wang, Y. F. Li et al., "Joint decision-making of parallel machine scheduling restricted in job-machine release time and preventive maintenance with remaining useful life constraints," *Reliability Engineering & System Safety*, vol. 222, p. 108429, 2022.

[7] X. Li, J. Cheng, H. Shao, K. Liu, and B. Cai, "A fusion CWSMM-based framework for rotating machinery fault diagnosis under strong interference and imbalanced case," *IEEE Transactions on Industrial Informatics*, p. 1, 2021.

[8] G. Y. Chen, C. F. Yan, J. D. Meng, H. B. Wang, and L. X. Wu, "Improved VMD-FRFT based on initial center frequency for early fault diagnosis of rolling element bearing," *Measurement Science and Technology*, vol. 32, no. 11, p. 115024, 2021.

[9] X. C. Zhu, X. Hu, D. Y. Li, and S. H. Peng, "A dual evaluation multi-scale template matching algorithm based on wavelet transform," *Electronics Letters*, vol. 58, 2022.

[10] Z. S. Chen, J. Fu, Y. J. Peng, T. H. Chen, L. K. Zhang, and C. F. Yuan, "Baseline correction of acceleration data based on a hybrid EMD-DNN method," *Sensors-Basel*, vol. 21, no. 18, 2021.

[11] H. Shao, J. Lin, L. Zhang, G. Diego, and K. Uday, "A novel approach of multisensory fusion to collaborative fault diagnosis in maintenance," *Information Fusion*, vol. 74, pp. 65–76, 2021.

[12] W. L. Zhao, Z. J. Wang, W. A. Cai et al., "Multiscale inverted residual convolutional neural network for intelligent diagnosis of bearings under variable load condition," *Measurement*, vol. 188, p. 110511, 2022.

[13] H. Li, T. Liu, X. Wu, and Q. Chen, "An optimized VMD method and its applications in bearing fault diagnosis," *Measurement*, vol. 166, 2020.

[14] T. Han and D. X. Jiang, "Rolling bearing fault diagnostic method based on VMD-AR model and random forest classifier," *Shock and Vibration*, vol. 2016, 11 pages, 2016.

[15] X. Zhang, Q. Miao, H. Zhang, and L. Wang, "A parameter-adaptive VMD method based on grasshopper optimization algorithm to analyze vibration signals from rotating machinery," *Mech Syst Signal Pr*, vol. 108, pp. 58–72, 2018.

[16] Y. Q. Li, D. R. Huang, and Z. X. Qin, "A classification algorithm of fault modes-integrated LSSVM and PSO with parameters' optimization of VMD," *Mathematical Problems in Engineering*, vol. 2021, 12 pages.

[17] A. Kumar, Y. Q. Zhou, and J. W. Xiang, "Optimization of VMD using kernel-based mutual information for the extraction of weak features to detect bearing defects," *Measurement*, vol. 168, 2021.

[18] Z. J. Wang, N. N. Yang, N. P. Li, W. H. Du, and J. Y. Wang, "A new fault diagnosis method based on adaptive spectrum mode extraction," *Structural Health Monitoring*, vol. 20, no. 6, pp. 3354–3370, 2021.

[19] W. Xu and J. F. Hu, "A novel parameter-adaptive VMD method based on grey wolf optimization with minimum average mutual information for incipient fault detection," *Shock and Vibration*, 14 pages, 2021.

[20] A. Hojjati, M. Monadi, A. Faridhosseini, and M. Mohammadi, "Application and comparison of NSGA-II and MOPSO in multi-objective optimization of water resources systems," *J Hydrol Hydromech*, vol. 66, no. 3, pp. 323–329, 2018.

[21] V. Modrak, R. S. Pandian, and S. S. Kumar, "Parametric study of wire-EDM process in Al-Mg-MoS2 composite using NSGA-II and MOPSO algorithms," *Processess*, vol. 9, no. 3, 2021.

[22] M. Rabbani, N. Oladzad-Abbasabady, and N. Akbarian-Saravi, "Ambulance routing in disaster response considering variable patient condition: NSGA-II and MOPSO algorithms," *J Ind Manag Optim*, 2022.

[23] J. B. Gai, J. X. Shen, Y. F. Hu, and H. Wang, "An integrated method based on hybrid grey wolf optimizer improved variational mode decomposition and deep neural network for fault diagnosis of rolling bearing," *Measurement*, vol. 162, 2020.

[24] M. S. Qi, R. Zhou, Q. Q. Zhang, and Y. S. Yang, "Feature classification method of frequency cepstrum coefficient based on weighted extreme gradient boosting," *Ieee Access*, vol. 9, pp. 72691–72701, 2021.

[25] X. Y. Bi, S. Q. Cao, and D. M. Zhang, "Diesel engine valve clearance fault diagnosis based on improved variational mode decomposition and bispectrum," *Energies*, vol. 12, no. 4, 2019.

[26] T. J. He, R. Z. Zhao, Y. C. Wu, and C. Yang, "Fault identification of rolling bearing using variational mode decomposition multiscale permutation entropy and adaptive GG clustering," *Shock and Vibration*, vol. 2021, 13 pages, 2021.

[27] A. Kumar, C. P. Gandhi, G. Vashishtha et al., "VMD based trigonometric entropy measure: a simple and effective tool for dynamic degradation monitoring of rolling element bearing," *Measurement Science and Technology*, vol. 33, no. 1, p. 014005, 2022.

[28] Z. He, H. Dong, Z. Ding, H. Jiang, and J. Cheng, "Modified deep auto-encoder driven by multi-source parameters for fault transfer prognosis of aero-engine," *IEEE Transactions on Industrial Electronics*, vol. 69, no. 1, pp. 845–855, 2022.

[29] G. R. Feng, H. R. Wei, T. Y. Qi, X. M. Pei, and H. Wang, "A transient electromagnetic signal denoising method based on an improved variational mode decomposition algorithm," *Measurement*, vol. 184, p. 109815, 2021.

[30] H. T. Wu, Y. R. Huang, L. Chen, Y. J. Zhu, and H. Z. Li, "Shape optimization of egg-shaped sewer pipes based on the nondominated sorting genetic algorithm (NSGA-II)," *Environmental Research*, vol. 204, p. 111999, 2022.

[31] Y. Zhang, D. W. Gong, and Z. H. Ding, "Handling multi-objective optimization problems with a multi-swarm cooperative particle swarm optimizer," *Expert Systems with Applications*, vol. 38, no. 11, pp. 13933–13941, 2011.

[32] S. Wei, D. Wang, H. Wang, and Z. K. Peng, "Time-varying envelope filtering for exhibiting space bearing cage fault features," *IEEE T Instrum Meas*, vol. 70, 2021.

[33] Y. Zhang, Z. Lian, W. Fu, and X. Chen, "An ESR quasi-online identification method for the fractional-order capacitor of forward converters based on variational mode decomposition," *IEEE Transactions on Power Electronics*, vol. 37, no. 4, pp. 3685–3690, 2022.

[34] *The data is from the bearing data center of Case Western Reserve University, USA* Website: https://csegroups.case.edu/.

Research Article

A Novel Anchorless Node Positioning Method for Wireless Sensor Network

Wenxiu He,[1] **Ran Cheng,**[2] **Keji Mao,**[2] **Ke Yan** (ID),[3] **Jianliang Wei** (ID),[4] **and Yingying Xu**[5]

[1]*Zhijiang College, Zhejiang University of Technology, China*
[2]*Zhejiang University of Technology, China*
[3]*Department of the Built Environment, National University of Singapore, Singapore*
[4]*School of Management Engineering and E-Commerce, Zhejiang Gongshang University, China*
[5]*School of Economics and Management, University of Science and Technology Beijing, China*

Correspondence should be addressed to Jianliang Wei; jianliang@zjgsu.edu.cn

Wireless sensor network sensing data is meaningless without any location information, and a large number of anchor node-based localization methods have been proposed to obtain the location information of nodes. However, this kind of method requires a certain number of anchor nodes deployed in the network and complex information interaction between nodes. Therefore, it is not ideal in positioning cost and effect. A WSN positioning method based on the steering antenna of the base station is proposed to address this problem. By rotating the orientation information of the antenna, accurate positioning can be achieved without the assistance of anchor nodes, and no signal interaction between nodes is required. Theoretically, the method is easier to be deployed in the actual scene to realize the positioning of sensor nodes. Experimental results show that the proposed method is better than most positioning methods assisted by anchor node in positioning accuracy, positioning time, and energy consumption.

1. Introduction

Wireless sensor networks (WSNs) are widely adopted in data perception and collection, but it is meaningless to perceive data without knowing its location information. For example, if a WSN is used to monitor a forest for fires, it is still meaningless to not know the location of the fire, even though the fire can be determined based on the sensory data of a node. The positioning of nodes with GPS modules on each sensor node is impractical for large-scale wireless sensor networks, so it is important to study accurate and low-energy WSN positioning methods.

Research on wireless sensor network positioning is mainly divided into several categories: (1) range-based positioning; (2) range-free positioning; (3) anchor-based positioning; (4) anchor-free positioning, etc. Among them, range-based positioning and anchor-based node positioning are generally combined with each other, such as using the Received Signal Strength Indication (RSSI) attenuation

of node interaction, signal Time of Arrival (TOA), signal Time Difference of Arrival (TDOA), and signal Angle of Arrival (AOA) model to calculate the distance between nodes and other information, and combining multiple anchor nodes can locate the positioning of unknown nodes. For example, Yan et al. studied the WSN positioning algorithm based on fuzzy decision-making, which is divided into several stages: knowledge accumulation, knowledge fusion, and knowledge expansion. In the knowledge accumulation stage, the RSS of the anchor node is obtained and processed as a position relation index; the knowledge fusion stage optimizes the membership degree of anchor nodes in different environments; in the knowledge expansion stage, the points with the highest matching degree are used to estimate the position of unknown nodes [1]. Furthermore, Yu et al. proposed a WSN node algorithm based on social spider optimization and opposition-based learning. Firstly, the Bounding-box method was used to know the possible region of unknown

nodes, and then, the opposition-based learning strategy is combined with the social spider optimization algorithm in the area to estimate the node locations. According to the simulation results, the positioning accuracy is higher than the traditional method [2]. Li et al. proposed a positioning method based on anchor nodes, using positioning priority to improve accuracy. This method reduces positioning errors by introducing a new concept that explores node positioning priorities.. Finally, the experiment compares and evaluates Simulated Annealing Location(SAL), Genetic Algorithm Locations (GAL), and the proposed method, showing that the priority-based positioning method has better positioning accuracy [3]. Xiong et al. proposed a hybrid positioning algorithm of RSS and TOA, which solved the multitarget positioning problem of wireless sensor networks in three-dimensional space and optimized the positioning results by using the least-squares method. The experiment comparing RSS ranging or TOA ranging alone has demonstrated that RSS combined with TOA has a higher accuracy rate [4].

Range-free positioning and anchorless node positioning are generally combined with each other. For example, Zhu et al. implemented a WSN indoor positioning method based on fingerprint matching. First, using the strength of the wireless signal to construct a basic fingerprint map, then constructing a high-resolution positioning fingerprint map with the Kriging interpolation algorithm, and finally optimizing the fingerprint matching result with K-means clustering algorithm to get the target position [5]. Messous et al. improved the DV-HOP positioning algorithm to investigate range-free localization algorithms in similar multihop wireless sensor networks, which optimizes the average hop length between nodes based on the recursive position of the positioning node, thereby reducing the positioning error [6]. Lee proposed a fingerprint database construction method for indoor fingerprint positioning, which can effectively solve the problem of large deviations in the fingerprint data collected due to the positioning environment during the construction of the fingerprint database. The method can improve positioning accuracy by studying the optimal number of clusters and combining the K-means method to obtain a more accurate radio fingerprint construction method [7]. To address the problem of outdoor parking difficulties, Postigo-Málaga et al. investigated a parking space location method based on RSS fingerprints of parking spaces. By collecting the signal strength of parking spaces during idle and busy hours, a fingerprint database was constructed, and then, the parking spaces were located by fingerprint matching [8].

The above analysis of range-based and range-free positioning methods reveals that they all require a certain number of anchor or beacon nodes to locate unknown nodes. Anchor nodes or beacon nodes require a large and complex workload and are subject to greater external interference, resulting in less than optimal positioning accuracy and deployment costs [9–11].

To address the above problem, this paper proposes a node positioning method based on the base station steering antenna, which can achieve high accuracy positioning without the need for an anchor node.

2. Related Assumptions and Positioning Model

2.1. Related Assumptions

(1) All nodes in the sensor network are deployed on the XY two-dimensional plane and cannot obtain their own position

(2) The signal energy emitted by the rotatable antenna mounted on the base station is mainly concentrated within its beam width, while the signal energy outside the beam width is weak and can be considered zero

(3) The base station adopts an active power supply and has strong calculation performance, supporting communication with ordinary nodes and complex calculations, and can achieve the purpose of adjusting the maximum communication distance by varying its transmission power Pt

(4) The location of the base station can be obtained by GPS technology

2.2. Positioning Model.
The positioning model proposed in this paper is shown in Figure 1. The Base Station (BS) is located at the origin O, and a Dynamic Antenna (DA) is erected at the position H above the base station. This antenna can transmit beacon frames to ordinary sensor nodes deployed in the XY plane. After receiving the beacon frame, the node determines its own position based on the horizontal rotation angle φ, the vertical elevation angle θ of the antenna, and the distance information from the node to the base station antenna. The positioning result of the node can be expressed in polar coordinates (ρ, φ), where ρ represents the distance between the node from the base station position O. The model satisfies the following conditions:

(1) The rotating antenna is a parabolic reflector-type directional antenna with a small beam width (θ_{bw})

(2) DA locates at height H above BS

(3) DA can rotate around the z-axis, and the included angle with the x-axis is $\varphi(0 \le \varphi \le 2\pi)$

(4) DA rotates around the z-axis, the smallest unit of each rotation is $\delta\phi(\delta\phi \le \theta_{bw}/2)$

(5) The elevation angle θ of DA is adjustable $(0 \le \theta \le \theta_{max})$, and θ_{max} can be used to calculate the position of the node farthest from BS

(6) The minimum adjustment unit of DA elevation angle θ is $\delta\theta(\delta\theta \le \theta_{bw}/2)$;

(7) By changing the φ and θ angles of the antenna, the base station signal can scan all nodes in the positioning area
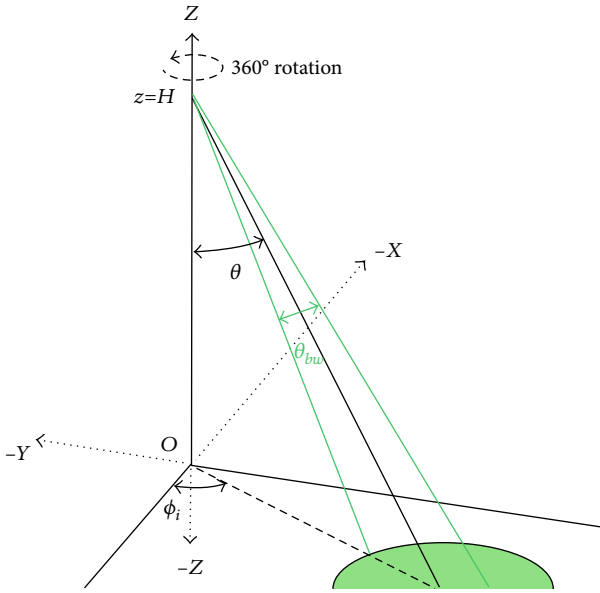
FIGURE 1: Positioning model diagram.
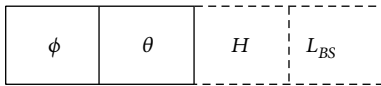
FIGURE 2: Beacon frame structure diagram.
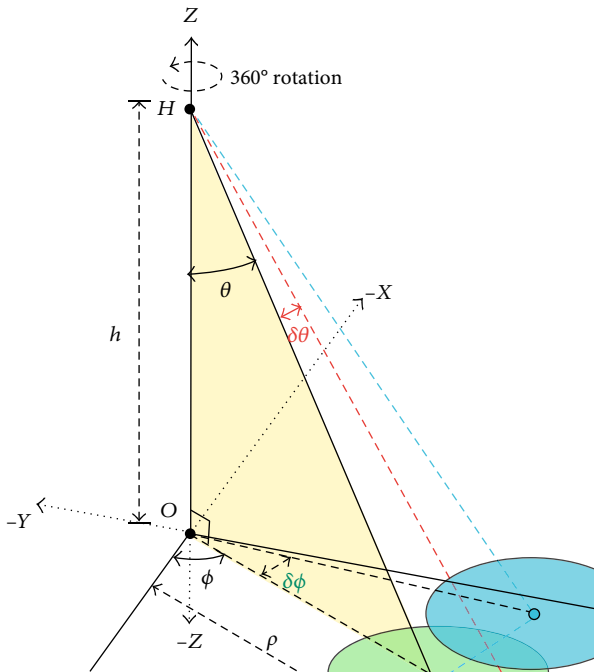
FIGURE 3: Positioning schematic diagram.

(8) Each time DA changes its position ($\delta\theta$ or $\delta\phi$), the beacon frame data is updated and the updated data frame is sent to ordinary nodes. The beacon frame includes antenna height H, elevation angle θ,

horizontal rotation angle φ, and the position of the base station

3. Anchorless Positioning Algorithm

This section introduces the proposed method for positioning wireless sensor networks without using anchor nodes, followed by a theoretical analysis of the performance associated with this positioning method.

3.1. Positioning Algorithm

3.1.1. Principle of Positioning. The positioning method proposed in this paper does not require frequent communication between anchor nodes and unknown nodes but achieves positioning through the beacon data interaction between the rotating antenna of the base station and the ordinary node.

The beacon frame format is shown in Figure 2, including the horizontal rotation angle φ, elevation angle θ of the rotating antenna, the height H of the antenna, and the location L_{BS} of the base station (obtained by GPS). When the antenna orientation is adjusted once, φ and θ are updated again, while the values of antenna height H and base station location L_{BS} are fixed.

The beam signal sent by the rotating antenna at angles φ and θ will get an elliptical signal coverage area in the XOY plane. If an ordinary node exists in this area at this time, the ordinary node can receive the beacon signal from the antenna, which contains the rotation angle φ, the elevation angle θ, and the height H of the rotating antenna. Ordinary nodes can calculate the distance ρ from the base station O based on these three parameters, as shown in Equation (1). Then, the position of the node can be expressed as φ, ρ, according to which the polar coordinate can be converted to the horizontal and vertical coordinates (x, y) of the node, and the conversion method is shown in Equation (2). As shown in Figure 3, it is assumed that the ordinary node is located at exactly point N, and it can calculate its own position based on the beacon frame.

When the rotating antenna rotates along the horizontal direction, each time rotating one unit angle $\delta\phi$(i.e., $\varphi = \varphi \pm \delta\phi$), then the signal coverage area will shift accordingly. As shown in Figure 3, the signal coverage area moves from the original position N to the position n_j. If there are ordinary nodes in the signal coverage area, the position coordinates of the ordinary nodes can also be obtained by the above method. When the steering antenna adjusts the elevation angle θ(i.e., $\theta = \theta \pm \delta\theta$), the coverage area of the signal from the steering antenna in the XOY plane will also change, such as moving from the original area with N as the signal coverage center to the coverage area with n_k as the center. If the magnitude of each adjustment of the steering antenna angle is relatively small, there is an overlap area in the signal coverage area between adjacent antenna angles, And the ordinary node in the overlapping area can receive a beacon signal at least once, and the number of times a node receives a beacon frame depends on the adjustment units $\delta\theta$ and $\delta\phi$ of the antenna angle. If a node receives n beacon frames,

The steps of BS positioning
Input: signal beam width (θ_{bw}), Antenna height (H), the smallest unit of antenna azimuth adjustment ($\delta\theta$ or $\delta\phi$);
Output: Updated beacon frame: beacon;
Steps:
1: Initialize angle θ and ϕ, $\theta = \theta_{bw}/2$, $\phi = 0°$;
2: According to the current antenna's azimuth information (beacon = {ϕ,θ,H,L_{BS}}), construct a beacon frame and send it;
3: while($\theta + \theta_{bw}/2 \leq \theta_{max}$)
4:      if($\phi < 2\pi$)
5:          Horizontal rotating antenna: $\phi = \phi + \delta\phi$;
6:      elseif$\phi == 2\pi$
7:          $\phi \leftarrow 0$;
8:          $\theta = \theta + \delta\theta$;
9:      endif
10:      Update the antenna's orientation information and construct new beacon frames: Beacon = {ϕ',θ',H,L_{BS}};
11:      Send beacon frames through the antenna;

ALGORITHM 1: BS positioning process.

The steps of ordinary node positioning
Input: Received beacon frames: beacon = {ϕ,θ,H,L_{BS}};
Output: Node coordinates:(x,y);
Steps:
1:   while(1)
2:       Node in listening state;
3:       recv ← Received data frames;
4:       if(recv is the end frame)
5:           break;
6:       else //Indicates beacon frames
7:           if(recv ≥ 1)
8:               if(recv > 1)
9:                   $\phi = \sum_{i=1}^{n}\phi_i/n, \theta = \sum_{i=1}^{n}\theta_i/n$
10:              endif
11:              $\rho = H \cdot \tan(\theta)$
12:              Node polar coordinates: (ρ,ϕ)
13:              (x,y)←(ρ,ϕ)
14:          endif
15:      endif
16:   endwhile

ALGORITHM 2: Ordinary node positioning process.

then the average antenna rotation angle and average elevation angle contained in these n beacon frames are calculated as shown in Equations (3) and (4). The average antenna rotation angle $\bar{\phi}$ and the average elevation angle $\bar{\theta}$ can be used to calculate the location of the ordinary node more accurately.

The specific steps of the tasks responsible for the base station in the positioning process are shown in Algorithm 1, and the tasks responsible for the ordinary nodes are shown in Algorithm 2.

$$\rho = H \cdot \tan(\theta), \qquad (1)$$

$$\begin{cases} x = \rho \cos(\theta) \\ y = \rho \sin(\phi) \end{cases}, \qquad (2)$$
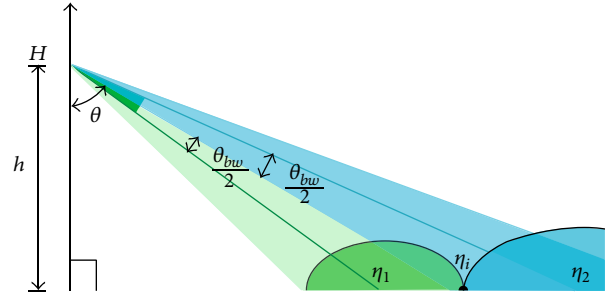
FIGURE 4: Maximum positioning error analysis.
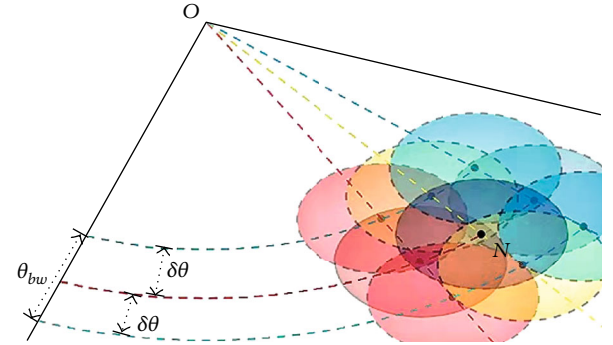
FIGURE 5: Beacon repeated reception principle.

$$\bar{\phi} = \frac{\sum_{i=1}^{n}\phi_i}{n}, \qquad (3)$$

$$\bar{\theta} = \frac{\sum_{i=1}^{n}\theta_i}{n}. \qquad (4)$$

The positioning method based on the rotating antenna of the base station has a maximum locating range. If this range is exceeded, the beacon signal cannot be received by the ordinary node, and it is naturally impossible to locate the ordinary node. The positioning distance is the distance between the node and the base station BS. Assuming that the farthest one sensor node from the base station node is n_a and the distance is ρ_{max}, then the antenna elevation angle

TABLE 1: Experimental parameters.

Symbol	Value
Positioning area A	$100 \, \text{m} \times 100 \, \text{m}$
Number of nodes deployed n	100
Antenna height H	Dynamically adjustable
Beam width θ_{bw}	Dynamically adjustable
Antenna elevation angle adjustment unit $\delta\theta$	$5°$
Antenna horizontal angle adjustment unit $\delta\phi$	$4°$
Initial angle of the antenna θ	0
Initial angle of the antenna ϕ	$\theta_{bw}/2$

(a)

(b)
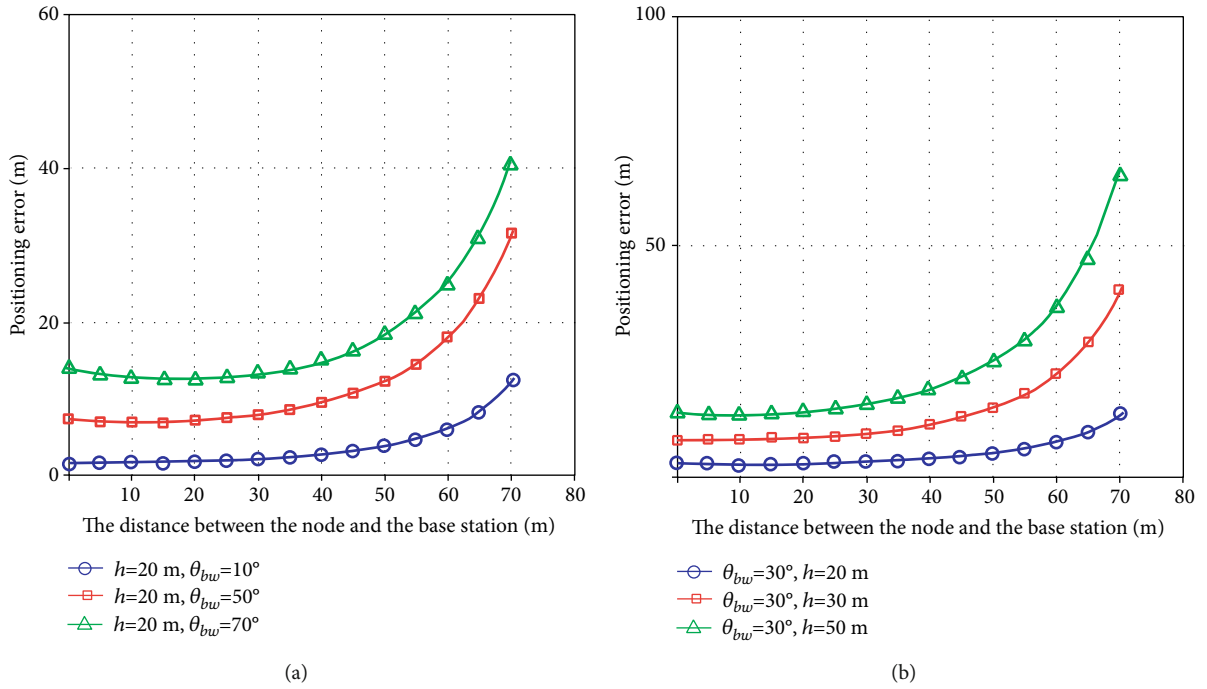
FIGURE 6: The effect of θ_{bw} and H on positioning.

$\theta_{\max}$ corresponding to this $\rho_{\max}$ is shown in Equation (5). Since the elevation angle of the antenna reaches 90°, the signal from the antenna is parallel to the XOY plane and cannot locate any node, so θ must be less than or equal to $90° - \theta_{bw}/2$. Then, the farthest localization distance $\rho_{\max}$ is shown in Equation (6).

$$\theta_{\max} = \arctan\left(\frac{H}{\rho_{\max}}\right), \tag{5}$$

$$\rho_{\max} \leq H \cdot \tan\left(90 - \frac{\theta_{bw}}{2}\right). \tag{6}$$

In Equations (5) and (6), H represents the antenna height, and θ_{bw} represents the signal beam width, both of which are known values.

3.1.2. Coordinate Conversion. Part (1) of Section 3.1 details the positioning method proposed in this paper, and based on this method, the coordinates (x, y) of ordinary nodes can be located, which is a coordinate system established with the base station as the origin and represents only the coordinates relative to the BS. Since the position of the BS can be obtained by GPS, the coordinates (x, y) of the ordinary node can also be converted to GPS coordinates based on the BS coordinates $(x_{BS}^{\circ} \boxtimes y_{BS}^{\circ})$. The conversion steps are as follows:

Step 1. Converting the position coordinates (x, y) of ordinary nodes into GPS coordinates requires knowing the relationship between latitude and longitude and the actual distance. The current commonly used conversion rate is $1° = 111.32 \, \text{km}$, which means that a difference of 1° in longitude or latitude will result in a difference of 111.32 km in the distance. Therefore, the ordinary node coordinates (x, y) are divided by 111.32 km to get the transformed coordinates, as shown in Equation (7).

$$\begin{cases} x_l^{\circ} = \dfrac{x}{111.32} \\ y_l^{\circ} = \dfrac{y}{111.32} \end{cases}. \tag{7}$$
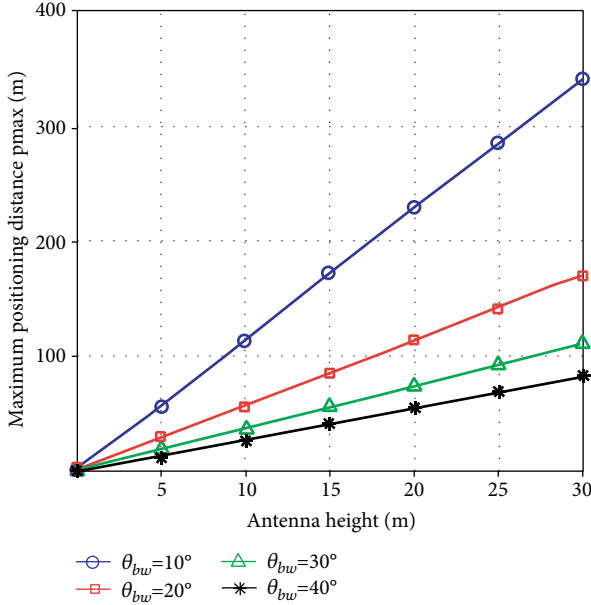
FIGURE 7: The effect of θ_{bw} and H on maximum locatable distance.

Step 2. Add the GPS coordinates of the BS and the coordinates (a, b) of the ordinary node to obtain the GPS coordinates (c, d) of the ordinary node, as shown in Equation (8).

$$\begin{cases} x_{GPS}^{\circ} = x_l^{\circ} + x_{BS}^{\circ} \\ y_{GPS}^{\circ} = y_l^{\circ} + y_{BS}^{\circ} \end{cases}. \tag{8}$$

3.2. Positioning Performance

3.2.1. Analysis of Positioning Error. When the signal from the steering antenna reaches the XOY plane, the signal coverage area is elliptical, as shown in Figure 4; as already described above, when a ordinary node can receive multiple beacon frames, the positioning accuracy can be improved by finding the positioning mean based on the data from multiple beacon frames. However, some nodes are located just on the boundary of the two signal coverage areas, as shown by n_i in Figure 4. The node at this location can only receive a beacon frame once, and it may belong to the signal coverage boundary centered on n_1, or it may belong to the signal coverage boundary centered on n_2. In this case, the positioning error is maximum, and its positioning error may be e_1 or e_2. Therefore, the maximum positioning error of the positioning algorithm is shown in Equation (9).

$$e = \max (e_1, e_2) = \max \left(H \cdot \tan (\theta) - H \cdot \tan \right.$$
$$\left. \cdot \left(\theta - \frac{\theta_{bw}}{2} \right), H \cdot \tan (\theta) - H \cdot \tan \left(\theta + \frac{\theta_{bw}}{2} \right) \right). \tag{9}$$

3.2.2. Analysis of Positioning Time. The time consumed by the positioning method proposed in this paper mainly includes the time T_{turn} for the base station to adjust the antenna orientation, the time T_B for the base station to update and send the beacon, and the position calculation

time T_P for the normal node after receiving the beacon. Therefore, the time T_{total} consumed in the whole process of positioning by this system is shown in Equation (10).

$$T_{total} = N_{step} \cdot (T_{turn} + T_B + T_P). \tag{10}$$

In Equation (9), N_{step} represents the number of adjustments of the steering antenna, and the amplitude of each adjustment is $\delta\theta$ or $\delta\phi$, and its value is shown in Equation (11).

$$N_{step} = N_{\varphi} + N_{\varphi} \cdot N_{\theta} \tag{11}$$

In Equation (11), $N_{\varphi} = 2\pi/\delta\varphi$, $N_{\theta} = \theta_{max}$.

3.2.3. Analysis of the Number of Beacon Frames Received. If the step value $\delta\theta$ and $\delta\phi$ of the steering antenna adjustment of the base station are relatively small, there will be a large overlap in the signal coverage area in the XOY plane. Therefore, ordinary nodes can receive multiple beacon frames in one rotation of the antenna, and the average position of the node is found based on the multiple beacon frames received, which is good for optimizing the positioning accuracy of the node. Assuming that the angle of each step of the steering antenna in the horizontal direction is $\delta\phi$, and the angle of each step of the elevation angle in the z-axis direction is $\delta\theta$. Under this condition, the maximum possible number of beacon frames Nrx received by the sensor node in the positioning area is shown in Equation (12). The position where the most beacon frames can be received is shown by the point N in Figure 5.

$$N_{rx} \le \left(\frac{\theta_{bw}}{\delta\theta} \times \frac{\theta_{bw}}{\delta\phi} \right). \tag{12}$$

4. Experiment Analysis

4.1. Analysis of Positioning Error. The performance of the algorithm proposed in this paper is verified through experimental analysis. The experiment uses MATLAB for simulation and randomly deploys 100 sensor nodes in a positioning area of $100 \, m \times 100 \, m$, and the base station is located in the center of the positioning area. Under this condition, the maximum positioning distance of the system is $\rho_{max} = 70.71 \, m$ (the distance from the base station to a vertex of the positioning area). In the experiment, the value of the signal beamwidth angle θ_{bw} and the steering antenna height H are dynamically adjusted. The specific parameters of the simulation experiment are shown in Table 1.

We analyze their influence on the positioning accuracy of the node by adjusting the height of the antenna and the beam width of the signal during the simulation. In the experiment, the experimental results obtained by varying the beam width (10°, 40°, and 70°) when the antenna height is all 20 m and analyzing the effect of beam width on positioning accuracy are shown in Figure 6(a). Then, change the antenna height when the beam width is all 30°, and analyze the effect on the positioning accuracy, the experimental

(a)

(b)
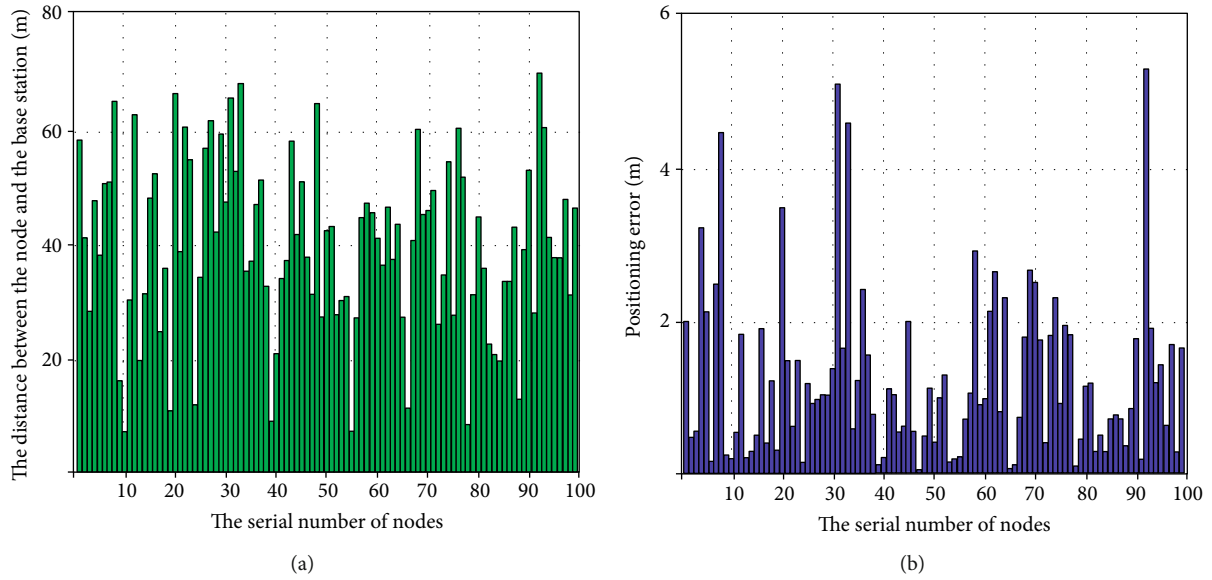
FIGURE 8: Node positioning error.

—— The distance between the actual position
and the estimated position of the node
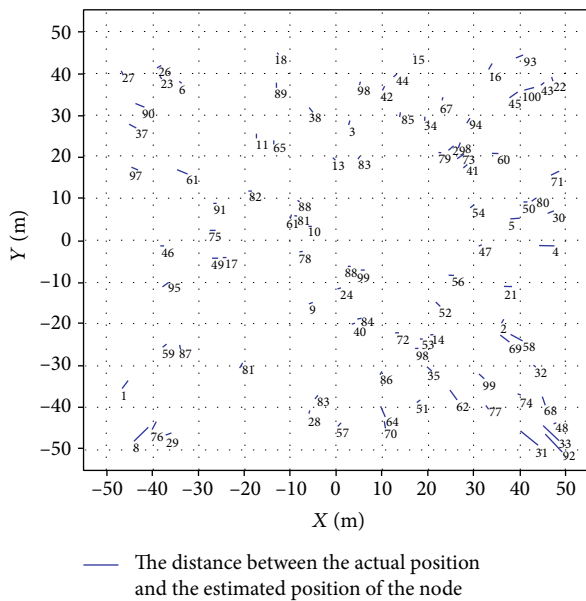
FIGURE 9: Positioning results.

FIGURE 10: The relationship between positioning error and positioning time.

results are shown in Figure 6(b). Both horizontal coordinates indicate the distance of the node from the base station and the vertical coordinates indicate the positioning error.

The experimental results in Figure 6(a) show that when the beam widths are 10°, 40°, and 70°, respectively, the localization error first increases gently as the distance between the node and the base station increases, and then increases faster when the distance from the base station is greater than 40 m. When the distance between the node and the base station is the same, the larger the beamwidth, the worse the positioning accuracy. Because the larger the beamwidth, the larger the area covered by the signal, and therefore, the positioning accuracy will be reduced. The experimental results in Figure 6(b) show that when the beamwidth is the

same, the higher the antenna height, the worse the corresponding positioning accuracy. Similarly, when the antenna height is higher, the signal coverage in the XOY plane is larger, resulting in worse positioning accuracy.

The maximum locatable distance $\rho_{\max}$ of the proposed positioning method is affected by the antenna height and beam width θ_{bw} (as in Equation (5)), which affects the maximum positioning range of the system when the antenna height or beam width is adjusted. The experimental results are shown in Figure 7, where the horizontal coordinates indicate the antenna height and the vertical coordinates indicate the maximum locatable range $\rho_{\max}$.

The experimental results are shown in Figure 7, which indicate that the maximum positioning distance ρmax grows
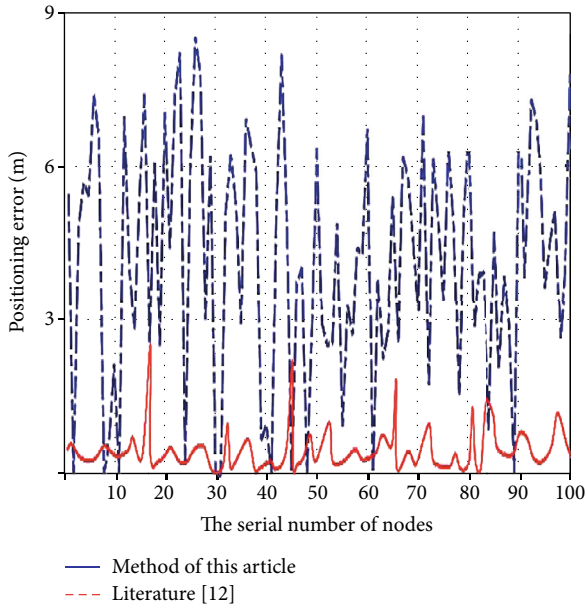
FIGURE 11: Comparison of positioning error.
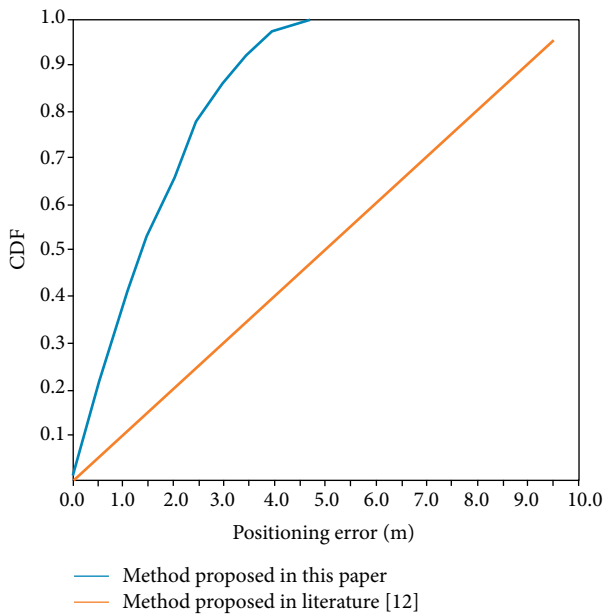
FIGURE 12: Cumulative error distribution results.

TABLE 2: . Energy consumption model parameter table.

Parameter	Value
E_{elec}	50 nJ/bit
E_{init}	0.5 J
E_{DA}	5 nJ/bit/signal
The size of Beacon packet	8bit

in a linear pattern with the increase of the antenna height. Equation (5) for calculating ρ_{max} shows that ρ_{max} is linearly related to H. So when the antenna height is the same, the larger the beam width θ_{bw} is, the smaller the maximum positioning distance ρ_{max} is. The distance of each node in the positioning area from the base station and the positioning error of each node are shown in Figures 8(a) and 8(b), respectively. The final positioning result of the node is shown in Figure 9. From the positioning results, it can be seen that the positioning error is relatively large for the node located in the lower left corner of the positioning area, while the positioning error located in the central area is the smallest, because the signal coverage at the positioning center area is strongest, and its positioning error is also the smallest.

The total time consumed by the proposed method to locate nodes in this paper includes the antenna azimuth adjustment time, the beacon frame construction and transmission time, and the node reception of beacon frames and localization calculation time. Therefore, the positioning time also reflects the distance between the node and the base station. This experiment analyzes the relationship between the positioning time and the positioning error of different nodes. The experimental results are shown in Figure 10.

The experimental results show that as the positioning time increases, the maximum positioning error of the node also increases, which indicates that the positioning error of the node far from the base station is greater. Also for a single node, the positioning error decreases as the localization time increases because the number of beacon frames received by the node increases with time, which optimizes the positioning results based on the mean value of the parameters of multiple beacon frames [12–15].

4.2. Positioning Comparison Experiment. The localization area of this experiment is a rectangle of $50 \, \text{m} \times 50 \, \text{m}$, and the signal strength-based localization optimization algorithm proposed in reference [16] is compared in the experiment, which uses a Kalman filter to filter the data collected from the optimal communication range and can easily solve the problem of perturbation of RSSI values. The variable relationship between communication distance and RSSI can be analyzed for more accurate optimization of node positioning. In reference [16], 20 anchor nodes and 100 ordinary nodes were deployed in the localization area, with 20 anchor nodes enabling the positioning of 100 nodes and all sensor nodes having a communication radius of 15 m. In contrast, the method proposed in this paper does not deploy anchor nodes, but only 100 ordinary nodes, and the height of the antenna is 10 m, the angle step unit $\delta\theta$ and $\delta\phi$ both are 4°, and the beam width θ_{bw} is 10°.

In Figure 11, the localization errors of 100 sensor nodes in the localization area are compared under the two methods. From the results, it can be seen that the maximum localization error of the localization method proposed in literature [16] is much higher than that of the localization method proposed in this paper, and the maximum localization error of the method proposed in this paper is less than
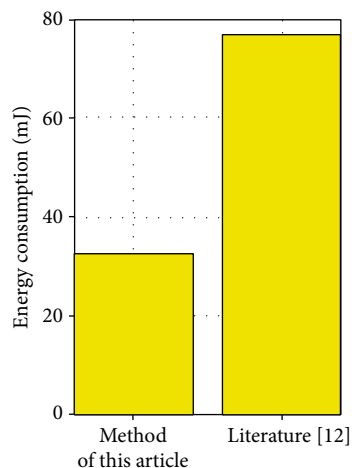
FIGURE 13: The energy consumption contrast.

FIGURE 14: Outdoor Wifi base station.

3 m, while the maximum error of the localization algorithm proposed in [16] is higher than 8 m.

The above experiments were verified 100 times and the results of the cumulative distribution of positioning errors were obtained as shown in Figure 12. The experimental results show that the positioning error of the positioning method proposed in this paper is basically in the range of 0-5 m in the positioning area of 50 m × 50 m, while the positioning error of the positioning method proposed in literature [16] is basically distributed in the range of 0-10 m. CDF denotes Cumulative Distribution Function.

Since the residual energy of sensor nodes is fixed and the residual energy of nodes decreases with the operation, if the energy consumption of the localization algorithm is too high, it is very detrimental to the long-term survival of the sensor network. Therefore, the energy consumption of the localization algorithm is one of the key metrics to measure its performance. This experiment is based on an experimental analysis of the common used energy consumption model (as presented in literature [17, 18]). The model parameters during the experiments are shown in Table 2. The total energy consumption of 100 nodes was compared in the experiment, and the results are shown in Figure 13.

To complete the localization of 100 nodes, the total energy consumed by the method proposed in this paper is about 33.6 mJ, and the total energy consumed by the localization method proposed in literature [16] is about 77.3 mJ. Because the localization method proposed in this paper does not require complex communication with anchor or neighboring nodes and only receives beacon data frames from the base station and is therefore less energy-intensive. In contrast, the localization method proposed in literature [16] requires communication with at least three surrounding anchor nodes and therefore consumes more energy than the method proposed in this paper. The actual experimental setup is deployed as shown in Figure 14. It is an outdoor Wifi Base Station with antenna.

5. Conclusion

As current wireless sensor network localization methods rely on anchor nodes or require complex data interaction to achieve localization, this paper proposes a localization method that does not require anchor nodes. The method uses base station steering antennas and interacts with the nodes to achieve node localization, and the experimental results show that the proposed method achieves good positioning accuracy and is of low energy consumption. In the future, we would further investigate the node localization method when the rotation angle of the steering antenna changes irregularly.

Data Availability

The data used in the study is available by sending an email to wenxiuhe@zjut.edu.cn.

Conflicts of Interest

The authors declare that they have no conflicts of interest.

Acknowledgments

References

[1] J. Yan, R. Qiao, L. Tang, C. Zheng, and B. Fan, "A fuzzy decision based WSN localization algorithm for wise healthcare," *China Communications*, vol. 16, no. 4, pp. 208–218, 2019.

[2] Y. Xiuwu, K. Zhang, Y. Liu, and R. Xiao, "WSN node localization based on social spider optimization and opposition based learning," *Control and Decision*, vol. 36, no. 10, pp. 2459–2466, 2021.

[3] J. Li, X. Peng, L. Tang, and Y. Zhang, "Using positioning priorities for accurate anchor-based node location over wireless sensor networks [C]//2017," in *IEEE 23rd International Conference on Parallel and Distributed Systems*, pp. 791–795, Shenzhen, China, Dec. 2017.

[4] H. Xiong, M. Peng, S. Gong, and Z. du, "A novel hybrid RSS and TOA positioning algorithm for multi-objective cooperative wireless sensor networks," *IEEE Sensors Journal*, vol. 18, no. 22, pp. 9343–9351, 2018.

[5] C. Zhu, Z. Hua, L. Chen, H. Xu, and K. Mao, "Indoor localization based on fingerprint matching in WSN," *Chinese Journal of Sensors and Actuators*, vol. 32, no. 3, pp. 451–457, 2019.

[6] S. Messous, H. Liouane, and N. Liouane, "Improvement of DV-hop localization algorithm for randomly deployed wireless sensor networks," *Telecommunication Systems*, vol. 15, pp. 33–46, 2020.

[7] S. G. Lee and C. Lee, "Developing an improved fingerprint positioning radio map using the K-means clustering algorithm," in *2020 International Conference on Information Networking*, pp. 761–765, Barcelona, Spain, Jan. 2020.

[8] M. Postigo-Málaga, L. P. Figueroa, and J. Chilo, "Low cost outdoors WSN parking system for metropolitan areas based on RSS," in *2019 10th IEEE international conference on intelligent data acquisition and advanced computing systems: technology and applications*, vol. 1, pp. 50–53, Metz, France, Sept. 2019.

[9] V. S. Chandrawanshi, R. K. Tripathi, and R. Pachauri, "An intelligent energy efficient clustering technique for multiple base stations positioning in a wireless sensor network," *Journal of Intelligent & Fuzzy Systems*, vol. 36, no. 3, pp. 2409–2418, 2019.

[10] A. Christy Jeba Malar, M. Deva Priya, J. Sengathir, N. Kiruthiga, R. Anitha, and T. Sangeetha, "An intelligent multi-floor indoor positioning system for cloud-based environment," *International Journal of Computers and Applications*, pp. 1–8, 2019.

[11] A. Courtay, M. Le Gentil, O. Berder, P. Scalart, S. Fontaine, and A. Carer, "Anchor selection algorithm for Mobile indoor positioning using WSN with UWB radio," in *2019 IEEE sensors applications symposium*, pp. 1–5, Sophia Antipolis, France, March 2019.

[12] S. NagaMallik Raj, D. Midhunchakkaravarthy, and D. Bhattacharyya, "Low Energy Utilization with Dynamic Cluster Head (LEU-DCH)—for reducing the energy consumption in wireless sensor networks," in *Machine Intelligence and Soft Computing*, Springer, Singapore, 2021.

[13] R. A. Pagare, S. Kumar, and A. Mishra, "Design and analysis of hybrid optical distribution network for worst-case scenario of E2-class symmetric coexistence 80 Gbps TWDM NG-PON2 architecture for FTTX access networks," *Optik*, vol. 228, p. 166168, 2021.

[14] S. Chaudhary, L. Wuttisittikulkij, M. Saadi et al., "Coherent detection-based photonic radar for autonomous vehicles under diverse weather conditions," *Plos One*, vol. 16, no. 11, article e0260799, 2021.

[15] J. Chen, L. Guo, Y. Shi, Y. Shi, and Y. Ruan, *An edge computing oriented unified cryptographic key management service for financial context*, Wireless Network, 2021.

[16] W. Wang, X. Liu, M. Li, Z. Wang, and C. Wang, "Optimizing node localization in wireless sensor networks based on received signal strength indicator," *IEEE Access*, vol. 7, pp. 73880–73889, 2019.

[17] X. Zhou, X. M. Zhu, L. J. Chen, K. Fang, Y. Lei, and K. Mao, "Design of an energy balance reliable routing protocol based on parking guidance system," *Chinese Journal of Sensors and Actuators*, vol. 9, pp. 1408–1417, 2015.

[18] P. Bakaraniya and S. Mehta, "K-LEACH: an improved LEACH protocol for lifetime improvement in WSN," *International Journal of Engineering Trends and Technology (IJETT)*, vol. 4, no. 5, pp. 1521–1526, 2013.

Research Article

An Improved Genetic Algorithm-Based Traffic Scheduling Model for Airport Terminal Areas

Junhao Liu [ID], Qing Cheng, Yuanji Wang, Changqi Yang, Rui Zhou, Xinping Zhu, Di Yao, Junjie Zhou, Yaqian Du, and Shanshan Yang

School of Air Traffic Management, Civil Aviation Flight University of China, Guanghan Sichuan 618307, China

Correspondence should be addressed to Junhao Liu; junhaoliu@cafuc.edu.cn

This paper takes the airport terminal area as the main research content and combines genetic algorithm with airport terminal area analysis theory to analyze and study the traffic scheduling in the airport terminal area. Based on the study of traditional traffic scheduling techniques and key techniques of genetic algorithms, this paper participates in the actual project of genetic algorithm-based traffic scheduling, analyzes the requirements of the project, focuses on the design and implementation of the traffic scheduling algorithm module in the genetic algorithm-based traffic scheduling system, and conducts further research on the pathfinding by constraints submodule. In this paper, the flight approach and departure sequencing problem and runway allocation problem are the main research objects. The dynamic optimal scheduling model of flight approach and departure is established by considering the interests and demands of airlines and airports, and a new scheduling algorithm is proposed. In this paper, a brief introduction to the airport terminal area is given, and the feasibility of the approach/departure optimal scheduling is introduced from the perspective of airlines with a long-range parallel two-runway airport as the research background. Secondly, through the analysis of the flight approach and departure process and the study of the approach and departure cooperative optimization strategy, a single-runway flight approach and departure traffic scheduling model under the joint sequencing strategy is established with the optimization objective of minimizing the total flight delay time, and the model is solved by using the sliding time window algorithm. Then, based on the single-runway scheduling model, a multirunway multiobjective flight optimal scheduling model is established with the objectives of minimizing total delay time, increasing runway throughput per unit time and fairness of flight delay time allocation, and a dynamic algorithm (STW-GA) combining sliding time window algorithm and dual-structured chromosome genetic algorithm is proposed to solve the model.

1. Introduction

With the rapid development of China's economy, the scale of the civil aviation industry is expanding; although the level of protection of all parties is constantly improving, the huge transport demand still brings many problems of unbalanced and uncoordinated development to the civil aviation industry, the use of airspace structure is becoming increasingly complex and diversified, and simple analysis and rough planning are no longer able to meet the requirements of safety and efficiency [1]. In addition, the root cause of ATC problems in flight delays is unreasonable airspace structure and inadequate overall airspace planning, so more accurate forecasting and long-term planning are fundamen-

tal methods to avoid flight delays, and in the airspace of dense and busy terminal areas of airports, there is a greater need for planning and management to keep up with the times. Therefore, airspace restructuring and operational optimization need to move from rough management based on experience to a refined management model based on scientific analysis, evaluation, and verification. In the State Council's opinion on promoting the development of civil aviation, it is stated that the structure of air routes in busy areas and the airspace structure of airport terminals should be scientifically optimized [2]. In addition, there is a growing demand for new airports in busy terminal areas. In 2020, the total number of civil airports in the layout plan reaches 244, including 97 new airports, and the number of new airports

in busy terminal areas is also increasing [3]. The main influencing factor of air traffic network congestion is the "bottleneck" effect caused by the capacity constraints of airports, terminal areas, and route intersections, and the terminal area, as one of the subsystems of the ATC system, is in a sense the most complex subsystem in terms of operational status. The airspace has a complex route structure, limited airspace resources, flight flow, and control difficulties, which become the bottleneck of the whole airspace efficiency [4]. Airspace planning is an important element in the field of airspace design and management and is an important method to improve airspace operational efficiency and air traffic service quality. The main influencing factor of air traffic network congestion is the "bottleneck" effect caused by the capacity constraints of airports, terminal areas, and route intersections. As one of the subsystems of the air traffic control system, the terminal area is, in a sense, one of the most complex subsystems; this airspace has complex characteristics such as complex route structure, limited airspace resources, and difficulty in-flight flow and control, which has become a bottleneck for improving the efficiency of the entire airspace. The research on how to reasonably plan the airspace of new airports in busy terminal areas is an important means to solve the effective allocation of airspace resources and alleviate the pressure on airspace, which is of great significance to improve the airspace management capacity of terminal areas in China. Therefore, this paper starts from the perspective of terminal area airspace planning, predicts the number of takeoffs and landings of airports in the busy terminal area and the distribution of flight traffic OD in the terminal area, establishes a terminal area route network optimization model based on the layout of waypoints, and ensures that the terminal area airspace can provide safe and efficient services for users.

Traffic scheduling is the problem of optimizing resource allocation for complex data flows in a cloud data center when sharing network resources and is directly related to the network transmission performance of applications with differentiated performance requirements in cloud data centers. Therefore, traffic scheduling has been the focus of industry and academia. To improve the convergence performance of the genetic algorithm, researchers apply various complex network models to the population structure design of the genetic algorithm and analyze how different population structures affect the performance of the genetic algorithm. With the explosive growth of cloud data center tenants and applications, cloud data center applications show significant differentiation in performance requirements. For example, some applications (e.g., online sales, web search, securities trading, and other services) have very small data traffic, typically a few kb to a few hundred kb [5]. These small chunks of data streams are very sensitive to latency during network transmission, and often a very small transmission delay can result in a large loss of revenue. Some other applications (e.g., data analysis, storage backup, virtual machine migration, and other services) generally have very large data traffic. These applications have little requirement for transmission latency, but because their data traffic is generally very large, they need to occupy a large amount of

bandwidth in the cloud data center to achieve network transmission. In practical application, the genetic algorithm does not have high requirements on the model of the optimization problem, and it also has good adaptability to the ambiguity of data when solving. It has been well applied in real life and is an efficient global search. The optimal algorithm has the advantages of strong applicability, strong robustness, and high efficiency. On the other hand, the lack of effective isolation of different application data streams in cloud data centers makes these data streams with differentiated performance requirements must compete for the same network resources frequently, thus posing a great challenge to cloud data center traffic management.

As a typical representative of the search algorithm that simulates the superiority and inferiority in nature, the genetic algorithm is fundamentally similar to a complex system; this system consists of a large number of individuals, and the individuals in the system interact with each other, thus having a large impact on the nature of the system; in other words, the population structure of the genetic algorithm has a significant impact on the transmission of genetic information in the population. The population structure of a genetic algorithm can adjust the propagation of genetic information in the population, thus having a significant impact on the convergence performance of the genetic algorithm [6]. To improve the convergence performance of genetic algorithms, researchers have applied various complex network models to the design of population structures of genetic algorithms and analyzed how different population structures affect the performance of genetic algorithms. The researchers classified these population topologies into two types: stationary and kinematic structures. For genetic algorithms that simulate natural evolutionary processes, the stationary structure does not reflect the changing interactions between individuals in the population, so it can limit the performance improvement of genetic algorithms [7]. The study of the kinematic structure is divided into two main categories: one is to adopt the corresponding adaptive scheme for the genetic algorithm and improve the structure according to the existing network model, and the other is to improve the original network structure according to the individuals in the population. In a sense, the real world can be seen as a relatively complex self-organizing complex network, and if the computational process of genetic algorithms can be designed according to the evolutionary process of self-organizing dynamic networks in the real world, the individuals in genetic algorithms can interact with each other like a biological population in nature. A genetic algorithm is a heuristic algorithm based on the genetic evolution mechanism of the natural population, which is widely used in global optimization search. It is different from the traditional search method. It randomly searches the target space by simulating the biological evolution process in nature. Moreover, the theory of complex networks can open new directions for the study of genetic algorithm performance improvement, so genetic algorithms can be analyzed and designed from the perspective of complex networks. However, few existing studies combine complex networks with genetic algorithm performance improvement, and the study

of genetic algorithm analysis and design based on complex network theory has significant research significance for genetic algorithm performance improvement. Complex network theory has been widely used in virtual communities, transportation systems, disaster spreading, and other fields.

2. Related Works

As an important area connecting the two sides of the airspace, the terminal area airspace has been studied in many developed countries. Mc Conkey firstly planned the airway network from two different perspectives of aircraft flight and control to meet the needs of both airspace users and studied the airway network in the terminal area and transition area by comparing the structure of the airway network under terminal area and normal flight [8]. In 2001, the "National Airspace System Operation Development Plan 2001-2010" was released to solve the problems of route congestion and airport congestion caused by various reasons and proposed measures to improve the security capacity of airport terminal areas by using ground-air data link and regional navigation. In 2007, the FAA found that airspace is another important factor, in addition to runways, limiting the capacity of airports, and explored the effect of increasing or improving air traffic control procedures and redesigning airspace structures on improving airport capacity [9]. Dual Serhan incorporates airline and passenger delay costs into an integrated airport ground and terminal airspace traffic management system, and Stavros Sidiropoulos constructs a framework for dynamic approach and departure routes to a multiairport terminal area, which leads to a significant improvement in the efficiency of the multiairport terminal area system [10]. In 2009, Hui Zhang established a terminal area Voronoi finite element profile model based on flight segments and combined traffic forecasting with route network optimization for sector classification, and proposed a "flight segment" theory for the characteristics of terminal area flight paths. In the same year, Rui Zhou proposed the "flight segment" theory for the characteristics of the terminal area flight path. In the same year, Rui Zhou conducted an in-depth and systematic study on the optimization of terminal airspace structure, proposed a terminal airspace route dynamic management model based on the principle of economic optimality, and established an evaluation system to evaluate the operational capacity and status of the route network. 2014, Li Yinfeng combined the analysis of the factors affecting terminal area capacity, established three types of terminal airspace resource allocation strategies to improve the guarantee capacity of the terminal area, which are runway operation mode adjustment, route structure optimization, and traffic flow optimization, and established a terminal area airspace resource allocation strategy evaluation model. Previous studies on terminal area airspace focused on traffic flow prediction, airport capacity assessment, flight approach and departure sequencing, etc., but less research was conducted on the overall planning of airspace in busy terminal areas.

The early (the early 1990s) traffic scheduling technology used in router-based core networks was Native IP. Native IP changed the path of service traffic by simply adjusting the routing weights/attributes of the interior gateway protocol (IGP) or by issuing access control list (ACL) policies on the router side. The ACL policy was issued at the router side, in order to change the path of service traffic and realize traffic scheduling. Fewer studies related to the aspect of airport scheduling for traffic scheduling algorithms are mostly focused on the study of heuristic algorithms. To minimize the delay cost, Xiaohang Cheng solves the single-runway entry scheduling problem by the essence adaptive genetic algorithm and optimizes the entry sequence of flights and the entry moment. To reduce the total flight delay time and cumulative landing time, a backtracking and swapping-based flight approach sequencing model is proposed [11]. The model effectively utilizes the spare time slots by the backtracking method and then determines the flight exchange rules by the cumulative landing factor and the delay factor. And the optimal values of the backtracking factor and weights are calculated through several simulations [12]. With the research objective of reducing the total flight delay time and increasing the airport capacity, the fusion backtracking algorithm is proposed based on the location-constrained exchange algorithm and the airway flow control model.

The genetic algorithm was first proposed by Professor J. Holland in 1975 in his monograph "Adaptation in Nature and Artificial Systems," which is a class of optimization algorithms that simulate natural selection and meritocracy in nature [13]. Genetic algorithms have no high requirements for the model of optimization problems in real-life applications, they also have good adaptability to the ambiguity of data in solving them, and they are well used in real life as an efficient global optimization-seeking algorithm with the advantages of high applicability, robustness, and efficiency. Well-adapted in real-life applications, it is an efficient global optimization-seeking algorithm with the advantages of high applicability, robustness, and efficiency. In practical applications, the standard genetic algorithm has many defects in maintaining population diversity, convergence accuracy, and convergence speed, which limit the development and application of genetic algorithms. Therefore, researchers have improved genetic algorithms in terms of parameter improvement and optimization, scheme adjustment, hybrid genetic algorithms, and improved neighborhood topology [14]. In terms of improvement and optimization of parameters and adjustment of the scheme, a new improved genetic algorithm is proposed, whose fitness function can change with individual states, while the variation operation is adjusted in the genetic algorithm, and it is experimentally found that the performance of the improved genetic algorithm is significantly improved, which makes the efficiency of solving complex problems significantly improved. To deal with optimization problems with large dimensions, an improved genetic algorithm is proposed. The improved genetic algorithm improves the strategy in selecting the initial population and adopts adaptive processing for the assignment of individuals, uses three individual assignment schemes, and applies the new strategy in selecting the initial population. It is found that the improved genetic algorithm

greatly improves the convergence speed of the algorithm and effectively improves the solution performance of the genetic algorithm. The operation operators of the genetic algorithm were optimally adjusted, the crossover and mutation operations in the genetic algorithm were adaptively processed, while the corresponding formulas were reasonably adjusted, and the elite retention strategy was optimized with a more reasonable and effective scheme. It is found that the improved genetic algorithm greatly reduces the production cost while effectively reducing the optimization time. In the research of combining with other algorithms, the standard genetic algorithm is combined with the particle swarm algorithm, and the improved algorithm carries out special retention for the elite individuals, and the particle swarm algorithm further optimizes the processing of the elite individuals, and the experiments find that the combination of the two algorithms effectively improves the performance of the algorithm. In recent years, with the popularity of the Internet and the rapid development of artificial intelligence algorithms, its application areas are also more and more extensive, in which the aerospace path planning problem can also be solved by artificial intelligence algorithms. A genetic algorithm is a common method for production scheduling problems. In many cases, the mathematical models established for production scheduling problems are difficult to solve accurately. After some simplifications in time, the solution can be solved, and the solution results are too different from the actual because of too much simplification. A genetic algorithm is an effective tool for solving complex scheduling problems. Genetic algorithms are characterized by strong robustness and outstanding global search capability and perform well in performing problem-solving [15]. Intelligent optimal collision avoidance techniques formed using genetic algorithms are used to solve the path planning problems, and the optimal fitness function is obtained by finding the optimal path points. An aircraft motion model is incorporated into the path planning for spaceflight, which can roughly evaluate the aircraft motion under the influence of external conditions.

3. Research on Airport Terminal Area Traffic Scheduling Model Based on Improved Genetic Algorithm

3.1. Improved Genetic Algorithm Design. A genetic algorithm is a heuristic algorithm based on the mechanism of the genetic evolution of the natural population, which is widely used with global optimization search. It differs from traditional search methods by simulating the biological evolution process in nature and performing a stochastic search of the target space. The genetic algorithm simulates the genetic phenomena of selection, crossover, and mutation in the process of natural selection and natural inheritance in Darwinian biological evolution, retains some candidate chromosomes in each iteration, selects the best performing chromosomes from these chromosomes according to certain indicators, uses selection, crossover, and mutation to combine these chromosomes again to produce a new generation

of chromosomes, and repeats until a chromosome is found that meets the target. The core idea is survival of the fittest, i.e., the better solutions are retained and passed on to the next generation, and the worse ones are eliminated [16]. Genetic algorithms provide a general framework for solving optimization problems for complex systems, which does not depend on the specific domain of the problem and is robust to the type of problem, so the method is widely used in various disciplines. For example, in function optimization: for some nonlinear, multimodel, multiobjective function optimization problems, which are difficult to solve by other optimization methods, genetic algorithms do facilitate better results. A genetic algorithm is a common method for production scheduling problems. In many cases, the mathematical model established for production scheduling problems is difficult to solve accurately, and even after some simplification, the solution can be solved too far from the actual result due to too much simplification. A genetic algorithm is an effective tool for solving complex scheduling problems.

3.1.1. Coding. The primary problem of applying a genetic algorithm is coding, which is the conversion of text, numbers, or other objects into a computer-recognizable language according to specified guidelines. The design of coding directly affects the successful operation of the algorithm, as well as the design of crossover operations, mutation operations, selection operations, and the evolutionary efficiency of the algorithm in genetic algorithms. The encoding of the genetic algorithm is to establish the mapping relationship between the genotype space of the expression space domain, as shown in Figure 1. Decoding, on the other hand, is the inverse process of encoding, converting computer language into human-understandable text. The topology management module inputs the topology information into the module, the policy management module also takes the policy conditions as the input of the module, and the traffic scheduling algorithm module selects one or more paths according to the traffic scheduling algorithm after acquiring the input information. The path planned by the traffic scheduling algorithm is the path that conforms to the policy and costs as little as possible. If no path that conforms to the policy is found, suboptimal pathfinding or priority preemption is performed as needed. This module mainly includes submodules of pathfinding according to constraints, multipath pathfinding, and priority preemption.

Through the analysis of the multirunway flight scheduling problem, it is known that the solution of the flight scheduling model is the optimal flight scheduling sequence and the corresponding approach and departure runways of the flights. Therefore, considering this feature of the solution of the flight scheduling model, this paper adopts a dual structure coding method in the coding of chromosomes The first structure is the flight information, which represents the queuing sequence of flights, and the second structure is the runway information, which represents the takeoff and departure runways of corresponding flights. Since the simulation information of the arithmetic example in this paper is based on parallel dual runways, the traditional numerical coding method is used in this paper, with 0 and 1
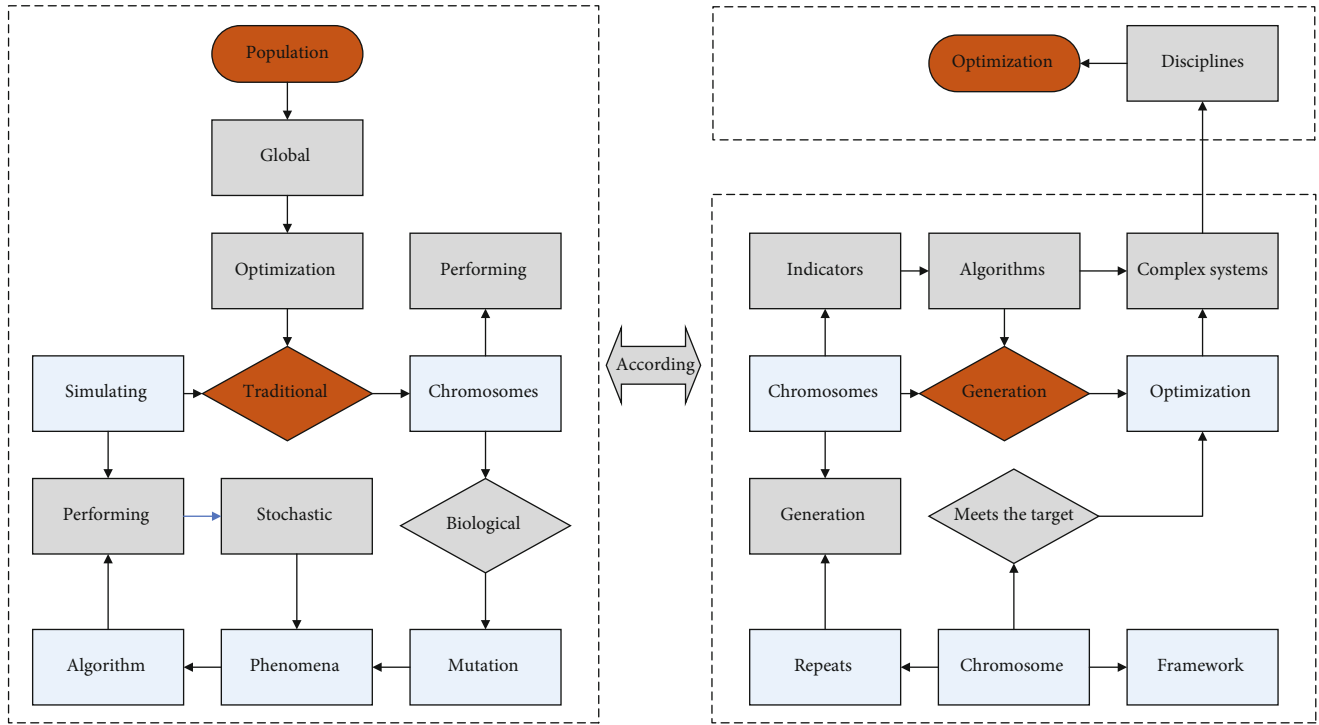
Figure 1: Genetic algorithm coding and decoding.

representing the two runways, respectively. But for the flight sequence chromosome, if the binary encoding is used to encode, it will generate meaningless encoding after the selection, crossover, and mutation operation regrets, which causes encoding mismatch and leads to the algorithm cannot continue to solve. Similarly, the same problem occurs if the original flight sequence number is encoded directly. Therefore, in this paper, GreenStreet codes are used to encode the flight sequence chromosomes in the first layer to ensure that no meaningless chromosomes are generated after the evolutionary operation and to reduce the complexity and difficulty of the algorithm.

3.1.2. Fitness Function. Genetic algorithms are heuristic algorithms, an intuitive or empirically constructed algorithm that does not rely on external information to validate the results during the search but rather calculates the fitness of feasible solutions as an important basis for evaluating the merit of chromosomes by including a fitness function in the algorithm. Also, the magnitude of chromosome fitness is used as an important basis for the probability of chromosomes being selected in the selection operation. Chromosomes with large fitness can be inherited to the next generation with greater probability, and conversely, chromosomes with small fitness lose their competitive advantage and have low selection probability. Limited by the planned, controlled, and fluctuating characteristics of traffic demand, empirical methods can only simply reflect the static mapping relationship between traffic flow parameters under certain operating scenarios and lack of in-depth exploration of the macrodynamic evolution of traffic flow under different congestion levels. The database of its influence mechanism.

Therefore, the correct construction of the fitness function directly affects the convergence result of the genetic algorithm and its convergence speed. And in general, the fitness function can be obtained directly by the transformation of the objective function. If the solution objective is a maximization problem, the fitness function is $Fitness(f(x_1)) = f(x_1)$, and if the solution objective is a minimization problem, the fitness function is $Fitness(f(x_1)) = f(x_1)$. However, since the model constructed in this paper is the objective minimization problem, and the selection operation in this paper is the choice of roulette wheel selection, the probability cannot be negative, so this paper adopts the bounds construction method and takes the inverse of the objective function as the fitness function for solving the minimization problem. And to prevent the denominator from being 0, a constant 1 is added to the denominator. In summary, the fitness function in the genetic algorithm is

$$Fitness(f(x_1)) = \frac{f(x_1)}{\sqrt{f(x_1) - 1}}. \tag{1}$$

3.1.3. Selection. The selection operation involves replicating chromosomes from a contemporary population into the next generation population with probability proportional to fitness. That is, chromosomes with higher fitness are better adapted to their environment and have a greater chance of replication. To make the optimal solution well preserved, this paper performs the selection operation using the best-preserved selection method. The roulette wheel selection method is used to select and preserve the individuals with higher fitness function values in the current population.

Probability of choice

48.9%

32.6%

9.5%

9.1%

Fitness (A)   Fitness (C)
Fitness (B)   Fitness (D)
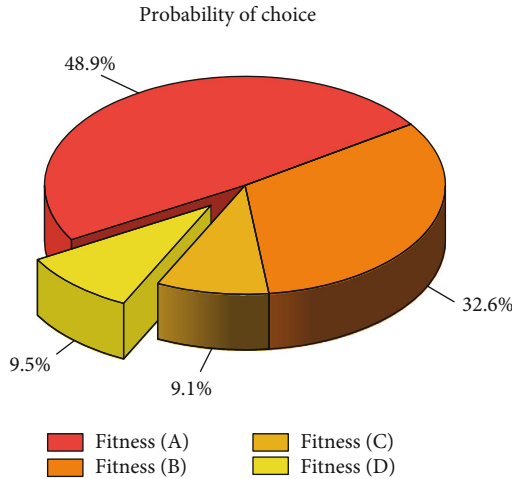
FIGURE 2: Transformation diagram of selection probabilities and fitness values.

The roulette wheel selection method is used to sum the fitness of all chromosomes in the contemporary population, and the chromosomes are transformed into selection probabilities in proportion to their fitness Pc. The principle of the transformation method is shown in Figure 2.

The traditional genetic algorithm encodes all the flight information, which makes the chromosome design complicated and computationally inefficient when the number of flights is large. The problem of coordinated release based on airport priority in the terminal area of multiple airports under an airport is newly added. A dual objective function is established to minimize the total flight delay cost and total delay time, and a multiairport coordinated release model based on airport priority is constructed considering the delay classification, and the multiobjective linear decreasing particle algorithm (LD-MPSO) is used to solve the model. And flight scheduling is a dynamic process, new flights will be added at any time, and the traditional genetic algorithm cannot be changed once the encoding is successful [17]. And the sliding time window algorithm studied in the previous chapter, although it is dynamic, for multirunway scheduling, not only need to assign flight approach and departure sequence and approach and departure time but also need to assign flight approach and departure runway, so the complexity of enumerating and arranging the flights in the time window will be greatly increased. Therefore, this paper combines the genetic algorithm and the sliding time window algorithm, combines the advantages of both, and designs an improved dynamic genetic algorithm. The algorithm steps are as follows.

Step 1. Output the initialization queue with the first w aircraft of the FCFS algorithm as the initial time window

Step 2. Based on the flight information in the time window, a two-layer structured chromosome coding is used to encode and generate the primitive population

Step 3. Calculate the fitness of individuals within the population

Step 4. Selection, crossover, and mutation operations are performed on chromosomes to generate a new generation of populations

Step 5. Determine if the genetic algorithm termination condition is satisfied; if so, continue to Step 6, and if not, skip Step 3

Step 6. Determine whether the time window reaches the right boundary; if it does, the final scheduling result is output, if there are still flights after the window, the optimization window is moved backward by s steps, and the remaining w-s aircraft in the previous window with the newly added s aircraft generates a new window consisting of w aircraft, jumping to Step 2. The flow chart of the algorithm is shown in Figure 3

3.2. Airport Terminal Area Traffic Scheduling Modeling. The strength of the terminal area route network structure affects whether the terminal area airspace can be operated safely and efficiently and whether the cost is reasonable. Waypoints are the connection points of various flight segments in the route network, and their spatial layout is the key to the topological characteristics of the route network [18]. Waypoints are the intersection of multiple flight paths, which can easily cause conflicts when multiple aircraft enter or breakaway, and determine the safety of air operation, and the spatial location of waypoints directly determines the operation cost of the flight path network, so the problem of flight path network optimization usually starts from the study of waypoint layout optimization. The waypoint layout problem is a mathematical problem to determine the optimization objectives, make them meet the established constraints, establish the corresponding optimization model, design a reasonable and effective algorithm to dynamically adjust the spatial geographic coordinates of waypoints, and finally optimize each optimization objective of the waypoint network. Another purpose of designing the double-crossing operator genetic algorithm is to accelerate the convergence speed of the algorithm; through the data statistics, the change curve of the sum of squares of the cost of each flight delay is shown in Figure 4. By analyzing the characteristics of the airway network in the terminal area, the problem of location selection of the new airport and the optimization of the airway network are transformed into the optimization of the waypoint layout, which is abstracted into the network topology structure composed of points and lines. Then a multiobjective optimization model that considers both economy and safety is established, with the constraints of not generating new intersections and selecting in characteristic regions.

Realistic problems can be expressed by the mathematical models developed, but the reality is often so intricate that the actual state cannot be fully reduced. The air-ground traffic network in the terminal area, as a special traffic network system that conveys flight flows, has nodes including airports, waypoints, and handover points. In this paper, as a theoretical study, to simplify the actual problem, reasonable assumptions are made to translate the important features of the research object into the mathematical language to describe it. Therefore, this paper uses the abstraction $G = (A, B, N)$ of the topology of the airway network to represent the airway network in the terminal area of the study. With the rapid development of my country's economy, the scale
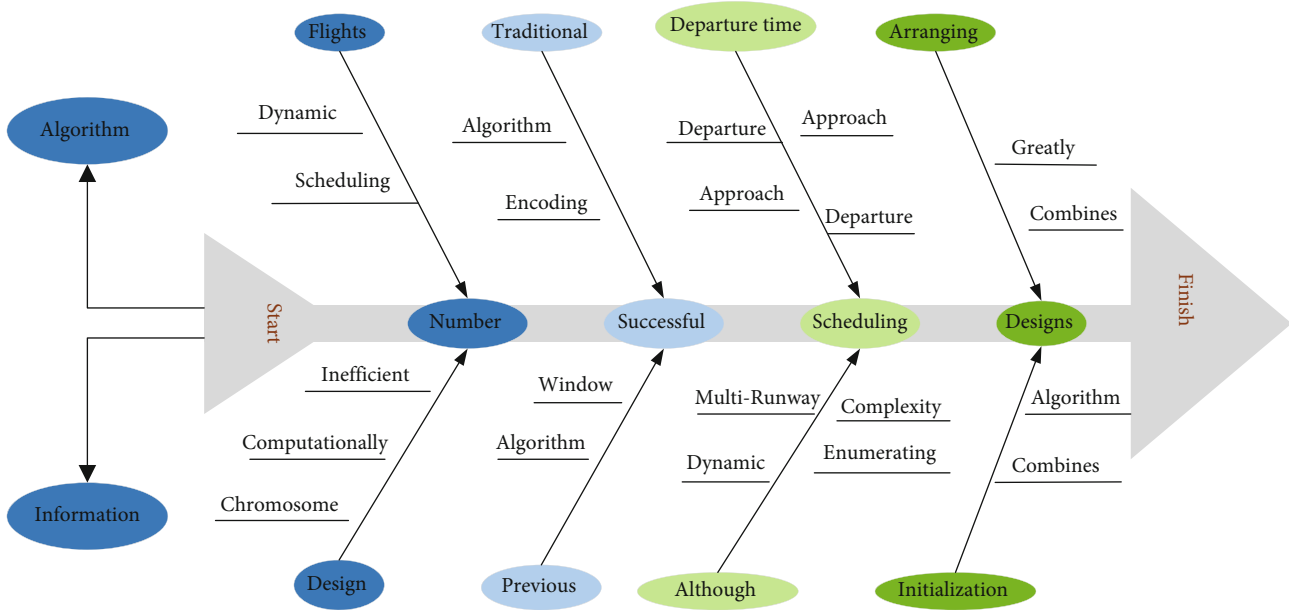
Figure 3: Genetic algorithm flow chart.
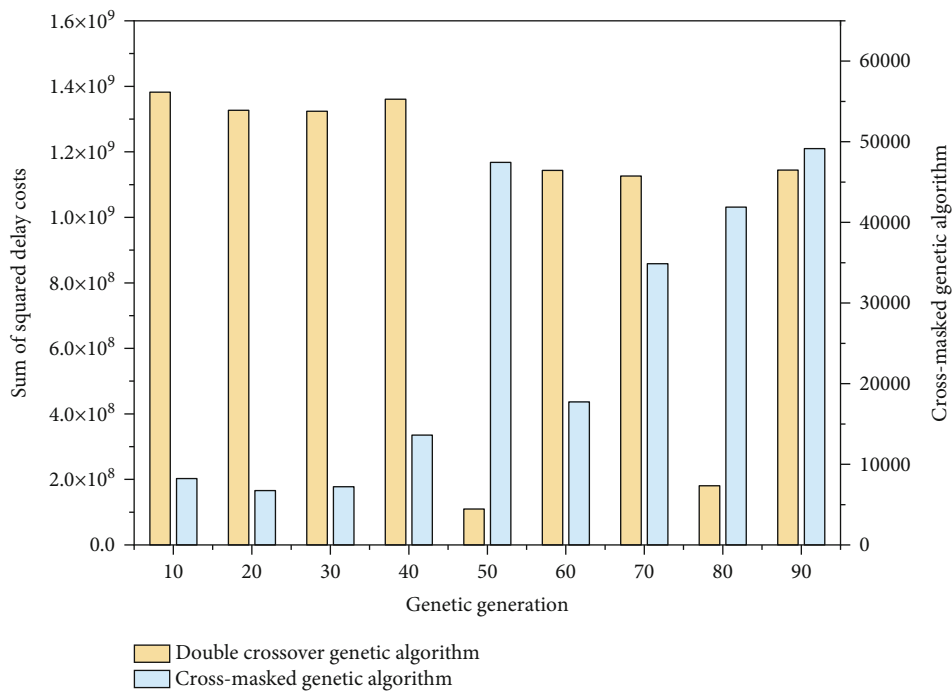
Figure 4: Plot of the sum of squares of the cost of delay.

of the civil aviation industry has continued to expand; although the level of support for all parties has continued to improve, the huge transportation demand still brings many problems of unbalanced and uncoordinated development to the civil aviation industry, and the use of airspace structure is becoming increasingly complex and diversified. With the increasing complexity and diversity, simple analysis and extensive planning can no longer meet the requirements of safety and efficiency. A indicates the set of airport points and boundary points in the terminal airway network that needs to be constructed, and since the boundary points have the same characteristics as the airport points, which both generate and absorb traffic, the boundary points and airport points are regarded as immovable points; B indicates the set of airway points in the terminal area as the optimization B denotes the set of waypoints in the terminal area, as the object of optimization in this paper, has movability; N denotes the set of flight segments in the route network.

$$\min d = \int_{i=1} \int_{j=1} f_{ij} d_{ij} + \int fij. \qquad (2)$$

In the terminal area route network optimization model established in this paper, the following premise assumptions are made: (1) all inbound and outbound flights in the terminal area fly according to the route structure, without considering the flight situation outside the route structure; (2) all aircraft fly at the same speed and uniform speed in the center of the route, without considering the overtaking and changing altitude layer situation, and without considering the type and performance differences; (3) since the research content of this thesis is terminal area route network planning, the scope is the approach and departure route network, so the route network can be seen as two-dimensional to study. (4) Aircraft are treated as an unconditional straight-line flight between node pairs, and the cost of the route network depends on the cost of each route. (5) To avoid the model solution from getting upside down in the planning and not being able to arrive at an optimal solution, each waypoint is allowed to search in a two-dimensional square space centered at its original position, with the range of square sides being 30 km. For the terminal area waypoint layout problem, the model can be described as follows: with the initial route network $G = (A, B, N)$ and the flight traffic distribution of each node known, adjust n waypoint locations in a given region to satisfy the maximum economy and safety of the route network and the best airline mobility and passenger experience. According to the above definition, the objective function of this mathematical model can be expressed as

$$\begin{cases} \min d = \sum_{n=1}^{i} \sum_{n=1}^{i} f_i d_j \\ \\ \min e = x \dfrac{f_1 f_2}{v} \sin \dfrac{1}{2} \\ \\ \min \theta = \int_{j}^{v} \partial_{ij}. \end{cases} \qquad (3)$$

The traffic scheduling algorithm module is the core of the traffic scheduling system and is the focus of this paper. The topology management module inputs the topology information into this module, the policy management module takes the policy conditions as input to this module as well, and the traffic scheduling algorithm module selects one or more paths according to the traffic scheduling algorithm after obtaining the input information. The path planned by the traffic scheduling algorithm is the path that conforms to the policy and costs as little as possible, and if a path that conforms to the policy cannot be found, then suboptimal pathfinding or priority preemption is performed on demand [19]. The main submodules under this module are pathfinding by constraint, multiple pathfinding, and priority preemption. Traffic scheduling is the problem of optimal resource allocation for complex data flows in cloud data centers when sharing network resources and is directly related to the network transmission performance of applications with differentiated performance requirements in cloud data centers. The main algorithm of pathfinding by constraint is a multiconstraint multiobjective pathfinding algorithm, which is a pathfinding algorithm under multiple constraints, where the multiple constraints include delay, jitter, packet loss rate, and bandwidth. The purpose of multiple pathfinding is to find multiple alternative paths between the source nodes to the destination node in the network to meet the user's selection needs for different paths. Priority preemption is to release the link resources occupied by low-priority service applications to plan paths for high-priority service applications when the paths cannot be computed by the multiconstraint multiobjective routing algorithm, and the system allows priority preemption. The overall design of the traffic scheduling algorithm is first described below. The demand for mandatory nodes, mandatory links, disabled nodes, and disabled links occurs in the actual network. The traffic scheduling algorithm first determines whether the required or disabled node links are needed, then performs pathfinding by constraint, and when the path planning by constraint fails and path preemption is allowed, priority preemption is performed to preempt the link resources occupied by the low-priority service flow. Figure 5 shows the overall flow design of the traffic scheduling algorithm. A waypoint is the intersection of multiple routes. When multiple aircraft enter or break free, it is easy to cause conflict, which determines the safety of air operations, and the spatial position of the waypoint directly determines what the route network is. Therefore, the route network optimization problem usually starts from the route network. Start with research on layout optimization.

4. Analysis of Results

4.1. Improved Genetic Algorithm System Analysis. Although the genetic algorithm has strong global searchability, the local searchability of the method is very poor, for the weak local searchability of the genetic algorithm "persistent problem," affecting the accuracy of the final search results of the algorithm, and the reactive optimization problem is nonlinear. In this paper, we introduce a nonlinear programming function, which has a strong local searchability in dealing with the nonlinear problem with constraints to find the minimum value. First, we use a mathematical multivariate function to perform a simple test of the improvement effect of the improved genetic algorithm proposed in this paper, and since $f(x)$ is a multivariate function in mathematics, we can calculate the minimum value of the also function as 2. Taking $f(x)$ as the objective function, we use the simple genetic algorithm with the improved genetic algorithm proposed in this paper to find the minimum value of this function as follows.

$$f(x_i) = \frac{\sin x_1 \sin x_2 \sin x_3 \sin x_4}{\sin 5x_1 \sin 5x_2 \sin 5x_3 \sin 5x_4}. \qquad (4)$$

The process of the improved genetic algorithm is somewhat different from that of the simple genetic algorithm. Its

FIGURE 5: Flow scheduling algorithm overall flow design diagram.

basic process first requires calculating the initial trend by PQ decomposition method, encoding the problem variables using a hybrid approach, and then calculating the fitness value of each individual in the population and secondly using the improved genetic algorithm to perform genetic operations to generate the new generation of individuals, in which the minion function is used to perform a nonlinear search for the optimum whenever the number of genetic generations is an integer multiple of 10 until the termination condition is satisfied to stop the genetic iteration process and output the optimal solution at this time as the global optimal solution. The genetic algorithm iteration diagram is shown in Figure 6.

The empirical traffic flow basic diagram effectively portrays the correlations of traffic flow parameters under real traffic demand and the characteristics of network supply and demand dynamics in the terminal area. However, limited by the planned, controlled, and fluctuating characteristics of traffic demand, the empirical method can only simply reflect the static mapping relationships among traffic flow parameters under certain operation scenarios and lacks the data basis to deeply explore the macroscopic dynamic evolution of traffic flow and its influence mechanism under different congestion levels. Given this, this section relies on the constructed traffic flow simulation platform in the terminal area and adopts the manual adjustment of parameters to reveal the spatial and temporal characteristics of the approach and departure traffic flow and its evolution law, analyze the sensitivity of the traffic flow phase threshold to the traffic flow operational parameters, and provide a theoretical basis for the design of the approach and departure air-ground integrated real-time control method. Under the simulation parameter environment, the traffic flow ratio of each approach and departure point is kept constant, and the traffic scenarios under the independent operation of the approach and departure field are designed in incremen-

tal steps of 0.1 vehicles/minute, and the duration of each scenario is 8 hours of continuous service request [20]. Based on the constructed CTM platform, we simulate the evolutionary trajectory of the macroscopic basic diagram of inbound/departure traffic flow under different scenarios, to reveal the characteristic patterns of traffic flow congestion evolution in the terminal area. For the genetic algorithm that simulates the natural evolution process, the static state structure cannot reflect the changing interaction relationship between the individuals in the population, so it will limit the performance improvement of the genetic algorithm. The research on the kinematic structure is mainly divided into two categories: one is to use the corresponding adaptive scheme for genetic algorithm and improve the structure according to the existing network model and the other is to use the original network structure according to the situation of the individuals in the population make improvements. According to the general transportation flow congestion evolution characteristics, combined with the critical traffic demand and demand change trend, three states of traffic congestion evolution in the terminal area are classified: (a) formation state: traffic demand continues to grow and is smaller than the critical demand, network throughput grows linearly with traffic demand, and traffic flow has a congestion formation trend but operates stably; (b) accumulation state: traffic demand reaches and exceeds its critical, network throughput tends to; (b) cumulative state: traffic demand reaches and exceeds its threshold, network throughput tends to saturate and decreases to some extent, and traffic flow congestion keeps increasing; and (c) dissipation state: traffic demand in the airspace gradually decreases, and traffic flow shows slow or rapid dissipation depending on the degree of network congestion. To deal with the large dimension of the optimization problem, an improved genetic algorithm is proposed. The improved genetic algorithm improves the strategy when selecting the initial population and adopts

FIGURE 6: Genetic algorithm iteration diagram.

adaptive processing for the allocation of individuals. Three individual allocation schemes are used, and a new strategy is applied when selecting the initial population.

$$C(t_1) = \min \int_{me} \int_{f_m} \int_t cf_{\sin}\left(t_{dc}^f - t_{ec}^f\right). \tag{5}$$

The FCFS algorithm, traditional genetic algorithm, segmented genetic algorithm, and STW-GA algorithm are compiled using PYTHON3 and solved by simulation with the algorithm examples. The results demonstrate that both the traditional genetic algorithm and STW-GA algorithm can significantly reduce the total delay time and increase the runway throughput efficiency compared with the FCFS algorithm, and the delay time is more equitably distributed. The STW-GA algorithm is also dynamic, feasible, and efficient. Traffic scheduling is a very important issue in cloud data centers and has been a challenge. The current traffic scheduling schemes in cloud data centers go to two extremes. Information agnostic schemes have a wide range of applicability and good deployability; however, they have very limited effectiveness in optimizing the performance of network transport. While information-aware traffic scheduling solutions achieve excellent network performance, they severely neglect the scope of the solution itself, and most information-aware traffic scheduling solutions require custom switches, making them not only very limited in scope but also difficult to deploy in current cloud data centers.

4.2. Airport Terminal Area Traffic Scheduling Implementation. By analyzing the characteristics of the airway network in the terminal area, the problem of siting new airports with airway network optimization is transformed into the problem of airway point layout optimization, which is abstracted into a network topology

composed of points and lines [21]. Then a multiobjective optimization model that considers economy and safety is established, with the constraints of not generating new intersections and selecting in the characteristic area. Afterward, an example analysis is conducted to process the airspace data within the terminal area of Shanghai, traffic data preprocessing, and position transformation coordination, and the differential evolutionary algorithm solution procedure is written using the MATLAB software, resulting in 19 waypoint locations being optimized, which proves the practical significance and feasibility of considering the location of the new airport site from the perspective of optimal route network in the terminal area (see Figure 7 for the clustering effect).

Based on the complex dynamic characteristics of traffic flow in the terminal area, the air-ground traffic flow congestion management solution for tactical operation is built from the perspectives of both traffic flow and controllers, covering "volume"-coordinated control of approach and departure launch rates, "sequence"-multisector approach traffic flow rate cooperative control, and "trace"-sector traffic flow horizontal trajectory management under multiple constraints, three major space-time overlapping functional modules, respectively, using air-ground meta cell network microsimulation platform, and terminal area airspace. The effectiveness of the solution is verified by using three methods: a macroscopic simulation platform for air-ground meta cell networks, a microscopic fast simulation platform for terminal area airspace, and a "human-in-the-loop" real-time simulation experiment. Genetic algorithm provides a general framework for solving complex system optimization problems; it does not depend on the specific field of the problem and has strong robustness to the types of problems, so the method is widely used in various disciplines. At the stage when the trajectory-based operation has not yet been carried
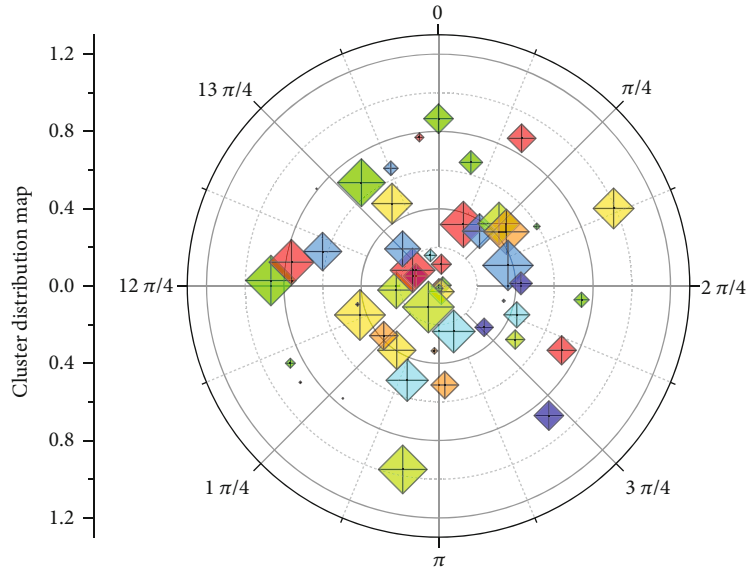
FIGURE 7: Clustering effect.

out, this solution can enrich and enhance the tactical/real-time level of the terminal area congestion mitigation methods and means for the external uncertain environment, thus improving the control capability and the safety and efficiency of traffic flow operation under congestion. It should be noted that the sector traffic flow "sequencing" control in this chapter only considers the first-come-first-served strategy based on the sector flow rate, and further attempts can be made to integrate with mature sequencing methods to generate more optimal and reasonable arrival times for sector exit point control. At the same time, the horizontal trajectory system can be extended to the network version and fused with the "volume" and "sequence" control modules to form a complete terminal area congestion decongestion system, and the joint operation experiment of multiple sectors in the terminal area can be designed for comprehensive verification. In addition, the horizontal trajectory management tool based on the inter-aircraft concept provides a strong reference for the four-dimensional trajectory planning in real-time under certain performance optimization objectives (fairness, economy, and efficiency) to support the development of performance-based higher-order air traffic management.

$$U_j\left(x_i, x_j\right) = \max_{ij} U\left(x_{i-j}, x_{i+j}\right). \tag{6}$$

For the problem of cooperative release based on airport priority in the terminal area of multiple airports under the addition of new airports, a dual objective function is established to minimize the total delay cost and total delay time of flights, a cooperative release model based on airport priority under consideration of delay classification is constructed, a multiobjective linear decreasing particle algorithm (LD-MPSO) is used to solve the model, and then an arithmetic example under the addition of new airports in the terminal area is. The simulation analysis is carried out to introduce

Before optimization
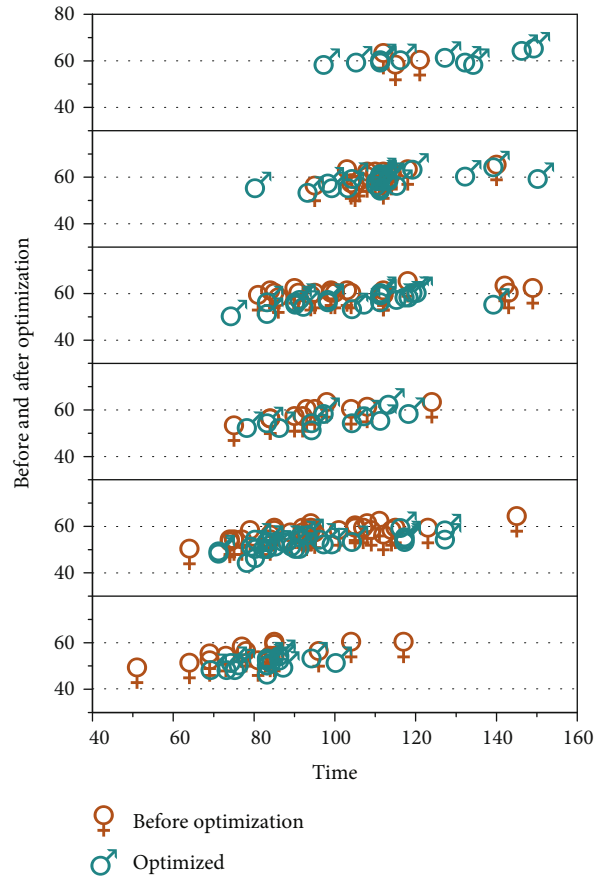
Optimized

FIGURE 8: Comparison of route network optimization results.

the operation of three airports in the terminal area, set the airport priority, and finally find the multiairport cooperative release strategy based on minimum delay time, based on minimum delay cost and considering both delay time and delay cost, respectively, and verify the validity of the model

through analysis and comparison, so as to provide a theoretical method and scientific basis for constructing a unified cooperative release mechanism in the multiairport terminal area. The comparison of the route network optimization results is shown in Figure 8.

5. Conclusion

Along with the rapid development of China's economy, the development of the civil aviation industry has also ushered in unprecedented opportunities and challenges. On the one hand, the number of flights has been increasing. On the one hand, the number of flights is increasing, the number of airports is increasing, and the civil aviation industry is thriving. On the other hand, however, airline congestion is becoming increasingly serious, and if not properly addressed, it will certainly hinder the progress of the aviation industry. The problem of flight sequencing in the terminal area has always been a key and difficult issue for research in the field of aviation control; especially in this era of rapid economic development, the phenomenon of congestion in the terminal area is extremely serious. With the development of the global air transport industry and the increasing number of aircraft, the flight sequencing problem has been categorized as an NP-hard problem. Genetic algorithms have advantages such as high global search capability and potential concurrency in solving such problems but also possess some disadvantages. By reading and studying the literature related to solving flight sequencing problems with genetic algorithms, it is found that simply setting the sequencing goal to the shortest total flight landing time is an oversimplified goal and the practicality of the sequencing results is not high. For the disadvantages of genetic algorithms such as instability and prematureness, an adaptive genetic algorithm is used to deal with it. At the same time, the convergence speed of the algorithm can be improved. The implementation of the terminal area flight scheduling system is carried out through the platform support provided by the national ATC scenario simulation system, and the improved sorting algorithm is applied to it. Through the analysis and comparison of the sorting results, the algorithm improvement is proved to be effective and achieves the research objectives.

Data Availability

The data used to support the findings of this study are available from the corresponding author upon request.

Conflicts of Interest

The authors declare that they have no known competing financial interests or personal relationships that could have appeared to influence the work reported in this paper.

Acknowledgments

References

[1] S. Mokhtarimousavi, D. Talebi, and H. Asgari, "A non-dominated sorting genetic algorithm approach for optimization of multi-objective airport gate assignment problem," *Transportation Research Record*, vol. 2672, no. 23, pp. 59–70, 2018.

[2] J. Tang, Y. Yang, W. Hao, F. Liu, and Y. Wang, "A data-driven timetable optimization of urban bus line based on multi-objective genetic algorithm," *IEEE Transactions on Intelligent Transportation Systems*, vol. 22, no. 4, pp. 2417–2429, 2021.

[3] J. Shouwen, L. Di, C. Zhengrong, and G. Dong, "Integrated scheduling in automated container terminals considering agv conflict-free routing," *Transportation Letters*, vol. 13, no. 7, pp. 501–513, 2021.

[4] N. Ding, K. Prasad, and T. T. Lie, "Design of a hybrid energy management system using designed rule-based control strategy and genetic algorithm for the series-parallel plug-in hybrid electric vehicle," *International Journal of Energy Research*, vol. 45, no. 2, pp. 1627–1644, 2021.

[5] N. Wichapa and P. Khokhajaikiat, "Solving a multi-objective location routing problem for infectious waste disposal using hybrid goal programming and hybrid genetic algorithm," *International Journal of Industrial Engineering Computations*, vol. 9, no. 1, pp. 75–98, 2018.

[6] R. K. Cecen, C. Cetek, and O. Kaya, "Aircraft sequencing and scheduling in TMAs under wind direction uncertainties," *The Aeronautical Journal*, vol. 124, no. 1282, pp. 1896–1912, 2020.

[7] Y. Tian, W. Hu, B. Du, S. Hu, C. Nie, and C. Zhang, "IQGA: a route selection method based on quantum genetic algorithm-toward urban traffic management under big data environment," *World Wide Web*, vol. 22, no. 5, pp. 2129–2151, 2019.

[8] Y. Sun, F. Lin, and H. Xu, "Multi-objective optimization of resource scheduling in Fog computing using an improved NSGA-II," *Wireless Personal Communications*, vol. 102, no. 2, pp. 1369–1385, 2018.

[9] W. Xu, P. Zhao, and L. Ning, "Last train delay management in urban rail transit network: bi-objective MIP model and genetic algorithm," *KSCE Journal of Civil Engineering*, vol. 22, no. 4, pp. 1436–1445, 2018.

[10] N. Li, G. Chen, M. Ng, W. K. Talley, and Z. Jin, "Optimized appointment scheduling for export container deliveries at marine terminals," *Maritime Policy & Management*, vol. 47, no. 4, pp. 456–478, 2020.

[11] Y. Liang and L. Wang, "Applying genetic algorithm and ant colony optimization algorithm into marine investigation path planning model," *Soft Computing*, vol. 24, no. 11, pp. 8199–8210, 2020.

[12] W. Osamy, A. A. El-Sawy, and A. M. Khedr, "Effective TDMA scheduling for tree-based data collection using genetic algorithm in wireless sensor networks," *Peer-to-Peer Networking and Applications*, vol. 13, no. 3, pp. 796–815, 2020.

[13] E. K. Elsayed, A. H. Omar, and K. E. A. Elsayed, "Smart solution for STSP semantic traveling salesman problem via hybrid ant colony system with genetic algorithm," *International*

Journal of Intelligent Engineering and Systems, vol. 13, no. 5, pp. 476–489, 2020.

[14] K. Gao, Y. Zhang, Y. Zhang, R. Su, and P. N. Suganthan, "Meta-heuristics for bi-objective urban traffic light scheduling problems," *IEEE Transactions on Intelligent Transportation Systems*, vol. 20, no. 7, pp. 2618–2629, 2019.

[15] F. Sabouhi, A. Bozorgi-Amiri, M. Moshref-Javadi, and M. Heydari, "An integrated routing and scheduling model for evacuation and commodity distribution in large-scale disaster relief operations: a case study," *Annals of Operations Research*, vol. 283, no. 1-2, pp. 643–677, 2019.

[16] M. Hafidi, M. Benaddy, and S. Krit, "Optimization and automation of air traffic control systems: an overview," *International Journal of Engineering, Science and Mathematics*, vol. 7, no. 3, pp. 104–116, 2018.

[17] R. Adhao and V. Pachghare, "Feature selection using principal component analysis and genetic algorithm," *Journal of Discrete Mathematical Sciences and Cryptography*, vol. 23, no. 2, pp. 595–602, 2020.

[18] L. Zhou, Y. Lin, X. Wang, and F. Zhou, "Model and algorithm for bilevel multisized terminal location-routing problem for the last mile delivery," *International Transactions in Operational Research*, vol. 26, no. 1, pp. 131–156, 2019.

[19] A. Dobrkovic, M. E. Iacob, and J. van Hillegersberg, "Maritime pattern extraction and route reconstruction from incomplete AIS data," *International journal of Data science and Analytics*, vol. 5, no. 2-3, pp. 111–136, 2018.

[20] Y. Song, F. Wang, and X. Chen, "An improved genetic algorithm for numerical function optimization," *Applied Intelligence*, vol. 49, no. 5, pp. 1880–1902, 2019.

[21] S. Harizan and P. Kuila, "Coverage and connectivity aware energy efficient scheduling in target based wireless sensor networks: an improved genetic algorithm based approach," *Wireless Networks*, vol. 25, no. 4, pp. 1995–2011, 2019.

Hindawi

Research Article

DeepNet-Based 3D Visual Servoing Robotic Manipulation

Abdulrahman Al-Shanoon, Yanjun Wang, and Haoxiang Lang (ID)

Department of Automotive and Mechatronics Engineering, Ontario Tech University, Oshawa, ON, Canada L1G 0C5

Correspondence should be addressed to Haoxiang Lang; haoxiang.lang@ontariotechu.ca

The fourth industrial revolution (industry 4.0) demands high-autonomy and intelligence robotic manipulators. The goal is to accomplish autonomous manipulation tasks without human interventions. However, visual pose estimation of target object in 3D space is one of the critical challenges for robot-object interaction. Incorporating the estimated pose into an autonomous manipulation control scheme is another challenge. In this paper, a deep-ConvNet algorithm is developed for object pose estimation. Then, it is integrated into a 3D visual servoing to achieve a long-range mobile manipulation task using a single camera setup. The proposed system integrates (1) deep-ConvNet training using only synthetic single images, (2) 6DOF object pose estimation as sensing feedback, and (3) autonomous long-range mobile manipulation control. The developed system consists of two main steps. First, a perception network trains on synthetic datasets and then efficiently generalizes to real-life environment without postrefinements. Second, the execution step takes the estimated pose to generate continuous translational and orientational joint velocities. The proposed system has been experimentally verified and discussed using the *Husky* mobile base and 6DOF *UR5* manipulator. Experimental findings from simulations and real-world settings showed the efficiency of using synthetic datasets in mobile manipulation task.

1. Introduction

The use of autonomous mobile manipulators (AMM) has grown in many industries with developments enabling these systems to transport, organize, and process various assets. The two main industries commonly utilize this technology are manufacturing facilities and courier services that maintain a large inventory and benefit from efficient robots. To evolve the performance in autonomy and versatility, applied robots make use of several sensing technologies and control algorithms. Two key steps are typically required to carry out autonomous mobile manipulation tasks: firstly, perception step based on sensor-fusion methods which are used to estimate objects and perceive surroundings and secondly, sensing-based robotic motion control technique. This sensory network, however, leads to complex and expensive robotic systems [1, 2].

Recent studies have aimed to use only vision sensors to perceive the robot's environment and gain adequate information about target objects [3]. However, preparation of training datasets requires effort and skills. As well as deep convolutional network training is computationally expensive and time-consuming [4]. Unlike 2D object detection, labeling 3D objects is a difficult task that requires a certain level of expertise. Although the use of synthetic datasets in the training of deep neural networks appeared and was discussed, it requires an endless supply of valuable prelabeled training datasets that are produced in a responsible manner [5]. Studies in [6] trained on synthetic and real-world dataset collections, including fine-tuning efforts. As a result, real-world applications of these methods are limited to structured backgrounds.

Another set of visual perception studies [7–9] requires complex vision-based setup to obtain the pose information of target objects. A stereo vision algorithm was proposed and tested in [3], using point cloud data from multiple stereo systems and utilizing iterative closest points. Vision-based mobile manipulator control was attempted in [10] using evaluation policy and requiring off-line training step. Minniti et al. in [11] addressed the whole-body control of

mobile manipulator without considering tracking a target object. Much of the latest studies [12] developed a mobile manipulation system that included kinematic model where a path planner, however, is still required.

Nevertheless, none of the prior works has demonstrated a complete and continuous framework, for achieving 3D visual servoing (VS) in mobile manipulator, based on synthetic-trained deep neural network. A novel long-range mobile manipulation system is proposed and verified in this paper. This combines a visual perception network with a VS technique for controlling robot motion. The system presents an end-to-end framework of deep net-based 3D VS for sophisticated robotic manipulation task. The perception network constantly estimates the full pose of target object. It is worthwhile to mention that perception network entirely trains on synthetic (only RGB images) datasets and then successfully generalizes to real-world experiments without postprocessing. To provide autonomous manipulation task, outputs of perception network are directly fed to the VS control scheme.

The proposed system was successfully implemented in the simulation environment as well as in real-world settings using the 6 degrees of freedom (DOF) manipulator arm mounted on 2DOF differential drive mobile base. The use of synthetic datasets was applied in the context of 6DOF object pose estimation from a single image and executed robustly in 3D continuous AMM task. The findings have shown the physical capabilities of generalization to novel environments for the handling of light conditions and occlusion variations.

The remainder of the paper is organized as follows: Section 2 reviews the related recent works. Section 3 illustrates the modeling of the perception network for object detection and pose estimation, manipulator, and visual servoing model development. Section 4 shows experimentation results with discussions. Lastly, the conclusions are set out in Section 5.

2. Related Work

This section briefly highlights the recent methods of detecting and estimating object's pose for manipulation applications. In the meantime, the control techniques of mobile manipulators are reviewed.

2.1. Target Pose Estimation for Visual Servoing Task. For robots to work effectively in unpredictable surroundings, they must understand the environment and possess adequate information on target objects, such as object pose information in the real world. Several studies use fiducial marker as a reference point for location of target objects in workspace. Additional research applied conventional computer vision approaches to determine the location of the target, for example, robot-object interaction tasks and model-based and feature-based methods. However, many inconveniences are associated with such methods such as limited background structure and poor performance with variations in lights and occlusion and require highly textured objects [13].

Robotic-object interaction task was conducted using convolution neural network (CNN). Recent studies were documented by Tekin et al. on single-shot network [9] and other networks such as BB8 [8] and SSD-6D [7]. Other works showed decent results and concentrated on problems like occlusions and different lighting conditions. The primary issue of training data, however, is how to generate an effective dataset. That presents sufficient variations for the deep net to learn from a wide range of lighting and pose conditions. Current labeling software like LabelFusion [14] has useful functionality for 3D object labelling. However, as far as we know, there is no simple and effective tool that helps to generate real-life training datasets, which can be used for 6DOF object pose estimation that is properly applied in mobile manipulation applications. Due to this difficulty, much of the existing studies presented systems for training deep network based on synthetic datasets [15, 16]. Finetuning efforts, however, are usually required to adjust the predictions in real-life settings and eliminate a problem known as reality gap. A recent solution was reported in [17], in which synthetic data is domain-randomized in nonrealistic manner. Training datasets include varieties of photorealistic and nonphotorealistic 3D backgrounds. This technique reinforces the deep net's understanding and prepares it to deal with real-world scenarios. In this paper, our perception network trains on only synthetic dataset that was proved in [5] as the state-of-the-art, which also covers adequate possibilities of various poses in different environments, for instance, excessive lighting or occlusions.

2.2. Mobile Manipulator Control. The configuration of the mobile manipulator has advantage of mobility achieved by the mobile base and dexterity executed by the manipulator. This type of robot is more flexible for manufacturing than any other traditional approach such as stationary manipulators or limited automatic guided vehicles (AGV). Implementing visual servoing control scheme into long-range manipulation could be challenging when the robot continuously operates in 3D space based on only visual features. In pose-based visual servoing (PBVS) control techniques, the measurement of the target is happening by utilizing the vision feedback signal that controls the movement of robot until the visual error becomes zero. Researchers in [18] used a hybrid control scheme that used the strengths of image-based and pose-based VS methods for aerial manipulation. The polar and Cartesian parameters of a target object were used in conjunction with a Jacobian equation to compute the camera pose relative to the target object. This hybrid method also creates an effective system for a manipulator by resolving the rotational and translational issues during object tracking [19]. The mobile manipulator configuration typically creates redundant joints, which may inhibit its functionality. Several published studies have established the generic kinematic modeling of mobile manipulator configuration. Researchers in [20] proposed metaheuristic algorithms to enhance the kinematic solutions of mobile manipulator designs. A different configuration for a mobile manipulator system was introduced in [21]. The mobile base has two types of wheels, including directional and fixed. The

system was tested in simulation environments but still lacked the guided vision-based method. The controller law in [22] used fuzzy logic to present the path planning of a mobile manipulator using vision-tracking system. However, soft computing concepts might propose approximation results, which may provide less accurate output. In [23], a multicamera VS system architecture was modeled and presented to control a robotic system where a target object is covered by multiple views. The controller could make different decisions since the pose estimation system was processed based on two perspectives. However, the computational level required longer processing times in addition to the limited applicable purposes.

The reviewed literature documented studies on mobile robots, while other publications focused on stationary robotic manipulators. However, combining the control techniques of mobile platforms and manipulators, both work based on deep nets, which is the challenge for new technologies. This work is, therefore, aimed at developing and testing a complete 3D visual servoing system that operates based on the collected feedback from a single camera. This paper focuses on an alternative solution that jointly uses DeepNet and PBVS to control an AMM system. This type of control scheme requires the pose parameters (related to a target object) that define the AMM robot's final pose. The underlying idea is how to control the pose of the mobile manipulator robot with respect to the detected object by using visual features synthetically trained.

3. Full System Model Development

The proposed system architecture consists of three interconnected phases. First, a deep-ConvNet predicts 2D objects and produces 2D belief maps using a single RGB image. Second, a pose estimation algorithm utilizes the belief maps to recover translational and rotational pose of a target object. Finally, the execution step achieves the desired pose between the end-effector and the target object, by employing the estimated target's pose and visual servoing control law. As the intention is to achieve 3D VS synthetically trained for the mobile manipulation system, we trained our system based on YCB images [24]. Figure 1 demonstrates the entire system architecture; the deep-ConvNet constantly detects and estimates the pose of the current object. The generated pose error stimulates the control law to send joint velocities and reduce the error by achieving a robot pose relative to the target object. The modeling of the system is illustrated in this section, which includes perception network and training, mobile manipulator robot kinematics, and the designing of VS control law based on the principle of Lyapunov.

3.1. Perception Network and Training Protocol. There are two main steps in the perception network: a deep-ConvNet step and a pose estimation step. Figure 2 depicts the deep-ConvNet architecture that trains directly on RGB image ($w \times h \times 3$), to predict the 2D key points of target object in the image. Transform-learning (of the first ten layers) is utilized as a feature extraction training step using VGG-19 model [25], pretrained on ImageNet [26]. Deep-

ConvNet contains multiple stages of convolutional neural network that is preceded by the feature extraction step. The input to each stage involves image feature map of transform-learning and belief maps of the prior stage. Each stage of deep-ConvNet generates 2D belief maps of a target object.

Feature dimensions are minimized from 512 to 128 by using two 3×3 convolutional neural layers. The feature map dimension-128 is the input to the first stage that contains three layers of $50 \times 50 \times 128$ and one layer of $50 \times 50 \times 512$. This stage produces belief map ($50 \times 50 \times 9$) and vector field ($50 \times 50 \times 16$) that both are fed to the next stage, in addition to the feature map ($50 \times 50 \times 128$). Similarly, the remaining stages (from 2 to 6) should have the same structure as the first stage. But the receiving dimension input ($128 + 9 + 16 = 153$) is different than a first stage. It is the output of the image feature map, as well as the belief map and vector field of the immediately preceding stage. In the remaining training stages, there are six layers of $50 \times 50 \times 128$ which provide belief map and vector field. The final stage produces nine belief maps. Each one represents a vertex which will be at the end 8 projected vertices for 3D bounding box and one vertex for the centroid. To detect the object's centroid, the network always seeks for local peaks from the belief maps. It uses the greedy algorithm that links the projected vertices to the indicated centroids.

Next, the object's projected vertices of the 3D bounding box are utilized by Perspective-n-Point (PnP) algorithm [27], similar to [9]. This is to retrieve the 6DOF pose of target object, as shown in Figure 3. In order to recover the target pose, the PnP process requires at least four vertices. The 2D object vertices output from belief maps are followed by PnP iterative approach to form 3D bounding box. To infer the translation and orientation of a target object relative to the camera frame, intrinsic camera parameters and object dimensions are required. The purpose of PnP problem is to estimate the translation and orientation of the calibrated camera from the known 3D points to the corresponding 2D image projections. This method helps to find the object pose from 3D-2D correspondence point. This is based on the Levenberg-Marquardt optimization approach [28]; proper object pose should be found by minimizing the reprojection error (RE). RE is the sum of squared distances between the observed 2D projection image points and projected 3D object points, as shown below.

$$x^2(m, b) = \Delta y_1^2 + \Delta y_2^2 + \Delta y_3^2 + \cdots, \tag{1}$$

where $x^2(m, b)$ is the error and Δy_n^2 is the difference (between observed key point and object point) for n point.

The inputs of PnP are the intrinsic camera parameters, object dimensions, and 2D observed points. The output retrieves the translational and rotational vectors of the 3D object into 2D image plane. We have three coordinate systems, namely, world, camera, and image plane coordinates. The 3D point $[x_i^w \quad y_i^w \quad z_i^w]^T$ is projected into the image plane m_i for $[u_i \quad v_i]^T$. The perspective transformation for
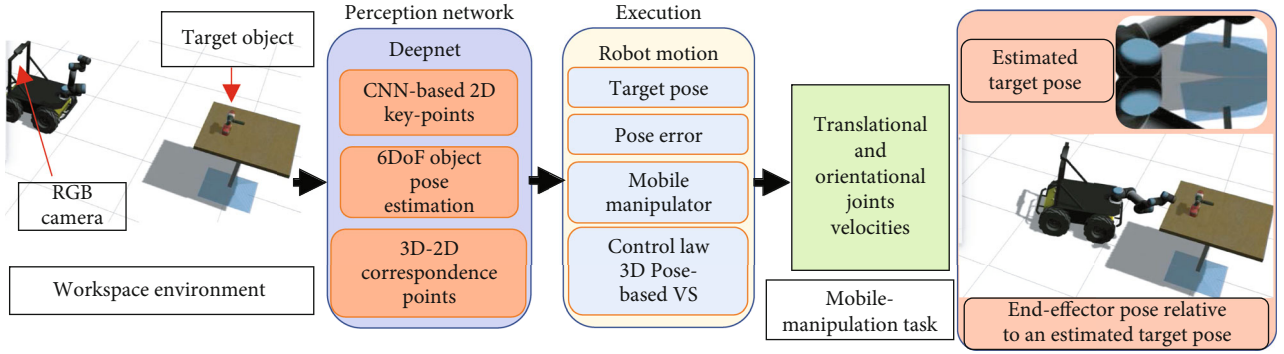
FIGURE 1: Overall system architecture.
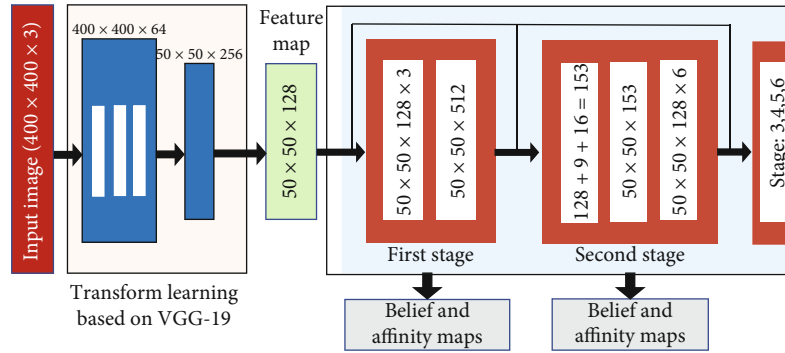
FIGURE 2: Deep-ConvNet architecture of the perception network.
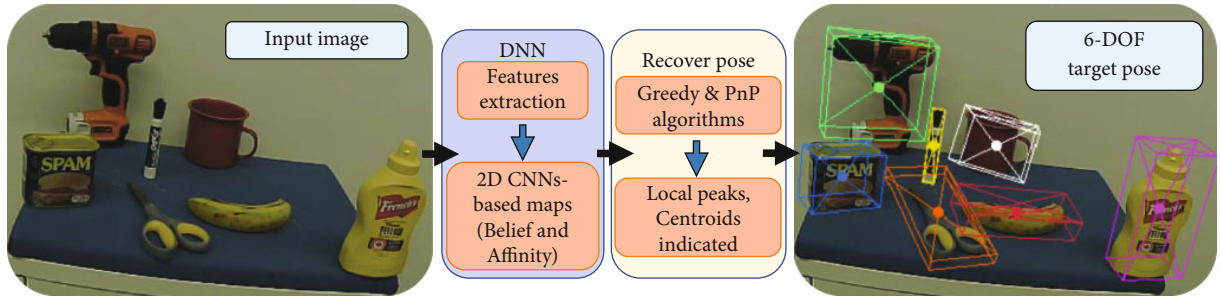
FIGURE 3: Pose estimation of multiple target objects.

the pinhole camera model is shown.

$$Sm_i = K[R \mid t]P_i^w,$$

$$S\begin{bmatrix} u_i \\ v_i \\ 1 \end{bmatrix} = \begin{bmatrix} f_x & 0 & c_r \\ 0 & f_y & c_c \\ 0 & 0 & 1 \end{bmatrix} \begin{bmatrix} r_{11} & r_{12} & r_{13} & t_x \\ r_{21} & r_{22} & r_{23} & t_y \\ r_{31} & r_{32} & r_{33} & t_z \end{bmatrix} \begin{bmatrix} x_i^w \\ y_i^w \\ z_i^w \\ 1 \end{bmatrix},$$

$$(2)$$

where K is the intrinsic camera matrix, $[R \mid t]$ is the extrinsic joint matrix which represents rotation and translation vectors, respectively. It is used to describe the homogeneous rigid motion of object point with respect to the camera coordinates. Also, it translates the coordinates of each 3D point into the coordinate system relative to the camera frame. S indicates the scalar projective factor. f_x and f_y are the focal length expressed in pixel coordinates. c_r and c_c are the principal point of the image center in pixel frame. The process, of changing $[R \mid t]$ and reducing RE, requires object dimensions and 2D observed projection points proposed by deep-ConvNet.

We leverage 60 k of single synthetic images during the training step, all collected from YCB object datasets [24]. Depth images and segmentation steps are not required. The system has been implemented on PyTorch platform [29] and trained on 4 GPUs (each one is GEFORCE RTX 2080 Ti) and processor Intel. Core i9-9820 for 70-80 epochs

with batch size of 64. The learning rate is 0.0001 based on network's optimizer, similar to Adam [30]. During the training, the regularization method of the loss function ($L2$) is used to calculate the loss error between the predicted output and the true value (ground truth) for each input. At the end of each epoch, the error value is accumulated by applying the mean square error (MSE) of each input. This is applied for the entire training phase which shows how the model learns by minimizing the square of the differences between the true and estimated values. Loss function will build and label belief and affinity maps. The used $L2$ loss function calculates the loss error between predicted belief maps and true value (ground truth) of the training data. In Equation (3), B_v^i is the CNN output for a belief map at stage $i \in (1 \cdots n)$ for vertex $v \in (1 \cdots m)$, where n is the stage number and m stands for the number of vertices. $\dot{B}_v$ is the ground truth. Similar to [31], the total loss in the stage i is the sum of losses $L = \sum_i^n L_i$. The deep-ConvNet utilizes intermediate supervision technique which replenishes the gradient at the end of each stage. The intermediate representations are significant to generate increasingly accurate belief maps. This technique provides essential structure to improve generalization by avoiding the well-known issue of vanishing gradient.

$$L_i = \frac{1}{n} \sum_{i=1}^{n} \sum_{v=1}^{m} \left(B_v^i - \dot{B}_v \right)^2. \tag{3}$$

3.2. Mobile Manipulator Model Development. The relationships between the wheel speeds of the mobile platform and the 6-joint velocities of the manipulator arm are presented in this section. Homogeneous representation is used to define the relationship between the frames of the mobile manipulator. The robot's rigid motion is demonstrated by the homogeneous transformation matrix (H) shown as

$$H_n^{n-1} = \begin{bmatrix} R^{3\times3} & d^{3\times1} \\ 0 & 1 \end{bmatrix}, \tag{4}$$

where $R^{3\times3}$ is a rotational matrix expressed in terms of Euler's angles (α, β, and γ) and $d^{3\times1}$ is a displacement vector. These both stand for defining the pose relationship between two coordinate frames. A Denavit-Hartenberg (DH) convention is used to define the coordinate frames of our model.

Figure 4 illustrates the schematic diagram of the mobile manipulator robot. The modeling of differential mobile base is analogous to two-joint manipulator that comprises of prismatic and revolute joints. The linear and angular velocities are the interpretations of the movements of prismatic and revolute joints of the mobile robot relative to the world frame. Along with the velocity of the base frame relative to the world frame, the angular and linear velocities of the mobile robot are obtained through forward kinematics. This is shown in the equation below, where J is the Jacobian

matrix that relates ${}_b^w V$ with $[\dot{\theta}n \quad \dot{d}n]^T$.

$$ {}_b^w V = J^{6\times8} \begin{bmatrix} \dot{\theta}_b \\ \dot{d}_b \end{bmatrix}. \tag{5}$$

In the term of the left and right wheel velocities, kinematics of a differential drive mobile robot (D) are required. In the presented work, the wheel diameter (d) and axle length (l) are 0.33 and 0.545 meters, respectively. Equation (6) demonstrates the relationship between the end-effector velocity relative to the joint's velocities (including two joints for the mobile robot and 6 joints for the manipulator arm). The final velocity equation of the system model is shown in Equation (7), where $E J D^{-1}$ relates end-effector velocity ξ_{ee}^{ee} to joint velocities $[{}_n d_n]^T$. This equation will be combined later with the derived control law of the visual servoing control scheme PBVS.

$$\xi_{ee}^{ee} = E^{-1} J D \left[\theta_1 \, d_2 \, \theta_2 \cdots \theta_n \right]^T, \tag{6}$$

$$\begin{bmatrix} \theta_n \\ d_n \end{bmatrix} = E J^\dagger D^{-1} \xi_{ee}^{ee}, \tag{7}$$

where $J^\dagger$ is the pseudoinverse method of Jacobian matrix that is used for solving inverse kinematics with J.

3.3. Mobile Manipulator Controller Design. The PBVS control aims to minimize the error between the desired and current end-effector pose, by regulating the movement of the robot through the determination of the necessary translational and rotational commands. Control law in PBVS is formulated from the perspective of the desired end-effector frame. The basis of the control law begins with Lyapunov's proportional control scheme, $\dot{e}(t) = -ke(t)$. The proportional gain is denoted as k and the solution yields an exponential decrease of error. Visual servoing error is defined by the difference between the current image and camera parameters (s) and the desired image and camera parameters (s_d), $e(t) = s - s_d$.

The used robotic system operates in three-dimensional Cartesian space; therefore, the error parameters must be defined by two vectors representing the position and orientation of end-effector. This data is obtained by means of pose estimation algorithms, which use a 3D model of a target object to refer to the image data for defining the pose end-effector. Equation (8) defines the results from the pose estimation algorithm.

$$s = (T_e^{e_d}, \phi_e^{ee_d}), s_d = (0, 0). \tag{8}$$

The first vector, $T_e^{e_d}$, is the position vector of current end-effector frame related to desired end-effector frame. The second vector, $\phi_e^{ee_d}$, is the orientation vector, in terms of Euler's angles, of current end-effector frame related to desired end-effector frame. The desired pose vector is zero, since all vectors are represented in relation to this desired frame. The main error equation is further expressed as
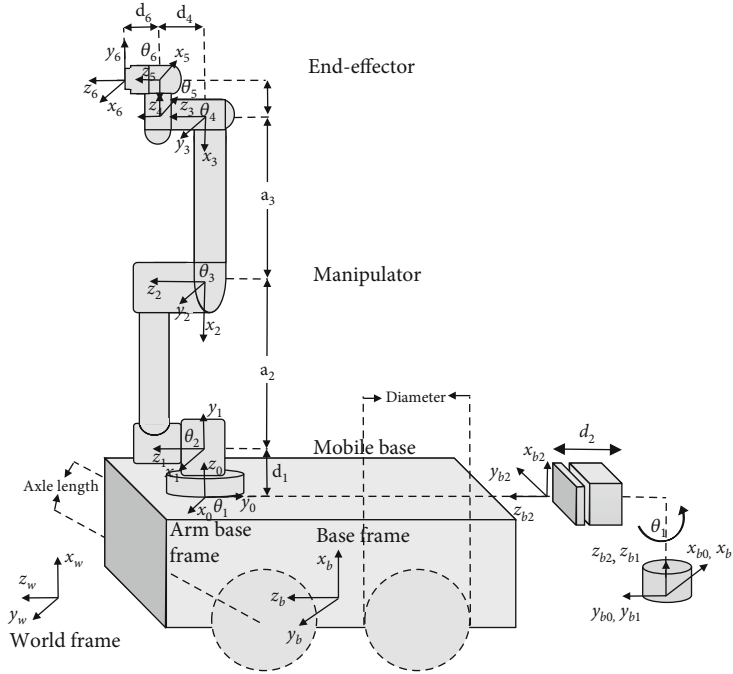
FIGURE 4: Schematic diagram and frames of interest for mobile manipulator robot.

follows.

$$e(t) = (T_e^{e_d}, \phi_e^{ee_d}). \qquad (9)$$

The overall control scheme is derived from both the position and orientation vectors introduced earlier. The change in position vector can be expressed in terms of a rotation matrix between current and desired end-effector pose, $R_e^{e_d}$, as seen in the following.

$$T_e^{ed} = (R_e^{e_d})^T T_e^{\dot{e}e_d}. \qquad (10)$$

Repeat the general process for the orientation vector seen in

$$w_e^{ed} = (R_e^{e_d})^T w_e^{\dot{e}e_d}. \qquad (11)$$

Angular velocities are determined by the rate of change in Euler angles found in $\phi_e^{ee_d}$ which are transformed using $T(\phi)$ defined in the following.

$$w_e^{\dot{e}e_d} = T(\phi) \, \phi_e^{ee_d}, \qquad (12)$$

where,

$$T(\phi) = \begin{bmatrix} 0 & -\sin\varphi & \cos\varphi * cos\theta \\ 0 & \cos\varphi & \sin\varphi * cos\theta \\ 1 & 0 & -\sin\theta \end{bmatrix}. \qquad (13)$$

Substituting Equation (12) into (11) determines the

velocity of the end-effector in terms of angular velocities.

$$w_e^{ed} = (R_e^{e_d})^T T(\phi) \, \phi_e^{ee_d}. \qquad (14)$$

Equation (10) also defines $T_e^{\dot{e}e_d}$ as the rate of change in translational error. This definition can produce the following formula.

$$T_e^{ed} = (R_e^{e_d})^T T_e^{\dot{e}e_d} = (R_e^{e_d})^T e(\dot{t})_t. \qquad (15)$$

Like the translational error, the rate of change in orientation error is defined by $\phi_e^{ee_d}$ when considering Equation (9) to generate the following equation.

$$w_e^{ed} = (R_e^{e_d})^T T(\phi) * e(\dot{t})_W. \qquad (16)$$

The control law for the velocities of end-effector is derived, as shown below, by applying Lyapunov's proportional control scheme from proportional error to Equations (15) and (16).

$$\xi_{ee}^{ee} = \begin{bmatrix} T_e^{ed} \\ w_e^{ed} \end{bmatrix} = -k \, L \, e(t), \qquad (17)$$

where L is known as the interaction matrix that relates the error value to the end-effector velocity.

The estimated pose error is the input to the controller, while end-effector velocity is the output. By combining this with the previous system model developed in Equation (7), the complete control law is designed and determined in Equation (18). This law controls the joint speeds in proportion to the error that happens between the current and
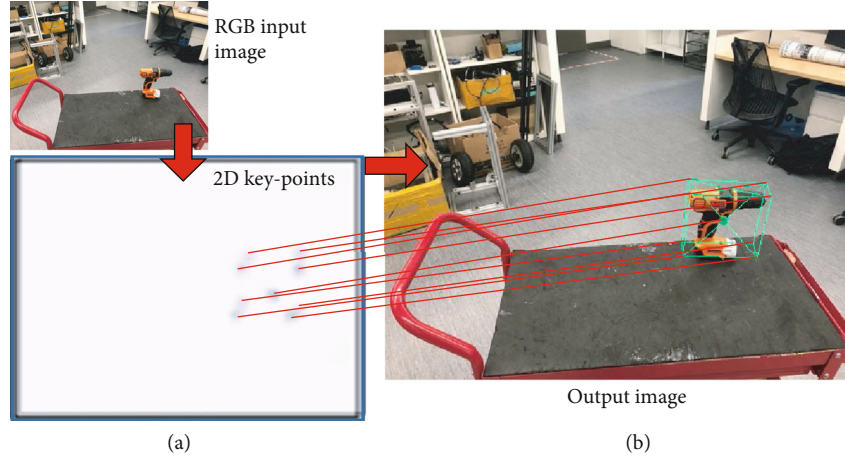
FIGURE 5: Single input image and 2D key points: (a) nine vertices of the final stage and (b) output image with a bounding box.

desired robot end-effector pose. In order to analyze the performance characteristics of the robot model, this control is implemented physically by experimentations in the following section.

$$[\theta_1 \quad \cdots \quad \theta_n]^T = -k\,E\,J^\dagger\,D^{-1}\,L\,e(t). \quad (18)$$

4. Experiments and Discussion

In this section, the experiments were carried out in simulation and real-world settings. Several tests of autonomous 3D visual servoing were conducted to show the performance of the entire system. The perception network has shown effective and robust findings that are reliably enough to be implemented in long-range mobile manipulator model designed in the previous section. The anticipated behavior of the robot during the experiments involves navigating the robot to a desired destination and orienting towards a target object. The target is constantly detected, including its pose estimation information. The controller law (designed in the prior section) is implemented in the experimentations. Training step is not required in the implementation with VS of mobile manipulator. The mobile manipulator robot consists of 6DOF manipulator arm (*UR5* developed by *Universal Robots*) mounted on top of differential mobile base (*A200 Husky* built by *Clearpath Robotics*).

4.1. Deep-Based 6DOF Object Pose Estimation. The perception network entirely trains on computer-generated images and then generalizes to operate on real-world experimentations. The single input image is processed to produce belief maps which hold probability values for each pixel of an image. Higher values represent target object location (target key points). Perception network detects the 2D key points associated with target object defining a bounding box. The detected key points include the centroid of target object with vertices of bounding box. A 3D pose of target object is retrieved by utilizing the estimated 2D key points, camera parameters, and target object dimensions. In contrary to recent researches [4, 8, 9] that demand complicated structure to segment target object in the input image, our deep-

TABLE 1: Speed network performance (sec.) for different stages on seven different objects.

Target objects	S-1	S-2	S-3	S-4	S-5	S-6
Drill	0.019	0.0424	0.062	0.079	0.098	0.182
Mug	0.05	0.0901	0.124	0.166	0.208	0.248
Banana	0.052	0.089	0.13	0.168	0.209	0.249
Scissors	0.05	0.094	0.125	0.167	0.21	0.261
Meat can	0.063	0.092	0.174	0.167	0.224	0.25
Marker	0.054	0.094	0.136	0.17	0.217	0.258
Mustard	0.048	0.089	0.125	0.169	0.209	0.239

TABLE 2: Average distance (mm) between the projected points and ground truth of seven different objects during different processing stages.

Target objects	S-1	S-2	S-3	S-4	S-5	S-6
Drill	51.21	22.49	9.366	6.66	3.587	1.462
Mug	91.15	18.79	11.243	3.933	1.934	0.949
Banana	92.04	26.93	17.129	7.725	4.525	1.841
Scissors	88.61	37.48	8.852	3.94	1.716	1.148
Meat can	117.7	33.56	14.298	9.722	6.084	2.61
Mustard	82.51	23.29	12.879	9.784	4.7147	1.907
Marker	94.52	37.85	22.98	13.01	5.58	1.717

ConvNet utilizes the threshold local peaks in the belief maps. Then, a greedy algorithm links the projected vertices to the indicated centroids.

As a result of feature extraction step, feature map is fed to a series of CNNs that output belief map tensor. Each belief map tensor represents one of each 9 vertices of the 3D bounding boxes. Figure 5(a) illustrates the combination of the 9 vertices (of the final stage) that can form bounding box as well as one belief map for the centroid. 2D key points are produced from a single input image. Similarly, a process works simultaneously to infer multiple instances of objects. Figure 5(b) is the output image with the combined vertices and bounding box.
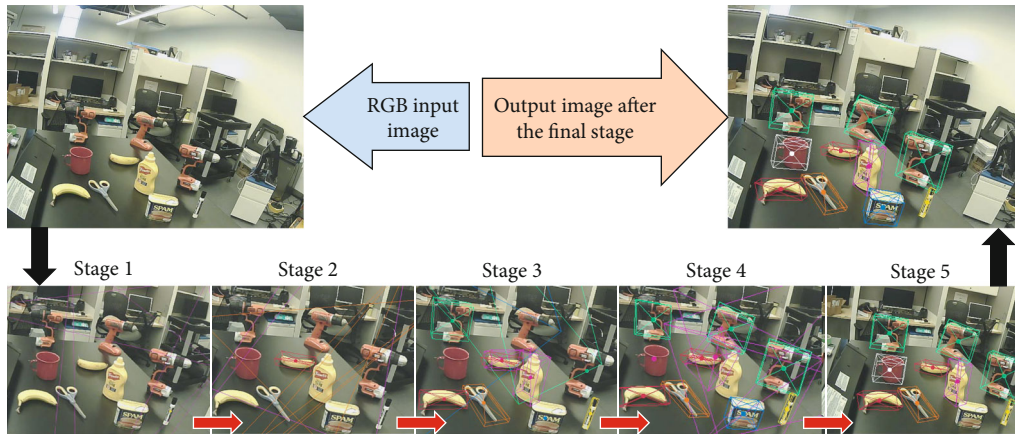
FIGURE 6: The process of 2D key point predictions throughout multistages.

FIGURE 7: Real-world performance of the perception network in difficult backgrounds operating on seven different objects.
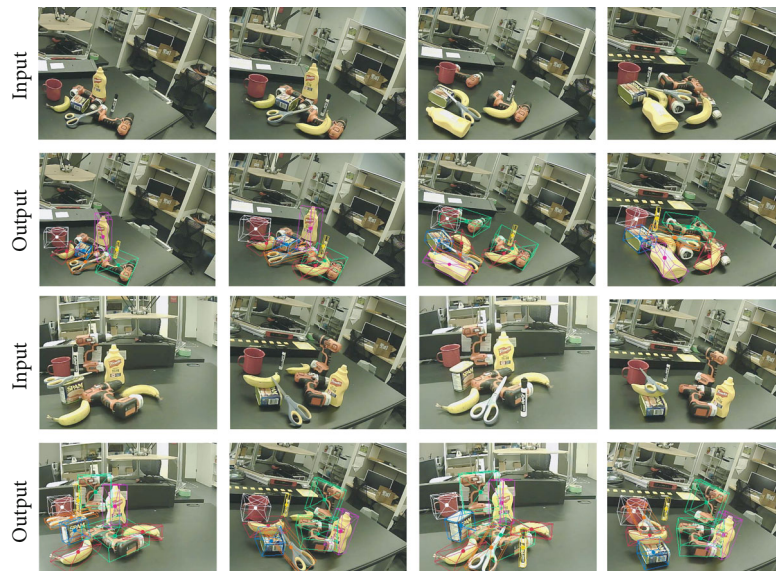
FIGURE 8: Perception network performance with occlusion events. Seven different objects are tested at the same time.

The entire execution time of the perception network is reported in Table 1, including object detection and pose estimation for different number of stages operating on seven different objects (drill, mug, banana, scissors, meat can, marker, and mustard). The average of the execution time of the entire network is about 0.24 sec.

Evaluation metric during multistages was calculated to find the accuracy performance. The average distance is the difference between the ground truth and the estimated key points from the perception network. Table 2 documents the findings of the average distance of seven different target objects. Table 2 shows how the accuracy improves throughout the stages, in which later stages resolve the ambiguities and result accurate performance. With lower distances between the centroids of ground truth and estimated 2D key points, the rate of the average distance (after the final stage) is around 1.66 mm. The accuracy threshold for the robotic manipulation was measured experimentally to find the necessary level of accuracy for grasping purposes. The accuracy threshold was found around 15 mm, by calculating the difference of centroids between ground truth and estimated points, using our robotic system (*UR5* manipulator, *Husky* mobile base, and 2-finger gripper from *RobotiQ*).

The early stages of generating 2D key points often produce ambiguities and unstable predictions that will be resolved by later stages. Figure 6 illustrates the process of generating 2D key points throughout multistages. Throughout the stages, the accuracy of predictions improves gradually. Poor performance of the first 3 stages is clearly indicated. However, the last 2 stages provide robust predictions where all target objects are well estimated by the final stage image.

The pose estimation of target objects is further examined in difficult unstructured backgrounds. Figure 7 demonstrates the performance of pose estimation operating on seven target objects with multiple poses in unprepared lab environment and difficult backgrounds.

The perception network is able to estimate the object's pose even when part of the object is invisible. Figure 8 shows instances of occlusions on different target objects. Object poses are well estimated even though objects obstruct each other randomly.

Another round of testing was necessarily carried out to show the network performance in various conditions of lighting. Figure 9 demonstrates the estimated poses of seven different objects in various illuminations. As seen in the figure, a light source was used closely to the target objects to disturb the image view and examine the perception capability in such lighting situations. The perception network performs robust and stable predictions of estimated poses of multitarget objects.

The ultimate tests of perception network have presented a sufficient model accuracy. That should be able to achieve 3D visual servoing in manipulation application. The next step is the implementation of a synthetically trained mobile manipulator system.

4.2. Visual Servoing for Long-Range Mobile Manipulator System.

After examining the perception network, a complete autonomous system of 3D VS should be implemented to extract the performance characteristics. There is no need to conduct postrefinements of the estimated object's pose. In addition, extra fine-tuning or retraining step is not required. Unlike a study in [32], our model detects and estimates the pose of target object with 3D bounding box regression. The estimated pose directly sends to the control scheme of the mobile manipulator system. The experiments of an entire AMM system were performed in simulation environment, as well as real-world settings.

In contrast to Bateux et al. in [33] who used gantry robot to execute 6DOF direct visual servoing task based on deep neural network method, our perception network does not rely on photometric details of an entire input image, in which image perturbations (such as pixel intensities) have no impact on VS performance. In addition, our robot model is applicable

FIGURE 9: Perception network performance during different lighting conditions.
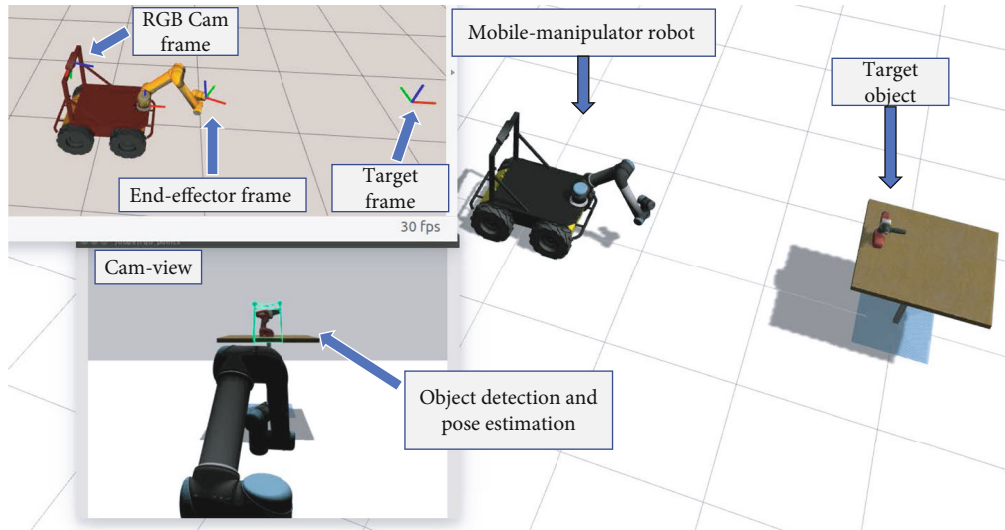
FIGURE 10: Experimental setup in simulation environment.

to both camera installations (eye-in-hand/eye-to-hand). This makes it more practical in a variety of scenarios.

4.2.1. Simulation Environment. Figure 10 demonstrates the experimental setup prepared in Gazebo (a 3D robotics simulator), a target object placed on the table is the desired pose of the robot end-effector. Frames of target object, camera, world base, and robot end-effector are processed by the robotics middleware ROS (Robot Operating System), all exhibited in 3D visualization tool called Rviz.

Multiple rounds of tests were carried out to show the performance of the entire system. A straight test is where the target object was placed in front of the robot. The end-effector of the robot moved as expected towards the detected target. Likewise, another test was performed but deliberately positioned target object at an angle to cause a curved trajectory for the end-effector.

4.2.2. Real-World Settings. Figure 11 shows the experimental setup carried out in the lab environment. *Husky* mobile base with 6DOF *UR5* manipulator, mounted on the top of the mobile robot, was used with uncostly single camera placed at the end-effector. Tracking test was required to investigate the physical capabilities of the proposed AMM system.

Figure 12 demonstrates a scene of the tracking test. Drill object was used as a target object. Figure 12(a) shows the frames of interest presented in Rviz visualizer, Figure 12(b)
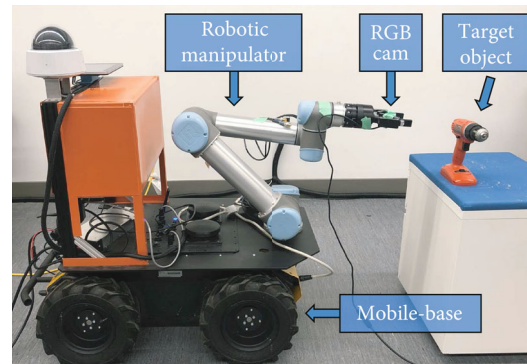
FIGURE 11: Experimental setup in unprepared lab environments.

indicates the estimated pose of the target object, Figure 12(c) is the third person view that covers the used robot with the target object. Eye-in-hand camera installation was considered during the tracking test. This shows a stable and robust performance of the entire manipulation system.

Figure 13 shows instances of the real-time tracking test, which occurs between the target object and end-effector of the AMM robot. Video recordings of the experiments have been provided to show the performance of the proposed AMM system. Comparing to such methods, our system estimates target competitively, which are trained only on
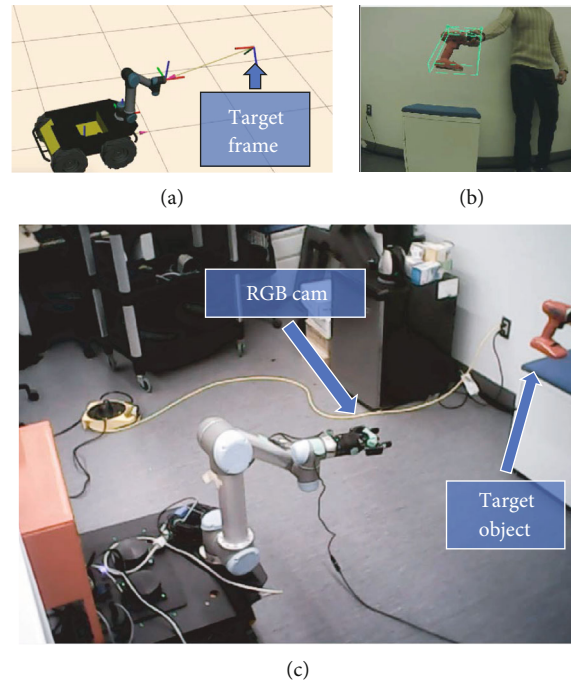
FIGURE 12: Real-world experiments: (a) frames of interest exhibited in the 3D visualizer (ROS-Rviz), (b) detected target object with its pose, and (c) mobile manipulator robot.
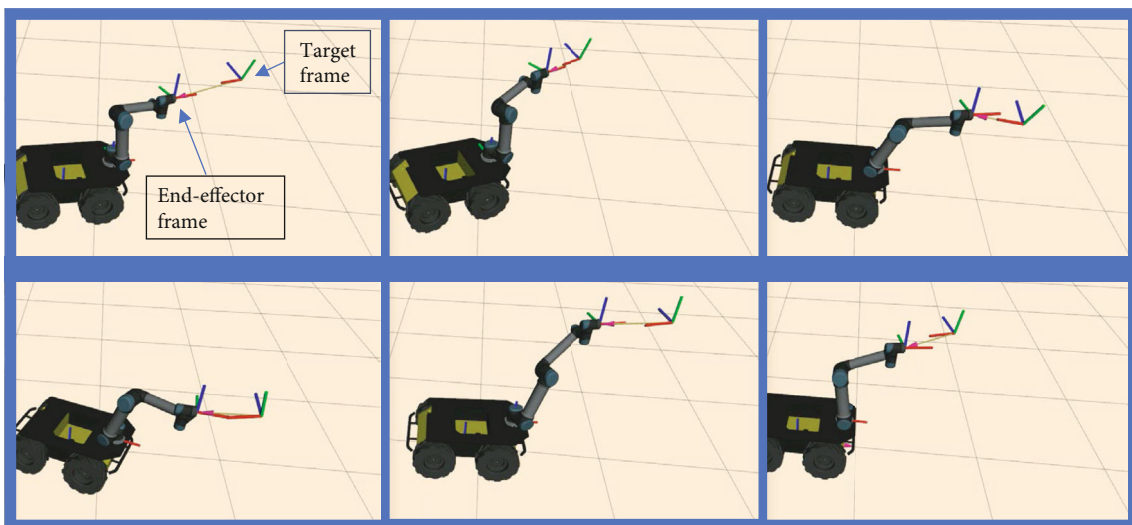
FIGURE 13: Instances of a real-time tracking test.

synthetic data and generalized to physical 3D pose-based VS implemented in long-range mobile manipulator.

4.2.3. Robotic Manipulation. The ultimate purpose of this research is to develop an autonomous framework for vision-based mobile manipulation system. The accuracy of a perception network is adequate to execute continuous 3D VS implemented on long-range mobile manipulator. The goal of experiment is to perform an end-to-end real-time tracking test. Unlike the study in [17], our robotic model is not restricted to static objects and does not require objects to be placed in structured settings. In addition, the proposed system could successfully approach target object with 6DOF

manipulation pose. This is different than traditional manipulation system in [34] which is only limited to top-down configuration. Moreover, our perception network entirely trains on computer-generated single images, and depth information or segmentation step is not required. This is unlike reference [6] which demands collections of synthetic and real-world dataset. Some recent studies might require manual data which gathered via human demonstration. It is worth mentioning that our robotic system is reliable to achieve tracking task with the 6DOF pose of dynamic object. This is appropriate to execute collaborative manipulation challenge (for instance handoff target object from the human to the robot).

To provide scalable visual manipulation system (unlike an approach in [35]), two different VS configurations (eye-in-hand and eye-to-hand) have been experimentally validated. Our robotic model can operate reliably even when the camera and target object are moving at the same time. This assists to overcome uncertainties of the environment and robotic kinematic model.

To demonstrate the proposed robotic system suitable for manipulation task, we carried out further experiments of the whole system. The robot was tasked to move to a desired pose relative to the target object. We ran 5 attempts per session for 5 different sessions. At each test, the starting pose of the end-effector was chosen differently. Similarly, target object was placed randomly within the workspace. The difference between the centroid of target object and end-effector frame was calculated as the average distance. This yields about 2-3 cm in any direction.

5. Conclusions

This work sets out to develop an autonomous 3D VS system based on DeepNet, implemented in a sophisticated mobile manipulator system, and utilized single RGB image. Two main steps construct the entire system: first, perception network to detect and estimate the pose of objects in 3D space, using an effective deep-ConvNet and pose estimation algorithms and model architecture. Second, the pose estimation data was then used in a 3D visual servoing scheme to control the motion of AMM system. Visual servoing control law was designed for the AMM model to avoid uncertain solutions of the inverse kinematics.

Perception network was entirely trained using computer-generated RGB images and depth images, and segmentations are not required. The system was, then, generalized successfully into real-world environment without fine-tuning or extra retraining. Besides simulation experiments, the proposed system was physically tested (on 6DOF manipulator arm mounted on differential robot base) to extract the performance characteristics of the robot model. The findings of experimentations have resulted in a robust and continuous 3D VS operations of AMM with handling occlusion and lighting variations. In terms of future work, it would be important to carry out further studies with the goal of applying object grasping.

Data Availability

All data related to the paper will be available upon request through the corresponding author: Haoxiang Lang (haoxiang.lang@ontariotechu.ca).

Disclosure

The earlier version of the paper has been presented as a thesis form (https://ir.library.dc-uoit.ca/bitstream/10155/1311/1/Al_Shanoon_Abdulrahman.pdf).

Conflicts of Interest

The authors declare that they have no conflicts of interest.

Acknowledgments

References

[1] V. Annem, P. Rajendran, S. Thakar, and S. K. Gupta, "Towards remote teleoperation of a semi-autonomous mobile manipulator system in machine tending tasks," in *International Manufacturing Science and Engineering Conference*, Erie, PA, USA, 2019.

[2] A. Dömel, S. Kriegel, M. Kaßecker, M. Brucker, T. Bodenmüller, and M. Suppa, "Toward fully autonomous mobile manipulation for industrial environments," *International Journal of Advanced Robotic Systems*, vol. 14, no. 4, 2017.

[3] F. Chen, M. Selvaggio, and D. G. Caldwell, "Dexterous grasping by manipulability selection for mobile manipulator with visual guidance," *IEEE Transactions on Industrial Informatics*, vol. 15, no. 2, pp. 1202–1210, 2018.

[4] Y. Xiang, T. Schmidt, V. Narayanan, and D. Fox, "Posecnn: a convolutional neural network for 6d object pose estimation in cluttered scenes," 2017, https://arxiv.org/abs/1711.00199.

[5] J. Tremblay, T. To, and S. Birchfield, "Falling things: a synthetic dataset for 3d object detection and pose estimation," in *Proceedings of the IEEE Conference on Computer Vision and Pattern Recognition Workshops*, pp. 2038–2041, Salt Lake City, UT, USA, 2018.

[6] G. Z. Gandler, C. H. Ek, M. Björkman, R. Stolkin, and Y. Bekiroglu, "Object shape estimation and modeling, based on sparse Gaussian process implicit surfaces, combining visual data and tactile exploration," *Robotics and Autonomous Systems*, vol. 126, article 103433, 2020.

[7] W. Kehl, F. Manhardt, F. Tombari, S. Ilic, and N. Navab, "Ssd-6d: making rgb-based 3d detection and 6d pose estimation great again," in *Proceedings of the IEEE International Conference on Computer Vision*, pp. 1521–1529, Venice, Italy, 2017.

[8] M. Rad and V. Lepetit, "Bb8: a scalable, accurate, robust to partial occlusion method for predicting the 3d poses of challenging objects without using depth," in *Proceedings of the IEEE International Conference on Computer Vision*, pp. 3828–3836, Venice, Italy, 2017.

[9] B. Tekin, S. N. Sinha, and P. Fua, "Real-time seamless single shot 6d object pose prediction," in *Proceedings of the IEEE Conference on Computer Vision and Pattern Recognition*, pp. 292–301, Salt Lake City, UT, USA, 2018.

[10] C. Wang, Q. Zhang, Q. Tian et al., "Learning mobile manipulation through deep reinforcement learning," *Sensors*, vol. 20, no. 3, p. 939, 2020.

[11] M. V. Minniti, F. Farshidian, R. Grandia, and M. Hutter, "Whole-body mpc for a dynamically stable mobile manipulator," *IEEE Robotics and Automation Letters*, vol. 4, no. 4, pp. 3687–3694, 2019.

[12] V. Pilania and K. Gupta, "Mobile manipulator planning under uncertainty in unknown environments," *The International*

Journal of Robotics Research, vol. 37, no. 2-3, pp. 316–339, 2018.

[13] B. Ahn, D. G. Choi, J. Park, and I. S. Kweon, "Real-time head pose estimation using multi-task deep neural network," *Robotics and Autonomous Systems*, vol. 103, pp. 1–12, 2018.

[14] P. Marion, P. R. Florence, L. Manuelli, and R. Tedrake, "Label fusion: a pipeline for generating ground truth labels for real rgbd data of cluttered scenes," in *2018 IEEE International Conference on Robotics and Automation (ICRA)*, pp. 3235–3242, Brisbane, QLD, Australia, 2018.

[15] M. Müller, V. Casser, J. Lahoud, N. Smith, and B. Ghanem, "Sim4cv: a photo-realistic simulator for computer vision applications," *International Journal of Computer Vision*, vol. 126, no. 9, pp. 902–919, 2018.

[16] G. Ros, L. Sellart, J. Materzynska, D. Vazquez, and A. M. Lopez, "The synthia dataset: a large collection of synthetic images for semantic segmentation of urban scenes," in *Proceedings of the IEEE conference on computer vision and pattern recognition*, pp. 3234–3243, Las Vegas, NV, USA, 2016.

[17] J. Tobin, R. Fong, A. Ray, J. Schneider, W. Zaremba, and P. Abbeel, "Domain randomization for transferring deep neural networks from simulation to the real world," in *2017 IEEE/RSJ international conference on intelligent robots and systems (IROS)*, pp. 23–30, Vancouver, BC, Canada, 2017.

[18] V. Lippiello, J. Cacace, A. Santamaria-Navarro et al., "Hybrid visual servoing with hierarchical task composition for aerial manipulation," *IEEE Robotics and Automation Letters*, vol. 1, no. 1, pp. 259–266, 2016.

[19] C. Y. Tsai, C. C. Wong, C. J. Yu, C. C. Liu, and T. Y. Liu, "A hybrid switched reactive-based visual servo control of 5-DOF robot manipulators for pick-and-place tasks," *IEEE Systems Journal*, vol. 9, no. 1, pp. 119–130, 2015.

[20] C. López-Franco, J. Hernández-Barragán, A. Y. Alanis, N. Arana-Daniel, and M. López-Franco, "Inverse kinematics of mobile manipulators based on differential evolution," *International Journal of Advanced Robotic Systems*, vol. 15, no. 1, 2018.

[21] O. F. Avilés, O. G. Rubiano, M. F. Mauledoux, A. J. Valencia, and R. Jiménez, "Simulation of a mobile manipulator on webots," *International Journal of Online Engineering*, vol. 14, no. 2, p. 90, 2018.

[22] A. T. Azar, H. H. Ammar, and H. Mliki, "Fuzzy logic controller ith color vision system tracking for mobile manipulator robot," in *International Conference on Advanced Machine Learning Technologies and Applications*, pp. 138–146, Springer, 2018.

[23] T. Kornuta and C. Zieliński, "Robot control system design exemplified by multi-camera visual servoing," *Journal of Intelligent & Robotic Systems*, vol. 77, no. 3-4, pp. 499–523, 2015.

[24] B. Calli, A. Singh, A. Walsman, S. Srinivasa, P. Abbeel, and A. M. Dollar, "The ycb object and model set: towards common benchmarks for manipulation research," in *2015 international conference on advanced robotics (ICAR)*, pp. 510–517, Istanbul, Turkey, 2015.

[25] K. Simonyan and A. Zisserman, "Very deep convolutional networks for large-scale image recognition," 2015, https://arxiv.org/abs/1409.1556.

[26] J. Deng, W. Dong, R. Socher, L. J. Li, K. Li, and L. Fei-Fei, "Imagenet: a large-scale hierarchical image database," in *2009 IEEE conference on computer vision and pattern recognition*, pp. 248–255, Miami, FL, USA, 2009.

[27] V. Lepetit, F. Moreno-Noguer, and P. Fua, "Epnp: an accurate o (n) solution to the pnp problem," *International Journal of Computer Vision*, vol. 81, no. 2, pp. 155–166, 2009.

[28] C. T. Kelley, *Iterative Methods for Optimization*, SIAM, Philadelphia, PA, USA, 1999.

[29] A. Paszke, S. Gross, S. Chintala et al., *Automatic Differentiation in Pytorch*, NIPS Workshop, 2017.

[30] D. P. Kingma and J. Ba, "Adam: a method for stochastic optimization," 2014, https://arxiv.org/abs/1412.6980.

[31] S. E. Wei, V. Ramakrishna, T. Kanade, and Y. Sheikh, "Convolutional pose machines," in *Proceedings of the IEEE conference on Computer Vision and Pattern Recognition*, pp. 4724–4732, Las Vegas, NV, USA, 2016.

[32] K. Ahlin, B. Joffe, A. P. Hu, G. McMurray, and N. Sadegh, "Autonomous leaf picking using deep learning and visual-servoing," *IFAC-PapersOnLine*, vol. 49, no. 16, pp. 177–183, 2016.

[33] Q. Bateux, E. Marchand, J. Leitner, F. Chaumette, and P. Corke, "Training deep neural networks for visual servoing," in *2018 IEEE international conference on robotics and automation (ICRA)*, pp. 3307–3314, Brisbane, QLD, Australia, 2018.

[34] E. Jang, S. Vijayanarasimhan, P. Pastor, J. Ibarz, and S. Levine, "End-to-end learning of semantic grasping," 2017, https://arxiv.org/abs/1707.01932.

[35] Q. Bateux and E. Marchand, "Particle filter-based direct visual servoing," in *2016 IEEE/RSJ International Conference on Intelligent Robots and Systems (IROS)*, pp. 4180–4186, Daejeon, Republic of Korea, 2016.

Research Article

A Sparsity-Limitation-Based High-Dimensional Distribution Searching Algorithm for Adversarial Attack

Chenxi Zhu [ID],[1] **Haobo Wang** [ID],[1] **Yan Zhuang** [ID],[1] **Jie Li** [ID],[1,2] **and Yangjie Cao** [ID] [1]

[1]*School of Cyber Science and Engineering, Zhengzhou University, Zhengzhou 450000, China*
[2]*Department of Computer Science and Engineering, Shanghai Jiaotong University, Shanghai 200240, China*

Correspondence should be addressed to Chenxi Zhu; chenxi_zhu@gs.zzu.edu.cn

Deep neural networks-based image classification systems could suffer from adversarial attack algorithms, which generate input examples by adding deliberately crafted yet imperceptible noise to original inputs. To reduce the impact on human visual sense and to ensure adversarial attack ability, the input image needs to be modified by pixels in considerable iterations which is time consuming. By using sparse mapping network to map the input into a higher dimensional space, searching space of adversarial perturbation distribution is enlarged to better acquire perturbation information. Taking both searching speed and searching effectiveness into consideration, sparsity limitation is introduced to suppress unnecessary neurons during parameter updating process. Based on different eye sensitivity of different colors, maps of each color channel are disturbed by perturbations with different strengths to reduce visual perception. Numerical experiments confirm that compared with the state-of-the-art adversarial attack algorithms, the proposed SparseAdv performs a relatively high attack ability, better imperceptible visualization, and faster generation speed.

1. Introduction

In recent years, artificial intelligence technology has ushered in rapid development, in which deep learning has emerged strongly. Deep learning has demonstrated outstanding results in a variety of domains, including image classification [1–3], speech recognition [4], object detection [5], and self-driving [6]. Though deep learning network shows excellent performance, its complicated internal structure and in-interpretability have raised security concerns, as such if a model might be compromised to make wrong prediction when exposed to adversarial attacks [7]. These attacks deliberately craft the input examples to mislead the deep learning network, and such modifications could be hard to be detected by bare human eyes [8]. The crafted examples are named as adversarial examples.

Discovery of adversarial examples has gained increasing attentions and researchers began to explore adversarial attack algorithms. According to generation methods of adversarial examples, the examples could be generated whether by directly modifying each input example or training a generator to achieve mass generation. The former generation methods are traditional adversarial example generation methods which update the input examples guided by feedback from specially designed loss function [7]. These methods achieve high successful attack rate, whereas sacrifice generation efficiency due to time cost on the change of each individual example. Especially in image classification domain, traditional generation methods need to alter all pixel values of an image during each updating iteration. For example, Carlini and Wagner (CW) attack [9] cost around two minutes to generate an adversarial example. Therefore, the latter generation methods which could speed up generation of adversarial examples have been proposed. AdvGAN [10] trained a generative adversarial network (GAN) to learn mapping from an original example to the adversarial one and the trained GAN could immediately alter the original input to its adversarial version. Moreover, authors of [11] utilized autoencoder as an auxiliary generator

to generate adversarial priors and thus reduced iterations for searching adversarial distributions. Instead of updating each pixels on the original input during the training process, the trained generator is able to mass generate adversarial examples in a fast speed.

The barely seeking local optimum, i.e., Nash equilibrium, with fluctuate results challenges the training process. Additionally, other generation methods mainly use generator as supplementary means, which still need abundant time-consuming iterations for further adversarial alteration. We try to realize and propose that an individual generator is enough to realize generator-based adversarial attacks and propose a new generator structure which maps the data from input space to high-dimensional space, and thus excavates more effective information for disturbing. Moreover, Kullback-Leibler divergence (KLD) is adopted for sparsity limitation on neurons in hidden layers. With sparsity limitation, computation complexity caused by high dimensional mapping could be reduced. To make the attack more imperceptible to human eyes, we conduct suitable operations on maps from different color channels based on biological characteristics of human visual system. Our contributions are summarized as follows:

(i) We search the required information in high-dimensional space and train a sparse mapping network as a generator, which can raise dimension of the input to dig out much effective perturbation and speed up generation process of adversarial examples

(ii) A KLD loss is added in loss function for sparsity limitation, so that neurons in the generator are selectively activated to make the training procedure more efficient

(iii) Based on different eye sensitivity of different colors, maps of each color channel are disturbed by perturbations with different strengths to reduce visual perception. Experimental results show that SparseAdv achieves higher successful rates of attacking and is also less perceptible in visual sense

The rest of this paper is organized as follows. Section 2 briefly overviews the related works of adversarial attacks. In Section 3, we specifically state the attack methodology of SparseAdv. We present the experimental results in Section 4 and conclude the paper in Section 5.

2. Related Work

2.1. White-Box Adversarial Attacks. Earlier adversarial attacks were mostly white-box adversarial attacks, in which attackers had access to all information (i.e., model structure, parameter, and hyper-parameter) of a target model. Adversarial attack was firstly proposed by Szegedy et al. [8] in 2013, they found that subtle modification of an example was able to mislead a deep learning model, which was then widely researched by experts from various fields. The example with nonsensitive (to human eye) yet misguiding (to deep learning model) perturbation was recognized as adversarial example. Goodfellow

et al. [7] proposed fast gradient sign method (FGSM), which used gradient direction to disturb clean examples and demonstrated that adversarial examples had unstable transferability among different target classifiers. Based on FGSM, a basic iterative method (BIM) [12] was subsequently proposed to superimpose the noise step by step. So that feedback of the gradient information could be fully used under the same disturbance and BIM was able to successfully achieve better results with a smaller disturbance effect. Considering that the complex nonlinear model might change drastically in a very small range, projected gradient descent [13] method used gradient feedback to limit the noise to a small range. CW attack [9] defined two impact factors according the two final goals—imperceptible visual effect to human and misleading result to the recognition model. CW attack updated the input by optimizing the two factors and showed excellent performance.

2.2. Black-Box Adversarial Attacks. In real scenarios, black-box attacks which do not need any information of the target model and show high transferability among various models have gained attention. The transferability of adversarial example refers to the successful attacking rate of the example set to a target model, could be almost the same when this set attacks another model. Therefore, concept of transferability means the ability to keep the performance when an adversarial example set changes the task environment, i.e., the target model to be attacked. As a result, transferability of adversarial examples indicates flexibility and adaptablity of an adversarial attack algorithm while facing different task environments. Moreover, higher transferability of adversarial example set in white-box research could make it more transferable to black-box adversarial attack. Dong et al. [14] proposed the Momentum Iterative Fast Gradient Sign Method (MI-FGSM) [14] in the Neural Information Processing Systems 2017 competition. MI-FGSM integrated the momentum term into iterative process, stabilizing the update direction and getting rid of undesirable local maximum. Diversity input method [15] proposed to enhance data diversity by randomly transforming clean examples, thereby improving transferability of adversarial examples. Translation Invariant Method [16] proposed a translation-invariant attack algorithm to generate adversarial examples that were less sensitive to white-box model and so that transferred better among black-box models. AutoZoom [11] added adversarial perturbation in low-dimensional space and mapped the perturbation to high-dimensional embedding space by autoencoder, thus reducing the mean query counts in finding successful adversarial examples. Inspired by AutoZoom, TREMBA [17] utilized AutoZoom's framework for gaining perturbation prior. Then by applying a standard black-box attack method such as Natural Evolution Strategy (NES) [18] on the embedding space, adversarial perturbations could be found efficiently for a target model.

2.3. Generator-Based Adversarial Attacks. When the adversarial examples are generated by altering the input to maximize the classification loss [8], it requires multiple iterations to modify on the input. Such iterations lower the efficiency of generating adversarial examples and thus consume much

time while facing the tasks that need to generate a plenty of adversarial examples. Generator-based adversarial attacks are thus proposed for fast adversarial example generation, including generating adversarial examples by general generators with neural network structure and by GAN. AutoZoom [11] and TREMBA [17], which were the black-box adversarial attacks mentioned above, both utilized autoencoder as a generator to generate perturbation prior. However, iterations on the input were still required for achieving the whole attack process. As for GAN, it is a generative network constituted by a generator and discriminator, which could be trained to learn the mapping between clean examples or random noise and adversarial examples. An adversarial example could be directly derived from trained network that generating iterations on each input is skipped [10, 19, 20]. Xiao et al. [10] proposed AdvGAN to generate an adversarial perturbation to be mapped from an original input by its generator, which was then added to this corresponding original image. The discriminator in AdvGAN judged whether the input example composed of original image and perturbation was an adversarial example. Based on AdvGAN, AdvGAN++ [19] proposed by Jandial et al. introduced latent vectors from the target classifier as the input of GAN to generate adversarial examples. Rob-GAN [20] introduced adversarial examples into GAN that not only could accelerate the training process by rapidly generating adversarial examples but also improve the quality of generating image and the robustness of discriminator. Zhao et al. [21] introduced Natural GAN model which could search adversarial example vector in low-embedding latent space and generate more targeted and natural adversarial perturbations. Deb et al. [22] focused on adversarial face synthesis and utilized human identity matching information to train GAN to gain face adversarial examples.

GAN performs well in speeding up adversarial example generation, whereas the two loss functions in generator and discriminator makes the convergence point hard to reach, which challenges the training process [23]. We propose to abandon discriminator which is used for confining pixel value to reduce visual effect on bare eye and conduct special noise adding method based on biological characteristics of the human eyes for better visualization. Therefore, the retained single loss function in training model could ease the convergence process. Researchers have performed diverse noise adding operations to balance visual effects and attack ability. Shamsabadi et al. [24] and Bhattad et al. [25] introduced unrestricted perturbations by exploiting image semantics such as color and texture to generate effective and photorealistic adversarial examples. Based on superpixel and attentional map, Dong et al. [26] preserved the attack ability even in highly constrained modification space, and it was robust to image processing based defense and steganalysis-based detection. Above methods focus on the machine's characteristics for recognizing images, which omit an important fact that perturbations added on adversarial examples are expected to be imperceptible to humans rather than machines. Human eyes are unevenly sensitive to red, green, and blue colors [27, 28], while convolution operations, which are conducted by machines, on maps from each color channel are the same. So that different perturbation values on different channels are necessary to achieve better balance between attack ability and visual effect. More specifically, weaker perturbations are added on maps from the color channel, to which human eyes are more sensitive, and stronger perturbations are added on maps from other color channels.

3. Attack Methodology

In this section, we first overview SparseAdv and then introduce each procedure in detail.

3.1. Overview of SparseAdv. In image classification area, adversarial examples are the clean image inputs added with specifically designed noise which could not only deceive the deep learning models based classifiers but are also least noticeable to human visual sense. The adversarial example generating framework SparseAdv is designed for the above task. As shown in Figure 1, SparseAdv contains a sparse mapping neural network that maps input image from input space to high-dimensional space to search special distribution which could potentially be the noise to mislead the categorization of target classifiers. This special distribution extracted by neural network in SparseAdv is then combined with its original image and fed into classifier. The image, disturbed by the searched distribution, tends thus to be classified into a category different from its true labeled class. Therefore, an adversarial example is then produced by the SparseAdv framework in theory. The loss function contains two parts, one of which is designed that the predicted label is guided to be the class with the secondary confidence [29] within four networks, which are ResNet-50 [30], VGG-16 [31], GoogleNet [32], and MobileNet-v2 [33], in our research. The other part introduces KLD, which is an indicator for sparsity measure. Suppression on KLD achieves sparsity limitation that benefits effective application of each neuron in a neural network. And then the whole loss function is fed back to update the parameters of sparse mapping neural network in SparseAdv. To increase the transferability, the overall loss function is constituted by the loss functions from each attack process on the four target networks. Successful adversarial attack means to generate perturbations which could change categorization result of the classifier, while to deceive human visual sense. Since human visualization is the focus, we follow the analysis of human eyes' biological characteristics in [27, 28] and learn that those are differently sensitive to different colors. Thus, different operations are conducted on maps from each color channel. For the insensitive color to human eyes, relatively strong noises are added on maps from corresponding color channels, while weak disturbing is conducted to reduce observability for the sensitive color. Note that strength of the noise is represented by the thickness of blue lines in Figure 1.

3.2. Formal Description. Once get the input image x, a sparse mapping network is used as a generator $\mathscr{G}(\cdot)$ and extract perturbation distribution $\mathscr{G}(x)$ from input space. We combine the generator operation with general adversarial attack algorithm, in which the input x with its adversarial perturbation δ is updated by minimizing the loss function $L_{\mathrm{adv}}(x, y)$ defined as follows from CW attack [29], which leads the label to another class with the secondary confidence:
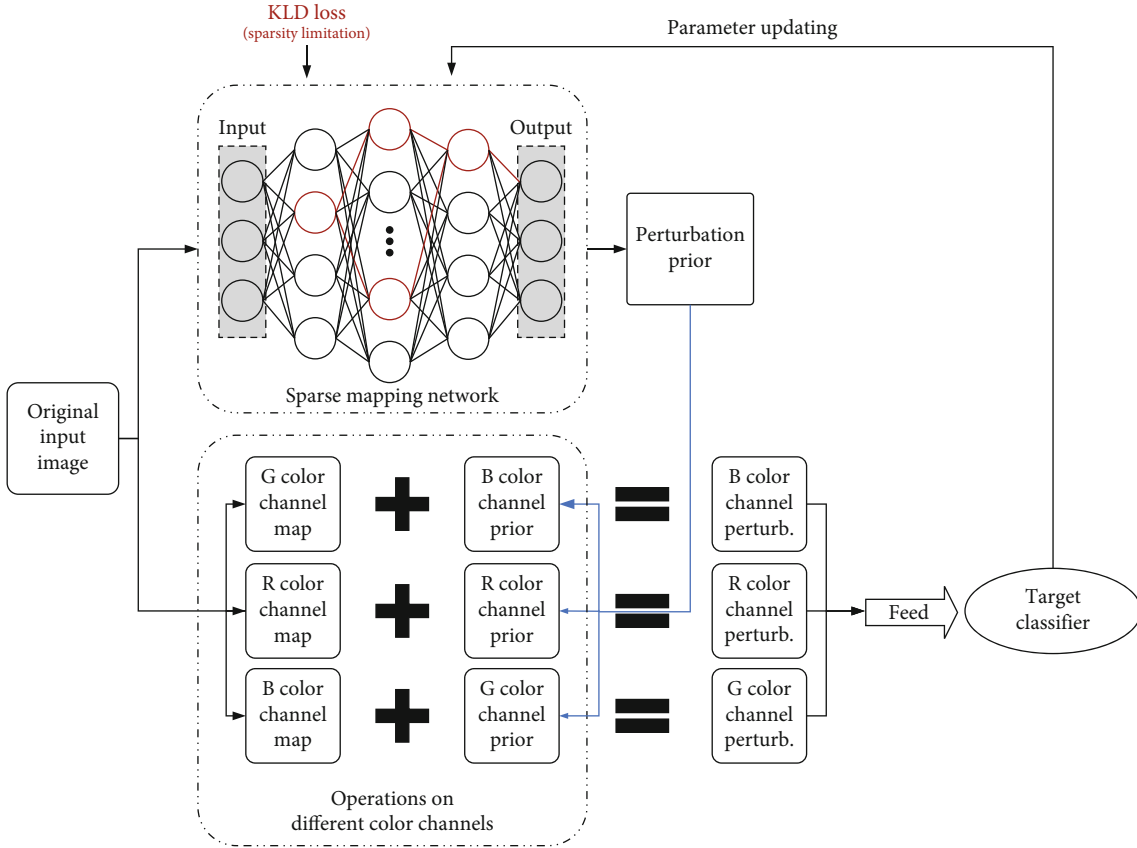
FIGURE 1: Overview of SparseAdv.

$$L_{\text{adv}}(x, y) = \left\{ -\kappa, \mathscr{C}[x + \delta]_y - \max_{c \neq y} \mathscr{C}[x + \delta]_c \right\}, \quad (1)$$

where (x, y) is the input x with its label y in a training set, $\mathscr{C}(\cdot)$ is the target classifier, and κ is a margin parameter which controls the strength of adversarial examples. So that the generated perturbation δ is substituted by $\mathscr{G}(x; \theta)$, generator $\mathscr{G}(\cdot)$ with input x and parameter θ, in Eq. (2):

$$L_{\text{adv}}(x, y) = \max \left\{ -\kappa, \mathscr{C}[x + \mathscr{G}(x; \theta)]_y - \max_{c \neq y} \mathscr{C}[x + \mathscr{G}(x; \theta)]_c \right\}. \quad (2)$$

Another penalty term KLD (i.e., $\text{KL}(\rho \| \widehat{\rho}_j(x)) = \sum_{i \in X} \rho \cdot \log (\rho / \widehat{\rho}_j(x)))$ is added to achieve sparsity limitation. Note that detailed introduction of KLD function is demonstrated in Section 3.4. Thus, the final loss function L_{final} is defined as follows:

$$L_{\text{final}}(x, y) = L_{\text{adv}}(x, y) + \text{KL}\left(\rho \Big\| \widehat{\rho}_j(x)\right). \quad (3)$$

Instead of directly updating the input image, SparseAdv updates the parameters θ of the generator. The upgrade process of parameter θ in sparse mapping network $\mathscr{G}$ according to loss function $L_{\text{final}}(x, y)$ is as follows:

$$\theta = \operatorname*{argmin}_{\theta} L_{\text{final}}\{\mathscr{C}[\mathscr{G}(x; \theta)], y\}. \quad (4)$$

The trained network $\mathscr{G}$ is thus able to generate adversarial perturbations once given the input images. Attack process is obtained by averaging out their loss functions as a new overall loss function shown below:

$$L_{\text{adv\_trans}}(x, y) = \frac{1}{N} \left\{ \sum_{n=1}^{N} L_{\text{final}}(x, y) \right\}, \quad (5)$$

where N denotes the number of target classifiers and n denotes the classifier index.

3.3. Sparse Mapping Network. Under recognition task, hidden layers in deep neural networks are designed for obtaining features, each layer of which chooses key information from the anterior layer for correct feature extraction. Therefore, size of the feature map generated by each hidden layer is diminishing as the layer goes deeper. General adversarial example generator follows such design, whereas ignores the fact that the key information under adversarial attack task requires disturbing ability rather than correct feature. Above analysis motivates us to abandon general structure design of neural network, which usually conducts down-sampling during feature extraction procedure, and raises the dimension of input image at
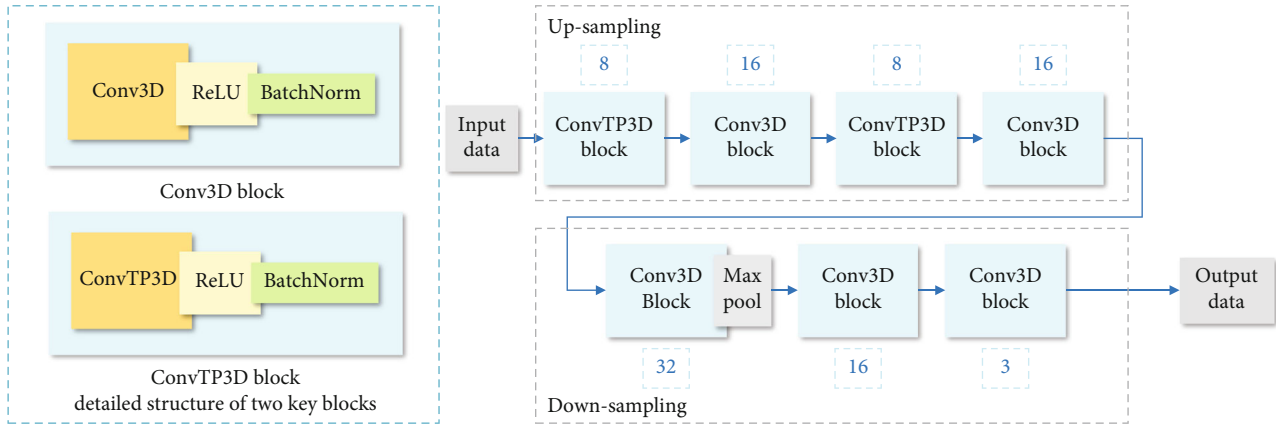
FIGURE 2: Sparse mapping network.
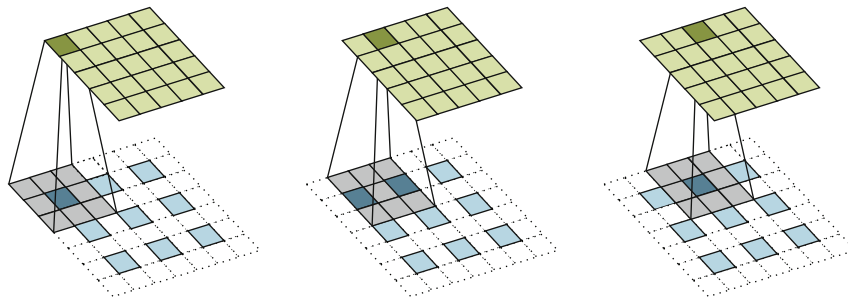
FIGURE 3: Deconvolutional operation.

shallow layers to enlarge the searching space for perturbation information.

In our SparseAdv framework, the sparse mapping network consists of an up-sampling module, which mainly utilizes the deconvolutional layer for dimension expansion, and a down-sampling module, which uses the convolutional layer for effective information extraction and the max-pooling layer for dimension adjusting. As shown in Figure 2, the right part of the figure demonstrates the structure of sparse mapping network, while the left part of the figure gives the detailed design of two key blocks including Conv3D block and ConvTP3D block. Each Conv3D block contains a three-dimensional convolutional layer (i.e., Conc3D in the figure), a rectified linear unit (ReLU) layer, and a batch normalization layer. Each ConvTP3D block has the same structure with the Conv3D block, except the first layer which is substituted by a three-dimensional deconvolutional layer (i.e., ConvTP3D in the figure).

The deconvolutional layer is designed for up-sampling, which is used to enlarge searching space in SparseAdv algorithm. Specifically, it is a special convolutional operation, before which the size of input image is enlarged by supplementing zeros in proportion. Figure 3 gives an example for deconvolutional operation, in which a 3×3 input is scaled up to the size of 5×5 after deconvolutional operation. The batch normalization layer speeds up the training process by using a higher learning rate, thus the retraining process consumes much less time. A max-pooling layer is invoked for down-sampling after some convolutional layers to adjust

data dimensions to the same size as the input image. Note that the introduction of nonlinear factors—ReLU—makes the model more controllable.

As a kind of GAN, AdvGAN contains a generator and a discriminator, each of which aims to converge its own loss function to optimal result. Generator of AdvGAN is used for misleading the target classifier, while the discriminator of it confines value change of pixels in an algorithm-allowed range. It would be a challenge on the overall gradient descent process because both functions have distinguish gradient directions [23]. Moreover, generator structure of GAN is designed as a normal autoencoder which maps the input to low-dimensional space, limiting access to effective perturbation information. We use sparse mapping network as is introduced above and conduct color-channel-based perturbation adding methods by analyzing biological characteristics of the human eyes to avoid loss function for those algorithm restrictions on pixel values. With our specially designed dimension raising structure and color-channel-based perturbation adding method, single loss function of SparseAdv is easy to be converged to expected point.

3.4. Kullback-Leibler Divergence. KLD is a method to describe difference between two probability distributions. Given a data set X and its two probability distribution P and Q, KLD $\mathrm{KL}(P\|Q)$ is defined as follows:

$$\mathrm{KL}(P\|Q) = \sum_{i \in X} P(i) \cdot \log \left(\frac{P(i)}{Q(i)} \right). \tag{6}$$

| | R channel | | | G channel | | | B channel | |
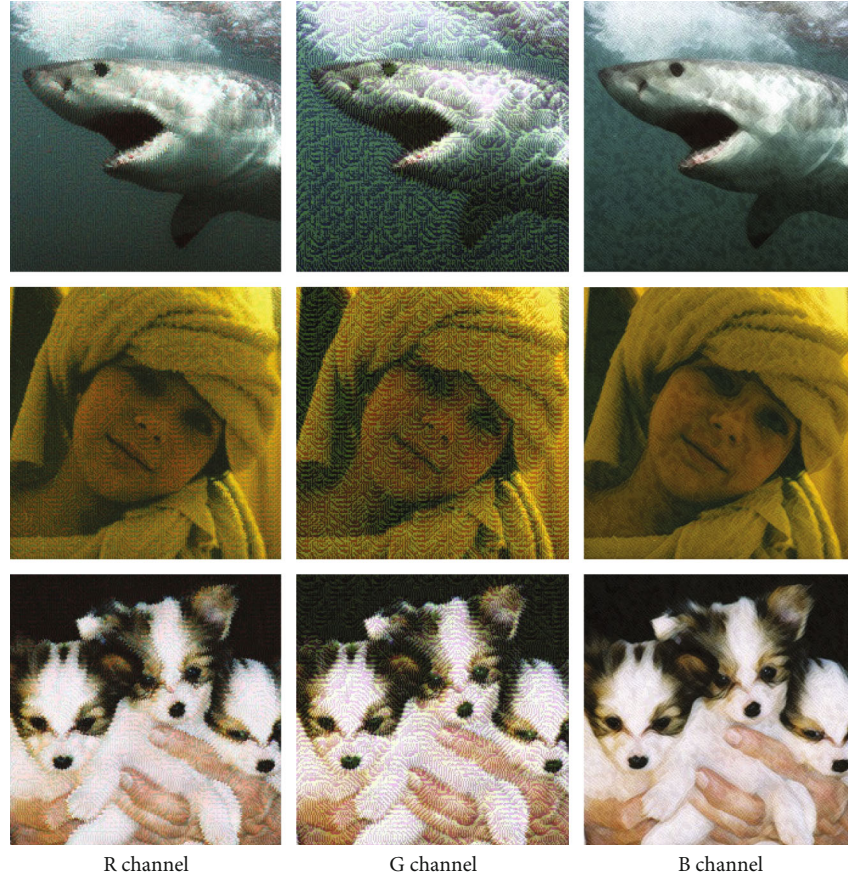
FIGURE 4: Visual comparisons on three channels.

TABLE 1: Comparison experiments of the four algorithms.

Attack	ResNet-50		VGG-16		GoogleNet		MobileNet-v2	
	Success (%)	Time	Success (%)	Time	Success (%)	Time	Success (%)	Time
AdvGAN	98.20	17.32 s	95.72	16.39 s	98.16	17.99 s	97.77	18.32 s
TREMBA	*99.52*	437.7 s	*100.0*	316.9 s	*99.85*	280.2 s	*100.0*	144.8 s
ColorFool	89.72	26.98 h	91.25	24.50 h	85.29	29.88 h	89.23	30.93 h
SparseAdv	97.26	*12.22 s*	96.32	*13.58 s*	99.02	*14.78 s*	95.35	*12.64 s*

∗The four compared algorithms include AdvGAN, TREMBA, ColorFool, and our SparseAdv. There are two performance metrics containing attack successful rate (%) and time of batch (1000) generation.

When there is a tremendous quantity of neurons in a neural network's hidden layers, some limitations are necessary for reducing computational complexity. Thus, KLD is added to the loss function to achieve sparsity limitation on sparse mapping network.

More specifically, given an input x, let $a_j(x)$ denote activation degree of the hidden neuron j, the average activation degree of j could be formalized as follows:

$$\widehat{\rho}_j = \frac{1}{M} \sum_{m=1}^{M} a_j\left(x^{(m)}\right), \tag{7}$$

where M denotes the number of samples in data set and m denotes index of each sample. We could define an sparsity parameter ρ, which is generally a low value close to 0 (e.g., $\rho = 0.05$). Thus, the average activation degree $\widehat{\rho}_j$ is expected to approach ρ for sparsity limitation. To achieve such limitation, an additional penalty factor is added to the loss function to punish those cases where ρ and $\widehat{\rho}_j$ are significantly different, so that the average activation degree of hidden neurons is kept within a small range. We choose KLD as a metric to measure the difference between ρ and $\widehat{\rho}_j$ as follows:

$$\mathrm{KL}\left(\rho \big\| \widehat{\rho}_j\right) = \sum_{i \in X} \rho \cdot \log\left(\frac{\rho}{\widehat{\rho}_j}\right). \tag{8}$$

| Original input | AdvGAN | TREMBA | ColorFool | SparseAdv |
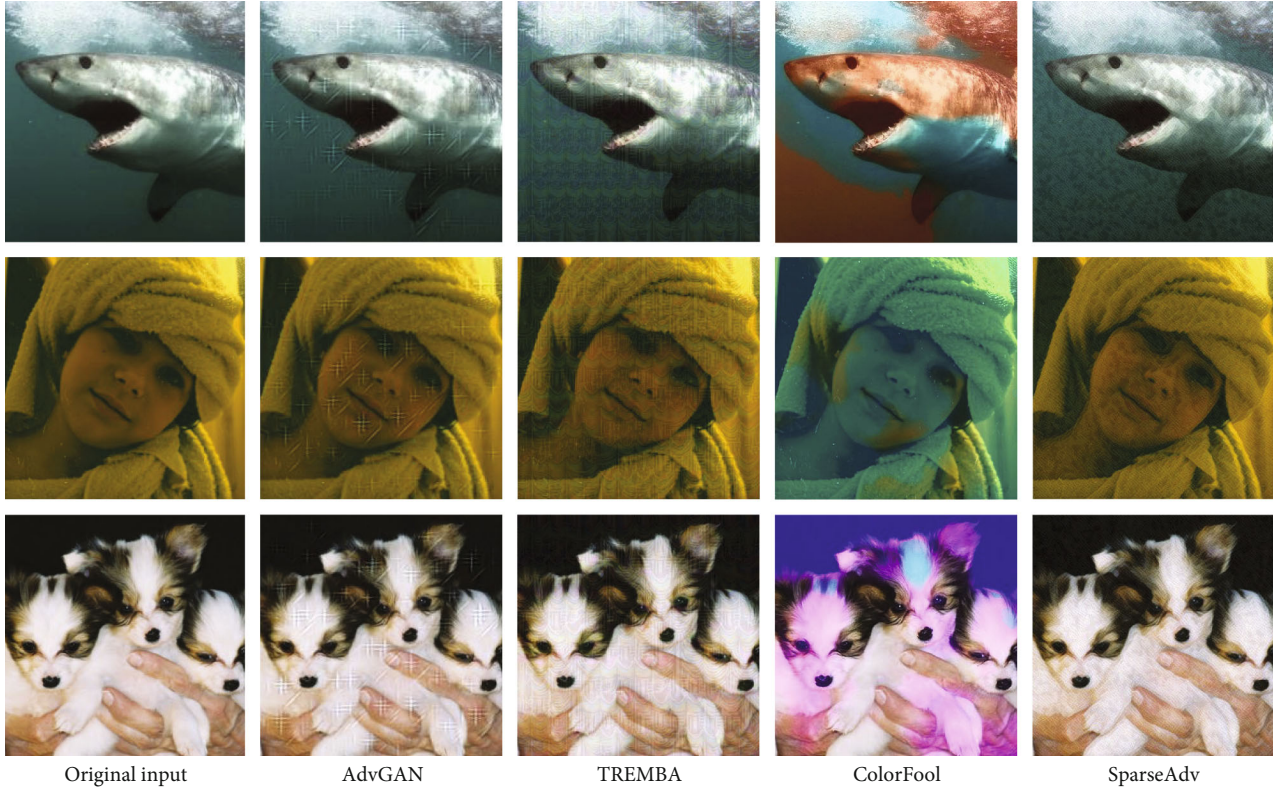
FIGURE 5: Visual comparisons of the adversarial examples generated by compared algorithms—AdvGAN, TREMBA, ColorFool, and our SparseAdv.

TABLE 2: Transferability of SparseAdv.

	MobileNet-v2	ResNet-50	VGG-16	GoogleNet
MobileNet-v2	*95.35*	57.90	53.26	15.88
ResNet-50	76.52	*97.26*	90.19	89.66
VGG-16	72.83	50.24	*96.32*	37.85
GoogleNet	73.29	69.18	84.66	*99.02*

∗The transferability is represented by attack successful rate (%) when the generated adversarial examples are fed into different deep learning models.

When ρ is equal to $\widehat{\rho}_j$, $\mathrm{KL}(\rho\|\widehat{\rho}_j)$ is equal to 0 and its value increases monotonically as the difference between ρ and $\widehat{\rho}_j$ increases. Therefore, minimizing the penalty $\mathrm{KL}(\rho\|\widehat{\rho}_j)$ has the effect of bringing $\widehat{\rho}_j$ closer to ρ, achieving sparsity limitation on the neural network.

3.5. Operations on Different Color Channels. We propose to choose a map from one color channel to be strongly disturbed and add weak perturbation on maps from other two channels. Exploration of biological characteristic of human eye shows that visual cones have different sensitivities to distinguished colors including red, green, and blue, according to the research of Dartnall et al. [27]. Cicerone et al. [28] measured the number of visual cones and found that the ratio of red-sensitive, green-sensitive, and blue-sensitive cones is approximately $40:20:1$. Such findings indicate that human eyes are least sen-

sitive to blue. However, convolutional neural networks (CNN) multiply the same weights of maps from three channels during feature extraction. Motivated by this finding, map from B channel is chosen to be added relatively strong perturbation since the sensitivity of blue color to human visualization is the lowest while its influence as a perturbation on CNN is equally of importance as the rest of two channels. Maps from the two other channels are perturbed by weaker perturbation compared with those added on maps from blue color channel. We implement the above methodology, attempting to achieve better visualization effects without confining pixel values of the adversarial examples. To verify the effectiveness of our color-channel-based operation, three groups of adversarial examples are generated, with each group containing three generated examples being strongly perturbed on R, G, and B channels, respectively. The adversarial examples are shown in Figure 4.

4. Experiments and Evaluations

4.1. Experimental Setup. The performance of SparseAdv on four networks: ResNet-50 [30], VGG-16 [31], GoogleNet [32], and MobileNet-v2 [33], was evaluated on dataset ImageNet-1000 [34]. Various experiments were set for different tasks: (1) for algorithm efficiency evaluation, SparseAdv was compared to AdvGAN [10], TREMBA [17], and ColorFool [24] in terms of generation efficiency of adversarial examples; (2) a transfer matrix was demonstrated to show transferability among the four networks (ResNet-50, VGG-

TABLE 3: Transferability of universal adversarial examples.

	MobileNet-v2	ResNet-50	VGG-16	GoogleNet	AlexNet	DenseNet	ResNet-152	ResNet-34
Universal adversarial example	95.98	97.32	96.65	95.06	75.46	86.75	82.09	88.24

∗The transferability is represented by attack successful rate (%) when the universal adversarial examples are fed into different deep learning models.

16, GoogleNet, and MobileNet-v2) and other networks including AlexNet [2], DenseNet [35], ResNet-152 [30], and ResNet-34 [30]; (3) SparseAdv was compared to AdvGAN [10], TREMBA [17], and ColorFool [24] to demonstrate its performance on reducing visual sense. Additionally, key parameters of the compared experiments are the default given optimal parameters by the previous researches as demonstrated in the literature for fair comparison.

Two indicators including attack successful rate (i.e., statistics the ratio of examples that are misclassified after attack from correctly classified before) and time of batch generation (i.e., record the time of generating 1000 adversarial-samples) were used for evaluating.

4.2. Comparison Experiments among Algorithms

4.2.1. Algorithm Efficiency. We set 1000 samples as a batch and compared the sample generating time by different algorithms. As shown in Table 1, SparseAdv achieves relatively high attack successful rate among the comparison results, whereas time consumption of each algorithm for generating adversarial examples demonstrates that SparseAdv saves considerable time compared to other algorithms.

4.2.2. Visual Comparisons. Several adversarial examples generated by the four algorithms are shown in Figure 5. It can be seen that those adversarial examples look similar, but SparseAdv realizes better visualization through our special perturbation adding approach. Compared to the rest of the adversarial attack algorithms, ours have finer-grained scratch at the background and are the most similar to the original images.

4.3. Transferability Evaluation. White-box attack was firstly conducted on each one of the four source models (ResNet-50, VGG-16, GoogleNet, and MobileNet-v2) and adversarial attack was transferred to the rest of the three models to evaluate the transferability of the proposed algorithm. The same attack was then conducted simultaneously on the four models. That is, the average of their four loss functions was used as an overall loss function for updating sparse mapping network to generate universal adversarial examples. We used those universal adversarial examples to test their transferability on the four target classifiers, and further tested their transferability on other target classifiers (AlexNet, DenseNet, ResNet-152, and ResNet-34). As shown in Table 2, the first four models in the left column are source models. And the four models in the top row are target models. Attack successful rate is used as transferability metric. As can be seen in the four rows of the table, values on the diagonal line from the upper left to the lower right are higher than the others. While the target model is different from the source model, attack successful rate drops down to different degrees. Structures and parameters of a

neural network are formulated from the feedback of its loss function [7]. The descendent and converge of the loss function guide the search to perturbation distributions. So, the searched perturbation distributions have strong correlation with such network's structure. When adversarial examples transfer among target models which have similar structures, they tend to be more transferable, and vice versa. That is the reason why adversarial examples' transferability shown in Table 2 is unstable.

Results in Table 3 reveal that transferability of the generated universal adversarial examples are more stable and higher. Because the universal adversarial examples are generated by the network which is used to simultaneously attack the four networks, they would then contain general information related to the four models' structures. Thus, the perturbation distributions would contain general structure information for more other models with higher probability, therefore easier to be transferable to more models which share this general structure information. Experimental results demonstrate that the four target models could be attacked with successful rate of no less than 95%. In addition, more neural networks with similar structure of all four target models could be successfully attacked by the universal adversarial examples, with a successful rate of no less than 75%.

5. Conclusion

In this paper, the purpose is to realize adversarial attack with better balance among attack ability, less time consumption, and more imperceptible visual result. Searching space is enlarged to obtain adversarial information, which could be used as the adversarial perturbation of the input example. A sparse mapping network is trained for fast adversarial perturbation generation and save considerable time than the traditional adversarial attack algorithms which need significant iterations for updating each input with pixels. To improve searching efficiency, KLD loss is introduced to selectively suppress unnecessary neurons, thus effectively reduces computation complexity. Based on eye sensitivity of different color channels, we add stronger perturbations on the B channel and add relatively weak noise on R and G channels to minimize the modifications under relatively eye-sensitive channels, for the goal of reducing the visual perception of the perturbations. SparseAdv could search universal adversarial information that contains general structure information for more models. Thus, the adversarial examples generated by those universal adversarial information have relatively high transferability. Experimental results show that the proposed SparseAdv spends 13.30 s on average, for generating 1000 adversarial examples, with an average successful rate of 96.99%, against four target deep learning models.

Data Availability

Conflicts of Interest

The authors declare that there is no conflict of interest regarding the publication of this paper.

Acknowledgments

References

[1] D. Lu and Q. Weng, "A survey of image classification methods and techniques for improving classification performance," *International Journal of Remote Sensing*, vol. 28, no. 5, pp. 823–870, 2007.

[2] A. Krizhevsky, I. Sutskever, and G. E. Hinton, "ImageNet classification with deep convolutional neural networks," *Advances in Neural Information Processing Systems*, vol. 25, pp. 1097–1105, 2012.

[3] K. He, X. Zhang, S. Ren, and J. Sun, "Delving deep into rectifiers: surpassing human-level performance on ImageNet classification," in *In Proceedings of the IEEE international conference on computer vision*, pp. 1026–1034, Santiago, Chile, 2015.

[4] O. Abdel-Hamid, A.-r. Mohamed, H. Jiang, L. Deng, G. Penn, and D. Yu, "Convolutional neural networks for speech recognition," *IEEE/ACM Transactions on audio, speech, and language processing*, vol. 22, no. 10, pp. 1533–1545, 2014.

[5] Z.-Q. Zhao, P. Zheng, S.-t. Xu, and X. Wu, "Object detection with deep learning: a review," *IEEE transactions on neural networks and learning systems*, vol. 30, no. 11, pp. 3212–3232, 2019.

[6] A. I. Maqueda, A. Loquercio, G. Gallego, N. Garc'ıa, and D. Scaramuzza, "Event-based vision meets deep learning on steering prediction for self-driving cars," in *In Proceedings of the IEEE Conference on Computer Vision and Pattern Recognition*, pp. 5419–5427, Salt Lake City, 2018.

[7] I. J. Goodfellow, J. Shlens, and C. Szegedy, "Explaining and harnessing adversarial examples," https://arxiv.org/abs/1412.6572.

[8] C. Szegedy, W. Zaremba, I. Sutskever et al., "Intriguing properties of neural networks," https://arxiv.org/abs/1312.6199.

[9] N. Carlini and D. Wagner, "Towards evaluating the robustness of neural networks," in *In 2017 ieee symposium on security and privacy (sp)*, pp. 39–57, San Jose, CA, USA, 2017.

[10] C. Xiao, B. Li, J. Y. Zhu, W. He, M. Liu, and D. Song, "Generating adversarial examples with adversarial networks," https://arxiv.org/abs/1801.02610.

[11] C.-C. Tu, P. Ting, P.-Y. Chen et al., "AutoZoom: autoencoder-based zeroth order optimization method for attacking black-box neural networks," in *Proceedings of the AAAI Conference on Artificial Intelligence*, pp. 742–749, Honolulu, Hawaii, USA, 2019.

[12] A. Kurakin, I. Goodfellow, and S. Bengio, "Adversarial machine learning at scale," https://arxiv.org/abs/1611.01236.

[13] A. Madry, A. Makelov, L. Schmidt, D. Tsipras, and A. Vladu, "Towards deep learning models resistant to adversarial attacks," https://arxiv.org/abs/1706.06083.

[14] Y. Dong, F. Liao, T. Pang et al., "Boosting adversarial attacks with momentum," in *In Proceedings of the IEEE conference on computer vision and pattern recognition*, pp. 9185–9193, Salt Lake City, 2018.

[15] C. Xie, Z. Zhang, Y. Zhou et al., "Improving transferability of adversarial examples with input diversity," in *In Proceedings of the IEEE/CVF Conference on Computer Vision and Pattern Recognition (CVPR)*, pp. 2730–2739, Long Beach California, June 2019.

[16] Y. Dong, T. Pang, H. Su, and J. Zhu, "Evading defenses to transferable adversarial examples by translation-invariant attacks," in *In Proceedings of the IEEE/CVF Conference on Computer Vision and Pattern Recognition*, pp. 4312–4321, Long Beach California, 2019.

[17] Z. Huang and T. Zhang, "Black-box adversarial attack with transferable model-based embedding," https://arxiv.org/abs/1911.07140.

[18] D. Wierstra, T. Schaul, T. Glasmachers, Y. Sun, J. Peters, and J. Schmidhuber, "Natural evolution strategies," *The Journal of Machine Learning Research*, vol. 15, no. 1, pp. 949–980, 2014.

[19] S. Jandial, P. Mangla, S. Varshney, and V. Balasubramanian, "AdvGAN++: harnessing latent layers for adversary generation," in *In Proceedings of the IEEE/CVF International Conference on Computer Vision (ICCV) Workshops*, Seoul Korea, 2019.

[20] X. Liu and C.-J. Hsieh, "Rob-GAN: generator, discriminator, and adversarial attacker," in *In Proceedings of the IEEE/CVF Conference on Computer Vision and Pattern Recognition (CVPR)*, pp. 11234–11243, Long Beach California, June 2019.

[21] Z. Zhao, D. Dua, and S. Singh, "Generating natural adversarial examples," https://arxiv.org/abs/1710.11342.

[22] D. Deb, J. Zhang, and A. K. Jain, "AdvFaces: Adversarial face synthesis," https://arxiv.org/abs/1908.05008.

[23] L. Mescheder, S. Nowozin, and A. Geiger, "The numerics of GANs," *In Advances in Neural Information Processing Systems*, vol. 30, 2017.

[24] A. S. Shamsabadi, R. Sanchez-Matilla, and A. Cavallaro, "ColorFool: semantic adversarial colorization," in *In IEEE/CVF Conference on Computer Vision and Pattern Recognition (CVPR)*, pp. 1151–1160, 2020.

[25] A. Bhattad, M. J. Chong, K. Liang, B. Li, and D. A. Forsyth, "Unrestricted adversarial examples via semantic manipulation," https://arxiv.org/abs/1904.06347.

[26] X. Dong, J. Han, D. Chen et al., "Robust superpixel-guided attentional adversarial attack," in *In IEEE/CVF Conference on Computer Vision and Pattern Recognition (CVPR)*, pp. 12895–12904, 2020.

[27] D. HJA, B. JK, and M. JD, "Human visual pigments microspectrophotometric results from the eyes of seven persons," *Proceedings of the Royal society of London. Series B. Biological sciences*, vol. 220, pp. 115–130, 1983.

[28] C. M. Cicerone and J. L. Nerger, "The relative numbers of long-wavelength-sensitive to middle-wavelength- sensitive

cones in the human fovea centralis," *Vision Research*, vol. 29, no. 1, pp. 115–128, 1989.

[29] N. Carlini and D. Wagner, "Towards evaluating the robustness of neural networks," in *In 2017 IEEE Symposium on Security and Privacy (SP)*, pp. 39–57, San Jose, CA, USA, 2017.

[30] K. He, X. Zhang, S. Ren, and J. Sun, "Deep residual learning for image recognition," in *In Proceedings of the IEEE Conference on Computer Vision and Pattern Recognition (CVPR)*, pp. 770–778, Las Vegas, Nevada, USA, 2016.

[31] K. Simonyan and A. Zisserman, "Very deep convolutional networks for large-scale image recognition," https://arxiv.org/abs/1409.1556.

[32] C. Szegedy, W. Liu, Y. Jia et al., "Going deeper with convolutions," in *Proceedings of the IEEE Conference on Computer Vision and Pattern Recognition (CVPR)*, pp. 1–9, Boston, Massachusetts, USA, 2015.

[33] M. Sandler, A. Howard, M. Zhu, A. Zhmoginov, and L.-C. Chen, "MobileNetV2: inverted residuals and linear bottlenecks," in *In Proceedings of the IEEE Conference on Computer Vision and Pattern Recognition (CVPR)*, pp. 4510–4520, Boston, 2018.

[34] O. Russakovsky, J. Deng, H. Su et al., "ImageNet large scale visual recognition challenge," *International Journal of Computer Vision*, vol. 115, no. 3, pp. 211–252, 2015.

[35] G. Huang, Z. Liu, V. Laurens, and K. Q. Weinberger, "Densely connected convolutional networks," in *In Proceedings of the IEEE conference on computer vision and pattern recognition 2017*, pp. 4700–4708, Las Vegas, Nevada, USA, 2016.

Research Article

Research on Intelligent Fault Diagnosis of Rolling Bearing Based on Improved ShufflenetV2-LSTM

Shaohui Ning [iD],[1] **Yansong Wang** [iD],[1] **Wenan Cai,**[2] **Zhenlin Zhang,**[3] **Yukun Wu,**[1] **Yonglei Ren,**[1] **and Kangning Du**[1]

[1]*School of Mechanical Engineering, Taiyuan University of Science and Technology, Taiyuan, Shanxi 030024, China*
[2]*School of Mechanical Engineering, Jinzhong University, Shanxi 030619, China*
[3]*North Automatic Control Technology Institute, Shanxi 030006, China*

Correspondence should be addressed to Shaohui Ning; ningshaohui@tyust.edu.cn

The timing characteristics of the fault vibration signal of the rolling bearing are ignored by the ShufflenetV2 network. For the bearing fault problem of multiple working conditions, the fault diagnosis signal is extracted by the feature, which cannot be performed efficiently and accurately. The ShufflenetV2 network has a deep number of layers and a large amount of parameters, which causes the network to be prone to overfitting. In response to the above problems, an improved ShufflenetV2-LSTM intelligent fault diagnosis system is proposed, which is a model in which the long short-term memory network (LSTM) layer and the Dropout layer are serially embedded in the ShufflenetV2 network. This method preserves the ability of the ShufflenetV2 network to extract features, and the advantage of the ability of LSTM to strengthen the data sequence is also inherited, so this improves the accuracy of fault diagnosis. The generalization ability of the model can be enhanced by Dropout, which can effectively suppress the degree of overfitting. In addition, this paper also optimized the activation function and optimizer in the model to make up for the additional time cost brought by the Dropout layer, so that the robustness of the system is improved and fault diagnosis can be analyzed efficiently. Experimental analysis shows that the diagnosis accuracy of the proposed algorithm is as high as 97% and early failures of rolling bearings can be effectively identified in real time.

1. Introduction

The rolling bearing in the mechanical transmission system is a key component, and its failure causes the equipment to be eccentrically loaded or the machine is destroyed. However, in actual production activities, due to internal factors (such as parts wear) or environmental factors (such as rapid temperature change), the occurrence of system failure is inevitable. Therefore, the early fault diagnosis of the rolling bearing is of great significance [1, 2]. A large amount of knowledge storage in signal processing is needed in the field of traditional fault diagnosis [3]. With the development of intelligent fault diagnosis methods, the ability of shallow machine learning structures to learn complex feature relationships is very limited [4]. All the above deep learning algorithms have been introduced in the field of

bearing fault diagnosis in recent years, making it more intelligent [5].

Deep learning is a branch of machine learning where multiple layers of data processing units are assembled into a deep architecture to extract multiple levels of data abstraction, and each layer automatically learns higher level of data representations from the output of the previous layer [6]. With the significant advantage of automatically learning data representations, it is considered as an advanced technique in big data analysis [7]. Therefore, deep learning-based intelligent diagnostic methods are more flexible and capable to deal with difficulties in real-world applications than traditional machine learning-based methods [8].

Most of the researches have realized the detection of bearing composite fault and fault degree through the analysis of vibration signals on experimental data or real-world

data. For instense, Zhang C install accelerometers on the running parts of high-speed trains to collect vibration signals and use adaptive deep filtering technology to realize composite fault detection of train bearings [9].

In 2012, the classic Alexnet network was the first to be applied to image classification and achieved excellent results [10]. Then, a large number of researchers applied the CNN model to the field of mechanical fault diagnosis and achieved remarkable success [11]. For example, Lu et al. proposed to convert one-dimensional vibration signals into two-dimensional gray maps and then use CNN for classification [12]. Li et al. proposed an intelligent fault diagnosis method for rolling element bearings based on the deep distance metric learning [13]. The VGG-16 network is used to process grayscale image signals [14]. The ShufflenetV2 network was used to process the two-dimensional time-frequency diagram of the fault signal, and it was found that the diagnosis result was better than other networks through a large number of experiments [15]. However, in complex working conditions and many types of faults, the diagnostic effect of a single CNN model is not ideal [16].

With the continuous improvement and development of intelligent fault diagnosis research, it is no longer enough to diagnose simple faults. In complex multiconditions or multiposition rolling bearing faults, the concept of time sequence needs to be introduced [17]. In other words, the ability to diagnose faults can be improved by realizing the connection of time information before and after. LSTM has the ability to remember information and transmit long-term time series information [18]. It is very effective to deal with a large amount of fault vibration data. The combination of whale algorithm and Adam optimizer optimizes LSTM, and the IWOA-LSTM algorithm is used for fault diagnosis [19]. After the signal is denoised by improved VMD, the variance is calculated. It inputs into LSTM network for rolling bearing life prediction [20]. However, the methods proposed in the above documents require feature preprocessing on the collected vibration signals, which does not meet the current requirements for real-time performance [21].

In response to the above problems, the lightweight ShufflenetV2 network is selected as the main body, in this article, and LSTM is embedded in it, constructing an improved ShufflenetV2-LSTM intelligent fault diagnosis system. In view of the fact that LSTM strengthens the time sequence of the data in order to learn hidden features, combining the ability to extract features and the advantages of lightweight networks, ShufflenetV2 deep structure makes up for the shortcomings of the single CNN model. This paper also uses Dropout layer to suppress the model overfitting, changes all the activation functions in the model to LeakyRelu, and uses the RMSprop algorithm to optimize the cross-entropy function. At the end of this article, we use ablation experiments and compare with other deep learning methods. The results show that the improved ShufflenetV2-LSTM system performs very well in terms of diagnostic efficiency and accuracy.

In summary, the main contributions of this study are shown as follows:

(1) The original vibration signal was decomposed by VMD to obtain several IMF components. The first three IMF components with the minimum envelope entropy were selected to reconstruct the signal, and the one-dimensional reconstructed signal was used to construct a 32 by 32 two-dimensional characteristic matrix by transverse interpolation

(2) In order to make use of LSTM's sensitivity to timing signals, the ShufflenetV2 network is selected as the main trunk, and LSTM modules are embedded in series after ShufflenetV2's global pooling layer. In order to reduce the degree of overfitting, an improved ShufflenetV2-LSTM intelligent fault diagnosis model for rolling bearings is proposed by connecting the Dropout layer after the LSTM

(3) The addition of Dropout layer to the ShufflennetV2-LSTM model brings additional time cost and reduces the overall robustness of the system. Therefore, the activation function and optimizer are optimized in this paper to solve this problem and improve also the diagnostic accuracy of the model

(4) Compared with other models the experimental results show that the proposed method can effectively diagnose faults. The process of LSTM learning fault features is shown by visualization technology

This paper is organized as follows: the theoretical background is given in Section 2. Section 3 presents the improved ShufflenetV2-LSTM fault diagnosis method. The implementation of the proposed method to deal with the fault diagnosis of data in Western Reserve University is illustrated in Section 4. Conclusions and future work are provided in Section 5.

2. The Basic Theory of the Model

2.1. ShufflenetV2. Traditional CNN models include convolutional layers, pooled layers, and fully connected layers. The existence of large convolution kernels and pooling layers makes the model computationally large. The model depth and size are increasing to improve the accuracy of the model. For some specific application scenarios such as mobile devices, because of their limited performance, the model requires high precision and small size.

ShuffleNetV1 solves the above problems. Based on the "Four Principles of Efficient Networks," ShufflenetV2 is modified from the ShufflenetV1 network and verified the superiority of ShufflenetV2 [22]. As a lightweight network, the structure of ShufflenetV2 is shown in Table 1. Each stage unit in the table is stacked by the unit structure shown in Figures 1(a) and 1(b).

When Stride = 1, the structure shown in Figure 1(a) is adopted. In order to meet the same number of input and output feature matrix channels in the G1 criterion.Firstly, the unit uses "Chanel Split" to divide the input feature channel into two parts c-c$'$and c$'$. Secondly, one of the branches

TABLE 1: ShufflenetV2 structure.

Layer	Convolution kernel	Stride	Repeat	Output channel
Conv1	3×3	2	1	24
Max pool	3×3	2	1	24
Stage 2		2	1	116
		1	3	
Stage 3		2	1	232
		1	7	
Stage 4		2	1	464
		1	3	
Conv5	1×1	1	1	1024
Global pool	7×7		1	
FC				40

is connected by a shortcut, and the other branch is used to deepen the number of network layers through 3-layer convolution. Finally, the left and right branches are connected in series through "Concat".

When Stride = 2, the structure shown in Figure 1(b) is adopted. This unit eliminates "Chanel Split" and performs convolution operations on the two branches, respectively. Therefore, the input feature width and height are reduced to achieve spatial downsampling. In order to compensate for the sudden decrease in parameters, the output results on the two branches are concatenated to double the channel.

At the end of the two units, channel shuffle is required to disrupt the order of output channels and ensure the exchange of characteristic information between the two branches.

ShufflenetV2 is the same as other lightweight models by scaling the number of filters to change the complexity of the model; "ShufflenetV2 s ×" means the complexity roughly s^2 times of ShufflenetV2 1 ×, but in this paper, we only consider ShufflenetV2 1 × case.

2.2. Long Short-Term Memory Network (LSTM).

LSTM is a variant of recurrent neural network (RNN) and solves the problem of gradient disappearance and gradient explosion [23]. The core design of LSTM is the cell state and the "gate" structure. The cellular state acts as a pathway for information to travel through a sequence. In theory, cell states can transmit information about sequence processing all the way down. Thus, even information of earlier time steps can be carried into the cells of later time steps, which overcomes the effect of short-term memory. Information is added and removed through a "gate" structure, which learns what information to save or forget during training. LSTM cleverly combines short- and long-term memory through gate control, which can effectively process time series signals, as shown in Figure 2 [24]. Therefore, it is more reasonable to use LSTM to process vibration signals with temporal characteristics on the basis of extracting features by CNN.

LSTM is mainly composed of input gate, forget gate, and output gate. In part one, the old information to be discarded is determined through the forgetting gate, and the input x_t at

t time and the output h_{t-1} of the hidden layer at the previous moment are used as the input of the forgetting gate. The calculation formula is as follows:

$$f_t = \text{sigmoid}\left(W_f \times [h_{t-1}, x_t] + b_f\right), \quad (1)$$

where sigmoid is the sigmoid activation function, W_f is the weight of the forgetting gate, b_f is the bias of the forgetting gate, and f_t is a measure of the importance of past memories.

In part two, the new information to be remembered is determined through the input gate. The input x_t at t time and the output of the hidden layer at the previous time are again calculated through formulas (2) and (3) to obtain the new information importance measurement factor i_t and candidate vector C_h. Finally, the cell state is updated by formula (4).

$$i_t = \text{sigmoid}(W_i \times [h_{t-1}, x_t] + b_i), \quad (2)$$

$$C_h = \tanh\left(W_c \times [h_{t-1}, x_t] + b_c\right), \quad (3)$$

$$C_t = f_t \times C_{t-1} + i_t \times C_h, \quad (4)$$

where W_i and W_c are the input gate weight and b_i and b_c are the input gate bias. C_{t-1} is the cell state at the previous moment, and C_t is the cell state of the updated input gate.

In part three, the output gate combines the results of the forget gate, and the final information to be output is determined. Firstly, the state of the cell at time t -1 is calculated by formula (5) to obtain part of the output O_t. What is more, the cell state at time t is normalized through the tanh function. Finally, multiply the two by formula (6) as the final output result.

$$o_t = \text{sigmoid}(W_o \times [h_{t-1}, x_t] + b_o), \quad (5)$$

$$h_t = o_t \times \tanh\left(C_t\right), \quad (6)$$

where W_o is the output gate weight and b_o is the output gate bias.

This study uses the sensitivity of LSTM to time series data and embeds LSTM in series after the global pool of ShufflenetV2 to strengthen the timing correlation of signals and suppress irrelevant features to improve training accuracy.

2.3. Dropout.

Compared with the training sample, there are too many parameters in the network model, which makes the training model prone to overfitting—the accuracy of the model on the training data is higher, but the accuracy on the test data is lower [25].

Stringing the Dropout layer in the network model can effectively improve the overfitting phenomenon [26]. In each training batch, the working principle of Dropout is to randomly shield some neurons each time by ignoring the connections between some neurons with a certain probability, as shown in Figure 3.

If N is the number of hidden cells in any layer, P is the probability of retaining a cell. In the expected case, only P

(a) Stride = 1: basic unit

(b) Stride = 2: unit for spatial down sampling
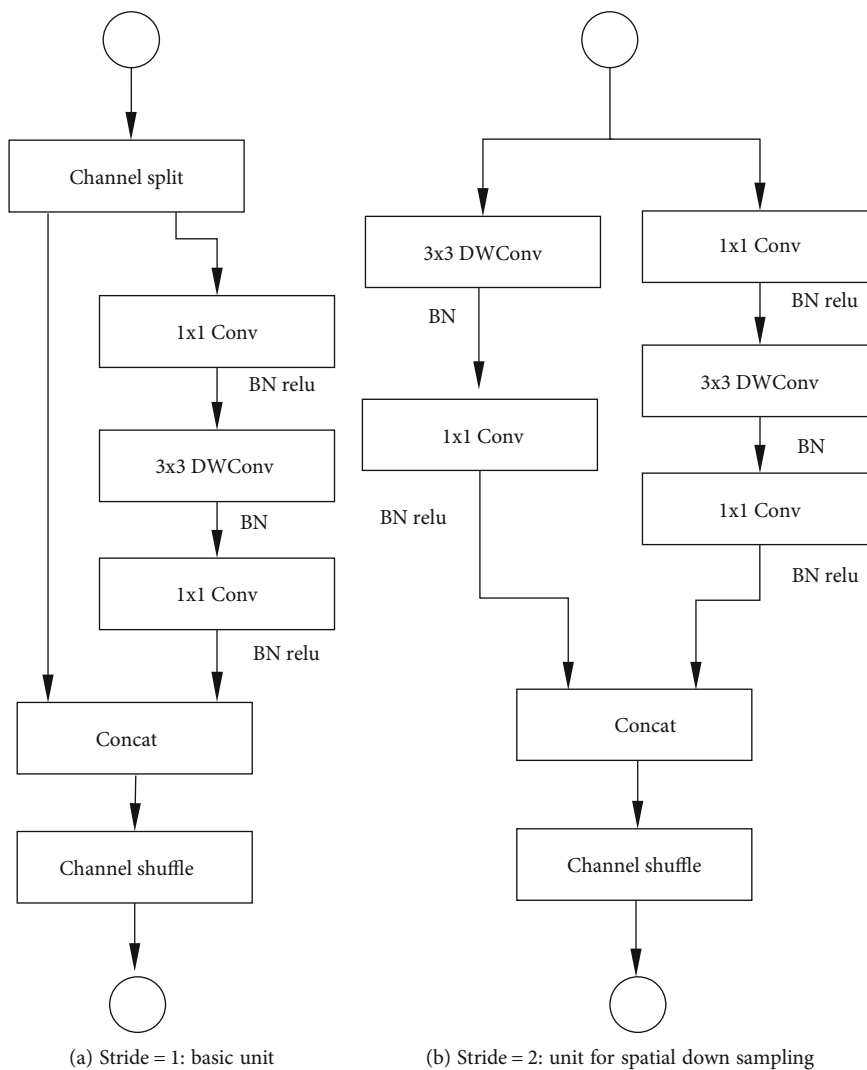
FIGURE 1: Blocks of ShufflenetV2 2.2 long short-term memory network (LSTM).

FIGURE 2: LSTM structure.

(a) Standard neural net

(b) After applying Dropout
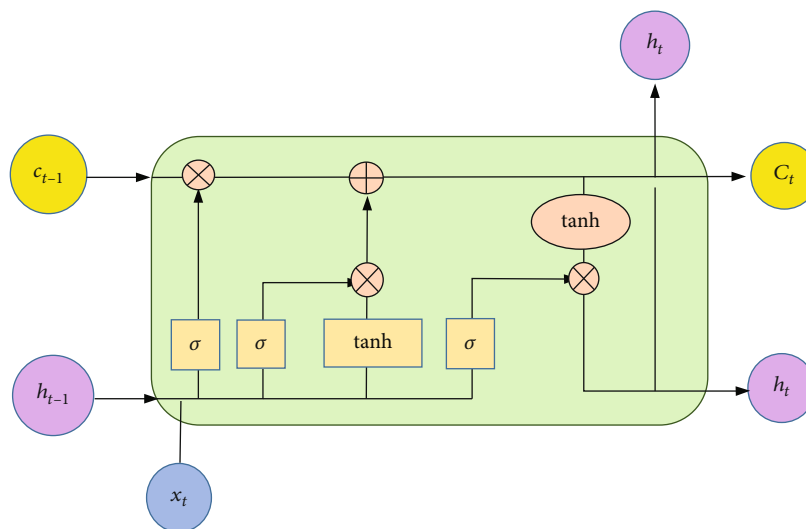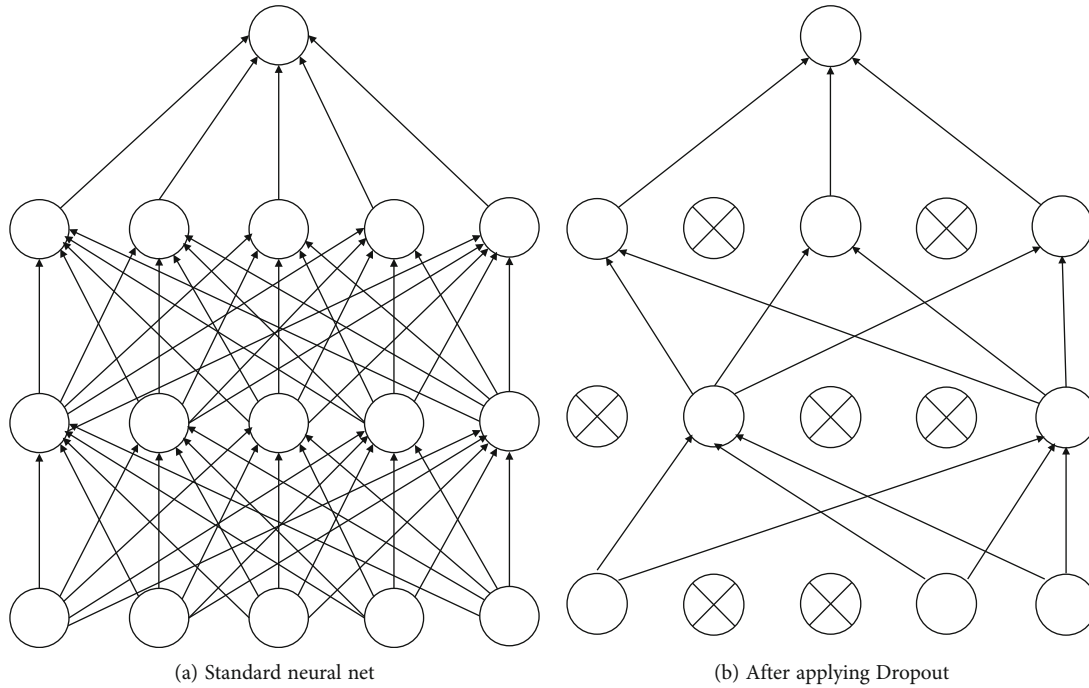
FIGURE 3: Dropout principle.

$\times N$ units will appear after the Dropout layer, instead of N hidden cells. This group of $P \times N$ units varied each time and did not allow the units to build coadaptations freely. Therefore, if a layer of size N is optimal for a standard neural network for any given task, then a good exit network should have at least N/P units.

Applying Dropout layer to a neural network is equivalent to extracting a "refined" network from it. The refined network consists of all the units that have survived from Dropout (Figure 3 (b)). Dropout introduces an additional hyperparameter, the probability of retaining unit P. This hyperparameter controls the intensity of Dropout. $P = 1$ means no Dropout, and a low P value means more Dropout. Typical P values for hidden units range from 0.5 to 0.8. A small P will slow down the training speed and lead to underfitting. Large P may not produce enough Dropout to prevent overfitting. According to experience, P is 0.5 in this study.

In this way, each neuron is not sensitive to another specific neuron. The parameters will not rely too much on the training data, which greatly enhances the generalization ability of the model. The Dropout layer connects to the back of the network which is more effective and needs to work with the fully connected layer. Therefore, a fully connected layer (FC1) and a layer of Dropout are serially connected after the LSTM, as shown in Figure 4.

3. The Improved ShufflenetV2-LSTM Rolling Bearing Fault Diagnosis System

The single ShufflenetV2 network cannot diagnose the bearing faults efficiently for multiposition and multiworking conditions. In order to introduce timing characteristics, improve training accuracy, and reduce overfitting degree, the ShufflenetV2 network is selected as the main stem in this paper. LSTM and Dropout modules are embedded in series after ShufflenetV2's global pool layer. An improved ShufflenetV2-LSTM fault diagnosis method is proposed. Combined with the sensitivity of LSTM to time series data, the system strengthens the time series correlation of signals and restrains irrelevant features to improve the training accuracy of model .In addition, the generalization ability of the model is increased by using Dropout random shielding neurons. However, during the experiment, it was found that the addition of Dropout module would reduce the overall robustness of the system and bring additional computational costs. In this study, we also improved the activation function and optimizer of the model to improve this problem and improve the diagnostic accuracy of the model.

3.1. Optimization Model

3.1.1. Activation Function. When improving the ShufflenetV2-LSTM system to identify bearing faults, the mapping relationship between fault types and labels is complicated. The activation function introduces nonlinear characteristics and transforms the current feature space to another space through a certain mapping [27]. The mapping ability of nonlinear equations for complex data learning is stronger than linear. In order for the data to be better classified, the selection of the activation function is crucial [28].

The activation function used by the original ShufflenetV2 is Relu, and its mathematical expression is as follows [29].

$$\mathrm{ReLU}(x) = \begin{cases} x & x > 0, \\ 0 & x \leq 0. \end{cases} \tag{7}$$
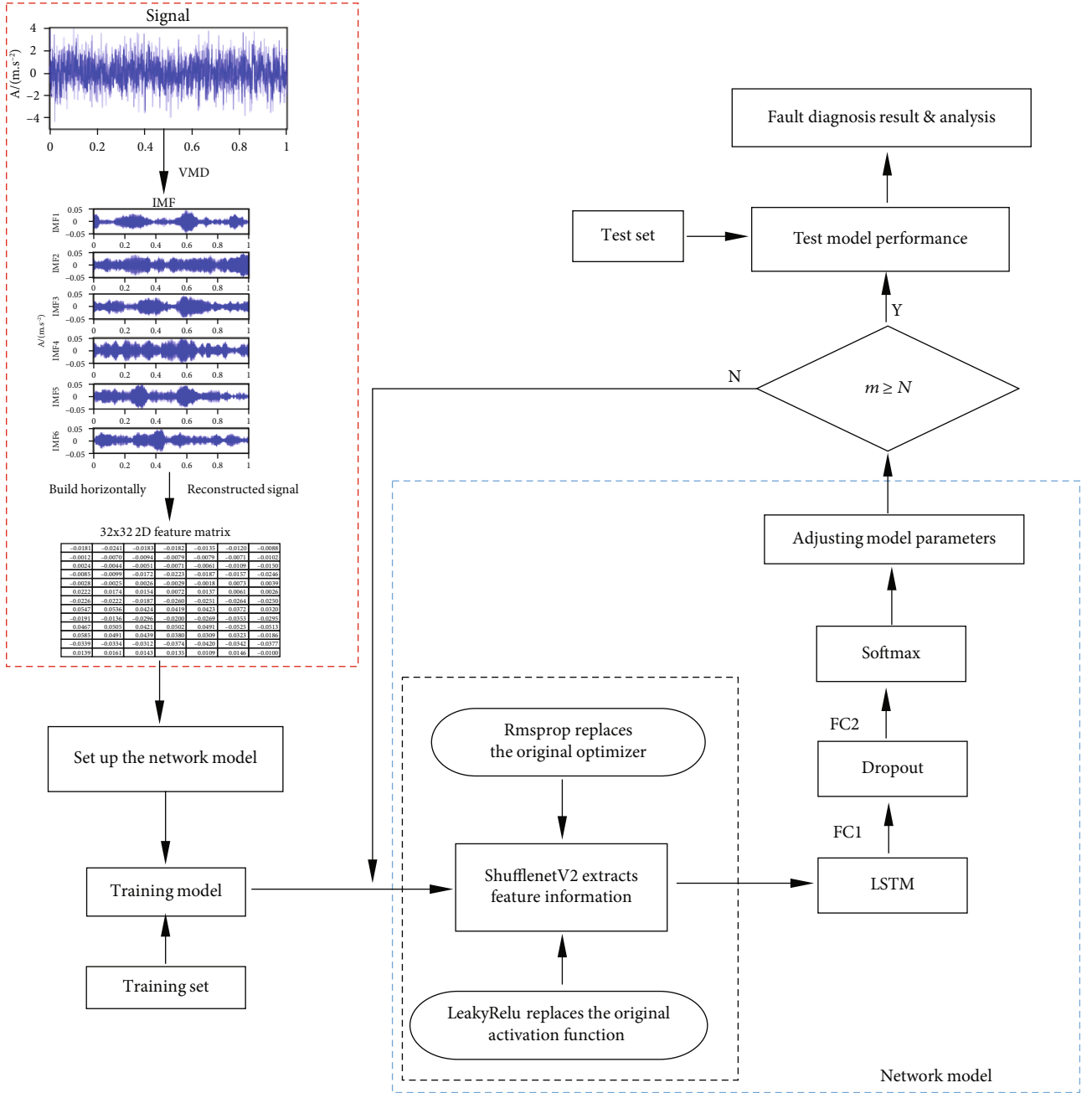
FIGURE 4: Intelligent fault diagnosis flow chart based on the improved ShufflenetV2-LSTM4

It can be seen from the expression that when $x \leq 0$, the output is 0 and its gradient is also 0. The neuron cannot update the parameters, which will cause the network to "necrotize." To solve this problem, the leakage value is introduced in the negative interval to obtain the LeakyRelu function [30].

$$
\text{LeakyReLU}(x) = \begin{cases} x & x > 0, \\ x/a & x \leq 0, \end{cases} \tag{8}
$$

where a is the fixed parameter in the $(1, +\infty)$ and x is the input. According to reference [30], the empirical a value is

100 in the study. By introducing leakage value, unilateral suppression is achieved, and part of negative gradient information is retained so that it is not completely lost. The LeakyRelu function ranges from minus infinity to infinity. This expands the range of values compared to Relu.

In order to accelerate the network convergence and enhance the robustness of the model, this research changes all the Relu in the original model to the LeakyRelu activation function.

3.1.2. Optimizer. During the training period of the model, the optimizer continuously optimizes the value of loss function by updating and calculating the network parameters of

the model, so that the model achieves the global optimal point [31]. In practical application, the selection of loss function and optimizer determines the convergence speed and effect of the model. The inappropriate loss function and the optimizer will cause the model to fall into the local optimal point, which is the value of loss function hovers around the local optimal point, unable to reach the global optimal point, resulting in poor accuracy of the final model.

In this paper, the cross-entropy cost function is used to calculate the difference between the current model probability distribution and the real distribution to obtain the loss function value. Equation (9) is a formula for the cross-entropy cost function, where a is the output value of the neuron activation function and y is the desired output value.

$$C = -\frac{1}{n} \sum [y \ln a + (1-y) \ln (1-a)]. \tag{9}$$

Therefore, the choice of the optimizer plays a crucial role in the training process [32]. RMSprop combines exponential moving average of gradient square to adjust the change of learning rate. This converges well in the case of nonstationary objective functions. The RMSprop optimizer introduces an attenuation factor β on the basis of AdaGrad and avoids the continuous accumulation of second-order momentum by focusing only on the descending gradient of the past period of time, thereby solving the problem of premature end of training [33]. The core part of RMSprop is the second-order momentum, which is calculated as follows:

$$V_t = \beta \times V_{t-1} + (1-\beta)dw^2, \tag{10}$$

where β is the attenuation factor, dw is the current gradient, and V_t is the second-order momentum at time t. Adam is an algorithm that combines the momentum and RMSprop [34].

$$m_t = \beta_1 \times m_{t-1} + (1-\beta_1)dw, \tag{11}$$

$$V_t = \beta_2 \times V_{t-1} + (1-\beta_2)dw^2, \tag{12}$$

where m_t is the first-order momentum, β_1 is the first-order momentum decay factor for formula (11), and other parameters in formula (12) have the same meaning as in formula (10).

Theoretically speaking, the optimization effect of Adam should be better than RMSprop [35], but in the experiment process of this study, it is found that the network model using RMSprop optimizer can converge stably within a certain period of time, but the model using Adam is still oscillating near the optimal value. The reason for the analysis may be that the oscillation of the acceleration learning rate of the first-order momentum in the later training period makes the model difficult to converge.

The improved ShufflenetV2-LSTM fault diagnosis system uses the RMSprop algorithm to optimize the cross-entropy loss function instead of Adam, which makes the network better converge to compensate for the additional time cost of Dropout.

TABLE 2: Experimental data set of CWRU.

Service load	Normal or fault (degree of damage)	Number of samples (training set/testing set)
0/1/2/3	N	100 (80/20)
	IR (7/14/21)	100 (80/20) × 3
	B (7/14/21)	100 (80/20) × 3
	OR (7/14/21)	100 (80/20) × 3

3.2. Improved ShufflenetV2-LSTM Basic Flow. An improved ShufflenetV2-LSTM fault diagnosis method for rolling bearings is proposed in this paper. The basic structure is shown in Figure 4, and the specific steps are as follows:

(1) Collect vibration signals of rolling bearing running state

(2) A series of IMF components were decomposed by VMD algorithm. The first three IMF components were selected to reconstruct the signal according to the envelope entropy value, and a 32 × 32 two-dimensional characteristic matrix was constructed by transverse interpolation

(3) Sample training set and test set are divided according to 8 : 2 ratio

(4) Set up network model and initialize parameters

(5) The training set trains the network model, and the model learns the fault characteristics, uses RMSprop algorithm to calculate the gradient of the loss function, and then updates the parameters

(6) Judge whether the training iteration number M reaches the preset value N. If so, proceed to the next step; otherwise, repeat the training

(7) Test set tests the trained model, outputs evaluation indicators, and finishes the training

The network model in Figure 2 mainly consists of the improved ShufflenetV2 module, the LSTM layer, the Dropout layer, and the Softmax layer. The detailed learning process is as follows: (1) input the 2d eigenmatrix into the network and firstly extract fault features using the improved ShufflenetV2 module; (2) LSTM is used to learn hidden features and discard noise features to retain the main feature information; (3) the Dropout layer is used to hide neurons with a certain probability. After the fault features pass through a full connection layer, Softmax calculates the probability of each type and outputs the fault classification results.

4. Experiments and Results

4.1. Data Set. This article uses a data set from the Rolling Bearing Experimental Center of Case Western Reserve University (CWRU) for experimental verification [36]. The bearing designation is 6205-2RS JEM SKF deep groove ball bearing, and the sampling frequency is 12 kHz. Bearing damage is a single-point damage made by EDM, which can

TABLE 3: Results of ablation experiments with data from CWRU.

Model	LSTM	Optimizer	Factor Dropout	Activation function	Training accuracy (%)	Test accuracy (%)	Time (min)
	0	0	0	0	92.19	88.25	$9'42$
	1	0	0	0	98.44	95.63	$9'57$
ShufflenetV2	0	1	0	0	100	94	$9'44$
	0	0	1	0	91.88	90.75	$20'39$
	0	0	0	1	94.44	89.37	$10'10$
This study	1	1	1	1	100	97.38	$9'23$

TABLE 4: Hyperparameter settings of each model.

Model	LSTM	Optimizer	Activation function	Dropout
Improved Alexnet	Add	RMSprop	LeakyRelu	Delete the original
Improved MobilenetV2	Add	RMSprop	LeakyRelu	Without
Improved Squeezenet	Add	RMSprop	LeakyRelu	Keep the original
Improved Resnet-18	Add	Adam	LeakyRelu	Without
Improved Xception	Add	Adam	LeakyRelu	Without

be divided into three types of failure locations: inner ring, rolling body, and outer ring failure. Each position is divided into 3 different levels of failure: minor failure (7 mils), moderate failure (14 mils), and serious failure (21 mils), plus a group of healthy rolling bearing operating status, a total of ten different bearing operating status. In order to verify that the improved model can be applied to different types of faults in different working conditions, each operating state distinguishes four workloads of 0, 1, 2, and 3 horsepower. Therefore, the data set in this article contains a total of 40 types of rolling bearing operating states, each of which has 100 small samples of data, and each small sample contains 1024 data points. According to reference [36], randomly select 80% of the samples from each type of running state for training set and the remaining 20% for testing set. The samples are arranged out of order. For the convenience of presentation, the inner ring, rolling body, and outer ring are represented by IR, B, and OR, respectively, and the normal state is represented by N. Details of the data set are shown in Table 2.

Before training the model, the data need to be preprocessed. For clarity, take the sample data of 0 horsepower slight inner ring failure as an example. Firstly, the sample of 1024 data points is decomposed by VMD to obtain 7 IMF components. Then the envelope entropy is used as the evaluation criterion [37], and the first three IMFs with the smallest entropy value are selected to reconstruct the signal. In order to meet the instantaneity, the vibration signal is directly used as the training set to maintain the timing characteristics of the vibration signal. Finally, the one-dimensional reconstruction signal is sequentially constructed in a horizontal order to construct a two-dimensional matrix of 32 by 32, which is used as the model input layer.

4.2. Ablation Experiment. In order to show that the various improvements made to the ShufflenetV2 network in this

TABLE 5: Diagnostic results of different models under CWRU bearing data set.

Model	Training accuracy (%)	Test accuracy (%)	Time (min)
Improved Alexnet	40.63	38.75	$25'16$
Improved MobilenetV2	98.44	94.63	$12'59$
Improved Squeezenet	39.04	32.37	$7'49$
Improved Resnet-18	96.88	91.87	$21'53$
Improved Xception	93.76	93.63	$31'53$
This study	100	97.38	$9'23$

article contribute to the improvement of the model's performance, an ablation experiment is carried out, where training accuracy, test accuracy, and training time are mainly used as evaluation indicators. During the experiment, the same sample data set was used, the learning rate was set to 0.001, the loss function used cross-entropy, the training iteration was 30 times, and the minimum batch was 64.

In order to prove that LSTM can improve the accuracy of the model, insert the LSTM after the global pooling layer of the ShufflenetV2 model. In order to prove that Dropout can prevent the model from overfitting, the fully connected layer and Dropout layer are connected in series after the LSTM layer. In order to prove the contribution of LeakyRelu activation function to the model, replace all activation functions in the network with LeakyRelu activation function. In order to prove that the RMSprop optimizer is more suitable for the model and accelerate the stable convergence of the model, a comparative experiment was designed and the Adam optimizer was changed to the RMSprop optimizer.
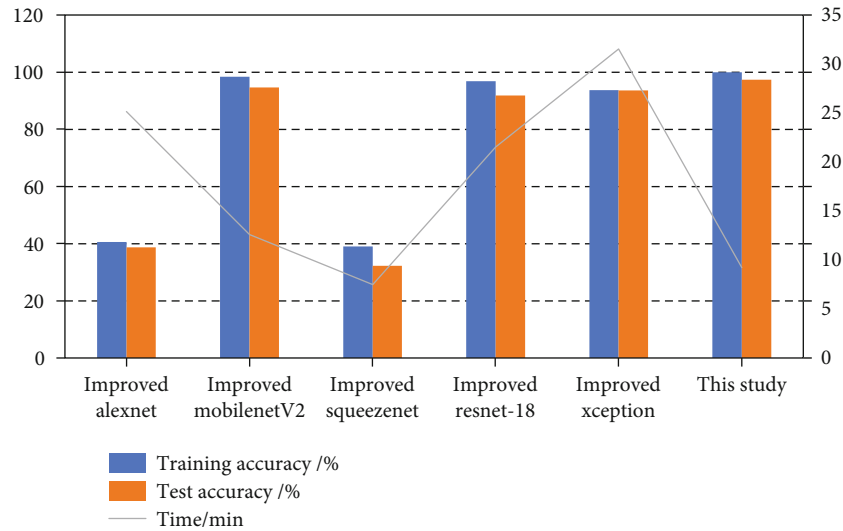
FIGURE 5: Classification accuracy of different algorithms based on the test bearing data set of Western Reserve University.

The experimental results are shown in Table 3. The temporal correlation between vibration data was enhanced by adding LSTM. The running time of the ShufflenetV2 network model is only increased by 15 s, but the accuracy rate can be increased by 7.38%. For the ShufflenetV2 model, the time cost of using RMSprop or Adam is the same basically. The accuracy rate of the model using the Adam optimizer can only oscillate around 92.19% at the end of the training. However, the model using the RMSprop optimizer can stably maintain 100% at the end of training, and the accuracy of the test set is 5.75% higher than that of Adam. This shows that the Adam optimizer will not always perform better than other optimizers, and the choice of optimizer cannot be generalized. Replace all model Relu activation functions with LeakyRelu activation functions to increase a small amount of time cost (28 s) in exchange for a certain classification accuracy rate. The improved model accuracy rate increased by 2.25%. For this model, adding, alone, the Dropout layer can reduce the degree of overfitting the difference between training accuracy, and test accuracy is reduced from 3.94% to 1.13%. However, the accuracy of the model will not be saturated until almost 2 times the time cost before the improvement as a cost. Therefore, it is not advisable to add alone the Dropout layer to avoid overfitting, and other improvements proposed in this paper are needed to compensate for the slow convergence rate and reduce the time cost.

Ultimately, the algorithm proposed in this research, introducing LSTM, selecting the RMSprop optimizer, using the LeakyRelu activation function, and adding the Dropout layer, reduces the degree of overfitting, improving the classification accuracy, and speeds up the model convergence speed to compensate for the additional time cost brought by the Dropout layer. The difference between the prediction accuracy and the training accuracy is reduced from 3.94% before the improvement to 2.62% in the rolling bearing data set. During the training process, the accuracy of the model can be stabilized at 100%, and the test accuracy can be as high as 97.38%, an increase of 9.13% compared to the model before the improvement.

4.3. Algorithm Comparison and Analysis. The current classic popular and lightweight neural network are selected for experimental comparison to compare with the method in this article in order to further verify the performance of this research method in the diagnosis of bearing faults. The experimental model selected Alexnet, MobilenetV2, Squeezenet, Resnet-18, and Xception.

It is necessary to improve the selected network model in order to ensure the fairness of the comparison experiment. Since the optimal hyperparameter settings of each network model are different for different networks, the optimization method proposed in this paper is not necessarily suitable for all the above models. Therefore, each of the above-mentioned network needs to pass ablation experiments to find the best hyperparameter settings of their respective networks with accuracy and time cost as indicators, as shown in Table 4.

A large number of experimental results show that no matter which type of network, embedding the LSTM can effectively improve the original network for the time series vibration signal from Table 4. The choice of the optimizer should be selected appropriately according to different networks. The only model in the table is MobilenetV2, which is replaced with LeakyRelu by the clippedRelu activation function, and the rest are Relu instead of LeakyRelu.

The above-mentioned improved network is compared with the research in this paper. The same sample data set is used during the experiment, and the other parameter settings are the same as those described above. The final experimental results are shown in Table 5 and Figure 5 (the data in Table 5 are plotted in Figure 5). It can be seen that the improved ShufflenetV2-LSTM model training set accuracy rate is the only one to reach 100% and the test set accuracy rate is as high as 97.38%, which is higher than the accuracy rate of other models. In addition, the loss function value is

(a) Features of the Input layer

(b) Features before the LSTM layer

(c) Features behind the LSTM layer

• N-0	• N-1	• N-2	• N-3	• IR 17-0	• IR 17-1	• IR 17-2	• IR 17-3	• IR 35-0	• IR 35-1
• IR 35-2	• IR 35-3	• IR 53-0	• IR 53-1	• IR 53-2	• IR 53-3	• B 17-0	• B 17-1	• B 17-2	• B 17-3
• B 35-0	• B 35-1	• B 35-2	• B 35-3	• B 53-0	• B 53-1	• B 53-2	• B 53-3	• OR 17-0	• OR 17-1
• OR 17-2	• OR 17-3	• OR 35-0	• OR 35-1	• OR 35-2	• OR 35-3	• OR 53-0	• OR 53-1	• OR 53-2	• OR 53-3
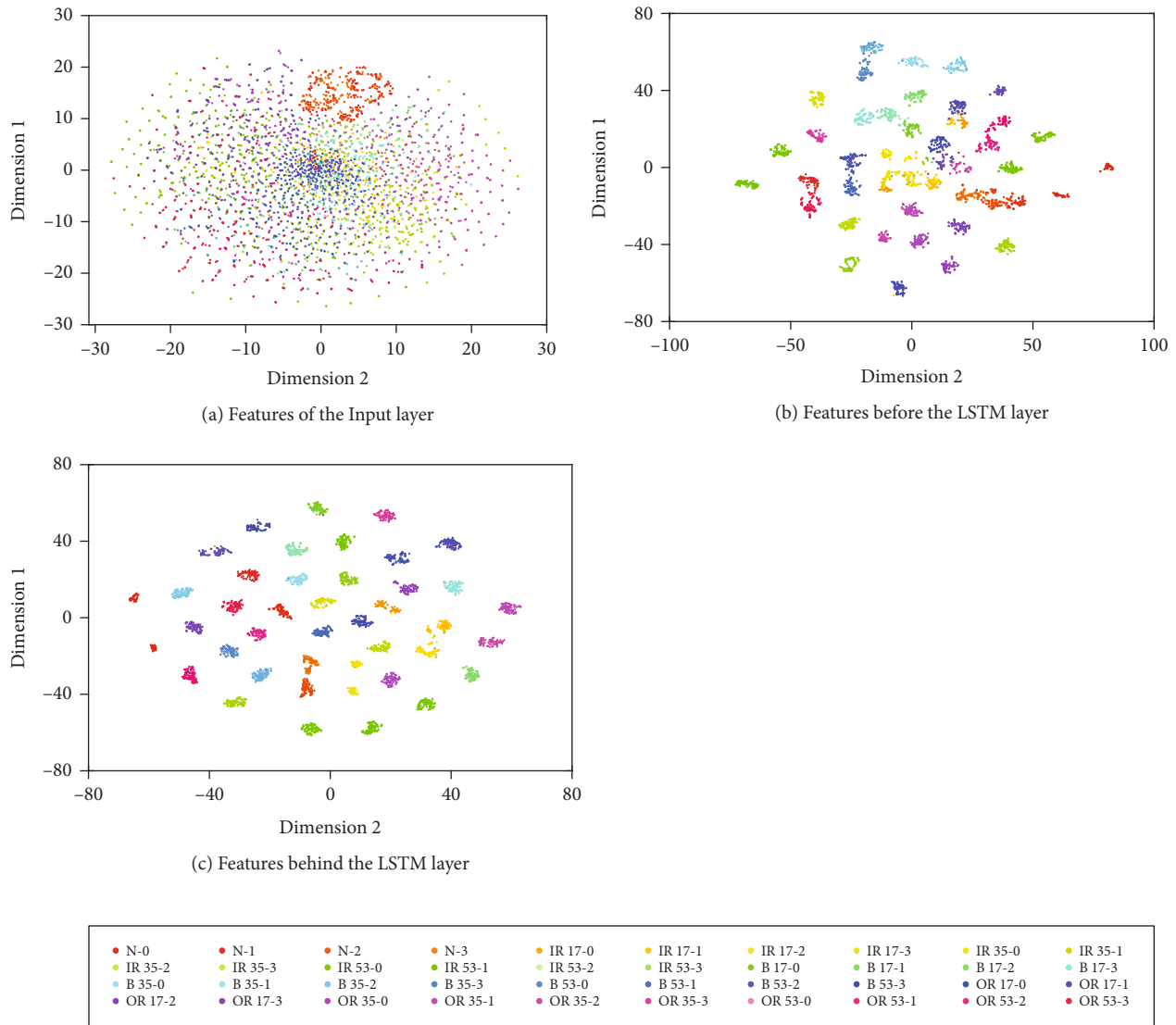
FIGURE 6: Visualization of training process in the improved ShufflenetV2-LSTM model using CWRU data sets 4.5 model generalization ability experiment and result analysis. (a) Features of the input layer. (b) Features before the LSTM layer. (c) Features behind the LSTM layer.

the lowest, indicating that there is little difference between the actual output and predicted value of the model. The training time of this model is shorter compared with other models, which is only longer than the improved Squeezenet model. The improved Squeezenet model has an accuracy rate of only 32.37%. The improved Alexnet is the network with the least number of convolutional layers in the table, with only 8 layers, but the time is nearly 3 times longer than the improved ShufflenetV2-LSTM. The test accuracy rate exceeds 90%: the improved MobilenetV2, the improved Resnet-18, and the improved Xception. However, it is, respectively, 2.75%, 5.51%, and 3.75% lower than the improved ShufflenetV2-LSTM and the time cost is also high. In particular, the Xception training time is 3 times that of the improved ShufflenetV2-LSTM.

Therefore, the improved ShufflenetV2-LSTM proposed in this article stands out in the face of many classification models, with the best timeliness and the highest accuracy,

FIGURE 7: Rolling bearing fault test rig.

(a) Inner ring failure   (b) Rolling body failure   (c) Outer ring failure
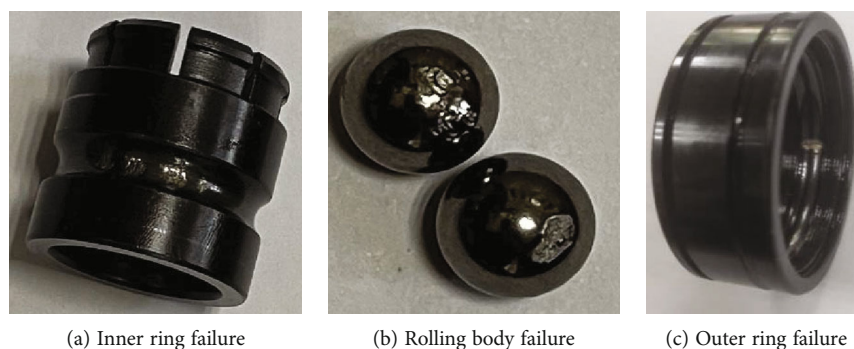
FIGURE 8: Fault bearings at different positions.

and can efficiently and reliably solve the problem of fault diagnosis of rolling bearings.

4.4. Data Visualization. In order to more intuitively study and analyze the model learning process and LSTM classification capabilities proposed, t-SNE (T-Stochastic Neighbor Embedding) technology is used to visualize the feature distribution and analyze the performance of the constructed model [37].

As shown in Figure 6(a), the input data is messy and difficult to classify. Though the features extraction of the multi-convolutional neural layers, some faults can be distinguished effectively. However, different working conditions of the same fault location cannot be effectively distinguished, for instance, the 2 and 3 horsepower conditions with moderate inner ring failure and the 0 and 1 horsepower conditions with serious outer ring failure. In addition, the minor and moderate rolling body failures cannot be effectively distinguished with the same 0 horsepower condition. It can be seen that LSTM strengthens the correlation of data timing characteristics, separating and gathering effectively the above-mentioned confusing faults comparing the two Figures 6(b) and 6(c). This shows that LSTM is sensitive to vibration signals and strengthens the ability to distinguish subtle faults. The model can extract and classify the forty types of fault features of rolling bearings under different working conditions and at different positions in the Figure 6(c). The model can effectively learn different fault features in order to realize diagnosis and classification.

4.5. Model Generalization Ability Experiment and Result Analysis. In order to further verify the generalization ability of the proposed method, a rolling bearing fault test bench was built, as shown in Figure 7. A rolling bearing of TYPE ER-16K was selected to set up inner ring fault, rolling body fault, and outer ring fault, plus a group of healthy bearings. There were four bearing state types, and the specific faults are shown in Figure 8. Twelve kinds of fault signals were measured under 150 kg, 300 kg, and 500 kg loads, respect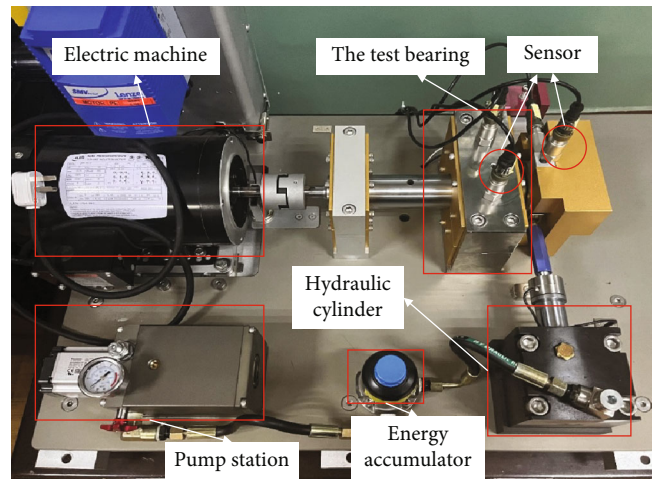ively. The sampling frequency was 12.8 kHz. Each small sample contained 1024 data points, and each type of signal was composed of 1280 small samples. 80% of the samples in the same category were randomly selected as the training set and the rest as the test set from Table 6 for data details. The same pretreatment is performed in Section 3.1: sample

TABLE 6: Data set of 12 bearing states.

Bearing state	Label			Number of samples (training set/testing set)
	150 kg	300 kg	500 kg	
Normal	N-150	N-300	N-500	1280 (1024/256) × 3
Inner ring fault	IR-150	IR-300	IR-500	1280 (1024/256) × 3
Rolling fault	B-150	B-300	B-500	1280 (1024/256) × 3
Outer ring fault	OR-150	OR-300	OR-500	1280 (1024/256) × 3

TABLE 7: Evaluation results of different models.

Model	Training accuracy (%)	Test accuracy (%)	Time (min)
Improved Alexnet	98.44	96.74	$16'40$
Improved MobilenetV2	100	97.66	26.33
Improved Squeezenet	87.50	81.93	$11'41$
Improved Resnet-18	100	98.8	$76'12$
Improved Xception	100	99.09	$70'02$
This study	100	98.86	$14'14$

signals are decomposed by VMD, the first three IMF components with the best entropy are reconstructed, and the two-dimensional characteristic matrix is constructed. The network model mentioned in the previous section is used for fault diagnosis. The results of diagnosis accuracy and training time are shown in Table 7.

It can be seen from Table 7 that when the fault categories are less, the diagnosis effect of the improved Alexnet model becomes better and the accuracy can reach 96.74%, but its accuracy and operation time are still inferior to the algorithm proposed in this paper. The test accuracy of this model is 98.86%, only lower than 99.09% of the improved Xception, but the training time of the improved Xception is up to 70 minutes. In the table, only the improved Squeezenet has a shorter calculation time than the model in this paper, but its test accuracy is 81.93%, which is the lowest among all models.

It can be seen that when the fault category becomes smaller, the gap between the algorithms is narrowed. However, considering the diagnosis accuracy and training time comprehensively, the improved ShufflenetV2-LSTM model still performs best. In addition, combined with the experimental fault diagnosis results in the previous section, it is shown that the proposed algorithm performs better than other algorithms and has certain reliability and generalization ability, which is suitable for intelligent diagnosis of various bearing faults.

5. Conclusion

This study proposes an improved ShufflenetV2-LSTM diagnosis system for the problem of rolling bearing fault diagnosis. Through the experimental study of the bearing failure data set, the following conclusions can be obtained:

(1) This model strengthens the time series correlation between vibration data through LSTM based on the capability to extract fault features of ShufflenetV2. It can be found that the ability to distinguish rolling bearing faults is significantly enhanced from the visual classification results. The experimental results of the two groups also show that compared with other network models, the proposed algorithm model can diagnose rolling bearing faults quickly and effectively and has excellent performance in diagnosis accuracy and training time

(2) In view of the problem of overfitting caused by many model parameters and small sample data, embedding the Dropout layer alone can effectively alleviate the degree of overfitting, but it will cause model instability and bring additional training time costs. This study proposes an improved method of replacing the Relu with LeakyRelu activation function and using the RMSprop optimizer to optimize the cross-entropy function to achieve the purpose of making up for the time cost of the Dropout layer. Experimental verification shows that the proposed improved method can not only avoid overfitting but also meet the real-time requirements

(3) Breaking the convention, this research found that the optimization effect of RMSprop is better than Adam for the model in this paper. It can be seen that the choice of optimizer cannot be generalized. For specific target tasks, how to select a suitable optimizer for a specific network model needs to be further explored in the future

Data Availability

The data used to support the findings of this study have not been made available because they are confidential.

Conflicts of Interest

The authors declare no conflicts of interest.

Authors' Contributions

Shaohui Ning conceived the experiments; Yansong Wang, Yukun Wu, and Yonglei Ren performed the experiments; Yansong Wang and Zhenlin Zhang programed the algorithm; Kangning Du and Wenan Cai processed the data; Shaohui Ning wrote the paper. All authors have read and approved the final manuscript.

Acknowledgments

References

[1] X. Li, J. Cheng, H. Shao, K. Liu, and B. Cai, "A fusion CWSMM-based framework for rotating machinery fault diagnosis under strong interference and imbalanced case," *IEEE Transactions on Industrial Informatics*, p. 1, 2021.

[2] Z. Wang, X. He, B. Yang, and N. Li, "Subdomain adaptation transfer learning network for fault diagnosis of roller bearings," *IEEE Transactions on Industrial Electronics*, vol. 69, p. 1, 2021.

[3] W. Yuanyuan, *Vibration and Acoustic Signal Analysis of Rolling Bearings*, Nanjing University of Aeronautics and Astronautics, 2014.

[4] M. Zhang, X. Li, and R. Wang, "Incipient fault diagnosis of batch process based on deep time series feature extraction," *Arabian Journal for Science and Engineering*, vol. 46, no. 10, pp. 10125–10136, 2021.

[5] X. Li, H. Jiang, M. Niu, and R. Wang, "An enhanced selective ensemble deep learning method for rolling bearing fault diagnosis with beetle antennae search algorithm," *Mechanical Systems and Signal Processing*, vol. 142, article 106752, 2020.

[6] Z. He, H. Shao, Z. Ding, H. Jiang, and J. Cheng, "Modified deep autoencoder driven by multi-source parameters for fault transfer prognosis of aeroengine," *IEEE Transactions on Industrial Electronics*, vol. 69, no. 1, pp. 845–855, 2022.

[7] L. Zhou, C. Zhang, F. Liu, Z. Qiu, and Y. He, "Application of deep learning in food: a review," *Comprehensive Reviews in Food Science and Food Safety*, vol. 18, no. 6, pp. 1793–1811, 2019.

[8] S. Zhang, S. Zhang, B. Wang, and T. G. Habetler, "Deep learning algorithms for bearing fault diagnostics-a review," in *in 2019 IEEE 12th International Symposium on Diagnostics for Electrical Machines, Power Electronics and Drives (SDEMPED)*, pp. 257–263, IEEE, 2019.

[9] C. Zhang, Y. Liu, F. Wan, B. Chen, and J. Liu, "Isolation and identification of compound faults in rotating machinery via adaptive deep filtering technique," *IEEE Access*, vol. 7, pp. 139118–139130, 2019.

[10] Z. Wang, W. Zhao, and W. Du, "Data-driven fault diagnosis method based on the conversion of erosion operation signals into images and convolutional neural network," *Process Safety and Environmental Protection*, vol. 149, pp. 591–601, 2021.

[11] J. Jiao, M. Zhao, J. Lin, and K. Liang, "A comprehensive review on convolutional neural network in machine fault diagnosis," *Neurocomputing*, vol. 417, pp. 36–63, 2020.

[12] C. Lu, Z. Wang, and B. Zhou, "Intelligent fault diagnosis of rolling bearing using hierarchical convolutional network based health state classification," *Advanced Engineering Informatics*, vol. 32, pp. 139–151, 2017.

[13] X. Li, W. Zhang, and Q. Ding, "A robust intelligent fault diagnosis method for rolling element bearings based on deep distance metric learning," *Neurocomputing*, vol. 310, pp. 77–95, 2018.

[14] X. Zhao Yukai and L. M. Gaowei, "Bearing fault diagnosis method based on VGG16 transfer learning," *Spacecraft Environmental Engineering*, vol. 37, no. 5, pp. 446–451, 2020.

[15] H. Liu, D. Yao, J. Yang, and X. Li, "Lightweight convolutional neural network and its application in rolling bearing fault diagnosis under variable working conditions," *Sensors*, vol. 19, no. 22, pp. 4827–4827, 2019.

[16] W. Zhao, Z. Wang, W. Cai et al., "Multiscale inverted residual convolutional neural network for intelligent diagnosis of bearings under variable load condition," *Measurement*, vol. 188, p. 110511, 2022.

[17] C. Baojia, C. Xueli, S. Baoming et al., "Application of CNN-LSTM deep neural network in rolling bearing fault diagnosis," *Journal of Xi'an Jiaotong University*, vol. 55, no. 6, pp. 28–36, 2021.

[18] T. Huang, Q. Zhang, X. Tang, S. Zhao, and X. Lu, "A novel fault diagnosis method based on CNN and LSTM and its application in fault diagnosis for complex systems," *Artificial Intelligence Review*, vol. 55, no. 2, pp. 1289–1315, 2022.

[19] Z. Zhi, Z. Huaqin, and P. Yue, "Fault diagnosis of rolling bearing based on improved whale algorithm to optimize LSTM," *Vibration and Shock*, vol. 40, no. 7, pp. 274–280, 2021.

[20] Z. Liang, J. Cao, X. Ji, and P. Wei, "Fault severity assessment of rolling bearings method based on improved VMD and LSTM," *Journal of Vibroengineering*, vol. 22, no. 6, pp. 1338–1356, 2020.

[21] Z. Wang, J. Zhou, and W. Du, "Bearing fault diagnosis method based on adaptive maximum cyclostationarity blind deconvolution," *Mechanical Systems and Signal Processing*, vol. 162, article 108018, 2022.

[22] M. A. Ning-ning, Z. H. A. N. G. Xiang-yu, and Z. H. E. N. G. Hai-tao, "Shufflenet V2: practical guidelines for efficient CNN architecture design," in *Proceedings of the European conference on computer vision*, pp. 116–131, 2018.

[23] S. Tao and L. Shunsheng, "Batch standardized CNN-LSTM diagnosis method for rolling bearing faults," *Computer Integrated Manufacturing System*, vol. 28, 2021http://kns.cnki.net/kcms/detail/11.5946.TP.20210330.1708.003.html.

[24] Q. Zhang, J. Zhang, J. Zou, and S. Fan, "A novel fault diagnosis method based on stacked LSTM," *IFAC-PapersOnLine*, vol. 53, no. 2, pp. 790–795, 2020.

[25] M. Zhao, B. Tang, L. Deng, and M. Pecht, "Multiple wavelet regularized deep residual networks for fault diagnosis," *Measurement*, vol. 152, p. 107331, 2020.

[26] S. Chunhe, Y. Li Zexi, L. Y. Hongxia, F. Tieying, and Z. Xuejian, "An oil well fault recognition method based on improved GoogLeNet," *Journal of Jiangsu University of Science and Technology (Natural Science Edition)*, vol. 35, no. 2, pp. 52–58, 2021.

[27] X. Wang, Y. Qin, Y. Wang, S. Xiang, and H. Chen, "ReLTanh: an activation function with vanishing gradient resistance for SAE-based DNNs and its application to rotating machinery fault diagnosis," *Neurocomputing*, vol. 363, pp. 88–98, 2019.

[28] D. Yao, H. Liu, J. Yang, and X. Li, "A lightweight neural network with strong robustness for bearing fault diagnosis," *Measurement*, vol. 159, p. 107756, 2020.

[29] K. Eckle and J. Schmidt-Hieber, "A comparison of deep networks with ReLU activation function and linear spline-type methods," *Neural Networks*, vol. 110, pp. 232–242, 2019.

[30] L. Chao, T. Lin, L. Yonghui, Z. Daomeng, and M. Yanchen, "Selective multilayer fusion neural network for face age estimation," *Journal of Transducer Technology*, vol. 33, no. 9, pp. 1313–1319, 2020.

[31] C. Zhang and Q. Li, "Distributed optimization for degenerate loss functions arising from over-parameterization," *Artificial Intelligence*, vol. 301, article 103575, 2021.

[32] Y. Zhu, G. Li, R. Wang, S. Tang, H. Su, and K. Cao, "Intelligent fault diagnosis of hydraulic piston pump based on wavelet analysis and improved AlexNet," *Sensors*, vol. 21, no. 2, p. 549, 2021.

[33] L. Jikeng, R. Yirui, S. Xin, L. Jun, Z. Mingyu, and W. Bo, "Power system fault probability diagnosis based on logistic regression deep neural network," *Journal of Tianjin University (Natural Science and Engineering Technology Edition)*, vol. 54, no. 2, pp. 186–195, 2021.

[34] C. Grover and N. Turk, "A novel fault diagnostic system for rolling element bearings using deep transfer learning on bispectrum contour maps," *International Journal*, vol. 31, p. 101049, 2022.

[35] G. Wenfeng, C. Hui, Z. Zehui, Z. Meiling, G. Cong, and W. Xin, "Research on intelligent fault diagnosis of rolling bearing based on improved convolutional neural network," *Chinese Journal of Vibration Engineering*, vol. 33, no. 2, pp. 400–413, 2020.

[36] W. Cai, J. Zhou, and J. Wang, "Interdependency and vulnerability of multipartite networks under target node attacks," *Complexity*, vol. 2019, 16 pages, 2019.

[37] Z. Wang, N. Yang, N. Li, W. du, and J. Wang, "A new fault diagnosis method based on adaptive spectrum mode extraction," *Structural Health Monitoring*, vol. 20, no. 6, pp. 3354–3370, 2021.

Research Article

Assured Deletion: A Scheme Based on Strong Nonseparability

Zhenjie Xie ⓘ, **Wei Fu** ⓘ, **Jianqiao Xu** ⓘ, **and Tingting Zhu** ⓘ

Department of Information Security, Navy University of Engineering, Wuhan, China

Correspondence should be addressed to Wei Fu; lukeyoyo@tom.com

Cloud storage services bring great convenience to users, but also make data owners lose direct control of their data. How to ensure that deleted cloud data can never be recovered by cloud servers or attackers is a key issue in the field of cloud storage security, which is important to protect user privacy and data confidentiality in the cloud environment. Most existing schemes have the drawbacks of overreliance on key destruction and having the ability to decrypt part of the ciphertext after cracking the key. To solve these problems, a novel cloud data assured deletion scheme based on strong nonseparability is presented. By combining XOR operation with the block cipher, the cipher data become strongly nonseparable; thus, destroying any piece of cipher data will result in unrecoverable original data. Theoretical analysis and experimental results both show that the scheme achieves the expected goals of assured deletion, which has obvious performance advantages and stronger security compared with similar schemes.

1. Introduction

In cloud storage application mode, users enjoy the benefits of flexible space, real-time sharing, disaster tolerance, and other benefits. However, they lose direct control over the data they own. When users want to delete data stored in the cloud, how to ensure that the deleted data will not be recovered by the cloud server or attackers, that is, assured deletion of cloud data, is a key issue to be solved in the field of cloud storage security. Because the cloud storage services are completely out of the direct control of users, there is no technical solution to ensure the direct destruction of cloud data at present; only the idea of "encrypt data, destroy key" [1] can indirectly achieve the assured deletion of cloud data.

The assured deletion schemes based on the above ideas destroy the key, but there are still complete cipher data on the cloud server. If the key is compromised or the cipher is violently cracked, the deleted original data is still at risk of being recovered. Even if it cannot be decrypted, the complete cipher data can still be used for ciphertext analysis. In addition, under the common working mode of block ciphers (e. g., ECB and CBC), if an attacker has the key, the intercepted cipher fragments can be decrypted. To deal with these threats, this paper presents a cloud data assured deletion

scheme based on strong nonseparability. By combining XOR operation with the block cipher, the cipher data are strongly nonseparable [2], that is, destroying any part of the whole cipher data will result in the original data not being recovered. Users host the key and some cipher data to a trusted third party, which destroys these cipher data and the key when the deletion operation is initiated. The strong nonseparability ensures that recovering any part of the original data without the complete cipher data is computationally infeasible, thus significantly enhancing the nonrecoverability of the data after the deletion operation. This scheme achieves the strong nonseparability by confusing data blocks directly participating in cryptographic operations through XOR operation, which reduces the number of cryptography computations. Therefore, it has obvious performance advantages and stronger security over existing similar assured deletion schemes.

2. Related Works

To realize the assured deletion of cloud data, Perlman first proposed the idea of "encrypt data, destroy key" [1]. Firstly, the user encrypts the original data by generating a random key, then uploads the ciphertext to the remote server, and

hosts the encryption key to a trusted third party. When performing data deletion, the trusted third party destroys the key to ensure that the cipher data on the remote server cannot be decrypted, thus achieving assured deletion. Tang et al. proposed FADE system [3, 4], which implements a policy-based assured deletion mechanism for cloud data. Mo et al. proposed a user-based assured deletion scheme [5] that does not rely on third parties; users only need to keep a small number of keys to achieve fine-grained assured deletion. Geambasu et al. proposed a scheme [6] which uses a threshold secret sharing mechanism to divide the encryption key and save it on a DHT (Distributed Hash Table) node, using the automatic update mechanism of DHT to delete the encryption key regularly. Feng and Tan proposed a data assured deletion scheme [7] based on trust value for cloud storage; the core is to evaluate the trustworthiness of DHT nodes, selecting a node with higher trustworthiness to store the key component, and reduce the probability that users cannot access their sensitive data during the authorized time.

Rivest pointed out that for existing encryption systems, as long as the key is mastered, part of the cipher data obtained can be decrypted [2]. This facilitates the attacker. On the one hand, any cipher fragments have a direct value because they can be decrypted to obtain the corresponding plaintext. On the other hand, any cipher fragment can provide useful information for cracking the key. To address these issues, Rivest proposed the concept of strongly nonseparable and proposed a way to construct a strongly nonseparable encryption scheme by existing cryptography technology and AONT (All-Or-Nothing-Transform) and an implementation scheme called Package Transform to accommodate scenarios with higher security requirements.

On the basis of Rivest's Package Transform scheme, Luo proposed a strongly nonseparable encryption scheme [8]. Luo's scheme first converts the original message sequence into a strongly inseparable pseudomessage sequence using AONT conversion and then encrypts the pseudomessage sequence using a random key to generate a cipher sequence. To improve the computational efficiency, Luo's scheme uses pseudorandom function (PRF) and hash operation to, respectively, replace two times block encryption in the Package Transform scheme. It is important to note that the Package Transform scheme implements AONT, which is a preprocessing process used to achieve strong nonseparability and cannot replace encryption operations by itself, while Luo's scheme is a complete encryption scheme which implements strong nonseparability. The scheme proposed by Zhang et al. [9, 10] uses a similar approach, but the use of bilinear mapping may result in high computational overhead.

Liu et al. proposed a blockchain-based verification scheme for deletion operation in the cloud [11]. Users invoke smart contracts to prove identity to the cloud server, and then, the cloud server deletes the data and generates a blockchain with deletion evidence embedded, while users can verify the results of data deletion without a trusted third party. Du et al. proposed a cloud data assured deletion scheme based on cipher reencryption combined with override verification [12]. By reencrypting and changing the

access control strategy corresponding to the ciphertext, data fine-grained deletion can be achieved. A searchable path hash binary tree based on dirty data block override is constructed to verify the correctness of the data to be deleted after overwriting. Zhang proposed an instantaneous deterministic deletion method of cloud storage data based on feature iteration [13], which extracts and classifies the features of redundant data in cloud storage data, iterates until convergence, and achieves high-performance deletion of redundant data. In addition, some assured deletion or self-destruction schemes for cloud data based on DHT [10, 14], attribute-based encryption [15–18], and identity-based encryption [19, 20] are proposed in recent years. Xiong et al. [21] made an in-depth analysis and comments on the related research work in recent years from three aspects: trusted execution environment, key management, and access control strategy.

The above schemes use some new technologies, but require considerable changes to the cloud storage service framework, making it difficult to directly apply them to existing cloud storage systems, complex to implementation, and significantly increasing the computational time cost or number of interactions, while the scheme in this paper does not change the existing system architecture, but fully exploits the mature cryptography technology, which achieves the goals of assured deletion by making the ciphertext strongly nonseparable.

3. Assured Deletion Scheme Based on Strong Nonseparability

The cloud storage system in reality is full of various security threats. To achieve assured deletion of cloud data, an efficient assured deletion scheme for cloud data based on strong nonseparability is proposed. This section first describes the assured deletion system from the perspective of the model, combs the real threats and proposes the expected design goals, then introduces the concept of strongly nonseparable, next describes the main algorithms, processes, and assured deletion mechanisms in detail, and finally gives the performance analysis of the scheme.

3.1. System Model

3.1.1. System Composition. To illustrate the assured deletion of cloud data, an assured deletion system with four entities is introduced, as Figure 1 illustrated.

Among them, the cloud storage server (CSS) provides users with cloud storage and data sharing services. Trusted third party (TTP) is the entity trusted by users, which is responsible for hosting keys and partial cipher data and for completely destroying the corresponding key and cipher data when performing the deletion operation. Data owner (DO) performs a specific encryption algorithm on the original data, uploads the output to CSS and TTP, and authorizes access for some users. Authorized users (AU) are those who are allowed to download and decrypt specific data. Assured deletion can be initiated by the DO or triggered by a strategy such as shelf life.
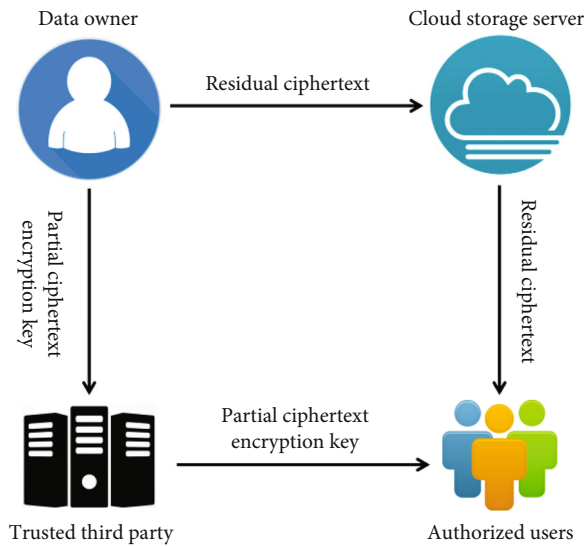
FIGURE 1: Assured deletion system model.

```
Input: F
Output: K, C'
Randomly generate an initial vector m'_0
Randomly generate a data encryption key K
for i in [1, n]:
        m'_i = m_i ⊕ m'_{i-1}
        c'_i = Enc_K(m'_i) ⊕ m'_{i-1}
end for
c'_0 = m'_0 ⊕ c'_1 ⊕ c'_2 ⊕ ⊕ c'_n
Make C' = (c'_0, c'_1, c'_2, ···, c'_n)
```

ALGORITHM 1

In fact, there is no credible third-party entity in some cloud storage systems. At this time, DO can retain the partial cipher data and destroy it when performing deletion.

3.1.2. Reality Threats. For traditional cloud storage systems, cloud data may still be retained after a deletion request, which poses a threat to user privacy and data confidentiality. Specifically, the implementation of assured deletion faces the following security threats:

(a) CSS does not perform data deletion operations, but only prohibits user access

(b) Attackers or malicious cloud service providers attempt to decrypt or mine the user data they hold

(c) Attackers intercept or crack the data encryption key to decrypt the acquired cipher data

3.1.3. Expected Goals. Within the framework of this system, in order to respond to these real threats and be operable, assured deletion should meet the following objectives:

(a) Assured deletion must be valid, that is, no one (including the DO) can recover all or part of the original data with limited computing resources after performing the data deletion

(b) Even if an attacker acquires all data stored by the CSS or if the cloud service provider itself is malicious, it cannot restore any of the original data

(c) Even if an attacker has the data encryption key, he cannot decrypt incomplete cipher data fragments

(d) The algorithm introduced by assured deletion must be easy to implement and will not significantly burden users

3.1.4. Safety Assumptions. To make the scheme feasible, the following assumptions need to be made:

(a) TTP is trustworthy and technically can ensure that the corresponding keys and data are securely destroyed

(b) The temporary data blocks generated by users will not be saved, that is, attackers cannot obtain the decrypted plaintext through the users

3.2. Strongly Nonseparable. Strongly nonseparable [2] introduced by Rivest guarantees that any missing cipher data will result in the failure to decrypt any part of the plaintext, as defined below.

Hypothesis Γ is a block cipher mechanism used to convert s plaintext sequence $m_1, m_2, \cdots, m_s$ to t cipher sequence $c_1, c_2, \cdots, c_t$. If it is satisfied that restoring any plaintext data before obtaining and decrypting all t cipher blocks is computationally infeasible, it is called the encryption mechanism Γ can make a sequence strongly nonseparable.

In the face of a strongly nonseparable encryption mechanism, the cipher fragments obtained by the attacker no longer have the value of direct decryption, nor can they provide a useful reference for cracking the key, so the security is significantly enhanced. Based on the definition of strongly nonseparable, we can use existing cryptographic technology to construct encryption schemes that satisfy the strong nonseparability.

3.3. Scheme Implementation. This section describes in detail the algorithms and processes for data encryption and data decryption of the scheme and gives the mechanism and security analysis of data deletion. Make Enc a block encryption algorithm, Dec the corresponding decryption algorithm for Enc, and $F = (m_1, m_2, \cdots, m_n)$ the original message sequence.

3.3.1. Data Encryption. The pseudocode for the data encryption algorithm is as follows.

The data encryption algorithm is executed by the DO. The execution process is shown in Figure 2. After execution, the DO randomly selects some data blocks in the cipher sequence C' to form a set Ψ. Specifically, make $\Psi = \{c'_0\}$; DO hosts Ψ and key K together to a TTP. The remaining
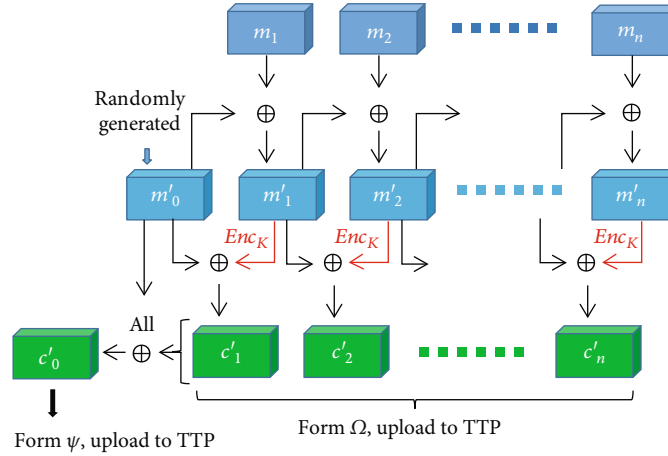
FIGURE 2: Data encryption process.
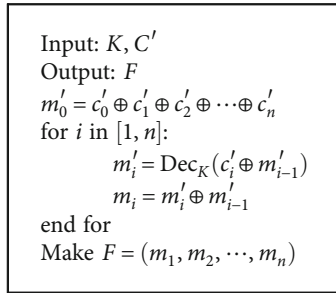
ALGORITHM 2
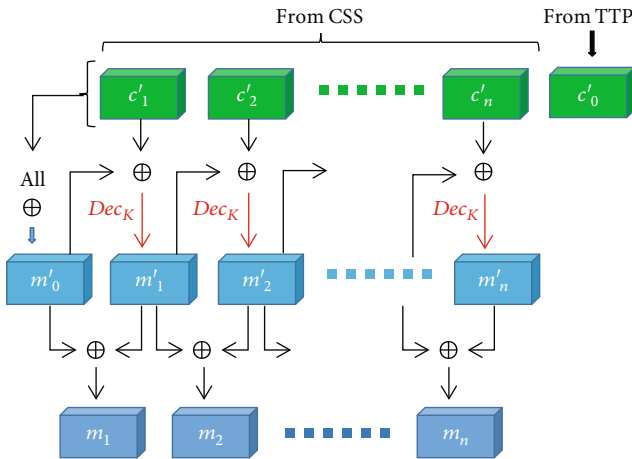
FIGURE 3: Data decryption process.

data blocks of cipher sequence C' form a set Ω and DO sends it to the CSS. DO grants access to some users.

3.3.2. Data Decryption. The pseudocode for the data decryption algorithm is as follows.

Data decryption algorithm is executed by AU when accessing cloud data. The execution process is shown in Figure 3. AU first retrieves the key K and the partial cipher data set Ψ from the TTP, then retrieves the remaining cipher data set Ω from the CSS, merges Ψ and Ω to get the com-

plete cipher sequence C', and then executes the data decryption algorithm to recover the original message sequence F.

It is worth mentioning that if all m'_{i-1} appearing in the above algorithms are fixed to the initial vector m'_0, the expected security characteristics can also be achieved. This simplifies the scheme representation further, but may result in the same plaintext blocks being converted to the same cipher blocks. Therefore, it is necessary to use the block cipher working mode other than ECB to hide the formatting rules and statistical characteristics of the plaintext. Experiments show that this simplification does not achieve performance improvement, so it will not be repeated later.

3.3.3. Data Delete Mechanism. When performing the deletion operation, the key K and the partial cipher data set Ψ are destroyed by the TTP. Due to the strong nonseparability of cipher data, any missing cipher data will result in the failure to decrypt any part of the plaintext.

The following security description analyzes whether the scheme achieves the expected security goals after performing deletion operations from the point of view of the strongest attacker.

TTP destroys the key K and the partial cipher data set Ψ (make $\Psi = \{c'_0\}$) after deletion. Assume that the strongest attacker A gets all remaining data Ω (make $\Omega = \{c'_1, c'_2, \cdots, c'_n\}$) stored by CSS and has the key K. However, A is infeasible to recover m'_0 without c'_0; thus, no fragment of the original message F can be recovered. Even if the attacker A gets part of the plaintext blocks (make it m_i), because A does not know m'_i, it is not possible to compute m'_0 contained in it; thus, no more plaintext blocks can be obtained.

In Luo's scheme [8], $m'_i = m_i \oplus f_{rk}(i)$; f is a pseudorandom function. Attacker A can get m'_i by decrypting c'_i. In the case of obtaining the plaintext block m_i, $f_{rk}(i)$ can be obtained. Pseudorandom functions usually do not satisfy the characteristics of cryptographic algorithms. As long as the seed rk is calculated inversely, other plaintext blocks can be restored.

TABLE 1: Performance analysis of schemes.

Scheme	Storage overhead	Calculation overhead	Communication overhead	Strong nonseparability	Confidentiality
Encryption only	$n\beta + k$	nENC	$n\beta + k$	No	Yes
Package Transform [2]	$(n + 1)\beta$	$3n\text{XOR} + 2n\text{ENC}$	$(n + 1)\beta$	Yes	No
Luo's scheme [8]	$(n + 1)\beta + k$	$2n\text{XOR} + n\text{HASH} + (n + 1)\text{ENC} + n\text{PRF}$	$(n + 1)\beta + k$	Yes	Yes
This scheme	$(n + 1)\beta + k$	Enc: $3n\text{XOR} + n\text{ENC} + 1\text{PRF}$ Dec: $3n\text{XOR} + n\text{ENC}$	$(n + 1)\beta + k$	Yes	Yes

TABLE 2: The configuration of experimental computer.

Item	Configuration
Machine type	PC
Operation system	Windows 10 64-bit
CPU	Intel Core i7-10710U
CPU quantity	6
Memory	16 GB LPDDR3 2133 MHz
Hard disk	SAMSUNG MZVLB512HBJQ-000L7

TABLE 3: The key operation implementation.

Operation	Implementation
Block encryption	*Python-Crypto.Cipher.AES*
Pseudorandom	*Python-random*
Hash	*Python-hashlib.md5*
Data block XOR	Python large integer bitwise XOR ("^")

To sum up, with limited computing resources and existing technology, an attacker cannot obtain any plaintext after performing the deletion operation under the assumptions. Therefore, the scheme achieves data assured deletion and has higher security than Luo's scheme.

3.4. Performance Analysis. This section makes a theoretical analysis of the scheme performance from three aspects: storage, calculation, and communication. Table 1 shows the performance analysis results of encryption only, Package Transform [2], Luo's scheme [8], and this scheme.

3.4.1. Storage Overhead. As mentioned earlier, for the original message sequence F with n blocks, the cipher sequence C' generated by the encryption algorithm has $(n + 1)$ blocks. Assuming that the size of each plaintext and cipher data block is β, the size of key K is k, and the partial cipher data set Ψ stored by TTP includes only one block. Thus, for each file stored, the storage overhead of CSS is $n\beta$, while it is $(\beta + k)$ for TTP. The overall storage overhead of the scheme is $(n + 1)\beta + k$. The DO does not need to save any data locally after uploading.

3.4.2. Calculation Overhead. The DO of this scheme needs $3 n \cdot \text{XOR} + n \cdot \text{ENC} + 1 \cdot \text{PRF}$ operations to perform the data encryption algorithm, while AU needs $3n \cdot \text{XOR} + n \cdot \text{ENC}$ operations to perform the data decryption algorithm. Among

them, XOR stands for data block XOR operation, ENC means block encryption/decryption operation, and PRF stands for pseudorandom operation (including randomly generating an initial vector). Luo's scheme [8] requires $2n \cdot \text{XOR} + n \cdot \text{HASH} + (n + 1) \cdot \text{ENC} + n \cdot \text{PRF}$ operations to perform file upload or download algorithms, where HASH refers to the hash operation. It can be seen that, compared with Luo's scheme, this scheme significantly reduces pseudorandom operations and avoids hash operations, thus significantly improving the computational efficiency.

3.4.3. Communication Overhead. After performing the data encryption algorithm, the DO uploads $n\beta$ data to CSS and $(\beta + k)$ data to TTP. Accordingly, AU downloads $n\beta$ data from CSS and $(\beta + k)$ data from TTP. The total communication overhead for a complete file upload or file access is $(n + 1)\beta + k$ regardless of the handshake cost required to establish the communication channel.

4. Experiments and Analysis

To verify the validity of this scheme, the main algorithms and processes of this scheme are implemented using Python programming; also, the schemes of encryption only, Package Transform [2], and Luo's [8] are implemented. The computational efficiency of the data encryption/decryption algorithms of each scheme is expected to be compared through comparative experiments.

4.1. Environment and Parameters. The configuration of the experimental computer is listed as Table 2.

128-bit key ($k = 16B$) was used in the experiments. The original file size was 10 MB (using 1 MB, 100 MB, 1 GB, and other sizes will get similar results; we use 10 MB file as an example), and the data block size β was 1 KB, 2 KB, 4 KB, 8 KB, and 16 KB in turn. Experiments with the same parameters were repeated 50 times, and their average values were taken as the final results.

Some Python libraries are used for key operations such as block encryption, hash, and pseudorandom involved in the algorithm. The specific implementation method is shown in Table 3.

To ensure the accuracy of the comparison, each scheme should be as consistent as possible in programming style, be optimized as possible in its own scheme framework, and use the same parameters.
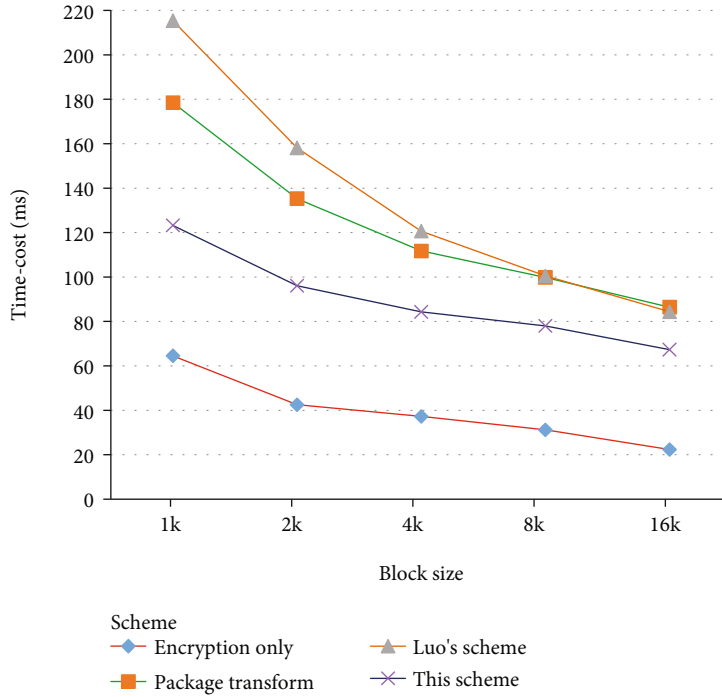
Figure 4: The data encryption time cost.
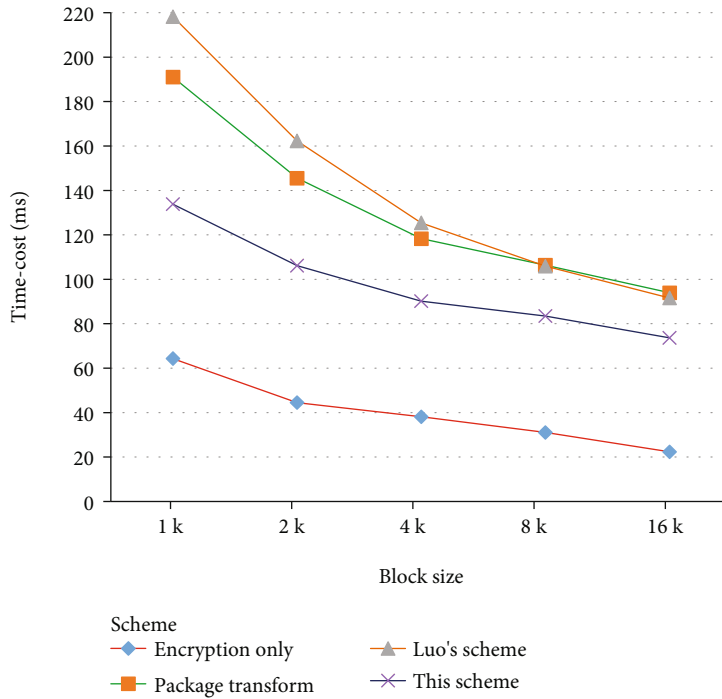
Figure 5: The data decryption time cost.

4.2. Data Encryption Test. In the data encryption test, each scheme executes the encryption algorithm for a random file of 10 MB in size, outputs a 10 MB file to upload to CSS, and also uploads a data block to TTP (except for encryption only). The time cost of performing the encryption algorithm of each scheme at different block sizes is shown in Figure 4.

Figure 4 shows that this scheme takes significantly less time cost to execute the encryption algorithm than Package Transform and Luo's scheme (about 2/3 to 3/4 of Luo's), which is about two to three times as long as encryption only. In addition, the time cost of each scheme decreases as the block size increases, because an increase in the block size

means a decrease in the total number of blocks, so the number of operations performed decreases.

4.3. Data Decryption Test. In the data decryption test, each scheme executes the decryption algorithm on the 10 MB file generated by its own execution of the encryption algorithm. The output file of each scheme is consistent with the original file through hash verification. The time cost of performing the decryption algorithm of each scheme at different block sizes is shown in Figure 5.

As can be seen from Figure 5, the decryption algorithm time consumed by each scheme is essentially the same as the encryption algorithm.

Combining the above test results, this scheme is an assured deletion encryption scheme based on strong nonseparability. It achieves greater security with only two to three times the computation overhead of encryption only. Because the hash operation is avoided and pseudorandom operation is reduced, the computation overhead is about 2/3 to 3/4 of Luo's scheme.

5. Conclusion

Aiming at the assured deletion of cloud data, a novel scheme based on strong nonseparability is presented. Compared with the traditional schemes of "encrypt data, destroy key," making the ciphertext strongly nonseparable is a promising way to achieve the assured deletion. By destroying the key and part of the cipher data through a TTP, the nonrecoverability of the original data after deletion operation is significantly enhanced. Compared with the existing similar schemes, this scheme achieves strong nonseparability by adding XOR operation instead of hash operation. The theoretical analysis and experimental results show that the proposed scheme achieves the expected design goals of assured deletion with less computation overhead, having obvious performance advantages and stronger security in similar schemes.

In fact, refining key management and realizing strong nonseparability of ciphertext are two ideas to realize assured deletion, which are not exclusive. If the two ideas are combined, the "credibility" of cloud data deletion will be further improved.

Data Availability

The codes and data used to support the findings of this study are available from the corresponding author upon request.

Conflicts of Interest

The authors declare that they have no conflicts of interest.

Acknowledgments

References

[1] R. Perlman, "File system design with assured delete," in *In Third IEEE International Security in Storage Workshop*, San Francisco, CA, USA, 2005.

[2] R. L. Rivest, "All-or-nothing encryption and the package transform," in *In International Workshop on Fast Software Encryption*, pp. 210–218, Springer, Berlin, Heidelberg, 1997.

[3] Y. Tang, P. Lee, J. Lui, and R. Perlman, "Fade: secure overlay cloud storage with file assured deletion," in *Security and Privacy in Communication Networks of Lecture Notes of the Institute for Computer Sciences, Social Informatics and Telecommunications Engineering*, S. Jajodia and J. Zhou, Eds., pp. 380–397, Springer Berlin Heidelberg, 2010.

[4] Y. Tang, P. Lee, J. Lui, and R. Perlman, "Secure overlay cloud storage with access control and assured deletion," *IEEE Transactions on Dependable and Secure Computing*, vol. 9, no. 6, pp. 903–916, 2012.

[5] Z. Mo, Y. Qiao, and S. Chen, "Two-party fine-grained assured deletion of outsourced data in cloud systems, in: distributed computing systems (ICDCS)," in *In 2014 IEEE 34th International Conference on Distributed Computing Systems*, pp. 308–317, Madrid, Spain, 2014.

[6] R. Geambasu, T. Kohno, A. A. Levy, and H. M. Levy, "Vanish: increasing data privacy with self-destructing data," *USENIX Security Symposium*, vol. 316, p. 10-5555, 2009.

[7] F. Guilan and T. Liang, "Data assured deletion scheme based on trust value for cloud storage," *Computer Science*, vol. 41, no. 6, pp. 108–122, 2014.

[8] Y. C. Luo, *Research on public auditing for shared data and assured deletion in cloud storage, [M.S. Thesis]*, National University of Defense Technology, Changsha, China, 2015.

[9] Z. Kun, Y. Chao, M. Jianfeng, and J. W. Zhang, "Novel cloud data assured deletion approach based on ciphertext sample slice," *Journal on Communications*, vol. 36, no. 11, pp. 108–117, 2015.

[10] W. Lina, Z.-W. Ren, R.-W. Yu, F. Han, and Y.-F. Dong, "A data assured deletion approach adapted for cloud storage," *Acta Electronica Sinica*, vol. 40, no. 2, pp. 266–272, 2012.

[11] L. Yining, Z. Yuanjian, L. Rushi, and C. Tang, "Blockchain-based verification scheme for deletion operation in cloud," *Journal of Computer Research and Development*, vol. 55, no. 10, pp. 2199–2207, 2018.

[12] D. Ruizhong, S. Pengliang, and H. Xinfeng, "Cloud data assured deletion scheme based on overwrite verification," *Journal on Communications*, vol. 40, no. 1, pp. 130–140, 2019.

[13] Z. Xinhua, "Instantaneous deterministic deletion of cloud storage data based on feature iteration," *Application Research of Computers*, vol. 37, no. 9, pp. 2840–2843, 2020.

[14] L. Chaoling, C. Yue, and Z. Yanzhou, "A data assured deletion scheme in cloud storage," *China Communications*, vol. 11, no. 4, pp. 98–110, 2014.

[15] W. Lina, Z. Ren, Y. Dong, R. Yu, and R. Deng, "A management approach to key-used times based on trusted platform module in cloud storage," *Journal of Computer Research and Development*, vol. 50, no. 8, pp. 1628–1636, 2013.

[16] Y. Yu, L. Xue, Y. Li, X. du, M. Guizani, and B. Yang, "Assured data deletion with fine-grained access control for fog-based industrial applications," *IEEE*, vol. 14, no. 10, pp. 4538–4547, 2018.

[17] L. Xue, Y. Yu, Y. Li, M. H. Au, X. du, and B. Yang, "Efficient attribute-based encryption with attribute revocation for assured data deletion," *Information Sciences*, vol. 479, pp. 640–650, 2019.

[18] X. Jinbo, Y. Zhiqiang, M. Jianfeng, F. Li, X. Liu, and Q. Li, "A secure self-destruction scheme for composite documents with attribute based encryption," *Acta Electronica Sinica*, vol. 42, no. 2, pp. 366–376, 2014.

[19] Y. Zhiqiang, X. Jinbo, M. Jianfeng, Q. Li, and X. Liu, "A secure electronic document self-destructing scheme in cloud computing," *Journal of Computer Research and Development*, vol. 51, no. 7, pp. 1417–1423, 2014.

[20] X. Jinbo, Y. Zhiqiang, M. Jianfeng, F. Li, and X. Liu, "A secure self-destruction scheme with IBE for the Internet content privacy," *Chinese Journal of Computers*, vol. 37, no. 1, pp. 139–150, 2014.

[21] X. Jinbo, L. Fenghua, W. Yanchao, J. Ma, and Z. Yao, "Research progress on cloud data assured deletion based on cryptography," *Journal on Communications*, vol. 37, no. 8, pp. 167–184, 2016.

Research Article

An In Situ Spectral Monitoring Scheme for Advanced Manufacturing of Novel Nanodevices

Hui Qi [ID][1,2] **and Xing Fu** [ID][1,3]

[1]*State Key Laboratory of Precision Measurement Technology and Instruments, Tianjin University, Tianjin 300072, China*
[2]*School of Precision Instrument and Opto-Electronics Engineering, Tianjin University, Tianjin 300072, China*
[3]*Tianjin Research Center of MicroNano Manufacturing Technology, Tianjin University, Tianjin 300072, China*

Correspondence should be addressed to Xing Fu; xingfu@tju.edu.cn

The advanced manufacturing of ultra-thin-film devices, especially the nano-semiconductor products, has drawn a significant research interest over the past decades. In this field, monitoring the properties and thickness of the semiconductor layers is of paramount importance, which has significant impact on the device quality. In this study, an in situ monitoring scheme for manufacturing of nanodevices has been proposed, which is able to accurately analyse the optical absorption properties of the semiconductor layers of varying thickness in nanodevices. The in situ reflectance spectral analysis of monolayer, bilayer, and bulk-phase samples confirms the practicability and reliability of the monitoring scheme. The findings reported in this study form the basis for the advanced manufacturing of nano- and sub-nanodevices in the future.

1. Introduction

The advanced manufacturing technologies have drawn a significant in recent years, including intelligent sensing, artificial intelligence, advanced monitoring, and other smart information technologies [1–6]. Owing to the critical role in advanced manufacturing, many researchers have attempted to exploit the opportunity of producing micro- and nanodevices in the past decades since the discovery of graphene in 2004 [7–10]. Particularly, the nanodevices based on two-dimensional (2D) materials have attracted great attention owing to their extraordinary properties, thus becoming the focus of research in the field of nanodevice manufacturing [11–16]. Considering material structure for nanodevices, the hybrid systems consisting of 2D and organic semiconductor thin films have sparked new research directions [17–21], and the combination of the advantages of both 2D and organic materials [22–24] has been widely con-

sidered to be promising for developing the novel nanodevices in the future. In recent years, the structures comprising van der Waals (vdW) epitaxial organic semiconductor films with controllable layers on the 2D material surface have emerged as one of the prime research highlights, as the properties and performance of the nanodevices based on such structures effectively correlate with the thickness of the organic layers [25–28]. Therefore, in order to satisfy the device functions and improve the production quality, a monitoring scheme, which is able to analyse the optical properties of thin films with different thicknesses, is essential for the advanced manufacturing of nano- and sub-nanodevices, especially the devices based on the structure of 2D/organic thin films which have been mentioned above.

In this paper, an in situ reflectance spectral monitoring scheme as microarea differential reflectance spectroscopy has been proposed for manufacturing the nano-thin-film devices, which is able to recognise and analyse the optical

absorption characteristics of the ultrathin films at the monolayer level. The differential reflectance spectroscopy (DRS) is a powerful tool to study the optical absorption characteristics of the thin and ultrathin films, which measures a normalized relative change in the reflectance of a surface, and the respective intensities of the reflected light from the covered adsorbate and the bare substrate are subsequently compared [29]. The DRS can be defined as [30–32]

$$\text{DRS} \equiv \frac{\Delta R}{R} := \frac{R(E, d) - R(E, 0)}{R(E, 0)} = \frac{I(E, d) - I(E, 0)}{I(E, 0)}, \quad (1)$$

where $R(E, 0)$ represents the reflectance from the clean substrate at a photon energy E and $R(E, d)$ represents the reflectance of the area covered by the films. The intensities of the light reflected from the clean surface and sample films are donated as $I(E, 0)$ and $I(E, d)$, respectively, which are used to calculate the DRS value. Owing to its high spectral resolution, the DRS technique has been successfully applied for the in situ investigation of the optical absorption properties of the organic semiconductive and 2D transition metal dichalcogenide (TMD) thin films [33–38]. The spectral resolution and measurement sensitivity of DRS at the monolayer and even sub-monolayer levels have been confirmed in the reported studies. For the 2D/organic structures mentioned above, which are randomly in the micrometer size owing to the dimensions of the mechanically exfoliated 2D materials [39–41], the spectral monitoring scheme should not only possess a high thickness resolution but also allow the selection of the detection range at the microscale of desired shape. Therefore, a DRS apparatus with the ability to select the measuring region of any size and at any position has been proposed here. In order to achieve the high resolution of the monolayer in the microarea, a high irradiation intensity Xenon lamp source and a large well depth scientific complementary metal oxide semiconductor (sCMOS) detector have been unitized for attaining the high signal to noise ratio. Moreover, based on the acquisition of signals by the sCMOS camera, the shape and position of the measurement region can be arbitrarily selected in the field of view. In particular, even one pixel can be selected as the measurement region. Furthermore, the 2D/organic semiconductor hybrid structure comprising of vdW epitaxial dimethyl-3,4,9,10-perylenetetracarboxilic diimide (Me-PTCDI) on the hexagonal boron nitride (h-BN) surface has been selected as the research target in this paper. The h-BN is widely used as the substrate for the nanodevices based on 2D materials due to its insulation [42–45], thus finding extensive use in the 2D/organic structures [25, 26]. Among the organic semiconductor materials, perylene dyes are significant owing to their optical and photoelectric properties [46–50]. Particularly, Me-PTCDI, a typical perylene dye molecule, is considered to be practical for producing novel nanodevices owing to its characteristics [51–54]. Consequently, the monolayer, bilayers, and bulk phase of Me-PTCDI thin films on the h-BN surface have been investigated by employing the microarea DRS. In addition, the phenomena such as peak broadening, orientation of peak shift, and changes in intensity of

the peaks in the experiments have been discussed in detail. The findings obtained in this paper not only provide the practical information for the fabrication of devices based on the h-BN/Me-PTCDI structures but also prove that the spectral scheme is able to detect the structures with different layers, which is highlighting the potential of the monitoring scheme for advanced manufacturing of the nano- and sub-nanodevices in the future.

2. Materials and Methods

2.1. Sample Preparation. The samples in this study consist of three materials from bottom to top: quartz (0001) substrate, h-BN film, and Me-PTCDI film. The samples have been prepared by using the following procedure:

Firstly, the h-BN thin film on the surface is prepared as follows:

Step 1. The pristine BN material is a single hexagonal bulk crystal. The bottom and top of a BN bulk piece are sandwiched between two pieces of tape, and the bulk is subsequently torn manually. At this stage, the BN bulk with a thickness about half of the original thickness is obtained.

Step 2. Step 1 is repeated several times until the h-BN thin film with the thickness at nanoscale is obtained gradually.

Step 3. The h-BN thin films are transferred onto the surface of an optical single crystal quartz (0001) substrate.

Secondly, the Me-PTCDI films with different numbers of layers are grown by van der Waals epitaxy on the h-BN/quartz substrate as follows [26]:

Step 1. The Me-PTCDI powder in a container is placed at the centre of the tube furnace, and the h-BN/quartz substrate is placed downstream at a suitable distance in the furnace.

Step 2. The tube is evacuated to 10^{-3} Pa.

Step 3. The Me-PTCDI powder is heated in the range 210-260°C to sublimate it, leading to the deposition on the h-BN surface. The process is continued until the film growth has been completed.

By controlling the factors such as the growing duration and the distance between the Me-PTCDI molecules and substrate, the Me-PTCDI thin films with varying number of layers are obtained successfully.

The optical microscope and photoluminescence (PL) images of a typical sample are shown in Figure 1.

The optical analysis has been carried out by using an optical microscope (Olympus BX-51) using a 20x objective lens, followed by the zooming out of the area of interest by using a 150x objective lens. The optical microscopy images in Figure 1 reveal that the samples exhibit a small size in the range of several micrometres. The PL properties of the Me-PTCDI thin films of different thicknesses illuminated by a 450 nm LED are shown in Figure 1(c). The green fluorescence region represents the film formed by a monolayer of Me-PTCDI, whereas the red fluorescence region represents the film formed by more than one layer of Me-PTCDI [26].

Figure 1 demonstrates that it is inevitable that the Me-PTCDI films deposited on the h-BN surface remain uniform
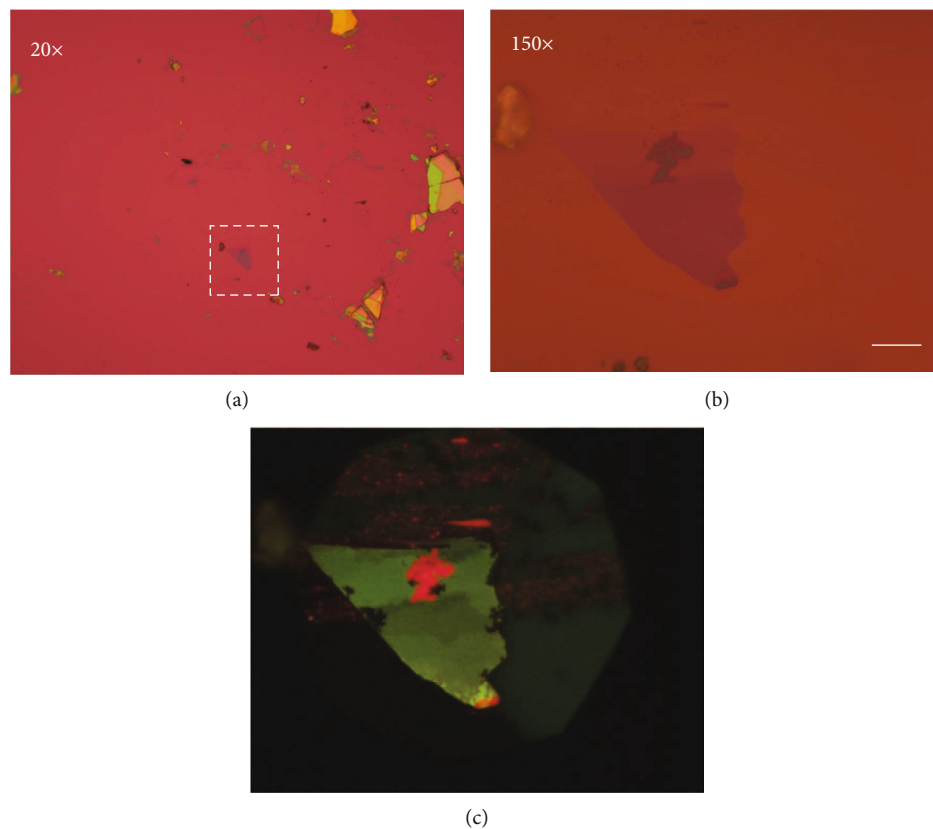
(a)

(b)

(c)

FIGURE 1: The characteristics of the samples: (a, b) optical microscopy images; (c) PL image (scale bar: 10 μm).
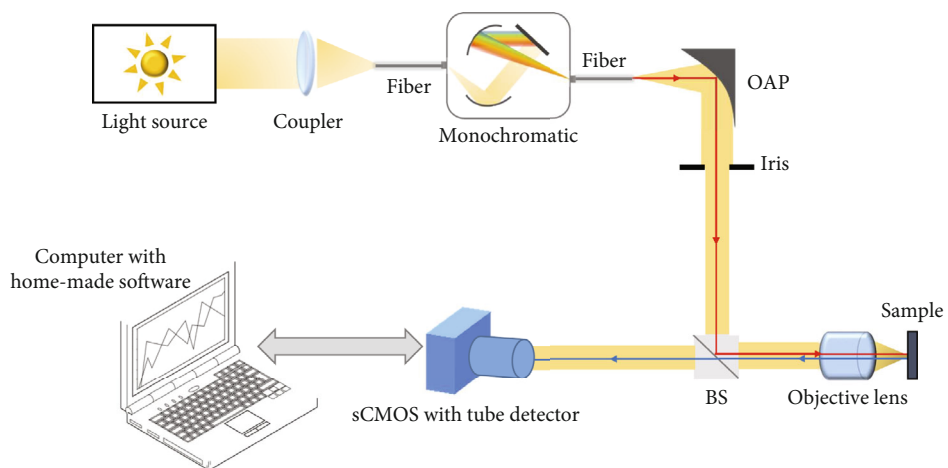

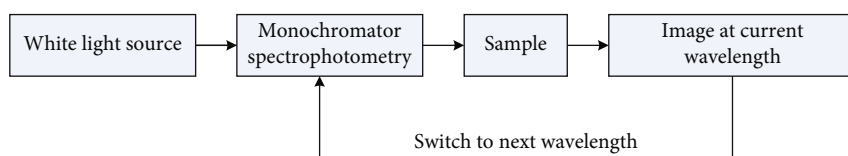FIGURE 2: Schematic illustration of the experimental system.

FIGURE 3: The flow chart depicting the acquisition of the spectral signals.
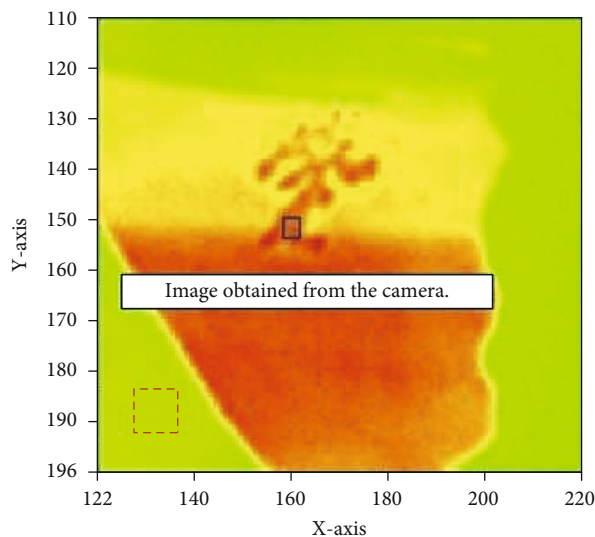
Figure 4: The selection of the experimental area of the sample in Figure 1.
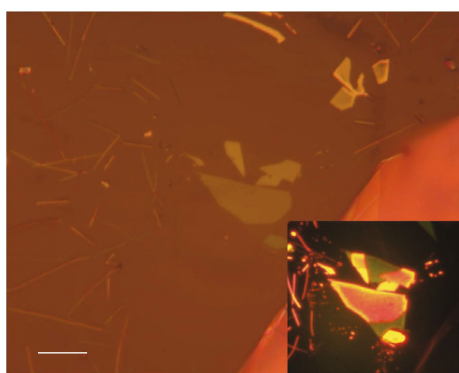
Figure 5: The optical and PL (inset) images of the Me-PTCDI films on the h-BN surface (scale bar: 10 μm).
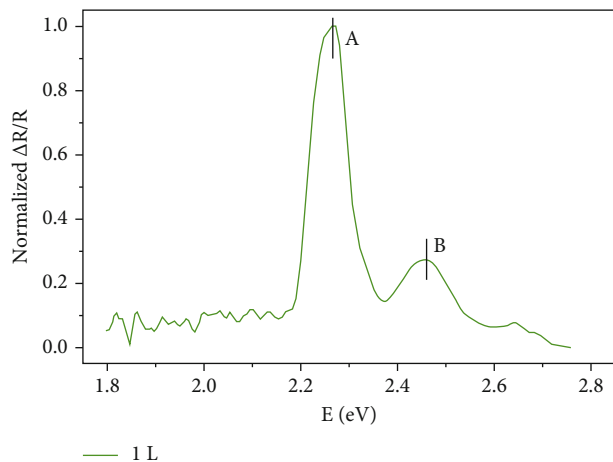
Figure 6: Normalized DRS of the Me-PTCDI monolayer at room temperature.

in such a microsize region. The mechanically exfoliated h-BN films are not only small but also random in size, shape, and surface quality. Besides, the deposition rates of the organic molecules on different areas are not the same. Therefore, the microarea DRS system with an ability to select the measuring region of any size and at any position is required.

2.2. Experimental Setup. The schematic illustration of the DRS system employed in this paper is presented in Figure 2. A brief introduction of the experimental system is given as follows.

In order to cover the range of the characteristic peaks of the organic molecules, which are always in the visible wavelength band, a 75 W Super-Quiet Xenon-lamp (Hamamatsu) has been used as the light source. A fiber coupler is utilized between the lamp and optical fiber to avoid the loss of intensity as much as possible. A monochromatic (SP2150, Princeton Instrument) with a grating flash at 500 nm has been used to obtain the single wavelength light. The off axis parabolic mirror (OAP, Thorlabs) functions as a collimator. The iris and the 50R/50 T beam splitter (BS, produced by Thorlabs) are placed before the 20x objective lens (Nikon CFI 60 TU Plan Epi). To match the light source with high intensity, a deep well miniature sCMOS camera (Panda 4.2 PCO) with a 200 mm tube lens (Edmund) is utilized as the detector, employed simultaneously with homemade software for spectral acquisition and recording.

2.3. Measurement Methods. The measurement methods consist of the three steps: acquisition of spectral signal, selection of measurement area, and the calculation of DRS, which are described in detail as follows.

2.3.1. Step 1: Acquisition of Spectral Signals. The steps for spectral signal acquisition are illustrated in Figure 3. The experimental parameters, including the start and end wavelength of the spectral detection range, step wavelength of the monochromator, exposure duration, and average times of a single acquisition, have been set according to the experimental requirements prior to the measurements. The reflected light intensity of the signals at all wavelengths is subsequently recorded.

2.3.2. Step 2: Selection of the Area of Measurement. The reflected intensity images at single wavelengths are imported into the computer by using the homemade software. Subsequently, the images are employed to select the measurement area. For instance, the image at 550 nm wavelength is used to select the measurement area, which has been shown in Figure 4. The range of the black solid rectangle is selected as the area covered by the Me-PTCDI film, and the range of the red dashed rectangle is selected as the substrate. The rectangular area is taken for example here. In fact, the selected area can be of any shape and size, even a single pixel.

2.3.3. Step 3: Calculation of DRS. The average reflected intensities of the experimental wavelengths from the selected area are calculated automatically by using the homemade

(a)

(b)

(c)
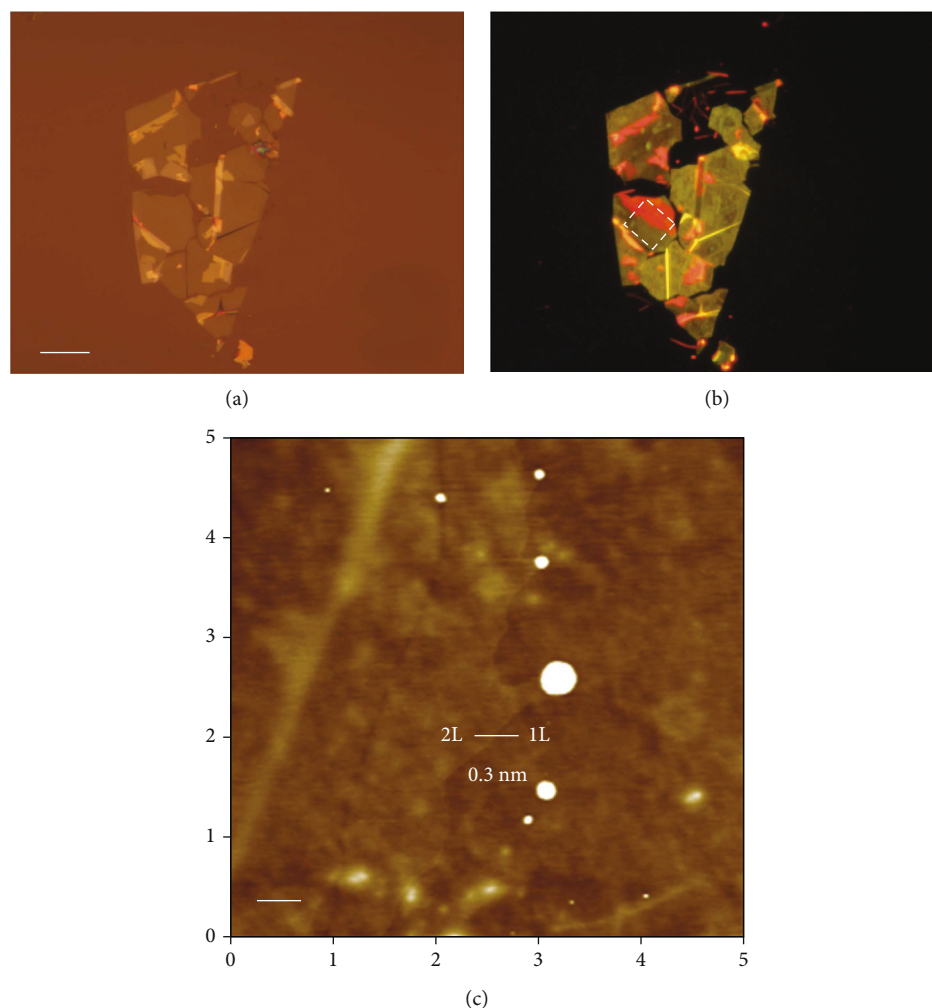
FIGURE 7: Images of the Me-PTCDI monolayer and bilayer films at the room temperature. (a) Optical microscopy image of the sample (scale bar: 10 μm). (b) PL image of the sample. (c) AFM image of the white dashed square region in (b) (scale bar: 500 nm).

software. Afterwards, the calculated average intensities for each wavelength from the sample area and substrate are incorporated into equation (1) as $I(E,d)$ and $I(E,0)$, respectively, to carry out the DRS analysis.

3. Experiments and Discussion

3.1. Absorption Characteristics of the Monolayer Me-PTCDI Film on the h-BN Surface. The optical microscopy and PL image of the sample including monolayer Me-PTCDI films are shown in Figure 5. Based on the PL characteristics of the Me-PTCDI film, the green fluorescence region can be confirmed as the monolayer, whereas the red fluorescence region represents the area covered with more than one layer of the Me-PTCDI molecules. In order to analyse the characteristics of the monolayer film, the samples are measured at room temperature by using the microarea DRS system proposed in this paper. The reflected intensities from the green area representing the monolayer Me-PTCDI on h-BN and the black area representing the quartz substrate are utilized as the signals of the monolayer film and substrate, respectively, to calculate DRS. The absorption of h-BN is noted

to be out of the range of experimental wavelengths; thus, the peaks in Figure 6 correspond to the characteristics of the Me-PTCDI monolayer.

Two peaks of the S0-S1 transition vibronic levels have been observed in the monolayer films. Peak A is observed at 2.26 eV whereas peak B is located at 2.46 eV. The positions of the two peaks are observed to be consistent with the characteristics of the Me-PTCDI monolayer film in the report earlier [26]. It proves that the microarea DRS system proposed in this paper is able to realize the spectral resolution at the monolayer level, even though the measuring area is extremely small, and the reflected intensity is relatively weak.

In addition, by comparing the position of the two peaks with those of the monomer in solution at room temperature [51], it can be observed that both peaks in the monolayer exhibit the redshift from the monomer. The redshift phenomena demonstrate that the first layer of the Me-PTCDI deposited on the h-BN substrate has assembled to form the J-aggregate, which has been extensively studied for novel applications [55–57]. It indicates that the structure based on the Me-PTCDI monolayer and h-BN is suitable for producing the sub-nano-thin-film devices.
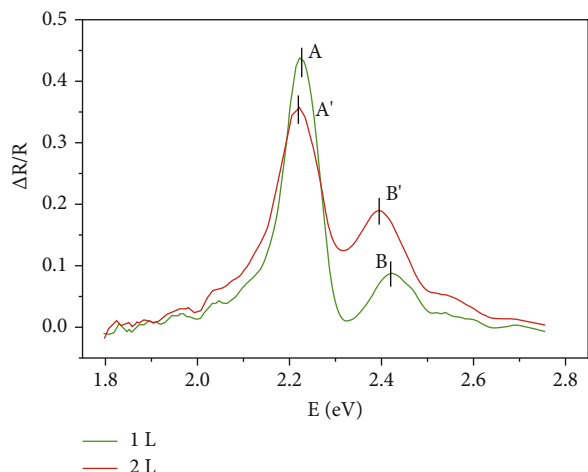
FIGURE 8: The DRS signal of the Me-PTCDI monolayer and bilayer films in Figure 7(c) at room temperature.
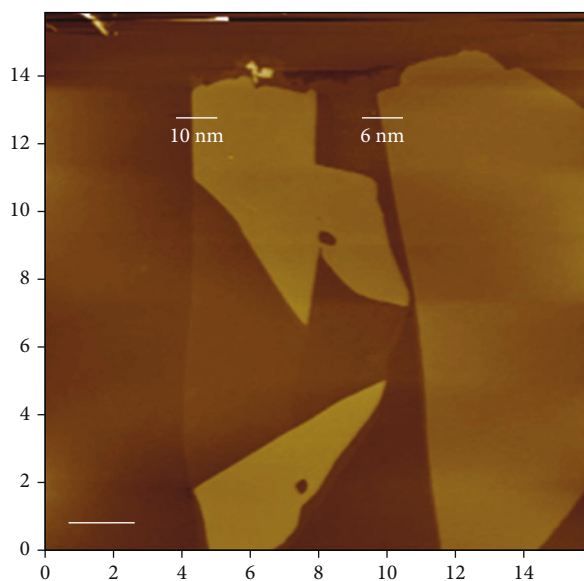
FIGURE 9: AFM image of the monolayer and multilayers of Me-PTCDI films on h-BN in Figure 5 (scale bar: 2 μm).

3.2. Absorption Characteristics of the Me-PTCDI Bilayers on the h-BN Surface.

The optical atomic force microscopy (AFM) images of the sample are shown in Figure 7. The measuring area of the monolayer film can be determined based on the PL image in Figure 7(b). According to the thickness of the monolayer film of Me-PTCDI on h-BN of about 0.3 nm [26], the area with a step of 0.3 nm from the monolayer region can be identified as bilayers in the AFM (Oxford Instruments Asylum Cypher) image. In addition, the DRS signals of the monolayer and bilayers in the area demonstrated in Figure 7(c) are shown in Figure 8.

It can be observed that the both characteristics peaks in the bilayers (peak A′ at 2.18 eV and peak B′ at 2.40 eV) have been slightly redshifted as compared to the

monolayer, which usually occurs during the film growth. However, the abnormal absorption has been observed that the intensity of peak B has increased while the intensity of peak A is decreased, although more molecules exist in the bilayer films.

The phenomenon is likely attributed to the influence of the different molecular aggregates in the Me-PTCDI monolayer and bilayer films. The Me-PTCDI monolayer films solely consist of the J-aggregates, formed by the head-to-tail orientation of the molecules on the surface. It is negative to the excitonic coupling, and the intensity of the spectral peaks is mostly generated by the Frenkel exciton (FE) transition. On the other hand, in bilayers, the H-aggregates formed by the molecules depicting the side-by-side orientation are noted to appear. It is positive to the excitonic coupling between the molecules, thereby resulting in the charge transfer (CT) transition, which has a narrower band gap and more easily realized transition behaviours as compared with FE. Thus, the slight redshifting of the peaks is attributed to the excitonic coupling in bilayers. Furthermore, once the second layer is deposited on the monolayer, a growing number of Me-PTCDI molecules enhance the absorption; however, the interaction generated by the H-aggregates represses the FE transition which has taken place in the monolayer. In addition, for the peaks at different energy positions, the two absorbing species function differently. For some typical organic thin films, the lowest excited state is almost pure FE exciton, whereas mixing between the FE and CT excitons occurs in the region of its vibronic replicas at higher energy positions [51].

Therefore, the experimental results indicate that for the lowest absorption transition contributing to peak A, the FE in the Me-PTCDI monolayer is so significant that the repression of the FE transition results in a decline in the absorption, although additional molecules exist in the bilayers. This observed DRS result also confirms the giant oscillator strength of the Me-PTCDI monolayer film reported in literature [26]. On the other hand, for peak B, which is the vibronic replica of peak A, the enhanced absorption generated by CT in bilayers dominates the characteristic behaviour, which represents an equilibrium between the two exciton species. Actually, the interesting phenomena have also been observed and investigated for the 3,4,9,10-perylenetetracarboxylic dianhydride (PTCDA) thin films [31–33], which is very similar to Me-PTCDI.

The experimental results prove the performance and reliability of the microarea DRS scheme, along with providing insights for producing devices, where the monolayer photoelectric devices based on ultrathin Me-PTCDI must exhibit a better performance at the sub-nanoscale as compared to the bilayer-based devices.

3.3. Absorption Characteristics of the Bulk-Phase Me-PTCDI Film on the h-BN Surface.

The multilayers of Me-PTCDI thin films have also been deposited on other areas of the sample in Figure 5. Combining the AFM topography in Figure 9 with the PL image in Figure 5, the target areas of the multilayer films with different thicknesses can be
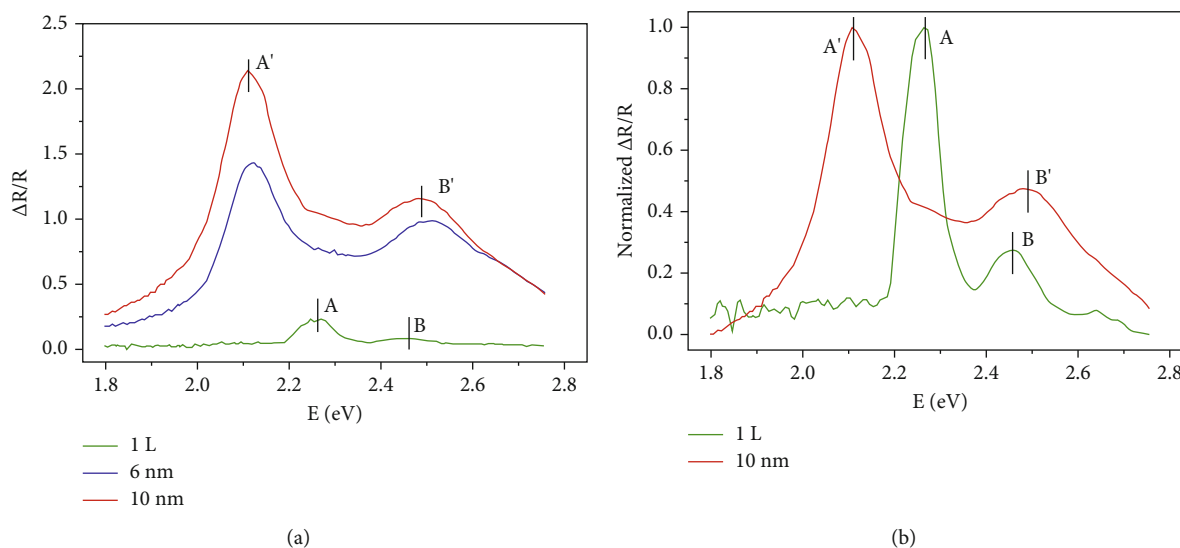
FIGURE 10: DRS of the Me-PTCDI films with different thicknesses on h-BN: (a) DRS of the films with monolayer and thickness of 6 nm and 10 nm and (b) the normalized DRS of the monolayer and 10 nm films.

selected. The DRS and normalized DRS results of the areas with different monolayers and thicknesses of 6 nm and 10 nm are illustrated in Figure 10.

The DRS signals for the sample films with monolayer (green curve), 6 nm (blue curve), and 10 nm (red curve) thicknesses are shown in Figure 10(a). Comparing the curves with different thicknesses, it is obvious that the absorption of the films increases with the thickness owing to the availability of an enhanced extent of molecules to absorb photons.

As shown in Figure 10(a), the positions of the two characteristic peaks (peak A' at 2.10 eV and peak B' at 2.48 eV) in the case of 6 nm and 10 nm films are almost the same, exhibiting independence on the film thickness. Therefore, such films can be regarded as the bulk-phase films.

To analyse the differences between the monolayer and bulk-phase films more effectively, the normalized DRS of the monolayer and 10 nm films is shown in Figure 10(b). The interesting phenomena of peak broadening and peak shift are described in the following.

By comparing the peak width of the bulk-phase film with the monolayer, the broadening phenomena have been observed apparently. The peaks observed in the case of the monolayer film are mostly attributed to FE, which results in the narrow peaks, while the coupling between the layers in bulk-phase films contributes to different excitons (such as FE, CT, and FE-CT) with different energy positions, which results in peak broadening. In addition, the scattering between the excitons and phonons in the thicker films at room temperature also contributes to peak broadening.

Furthermore, it is interesting to note that peak A has been redshifted from the monolayer to the bulk phase, while peak B has been blueshifted. It is likely due to the impact of the substrate described as follows.

In the monolayer film, the π-π conjugation is not formed among the molecules owing to the molecular J-aggregates, while in the bulk-phase films consisting of both J-aggregates and H-aggregates, the π-π bond can be formed between the adjacent layers of molecules. It leads to the electronic coupling, which leads to that the Coulomb potential of molecules has been decreased. Therefore, the characteristic peaks of the multilayer films must move to the lower energy positions in case the interaction among the molecules functions alone.

However, the Coulomb potential between h-BN and Me-PTCDI is different from the Coulomb energy among the Me-PTCDI molecules, also affecting the excitonic transition at the same time. It is commonly reported that the initial layers (especially the first layer) of the organic film are influenced by the substrate significantly, while the impact decreases in the subsequent molecular layers. As a result, the films tend to become stable and form a bulk phase gradually [33–37].

Therefore, the peak shifting from the monolayer to bulk crystal is the combination of the two kinds of different Coulomb energy interactions mentioned above. With respect to the different peak shift phenomena, it is likely that the interaction between the h-BN substrate and Me-PTCDI contributes to locating the peaks in the monolayer to a lower energy position, but the impact degrees of substrate on the two characteristic peaks are different. For the lowest exited transition (peak A and peak A'), the impact of the h-BN substrate is weaker than the effect of Me-PTCDI molecular layers; thus, peak A has been redshifted to peak A' from the monolayer to bulk phase, while for the vibronic replicas of the lowest transition (peak B and peak B'), the impact of the substrate is more significant than the effect of molecules so that peak B in the monolayer is located at a rather lower energy positon as compared to peak B' in bulk crystal, which results in the blueshift phenomena.

The experimental results demonstrate that the microarea DRS scheme is practical at both sub-nano- and nanoscales. Also, the important information for producing devices is revealed that the substrate influences the performance of ultrathin films devices apparently and the devices based on bulk crystal Me-PTCDI must function differently as compared to the devices based on the monolayer films.

4. Conclusions

In this paper, an in situ microarea DRS scheme has been applied to investigate the dependence of the absorption properties on the thickness of the Me-PTCDI films on the h-BN surface, which is a typical structure contained in the nanodevices. The experimental results obtained in this study demonstrate the successful application of the scheme to the monolayer level.

The optical performance of the monolayer, bilayers, and bulk phase of the Me-PTCDI films on the h-BN surface has been analysed by using microarea DRS. Several interesting phenomena and critical properties of the Me-PTCDI/h-BN structure have been revealed. It is demonstrated that the ultrathin Me-PTCDI films on h-BN can be utilized for the sub-nanophotoelectric devices. In particular, the performance of the monolayer device is noted to be superior owing to its greater absorption. In addition, the substrate material for the monolayer devices is also vital due to its significant impact on the monolayer absorption. Furthermore, for the devices produced by incorporating the bulk phase Me-PTCDI films on h-BN at the nanoscale, the performance based on absorption properties can be improved by increasing film thickness, which will function at different characteristic wavelengths with a wider band as compared to the monolayer devices.

The findings reported in this study prove that the microarea DRS scheme is able to detect and analyse the thickness and optical properties of the ultrathin films in the nano- and sub-nanodevices. The scheme is practical and potentially promoted for advanced manufacturing of the nano-thin-film devices in the future.

Data Availability

All data used to support the findings of this study are included within the article.

Conflicts of Interest

The authors declare they have no competing interests.

Acknowledgments

References

[1] D. Li, K. Yao, Z. Gao, Y. Liu, and X. Yu, "Recent progress of skin-integrated electronics for intelligent sensing," *Light: Advanced Manufacturing*, vol. 2, no. 1, pp. 39–58, 2021.

[2] H. Shao, L. Jing, L. Zhang, D. Galar, and U. Kumar, "A novel approach of multisensory fusion to collaborative fault diagnosis in maintenance," *Information Fusion*, vol. 74, pp. 65–76, 2021.

[3] S. Tofail, A. Mani, J. Bauer, and C. Silien, "In situ, real-time infrared (IR) imaging for metrology in advanced manufacturing," *Advanced Engineering Materials*, vol. 20, no. 6, 2018.

[4] H. Ding, R. Gao, A. Isaksson, R. G. Landers, T. Parisini, and Y. Yuan, "State of AI-based monitoring in smart manufacturing and introduction to focused section," *IEEE/ ASME Transactions on Mechatronics*, vol. 25, no. 5, pp. 2143–2154, 2020.

[5] Z. He, H. Shao, X. Zhong, and X. Zhao, "Ensemble transfer CNNs driven by multi-channel signals for fault diagnosis of rotating machinery cross working conditions," *Knowledge-Based Systems*, vol. 207, article 106396, 2020.

[6] B. Li, B. Hou, W. Yu, X. B. Lu, and C. W. Yang, "Applications of artificial intelligence in intelligent manufacturing: a review," *Frontiers of Information Technology & Electronic Engineering*, vol. 18, pp. 86–96, 2017.

[7] J. A. Liddle and G. M. Gallatin, "Nanomanufacturing: a perspective," *ACS Nano*, vol. 10, no. 3, pp. 2995–3014, 2016.

[8] F. Fang, X. Zhang, W. Gao, Y. B. Guo, G. Byrne, and H. N. Hansen, "Nanomanufacturing—perspective and applications," *CIRP Annals*, vol. 66, no. 2, pp. 683–705, 2017.

[9] K. S. Novoselov, A. K. Geim, S. V. Morozov et al., "Electric field effect in atomically thin carbon films," *Science*, vol. 306, no. 5696, pp. 666–669, 2004.

[10] L. Lv, F. Zhuge, F. Xie et al., "Reconfigurable two-dimensional optoelectronic devices enabled by local ferroelectric polarization," *Nature Communications*, vol. 10, no. 1, p. 3331, 2019.

[11] J. Tao, W. Shen, S. Wu et al., "Mechanical and electrical anisotropy of few-layer black phosphorus," *ACS Nano*, vol. 9, no. 11, pp. 11362–11370, 2015.

[12] G. Iannaccone, F. Bonaccorso, L. Colombo, and G. Fiori, "Quantum engineering of transistors based on 2D materials heterostructures," *Nature Nanotechnology*, vol. 13, pp. 183–191, 2018.

[13] A. Islam, A. Akker, and P. Feng, "Polarization sensitive black phosphorus nanomechanical resonators," *Optical Materials Express*, vol. 9, no. 2, pp. 526–535, 2019.

[14] B. Radisavljevic, A. Radenovic, J. Brivio, V. Giacometti, and A. Kis, "Single-layer MoS_2 transistors," *Nature Nanotechnology*, vol. 6, no. 3, pp. 147–150, 2011.

[15] J. Shim, A. Oh, D. Kang et al., "High-performance 2D rhenium disulfide (ReS2) transistors and photodetectors by oxygen plasma treatment," *Advanced Materials*, vol. 28, no. 32, pp. 6985–6992, 2016.

[16] H. Huang, J. Wang, W. Hu et al., "Highly sensitive visible to infrared $MoTe_2$ photodetectors enhanced by the photogating effect," *Nanotechnology*, vol. 27, no. 44, article 445201, 2016.

[17] X. Liu, J. Gu, K. Ding et al., "Photoresponse of an organic semiconductor/two-dimensional transition metal dichalcogenide heterojunction," *Nano Letters*, vol. 17, no. 5, pp. 3176–3181, 2017.

[18] H. Huang, S. Chen, X. Gao, W. Chen, and A. T. Wee, "Structural and electronic properties of PTCDA thin films on epitaxial graphene," *ACS Nano*, vol. 3, no. 11, pp. 3431–3436, 2009.

[19] I. A. Pshenichnyuk, P. B. Coto, S. Leitherer, and M. Thoss, "Charge transport in pentacene-graphene nanojunctions," *Journal of Physical Chemistry Letters*, vol. 4, no. 5, pp. 809–814, 2013.

[20] X. Liu, X. Chen, J. Yi et al., "Organic charge-transfer interface enhanced graphene hybrid phototransistors," *Organic Electronics*, vol. 64, pp. 22–26, 2018.

[21] Q. Wang and M. C. Hersam, "Room-temperature molecular-resolution characterization of self-assembled organic monolayers on epitaxial graphene," *Nature Chemistry*, vol. 1, no. 3, pp. 206–211, 2009.

[22] J. Yang, D. Yan, and T. S. Jones, "Molecular template growth and its applications in organic electronics and optoelectronics," *Chemical Reviews*, vol. 115, no. 11, pp. 5570–5603, 2015.

[23] J. Liu, H. Zhang, H. Dong et al., "High mobility emissive organic semiconductor," *Nature Communications*, vol. 6, pp. 1–8, 2015.

[24] H. Ling, S. Liu, Z. Zheng, and F. Yan, "Organic flexible electronics," *Small Methods*, vol. 2, no. 10, article 1800070, 2018.

[25] Y. Zhang, J. Qiao, S. Gao et al., "Probing carrier transport and structure-property relationship of highly ordered organic semiconductors at the two-dimensional limit," *Physical Review Letters*, vol. 116, no. 1, article 016602, 2016.

[26] H. Zhao, Y. Zhao, Y. Song et al., "Strong optical response and light emission from a monolayer molecular crystal," *Nature Communications*, vol. 10, no. 1, p. 5589, 2019.

[27] W. He, H. Zang, S. Cai et al., "Intercalation and hybrid heterostructure integration of two-dimensional atomic crystals with functional organic semiconductor molecules," *Nano Research*, vol. 13, no. 11, pp. 2917–2924, 2020.

[28] D. He, Y. Zhang, Q. Wu et al., "Two-dimensional quasi-freestanding molecular crystals for high-performance organic field-effect transistors," *Nature Communications*, vol. 5, no. 1, p. 5162, 2014.

[29] J. D. E. Mcintyre and D. E. Aspnes, "Differential reflection spectroscopy of very thin surface films," *Surface Science*, vol. 24, no. 2, pp. 417–434, 1971.

[30] H. Zaglmayr, C. Hu, L. Sun, and P. Zeppenfeld, "Optical referencing in differential reflectance spectroscopy," *Measurement Science and Technology*, vol. 25, article 115603, 2014.

[31] R. Forker and T. Fritz, "Optical differential reflectance spectroscopy of ultrathin epitaxial organic films," *Physical Chemistry Chemical Physics*, vol. 11, no. 13, pp. 2142–2155, 2009.

[32] R. Forker, M. Gruenewald, and T. Fritz, "Optical differential reflectance spectroscopy on thin molecular films," *Annual Reports on the Progress of Chemistry, Section C: Physical Chemistry*, vol. 108, pp. 34–68, 2012.

[33] H. Proehl, T. Dienel, R. Nitsche, and T. Fritz, "Formation of solid-state excitons in ultrathin crystalline films of PTCDA: from single molecules to molecular stacks," *Physical Review Letters*, vol. 93, no. 9, article 097403, 2004.

[34] H. Proehl, R. Nitsche, T. Dienel, K. Leo, and T. Fritz, "In situ differential reflectance spectroscopy of thin crystalline films of PTCDA on different substrates," *Physical Review B*, vol. 71, no. 16, article 165207, 2005.

[35] L. Zhang, X. Fu, C. Hu et al., "Optical and structural properties of the pentacene/quartz (0001) interface," *Physical Review B*, vol. 93, no. 7, 2006.

[36] L. Zhang, X. Fu, M. Hohage, P. Zeppenfeld, and L. D. Sun, "Growth of pentacene on α-Al 2 O 3 (0001) studied by in situ optical spectroscopy," *Physical Review Materials*, vol. 1, no. 4, 2017.

[37] L. Zhang, C. Hu, X. Fu, M. Jiang, Q. Sui, and L. Jia, "Pentacene crystal transition during the growth on SiO2 studied by in situ optical spectroscopy," *Synthetic Metals*, vol. 231, pp. 65–69, 2017.

[38] Y. Wang, L. Zhang, S. Lv et al., "In-situ variable reflectance spectra model of two-dimensional material prepared by CVD," *Journal of Crystal Growth*, vol. 559, article 126034, 2021.

[39] C. An, Z. Xu, W. Shen et al., "The opposite anisotropic piezoresistive effect of ReS2," *ACS Nano*, vol. 13, no. 3, pp. 3310–3319, 2019.

[40] W. Shen, C. Hu, J. Tao et al., "Resolving the optical anisotropy of low-symmetry 2D materials," *Nanoscale*, vol. 10, no. 17, pp. 8329–8337, 2018.

[41] M. Zhong, H. Meng, S. Liu et al., "In-plane optical and electrical anisotropy of 2D black arsenic," *ACS Nano*, vol. 15, no. 1, pp. 1701–1709, 2021.

[42] L. Liu, Y. Feng, and Z. Shen, "Structural and electronic properties of h-BN," *Physical Review B*, vol. 68, article 104102, 2003.

[43] J. D. Caldwell, I. Aharonovich, G. Cassabois, J. H. Edgar, B. Gil, and D. N. Basov, "Photonics with hexagonal boron nitride," *Nature Reviews Materials*, vol. 4, pp. 552–567, 2019.

[44] C. Dean, A. F. Young, I. Meric et al., "Boron nitride substrates for high-quality graphene electronics," *Nature Nanotech*, vol. 5, pp. 722–726, 2010.

[45] A. Pakdel, Y. Bando, and D. Golberg, "Nano boron nitride flatland," *Chemical Society Reviews*, vol. 43, no. 3, pp. 934–959, 2014.

[46] T. Kaiser, H. Wang, V. Stepanenko, and F. Würthner, "Supramolecular construction of fluorescent J-aggregates based on hydrogen-bonded perylene dyes," *Angewandte Chemie*, vol. 119, no. 29, pp. 5637–5640, 2007.

[47] H. Wang, T. E. Kaise, S. Uemura, and F. Würthner, "Perylene bisimide J-aggregates with absorption maxima in the NIR," *Chemical Communications*, vol. 10, pp. 1181–1183, 2008.

[48] F. Zhao, X. Luo, J. Liu et al., "Toward high performance broad spectral hybrid organic–inorganic photodetectors based on multiple component organic bulk heterojunctions," *Journal of Materials Chemistry C*, vol. 4, pp. 815–822, 2016.

[49] M. Meissner, M. Gruenewald, F. Sojka, C. Udhardt, R. Forker, and T. Fritz, "Highly ordered growth of PTCDA on epitaxial bilayer graphene," *Surface Science*, vol. 606, no. 21-22, pp. 1709–1715, 2012.

[50] M. Gruenewald, C. Sauer, J. Peuker et al., "Commensurism at electronically weakly interacting phthalocyanine/PTCDA heterointerfaces," *Physical Review B*, vol. 91, no. 15, 2015.

[51] M. Hoffmann, K. Schmidt, T. Fritz, T. Hasche, V. M. Agranovich, and K. Leo, "The lowest energy Frenkel and charge-transfer excitons in quasi-one-dimensional structures: application to MePTCDI and PTCDA crystals," *Chemical Physics*, vol. 258, no. 1, pp. 73–96, 2000.

[52] W. Tress, A. Petrich, M. Hummert, M. Hein, K. Leo, and M. Riede, "Imbalanced mobilities causing S-shaped IV curves in planar heterojunction organic solar cells," *Applied Physics Letters*, vol. 98, article 063301, p. 23, 2011.

[53] H. Yu, J. H. Kim, W. Chen, D. Kim, J. Guo, and F. So, "Effect of nano-porosity on high gain permeable metal-base transistors,"

Advanced Functional Materials, vol. 24, no. 38, pp. 6056–6065, 2014.

[54] J. Zhang, X. Ye, C. Gu et al., "Non-covalent interaction controlled 2D organic semiconductor films: molecular self-assembly, electronic and optical properties, and electronic devices," *Surface Science Reports*, vol. 75, article 100481, 2020.

[55] M. Y. Losytskyy and V. M. Yashchuk, "Fluorescent J-aggregates and their biological applications," in *Advanced Fluorescence Reporters in Chemistry and Biology II*, vol. 9 of Springer Series on Fluorescence, pp. 135–157, Springer, Berlin, Heidelberg, 2010.

[56] F. C. Spano and C. Silva, "H- and J-aggregate behavior in polymeric semiconductors," *Annual Review of Physical Chemistry*, vol. 65, pp. 477–500, 2014.

[57] G. D. Scholes, G. R. Fleming, L. Chen et al., "Using coherence to enhance function in chemical and biophysical systems," *Nature*, vol. 543, no. 7647, pp. 647–656, 2017.

Research Article

Position Encoder Analysis and Low Delay Control for a Medical Robot with Six DoFs

Wenyuan Liang [ID],[1,2] **Xiaobo Zhou,**[3] **and Qing Lan** [ID][3,4]

[1]*College of Engineering, Peking University, Beijing, China*
[2]*National Research Center for Rehabilitation Technical Aids, Beijing, China*
[3]*Suzhou Key Laboratory of Minimally Invasive Neurosurgery, Suzhou, China*
[4]*Department of Neurosurgery, The Second Affiliated Hospital of Soochow University, Suzhou, China*

Correspondence should be addressed to Wenyuan Liang; lwy123@hotmail.com and Qing Lan; szlq006@163.com

Medical robots are in great demand for orthopedic surgery. The robotic control could be divided into two layers, the top layer and the bottom layer (also called joint control). However, how to improve the dynamic performance of joint control is still a challenging issue. Traditional PID control and PID-based sliding mode control are commonly used methods for the joint control of medical and industrial robots. In this paper, the proposed joint control is based on dynamic compensation. Dynamic compensation includes inertia and friction. The joint control diagram includes PID, sliding mode control, and adaptive dynamic compensation as a module unit. The design of the proposed joint control method could overcome the disadvantages of model uncertainty and dynamic disturbances and improve robot dynamic performance. Additionally, since control feedback is based on the joint position encoder, position encoder analysis is included in this paper. The dynamic performance of the proposed joint control was tested on the six-DoF medical robot, and the indexes of rising time, task space tracking, and contact space tracking were adopted to evaluate the dynamic performance. The experimental results show that the proposed control method has a much smaller rising time than the commercial controller product. The control proposed in this paper realized low delay control and improved the dynamic response of the control.

1. Introduction

Many medical robots are being developed for surgery (Figure 1 shows examples of medical robot applications) to realize better operation performance that is more precise and minimally invasive, compared with traditional manual procedures.

Research related to medical robots for orthopedic surgery began in the mid-1980s [1, 2]. The orthopedic medical robots are supposed to play an important role in orthopedic surgery. The role of orthopedic medical robots is divided into two kinds of essential features. The first feature is that the orthopedic medical robots can be used for bone cutting/drilling/milling, and the second feature is that the orthopedic medical robots can be used for holding/placing surgical tools [3].

The basic requirements for medical robots are safe, reproducible, and precise [1]. One of these mentioned requirements is to provide more precise control during robotic surgical procedures. The robotic control could be divided into two layers (see Figure 2), the top layer and the bottom layer. The top layer focuses on manipulation planning, and the bottom layer focuses on joint control [4, 5]. Both the top layer and the bottom layer could improve the precise control of the robot.

This paper will focus on the joint control of the medical robot. For the joint control, the key is its dynamic performance. The indexes of the dynamic performance of joint control are included in [4, 6]. In this paper, the indexes of rising time, task space tracking, and contact space tracking will be adopted to test the dynamic performance of the controller.

Diseased joint

Bones cut
and shaped

Implants in place

(a)

(b)
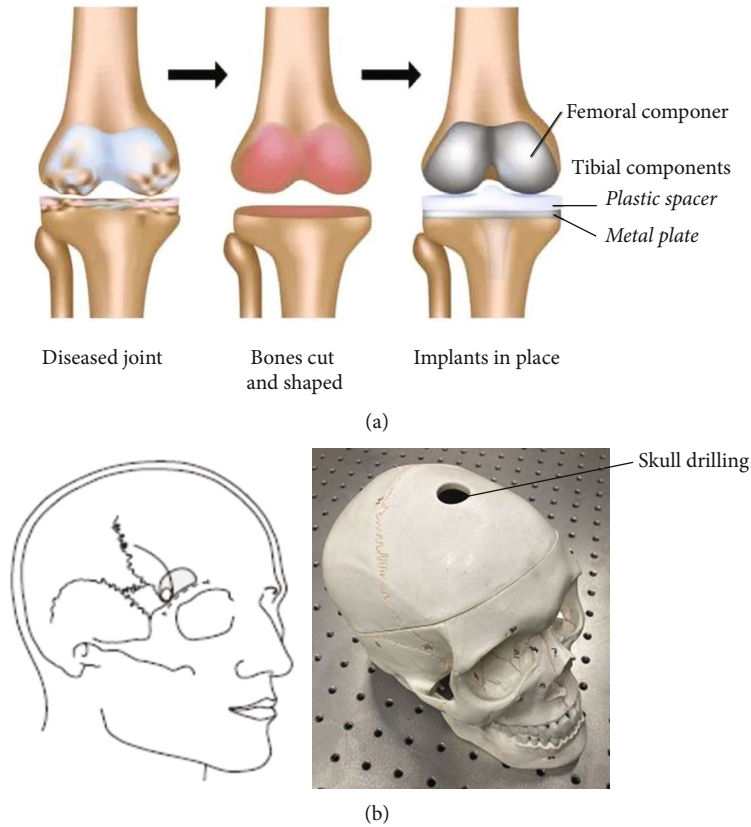
FIGURE 1: Examples of medical robot applications in surgery: (a) orthopedic surgery and (b) neurosurgery.
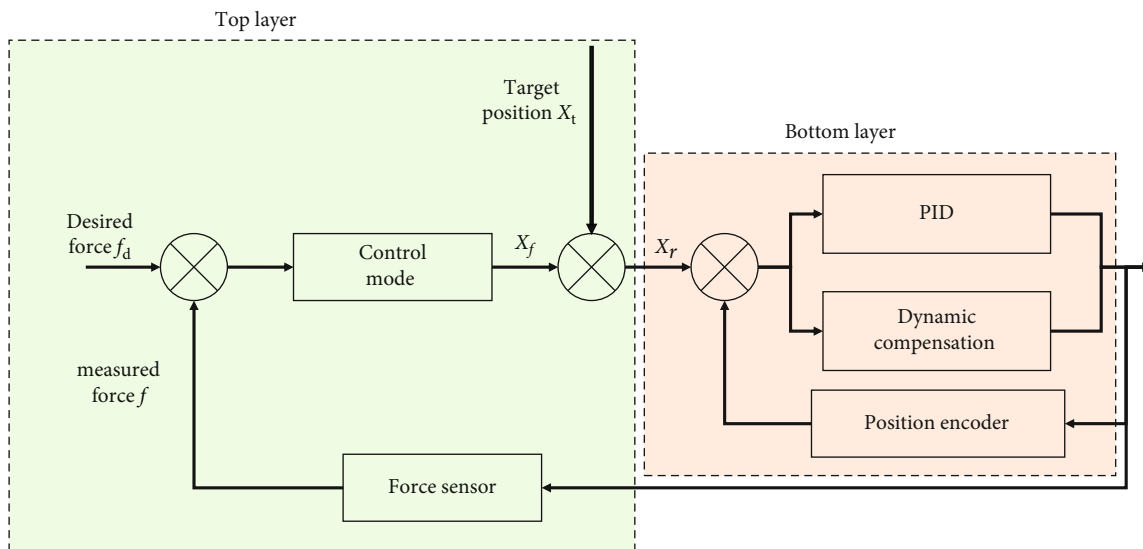
FIGURE 2: General robotic control diagram (top layer and bottom layer).

To date, orthopedic medical robots, such as MAKO, Robodoc, Praxim, and Navio, have good performance on clinical surgical tasks [7]. However, how to improve the control performance and reduce the delay time of joint control [8] is still a challenging issue in robotics.

In early robotic applications, because PID control [9] has a simple structure and easy adjustment, PID control is used as a component of joint control and is widely used in both indus-

trial robots and medical robots. With the development of robotic applications, traditional joint control cannot meet the requirements that are of good dynamic characteristics and high precision result [10]. Therefore, many improved joint control methods have been proposed [11–13]. Intelligent methods for PID tuning are adopted to improve the joint control performance. In [11], some autotuning methods have been proposed by researchers. Since PID fails in the case of

uncertain environment, to realize high-precision trajectory tracking under model uncertainty and external disturbances, researchers have adopted a sliding mode control (SMC) method that includes PID and sliding mode control. In [12], it lists different configurations of PID-based SMC to overcome the drawbacks of PID. In [13], researchers combine the fuzzy gain tuning, the robustness of the sliding mode controller, and the rapid response characteristics of the PID, which effectively reduces the chattering caused by the sliding mode controller and improves the stability of the system. Although PID-based SMC has the advantages of tracking trajectory with high precision and overcoming the uncertain environment, it still has a limit on dynamic performance.

The essence of dynamic performance of the joint control is bandwidth. Both tuning control parameters and dynamic compensation are approaches to improve bandwidth. Improving the bandwidth could reduce the delay time of the control response [14]. However, researchers [9–13] focus on tuning the control parameters, and the research on the dynamic compensation of the joint control (bottom layer) is much less.

By considering that dynamic compensation is also a good approach to reduce the delay time of the joint control, this paper will improve the dynamic characteristics of the joint control by adding dynamic compensation. Dynamic compensation includes inertia and friction.

In this paper, the main contribution of the proposed method over the previous methods is the joint control diagram which includes PID, sliding mode control, and adaptive dynamic compensation as a module unit. The design of the proposed joint control method could overcome the disadvantages of model uncertainty and dynamic disturbances and improve the dynamic performance of robot.

The structure of this paper is as follows. In the second section, the VDC method [5] is used to build the kinematics of the 6-DoF medical robot. In the third section, it shows an improved control approach that combines joint control and dynamic compensation. Since control feedback is based on the joint position encoder, the position encoder analysis included in the fourth section will discuss how to determine the data bits and sampling time. The control performance is shown in the fifth section.

2. Kinematics of the 6-DoF Medical Robot

In this paper, the medical robot is with six DoFs (see Figure 3), and its load capacity is 10 kg. In the project, this robot is supposed to be used for drilling and placing. From the base to the end effector, the six joints are labeled as J1–J6. All six joints are the type of rotational joint.

For the 6-DoF robot, the inertial coordinate frame is defined as F_0-$x_0 y_0 z_0$; the coordinate frame for the end effector is labeled as F_{ee}-$x_{ee} y_{ee} z_{ee}$; the coordinate frame for the ith ($i = 1, 2, \cdots, 6$) joint is F_i-$x_i y_i z_i$, and the direction of the axis z_i aligns with the rotational axis of the ith joint, respectively.

Based on the VDC method [5], the 6-DoF robot is virtually decomposed into six subsystems by placing six cutting points at the six joints, respectively. As illustrated in Figure 4, a cutting point is an interface of separation that virtually cuts through the ith joint. The ith joint is located between the $(i - 1)$th link

and the ith link. For the ith joint, two coordinate frames are defined. The first is the inboard frame $F_{\hat{i}}$ which is attached on Link i-1 and labeled with $F_{\hat{i}} - x_{\hat{i}} y_{\hat{i}} z_{\hat{i}}$, and the second is the outboard frame F_i which is attached on Link i and labeled with F_i-$x_i y_i z_i$. Therefore, while the ith joint rotates with θ_i, the outboard frame F_i will rotate along the axis $z_{\hat{i}}$ as θ_i with respect to the inboard frame $F_{\hat{i}}$. If $\theta_i = 0$, frame F_i and frame $F_{\hat{i}}$ will share the same position and orientation at the cutting point. Since frame $F_{\hat{i}}$ and frame F_{i-1} are attached on the same Link $i - 1$, the rotation matrices ${}^{i-1}C_{\hat{i}}$ between frame F_{i-1} and frame $F_{\hat{i}}$ are constant. The rotation matrices associated with inboard frame and outboard frame can be expressed as

$$
{}^iC_{\hat{i}} = \begin{bmatrix} \cos\theta_i & -\sin\theta_i & 0 \\ \sin\theta_i & \cos\theta_i & 0 \\ 0 & 0 & 1 \end{bmatrix}. \tag{1}
$$

The transformation matrices between inboard frame and outboard frame are defined as

$$
{}^{\hat{i}}T_{i-1} = \begin{bmatrix} {}^{\hat{i}}C_{i-1} & -{}^{\hat{i}}C_{i-1} \cdot \left({}^{i-r}r_{i-1,\hat{i}} \right) \\ 0_{3\times3} & {}^{\hat{i}}C_{i-1} \end{bmatrix}, \tag{2}
$$

$$
{}^{\hat{i}}T_{i-1} = \begin{bmatrix} {}^{\hat{i}}C_i & 0_{3\times3} \\ 0_{3\times3} & {}^{\hat{i}}C_i \end{bmatrix}, \tag{3}
$$

where in Equation (2), is ${}^{i-r}r_{i-1,\hat{i}}$ the position vector between the origin of frame $F_{\hat{i}}$ and the origin of frame F_{i-1} that is expressed in frame F_{i-1}, and the cross-product operator is defined as

$$
(r \times) = \left(\begin{bmatrix} r_1 \\ r_2 \\ r_3 \end{bmatrix} \times \right) = \begin{bmatrix} 0 & -r_3 & r_2 \\ r_3 & 0 & -r_1 \\ -r_2 & r_1 & 0 \end{bmatrix}. \tag{4}
$$

Based on Table 1, which shows the D-H parameters of the 6-DoF robot, it can derive the following.

$$
\begin{aligned}
&{}^0r_{0,\hat{1}} = [0, 0, a_0]', \, {}^0C_{\hat{1}} = [-1, 0, 0\,;0, -1, 0\,;0, 0, 1]', \\
&{}^1r_{1,\hat{2}} = [0, 0, a_1]', \, {}^1C_{\hat{2}} = [0, -1, 0\,;0, 0, -1\,;1, 0, 0]',
\end{aligned} \tag{5}
$$

$$
\begin{aligned}
&{}^2r_{2,\hat{3}} = [a_2, 0, 0]', \, {}^2C_{\hat{3}} = [0, -1, 0\,;-1, 0, 0\,;0, 0, -1]', \\
&{}^3r_{3,\hat{4}} = [0, -a_3, 0]', \, {}^3C_{\hat{4}} = [1, 0, 0\,;0, 0, -1\,;0, 1, 0]', \\
&{}^4r_{4,\hat{5}} = [0, 0, a_4]', \, {}^4C_{\hat{5}} = [1, 0, 0\,;0, 0, 1\,;0, -1, 0]', \\
&{}^5r_{5,\hat{6}} = [0, -a_5, 0]', \, {}^5C_{\hat{6}} = [1, 0, 0\,;0, 0, -1\,;0, 1, 0]'.
\end{aligned} \tag{6}
$$

Hence, for the 6-DoF robot, the transformation matrix from the base to the end effector is
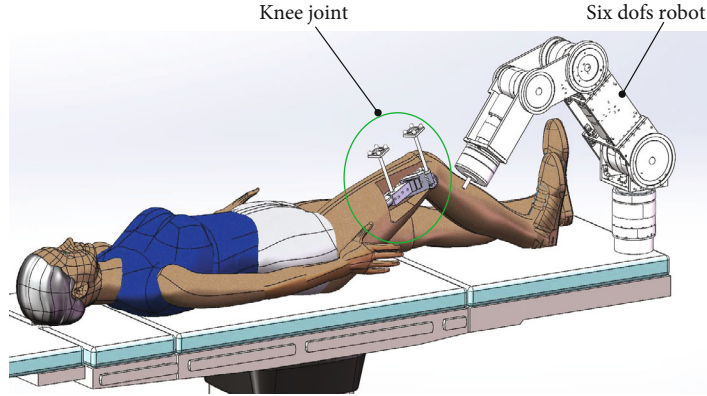
FIGURE 3: Medical robot with six DoFs for knee joint surgery.
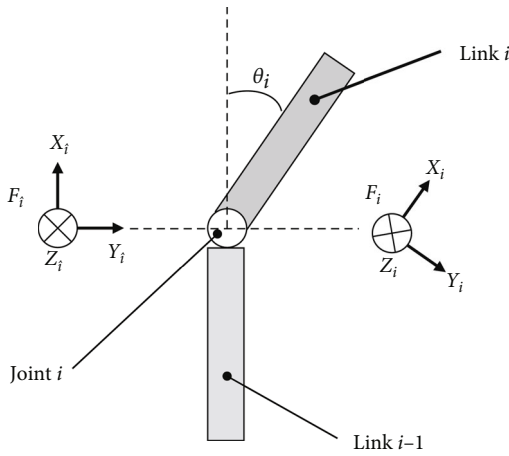
FIGURE 4: Inboard frame and outboard frame of the ith joint.

TABLE 1: D-H parameters of the 6-DoF robot.

	θ_i	d_i (unit: m)	a_{i-1} (unit: m)	α_{i-1}
Joint 1	θ_1	0.26	0	90°
Joint 2	θ_2	0	0.48	180°
Joint 3	θ_3	0	0	90°
Joint 4	θ_4	0.52	0	−90°
Joint 5	θ_5	0	0	90°
Joint 6	θ_6	0.196	0	0°

$$^0T_6 = {}^0T_{\hat{1}} \cdot {}^{\hat{1}}T_1 \cdot {}^1T_{\hat{2}} \cdot {}^{\hat{2}}T_2 \cdot {}^2T_{\hat{3}} \cdot {}^{\hat{3}}T_3 \cdot {}^3T_{\hat{4}} \cdot {}^{\hat{4}}T_4 \cdot {}^4T_{\hat{5}} \cdot {}^{\hat{5}}T_5 \cdot {}^5T_{\hat{6}} \cdot {}^{\hat{6}}T_6. \tag{7}$$

3. Dynamics and Controller of the 6-DoF Medical Robot

In this paper, the control is model-based. The classical adaptive identification method [15, 16] was adopted to identify the inertial parameters in this research project. However, in previous research, the adaptive identification method was not included in the joint control structure of joint con-

trol, and it was included in the top layer of the control of the system.

In this section, the first part will build the dynamics of the subsystem, and the second part will show the joint control based on dynamic compensation.

3.1. Dynamics of the Subsystem. As mentioned above, the full system of the 6-DoF robot is virtually decomposed into six subsystems. This part will discuss the velocity transformation, force transformation, and dynamics of the subsystem.

For the velocity transformation, the defined labels have the corresponding meanings: ^iv_i represents that the linear velocity of target (v_i) is with respect to the origin of the frame F_i and is expressed in frame F_i; $^i\omega_i$ represents that the angular velocity of the target (ω_i) is with respect to the origin of the frame F_i and is expressed in frame F_i. Then, the following will hold:

$$
\begin{bmatrix} ^iv_i \\ ^iw_i \end{bmatrix} = {}^iT_{\hat{i}} \cdot \begin{bmatrix} ^{\hat{i}}v_{\hat{i}} \\ ^{\hat{i}}w_{\hat{i}} \end{bmatrix} + \begin{bmatrix} 0_{3\times1} \\ \vec{z}_i \end{bmatrix} \cdot \dot{\theta}_i,
$$

$$
\begin{bmatrix} ^{\widehat{i+1}}v_{\widehat{i+1}} \\ ^{\widehat{i+1}}w_{\widehat{i+1}} \end{bmatrix} = {}^{\widehat{i+1}}T_i \cdot \begin{bmatrix} ^iv_i \\ ^iw_i \end{bmatrix},
$$

$$
^iT_{\hat{i}} = \begin{bmatrix} ^iC_{\hat{i}} & 0_{3\times3} \\ 0_{3\times3} & ^iC_{\hat{i}} \end{bmatrix},
$$

$$
^{\widehat{i+1}}T = \begin{bmatrix} ^{\hat{i}}C_i & -^{\hat{i}}C_i \cdot ({}^ir_{i,mi} \times) \\ 0_{3\times3} & ^{\hat{i}}C_i \end{bmatrix},
$$

(8)

where $^ir_{i,mi}$ is the CoM (center of mass) position of Link i that is expressed in frame F_i.

For the force transformation, the defined labels have the corresponding meanings: $^if_{net,i}$ represents the vector sum of the force (except the gravitational force) that is acting on Link i and expressed in frame F_i; $^im_{net,i}$ represents the vector sum of the moment of force (except the contribution of the gravitational force) that is acting on Link i and expressed in
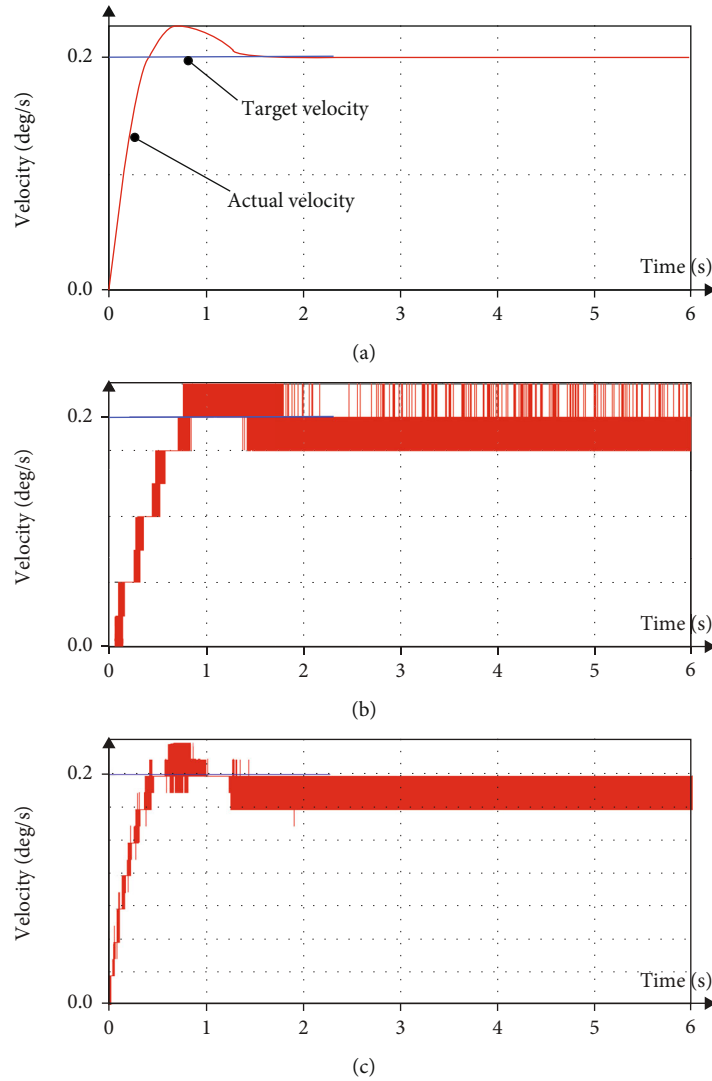
FIGURE 5: Encoder output comparison with different data bits.

frame F_i. $\tau_{\text{net},i}$ represents the sum of torque that is acting on the ith joint. Then, Equations (9) and (10) will hold.

$$\begin{bmatrix} {}^i f_i \\ {}^i m_i \end{bmatrix} = {}^{i+1}\widehat{T}_i^T \cdot \begin{bmatrix} \widehat{{}^{i+1} f_{i+1}} \\ \widehat{{}^{i+1} m_{i+1}} \end{bmatrix} + \begin{bmatrix} {}^i f_{\text{net},i} \\ {}^i m_{\text{net},i} \end{bmatrix}, \quad (9)$$

$$\begin{bmatrix} \widehat{{}^i f_{\widehat{i}}} \\ \widehat{{}^i m_{\widehat{i}}} \end{bmatrix} = {}^i\widehat{T}_{\widehat{i}}^T \cdot \begin{bmatrix} {}^i f_i \\ {}^i m_i \end{bmatrix} + \begin{bmatrix} 0_{3\times 1} \\ \vec{z}_i \end{bmatrix} \cdot {}^i \tau_{\text{net},i}, \quad (10)$$

where in Equations (9) and (10), $[{}^i f_i, {}^{\widehat{i}} f_{\widehat{i}}, {}^{i+1} f_{\widehat{i+1}}]$ and $[{}^i m_i, {}^{\widehat{i}} m_{\widehat{i}}, {}^{i+1} m_{\widehat{i+1}}]$ are all the intermediate calculation results.

For the ith subsystem, m_i is the mass of Link i, I_i is the moment of inertia of Link i which is with respect to the CoM of Link i, and $\vec{g}$ is the gravity vector. Then, the dynam-

ics of the ith subsystem is expressed as

$$M_i \bullet \begin{bmatrix} {}^i \dot{v}_i \\ {}^i \dot{\omega}_i \end{bmatrix} + C_i \bullet \begin{bmatrix} {}^i v_i \\ {}^i \omega_i \end{bmatrix} + G_i = \begin{bmatrix} {}^i f_{\text{net},i} \\ {}^i m_{\text{net},i} \end{bmatrix}, \quad (11)$$

where

$$M_i = \begin{bmatrix} m_i \bullet I_{3\times 3} & -m_i \bullet ({}^i r_{i,mi} \times) \\ m_i \bullet ({}^i r_{i,mi} \times) & I_i - m_i \bullet ({}^i r_{i,mi} \times)^2 \end{bmatrix},$$

$$C_i = \begin{bmatrix} m_i \bullet ({}^i \omega_i \times) & -m_i \bullet ({}^i \omega_i \times) \bullet ({}^i r_{i,mi} \times) \\ m_i \bullet ({}^i r_{i,mi} \times) \bullet ({}^i \omega_i \times) & \begin{array}{l} ({}^i \omega_i \times) \bullet I_i + I_i \bullet ({}^i \omega_i \times) - \\ m_i \bullet ({}^i r_{i,mi} \times) \bullet ({}^i \omega_i \times) \bullet ({}^i r_{i,mi} \times) \end{array} \end{bmatrix},$$

$$G_i = \begin{bmatrix} -m_i \bullet {}^i C_0 \bullet \vec{g} \\ -m_i \bullet ({}^i r_{i,mi} \times) \bullet {}^i C_0 \bullet \vec{g} \end{bmatrix}. \quad (12)$$

FIGURE 6: Encoder output comparison with different sampling times.

3.2. Control Based on Dynamic Compensation.

In this paper, the model-based design is adopted to set up the controller. The classical adaptive identification method [15, 16] was adopted to identify the inertial parameters in the bottom layer of control. Additionally, joint control is the basic of full-system control. Optimizing the joint control can improve reducing the delay time of the dynamic response. Therefore, in this part, the discussions will focus on joint control.

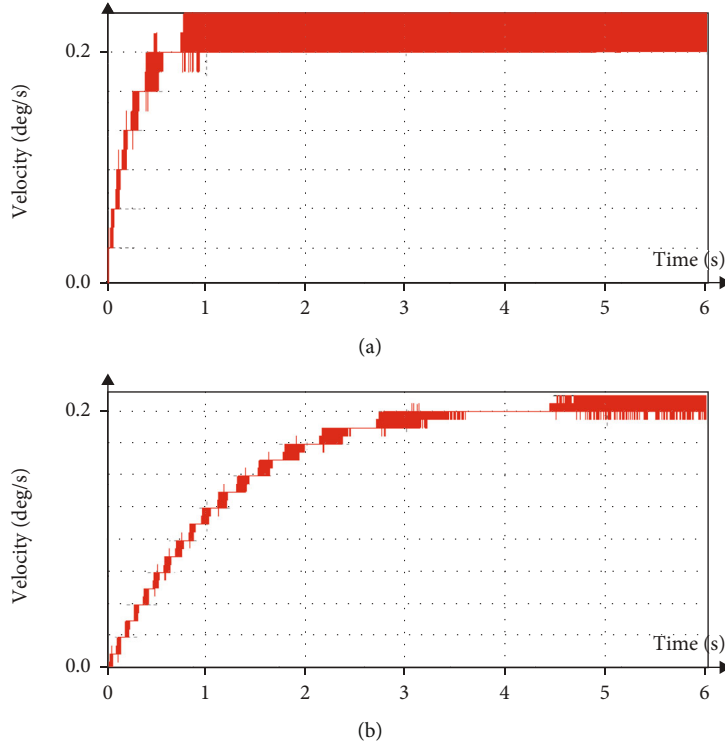In Equation (13), it shows the common sliding mode control. $\theta_{d,i}$ and $\dot{\theta}_{d,i}$ are the command of the ith joint position and velocity, respectively. For the control coefficient, there is $\lambda_i > 0$.

$$\dot{\theta}_{r,i} = \dot{\theta}_{d,i} + \lambda_i \bullet (\theta_{d,i} - \theta_i). \tag{13}$$

For the ith joint, its control law is defined as Equation (14). In the right part of Equation (14), the first three items play the role of dynamic compensation, and the last three items play the role of control.

$$
{}^i\tau_{\mathrm{net},i} = I_{j,i} \bullet \ddot{\theta}_{r,i} + \widehat{k}_{c,i} \bullet \mathrm{sign}\left(\dot{\theta}_{r,i}\right) + \widehat{k}_{v,i} \bullet \dot{\theta}_{r,i} \\
+ k_{P,i} \bullet \theta_{e,i} + k_{I,i} \bullet \int \theta_{e,i} + k_{D,i} \bullet \dot{\theta}_{e,i}. \tag{14}
$$

Additionally, $\theta_{e,i} = \theta_{d,i} - \theta_i$, $\dot{\theta}_{e,i} = \dot{\theta}_{d,i} - \dot{\theta}_i$; $\widehat{k}_{c,i}$ is the estimated value for the Coulomb friction coefficient of the ith joint, and $\widehat{k}_{v,i}$ is the estimated value for the viscous friction

TABLE 2: Control parameters of the six joints.

Joint	6	5	4	3	2	1
$k_{P,i}$	0.2	0.2	1.2	1.2	3.1	3.1
$k_{I,i}$	0.06	0.06	0.5	0.5	1.2	1.2
$k_{D,i}$	0.01	0.01	0.1	0.1	0.23	0.23
t_{rise} (ms)	68	53	51	57	50	50
$t_{c,\mathrm{rise}}$ (ms)			110			
$\frac{t_{c,\mathrm{rise}} - t_{\mathrm{rise}}}{t_{c,\mathrm{rise}}}$ (%)	38.2%	51.8%	53.6%	48.2%	54.4%	54.5%

coefficient of the ith joint; $k_{P,i}$, $k_{I,i}$, and $k_{D,i}$ are the PID control parameters.

In Equation (14), $I_{j,i}$, $\widehat{k}_{c,i}$, and $\widehat{k}_{v,i}$ are the unknown variables. The inertial variable $I_{j,i}$ was identified based on the classical adaptive identification method [15, 16] by the top layer of control. $\widehat{k}_{c,i}$ and $\widehat{k}_{v,i}$ are identified by using the following equations: Equations (15)–(17). $\bar{k}_{c,i}$ and $\underline{k}_{c,i}$ are supremum and infimum for $k_{c,i}$, respectively; $\bar{k}_{v,i}$ and $\underline{k}_{v,i}$ are supremum and infimum for $k_{v,i}$, respectively. The function $\mathscr{P}$ is the identification function [4], and its time derivative is shown in Equation (17).

$$
\begin{bmatrix} s_{c,i} \\ s_{v,i} \end{bmatrix} = \begin{bmatrix} \mathrm{sign}\left(\dot{\theta}_{r,i}\right) \\ \dot{\theta}_{r,i} \end{bmatrix} \bullet \left(\dot{\theta}_{e,i} + \lambda_i \bullet \theta_{e,i}\right), \tag{15}
$$
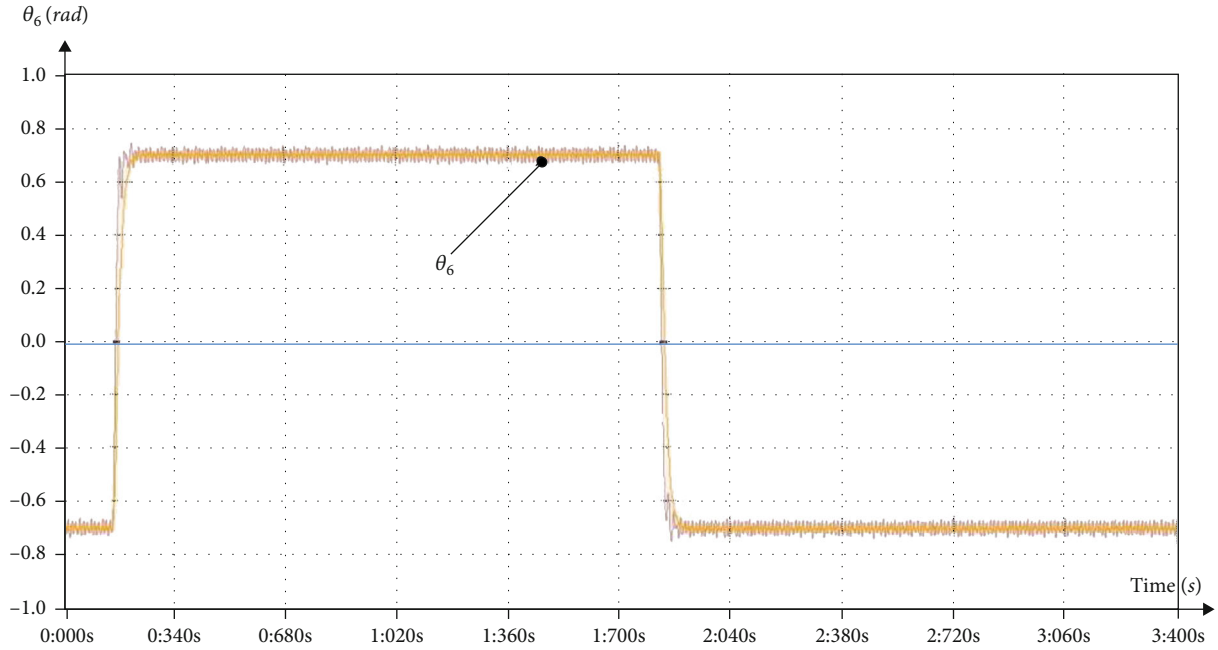
Figure 7: Joint control performance of Joint 6.
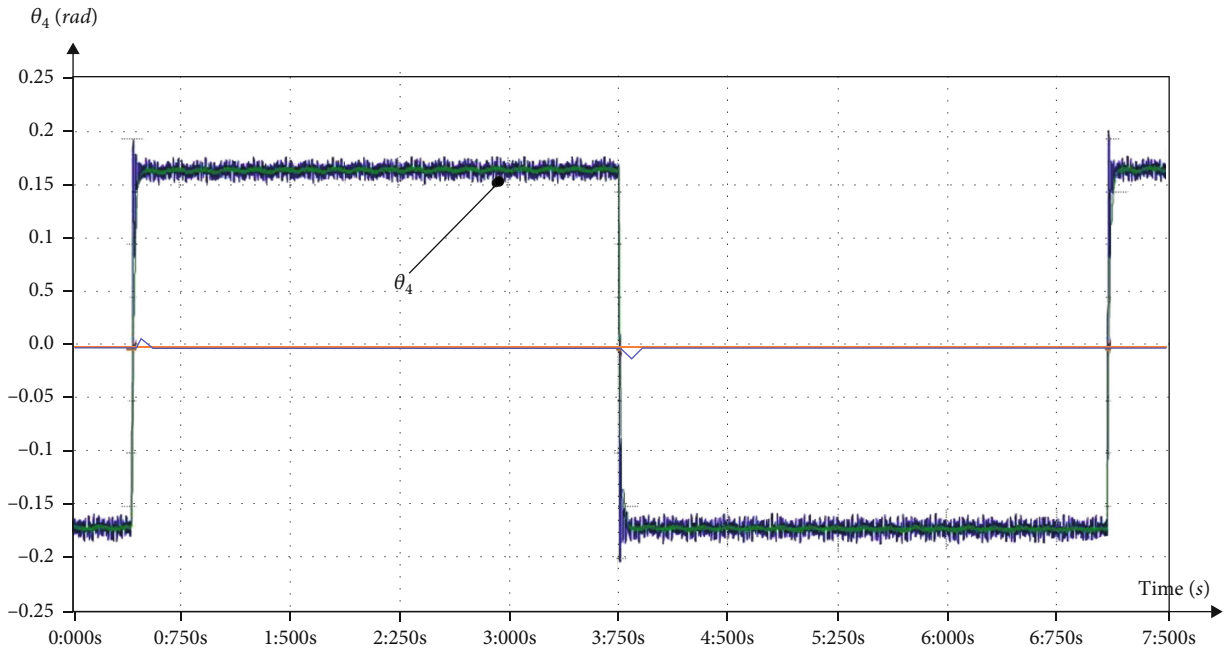
Figure 8: Joint control performance of Joint 4.

$$\begin{bmatrix} \widehat{k}_{c,i} \\ \widehat{k}_{v,i} \end{bmatrix} = \begin{bmatrix} \mathscr{P}_{c,i}\left(s_{c,i}, \rho_{c,i}, \bar{k}_{c,i}, \underline{k}_{c,i}, t\right) \\ \mathscr{P}_{v,i}\left(s_{v,i}, \rho_{v,i}, \bar{k}_{v,i}, \underline{k}_{v,i}, t\right) \end{bmatrix}, \qquad (16)$$

$$\dot{\mathscr{P}}\left(s(t), \rho, \bar{k}, \underline{k}, t\right) = \begin{cases} 0, \text{ if } \mathscr{P} \geq \bar{k} \text{ and } s \geq 0, \\ 0, \text{ if } \mathscr{P} \leq \underline{k} \text{ and } s \leq 0, \\ \rho \bullet s(t), \text{ otherwise.} \end{cases} \qquad (17)$$

Finally, the computation result of ${}^{i}\tau_{\text{net},i}$ in Equation (14) is substituted into Equation (10). Then, a complete dynamic equation of the subsystem shown in Equation (11) is obtained. The matrices of M_i, C_i, and G_i are also identified based on the classical adaptive identification method [15, 16].

4. Position Encoder Analysis

In this paper, the position encoders are fixed on the motor axis of each joint. In this section, it will discuss how to choose the position encoders based on the simulation analysis.
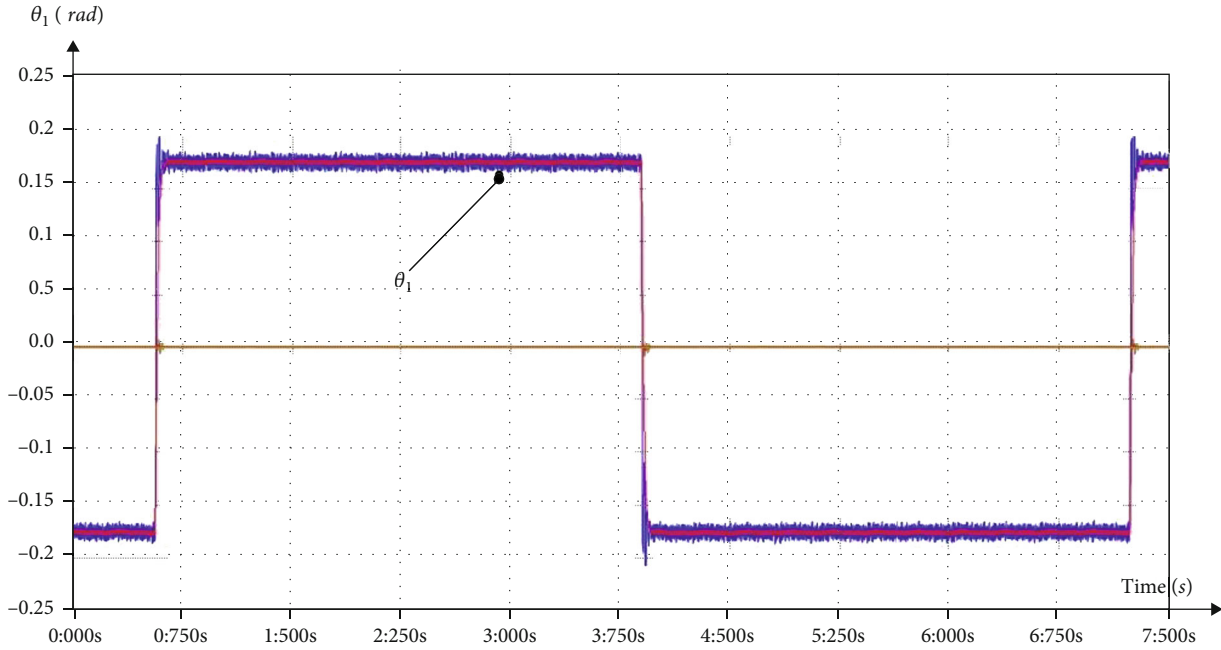
FIGURE 9: Joint control performance of Joint 1.
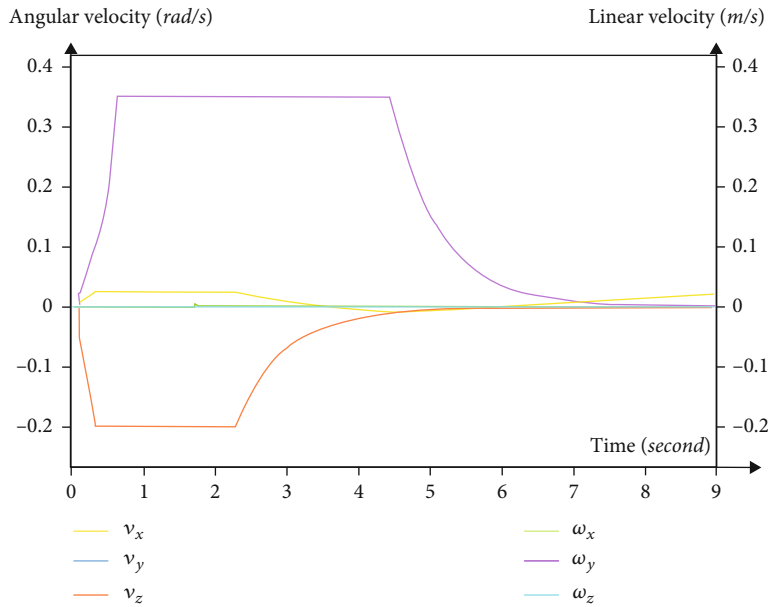
FIGURE 10: The commanded velocities of the end effector.

4.1. Data Bits Requirement Analysis. As well known, data bits output by the encoder during one round of the encoder shaft will determine the encoder resolution. If an encoder has insufficient resolution, it will not provide effective feedback to the controller, and the system will not perform as required.

In the data bits analysis, the target velocity is set as 0.2 deg/s (see Figure 5(a)), and the gear ratio for each motor is 160 : 1. Two types of encoder are adopted to detect the actual velocity. Figure 5(b) shows the recording result of the encoder with 15 data bits. Figure 5(c) shows the recording result of the encoder with 16 data bits.

Based on the comparisons, especially in the duration from start to 1 second, it shows that the encoder with 16 data bits has better tracking performance than the encoder with 15 data bits. Therefore, in this paper, the robot controller is based on the position encoders with 16 data bits.

4.2. Sampling Time Requirement Analysis. Since the computation resource is limited, it is needed to choose an appropriate sampling time of the encoder. Figure 6(a) shows the recording result of the encoder with a sampling time of 0.1 ms. Figure 6(b) shows the recording result of the encoder with sampling time of 0.25 ms.
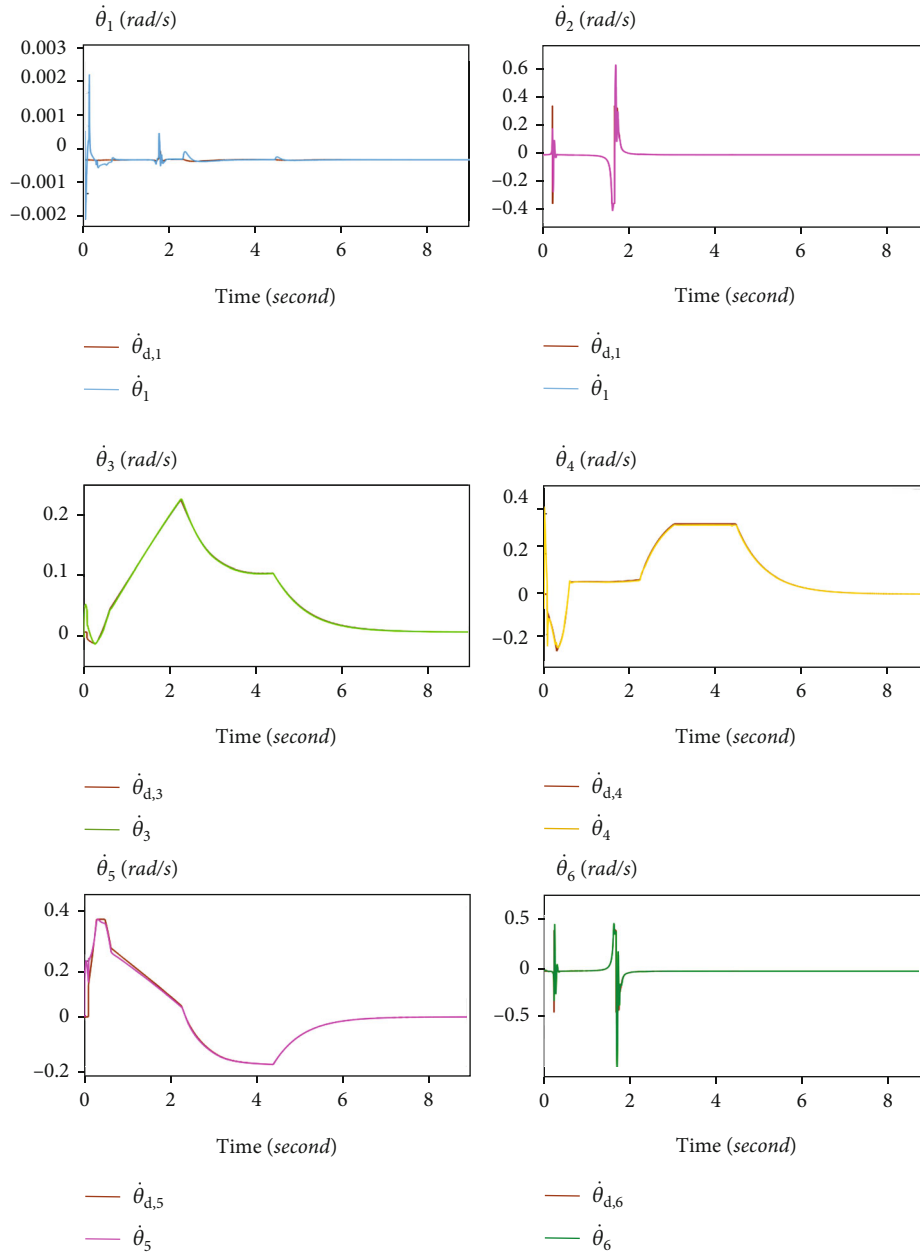
FIGURE 11: Tracking velocities of six joints.

By comparing the encoder performance of recording continuity, it shows that the encoder with 0.1 ms sampling time is better. Therefore, in this paper, the robot controller is based on position encoders with a sampling time of 0.1 ms sampling time.

5. Control Performance

In control processing, the hardware is based on the BECKH-OFF TwinCAT 3 real-time platform, and the communication protocol is EtherCAT.

In this section, the experimental test of the proposed controller follows the performance criteria shown in [6]. The criteria include the tests of step response, trajectory tracking without load, and payload verification. The experi-

mental tests of control performance are based on the 6-DoF medical robot platform. As shown in Table 2, the control parameters for the six joints are listed in detail.

5.1. Joint Control Performance. To reduce the delay time of the dynamic response, in this part, this paper will focus on the rising time for each joint under the command of a sequence of step-square waves. The dynamic joint response can be recorded by TwinCAT 3, and then, the rising time based on the recorded curves can be detected.

Based on the control proposed in the last section, the joint control performances are shown in Figures 7–9.

In Figures 7–9, all figures show that each joint control can achieve the goal with high precision and well dynamic response. More details are shown in Table 2. The rising time
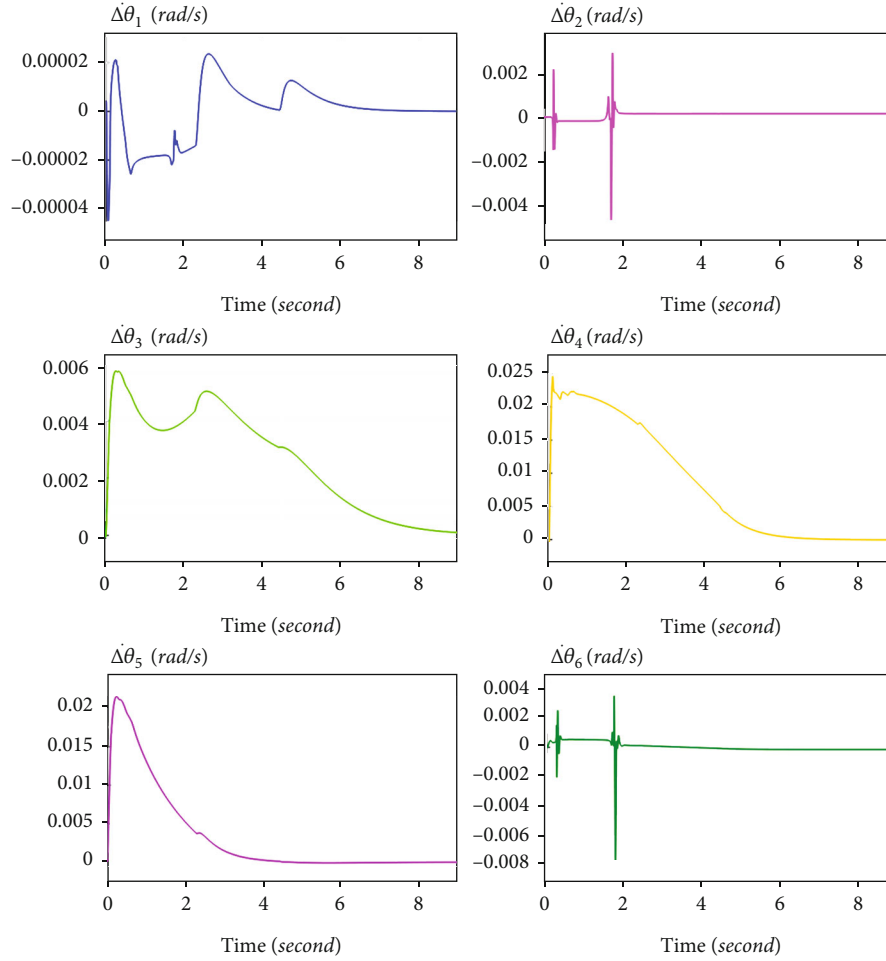
FIGURE 12: Tracking velocity errors of six joints.

for each joint is 68 ms, 53 ms, 51 ms, 57 ms, 50 ms, and 50 ms, respectively.

For comparison, a commercial controller was adopted to control this 6-DoF robot, and the rising time of joint response ($t_{c,\text{rise}}$) was about 110 ms based on the commercial controller. Compared with the commercial controller, the controller proposed in this paper could reduce the rising time of joint response by almost more than 50% (see Table 2). Hence, the controller proposed in this paper realized low delay control and improved the dynamic response of control.

5.2. Task Space Tracking Performance. To test the tracking performance of the 6-DoF robot in the task space, a set of commanded velocities of the end effector is adopted as shown in Figure 10.

In Figure 10, the path planning for the commanded velocities follows three steps, speed up, constant speed, and slow down.

Based on the commanded velocities of the end effector, the six joints of the robot will track the commanded velocities in the joint space. As shown in Figure 11, it shows the tracking results of the joint velocities. For the ith joint, $\dot{\theta}_{d,i}$ is the commanded joint velocity, and $\dot{\theta}_i$ is the real joint velocity ($i = 1, 2, \cdots, 6$). Figure 11 shows that the six joints could follow the commanded velocities well.

In Figure 12, it shows the tracking error of the six joints. The tracking error is small and converging to zero.

Therefore, based on the experimental results shown in Figures 11 and 12, the controller shown in this paper could realize the good tracking performance of the 6-DoF robot in the task space.

5.3. Contact Space Tracking Performance. To test the tracking performance of the 6-DoF robot in the contact space, the test experiments include plate surface contact test and curved surface contact test (see Figure 13). In both tests, the robot is expected to move along the surface with a stable contact force.

In Figure 14, it shows the trajectory of the contact force when the robot is required to move along the plate surface. The contact force is recorded by a six-dimensional force sensor. The commanded contact force is set as 5 N.

In Figure 15, it shows the trajectory of the contact force when the robot is required to move along the curved surface. The commanded contact force is set as 10 N.

Both in Figures 14 and 15, the robot could track the surface well. In particular, in the test of curved surface, the end

Plate surface   Curved surface
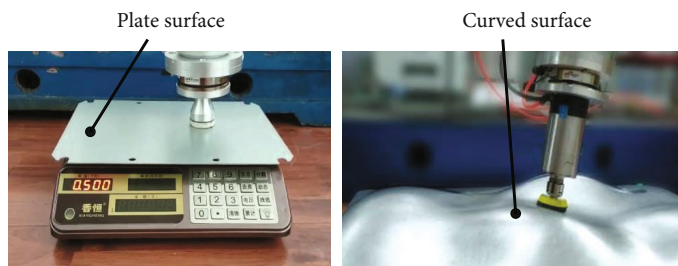
FIGURE 13: Contact space test (plate surface and curved surface).
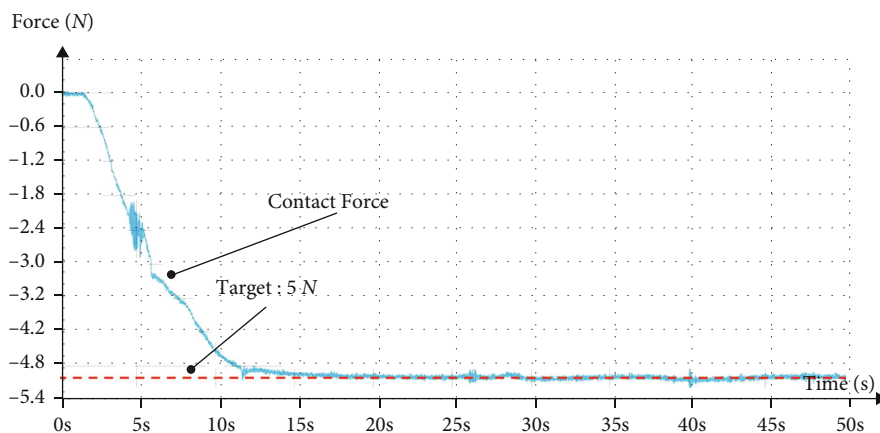
FIGURE 14: Plate surface contact tracking performance.
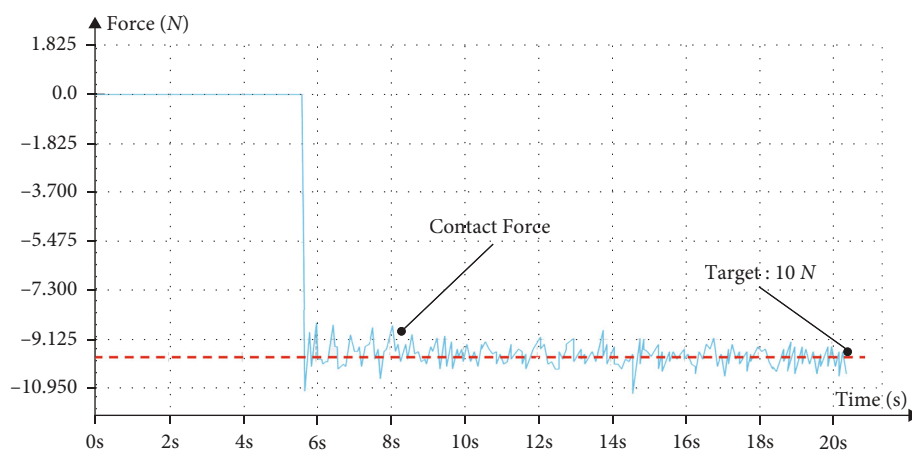
FIGURE 15: Curved surface contact tracking performance.

of the robot could keep a stable contact force on the complex curved surface. The experimental results of the contact space tracking show the controller have well dynamic performance.

6. Conclusions

In this paper, a method for joint control in robot-assisted orthopedic surgery was proposed. Compared to traditional joint control, improved joint control includes PID, sliding mode control, and adaptive dynamic compensation as a module unit. The performance of the proposed joint control

was tested on a six-DoF robot. The experimental results of the joint dynamic response under square waves show that the proposed control method has a much smaller rising time than the commercial controller product, which means better performance in high dynamic response for the robot. The experimental results of the tracking performance in the task space and contact space show that the robot could follow the commanded velocities well.

In the near future, the proposed joint control method will be applied for real orthopedic surgery experiments. And further research will focus on improving human-machine collaboration based on the proposed control method.

Data Availability

The data used to support the findings of this study are available from the corresponding author upon request.

Conflicts of Interest

The authors declare that there is no conflict of interest regarding the publication of this paper.

Acknowledgments

References

[1] W. L. Bargar, "Robots in orthopaedic surgery," *Clinical Orthopedics and Related Research*, vol. 463, pp. 31–36, 2007.

[2] F. Picard, A. H. Deakin, P. E. Riches, K. Deep, and J. Baines, "Computer assisted orthopaedic surgery: past, present and future," *Medical Engineering and Physics*, vol. 72, pp. 55–65, 2019.

[3] J. Kubicek, F. Tomanec, M. Cerny, D. Vilimeck, M. Kalova, and D. Oczka, "Recent trends, technical concepts and components of computer-assisted orthopedic surgery systems: a comprehensive review," *Sensors*, vol. 19, no. 23, pp. 5199–5233, 2019.

[4] D. Kortenkamp and R. Simmons, "Robotic systems architectures and programming," in *Springer Handbook of Robotics*, O. Khatib and B. Siciliano, Eds., pp. 187–206, Springer, 2008.

[5] W. H. Zhu, *Virtual decomposition control: toward hyper degrees of freedom robots*, Springer, [New York, NY], 2012.

[6] P. Chiacchio, F. Pierrot, L. Sciavicco, and B. Siciliano, "Robust design of independent joint controllers with experimentation on a high-speed parallel robot," *IEEE Transactions on Industrial Electronics*, vol. 40, no. 4, pp. 393–403, 1993.

[7] M. W. Allen and D. J. Jacofsky, "Evolution of robotics in arthroplasty," in *Robotics in Knee and Hip Arthroplasty*, pp. 14–25, Springer, 2019.

[8] X. Tian and Y. Xu, "Low delay control algorithm of robot arm for minimally invasive medical surgery," *IEEE Access*, vol. 8, pp. 93548–93560, 2019.

[9] K. J. Strm and T. Hgglund, *PID Controllers: Theory, Design and Tuning*, The Instrumentation, Systems and Automation Society, 1995.

[10] C. A. Nelson, M. A. Laribi, and S. Zeghloul, "Multi-robot system optimization based on redundant serial spherical mechanism for robotic minimally invasive surgery," *Robotica*, vol. 37, no. 7, pp. 1202–1213, 2019.

[11] R. P. Borase, D. K. Maghade, S. Y. Sondkar, and S. N. Pawar, "A review of PID control, tuning methods and applications," *International Journal of Dynamics and Control*, vol. 9, no. 2, pp. 818–827, 2021.

[12] S. J. Gambhlre, D. R. Klshore, P. S. Londhe, and S. N. Pawar, "Review of sliding mode based control techniques for control system applications," *International Journal of Dynamics and Control*, vol. 9, no. 1, pp. 363–378, 2021.

[13] X. Wang, H. Lan, and K. Li, "Treatment of femoral neck fractures with cannulated screw invasive internal fixation assisted by orthopaedic surgery robot positioning system," *Orthopedic Surgery*, vol. 11, no. 5, pp. 864–872, 2019.

[14] S. D. Eppinger, "Understanding bandwidth limitations in robot force control," in *Proceedings of the IEEE International Conference on Robotics and Automation*, pp. 904–909, North Carolina, USA, 1987.

[15] J. Wu, J. Wang, and Z. You, "An overview of dynamic parameter identification of robots," *Robotics and Computer-Integrated Manufacturing*, vol. 26, no. 5, pp. 414–419, 2010.

[16] W. Khalil, M. Gautier, and P. Lemoine, "Identification of the payload inertial parameters of industrial manipulators," in *Proceedings of the IEEE International Conference on Robotics and Automation*, pp. 4943–4948, Roma, Italia, 2007.

Research Article

Feature Fusion for Weld Defect Classification with Small Dataset

Wenhui Hou [ID]**, Lulu Rao, Andong Zhu, and Dashan Zhang** [ID]

Anhui Provincial Engineering Laboratory of Intelligent Agricultural Machinery, School of Engineering,
Anhui Agriculture University, No. 130 West Changjiang Road, Hefei 230026, China

Correspondence should be addressed to Dashan Zhang; zhangds@mail.ustc.edu.cn

Detecting defects from weld radiography images is an important topic in the field of nondestructive testing. Many intelligent detection systems are constructed based on computer. Feature extraction is critical for constructing such system to recognize and classify the weld defects. Deep neural networks have powerful ability to learn representative features that are more sensitive to classification. However, a large number of samples are usually required. In this paper, a stacked autoencoder network is used to pretrain a deep neural network with a small dataset. We can learn the hierarchical feature from the network. In addition, two kinds of traditional manual features are extracted from the same set. These features are combined into new fusion feature vectors for classifying different weld defects. Two evaluation methods are used to test the classification performance of these features through several experiments. The results show that deep feature based on stacked autoencoder network performs better than the other features. The classification performance of fusion features is better than single feature.

1. Introduction

As a basic technology, welding is widely used in many areas, such as aerospace manufacturing, bridge engineering, and mechanical manufacturing. Due to the complexity of the welding process, the instability of the welding parameters, or the influence of the welding stress and deformation in the structure, welding defects are inevitable, such as the lack of penetration, porosity, slag inclusion, and crack. The appearance of welding defects directly affects the quality of welding products, which causes the failure of welding structure and even safety accidents. Therefore, it is necessary to detect and classify the welding defects.

Detection of welding defects is an important task of nondestructive testing of welding materials. Among them, X-ray testing is the most common preferred technique for examining the quality of welded joints. For this, experienced workers need to inspect the defects from the radiography film generated in X-ray testing. This process is not only time-consuming but also subjective [1]. Many scholars have been committed to building an objective and intelligent detection systems for weld defects. Such system based on digital radiography images often involves feature extraction and pattern recognition.

Feature extraction from weld images is the core of intelligent detection systems. According to the investigation, D' Angelo and Rampone [2] pointed out that the key to the system for recognizing the structure defects is to extract the features that can express the defects more uniquely. The pattern recognition is conducted for classifying different types of defects. In the initial testing, the geometrical and the texture features are commonly used for classifying the weld defects [3–7]. The geometrical features which describe the shape and orientation of defects are usually defined by experts. Boaretto and Centeno [5] extracted several geometrical features (area, eccentricity, solidity, ratio, etc.) from the discontinuities detected in weld bead region. Then, a multilayer perceptron (MLP) was used to classify discontinuities as defect or no-defect through these features and achieved an accuracy of 88.6%. In addition, they also tried to classify the different defects, but the attempt was not successful because of the unbalanced data. In these works, the geometric features extracted by different scholars are not the same. Kumar et al. [7] used texture features based on the gray level cooccurrence matrix (GLCM) as input features of back propagation (BP) neural network, achieving a classification accuracy of 86.1%. Furthermore, they simultaneously
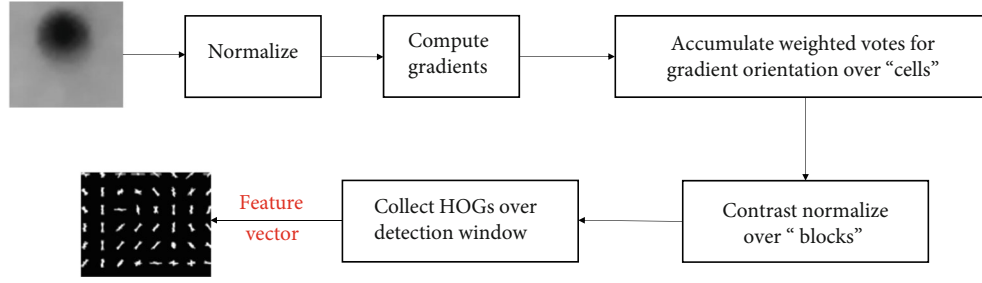
FIGURE 1: The flowchart of extracting HOG feature.

extracted both texture and geometric features, eventually achieving an accuracy of 87.34% [8]. Wang and Guo [9] extracted three numeral features from potential region and used support vector machines (SVM) to distinguish real defects from potential defects. The physical meaning of each feature is different. In addition, the Mel-frequency cepstral coefficients and polynomial coefficients were used as the classification features in weld detection [10, 11]. These features can be collectively known as manual features. However, the manual extraction of features has significant drawback: it is task intensive [12]. The extracted features are inconsistent, and it is difficult to find the general features for varying task.

Recently, deep learning has been a significant breakthrough in image analysis and interpretation. The popular deep learning techniques including deep belief network (DBN), recurrent neural network (RNN), and convolutional neural network (CNN) have attracted increasing attention and become the popular tools for fault diagnosis and defect detection [13–15]. These networks can automatically extract the features without any hand operation for detecting the weld images. The classification performance of deep features through deep neural network is better [16]. However, the deep CNN got poor classification performance when the training dataset is small [17]. This is just because of the characteristic of deep learning: the good performance of deep networks benefits from the training by lots of data. However, it is not easy to collect big dataset of weld defects because the resolution of radiography image for weld seam is usually high. Stacked autoencoder (SAE) [18] is proposed as an alternative to restricted Boltzmann machine (RBM) [19, 20] in pretraining [21, 22]. SAE is used to pretrain a deep neural network with a small dataset. In our work, we use SAE for pretraining and fine-turning strategies to train a deep neural network (DNN).

In this paper, we applied information fusion technology to combine different features for weld defect classification. The workflow of classification is given in the following parts. Firstly, feature extraction is discussed in Section 2. HOG features and texture features are introduced. In addition, a SAE network is constructed to learn multilevel features. Moreover, we investigate pretraining and fine-turning strategies to get better features. Secondly, in Section 3, the above features are combined with each other. Thirdly, an experiment about weld defect classification is shown in Section 4. In this part, we investigated the classification performance of different kinds of features and fusion features. The experiment
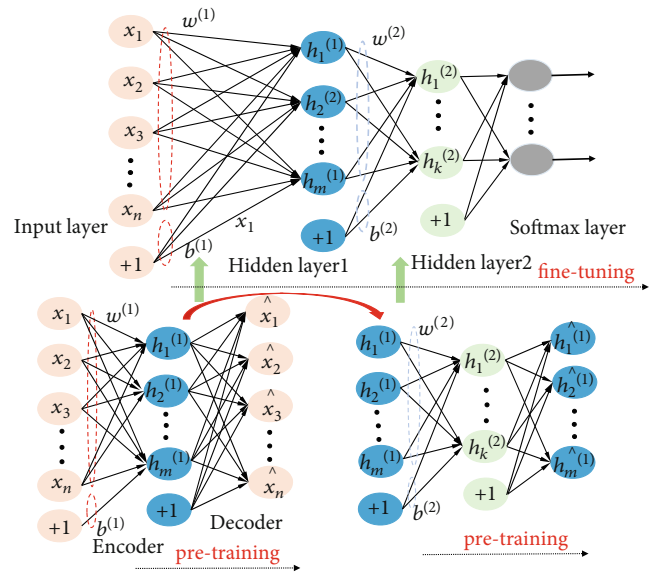
FIGURE 2: The structure of SAE.

results are discussed, and suggestions are given for future research in Section 5.

2. Feature Extraction

Different defects in radiography image exhibit various visual properties in shapes, sizes, textures, and positions. In order to recognize various defects, the important features of the specific type of defects should be artificially selected. The characteristics based on intensity contrast are very useful to classify weld defects because of different gray value distributions of different defect types. In this section, two traditional manual features based on gray level distribution are introduced. In addition, a feature learning technology based on DNN is elaborated.

2.1. HOG Feature Vector. Histograms of oriented gradient (HOG) descriptors based on a statistical evaluation of a series of normalized local gradient direction histograms of the image window are first proposed by Dalal and Triggs for human detection [23]. They capture the gradient or edge direction characterizing the appearance and shape of the local objects. They are robust to small changes in image contour locations and directions and significant change in image illumination. The features of descriptors are extracted as
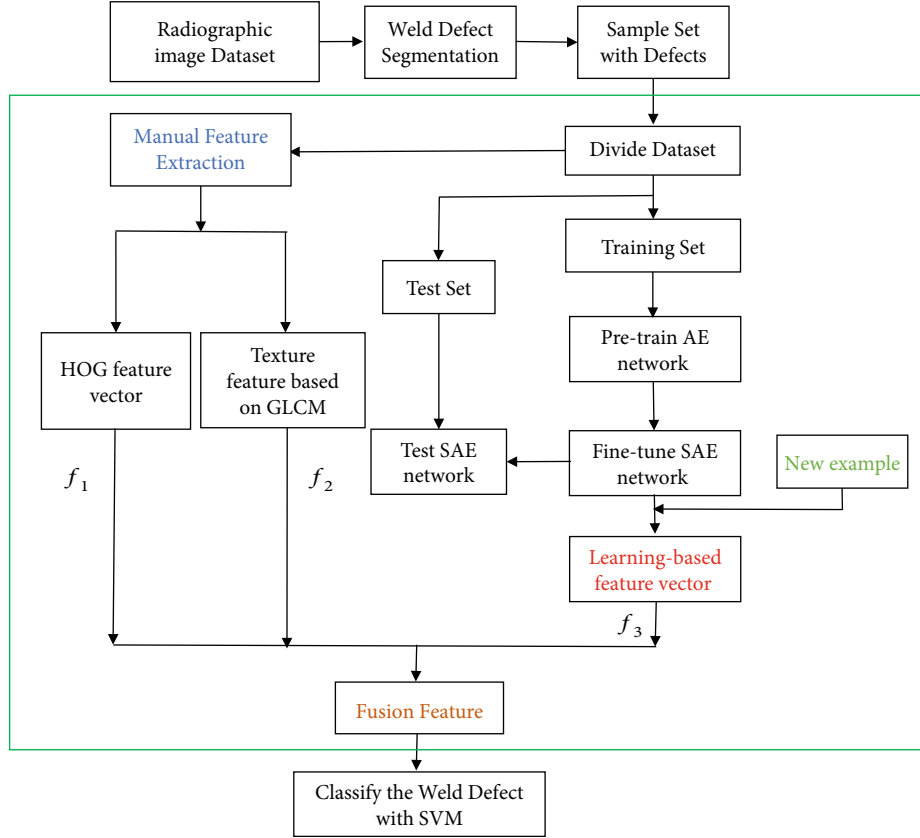
FIGURE 3: Workflow of weld classification.

(a) Original radiography image

(b) Segmented weld defect

FIGURE 4: The example of weld defect segmentation.

discriminative and separable as possible. In this paper, the HOG features are used for presenting the local weld defect in radiography images. The flowchart of algorithm is shown in Figure 1.

2.2. Texture Feature Vector Based on GLCM. Gray level cooccurrence matrix (GLCM) theory is an important second-order statistical method for texture analysis [24, 25]. It reflects the spatial complexity, pixel distribution, and roughness of the image through the joint probability density of two pixels in different positions. The element of matrix is expressed as $P_{(i,j,d,\theta)}$, which is the probability of the occurrence pixel pairs (i, j). d is the distance between i and j. θ is the position relation of pixel pairs (i, j), which is usually $0°, 45°, 90°$, and $135°$. Haralick et al. [26] defined 14 statistical parameters as texture features. In this paper, we used these features for describing the weld defect. 5 pivotal parameters are listed here.

$$SE = \sum_{i=0}^{L-1} \sum_{j-0}^{L-1} \{P(i, j \mid d, \theta)\}^2, \tag{1}$$

where L is the number of gray level. S_E is the energy feature, which is a second-moment measuring homogeneity of the image.

$$S_{\text{Con}} = \sum_{n=0}^{L-1} n^2 \sum_{i=1}^{L-1} \sum_{j=1}^{L-1} P(i, j \mid d, \theta), \tag{2}$$

where S_{Con} is the contrast feature, which is the difference moment of the matrix measuring the contrast or the amount of local variations in the image.

$$S_{\text{Cor}} = \frac{1}{\sigma_x \sigma_y} \sum_{i=1}^{L-1} \sum_{j=1}^{L-1} \left(ij \cdot P(i, j \mid d, \theta) - \mu_x \mu_y\right)^2, \tag{3}$$

(a) PO

(b) ND

(c) CR

(d) LOP

(e) SI
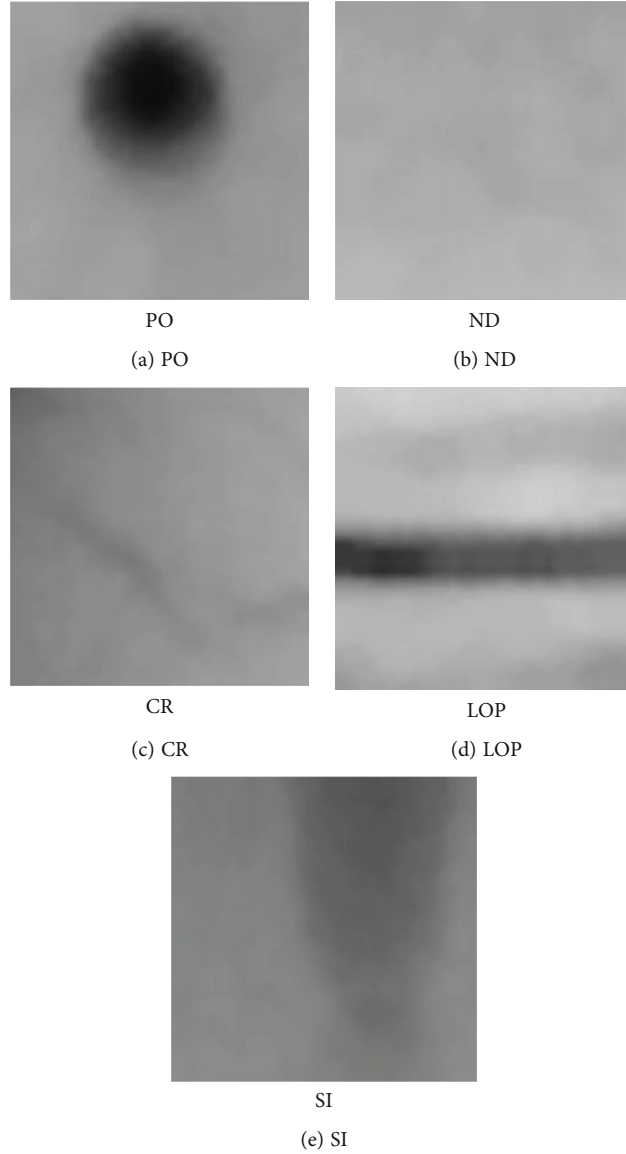
FIGURE 5: The samples of different weld defects.

where $\mu_x, \mu_y, \sigma_x,$ and σ_y are average value and standard deviation, respectively. S_{Cor} is the correlation feature measuring the similarity in one direction.

$$S_S = -\sum_{i=1}^{L-1}\sum_{j=1}^{L-1} P(i,j\mid d,\theta) \log\left[P(i,j\mid d,\theta)\right], \qquad (4)$$

where S_S is the entropy feature measuring the complexity of image.

$$D = \sum_{i=1}^{L-1}\sum_{j=1}^{L-1} P(i,j\mid d,\theta)\frac{1}{1+(i-j)^2}, \qquad (5)$$

where D is the inverse difference moment reflecting the homogeneity of the image texture and measuring the local amount of variations of the texture.

2.3. Feature Based on Learning through SAE. Autoencoder (AE) is a simple neural network containing input, hidden, and output layers. It trains the network in an unsupervised manner by reconstructing the input in output layer. The process is divided into two parts: encoding and decoding. The encoding is a connection from the input layer to hidden layer. It can be expressed as $h = f(W^{(1)}x + b^{(1)})$, where h is the activation value of hidden layer, $W^{(1)}$ and $b^{(1)}$ are weight matrix and bias of encoding, and f is the encoding function. Similarly, from the hidden layer to output layer, decoding is expressed as $x^\wedge = g(W^{(1)'}x + b^{(1)'})$, where $x^\wedge$ is the reconstruction of input, $W^{(1)'}$ and $b^{(1)'}$ are the corresponding parameters of decoding, and g is the encoding function. The back propagation algorithm is used to obtain the optimal parameters of the network for minimizing the cost function. For better feature, some restrictive constraints are imposed on the hidden layer. The cost function of network

Table 1: The sample numbers of different defect types.

Defect types	Number in training set	Number in test set
CR	868	372
IP	839	360
ND	868	372
PO	868	372
SI	869	372
Total	4312	1848
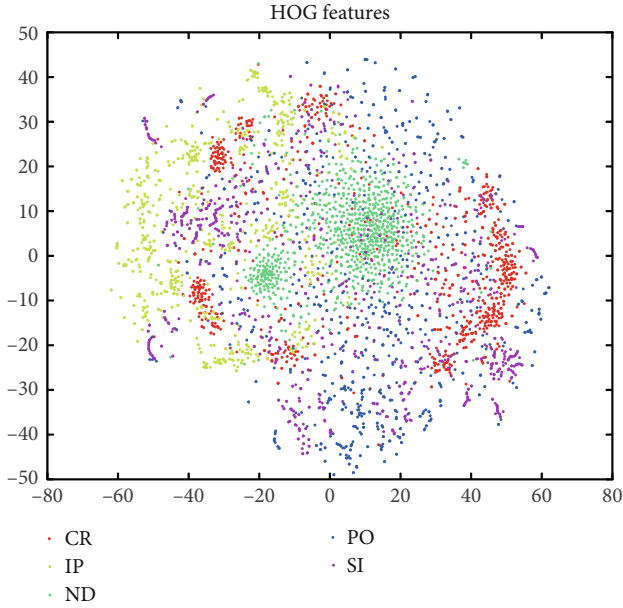
Figure 6: The t-SNE distribution map of HOG feature vectors.
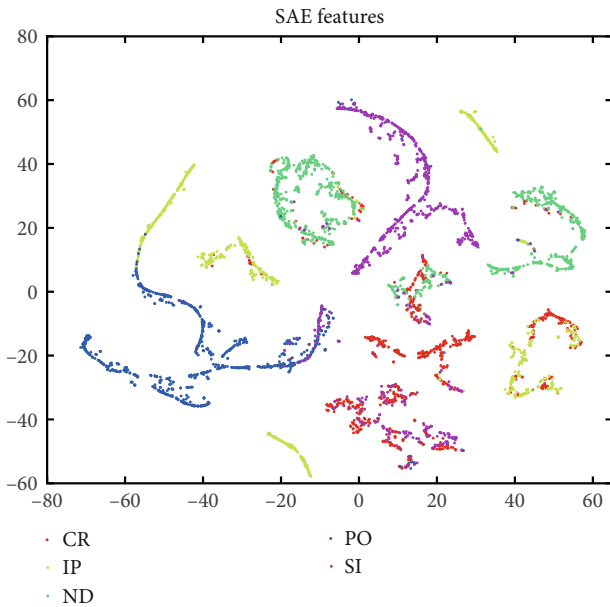
Figure 7: The t-SNE distribution map of SAE feature vectors.
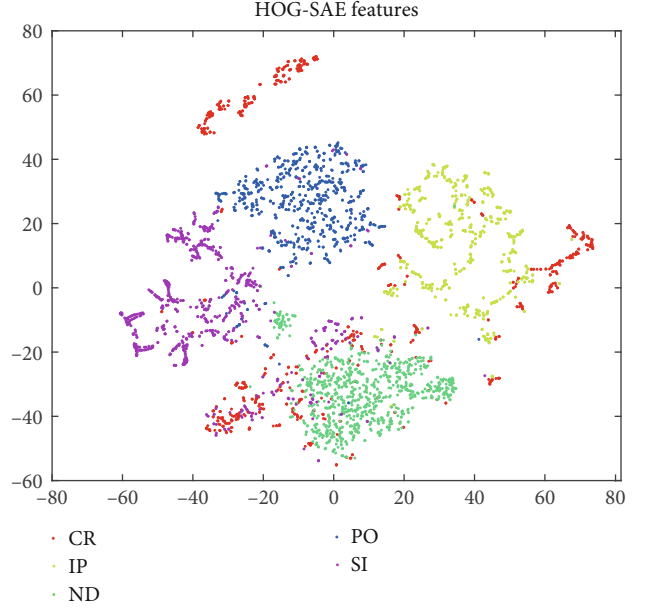
Figure 8: The t-SNE distribution map of fusion feature of HOG-SAE feature.

is described as Equation (6).

$$J(W, b) = \frac{1}{2m} \sum_i \left(\hat{x} - x \right)^2 + \frac{\lambda}{2m} \sum W^2 + \beta \sum_j KL\left(\rho \left\| \hat{\rho}_j \right. \right),$$

(6)

where m is the number of samples, $\beta \sum_j KL(\rho \| \rho_j^{\wedge})$ is the sparse penalty term, and β is the weight of this term.

As is shown in Figure 2, we construct a deep neural network (100-50-5) by stacking two AEs and a softmax layer for supervised learning. The network initializes the parameters by training each AE layer by layer. Once the pretraining of AE is finished, the decoder is discarded. The activation of previous AE in hidden layer is the input of the next AE. For best parameter, the fine-tuning step is implemented by supervised learning through training set.

3. Feature Fusion

It is critical to select appropriate features to classification of weld defects. Silva et al. [27] pointed out that the mass of features used for classification is more important. The weld defects are usually distributed in the local space of the radiography images with linear, circular, and other irregular shapes. The HOG feature is sensitive to gradient and direction; thus, it focuses on describing the structure and contour of objects. The HOG description has strong ability on identifying local regions. The Haralick feature based on GLCM describes the texture of the image by counting the frequency of pixel pairs with a particular relationship. The two kinds of features with specific physical significance are useful for classifying the defects. However, it is not sufficient to describe the image comprehensively by using each single feature. In addition, the DNN can learn hierarchical features

FIGURE 9: The t-SNE distribution map of texture feature based on GLCM.

FIGURE 10: The t-SNE distribution map of fusion feature of HOG-GLCM feature.

FIGURE 11: The t-SNE distribution map of fusion feature of SAE-GLCM feature.

are encircled by the green rectangular box (feature extraction and fusion).

As is shown in Figure 3, there are two ideas of fusion: one is the fusion of two different manual features, and the other one is the fusion of manual features and learning-based features. Characteristic-level fusion is adopted, which involves various feature extractions of images and then integrates the different feature vectors. In the extraction for HOG feature vector f_1, the cell size is 4×4. Thus, the dimension of the vector is 1×5184. For the texture feature based on GLCM f_2, the mean and standard deviation of 14 features are calculated in 3 different distances. Thus, the dimension of the vector is 1×84. We obtain the vector (1×5) in the softmax layer for learning-based feature based on SAE f_3. The parameters used in network are: $\lambda = 4e - 3$ and $\beta = 3$. The fusion feature is noted as $f_{fusion} = [f_i, f_j], i \neq j$.

4. Experimental Results and Discussion

In this section, several experiments are implemented based on MATLAB for investigating the classification performance of different features. Datasets, evaluation methods, and results of experiments are introduced.

4.1. Experimental Database. The database for subsequent learning is from the "welds" group in a public database called GDXray [28]. An example of radiography images is shown in Figure 4(a). Morphological analysis is used in this paper for segmented weld defects. The processed result is shown in Figure 4(b). Based on the results, we cropped the patches with defects to form a Dataset _RUS [16]. In our previous work, we used CNN for defect classification on this dataset; however, the result is not good. Dataset _RUS includes 6,160 cropped image patches with different weld defects, including lack of penetration (LOP), porosity (PO),

automatically; however, physical significance of these features is undefined. For a more comprehensive description of the objects, we tried to fuse these features.

The workflow of weld classification in this paper is shown in Figure 3. Firstly, the weld defects are segmented. Secondly, the samples with defects are formed. Thirdly, two manual features are extracted. Meanwhile, the SAE networks are trained and fine-tuned for learning feature. Finally, the fusion features are imported into the SVM for classification. Our work mainly focused on the steps which

TABLE 2: The classification accuracies of different features.

Feature types	CR	LOP	ND	PO	SI	Mean
GLCM feature	75.2%	63.2%	74.3%	75.2%	61.7%	73.2%
HOG feature	69.1%	84.7%	86.6%	74.7%	69.1%	76.8%
SAE feature	79.8%	91.1%	94.6%	78.8%	74.2%	83.7%
HOG-GLCM feature	80.9%	95.6%	79.3%	87.6%	96.0%	87.8%
HOG-SAE	83.3%	93.9%	89.5%	84.9%	86.8%	87.7%
SAE-GLCM	92.7%	88.3%	91.9%	92.5%	98.9%	92.9%

slag inclusion (SI), and crack (CR). The patches without defect are noted as ND. Some samples with different defects are shown in Figure 5. The dataset is divided into the training set and testing set on a scale of 7 : 3 for later experiments. The sample numbers of each defect patches are shown in Table 1.

4.2. Results of Visualization. We extract the HOG feature vector, texture feature vector based on GLCM, and learning-based feature from 4312 patches (training set). In order to show the performance of the abovementioned features and fusion features more intuitively, the t-SNE method is used for visualizing the features through 2D maps. The t-SNE distribution maps of features are shown below.

The t-SNE method shows the high-dimensional data in low-dimensional maps. Thus, the dimension of data should be considered in fusion. The dimension of HOG feature is too high, and PCA algorithm is adopted beforehand to reduce the dimension to 5. Then, it is fused with a SAE feature, namely HOG-SAE feature. Figures 6 and 7 show the distribution of single HOG feature and SAE feature. Figure 8 shows the distribution map of the fusion feature. In terms of the color distribution, the separability of fusion feature is better.

For texture features, we select 5 listed in Section 2 showing the t-SNE distribution map in Figure 9. The distribution of texture feature is rambling. From the visual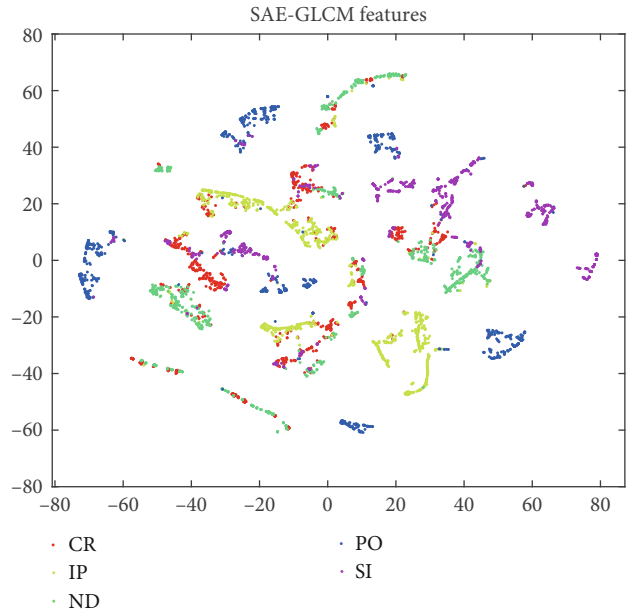 effects, the conclusion is that the deep features perform better than manual features for classification (this is consistent with our previous result). Then, the feature vector is fused with HOG feature and SAE feature, namely HOG-GLCM feature and SAE-GLCM feature. The t-SNE distribution maps are shown in Figures 10 and 11. Compared to the single GLCM feature, the performance of fusion feature improved. However, it is not noticeable when comparing with HOG feature or SAE feature from the visual effect. To evaluate the performance of each feature more objectively, a quantitative evaluation method is needed.

4.3. Results of SVM Classification. Support vector machine (SVM) is developed based on the statistical learning theory, which is suitable for use in solving high-dimensional classification problems with small samples. Thus, it is popular in the classification and diagnosis of weld defects in recent years [29, 30]. In this paper, SVM is used to build the relation model concerning features and weld defects. To reduce the training time, the kernel function of the SVM adopted is linear. The classification performance of the features is eval-

TABLE 3: The classification accuracies of HOG-GLCM feature in different weights.

k_1	CR	LOP	ND	PO	SI	Mean
0.6	80.6%	95.3%	92.7%	89.8%	93.0%	90.3%
0.7	89.0%	94.7%	92.5%	89.0%	91.9%	91.4%
0.8	87.1%	93.6%	92.5%	88.4%	91.4%	90.6%
0.9	84.7%	92.5%	90.6%	87.9%	89.5%	89.0%

TABLE 4: The classification accuracies of HOG-SAE feature in different weights.

k_1	CR	LOP	ND	PO	SI	Mean
0.6	83.6%	95.0%	93.8%	85.8%	83.9%	88.4%
0.7	84.7%	93.6%	93.3%	85.8%	80.4%	87.5%
0.8	83.9%	92.5%	93.0%	84.4%	75.8%	85.9%
0.9	82.3%	91.7%	93.0%	84.1%	73.1%	84.8%

TABLE 5: The classification accuracies of SAE-GLCM feature in different weights.

k_1	CR	LOP	ND	PO	SI	Mean
0.6	94.4%	94.2%	97.0%	93.5%	98.1%	95.5%
0.7	94.9%	95.0%	97.0%	93.3%	97.6%	95.6%
0.8	93.3%	94.7%	97.3%	93.3%	96.0%	94.9%
0.9	92.5%	94.4%	95.7%	92.2%	94.9%	93.9%

uated through accuracy rates and their mean of various types. The classification rates are shown in Table 2.

The classification ability of deep features is stronger than the manual features. However, the DCNN networks perform poorly when the sample set is small [17]. In this paper, the accuracies of different single features in the table demonstrate that the learning feature based on SAE network performs better than the manual features. This is consistent with the above analysis.

The classification performance of fusion feature with two different features is better than that of single features. Among them, the fusion feature of texture feature based on GLCM and learning feature based on SAE (SAE-GLCM feature) perform best. The average accuracy achieves 92.9%.

The table shows the separability of three single features clearly. Based on this, we try to apply different weights on each feature during fusion, namely $f_{\text{fusion}} = [k_1 f_i, k_2 f_j], i \neq j$

, $k_1 + k_2 = 1$. Several experiments are set to test the classification performance of three fusion feature vectors with different weights. The results are shown in Tables 3–5.

From the tables, it is obvious that the classification accuracies of fusion features with weights improved, especially the fusion of SAE feature and GLCM feature (SAE-GLCM feature). The best accuracy achieves 95.6%.

5. Conclusion and Future Work

Considering that deep convolutional neural networks are not suitable for the classification of small sample sets, a SAE network is used to learn feature from the patches of radiography images for classifying the weld defects in this paper. Meanwhile, two kinds of different manual features are extracted. In order to express the objectives more comprehensively, we fuse the features for combining different information. The t-SNE distribution of these features and their fusion feature is shown in figures for intuitive display. We use SVM to classify the weld defects for evaluating the performance of the different features objectively. The results demonstrate that the fusion features perform better than the single features on the classification ability. The fusion of texture feature based on GLCM and learning feature based on SAE network has the best performance. The classification power of the feature vectors becomes stronger when the fusion is weighted. However, the performance promotion of fusion of HOG feature and SAE feature is limited. This may result from the large difference in the dimensionality of the two features.

In the future, we will consider optimizing the weight adopted in fusion. The fusion model will be used to the entire X-ray image for detection of defects.

Data Availability

The data that support the findings of this study are available from the corresponding author upon reasonable request.

Conflicts of Interest

The authors declare no conflicts of interest.

Acknowledgments

References

[1] I. Valavanis and D. Kosmopoulos, "Multiclass defect detection and classification in weld radiographic images using geometric and texture features," *Expert Systems with Applications*, vol. 37, no. 12, pp. 7606–7614, 2010.

[2] G. D'Angelo and S. Rampone, "Feature extraction and soft computing methods for aerospace structure defect classification," *Measurement*, vol. 85, pp. 192–209, 2016.

[3] J. Hassan, A. M. Awan, and A. Jalil, "Welding defect detection and classification using geometric features 2012," in *10th international conference on Frontiers of information technology*, pp. 139–144, Islamabad, Pakistan, 2012.

[4] J. Zapata, R. Vilar, and R. Ruiz, "Performance evaluation of an automatic inspection system of weld defects in radiographic images based on neuro-classifiers," *Expert Systems with Applications*, vol. 38, pp. 8812–8824, 2011.

[5] N. Boaretto and T. M. Centeno, "Automated detection of welding defects in pipelines from radiographic images DWDI," *NDT&E International*, vol. 86, pp. 7–13, 2017.

[6] D. Mery and M. A. Berti, "Automatic detection of welding defects using texture features," *Insight-Non-Destructive Testing and Condition Monitoring*, vol. 45, no. 10, pp. 676–681, 2003.

[7] J. Kumar, R. S. Anand, and S. P. Srivastava, "Multi-class welding flaws classification using texture feature for radiographic images," in *International Conference on Advances in Electrical Engineering*, Vellor, India, 2014.

[8] J. Kumar, R. S. Anand, and S. P. Srivastava, "Flaws classification using ANN for radiographic weld images," in *2014 International Conference on Signal Processing and Integrated Networks (SPIN)*, pp. 145–150, Noida, India, 2014.

[9] Y. Wang and H. Guo, "Weld defect detection of X-ray images based on support vector machine," *IETE Technical Review*, vol. 31, no. 2, pp. 137–142, 2014.

[10] H. Kasban, O. Zahran, H. Arafa, M. El-Kordy, S. M. S. Elaraby, and F. E. A. El-Samie, "Welding defect detection from radiography images with a cepstral approach," *Ndt & E International*, vol. 44, no. 2, pp. 226–231, 2011.

[11] O. Zahran, H. Kasban, M. El-Kordy, and F. E. Abd El-Samie, "Automatic weld defect identification from radiographic images," *NDT & E International*, vol. 57, pp. 26–35, 2013.

[12] M. Xia, H. Shao, D. Williams, S. Lu, L. Shu, and C. W. de Silva, "Intelligent fault diagnosis of machinery using digital twin-assisted deep transfer learning," *Reliability Engineering & System Safety*, vol. 215, article 107938, 2021.

[13] H. Shao, H. Jiang, H. Zhang, and T. Liang, "Electric locomotive bearing fault diagnosis using a novel convolutional deep belief network," *IEEE Transactions on Industrial Electronics*, vol. 65, no. 3, pp. 2727–2736, 2018.

[14] M. Xia, H. Shao, X. Ma, and C. W. de Silva, "A stacked GRU-RNN-based approach for predicting renewable energy and electricity load for smart grid operation," *IEEE Transactions on Industrial Informatics*, vol. 17, no. 10, pp. 7050–7059, 2021.

[15] N. Yang, H. Niu, and L. Chen, "X-ray weld image classification using improved convolutional neural network," *AIP Conference Proceedings*, vol. 1995, no. 1, article 020035, 2018.

[16] W. Hou, Y. Wei, Y. Jin, and C. Zhu, "Deep features based on a DCNN model for classifying imbalanced weld flaw types," *Measurement*, vol. 131, pp. 482–489, 2019.

[17] S. Feng, H. Zhou, and H. Dong, "Using deep neural network with small dataset to predict material defects," *Materials & Design*, vol. 162, pp. 300–310, 2019.

[18] H. Shao, M. Xia, J. Wan, and C. De Silva, "Modified stacked auto-encoder using adaptive Morlet wavelet for intelligent fault diagnosis of rotating machinery," *IEEE/ASME Transactions on Mechatronics*, 2021.

[19] G. E. Hinton and R. R. Salakhutdinov, "Reducing the dimensionality of data with neural networks," *Science*, vol. 313, no. 5786, pp. 504–507, 2006.

[20] G. E. Hinton, S. Osindero, and Y. W. Teh, "A fast learning algorithm for deep belief nets," *Neural Computation*, vol. 18, no. 7, pp. 1527–1554, 2006.

[21] Y. Bengio, P. Lamblin, D. Popovici, and H. Larochelle, "Greedy layer-wise training of deep networks," *Advances in Neural Information Processing Systems*, vol. 19, pp. 153–160, 2007.

[22] L. Yang and H. Jiang, "Weld defect classification in radiographic images using unified deep neural network with multi-level features," *Journal of Intelligent Manufacturing*, vol. 32, no. 2, pp. 459–469, 2021.

[23] N. Dalal and B. Triggs, "Histograms of oriented gradients for human detection computer vision and pattern recognition," in *IEEE*, vol. 1, pp. 886–893, San Diego, CA, 2005.

[24] D. A. Clausi, "An analysis of co-occurrence texture statistics as a function of grey level quantization," *Canadian Journal of Remote Sensing*, vol. 28, pp. 45–62, 2002.

[25] L. K. Soh and C. Tsatsoulis, "Texture analysis of SAR sea ice imagery using gray level co-occurrence matrices," *IEEE Transactions on Geoscience and Remote Sensing*, vol. 37, no. 2, pp. 780–795, 1999.

[26] R. M. Haralick, K. Shanmugam, and I.'. H. Dinstein, "Textural features for image classification," *IEEE Transactions on Systems, Man, and Cybernetics*, vol. SMC-3, no. 6, pp. 610–621, 1973.

[27] R. R. Da Silva, L. P. Calôba, M. H. S. Siqueira, L. V. S. Sagrilo, and J. M. A. Rebello, "Evaluation of the relevant characteristic parameters of welding defects and probability of correct classification using linear classifiers," *Insight*, vol. 44, no. 10, pp. 616–622, 2002.

[28] D. Mery, V. Riffo, U. Zscherpel et al., "GDXray: the database of X-ray images for nondestructive testing," *Journal of Nondestructive Evaluation*, vol. 34, no. 4, pp. 1–12, 2015.

[29] D. You, X. Gao, and S. Katayama, "WPD-PCA-based laser welding process monitoring and defects diagnosis by using FNN and SVM," *IEEE Transactions on Industrial Electronics*, vol. 62, no. 1, pp. 628–636, 2014.

[30] M. S. El-Tokhy and I. I. Mahmoud, "Classification of welding flaws in gamma radiography images based on multi-scale wavelet packet feature extraction using support vector machine," *Journal of Nondestructive Evaluation*, vol. 34, no. 4, 2015.

Research Article

Fast Method of Detecting Packaging Bottle Defects Based on ECA-EfficientDet

Zhenwen Sheng and Guiyun Wang (ORCID)

Shandong Xiehe University, Jinan, China

Correspondence should be addressed to Guiyun Wang; xiehewsq@sdxiehe.edu.cn

Conventional methods of detecting packaging defects face challenges with multiobject simultaneous detection for automatic filling and packaging of food. Targeting this issue, we propose a packaging defect detection method based on the ECA-EfficientDet transfer learning algorithm. First, we increased the complexity in the sampled data using the mosaic data augmentation technique. Then, we introduced a channel-importance prediction mechanism and the Mish activation function and designed ECA-Convblock to improve the specificity in the feature extractions of the backbone network. Heterogeneous data transfer learning was then carried out on the optimized network to improve the generalization capability of the model on a small population of training data. We conducted performance testing and a comparative analysis of the trained model with defect data. The results indicate that, compared with other algorithms, our method achieves higher accuracy of 99.16% with good stability.

1. Introduction

To guarantee high-quality products from automatic packaging production lines, defect inspections are indispensable. Usually, such inspections look for defects in the caps, labels, packaging, spraying code, etc. In particular, the cap and label significantly affect product quality and their appearance and inspection are therefore of great importance.

Conventional packaging defect inspections are mostly made using equipment based on image processing techniques. For instance, Toxqui-Quitl et al. [1] proposed a PET bottle defect inspection method with self-adaptive gamma adjustments to bottle images through a frequency filtering technique for highly accurate inspections of the face, wall, and bottom of bottles. Zheng et al. [2] proposed a texture area defect detection algorithm based solely on phase change. Zhou et al. [3] combined mean squared cyclic detection and entropy partition and proposed an improved random cyclic detection method to determine defective regions on the bottoms of bottles. The above-mentioned works use image processing for packaging defect inspection. However, they require many experiments to determine the

judgment rules. In addition, they require complex inspection environments and face challenges with simultaneous detections in multiple categories. Therefore, their advantages for practical inspection are limited.

Simultaneously detecting defects in multiple categories thus remains an issue to be solved. Deep learning has recently shown potential in the field of classification and detection and is a promising solution in the field of packaging defect inspection.

The development of deep learning techniques began with the representative convolution neural network architecture, LeNet-5 [4], followed by the iconic deep learning algorithm, AlexNet [5]. Later algorithms included VGG [6], ResNet [7], MobileNet [8], and EfficientNet [9]. Zhou et al. [10] improved the size and number of kernels on the standard LeNet5 model and integrated the PSO optimization algorithm and proposed an improved LeNet5 model for fault detection of liquid plunger pumps. Wang et al. [11] proposed an AlexNet-based convolutional neural network method to deal with defects from a data-driven perspective. Zhang et al. [12] proposed a cost-sensitive residual convolutional neural network for unbalanced data defect detection.

Marques [13] proposed a convolutional neural network diagnosis system using EfficientNet, which effectively improved the accuracy of the medical decision-making system. Michele et al. [14] explored the applicability of the MobileNet V2 deep convolutional network by fine-tuning the pretrained MobileNet neural network. The results show that 100% classification accuracy can be achieved based on MobileNet V2. As network architectures became more complex, their feature extraction capabilities increased as well. Deep learning networks have demonstrated outstanding performance in the field of image identification. In particular, feature extraction networks based on deep learning have made great progress in object detection. Object detection falls into two categories: one- stage object detection and two-stage object detection. One-stage object detection has a broader range of applications, due to its superior balancing of speed and accuracy. EfficientDet, proposed by Tan et al. [15] from the Google Brain Team, and YOLOv4, proposed by Bochkovskiy et al. [16], are the best-performing object detection models. However, there is little research on the use of object detection for packaging defect inspection. We used EfficientDet in this study because it is more accurate than YOLOv4.

In addition, the object detection algorithm requires a large amount of data to build the model. However, it is difficult to obtain packaging defect samples. Therefore, to improve the model's generalization capability, the model must be specifically designed and the data must be processed. Regarding the latter, data augmentation and transfer learning are effective techniques to improve model accuracy with small datasets. Regarding the model design, effective channel feature importance prediction can improve the generalization capability. For example, Hu et al. [17] proposed the squeeze-and-excitation network (SE-Net), which makes predictions on channel importance during convolution to improve the overall accuracy of the model. Subsequently, a large number of scholars applied SE to some networks [18, 19]. Wang et al. [20] showed that SE-Net can also be used for dimension reduction. To prevent any unnecessary loss in accuracy due to dimension reduction, they designed the effective channel attention network (ECA-Net) for improved model accuracy.

In summary, conventional imaging processing methods have difficulties simultaneously detecting defects in multiple categories. Moreover, the scarcity of defect samples renders trained models weak in terms of generalization. Thus, we propose a fast packaging defect detection method based on the ECA-EfficientDet transfer learning algorithm. The contributions of this study are twofold. First, we incorporated the ECA mechanism in a backbone feature extraction network and designed an ECA-Convblock convolution block that is capable of predicting the channel importance during convolution. This suppresses channels that carry no information, to make specific representations of object features and improve the defect detection accuracy. Second, we used the mosaic augmentation technique on our sample data. This effectively enhanced the sample complexity and therefore improved the generalization capability. In addition, we adopted heterogeneous data transfer learning during the
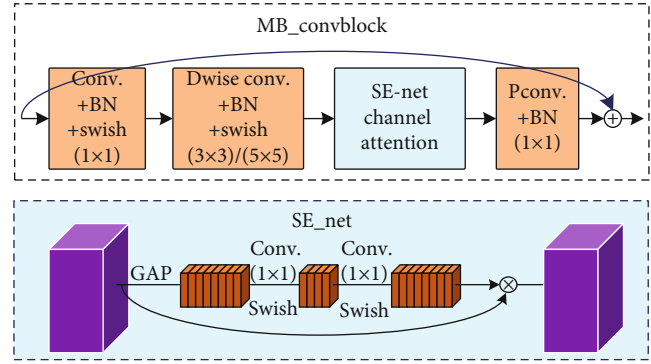
Figure 1: MB_Convblock convolution block.

training process and we utilized the Mish activation function to improve the robustness of our model in complex environments.

The remainder of this paper is organized as follows: Section 2 provides an overview of the structure of the EfficientDet algorithm. Section 3 describes the framework and design of the packaging bottle defect detection model. In Section 4, we describe our evaluation of the proposed method through the analysis and comparison of simulation results. Section 5 offers conclusions.

2. EfficientDet Model Architecture

EfficientDet [21] is an object detection algorithm proposed by the Google Brain Team at CVPR2020. It can be viewed as an extension of EfficientNet [9], extending from classification to object detection. EfficientDet balances efficiency and accuracy. Its overall architecture consists of the backbone feature extraction network, an enhanced feature extraction network, and box/class determination.

The backbone feature extraction network for EfficientNet contains eight convolution layers. Except for the ordinary convolution (Conv. + BN + Swish) operation in the first layer, all the other layers are formed by piling up the convolution block (MB_Convblock), as illustrated in Figure 1. The overall structure is illustrated in Figure 2(c1, I). First, the dimensions are increased through an ordinary 1 1 convolution. Then, a 3 3 or 5 5 deep separable convolution is carried out with the SE-Net channel attention mechanism. The remaining seven layers of the network can be described as follows: MB_Convblock piles once in the second and eighth layers, piles twice in the third and fourth layers, piles three times in the fifth and sixth layers, and piles four times in the seventh layer. The fourth, sixth, and seventh layers all adopt 5 5 separable convolution (whereas the other layers use 3 3). Therefore, the depth of the feature extraction network increases. Finally, the fourth, sixth, and eighth layers (P3–P7) of the backbone network are outputted as effective feature layers for the next stage of feature fusion and reuse.

The enhanced feature extraction network repeatedly performs upsampling and downsampling on the features extracted by the backbone network to achieve effective fusion and high utility of the extracted features, as illustrated
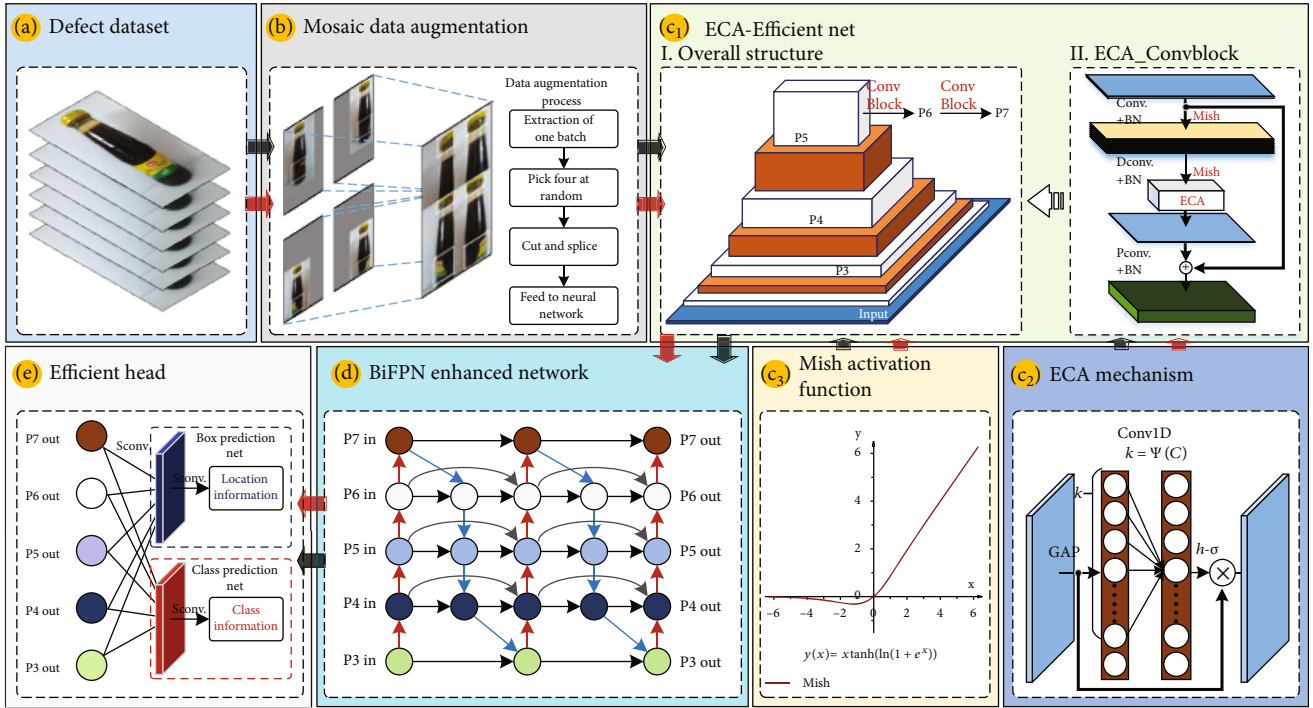
FIGURE 2: Framework for the defect inspection method based on the ECA-EfficientDet algorithm.

in Figure 3. The enhanced feature extraction network is formed by three serially connected BiFPNs. Feature layers P6 and P7 are obtained by downsampling from P5. After fusing the features, five feature maps with rich semantic information are outputted for the final class and box information detection. Two deep, separable convolution operations on the fused five feature maps are thus used to predict the final class and box information.

3. Research on EfficientDet Optimization

The subject of our study is the detection of packaging defects. Since there are many categories of defects but samples of defects are few, directly implementing the current algorithms cannot meet the accuracy requirements of practical production. Since the backbone feature extraction network is directly related to the feature extraction capability, we optimize three aspects of the backbone network. First, we utilize data augmentation to improve as much as possible the complexity of the sample data to enhance the model's generalization capability. Second, we modify the structure of the network to enhance the feature extraction capability. And third, we conduct transfer learning on the optimized model to improve the overall robustness of the model. Our design of the bottle packaging defect detection model is illustrated in Figure 2. It consists of five parts: sample input (a), mosaic data augmentation (b), the ECA-EfficientNet backbone feature extraction network (c1–c3), the BiFPN enhanced feature extraction network (d), and the efficient head box/class result output (e).

The detection flow can be generally described as follows. First, before training, we perform random mosaic data augmentation. Then, we feed the augmented data into the opti-
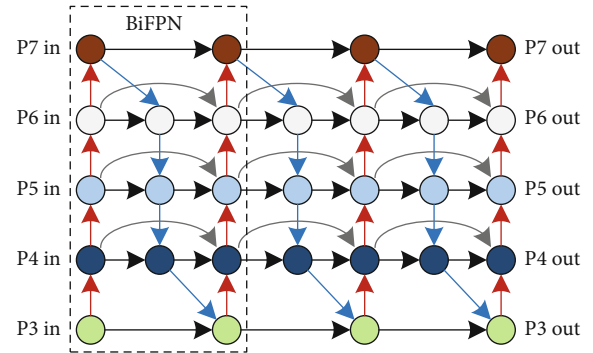
FIGURE 3: BiFPN-enhanced feature extraction network.
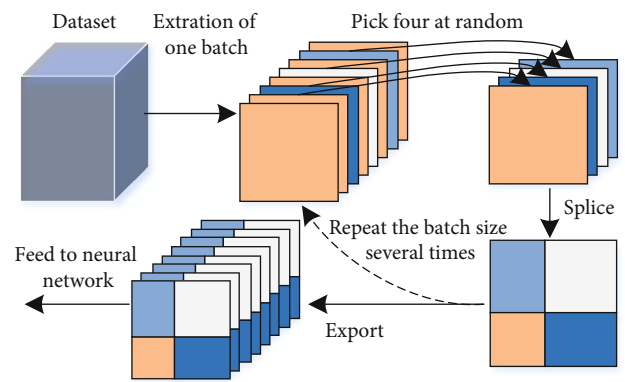
FIGURE 4: Mosaic data augmentation flow.

mized ECA-EfficientNet backbone network for multiscale feature extraction. Five feature maps (P3–P7) of different scales are obtained as a result. Next, we input the acquired
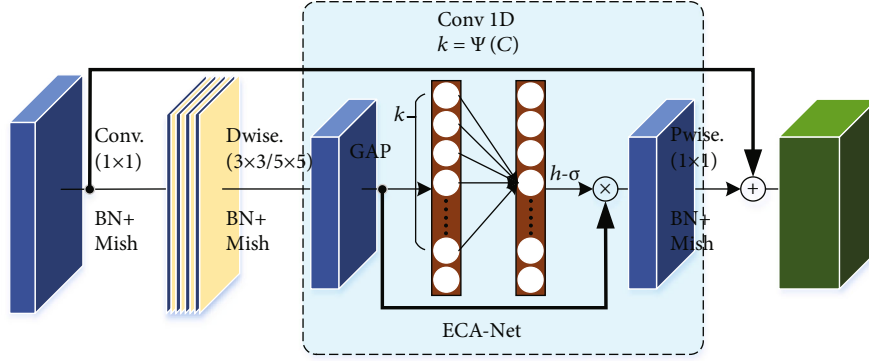
FIGURE 5: ECA_Convblock convolution block.

feature maps into the enhanced feature extraction network, which is formed by three BiFPN modules concatenated serially for feature fusion and reuse. Finally, we conduct deep separable convolution on the five fused feature maps to detect the box and class information of the defect samples.

3.1. Mosaic Data Augmentation Structure. Mosaic data augmentation [16] is a new type of data augmentation scheme proposed at the same time as the YOLOv4 algorithm. It was developed from CutMix augmentation [22] and is capable of improving the image background complexity with a small population of samples to improve the generalization capability of models. Therefore, we adopted mosaic augmentation in this study. Considering that EfficientDet is an end-to-end network, we also adopted an end-to-end network and embedded data augmentation into model training. The procedures are illustrated in Figure 4.

First, we select a batch from the defect sample set. Next, we randomly pick four images from the batch and generate a new image by stitching the top-left, top-right, bottom-left, and bottom-right sections of the four selected images. This step is repeated until a new batch is created. Finally, the newly generated batch and previous samples are fed to the model for training. Notice that the total number of samples used for training does not change, which enables the network to perform data augmentation before training in an end-to-end manner.

3.2. Reconstruction of the Backbone Feature Extraction Network

3.2.1. Design of the ECA-Convblock Convolution Block. The backbone network of EfficientDet is EfficientNet, which is described above. The backbone network is all piled from the MB_Convblock convolution block, as illustrated in Figure 1. In terms of algorithm design, EfficientNet adopts deep, separable convolution to decrease the number of parameters in the model. To avoid insufficiency in feature extraction, the authors of the algorithm utilized the SE-Net [17] channel attention mechanism after layer-by-layer convolution to improve the specificity in the extracted features by predicting channel importance during the convolution. However, according to the structural principles of SE-Net,
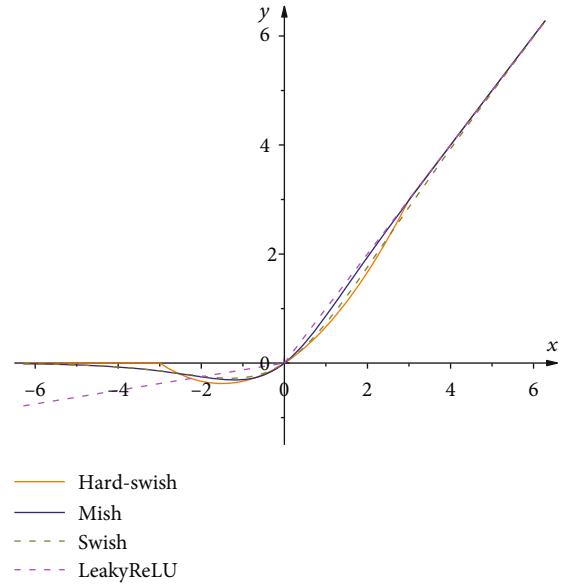
FIGURE 6: Various activation functions.

there is a reduction in feature dimensions when applying the attention mechanism, resulting in a loss in model accuracy. To avoid this, we introduce an ECA_Convblock convolution block as illustrated in Figure 5 to prevent accuracy loss due to the dimension reduction when applying SE-Net.

The structure of the ECA_Convblock convolution block is very similar to that of MB_Convblock. The major difference is that there is no dimension reduction in the ECA channel importance prediction. Instead, the weighted channel is obtained from a 1D convolution of size k, avoiding loss in accuracy due to dimension reduction. Here, k is obtained self-adaptively from the number of input feature map channels. The equation can be written as follows [20].

$$k = \psi(C) = \left| \frac{\log_2(C)}{\gamma} + \frac{b}{\gamma} \right|_{\text{odd}}, \qquad (1)$$

where C is the number of input sample channels, odd means taking the odd integer number of the input, and b and γ are heuristic parameters, which are set to $b = 2$ and $\gamma = 1$, per the

FIGURE 7: Sample of the packaging bottle defect dataset; the red frame is the ground-truth box.

values provided by the ECA authors. We maintain the outmost residual edge, which many researchers have shown is beneficial for stability when updating weights.

3.2.2. Introduction of the Mish Activation Function. After showing the ECA's improvement in model's accuracy, we proceed to discuss the impact of the activation function on model accuracy. EfficientNet adopts Swish as the activation function [23]. Based on the backbone feature extraction network, we experimented with three other activation functions: the hard-Swish function [24], the LeakyReLU function [25], and the Mish function [26], as illustrated in Figure 6.

Figure 6 shows that all four activation functions make adjustments in the negative value region. These are beneficial for preventing some of the weights from losing gradients during model training. However, the excessive dispersion of LeakyReLU in the negative value region makes updating the weights unstable. The hard-Swish function, on the other hand, has poor gradient flow during weight updating, since it utilizes a hard zero boundary. Only the Mish function, similar to the Swish function, avoids saturation by clipping the positive value region and smoothly processing the negative value region, stabilizing weight updating during the iterations to achieve good generalization capability. Therefore, we adopted the Mish activation function in our model. Through comparison, we found that the Mish function's performance is excellent.

3.2.3. Heterogeneous Data Transfer Learning. It is well known that transfer learning is capable of applying model parameters and weights learned from a large amount of data to a small dataset to improve the generalization capability when the relevant dataset is small. Therefore, to further improve the overall robustness of the model after structural optimization and because the number of defect samples is small, we adopted transfer learning to improve the model's generalization capability.

When training the optimized model (ECA-EfficientDet), in the early stage, we utilized the VOC2007 dataset. VOC2007 is a comparatively large dataset for object detection. It contains rich data types and objects. However, due to the differences between VOC2007 and the defect sample data, transfer learning is heterogeneous in nature. After the first stage, we transferred the obtained weights to the second stage of training with defect sample data, after which we obtained the model for defect detection.

4. Experiments and Results

4.1. Source of Data. For practical packaging defect inspection, we obtained defect samples from a common production line packaging product, namely, bottles. A total of 1200 samples were collected with cap and label defects. Cap defects included mislocated caps, absent caps, and normal caps. Label defects included mislocated labels, absent label, damaged labels, and normal labels. The sample of the packaging bottle defect image is shown in Figure 7, and the number details are summarized in Table 1.

We utilized professional labeling software, LabelImg, to build the ground-truth from the sample data and automatically generated XML files to store practical information about the defect data, which were used together with the samples during model training and testing.

4.2. Model Training and Evaluation Metrics. Our experimental environment was Windows 10 OS, Anaconda Python 3.7, NVIDIA RTX 2070 GPU, CUDA 10.1, and cuDNN 7.6.5.32. We used the Keras library for programming. For data allocation, we selected 1000 samples from the dataset for training, among which 900 samples were used for model training and the other 100 for crossvalidation. The remaining 200 samples were used for performance testing after model training. In terms of the training methodology, we adopted transfer learning for overall model training. Then, we conducted model optimization using our own defect sample data. We

TABLE 1: Defect sample number by category.

Category	Count
Cap defect	
No cap	263
Misloc cap	612
Normal cap	325
Label defect	
No label	293
Misloc label	335
Damaged label	345
Normal label	227

configured hyperparameters with 512×512 input data. We enabled early-stop, such that the iterations would not continue after the model had optimally converged. To speed up the training, we froze the backbone network during the first 50 epochs, during which time only the enhanced feature extraction network's weights were updated. The batch size was set to 8, and the initial learning rate was 0.001. In the next 50 epochs, we unfroze the backbone network for weight updating to optimize the global network. During this time, the batch size was set to 4 and the initial learning rate was 0.00005.

We used two commonly used metrics for object detection model evaluation, precision (P) and recall (R) [27].

$$P = \frac{TP}{TP + FN},$$
$$R = \frac{TP}{TP + FP}, \tag{2}$$

where TP is the number of samples that the model correctly detected, FN is the number of samples that the model failed to detect, and FP is the number of samples that the model falsely detected. Considering that the precision and recall can vary for different confidence thresholds, we also recorded the *P-R* (precision-recall) to obtain the average precision (AP) [27].

$$AP = \int_0^1 P(R)dR. \tag{3}$$

The AP value is the area under the *P-R* curve, where *P* represents precision and *R* represents recall. For multicategory defects, it is common to use the mean average precision (mAP) of all categories for overall evaluation.

4.3. Model Evaluation and Performance Comparison and Analysis

4.3.1. Evaluation of Model Training. It can be observed in Figure 8 that, in general, the loss gradually decreases as the number of epochs increase until convergence, indicating that the model's prediction error gradually decreases. In addition, there is a sudden drop in the loss curves for the crossvalidation set after epoch 43. This is because the model freezes the
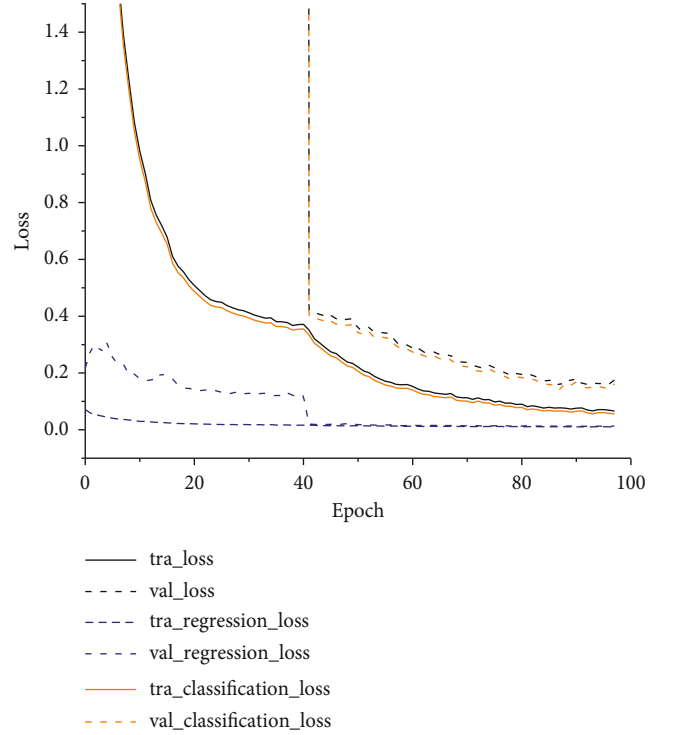
FIGURE 8: Model loss function.

Legend:
- tra_loss
- val_loss
- tra_regression_loss
- val_regression_loss
- tra_classification_loss
- val_classification_loss

mAP=99.16%

FIGURE 9: *P-R* curve.

Legend:
- Uncapped AP = 100%
- Skew cap AP = 99.02%
- Normal cap AP = 99.58%
- Unlabeled AP = 100%
- Skew label AP = 96.47%
- Damaged label AP = 99.04%
- Normal label AP = 100%
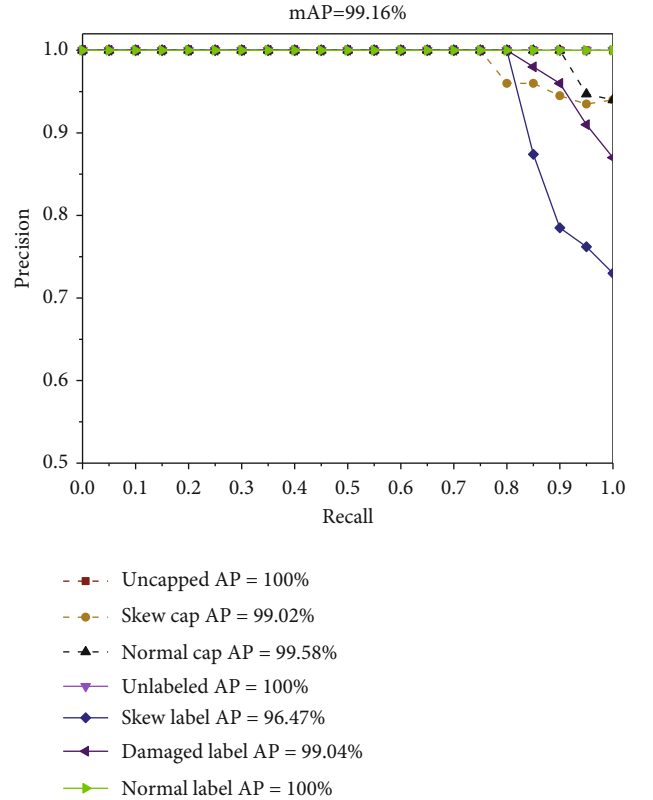
backbone network in the early stage of the training. In later iterations, after unfreezing the network, the model is trained globally and the loss of the crossvalidation set approaches

TABLE 2: Impact of transfer learning and ECA on model performance.

Method	Parameters (10^7)	FPS	Transfer learning?	mAP (/%)	Standard deviation (mAP)
EfficientDet	0.389	45.62	Yes	97.75	0.62
			No	23.12	0.65
(Mish)ECA-EfficientDet	**0.325**	**41.72**	**Yes**	**99.16**	**0.54**
			No	30.12	0.61

TABLE 3: Impact of mosaic trick on model performance.

Method	Parameters (10^7)	FPS	Mosaic trick?	mAP (/%)	Standard deviation (mAP)
EfficientDet	0.389	45.62	Yes	97.75	0.62
			No	95.45	0.59
(Mish)ECA-EfficientDet	**0.325**	**41.72**	**Yes**	**99.16**	**0.54**
			No	97.88	0.63

that of the training set, indicating a progressive improvement in the model's generalization capability.

4.3.2. Performance Testing.
After model training, we imported the files containing the learned weights into our program and tested the model with 200 samples. The results are illustrated in Figure 9 as P-R curves. The solid lines denote label defects and the dashed lines denote cap defects.

From the P-R curve, the AP value for each type of defect can be readily obtained. Overall, our method achieved a mAP of 99.16%. For each individual defect category, except for a slightly lower precision for mislocated labels, our method achieved accuracy above 99% for all the other categories. This indicates that our method is capable of meeting the practical needs of applications.

4.3.3. Performance Comparison and Analysis.
In our investigation, we conducted several experimental simulations to validate the optimized model and demonstrate the advantages of our method. In Tables 2–5, the results of our method or strategy are presented in bold.

First, we investigated the impact of transfer learning and the ECA mechanism on model performance. We compared ECA-EfficientDet and EfficientDet with and without transfer learning. The simulation results are summarized in Table 2.

It can be observed in Table 2 that, compared with the model without transfer learning, the precision of the model with transfer learning was substantially higher. This demonstrates the effectiveness of transfer learning for small-sized sample data and its ability to avoid hindering the model's generalization capability due to limited samples. In addition, the ECA mechanism improved the model's precision as well, albeit at the cost of some loss in detection speed.

Next, in order to prove the necessity of the mosaic method. We compared ECA-EfficientDet and EfficientDet (transfer learning) with and without mosaic trick. The results are shown in Table 3.

It can be seen from the results that the mosaic trick can effectively improve the performance of ECA-EfficientDet and EfficientDet. In addition, we also compared various acti-

TABLE 4: Impact of activation functions on model performance.

Method	Activation function	mAP (/%)	Standard deviation (mAP)	FPS
ECA-EfficientDet	Swish [23]	98.63	0.58	45.98
	Hard-Swish [24]	95.64	0.61	44.08
	Hard-Swish [24]	97.12	0.59	49.36
	Mish [19]	**99.16**	**0.54**	**41.72**

TABLE 5: Performance of the proposed method compared with other single-stage object detection algorithms.

Method	Parameters (10^7)	mAP (/%)	Standard deviation (mAP)	FPS
YOLOv3 [28]	6.200	92.60	0.66	31.08
YOLOv4 [16]	6.443	97.22	0.58	22.64
YOLOv4-tiny [16]	0.606	91.23	0.63	157.47
SSD [29]	2.628	97.55	0.71	62.56
EfficientDet [21]	0.389	97.75	0.62	45.62
Our method	**0.325**	**99.16**	**0.54**	**41.72**

vation functions on the ECA-EfficientDet with transfer learning. The results are summarized in Table 4.

It can be observed in Table 4 that the Mish function has higher precision than EfficientDet's default activation function, Swish. However, Mish function's detection speed is lower than that of the others.

Because our method performs end-to-end single-stage object detection, we compared our ECA-EfficientDet (with Mish as the activation function) with transfer learning to other object detection algorithms. The results are summarized in Table 5.

It can be observed in Table 5 that our method achieved higher precision (mAP = 99.16%) than the other five
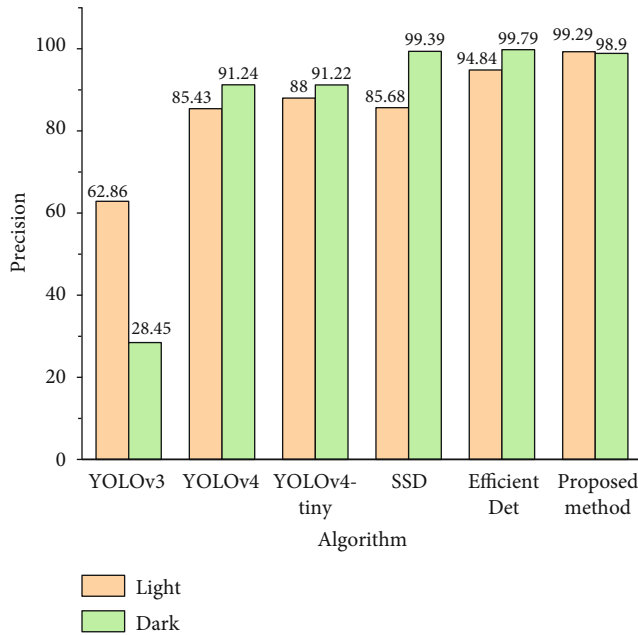
FIGURE 10: Comparison of our method to other object detection algorithms in light and dark environments.

single-stage object detection algorithms. In terms of detection speed, our method was faster than YOLOv3 and YOLOv4 and close to EfficientDet. In addition, although YOLOv4-tiny had the fastest detection speed, its accuracy was the worst, rendering it disadvantageous in practical applications.

To test the model's stability in complex environments, we lightened and darkened the 200 test samples using the OpenCV library, thus generating two subsets that simulated detection in light and dark environments. We tested our object detection algorithm with these two subsets. The results are illustrated in Figure 10. The dark color represents testing in a dark environment, and the light color represents testing in a light environment.

It can be observed in Figure 10 that, compared with other object detection algorithms, our method was more precise in both environments and there were few differences between the two subsets, indicating good model stability.

In summary, although our method is slightly inferior in terms of detection speed, it shows good performance in terms of precision and stability. Our detection speeds can meet the needs for practical inspection. Therefore, we expect that our method will be advantageous for applications of packaging defect detection.

5. Conclusions

We proposed a packaging defect detection method based on the ECA-EfficientDet object detection algorithm. We validated its effectiveness and advantages on a sample dataset of defects. Our results show the following: (1) The proposed method solves a challenging problem in conventional machine vision algorithms. It can simultaneously detect multiple defect objects, effectively reducing inspection costs

on production lines. (2) Our design of ECA-Convblock in the backbone feature extraction network prevents dimension reduction in model channel importance prediction and enhances high-quality expressions of object features, effectively improving the defect detection accuracy. (3) The incorporation of Mosaic data augmentation and the Mish activation function into the model and the adoption of heterogeneous-data-based transfer learning for model training effectively enhance the model's generalization capability and improve its robustness in complex environments. It should be pointed out that the algorithm has obvious advantage in accuracy performance and algorithm stability, but it is slightly insufficient in detection speed. Therefore, combining light weight with the model in this paper to improve the model's actual generation and detection will be carried out in the follow-up research.

Data Availability

The data used to support the findings of this study are available from the corresponding author upon request.

Conflicts of Interest

The authors declare that they have no conflicts of interest.

References

[1] C. Toxqui-Quitl, J. Cardenas-Franco, A. Padilla-vivanco, and J. Valdiviezo-Navarro, "Bottle Inspector Based on Machine Vision, Proc," in *Image Processing: Machine Vision Applications VI*, pp. 1–10, International Society for Optics and Photonics, 2013.

[2] Y. Zheng, Y. Wang, X. Zhou, X. Jiang, Y. Peng, and Y. Liu, "Empty bottle texture area defect detection based on POBT," *Journal of Electronic Measurement and Instrumentation*, vol. 31, no. 4, pp. 549–558, 2017.

[3] X. Zhou, Y. Wang, Q. Zhu et al., "A surface defect detection framework for glass bottle bottom using visual attention model and wavelet transform," *IEEE T. Ind. Inform.*, vol. 16, no. 4, pp. 2189–2201, 2020.

[4] Y. Lecun, L. Bottou, Y. Bengio, and P. Haffner, "Gradient-based learning applied to document recognition," *Proceedings of the IEEE*, vol. 86, no. 11, pp. 2278–2324, 1998.

[5] A. Krizhevsky, I. Sutskever, and G. Hinton, "ImageNet classification with deep convolutional neural networks," *Communications of the ACM*, vol. 60, no. 6, pp. 84–90, 2017.

[6] Z. J. Gao, Y. J. Zhang, and Y. Li, "Extracting features from infrared images using convolutional neural networks and transfer learning," *Infrared Physics & Technology*, vol. 105, p. 103237, 2020.

[7] K. He, X. Zhang, S. Ren, and J. Sun, "Deep residual learning for image recognition," in *Proc. 2016 IEEE Conference on Computer Vision and Pattern Recognition (CVPR)*, pp. 770–778, 2016.

[8] A. G. Howard, "MobileNets: efficient convolutional neural networks for mobile vision applications," *Computer Vision and Pattern Recognition*, 2017, arXiv: 1704.04861v1.

[9] M. Tan and Q. V. Le, "EfficientNet: rethinking model scaling for convolutional neural networks, Proc," in *2019*

International Conference on Machine Learning(ICML), pp. 1–11, 2019.

[10] Y. Zhou and G. P. Li, "Intelligent fault diagnosis of hydraulic piston pump combining improved LeNet-5 and PSO hyperparameter optimization," *Applied Acoustics.*, vol. 183, p. 108336, 2021.

[11] Z. J. Wang, W. L. Zhao, and W. H. Du, "Data-driven fault diagnosis method based on the conversion of erosion operation signals into images and convolutional neural network," *Process Safety and Environmental Protection*, vol. 149, pp. 591–601, 2021.

[12] H. Zhang, L. X. Jiang, and C. Li, "CS-ResNet: cost-sensitive residual convolutional neural network for PCB cosmetic defect detection," *Expert Systems With Applications*, vol. 185, p. 115673, 2021.

[13] G. Marques, "Automated medical diagnosis of COVID-19 through EfficientNet convolutional neural network," *Applied Soft Computing Journal*, vol. 96, 2020.

[14] A. Michele, V. Colin, and D. D. Santika, "MobileNet convolutional neural networks and support vector machines for palmprint recognition," in *4th International Conference on Computer Science and Computational Intelligence*, vol. 157, pp. 110–117, 2019.

[15] T M P R, "Efficient Det: scalable and efficient object detection," in *Proc. 2020 IEEE/CVF Conference on Computer Vision and Pattern Recognition (CVPR)*, pp. 10778–10787, 2020.

[16] A. Bochkovskiy, C. Wang, and H. Liao, "YOLOv4: optimal speed and accuracy of object detection," 2020, arXiv preprint, arXiv: 2004.10934v1.

[17] J. Hu, L. Shen, G. Sun, and S. Albanie, "Squeeze-and-excitation networks," *IEEE Transactions on Pattern Analysis & Machine Intelligence*, vol. 42, no. 8, 2020.

[18] X. Li, X. Shen, Y. Zhou, X. Wang, and T. Q. Li, "Classification of breast cancer histopathological images using interleaved DenseNet with SENet (IDSNet)," *PloS one*, vol. 15, no. 5, 2020.

[19] Z. Li, K. Jiang, S. Qin, Y. Zhong, and A. Elofsson, "GCSENet: A GCN, CNN and SENet ensemble model for microRNA-disease association prediction," *PLOS Computational Biology*, vol. 17, no. 6, p. e1009048, 2021.

[20] Q. Wang, B. Wu, P. Zhu, P. Li, and Q. Hu, "ECA-net: efficient channel attention for deep convolutional neural networks," in *Proc. 2020 IEEE/CVF Conference on Computer Vision and Pattern Recognition (CVPR)*, pp. 11531–11539, 2020.

[21] M. T. R. Pang and Q. V. Le, "EfficientDet: scalable and efficient object detection," in *Proc. 2020 IEEE/CVF Conference on Computer Vision and Pattern Recognition (CVPR)*, pp. 10778–10787, 2020.

[22] S. Yun, D. Han, S. J. Oh, S. Chun, J. Choe, and Y. Yoo, "Cut-Mix: regularization strategy to train strong classifiers with localizable features," 2019, arXiv preprint, arXiv: 1905.04899v1.

[23] P. Ramachandran, B. Zoph, and Q. V. Le, "Swish: a self-gated activation function," 2017, arXiv preprint arXiv:1710.05941v1.

[24] A. Howard, "Searching for MobileNetV3," in *Proc. 2019 IEEE/ CVF International Conference on Computer Vision (ICCV)*, pp. 1314–1324, 2020.

[25] A. L. Maas, A. Y. Hannun, and A. Y. Ng, "Rectifier nonlinearities improve neural network acoustic models, proc," in *Proceedings of the 30th International Conference on Machine Learning*, pp. 1–6, 2013.

[26] D. Misra, "Mish: a self regularized non-monotonic neural activation function," 2019, arXiv preprint arXiv:1908.08681v1.

[27] K. Li and L. Cao, "A review of object detection techniques," in *Proc. 2020 5th International Conference on Electromechanical Control Technology and Transportation (ICECTT)*, pp. 385–390, 2020.

[28] J. Redmon and A. Farhadi, "YOLOv3: an incremental improvement," *Computer Vision and Pattern Recognition*, 2018, arXiv: 1804.02767v1.

[29] W. Liu, D. Anguelov, D. Erhan et al., "SSD: single shot multi box detector," in *Proc. 14th European Conference on Computer Vision (ECCV)*, pp. 21–37, Springer International Publishing, 2016.

Research Article

Improved SiamFC Target Tracking Algorithm Based on Anti-Interference Module

Yejin Yan ⓘ, **Wenxiao Huo** ⓘ, **Jiayu Ou** ⓘ, **Zhifeng Liu** ⓘ, **and Tianping Li** ⓘ

College of Physics and Electronic Science, Shandong Normal University, 250300 Shandong, China

Correspondence should be addressed to Tianping Li; sdsdltp@sdnu.edu.cn

The SiamFC target tracking algorithm has attracted extensive attention because of its good balance between speed and performance, but the tracking effect of the SiamFC algorithm is not satisfactory in complex background scenes. When SiamFC algorithm uses deep semantic features for tracking, it has good recognition ability for different types of objects, but it has insufficient discrimination for the same types of objects. Therefore, we propose an effective anti-interference module to improve the discrimination ability of the algorithm. The anti-interference module uses another feature extraction network to extract the features of the candidate target images generated by the SiamFC main network. In addition, we set up the feature vector set to save the feature vectors of the tracking target and the template image. Finally, the tracking target is selected by calculating the minimum cosine distance between the feature vector of the candidate target and the vector in the feature vector set. A large number of experiments show that our anti-interference module can effectively improve the performance of SiamFC algorithm, and the performance of this algorithm can be comparable to the popular algorithms.

1. Introduction

The field of computer vision has advanced rapidly in recent years, and the direction of target tracking has become a research hotspot for many research institutions and universities. Current target tracking is typically based on delimiting the target area in the first frame of the video sequence and then tracking the target in the subsequent frame [1]. Target tracking has a wide range of applications, such as autonomous driving [2], video surveillance, and human-computer interaction [3]. However, many problems still exist in the field of target tracking, such as complex background, target occlusion, and scale change [4].

Current mainstream target tracking algorithms can be divided into two categories. One category is based on the Siamese network [5–13]. Algorithms in this category are designed using the Siamese network structure and have achieved good results. The other category is based on a non-Siamese network [14–18], which is mostly studied using correlation filter (CF) [19–22]; however, because algorithms in this category are constantly improving, their tracking speed and performance based on CF cannot be well balanced. The majority of researchers

prefer a Siamese network-based target tracking algorithm, and its classical algorithm SiamFC [5] has become a milestone algorithm. It can effectively balance the speed and accuracy of target tracking and has become the cornerstone of many subsequent improved algorithms. However, these improved algorithms [5–9] cannot effectively solve the intraclass interference problem of target tracking in a complex background because they do not effectively distinguish the tracking target from the interference target. Moreover, we believe that simply relying on an improved network model to improve the anti-interference ability of the target cannot meet the requirements. In some cases, the response value of the interference target in the tracking process exceeds the response value of the tracking target, as shown in Figure 1. However, this is inevitable because a convolutional neural network (CNN) cannot obtain such a high discriminant network model to avoid the overfitting problem in the training process. If we want to further improve the discrimination ability of the target while also considering the universality of the target tracking effect, we must increase the number of training parameters and the training set. These two requirements have significant limitations in terms of current conditions.
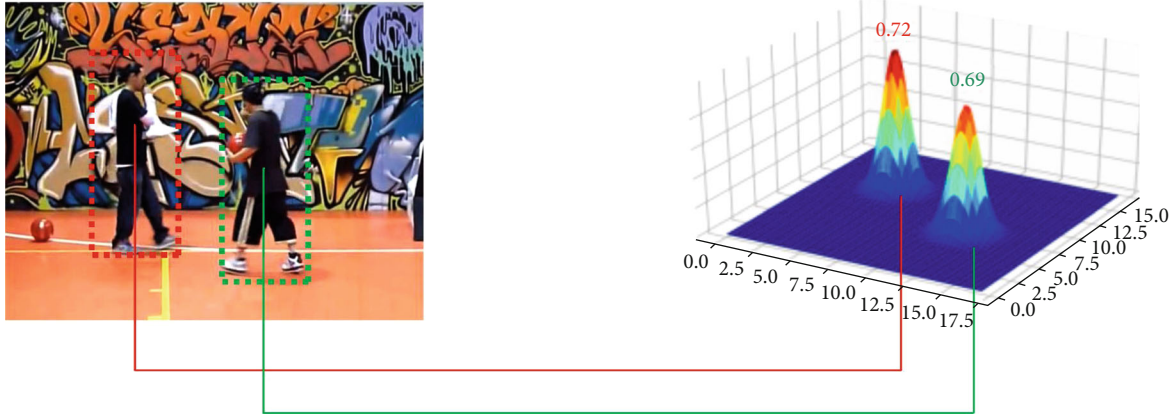
Figure 1: Response scores of SiamFC algorithm. Red box target for interference target, and green box target for tracking target.

The similarities between these algorithms [5–8] are all based on the screening of candidate targets, with the majority of the screening aimed at selecting the target with the highest score in the score map. SiamFC [5] is screened directly based on the score map after cross-correlation operation, SiamRPN [6] is screened directly based on the score map after nonmaximum suppression, and DaSiamRPN [7] is the same as SiamRPN [6]. However, in the complex background, the response value of the target is close to the interference target, and even the response value of the interference target is higher than that of the tracking target, which will inevitably affect the tracking effect.

Based on this background, this study proposes an anti-interference module and designs an appearance feature extraction network. First, it extracts features of the tracking target in recent and initial frames and then extracts features of the candidate target in the current frame. Finally, it judges the best tracking target by calculating the minimum cosine distance of the feature vectors of the two parts and finally realizes the effective judgment of the candidate target frame.

The main contributions of this paper are as follows:

(1) The anti-interference module is designed to improve the robustness of the algorithm to complex background scenes

(2) An appearance feature extraction network which can effectively extract the appearance features of the target is designed. Multiple candidate boxes are extracted on the basis of SiamFC, and the candidate boxes are input into the appearance feature extraction network to finally obtain the correlation vector

(3) The feature vector set is designed, which can save the tracking target feature vector in recent frames and the template image

(4) The cosine distance between the vector in the feature vector set and the feature vector of the candidate target is calculated to determine the tracking target, which solves the disadvantage that only template image features can be used in SiamFC algorithm

and improves the performance of the algorithm for long-time tracking

2. Related Works

2.1. Target Tracking Algorithm Based on Deep Learning. In recent years, due to the continuous expansion of available datasets and the improvement in computing power, the advantages of deep learning (DL) methods have gradually become evident. DL methods are far more powerful than traditional algorithms in terms of target tracking. In addition, the great potential of DL direction has piqued the interest of an increasing number of researchers. The advantage of a DL algorithm lies in the strong feature extraction ability and representation ability of its network model. At present, methods based on the DL network model are mainly divided into the following categories: CNN method, recurrent neural network (RNN) method, and generative adversarial network (GAN) method. The most popular DL network model in the field of computer vision is CNNs, and RNNs are more commonly used in natural language processing. Although GANs have some applications in image processing, they are limited to data processing. DL was first applied to target tracking in [23], and a target tracking framework based on offline training and online fine-tuning was proposed. Several subsequent algorithms have been improved on this network framework and have achieved good results.

2.2. Convolutional Neural Network-Based Methods. In recent years, CNNs have swept through the field of DL. From natural language processing to image processing, computer vision has also made great progress through the continuous improvement of CNNs. In 2012, the success of the AlexNet network model on the ImageNet classification dataset sparked a surge in researchers' interest in DL. There are three popular network models: AlexNet [24], VggNet [25], and ResNet [26]. AlexNet [24] has a network structure of only eight layers, of which five layers are convolution layers and the other three layers are fully connected layers. Compared with AlexNet [24], VggNet [25] has more network depth, so the tracking effect is greatly improved. However, with the increase in network depth, grid degradation will occur. At this time, the emergence of ResNet

[26] introduces neural networks in a new direction. ResNet [26] connects network layers through the jump connection, which effectively solves the problem of grid degradation when the network depth is deepened. Finally, ResNet [26] won ImagNet2015 [27]. In recent years, lightweight models have attracted increasing attention. MobileNetV1 [28] uses depthwise (DW) separable convolutions, ignores the pooling layer, and uses convolution with a stripe equal to 2. Compared with V1, MobileNetV2 [29] introduces a residual structure. Before DW, 1×1 convolution is used to increase the feature map channel. After pointwise, a rectified linear unit (ReLU) is abandoned and replaced with a linear activation function to prevent the destruction of features by ReLU. MobileNetV3 [30] integrates the depth separable convolution of V1 and the inverse residual structure of V2 and introduces the h-swish activation function. EffNet [31] decomposes the DW layer of MobileNetV1 into 3×1 and 1×3 convolutions. After the first layer, pooling is adopted to reduce the amount of calculation in the second layer. The smaller the size of the model, the higher the accuracy is obtained. EfficientNet [32] designs a standardized convolution network expansion method to optimize the efficiency and accuracy of the network from the three dimensions of balance resolution, depth, and width. ShuffleNetV1 [33] reduces computation complexity by grouping convolution and enriches channel information by reorganizing channels. ShuffleNetV2 [34] mainly designs and uses more efficient CNN network structure design criteria.

CNNs typically extract the deep semantic features of images through deep neural networks and then use the appropriate classifier to extract the target. At present, the full CNN is the most popular; that is, there is no full connection layer in the entire network model, which greatly reduces the number of network parameters and increases the running speed. In SiamFC [5] tracking algorithm, the network model is improved on the basis of AlexNet [24], removing the final full connection layer and part of the convolution layer. Finally, the target tracking problem is transformed into a similarity matching problem, and the location of the target is judged by a cross-correlation operation. SiamRPN [6] algorithm introduces the RPN [35] network to target detection based on the SiamFC algorithm, significantly improving the accuracy of target tracking through classification and regression. DaSiamRPN [7] optimizes the imbalance of positive and negative samples in the training process based on SiamRPN. SiamRPN + + [8] increases the network depth based on SiamRPN [6] and has achieved good results. CFNet [9] adds the CF layer based on the SiamFC [5] structure to realize the end-to-end training of the network, which proved that this network structure could use fewer convolution layers of the network without degrading accuracy. The main improvement of SiamFC++ [36] is to add a boundary box regression branch and quality estimation branch based on SiamFC [5]. In [37], the authors propose a multilevel similarity model under a Siamese framework for robust TIR object tracking, which solves the problem that only RGB images can be used in the training process. Motivated by the forward-backward tracking consistency of a robust tracker, self-SDCT [38] proposes a multicycle consistency loss as self-supervised information for learning feature extraction network from adjacent video frames. TRBACF [39] proposes a temporal regular-

ization strategy based on the correlation filter, which effectively solves the problem that the model can not adapt to tracking scene changes and improves the robustness and accuracy of the algorithm.

2.3. Image Similarity Judgment. At present, there are several ways to judge the similarity of images. The first method is based on histograms. The histogram method judges the similarity by describing the color distribution in an entire image, but a histogram is too simple to capture the similarity of color information and cannot use more information. The second method is to calculate the mutual information about two images. Although this method is accurate, it has great limitations. It requires that the size of the two images must be the same. If the two images are cut into the same size, it is bound to lose a lot of information, thereby degrading accuracy. The third method is the cosine distance judgment method. Images are represented as vectors, and the cosine distance between these vectors is calculated to determine the similarity. The cosine distance pays more attention to the direction of the vector to avoid the influence of the absolute value of the vector on the similarity judgment. It is very suitable for us to extract the target feature and use the vector for similarity judgment.

3. The Proposed Algorithm

In the classical SiamFC [5] algorithm, an improved network on AlexNet [24] is used as the backbone network of the tracking network. The Siamese network is used to extract the feature of the search and template images, respectively. Finally, the position score map of $17 \times 17 \times 1$ is obtained by a cross-correlation operation, as shown in Figure 2.

However, the resolution of the feature map calculated using the two feature branches in SiamFC [5] is too small. Although it can effectively search the target, it cannot effectively distinguish the target within a class. As shown in Figure 1(b), the interference target even produces a higher thermal value than the tracking target. Inspired by the appearance feature module in DeepSort [40], we consider whether we can construct another special appearance feature extraction network to extract the appearance feature of the target to better distinguish intraclass targets.

Thus, we design a new type of target anti-interference module. The main body of the anti-interference module is composed of a feature extraction network and similarity calculation. Unlike other algorithms for suppressing the interference target, we choose the tracking results of several adjacent frames of the tracking target to measure the tracking target twice.

We will describe the overall framework of the algorithm in Section 3.1. Section 3.2 focuses on the main framework of the benchmark algorithm SiamFC [5]. Section 3.3 describes the main network of our anti-interference module. Section 3.4 mainly describes the working mode of the anti-interference module and how to determine the position of the final target box.
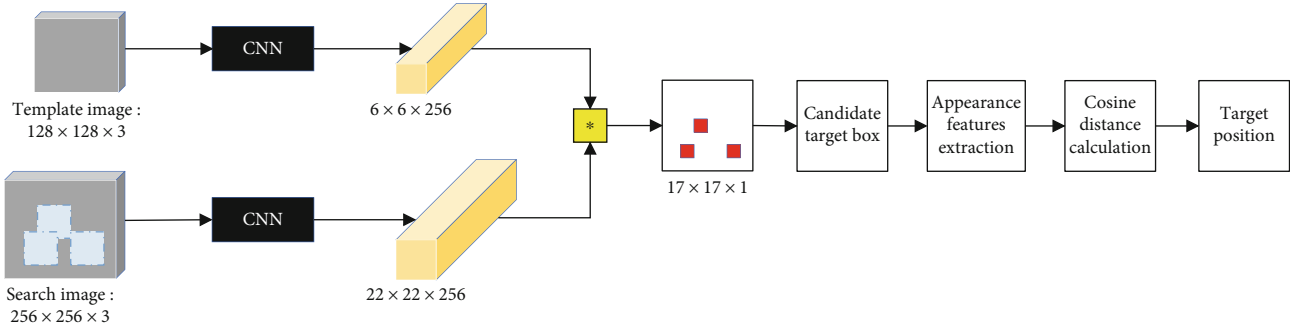
FIGURE 2: Overall frameworks.

3.1. Overall Framework. The algorithm is mainly composed of two parts. The first part is the main framework of SiamFC [5], as shown in the red box in Figure 2. The main role is to extract features and generate candidate targets. Different from SiamFC [5], where only one target box is generated in SiamFC [5], multiple candidate boxes are selected in our algorithm. The second part is our anti-interference module, such as the green box in Figure 2. The main function is to process the multiple candidate boxes generated in the first part to output the final target position. Figure 2 shows the overall frame diagram.

3.2. The SiamFC Framework. The main framework of SiamFC [5] is divided into two branches: template and search branches. The main network of SiamFC [5] is improved on the basis of AlexNet [24], removing the full connection layer and partial convolution layer. There are only Conv and pooling layers in the entire network structure, and the template branch shares the same network parameters with the search branch, which satisfies the definition of full convolution and twin network. The processing of the original image in SiamFC [5] is as follows: we select the first frame image of the video sequence as the template image and other images as the search image. We use 127×127-pixel template images and 255×255-pixel search images. To facilitate the extraction of appearance features by the anti-interference module, we cut the template image to 128×128 pixels and the search image to 256×256 pixels. The specific feature processing process of SiamFC is as follows. A template image of $128 \times 128 \times 3$ is input into the template branch to obtain the feature map of $6 \times 6 \times 128$. Similarly, a search image of $256 \times 256 \times 3$ is input into the search branch to obtain the feature map of $22 \times 22 \times 128$. A template image feature is used as the convolution kernel, and the two feature maps are cross-correlated; sliding window detection is performed on the features of the search image. Then, we obtain a $17 \times 17 \times 1$ score map about the target location information. The cross-correlation operation formula is as follows:

$$F(Z, X) = \varphi(Z) * \varphi(X) + b_i. \tag{1}$$

$\varphi(Z)$ and $\varphi(X)$ represent the extracted template and search image features, respectively. The symbol $*$ indicates convolution operation, where b_i denotes a signal that takes the value $b \in R$ in every location.

In the actual tracking process, our template branch only needs to be executed once to obtain the features of a template image. In the subsequent tracking process, information about the target position can be obtained by convolution operation between the extracted features of the search image and the features of the template image. The position of the target in the original image is obtained by upsampling according to the score map of $17 \times 17 \times 1$.

3.3. Extract Appearance Features. Figure 3 is our appearance feature extraction network, which is also the main part of the anti-interference module. It is mainly composed of two convolution layers and six residual blocks. The GOT10k [41] dataset is used to train the residual network model offline and output the normalized characteristics. Candidate boxes are reshaped into $128 \times 128 \times 3$ images, which are then input into the feature extraction network, producing 256-dimensional vectors. Finally, the normalization operation is performed to facilitate subsequent calculation.

3.4. Determination of Target Position by Minimum Cosine Distance. First, the network extracts the appearance features of five adjacent target frames and the initial frame and saves them to the feature vector set. Then, the vector of multiple prediction target frames in the current frame is extracted. The best tracking target is judged by calculating the cosine distance between the multiple candidate target features and the feature vector set of the current frame. Then, the feature vector set is updated according to the predicted target. The specific flowchart is shown in Figure 4. There are typically six vectors in the feature vector set, including five adjacent frame vectors and one initial frame vector. The selection of the prediction target box is based on the score map of $17 \times 17 \times 1$ generated by SiamFC [5]. First, we normalize and sort the score map of $17 \times 17 \times 1$ and then select the maximum three values. Take out the candidate target boxes corresponding to the three values. Then, their feature vectors are obtained using the feature extraction network. By calculating the cosine distance between the feature vector set and the feature vectors of the three prediction target boxes, the matrix of 3×6 can be obtained. The formula for calculating the single value of matrix $R(i, j)$ is as follows:

$$R(i, j) = 1 - r_i^T r_j \quad i \in (1, 3), \quad j \in (1, 6). \tag{2}$$

$128 \times 128 \times 3$ $128 \times 128 \times 32$ $64 \times 64 \times 32$ $32 \times 32 \times 64$ $1 \times 1 \times 256$
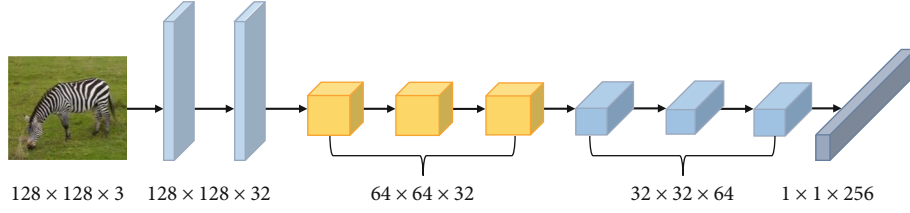
FIGURE 3: Deep appearance feature extraction network structure diagram.
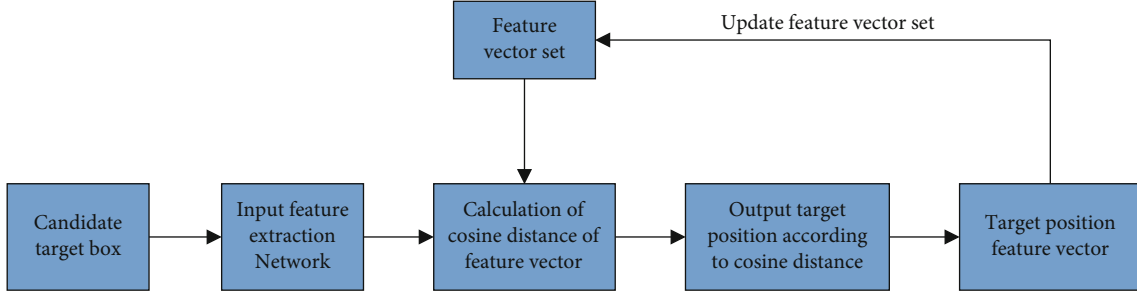
FIGURE 4: Flowchart of anti-interference module.
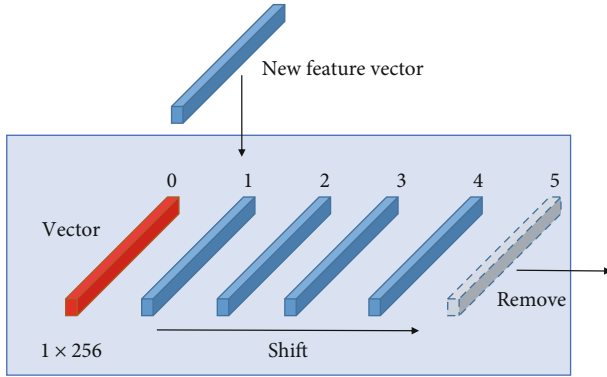
FIGURE 5: Update feature vector set.

The value of each row of the matrix is calculated by linear weighting. The formula is as follows:

$$R[i] = k1R(i,1) + k2\sum_{j=1}^{6} R(i,j), \quad i \in (1,3). \tag{3}$$

$k1$ and $k2$ are hyperparameters, typically $k1 = 0.35$ and $k2 = 0.65$.

Select the smallest $R[i]$ value as the final target location. The cosine distance can judge the similarity between vectors by calculating the angle between the directions of vectors, which effectively avoids the effect of the difference in absolute values of image pixels on the similarity judgment.

For update feature vector set, as shown in Figure 5, the feature vector set saves the feature vectors of our last five frames (as shown in Figure 5, blue vector) and template pictures (as shown in Figure 5, red vector). When we deter-

mine the position of the target in the current frame, we save the appearance feature vector obtained from the corresponding target candidate box to our feature vector set and remove the last feature vector.

4. Experiments

4.1. Experimental Configuration. We conducted experiments on a Linux system, and the experimental code was written in Python language and the PyTorch [42] framework. The experimental system configuration is Inter Core i7-10700 k CPU @ 3.80 GHz ×16, and a single GTX1070ti GPU.

4.2. Training Process. The training CNN part uses ILSVRC15 [27] and GOT10k [41] datasets for training. The appearance feature extraction network is trained using GOT10k [41].

4.3. Test Process. The OTB2015 [43] dataset is used for performance tests, and the VOT2016 [44] and VOT2017 [45] datasets are used to test the universality of the algorithm. To verify the effectiveness of the anti-interference module, we first compare the discrimination ability of the anti-interference module with the original algorithm, and then, we conduct tracking experiments on public datasets OTB2015 [43], VOT2016 [44], and VOT2017 [45] to prove the effectiveness and universality of our algorithm.

4.4. Single Discriminant Ability Experiment. Figure 6(a) is the first frame in the OTB2015 [43] video sequence "Board," where the green frame is the selected tracking target. Figure 6(b) is the SiamFC [5] tracking failure frame, where the red frame is the SiamFC [5] tracking failure position, and the green frame is the ground truth of the tracking target. To verify the effectiveness of our anti-interference

(a)   (b)

(c)   (d)

(e)
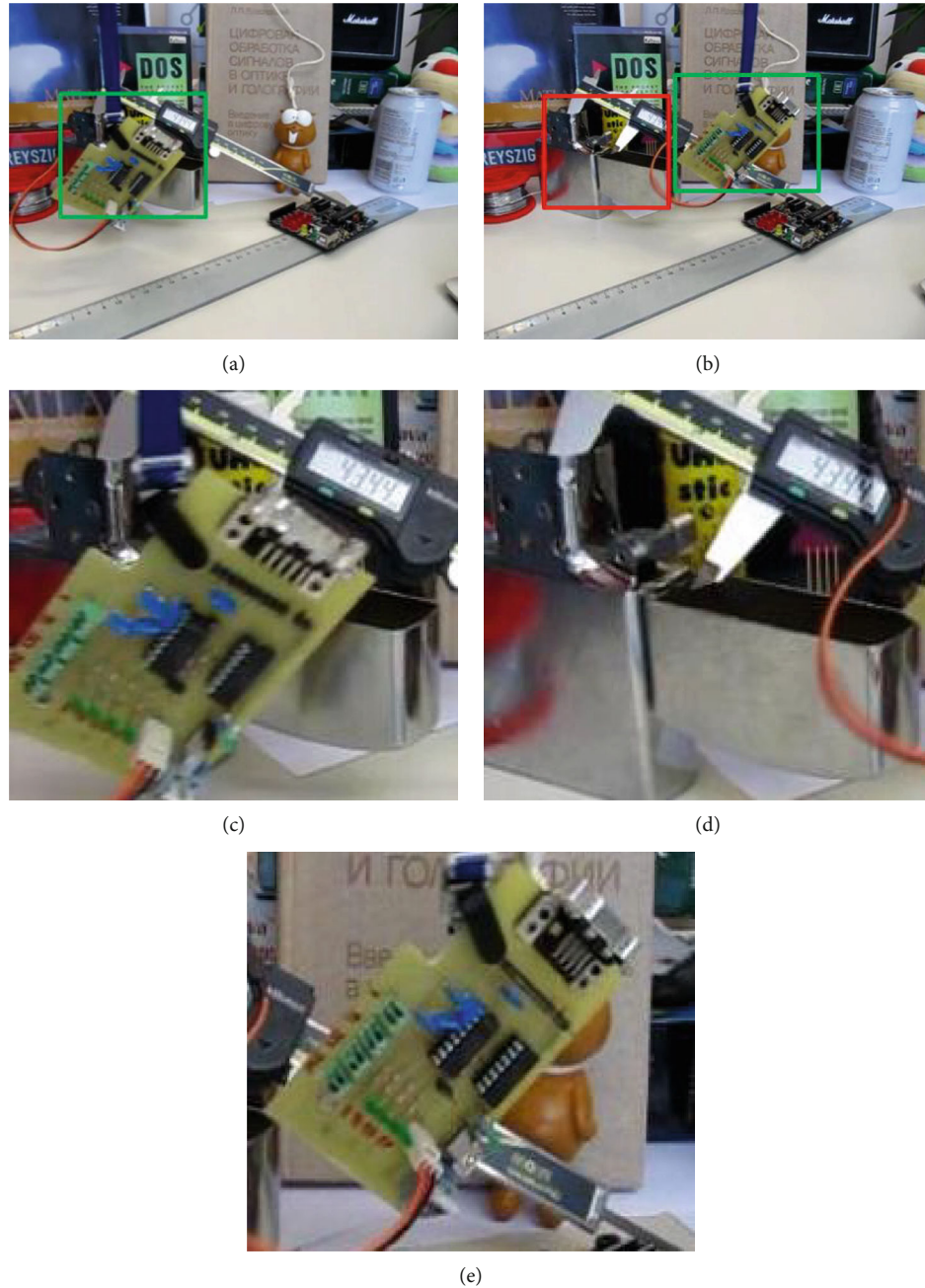
Figure 6: (a, b) The initial frame and SiamFC [5] tracking failure frame images, respectively. (c–e) The input images of the anti-interference module.

module, we first input the initial frame part as Figure 6(c) into our anti-interference module to obtain the feature vector. Then, we extract the tracking failure frame part, as shown in Figure 6(d), and the tracking target of the first frame, as shown in Figure 6(e). After that, we input Figures 6(d) and 6(e) into our anti-interference module to obtain the corresponding vector and then calculate the cosine distance using the feature vector of the initial frame tracking target. Finally, the cosine distance between the failure target and the initial frame is 0.73, and the cosine distance obtained from the ground truth part is 0.92. The higher the similarity, the closer the cosine dis-

tance is to 1. Thus, our anti-interference module can effectively judge the intraclass interference target, allowing our algorithm to outperform the baseline algorithm SiamFC [5].

4.5. Experiments in OTB2015. The OTB2015 [43] dataset is the benchmark dataset to test the performance of the target tracking algorithm. The dataset contains 100 manually annotated video sequences. The dataset mainly has two evaluation indexes: success and precision rates. The success rate is determined by whether the overlap rate between the bounding box and ground truth obtained using a frame during the tracking

(a)

(b)
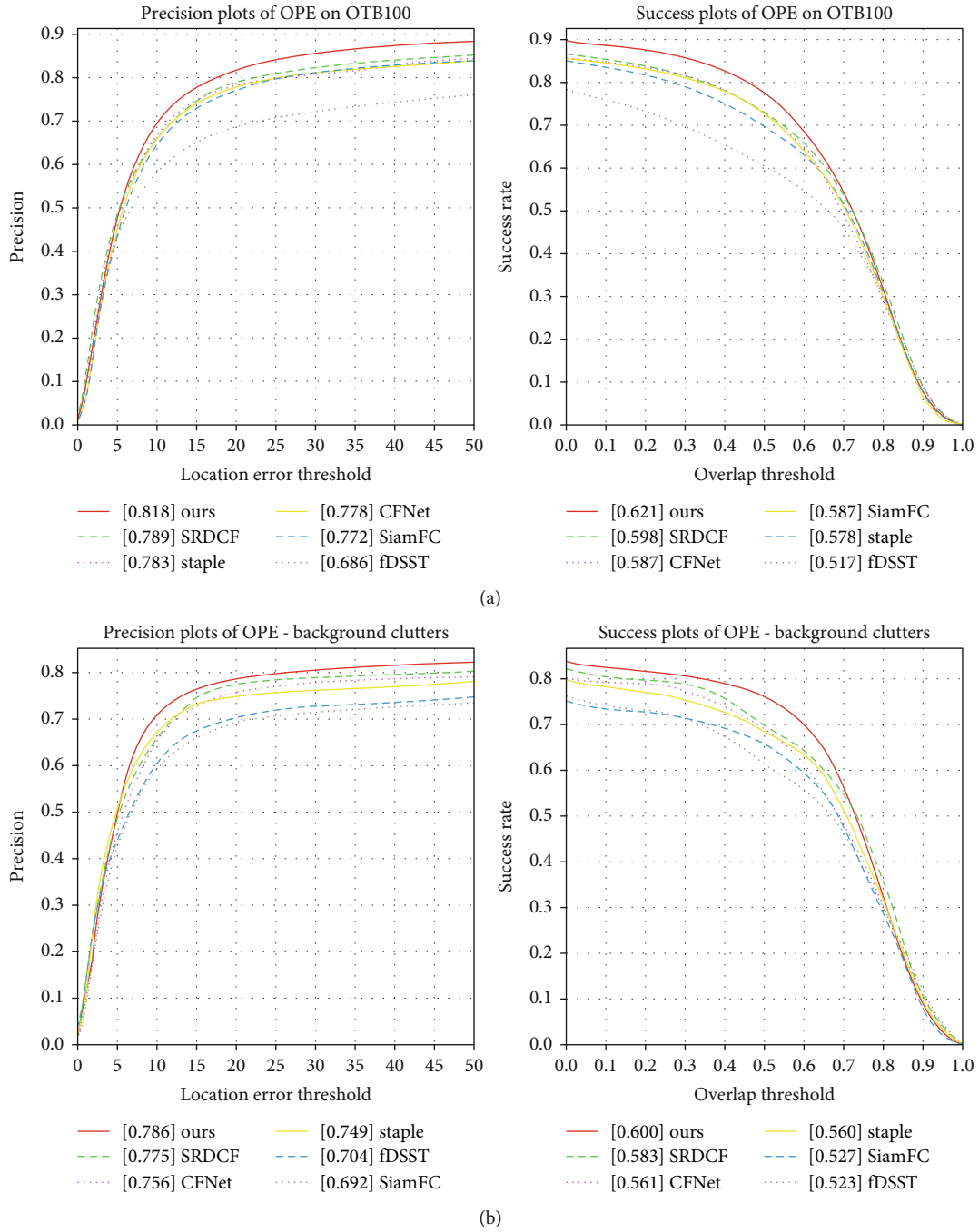
FIGURE 7: (a) The comparison of our algorithm with other algorithms on the OTB2015 dataset [43]. (b) The comparison of our algorithm with other algorithms on the OTB2015 [43] complex background dataset.

process exceeds a certain threshold; if so, the frame is regarded as a successful tracking frame. The percentage of successful frames in all frames is the success rate. The precision rate is defined as the center point of the target bounding box estimated by the tracking algorithm and the center point of the target manually labeled ground truth, and the distance between the two is less than the percentage of the video frames in a given threshold. Different thresholds have different percentages, and the general threshold is set to 20 pixels.

Figure 7(a) shows the comparison of our algorithm with other popular algorithms and benchmark algorithm SiamFC [5] on the OTB2015 [43] dataset. Other algorithms are SRDCF [46], Staple [47], CFNet [9], and fDSST [48]. Figure 7(b) shows the experimental results on the dataset in the OTB2015 complex background section. Figure 7 shows that the effect of our algorithm on the overall dataset has been compared to several existing popular algorithms. Our algorithm outperforms the benchmark algorithm SiamFC [5] in terms of accuracy and
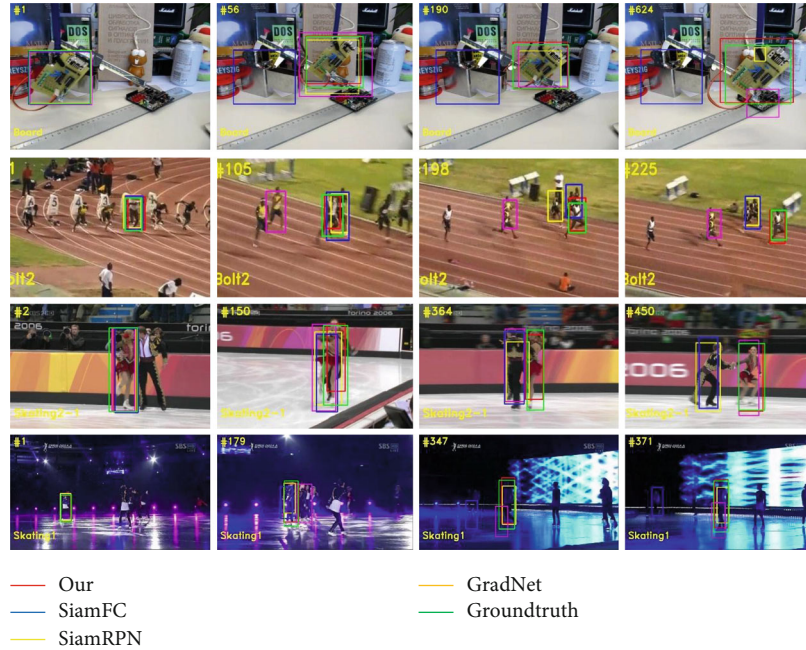
FIGURE 8: Comparison of tracking effects between our algorithm and other algorithms.

TABLE 1: Comparison of VOT2016 algorithm results.

Tracker	EAO	A	R	EFO
Our	0.301	0.558	0.286	3.857
SiamFC [5]	0.277	0.549	0.382	5.444
Staple [46]	0.295	0.544	0.378	11.114
CCOT [48]	0.331	0.539	0.238	0.507
TCNN [49]	0.325	0.554	0.268	1.049
DDC [44]	0.293	0.541	0.345	0.198
EBT [50]	0.291	0.465	0.252	3.011
STAPLEp [44]	0.286	0.557	0.368	44.765
DNT [51]	0.278	0.515	0.329	1.127
DeepSRDCF [52]	0.276	0.528	0.380	0.380
MDNet_N [53]	0.257	0.541	0.337	0.534

success rates. In particular, our algorithm has a good tracking effect in the case of complex background, which also shows that our algorithm can effectively distinguish between intraclass targets, reducing the misjudgment rate. In terms of running speed, SiamFC [5] is 80 fps, whereas our algorithm is 56 fps. Although the tracking speed of our algorithm is lower than that of the SiamFC algorithm, it still exceeds 30 fps, meeting the speed requirements of real-time target tracking. Figure 8 shows the comparison of tracking effects between our algorithm and other algorithms.

4.6. Experiments in VOT2016.
To verify the universality of the improved algorithm, we also conducted experiments on the VOT2016 [44] dataset. The VOT challenge is one of the most influential competitions in the field of computer vision. The VOT2016 [44] benchmark dataset consists of 60 video sequences, and all are color sequences. There are three main evaluation indicators in VOT2016 [44]: accuracy (A), equivalent filter operations (EFO), robustness (R), and expected average overlap (EAO). Accuracy is the accuracy of the target tracking, that is, the average overlap between the target box and the true value box during successful tracking. Robustness (R) is defined as the number of tracking failures. EAO represents the average value of the intersection and union ratio between the prediction box and the true ground-truth box in the entire video sequence. EFO is used to measure the tracking speed of the tracker.

We compare our algorithm with ten other popular algorithms on the VOT2016 [44] dataset, including the benchmark algorithm SiamFC [1] and nine other popular algorithms: Staple [47], CCOT [49], TCNN [50], DDC [44], EBT [51], STAPLEp [44], DNT [52], DeepSRDCF [53], and MDNet_N [54]. The comparison results are shown in Table 1. The chart shows that CCOT [38] has the best EAO of 0.331, our algorithm has the best accuracy of 0.558, CCOT [48] has the best robustness of 0.238, and STAPLEp [44] has the best tracking speed EFO of 44.745.

From the comparison results, our algorithm outperforms the benchmark algorithm SiamFC [5] in terms of EAO, accuracy, and robustness. In particular, the robustness of our algorithm is greatly improved compared with the original algorithm SiamFC [5]. This is because our anti-interference module effectively reduces the number of tracking failures, thereby improving the robustness of tracking. The accuracy of the algorithm is also improved compared with SiamFC [5], and it is better than other algorithms. This is because the tracking robustness can be increased after screening candidate targets through the anti-interference module. Second, our anti-interference module uses the minimum cosine distance to judge similar targets and processes the tracking target vector

TABLE 2: Comparison of VOT2017 algorithm results.

Tracker	SiamNAB	SiamFC	ECOHC	KFebT	ASMS	SSKCF	CSRDCF	UCT	MOSSEca
A	0.517	0.502	0.494	0.451	0.489	0.513	0.475	0.490	0.400
R	0.486	0.604	0.571	0.684	0.627	0.656	0.646	0.777	0.810
EAO	0.215	0.182	0.177	0.169	0.168	0.158	0.158	0.145	0.139

of recent frames in a weighted way, which reduces the probability of losing targets in the tracking process and improves the performance of long-time tracking. Therefore, accuracy can be improved. However, the accuracy has not been greatly improved. We believe that this is because the SiamFC regression is not sufficiently accurate. Compared with other algorithms, even though our indicators are not the highest, we do a good job of balancing speed and performance. For example, although the EAO value of CCOT reaches 0.331, its tracking speed is very slow; its EFO is only 0.507, whereas ours reaches 3.857.

4.7. Experiments in VOT2017. In this experiment, we evaluated the proposed algorithm on the VOT2017 [45] benchmark dataset. Then, we compared its accuracy, robustness, and EAO score with SiamFC [5] and the seven popular real-time tracker algorithms in VOT2017 [45]. These trackers are SiamFC, ECOHC [55], KFebT, ASMS, SSKCF, CSRDCF, UCT [56], and MOSSEca. Table 2 presents the experimental results. It can be seen from Table 2 that all indexes of our algorithm are better than other algorithms, and the accuracy is improved by 1.5% compared with the benchmark algorithm SiamFC. Especially in terms of robustness, our algorithm has great advantages over other methods; we believe that this is because the anti-interference module reduces the error rate in complex background. In addition, combined with the characteristics of targets in recent frames, the robustness of the algorithm for long-time tracking is also improved. The above experiments showed that on the VOT2017 [45] dataset, the proposed method is highly competitive with other most advanced trackers.

5. Conclusions

In this study, a new anti-interference module is proposed. Based on the benchmark algorithm SiamFC [5], another feature extraction network is designed, and its intraclass discriminant ability is trained on the GOT10k [41] dataset. The cosine distance is used to select the best tracking target by extracting the vector of the target frame. The experimental results show that, compared with the original benchmark algorithm SiamFC [5], our algorithm can well cope with the effect of intraclass targets on tracking performance in a complex background, thereby improving tracking accuracy; this also proves the effectiveness of the proposed anti-interference module. In the future, we will incorporate the anti-interference module into more advanced algorithms for research.

Data Availability

The test results already exist in the manuscript.

Conflicts of Interest

The authors declare that they have no conflicts of interest.

References

[1] S. Hare, S. Golodetz, A. Saffari et al., "Struck: structured output tracking with kernels," *IEEE Transactions on Pattern Analysis and Machine Intelligence*, vol. 38, no. 10, pp. 2096–2109, 2015.

[2] S. S. Rautaray and A. Agrawal, "Vision based hand gesture recognition for human computer interaction: a survey," *Artificial Intelligence Review*, vol. 43, no. 1, pp. 1–54, 2015.

[3] L. Mao, X. Li, D. Yang, and R. Zhang, "Convolutional feature frequency adaptive fusion object detection network," *Neural Process Letter*, vol. 53, no. 5, pp. 3545–3560, 2021.

[4] S. T. Cheng, C. W. Hsu, G. J. Horng, and S. Y. Chen, "Across-camera object tracking using a conditional random field model," *The Journal of Supercomputing*, pp. 1–28, 2021.

[5] L. Bertinetto, J. Valmadre, J. F. Henriques, A. Vedaldi, and P. H. Torr, "Fully-convolutional siamese networks for object tracking," in *European conference on computer vision*, pp. 850–865, Springer, Cham, 2016.

[6] B. Li, J. Yan, W. Wu, Z. Zhu, and X. Hu, "High performance visual tracking with Siamese region proposal network," *Proceedings of the IEEE Conference on Computer Vision and Pattern Recognition*, pp. 8971–8980, 2018.

[7] Z. Zhu, Q. Wang, B. Li, W. Wu, J. Yan, and W. Hu, "Distractor-aware Siamese networks for visual object tracking," in *Proceedings of the European Conference on Computer Vision (ECCV)*, pp. 101–117, 2018.

[8] B. Li, W. Wu, Q. Wang, F. Zhang, J. Xing, and J. Yan, "SiamRPN++: evolution of Siamese visual tracking with very deep networks," in *Proceedings of the IEEE/CVF Conference on Computer Vision and Pattern Recognition*, pp. 4282–4291, 2019.

[9] J. Valmadre, L. Bertinetto, J. F. Henriques, A. Vedaldi, and P. H. Torr, "End-to-end representation learning for correlation filter based tracking," in *2017 IEEE Conference on Computer Vision and Pattern Recognition*, pp. 2805–2813, 2017.

[10] P. Gao, R. Yuan, F. Wang, L. Xiao, H. Fujita, and Y. Zhang, "Siamese attentional keypoint network for high performance visual tracking," *Knowledge-Based Systems*, vol. 193, p. 105448, 2020.

[11] L. Zheng, Y. Chen, M. Tang, J. Wang, and H. Lu, "Siamese deformable cross-correlation network for real-time visual tracking," *Neurocomputing*, vol. 401, pp. 36–47, 2020.

[12] K. Yang, Z. He, Z. Zhou, and N. Fan, "Siam Att: Siamese attention network for visual tracking," *Knowledge-Based Systems*, vol. 203, p. 106079, 2020.

[13] D. Li, F. Porikli, G. Wen, and Y. Kuai, "When correlation filters meet Siamese networks for real-time complementary tracking," in *IEEE Transactions on Circuits and Systems for Video Technology*, pp. 509–519, 2020.

[14] C. Ma, J. Huang, J. B. Yang, X. Yang, and M. H. Yang, "Hierarchical convolutional features for visual tracking," in *Proceedings of the IEEE international conference on computer vision*, pp. 3074–3082, 2015.

[15] Y. Song, C. Ma, X. Wu et al., "Vital: visual tracking via adversarial learning," *Proceedings of the IEEE Conference on Computer Vision and Pattern Recognition*, pp. 8990–8999, 2018.

[16] H. Fan and H. Ling, "Sanet: structure-aware network for visual tracking," in *Proceedings of the IEEE conference on computer vision and pattern recognition workshops*, pp. 42–49, 2017.

[17] M. Zhang, J. Xing, J. Gao, X. Shi, Q. Wang, and W. Hu, "Joint scale-spatial correlation tracking with adaptive rotation estimation," in *in Proceedings of the IEEE international conference on computer vision workshops*, pp. 32–40, 2015.

[18] Y. Song, C. Ma, L. Gong, J. Zhang, R. W. Lau, and M. H. Yang, "Crest: convolutional residual learning for visual tracking," in *Proceedings of the IEEE international conference on computer vision*, pp. 2555–2564, 2017.

[19] D. S. Bolme, J. R. Beveridge, B. A. Draper, and Y. M. Lui, "Visual object tracking using adaptive correlation filters," in *IEEE Conference on Computer Vision and Pattern Recognition*, pp. 2544–2550, 2010.

[20] J. F. Henriques, R. Caseiro, P. Martins, and J. Batista, "Exploiting the circulant structure of tracking-by-detection with kernels," in *European conference on computer vision*, pp. 702–715, Springer, Berlin, Heidelberg, 2012.

[21] J. F. Henriques, R. Caseiro, P. Martins, and J. Batista, "High-speed tracking with kernelized correlation filters," *IEEE Transactions on Pattern Analysis and Machine Intelligence*, vol. 37, no. 3, pp. 583–596, 2015.

[22] P. Zhang, Q. Guo, and W. Feng, "Fast and object-adaptive spatial regularization for correlation filters based tracking," *Neurocomputing*, vol. 337, no. 14, pp. 129–143, 2019.

[23] N. Y. Wang and D. Y. Yeung, "Learning a deep compact image representation for visual tracking," in *Proceedings of the Advances in Neural Information Processing Systems*, pp. 809–817, 2013.

[24] A. Krizhevsky, I. Sutskever, and G. E. Hinton, "Imagenet classification with deep convolutional neural networks," *Advances in Neural Information Processing Systems*, vol. 25, pp. 1097–1105, 2012.

[25] K. Simonyan and A. Zisserman, "Very deep convolutional networks for large-scale image recognition," 2014, http://arxiv.org/abs/1409.1556.

[26] K. He, X. Zhang, S. Ren, and J. Sun, "Deep residual learning for image recognition," in *Proceedings of the IEEE conference on computer vision and pattern recognition.*, pp. 770–778, 2016.

[27] O. Russakovsky, J. Deng, H. Su et al., "Image net large scale visual recognition challenge," *International Journal of Computer Vision*, vol. 115, no. 3, pp. 211–252, 2015.

[28] A. G. Howard, M. Zhu, B. Chen et al., "MobileNets: efficient convolutional neural networks for mobile vision applications," 2017, http://arxiv.org/abs/1704.04861.

[29] M. Sandler, A. Howard, M. Zhu, A. Zhmoginov, and L. C. Chen, "MobileNetV2: inverted residuals and linear bottlenecks," in *Proceedings of the IEEE Conference on Computer Vision and Pattern Recognition*, pp. 4510–4520, 2018.

[30] A. Howard, M. Sandler, G. Chu et al., "Searching for MobileNetV3," *Proceedings of the IEEE/CVF International Conference on Computer Vision*, pp. , 20191314–1324, 2019.

[31] I. Freeman, L. Roese-Koerner, and A. Kummert, "Effnet: an efficient structure for convolutional neural networks," in *2018 25th ieee international conference on image processing (icip)*, pp. 6–10, 2018.

[32] M. Tan and Q. Le, "Efficientnet: rethinking model scaling for convolutional neural networks," in *International Conference on Machine Learning*, pp. 6105–6114, 2019.

[33] X. Zhang, X. Zhou, M. Lin, and J. Sun, "Shufflenet: an extremely efficient convolutional neural network for mobile devices," in *Proceedings of the IEEE Conference on Computer Vision and Pattern Recognition*, pp. 6848–6856, 2018.

[34] N. Ma, X. Zhang, H. T. Zheng, and J. Sun, "ShuffleNet V2: practical guidelines for efficient cnn architecture design," in *Proceedings of the European conference on computer vision*, pp. 116–131, 2018.

[35] S. Ren, K. He, R. Girshick, and J. Sun, "Faster R-CNN: towards real-time object detection with region proposal networks," *IEEE Transactions on Pattern Analysis & Machine Intelligence*, vol. 39, no. 6, pp. 1137–1149, 2017.

[36] Y. Xu, Z. Wang, Z. Li, Y. Yuan, and G. Yu, "Siam FC++: towards robust and accurate visual tracking with target estimation guidelines," in *Proceedings of the AAAI Conference on Artificial Intelligence*, vol. 34no. 7, pp. 12549–12556, 2020.

[37] Q. Liu, X. Li, Z. He, N. N. Fan, D. Yuan, and H. P. Wang, "Learning deep multi-level similarity for thermal infrared object tracking," *IEEE Transactions on Multimedia*, pp. 2114–2126, 2020.

[38] D. Yuan, X. Chang, P. Y. Huang, Q. Liu, and Z. He, "Self-supervised deep correlation tracking," *IEEE Transactions on Image Processing*, vol. 30, pp. 976–985, 2020.

[39] D. Yuan, X. Shu, and Z. He, "TRBACF: learning temporal regularized correlation filters for high performance online visual object tracking," *Journal of Visual Communication and Image Representation*, vol. 72, p. 102882, 2020.

[40] N. Wojke, A. Bewley, and D. Paulus, "Simple online and real-time tracking with a deep association metric," in *2017 IEEE international conference on image processing (ICIP). IEEE*, pp. 3645–3649, 2017.

[41] L. Huang, X. Zhao, and K. Huang, "GOT-10k: a large high-diversity benchmark for generic object tracking in the wild," *IEEE Transactions on Pattern Analysis and Machine Intelligence*, vol. 43, no. 5, pp. 1562–1577, 2021.

[42] A. Paszke, S. Gross, S. Chintala, and G. Chanan, "Pytorch: Tensors and dynamic neural networks in python with strong gpu acceleration," *PyTorch: Tensors and Dynamic Neural Networks in Python with Strong GPU Acceleration*, vol. 6, no. 3, 2017.

[43] Y. Wu, J. Lim, and M. H. Yang, "Object tracking benchmark," in *IEEE Transactions on Pattern Analysis & Machine Intelligence*, pp. 1834–1848, 2015.

[44] M. Kristan, A. Leonardis, J. Matas, M. Felsberg, and R. Pflugfelder, "The visual object tracking VOT2016 challenge results," in *European conference on computer vision*Springer.

[45] M. Kristan, A. Leonardis, J. Matas et al., "The visual object tracking VOT2017 challenge results," in *2017 IEEE International Conference on Computer Vision Workshop (ICCVW)*IEEE.

[46] M. Danelljan, G. Hager, F. Shahbaz Khan, and M. Felsberg, "Learning spatially regularized correlation filters for visual tracking," in *Proceedings of the IEEE international conference on computer vision*, pp. 4310–4318, 2015.

[47] L. Bertinetto, J. Valmadre, S. Golodetz, O. Miksik, and P. H. Torr, "Staple: complementary learners for real-time tracking," in *Proceedings of the IEEE conference on computer vision and pattern recognition.*, pp. 1401–1409, 2016.

[48] M. Danelljan, G. Häger, F. S. Khan, and M. Felsberg, "Discriminative scale space tracking," *IEEE Transactions on Pattern Analysis and Machine Intelligence*, vol. 39, no. 8, pp. 1561–1575, 2017.

[49] M. Danelljan, A. Robinson, F. S. Khan, and M. Felsberg, "Beyond correlation filters: learning continuous convolution operators for visual tracking," in *European Conference on Computer Vision*, pp. 472–488, Springer, 2016.

[50] H. Nam, M. Baek, and B. Han, "Modeling and propagating CNNs in a tree structure for visual tracking," 2016, http://arxiv.org/abs/1608.07242.

[51] G. Zhu, F. Porikli, and H. Li, "Beyond local search: tracking objects everywhere with instance-specific proposals," in *Proceedings of the IEEE conference on computer vision and pattern recognition*, pp. 943–951, 2016.

[52] Z. Chi, H. Li, H. Lu, and M. H. Yang, "Dual deep network for visual tracking," *IEEE Transactions on Image Processing*, vol. 26, no. 4, pp. 2005–2015, 2017.

[53] M. Danelljan, G. Hager, F. Shahbaz Khan, and M. Felsberg, "Convolutional features for correlation filter based visual tracking," in *Proceedings of the IEEE international conference on computer vision workshops*, pp. 58–66, 2015.

[54] H. Nam and B. Han, "Learning multi-domain convolutional neural networks for visual tracking," in *Proceedings of the IEEE conference on computer vision and pattern recognition*, pp. 4293–4302, 2016.

[55] M. Danelljan, G. Bhat, F. Shahbaz Khan, and M. Felsberg, "Eco: efficient convolution operators for tracking," in *Proceedings of the IEEE conference on computer vision and pattern recognition*, pp. 6638–6646, 2017.

[56] Z. Zhu, G. Huang, W. Zou, D. Du, and C. Huang, "UCT: learning unified convolutional networks for real-time visual tracking," in *Proceedings of the IEEE international conference on computer vision workshops*, pp. 1973–1982, 2017.

Research Article

An Improved Security Authentication Protocol for Lightweight RFID Based on ECC

Guo-heng Wei, Yan-lin Qin (ID)**, and Wei Fu**

Information Security Department, Naval University of Engineering, Wuhan, 430033 Hubei, China

Correspondence should be addressed to Yan-lin Qin; qinyanlincool@163.com

The security, privacy, and operation efficiency of radio frequency identification (RFID) must be fully measured in practical use. A few RFID authentication schemes based on elliptic curve cryptography (ECC) have been proposed, but most of them cannot resist the existing attacks. The scheme presented by Qian et al. could not resist impersonation attack according to our security analysis. Then, we propose a novel lightweight RFID authentication scheme, which is proved that it can resist server spoofing attack, tag masquerade attack, and provide other security properties of a RFID authentication scheme. Comparisons of computation and communication cost demonstrate that the proposed scheme is more suitable for the resource-constrained RFID authentication.

1. Introduction

Radio frequency identification (RFID) is a noncontact automatic identification technology, and the basic principle is to use the transmission characteristics of the RF signal space coupling (inductive or electromagnetic coupling) or reflection to achieve automatic identification of the object. An RFID system usually consists of tags, readers, and a back-end server [1]. In recent years, radio frequency identification technology has developed rapidly and been widely used in various fields. However, due to the openness of the channel between the tag and the reader, the security and privacy problems it faces have become increasingly prominent. In particular, the processing capacity, storage space, and energy supply of tag chips are very limited, and many mature security schemes cannot be applied to RFID. Hence, higher security level, lightweight, and efficient RFID authentication scheme has become the new research goal.

At present, several lightweight RFID authentication schemes using cryptography have been successively proposed. These schemes can be roughly divided into the following categories: the schemes using simple bitwise logic operation, the schemes based on hash function, the schemes based on symmetric cryptosystem (AES and others), and the schemes based on public key cryptosystem. Among them,

lightweight authentication scheme using simple bitwise logic operations satisfies the properties of low calculation amount, low power consumption, and small chip area, but the security cannot be well guaranteed. At the same time, the authentication scheme using only the hash function and the symmetric cryptographic algorithms has also been proved to be unable to fully meet the security requirements of RFID authentication [2]. Therefore, scholars have carried out research on lightweight authentication schemes based on public key cryptography. In this paper, we propose an improved RFID authentication scheme based on the security analysis of the scheme proposed by Qian et al. [3], analyze the security of the improved scheme, and compare its performance with the existing similar schemes. The security and efficiency comparison results show that the proposed scheme is more secure and has superior computing performance.

2. Related Work

In recent years, the public key cryptosystem has been introduced into the RFID authentication schemes. Chen et al. [4] proposed the RFID authentication scheme based on the quadratic residues for the first time, but Cao et al. [5]found that it could not resist tag impersonation and desynchronization

attacks [5]. Yeh et al. [6] further proved that the scheme in [4] could not provide location privacy and resistance to replay attacks and proposed an improved scheme.

Compared with public key cryptosystem based on quadratic residues [7] and other public key cryptosystems (such as RSA and ElGamal), elliptic curve public key cryptography (ECC) requires a much shorter key length while providing the same security strength, so it is especially suitable for environments with limited computing resources and storage space. Lee et al. [8] proposed an ECC-based RFID authentication scheme—EC-RAC—which proved to be unable to resist impersonation attacks and location tracking attacks [9]. Aiming at the security problems in the EC-RAC scheme [10], Zhang et al. [11] proposed a randomized key RFID authentication scheme based on the elliptic curve discrete logarithm problem and proposed an improved scheme for the classic Schnorr authentication scheme at the same time. Babaheidarian et al. [12] pointed out that both of the two improved schemes proposed in [11] have security problems: the improved scheme for EC-RAC has the risk of tag impersonation attack and cannot provide mutual authentication between the server and the tag; the improved scheme for the classic Schnorr authentication scheme is difficult to resist location tracking attack and desynchronization attack. Liao and Hsiao [13] proposed an ECC-based RFID authentication scheme, which does not need to update the data in the server and tag memory and has high computational efficiency. However, Peeters and Hermans [14] proved that there is a server counterfeiting attack, and the attacker can obtain the identity authentication factor of the tag by insertion attack, so it is also difficult to resist the tag impersonation attack. He et al. [15] improved the authentication scheme in [13], but Wei et al. [16] found that the improved scheme [15]could not resist the server impersonation attack. This paper focuses on the analysis to another ECC-based authentication scheme proposed by Qian et al. [3] recently. Through analysis, we found that the scheme still has loopholes for attacks such as server impersonation and tag impersonation.

3. Security Analysis of the RFID Authentication Scheme Proposed by Qian et al.

3.1. The Authentication Scheme Proposed by Qian et al. Qian et al. proposed an ECC-based RFID authentication scheme in [3]. The detailed steps of this scheme are shown in Figure 1.

3.2. Attacks against the Scheme

(i) Server impersonation attack

Assuming that the attacker can obtain the tag's internal ID information, he can impersonate database and reader to interact with the tag and can pass the tag's authentication.

The specific attack steps are as follows:

(a) Attacker→tag: The attacker generates a random number R' and sends $M_1' = \{R', \text{Query}\}$ to the tag

(b) Tag→fake reader: Upon receiving query and R', the tag computes $M_2' = \{M(ID) + tP_s + R', P_t + R'\}$ and sends it to the fake reader

(c) Fake reader→fake database: The fake reader sends $\{M_2', R'\}$ to the fake database

(d) Fake database→tag: The fake database generates a random number k', calculates $K' = k'G$ and $M_4' = \{H(ID) \oplus K_x', (K_x' + R') \oplus H(ID)\}$, and sends M_4' to the tag

(e) Tag: Upon receiving M_4', the tag checks that $(M_4'^{(1)} \oplus H(ID) + R_x') \oplus M_4'^{(2)} = H(ID)$ holds

Therefore, the tag believes that the attacker is a legitimate database, and the successful attack proves that the scheme is unable to resist server impersonation attacks.

(ii) Tag impersonation attack

Supposing that after the attacker intercepting message M_2 that the tag sent to the reader, he can calculate $M(ID) + tP_s = M_0 - R$ and then can impersonate the tag to interact with the reader and database and pass the reader's authentication.

The specific steps are as follows:

(1) Attacker→reader: When the attacker receives query and random number R', he calculates $M_2' = \{M_0 - R + R', P_t + R'\} = \{M_0', P_t + R'\}$ and sends M_2' to the reader

(2) Reader→server: The reader sends $M_3' = \{M_2', R'\}$ to the server

(3) Server: The server computes $M(ID) = M_0' - R' - nP_t = M_0 - R - nP_t = (M(ID) + tP_s) - nP_t$ and compares $M(ID)$ with $M(ID')$ stored locally and finds that it is consistent, so it verifies the fake tag.

Therefore, the database is made to consider the attacker to be a legitimate tag, and the attack is successful, which proves that the scheme is unable to resist the tag impersonation attack.

At the same time, since the authentication scheme of Qian et al. is difficult to resist server and tag impersonation attacks, it is easy to prove that it cannot resist location tracking attacks nor does it satisfy anonymity and forward security.

4. The Improved Scheme

To resist the above server and tag impersonation attacks, the authentication scheme proposed by Qian et al. has been modified. The detailed process is as follows:

4.1. System Parameter Setting

Public/private key pair (n, P_s) Public/private key pair (t, P_t)

DataBase   Reader   Tag

①

$$M_1 = R$$

③   ②

$$M_3 = (M_2, R)$$

$$M_2 = \{M(ID) + tP_s + R, P_t + R\}$$
$$= \{M_0, P_t + R\}$$

④   ⑤

M_4 Forward M_4

Calculate $M(ID) = M_0 - R - nP_t$, compare it with stored $M(ID')$, if it is consistent, the tag is authenticated. Generate a random number r, calculate $K = rG$ and $M_4 = \{H(ID') \oplus K_x, (K_x + R_x) \oplus H(ID')\} = \{M_4^{(1)}, M_4^{(2)}\}$.

Calculate $H(ID') = (M_4^{(1)} \oplus H(ID) + R_x) \oplus M_4^{(2)}$, if $H(ID') = H(ID)$ holds, the tag authenticates the reader as legal.
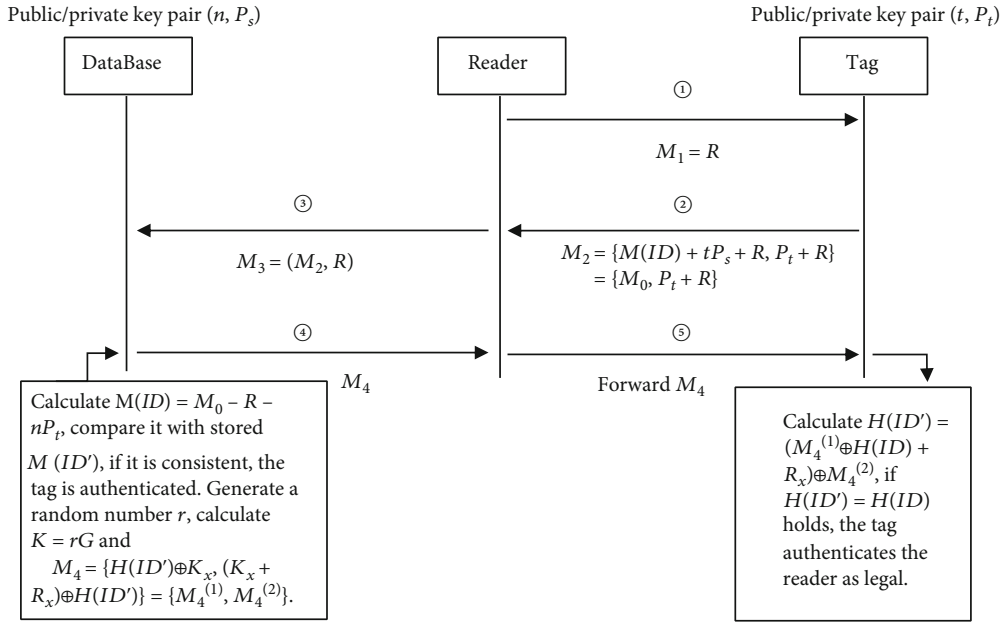
FIGURE 1: ECC-based RFID authentication scheme proposed by Qian et al.

TABLE 1: Comparison of computational overhead of the scheme in this paper and the existing schemes.

	Qian et al.'s scheme [3]	Lee et al.'s scheme [8]	Zhang et al.'s scheme I [11]	Zhang et al.'s scheme II [11]	He et al.'s scheme [15]	Wei et al.'s scheme [16]	Our scheme
Server	3SM+2TA	4SM+2TA	5SM+3TA	3SM+2TA	3SM+4TA	4SM+1TA	4SM +1TA
Tag	1SM+3TA	2SM	2SM	1SM	3SM+4TA	5SM+1TA	4SM +1TA

TABLE 2: Comparison of communication overhead of the scheme in this paper and the existing schemes.

	Qian et al.'s scheme [3]	Lee et al.'s scheme [8]	Zhang et al.'s scheme I [11]	Zhang et al.'s scheme II [11]	He et al.'s scheme [15]	Wei et al.'s scheme [16]	Our scheme
Server	640 bits	160 bits	160 bits	160 bits	640 bits	640 bits	640 bits
Tag	640 bits	800 bits	960 bits	640 bits	640 bits	960 bits	640 bits

(1) Generate a large prime number q, and $F(q)$ is a finite field, where q represents the number of elements in the finite field.

(2) Choose a safe elliptic curve $y^2 = x^3 + ax + b$, where $a, b \in F(q)$. Select the points on the elliptic curve to form an additive cyclic group $(P, +)$ with order t, and G is a generator of P. The reader, database, and each tag store the elliptic curve parameters $\{q, a, b, G, t\}$ locally.

(3) The server selects $n \in Z_t^*$ as its private key and computes $P_s = nG$ as its public key and selects a random value ID as the identity information of each tag and encodes it as a point on the elliptic curve, denoted as $M(ID)$. The server saves $M(ID)$ and stores its public key P_s together with $M(ID)$ in the memory of the tag.

(4) Select a secure hash function: $H : (P, +) \longrightarrow \{0, 1\}^*$

4.2. The Authentication Process

(1) Reader→tag: The reader generates a random number r_1, computes $R_1 = r_1 G$, and sends $M_1 = \{R_1, Query\}$ to the tag

(2) Tag→reader: Upon receiving M_1, the tag generates a random number r_2, computes $R_2 = r_2 G$ and $M_2 = H(M(ID) + r_2 P_s) \oplus H(r_2 R_1)$, and sends $\{M_2, R_2\}$ to the reader

(3) Reader→database: Upon receiving $\{M_2, R_2\}$, the reader sends $M_3 = \{M_2, R_2, r_1\}$ to the database

(4) Database→reader: Upon receiving M_3, the database uses stored tag identity information ID' to verify whether $H(M(ID') + nR_2) \oplus M_2 = H(r_1 R_2)$ holds. If so, it will compute $M_4 = nR_2$ and send M_4 to the reader

TABLE 3: Comparison of security performance of the scheme in this paper and the existing schemes.

	Qian et al.'s scheme [3]	Lee et al.'s scheme [8]	Zhang et al.'s scheme I [11]	Zhang et al.'s scheme II [11]	He et al.'s scheme [15]	Wei et al.'s scheme [16]	Our scheme
Mutual authentication	×	×	×	×	×	√	√
Confidentiality of authentication factor	√	√	√	×	√	√	√
Anonymity	×	×	√	×	√	√	√
Practicability	√	√	×	×	√	√	√
Perfect forward security	×	√	√	√	√	√	√
Scalability	√	√	×	×	√	√	√
Resistance to replay attack	√	√	√	√	√	√	√
Resistance to tag impersonation attack	×	×	×	√	√	√	√
Resistance to server impersonation attack	×	×	×	×	×	√	√
Resistance to DoS attack	√	√	×	×	√	√	√
Resistance to location tracking attack	×	×	√	×	√	√	√

√ means providing; × means not providing.

(5) Reader→tag: The reader forwards M_4 to the tag

(6) Tag: Upon receiving M_4, the tag checks whether $M_4 = r_2 P_s$ holds, and if so, the reader and database are authenticated.

5. Security Analysis of the Improved Scheme

(i) Resistance to server impersonation

Assume that the attacker can obtain the tag's internal information $M(ID)$ and uses reader and database impersonation attacks.

(a) Attacker→tag: The attack impersonates the reader to generate a random number r_1', calculates $R_1' = r_1' G$, and sends R_1' to the tag

(b) Tag→fake reader (attacker): Upon receiving R_1', the tag generates a random number r_2', computes $M_2' = H(M(ID) + r_2' P_s) \bigoplus H(r_2' R_1')$, and sends $\{M_2', R_2'\}$ to the fake reader (the attacker)

(c) Fake reader→fake database (attacker): The fake reader sends $M_3' = \{M_2', R_2', r_1'\}$ to the fake database (the attacker)

(d) Fake database: The fake database must forge $M_4' = nR_2'$ to pass the authentication of the tag. Because of the unidirectionality of the hash function, the attacker cannot recover out $M_4' = nR_2' = r_2' P_s$ even though he obtains the $M(ID)$ and uses M_2', R_2', r_1' to calculate $H(M(ID) + r_2' P_s) = M_2' \bigoplus H(r_2' R_1')$. Meanwhile, the attacker cannot obtain the database's private key n or the random number r_2' generated by the tag, so it is unable for him to forge M_4'

(ii) Resistance to tag impersonation

(a) The attacker impersonates the tag to attack: Upon receiving the message $M_1' = \{R_1', \text{Query}\}$ of the reader, the fake tag selects a random number r_2' and calculates $R_2' = r_2' G$. However, it is unable to recover the tag's legal $M(ID)$, so the attack fails because he cannot generate legal authentication information $M_2' = H(M(ID) + r_2' P_s) \bigoplus H(r_2' R_1')$

(b) Assuming that the attacker takes an active attack: The attacker selects a random number r_1', calculates $R_1' = r_1' G$, and sends R_1' to the tag. Upon receiving R_1', the tag generates a random number r_2', computes $R_2' = r_2' G$ and $M_2' = H(M(ID) + r_2' P_s) \bigoplus H(r_2' R_1')$, and sends $\{M_2', R_2'\}$ to the reader. After the attacker intercepts $\{M_2', R_2'\}$, he can calculate $H(r_1' R_2') \bigoplus M_2' = H(M(ID) + r_2' P_s)$, but cannot obtain tag's $M(ID)$ because of the unidirectionality of the hash function

(iii) Resistance to replay attack

In replay attack, the attacker can intercept the reader's past authentication information $M_4 = nR_2 = r_2 P_s$ sent to the tag and resend it to the tag. Upon receiving the replay information, the tag can compute $M_4' = r_2' P_s$ using its current one-time random number r_2'. $M_4 \neq M_4'$, and it can be determined that M_4 is a replay information. The attacker can also intercept the tag's past authentication information $\{M_2, R_2\}$ sent to reader and send it to the reader. Upon receiving $\{M_2, R_2\}$, the reader combines it with the random number r_1' (it currently generates to get $M_3' = \{M_2, R_2, r_1'\}$) and forward M_3' to the database. Upon receiving M_3', the database checks that $H(M(ID') + nR_2) \bigoplus M_2 \neq H(r_1' R_2)$ to identify replay attack.

(iv) Forward security

Forward security ensures that attacker cannot associate the past interaction information with tag's identity. Assume that the attacker can obtain tag's identity information $M(ID)$ and intercept the past interaction information $M_1 = \{R_1, \text{Query}\}$, $\{M_2, R_2\}$, and M_4, among them $R_1 = r_1 G$, $R_2 = r_2 G$, and $M_2 = H(M(ID) + r_2 P_s) \bigoplus H(r_2 R_1)$. Without obtaining one-time random numbers r_1 and r_2 and database's private key n, the attacker cannot confirm the intercept information M_1, $\{M_2, R_2\}$, and M_4 is related to the tag's identity $M(ID)$ that he knows.

(v) Mutual authentication

The attacker can eavesdrop on the information passed between the reader and tag to get the message $M_2 = H(M(ID) + r_2 P_s) \bigoplus H(r_2 R_1)$. Due to the unidirectionality of hash function, he cannot get $M(ID)$, so he cannot generate the legitimate information that can pass authentication. At the same time, the database can use stored ID' to check whether $H(M(ID') + nR_2) \bigoplus M_2 = H(r_1 R_2)$ holds to authenticate the tag. In addition, in the authentication process of the tag to reader, the tag authenticates reader by verifying whether $M_4 = r_2 P_s$ is true. If the attacker does not have private key n of the legitimate database or the one-time random number r_2, it is difficult to calculate M_4 and unable to pass the authentication of the tag.

(vi) Confidentiality of the identity information $M(ID)$

In the improved scheme in this paper, the $M(ID)$ information of the tag is only contained in M_2. Due to the unidirectionality of hash function, the attacker cannot intercept the previous interaction information between the reader and tag to obtain the tag's legitimate $M(ID)$. Similar to the antitag impersonation attack analysis mentioned above, the attacker is also difficult to obtain the tag's $M(ID)$ through active attack.

(vii) Resistance to location tracking attack

We assume that the attacker has mastered the tag's $M(ID)$ and intercepted the interaction information M_1, M_2, R_2. Since the attacker cannot obtain the database's private key n, the reader's random number r_1, and the tag's random number r_2, so it is impossible to use $H(M(ID) + nR_2) \bigoplus M_2 = H(r_1 R_2)$ to associate the intercepted interaction information with a specific tag. Therefore, the improved scheme can resist location tracking attack.

(viii) Anonymity

Anonymity of the scheme requires that the attacker cannot associate the interaction information with tag's identity. According to the previous analysis, it is difficult for an attacker to recover the tag's $M(ID)$ from the interaction information between the reader and tag, and each interaction uses different random numbers r_1 and r_2, so the attacker cannot associate the interaction information with tag's specific identity, which ensures the anonymity.

(ix) Resistance to denial-of-service (DOS) attack

From the above analysis of the confidentiality of the tag's $M(ID)$, it can be seen that the tag's $M(ID)$ can be well protected, and it is difficult for an attacker to obtain the tag's $M(ID)$ from the interaction information between the reader and the tag. Therefore, the authentication scheme in this paper does not need to update tag's $M(ID)$, which can effectively resist DOS attack.

6. Efficiency and Security Performance Comparisons

We compared the computing efficiency, communication overhead, and security of the improved authentication scheme with similar schemes. For the convenience of comparison, the scalar dot product operation on the elliptic curve is denoted as SM and the point addition operation as TA. At the same time, assume that all schemes use the elliptic curve with a key length of 160 bits, and the data length of a point on the elliptic curve is 320 bits. Table 1 shows the comparison of computational overhead between the schemes in References [3, 8, 11, 15, 16] and the schemes in this paper, among which scheme I in [11] refers to the improvement of EC-RAC scheme, and scheme II in [11] refers to the improved scheme of Schnorr authentication scheme.

The communication overhead refers to the length of the authentication information transmitted by the server and the tag during the execution of the authentication scheme. Table 2 gives the comparison of communication overhead between the schemes in [3, 8, 11, 15, 16] and the improved schemes. Only the length of communication data between the server (or reader) and the tag is considered here, and data interactions between the server and reader are ignored.

It can be seen from Table 2 that the length of data transmitted by the tag and server in the scheme in this paper is basically equal to that in the schemes in [3, 15]. Table 3 shows the comparison of security performance between the proposed scheme and the existing schemes.

Through the above analysis, the scheme proposed in this paper is basically the same as the original scheme in terms of computational and communication overhead, which can satisfy the practical application of low-cost tags, but compared with other typical schemes with similar structure, this scheme has a superior security advantage, which can fully meet various security requirements such as mutual authentication and privacy protection in the RFID authentication process.

7. Conclusion

This paper analyzes the security performance of the improved scheme proposed by Qian et al. and proves that it is difficult to resist server and tag impersonation and thus cannot realize the mutual authentication between the server and the tag. On this basis, we improved the scheme proposed by Qian et al. Security analysis and efficiency comparison show that compared with similar schemes, the

proposed scheme has higher security while ensuring high computing performance and can fully meet the security requirements of mutual authentication and privacy protection in the RFID authentication process.

Data Availability

The experimental data used to support the findings of this study are included within the article.

Conflicts of Interest

The authors declare that they have no conflicts of interest.

References

[1] C. Roberts, "Radio frequency identification (RFID)," *Journal of Computer Security*, vol. 25, no. 1, pp. 18–26, 2006.

[2] M. Burmester, B. Medeiros, and R. Motta, *Anonymous RFID Authentication with Constant Key-Lookup*, ACM, 2007, Cryptology ePrint Archive: Listing for 2007 (2007/402).

[3] Q. Qian, Y.-L. Jia, and R. Zhang, "A lightweight RFID security scheme based on elliptic curve cryptography," *International Journal of Network Security*, vol. 18, no. 2, pp. 354–361, 2016.

[4] Y. Chen, J. S. Chou, and H. M. Sun, "A novel mutual authentication scheme based on quadratic residues for RFID systems," *Computer Networks*, vol. 52, no. 12, pp. 2373–2380, 2008.

[5] T. Cao, P. Shen, and E. Bertino, "Cryptanalysis of some RFID authentication protocols," *The Journal of Communication*, vol. 3, no. 7, pp. 20–27, 2008.

[6] T. C. Yeh, C. H. Wu, and Y. M. Tseng, "Improvement of the RFID authentication scheme based on quadratic residues," *Computer Communications*, vol. 34, no. 3, pp. 337–341, 2011.

[7] R. Doss, S. Sundaresan, and W. Zhou, "A practical quadratic residues based scheme for authentication and privacy in mobile RFID systems," *Ad Hoc Networks*, vol. 11, no. 1, pp. 383–396, 2013.

[8] Y. K. Lee, L. Batina, and I. Verbauwhede, "EC-RAC (ECDLP based randomized access control): provably secure RFID authentication protocol," in *2008 IEEE International Conference on RFID*, pp. 97–104, Las Vegas, NV, USA, 2008.

[9] T. Van Deursen and S. Radomirovic, *Attacks on RFID Schemes [EB/OL]*, ACM, 2008, Cryptology ePrint Archive, Report 2008/310, 2008. http://eprint.iacr.org/.

[10] J. Bringer, H. Chabanne, and T. Icart, "Cryptanalysis of EC-RAC, a RFID identification scheme," in *CANS, volume 5339 of Lecture Notes in Computer Science*, pp. 149–161, Springer, 2008.

[11] X. Zhang, L. Li, Y. Wu, and Q. Zhang, "An ECDLP-based randomized key RFID authentication protocol," in *2011 International Conference on Network Computing and Information Security*, pp. 146–149, Guilin, China, 2011.

[12] P. Babaheidarian, M. Delavar, and J. Mohajeri, "On the security of an ECC based RFID authentication scheme," in *2012 9th International ISC Conference on Information Security and Cryptology*, Tabriz, 2012.

[13] Y. Liao and C. Hsiao, "A secure ECC-based RFID authentication scheme integrated with ID-verifier transfer protocol," *Ad Hoc Networks*, vol. 18, pp. 133–146, 2014.

[14] R. Peeters and J. Hermans, *Attack on Liao and Hsiao's Secure ECC Based RFID Authentication Scheme Integrated with ID-Verifier Transfer Scheme [EB/OL]*, ACM, 2013, Cryptology ePrint Archive, Report 2013/399, http://eprint.iacr.org/.

[15] D. He, N. Kumar, N. Chilamkurti, and J.-H. Lee, "Lightweight ECC based RFID authentication integrated with an ID verifier transfer protocol," *Journal of Medical Systems*, vol. 38, no. 10, pp. 116–118, 2014.

[16] W. Guoheng, Q. Yanlin, and Z. Huanguo, "Security authentication scheme for lightweight radio frequency identification based on ECC," *Journal Huazhong University of Science and Technology (Natural Science Edition)*, vol. 46, no. 1, 2018.

Research Article

A Crowdsourcing Information Obtaining Scheme Aiming at Senior Netizens Based on Blockchain

Yanlin Qin, Xueguang Zhou, and Guoheng Wei (ORCID)

Department of Information Security, Naval University of Engineering, Wuhan 430033, China

Correspondence should be addressed to Guoheng Wei; wgh7929@aliyun.com

Senior netizens play a unique role in crowdsourcing information obtaining, but the traditional crowdsourcing information obtaining scheme based on intermediary platform cannot satisfy the senior netizens' strong reliability on anonymity. Malicious intermediary platform may leak out the privacy information of both parties. Data stored in intermediary platform may be intercepted, tampered, and fraudulently used by attackers, so smooth crowdsourcing information transactions cannot be ensured. In order to achieve secure and reliable crowdsourcing information obtaining, blockchain technology with decentralization and nontampering was used to propose a crowdsourcing information obtaining scheme, which is independent on intermediary platform. During processes of requirements releasing, information submitting, and rewarding, privacy protection techniques were used to preserve the anonymity of participants and confidentiality of data. Compared with the existing protocols, the proposed scheme has obvious advantages in privacy protection.

1. Introduction

The concept of crowdsourcing was proposed by Howe [1] and refers to outsourcing tasks to unspecified mass networks in a free and voluntary way. The basic model of traditional crowdsourcing includes the outsourcer, the contractors, and the crowdsourcing intermediary, which constitute the crowdsourcing operation organization. The outsourcer issues requirements and the intermediary provides tasks; the contractors submit the information, and the intermediary feedbacks contractors' submission. Crowdsourcing activities often involve many people in bidding for a task, and the evaluation process is mainly based on the satisfaction of the outsourcer of the task. According to the purpose of crowdsourcing, it can be divided into crowd wisdom [2], crowd creation, crowd voting, and crowdfunding. Crowdsourcing information obtaining activities are crowd wisdom activities, in which the outsourcer attracts netizens to participate voluntarily, and the contracting netizens collect and provide the information to the outsourcer through Web pages, newspapers, and magazines and field investigations, and the outsourcer screens the effective crowdsourcing information manually and systematically and gives appropriate rewards

to the participants. In the crowdsourcing information obtaining scheme in this paper, the contractors mainly consist of senior netizens, because the space-time extension and anonymity of the network attract senior netizens to stay on the Internet for a long time, which is an important force to participate in network activities. However, in the traditional crowdsourcing information obtaining scheme that relies on the intermediary platform, it is difficult to ensure senior netizens' strong requirement of anonymity, and the intermediary platform, driven by its interests, may disclose the private data of the outsourcer and the contractors in the process of crowdsourcing information transactions. At the same time, attackers will take various measures to intercept, tamper, and fraudulently use key data stored in the intermediary platform. Once the intermediary platform is attacked, it will directly threaten the fluent operation of the whole crowdsourcing transaction mechanism.

The main work of this paper is as follows:

(1) Establish a decentralized and nontampered crowdsourcing information obtaining framework based on blockchain. Before joining the crowdsourcing information obtaining blockchain, the key generation

center generates certificateless public and private key pairs, including initialization parameter generation and nodes' public/private key pair generation

(2) Design the release algorithm of the crowdsourcing information requirements. The certificateless multi-receiver anonymous signcryption scheme is used to complete the release of the requirements, and the blockchain address of the outsourcer, the information requirements, and reward is encrypted together. Except for the intended contractors, other nodes cannot know the information such as requirements and rewards. In the signcryption information issued by the outsourcer, the blockchain address of the contractor is hidden to prevent other nodes in the network from tracking its identity through the blockchain address of the contractor. At the same time, each contractor only uses its private key and blockchain address in the process of unsigncrypt and does not need addresses of other contractors, thus, ensuring mutual anonymity among contractors

(3) Design the submission algorithm of the crowdsourcing information using the idea of random address, the outsourcer generates a temporary public key address and records it in the blockchain. The contractor uses its long-term private key to calculate the temporary private key for the information submission. After receiving the crowdsourcing information returned by the contractor, the outsourcer decrypts and verifies it, thus, realizing the confidentiality of the crowdsourcing information and preventing the identity of the contractor from being exposed in the process of submitting the information many times

(4) Design the reward accounting algorithm of the crowdsourcing information. The outsourcer determines the reward accounting of crowdsourcing information by generating ring signcryption, so as to prevent the leakage of identity privacy in the process of awarding. The contractor uses the temporary private key to decrypt the ring signcryption of the outsourcer and confirm the legal reward from the outsourcer. When using legal rewards, the contractor only needs to use its temporary private key to complete the signature, and the payee can verify the signature by using the temporary public key of the contractor recorded in the blockchain. Because the temporary public key addresses of the contractor are different in each crowdsourcing information transaction, the consumer anonymity of the contractor is realized

(5) Analyze the privacy protection effect and operation efficiency of the scheme proposed in this paper. In terms of privacy protection, this scheme is compared with existing information sharing schemes based on blockchain, mainly from three dimensions: outsourcer privacy protection, contractor privacy protection,

and transaction data privacy protection. By comparison, it is verified that this scheme has obvious advantages over other schemes in privacy protection and has higher calculation efficiency

2. Relevant Work

Traditional crowdsourcing information obtaining is composed of the outsourcer, the crowdsourcing intermediary platform, and the contractors, and the crowdsourcing information obtaining task is completed through 9 steps. In the traditional process of obtaining crowdsourcing information, the outsourcer and the contractor need to release and submit the information through the intermediary crowdsourcing platform, which brings extra cost to both parties. On the other hand, there is no completely trusted intermediary in the real network, and the malicious crowdsourcing intermediary platform may sell the private information of both parties in crowdsourcing information transactions for its own benefits. At the same time, once the intermediary platform is attacked, the whole crowdsourcing transaction mechanism will be paralyzed and chaotic. Therefore, we can introduce decentralized blockchain technology into crowdsourcing information transaction to remove the dependence on crowdsourcing intermediary platform. The traditional crowdsourcing information obtaining process is shown in Figure 1.

Because blockchain technology has the characteristics of no center, anti-tamper, and anonymity, scholars have applied blockchain technology to the field of network information sharing. Rawat et al. [3] designed a multimember information sharing framework based on blockchain technology, in which nodes in blockchain can share network security protection schemes, and analyzed possible attack behaviors in the system based on game theory. Huang et al. [4] designed a network security threat intelligence sharing model based on blockchain to solve the privacy protection demand of users in the process of threat intelligence sharing. However, this model directly uses the anonymity of users' accounts in the blockchain to protect the identity privacy of both parties in the threat intelligence sharing, which can only provide weak anonymity. In the frequent information sharing process between the two parties, attackers can infer the true identity of users by analyzing the correlation between transactions, statistical characteristics, and transaction amounts. At the same time, the status of the threat intelligence center in the model is not equal to that of the organization, and the organization needs to register at the threat intelligence center when joining the threat intelligence sharing blockchain. Wang et al. [5] proposed a private data sharing model of medical blockchain based on ring signature. However, this model only considers the anonymity protection of transaction outsourcer and lacks the anonymity protection mechanism of contractor. At the same time, the ring signature message is not encrypted, which easily leads to the leakage of users' private data. He et al. [6] proposed an incentive mechanism for crowdsensing applications based on blockchain technology, which uses digital signature and watermarking technology
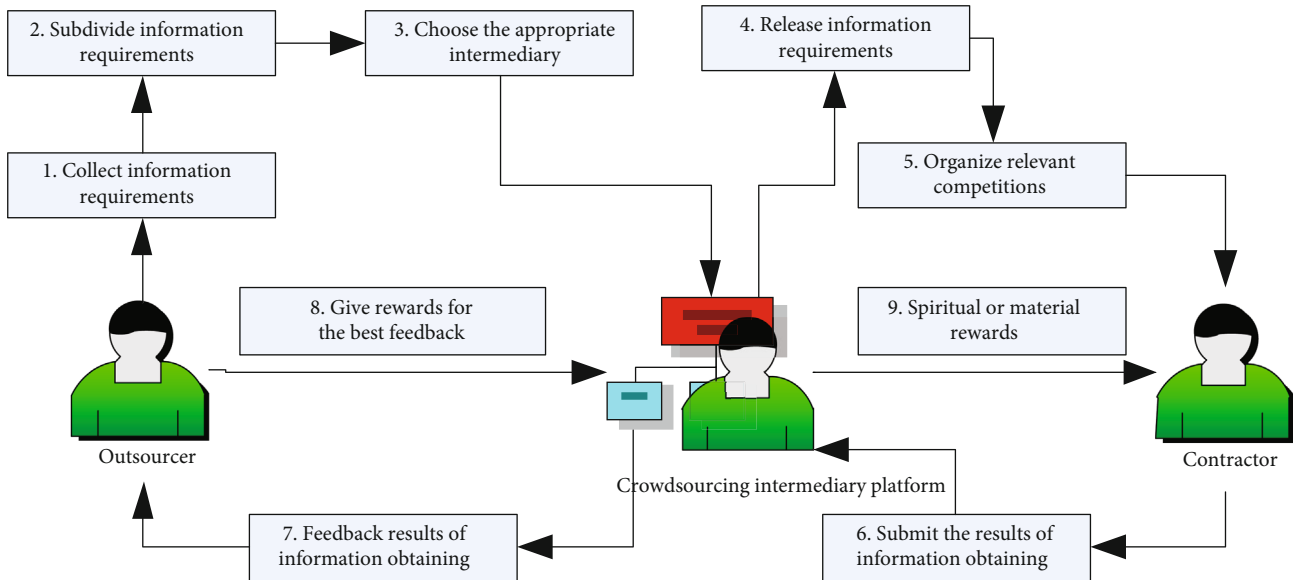
FIGURE 1: Flowchart of traditional crowdsourcing information obtaining.

to prevent the sensing data from being tampered and used under false pretences, but this scheme does not protect the confidentiality of the sensing data and the identity privacy of the sensing users. Cheng et al. [7] designed a framework of network threat intelligence sharing and rating system based on blockchain, but did not give technical details to protect the confidentiality of threat intelligence and the anonymity of nodes. Cai et al. [8] designed the application framework of Internet public welfare crowdfunding platform on blockchain, but also did not involve specific measures to protect the privacy of platform users and the security of crowdfunding data. Xu et al. [9] designed a privacy protection scheme for electronic health records based on blockchain and homomorphic encryption, which uses proxy reencryption technology to protect the security of patient's privacy data. However, the protection of patient's identity privacy only depends on the anonymity of the patient's Ethereum address, and there is still the risk of identity being tracked and leaked during the frequent use. Sandro et al. [10] designed a secure sharing framework of personal health data based on blockchain, which mainly relies on the anonymity of blockchain addresses to protect user's personal privacy. Li et al. [11] established a trusted big data sharing model without center by using blockchain and smart contract, but the privacy protection of data provider and data demander mainly depends on the anonymity of blockchain address. Mohammad et al. [12] proposed a data sharing framework based on licensed blockchain to ensure real-time authentication of shared data and tracking audit of data access in blockchain. The scheme uses the public key of data subject to encrypt access records, which protects the privacy of data subject, but does not protect the privacy of data accessor. Fan et al. [13] proposed a data sharing scheme for content-centric 5G networks based on blockchain. The scheme issues identity certificates to each user and uses encryption technology to ensure the confidentiality of data in the network, but it lacks protection measures for

the identity privacy of data sharing parties in blockchain. Qiao et al. [14] designed a data sharing scheme for 5G IoT based on blockchain to solve the privacy of transactions under the chain, but did not discuss the privacy protection strategy of both parties in the chain cash withdrawal transaction.

The research of blockchain's application in information sharing in other industries has made some progress, but these research results cannot be directly applied to crowdsourcing information obtaining. It is difficult to meet the special needs of both parties of crowdsourcing transactions for personal identity privacy and transaction privacy. To solve the above problems, this paper designs a crowdsourcing information obtaining scheme based on blockchain. The scheme uses a certificateless multireceiver anonymous signcryption scheme with anonymous to release crowdsourcing information requirements and rewards, which not only protects the confidentiality of information requirements but also ensures the anonymity of the outsourcer and the contractor. To generate a temporary public-private key pair for the contractor, the contractor uses the temporary private key to signcrypt the collected crowdsourcing information to ensure the secrecy of the returned information and the identity untraceablity of the contractor. The One-Time-Pad ring signcryption algorithm is used to ensure the anonymity of the outsourcer in the reward payment transaction and the secrecy of the reward amount, and at the same time, the untraceability of the contractor in the process of using the reward for consumption is realized.

3. Background Knowledge

3.1. Blockchain Technology Foundation. Blockchain is a distributed ledger that records transaction data permanently [15], which is formed by linking some ordered data structures (also called blocks). All nodes in the blockchain
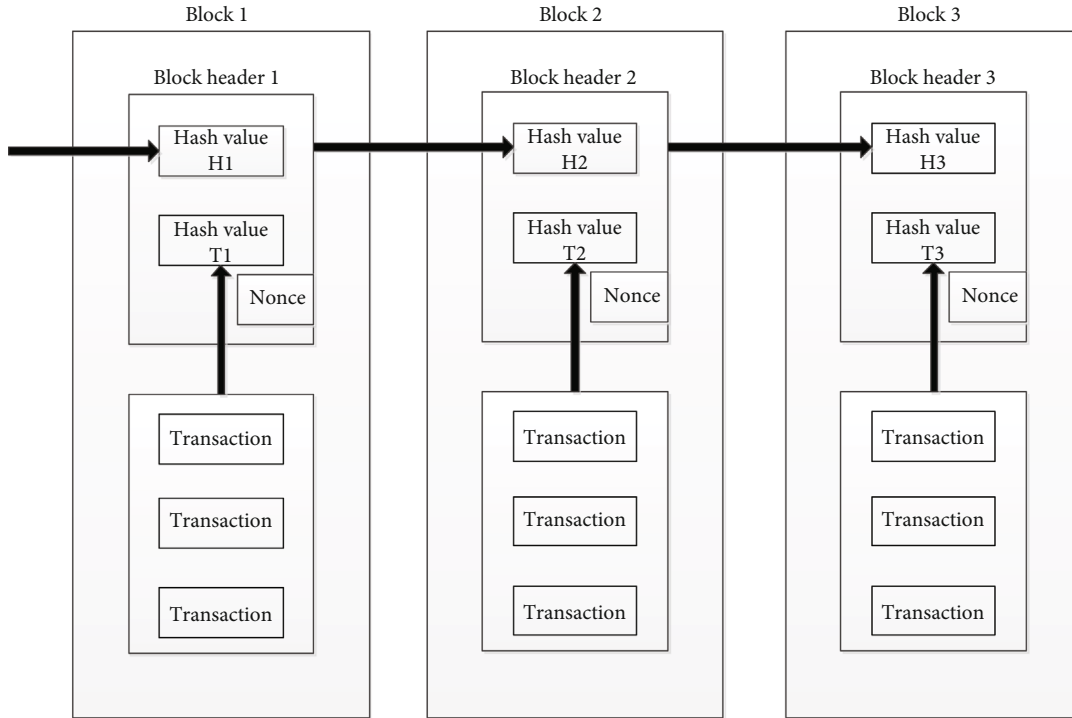
FIGURE 2: Data structure of blockchain.

network share a complete ledger, and once the transactions recorded in any ledger are released, it is difficult to modify them. Due to the difference of decentralization degree, there are two forms of blockchain [16]: the unlicensed chain and the licensed chain. The unlicensed chain is completely decentralized, and nodes are free to join and exit. It is suitable for a completely open and highly autonomous application environment. In the licensed chain, there are a few nodes that have higher authority than ordinary nodes. When joining, the nodes need to be authorized by the central node. The licensed chain is mainly suitable for small-scale internal data sharing.

The data structure of blockchain consists of transaction records and blocks [17]. First, both parties create a new transaction and broadcast it to the blockchain. Miner nodes package and merge the transactions generated and verified to be legal within a certain period into blocks, compete for the bookkeeping right through the Proof of Work (PoW) mechanism, and then add the new blocks to the blockchain.

The core unit of blockchain is block, which is composed of block header to ensure the orderly and complete block data and block body containing several transaction records. The block header stores the hash value of the block header of the previous block, Merkleroot, which is the overall hash value of all transaction data in this block, and a random number named nonce, timestamp, and other structured information; The block body is used to record the summary information of all verified transactions and a Merkle Tree [18] which ensures that transactions cannot be tampered. Figure 2 shows the data structure of blockchain.

3.2. Unlicensed Signcryption Scheme [19]. The scheme includes signer (ID_A), signcryption receiver (ID_B), and key generation center (KGC). The algorithm includes seven steps:

(1) *Setting of System Parameter.* Enter the security parameter η, KGC sets the system public parameters, generates the system master key s, and keeps it secretly

(2) *Setting of Partial Public and Private Keys.* Enter system parameters, master key s and user's identity ID_i, and KGC sets user's partial public and private key (D_i, u_i)

(3) *Setting of User's Secret Value.* Taking system parameters and user's identity ID_i as input, the user sets its secret value x_i and keeps it secretly

(4) *Setting of Complete Private Key.* Taking system parameters, user's identity ID_i, partial private key u_i, and secret value x_i as inputs, the user sets its complete private key (x_i, u_i)

(5) *Setting of Complete Public Key.* Taking system parameters, user's identity ID_i, partial public key D_i, and secret value x_i as inputs, the user sets its complete public key (X_i, D_i)

(6) *Signcryption.* Take system parameters, message m, signer's identity ID_A, private key (x_A, u_A), receiver's identity ID_B, and public key (X_B, D_B) as input, the signer outputs the signcryption σ of message m

(7) *Verification of Signcryption.* Take system parameters, σ, signer's identity ID_A, public key (X_A, D_A), receiver's identity ID_B and private key (X_B, D_B) as

input, receiver performs decryption and verification, then outputs that m is "True" or "Rejected"

3.3. CryptoNote Protocol [20]. To protect the identity anonymity of blockchain nodes, that is, to prevent attackers from gradually analyzing the identity information corresponding to their addresses through transaction records. The following is a brief description of the process of using one-time public and private keys to protect the anonymity of the contractor's identity in CryptoNote protocol: assume that the contractor's public and private key pair is (A, B)/(a, b), which satisfies $A = aG$, $B = bG$. Both parties conduct transactions through the following steps:

(1) The outsourcer randomly selects an integer r and calculates $R = rG$; use the public key (A, B) of the contractor to calculate the one-time transaction public key $P = H(rA)G + B$

(2) The outsourcer initiates the transaction and releases R, P, and the transaction amount on the blockchain

(3) The contractor calculates $P' = H(aR)G + bG$ by using its private key and compares it with the one-time public key included in the transaction initiated by the outsourcer. If it is consistent, it is determined that it is the legal contractor of the transaction

(4) The legal contractor calculates the one-time private key $x = H(aR) + b$ corresponding to the one-time public key and uses this private key to sign and consume the transaction revenues

4. A Crowdsourcing Information Obtaining Scheme Based on Blockchain

4.1. Overall Description of the Scheme. Because the contractors of the crowdsourcing information obtaining scheme in this paper are senior netizens in the network, and the senior netizens often have characteristics such as self-dependence, independence, alertness, and low self-exposure, the anonymity of the network plays a vital role in stimulating senior netizens to participate in crowdsourcing information obtaining. The unlicensed blockchain can be completely decentralized, allowing nodes to freely join and exit the network. This high autonomy is completely consistent with the strong dependence of senior netizens on network anonymity, which can give full play to their own advantages. Therefore, this paper designs a crowdsourcing information obtaining scheme in unlicensed blockchain. The network nodes include the outsourcer node, the contractor node, and the miner node. Among them, miner nodes compete to obtain the bookkeeping right through the PoW mechanism, verify the crowdsourcing transactions, and package the verified transactions into the new block. All miners are jointly responsible for the maintenance of the blockchain. For the sake of simplification, it is assumed that there is one outsourcer node F and multiple contractor nodes $J_1, J_2, \cdots, J_k$ in the network, and the scenarios of multiple outsourcers and multiple contractor nodes can be discussed similarly. Before joining the

crowdsourcing information obtaining blockchain, the outsourcer node and the contractor node need to generate their own public and private key pairs and blockchain transaction addresses.

The crowdsourcing information obtaining scheme based on blockchain mainly consists of the following three stages:

(1) *Release Stage of Crowdsourcing Information Requirements.* The outsourcer collects information requirements and sends the requirements and reward to the contractor (senior netizens). The release algorithm of the crowdsourcing information requirements in 4.3 will be used in this stage

(2) *Submission Stage of Crowdsourcing Information.* The contractor makes full use of its superior resources to collect the information meeting the task requirements and submit the required information to the outsourcer. The submission algorithm of crowdsourcing information in 4.4 will be used in this stage

(3) *Evaluation and Reward Stage of Crowdsourcing Information.* The outsourcer evaluates the quality, timeliness, and benefit of the crowdsourcing information submitted by the contractor, selects the best result to pay remuneration, and realizes the incentive for the contractor to participate in the crowdsourcing information collection. The reward accounting algorithm of the crowdsourcing information in 4.5 will be used to generate a reward transaction and broadcast the transaction to the crowdsourcing information obtaining blockchain. The basic architecture of crowdsourcing information obtaining scheme based on blockchain is shown in Figure 3

4.2. Initialization Settings. Before joining the crowdsourcing information obtaining blockchain, the outsourcer node and the contractor node first generate certificateless public and private key pairs.

Client wallet performs the following steps to set system parameters and generate certificateless public and private key pairs for nodes:

(1) Generation of initialization parameters

Select elliptic curve addition group G with large prime order q, P is a generator of G; define the following four secure Hash functions:

$$H0 : \{0, 1\}^* \times G \times G \longrightarrow Z_q^*, \quad (1)$$

$$H1 : G \times \{0, 1\}^* \times G \longrightarrow Z_q^*, \quad (2)$$

$$H2 : G \longrightarrow \{0, 1\}^*, H3 : \{0, 1\}^* \longrightarrow Z_q^*, \quad (3)$$

$$H4 : G \longrightarrow Z_q^*. \quad (4)$$

$s \in Z_q^*$ is the master key of the client wallet, $PK_m = sP$ is its corresponding public key, and the system parameters $(q, PK_m, H_0, H_1, H_2, H_3, H_4)$ are disclosed to the public.
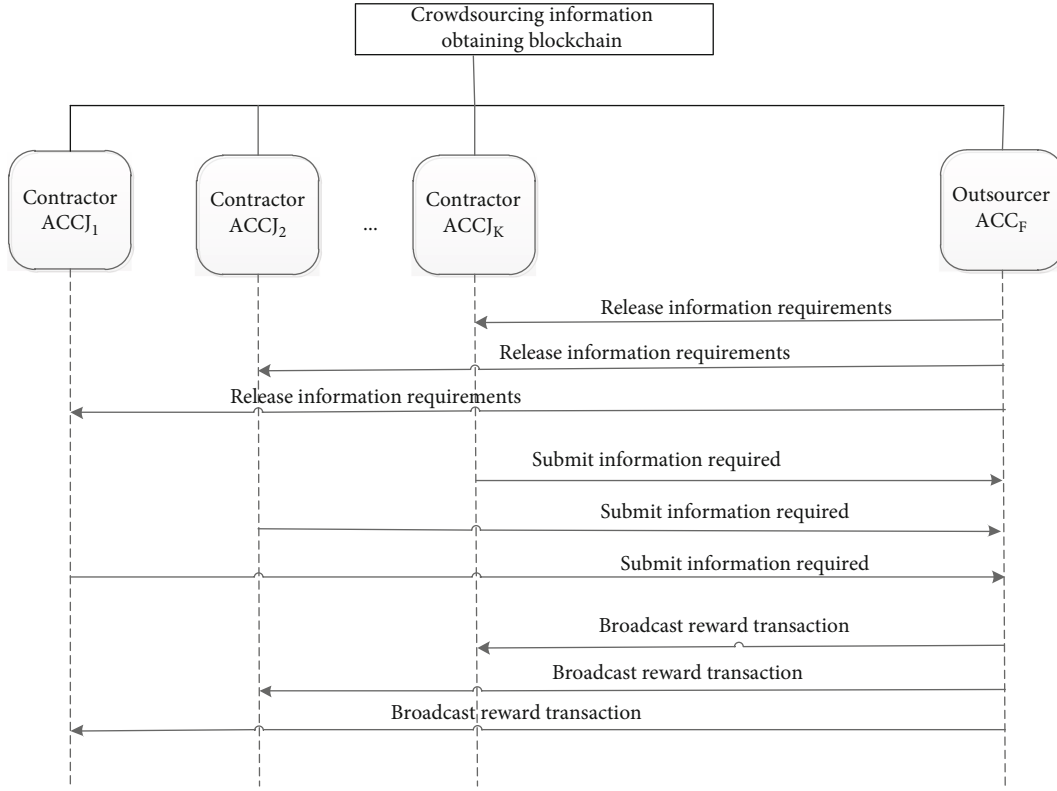
FIGURE 3: Basic architecture of crowdsourcing information obtaining scheme based on blockchain.

(2) Generation of node's public/private key pair

Node ID_i selects a random number $x_i \in Z_q^*$ as its secret value, calculates $X_i = x_iP$, and sends $X_i\|ID_i$ to the client wallet.

Client wallet selects random number $d_i \in Z_q^*$ and calculates

$$D_i = d_iP, u_i = d_i + sH_0(ID_i, D_i, X_i). \tag{5}$$

Then, returns to part of the user's partial public-private key pair D_i/u_i and the node ID_i obtains its complete public-private key pair $(X_i, D_i)/(x_i, u_i)$.

According to the key generation algorithm, the public and private key pair generated for the outsourcer node is $(X_F, D_F)/(x_F, u_F)$, and then the blockchain address is $ACC_F = H_0(ID_F, D_F, X_F)$ calculated from the public key; the certificateless public-private key pair of the contractor node is $(X_{J_i}, D_{J_i})/(x_{J_i}, u_{J_i})$, and the blockchain address is $ACC_{J_i} = H_0(ID_{J_i}, D_{J_i}, X_{J_i})$, $1 \le i \le k$.

4.3. Release Algorithm of the Crowdsourcing Information Requirements.
The first stage of the crowdsourcing information obtaining scheme based on blockchain is the release of information requirements and rewards: the outsourcer collects the information requirements of decision makers, subdivides the information requirements, and sends the information requirements and rewards to the senior netizens (contractors) positioned in the early stage. In order to ensure the identity anonymity of the outsourcer and the contractor in the process of releasing crowdsourced information requirements and to realize the privacy of crowdsourcing information and rewards, the certificateless multireceiver anonymous signcryption scheme proposed in reference [19] is used to sign the requirements and rewards. Set $M = (T\|requirements\|reward)$, where T is a timestamp.

The outsourcer releases M by the following algorithm:

(1) Randomly select a number $r_1 \in Z_q^*$ calculate $R_1 = r_1P$ and $h = H_1(R_1 + X_F, ACC_F, M, D_F)$, $SIG = r_1 + x_F/x_F + hu_F$

(2) Randomly select $r_2 \in Z_q^*$, calculate $R_2 = r_2P$

$$C = H_2(R_2) \bigoplus (M\|ACC_F\|SIG); \tag{6}$$

(3) Calculate $y_i = H_3(ACC_{J_i})$, $1 \le i \le k$, and calculate Lagrange interpolation polynomial

$$f_i(x) = \prod_{1 \le j \ne i \le k} \frac{y - y_j}{y_i - y_j} = c_{i1} + c_{i2}y + \cdots c_{ik}y^{k-1}, \tag{7}$$

where $c_{i1}, c_{i2}, \ldots, c_{ik} \in Z_q^*$

(4) Calculate

$$Y_i = r_2 \left(X_{J_i} + D_{J_i} + ACC_{J_i} PK_m \right), \quad V_i = \sum_{j=1}^{k} c_{ji} Y_j, \quad (8)$$

$$1 \le i \le k \quad (9)$$

(5) The outsourcer broadcasts ciphertext $\sigma = (V_1, V_2, \cdots, V_k, R_1, C)$ to the group of the contractors

After receiving it, the contractor executes the following algorithm for unsigncryption:

(1) Calculate

$$y_i = H_3 \left(ACC_{J_i} \right), \quad (10)$$

$$Y'_i = V_1 + y_i V_2 + \cdots y_i^{k-1} (\mathrm{mod} \, q) V_k. \quad (11)$$

Calculate $R'_2 = (x_{J_i} + u_{J_i})^{-1} Y'_i$, recover the original message and signature $(M \| ACC_F \| SIG) = H_2(R'_2) \oplus C$.

(2) Get the blockchain address ACC_F of the outsourcer from the recovered message, and then calculate

$$h' = H_1(R_1 + X_F, ACC_F, M, D_F); \quad (12)$$

(3) Verify the equation by using the public key (X_F, D_F) and address ACC_F of the contractor

$$h' = H_1 \left(SIG \left(X_F + h'(D_F + ACC_F PK_m) \right), ACC_F, M, D_F \right). \quad (13)$$

Whether it is true or not, if so, the contractor confirms that the received signcryption is truly from the address ACC_F, otherwise, it refuses the signcryption.

In the above algorithm, the outsourcer encrypts its blockchain address, information requirements, and reward amount, which makes it impossible for other nodes in the blockchain to know from which blockchain address the information requirements are released, except for the nodes in the intended contractor group. At the same time, in the signcryption information released by the outsourcer, the blockchain address of each contractor is also hidden. Not only can the nodes outside the contractor group not know the blockchain address of the contractor but also the contractor only uses its private key and blockchain address in the decryption process and does not use the address of other contractors. This ensures that each contractor cannot know each other's blockchain address, that is, it can achieve mutual anonymity, which is consistent with the contractor's requirement for privacy protection.

4.4. Submission Algorithm of the Crowdsourcing Information. After receiving the crowdsourcing information requirements released by the outsourcer, the senior netizens voluntarily decide whether to join the crowdsourcing information obtaining blockchain network based on their own expertise and accumulated network resources. After collecting the required information, the contractor submits the information to the outsourcer. Although there is no direct relationship between the blockchain address of the contractor and the identity of senior netizens, which ensures the anonymity of the contractor to a certain extent, the contractor still has the risk of leaking his identity in the process of using the same address for multiple crowdsourcing information transactions with the outsourcer. Therefore, this paper uses the idea of random address in CryptoNote [20]. First, the outsourcer performs the following steps to generate a temporary public key address for each intended contractor and record it in the blockchain:

(1) Randomly select a number $t_{i1}, t_{i2} \in Z_q^*$, calculate $T_{i1} = t_{i1}P$, $T_{i2} = t_{i2}P$, $1 \le i \le k$

(2) Calculate the temporary public key address of this crowdsourcing information transaction $ACC'_{J_i} = (X'_{J_i}, D'_{J_i}) = (H_4(t_{i1}X_{J_i})P, H_4(t_{i2}(D_{J_i} + ACC_{J_i}PK_m))P)$, $1 \le i \le k$

(3) Record T_{i1}, T_{i2}, and $ACC'_{J_i} = (X'_{J_i}, D'_{J_i})$, $1 \le i \le k$, in the blockchain

The contractor uses its long-term private key (x_{J_i}, u_{J_i}), to calculate the temporary private key $(x'_{J_i}, u'_{J_i}) = (H_4(x_{J_i}T_{i1}), H_4(u_{J_i}T_{i2}))$ for the information submission this time, and then executes the following algorithm to signcrypt $I = (T \| \text{information data})$ and return the signcryption to the outsourcer:

(1) Randomly select a number $z_i \in Z_q^*$, calculate $Z_i = z_iP$, $h_i = H_1(Z_i + X'_{J_i}, ACC'_{J_i}, I, D'_{J_i})$

(2) Generate the signature of I

$$SIG_{J_i} = \frac{z_i + x'_{J_i}}{x'_{J_i} + h_i u'_{J_i}}; \quad (14)$$

(3) Calculate

$$V_{J_i} = \left(z_i + x'_{J_i} \right) (X_F + D_F + ACC_F PK_m), \quad (15)$$

$$C = H_2(V_{J_i}) \oplus (I \| \text{SIG}_{J_i}). \tag{16}$$

Send signcryption $\sigma = \{Z_i, C\}$ to the outsourcer F.

After receiving the signcryption returned by the contractor, the outsourcer performs the following steps to decrypt and verify:

(1) Calculate $V_F = (Z_i + X'_{J_i})(x_F + u_F)$

(2) Recover the data returned by the contractor

$$I \| \text{SIG}_{J_i} = H_2(V_F) \oplus C. \tag{17}$$

(3) Calculate

$h_i = H_1(Z_i + X'_{J_i}, \text{ACC}'_{J_i}, I, D'_{J_i})$ and verify

$$h_i = H_1\left(\text{SIG}_{J_i}\left(X'_{J_i} + h_i D'_{J_i}\right), \text{ACC}'_{J_i}, I, D'_{J_i}\right). \tag{18}$$

Whether it is true or not, if it is true, confirm that the information comes from the contractor corresponding to the blockchain address ACC'_{J_i}.

In the above algorithm, the contractor uses the temporarily generated private key to submit the data, so as to ensure the confidentiality of the data and prevent exposing its identity in the process of submitting. Normally, in order to protect the contractor's enthusiasm to collect information, no disciplinary measures are taken for the contractor submitting information with low quality. If very few contractors maliciously submit irrelevant data for many times, the outsourcer can trace the blockchain address information of the malicious contractor according to the corresponding relationship between its retained contractor blockchain address and the temporary address, thus, excluding the malicious contractor address from the contractor set in the future information requirements release.

4.5. Reward Accounting Algorithm of the Crowdsourcing Information.
In order to encourage the contractor to complete the collection and submission of crowdsourcing information with high quality, the following is the reward accounting algorithm of the crowdsourcing information. After receiving the information provided by the contractor, the outsourcer screens out valuable information manually and systematically and pays appropriate remuneration to the corresponding contractor. The higher the quality of the submitted crowdsourcing information, the higher the amount of reward. At the same time, in order to realize the identity anonymity of the outsourcer and the contractor and the reward confidentiality in the process of crowdsourcing information reward transaction, the following One-Time-Pad ring signcryption algorithm [21] will be improved and the following reward accounting algorithm of crowdsourcing information will be given to ensure that the transaction record will not expose the specific identity of the

outsourcer and the contractor in the blockchain and will not expose the reward amount m:

(1) The outsourcer selects the one-time random key k_F, calculates the corresponding public key $K_F = k_F P$, and then constructs the public key set $\{K_1, K_2 \cdots, K_n\}$, which does not contain the one-time public key K_F

(2) The outsourcer selects $a_i, b_i \in Z_q^*(1 \le i \le n)$ to set the attribute value for the public key in the public key set:

$$A_i = a_i P + b_i K_i, B_i = a_i H_2(K_i) + b_i k_F H_2(K_F), 1 \le i \le n. \tag{19}$$

Select $a_F, b_F \in Z_q^*$ to set the attribute value for the random public key K_F:

$$A_F = a_F P, B_F = a_F H_2(K_F). \tag{20}$$

(3) Set $s_i = b_i, c_i = a_i, 1 \le i \le n$

(4) Calculate $s_F = H_0(m, A_1, A_2, \cdots, A_n, A_F, B_1, B_2, \cdots B_n, B_F) - \sum_{i=1}^n s_i$.

(5) Calculate $c_F = a_F - s_F k_F$, and

$$X_F = (m, s_1, s_2, \cdots, s_n, s_F, c_1, c_2, \cdots, c_n, c_F). \tag{21}$$

(6) Select random number v_F and calculate

$$V_F = v_F P, C = H_2(V_F) \bigoplus X_F. \tag{22}$$

(7) Calculate $W_F = v_F(X'_{J_i} + D'_{J_i})$

The above algorithm is the process of generating ring signcryption by the outsourcer.

(8) Define the reward transaction of crowdsourcing information as <time stamp T, $\{K_1, K_2, \cdots, K_n, K_F\}$, ACC'_{J_i}, (W_F, C) >, and broadcast the transaction to the crowdsourcing information obtaining blockchain

After receiving the award transaction broadcasted by the outsourcer, the contractor uses its long-term private key (x_{J_i}, u_{J_i}), calculates $(X'_{J_i}, D'_{J_i}) = (H_4(x_{J_i} T_{i1})P, H_4(u_{J_i} T_{i2})P)$, and compares it with the temporary public key address ACC'_{J_i} of the contractor recorded in the transaction. If it is consistent, it is determined that the crowdsourcing information provided by itself has received the reward from the

outsourcer and then performs the following steps to decrypt and verify the ring signcryption of the outsourcer:

(1) Calculate with its temporary private key

$$V_{J_i} = \left(x'_{J_i}, u'_{J_i}\right)^{-1} W_F. \tag{23}$$

(2) Restore the ring signature $X_F = H(V_{J_i}) \oplus C$

(3) Calculate $A'_i = c_i P + s_i K_i$

$$B'_i = c_i H_2(K_i) + s_i k_F H_2(K_F), \tag{24}$$

$$A'_F = c_F P + s_F K_F, \tag{25}$$

$$B'_F = c_F H_2(K_F) + s_F k_F H_2(K_F). \tag{26}$$

(4) Verify the equation

$$s_F + \sum_{i=1}^{n} s_i = H_0\left(m, A'_1, A'_2, \cdots, A'_n, A'_F, B'_1, B'_2, \cdots B'_n, B'_F\right). \tag{27}$$

Whether it is true, if so, confirm that the electronic money is the legal reward from the outsourcer for providing crowdsourcing information, otherwise, refuse it.

When the contractor uses the obtained reward for consumption, it only needs to use its temporary private key to sign m, without using its long-term private key; the payee uses the temporary public key address of the contractor recorded in the blockchain for verification. Because the temporary public key addresses of the contractor are different from each other in each crowdsourcing information transaction, the nodes in the crowdsourcing blockchain cannot link the real identity of the contractor with its consumption behaviors, thus, realizing the consumer anonymity of the contractor.

5. Privacy Protection and Efficiency Analysis of our Scheme

5.1. Privacy Protection Analysis. The crowdsourcing information obtaining scheme based on blockchain is mainly realized by the certificateless multireceiver anonymous signcryption scheme [19] and one-time pad ring signature algorithm [21] in the stage of crowdsourcing information requirements release, crowdsourcing information submission by the contractor and crowdsourcing information evaluation and reward. The security of the algorithm has been proved in detail in relevant references, so it will not be described in detail. In this paper, based on the above algorithm, the idea of temporary public key address and tempo-

rary private key is introduced to protect the identity anonymity and data privacy of the outsourcer and the contractor. The privacy protection effect of the scheme is analyzed emphatically below:

(1) *Releasing of Information Requirements.* In this stage, the outsourcer signed the blockchain address, released requirements, and reward together with the public key of the contractor, so that other nodes in the blockchain network could not know the specific information requirements and could not track the specific identity information of the outsourcers from the release of the crowdsourcing information task. In addition, in the signcryption released by the outsourcer, Lagrange interpolation polynomial is used to hide the blockchain address of each contractor, so as to prevent the blockchain address of each contractor from being exposed in the blockchain. Meanwhile, each contractor in the contractor node set only uses its private key and blockchain address information to decrypt the signcryption, and cannot use the addresses of other contractors, thus ensuring mutual anonymity among each contractor

(2) *Submission of Crowdsourcing Information by the Contractor.* In this stage, the contractor does not directly use the private key corresponding to its blockchain address to submit the collected crowdsourcing information, but the outsourcer first uses the public key of the contractor to generate the temporary public key of the contractor for this submission, and then the contractor uses the temporary private key corresponding to the temporary public key to signcrypt and transmit the collected information to the outsourcer. Because the contractor uses different temporary private keys every time, it can ensure the confidentiality of the data and prevent its identity from being exposed in the process of submitting the crowdsourcing information many times

(3) Evaluation and Reward Stage of Crowdsourcing Information. In this stage, in order to prevent the identity of the outsourcer from leaking in the process of multiple awards, the outsourcer uses a ring signcryption algorithm to sign the reward amount and then publishes the crowdsourcing information reward transaction in the blockchain. Attackers cannot associate the reward transaction with the real address of the outsourcer, and at the same time, the temporary public key address of the contractor is published in the transaction to prevent attackers from tracking its identity by using the public key address of the contractor

(4) When the contractor uses the obtained for consumption, it only needs to use its temporary private key to sign the reward m, and the payee uses the contractor's temporary public key address for verification. Because the contractor's temporary public key

TABLE 1: Comparison of privacy protection property.

	[4]	[5]	[6]	[7]	[8]	[9]	[10]	[11]	[12]	[13]	[14]	Ours
Privacy protection of outsourcer	Weak anonymity	Strong anonymity	×	×	×	Weak anonymity	Weak anonymity	Weak anonymity	Weak anonymity	×	×	Strong anonymity
Privacy protection of contractor	Weak anonymity	Weak anonymity	×	×	×	Weak anonymity	Weak anonymity	Weak anonymity	×	×	×	Strong anonymity
Privacy protection of transaction data	No protection of transaction amount	×	×	×	×	√	√	√	√	√	√	√

TABLE 2: Statistics of scheme's calculation cost.

	Release algorithm	Submission algorithm	Reward accounting algorithm
Outsourcer	$(k^2 + k + 2)$SM	$(4k + 3)$SM	$(2n + 3)$SM
Contractor	$(k + 2)$SM	4SM	$(2n + 3)$SM

address is different from each other in each transaction, it realizes the anonymity of the contractor's consumption

In the following, the privacy protection performance of the scheme in this paper is compared with the existing information sharing scheme based on blockchain. Here, we define the scheme that only relies on the anonymity of user's blockchain address to protect the anonymity of user's identity as satisfying weak anonymity and define the scheme that uses other special technologies to ensure the anonymity of user's identity as satisfying strong anonymity. The results are shown in Table 1. The scheme in this paper has obvious advantages over other schemes in privacy protection.

5.2. Efficiency Analysis. In this section, the calculation efficiency of this scheme is quantitatively evaluated. The calculation cost of the scheme mainly depends on the calculation amount of the outsourcer and the contractor in the release of the requirements, the submission of the information, and the reward accounting. In order to improve the calculation efficiency, the above algorithms do not use bilinear pairing operation and exponential operation on multiplication group [22], but mainly use scalar multiplication operation on elliptic curve to design. "SM" is used to represent scalar multiplication operation on elliptic curve. Table 2 shows the calculation statistics of the outsourcer and the contractor in the scheme. Because other operations (hash operation and point addition operation) consume much less time than scalar multiplication operation, they are not included in the statistics here.

Among them, the parameter k is the number of contractors in the crowdsourcing blockchain, and n is the number of public keys in the public key set in the ring signature algorithm (which is a fixed parameter). If choose a 160-bit elliptic curve group on a hypersingular curve over a 512-bit finite field based on PBC library (Version 0.5.14), one SM operation takes about 1.51 ms [23]. It can be seen from Table 2 that the calculation cost of the outsourcer in the three algorithms of crowdsourcing information obtaining scheme is $O(k^2)$, $O(k)$, and $O(1)$, which are all effective polynomial time algorithms; as a contractor with weak computing power, the computational overhead in the three algorithms is $O(k)$, $O(1)$, and $O(1)$ separately, which are all effective polynomial time algorithms with less computation, especially in the submission and reward accounting algorithms that the contractor frequently participates in.

6. Conclusion

On the basis of traditional crowdsourcing information obtaining scheme based on intermediary platform, this paper designs a crowdsourcing information obtaining scheme aiming at senior netizens based on blockchain. The scheme does not need intermediary platform, and in order to satisfy the absolute dependence of senior netizens on personal anonymity, the scheme uses the certificateless multireceiver anonymous signcryption scheme to release information requirements and rewards, so as to ensure the identity anonymity of the outsourcer and the contractor and the confidentiality of crowdsourcing information. In the submission stage, a temporary public-private key pair is generated for the contractor, and the contractor uses the temporary private key to sign and return the data to ensure the identity anonymity of the contractor in the process of submitting information for many times; in the process of reward accounting, the outsourcer uses the one-time temporary public key of the contractor to signcrypt the reward, so as to ensure the anonymity of its identity and the secrecy of the remuneration, and at the same time realize the untraceability of the consumption. Compared with the privacy protection of similar schemes, this scheme has obvious advantages.

Data Availability

The experimental data used to support the findings of this study are included within the article.

Conflicts of Interest

The authors declare that they have no conflicts of interest.

References

[1] J. Howe, "The rise of crowdsourcing," *Wired Magazine*, vol. 14, no. 6, pp. 1–4, 2006.

[2] N. D. Lane, E. Miluzzo, H. Lu, D. Peebles, T. Choudhury, and A. Campbell, "A survey of mobile phone sensing," *IEEE Communications Magazine*, vol. 48, no. 9, pp. 140–150, 2010.

[3] D. B. Rawat, L. Njilla, K. Kwiat, and C. Kamhoua, "iShare: blockchain based privacy-aware multi agent information sharing games for cyber-security," in *2018 International Conference on Computing, Networking and Communications (ICNC)*, pp. 425–431, Piscataway, NJ, March 2018.

[4] H. Kezhen, L. Yifeng, and F. Dengguo, "Cyber security threat intelligence sharing model based on blockchain," *Journal of Computer Research and Development*, vol. 57, no. 4, pp. 836–846, 2020.

[5] W. Ruijin, Y. Suzhe, L. Y. T. Yucheng, and Z. Fengli, "Medical blockchain of privacy data sharing model based on ring signature," *Journal of University of Electronic Science and Technology of China*, vol. 48, no. 6, pp. 886–892, 2019.

[6] H. Yunhua, L. Mengru, L. Hong, S. Limin, X. Ke, and Y. Chao, "A blockchain based incentive mechanism for crowdsensing applications," *Journal of Computer Research and Development*, vol. 56, no. 3, pp. 544–554, 2019.

[7] C. Yexia, F. Jun, and C. D. Yuejin, "Research on threat intelligence sharing and rating technology based on blockchain," *Information and Communications Technology and Policy*, vol. 2, pp. 19–24, 2020.

[8] C. Mingzhang, W. Lin, and W. Jiang, "Research on the application of blockchain technology in the field of internet public welfare crowdfunding," *Library and Information*, vol. 2, pp. 76–80, 2020.

[9] X. Wenyu, W. Lei, and Y. Yunxue, "Privacy-preserving scheme of electronic health records based on blockchain and homomorphic encryption," *Journal of Computer Research and Development*, vol. 55, no. 10, pp. 2233–2243, 2018.

[10] S. Amofa, E. B. Sifah, K. O. -B. Obour Agyekum, S. Abla, X. Qi, C. G. James, and G. Jianbin, Eds.J. Gao, "A blockchain-based architecture framework for secure sharing of personal health data," in *2018 IEEE 20th International Conference on e-Health Networking, Applications and Services (Healthcom)*, pp. 1–6, Vitkovice, September 2018.

[11] L. Yue, H. Junqin, and Q. Shengzhi, "Big data model of security sharing based on blockchain," in *2017 3rd International Conference on Big Data Computing and Communications (BIGCOM)*, pp. 117–121, Cheng Du, China, August 2017.

[12] M. J. M. Chowdhury, A. Colman, M. A. K. J. Han, and P. Sarda, "Blockchain as a notarization service for data sharing with personal data store," in *2018 17th IEEE International Conference On Trust, Security And Privacy In Computing And Communications/ 12th IEEE International Conference On Big Data Science And Engineering (TrustCom/BigDataSE)*, pp. 1330–1335, New York, USA, August 2018.

[13] F. Kai, R. Yanhui, W. Yue, L. Hui, and Y. Yingtang, "Blockchain-based efficient privacy preserving and data sharing scheme of content-centric network in 5G," *The Institution of Engineering and Technology*, vol. 12, no. 5, pp. 527–532, 2018.

[14] Q. Kang, Y. Wei, W. Lingwei, and T. Hongbo, "Data sharing scheme for 5G IoT based on blockchain," *Chinese Journal of Network and Information Security*, vol. 6, no. 4, pp. 45–55, 2020.

[15] D. Valadeolmillos, Y. Mezquita, and A. Gonzalez Briones, "Blockchain technology: a review of the current challenges of cryptocurrency," in *International congress on Blockchain and Applications*, pp. 153–160, Atlanta, USA, 2019.

[16] H. Xuan, Y. Yong, and W. FeiYue, "Security problems on blockchain: the state of the art and future trends," *Acta Automatica Sinica*, vol. 45, no. 1, pp. 206–225, 2019.

[17] Z. Jun, Z. Haining, and T. Yi, *Blockchain Technology Guide*, China Machine Press, Beijing, 2016.

[18] Z. Shiqin, H. Ru, H. Tao, L. Jiang, W. Shuo, and F. Wei, "Survey of blockchain: principle, progress and application," *Journal on Communications*, vol. 41, no. 1, pp. 134–151, 2020.

[19] Q. Yanlin, W. Xiaoping, and H. Wei, "Efficient certificateless multi-receiver anonymous signcryption scheme," *Journal on Communications*, vol. 37, no. 6, pp. 129–138, 2016.

[20] N. Van Saberhagen, "CryptoNote v 2.0," 2020, http://coinpaprika.com/storage/cdn/jwhitepapers/1611.pdf.

[21] M. Dai, S. Zhang, H. Wang, and S. Jin, "A low storage room requirement framework for distributed ledger in blockchain," *IEEE Access*, vol. 6, pp. 22970–22975, 2018.

[22] MIRACL, "Multiprecision integer and rational arithmetic C/C++ library," 2020, https://indigo.ie/mscott/.

[23] D. Sheng, C. Jin, and L. Hui, "Efficient pairing-free CP-ABE based on ordered binary decision diagram," *Journal on Communications*, vol. 40, no. 12, pp. 1–8, 2019.

Research Article

Parallel Cross-Sparse Filtering Networks and Its Application on Fault Diagnosis of Rotating Machinery

Shan Wang [iD],[1] **Baokun Han** [iD],[1] **Huaiqian Bao** [iD],[1] **Jinrui Wang** [iD],[1] **and Zongzhen Zhang** [iD][1,2]

[1]*College of Mechanical and Electronic Engineering, Shandong University of Science and Technology, Qingdao 266590, China*
[2]*College of Energy and Power Engineering, Nanjing University of Aeronautics and Astronautics, Nanjing 210016, China*

Correspondence should be addressed to Zongzhen Zhang; zhzz18@126.com

Intelligent diagnosis method has become a new focus for researchers, which can get rid of the dependence of diagnostic experience and prior knowledge. However, in practical application, to deal with the new fault type of mechanical equipment, the number of fault labels of the diagnosis model needs to be increased. We must retrain the whole training model, which is a time-consuming process. To solve this problem, higher requirements are put forward for the generalization ability and universality of the algorithm. In view of the feature extraction advantages of cross-sparse filtering (Cr-SF), which can be regarded as an unsupervised minimum entropy learning method using the maximization of the proxy of sparsity, this paper proposed a parallel network based on Cr-SF. The feature extraction process of each sample is independent, and the feature extraction and classifier training process are separated. Therefore, the most prominent advantage of the proposed method is that when a new fault occurs, it only needs to extract the feature of the new fault separately and then input it to the classifier at the last layer for training. The experimental results show that the proposed method can obtain high accuracy and stability and can significantly improve the adaptability of intelligent fault diagnosis in practical application.

1. Introduction

As the key parts of mechanical transmission, bearings and gears are prone to failure during the runtime, which may reduce the working efficiency and even cause accidents and disasters [1]. Therefore, accurate early warning and corresponding maintenance measures when bearing and gear failure are of great significance to ensure the safe operation of mechanical equipment [2]. With the rapid development of machine learning theory, intelligent fault diagnosis method of rotating machinery has become an important topic in the area of health monitoring of mechanical equipment [3, 4].

Recently, deep learning-based intelligent rotating machinery fault diagnosis, which can automatically extract the features from original data, has achieved remarkable success [5–7]. These methods have great performance to overcome the inherent disadvantages of traditional machine learning methods, such as Support Vector Machine (SVM),

Artificial Neural Network (ANN), and Principal Component Analysis (PCA). Jia et al. [8] proposed a novel intelligent method based on DNNs to overcome the shortcomings of the traditional methods, which can adaptively learn the fault features and obtain superior diagnostic accuracy and robustness. Wang et al. [9] improve the computation efficiency of feature extraction using batch normalization based Stacked Autoencoders (SAEs). Li et al. [10] enhanced the feature learning ability using S-transform (ST) algorithm and connected convolutional neural networks (CNN). Shao et al. introduced Gaussian visible units to the electric locomotive bearing fault diagnosis based on Convolutional Deep Belief Network (CDBN) [11, 12]. The literature [13] presented a novel deep autoencoder loss function based on maximum corr-entropy to eliminate the effects of background noise. To estimate the irregularity of the collected time series, Li et al. [14] proposed a multiscale symbolic Lempel-Ziv- (MSLZ-) based intelligent fault diagnosis method and successfully
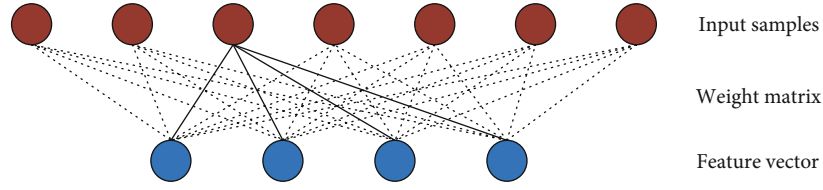
FIGURE 1: Architecture of sparse filtering.

applied it the multiple fault diagnosis of railway vehicle systems. In [15], a novel feature learning method named multiscale symbolic dynamic entropy (MSDE) was firstly proposed and then combined with transfer learning to obtain the mapping matrix and achieve the novel cross-domain intelligent fault diagnosis. In [16], the MSDE-based fault diagnosis method was applied to the planetary gearboxes and shows superior advantages in terms of computation efficiency and robustness. Wang et al. [17] proposed subdomain adaptation transfer learning network to reduce adaptively marginal and conditional distribution biases. Jia et al. [18] proposed a partial transfer fault diagnosis model based on a weighted subdomain adaptation network (WSAN), which focuses on the distribution of local feature while aligning the global distribution.

However, deep learning requires training all types of fault samples simultaneously. Therefore, if new fault types appear in the application process, we need to retrain and reoptimize a lot of parameters simultaneously with a large number of training data. This is a time-consuming process and will affect the real-time application of the monitoring system. The main reason for this problem is that deep learning requires all label data to participate in feature extraction and classification training. Lei et al. [19] applied sparse filtering and softmax classifier to the intelligent diagnosis bearing faults, which is a two-stage model, and feature learning and classification training are independent of each other. Although the feature learning and classifier training of these methods are separated, the feature learning is still carried out simultaneously for all fault types. Parallel network structure is an effective way to solve this problem, in which each fault can be trained separately. In this way, the feature learning process is an independent process for each type of fault condition. In [20], a concurrent convolution neural network (C–CNN) composed of multiple branches was proposed for bearing fault diagnosis, in which the convolutional layer of different branches selects the kernels with different scales in same level. In view of gearbox structure and operating condition, Guo et al. [21] established reinforced input-based multitask parallel convolutional neural network for coupling fault diagnosis of gearbox that has parallel submultiple classifiers and convolutional neural networks. This method is to overcome the problem that all kinds of shared features of multiparts cannot be adequately extracted simultaneously. The independent training of single fault sample cannot be realized.

The independent training of samples puts forward higher requirements for the feature extraction algorithm. In an unsupervised learning method, sparse representation is the core principle [22]. Data sparsity corresponds to information entropy. The sparser the data is, the smaller the entropy is. In [23], Zennaro and Ken's study a thorough theoretical analysis of SF and the corresponding performance and proved that the SF works by explicitly maximizing the entropy of the learned representations through the maximization of the proxy of sparsity. Zhang et al. introduced generalized normalization to the sparse filtering and discussed the lifetime and population sparsity [24]. In [25, 26], Intrinsic Component Filtering (ICF) and Cr-SF, the improved variants of standard SF, were proposed for the in intelligent fault diagnosis, weak feature extraction, and compound separation. Cr-SF is a variant of SF. Therefore, Cr-SF can be regarded as an unsupervised minimum entropy feature learning method, in which the entropy of the extracted features is measured as cross-sparsity. Considering the advantages of Cr-SF in extracting features of small sample [25], this paper proposes parallel Cr-SF networks.

Firstly, each type of fault sample is trained through Cr-SF to learn the weights of each fault condition. The second step is feature selection and optimization, in which the most representative features are selected to arrange and combine the features of the whole fault conditions. The third step is to input the entire features and label data into the classifier for training. In this way, when new fault type data appears and the trained monitoring system needs to be upgraded, we only need to extract the features of the newly added data and add the features to the existing feature matrix to retrain the classifier. There is no need to retrain all training samples, which saves the time of system upgrade.

The rest of this study is organized as follows. Section 2 introduces Cr-SF and the proposed structure of parallel network. Section 3 verifies the effectiveness of the proposed method through rolling bearing and planet gear fault datasets. The visualization of weights and features is discussed in Section 4. Finally, the conclusions are given in Section 5.

2. Proposed Method

2.1. Cross-Sparse filtering. As shown in Figure 1, cross sparse filtering is the variant of SF, Which can be regarded as a two-layer neural network. The optimization process of Cr-SF is simultaneous for the rows and columns of feature matrix. Therefore, the objective function is composed of two terms: $l_{1/2}$-norms of rows and $l_{1/2}$-norms of columns of feature matrix. Suppose the input dimension and output dimension of Cr-SF are N_{in} and N_{out}. The collected original signal $\mathbf{x} \in \mathfrak{R}^N$ is randomly segmented into a matrix segment matrix $\mathbf{S} \in \mathfrak{R}^{N_{in} \times M}$, where $M = N_{s1} \times m$, m is training samples number, and N_{s1} is the segment number.

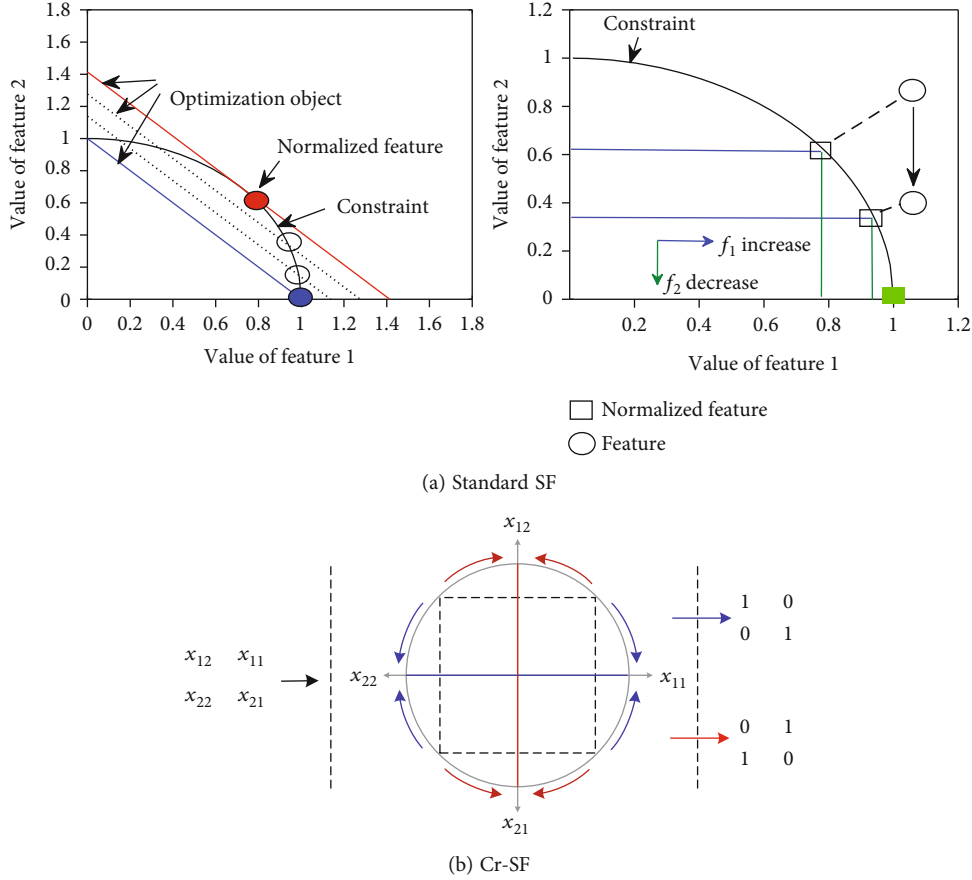(a) Standard SF

(b) Cr-SF

FIGURE 2: Schematic diagram of the optimization target and the constraints of various methods.

First, the local feature matrix $\mathbf{F} \in \mathfrak{R}^{N_{\text{out}} \times M}$ is activated by the product of weight matrix $\mathbf{W} \in \mathfrak{R}^{N_{\text{out}} \times N_{\text{in}}}$ and input matrix $\mathbf{S} \in \mathfrak{R}^{N_{\text{in}} \times M}$, that is, $\mathbf{F} = \mathbf{WS}$.

Second, the objective function of Cr-SF can be constructed by the $l_{1/2}$-norms of rows and $l_{1/2}$-norms of columns of the feature matrix $\mathbf{F}$. The two terms can be written as

$$\mathcal{L}_1 = \left\| \frac{F^i}{\left\| F^i \right\|_2} \right\|_1, \tag{1}$$

$$\mathcal{L}_2 = \left\| \frac{F_j}{\left\| F_j \right\|_2} \right\|_1. \tag{2}$$

Then, weight vectors are constrained to its l_2-norm sphere to eliminate the influence of redundancy in an optimization process. Therefore, the final objective function of the Cr-SF can be expressed as

$$\mathcal{L} = \sum_i^M \mathcal{L}_1 + \lambda \sum_j^{N_{\text{in}}} \mathcal{L}_2 S \cdot T \left| W^i \right|_2 = 1, \tag{3}$$

where $\lambda \geq 0$ is an adjustable parameter that adjusts the priority of two items in the sparse optimization process. According to the discussion of references [26], the value of λ is 1 in this

paper. Due to the fact that $\mathcal{L}$ is nonconvex and nonsmooth. $|\mathbf{F}|$ is replaced by a soft-absolute function $\sqrt{\mathbf{F}^2 + \varepsilon}$, where ε is a small number and equals 1×10^{-8}.

Third, the sparse optimization process uses the L-BFGS algorithm. The gradient function of the objective function can be given by

$$\frac{\partial \mathcal{L}}{\partial \mathbf{w}} = \left[\left(\frac{O}{\left(\sum_j^{N_{\text{in}}} \left| \mathbf{F}^i \right|^2 \right)^{1/2}} - \frac{\mathbf{F} \cdot \sum_j^{N_{\text{in}}} \left(\mathbf{F}^i \right)}{\left(\sum_j^L \left| \mathbf{F}^i \right|^2 \right)^{3/2}} \right) + \left(\frac{\mathbf{O}}{\left(\sum_i^M \left| \mathbf{F}_j \right|^2 \right)^{1/2}} - \lambda \frac{\mathbf{F} \cdot \sum_i^M \left(\mathbf{F}_j \right)}{\left(\sum_i^M \left| \mathbf{F}_j \right|^2 \right)^{3/2}} \right) \right] \cdot \frac{\mathbf{f}}{|\mathbf{f}|} \cdot \mathbf{x}', \tag{4}$$

where $\mathbf{o} \in \mathfrak{R}^{N_{\text{in}} \times M}$ is a matrix of all ones.

As discussed earlier, the optimization of Cr-SF is a cross-sparse optimization process. In order to show more clearly, we present the optimization diagram of SF and Cr-SF in Figure 2. It can be seen that the optimization of SF is a process in which the column features are gradually sparse under row competition constraints. As one feature increases, the other must decrease to ensure the direction of optimization. Cr-SF is a sparse optimization of column features and row
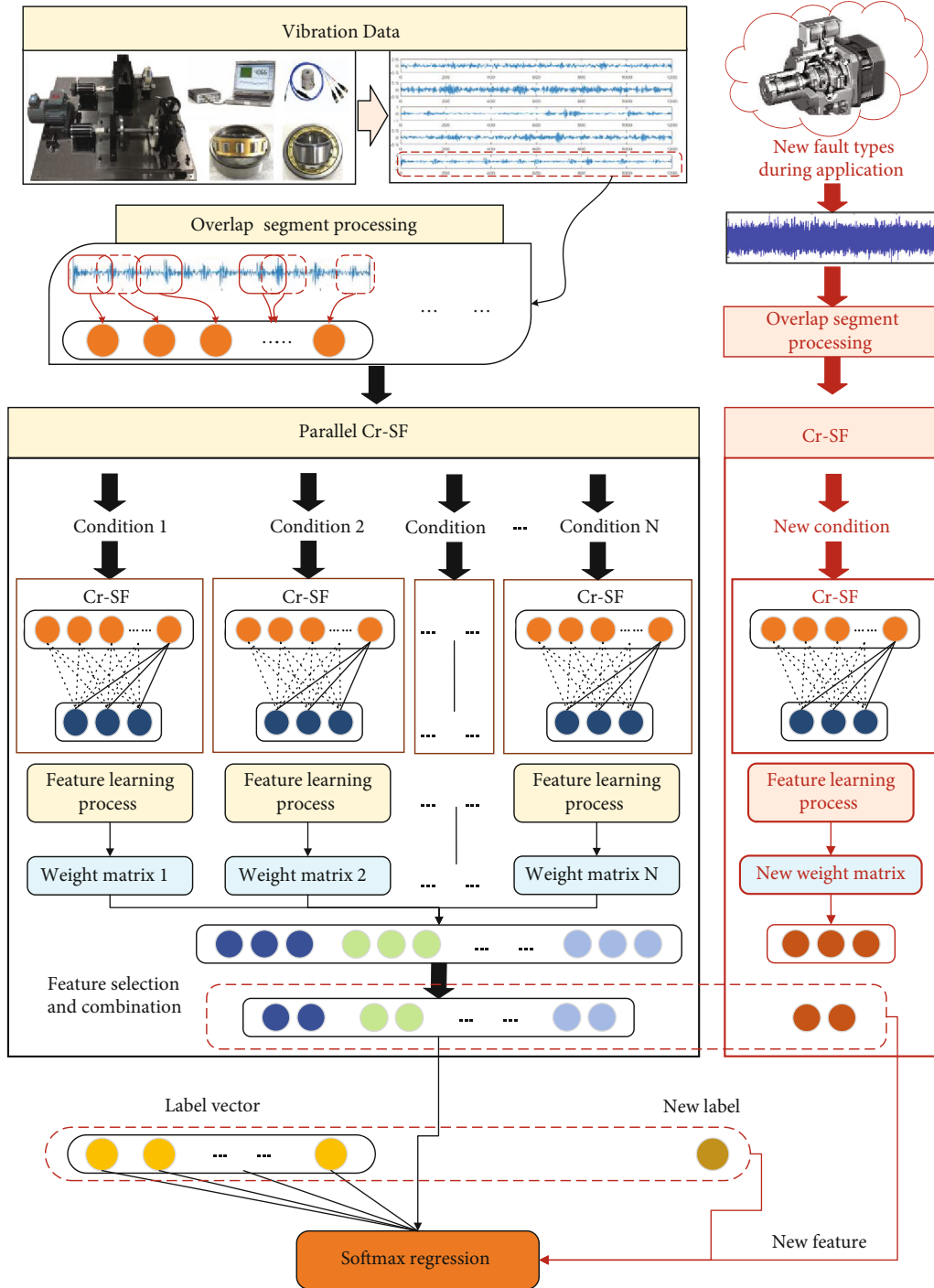
Figure 3: Parallel network structure of the proposed method.

features at the same time. The sparse process between column feature and row feature is separate. For a 2-to-2 matrix, the ideal result of Cr-SF will become a standard orthogonal matrix.

2.2. Parallel Networks Using Cr-SF. This section presents the parallel networks based on the Cr-SF. Figure 3 shows the flow chat of the parallel diagnosis model. The general procedures can be summarized as follows.

(Step 1) Model training: different from the traditional intelligent fault diagnosis methods, the proposed method trains different fault conditions separately. Specifically, suppose that the number of input fault types is L. The fault datasets with same fault type are input into Cr-SF, respectively. Each sample is randomly segmented into a matrix. The sample features are activated through formulas (1)–(3), and the

weights are optimized following formula (4). The trained weights $\mathbf{W}_i$ are obtained, where i is the number of fault type.

(Step 2) Feature selection and arrangement: local features $\mathbf{F}_i \in \mathfrak{R}^{N_{\text{out}} \times M}$ can be calculated using the non-linear activation function and the trained weights, $\mathbf{F}_i = \text{Log}(1 + \mathbf{W_i S_i})$. The local features are averaged to obtain the features of each fault sample, $\mathbf{f}_i = (\sum_{j=1}^{Ns} F_i^j)/N_{s2}$, where N_s is the number of segments. According to the order of eigenvalues from large to small, n features are selected as the final features of fault samples. Then, the features of all fault samples are arranged and combined into a feature matrix $\mathbf{f} = \mathfrak{R}^{n \times m}$ as the input of softmax, where m is the number of training samples.

(Step 3) Classifier training using the learned features $\{\mathbf{f}^i\}_{i=1}^m$ and the corresponding label set $\{y^i\}_{i=1}^m$. $\{\mathbf{f}^i\}_{i=1}^m$ and $\{y^i\}_{i=1}^m$ are fed into the softmax classifier, where $y^i \in \{1, 2, 3, \cdots, k\}$ denotes the label vector of each fault type. The hypothesis $h_\theta(\mathbf{f})$ can be written as

$$h_\theta\left(x^i\right) = \frac{1}{\sum_{j=1}^k \exp\left(\theta_j^T f^i\right)} \begin{bmatrix} \sum_{j=1}^k \exp\left(\theta_1^T f^i\right) \\ \sum_{j=1}^k \exp\left(\theta_2^T f^i\right) \\ \vdots \\ \sum_{j=1}^k \exp\left(\theta_k^T f^i\right) \end{bmatrix}, \quad (5)$$

where $p(y^i = j \mid \mathbf{f})$ means the probability for each feature and $\theta_1, \theta_2, \cdots, \theta_k$ are the parameters of softmax model.

The cost function of the softmax regression is a cross-entropy function and takes the form

$$J(\theta) = -\frac{1}{m} \sum_{i=1}^m \sum_{j=1}^k 1\{y^i = 1\} \lg \frac{\exp\left(\theta_j^T f^i\right)}{\sum_{l=1}^k \exp\left(\theta_l^T f^i\right)} + \frac{\lambda}{2} \sum_{k=1}^K \sum_{l=1}^N \theta_{kl}^2, \quad (6)$$

where m is the training samples number and k is the category number and $1\{\bullet\}$ is the indicator function.

After the model is trained, the features of the online monitoring data are extracted through the trained weights and then input into the softmax classifier to realize feature recognition.

As shown in Figure 3, when a new fault needs to be added, the features of the new fault sample data can be trained through Cr-SF, and then the trained weights and fea-

TABLE 1: Description of the ten bearing working conditions.

Fault condition	Fault diameter (mm)	Motor load (HP)	Sample number	Condition label
NC	—	0	400	1
OF	0.18	0	400	2
OF	0.36	0	400	3
OF	0.53	0	400	4
IF	0.18	0	400	5
IF	0.36	0	400	6
IF	0.53	0	400	7
BF	0.18	0	400	8
BF	0.36	0	400	9
BF	0.53	0	400	10

tures are selected and arranged according to the way in Step 2 to establish a new weight matrix, and then feature extraction and classifier training are carried out for all fault samples. In this way, the newly added fault data does not need to be trained at the same time with the existing fault data. It only needs to train the classifier after combining the trained features.

3. Experimental Validation

In this paper, the planetary gear and rolling bearing datasets are employed to demonstrate the proposed parallel diagnosis model. It should be noted that the proposed model is actually a process of adding new faults when training multiple fault types. Therefore, this study does not separately verify the accuracy of the experiment adding new faults. We only need to compare the accuracy of multifault diagnosis and the training time of adding a new fault.

3.1. Rolling Bearing Data Verification. In this experiment, the rolling bearings fault datasets, which provided from the Case Western Reserve University Lab, are used to demonstrate the diagnostic performance of the proposed method. The motor bearing test bench is mainly composed of an induction electrical motor, the testing bearings, and an acceleration sensor. Two vibration sensors are installed at the drive end and output end of the motor, respectively. This experiment consists of four different fault types: normal condition (NC), inner race fault condition (IF), outer race fault condition (OF), and roller fault condition (RF). For each fault type, three different severity levels (0.18, 0.36, and 0.53 mm) are designed. Therefore, this experiment totally contains ten kinds of fault conditions. During data acquisition, the sampling frequency is set to 12 kHz. Each sample contains 1200 data points. Each health condition includes 100 vibration samples under one load, and there are 1000 samples for this study, as shown in Table 1.

In the experimental verification, the output dimension N_{out} of the parallel neural unit is 20 and the input dimension N_{in} is 100. Figure 4 shows the comparison of accuracy, standard deviation, and computational time obtained by different methods with the change of percentage of training
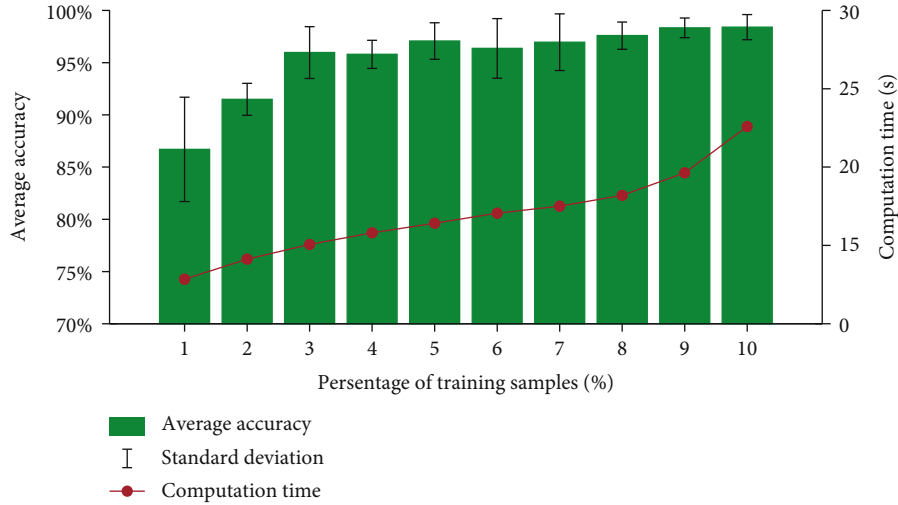
Figure 4: Diagnostic results of parallel SF with different percentage of training data.
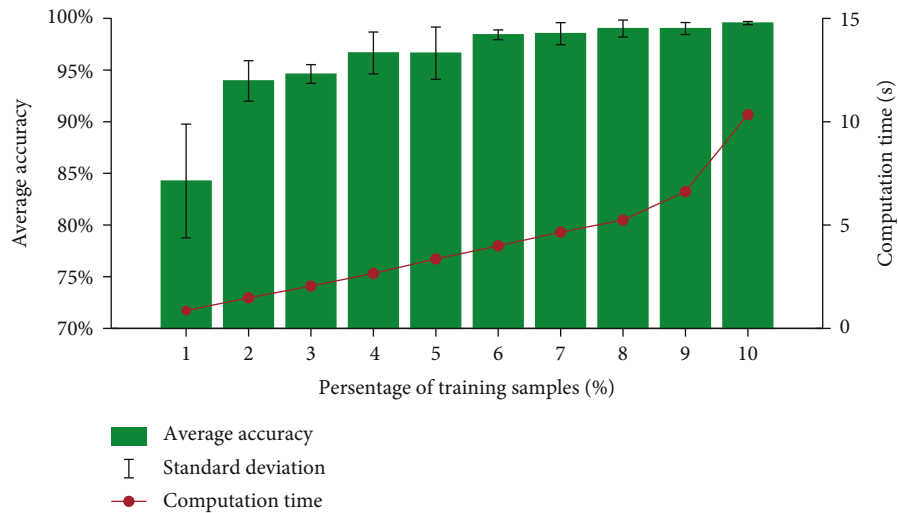

Figure 5: Diagnostic results of traditional structure with different percentage of training data.

data. Firstly, by comparing Figures 5 and 4, it can be seen that under the same output dimension, the parallel structure performs a negative impact on the accuracy and calculation time. When the standard SF algorithm is transformed to parallel network, the accuracy decreases and the calculation time is longer. The reason may be that the structure needs to calculate more times and the number of training samples of each parallel neural unit is much smaller than that of the traditional structure. Therefore, the experimental results also verify the problem mentioned in the preface: the parallel structure requires higher feature extraction ability of neural units in small samples.

As can be seen from Figure 6, compared with the other methods, a parallel Cr-SF network has significantly improved in the accuracy due to the stronger feature extraction ability of Cr-SF. For example, when the proposed method is trained with by only 2% data, the accuracy is above 99% and the standard deviation is only 0.81%. While when the parallel SF network is trained with 15% samples, the accuracy rate is only 98.4% and standard deviation is 1.2%. With the increasing of

the percentage of training data, the accuracy increases. When the percentage of training data is above 3%, the accuracy of the proposed method can reach a relatively stable state. The experimental results show that the proposed method has higher accuracy and better robustness in case of small samples. The accuracy and stability of feature extraction based on Cr-SF are the premise to ensure the use of parallel network structure.

Figures 7 and 8 show the impact of the different feature dimension of each condition on the diagnosis performance. The output dimension N_{out} of the parallel neural unit is 20, the input dimension N_{in} is 100, and the percentage of training data is 10%. It can be observed that the test accuracy of parallel SF gradually increases, when the dimension is 20, which means the input dimension of softmax is 200, the accuracy is 98.4%, and the standard deviation is 1.2%. However, when the dimension is greater than 8, the accuracy of parallel Cr-SF is relatively stable, and the accuracy can achieve above 99.9%. In this case, the input dimension of softmax is only 80.
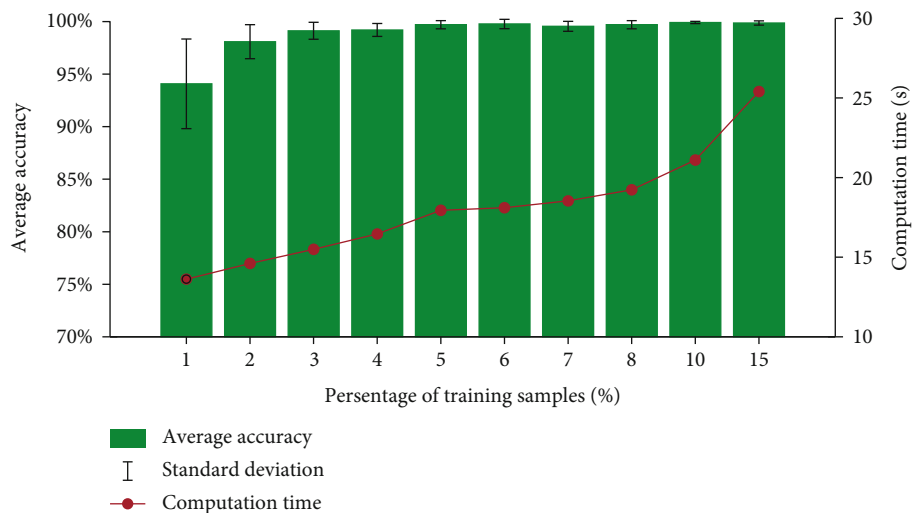
Figure 6: Diagnostic results of parallel Cr-SF with different percentage of training data.
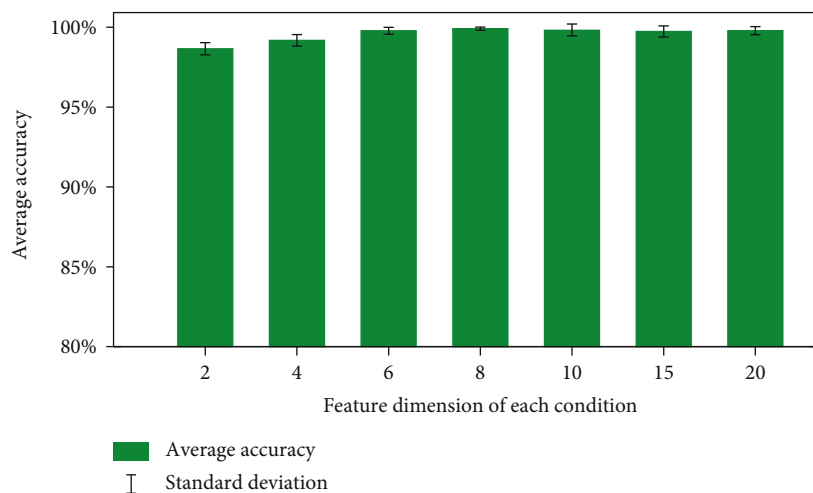

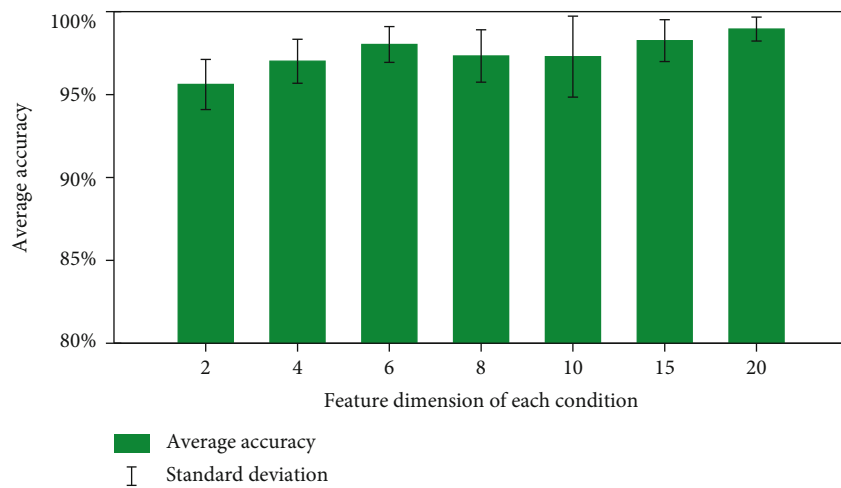Figure 7: Diagnostic results of parallel Cr-SF with different feature dimension of each condition.

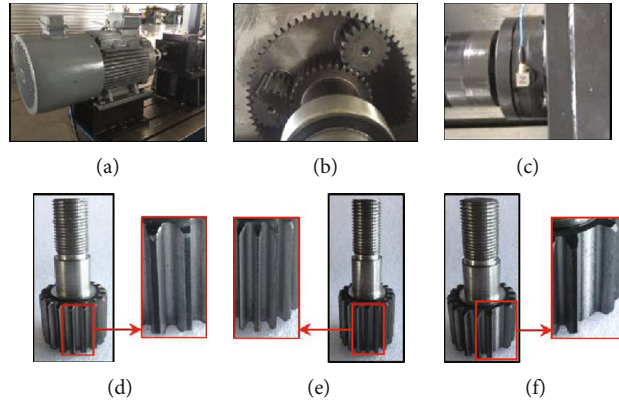Figure 8: Diagnostic results of parallel SF with different feature dimension of each condition.

FIGURE 9: Gear fault feature and test bench diagrams. (a) Test rig, (b) schematic of the gearbox, (c) triaxial accelerometer, (d) normal gear, (e) worn teeth, and (f) broken teeth.
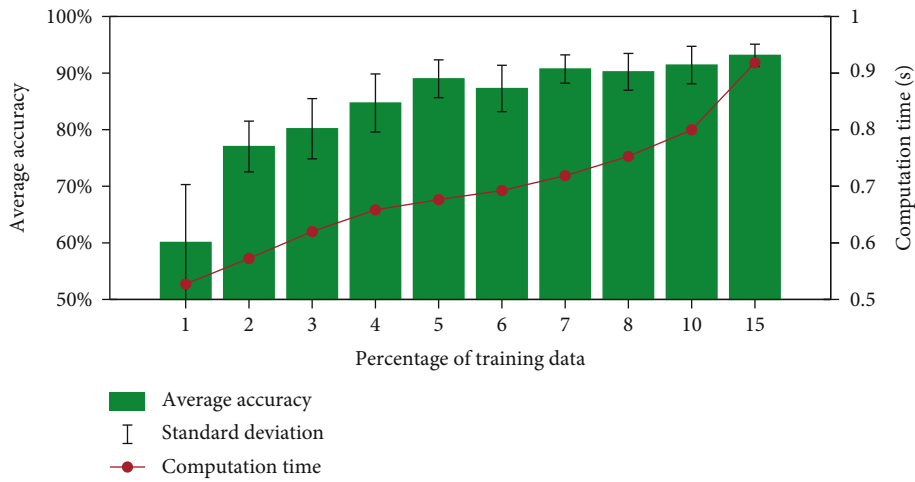

FIGURE 10: Diagnostic results of parallel SF with different percentage of training data.
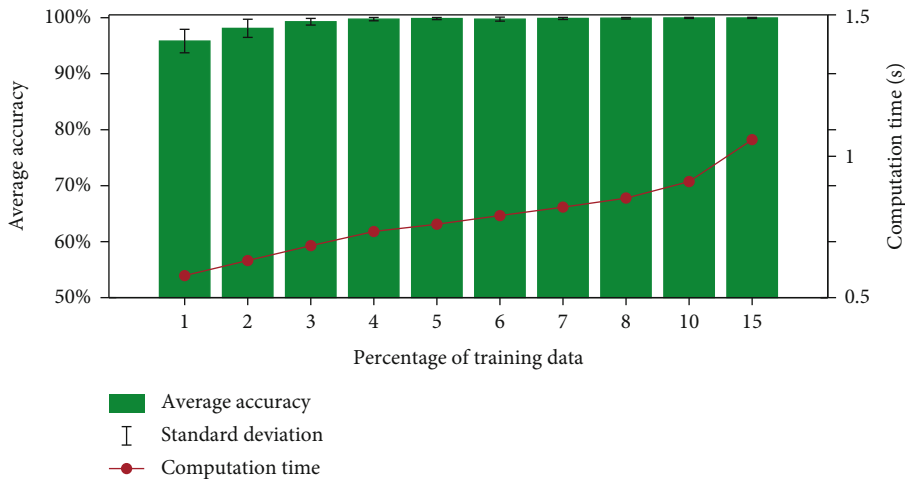
FIGURE 11: Diagnostic results of parallel Cr-SF with different percentages of training data.

3.2. Gear Data Verification and Analysis. In this experiment, the vibration data is collected from the driving end of the planetary gearbox on the test bench, as shown in Figure 9. The test bench is composed of a motor with a rated speed of 1500 rpm, a planetary gearbox with three planetary gears, a multichannel data acquisition system, a three-way acceleration sensor, and a tachometer. In order to increase the interference of the environment, the test-bed is placed in an assembly workshop, and the base of the test-bed has no shock absorber. This test simulates four health conditions
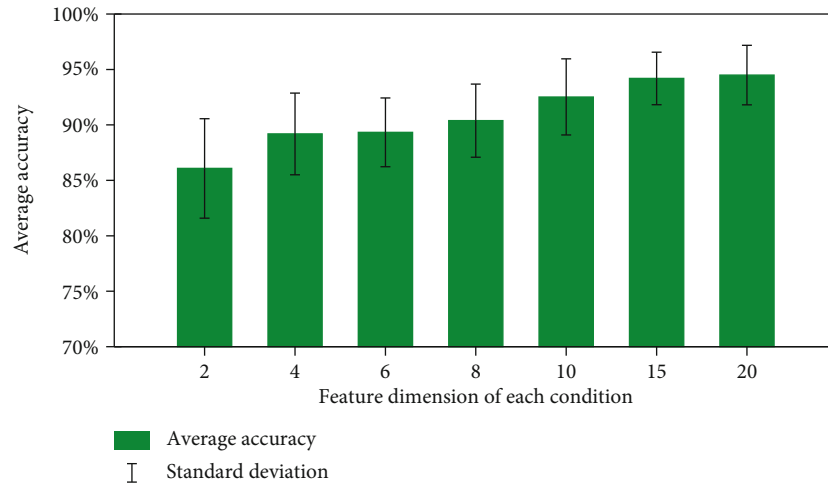
FIGURE 12: Diagnostic results of parallel SF with different feature dimensions of each condition.
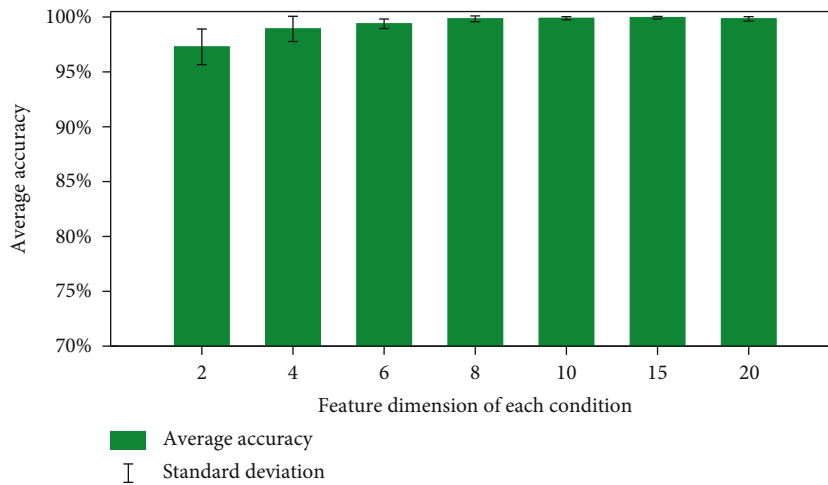

FIGURE 13: Diagnostic results of parallel Cr-SF with different feature dimensions of each condition.

of planetary gears, namely, normal working condition (NC), planetary gear wear fault (WF), planetary gear broken tooth (BT), and compound fault of broken tooth and wear (CF). The sampling frequency is set as 12.8 kHz. There are 600 samples under each health condition. Each test data includes 2400 sample points.

The diagnostic results using parallel SF and Cr-SF with various percentage of training data are shown in Figures 10 and 11. In this experiment, the parameter settings are consistent with the previous verification. The diagnostic results show a pattern similar to that in the previous section. With the increase of the percentage of training data, the accuracy increases gradually. The diagnostic results of parallel SF were significantly worse than those of parallel Cr-SF. Taking the training percentage of 3% as an example, the accuracy of parallel Cr-SF is 99.28% ± 0.59%, but the accuracy of parallel SF is only 80.17% ± 5.3%. When the training percentage is greater than 3%, the accuracy is above 99%. The diagnostic results show that the proposed method can ensure higher diagnosis accuracy and robustness with fewer samples.

Figures 12 and 13 show the changes of accuracy and standard deviation of the two methods with the increase of feature dimension of each condition. The percentage of training samples was 10%. When only two features are used to express the fault condition, the accuracy of the proposed method can reach 97.28%, and the standard disassembly is only 1.62%, which is much better than parallel SF. When the feature dimension is equal to 8, the accuracy can reach 99.83%.

4. Discussion on Feature and Weight Visualization

In order to further intuitively explain the performance of the proposed method and its feature extraction process, the visualization of weights and features are studied in case of 10% of training samples.

As shown in Figure 14, it is obvious that the learning features of Cr-SF are sparser, and there are only a few principal components in the features, which can explain why the
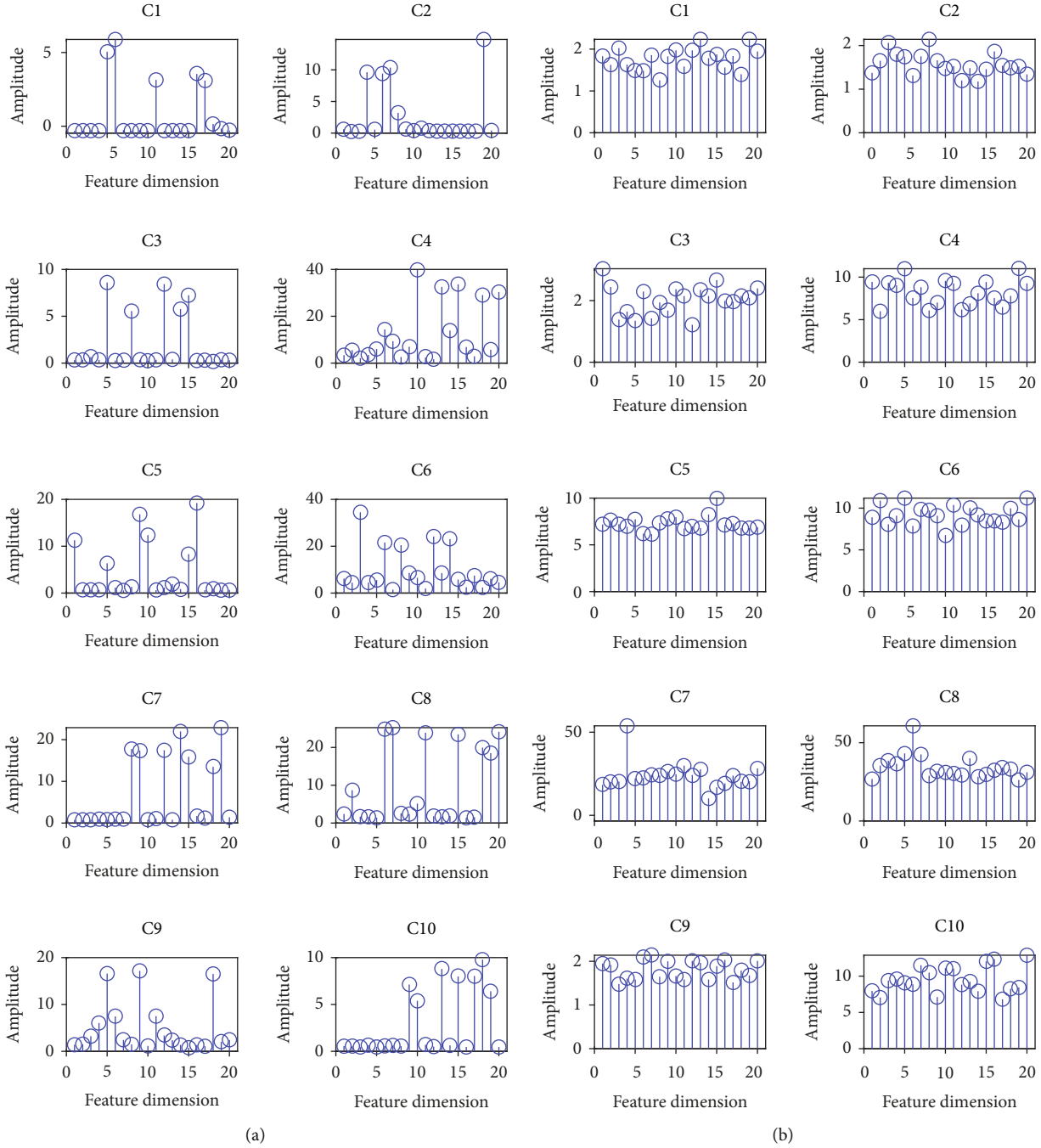
FIGURE 14: Learned feature vectors of each condition: (a) parallel Cr-SF and (b) parallel SF.

accuracy of the proposed method does not change signifi-cantly after the feature number is 8; all the main features have been selected in this case. The value of features of SF has little change and performs poor sparsity. At this case, more features need to be selected to express the main fault information to achieve high diagnostic accuracy. Therefore, the feature learning process of Cr-SF performs stronger robustness and better sparsity, which is the key to ensure the accuracy and robustness of the proposed algorithm in the diagnosis process.

In order to further explain the sparsity of features, Fou-rier transform is carried out on the learned filters to obtain the corresponding spectrum, as shown in Figure 15. It can be seen that the frequency components of the filters learned by the proposed method are clearer, and the energy of the filters is concentrated in a specific frequency range. How-ever, the noise interference of the filters learned by SF is obvious. Compared with Cr-SF, there are many noise distur-bances, especially in the low frequency band. It should be noted that some filters learned by Cr-SF contains high-
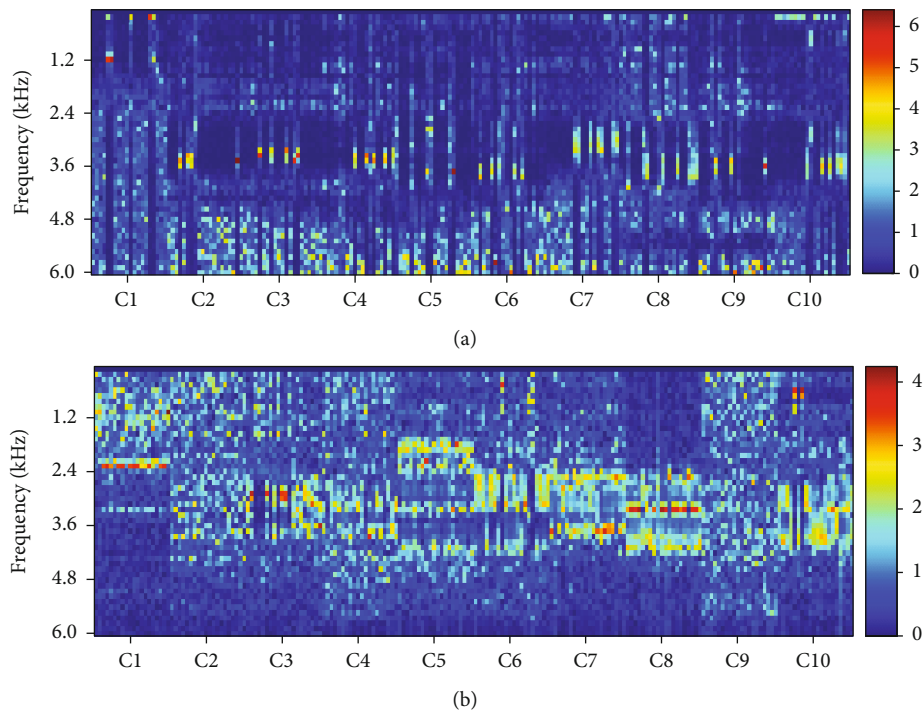
(a)

(b)

FIGURE 15: Learned weights of each condition: (a) parallel Cr-SF and (b) parallel SF.

frequency noise. However, we find that the peak value of characteristic frequency in these filters is small. The corresponding feature value is very small. The characteristic amplitudes corresponding to these filters are close to 0. Therefore, these features can be discarded in the process of feature selection.

5. Conclusions

This paper presents a parallel network structure based on the Cr-SF, a minimum entropy unsupervised learning method. The proposed method solves the problem that the detection system is required to retrain the whole model when new faults are added in real industrial application. The experimental verification is carried out using the fault data of bearing and planetary gearbox. The results confirm that the proposed method can ensure the sparsity and training robustness of the feature extraction process and performs superior diagnostic accuracy, stability and computational efficiency comparing with the traditional methods. In the proposed method, fault feature training and classifier training are separated, and the training of each fault type is implemented independently. When a new fault is added, it only needs to extract the features of the new fault and then input them into the classification for retraining.

The limitation of the proposed method is that there is no clear judgment principle in the feature selection process. In some cases, the magnitude of the amplitude does not indicate the importance of the feature, especially in the strong interference environment. Therefore, the future works of authors will focus on more advanced feature selection methods to further improve the performance of the proposed algorithm.

Data Availability

The data used to support the findings of this study are available from the corresponding author upon request.

Conflicts of Interest

The authors declare that they have no conflicts of interest.

Acknowledgments

References

[1] X. Li, J. Cheng, H. Shao, K. Liu, and B. A. Cai, "A fusion CWSMM-based framework for rotating machinery fault diagnosis under strong interference and imbalanced Case," *IEEE Transactions on Industrial Informatics*, p. 1, 2021.

[2] Z. He, H. D. Shao, Z. Y. Ding, H. K. Jiang, and J. S. Cheng, "Modified deep auto-encoder driven by multi-source parameters for fault transfer prognosis of aero-engine," *IEEE Transactions on Industrial Electronics*, vol. 69, no. 1, pp. 845–855, 2022.

[3] H. Chen, B. Jiang, and S. Ding, "Data-driven fault diagnosis for traction systems in high-speed trains: a survey, challenges, and perspectives," *IEEE Transactions on Intelligent Transportation Systems*, pp. 1–17, 2020.

[4] Z. Z. Zhang, S. M. Li, J. T. Lu, J. R. Wang, and X. X. Jiang, "A novel intelligent fault diagnosis method based on fast intrinsic

component filtering and pseudo-normalization," *Mechanical Systems and Signal Processing*, vol. 145, article 106923, 2020.

[5] S. S. Ji, B. K. Han, Z. Z. Zhang, and J. R. Wang, "Parallel sparse filtering for intelligent fault diagnosis using acoustic signal processing," *Neurocomputing*, vol. 462, pp. 466–477, 2021.

[6] C. Li, S. H. Zhang, Y. Qin, and E. Estupinan, "A systematic review of deep transfer learning for machinery fault diagnosis," *Neurocomputing*, vol. 407, pp. 121–135, 2020.

[7] R. Q. Yan, X. F. Chen, P. Wang, and M. Darian, "Deep learning for fault diagnosis and prognosis in manufacturing systems," *Computers in Industry*, vol. 110, pp. 1-2, 2019.

[8] F. Jia, Y. G. Lei, J. Lin, X. Zhou, and N. Lu, "Deep neural networks: a promising tool for fault characteristic mining and intelligent diagnosis of rotating machinery with massive data," *Mechanical Systems and Signal Processing*, vol. 73, pp. 303–315, 2016.

[9] J. R. Wang, S. M. Li, Z. H. An, X. Jiang, W. Qian, and S. Ji, "Batch-normalized deep neural networks for achieving fast intelligent fault diagnosis of machines," *Neurocomputing*, vol. 329, pp. 53–65, 2019.

[10] G. Li, C. Deng, and J. Wu, "Sensor data-driven bearing fault diagnosis based on deep convolutional neural networks and S-transform," *Sensors*, vol. 19, no. 12, p. 2750, 2019.

[11] H. Shao, H. Jiang, H. Zhang, W. Duan, T. C. H. Liang, and S. H. P. Wu, "Rolling bearing fault feature learning using improved convolutional deep belief network with compressed sensing," *Mechanical Systems and Signal Processing*, vol. 100, pp. 743–765, 2018.

[12] H. Shao, H. Jiang, H. Zhang, T. Liang, and S. H. P. Wu, "Electric locomotive bearing fault diagnosis using a novel convolutional deep belief network," *IEEE Transactions on Industrial Electronics*, vol. 65, no. 3, pp. 2727–2736, 2018.

[13] H. Shao, H. Jiang, H. Zhao, and F. Wang, "A novel deep autoencoder feature learning method for rotating machinery fault diagnosis," *Mechanical Systems and Signal Processing*, vol. 95, pp. 187–204, 2017.

[14] Y. B. Li, F. Liu, S. Wang, and J. Yin, "Multiscale symbolic Lempel-Ziv: an effective feature extraction approach for fault diagnosis of railway vehicle systems," *IEEE Transactions on Industrial Electronics*, vol. 17, no. 1, pp. 199–208, 2021.

[15] Y. B. Li, Y. Ren, H. Zheng, Z. Deng, and S. Wang, "A novel cross-domain intelligent fault diagnosis method based on entropy features and transfer learning," *IEEE Transactions on Instrumentation and Measurement*, vol. 70, pp. 1–14, 2021.

[16] Y. B. Li, S. Wang, N. Li, and Z. Deng, "Multiscale symbolic diversity entropy: a novel measurement approach for time-series analysis and its application in fault diagnosis of planetary gearboxes," *IEEE Transactions on Industrial Informatics*, vol. 18, no. 2, pp. 1121–1131, 2022.

[17] Z. Wang, X. He, B. Yang, and N. Li, "Subdomain adaptation transfer learning network for fault diagnosis of roller bearings," *IEEE Transactions on Industrial Electronics*, p. 1, 2021.

[18] S. X. Jia, J. R. Wang, X. Zhang, and B. K. Han, "A weighted subdomain adaptation network for partial transfer fault diagnosis of rotating machinery," *Entropy*, vol. 23, no. 4, p. 424, 2021.

[19] Y. Lei, F. Jia, J. Lin, S. Xing, and S. Ding, "An intelligent fault diagnosis method using unsupervised feature learning towards mechanical big data," *IEEE Transactions on Industrial Electronics*, vol. 63, no. 5, pp. 3137–3147, 2016.

[20] Y. H. Chang, J. L. Chen, C. Qu, and T. Y. Pan, "Intelligent fault diagnosis of wind turbines via a deep learning network using parallel convolution layers with multi-scale kernels," *Renewable Energy*, vol. 153, pp. 205–213, 2020.

[21] S. Guo, T. Yang, H. C. Hua, and J. W. Cao, "Coupling fault diagnosis of wind turbine gearbox based on multitask parallel convolutional neural networks with overall information," *Renewable Energy*, vol. 178, pp. 639–650, 2021.

[22] J. Ngiam, Z. Chen, S. A. Bhaskar, P. W. Koh, and A. H. Ng, "Sparse filtering," *Advances in Neural Information Processing Systems*, pp. 1125–1133, 2011.

[23] F. M. Zennaro and K. Chen, "Towards understanding sparse filtering: a theoretical perspective," *Neural Networks*, vol. 98, pp. 154–177, 2018.

[24] Z. Z. Zhang, S. M. Li, J. R. Wang, Y. Xin, and Z. H. An, "General normalized sparse filtering: a novel unsupervised learning method for rotating machinery fault diagnosis," *Mechanical Systems and Signal Processing*, vol. 124, pp. 596–612, 2019.

[25] Z. Z. Zhang, S. M. Li, J. T. Lu, Y. Xin, and H. J. Ma, "Intrinsic component filtering for fault diagnosis of rotating machinery," *Chinese Journal of Aeronautics*, vol. 34, no. 1, pp. 397–409, 2021.

[26] Z. Z. Zhang, S. M. Li, J. T. Lu, J. R. Wang, and X. X. Jiang, "A novel unsupervised learning method based on cross-normalization for machinery fault diagnosis," *IEEE Access*, vol. 8, pp. 92407–92417, 2020.

Research Article

Series Arc Fault Detection in a Low-Voltage Power System Based on CEEMDAN Decomposition and Sensitive IMF Selection

Guixia Fu,[1] **Guizhen Chen,**[1] **Wei Wang,**[1] **Qinbing Wang,**[2] **and Guofeng Zou** ORCID[1]

[1]*School of Electrical and Electronic Engineering, Shandong University of Technology, Zibo, Shandong 255049, China*
[2]*Gaoqing County Power Supply Company, State Grid Shandong Electric Power Corporation, Gaoqing, Shandong 255000, China*

Correspondence should be addressed to Guofeng Zou; zgf841122@163.com

In the series arc fault detection of a low-voltage distribution network, the features of the fault current signal are easily submerged and arc fault features are difficult to be represented, which greatly increases the difficulty of fault arc detection based on current signals. To solve these problems, a series arc fault detection method combining CEEMDAN decomposition and sensitive IMF selection is proposed. In this paper, the CEEMDAN algorithm is first applied to complete decomposition of the arc current in series faults. Then, 12 feature indicators of the arc current are defined and the frequency band division of the IMF component is realized according to the kurtosis index and energy feature which are more sensitive. The time window-based feature calculation method is proposed to obtain the local features of the time scale of each high-frequency IMF component. Accurate selection of sensitive IMF components is realized by comparing feature indexes such as the variance and root mean square value. Finally, for the current feature set, the second dimension reduction is realized by the subspace transformation algorithm and the series arc fault detection is realized based on the SVM. The actual experiments show that the optimal detection accuracy of the proposed method is 91.67% and the average accuracy of 10 crossvalidation experiments is 88.33%. It shows that the proposed sensitive IMF selection method can effectively capture the fault component signals in the current and the proposed fault feature description method has good representation and discrimination ability.

1. Introduction

In the low-voltage distribution network, arc fault is easily caused by line insulation damage and loose terminal. Local high temperature associated with arc fault can easily lead to electrical fire accident. Arc faults are divided into series arc, parallel arc, and ground arc. When a series arc fault occurs, it is equivalent to a series of time-varying resistor in the circuit, which will easily lead to the fault current similar to the load current. Sometimes, the waveform characteristics of the fault current are difficult to distinguish from the characteristics of the nonlinear load current [1–3]. It is the above factors that bring great difficulties to series arc detection and make it become a hot and difficult research area of arc detection [4, 5].

Arc fault detection methods can be divided into two categories: (1) arc detection based on the physical characteristics of arc light, arc sound, and temperature and (2) arc

detection based on time-frequency domain analysis of the arc voltage or current signal [6, 7]. Due to the randomness of the location of the arc fault, the first detection method is mostly used in electrical switchgear and its application in line arc fault detection is limited [8, 9]. The time-frequency analysis method based on current and voltage signals of monitoring points has become a research hotspot in arc fault detection. The current detection method can protect the downstream branch arc fault by installing the monitoring point in the upstream of the line. Therefore, compared with the voltage detection method [10], its applicability and flexibility is stronger and more favored by researchers [11, 12].

Fourier transform is widely used in early arc fault detection [13]. The essence of this method is to decompose the electrical signal into the superposition sum of multifrequency sine waves, which transform the time domain problem into the frequency domain for analysis. Fourier transform realizes the correlation between the time domain

and frequency domain of electrical signals, but signal analysis can only be implemented independently in the time domain or frequency domain, not simultaneously. Due to the sound adaptability, wavelet transform can realize multi-scale time-frequency analysis of the signal, which has been applied in the analysis of mechanical fault signals [14] and arc fault signals [15, 16]. Wang et al. [17] proposed a hybrid time and frequency analysis and fully connected neural network- (HTFNN-) based method to identify the series AC arc fault. Firstly, the samples are roughly divided into the resistive category, capacitive-inductive category, and switching category. Then, in each category, a separate fully connected neural network is used to identify the fault and the method achieves high identification accuracy. Chu et al. [18] proposed a novel high-frequency coupling sensor for extracting the features of low-voltage series arc faults. In the method, high-frequency feature signals under different loads are collected and transformed into two-dimensional feature gray images, which are used to train the convolutional neural network to realize series arc fault detection. Experiments show that the method is stable and universal.

Hilbert-Huang transform (HHT) [19] is a typical non-linear and nonstationary signal processing method, and its key step is empirical mode decomposition (EMD). EMD can decompose complex signals adaptively into several intrinsic mode functions (IMF), but this method has a serious mode mixing problem, which affects the performance of HHT [20]. Therefore, Wu and Huang [21] proposed the ensemble empirical mode decomposition (EEMD). By introducing Gaussian white noise with uniform frequency distribution into the signal to be decomposed, EEMD overcomes the problem of intermittent signal and avoids mode mixing. However, due to the interference of white noise, the reconstructed signal is easy to be distorted. Cheng et al. [22] proposed an enhanced periodic mode decomposition (EPMD) algorithm for accurate extraction of periodic pulses from rolling bearing composite fault signals, which effectively improved the accuracy of bearing fault diagnosis.

In 2011, Torres et al. [23] proposed the complete ensemble empirical mode decomposition with adaptive noise (CEEMDAN), which further improves the accuracy and completeness of decomposition signals and effectively overcomes the problem of mode mixing. However, the CEEMDAN algorithm has not been applied in arc current signal analysis. CEEMDAN can achieve complete signal decomposition, but in arc fault detection, usually, only a few IMF components are sensitive to the arc fault and can reflect the characteristics of the fault arc. Most of the other IMF components are invalid for arc detection and even contain more interference information. Therefore, it is extremely difficult to extract fault identification features from all IMF components obtained by CEEMDAN decomposition and the interference features easily affect the accuracy of arc fault detection.

Based on the above analysis, in this paper, a series arc fault detection method based on CEEMDAN decomposition and sensitive IMF selection is proposed. The CEEMDAN algorithm is used to decompose the current signal and obtain the complete IMF components. Then, this paper proposes a strategy to automatically select the sensitive IMF

from the all IMF components. In this strategy, the kurtosis index and energy feature are taken as the basis to determine the fundamental frequency boundary and achieve frequency division. For high-frequency IMF, we design a local feature extraction method based on the time window. Using the number of fundamental frequency periods as the interval, IMF in the high-frequency band is divided into some non-overlapping time windows and the feature indexes of the signal are calculated in each time window. The sensitive IMF component with the strongest discriminability is selected adaptively based on the feature indexes such as variance and root-mean-square amplitude. After sensitive IMF selection, the local features of the best IMF component are used as the feature description of the current signal, which can be used to construct the current feature database. Finally, the subspace transformation algorithm is used to implement secondary dimension reduction for current features and the support vector machine (SVM) is used to the series arc fault detection. Experimental results show that the combination of CEEMDAN decomposition and sensitive IMF selection strategy, as well as the local feature construction method based on the time window, can effectively capture the discriminant features of the series arc, which realize the reliable detection of the arc fault.

The main highlights of the proposed method are generalized as follows:

(1) To obtain complete decomposition results of fault current signals, the CEEMDAN decomposition algorithm is first applied to current signal decomposition

(2) To extract the strongest discriminative IMF component, a method of frequency division and an accurate selection method of sensitive IMF are proposed

(3) To overcome the difficulty in fault feature representation, a local feature calculation method based on the time window is proposed and 12 feature indexes are defined to express fault features

(4) To better improve the effectiveness of series arc fault features and fault detection accuracy, this paper adopts subspace transformation for feature compression and SVM for fault detection

The remainder of this paper is structured as follows: in Section 2, the CEEMDAN algorithm is described. The feature calculation methods of the current signal are illustrated in Section 3. In Section 4, the selection method of the sensitive IMF component and the series arc fault detection method are proposed. Detailed experiments and analyses are performed in Section 5. In Section 6, the conclusions are drawn.

2. CEEMDAN Algorithm

Mode mixing refers to the phenomenon that a single IMF component contains multiple components with different frequencies or the same frequency component is decomposed into different IMF components. Mode mixing is usually

caused by the intermittency of the signal. Therefore, the EEMD algorithm introduces Gaussian white noise into the signal to be decomposed, which makes the signal become continuous at different scales and alleviates the mode mixing problem. However, the EEMD algorithm cannot completely eliminate the introduced noise interference, which makes the reconstructed signal distortion. In each stage of EMD decomposition of signals, the CEEMDAN algorithm adaptively adjusts the noise coefficient to generate Gaussian noises with different SNR introduced into the signals to be decomposed, which can avoid mode mixing and eliminate the interference of false information. The algorithm steps are as follows:

(1) Gaussian white noise $n_i(t)$ is added to the original signal $x(t)$. The signal with added noise is $x(t) + \gamma_0 n_i(t)$, where γ_0 is the noise coefficient. EMD is used to perform I decomposition for the signal with noise. The first IMF component $\mathrm{IMF}_1(t)$ and the corresponding residual component $r_1(t)$ of CEEMDAN are obtained through integration averaging:

$$\mathrm{IMF}_1(t) = \frac{1}{I}\sum_{i=1}^{I}\mathrm{IMF}_{i1}(t),$$
$$r_1(t) = x(t) - \mathrm{IMF}_1(t),$$
(1)

where I is the number of decomposition

(2) Assume that $\mathrm{EMD}_j(\cdot)$ is the jth mode function of EMD decomposition. Decompose the signal $r_1(t) + \gamma_1 \cdot \mathrm{EMD}_1[n_i(t)]$ to obtain the second IMF component of CEEMDAN:

$$\mathrm{IMF}_2(t) = \frac{1}{I}\sum_{i=1}^{I}\mathrm{EMD}_1(r_1(t) + \gamma_1 \cdot \mathrm{EMD}_1[n_i(t)]) \quad (2)$$

(3) Calculate the k-order residual component:

$$r_k(t) = r_{k-1}(t) - \mathrm{IMF}_k(t),\quad (3)$$

where $\mathrm{IMF}_k(t)$ is the kth IMF component. EMD decomposition is performed for the kth signal $r_k(t) + \gamma_k \mathrm{EMD}_k(n_i(t))$ until the first IMF component is obtained. On this basis, the $(k + 1)$th IMF component of CEEMDAN is calculated:

$$\mathrm{IMF}_{k+1}(t) = \frac{1}{I}\sum_{i=1}^{I}\mathrm{EMD}_1(r_k(t) + \gamma_k \cdot \mathrm{EMD}_k[n_i(t)]) \quad (4)$$

(4) The above calculation steps are repeated until the residual components can no longer be decomposed

and all K IMF components of CEEMDAN are obtained; the remaining residual $R(t)$ is

$$R(t) = x(t) - \sum_{k=1}^{K}\mathrm{IMF}_k(t).\quad (5)$$

Therefore, after decomposition, the initial signal can be expressed as

$$x(t) = \sum_{k=1}^{K}\mathrm{IMF}_k(t) + R(t).\quad (6)$$

The CEEMDAN method can realize complete reconstruction of the original signal based on noise-assisted analysis. Gaussian noises with different SNR are adjusted adaptively by noise coefficient and introduced into the signal to be decomposed, which improves the decomposition effect of EMD effectively

3. Feature Calculation of the Current Signal

Learn from the feature calculation method commonly used in mechanical fault diagnosis [24, 25], for each IMF component of the current signal; this paper defines 9 statistical feature indicators, as well as the energy feature, entropy feature, and energy entropy feature to form a 12-dimensional current feature vector. Assume that K IMF components are obtained after CEEMDAN decomposition and each component sequence contains N sampling points, i.e., $x_1, x_2, \cdots, x_i, \cdots x_N$, where i represents the ith sampling point. The 12 feature indicators are defined as follows:

The mean value is

$$\bar{X} = \frac{1}{N}\sum_{i=1}^{N}x_i.\quad (7)$$

The variance is

$$\sigma^2 = \frac{1}{N\text{-}1}\sum_{i=1}^{N}\left(x_i - \bar{X}\right)^2 \quad (8)$$

The root-mean-square value is

$$X_{RMS} = \sqrt{\frac{1}{N}\sum_{i=1}^{N}(x_i)^2}\quad (9)$$

The root amplitude is

$$X_r = \left(\frac{1}{N}\sum_{i=1}^{N}|x_i|\right)^2 \quad (10)$$

The average amplitude is

$$\bar{X}_a = \frac{1}{N} \sum_{i=1}^{N} |x_i| \tag{11}$$

The peak is

$$X_p = \max\left(|x_i|\right) \tag{12}$$

The kurtosis is

$$K = \frac{1}{N-1} \sum_{i=1}^{N} \frac{\left(x_i - \bar{X}\right)^4}{\sigma^4} \tag{13}$$

The kurtosis index is

$$K_f = \frac{K}{X_{\mathrm{RMS}}^4}. \tag{14}$$

The margin index is

$$L_f = \frac{X_p}{X_r}. \tag{15}$$

The energy feature is

$$E = \sum_{i=1}^{N} (x_i)^2. \tag{16}$$

The entropy feature is

$$H = -\sum_{i=1}^{N} P(x_i) \lg P(x_i), \tag{17}$$

where $P(\cdot)$ is the probability.

The energy entropy features are

$$H_{EN} = -\sum_{i=1}^{N} P_i \lg P_i, \tag{18}$$

where $P_i = E_i / \sum_{i=1}^{K} E_i$ and E_i represents the energy of the ith IMF component.

After the above calculation, each IMF component containing N sampling points is transformed into a 12-dimensional eigenvector, which reflects the overall state of the signal sequence.

4. Selection of the Sensitive IMF Component and Series Arc Fault Detection

4.1. Fundamental Frequency Determination and Frequency Division. The 12 feature indexes defined in this paper reflect the characteristics of IMF components at different frequencies, among which the kurtosis index and energy feature have strong sensitivity to current signal fluctuations. Therefore, based on these two indicators, this paper divides the
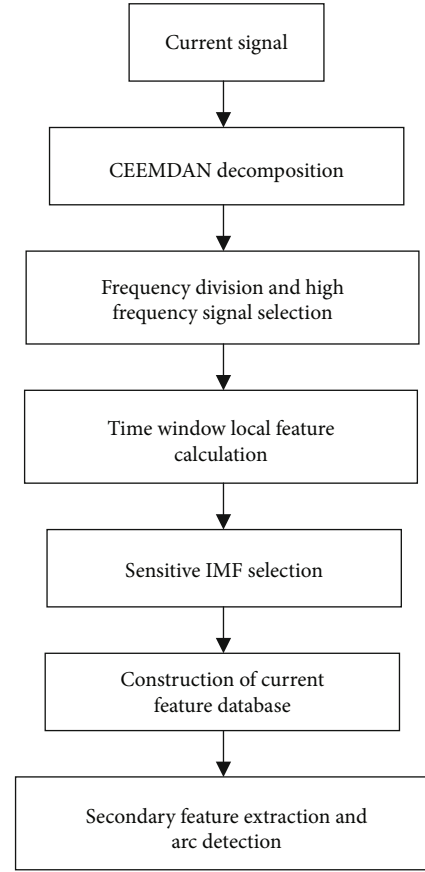

Figure 1: The overall flow chart of the proposed algorithm.

frequency bands for all IMF components. In our study, it is found that when the kurtosis index is the minimum value and the energy feature is the maximum value, the corresponding IMF component has the smallest fluctuation range and contains the most information. This component is the fundamental frequency component of the arc current signal, which is selected as the boundary of division. Therefore, the IMF component above this frequency is the high-frequency signal and the IMF component below this frequency is the low-frequency signal.

Since the current that causes the arc fault is usually a high-frequency signal, so after frequency division, feature index calculation and feature extraction only need to be carried out for the initially selected high-frequency signals. It can not only reduce the complexity of feature index calculation, feature extraction, and fault detection but also avoid the interference of low-frequency signals and improve the accuracy of arc detection.

4.2. Local Feature Calculation and Selection of Sensitive IMF Components. The global feature obtained from all N sampling points of IMF component data participating in index calculation can reflect the overall change of signals, which reflects the characteristics of signals of different frequency components in a macroscopic view. In the high-frequency band, the global features of some IMF components with similar frequencies are almost the same and the crucial features

Schematic diagram of series fault arc generation circuit
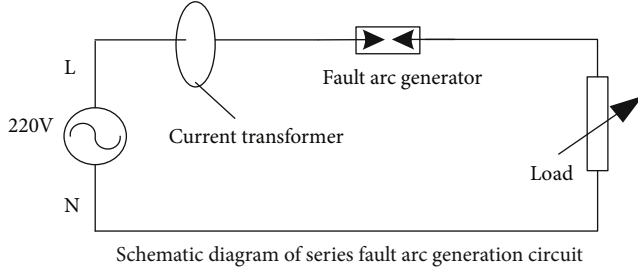
(a) Schematic diagram of the series fault arc generation circuit
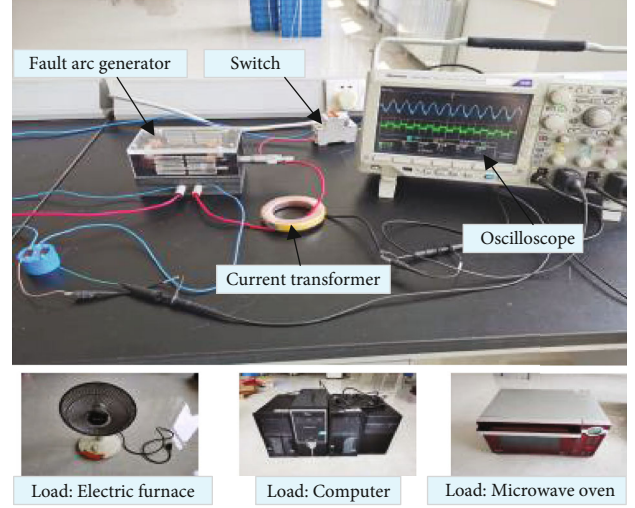
(b) Series fault arc generation circuit

FIGURE 2: Series fault arc generation platform.

that distinguish fault current signals are easily covered up. Therefore, from the microviewpoint that the feature indexes need to fully reflect the local changes of the arc current signal, a calculation method of local feature indexes based on the time window is proposed. Then, the most sensitive IMF component is accurately selected from the high-frequency IMF components based on the time window local features. The algorithm steps are as follows:

(1) Determine the period number M of the fundamental frequency IMF

(2) According to period number M, the high-frequency IMF components are divided into M nonoverlapping time windows, namely, $\text{IMF}_1^i, \text{IMF}_2^i, \cdots, \text{IMF}_M^i$, where i represents the ith IMF high-frequency component

(3) For M time windows of the ith IMF component, 12 feature values are calculated according to the index definition formula, e.g., the feature of the jth window $F_j^i = [\bar{X}, \sigma^2, X_{\text{RMS}}, X_r, \bar{X}_a, X_p, K, K_f, L_f, E, H, H_{EN}]$. Therefore, the feature formed by the ith IMF component is $M \times 12$ dimensions, i.e., $F^i = [F_1^i, F_2^i, \cdots, F_M^i]$

(4) The variance σ^2, root mean square value X_{RMS}, root amplitude X_r, average amplitude $\bar{X}_a$, energy feature E, and energy entropy feature H_{EN} of each time window in the IMF component are selected as the judgment indexes

If the fluctuation of the above judgment indexes in the front and back time windows (such as the jth and $(j+1)$th windows) is less than the threshold θ, it indicates that the signals in each window of the IMF component are stable. That is, the IMF does not contain the current information causing the fault arc.

If the judgment indexes in the front and back time windows (such as the jth and $(j+1)$th windows) have obvious

TABLE 1: Current dataset under different loads.

Load type	Normal data (group)	Fault data (group)
Electric furnace (400 W)	10	30
Electric furnace (800 W)	10	30
Computer	10	30
Microwave oven	10	30

jump changes and the jump amplitude is greater than or equal to the threshold θ, it indicates that the signal in the IMF component is not stable. That is, the IMF contains the current information causing the fault arc.

(5) Through above calculation and comparison, the IMF component with the largest jump amplitude is selected from the IMF components whose jump value of the feature indexes in the front and back time windows exceeded the threshold θ, which is the sensitive IMF component. So, this component has the strongest discrimination in the series arc fault detection

Local features with periodicity are captured by local feature calculation based on the time window, which can express the signal change of the time scale in more detail. It has obvious advantages and distinct degree for analyzing the high-frequency signal fluctuation caused by the arc fault. Based on this work, the selected sensitive IMF component can better describe the key features of signals and improve the accuracy of arc fault detection.

4.3. Series Arc Fault Detection. After the CEEMDAN decomposition, sensitive IMF selection, and local feature calculation, the feature information of the best IMF component in
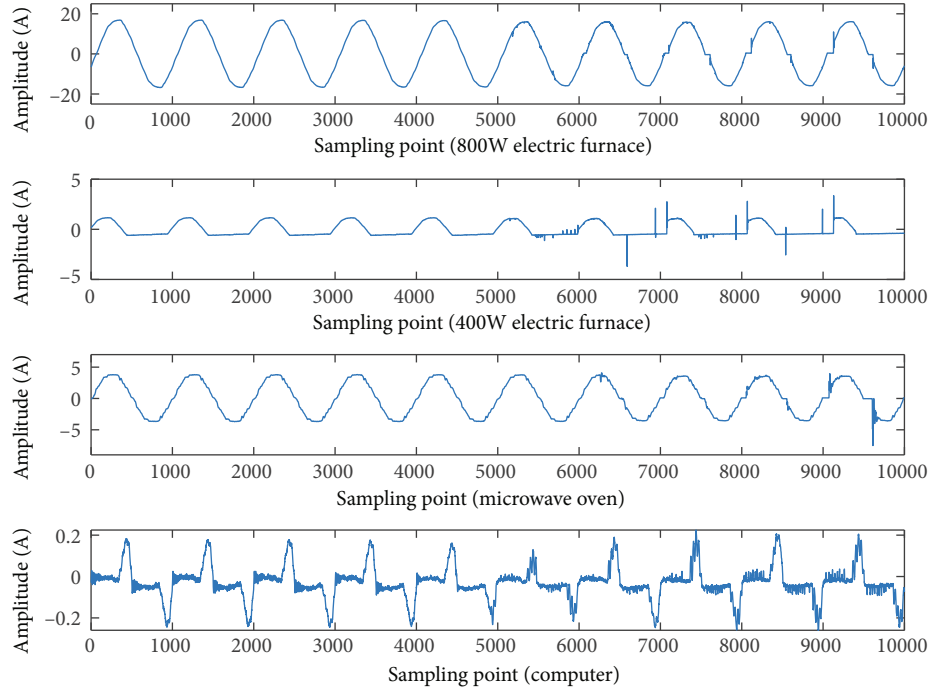
FIGURE 3: Fault arc current waveforms under different loads.

the arc current is obtained. However, these features still contain a lot of redundant information, even interference information. Therefore, to improve the discriminant ability of the features, it is very important to perform secondary feature extraction and dimension reduction for the preliminary arc current features.

Subspace mapping is to map feature vectors from the original space to the new space by mathematical transformation, and the feature vectors in the new space have lower dimension and more significant discriminant ability. Now, the classic subspace feature extraction methods in machine learning include PCA, LDA, ICA, KPCA, and KLDA [26]. In this work, the linear subspace mapping PCA and LDA algorithms and the nonlinear subspace mapping KPCA and KLDA algorithms are used for the secondary extraction and dimension reduction of arc current features.

The support vector machine (SVM) [27] is a typical binary classifier, which has unique advantages in solving small sample, nonlinear, and high dimension pattern recognition problems. It can mine the hidden decision information of sample features to the maximum extent, and it is widely used in the field of fault diagnosis. Therefore, in this paper, the SVM is selected as the classifier of series arc fault detection.

In summary, the overall flow of the proposed algorithm is shown in Figure 1.

5. Experiment and Analysis

5.1. Current Signal Acquisition Platform.
The circuit principle of the series fault arc generation platform is shown in Figure 2. The input voltage is 220 V and LPCT with a bandwidth of 200 kHz is used as the current sensor. The arc fault

generator uses a copper electrode with a diameter of 10.0 mm as the moving contact and a graphite electrode with a diameter of 8.0 mm as the reference static contact.

5.2. Current Dataset Construction.
Based on the fault arc generation circuit shown in Figure 2, the current signal is collected by a recording device. The sampling frequency is set to 50 kHz, and the sampling length is set to 20 ms. The current dataset constructed under different loads is shown in Table 1.

Considering the load in the actual circuit can be divided into three types: pure resistor load, resistor-inductance load, and nonlinear load. The 800 W electric furnace is selected as the pure resistor load. When the furnace works at 400 W, it works in the state of half-wave rectification. Therefore, 800 W and 400 W electric furnaces basically cover the current characteristics of resistor loads. A computer is a nonlinear load, and its current waveform can represent most of the switching power supply loads. A microwave oven belongs to the nonlinear load with more inductance, which can represent the current characteristics of most resistor-inductance loads. The above 4 kinds of loads are commonly used household appliances with higher frequency in life and can represent most loads, with typicality. In the experiment, 10 groups of normal current data and 30 groups of fault current data are collected under each load. Figure 3 shows the comparison of current waveforms before and after the arc fault, in which the first 5 periods are fault-free signals and the last 5 periods are fault signals.

5.2.1. Training Dataset.
In the experiment, we randomly select 5 groups of normal current data and 20 groups of fault

(a) Current waveform under computer load
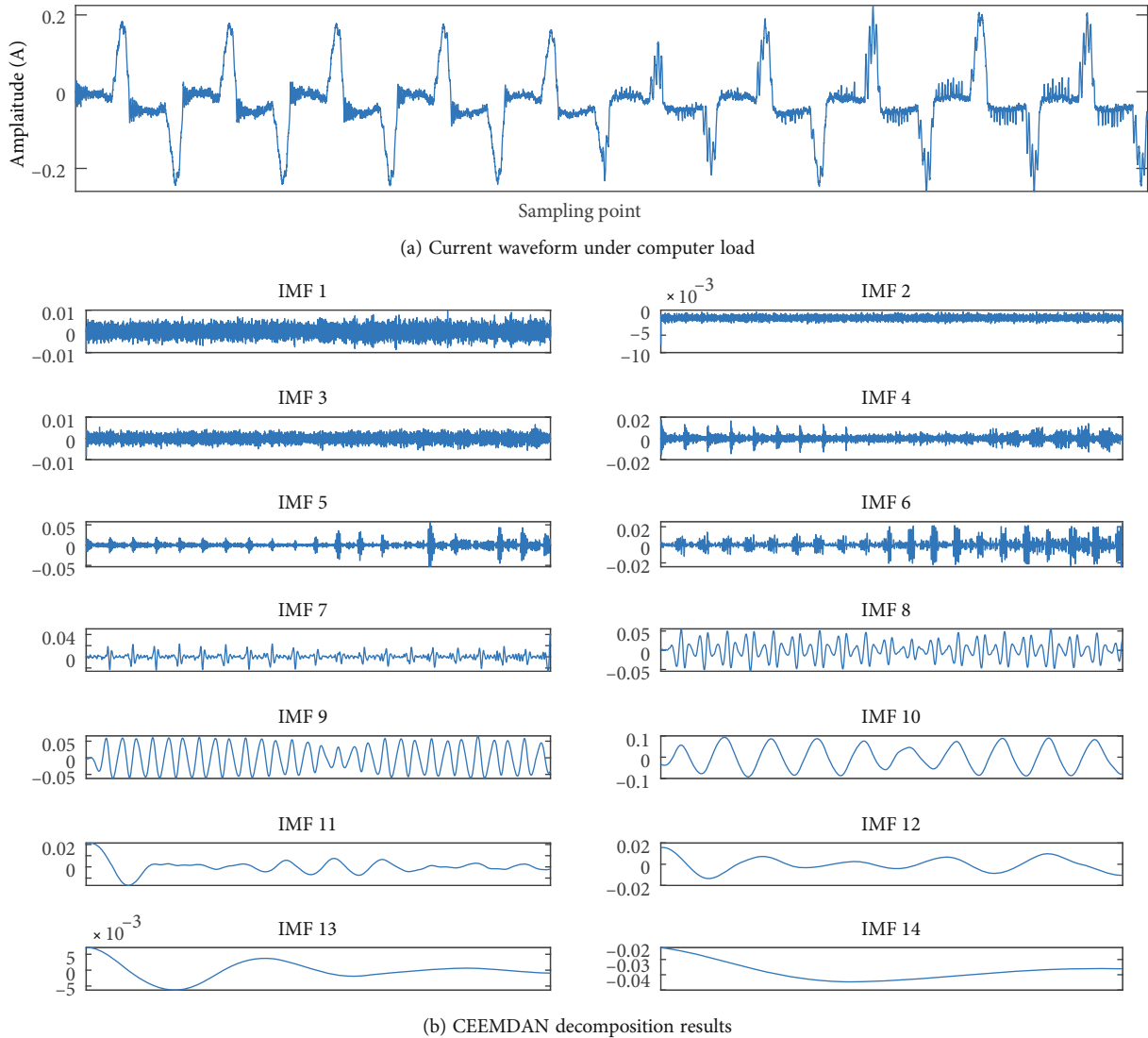

(b) CEEMDAN decomposition results

FIGURE 4: Fault arc current and decomposition results under computer load.

arc current data under 4 kinds of loads as training samples. Therefore, the training sample set size is 100.

5.2.2. Test Dataset. The remaining 5 groups of normal current and 10 groups of fault arc current under 4 kinds of loads are taken as the test sample set, and the total number of test samples is 60. In order to ensure reliable detection results, the average accuracy of the proposed algorithm is evaluated by 10 cross tests.

5.3. Decomposition Experiment of the Current Signal. In this work, the CEEMDAN algorithm is used to decompose the arc current signal and the results are shown in Figures 4 and 5. Figures 4(a) and 5(a) show the arc fault current waveform when the computer is used as the load and the microwave oven is used as the load. The first 5 periods are normal current waveform and the last 5 periods are fault current waveform.

Experiments show that the CEEMDAN algorithm adaptively decomposes the current signals under computer load

and microwave load into 14 components and realizes the detailed and complete decomposition of arc current signals in different frequency ranges, which can effectively overcome the mode mixing problem of the EMD decomposition algorithm. Observing the decomposition results of Figures 4(b) and 5(b), the component IMF10 contains 10 complete sinusoidal periodic signals whose frequency is consistent with the original current signal. Therefore, IMF10 corresponds to the fundamental frequency component. With IMF10 as the boundary, IMF1 to IMF9 are classified as high-frequency signals, and IMF11 to IMF14 are classified as low-frequency signals. The simple and clear division of each frequency band indicates that the signal decomposition is complete and no mode mixing occurs.

In addition, under computer load, high-frequency decomposition signals show that IMF4, IMF5, and IMF6 components have significant differences in the time scale, especially IMF5 and IMF6 which have good discrimination. Under microwave load, the waveforms from IMF4 to IMF7 are significantly different before and after arc occurrence,

(a) Current waveform under microwave oven load

CEEMDAN decomposition results
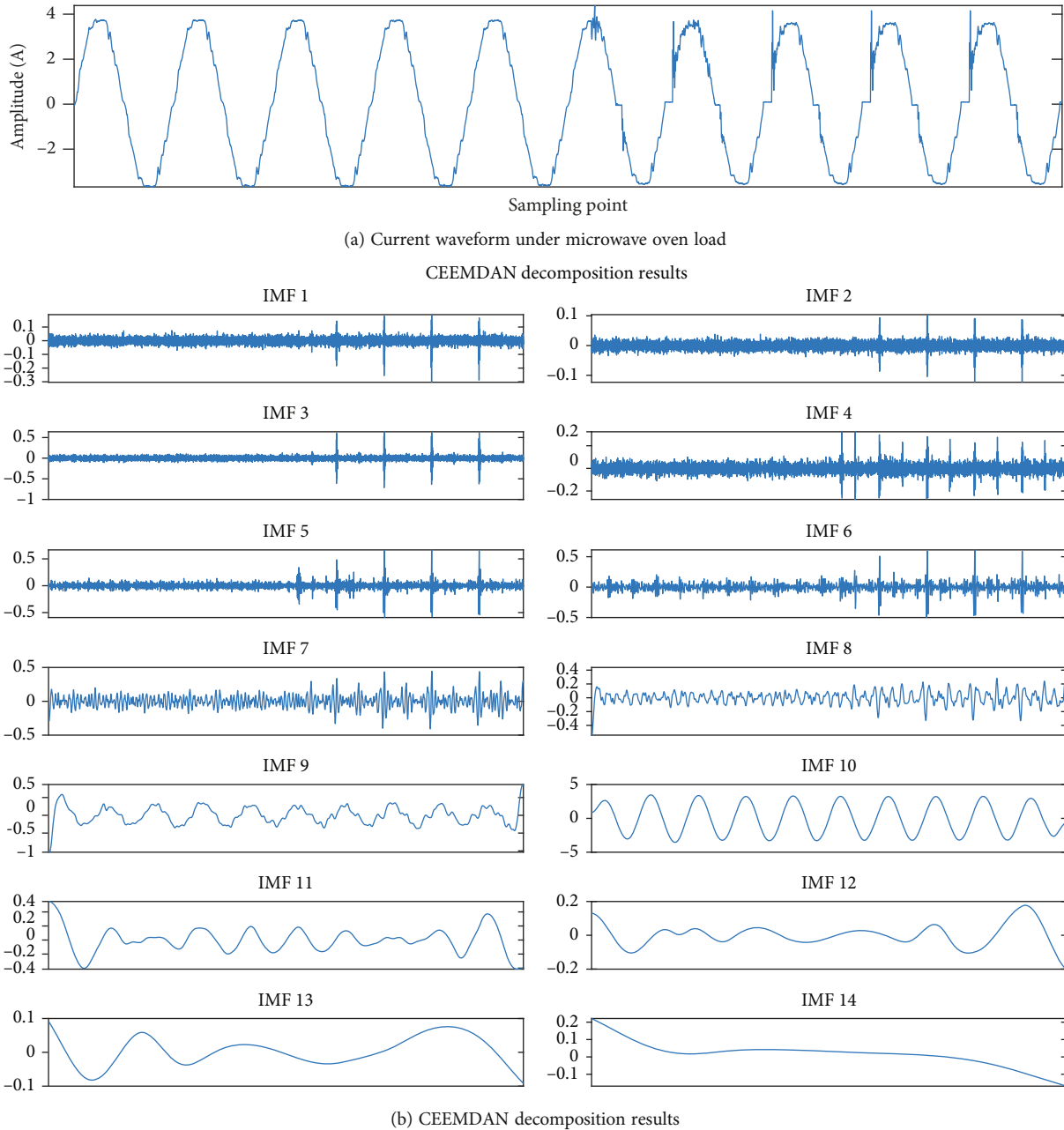

(b) CEEMDAN decomposition results

FIGURE 5: Fault arc current and decomposition results under microwave oven load.

especially IMF4 and IMF5 which have good differentiation which contributes greatly to arc fault detection.

In conclusion, the CEEMDAN decomposition strategy has a significant advantage in overcoming mode mixing and the discriminant of decomposed component signals is strong. Thus, it is feasible to select the CEEMDAN algorithm for arc current signal decomposition in this paper.

5.4. Feature Calculation of the Arc Fault Current and Sensitive IMF Selection. In order to make a better mathematical description of each IMF component and reduce the complexity of the fault detection operation, we adopt statistical feature indexes such as the mean and variance, as well as the energy feature, entropy feature, and energy entropy

feature, a total of 12 feature values as the feature description of each IMF component. Taking the decomposition results shown in Figure 5(b) as an example, 12 features of 14 IMF components are calculated and the feature matrix of 14×12 dimension is constructed as shown in Table 2.

The data in Table 2 show that the 12 feature indexes reflect different characteristics of multiscale IMF components, among which the kurtosis index and energy feature have strong discrimination. Therefore, by comparing the kurtosis index and energy feature of each IMF component, it can be clearly judged that IMF10 is the fundamental frequency component. This component can be used as the boundary of frequency division. IMF1–IMF9 correspond to the high-frequency signals and IMF11–IMF14 correspond

TABLE 2: Calculation results of global eigenvalues of different IMF components.

IMF name	Mean	Variance	Root mean square	Square root amplitude	Average amplitude	Peak
IMF1	$-1.03e-4$	$4.75e-4$	0.0218	$2.48e-4$	0.0157	0.3038
IMF2	$-1.61e-4$	$1.41e-4$	0.0119	$7.45e-5$	0.0088	0.1235
IMF3	$2.37e-5$	0.0027	0.0517	0.0010	0.0316	0.7145
IMF4	$1.02e-4$	0.0016	0.0405	$8.39e-4$	0.0290	0.3235
IMF5	$1.37e-4$	0.0047	0.0682	0.0017	0.0408	0.6673
IMF6	$-3.57e-4$	0.0065	0.0803	0.0028	0.0528	0.6124
IMF7	$2.58e-4$	0.0090	0.0950	0.0050	0.0704	0.4450
IMF8	$-2.21e-4$	0.0084	0.0918	0.0046	0.0682	0.5403
IMF9	0.0012	0.0572	0.2391	0.0369	0.1920	1.0379
IMF10	**0.0129**	**5.1018**	**2.2588**	**4.1063**	**2.2064**	**3.5617**
IMF11	-0.0034	0.0300	0.1731	0.0165	0.1286	0.5487
IMF12	$9.22e-4$	0.0043	0.0653	0.0024	0.0488	0.2004
IMF13	0.0034	0.0017	0.0415	0.0012	0.0342	0.0917
IMF14	0.0160	0.0048	0.0711	0.0027	0.0520	0.2212
IMF name	Kurtosis	Kurtosis index	Margin index	Energy feature	Entropy feature	Energy entropy feature
IMF1	19.441	$8.6e+7$	$1.23e+3$	4.754	1.099	0.000841
IMF2	11.857	$5.99e+8$	$1.59e+3$	1.407	1.211	0.00028
IMF3	45.485	$6.37e+6$	713.93	26.72	0.731	0.00376
IMF4	10.377	$3.85e+6$	385.19	16.408	1.516	0.00263
IMF5	27.132	$1.25e+6$	401.82	46.523	1.046	0.00626
IMF6	13.898	$3.34e+5$	219.92	64.537	1.438	0.00828
IMF7	5.347	$6.57e+4$	89.717	90.227	2.199	0.01071
IMF8	6.987	$9.85e+4$	116.22	84.25	1.954	0.00986
IMF9	4.039	$1.243+3$	28.16	571.788	2.336	0.04906
IMF10	**1.539**	**0.0591**	**0.8674**	**$5.102e+4$**	**3.264**	**0.02517**
IMF11	3.99	$4.44e+3$	33.18	299.706	2.796	0.03512
IMF12	3.847	$2.11e+5$	84.24	42.66	2.691	0.00541
IMF13	2.323	$7.82e+5$	78.51	17.23	3.104	0.00095
IMF14	4.5012	$1.76e+5$	81.89	50.51	2.548	0.00336

to the low-frequency signals. This conclusion is identical with that obtained from the direct observation of Figure 5(b) in Section 5.3. It further proves that the proposed frequency division strategy is effective.

The current signals collected in our experiment all contain 10 periods. Therefore, according to the local feature calculation method of the time window, each IMF component in the high-frequency band can be divided into 10 windows. Then, 12 feature indexes such as the mean and variance are calculated for each window. Table 3 shows the feature calculation results of IMF5 divided into 10 time windows in Figure 5(b).

According to the data in Table 3, by comparing the indexes such as the variance, root mean square, root amplitude, average amplitude, energy feature, and energy entropy feature, we can see that the index values of the first 5 periods are significantly different from those of the last 5 periods. It shows that this IMF component contains the information

that causes the arc fault, so this IMF component can be used as one of the candidates of sensitive IMF components.

To accurately select the most sensitive IMF component, in our experiment, the decomposition results under microwave oven load are taken as an example. We calculate the local features of the time window of 9 high-frequency components including IMF1 to IMF9. After comprehensive comparison of all feature values, it is found that the features of IMF4 in the first 5 periods and the last 5 periods had the largest variation amplitude and the strongest distinguishing significance. The feature values of other IMF components in the first and last 5 periods also changed to some extent, but the amplitude of change is lower than IMF4, and the differentiation degree is weak. Therefore, the IMF4 component is selected as the most sensitive component according to the principle of significant differentiation and maximum variation amplitude. Similarly, in the decomposition results under the computer load in Figure 4(b), IMF6 is the most sensitive component.

TABLE 3: Calculation results of local eigenvalues of IMF5 components in the time window.

| Window	Mean	Variance	Root mean square	Square root amplitude	Average amplitude	Peak
Window 1	$-5.96e-4$	0.0014	0.0372	0.00084	0.029	0.1433
Window 2	$-1.49e-4$	0.0017	0.0416	0.0011	0.033	0.1155
Window 3	$1.98e-4$	0.0015	0.0390	0.00097	0.0312	0.1363
Window 4	$3.05e-4$	0.0017	0.0416	0.0011	0.0335	0.1367
Window 5	**$3.53e-4$**	**0.0014**	**0.0381**	**0.00092**	**0.0303**	**0.1157**
Window 6	**$9.08e-4$**	**0.0046**	**0.0681**	**0.0021**	**0.0475**	**0.3939**
Window 7	$1.98e-4$	0.0079	0.0866	0.0031	0.0556	0.4836
Window 8	$-2.20e-6$	0.0090	0.0947	0.0025	0.0503	0.6613
Window 9	$5.45e-6$	0.0085	0.0924	0.0024	0.0493	0.6673
Window 10	$1.47e-4$	0.0087	0.0933	0.0025	0.0499	0.6508
Window	Kurtosis	Kurtosis index	Margin index	Energy feature	Entropy feature	Energy entropy feature
Window 1	3.127	$1.795e+6$	170.022	1.382	2.616	0.1045
Window 2	2.839	$0.951e+6$	136.19	1.728	2.951	0.1223
Window 3	2.989	$1.292e+6$	140.39	1.521	2.721	0.1118
Window 4	2.967	$0.991e+6$	121.95	1.7306	2.767	0.1224
Window 5	**2.900**	**$1.38e+6$**	**125.75**	**1.4501**	**2.792**	**0.1081**
Window 6	**9.207**	**$3.821e+5$**	**166.12**	**4.634**	**1.868**	**0.2597**
Window 7	11.549	$1.873e+5$	156.64	7.851	1.815	0.3003
Window 8	21.454	$2.66e+5$	261.49	8.974	1.277	0.3174
Window 9	22.105	$3.03e+5$	274.82	8.541	1.208	0.3120
Window 10	21.142	$1.783e+5$	261.49	8.709	1.195	0.3126
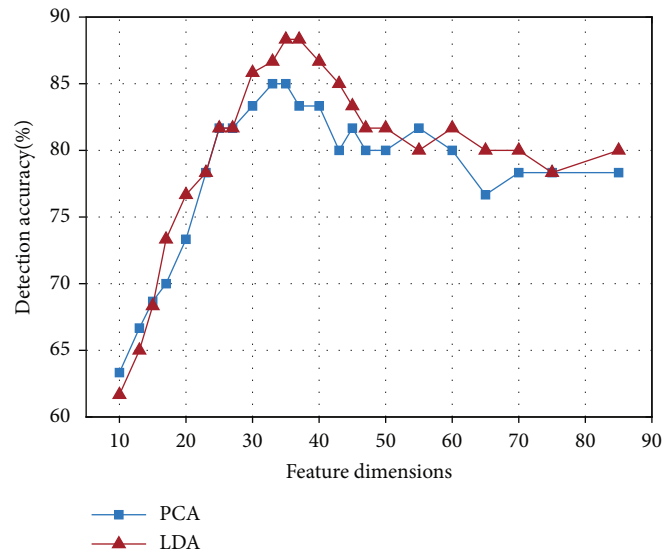
FIGURE 6: The influence of PCA and LDA feature dimensions on detection accuracy.

In summary, in this paper, we accurately select the most discriminating sensitive IMF component, and then, the fault arc current signal is characterized by 10 time windows and 12 feature indexes. Thus, the original current signal with each set of 10,000 sampling points is converted into a vector with 120 feature values. After local feature extraction of the time window, 160 groups of normal current and fault arc current data under 4 load types finally form a current feature database with a scale of 160×120.

5.5. Fault Arc Detection Experiment. The 160×120 dimension current feature database still contains some redundant
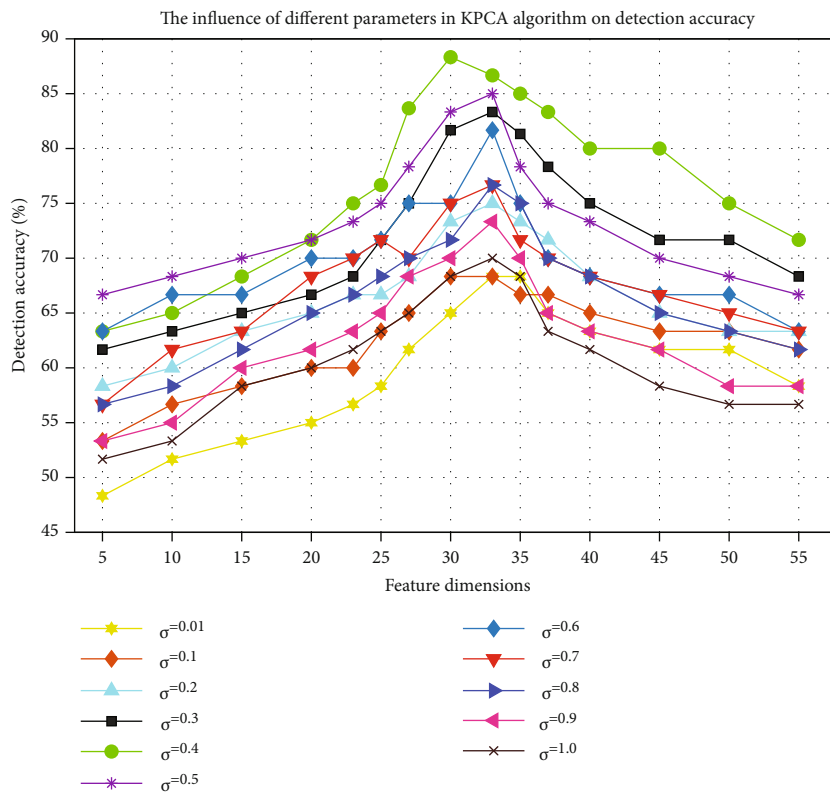
(a) The influence of different parameters in the KPCA algorithm on detection accuracy
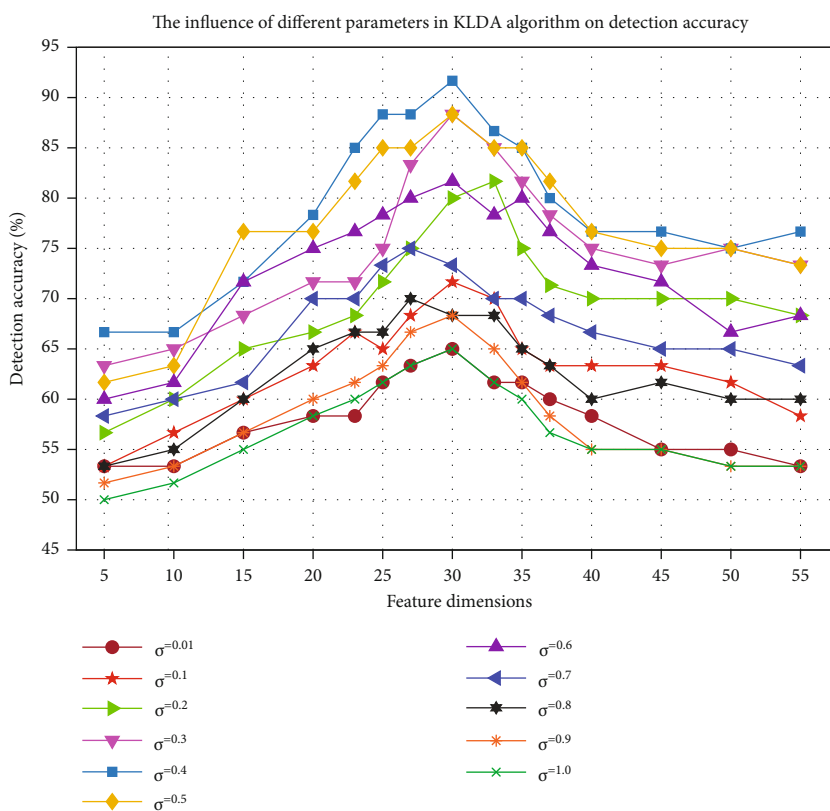
(b) The influence of different parameters in the KLDA algorithm on detection accuracy

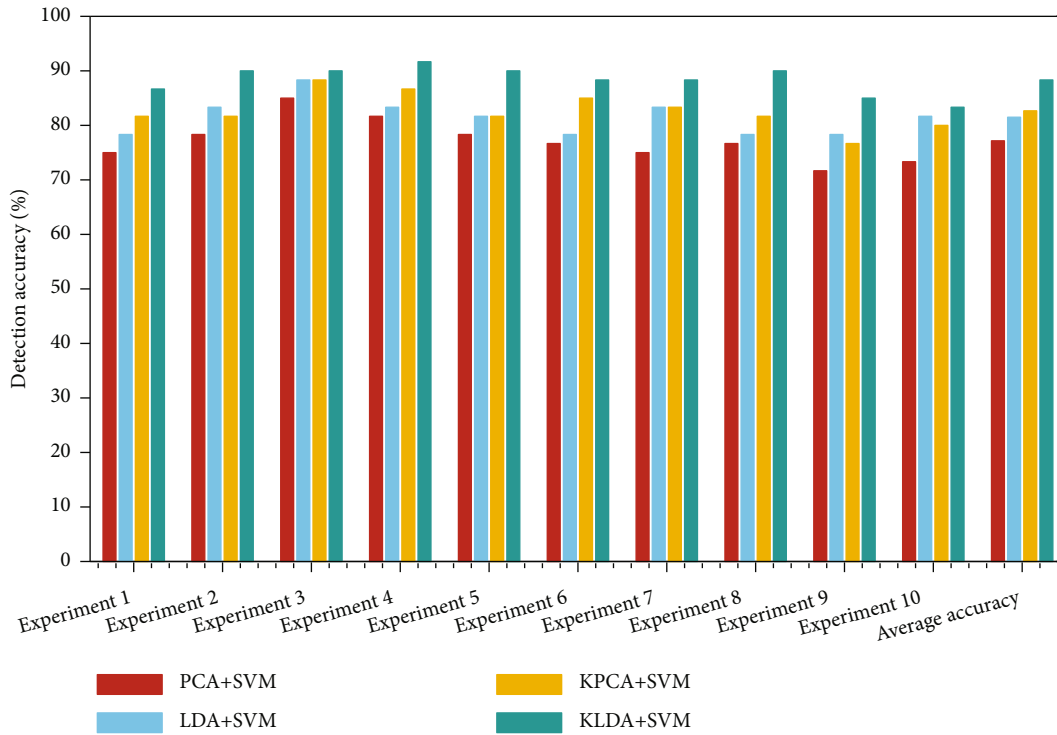FIGURE 7: Detection accuracy of KPCA and KLDA under different parameters.

FIGURE 8: The detection accuracy of crossvalidation experiments.

information and interference information, which not only increases the complexity of arc fault detection but also affects the accuracy of detection. Therefore, to mine the features with higher discrimination, the subspace transformation method is used to perform secondary feature extraction for the current feature. The subspace transformation methods adopted in this paper include linear subspace methods PCA and LDA and nonlinear subspace methods KPCA and KLDA.

Series fault arc detection is a binary classification problem and the SVM is used as the fault detector in this paper. In the experiment, Gaussian kernel is used in the kernel function of the SVM and the optimal penalty factor of the SVM is determined to be 10 and the adjustable parameter of kernel function is determined to be 0.55 through the cross verification grid search method.

The main influencing factor of PCA and LDA is the retained feature dimension d during feature extraction. The influence factors of KPCA and KLDA include reserved feature dimension d and adjustable parameter σ in kernel function. Therefore, comparison experiments are performed to determine the parameter settings for optimal performance of each algorithm. Figure 6 shows the influence of PCA and LDA feature dimensions on detection accuracy in a cross experiment. Figure 7 shows the influence of KPCA and KLDA feature dimensions and the kernel function adjustable parameter on detection accuracy in a cross experiment.

As shown in Figure 6, the curves of arc fault detection accuracy have similar trends. When the dimension is lower than 25, the detection accuracy is generally low. At this stage, as the dimension gradually increases, the effective information contained in the feature gradually increases, so

the detection accuracy increases rapidly. When the dimension is 30–45, the detection accuracy reaches a high value but there is a small fluctuation affected by the validity of the feature. When the dimension exceeds 45, interference information will be introduced into retained features, so the detection accuracy will decrease slightly. At this stage, as the dimension continues to increase, the detection accuracy is generally stable, remaining at around 80%.

In addition, because LDA is a supervised algorithm, while PCA is an unsupervised feature extraction algorithm, LDA is easier for capturing strong discriminant features than PCA. Therefore, LDA shows more excellent detection performance. In this experiment, when the feature dimension is 34, the optimal detection accuracy of PCA-SVM is 85%. When the feature dimension is 35, the optimal detection accuracy of LDA-SVM is 88.33%. After 10 crossvalidation experiments, the average detection accuracy of PCA-SVM is 77.2%. The average detection accuracy of the LDA-SVM algorithm is 81.5%.

Figure 7 shows the influence of feature dimensions on detection accuracy when the kernel function adjustable parameter has different values. It is found that the effect of the feature-retained dimension on detection accuracy is similar to that of the linear subspace algorithm. The adjustable parameter of kernel function plays a key role in improving the detection accuracy. As shown in Figure 7, the optimal value of the adjustable parameter of the KPCA algorithm is 0.4 and the optimal feature-retained dimension is 30 and the highest detection accuracy is 88.33%. The optimal value range of the adjustable parameter of the KLDA algorithm is 0.3-0.4, and the optimal feature-retained dimension is 30,

and the highest detection accuracy reaches 91.67%. After comprehensive analysis, the kernel function adjustable parameter of the KLDA algorithm is set to 0.35. The optimal feature dimension of both algorithms is 30.

In order to prove the reliability and effectiveness of the proposed algorithm, 10 crossvalidation experiments are performed and the average detection accuracy of all experiments is calculated as the final performance evaluation. The results and average accuracy of 10 crossvalidation experiments are shown in Figure 8.

In general, the performance of the nonlinear subspace transformation algorithm is better than that of the linear algorithm. Although the detection performance of the LDA-SVM algorithm is better than the KPCA-SVM algorithm in the 1st, 9th, and 10th experiments, the overall average detection accuracy of KPCA-SVM is 82.7%, which is better than that of LDA-SVM 81.5%. It shows that the feature extraction ability of nonlinear subspace transformation is better than that of linear subspace transformation and the feature set contains more nonlinear information. In addition, the KLDA-SVM algorithm has the highest average detection accuracy of 88.33%. The advantage of the KLDA algorithm lies in the guidance of supervision information. Under the same condition of retaining 30-dimensional features, the KLDA algorithm can capture features with more significant discrimination and stronger classification ability. Therefore, compared with the KPCA-SVM algorithm, the detection accuracy of the KLDA-SVM improved by about 5%.

6. Conclusions

In order to realize arc detection of series faults accurately and efficiently, a detection algorithm based on CEEMDAN decomposition and sensitive IMF selection is proposed. In this paper, a series arc generation platform is built and the current data of four kinds of loads are collected. Based on the CEEMDAN algorithm, arc current decomposition is implemented and a frequency division strategy is proposed to realize high-frequency signal rough selection. Then, an accurate selection strategy for the sensitive IMF component is proposed, which eliminates the interference of invalid IMF components and reduces the complexity of fault detection. A local feature construction method based on the time window is proposed to realize local feature extraction of the sensitive IMF component and enhance the contrast and discrimination of arc current features. Subspace transformation is used to extract secondary feature and the reduce dimension, and the support vector machine is used to detect the series fault arc. The optimal average detection accuracy of the proposed algorithm is 88.33%, which proves the effectiveness of the proposed algorithm and provides an important reference for fault arc detection technology and device design.

Data Availability

The dataset used in the experiment can be obtained by contacting the corresponding author.

Conflicts of Interest

The authors declare no conflict of interest.

Authors' Contributions

Fu Guixia proposed the original idea and wrote this paper; Chen Guizhen analyzed the data and corrected the translation; Wang Wei and Wang Qinbing collected the experimental data. Zou Guofeng participated in the reasonableness demonstration and manuscript modification.

Acknowledgments

References

[1] G. G. Liu, S. J. Du SH, and X. Han, "Research on LV arc fault protection and its development trends," *Power System Technology*, vol. 1, pp. 321–329, 2017.

[2] B. Basnet, H. Chun, and J. Bang, "An intelligent fault detection model for fault detection in photovoltaic systems," vol. 2020, pp. 1–11, 2020.

[3] N. Qu, J. Wang, J. Liu, and Z. Wang, "An arc fault detection method based on multidictionary learning," *Mathematical Problems in Engineering*, vol. 2018, 8 pages, 2018.

[4] Y. Kai, Z. Rencheng, Y. Jianhong, D. Jianhua, C. Shouhong, and T. Ran, "Series arc fault diagnostic method based on fractal dimension and support vector machine," *Transactions of China Electrotechnical Society*, vol. 31, no. 2, pp. 70–77, 2016.

[5] T. J. Zhao, J. Meng, Y. Q. Song, X. Y. Xie, and M. C. Zhang, "Series arc detection and protection on the DC side of string-type PVs," *Power System Protection and Control*, vol. 48, no. 20, pp. 74–82, 2020.

[6] Q. W. Lu, T. Wang, Z. R. Li, and C. Wang, "Detection method of series arcing fault based on wavelet transform and singular value decomposition," *Transactions of China Electrotechnical Society*, vol. 17, pp. 212–221, 2017.

[7] N. Qu, J. Chen, J. Zuo, and J. Liu, "PSO–SOM neural network algorithm for series arc fault detection," *Adv. Math. Phys.*, vol. 2020, pp. 1–8, 2020.

[8] J. G. Wang, W. Lin, Z. Wang, J. Li, W. He, and P. Wang, "Online detecting device for switchgear arc based on ultraviolet detection," *Power System Protection and Control*, vol. 39, no. 5, pp. 128–133, 2011.

[9] B. R. Pan, C. Wei, X. Z. Gui, and L. P. Zhang, "Development and application of a portable arc protection tester," *Power System Protection and Control*, vol. 48, no. 13, pp. 149–155, 2020.

[10] J. C. Kim, D. O. Neacşu, B. Lehman, and R. Ball, "Series AC arc fault detection using only voltage waveforms," in *2019 IEEE Applied Power Electronics Conference and Exposition (APEC)*, pp. 2385–2389, Anaheim, CA, USA, 2019.

[11] Y. Wang, L. Hou, K. C. Paul, Y. Ban, C. Chen, and T. Zhao, "ArcNet: series AC arc fault detection based on raw current and convolutional neural network," *IEEE Transactions on Industrial Informatics*, vol. 18, no. 1, pp. 77–86, 2022.

[12] J. Jiang, W. Li, Z. Wen, Y. Bie, H. Schwarz, and C. Zhang, "Series arc fault detection based on random forest and deep neural network," *IEEE Sensors Journal*, vol. 21, no. 15, pp. 17171–17179, 2021.

[13] N. Hadziefendic, M. Kostic, and Z. Radakovic, "Detection of series arcing in low-voltage electrical installations," *European Transactions on Electrical Power*, vol. 19, no. 3, pp. 423–432, 2009.

[14] A. G. Kavaz and B. Barutcu, "Fault detection of wind turbine sensors using artificial neural networks," *Journal of Sensors*, vol. 2018, 11 pages, 2018.

[15] G. Artale, A. Cataliotti, V. C. Nuccio, D. Di Cara, G. Tinè, and G. Privitera, "A set of indicators for arc faults detection based on low frequency harmonic analysis," in *2016 IEEE international instrumentation and measurement technology conference*, pp. 1–6, Taipei, 2016.

[16] Y. Kun, M. Shang, W. Wei, D. Peng, and X. Zebao, "Simulation and research of low voltage series arc discharge detection and fault protection based on Cassie model and wavelet analysis," *Electrical & Energy Management Technology*, vol. 18, pp. 48–52, 2019.

[17] Y. Wang, F. Zhang, X. Zhang, and S. Zhang, "Series AC arc fault detection method based on hybrid time and frequency analysis and fully connected neural network," *IEEE Transactions on Industrial Informatics*, vol. 15, no. 12, pp. 6210–6219, 2019.

[18] R. Chu, P. Schweitzer, and R. Zhang, "Series AC arc fault detection method based on high-frequency coupling sensor and convolution neural network," *Sensors*, vol. 20, no. 17, pp. 4910–4919, 2020.

[19] N. E. Huang, Z. Shen, S. R. Long et al., "The empirical mode decomposition and the Hilbert spectrum for nonlinear and non-stationary time series analysis," *Proceedings of the Royal Society*, vol. 454, no. 1971, pp. 903–995, 1998.

[20] G. Rilling, N. P. Flandr, and P. Goncalves, "On empirical mode decomposition and its algorithms," in *IEEE-EURASIP workshop on nonlinear signal and image processing, NSIP-03, Grado (I)*, pp. 9–11, Italy, 2003.

[21] Z. Wu and N. E. Huang, "Ensemble empirical mode decomposition: a noise-assisted data analysis method," *Advances in Adaptive Data Analysis*, vol. 1, no. 1, pp. 1–41, 2009.

[22] J. Cheng, H. S. Yang, H. Shao, H. Pan, J. Zheng, and J. Cheng, "Enhanced periodic mode decomposition and its application to composite fault diagnosis of rolling bearings," *ISA Transactions*, vol. 113, 2021.

[23] M. E. Torres, M. A. Colominas, G. Schlotthauer, and P. Flandrin, "A complete ensemble empirical mode decomposition with adaptive noise," in *IEEE International Conference on Acoustics, Speech and Signal Processing*, pp. 4144–4147, Prague, Czech Republic, 2011.

[24] G. Zhiqiang and L. Yuedie, "Fault diagnosis of rolling bearing based on improved LMD and comprehensive characteristic index," *Journal of Hefei University of Technology: Natural Science*, vol. 44, no. 2, pp. 145–150, 2021.

[25] J. Lingli, C. Liman, T. Hongchuang, and L. Xuejun, "Fault diagnosis of spiral bevel gear based on CEEMDAN permutation entropy and SVM," *Journal of Vibration, Measurement & Diagnosis*, vol. 41, no. 1, pp. 33–40, 2021.

[26] K. C. Kempfert, Y. Wang, C. Chen, and S. W. K. Wong, "A comparison study on nonlinear dimension reduction methods with kernel variations: visualization, optimization and classification," *Intelligent Data Analysis*, vol. 24, no. 2, pp. 267–290, 2020.

[27] W. Miao, Q. Xu, K. H. Lam, P. W. T. Pong, and H. V. Poor, "DC arc-fault detection based on empirical mode decomposition of arc signatures and support vector machine," *IEEE Sensors Journal*, vol. 21, no. 5, pp. 7024–7033, 2021.

Research Article

Tradeoff Optimization Technology of Effectiveness-Cost for Satellite-Based on CAIV Method

Zhiwei Chen [ID],[1] Jian Jiao [ID],[2] Xinlin De [ID],[3] and Dongming Fan [ID][2,4]

[1]*Unmanned System Research Institute, Northwestern Polytechnical University, Xi'an 710109, China*
[2]*School of Reliability and Systems Engineering, Beihang University, Beijing 100191, China*
[3]*Beijing Institute of Structure & Environment Engineering, Beijing 100076, China*
[4]*School of Transportation Science and Engineering, Beihang University, Beijing, China*

Correspondence should be addressed to Jian Jiao; jiaojian@buaa.edu.cn

The tradeoff of effectiveness and cost is a vital problem for complex industrial systems, mainly applied in the weapons and aviation fields. As a typical complex industrial system, the effectiveness-cost tradeoff of the satellites becomes challenging and interesting. This paper takes a remote sensing satellite as a research object, and an integrated approach to assess and optimize its effectiveness and cost is proposed. The characteristic parameters are selected according to an analysis of its structure and mission. Furthermore, the effectiveness evaluation model is established based on the Availability-Dependability-Capability (ADC) model, and the cost parameter model is developed using historical data and regression analysis. According to the Cost as Independent Variable (CAIV) method, the objective function of the satellite effectiveness-cost with the effectiveness-cost tradeoff space is established. The objective function is solved and optimized using a genetic algorithm to achieve a more efficient and economical satellite design scheme.

1. Introduction

The ability to complete missions efficiently by making the most of available resources, i.e., the ability to make a tradeoff between cost and effectiveness, has become a focus in complex industrial systems. There is a great deal of effectiveness study in industrial fields such as military, machinery manufacturing, and civil aviation [1–6], and many classical effectiveness evaluation methods have been proposed, such as the Weapons System Effectiveness Industry Advisory Committee (WSEIAC) model [7], the index method [8], and the system effectiveness analysis (SEA) [3]. However, due to significant differences between the working environment and mission characteristics, applying these methods directly in satellites for effectiveness evaluation is challenging and interesting. In studies about satellite effectiveness, Elhady [9] considered that effective measures usually depend on system performance, availability, reliability, and product quality. The effectiveness of the satellite was calculated semi-

quantitatively in the literature [10–12]. These studies made some improvements in effectiveness evaluation, but they mainly focused on the functions and structure of satellites rather than the mission process. Based on system state transformations that occur throughout missions, De et al. [13] refined the effectiveness definition of remote sensing satellites and assessed the effectiveness of different satellite states, but the analysis was relatively simple.

With increasing demands for satellite applications, the cost of satellites has also become a significant problem. Currently, different cost estimation models commonly used for spacecraft include the Unmanned Space Vehicle Cost Model (USCM) [14], the NASA/Air Force Cost Model (NAFCOM) [15], and the Small Satellite Cost Model (SSCM) [16], most of which are based on satellite mass and other performance factors [17]. Furthermore, the Performance-Based Cost Model (PBCM) [18] and KAU Earth Observation Satellite Cost Model (KEOSCM) [19] are proposed to improve the existing models. While cost estimation studies of spacecraft

are conducive to reducing the cost of satellites, cost reduction cannot sacrifice system effectiveness, which means that a rational balance between effectiveness and cost is needed.

The US military proposed the CAIV methodology in the 1990s to resolve the contradiction between the shortage of military expenditure and the expansion of demand [20]. This methodology defines cost as an input variable and emphasizes the tradeoff between effectiveness and cost. At present, some scholars have applied the CAIV methodology to the military field [21–23]. The CAIV methodology is used to support the tradeoff of the environmental exploration satellite system, and a tradeoff model of the performance and cost is established in [24]. Apgar discussed [25] the different initiatives to control space mission costs, including CAIV. In this paper, the system effectiveness and cost model are established by analyzing a remote sensing satellite as an object. Then, we optimize the satellite design by analyzing the tradeoff between effectiveness and cost (based on the CAIV methodology) and ensure that the design meets performance requirements at an affordable cost. Although we present this effectiveness-cost modeling and tradeoff analysis methodology for remote sensing satellites, this method can be applied to other space products with minor modifications.

The following sections of the paper are organized as follows. Section 2 mainly analyzes the structure and mission characteristics of a satellite and selects characteristic parameters. Section 3, combined with the mission process of the remote sensing satellite, establishes the evaluation model of effectiveness and cost of the remote sensing satellite, respectively. Section 4 proposes the tradeoff model based on the CAIV method, as well as the effectiveness assessment and cost estimation models established in Section 3, and uses a genetic algorithm to optimize the effectiveness-cost model in the tradeoff space, and finally arrives at the remote sensing satellite design solution with the optimal effectiveness-cost ratio. Finally, the discussion and conclusion are summarized in Section 5.

2. Structure and Mission of Remote Sensing Satellite

2.1. Structure and Characteristics of Satellite.
According to its essential functions, the structure of the satellite, specifically a microwave imaging observation satellite, can be divided into payloads and satellite platforms. The specific composition is shown in Figure 1.

2.1.1. Payloads.
The payloads of microwave imaging observation satellites mainly include various remote imaging sensors for earth observation, which is the core part of the satellite.

2.1.2. Satellite Platform.
Satellite platforms can be divided into different subsystems, including structures-and-mechanisms, thermal control, power, control, propulsion, tracking, telemetry and command (TT&C), data management, and data transmission, which provide support, control, command, and management services.

Limited by the size of the carrier, the materials and instruments used in a satellite must satisfy the requirements of negligible mass, small volume, and low power consumption. Additionally, remote sensing satellites have other working, and technical characteristics, including long life and high reliability, a high degree of automation, and a technology-intensive design, and must suit particular environmental conditions.

(1) Special environmental conditions. A remote sensing satellite is subjected to severe shocks such as overload, vibration, and noise during launch and operates in a space environment with microgravity, intense radiation, and ultralow temperatures

(2) Long life and high reliability. A remote sensing satellite needs to work continuously in orbit for several years, during which it is almost impossible to perform replenishment, maintenance, repair, or replacement. Therefore, long life and high reliability are essential characteristics for a satellite

(3) The high degree of automation. The control of remote sensing satellites is mainly accomplished through the ground station and the TT&C subsystem. As satellite function improves, the degree of automation increases and the ability for autonomous control

(4) Technology-intensive. A satellite is a technology-intensive system, and satellite platforms and payloads apply specific theories, different materials, and equipment, involving many fields of science and technique

2.2. Capability and Mission Analysis of Satellite.
To quickly obtain detailed information about a target, a remote sensing satellite needs to adjust its attitude in a short time after receiving control information from the ground station. Moreover, it should also change the angle of the remote sensor rapidly according to user's needs to observe the target quickly and efficiently. When the satellite reaches the predetermined area, target's electromagnetic wave radiated and reflected can be collected and preprocessed by the sensors to realize continuous imaging. The quality of the image will directly affect subsequent decision-making. After obtaining target information, the satellite needs to transmit the information to the ground station for reprocessing in a short time to ensure the timeliness of the information. Hence, a high capability of information processing and transmission is demanded.

According to the application and mission process of a remote sensing satellite, three main functional characteristics of the satellite can be concluded: the high-speed attitude maneuvering capability, the high-resolution imaging capability, and the ability to transmit large bandwidth information. In order to quantitatively measure satellite capabilities, these three functions or capabilities can be divided based on the composition of the satellite and described using design parameters so that they can be evaluated using the
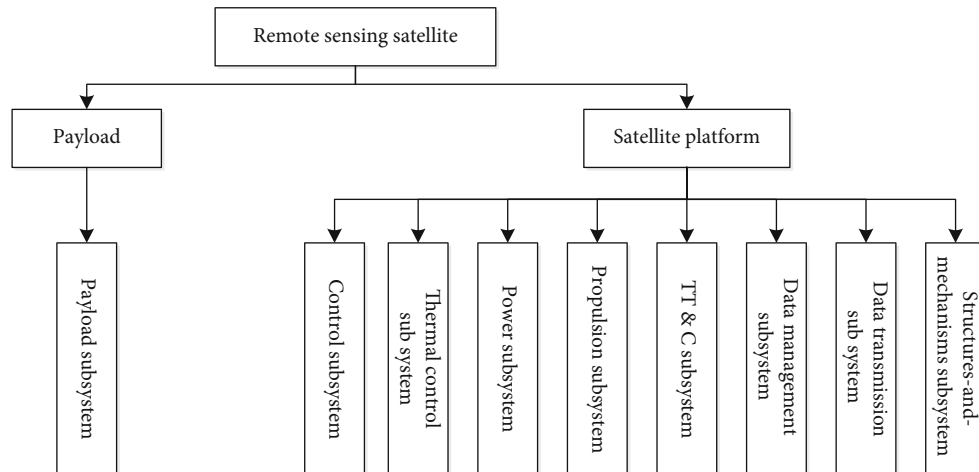
Figure 1: The composition of remote sensing satellite.
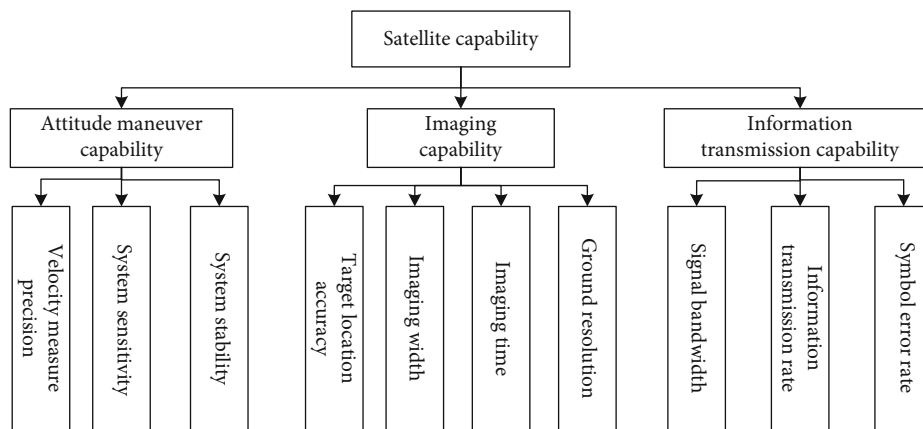

Figure 2: Capability indicators of remote sensing satellite.

performance of the satellite. After discussing with aerospace experts, some representative parameters are chosen as capability indicators to measure system capacity according to the function and structure of the satellite. For example, the imaging capability is measured by target location accuracy, imaging width, imaging time, and ground resolution. The specific composition is shown in Figure 2.

Among these three capabilities, high-resolution imaging is the central capability that is fundamental in determining the whole satellite's capability. At the same time, the attitude maneuvering and information transmission capabilities support the capability of the satellite platform from the perspective of satellite design and operation, reflecting the capability of coordinating and matching with imaging capability.

Based on the analysis of the structural characteristics and central capabilities of remote sensing satellites, we can safely conclude that the subsystems influencing the capability of satellites are payloads, control, propulsion, and data transmission subsystems; the subsystems that indirectly impact the capability are structures-and-mechanisms, thermal control, power, TT & C, and data management subsystems. Therefore, the satellite structure is moderately simplified. The indirect impact subsystems are collectively called auxil-

iary subsystems; furthermore, the reliability of the structures-and-mechanisms subsystem is regarded as one. Its impact on the capability of the satellite could be ignored because it adopts margin design based on safety factors. The logical relationships between the structure and the mission capability of remote sensing satellites are shown in Figure 3.

The state changes of each subsystem will affect different capability indicators, that will in turn affect the overall capability of the satellite. The arrows between the elements in Figure 3 indicate their relationships of influence. For example, the payload subsystem impacts all the capability indicators of the imaging capability and has a specific influence on the information transmission capability of the satellite. The auxiliary subsystem does not directly affect the capability index in the mission process, but it plays a fundamental role in supporting the remote sensing satellite and indirectly impacts all the capability indicators.

The propulsion, control, payload, data transmission, and auxiliary subsystems are represented by N_1, N_2, N_3, N_4, N_5, respectively, and each subsystem has two states: normal (N) and fault ($\bar{N}$). Therefore, there are 32 possible system states of the satellite. However, according to the actual operation of the satellite and the practical significance of these states, when
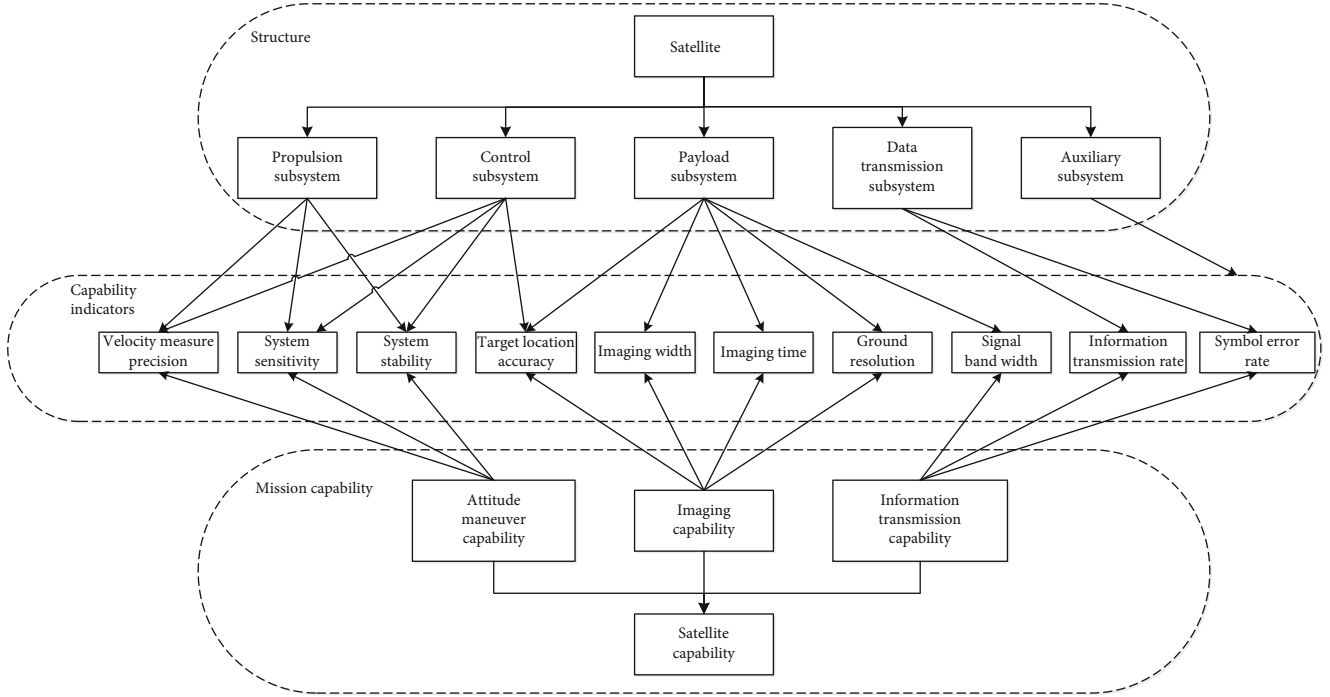
FIGURE 3: The logical relationship between the structure and mission capability of the satellite.

TABLE 1: The meanings of remote sensing satellite states.

State number	System state	Capability situation
1	$N_1N_2N_3N_4N_5$	Satellite capabilities are standard, and remote sensing missions can be carried out.
2	$\bar{N}_1N_2N_3N_4N_5$	Attitude maneuver capability is impaired, and satellite capabilities are slightly reduced.
3	$N_1\bar{N}_2N_3N_4N_5$	Capabilities of attitude maneuver and imaging are impaired, and satellite capabilities are slightly reduced.
4	$N_1N_2\bar{N}_3N_4N_5$	Capabilities of information transmission and imaging are impaired, and satellite capabilities are significantly reduced.
5	$N_1N_2N_3\bar{N}_4N_5$	Information transmission capabilities are impaired, and satellite capabilities are slightly reduced.
6	$\bar{N}_1\bar{N}_2N_3N_4N_5$	Capabilities of attitude maneuver and imaging are impaired, and satellite capabilities are significantly reduced.
7	$\bar{N}_1N_2\bar{N}_3N_4N_5$	Three capabilities are impaired, and satellite capabilities are critically reduced.
8	$\bar{N}_1N_2N_3\bar{N}_4N_5$	Capabilities of attitude maneuver and information transmission are impaired, and satellite capabilities are significantly reduced.
9	$N_1\bar{N}_2\bar{N}_3N_4N_5$	Three capabilities are impaired, and satellite capabilities are critically reduced.
10	$N_1\bar{N}_2N_3\bar{N}_4N_5$	Three capabilities are impaired, and satellite capabilities are critically reduced.
11	$N_1N_2\bar{N}_3\bar{N}_4N_5$	Capabilities of information transmission and imaging are critically impaired, and satellite capabilities are reduced.
12	Error	Satellite capabilities are lost, and remote sensing missions cannot be carried out.

the auxiliary subsystem fails or the fault number of other subsystems is greater than or equal to three (≥3), it can be regarded that the remote sensing satellite has lost its essential capability and cannot continue to perform the mission. The states in which the satellite cannot continue to perform its mission are classified as ERROR states, and thus, the number of system states of the satellite is simplified to 12. The specific meanings of each state are shown in Table 1.

3. Modeling of Effectiveness and Cost for Remote Sensing Satellite

3.1. Effectiveness Model for Remote Sensing Satellite. Effectiveness is a widely applied concept, so it should be precisely defined before analysis. The most common understanding of effectiveness is the real-world ability of a specific system to accomplish a specific mission. Based on the above discussion

about capability and mission characteristics, the definition of the effectiveness of a remote sensing satellite can be summarized as *the ability to carry out mission-specific remote sensing continuously within a designated area and a specified period of time, where the collected information should meet a specific requirement.*

In this paper, the effectiveness of the satellite is calculated using the ADC model [7]. The ADC model was proposed by WSEIAC, in which system effectiveness is regarded as a measure of the degree to which a system can meet a set of mission requirements and is the comprehensive embodiment of system availability (A), dependability (D), and capability (C). By combining the *ADC* model with probability theory, the effectiveness of remote sensing satellite can be expressed as:

$$E = A \bullet D \bullet C_a, \tag{1}$$

where A is an availability vector, representing the probabilities of the satellite in different states when it begins its mission. D is a dependability matrix representing the transition probability between different system states during the mission. C_a is a capability vector, representing the inherent capability of the satellite under different states. The detailed expression of A, D, and C_a will be discussed in the following sections.

3.1.1. Availability of Remote Sensing Satellite. The availability of remote sensing satellites is represented by a row vector A, that is, $A = [A_1, A_2 \cdots A_i \cdots A_n]$, where A_i is the probability that the satellite is in the state i at the beginning of the mission, n is the total number of satellite states, and $\sum_{i=1}^{n} A_i = 1$. Since the analyzed satellite is a single satellite and there is no backup, only repairable faults are considered, and nonrepairable faults will result in mission failure. Using a_1, a_2, a_3, a_4, a_5 represents the probabilities, respectively, that five subsystems (shown in Figure 3) can operate normally, and let MTBF and MTTR represent the average time between fault and the average repair time of these subsystems, respectively; thus,

$$a_i = \frac{\mathrm{MTBF}_i}{(\mathrm{MTBF}_i + \mathrm{MTTR}_i)}. \tag{2}$$

And the probabilities that the subsystems cannot operate normally at the beginning are

$$\bar{a}_i = 1 - a_i. \tag{3}$$

There are twelve states in remote sensing satellites (shown in Table 1). The probability that the satellite is in a particular state at the beginning of the mission is the product of the state probabilities of five subsystems, for example, $A_1 = a_1 a_2 a_3 a_4 a_5$. So, the availability vector is:

$$A = [A_1 \quad A_2 \quad A_3 \quad A_4 \quad A_5 \quad A_6 \quad A_7 \quad A_8 \quad A_9 \quad A_{10} \quad A_{11} \quad A_{12}]. \tag{4}$$

3.1.2. Dependability of Remote Sensing Satellite. The dependability matrix (D) of the remote sensing satellite is an n-order-matrix, that is, $D = [d_{ij}]_{n \times n}$, where $d_{ij}(i, j = 1, 2, \cdots, n)$ represents the probabilities of transitions from initial state i to state j during the mission. Therefore, the state changes of the satellite can be expressed mathematically as a stochastic process, $\{X(t), t \geq 0\}$, where t is time. In the stochastic process, the probability of the satellite transferring from one state to another is only related to the present state so that the process can be transformed into continuous-time Markov chains. The mathematical expression of continuous Markov chains is:

$$P\{X(t + u) = j | X(u) = i\} = p_{ij}(u, t). \tag{5}$$

It represents the probability that the system is in state i at time u and is transferred to state j after time interval t. According to the historical data of similar satellites, it can be assumed that the reliability of the subsystems is subject to exponential distribution, so the probability of state transition is independent of the time u. Therefore, $p_{ij}(u, t)$ can be written as $p_{ij}(t)$.

In the state transition process, we assume that two or more faults cannot cooccur in the satellite [13], and the satellite state does not change within an operation time of $\Delta t (\Delta t \longrightarrow 0)$ after a state transition. This assumption is also in line with the actual situation and can significantly reduce the computational complexity. Then, the transition probability $p_{ij}(t)$ satisfies regularity condition:

$$\lim_{t \longrightarrow 0} p_{ij}(t) = \begin{cases} 1, i = j, \\ 0, i \neq j. \end{cases} \tag{6}$$

For any fixed $i, j \in I$, $p_{ij}(t)$ is a consistent, continuous function of t and has the following limits:

$$\begin{cases} \lim_{\Delta t \longrightarrow 0} \dfrac{p_{ij}(\Delta t) - 1}{\Delta t} = q_{ij}, i = j, \\ \lim_{\Delta t \longrightarrow 0} \dfrac{p_{ij}(\Delta t)}{\Delta t} = q_{ij}, i \neq j, \end{cases} \tag{7}$$

where q_{ij} is called transfer intensity of a homogeneous Markov process. The transfer intensity of homogeneous Markov chains of continuous-time can form a matrix shown below:

$$Q = \begin{bmatrix} q_{11} & q_{12} & \cdots & q_{1n} \\ q_{21} & q_{22} & \cdots & q_{2n} \\ \cdots & \cdots & q_{ij} & \cdots \\ q_{n1} & q_{n2} & \cdots & q_{nn} \end{bmatrix}. \tag{8}$$

From the matrix Q, the equation can be deduced to evaluate the transition probability for any time interval t, which can be expressed by the Kolmogorov forward:

$$\frac{dp_{ij}(t)}{dt} = \sum_{k} p_{ik}(t) q_{kj}, \tag{9}$$

where the initial conditions are $p_{ij}(0) = \begin{cases} 1, i = j \\ 0, i \neq j \end{cases}$, and $P(t)$ can be written in matrix form:

$$P(t) = \frac{d}{dt} P(t) Q^{-1}. \tag{10}$$

The transfer intensity matrix Q can be obtained based on the fault rates of the satellite subsystems, and then, the state transition probability matrix $P(t)$ after a time interval t, i.e., the dependability matrix D, of the satellite can be calculated. According to the definition of satellite effectiveness, the remote sensing mission of the satellite is a continuous process, so the mission will fail once the satellite fails. Therefore, the dependability matrix D is an upper triangle matrix without considering the maintenance of the satellite during the mission.

Due to space constraints, only the fourth row of matrix D is used as an example, where $\lambda_1, \lambda_2, \lambda_3, \lambda_4, \lambda_5$ represent the propulsion, control, payloads, data transmission, and auxiliary subsystems' failure rates. In the same way, other elements in matrix D can be deduced.

$$
\begin{aligned}
&D_{4,1} = D_{4,2} = D_{4,3} = D_{4,5} = D_{4,6} = D_{4,8} = D_{4,10} = 0, \\
&D_{4,4} = e^{-t(\lambda_1+\lambda_2+\lambda_4+\lambda_5)}, \\
&D_{4,7} = e^{-t(\lambda_2+\lambda_4+\lambda_5)} - e^{-t(\lambda_1+\lambda_2+\lambda_4+\lambda_5)}, \\
&D_{4,9} = e^{-t(\lambda_1+\lambda_4+\lambda_5)} - e^{-t(\lambda_1+\lambda_2+\lambda_4+\lambda_5)}, \\
&D_{4,11} = e^{-t(\lambda_1+\lambda_2+\lambda_5)} - e^{-t(\lambda_1+\lambda_2+\lambda_4+\lambda_5)}, \\
&D_{4,12} = 2e^{-t(\lambda_1+\lambda_2+\lambda_4+\lambda_5)} - e^{-t(\lambda_1+\lambda_2+\lambda_5)} - e^{-t(\lambda_1+\lambda_4+\lambda_5)} \\
&\qquad\quad - e^{-t(\lambda_2+\lambda_4+\lambda_5)} + 1.
\end{aligned}
\tag{11}
$$

3.1.3. Capability of Remote Sensing Satellite. The column vector C_a represents the capability of remote sensing satellites, $C_a^T = [C_{a1}, C_{a2} \cdots C_{ak} \cdots C_{an}]$, where C_{a1} implies the perfect performance state and C_{an} implies the worst state. Therefore, when calculating the capability of remote sensing satellites, C_{a1} should be calculated first, and the remaining capability values can be evaluated by comparing them with C_{a1}. It is obvious that the capability indicators shown in Figure 2 cannot be directly calculated, so they should first be normalized and transformed into a unified quantitative style. The design range of the indicator P_i can be divided into subranges, and the evaluation value $u(P_i)$ can be determined according to the normalization function. Equation (12) is an example of a normalization function, in which the design range of the indicator P_i is divided into five subranges, and different evaluation values $u(P_i)$ are assigned using the functions, where 10 represents the best performance, and 0 represents the worst.

$$
u(P_i) = \begin{cases}
0, \wedge P_i \leq p_1, \\
10 \times \dfrac{P_i - p_1}{p_2 - p_1}, \wedge p_1 < P_i < p_2, \\
10, \wedge p_2 \leq P_i \leq p_3, \\
10 \times \left(1 - \dfrac{P_i - p_3}{p_4 - p_3}\right), \wedge p_3 < P_i < p_4, \\
0, \wedge P_i \geq p_5.
\end{cases}
\tag{12}
$$

For capability indicators that are difficult to evaluate using a linear function in Equation (12), the piecewise interval evaluation method can be adopted. According to the data variation range of specific capability indicators, the dividing point and number of capability evaluation intervals are determined, and the corresponding capability evaluation value $u(P_i)$ is given. Taking the symbol error rate as an example, the lower rate corresponds to a better capability evaluation value. The capability evaluation interval of this indicator has five ranges, namely $[0, 10^{-8}]$, $[10^{-8}, 10^{-7}]$, $[10^{-7}, 10^{-6}]$, $[10^{-6}, 10^{-5}]$, and $[10^{-5}, \infty]$, and the corresponding evaluation value is 10, 8, 6, 4, and 0, respectively.

Then, the AHP [26] is introduced to determine the weight of the capability indicators so that the capability of the satellite can be assessed quantitatively. A hierarchical structure model is established according to the structure of capability indicators in Figure 2, and values of pairwise contrast are scored by discussing with experts in the aerospace industry in order to construct judgment matrices. Then, the order of importance and consistency test is performed on the indicators of the same level to get the weight w_i of each indicator in the hierarchical model. Using the weights and the evaluation values $u(P_i)$, the capability of the satellite to accomplish the mission in a normal state can be calculated, i.e., $C_{a1} = \sum w_i \cdot u(P_i)$.

According to the definition of different satellite states (shown in Table 1), the capability of satellites in other states can be regarded as a reduction of capability in normal states because the state of the satellite subsystems impacts the capability indicators. An influence coefficient of capability indicators (ρ) is introduced to represent the extent to which the satellite subsystems impact each capability indicator under different conditions, where $\rho = 0$ means that the subsystem failure does not influence the capability indicator, while $\rho = 1$ means that the subsystem fault has a decisive influence. Thus, the reduction of the capability indicator is shown in the following equation:

$$
\begin{cases}
u(P_i)' = \left(1 - \sum \rho\right) \cdot u(P_i), \left(\sum \rho \leq 1\right), \\
u(P_i)' = 0, \left(\sum \rho > 1\right),
\end{cases}
\tag{13}
$$

where $u(P_i)$ is the evaluation value of capability indicator in the normal state and $u(P_i)'$ is the reduction value. Thus, the capabilities of the satellite in other states are $C_{ak} = \sum w_i \cdot u(P_i)'$.
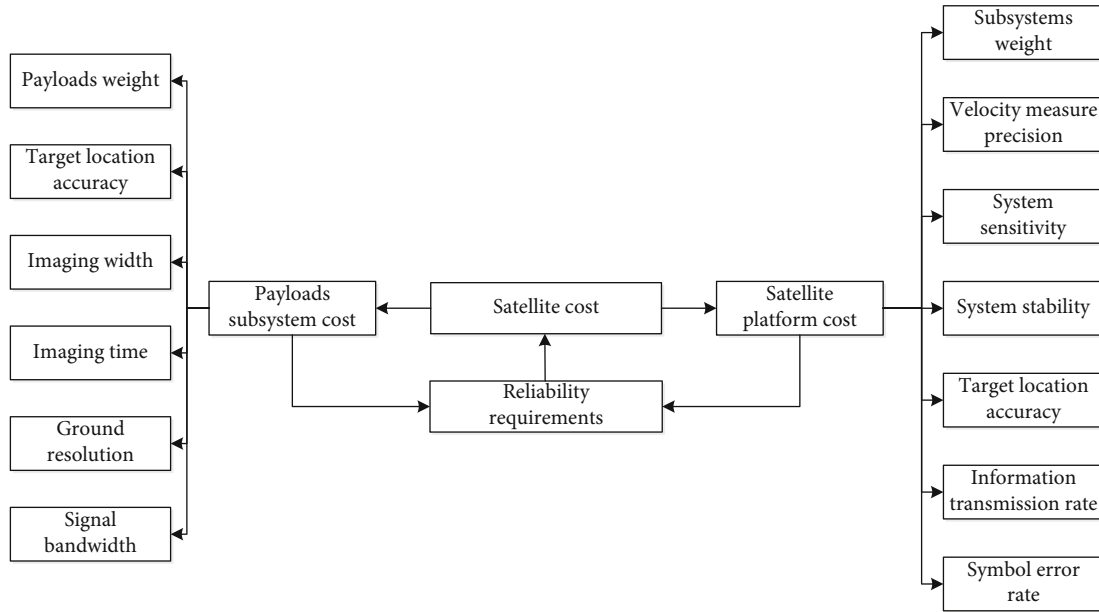
FIGURE 4: The cost relationship structure for a remote sensing satellite.

3.2. Cost Model for Remote Sensing Satellite. The cost of research and development can be quickly and efficiently estimated based on the design parameters, which is usually called parameter cost estimation [27]. Similarly, the cost of remote sensing satellites is evaluated based on the analysis of system composition. The functional relationship between each subsystem cost and design parameters is established based on the physical characteristics, design parameters, and cost data from similar historical data. This study only considered the cost associated with satellite design, development, and test.

3.2.1. Establish the Cost Relationship Structure for Remote Sensing Satellite. The cost relationship between the structure and mission capability of the satellite is shown in Figure 4. The cost of the satellite consists of the payload subsystem and satellite platform subsystems, i.e.,

$$C_o = \sum_i C_{oi}, \qquad (14)$$

where C_{oi} is the cost of each subsystem of the satellite. The cost is affected by many factors, such as weight, capability indicators, and reliability requirements. The specific impacts and cost models for each subsystem are discussed below.

3.2.2. Cost Models of Satellite Subsystems. According to the USCM, which is widely used for cost estimation of satellites [14], the cost model of the satellite subsystem is:

$$C_{oi} = a_i X^{b_i}, \qquad (15)$$

where C_{oi} is the cost of the satellite subsystem, X is the weight of subsystem, and a_i and b_i are correction coefficients. Based on the cost relationship structure of the remote sensing satellite, the original USCM is amended, and differ-

ent capability indicators are introduced as correction variables so that the cost models of different subsystems can be obtained. The correction coefficients in the models can be calculated using regression analysis on historical data.

(1) The Cost Model of the Propulsion Subsystem

$$C_{o1} = A_1 \bullet X^{a_1} \bullet P_1^{b_1} \bullet P_2^{c_1} \bullet P_3^{d_1} \bullet P_4^{f_1}, \qquad (16)$$

where C_{o1} is the cost of the propulsion subsystem, X is the total weight of the propulsion subsystem, P_1 is the velocity measure precision, P_2 is the system sensitivity, P_3 is the system stability, P_4 is the reliability requirement, and A_1, a_1, b_1, c_1, d_1, and f_1 are the correction coefficients.

(2) The Cost Model ofthe Data Transmission Subsystem

$$C_{o2} = A_2 \bullet X^{a_2} \bullet P_5^{b_2} \bullet P_6^{c_2} \bullet P_4^{f_2}, \qquad (17)$$

where C_{o2} is the cost of the data transmission subsystem, X is the total weight of the data transmission subsystem, P_5 is the information transmission rate, P_6 is the symbol error rate, P_4 is the reliability requirement, and A_2, a_2, b_2, c_2, d_2, and f_2 are the correction coefficients.

(3) Cost Model ofPayload Subsystem

$$C_{o3} = A_3 \bullet X^{a_3} \bullet P_7^{b_3} \bullet P_8^{c_3} \bullet P_9^{d_3} \bullet P_{10}{}^{e_3} \bullet P_{11}{}^{g_3} \bullet P_4^{f_3}, \qquad (18)$$

where C_{o3} is the cost of the payload subsystem, X is the total weight of the payload subsystem, P_7 is the target location accuracy, P_8 is the imaging width, P_9 is the imaging time, P_{10} is the ground resolution, P_{11} is the signal bandwidth, P_4 is the reliability requirement, and $A_3, a_3, b_3, c_3, d_3, e_3, f_3$, and g_3 are the correction coefficients.

TABLE 2: The reliability of subsystems.

Subsystem	1	2	3	4	5	6	7	8
Propulsion subsystem	0.9859	0.9859	0.988	0.988	0.988	0.988	0.988	0.985
Control subsystem	0.9033	0.9253	0.9338	0.9338	0.925	0.921	0.92	0.944
Payloads subsystem	0.902	0.8300	0.9266	0.926	0.901	0.895	0.808	0.8965
Data transmission subsystem	0.9495	0.9171	0.9675	0.9675	0.977	0.966	0.976	0.847
Auxiliary subsystem	0.9189	0.8914	0.8868	0.8868	0.9307	0.8791	0.9448	0.8846

TABLE 3: The weight of subsystems (kg).

Subsystem	1	2	3	4	5	6	7	8
Propulsion subsystem	96	111	103	103	75	45.5	55	175
Control subsystem	191	220.2	234	234	183	170.77	172	330
Payloads subsystem	606	729.8	798	750	475	940	392	742
Data transmission subsystem	136	175.2	190	190	72	63.3	125	227
Auxiliary subsystem	895	964	971	971	907	793.09	534	1162

TABLE 4: The cost of subsystems (RMB).

Subsystem	1	2	3	4	5	6	7	8
Propulsion subsystem	2018	2384	2517	2517	1829	1578	1528	3112
Control subsystem	1786	2251	2862	2862	1151	1011	1001	4207
Payloads subsystem	4884	3956	6497	6021	3264	6449	1687	5453
Data transmission subsystem	2247	2240	3130	3130	1223	1288	2484	2834
Auxiliary subsystem	14013	13244	13256	13256	15308	11128	10898	13404

(4) The Cost Model of the Control Subsystem

$$C_{o4} = A_4 \bullet X^{a_4} \bullet P_1^{b_4} \bullet P_2^{c_4} \bullet P_3^{d_4} \bullet P_7^{e_4} \bullet P_4^{f_4}, \qquad (19)$$

where C_{o4} is the cost of the control subsystem, X is the total weight of the control subsystem, P_1 is the velocity measure precision, P_2 is the system sensitivity, P_3 is the system stability, P_7 is the target location accuracy, P_4 is the reliability requirement, and $A_4, a_4, b_4, c_4, d_4, e_4$, and f_4 are the correction coefficients.

(5) The Cost Model of the Auxiliary Subsystem

$$C_{o5} = A_5 \bullet X^{a_5} \bullet P_4^{f_5}, \qquad (20)$$

where C_{o5} is the cost of the auxiliary subsystem, X is the total weight of the auxiliary subsystem, P_4 is the reliability requirement, and A_5, a_5, and f_5 are the correction coefficients.

By collecting and preprocessing the historical data of remote sensing satellites, the design parameters and cost of each subsystem of similar satellites can be estimated. Since there are price fluctuations throughout different years, all costs of historical satellites will be converted to the price in 2016 to maintain a uniform measurement of the fitted data. The detailed data can be found in Tables 2–6. Nonlinear multivariate regression analysis is performed to evaluate the parameters in the above cost models. The Levenberg-

Marquardt algorithm [28] is chosen to ensure the stability of the model and reduce the number of calculations and fitting errors of the correction coefficients.

Nonlinear models are complex compared to other models, and it is difficult to obtain their regression parameters. Marquard introduced the damping factor based on the Gauss-Newton method and proposed the Marquardt algorithm. The method has a high fitting efficiency and low error for nonlinear model fitting. It inherits the global optimization-seeking feature of the original algorithm and speeds up the convergence speed. The basic principle of the Marquardt method is to calculate the sum of squares of residuals through continuous data iteration, which is used to evaluate whether the fitted parameters achieve the best fitting effect. When the sum of squares of the residuals reaches a minimum value, the iterative process ends, and the resulting regression parameters are the final results of the cost curve fitting, which leads to the cost estimation model for each subsystem.

The cost models for each subsystem are listed in Table 7.

4. Tradeoff Optimization between Effectiveness and Cost of Remote Sensing Satellite

4.1. The Methodology of Cost as an Independent Variable (CAIV). The US military proposes the CAIV methodology to solve the contradiction between the limitation of system resources and the unlimited expansion of demand. The two most fundamental characteristics in the CAIV

TABLE 5: The capability indicators of satellites.

Capability indicator	1	2	3	4	5	6	7	8
Velocity measure precision (m/s)	4	2	1.8	1.8	6	6	6	1
System sensitivity (°)	5	5	6	6	4	4	4	8
System stability (°/s)	0.55	0.5	0.6	0.6	0.4	0.35	0.35	0.6
Target location accuracy (m)	35	40	30	30	40	30	40	35
Imaging width (km)	25	25	28	25	18	28	18	30
Imaging time (h)	2	1.8	2.5	2	1.5	2.5	1	2.5
Ground resolution (m)	3	3	4	4.5	10	2	10	4
Signal bandwidth (mhz)	600	600	580	580	550	500	500	600
Information transmission rate (Gbps)	15	14	16	16	15	13	13	17
Symbol error rate	10^{-7}	10^{-7}	10^{-8}	10^{-8}	10^{-6}	10^{-6}	10^{-6}	10^{-8}

TABLE 6: The value range of satellite capability indicators.

Velocity measure precision (m/s)	System sensitivity (°)	System stability (°/s)	Target location accuracy (m)	Imaging width (km)
0.5-10	4-8	0.35-0.7	30-50	10-30
Imaging time (h)	Ground resolution (m)	Signal bandwidth (mhz)	Information transmission rate (Gbps)	Symbol error rate
0.5-3.5	0.5-20	100-600	5-20	$1*10^{-8}-1*10^{-5}$

methodology are that it takes cost as an input variable rather than an output variable and emphasizes the optimization of the tradeoff between cost and effectiveness. In the process of tradeoff and optimization, cost, like other input indicators, is managed and controlled as a constraint by imposing upper and lower limits. Therefore, when determining the cost range, we should not set a particular target arbitrarily but conduct a series of cost and effectiveness analyses to comprehensively understand what cost changes can improve the effectiveness and which parameters can effectively control cost.

To define the value range for each parameter and cost, the CAIV methodology also proposed the concept of the *tradeoff optimization space*. The tradeoff optimization space can be defined using cost and effectiveness and regarded as a set of all feasible alternatives, and each element in it represents a feasible alternative. For the cost of a satellite, it is necessary to determine the upper limit of C_{omax} within the economically affordable range, and the lower limit C_{omin}, if necessary, it also needs to be determined. On the other hand, we need to determine the ranges of the design parameters used to measure effectiveness. For design parameters, we need to know the constraints of equipment capabilities and the level of the existing technology. Take a certain indicator P_i for example, if the lowest value that can meet the mission requirement is P_i^L, and the highest value that can be achieved under the current technical level is P_i^U, then the value range of the indicator is $P_i^L \leq P_i \leq P_i^U$. Of course, for some indicators, a smaller value is better than a larger value so that the range will be $P_i^U \leq P_i \leq P_i^L$.

4.2. Building and Solving the Tradeoff Optimization Model of Satellite. The designers of remote sensing satellites need to select the best design scheme among all alternatives in the established tradeoff optimization space. There are many evaluation criteria for measuring the effectiveness and cost of a design scheme. This paper takes the effectiveness-cost ratio as the criteria, and the tradeoff optimization space is taken as the constraint condition. The tradeoff optimization model of a remote sensing satellite is established as follows:

$$\begin{cases} \max K = E/C_o, \\ \text{s.t.} E = F(P_1, \cdots, P_n), \\ C_o = \varphi(P_1, \cdots, P_n), \\ E \geq 6, \\ 10000 \leq C_o \leq 30000, \\ P_i^L \leq P_i \leq P_i^U, i = 1, \cdots, n, \end{cases} \quad (21)$$

where K represents the value of the effectiveness-cost ratio, and the larger the value, the better the satellite design scheme. $E = F(P_1, \cdots, P_n)$ is the effectiveness evaluation model of satellite, which can be calculated based on Equations (1)–(13). According to design's requirements, satellite's effectiveness after running for 10,000 hours must be higher than 6. $C_o = \varphi(P_1, \cdots, P_n)$ is the satellite cost model, which can be calculated using Equations (14)–(20). According to the design requirements, the total cost of remote sensing satellite is estimated to be between 100 million and 300 million (RMB). $P_1, \cdots, P_n$ represent all kinds of parameters of the satellite, and their ranges can be estimated according to the mission requirements.

The tradeoff optimization model can be transformed into an extremum problem of the function with multiple constraints. To avoid the problem of a locally optimal solution in the solving process, a generalized genetic algorithm

Table 7: Cost models for subsystems.

Subsystem	Cost model
Propulsion subsystem	$C_{o1} = 832.3837X^{0.3167} \bullet P_1^{-0.1751} \bullet P_2^{c0.0200} \bullet P_3^{0.0530} \bullet P_4^{22.0525}$
Data transmission subsystem	$C_{o2} = 2.0764X^{1.2182} \bullet P_5^{0.3836} \bullet P_6^{-0.0007} \bullet P_4^{2.6665}$
Payload subsystem	$C_{o3} = 2.5742X^{0.7652} \bullet P_7^{-0.0032} \bullet P_8^{0.0569} \bullet P_9^{0.0236} \bullet P_{10}^{-0.1204} \bullet P_{11}^{0.4727} \bullet P_4^{4.2080}$
Control subsystem	$C_{o4} = 392.1322X^{0.4898} \bullet P_1^{-0.3508} \bullet P_2^{0.0587} \bullet P_3^{0.8144} \bullet P_7^{-0.0464} \bullet P_4^{0.1023}$
Auxiliary subsystem	$C_{o5} = 282.4148X^{0.6225} \bullet P_4^{3.8215}$

Table 8: The value of the capability indicators.

Velocity measure precision (m/s)	System sensitivity (°)	System stability (°/s)	Target location accuracy (m)	Imaging width (km)
9.7323	7.8769	0.6765	30.7965	20.0000
Imaging time (h)	Ground resolution (m)	Signal bandwidth (mhz)	Information transmission rate (Gbps)	Symbol error rate
3.4614	8.0000	237.8178	7.8004	5.0592×10^{-6}

Table 9: The weight and reliability requirements of each subsystem.

Parameter	Propulsion subsystem	Control subsystem	Payloads subsystem	Data transmission subsystem	Auxiliary subsystem
Weight (kg)	185	51	571	255	883
Reliability	0.9804	0.9959	0.9683	0.9733	0.8022

[29, 30] is introduced to solve the extreme value of the effectiveness-cost ratio of the model. The core idea of this algorithm is to perform selection, crossover, mutation, and other related operations on a biological population consisting of a certain number of individuals by simulating the evolutionary laws of organisms in nature to find the optimal solution or approximate solution according to the target requirements. On this basis, other scholars have continued to supplement and develop the genetic algorithm to the completeness, and it has become the most widely used optimization algorithm. The basic parameters of the algorithm are set as follows:

(i) The population size is 100

(ii) Mutation probability is 0.01

(iii) Crossover probability is 0.6

After 30 iterations, the optimization results tend to be stable, and the highest value of effectiveness-cost ratio that can be obtained in the tradeoff optimization space is 4.0705×10^{-4}, where the effectiveness value is 6.8421, the cost value is 168 million (RMB). The value of satellite's capability indicators is shown in Table 8, and the weight and reliability requirements of each subsystem are shown in Table 9.

Before performing the tradeoff optimization of effectiveness-cost, the effectiveness of the satellite is 6.7794, and the cost is about 251 million (RMB), meaning the effectiveness-cost ratio is 2.7047×10^{-4}. Compared with the tradeoff design scheme, the effectiveness of the satellite has increased by 0.9249%, the cost of the satellite has reduced by 33%, and the satellite effectiveness-cost ratio has increased significantly. The tradeoff design scheme of the satellite is more practical than the original design based on meeting performance requirements and affordability.

5. Discussion and Conclusion

Based on the idea of the CAIV methodology, this paper proposes a tradeoff optimization method of effectiveness-cost for a remote sensing satellite, in which multiple models are combined synthetically to improve satellite's design scheme. Compared with the other tradeoff optimization methods, the input cost is taken as an independent variable and is considered in the whole tradeoff process in this work. The proposed approach emphasizes that cost is integral to design indicators to ensure that the input cost is within the tolerable limit. Under the premise of meeting the performance requirements of the satellite, the proposed method can find the optimal scheme from the whole feasible design domain, which is different from selecting the design scheme with the highest effectiveness-cost ratio from several alternative design schemes as the decision result. The tradeoff optimization between cost and effectiveness can efficiently yield calculated results close to the actual use situation, which is beneficial to discover unreasonable links and helps improve the design scheme.

Compared with the original design and effectiveness-cost ratio, the optimized design scheme is more competitive, as we can see from the case study. However, since the evaluation criteria in the tradeoff optimization model are only related to the effectiveness and cost of the satellite, the results

will be affected by the accuracy of the effectiveness and cost models. Therefore, we need to make more precise calculations on the cost and effectiveness of satellites in future research. Additionally, the subjective preference of decision-makers for effectiveness and cost also affects the final satellite design scheme in the actual decision-making process, which is difficult to quantify and should be further discussed.

Data Availability

All of the data used to support the findings of this study are included in the article.

Conflicts of Interest

The authors declare no conflict of interest.

Authors' Contributions

Jian Jiao and Zhiwei Chen prepared the conception and the formal description of the proposed solution; they both made the literature review; Dongming Fan analyzed the data; and Zhiwei Chen and Xinlin De implemented the proposed solution and wrote the paper.

References

[1] D. Cave, "Systems effectiveness analysis tool for evaluating guided interceptors," in *32nd Aerospace Sciences Meeting and Exhibit; American Institute of Aeronautics and Astronautics*, Reno, NV, U.S.A, 1994.

[2] W. Guo and X. Shao, "Detection effectiveness of ship-borne radar under interference environment based on ADC model," *Command Control & Simulation*, vol. 3, pp. 47–49, 2014.

[3] H. Shao, H. Jiang, X. Zhang, and M. Niu, "Rolling bearing fault diagnosis using an optimization deep belief network," *Measurement Science and Technology*, vol. 26, no. 11, article 115002, 2015.

[4] W. Bi, F. Gao, and A. Zhang, "A novel weapon system effectiveness assessment method based on the interval-valued evidential reasoning algorithm and the Analytical Hierarchy Process," *IEEE Access*, vol. 9, pp. 53480–53490, 2021.

[5] S. Zhao, S. Song, Q. Qi, and W. Lei, "Cost-efficiency tradeoff is optimized in various cancer types revealed by genome-wide analysis," *Molecular Genetics and Genomics*, vol. 296, no. 2, pp. 369–378, 2021.

[6] L. Washington and A. Levis, "Effectiveness analysis of flexible manufacturing systems," in *Proceedings. 1986 IEEE International Conference on Robotics and Automatio*, pp. 1821–1826, San Francisco, CA, USA, April 1986.

[7] W. F. Stevens, *Weapon System Effectiveness Industry Advisory Committee*, SAE Technical Paper, 1964.

[8] T. N. Dupuy, *Application of the Quantified Judgment Method of Analysis of Historical Combat to Current Force Assessments*, Springer, Boston, MA: Military Strategy and Tactics, 1975.

[9] A. M. Elhady, "Remote sensing satellite system overall effectiveness analysis and modeling," in *2014 IEEE Aerospace Conference*, pp. 1–10, Big Sky, MT, USA, 2014.

[10] L. Tao, "Study of system effectiveness evaluation for optical imaging reconnaissance satellite based on fuzzy theory," in *3rd International Symposium of Space Optical Instruments and Applications*, vol. 192 of Springer Proceedings in Physics, Springer, Cham.

[11] P. Qin, "Effectiveness evaluation for remote sensing satellite application system based on AHP, ADC and gray theory," *Modeling and Simulation*, vol. 6, pp. 218–227, 2017.

[12] H. Chen and Y. Li, "Effectiveness evaluation and evaluating method innovation for weapon system," *Journal of Institute of Command & Technology*, vol. 15, pp. 1–5, 2004.

[13] X. De, J. Jiao, and Y. Zhu, "Modeling and evaluation for effectiveness of remote sensing satellite based on ADC model," in *Proceedings of the 2018 International Conference on Mathematics, Modelling, Simulation and Algorithms ((MMSA 2018)*, Chengdu, China, 2018.

[14] P. Nguyen, L. Lozzi, and W. Galang, *Unmanned Space Vehicle Cost Model*, US Air Force Space and Missile Systems Center (SMC/FMC), California, 2002.

[15] S. Winn and J. Hamcher, *NASA/Air Force Cost Model NAF-COM*, Science Applications International Corporation, 2002.

[16] "Small satellite cost model website," 2018, http://www.aero.org/capabilities/sscm/index.html.

[17] J. R. Wertz, D. F. Everett, and J. J. Puschell, *Space Mission Engineering: the New SMAD; Space Technology Library*, Microcosm Press, El Segundo, 2011.

[18] A. Shao, E. A. Koltz, and J. R. Wertz, "Quantifying the cost reduction potential for earth observation satellites," in *Proceedings of the 12th Reinventing Space Conference*, pp. 199–210, London, UK, 2014.

[19] Y. K. Chang, H. Kim, and J. S. Kang, "Development of reliability-corrected cost model for small earth observation satellites," *Acta Astronautica*, vol. 88, pp. 163–175, 2013.

[20] C. M. A. Kaye, D. R. Graham, and A. L. Gotwald, *Cost as an Independent Variable: Principles and Implementation*, Space and Missile Systems Center Los Angeles Afb Ca, 2000.

[21] Y. T. Tan and B. A. Guo, "Effectiveness-cost analysis & target demonstration method based-on CAIV," *Systems Engineering - Theory & Practice*, vol. 27, pp. 48–53, 2007.

[22] Q. L. Han, X. J. Cheng, and D. Xu, "Mechanical product design cost-effective tradeoff based on CAIV," *Control and Decision*, vol. 29, pp. 1522–1526, 2014.

[23] L. Gu, X. Xi, K. Liu, and S. Wang, "Cost effectiveness model and optimization of weapon system based on cost as an independent variable," in *2016 12th World Congress on Intelligent Control and Automation (WCICA)*, pp. 2455–2459, Guilin, China, 2016.

[24] P. E. Ardanuy, C. F. Schueler, S. W. Miller, K. Jensen, and W. J. Emery, "Use of CAIV techniques to build advanced VIIRS approaches for NPOESS key EDRs," in *Proceedings of the SPIE(2002)*, pp. 142–151, Seattle, United States, 2002.

[25] H. E. Apgar, "Affordable space systems," in *Proceedings of AIAA SPACE 2013 Conference and Exposition*, pp. 1–15, San Diego, United States, 2013.

[26] T. L. Saaty, "How to make a decision: the analytic hierarchy process," *European Journal of Operational Research*, vol. 48, pp. 9–26, 1990.

[27] P. Duverlie and J. M. Castelain, "Cost estimation during design step: parametric method versus case based reasoning method," *The International Journal of Advanced Manufacturing Technology*, vol. 15, pp. 895–906, 1999.

[28] D. W. Marquardt, "An algorithm for least-squares estimation of nonlinear parameters," *Journal of the Society for Industrial and Applied Mathematics*, vol. 11, pp. 431–441, 1963.

[29] C. Dong and X. H. Guo, "A global optimization algorithm based on generalized genetic algorithm," *Computer Science*, vol. 26, pp. 7–10, 1999.

[30] Z. Chen, T. Zhao, J. Jiao, and F. Ren, "Availability analysis and optimal design of multistate weighted k-out-of-n systems with component performance requirements," *IEEE Access*, vol. 6, pp. 51547–51555, 2018.

Research Article

Research on Wireless Sensor Network Access Control and Load Balancing in the Industrial Digital Twin Scenario

Wei Zhou ID

Information Engineering Department, Suzhou University, Suzhou 234000, China

Correspondence should be addressed to Wei Zhou; weizhou@ahszu.edu.cn

Wireless sensor networks which are based on distributed information processing technology are taking an increasingly key role in industrial digital twin scenarios. There are many important issues in the access of networks. One of the most important issues is how to improve network access control and the effectiveness of load balancing. Based on the industrial digital twin technology, this article first introduces several typical network access and network loads and performs tree-structured processing on the outliers generated during the chain formation process to reduce the length of the data transmission path, optimize the main chain head and subchain chain head selection strategy and chaining rules, and perform nonchain operations on common nodes and chain heads near sink to reduce data inverse transfer. The experimental results show that this paper uses the digital twin calculation formula to accurately and objectively determine the remaining cluster head and the distance head and the base station, so that when the node distance is limited, the network energy consumption can be balanced as much as possible, and the network load is promoted.

1. Introduction

Wireless sensor networks integrate sensor technology, computing, and communication technology and become an active research branch in the field of computer science. In the wireless sensor network architecture, the digital twin technology at the network layer is crucial to the life cycle of the wireless sensor network [1]. The network load algorithm has become the digital twin technology that is currently the focus of research. The digital twin protocol is the core technology of the wireless sensor network layer. While discovering a path with a smaller delay, it avoids network congestion and balances network energy consumption. For different application environments, the digital twin protocol can be divided into network access protocol, network load protocol, and geographic digital twin protocol. When designing a digital twin protocol, an important challenge will be faced, that is, how to complete the sensing, communication, and control functions under the condition that the node's energy resources, computing capabilities, storage space, and communication capabilities are highly restricted. For this reason, the main goals of the wireless

sensor network digital twin protocol design are establishing an energy efficiency path, forming a reliable data forwarding mechanism, and maximizing the network life cycle [2–5].

With the rapid rise of the Internet and the Internet of Things, as well as the rapid development of microelectromechanical systems (MEMS), distributed information processing, radio communications, multifunction sensors, embedded software, and hardware technologies have matured day by day, and wireless sensor networks have become a representative of emerging fields. When it was born, these software and hardware technologies have provided great help to promote the rapid development of WSN technology [6–8]. WSN uses a variety of highly integrated and low-cost micro wireless sensor nodes to collaborate to achieve real-time monitoring and perception in different application environments and collect relevant data or other object data of interest [6], and then, the embedded system performs preliminary processing on the monitoring data [7], and then, the network sends these data digital twins to the control center according to the defined transmission protocol. It divides a network with a large range and nodes into multiple smaller clusters according to specified rules, making

the network hierarchy clearer and more scalable. Since most of the non-cluster-head nodes can close the communication module for a long time, for the traditional uniform network load protocol, due to the multihop transmission between clusters, the cluster head node near the base station takes on more forwarding tasks, which consumes more energy and causes the problem of uneven network energy consumption [9–11].

Based on the study of multiple clustering and chained digital twin algorithms, this paper proposes a tree-shaped chained multihop digital twin algorithm (TUCM). The algorithm introduces angle control between candidate cluster heads to optimize the selection method of cluster heads, builds a tree-shaped chain structure to optimize the strategy, uses a hybrid hierarchical network topology structure, and improves the path selection probability model of the ant colony algorithm. And the pheromone update model realizes the mixed multihop data transmission to eliminate the shortcomings of the digital twin and other network load algorithms in the large-area measurement area environment of the cluster node to the sink node in the long-distance single-hop transmission. Aiming at the problem of random selection when selecting candidate cluster heads, this paper sets a threshold calculation formula for each node according to the remaining energy. By considering the remaining energy of the node in the selection of the threshold, the threshold generated by the node with less energy is smaller, so that it has a smaller probability to become a candidate cluster head node. The bottom layer constructs the network nodes into multiple subchains and selects the main chain head and the subchain heads to construct the top-level chain head chain. In order to improve the success rate of data transmission between clusters, this paper adopts Bayesian link estimation for each cluster head node after each round of cluster formation.

2. Related Work

Due to the huge application value of wireless sensor network technology, which has a profound impact on the development of the country and society, domestic and foreign scientific researchers have conducted in-depth research on it from different directions. Because of the special application environment of WSN, which is often unattended, the design of the digital twin protocol plays a vital role in whether the network can be used normally and how long it can be used. Because traditional networks do not have these new features, many different WSN digital twin algorithms have emerged. The following briefly describes the current research status of WSN at home and abroad [12].

Regarding network topology control, the existing research results mainly have two ideas. One uses the positioning mechanism to accurately and effectively divide the network. However, the positioning mechanism is more expensive and generates greater internal friction; the other is to use level type topology (clustering algorithm) takes some nodes and then constructs a backbone network responsible for data processing and forwarding. The rest of the noncluster head nodes are mainly used to sense and collect nearby information. And in the cluster head election stage, the communication module is temporarily closed, and the sleep mode is entered to save energy. At present, some domestic and foreign scholars have conducted research on this aspect as follows: Zheng and Sivabalan [13] proposed a classic clustering protocol LEAcH. The protocol periodically performs two phases: cluster establishment and data communication. In the cluster establishment stage, the nodes in the network are randomly selected as cluster heads, and the nodes that are not selected as cluster heads choose to join the clusters that are closer to them. Leng et al. [14] believe that in the data communication stage, the member nodes in the cluster will transmit the collected information to the cluster head, and the data will be fused in the cluster head node. Compared with traditional network access protocols, this algorithm extends the network life cycle by about 15%. However, this algorithm selects cluster head nodes randomly, which can easily cause uneven distribution of cluster head nodes.

The HEED protocol proposed in Li et al. [15] uses a different competition mechanism from the LEAcH protocol to select cluster head nodes. The HEPrint protocol fully considers the role of node residual energy in selecting cluster heads, so that the selected cluster heads can construct a more reasonable network topology. Lim et al. [16] believe that this protocol requires all nodes to communicate directly with the base station, which requires relatively high hardware requirements for sensor nodes. Both of the above two protocols use single-hop communication within the cluster to directly transmit the data collected by the member nodes to the cluster head node. This single-hop communication method within a cluster is simple and easy to expand. However, Barykin et al. [17] did not consider the cluster head. For member nodes far away from the cluster head, energy consumption may be too fast due to long-distance transmission. With the in-depth study of the digital twin protocol, another multihop communication method within the cluster has emerged. According to the effectiveness and timeliness of the regional coverage of WSN in the monitoring environment, scholars proposed a nonuniform clustered wireless sensor network digital twin algorithm based on energy efficiency improvement [18–21]. This algorithm first optimizes the cluster head election based on the node distribution density and then controls the competition radius of the clusters to achieve nonuniform clustering. Then, each cluster head calculates the distance coefficient and the dispersion coefficient to determine the internal communication mode of each cluster. It adopts single-hop and multihop transmission mechanism. The results show that improves the energy efficiency of network nodes, avoids the "hot spot" problem of WSN, delays the dead time of network nodes, and improves the effective coverage time of the monitoring area and the overall network life cycle [22–25].

3. Network Construction of Industrial Digital Twin Scene

3.1. Industrial Digital Network Cycle. In the structure of the industrial digital network, the SU is responsible for

collecting the required data information in the area to be tested and then using corresponding means to send the data information to the corresponding relay station; the DPU is mainly composed of low-power embedded microcontrollers, capable of coordinate various operations of the management node, such as processing and saving the data collected by the sensor unit; TU is mainly composed of low-power communication, etc., managing the communication process between nodes, and at the same time exchanging related data information; currently, PU mainly adopts that alkaline batteries or lithium batteries are responsible for providing energy for the work of nodes, and the energy unit is related to the lifetime of the entire network.

$$\sum I(i,j) - \sum \bar{\delta}(i,j) + \bar{\delta} \max \sqrt{i^2 + j^2} = 0. \quad (1)$$

Many small nodes are scattered in the environment to be tested, and nodes with specific functions form a wireless network. Finally, the monitoring center also real-time control and management of network nodes can be achieved through the received information.

Since the functional characteristics of the sink node determine its stronger data processing, fusion and information transmission capabilities than ordinary nodes, it can not only realize the connection between WSN and the Internet and other external networks but also send the collected data information to the external network.

$$\lim_{x \to \infty} (\bar{\delta} \max - \bar{\delta} \min) - \lim_{x \to \infty} (\bar{\delta}(i,j) + \bar{\delta} \max) = 0. \quad (2)$$

With the collection and transmission of data, network nodes gradually exhaust their own energy. Natural and human factors may also cause node failure or death, communication link quality, and wireless medium's own factors will affect the normal operation of the entire network. These are several types of cause networks. At this time, if the network is paralyzed and the tasks delivered by the user cannot be completed normally, it means that the network does not have good robustness, and the design of the digital twin protocol must consider good robustness or robustness. In a specific environment, robustness is difficult to evaluate by a single value, and it is usually discussed in detail based on node and link models.

3.2. Distribution of Sensor Node System. A wireless sensor network system usually includes a sensor node, a base station node, and an application node. A large number of sensor nodes are arbitrarily scattered in the designated sensor field. Each node can collect the information of the sensing object in Figure 1. After the query is sent for a period of time, the sink starts to receive the returned information from multiple paths. At this time, it selects the optimal path from it and sends a "path strengthening" message to the corresponding neighboring node. The "path enhancement" message is also a query command, which is different from the previous one in that it contains a larger information collection rate.

The "path strengthening" message is transmitted hop by hop along the optimal path to the sensor node being queried. This path becomes the "main path," and the other paths become the backup paths accordingly. After the sensor node receives the "path enhancement" message, it will collect the information according to the required rate in Table 1.

The closer the node is to the base station, the smaller the node's competition radius. Correspondingly, the cluster structure closer to the base station is smaller, which will reduce the energy consumption of data communication in the cluster, and can reserve more energy for the relay and forwarding services between clusters.

In the network access protocol, each wireless sensor node in the network is homogeneous, that is, has the same state, and is randomly distributed at any location in the network. The disadvantage is that the cost of establishing and maintaining a digital twin is high, and the number of data transmission hops is large, which is not suitable for large-scale network applications.

There is no hierarchy of nodes in the network access protocol. The node sends data directly to the sink node, or it can be forwarded to the sink node. The flooding digital twin protocol is that after each node receives the information, it forwards data packets to neighboring nodes in the form of broadcast.

$$\text{for}(t, t-1 \in C(r,t)), A_t(\alpha, \beta) = F[A(t, t-1), M(i,t)]. \quad (3)$$

Flooding the digital twin agreement is prone to implosion. The normal node first sends data to each neighboring node to receive the data and sends it to other nodes except itself. And so on, until the collected data information is transmitted to the sink node, or until the node information data expires. The biggest problem with this protocol is that it generates a large number of duplicate data packets and occupies a large amount of network resources, which makes the digital twin and link resources too wasteful, resulting in low efficiency.

3.3. Cluster before Digital Information Update. The GEAR digital twin mechanism establishes an optimized event area, avoiding flooding propagation, thereby reducing the cost of establishing the digital twin. The future situation prediction stage is based on the law of the development of the network load process to realize the trend prediction of the future operation state of the system. The future forecast results will be submitted to the operation dispatcher for decision-making and use, and the closed-loop control of the network load will be realized.

$$\iint A_t(\alpha, \beta) dadb - \iint [A(t, t-1), M(i,t)] dt d(t-1) = 0. \quad (4)$$

In the GEAR digital twin, the wireless links between nodes are symmetrical. The query message propagation in the GEAR route includes two stages. This link is the core of the entire situational awareness process. It also runs through the entire situational awareness process.
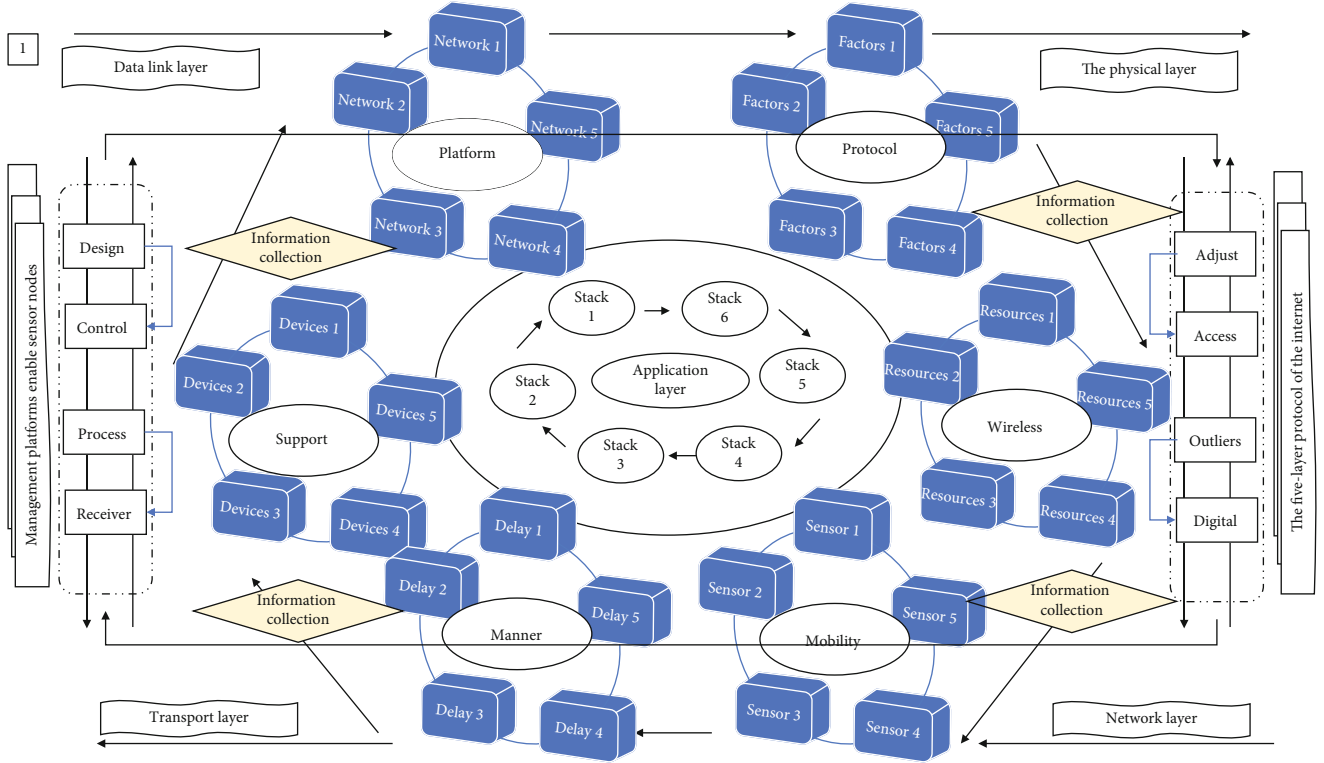
FIGURE 1: Sensor node system distribution topology.

TABLE 1: Data forwarding in the sensor network.

Data number	Sensor network 1	Sensor network 2	Sensor network 3
1	16.77	44.29	7.26
2	16.89	44.44	7.33
3	17.42	45.07	7.64
4	18.11	45.92	8.04
5	18.79	46.73	8.43
6	19.31	47.37	8.74
7	19.62	47.74	8.92

$$\beta_t = \begin{cases} \alpha_1 - \dfrac{(\lambda_2 - \lambda_1)}{(\lambda_2 + \lambda_1)}, & t \le 0, \\ \alpha_1 - 1, & t > 0. \end{cases} \tag{5}$$

The chain head node will generate a token that can control the transmission of data along the direction of the chain head leader node. In each subsequent round, the node closest to the end of the chain will join the current chain and become the new end of the chain. When all sensor nodes have joined the chain, the final network node chain structure is formed.

In the chain structure, when a node dies, the chain structure needs to be reconstructed to prevent the chain from breaking. In each round, the leader node at the head of the chain stays with the node, and the remaining nodes only collect and receive data and merge them, and forward the

fused data along the chain to the next-hop neighbor nodes in Figure 2.

The directed diffusion protocol is a query-based digital twin protocol and a data-centric digital twin protocol. The agreement is divided into three stages: interest diffusion, gradient establishment, and path strengthening. The sink node determines the best path according to the magnitude of the "gradient" value. This protocol is very energy-efficient, but it is to establish the best path and consumes energy during the digital twin.

3.4. Network Load Balancing Overlap. Because wireless sensor networks are different from traditional wireless networks, other wireless sensor network digital twin algorithms cannot be simply applied to wireless sensor networks. A suitable digital twin algorithm must be designed according to the characteristics of the wireless sensor network itself for network access algorithms and network load algorithms.

$$\prod_{\alpha_1}^{\alpha_1 - 1} (\alpha_2 + \alpha_1)\left(E_n^1 + \lambda_1\right) \prod_{\alpha_1}^{\alpha_1 - 1} \frac{(\alpha_2 + \alpha_1)}{\left(E_n^1 + \lambda_1\right)} = 1. \tag{6}$$

When there is a corresponding request, the data information is sent to the destination. During data transmission or reception, each node in Figure 3 first detects the energy status, and if it is in a low energy status, it stops some unimportant operations, such as stopping as a relay node. But the message sent by the publisher is asynchronous, there is no need to wait for the subscriber to subscribe, and it does not care whether the subscriber subscribes or not.
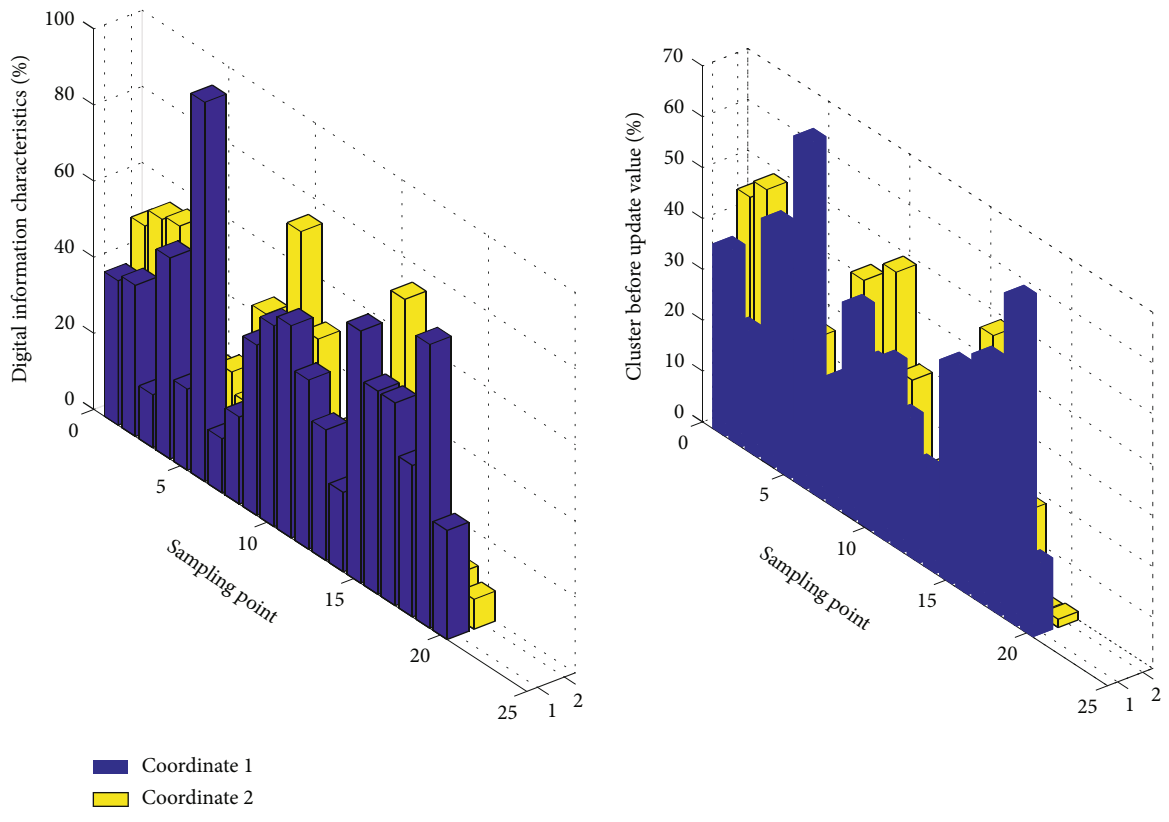
FIGURE 2: Cluster histogram before digital information update.
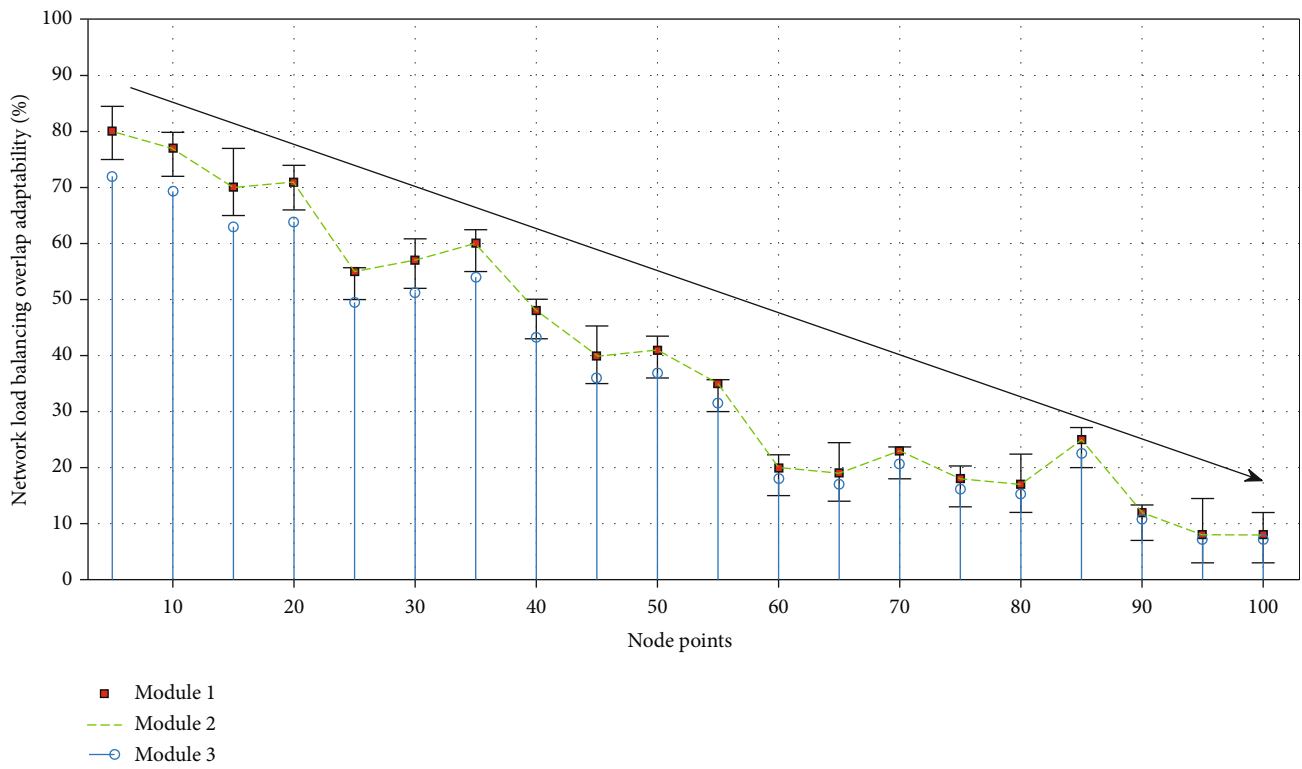
FIGURE 3: Analysis of overlapping fitness of network load balancing.

The real-time situation understanding stage is mainly to obtain network load data and information for integration and analysis and then conduct situation assessment and comprehensively evaluate the stability of network load through the establishment of various stability indicators and systems.

The advantage of the SPIN protocol is that the use of a metadata negotiation mechanism eliminates the entire network and solves the problems of implosion and overlap.

First of all, the protocol is established on a relatively abstract level to analyze and design sensor networks, without a more practical wireless network model. Secondly, the volatility of network nodes and links is not taken into consideration, and fault-tolerant technology is not supported. Finally, the resource adaptive technology proposed is relatively simple, not complete enough, and not suitable for actual wireless sensor network applications.

$$G\left(x, t, n \mid x^2 - t^2 = 0\right) - \left\| \begin{matrix} \alpha_2 + \alpha_1 & E_n^1 + \lambda_1 \\ E_n^1 - \lambda_1 & \alpha_2 - \alpha_1 \end{matrix} \right\| = 0. \quad (7)$$

For the digital twin protocol, the cluster heads are randomly selected in a probabilistic manner. Currently, various types of network load data information that can be collected mainly include network topology, real-time operation data, equipment component information, and network load.

The entire network topology is constantly changing, and the lifespan is short; the entire network chain digital twin of the protocol causes 99% of the nodes to need to fuse data, the first node of the chain has a large load and high energy consumption, and the data transmission delay of the end node is high. A WSN collaborative network load design method based on hierarchical area division (CCRD-HRD) is proposed. Based on SCA-HRD, this method adds consideration to discrete clusters and designs collaborative digital twins.

4. Wireless Sensor Network Access Control and Load Balancing Model Construction in the Industrial Digital Twin Scenario

4.1. Industrial Digital Hierarchical Topology.
For wireless sensor networks, network topology control has a particularly important meaning. Using real-life temperature data for simulation, the results show that compared with existing data collection methods at different decoding rates, the solution proposed in this chapter can always obtain better data quality without the need to deploy a dedicated sensor network.

$$\text{for}(r, t - 1 \in C(r - 1, t)), \sum Q_k * g_i y_{ik}^2 = \frac{\sum g_i y_{ik}^2}{\sum Cx * g_i y_{ik}^2}. \quad (8)$$

Situational awareness is the core link to realize real-time monitoring of large network loads. It extracts, analyzes, evaluates, and predicts network load and stable behavior based on the wide-area operating status information of the network load, in order to realize online secu-

rity early warning and intelligence to lay the foundation for active regulation.

Among them, the prerequisite for the whole network load situation awareness is to realize the extraction of situation elements first, and its purpose is to monitor the state of the power system and obtain data information. With the expansion and development of the power system in Table 2, the collection scope and technical means of situation elements are constantly expanding.

In addition to traditional power control and hierarchical topology control, people have also proposed heuristic node wake-up and sleep mechanisms. This mechanism enables the node to set the communication module to sleep when no event occurs and automatically wakes up and wakes up neighboring nodes in time when an event occurs. This mechanism cannot be used independently as a topology control mechanism and needs to be used in conjunction with other topology control algorithms.

4.2. Wireless Sensor Network Protocol Stack.
Due to the limitations of sensor node energy, computing, and storage capabilities, as well as the constant changes in sensor network topology and network resources, traditional network protocols cannot be used in wireless nodes. In wireless sensor networks, the digital twin protocol not only cares about the energy consumption of a single node but also cares about the balanced network. At the same time, the wireless sensor network is data-centric and establishes a forwarding path from the data source to the sink node based on the data of interest.

$$\left\langle \begin{matrix} \alpha_2 + \alpha_1 & E_n^1 + \lambda_1 \\ E_n^1 - \lambda_1 & \alpha_2 - \alpha_1 \end{matrix} \middle| \begin{matrix} 1 & 0 \\ 0 & 1 \end{matrix} \right\rangle = \left\langle \begin{matrix} \lambda & -1 \\ 1 & \lambda \end{matrix} \middle| \begin{matrix} \alpha_1 & 1 \\ 1 & \alpha_1 \end{matrix} \right\rangle. \quad (9)$$

By placing a large number of sensor nodes, enough paths are provided to satisfy the survival of the network and adapt to the environment. The system must also consider some important parameter settings, such as network size, node density, and the trade-off between energy consumption, reliability, and response time. Subscribers can subscribe to multiple channels, and publishers can send messages to subscribers through channels.

The energy waste at the MAC layer is mainly manifested in idle listening, receiving unnecessary data, and collision retransmissions. Assuming that the transmitting radius of the node is R, the farthest distance from the base station to the monitoring area is D. The base station in Figure 4 first determines its own gradient level as O and calculates the number of gradient levels $N = [D/R]$ to be divided.

The node that has not received the gradient message determines that its gradient is n after receiving the message, and the node that has determined its gradient discards it when it receives this message. After the gradient is established, the node sends interactive information to neighboring nodes and saves the received interactive information.

After the interaction is completed, the node calculates and updates its own comprehensive weight based on the

TABLE 2: Backbone network node communication module.

Node ID	Distance from the node	Neighbor node status
(S1, S2, S3)	D12	Route_flag 1
(S2, S2, S3)	D21	Power control 1
(S3, S2, S3)	D33	Power control 2
(S1, S1, S3)	D14	Route_flag 2
(S1, S3, S3)	D42	Route_flag 3
(S1, S2, S1)	D24	Power control 3
(S1, S2, S2)	D13	Power control 4

interaction by the neighboring node. In the clustering stage, the node first uses the updated weight to compare with the weight of the neighbor set: if the comparison between node a and any node b in the neighbor set meets any of the following rules, then the weight ratio of node a is considered.

$$\frac{\partial}{\partial W_{ij}{}^l} J(w,b) - \iint \frac{\partial}{\partial W_{ij}{}^l} A_t(\alpha, \beta) da db = 0. \quad (10)$$

In order to reduce energy consumption, the MAC protocol usually adopts an alternate wireless channel listening mechanism of "listening/sleeping." The sensor node only listens to the wireless channel when it needs to send and receive data, and try to enter the sleep state when there is no data to send and receive. Since the wireless sensor network is an application-related network, when the application requirements are different, the network protocol often needs to be customized according to the application type or the characteristics of the application target environment. No single protocol can fully adapt to a variety of different applications.

4.3. Network Algorithm Clustering Results. In the clustering process of the network algorithm, first calculate the optimal number of clusters for each divided area according to a certain strategy, and then use the digital twin algorithm to perform the first round of random clustering for each divided area intermittently, and only need to cluster later internal adjustment, and consider the nodes in Table 3, to avoid the nodes of the whole network periodically and frequently clustering and consuming too much energy and low-energy nodes serving as cluster head nodes multiple times.

In multihop data transmission between clusters, a threshold TD-MAx is introduced. If the distance between the cluster head node and the base station is less than TD-MAx, the cluster head node directly transmits the data to the base station. On the contrary, use the method described below as much as possible to transmit the collected data.

When the intercluster multihop transmission starts, each cluster head broadcasts a NoDE-s containing the cluster head ID, the current remaining energy, and its distance to the base station with the same power; it will maintain a set of candidate digital twin nodes according to the received message. The node decides whether to join the cluster head competition according to its own remaining energy.

$$\frac{\nabla J(w,b)}{\nabla J(b)} - \nabla \frac{1}{b} \sum_{i=1}^{m} J(w,b;x^i,y^i) + \lambda W_{ij}{}^l = 0. \quad (11)$$

The number of clusters is then refined into each divided area, and each divided area is intermittently used to perform specific clustering with the improved combination of digital twin and PEGASIS algorithm. Once the clustering is done, each divided region is formed. The member nodes in the cluster perform data collection, and cluster head nodes perform data fusion. Finally, each cluster head node forwards the fused data through the collaborative data transmission digital twin between the clusters and finally transmits it to the sink node. This process continues until the end of the wireless sensor network life cycle, and the duration is as long as possible.

5. Application and Analysis of Wireless Sensor Network Access Control and Load Balancing Model in the Industrial Digital Twin Scenario

5.1. Industrial Digital Data Element Preprocessing. In the wireless sensor network, the energy consumption of the wireless communication module of the sensor node in the idle state is equivalent to that in the transceiver state, so only by turning off the node's communication module can the energy consumption of the wireless communication module be greatly reduced, considering a certain mechanism choice.

A subscriber, such as a client, expresses an event or a type of event that it is interested in receiving in the form of event subscription. Some nodes are used as backbone network nodes, and their communication modules are turned on, and the communication modules of nonbackbone nodes are turned off. The backbone nodes build a network to be responsible for the digital twin forwarding of data.

$$\frac{\partial J(w,b;x^i,y^i)}{J(x^i,y^i)} = \frac{\partial f(x^i,y^i)}{\partial f(x,y)}. \quad (12)$$

After the wireless sensor network monitoring area is divided into hierarchical regions, the first-level region closest to the sink node is first used to calculate the probability and the principle of minimizing total energy consumption and then based on the total energy between regions.

Among them, the cluster head selection probability of each area in Table 4 is different, and it becomes smaller as the distance from the sink node increases, so as to ensure the nonuniform clustering of the entire network. Through this algorithm, participants can compress the sensory data collected in the target area into CS measurement values. In order to improve data quality, a data reconstruction algorithm based on multiple rounds is further proposed.

A good clustering algorithm can provide a foundation for data fusion, time synchronization, target positioning, and network management and is beneficial to extending the time of the entire network. Based on a reasonable and effective network clustering structure, it is possible to
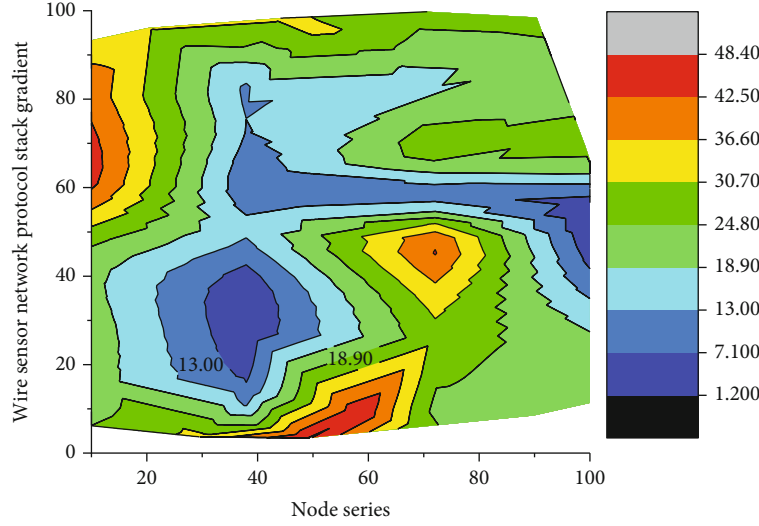
FIGURE 4: Gradient distribution of wireless sensor network protocol stack.

TABLE 3: Data transmission delay of chain end node.

Parameters	Transmission node 1	Transmission node 2	Transmission node 3
Distribution area	509.26	32.10	14.14
Base station coordinates	509.88	31.49	11.30
Number of nodes	510.49	32.94	8.60
Data packet size	511.11	36.27	6.69
Node initialization energy	511.73	40.85	6.19
Signal threshold	512.35	45.76	7.39
State cluster	512.96	50.07	10.14

TABLE 4: Algorithm of optimal cluster number for hierarchical area.

Circle steps	Algorithm meaning	Step codes
1	Upper-layer applications in X_i	% Program P1_1
2	An efficient network control system	% Generation of a Unit Sample Sequence
3	The cluster head selection probability $\bar{X}$	Clf;
4	Logical network structure as $X_i - \bar{X}$	% Generate a vector from -10 to 20
5	A reasonable and effective network	N = -10:20;
6	The distance from the sink node $\sum_{i=1}^{n} \kappa X_i$	% Generate the unit sample sequence
7	In networks depends on the clustered $\mu_X(\kappa - t)$	U = [zeros (1,3) ones(1,28)];
8	A foundation for data fusion in $\left(X_i + \bar{X}\right)^2$	% Plot the unit sample sequence
9	Good clustering algorithm	Stem (n,u);
10	It becomes smaller as the distance $\sum_{i=1}^{n} \left(X_i + \bar{X}\right)^2$	Xlabel ('Time index n'); ylabel ('Amplitude');
11	It is possible to establish $\mathbb{Z}[0, 1]$	Title ('Unit Step Sequence');
12	The application of many protocols	Axis ([-10 20 0 1.2]);
13	So as to ensure the nonuniform $A(t, t - 1)$	Clf; % Clear old graph
14	It provides channel control in cov $\left(X_i - \bar{X} \mid X\right)$	Stem (n,x); % Plot the generated sequence
15	It is beneficial to extending the lifetime	Axis ([0 40 -4 4]);
16	A foundation for data fusion in $\lim_{x \longrightarrow \infty} \left[\left(X_i - \bar{X}\right)^2\right]$	Grid;

establish an efficient network control system, realize effective resource scheduling and application including bandwidth allocation and frequency reuse, provide channel access control, efficient digital twin computing, and establish virtual circuits and other functions.

The application of many protocols in sensor networks depends on the clustered logical network structure, and many upper-layer applications can run on this structure. By introducing a new spatiotemporal data abstract model in the target perception area, the participant's movement process is represented as a random measurement of the perception task.

$$\frac{\partial J(w, b; x^i, y^i)}{\partial J(w, b)} = \frac{\partial f(w, b)}{\partial f(w) \partial f(b)}. \tag{13}$$

The protocol uses digital twins in the multihop phase between clusters to adaptively determine the weight coefficients occupied by multiple metric factors. The selection of each metric factor is of great significance for the node when selecting the next hop standard for evaluating the network survival time, and the distance can reduce the number of hops and reduce the transmission delay.

The quality status can estimate the reliability of the wireless link transmission channel, and they reserve more energy for intercluster data forwarding. In this paper, when the cluster head node selects the next hop node in the multihop phase between clusters, it is based on a cost function improved from the protocol, which includes the cluster head. The number of internal members is used as a measurement factor, and the weight coefficients occupied by each measurement factor in the cost function are objectively and adaptively calculated using digital twins.

5.2. Realization of Wireless Sensor Network Access Control Simulation. Assuming that nodes in the wireless sensor network access control, each node calculates the probability of becoming a candidate cluster head according to the formula. In each round of selection of cluster heads, the percentage of candidate cluster heads to all nodes is p. For all nodes N, the number of candidate cluster heads will be approximately $N \times p$, and HEAD_MsG will be broadcast.

$$\begin{cases} \lim_{x \to \infty} A(t, t-1) - M(i, t) = \mathbb{Z}[0, 1], \\ \lim_{x \to \infty} A(t) - M(t) = \mathbb{Z}[0, 0]. \end{cases} \tag{14}$$

After that, if K nodes are generated from these candidate cluster head nodes as cluster head nodes in this round, it is necessary to broadcast MsG messages with the largest energy and MsG messages for successful elections. Finally, the remaining N-K ordinary nodes in the network select the cluster head node with a stronger signal according to the received signal strength.

The cluster head node in Figure 5 calculates and sends K time slot information to the member nodes in the cluster. Based on the above analysis, in each round of cluster formation, the total number of messages in the network is $N \times p$.

Experimental results show that compared with existing collection methods, the proposed scheme can obtain better data quality under different decoding rates.

This article will use OMNeT++ (Objective Modular Network Testbed in C++) as a simulation platform tool. This software is a component-based, object-oriented modular simulation software. OMNeT++ provides a graphical network editor and network data stream viewing tool and can run on multiple operating system platforms. It uses events as the basic communication mechanism to provide the loosely coupled interaction mode required by large-scale systems.

On the OMNeT++ platform, the network protocol is written in "+" language, and the user-defined language "NE0" is used to construct the network model. Compared with simulation platforms such as Ns-2 and OPN, OMNe ++ not only can easily define the network topology and has obvious advantages in the perfection of the model library and the support for debugging and tracing of the protocol code.

$$\begin{bmatrix} Q_k * g_i y_{ik}{}^2 & Cx \\ -Cx & Q_k * g_i y_{ik}{}^2 \end{bmatrix} \times \begin{bmatrix} \sin\theta & -\cos\theta \\ \cos\theta & -\sin\theta \end{bmatrix} = 1. \tag{15}$$

The main documents are introduced as follows: (1) need file: use ned language to describe the network topology, network simulation parameters, and network connections between nodes; (2) cc file: use "+ language to write each module algorithm; (3) msg file: message file, mainly used to simulate various events, messages, frames, etc. in the transmission process; (4) I.b file: the kernel library and user connection library used in the simulation process; (5) ini file: users set various parameters in the simulation module; and (6) -vec and -sna files: output vector files and output scalar files, mainly it is used to store data and record the simulation results.

$$\sum_{i=1}^{n} \kappa X_i Z(i) - \sum_{i=1}^{n} \kappa X_i + \mu_X = \sum_{i=1}^{n} \mu_X (\kappa - t) X_i. \tag{16}$$

According to two different values of c, the sensory data collected by each participant in the target area during a period of time will be compressed into a measured value. The original data is reconstructed by an iterative algorithm using the measurement matrix and measured values. In order to improve the quality of data reconstruction, a data recovery algorithm based on multiple rounds is further proposed by using the time correlation between the data.

5.3. Case Application and Analysis. In this paper, the algorithm is mainly simulated and tested. In the case of limited experimental conditions, MATLAB is mainly used as an experimental simulation tool to simulate the setting of WSN simulation scenarios and simulation parameters, and the experimental simulation is performed based on the simulation performance metrics.
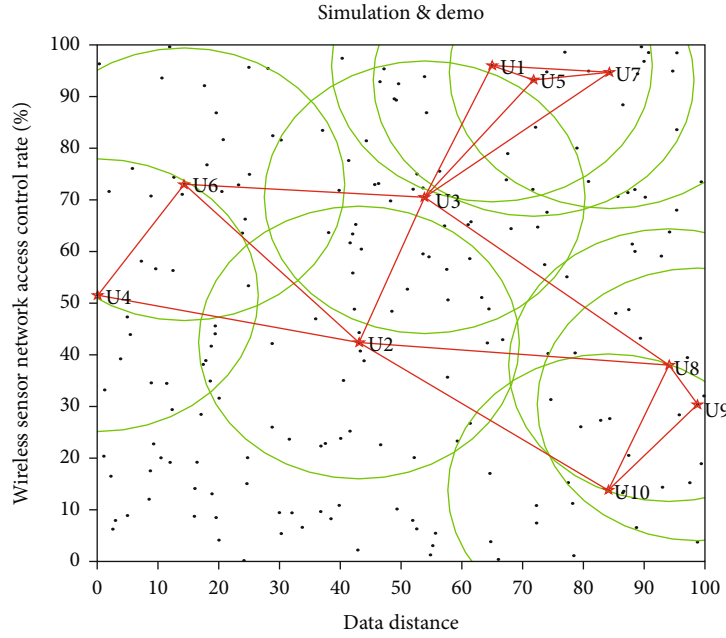
FIGURE 5: Distribution of wireless sensor network access control nodes.

Through several simulations in MATLAB, better simulation analysis results of the network survival time and total energy consumption of the three algorithms are obtained. For the simulation results of the network survival time in Figure 6, we, respectively, counted the number of rounds of the three algorithms at the beginning of dead nodes, 10% node deaths, 50% node deaths, 70% node deaths, and the entire network node death.

This article is the effect diagram of the nonuniform clustering of the protocol formed by 100 nodes in a square network with a side length. Among them, the first to sixth steps are the cluster formation stage, and the seventh to eighth steps are the intercluster multihop data transmission stage.

In the first step of the protocol, network initialization for the base station sends a start message to all nodes. All nodes calculate the approximate distance from the base station based on the received signal strength. The dead node no longer establishes any contact with the base station. When the participants move to some monitoring points to collect data, the movement of the monitoring points is similar to the random walk between nodes in WSNs to collect data.

$$\text{cov}\left(X_i - \bar{X} \mid X\right) = \sum_{i=1}^{n} \left(X_i - \bar{X}\right)^2 + \sum_{i=1}^{n} \left(X_i + \bar{X}\right)^2 + \sum_{i=1}^{n} \left(X_i\right)^2. \tag{17}$$

In the text, the green dot represents the broadcast message, and the straight line with the arrow represents the wireless communication connection established by the node and the base station; the right picture shows the start of the surviving node in the network receiving the base station transmission, where the white dots represent nodes that died

due to exhaustion of energy, and no communication connection with the base station is established.

It can be seen that the algorithm prolongs the network lifetime more effectively. For the simulation results of the network, the number of rounds in which the three algorithms consume 10% of the total energy, 50% of the total energy, 70% of the total energy, and total energy consumption of the three algorithms is, respectively, counted. In a sense, its trajectory can completely cover the target area. In this topic, a distributed coding algorithm based on compressed sensing is proposed.

All nodes in the network in Figure 7 enter the dormant state. Each node that becomes a candidate cluster head will broadcast the message according to its own competition radius. After receiving the message, the other candidate in the election before will be awakened from the dormant state.

The message with stronger signal is selected, and the message is sent to it to apply to join the cluster. The cluster head node will calculate the TDMA time slot according to the number of members in the cluster and send it to the establishment of the cluster which is completed. First, we simulate the movement trajectory of the participant and obtain the respective measurement vector of the participant through the trajectory position. Multiple participant trajectories can obtain a binary measurement matrix.

$$\frac{\text{cov}\left(X_i - \bar{X} \mid X\right)}{\text{cov}\left(X_i + \bar{X} \mid X\right)} = \lim_{x \to \infty} \left[\left(X_i - \bar{X}\right)^2\right] \times \frac{\sum_{i=1}^{n} \left(\sum_{i=1}^{n} \left(X_i - \bar{X}\right)^2\right)^2}{\sum_{i=1}^{n} \left(X_i + \bar{X}\right)^2}. \tag{18}$$

After the cluster in each level area is formed in the cluster domain, it will allocate time slots according to the TDMA
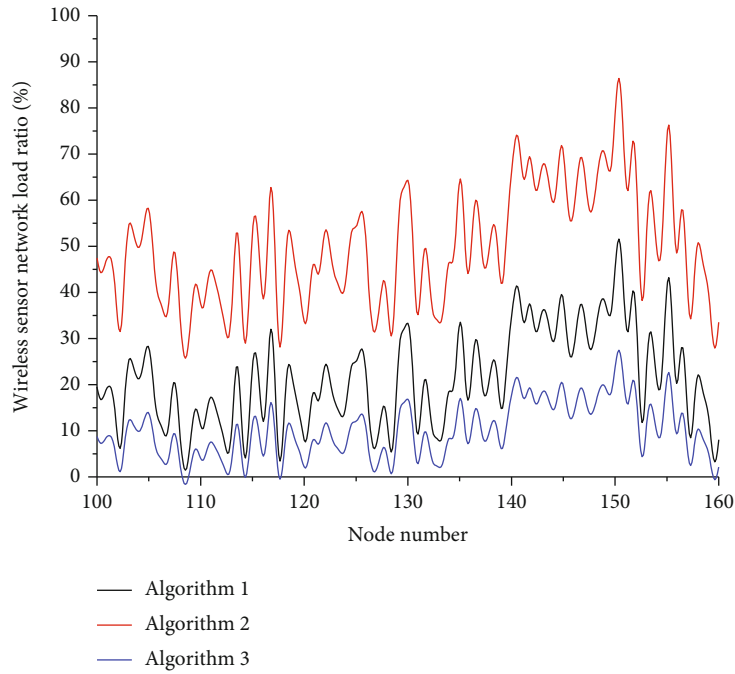
Figure 6: Comparison distribution of total energy consumption of wireless sensor network load.
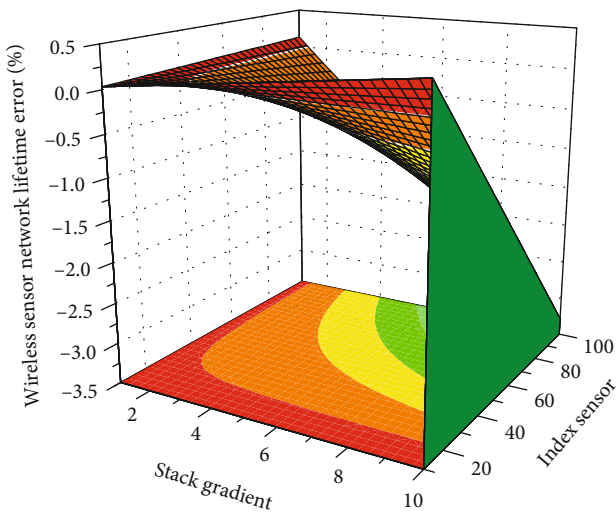
Figure 7: Three-dimensional distribution of the survival time of wireless sensor network.

scheduling method. At the beginning, the member nodes in the cluster are in a dormant state. When the participants move to some monitoring points to collect data, the movement of the monitoring points is similar to the random walk between nodes in WSNs to collect data.

When the node is activated, the member nodes in the nonchain structure collect data and send it to the cluster head in a single hop, while the cluster node in the chain structure needs to transmit the data along the chain after collecting the data pairs. If the node meets the conditions, it will become a candidate cluster head, and then, the candidate cluster head selects the final cluster head node through regional competition.

6. Conclusion

In the homogeneous node environment, based on the network load algorithm, this paper optimizes the digital twin topology structure, divides the network nodes into two layers, constructs the network nodes into multiple subchains at the bottom layer, and selects the main chain head and the branch chain heads to construct the top-level chain head chain. Secondly, the isolated points generated in the chain formation process are processed in a tree structure to reduce the length of the data transmission path, optimize the selection strategy of the main chain head and the branch chain head and the chaining rules, and compare the common nodes and chain heads near the sink. The number of clusters generated is small, and the packet delivery delay is low; but the overlap between the generated clusters is large, the cluster head nodes are often overloaded, and the load among the cluster heads is extremely uneven. At the same time, the gateway node serves as another cluster head to share part of the nodes, which not only maintains the advantages of the original algorithm with less packet delivery delay but also reduces the burden on the cluster head node that is overloaded. Finally, the digital twin algorithm is studied in detail, and an energy adaptive nonuniform clustering algorithm based on digital twin is designed. In addition, the idea of nonuniform clustering is introduced in the single-hop mode, and the clustering radius is determined by integrating node connectivity and the distance between the node and the base station, so that the cluster head far away from the base station manages fewer nodes. The experimental results show that the protocol proposed in this paper is stable in the network, network energy efficiency, and data transmission efficiency. It is superior to other comparison protocols in terms of it and can improve the success rate of data transmission.

Data Availability

The data used to support the findings of this study are available from the corresponding author upon request.

Conflicts of Interest

The author declares that there are no known competing financial interests or personal relationships that could have appeared to influence the work reported in this paper.

Acknowledgments

References

[1] C. Gehrmann and M. Gunnarsson, "A digital twin based industrial automation and control system security architecture," *IEEE Transactions on Industrial Informatics*, vol. 16, no. 1, pp. 669–680, 2019.

[2] M. Redeker, J. N. Weskamp, B. Rössl et al., "Towards a digital twin platform for Industrie 4.0," *Industrial Cyber-Physical Systems*, pp. 39–46, 2021.

[3] Q. Qi, F. Tao, T. Hu et al., "Enabling technologies and tools for digital twin," *Journal of Manufacturing Systems*, vol. 58, pp. 3–21, 2021.

[4] H. X. Nguyen, R. Trestian, D. To, and M. Tatipamula, "Digital twin for 5G and beyond," *IEEE Communications Magazine*, vol. 59, no. 2, pp. 10–15, 2021.

[5] E. B. Priyanka, S. Thangavel, X. Z. Gao, and N. S. Sivakumar, "Digital twin for oil pipeline risk estimation using prognostic and machine learning techniques," *Journal of industrial information Integration*, p. 100272, 2021.

[6] Y. Lu, X. Huang, K. Zhang, S. Maharjan, and Y. Zhang, "Communication-efficient federated learning for digital twin edge networks in industrial IoT," *IEEE Transactions on Industrial Informatics*, vol. 17, no. 8, pp. 5709–5718, 2020.

[7] D. Lee and S. H. Lee, "Digital twin for supply chain coordination in modular construction," *Applied Sciences*, vol. 11, no. 13, p. 5909, 2021.

[8] P. Conejos Fuertes, F. Martínez Alzamora, M. Hervás Carot, and J. C. Alonso Campos, "Building and exploiting a digital twin for the management of drinking water distribution networks," *Urban Water Journal*, vol. 17, no. 8, pp. 704–713, 2020.

[9] L. Zhao, G. Han, Z. Li, and L. Shu, "Intelligent digital twin-based software-defined vehicular networks," *IEEE Network*, vol. 34, no. 5, pp. 178–184, 2020.

[10] R. Anderl, S. Haag, K. Schützer, and E. Zancul, "Digital twin technology–an approach for Industrie 4.0 vertical and horizontal lifecycle integration," *it-Information Technology*, vol. 60, no. 3, pp. 125–132, 2018.

[11] R. Minerva, G. M. Lee, and N. Crespi, "Digital twin in the IoT context: a survey on technical features, scenarios, and architectural models," *Proceedings of the IEEE*, vol. 108, no. 10, pp. 1785–1824, 2020.

[12] R. B. Roy, D. Mishra, S. K. Pal et al., "Digital twin: current scenario and a case study on a manufacturing process," *The International Journal of Advanced Manufacturing Technology*, vol. 107, no. 9, pp. 3691–3714, 2020.

[13] P. Zheng and A. S. Sivabalan, "A generic tri-model-based approach for product-level digital twin development in a smart manufacturing environment," *Robotics and Computer-Integrated Manufacturing*, vol. 64, p. 101958, 2020.

[14] J. Leng, Q. Liu, S. Ye et al., "Digital twin-driven rapid reconfiguration of the automated manufacturing system via an open architecture model," *Robotics and Computer-Integrated Manufacturing*, vol. 63, p. 101895, 2020.

[15] M. Li, Z. Li, X. Huang, and T. Qu, "Blockchain-based digital twin sharing platform for reconfigurable socialized manufacturing resource integration," *International Journal of Production Economics*, vol. 240, p. 108223, 2021.

[16] K. Y. H. Lim, P. Zheng, and C. H. Chen, "A state-of-the-art survey of digital twin: techniques, engineering product lifecycle management and business innovation perspectives," *Journal of Intelligent Manufacturing*, vol. 31, no. 6, pp. 1313–1337, 2020.

[17] S. Y. Barykin, I. V. Kapustina, S. M. Sergeev et al., "Developing the physical distribution digital twin model within the trade network," *Academy of Strategic Management Journal*, vol. 20, pp. 16–18, 2021.

[18] T. Zhang, X. Liu, Z. Luo, F. Dong, and Y. Jiang, "Time series behavior modeling with digital twin for Internet of Vehicles," *EURASIP Journal on Wireless Communications and Networking*, vol. 2019, no. 1, 11 pages, 2019.

[19] Y. He, J. Guo, and X. Zheng, "From surveillance to digital twin: challenges and recent advances of signal processing for industrial Internet of Things," *IEEE Signal Processing Magazine*, vol. 35, no. 5, pp. 120–129, 2018.

[20] A. Z. Abideen, V. P. K. Sundram, J. Pyeman, A. K. Othman, and S. Sorooshian, "Digital twin integrated reinforced learning in supply chain and logistics," *Logistics*, vol. 5, no. 4, p. 84, 2021.

[21] H. Zhang, Q. Yan, and W. Zhenghua, "Information modeling for cyber-physical production system based on digital twin and AutomationML," *The International Journal of Advanced Manufacturing Technology*, vol. 107, no. 3-4, pp. 1927–1945, 2020.

[22] S. Mi, Y. Feng, H. Zheng, Y. Wang, Y. Gao, and J. Tan, "Prediction maintenance integrated decision-making approach supported by digital twin-driven cooperative awareness and interconnection framework," *Journal of Manufacturing Systems*, vol. 58, pp. 329–345, 2021.

[23] T. R. Wanasinghe, L. Wroblewski, B. K. Petersen et al., "Digital twin for the oil and gas industry: overview, research trends, opportunities, and challenges," *IEEE Access*, vol. 8, pp. 104175–104197, 2020.

[24] Q. Lu, A. K. Parlikad, P. Woodall et al., "Developing a digital twin at building and city levels: case study of West Cambridge campus," *Journal of Management in Engineering*, vol. 36, no. 3, 2020.

[25] N. Kousi, C. Gkournelos, S. Aivaliotis, C. Giannoulis, G. Michalos, and S. Makris, "Digital twin for adaptation of robots' behavior in flexible robotic assembly lines," *Procedia manufacturing*, vol. 28, pp. 121–126, 2019.

Research Article

A Novel Data Analytics Oriented Approach for Image Representation Learning in Manufacturing Systems

Yue Liu [ID],[1,2] **Junqi Ma** [ID],[1] **Xingzhen Tao** [ID],[1] **Jingyun Liao** [ID],[3] **Tao Wang** [ID],[4] **and Jingjing Chen** [ID][4,5]

[1]*Jiangxi College of Applied Technology, China*
[2]*Guangzhou University, China*
[3]*Guangzhou Panyu Polytechnic, China*
[4]*Zhijiang College, Zhejiang University of Technology, China*
[5]*School of Economics, Fudan University, China*

Correspondence should be addressed to Tao Wang; wt@zzjc.edu.cn

In the era of digital manufacturing, huge amount of image data generated by manufacturing systems cannot be instantly handled to obtain valuable information due to the limitations (e.g., time) of traditional techniques of image processing. In this paper, we propose a novel self-supervised self-attention learning framework—TriLFrame for image representation learning. The TriLFrame is based on the hybrid architecture of Convolutional Network and Transformer. Experiments show that TriLFrame outperforms state-of-the-art self-supervised methods on the ImageNet dataset and achieves competitive performances when transferring learned features on ImageNet to other classification tasks. Moreover, TriLFrame verifies the proposed hybrid architecture, which combines the powerful local convolutional operation and the long-range nonlocal self-attention operation and works effectively in image representation learning tasks.

1. Introduction

The researchers in the field of computer vision have already achieved great progress in the techniques for image recognition; most of these achievements are based on supervised learning methods. For example, ImageNet [1] acts as a large-scale labelled image dataset applicable for all kinds of image learning tasks, among which supervised methods, e.g., ResNet [2] and AlexNet [3], are dominating and providing the state-of-the-art performances. Although with the thriving of semisupervised learning, unsupervised learning, and self-supervised learning, some competitive methods are emerging, e.g., fast-SWA [4], VAT [5], CPC [6], DIM [7], AMDIM [8], and IIC [9]. These methods show that the performance gap between reduced supervised and supervised methods is shrinking; the amount of labels required for training a competitive unsupervised or self-supervised method is dramatically decreasing. It is noted that certain amount of labels as guiding reference for learning methods is too valuable to ignore that usually results in the gradually decreased adoptions of fully unsupervised methods [10]. All these studies above imply that self-supervised methods are becoming more and more promising in the area of image representation learning, yet we have not seen any self-supervised learning method that surpasses the performance of supervised methods in a general perspective. On the other hand, considering the huge amount of image data being generated every day by manufacturing systems, it is reasonable to rethink the methodology of image learning. Specifically, in the environment of manufacturing systems, applications such as robotics, autopilot systems, medical diagnosis, smart home, and smart city systems are generating significant amount of data every day. It is notable that a large portion of data produced in manufacturing systems is image, as shown in Figure 1.
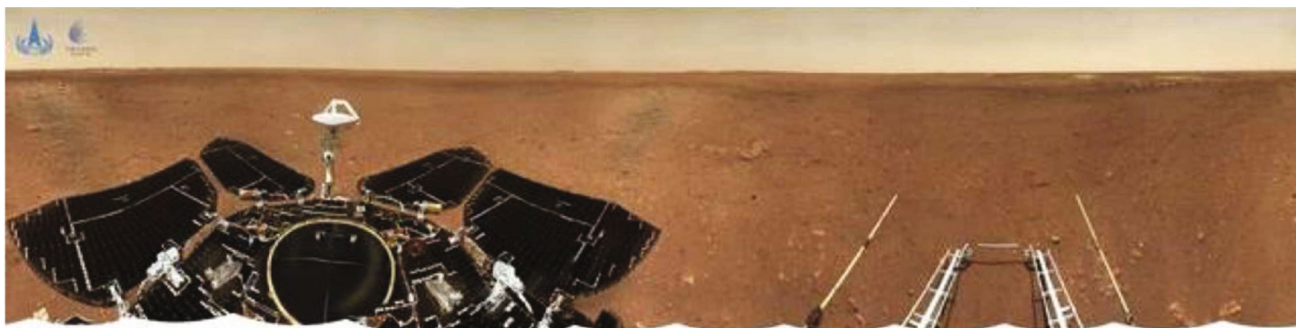
(a)
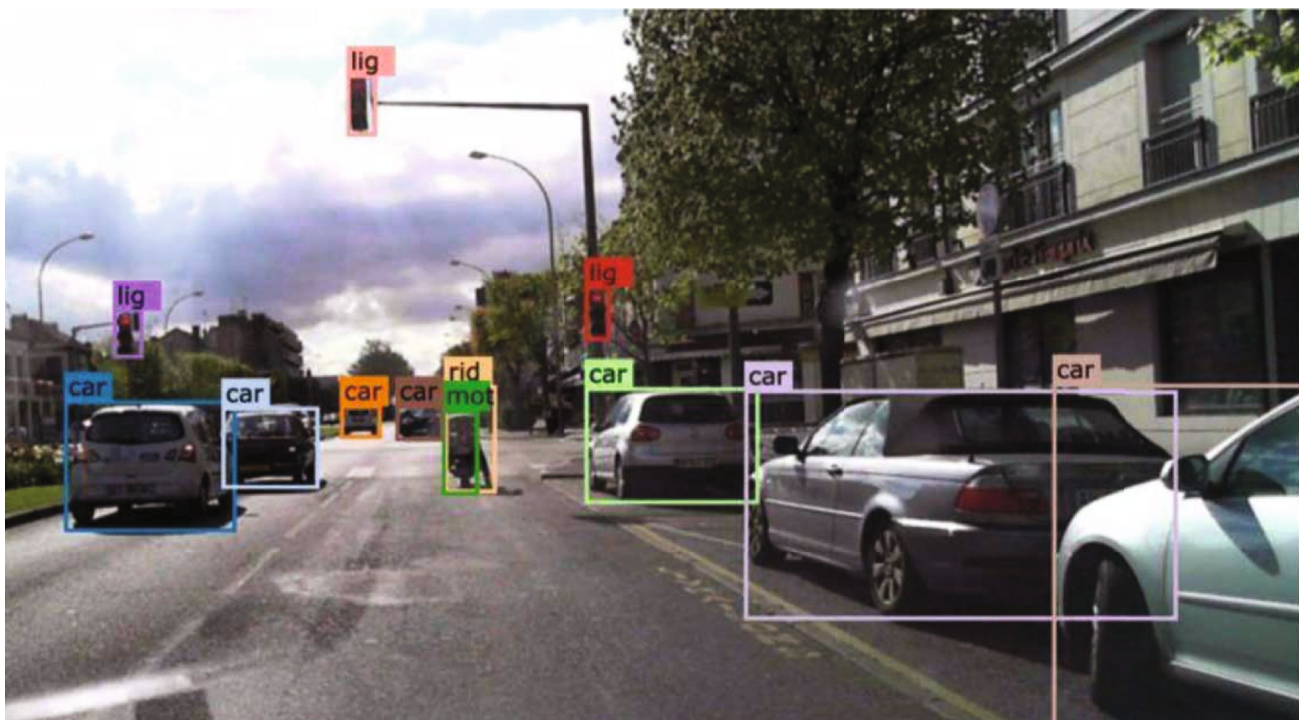
(b)

FIGURE 1: Continued.
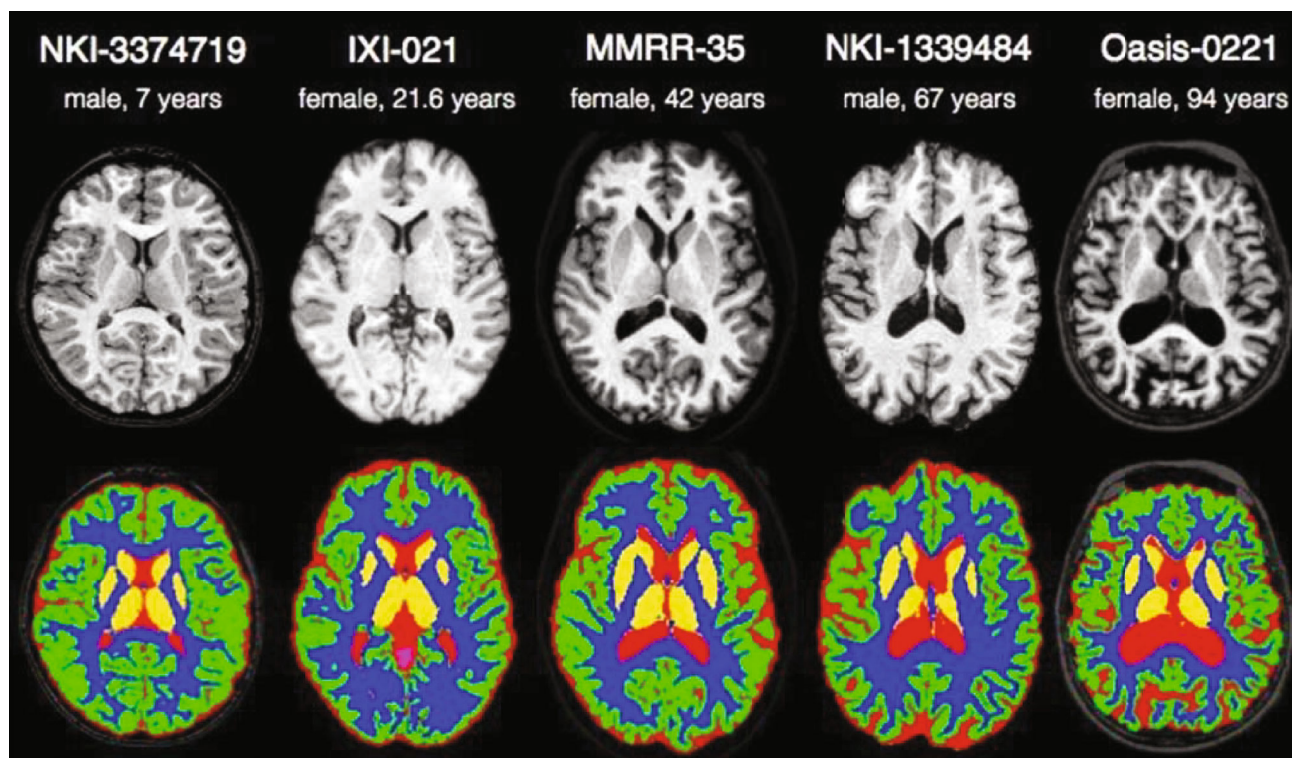
(c)
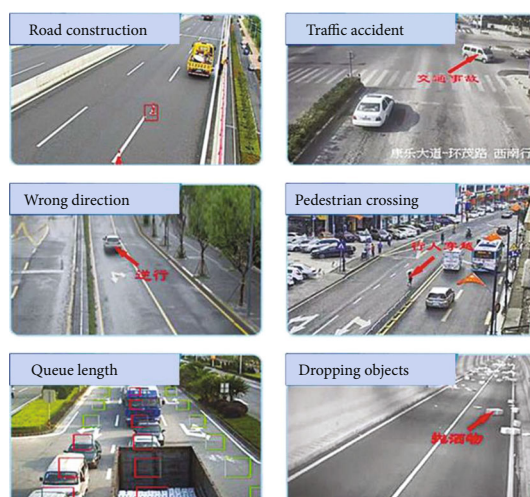
(d)

Figure 1: (a) A picture by a navigation terrain camera; (b) the object recognition result of pictures captured by camera mounted on an autopilot vehicle; (c) the diagram of individual differences in brain area and shape, captured for further medical diagnosis; (d) images from surveillance cameras of smart city system being processed for incident detection.

Images are generated by various kinds of manufacturing systems in a sharp speed and are ready to be analyzed though technologies like image classification, object detection, image segmentation, image filtering, denoising, etc. However, it is noted that image data cannot be instantly processed due to performance limitations by the manufacturing systems. Although with the research focus being transferred to subdivision fields of image learning, e.g., medical image processing [11], face recognition [12], image analysis in autonomous vehicle [13], and fault diagno-

sis in manufacturing system [14–17], the capability is gradually catching up with the explosive growth of image data being generated in manufacturing environments. It should be also well noted that, in order to equip models with specific processing capability in subdivision fields, many task-specific image datasets with accurate labelling are created for supervised training. The fact that, it demands tremendous effort to label every image according to the training target, directly strangles the development of supervised learning methods. Thus, many researchers attempt to

exploring alternatives of supervised learning, for example, self-supervised methods using the structural information of the image data to supervise the learning process. In this paper, we propose a general solution for image representation learning based on the self-supervised method, with the capability of transferring to subdivision fields with trivial effort.

Current methods of self-supervised learning for image processing can roughly be divided into the following two categories: generative methods and contrastive methods. Generative methods based on Auto-Encoder [18–20] and generative adversarial networks (GAN) [21–23] rely on reconstruction error in pixel-level to learn image representation. Relying on pixel-based objectives significantly reduces the capability to model correlations or complex structures and makes model heavily focus on low-level features instead of abstract representative features. Contrastive methods [6, 7, 24–27] learn image representations by contrasting positive and negative samples in the latent space, which forces model to discard pixel-wise information and focus on the structure and correlation of the image as a whole. While executing an image learning task, the aim is to get a semantic structural embedding of image which is generalized and can be transferred to subdivision tasks which do not dependent on pixel-level details; thus, contrastive methods better fit our purpose. We are inspired by Contrastive Predictive Coding (CPC) introduced in [6] which utilizes a probabilistic contrastive loss (called "the InfoNCE") to force the model to learn the underlying semantic information that is shared among the input sequence. However, when applying CPC to image representation learning, a major issue needs to be addressed properly; as shown in Figure 2, it is difficult to predict image patches which contain objects that never appear in previous content as CPC lacks of knowledge of long-range dependencies across the entire image. In this paper, we equip the CPC framework with the power of self-attention [28] which is skilled in capturing nonlocal long-range dependencies, in order to learn a better semantic structural representation of image. The intuition is that if sending the latent embeddings of image patches through the self-attention framework (i.e., a transformer encoder architecture), then each patch embedding will have an impression of the content of other patches, and features of more correlation with others will be emphasized as a result. This process facilitates the learning of nonlocal high-level representation of image.

In this paper, we propose a novel data analytics oriented approach for image representation learning with self-supervised learning and self-attention for manufacturing systems—TriLFrame. The framework is aimed at learning nonlocal semantic features of image with the ability to predict the missing patches of image in latent space. Although following the idea of contrastive self-supervision, TriLFrame is different from [6, 25] in major aspects: first, TriLFrame applies self-attention mechanism on the top of backbone convolutional operations to capture long-range dependencies; second, TriLFrame makes use of nonlocal image patches with no overlap to construct positive and negative samples for contrastive learning; and third, we introduce a

progressive prediction strategy instead of the simple linear transformation used in [6]. It should also be noted that this paper is an extension of our previous work CPCTR [29], which is a self-supervised self-attention framework for video representation learning. CPCTR utilizes self-attention operations to encode long-range spatio-temporal correlations of video data in order to capture "slow features" in video. Different from CPCTR, this paper makes the following novel contributions: first, specifically for image data processing, we design a new self-supervision pretext, which is the first few to introduce self-attention to contrastive image representation learning; second, a novel positive and negative sample construction is designed for contrastive learning which only requires spatial information of data; and third, under the context of manufacturing systems, we conduct experiments on different image datasets to show the effectiveness of the proposed method.

The contribution in this paper is summarized as follows: (1) we propose the self-supervised self-attention coding framework for image learning in manufacturing environment; (2) we apply the transformer encoder to TriLFrame to learn nonlocal spatial dependencies to better learn the semantic representation of image, and we experiment on the self-attention module in TriLFrame to reveal its effectiveness; and (3) we evaluate TriLFrame on the ILSVRC ImageNet competition dataset [30] as many authors [31–33]. With unlabeled image data, we show that a pretrained TriLFrame can be easily transferred to image classification tasks with competitive performances.

2. Related Literatures

2.1. Contrastive Learning. Based on the theory of Noise Contrastive Estimation (NCE) [34], contrastive learning uses classification tasks to discriminate positive sample from negative sample. The learning process is greatly dependent on operation on the latent space of input data (i.e., input data is preprocessed to reduce dimension), which forces contrastive learning to pay more attention to semantic structural representations while less attention to low-level pixel-wise features. In order to improve the efficiency of contrastive learning, users are required to carefully select positive and negative samples. Generally, negative samples that are hard to discriminate can improve the learning quality greatly. Contrastive learning has been proven competitive in the contexts of natural language processing [35, 36], audio processing [6], image processing [24, 27], video understanding [37, 38], etc., and a number of researches have been investigating the prospect of contrastive learning using no negative pairs [39] and no momentum encoder [40]. Its performance shows a promising prospect of contrastive learning. Recently, a new contrastive learning approach, Contrastive Predictive Coding (CPC) in [6], proposes an effective framework that can be applied to sequenced data modality, e.g., natural language, audio, video, or image (an image can be cut into a spatial sequence of image patches). CPC encodes underlying shared features that is slowly varying across data sequences and discarding local information. These shared features are called "slow features," which refers to these
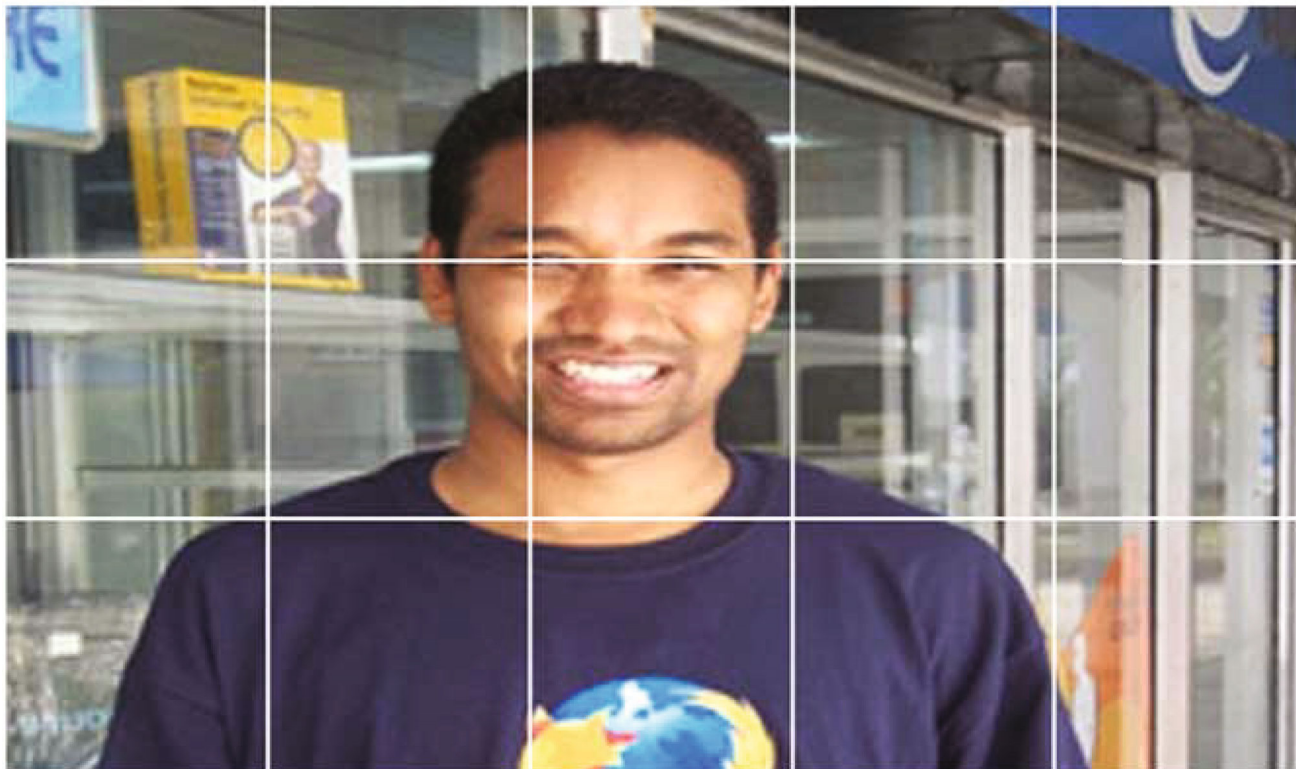
(a)

Figure 2: Continued.

(b)

FIGURE 2: (a) The upper part of a full image. (b) The full image labelled as "Mobile Phone" in the ImageNet dataset.

features that are slowly varying across time, e.g., the identity of a speaker in an audio signal, an activity carried out in a video, and an object in an image.

2.2. Self-Supervised Learning for Image. With the development of self-supervised learning, especially the wide adoption of contrastive learning, self-supervised methods have shown a promising prospect for the images learning [6, 24, 25, 27, 31, 41]. CPC [6] using self-supervised training on unlabeled ImageNet dataset and fine-tuned with linear classification already outperform the supervised AlexNet [3]; Data-Efficient CPC [25] as an extended work has scaled up CPC and achieved Top 1 accuracy of 71.5% on the image classification task on ImageNet; it also exhibits high data efficiency when fine-tuning with labelled data compared with fully supervised methods. Deep InfoMax (DIM) [7] learns image representations through the internal structure information. A follow-up work of DIM and Augment Multiscale DIM (AMDIM) [8] utilizes invariant features across data augmentations, e.g., color jittering and random cropping; it gets Top 1 accuracy of 68.4% on ImageNet with unsupervised pretraining and evaluated by linear classification task. Contrastive Multiview Coding (CMC) [26] learns representations using different versions of the same image,

e.g., image of different angles, as data transformations which the representation should cope with. In the conventional formulation of contrastive learning, the size of minibatch restricts the total number of negative samples; Momentum Contrast (MoCo) [24] effectively lifts this restriction by maintaining a long queue of all negative samples, when training the negative encoder does not update with the positive encoder. The experiment results show that MoCo outperforms supervised models in several downstream tasks on different image datasets. Typically, these image downstream tasks need supervised training with labelled image to achieve good results; however, MoCo shows that the performance gap between supervised and unsupervised methods has largely been closed.

2.3. Self-Attention. TriLFrame also adopts the idea of self-attention mechanism [28], in which we know the emerging transformer architecture. A self-attention operation calculates the response of a position in an input sequence by paying attention to every position in the sequence and uses the average in the representation space, resulting each response being embedded with correlations with every other position regardless of their distance. Self-attention also carries a major merit, i.e., self-attention module can be calculated simultaneously, which dramatically accelerate the training process. Self-attention, or transformer, already becomes the de facto standard for natural language processing (NLP) tasks [42, 43], and recently, many researches explore their application in computer vision, e.g., object detection [44], image classification [45], video classification [46], and video segmentation [47]. Vision Transformer (ViT) [45] is constructed with pure transformer encoders and is applied directly to a sequence of image patches; ViT achieves competitive results on image classification tasks. After training ViT on large-scale image datasets and transferred to image recognition benchmarks, ViT gets remarkable results compared to state-of-the-art CNNs. However, there is a major drawback of ViT, i.e., it requires substantially more image data and computational resources to train compared to CNNs. Thus, the self-attention architecture (just the transformer encoder) is applied to a sequence of patch embeddings of image (preprocessed by CNNs, e.g., ResNet [2]), aiming to learn nonlocal correlations to implement the learning of semantic structural representation image.

2.4. Image Classification. Traditional image classification architectures [2, 3, 48] take advantage of convolutional networks for processing images and get remarkable performance. Convolutional network is still the de facto standard for image processing tasks and has been implemented in many practical applications. In recent research, new architectures, e.g., networks using transformer [45, 49, 50] or multilayer perceptron (MLP) [51–53], are challenging the leading position of CNNs. We also note that hybrid CNN-Transformer architecture [54–57] argues that the combination of local convolutional operation and nonlocal self-attention operation is the optimal solution for computer vision tasks. All recent works are trying to break the limitation of CNNs. Here, in our work, RGB image data is utilized

to train a hybrid CNN-Transformer architecture in a self-supervised manner, and then, the model is fine-tuned for image classification tasks; it is also an attempt to explore new framework of image processing.

3. Self-Supervised Self-Attention Learning Method

In this section, the core components and implementations of TriLFrame which include the learning framework, the sample construction, and the self-attention module are presented.

3.1. Framework. The aim of TriLFrame is to learn a nonlocal semantic representation of image. The image is first processed by a convolutional operation, and then, patches of latent representations are unfolded for self-attention operation. As illustrated in Figure 3, TriLFrame takes an RGB image as input and unfolds the latent embedding into a number of patches (16 patches as in the experiment), given the former part of patches the TriLFrame predicts the latter part of patches. We use the latter part patches and the predicted patches to construct positive and negative samples for contrastive learning. First step, the RGB image is preprocessed, and a convolutional operation $f(.)$ computes the image embedding X:

$$X = f(\text{image}), \tag{1}$$

where X has dimension $\mathbb{R}^{C \times H \times W}$. As same as ViT, we break apart the latent embedding X along the spatial dimension $\mathbb{R}^{H \times W}$ to get patch 1 to patch 16, where each patch is named as $x_i \in \mathbb{R}^C$, and we have $X = \{x_i \in \mathbb{R}^C, i \in \{1, 2, \cdots, H \times W\}\}$. These patches are sent to the self-attention function transEnc(.) to compute nonlocal correlations:

$$Z = \text{transEnc}(X), \tag{2}$$

where $Z = \{z_i \in \mathbb{R}^C, i \in \{1, 2, \cdots, H \times W\}\}$.

Afterwards, patches are accumulated along the patch sequence by an aggregation function $g(.)$ to get a context c_i:

$$c_i = g(z_1, z_2, \cdots, z_i). \tag{3}$$

The accumulated context c_i is of the same dimension as x_i and z_i. In our initial settings, $x_i, z_i, c_i \in \mathbb{R}^{256}$.

If feature vector $z_1, z_2, \cdots, z_i$ have embedded with semantic structural features, e.g., the key features of image patch and have been aware of the correlation with other patches, then the accumulated context c_i can predict embeddings of the rest patches by using a simple inference function $\varphi(.)$:

$$\hat{z}_{i+1} = \varphi(c_i) = \varphi(g(z_1, z_2, \cdots, z_i)), \tag{4}$$

$$\hat{z}_{i+2} = \varphi(c_{i+1}) = \varphi(g(z_1, z_2, \cdots, z_i, \hat{z}_{i+1})), \tag{5}$$

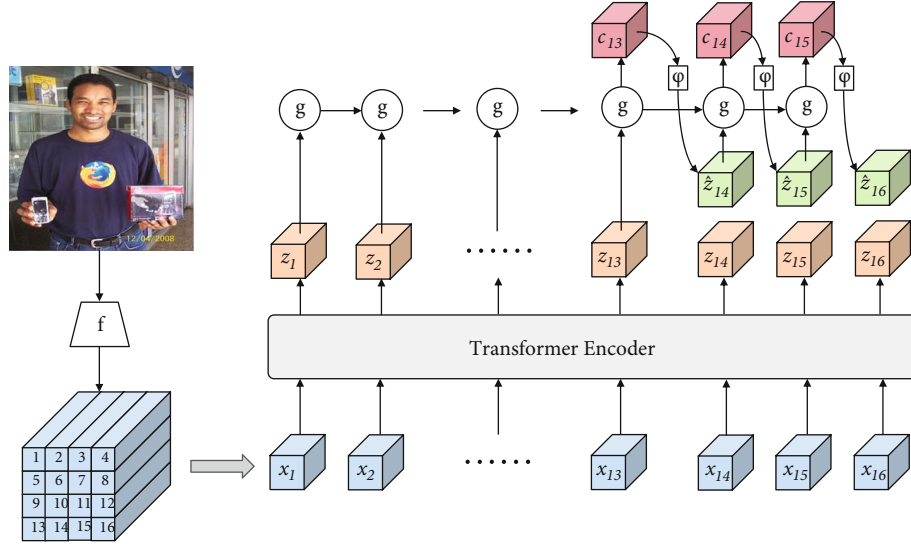where $\hat{z}_{i+1}$ is the predicted embedding of patch $i + 1$. As

FIGURE 3: A diagram of self-supervised self-attention learning framework.

instructed in Seq2Seq [58], we infer future embeddings in a sequential mode. For the prediction of patch $i + 2$, the context c_{i+1} which accumulates every past embeddings including the latest predicted $\hat{z}_{i+1}$, as illustrated in Equation (5). We totally infer q patches for one image.

3.2. Contrastive Learning. In TriLFrame, contrastive learning is implemented by discriminating positive "Predicted Patch - Ground-truth Patch" sample pair (named "Pred-GT" sample pair) and negative Pred-GT sample pair. Follow the idea of NCE [34] and CPC [6], a NCE variant is adopted as our contrastive loss for contrastive image learning. The proposed contrastive loss draws the predicted patches closer to the ground-truth patches while the Pred-GT sample pair does not need to be completely the same, i.e., model just needs to learn nonlocal semantic structural representation without paying attention to pixel-level details or noises.

As illustrated in Figure 4, the red arrow line connects the only positive sample pair, and the dashed black arrow line shows two negative sample pairs constructed by (1) the predicted patch embedding and a random ground-truth patch embedding of the same image and (2) the predicted patch embedding and the patch embedding of an image from the same minibatch. In TriLFrame, we break down an image representation X of dimension $\mathbb{R}^{C \times H \times W}$ into $H \times W$ patches, for i-th image patch; the ground-truth latent embedding z_i is couple with its predicted latent embedding $\hat{z}_i$; both embeddings are of the same dimension $\mathbb{R}^C$. As illustrated in Figure 4, we construct positive sample pairs with a prediction embedding and its corresponding ground-truth embedding and negative sample pairs with a prediction embedding and ground-truth embeddings at other spatial positions of the same image. We further utilize patch embeddings of images from the same minibatch to produce more negative Pred-GT pairs for contrastive learning.

The similarity score of the Pred-GT sample pair is calculated by dot product as $\hat{z}_i^T \bullet z_j$ where $\hat{z}_i^T, z_j \in \mathbb{R}^c$, i and j

denote i-th and j-th patch ($i, j \in \{1, 2, \cdots, H \times W\}$). Hence, TriLFrame is to optimize the contrastive loss:

$$\mathcal{L} = -\sum_i \left[\log \frac{\exp\left(\hat{z}_i^T \bullet z_i\right)}{\sum_j \exp\left(\hat{z}_i^T \bullet z_j\right)} \right]. \quad (6)$$

The loss function in the above equation is typically the cross-entropy loss for distinguishing positive Pred-GT sample pairs from negative sample pairs. When training with minibatch, we define the following types of negative Pred-GT sample pairs to define the construction of negative samples:

(i) *Easy Negatives.* In the same minibatch, easy negatives are Pred-GT sample pairs from two images. Easy negatives are relatively easy to discriminate in general, but there exist similar patches from different images; for instance, image patches both contain a football

(ii) *Spatial Negatives.* In the same image, spatial negatives are constructed with predicted patch and ground-truth patch embeddings, where the two patches are at different spatial locations in the image, i.e., $(\hat{z}_i, z_j)$ pair with $i \neq j$

3.3. Transformer Encoder. We implement the conventional transformer architecture [28] as the transformer in TriLFrame except that the transformer decoder and the positional encoding are discarded. Although it is proven that positional embeddings make self-attention operation be aware of sequential information to some degree [44, 45], when using self-attention on image patches, the goal is to embed nonlocal correlations between patches of image, so it is not important to be aware of sequential information of patches.

As illustrated in Figure 5, the conventional transformer encoder operation gets a one-dimensional sequence of patch
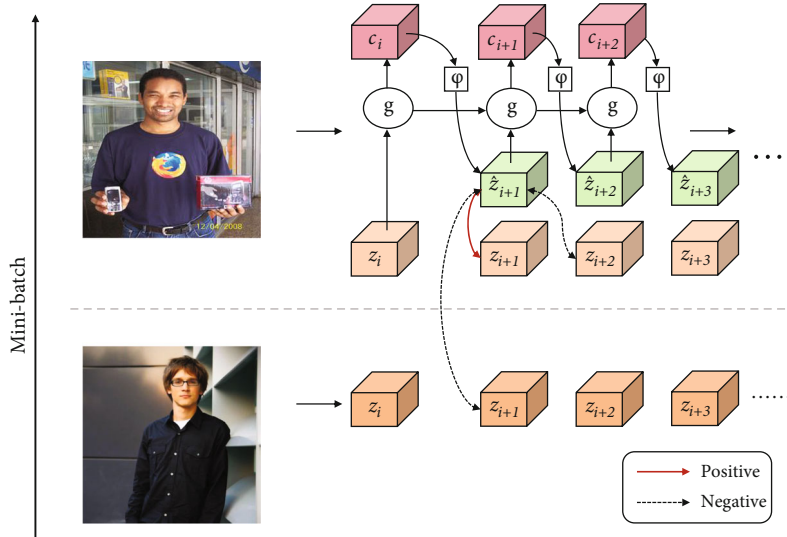
FIGURE 4: The construction of positive and negative samples of contrastive learning.
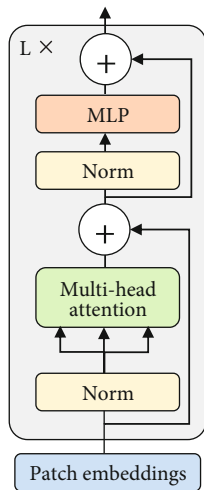
FIGURE 5: The architecture of transformer encoder applied in TriLFrame.

embeddings. To make the transformer applicable in three-dimensional latent embeddings of images, we break apart the image embedding $X \in \mathbb{R}^{C \times H \times W}$ along the spatial dimension $\mathbb{R}^{H \times W}$ to a series of one-dimensional patches $x_i \in \mathbb{R}^C$. Transformer encoder takes a total number of $H \times W$ patches as input. In our implementation, the transformer encoder is repeated L times, with a shared feature vector dimension C at all layers. Each layer has one multihead self-attention operation and one MLP operation, where the number of heads is H. After each transformer encoder, we get an output $Z \in \mathbb{R}^{C \times H \times W}$. Through the transformer encoder operation, each patch of image links to every other patch; thus, the nonlocal spatial dependencies are computed.

3.4. Image Processing Workflow. Due to the diversity of images generated by manufacturing systems, e.g., images of different resolution, images from different angles, pano-

ramas or close shot, grey-scale image or RGB image, infrared images, and medical images (magnetic resonance imaging images, CT images), image data must be preprocessed for self-supervised learning afterwards. To help the model learn nonlocal semantics, we deploy the following frame-wise augmentation methods to every image in a minibatch, such as color jittering which includes random contrast, random brightness, random hue, random saturation, and random greyscale during self-supervised training. It is noted that, by introducing self-attention, in contrast to CPC, TriLFrame does not require image patches to be overlapped; this effectively avoids the network to perform feature extrapolation as the prediction.

In contrast to the one-off prediction of the latter patches presented in [6], we implement a successive predictive mechanism (i.e., latter patches are predicted in a progressive manner). As described in Equations (4) and (5), all previous context of the image (an aggregated context) is utilized to make the next inference. This successive prediction process ensures that the model makes use of every previous image patch when predicting the next patch embedding.

Batch normalization [59] (BN) is a conventional practice in deep neural networks; however, it is not adopted in CPC [6]. We argue that BN is necessary in TriLFrame, and it gives 2%-4% accuracy improvement in classification tasks we performed. It is difficult to train a hybrid CNN-transformer network without normalization either in self-supervised training stage or supervised fine-tuning stage. In this paper, BN is adopted for convolutional function and transformer encoder.

4. Experiments and Analysis

We show the experiment setups and the self-supervised training procedure in the following section, and then, we show the ablation study of TriLFrame and the evaluation of the model.

4.1. Experiment Setting

4.1.1. Network Architecture. A conventional ResNet [2] is implemented as the convolutional operation $f(.)$; ResNet consists of four residual blocks wrapping up with final channel dimension of 256. We use the output from the fourth residual block as the input to transformer encoder. In our experiments, ResNet18 is implemented. After ResNet encoder, the latent representation of an image is cut into a sequence of patches and then processed by transformer as [28] without the positional encoding module. Taking account of the number of the image patches, we set the number of attention heads and encoder layers to 2 and 1, respectively, in our experiments. This setting of transformer also forces encoder $f(.)$ to learn a better quality of semantic structural representation of image, i.e., in order to train a strong feature encoder, a weak self-attention operation transEnc(.) and aggregation operation $g(.)$ is preferable. Thus, we apply a simple Convolutional Gated Recurrent Unit with the smallest kernel size (1, 1) as our aggregation operation. For inference, one simple MLP is applied in a progressive manner.

4.1.2. Self-Supervised Training. In our experiments, we use the ILSVRC ImageNet competition dataset [30] for self-supervised training. The ImageNet dataset has been used to evaluate unsupervised vision models by many works. Before encoder function $f(.)$, images are preprocessed for data augmentation; we implement random grey, random flip, random crop, and color jittering for each image before feeding to ResNet18. These augmentations help the network to avoid shortcuts, i.e., feature extrapolation, as discussed in Section 3.4.1. For self-supervision, we train TriLFrame end-to-end with Adam optimizer; we start with an initial learning rate of $10e$-3 and weight decay rate of $10e$-5. The learning rate is decayed by a linear function every 100 epoch and is settled at the rate of 10-5.

4.2. Evaluation Methods

4.2.1. Self-Supervised Learning Evaluation. The TriLFrame is first training with self-supervision on the ILSVRC ImageNet. Self-supervised training is initially evaluated by the validation Top 1 accuracy, i.e., the Top 1 accuracy of classifying the positive Pred-GT sample pairs from others in the validation set. Self-supervision with high validation accuracy tells that the model learns a good distribution of image embeddings. After self-supervised training, TriLFrame is further evaluated by downstream tasks, especially the image classification task on the ILSVRC ImageNet. TriLFrame is fine-tuned with a simple classification layer on the ILSVRC ImageNet in a supervised manner; after model converges, TriLFrame is then evaluated by the classification task on the ILSVRC ImageNet. We report all accuracy results as Top 1 accuracies.

4.2.2. Image Classification. Image classification is an important metric for evaluation on the self-supervised image learning approaches; thus, we take the image classification task to evaluate the TriLFrame.

After contrastive learning, the model should be able to encode the semantic structural representation of an input image from any source in manufacturing systems, and the image representation can then be used in classification task. The last aggregated context representation c is utilized to construct the image classification network as follows: at first stage, we first encode an image with the convolutional operation $f(.)$ to get the latent embedding X, which is subsequently broken into a sequence of image patches with no overlapping. The patch sequence is then sent to the self-attention operation transEnc(.) to capture nonlocal dependencies, and finally, we use the aggregation function $g(.)$ to aggregate the whole sequence of patch embeddings into a context representation c which is a feature vector of the image. At second stage, the representation c is passed to a FC layer and a *Softmax* function to get the probabilities for image classification. The classification network is trained by Adam optimizer; we start with the learning rate of $10e$-3 and a weight decay rate of $10e$-3. Because TriLFrame is fine-tuned for image classification, so the initial learning rate of the convolutional operation $f(.)$, the self-attention operation transEnc(.), and the aggregation operation $g(.)$ is set to 10^{-4}. At prediction stage, an image is preprocessed except for random crop. The final classification result is given by the *Softmax* probability.

4.3. Performance Analysis

4.3.1. Ablation Study. We conduct several ablation studies on the TriLFrame architecture, especially on the backbone encoder and transformer encoder module, to show the contribution of each module of TriLFrame and the effectiveness of deeper convolutional encoder. The ablation study is first conducted with ResNet18 as encoder, and the results are given in the upper part of Table 1. The baseline model is set up with random initialization and trained only in supervision for image classification on the ILSVRC ImageNet dataset. TriLFrame is pretrained with contrastive learning and fine-tuned with supervised learning on ILSVRC. We observe that Top 1 accuracy increases from 54.1% to 75.6%, after TriLFrame is pretrained with self-supervision. Also, it is obvious that after removing the transformer module transEnc(), the Top 1 accuracy incurs a significant drop: from 75.6% to 66.8%. This ablation study demonstrates that the TriLFrame framework is effective in capturing the semantic representation of image, and that the self-attention module plays an important role in the framework.

We also try to use deeper convolutional networks, e.g., ResNet50 and ResNet101. The results are given in the lower part of Table 1. It empirically shows that deeper convolutional encoders contribute to better self-supervised accuracy as well as better image classification accuracy. When adopting ResNet101 as backbone encoder, we observe that Top 1 accuracy of classification accuracy reaches 81.2%, which is a considerable increase compared with 75.6% by ResNet18 and 78.3% by ResNet50. This ablation study proves that deeper convolutional encoder plays a more effective role in TriLFrame architecture.

TABLE 1: The result of ablation studies on TriLFrame architecture. The model is pretrained with contrastive learning and then fine-tuned with supervised learning classification task on the ILSVRC ImageNet dataset. "Random Init." that represents random initialization is used for setting up. "Remove transEnc()" that represents the transformer of TriLFrame is removed; patch embeddings are aggregated without transformer encoder.

| Encoder | Self-Sup. (ILSVRC) | | Sup. (ILSVRC) |
	Setting	Top1 Acc.	Top1 Acc.
ResNet18	Random Init.	—	54.1
ResNet18	Remove transEnc()	68.8	66.8
ResNet18	TriLFrame	80.9	75.6
ResNet50	TriLFrame	83.7	78.3
ResNet101	TriLFrame	88.5	81.2

FIGURE 6: The correlation of self-supervision accuracy and image classification accuracy.

4.3.2. Self-Supervision Accuracy Compared with Classification Accuracy.

We also conduct experiments to show the correlation of self-supervision and image classification tasks. During self-supervised training TriLFrame on the ILSVRC dataset, we perform several early stops at different self-supervision accuracy and fine-tune with supervision for image classification. Then, we demonstrate the relationship of self-supervision accuracy and image classification accuracy. For simplicity, the correlation experiments are conducted with ResNet18 as backbone encoder. The following Figure 6 shows our findings.

As shown in Figure 6, TriLFrame is trained using self-supervision on the ILSVRC dataset and is early-stopped at validation Top 1 accuracy of {54.8, 64.0, 71.4, 80.9}; for each early stop, the model is then fine-tuned with supervision for image classification. It is obvious that the performance of TriLFrame on downstream classification task is dependent on the self-supervision accuracy, i.e., TriLFrame of higher self-supervision accuracy yields higher accuracy of image classification. This correlation of self-supervision accuracy and classification accuracy shows that the image representation learnt in self-supervised training effectively capture semantic structural features which is generalized and can be used at downstream classification tasks.

4.4. Comparison with State-of-the-Art Methods.

We show the comparison with state-of-the-art self-supervised methods using linear probing. Results of state-of-the-art methods are reported by the implementation in [39, 60, 61]. For fair comparison, all methods are pretrained with 224×224 image crop from the ILSVRC ImageNet dataset; data augmentation is applied accordingly. Note that we try ResNet18, ResNet50, and ResNet101 as backbone encoder in TriL-Frame to show comparable results, which is different from other model settings. The results are given in Table 2. It shows that: first, the proposed TriLFrame framework outperforms the state-of-the-art method with 81.2% Top 1 accuracy, but it has a relatively large parameters of 485 M compared with other methods listed in the table. Second, when constructed with a shallow convolutional network ResNet18, TriLFrame is a quite light-weight architecture of only 75 M parameters, which is significantly less than other
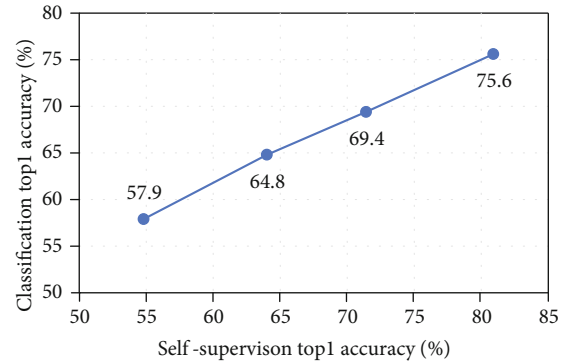
methods with close performance (CMC has a 94 M parameters but only 70.6% accuracy). This proves that the hybrid CNN-Transformer architecture which combines local convolutional operation and nonlocal self-attention operation is quite effective and efficient in capturing nonlocal semantic image features.

4.5. Transfer to Other Image Classification Tasks.

Another important experiment to test whether self-supervised learning captures key semantic features is transfer learning. Model is first trained with self-supervision on the ImageNet; when the model settles, we follow the classification model setting as described in Section 4.2.2 except that the model will be fine-tuned end-to-end for transfer learning. Specifically, the parameters learned from self-supervision on ImageNet dataset are used to initialize the classification model, and then, the entire model will be trained with supervised learning on other image datasets. We follow the transfer learning settings and evaluation protocol in [39], and we use image datasets CIFAR [62], VOC2007 [63], Pets [64], and Flowers [65]. If features learned from self-supervision are generic and contain key semantic features, then they should be helpful in other the image datasets mentioned above. Please note that TriLFrame uses ResNet50 as encoder, which matches the conventional architecture setting. The transfer learning results are given in Table 3.

Although TriLFrame only surpasses other methods in one of the five classification tasks, it achieves competitive performances compared with state-of-the-art methods. We note that TriLFrame performs better with larger dataset; for example, TriLFrame achieves the highest accuracy on CIFAR100 and the second highest accuracy on CIFAR10; both datasets have more training samples than VOC2007, Pets, and Flowers. This characteristic of TriLFrame accords with ViT which also requires large amount of training data to get competitive performances.

4.6. Discussion.

Through ablation study on the TriLFrame framework and comparison with SOTA models, we believe that the following factors contribute to the achievements of TriLFrame: First, the contrastive self-supervised training process forces the model to learn a strong semantic structural embedding of image through predicting

TABLE 2: The comparison with state-of-the-art self-supervised methods in ImageNet classification, evaluated by linear probing. "Params" and "Architecture" column shows the basic features of the corresponding method. "Top1 Acc." and "Top5 Acc." are reported by a linear classification on the ImageNet dataset, after models are pretrained with self-supervision.

Method	Params	Architecture	Top1 Acc. (%)	Top5 Acc. (%)
CMC	94 M	ResNet50 ×2	70.6	89.7
CPC v2	305 M	ResNet161	71.5	90.1
BYOL	375 M	ResNet50 ×4	78.6	94.2
SimCLR	375 M	ResNet50 ×4	76.5	93.2
MoCo v3	304 M	ViT-L/16	77.6	—
MoCo v3	304 M	ViT-BN-L/7	81.0	—
TriLFrame (ours)	75 M	ResNet18 + transformer	75.6	92.1
TriLFrame (ours)	265 M	ResNet50 + transformer	78.3	93.6
TriLFrame (ours)	485 M	ResNet101 + transformer	81.2	94.7

TABLE 3: Transfer learning results. Models are initialized with parameters from self-supervised learning on ImageNet dataset and are fine-tuned for classification task on relative datasets. A supervised training (on ImageNet) version "Supervised-IN" is also provided for comparison.

Method	Dataset Classes	CIFAR10 10	CIFAR100 100	VOC2007 20	Pets 37	Flowers 102
BYOL [39]		97.8	86.1	85.4	91.7	97.0
SimCLR [27]		97.7	85.9	84.1	89.2	97.0
Supervised-IN [27]		97.5	86.4	85.0	92.1	97.6
MoCo v3 [61]		98.9	90.5	—	93.2	97.7
TriLFrame (ours)		98.2	90.7	85.2	91.5	96.2

nondeterministic image patch embeddings given previous context knowledge of the image. Second, it is apparent that the hybrid CNN-Transformer architecture which combines local convolutional operation and nonlocal self-attention operation is quite effective and efficient in capturing nonlocal semantic image features. Third, we trust that the framework design of TriLFrame, which makes use of convolutional operation, self-attention operation, and aggregation operation, shows great performance and suits image learning tasks.

5. Conclusion

In this paper, we propose a novel self-supervised self-attention framework TriLFrame for image representation learning in manufacturing systems. TriLFrame combines the powerful local convolutional operation and the long-range nonlocal attention operation; TriLFrame learns image representation through contrasting predicted image patches and ground-truth image patches. We show that the proposed TriLFrame achieves state-of-the-art performances on image classification task on the ImageNet, with a Top 1 accuracy of 81.2%; TriLFrame also achieves competitive performance with a light-weight architecture of only 75 M parameters. When tested in transfer learning, TriLFrame is proven to be reliable in capturing semantic features for image classification tasks.

The work demonstrated shows that TriLFrame has a promising future in image-related tasks in manufacturing

systems; it can be quickly transferred and deployed to applications such as anomaly detection, medical diagnosis, and road analysis. Nevertheless, TriLFrame requires extra supervision information (e.g., image labels and segmentation information) if it is to be deployed in manufacturing systems for a specific task, and the supervision information may require exquisite design and significant amount of effort. Therefore, we hope the proposed TriLFrame can be considered as a baseline or backbone framework when solving image-related tasks in manufacturing systems in the future.

Data Availability

The data that support the findings of this study are available on request from the corresponding author.

Conflicts of Interest

The authors declare no conflict of interest.

Acknowledgments

References

[1] J. Deng, W. Dong, R. Socher, L.-J. Li, K. Li, and L. Fei-Fei, "ImageNet: a large-scale hierarchical image database," in *2009 IEEE Conference on Computer Vision and Pattern Recognition*, Miami, FL, USA, 2009.

[2] K. He, X. Zhang, S. Ren, and J. Sun, "Deep residual learning for image recognition," in *Proceedings of the IEEE Conference on Computer Vision and Pattern Recognition (CVPR)*, Las Vegas, U.S.A, 2016.

[3] A. Krizhevsky, I. Sutskever, and G. E. Hinton, "ImageNet classification with deep convolutional neural networks," in *Conference and Workshop on Neural Information Processing Systems (NeurIPS)*, Lake Tahoe, U.S.A, 2012.

[4] B. Athiwaratkun, M. Finzi, P. Izmailov, and A. G. Wilson, Eds., "There are many consistent explanations of unlabeled data: why you should average," in *International Conference on Learning Representations (ICLR)*, New Orleans, U.S.A, 2019.

[5] T. Miyato, S.-i. Maeda, M. Koyama, and S. Ishii, "Virtual adversarial training: a regularization method for supervised and semi-supervised learning," *IEEE Transactions on Pattern Analysis and Machine Intelligence*, vol. 41, no. 8, pp. 1979–1993, 2018.

[6] A. Van Den Oord, Y. Li, and O. Vinyals, "Representation learning with contrastive predictive coding," 2018, https://arxiv.org/abs/1807.03748.

[7] R. D. Hjelm, A. Fedorov, S. Lavoie-Marchildon et al.2019, https://arxiv.org/abs/1808.06670.

[8] P. Bachman, R. D. Hjelm, and W. Buchwalter, "Learning representations by maximizing mutual information across views," 2019, https://arxiv.org/abs/1906.00910.

[9] X. Ji, J. F. Henriques, and A. Vedaldi, "Invariant information clustering for unsupervised image classification and segmentation," in *Proceedings of the IEEE/CVF International Conference on Computer Vision (ICCV)*, Seoul, Korea, 2019.

[10] L. Schmarje, M. Santarossa, S.-M. Schröder, and R. Koch, "A survey on semi-, self- and unsupervised techniques in image classification," 2020, https://arxiv.org/abs/2002.08721.

[11] G. Litjens, T. Kooi, B. E. Bejnordi et al., "A survey on deep learning in medical image analysis," *Medical Image Analysis*, vol. 42, no. 9, pp. 60–88, 2017.

[12] Y. Taigman, M. Yang, M.'. A. Ranzato, and L. Wolf, "DeepFace: closing the gap to human-level performance in face verification," in *Proceedings of the IEEE Conference on Computer Vision and Pattern Recognition (CVPR)*, Columbus, U.S.A, 2014.

[13] J. Janai, F. Güney, A. Behl, and A. Geiger, "Computer vision for autonomous vehicles: problems, datasets and state of the art," in *IEEE Conference on Computer Vision and Pattern Recognition (CVPR)*, Honolulu, U.S.A, 2017.

[14] H. Zhiyi, S. Haidong, Z. Xiang, Y. Yu, and C. Junsheng, "An intelligent fault diagnosis method for rotor-bearing system using small labeled infrared thermal images and enhanced CNN transferred from CAE," *Advanced Engineering Informatics*, vol. 46, article 101150, 2020.

[15] K. Yan, "Chiller fault detection and diagnosis with anomaly detective generative adversarial network," *Building and Environment*, vol. 201, article 107982, 2021.

[16] K. Yan, J. Su, J. Huang, and Y. Mo, "Chiller fault diagnosis based on VAE-enabled generative adversarial networks," *IEEE Transactions on Automation Science and Engineering*, vol. 19, no. 1, pp. 387–395, 2020.

[17] K. Yan, J. Huang, W. Shen, and Z. Ji, "Unsupervised learning for fault detection and diagnosis of air handling units," *Energy and Buildings*, vol. 210, article 109689, 2020.

[18] G. E. Hinton and R. R. Salakhutdinov, "Reducing the dimensionality of data with neural networks," *Science*, vol. 313, no. 5786, pp. 504–507, 2006.

[19] P. Vincent, H. Larochelle, Y. Bengio, and P.-A. Manzagol, Eds., "Extracting and composing robust features with denoising autoencoders," in *ICML '08: Proceedings of the 25th international conference on Machine learning*, Helsinki, Finland, 2008.

[20] D. P. Kingma and M. Welling, "Auto-encoding variational Bayes," 2014, https://arxiv.org/abs/1312.6114.

[21] I. J. Goodfellow, J. Pouget-Abadie, M. Mirza et al., "Generative adversarial networks," *Advances in Neural Information Processing Systems*, vol. 3, pp. 2672–2680, 2014.

[22] A. Radford, L. Metz, and S. Chintala, "Unsupervised representation learning with deep convolutional generative adversarial networks," 2016, https://arxiv.org/abs/1511.06434.

[23] J. Bao, D. Chen, F. Wen, H. Li, and G. Hua, "CVAE-GAN: fine-grained image generation through asymmetric training," in *Proceedings of the IEEE International Conference on Computer Vision (ICCV)*, Venice, Italy, 2017.

[24] K. He, H. Fan, Y. Wu, S. Xie, and R. Girshick, "Momentum contrast for unsupervised visual representation learning," *Proceedings of the IEEE/CVF Conference on Computer Vision and Pattern Recognition (CVPR)*, 2019, pp. 9729–9738, 2020.

[25] O. J. Hénaff, "Data-efficient image recognition with contrastive predictive coding," in *Proceedings of the 37th International Conference on Machine Learning*, Long Beach, U.S.A, 2019.

[26] Y. Tian, D. Krishnan, and P. Isola, "Contrastive multiview coding," in *IEEE Conference on Computer Vision and Pattern Recognition (CVPR)*, Long Beach, U.S.A, 2019.

[27] T. Chen, S. Kornblith, M. Norouzi, and G. Hinton, "A simple framework for contrastive learning of visual representations," in *Proceedings of the 37th International Conference on Machine Learning,*, 2020.

[28] A. Vaswani, N. Shazeer, N. Parmar et al., "Attention is all you need," in *31st Conference on Neural Information Processing Systems (NIPS 2017)*, Long Beach, CA, USA, 2017.

[29] Y. Liu, J. Ma, Y. Xie et al., "Contrastive predictive coding with transformer for video representation learning," *Neurocomputing*, 2021.

[30] O. Russakovsky, J. Deng, H. Su et al., "ImageNet large scale visual recognition challenge," *International Journal of Computer Vision*, vol. 115, no. 3, pp. 211–252, 2015.

[31] C. Doersch, A. Gupta, and A. A. Efros, "Unsupervised visual representation learning by context prediction," in *Proceedings of the IEEE International Conference on Computer Vision (ICCV)*, pp. 1422–1430, Santiago, Chile, 2015.

[32] R. Zhang, P. Isola, and A. A. Efros, "Colorful image colorization," in *Computer Vision – ECCV 2016. ECCV 2016*, B. Leibe, J. Matas, N. Sebe, and M. Welling, Eds., vol. 9907 of Lecture Notes in Computer Science, pp. 649–666, Springer, Cham, 2016.

[33] C. Doersch and A. Zisserman, "Multi-task self-supervised visual learning," in *Proceedings ofthe IEEE Conference on Computer Vision and Pattern Recognition*, pp. 2051–2060, Honolulu, U.S.A, 2017.

[34] M. U. Gutmann and A. Hyvarinen, *Noise Contrastive Estimation: A New Estimation Principle for Unnormalized Statistical Models*, AISTATS, 2010.

[35] H. Fang, S. Wang, M. Zhou, J. Ding, and P. Xie, "CERT: contrastive self-supervised learning for language understanding," 2005, https://arxiv.org/abs/2005.12766.

[36] J. M. Giorgi, O. Nitski, G. D. Bader, and B. Wang, "DeCLUTR: deep contrastive learning for unsupervised textual representations," 2006, https://arxiv.org/abs/2006.03659.

[37] T. Han, W. Xie, and A. Zisserman, "Video representation learning by dense predictive coding," in *Proceedings of the IEEE/CVF International Conference on Computer Vision (ICCV)*, Venice, Italy, 2020.

[38] T. Han, W. Xie, and A. Zisserman, "Memory-augmented dense predictive coding for video representation learning," in *European Conference on Computer Vision (ECCV)*, 2020.

[39] J.-B. Grill, F. Strub, F. Altché et al., "Bootstrap your own latent: a new approach to self-supervised learning," 2020, https://arxiv.org/abs/2006.07733.

[40] X. Chen and K. He, "Exploring simple Siamese representation learning," in *Proceedings of the IEEE/CVF Conference on Computer Vision and Pattern Recognition (CVPR)*, 2021.

[41] M. Caron, P. Bojanowski, A. Joulin, and M. Douze, "Deep clustering for unsupervised learning of visual features," in *Proceedings of the European Conference on Computer Vision (ECCV)*, pp. 132–149, Munich, Germany, 2018.

[42] J. Devlin, M. W. Chang, K. Lee, and K. Toutanova, "BERT: pre-training of deep bidirectional transformers for language understanding," 2018, https://arxiv.org/abs/1810.04805.

[43] A. Radford, K. Narasimhan, T. Salimans, and I. Sutskever, *Improving Language Understanding by Generative Pre-Training*, OpenAI, 2018.

[44] N. Carion, F. Massa, G. Synnaeve, N. Usunier, A. Kirillov, and S. Zagoruyko, "End-to-end object detection with transformers," in *Computer Vision – ECCV 2020. ECCV 2020*, vol. 12346 of Lecture Notes in Computer Science, Springer, Cham.

[45] A. Dosovitskiy, L. Beyer, A. Kolesnikov et al., "An image is worth 16x16 words: transformers for image recognition at scale," 2021, https://arxiv.org/abs/2010.11929.

[46] X. Wang, R. Girshick, A. Gupta, and K. He, "Non-local neural networks," in *Proceedings of the IEEE Conference on Computer Vision and Pattern Recognition (CVPR)*, pp. 7794–7803, Salt Lake City, U.S.A, 2018.

[47] Y. Wang, X. Zhaoliang, X. Wang et al., "End-to-end video instance segmentation with transformers," in *Proceedings of the IEEE/CVF Conference on Computer Vision and Pattern Recognition (CVPR)*, 2021.

[48] M. Tan and V. L. Quoc, "EfficientNet: rethinking model scaling for convolutional neural networks," in *Proceedings of the 36th International Conference on Machine Learning*, Long Beach, U.S.A, 2019.

[49] D. Zhou, B. Kang, X. Jin, L. Yang, X. Lian, Z. Jiang, Q. Hou, and J. Feng, Eds., "DeepViT: towards deeper vision transformer," 2021, https://arxiv.org/abs/2103.11886.

[50] H. Touvron, M. Cord, M. Douze, F. Massa, A. Sablayrolles, and H. Jégou, Eds., "Training data-efficient image transformers & distillation through attention," in *Proceedings of the 38th International Conference on Machine Learnin*, 2021.

[51] Q. Hou, Z. Jiang, L. Yuan, M.-M. Cheng, S. Yan, and J. Feng, Eds., "Vision permutator: a permutable MLP-like architecture for visual recognition," 2021, https://arxiv.org/abs/2106.12368.

[52] H. Touvron, P. Bojanowski, M. Caron et al., "ResMLP: feedforward networks for image classification with data-efficient training," 2021, https://arxiv.org/abs/2105.03404.

[53] I. Tolstikhin, N. Houlsby, A. Kolesnikov et al., "MLP-mixer: an all-MLP architecture for vision," 2021, https://arxiv.org/abs/2105.01601.

[54] T. Xiao, M. Singh, E. Mintun, T. Darrell, P. Dollár, and R. Girshick, Eds., "Early convolutions help transformers see better," in *IEEE/CVF Conference on Computer Vision and Pattern Recognition (CVPR)*, 2021.

[55] I. Bello, B. Zoph, A. Vaswani, J. Shlens, and V. L. Quoc, Eds., "Attention augmented convolutional networks," in *Proceedings of the IEEE/CVF International Conference on Computer Vision (ICCV)*, Seoul, Korea, 2019.

[56] C. Li, T. Tang, G. Wang et al., "BossNAS: exploring hybrid CNN-transformers with block-wisely self-supervised neural architecture search," https://arxiv.org/abs/2103.12424.

[57] J. Chen, T. Cai, W. He et al., "A blockchain-driven supply chain finance application for auto retail industry," *Entropy*, vol. 22, no. 1, p. 95, 2020.

[58] I. Sutskever, O. Vinyals, and V. L. Quoc, "Sequence to sequence learning with neural networks," in *Conference and Workshop on Neural Information Processing Systems (NeurIPS)*, Montréal, Canada, 2014.

[59] S. Ioffe and C. Szegedy, "Batch normalization: accelerating deep network training by reducing internal covariate shift," in *Proceedings of the 32nd International Conference on Machine Learning*, pp. 448–456, Lille, France, 2015.

[60] X. Chen, H. Fan, R. Girshick, and K. He, "Improved baselines with momentum contrastive learning," https://arxiv.org/abs/2003.04297.

[61] X. Chen, S. Xie, and K. He, "An empirical study of training self-supervised vision transformers," 2021, https://arxiv.org/abs/2104.02057.

[62] A. Krizhevsky, *Learning Multiple Layers of Features from Tiny Images*, Technical report, University of Toronto, 2009.

[63] M. Everingham, L. Van Gool, C. K. I. Williams, J. Winn, and A. Zisserman, "The Pascal visual object classes (VOC) challenge," *International Journal of Computer Vision*, vol. 88, no. 2, pp. 303–338, 2010.

[64] O. M. Parkhi, A. Vedaldi, A. Zisserman, and C. V. Jawahar, "Cats and dogs," in *2012 IEEE Conference on Computer Vision and Pattern Recognition*, Providence, RI, USA, 2012.

[65] M.-E. Nilsback and A. Zisserman, "Automated flower classification over a large number of classes," in *2008 Sixth Indian Conference on Computer Vision, Graphics & Image Processing*, Bhubaneswar, India, 2008.

Research Article

A Novel Generative Method for Machine Fault Diagnosis

Zhipeng Dong,[1] Yucheng Liu,[2,3] Jianshe Kang 🆔,[1] and Shaohui Zhang 🆔[2]

[1]*Army Engineering University of PLA, Shijiazhuang, China*
[2]*School of Mechanical Engineering, Dongguan University of Technology, Dongguan 523808, China*
[3]*College of Mechatronics and Control Engineering, Shenzhen University, Shenzhen 518060, China*

Correspondence should be addressed to Shaohui Zhang; zhangsh@dgut.edu.cn

Deep learning is widely used in fault diagnosis of mechanical equipment and has achieved good results. However, these deep learning models require a large number of labeled samples for training, which is difficult to obtain enough labeled samples in the actual production process. However, it is easier to obtain unlabeled samples in the industrial environment. To overcome this problem, this paper proposes a novel method to generative enough label samples for training deep learning models. Unlike the generative adversarial networks, which required complex computing time, the calculation of the proposed novel generative method is simple and effective. First, we calculate the Euclidean distance between the training sample and the test sample; then, the weight coefficient between the training sample and the test sample is settled to generate pseudosamples; finally, combine with the pseudosamples, the deep learning method is training for machine fault diagnosis. In order to verify the effectiveness of the proposed method, two experiment datasets with planetary gearboxes and wind gearboxes are carried out with different activation functions. Experimental results show that the proposed method is effective for most activation function models.

1. Introduction

With the continuous development of industrial intelligence, people are focusing on equipment health monitoring and fault diagnosis. Gearboxes are widely used in mechanical equipment, especially in large and complex equipment, and gearboxes are the main transmission device. Therefore, condition monitoring and fault diagnosis of gearboxes are very important [1, 2]. In the manufacturing industry, machine fault will directly affect machining accuracy and machining quality, reducing production efficiency [3]. Equipment status monitoring and fault diagnosis are essential to ensure the machine's normal operation, reduce maintenance costs, and improve production efficiency. Therefore, it is of great significance to conduct health monitoring and fault diagnosis of mechanical engineering equipment.

The data-driven fault diagnosis method usually includes three stages: (1) using sensors to obtain sample data; (2) denoising the sample data and extracting features; (3) inputting the extracted features into the classification algorithm

for fault identification [4]. Deep learning is an effective method of fault diagnosis. In order to improve the accuracy of fault diagnosis, researchers have developed several deep learning networks. Such as recurrent neural networks (RNN) [5], autoencoder(AE) [6, 7], long short-term memory (LSTM) [8], deep belief network (DBN) [9], and convolutional neural network (CNN) [10], the advantage of these deep learning algorithms is to reduce feature redundancy and extract more information features for predictive models. Deep learning technology has shown good performance in fault detection and diagnosis with its powerful feature extraction ability and excellent classification performance, thus, it has become a research hotspot. Guo et al. [11] proposed an intelligent method based on deep belief network (DBN) and hyperparameter optimization for fault diagnosis of rolling bearings. Li et al. [12] proposed a deep autoencoder network for cross-machine fault diagnosis. Zhou et al. [13] designed a new generative confrontation network generator and discriminator, using a global optimization scheme to generate more discriminable fault samples. Ma

and Mao [14] developed a novel deep neural network, a convolution-based long short-term memory (CLSTM) network, to predict the remaining service life (RUL) of rotating machinery in field vibration data. Wang et al. [15] formed a new fault diagnosis method by integrating the deformable convolutional neural network (CNN), deep long short-term memory (DLSTM), and transfer learning strategies. Singh et al. [16] proposed a deep learning-based domain adaptation (DA) method for fault diagnosis of gearboxes when the speed changes significantly. Xue et al. [17] proposed an enhanced deep sparse autoencoder (ADSAE) for diagnosing gear pitting faults. He et al. [18] proposed an improved deep autoencoder (MDAE) driven by multisource parameters for cross-domain fault prediction.

Deep learning has a good effect on fault diagnosis; however, it requires a large number of condition samples in the training process to achieve satisfactory accuracy. The limited number of samples will directly lead to a reduction in model performance. Due to different working conditions, it is difficult and expensive to collect enough fault samples for training models in actual industrial production. Therefore, it is important to research the deep learning method for machine fault diagnosis in small samples situation. Li et al. [19] proposed a fusion framework based on the confidence weight support matrix machine (CWSMM) for strong interference and unbalanced data sets. Ti et al. [20] proposed a weighted extended neural network (W-ENN) model for fault diagnosis of a small piece of steam turbine generator sets. He et al. [21] suggested using depth transfer multiwavelet autoencoder to diagnose the gearbox fault with a few training samples. Zhang et al. [22] used generative adversarial networks to learn the mapping between noise distribution and actual mechanical time vibration data and then generate similar fake samples to expand further the available data set for fault diagnosis. Xiao et al. [23] proposed a fault diagnosis framework using an improved TrAdaBoost algorithm and a convolutional neural network for a small amount of target data for transfer learning. Meng et al. [24] proposed a data enhancement method that divides a single sample into multiple cells and then reorganizes the cells to increase the number of data samples. Li et al. [25] proposed an enhanced generative adversarial network (EGAN), which uses a generator to generate specified samples and automatically enrich small sample data sets for fault diagnosis of rotating machinery. In order to solve the problem of unbalanced sample allocation, Zhang et al. [26] designed a weighted minority oversampling (WMO) comprehensive oversampling method.

Although the deep learning model has high diagnostic accuracy and prediction accuracy, it requires a large number of label samples for training. Otherwise, the diagnostic accuracy will be greatly reduced. Since several novel deep learning methods have been proposed to overcome the problem of the small sample, most of these methods are based on deep learning network architecture and require a lot of computing time. Therefore, a novel method with litter computing time has been proposed for the small sample problem. The main contributions of the paper contains (1) a novel, low-computing, and effective intelligent diagnosis method is proposed for small samples problem; (2) the proposed

method calculates the Euclidean distance between a small label samples and a large number of unlabeled samples and generates pseudo samples with labels by a weight; (3) the proposed method is used for fault detection of planetary gearboxes, and the accuracy has been greatly improved.

The other sections of this paper are arranged as follows. The second section mainly introduces the theory of the proposed method. Sections 3 and 4 discuss the arrangement of experiments on planetary gearboxes and industrial robots and the analysis of the corresponding results. Finally, Section 5 introduces the relevant conclusions.

2. Methodology

For the small sample problem of fault diagnosis, we use unknown as training samples X_{train} and then use a number of label samples as test samples X_{test}. The training sample matrix is composed of $m \times n$ dimensional vectors, expressed as

$$X_{\text{train}} = [x_{11}, x_{12}, \cdots, x_{1n}; \cdots; x_{m1}, x_{m2}, \cdots, x_{mn}] X_{train} \in R^{\text{m} \times n}. \tag{1}$$

Similarly, the test sample matrix is composed of $f \times n$ dimensional vectors, expressed as

$$X_{\text{test}} = [x_{11}, x_{12}, \cdots, x_{1n}; \cdots; x_{f1}, x_{f2}, \cdots, x_{fn}] X_{test} \in R^{f \times n}. \tag{2}$$

By calculating the Euclidean distance between the test sample and the training sample and comparing the distance, find the training sample point closest to the test sample.

2.1. Novel Generative Method. Euclidean distance is the actual distance between two points in n-dimensional space or the distance from the point to the origin (that is, the length of the vector). The Euclidean distance obtained in two and three dimensions is equal to the actual distance between two points. It is the simplest and most direct method to calculate the distance between data sample points. Suppose two n-dimensional vectors $A = [a_1, a_2, \cdots, a_n]$ and $B = [b_1, b_2, \cdots, b_n]$, then, the Euclidean distance formula in n-dimensional space is

$$\text{Dist}_{(A,B)} = \sqrt{(a_1 - b_1)^2 + (a_2 - b_2)^2 + \cdots + (a_n - b_n)^2}. \tag{3}$$

The above formula can calculate the Euclidean distance between the vectors, extended from the Euclidean distance between the vectors to the Euclidean distance between the matrices. Let $i \times n$ dimensional matrix C as $C = [x_{11}, x_{12}, \cdots, x_{1n}; \cdots; x_{i1}, x_{i2}, \cdots, x_{\text{in}}]$, $j \times n$ dimensional matrix D as $D = [y_{11}, y_{12}, \cdots, y_{1n}; \cdots; y_{j1}, y_{j2}, \cdots, y_{jn}]$. Calculating the Euclidean distance of matrix C and matrix D will get distance matrix E. The formula for calculating Euclidean distance between matrices is

$$\text{Dist}_{c_{ij}} = \sqrt{\left(x_{i1} - y_{j1}\right)^2 + \left(x_{i2} - y_{j2}\right)^2 + \cdots + \left(x_{in} - y_{jn}\right)^2}. \tag{4}$$

The above formula can be found that each row vector of matrix C has been calculated j times (the number of rows in D). Therefore, the calculation of the Euclidean distance between the matrices relies on the measure of the Euclidean distance between the vectors, so the dimension of the matrix E is $i \times j$. After calculating the Euclidean distance of the data sample points, compare the distance between the sample points. Find the test sample point $\text{Dist}_{\min}$ with the smallest Euclidean distance from the training sample in the test sample and then generate the label sample by calculating the following formula.

$$X_{\text{new}} = (\text{dist}_{\min}, :) \times k + X_{\text{test}}. \tag{5}$$

In the formula, X_{new} represents a new sample, and k represents a scale factor. We automatically classify sample points with sufficiently small distance into one category, generate a unique sample point at the distance k between the two sample points with the shortest distance, and expand the data sample by this method in Figure 1.

2.2. SAE-Based Network Model

2.2.1. Autoencoder (AE).
Autoencoders were used for dimensionality reduction processing and feature learning of high-dimensional complex data, which has a positive effect on the development of deep learning neural networks. The autoencoders use unsupervised neural network learning methods to learn unlabeled raw data and extract low-dimensional data features of high-dimensional complex data. The network structure of the autoencoder is shown in Figure 2. It is composed of three layers of neural networks, namely, the input layer, the hidden layer, and the output layer. The hidden layer means that the high-dimensional data is processed to obtain the low-dimensional data features. The output layer has the same number of nodes as the input layer, which means that the input and output data dimensions are the same. The autoencoder aims to reconstruct its input; that is, it uses the backpropagation algorithm to make the output equal to the input as much as possible. A function that the self-encoding neural network tries to learn is

$$y_{w,b}(x) \approx x. \tag{6}$$

The autoencoder tries to approximate an identity function so that the output $y(i)$ approximates the input $x(i)$. By minimizing the reconstruction error, the input data can be reconstructed as much as possible in the output layer, thereby exerting the unsupervised learning effect and effectively extracting low-dimensional data features. The autoencoder method has been widely used in fault diagnosis.

The autoencoders are composed of a three-layer neural network, which can also be seen as composed of two parts: encoder and decoder. The encoder consists of an input layer and a hidden layer. Through training, the input layer data x
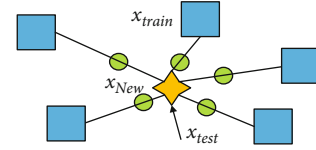
FIGURE 1: Pseudosample generation.
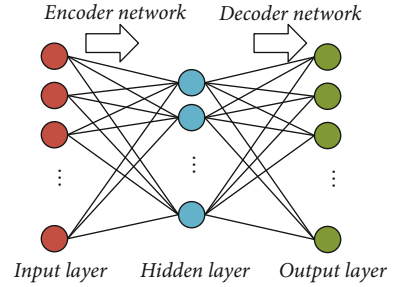
FIGURE 2: The structure of an AE neural network.
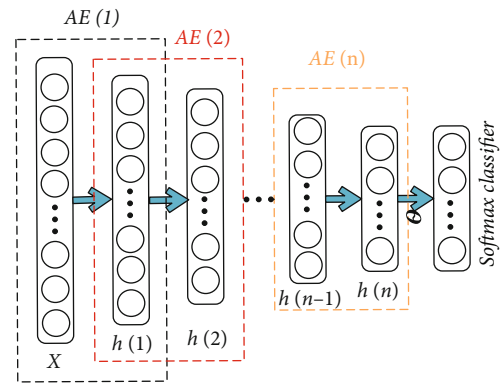
FIGURE 3: The structure of the SAE network.

is encoded and converted into a deterministic mapping of the feature form h of the hidden layer. It can perform affine mapping and nonlinear mapping. The coding network is defined as

$$\boldsymbol{h} = f_\theta(\boldsymbol{w}_1 x + \boldsymbol{b}_1), \tag{7}$$

where f_θ is the activation function in the coding network, w_1 is the weight vector of the coding stage, b_1 is the offset vector of the coding stage, and $\theta = \{w_1, b_1\}$ is the trainable parameter set of the encoder and decoder. Then, in the decoding stage, the decoder consists of a hidden layer and an output layer. The decoding network maps the feature h of the hidden layer to the input layer, reconstructs the input data x, and obtains the output layer data with the same dimensions. Similarly, the decoding process can be defined as

$$x' = y_{w,b}(x) = f'_\theta(\boldsymbol{w}_2 h + \boldsymbol{b_2}). \tag{8}$$

The vector of approximate input data is reconstructed by the output layer, the activation function in the decoding network, w_2 is the weight vector of the decoding stage, b_2 is the
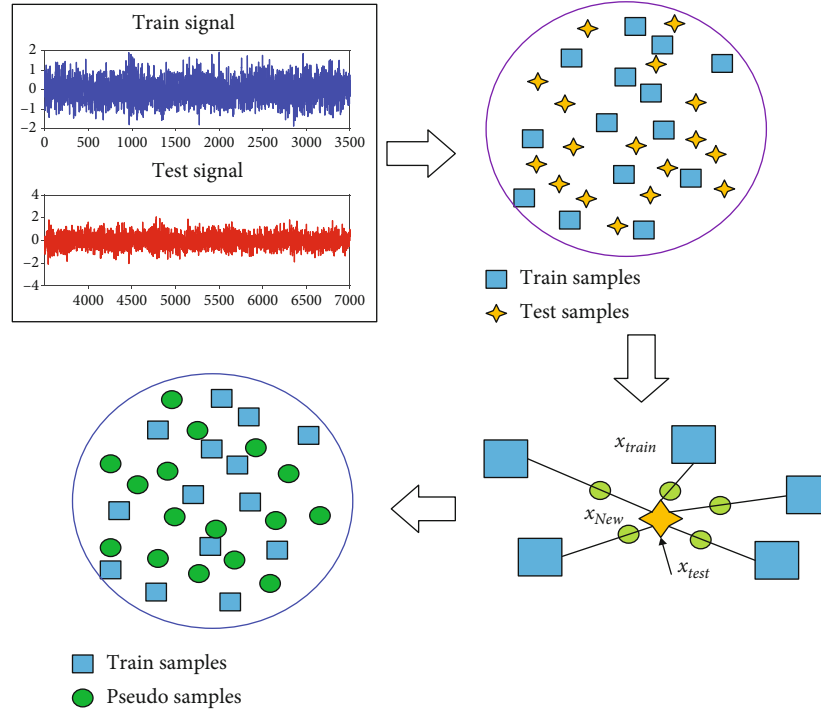
FIGURE 4: The overall proposed fast generative samples structure.

offset vector of the decoding stage, and $\theta = \{w_2, b_2\}$ is the trainable parameter set of the encoder and decoder. The reconstruction error $J(w, b; x, x')$ between the output x' and the input x is expressed as

$$J\left(\boldsymbol{w}, \boldsymbol{b}; \boldsymbol{x}, \boldsymbol{x}'\right) = \frac{1}{2}\left\|\boldsymbol{x} - \boldsymbol{x}'\right\|^2. \tag{9}$$

In the training process, given a training set of m samples, we define the total cost function as

$$J(\boldsymbol{w}, \boldsymbol{b}) = \left[\frac{1}{m}\sum_{i=1}^{m} J\left(\boldsymbol{w}, \boldsymbol{b}; \boldsymbol{x}, \boldsymbol{x}'\right)\right] + \lambda T, \tag{10}$$

where $J(w, b)$ represents the total cost function of the entire data set, the last term is the average sum of square error, λT is the regularization term (also called the weight penalty term), and the weight penalty parameter λ is used to limit the weight in order to achieve the purpose of preventing overfitting.

2.2.2. SAE-Based Network. The SAE network structure is composed of multiple autoencoder structure hierarchically, and there is a classifier in the output layer. The SAE network structure is shown in Figure 3.

The AE network has the problem of extracting feature redundancy. In order to solve this problem, regularization constraints are introduced in the SAE network, and constraints are added to the hidden layer neurons. In the encoding and decoding process, in order to make the hidden layer sparse, we need to add constraints to each hidden layer.
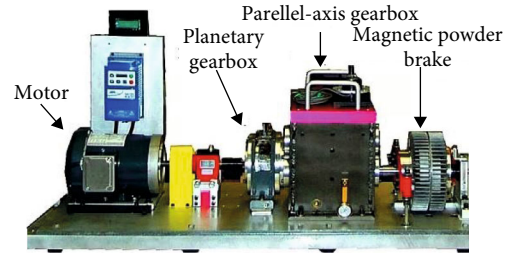
FIGURE 5: The drivetrain diagnostics simulator.

Only a few neuron nodes are active. The average activation degree of the hidden layer neural unit node j can be described as

$$\boldsymbol{\rho}_j = \frac{1}{m}\sum_{i=1}^{m}\left[h_j(x(i))\right]. \tag{11}$$

The average activation degree of the hidden layer neuron nodes generally approaches 0; that is, most neuron nodes are disabled. Therefore, in order to ensure that the activation degree of each node is close to 0, additional penalty terms need to be added to the cost function, which is described by the mathematical formula as follows:

$$KL\left(\rho\|\rho_j\right) = \rho \log \frac{\rho}{\rho_j} + (1-\rho) \log \frac{1-\rho}{1-\rho_j}, \tag{12}$$

where ρ is the sparsity parameter, and $KL(.)$ is the Kulback-Leibler divergence used as a penalty metric between the

TABLE 1: Faulty patterns set in the experiments.

Faulty pattern	Fault type	Load condition	Faulty pattern	Fault type	Load condition
F1	Surface wear	0 nm	F11	Chipped tooth	2.8 nm
F2	Surface wear	1.4 nm	F12	Chipped tooth	5.2 nm
F3	Surface wear	2.8 nm	F13	Missing tooth	0 nm
F4	Surface wear	5.2 nm	F14	Missing tooth	1.4 nm
F5	Crack tooth	0 nm	F15	Missing tooth	2.8 nm
F6	Crack tooth	1.4 nm	F16	Missing tooth	5.2 nm
F7	Crack tooth	2.8 nm	F17	Normal	0 nm
F8	Crack tooth	5.2 nm	F18	Normal	1.4 nm
F9	Chipped tooth	0 nm	F19	Normal	2.8 nm
F10	Chipped tooth	1.4 nm	F20	Normal	5.2 nm

expected distribution and the actual distribution. The penalty term has the property that when $\rho_{j=}\rho$, $KL(\rho\|\rho_j) = 0$. In the SAE network, the sparse penalty is added to the cost function, which can be expressed by the following formula:

$$J_{\text{sparse}}(w, b) = J(w, b) + \beta \sum_{j=1}^{s} KL\left(\rho\|\rho_j\right), \qquad (13)$$

where β is the weight of the sparsity parameter. The parameters $\{w, b\}$ can be updated using a stochastic gradient descent algorithm.

2.3. Classical Activation Functions. The input datasets of the neural network are weighted and, applied to the activation function, which can enhance the nonlinearity of the entire network model. Since the activation function can introduce nonlinearity to neurons, the expressive ability of the network model becomes stronger. The Sigmoid function is a commonly used activation function, but it has the problem of vanishing gradient. In order to solve the problem of vanishing gradient, many activation functions have been developed. In order to verify the effectiveness of the proposed method, the following activation functions are used in the SAE model.

(1) According to the literature [27], the expression of Tanh function is

$$\text{Tanh}(\boldsymbol{x}) = \frac{e^x - e^{-x}}{e^x + e^{-x}}, \qquad (14)$$

$$\text{Tanh}'(\boldsymbol{x}) = \frac{4}{(e^x + e^{-x})^2}. \qquad (15)$$

Tanh is a common activation function, and its value range is [-1, 1]. Compared with Sigmoid, its output mean value is 0, and the number of iterations is less. Moreover, the convergence speed is faster. Note that the Tanh has soft saturation and will cause the problem of gradient disappearance.

(2) According to the literature [28], the expression of RelTanh function is

$$\text{RelTanh}(\boldsymbol{x}) = \begin{cases} \text{Tanh}'(\lambda^+)(x - \lambda^+) + \text{Tanh}(\lambda^+) & x \geq \lambda^+, \\ \text{Tanh}(x) & \lambda^- < x < \lambda^+, \\ \text{Tanh}'(\lambda^-)(x - \lambda^-) + \text{Tanh}(\lambda^-) & x \leq \lambda^-. \end{cases}$$
$$(16)$$

The RelTanh activation function is composed of a linear function at both ends and a nonlinear Tanh function at the middle. Therefore, it can solve the problems of the Tanh function and ReLU function. λ^+ and λ^- are mainly used to constrain the learnable range of the slope and avoid the disappearance of the gradient. The initial threshold will be set to $\lambda^+ = 0$ and $\lambda^- = -1$.

(3) According to the literature [29], the expression of ELU function is

$$\text{ELU}(\boldsymbol{x}) = \begin{cases} x & x \geq 0, \\ \alpha(\exp(x) - 1) & x < 0. \end{cases} \qquad (17)$$

ELU is an improved version of the ReLU function. Through the parameter α, the output of the negative interval is no longer to zero. The output has a certain degree of anti-interference ability and enhances the robustness to noise; however, it still has gradient disappearance.

2.4. The Proposed Algorithm. This paper proposes a novel generative method to provide enough label samples for training deep learning models. By calculating the relationship between the label samples and their nearest unlabeled samples, the proposed method can generate enough pseudosamples with labels. Combine with the pseudosamples, the deep learning method is training for machine fault diagnosis. The structure of proposed in this paper is shown in Figure 4 and summarized as follows.
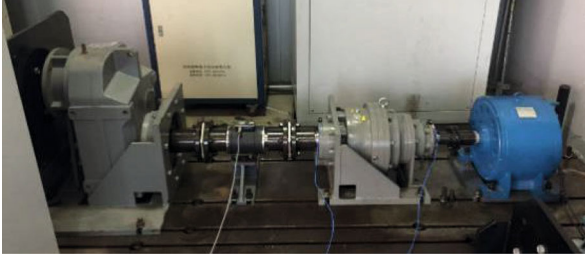
Figure 6: Wind gearboxes test rig.

Table 2: Faulty patterns set in the experiments.

Faulty pattern	Fault location	Degree of failure
A	Normal	Normal
B	Planet gear	Broken
C	Planet gear	Moderate
D	Ring left	Moderate
E	Sun gear	Broken

Table 3: The average accuracy of 100_train samples.

Samples Function	100	500	700	900
Reltanh	0.3827	0.3600	0.4984	0.5637
Tanh	0.3535	0.3942	0.3705	0.4228
ELU	0.3476	0.4142	0.3700	0.4561

(1) Collected the condition data set from machine experiments

(2) Divide data into training and testing data set

(3) Calculating the Euclidean distance between the test sample and the training sample, and comparing the distance

(4) Finding the training sample point closest to the test sample and generative the pseudosamples with labels

(5) Train SAE model with different activation functions

Fault classification using the trained SAE model and evaluate the accuracy.

3. Experiments

3.1. Fault Experiment of Planetary Gearbox. Design experiments to verify the validity of the proposed method. The experimental device used the power transmission fault diagnosis experiment platform (DDS) designed by SpectraQuest, as shown in Figure 5.

The failure of the transmission system is mainly caused by the wear of the tooth surface in the spur gear and the helical gear, the crack of the tooth surface, the pitting of the tooth surface, and the lack of teeth. Therefore, this experiment sets these four types of failures. Since the planetary

Table 4: The average accuracy of 200_train samples.

Samples Function	200	1000	1400	1800
Reltanh	0.4893	0.6313	0.61660	0.6691
Tanh	0.4662	0.6416	0.5314	0.6267
ELU	0.4779	0.4640	0.5371	0.6084

Table 5: The average accuracy of 300_train samples.

Samples Function	300	1500	2100	2700
Reltanh	0.5767	0.7334	0.7435	0.7834
Tanh	0.5082	0.6410	0.7318	0.7547
ELU	0.5671	0.6450	0.6907	0.8212

Table 6: The average accuracy of 400_train samples.

Samples Function	400	2000	2800	3600
Reltanh	0.7036	0.7355	0.7667	0.8500
Tanh	0.5928	0.5696	0.6685	0.8304
ELU	0.6548	0.5851	0.7455	0.8058

Table 7: The average accuracy of 500_train samples.

Samples Function	500	2500	3500	4500
Reltanh	0.7725	0.8266	0.8674	0.8675
Tanh	0.6695	0.7410	0.7589	0.8276
ELU	0.7809	0.7910	0.8004	0.8776

gearbox's secondary sun gear has a relatively high probability of failure, this experiment's focus is to test the secondary sun gear of the planetary gearbox. In order to obtain a variety of vibration signals, by controlling the magnetic brake under four different load conditions (0 Nm, 1.4 Nm, 2.8 Nm, and 5.2 Nm), the vibration signals of normal conditions and four fault conditions are collected. A total of 20 groups of vibration signals, as shown in Table 1.

3.2. Fault Experiment of Wind Gearboxes. In order to further verify the effectiveness and versatility of the method, we use the wind gearboxes failure data set to test the method again. The experiment was carried out on the industrial robot experimental platform, as shown in Figure 6. The test bench consists of a 3.7 kW electric motor, a two-stage parallel gearbox with a speed increase ratio of 20, a 3 kW permanent magnet synchronous motor, and a 3 kW load box. In order to ensure the rationality of the collected signals, the sensor is installed on the bearing chock of the gearbox, and the sensor is connected to the computer to store the signal data. In this case, it can better reflect the advantages of the proposed method in adapting to different types of data sets under small sample conditions.
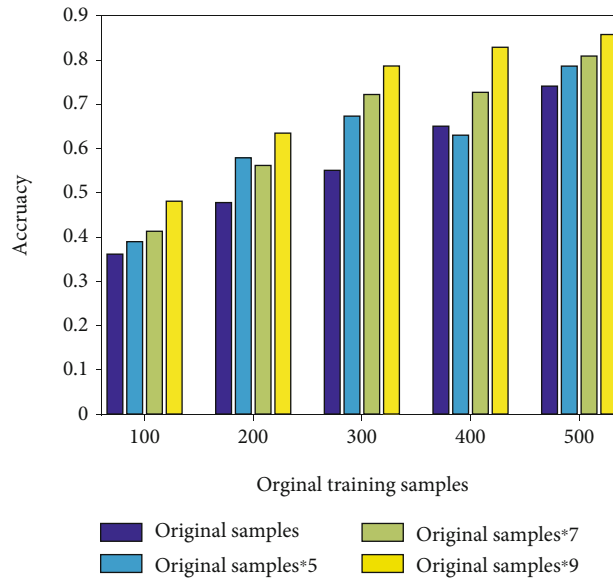
FIGURE 7: Average accuracies of all activation functions.

The gearbox is a key component to ensure the normal operation of the wind. The gearbox is mainly composed of the two-stage parallel gearbox. As the internal gear is prone to pitting and cracking failures, it will lead to reduced work efficiency. Therefore, in this experiment, the sun gear and planetary gears are tested, and a set of normal modes and four sets of failure modes are set. Table 2 shows the detailed description of the gear fault location and fault degree of the gear simulated in this experiment. The experiment is carried out under the condition that the motor speed is 300 r/min and no load.

4. Fault Diagnosis and Result Analysis

4.1. Fault Diagnosis and Result Analysis for Planetary Gearbox. By analyzing the fault diagnosis accuracy of each activation function in the experiment, the effectiveness of the method under the condition of small samples is verified. In order to avoid the problem of the disappearance of the gradient of the activation function, a 4-layer SAE network structure was constructed, and different activation functions were applied when experimenting with the gearbox. In order to ensure the universality and reliability of the experimental results of this method under small sample conditions, we conducted experiments based on five groups of different sample numbers. In the experiment, the basic numbers of samples are 100, 200, 300, 400, and 500. To ensure the validity of the experimental results, in the experiment, each group of basic samples used the method proposed in this paper to carry out three generate sample, and four independent experiments were carried out after each generate. The average diagnostic accuracy is a key measurable indicator that reflects the functional differences between activation functions and compares the performance of activation functions.

The proposed method is used to generate the label samples, and then deep learning models with different activation functions are used for fault diagnosis. The average accuracy of each activation function under different sample sizes is listed in Tables 3 to 7.

In the case of 100 train samples, the activation functions, as RelTanh, Tanh, and ELU, have improved diagnostic accuracy. When the train samples extended to 900, the highest accuracy of activation function is RelTanh, which exceeds 50% (as shown in Table 3). For the basic samples number is 200, the classification rate of the activation function is ranging from 46.62% to 48.93%. When the training samples are increasing to 1,800 by the proposed method, the accuracy of the activation functions is above 60%. As the number of train samples increases, the accuracy of overall function is significantly improved. When the train samples is 300 and without samples generation, the accuracy of the activation function range between 50.82% and 57.67%. Since the number of train samples becomes 2700 with generated method, the average diagnostic accuracy of the ELU function reaches 82.12%. In the case of the original train samples is 400, the diagnostic accuracy of the activation function is significantly improved, and the diagnostic accuracy of RelTanh and Tanh are exceeded 80%. For the original train samples is 500, the accuracy of the activation function is ranging from 66.95% to 78.09%. The accuracy of RelTanh, Tanh, and ELU are still the highest. From Tables 3 to 7, it can be shown that the average accuracy of RelTanh and Tanh functions is higher in these cases, since they overcome the vanishing gradient problem and the diagnostic accuracy will increase as the number of samples increases.

The average accuracies of each activation function with the proposed generate method are compared with the original method, as shown in Figure 7. Form the Figure 7, it shows that the fault diagnosis accuracy of activation function is significantly improved as increasing the training samples, which proves the effectiveness of the proposed method.

The ELU function has an average diagnostic accuracy rate of 87.76% when the sample base is expanded from 500 to 4500, which has an absolute advantage over the activation
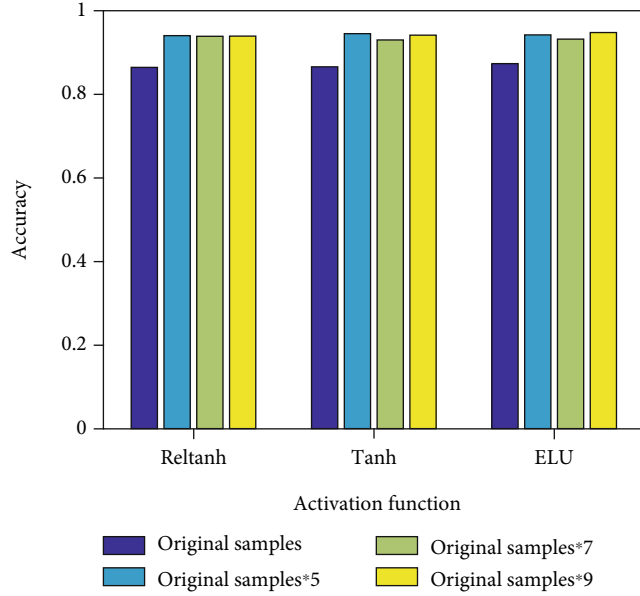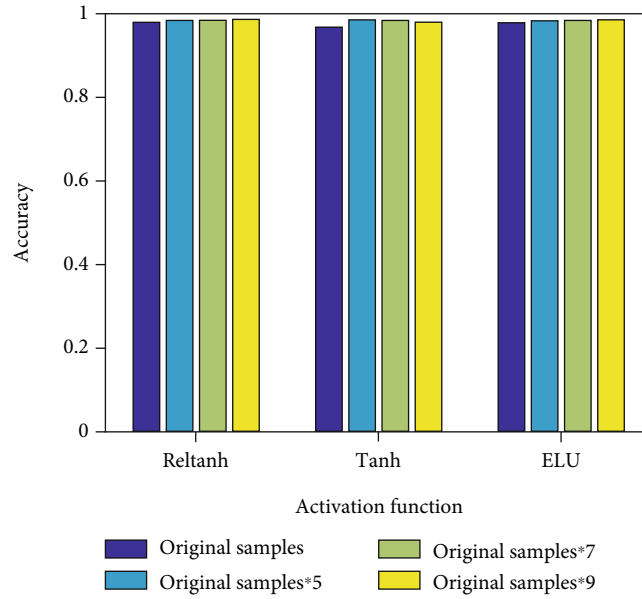
FIGURE 8: Average accuracies of all activation functions based on 100 train samples.
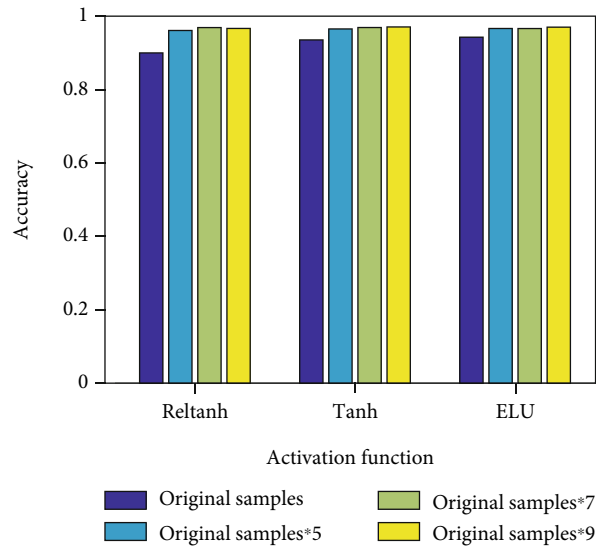
FIGURE 9: Average accuracies of all activation functions based on 200 train samples.

function of other functions. The ELU function negative interval is saturated, allowing negative abnormal input and avoiding a certain degree of gradient disappearance while having stronger noise robustness. In summary, the ELU, RelTanh, and Tanh function of our proposed sample expansion method perform best. It is worthy of further development and application in the case of small samples.

4.2. Fault Diagnosis and Result Analysis for Wind Gearboxes. Like the experiment introduced in Section A, we use the SAE network model in the wind gearboxes fault diagnosis experiment. In the experiment, this method is used to expand and train five groups of different numbers of samples. In order to ensure the validity and rationality of the results, three gener-

ate sample experiments were carried out for each group of samples, and four independent experiments were carried out for each group of generated the sample.

In the wind gearboxes fault diagnosis experiment, each activation function average diagnosis accuracy under different sample bases is shown in Figures 8 to 12. Experimental results show that the proposed method has certain effects in the case of small samples, and the activation function (Reltanh) has highest diagnostic accuracy. The diagnostic accuracy is increasing as generates training samples increases. For the original train samples is 100 (as shown in Figure 8), the accuracy of Reltanh is ranging from 0.8743 to 0.9511. When the sample base is 200, the diagnosis accuracy rates are ranging from 0.9009 to 0.9700, 0.9364 to
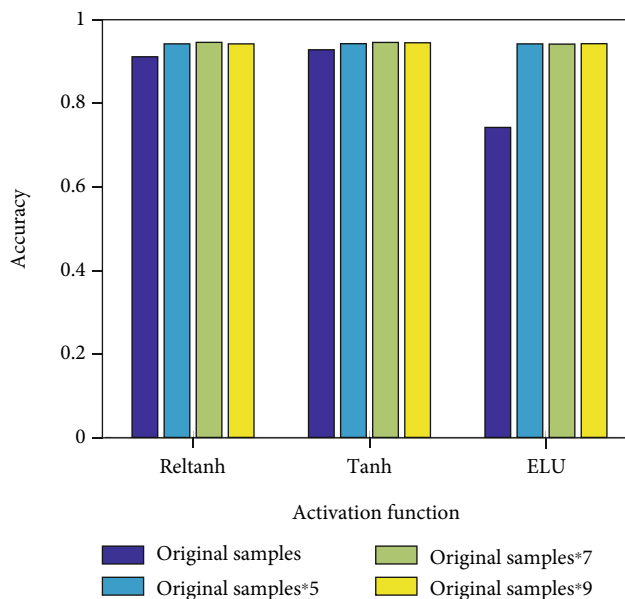
FIGURE 10: Average accuracies of all activation functions based on 300 train samples.
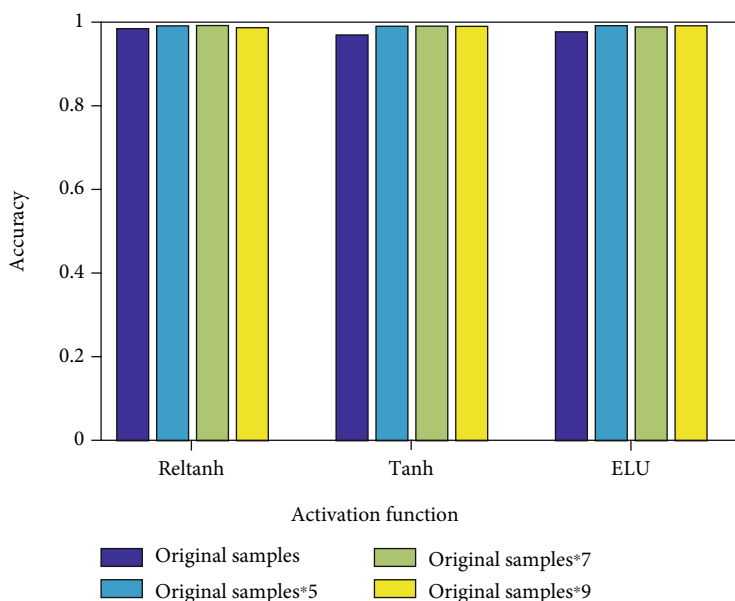
FIGURE 11: Average accuracies of all activation functions based on 400 train samples.

0.9717, and 0.9438 to 0.9711 for Reltanh, Tanh, and ELU, respectively. For the original samples is 300 (as shown in Figure 10), the accuracy rate is ranging between 0.7697 and 0.9626 without samples generated. However, the accuracy rates increase to more than 0.9766 under the proposed method.

In the case of the sample base is 400, the diagnosis accuracy rate of Reltanh is 97.56 ~ 98.30%. The Tanh function accuracy is increased by 2.09%, when the samples are increased to 2,800. When the basic sample number is 500, the diagnostic accuracy rate of the Reltanh function reaches to 98.50% (as shown in Figure 12).

From Figures 8–12, it can be seen that the Reltanh function has the highest fault diagnosis accuracy. As the sample size increases, the diagnostic accuracy of all activation functions has raised with different degrees. This result proved the effectiveness of the proposed method. In general, our method has strong stability in the case of small samples and has good results on different data sets with small training samples.

The average accuracies of each activation function with the proposed generate method are compared with the original method, as shown in Table 8. It should be noted that nine-time of the original train samples is generated by the

FIGURE 12: Average accuracies of all activation functions based on 500 train samples.

TABLE 8: Average accuraciesof all activation functions.

Training samples	The SAE-based DNNs	The proposed method
100	87.78%	95.04%
200	92.70%	96.82%
300	89.25%	97.84%
400	96.82%	98.14%
500	97.38%	98.26%

proposed method, and the average accuracies are calculated. The average accuracy of the proposed method is better than that of the SAE-based DNNs method for different training samples. The accuracy is increased by 0.88% to 8.59% for different training samples, when the samples are increased by the proposed method.

5. Conclusions

Deep learning has been widely used in fault diagnosis of mechanical equipment and has achieved ideal results. To overcome the problem of the small sample, this paper proposed a novel generative method to provide enough label samples for deep learning model. First, the Euclidean distance between a label sample and unlabeled samples is calculated, and the nearest samples are selected to generate new label samples. Then, the pseudosamples with label samples are altogether for training deep model. The results of fault diagnosis on planetary gearboxes and wind gearboxes show that the proposed method can greatly improve accuracy. It is worth noting that the effect of this method is related to the activation function. In the gearbox experiment, as the number of original samples increases, the proposed method has a good effect on most activation functions, and "ReLTanh," "Tanh," or "ELU" is the best activation function.

Data Availability

The data used to support the findings of this study are available from the author upon request.

Conflicts of Interest

The authors declare that they have no conflicts of interest.

References

[1] Z. Feng, A. Gao, K. Li, and H. Ma, "Planetary gearbox fault diagnosis via rotary encoder signal analysis," *Mechanical Systems and Signal Processing*, vol. 149, article 107325, 2021.

[2] M. S. Raghav and R. B. Sharma, "A review on fault diagnosis and condition monitoring of gearboxes by using AE technique," *Archives of Computational Methods in Engineering*, vol. 28, no. 4, pp. 2845–2859, 2021.

[3] A. Kumar, C. Gandhi, Y. Zhou, R. Kumar, and J. Xiang, "Improved deep convolution neural network (CNN) for the identification of defects in the centrifugal pump using acoustic images," *Applied Acoustics*, vol. 167, article 107399, 2020.

[4] Z. Hu, Y. Wang, M. Ge, and J. Liu, "Data-driven fault diagnosis method based on compressed sensing and improved multiscale network," *IEEE Transactions on Industrial Electronics*, vol. 67, no. 4, pp. 3216–3225, 2020.

[5] J. Wang and C. Zhang, "Software reliability prediction using a deep learning model based on the RNN encoder-decoder,"

Reliability Engineering & System Safety, vol. 170, pp. 73–82, 2018.

[6] H. Zhu, J. Cheng, C. Zhang, J. Wu, and X. Shao, "Stacked pruning sparse denoising autoencoder based intelligent fault diagnosis of rolling bearings," *Applied Soft Computing*, vol. 88, article 106060, 2020.

[7] J. Liu, K. Zhou, C. Yang, and G. Lu, "Imbalanced fault diagnosis of rotating machinery using autoencoder-based supergraph feature learning," *Frontiers of Mechanical Engineering*, pp. 1–11, 2021.

[8] J. Lei, C. Liu, and D. Jiang, "Fault diagnosis of wind turbine based on long short-term memory networks," *Renewable Energy*, vol. 133, pp. 422–432, 2019.

[9] C. Shen, J. Xie, D. Wang, X. Jiang, J. Shi, and Z. Zhu, "Improved hierarchical adaptive deep belief network for bearing fault diagnosis," *Applied Sciences*, vol. 9, no. 16, p. 3374, 2019.

[10] Z. Chen, A. Mauricio, W. Li, and K. Gryllias, "A deep learning method for bearing fault diagnosis based on cyclic spectral coherence and convolutional neural networks," *Mechanical Systems and Signal Processing*, vol. 140, article 106683, 2020.

[11] C. Guo, L. Li, Y. Hu, and J. Yan, "A deep learning based fault diagnosis method with hyperparameter optimization by using parallel computing," *IEEE Access*, vol. 8, pp. 131248–131256, 2020.

[12] X. Li, X.-D. Jia, W. Zhang, H. Ma, Z. Luo, and X. Li, "Intelligent cross-machine fault diagnosis approach with deep autoencoder and domain adaptation," *Neurocomputing*, vol. 383, pp. 235–247, 2020.

[13] F. Zhou, S. Yang, H. Fujita, D. Chen, and C. Wen, "Deep learning fault diagnosis method based on global optimization GAN for unbalanced data," *Knowledge-Based Systems*, vol. 187, article 104837, 2020.

[14] M. Ma and Z. Mao, "Deep convolution-based LSTM network for remaining useful life prediction," *IEEE Transactions on Industrial Informatics*, vol. 17, no. 3, pp. 1658–1667, 2021.

[15] Z. Wang, Q. Liu, H. Chen, and X. Chu, "A deformable CNN-DLSTM based transfer learning method for fault diagnosis of rolling bearing under multiple working conditions," *International Journal of Production Research*, vol. 59, pp. 1–15, 2021.

[16] J. Singh, M. Azamfar, A. Ainapure, and J. Lee, "Deep learning-based cross-domain adaptation for gearbox fault diagnosis under variable speed conditions," *Measurement Science and Technology*, vol. 31, no. 5, article 055601, 2020.

[17] L. Xueyi, L. Jialin, Q. Yongzhi, and H. David, "Semi-supervised gear fault diagnosis using raw vibration signal based on deep learning," *Chinese Journal of Aeronautics*, vol. 33, no. 2, pp. 418–426, 2020.

[18] Z. He, H. Shao, Z. Ding, H. Jiang, and J. Cheng, "Modified deep autoencoder driven by multisource parameters for fault transfer prognosis of aeroengine," *IEEE Transactions on Industrial Electronics*, vol. 69, no. 1, pp. 845–855, 2022.

[19] X. Li, J. Cheng, H. Shao, K. Liu, and B. Cai, "A fusion CWSMM-based framework for rotating machinery fault diagnosis under strong interference and imbalanced Case," *IEEE Transactions on Industrial Informatics*, p. 1, 2021.

[20] W. Tichun, W. Jiayun, W. Yong, and X. Sheng, "A fault diagnosis model based on weighted extension neural network for turbo- generator sets on small samples with noise," *Chinese Journal of Aeronautics*, vol. 33, no. 10, pp. 2757–2769, 2020.

[21] Z. He, H. Shao, P. Wang, J. J. Lin, J. Cheng, and Y. Yang, "Deep transfer multi-wavelet auto-encoder for intelligent fault diagnosis of gearbox with few target training samples," *Knowledge-Based Systems*, vol. 191, article 105313, 2020.

[22] W. Zhang, X. Li, X.-D. Jia, H. Ma, Z. Luo, and X. Li, "Machinery fault diagnosis with imbalanced data using deep generative adversarial networks," *Measurement*, vol. 152, article ???, 2020.

[23] D. Xiao, Y. Huang, C. Qin, Z. Liu, Y. Li, and C. Liu, "Transfer learning with convolutional neural networks for small sample size problem in machinery fault diagnosis," *Proceedings of the Institution of Mechanical Engineers, Part C: Journal of Mechanical Engineering Science*, vol. 233, no. 14, pp. 5131–5143, 2019.

[24] Z. Meng, X. Guo, Z. Pan, D. Sun, and S. Liu, "Data segmentation and augmentation methods based on raw data using deep neural networks approach for rotating machinery fault diagnosis," *IEEE Access*, vol. 7, pp. 79510–79522, 2019.

[25] Q. Li, L. Chen, C. Shen, B. Yang, and Z. Zhu, "Enhanced generative adversarial networks for fault diagnosis of rotating machinery with imbalanced data," *Measurement Science and Technology*, vol. 30, no. 11, article 115005, 2019.

[26] Y. Zhang, X. Li, L. Gao, L. Wang, and L. Wen, "Imbalanced data fault diagnosis of rotating machinery using synthetic oversampling and feature learning," *Journal of Manufacturing Systems*, vol. 48, pp. 34–50, 2018.

[27] E. Fan, "Extended tanh-function method and its applications to nonlinear equations," *Physics Letters A*, vol. 277, no. 4-5, pp. 212–218, 2000.

[28] X. Wang, Y. Qin, Y. Wang, S. Xiang, and H. Chen, "ReLTanh: an activation function with vanishing gradient resistance for SAE- based DNNs and its application to rotating machinery fault diagnosis," *Neurocomputing*, vol. 363, pp. 88–98, 2019.

[29] D.-A. Clevert, T. Unterthiner, and S. Hochreiter, "Fast and accurate deep network learning by exponential linear units (elus)," https://arxiv.org/abs/1511.07289, 2015.

Research Article

Multilayer Extreme Learning Convolutional Feature Neural Network Model for the Weak Feature Classification and Status Identification of Planetary Bearing

Rui Yang [ID], Zenghui An, and Shijun Song

School of Mechanical and Electronic Engineering, Shandong Jianzhu University, Jinan 250101, China

Correspondence should be addressed to Rui Yang; woyangr@126.com

A convolutional neural network has the characteristics of sharing information between layers, which can realize high-dimensional data processing. In general, the convolutional neural network uses a feedback mechanism to realize parameter self-regulation, which solves the disadvantages of manual parameter adjustment. However, it is unable to determine the iteration number with the best calculation accuracy. Calculation efficiency cannot be guaranteed while achieving the best accuracy. In this paper, a multilayer extreme learning convolutional neural network model is proposed for feature recognition and classification. Firstly, two-dimensional spatial characteristics of planetary bearing status data were enhanced. Then, extreme learning machine is embedded in a convolution layer to solve convex optimization problems. Finally, the parameters obtained from the training model were nested into a network to initialize the model parameters to separate each status feature. Planetary bearing experimental cases show the effectiveness and superiority of the proposed model in the recognition and classification of weak signals.

1. Introduction

With the improvement of automation level in a modern production system, rotating machinery presents the development direction of high speed, high efficiency, and maximum economic benefit. However, a continuous production process makes the equipment run under heavy load for a long time, which will easily lead to accelerated fatigue of transmission parts. Furthermore, tight connections between devices make the health status of an individual component affect the efficiency and quality of the entire system. Once the transmission parts fail, it will lead to a series of chain reactions and even make the whole equipment or even the whole production line stop working. Therefore, reliable monitoring of transmission parts is crucial to maintain the whole safety production process.

In recent years, a planetary gearbox with dual rotor bearings has become the main transmission component due to its series of advantages with compact structure, large transmission ratio, light weight, and strong bearing capacity. It

is widely used in automotive, wind power, aerospace, and other fields. Because the equipment works in complex environment for a long time, it is easy to cause accelerated fatigue of transmission parts [1]. For example, wind energy as green energy has promoted wind power generation to become one of the fastest growing branches of the current power generation field. Typically, a wind turbine consists of a planetary gear train (I level transmission) and two fixed-shaft gear trains (II level and III level transmission), as shown in Figure 1. Planetary gear trains are usually mounted at the low-speed end to withstand greater torque. In addition, wind turbines are usually located in a relatively wide-open area or offshore areas and often affected by irregular variable speed winds and the external ambient temperature that change with the season. Due to the complex working environment, the key components (gears and bearing) of the planetary gearbox are easily damaged. For example, the G52-850 wind turbine, consisting of Gamesa and Echesa speed-increasing gearboxes and INDER generators, showed abnormalities after 5-year work. Through
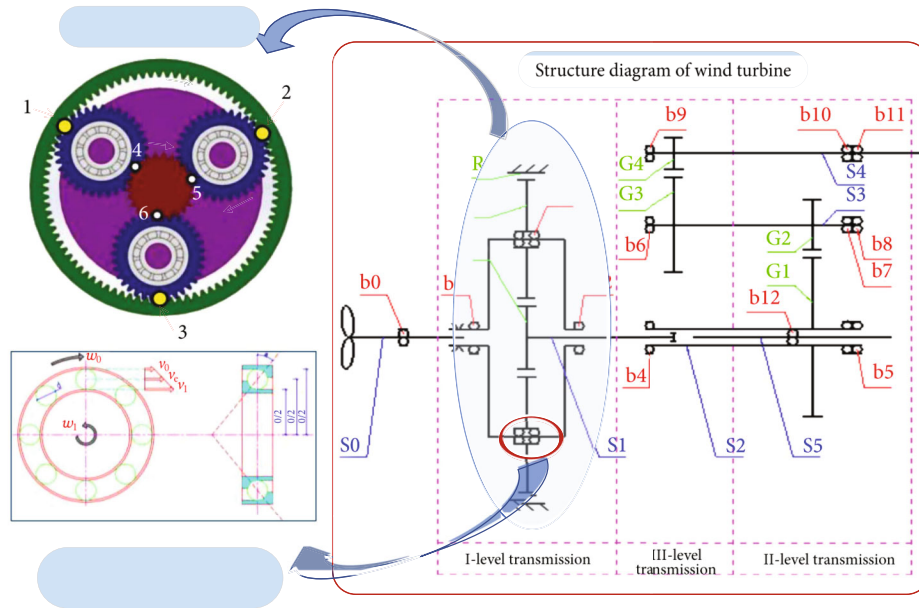
FIGURE 1: Layout of wind turbine transmission components and schematic diagram of planetary bearings.

endoscopic and unpacking tests, it was found that the fault was caused by planetary bearings [2]. It is the key to maintain the whole safety production process to adopt a reliable monitoring method to monitor the equipment condition. Therefore, the working efficiency and safety of a wind power generation system can be greatly improved when the planetary bearing is operated in stable status.

From the evolution process of bearing failure (Figure 2), it can be seen that the initial stage of failure accounts for a larger proportion of the entire damage. As the fault continues to deteriorate, the degradation rate increases exponentially. In the early stage of failure, the abnormal symptoms are slight, the impact on the mechanical system is small, and the maintenance cost is relatively low. If fault goes undiagnosed or unnoticed at an early stage, it will lead to a catastrophic accident when early fault develops and accumulates to a certain extent. Therefore, early detection, early diagnosis, and early maintenance are essential to ensure the safe operation of high-precision equipment. In addition, under the demand of intelligent devices, the amount of data that needs to be analyzed is also large. Traditional fault diagnosis based on point-by-point single-signal analysis is difficult to detect the characteristic components related to fault quickly and accurately, which seriously hinders the development process of high precision, high speed, and high reliability of high-end equipment, whereas intelligent fault diagnosis based on "data-driven" can solve this problem with high precision, high speed, and high reliability [3].

In 2006, the birth of the deep learning algorithm [4, 5] marks the development of fault diagnosis towards rapidity, efficiency, and intelligence. High target feature resolution of a data set will get accurate fault diagnosis results, and complete data volume can improve model learning ability. These existing data-driven neural network models have achieved good results in some ideal environments. However, there are still some factors restricting their application in the

field of fault diagnosis. However, due to the randomness and uniqueness of faults, the field of intelligent diagnosis faces some bottlenecks. Rotating machinery is in a healthy status for a long time, and most of the collected signals are in a healthy status. Due to the high cost of collecting measured fault samples, it is difficult to obtain all types of fault samples, which makes the sample set unbalanced. Besides, in case of early fault or large external interference, the fault characteristic information is weak or even submerged. The model may give interference information a high confidence output. Aiming at the incomplete characteristics of the fault data set, Gao et al. and Liu et al. are committed to using finite element method simulation to simulate a sample with different fault statuses [6, 7]. An et al. [8] proposed a self-learning transferable neural network for fault intelligence diagnosis with unlabeled and imbalanced data. Most of the weak fault intelligent diagnosis methods [9, 10] use traditional fault feature extraction as the preprocessing to extract sensitive information, and there is a lack of research on improving the robustness of the model itself.

A convolutional neural network (CNN) [11, 12] is one of the representative models for intelligent recognition and classification of weak fault signals of bearings. It has attracted the attention of many researchers and been widely used in many fields such as bearing fault diagnosis. Fu et al. [13] used 1D convolution kernels of different scales to extract multiscale features and performed dimensional assimilation on feature space of different scales based on fusion theory to adapt to convolution operation. Zhao et al. [14] converted one-dimensional time-domain signal into 2D grayscale images, which were used as the analysis sample data of the CNN model. This solved the problem of insufficient data and avoided the process of artificial feature extraction. Cyclic spectral coherence was adopted as preprocessing to extract information that best characterized the status of bearing [15]. Then, group normalization
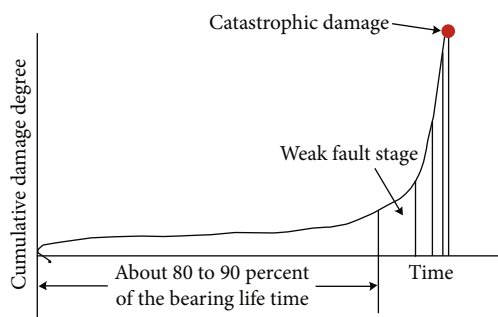
Figure 2: Failure development trend chart.

calculation was introduced to balance the distribution difference of data. Ye et al. [16] proposed a new method called deep morphological convolutional network, which consists of two parallel branches: noise filtering and feature selection algorithm. Noise filtering can update structure elements based on backpropagation. A feature selection algorithm was based on kurtosis weight fusion. Besides, values of various hyperparameters directly affect the training speed and accuracy of the CNN model. Currently, an error backpropagation (EBP) mechanism was often used to modify the model parameters. In the process of parameter adjustment, the initialization values of some parameters may also affect the classification results of the model. In addition, the range of adjustable parameters involved in the algorithm directly affects the computational complexity. Therefore, the CNN model is not suitable for rapid online monitoring, especially for early diagnosis of weak faults. An effective model is urgently needed to improve the performance of online monitoring.

In order to build a model framework with superior performance, the extreme learning machine (ELM) principle is adopted to deal with the convex optimization problem of a convolution layer. ELM was firstly proposed by Huang et al. [17] for a feedforward single-layer neural network. Subsequently, ELM was gradually introduced into the multilayer model structure [18, 19]. Compared with other models such as Deep Belief Network (DBN) [20, 21] and Stacked Autoencoder (SAE) [22], the ELM model involves fewer parameters and has higher computational efficiency and less complexity. Therefore, ELM has been favored by researchers in many fields, such as image processing [23], objective optimization [24, 25], dimensionality reduction [26], and fault diagnosis [27–29].

ELM was combined with other models to improve the training efficiency and recognition accuracy. For example, ELM was combined with an autoencoder to mine deep features of training data and proved to be superior to ELM, SAE, and CNN [30]. Online sequential ELM was proposed to classify and recognize the low-dimensional features extracted from the SAE model, whose effectiveness of this method has been proven for tool wear status recognition [31]. ELM was used as an enhanced classifier to improve the recognition accuracy of an integrating CNN model. Its superiority in training speed and accuracy was verified by comparing with other 6 models [32].

In general, ELM plays a role of an efficient classifier in the hybrid model. The existing model framework based on multilayer perceptron has shortcomings in improving the training speed. The goal of this paper presented here is to find a training model mechanism to improve the training accuracy and speed. Based on this, a fast and effective embedded hybrid model structure, called multilayer extreme learning convolutional feature neural network model (M_ELMConvNet), was proposed. The main contributions here are twofold.

(1) The wavelet cyclic spectrum feature extraction method [33] was used to convert the time-domain signal into a two-dimensional image. Then, the obtained image is partitioned, which is more suitable for CNN analysis

(2) A new model training mechanism of embedding ELM into a convolutional layer was proposed to improve the calculation speed and classification accuracy. The final classification and recognition results are obtained by multilayer stacking structure. The computational speed and accuracy of the proposed algorithm are verified by comparing with the results of other models

The remainder of this paper is structured as follows: the relevant theoretical research background contents, such as CNN and ELM models, are shown in Section 2. The proposed model framework and implementation process are introduced in Section 3. The proposed method is applied to the experimental data in Section 4. Finally, conclusions and the next step are described in Section 5.

2. Theoretical Background

2.1. CNN. CNN is a self-learning model that can automatically extract the internal feature information of the input data and implement classification tasks. Different from traditional neural networks, CNN generally contains a convolution layer and a subsampling layer (also called pooling layer). CNN learns hidden features by continuously running the convolutional layer in a loop and performing pooling operations. The convolution layer is used to convolute the original input data with multiple local filters to generate locally invariant feature information, which is used as the input of the pooling layer to extract representative features. The procedure is shown in Figure 3.

Suppose the size of the input layer is Height × Width = $a \times b$, and the number of input layers is c which is the number of channels. Define a convolution kernel as K, whose size is $n \times n$. The entire operation process of the convolution layer is to continuously perform convolution operations on the input layer data and the convolution kernel. The features extracted by the convolutional layer are served as the input of the pooling layer to further reduce the dimension of the feature matrix by calculating the local average or maximum. Subsequently, the fully connection layer tiles the output matrix of the pooling layer. The main task of each layer before the fully connected layer is feature extraction. The
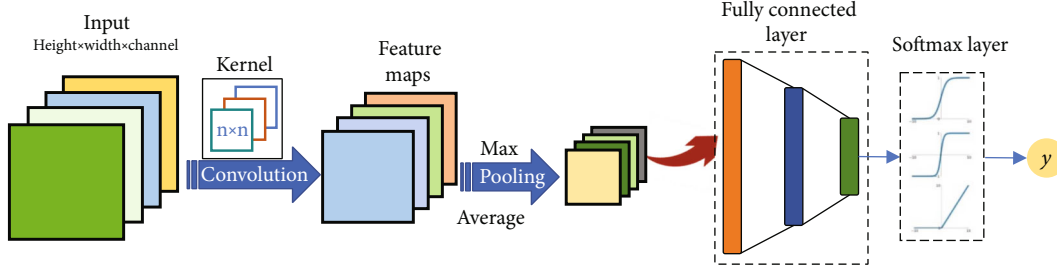
FIGURE 3: CNN model frame diagram.

classification task starts at the fully connection layer. Generally, there are multiple full connection layers in the whole network structure. Because the single-layer structure can only solve the linear classification problem and most of the problems in real life are nonlinear problems, the softmax layer is also connected behind the full connection layer to further predict the label. By calculating the probability of each sample's category, the label category with the largest probability value is assigned to the sample data.

2.2. ELM. ELM uses randomness and Moore-Penrose generalized inverse theory to calculate parameters, which avoids the use of EBP and greatly improves the training speed. The input layer data is usually nonlinear and separable. The core idea of the ELM algorithm is to map the original data into a high-dimensional feature space by adding hidden layer nodes on the premise that the input data is linearly separable. The connection weights between the input layer and the hidden layer are randomly generated. The connection matrix between the hidden layer and the output layer is calculated by Moore-Penrose generalized inverse. The entire training process only needs to adjust the number of hidden layer nodes. The schematic diagram is shown in Figure 4.

3. Proposed Architecture and Method

3.1. Formulated General Model Framework. Suppose there is a set of bearing status data to be classified. The data set are $D_x = \{x_1, \cdots, x_N\}, x_j \in R^{1 \times n \times c}$, and the target matrix is $D_Y = \{Y_1, \cdots, Y_N\}, Y_j \in R^C$, where n and c are the length and the number of channels of the input data, respectively. N is the number of samples in the data set. C is the number of target category to which the input data belongs. The relationship between the sample set and the label matrix can be achieved by the classification function, as shown in the following formula:

$$D_Y = f_c(D_x), \tag{1}$$

where f_c is the classification function of D_x.

3.2. Data Graphical Processing and Enhancement. In order to improve the accuracy of model recognition, the two-dimensional CNN model was used for data processing. The original sample data is one-dimensional, which reflects the time-domain waveform information and often overwhelms some fault active components. In this paper, one-

dimensional time-domain data are converted into 2D images based on wavelet cyclic spectrum theory [33] and the periodic characteristics of nonstationary bearing information are extracted. The local information in cycle spectrum of each fault type is similar. In order to make up for the shortage of faulty data samples and improve the quality of sample data, the converted image is further processed by block localization. Suppose that $W_s = \{S_1, \cdots, S_N\}, S_j \in R^{w \times h \times c}$ is the 2D cyclic spectrum sample matrix, w and h are the width and height of each single image sample matrix, respectively, and the label matrix is $W_L = \{L_1, \cdots, L_N\}, L_j \in R^L$. For the sample W_s, we regard it as being composed of several submodules W_P. $P_s = \{S_1^P, \cdots, S_N^P\} \subseteq W_P$, and corresponding labels $P_L = \{L_1^P, \cdots, L_N^P\}$.

$$P_L = f_p(P_I), \tag{2}$$

$$W_L = f_q\left(f_p \otimes W_P\right), \tag{3}$$

where $\otimes$ is the tensor product and f_p and f_q are the classification functions for P_I and W_s, respectively.

3.3. Parameter Transfer

3.3.1. Convolution Layer Detector Based on ELM. The ELM algorithm is integrated into the model to further improve the classification characteristics of the algorithm. As mentioned above, ELM is superior in complexity and accuracy compared with other algorithms [34]. The weight matrix of the input layer is randomized; that is, the weight matrix of the input layer and the input data are independent of each other. We can set it arbitrarily according to some distribution theories. The output matrix of the hidden layer and the weight matrix between the hidden layer and output layer need to be calculated relying on label data.

The specific implementation process is as follows:

Assuming there are N test samples (X_j, L_j), $X_j = \{x_{j,1}, x_{j,2}, x_{j,3}, \cdots x_{j,n}\}^T$ and corresponding labels are $L_j = \{l_{j,1}, l_{j,2}, l_{j,3}, \cdots l_{j,n}\}^T$. N_H is the number of hidden layer nodes. Hidden layer output can be expressed as

$$H_o = W_i \bullet X_j + b_i, \tag{4}$$

where $W_i = \{w_{i,1}, w_{i,2} \cdots w_{i,n}\}$ is the connection matrix between the input layer and hidden layer and b_i is the offset

(a) ELM network structure diagram and its parameterized model

(b) Spatial model diagram of ELM. The nonlinear characteristics of the input data are fitted by multiple mappings
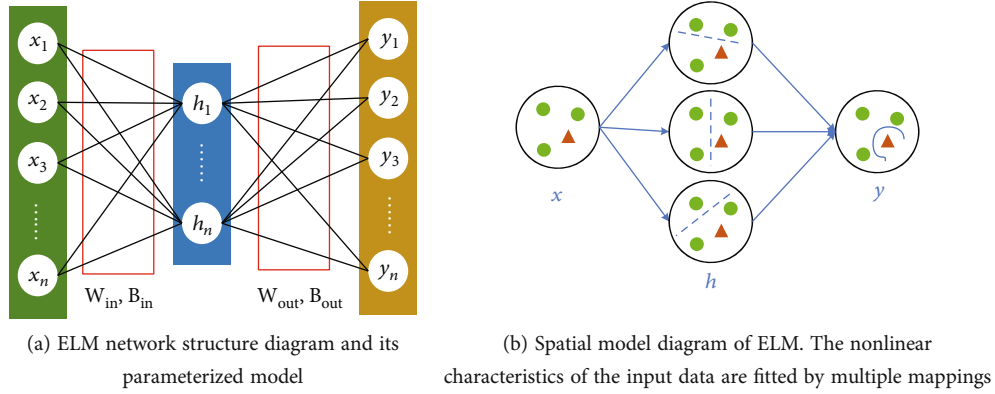
FIGURE 4: Schematic diagram of ELM structure and principle.

vector. Both of them are randomly generated. The output layer matrix can be expressed as

$$O_j = \begin{bmatrix} f(W_1 \bullet X_1 + b_1) & \cdots & f(W_{N_H} \bullet X_1 + b_{N_H}) \\ \vdots & & \\ f(W_1 \bullet X_n + b_1) & \cdots & f(W_{N_H} \bullet X_n + b_{N_H}) \end{bmatrix} \begin{bmatrix} \beta_1 \\ \beta_2 \\ \vdots \\ \beta_{N_H} \end{bmatrix} = f(H_o)\beta_i,$$

$$f(H_o) = \begin{bmatrix} \sigma_{\mathrm{sig}}(W_1 \bullet X_1 + b_1) & \cdots & \sigma_{\mathrm{sig}}(W_{N_H} \bullet X_1 + b_{N_H}) \\ \vdots & & \\ \sigma_{\mathrm{sig}}(W_1 \bullet X_n + b_1) & \cdots & \sigma_{\mathrm{sig}}(W_{N_H} \bullet X_n + b_{N_H}) \end{bmatrix}. \quad (5)$$

$O_j = \{o_1, o_2, \cdots o_n\}$ indicate the categories of the output target label. β_i is the layer connection weight (LW) between the hidden layer and output layer. β_i is unknown and must be calculated based on the label data in the process of prediction classification results of the ELM algorithm. The expression is

$$\beta = H_o^{-1}L. \quad (6)$$

In the training stage, the number of hidden layer nodes is an uncertain factor, which has an impact on the prediction performance. In order to evaluate the performance of the parameters calculated by the model, the error minimization loss function was used as an evaluation index of prediction ability, shown as

$$E = \min \sum_{j=1}^{N} \|O_j - L_j\|, \quad j = 1, 2, 3 \cdots N. \quad (7)$$

The parameters corresponding to the minimum E value are the optimal values that best characterize the target features. Finding the minimum number of hidden layers while ensuring the highest accuracy is another factor to improve operation efficiency.

3.3.2. Pooling Layer. The pooling layer is actually a down-sampling layer, which is mainly used to extract local features and prevent overfitting. The procedure is as follows: first, define the size and step of the local pool module. Then, the local feature extraction method is determined. The most common method is to calculate the average or maximum value of each module. In this paper, the pooling layer is followed by the random parametric dimension reduction layer, as shown in equation (4). The pooling process adopts the method of calculating the average value as shown in

$$A(u_1, u_2) = \sum_{u_1=1}^{N_H} \sum_{u_2=1}^{N_H} \frac{1}{r \times r} \sum_{i=1}^{r} \sum_{j=1}^{r} O(i + (u_1 - 1) \times r, j + (u_2 - 1) \times r), \quad (8)$$

where r is the size of each step.

3.3.3. Normalization. After the pooling layer and before the ELM classification layer, a min-max standardization process was added to prevent the occurrence of gradient disappearance. The normalization result is obtained by

$$S_x = \frac{A_x - \min(A_x)}{\max(A_x) - \min(A_x)} \times (N_{\max} - N_{\min}) + N_{\min}, \quad (9)$$

where min and max are operators for calculating the maximum and minimum elements in the matrix A_x, respectively. $N_{\max}$ and $N_{\min}$ are the range of the interval for normalizing the matrix.

3.4. Test Model. Intelligent diagnosis methods based on deep learning theory mostly rely on a large amount of training data to achieve classification and recognition. The premise is that the performance of connection weights must be evaluated and modified on the basis of data with accurate label. In this paper, a method based on parameter transfer theory is proposed. The existing labeled data is input into the supervised model for training, and the connection weights of each module are obtained. Afterward, interlayer connection matrices are input into the test model to recognize and classify the unlabeled data.
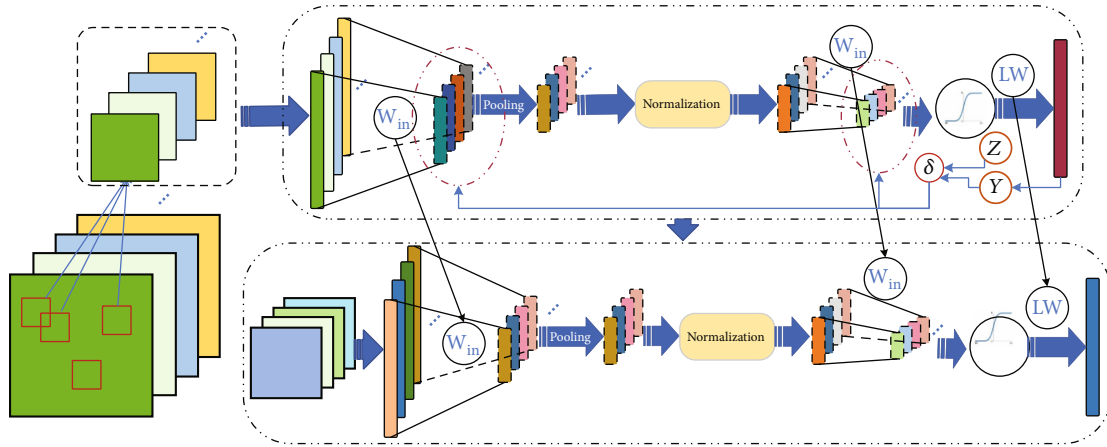
FIGURE 5: Framework of the proposed algorithm.

3.5. Fault Diagnosis Method Based on M_ELMConvNet. This paper presents a fast feature learning method based on two-dimensional CNN and ELM, and the model frame is shown in Figure 5.

Figure 6 shows the flowchart of the present method, and the procedures are as follows:

Firstly, samples were collected and processed with 2D data transformation and enhancement.

(1) The acceleration signals of bearings in four different working conditions were collected. About 85% of the data were labeled as training samples. The rest of the data is unmarked and is considered the test sample

(2) The original data is transformed into a 2D image by wavelet cyclic spectrum analysis

(3) Subsequently, the obtained image is partitioned to enhance the data according to equation (3)

Secondly, an efficient and accuracy neural network classification model is constructed.

(1) The entire model framework consists of two parts. One is the training process for labeled data, and the other is the predictive classification process for unlabeled data

(2) The labeled data is input into the supervised training model. The first step of this model is to reduce the dimension of the data by randomizing the connection matrix. The specific implementation process was based on the ELM training principle, as shown in equation (4). Then, the dimensionless data is entered into the pooling layer and standardized. Finally, the data is input to ELM for supervisory testing. The error rate between the test data and the label data is used as the loss function to adjust the random parameterized dimensionality reduction and the number of ELM hidden nodes. Subsequently, the optimal node number was assigned to the model to predict the connection matrix between each layer

(3) In the prediction process of the test sample set, based on the idea of parameter transfer, the connection matrix $W_{1\text{in}}$, $W_{2\text{in}}$ and layer connection weight LW obtained by the supervised test process were input into the test model of the corresponding prediction sample as the preset model parameter values, and the final prediction results were obtained

Thirdly, the whole training process is applied to the recognition and classification of bearing status data.

4. Experimental Validation

The data for verifying the effectiveness of the proposed algorithm were obtained from the comprehensive test bench for power transmission fault diagnosis. The sample data analyzed were measured under different conditions at different times.

4.1. Experiment Setup and Data Description. The power transmission system of the testbed consists of a planetary gearbox, a parallel shaft gearbox supported by rolling bearings or sleeve bearings, bearing load, and programmable magnetic brake, as shown in Figure 7. The testbed includes all the necessary powertrain configurations for studying gearbox dynamics and noise characteristics, health monitoring techniques based on vibration signal analysis, lubrication conditions, and wear particle analysis. The testbed has stable performance and can withstand strong load impact. There is enough space for the replacement and installation of gears and the installation of a monitoring device. Planetary gear systems, sun gears, planetary gears and gear rings, brackets, and bearings are easy to be disassembled.

The vibration signals under four statuses: no damage, first-stage planetary bearing outer ring failure, first-stage planetary bearing inner ring failure, and first-stage planetary bearing ball failure, were collected for analysis. In the experiment, the relevant parameters are set as follows: sampling frequency is 15360 Hz and motor speed is 2100 r/min. Multiple acceleration signals under different working conditions were collected. The data collected under each health condition were separated into 470 equal parts. Randomly select
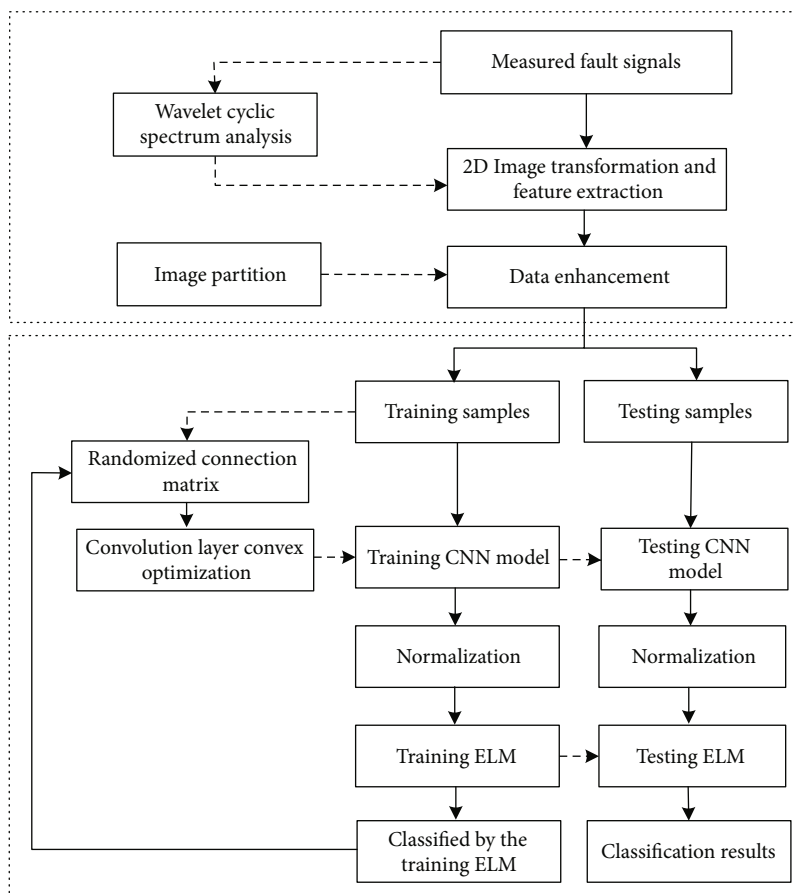
FIGURE 6: The flowchart of the proposed fault diagnosis method.

FIGURE 7: Comprehensive test bench for power transmission fault diagnosis.

TABLE 1: Description of status data sample set.

Planetary bearing damage statuses	No damage	Inner-race fault	Outer-race fault	Ball fault
Number of training samples	400	400	400	400
Number of test samples	70	70	70	70
Label	1	2	3	4

400 pieces of data in these four statuses as the training data set and 70 pieces as the test data set, respectively. A detailed partition of the sample set for status data analysis is shown in Table 1. The time waveforms for 2.5 s and the spectrum with bandwidth [0 Hz 2500 Hz] of the vibration signal for four statuses are shown in Figure 8. It can be seen from Figure 8 that the time-domain waveforms and spectrums for different four-status signals are inevitably affected by external interference information, which is also one of the factors that reduce the ability of model recognition.

4.2. Result Analysis. The purpose of this paper is to propose a fast and effective intelligent classification method for weak fault data of planetary bearings. In order to further verify the effectiveness of the proposed M_ELMConvNet neural network model, the experimental data were analyzed by the algorithm described in Section 3.5. For comparison, three other models including ELM, BP-based CNN, and Deep Autoencoder (DAE) were also applied to status identification of experimental data.

The average recognition accuracy of the algorithm under different hidden layer nodes is calculated by executing the model for 20 times. The results are shown in the box diagram in Figure 9. As shown in Figure 9, the prediction accuracy rate of most testing results was above 98%. The validity of M_ELMConvNet in planetary bearing status recognition is further verified. With the increase in the number of hidden layer nodes, the recognition accuracy rate fluctuates slightly. When the number of hidden layer nodes is set to 290, the average prediction accuracy is relatively high and

(a)

(b)

(c)

(d)

(e)

(f)

(g)

(h)
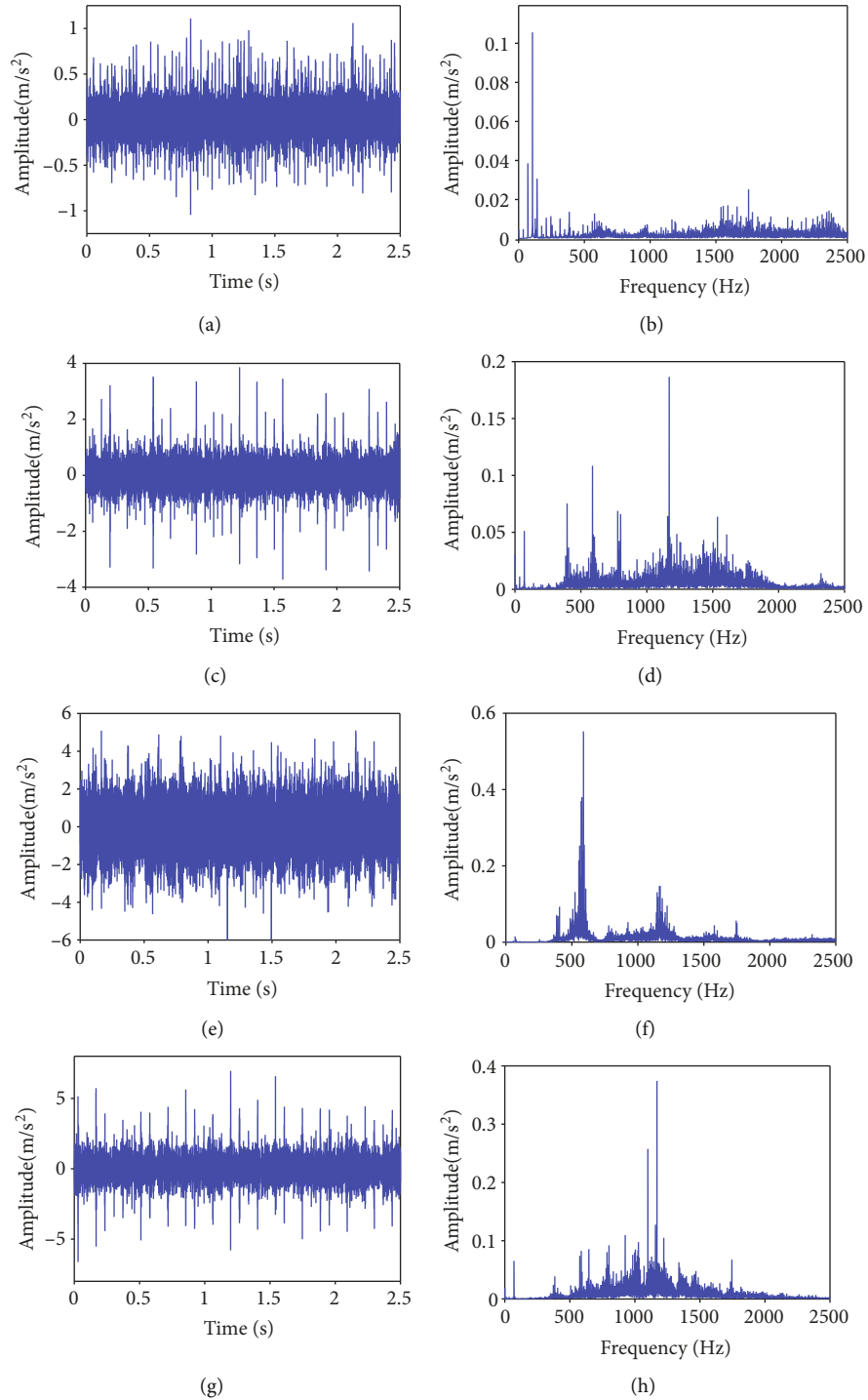
FIGURE 8: Signal waveforms listed in Table 1: (a) no-damage bearing signal in the time domain; (b) the spectrum of no-damage bearing signal; (c) inner-race fault bearing signal in the time domain; (d) the spectrum of inner-race fault bearing signal; (e) outer-race fault bearing signal in the time domain; (f) the spectrum of outer-race fault bearing signal; (g) ball fault bearing signal in the time domain; (h) the spectrum of ball fault bearing signal.

the stability is strong. Meantime, the model training time also showed an exponential growth trend, as shown in Figure 10. In the subsequent analysis, the number of hidden layer nodes was set to 290 based on the balance training time and prediction accuracy.

Figure 11 is the confusion matrix of multistatus classification and recognition accuracy based on the proposed method. As can be seen from Figure 11, the highest prediction accuracy is 100% for status 4. The minimum recognition accuracy is status 3 because there is no obvious
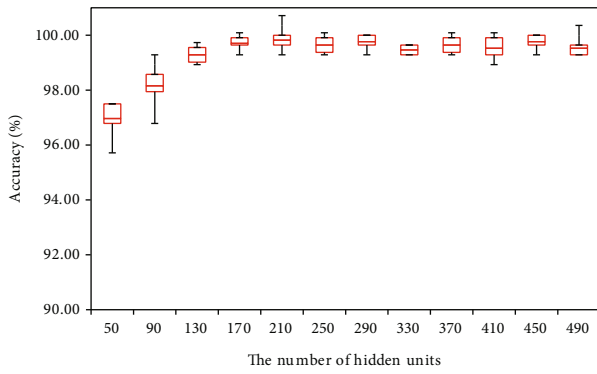
FIGURE 9: Boxplot of prediction accuracies with different numbers of hidden units.
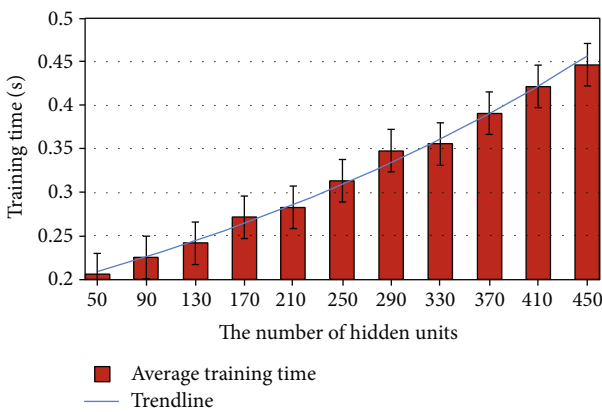
FIGURE 10: Training time of M_ELMConvNet with different numbers of hidden units.

FIGURE 11: Confusion matrix of multistatus classification and recognition accuracy based on M_ELMConvNet.

distinction between status 2 and status 3. In general, the proposed method in this paper can achieve high predictive recognition accuracy in each status.

4.3. Comparative Verification. The diagnosis performances of the original data and multiparameters DAE and CNN
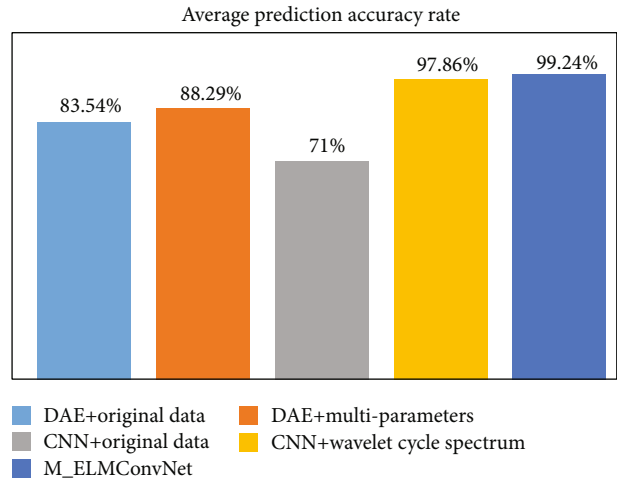
FIGURE 12: Evaluate classifiers' performance by comparison.
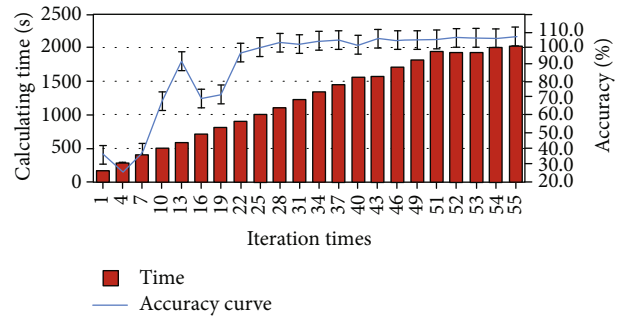
FIGURE 13: The result of different iteration times of the CNN model based on BP for planetary bearing status recognition.

with the original data and wavelet cycle spectrum were also compared with the M_ELMConvNet proposed in this paper. Each model was executed multiple times, and the average result was calculated. Figure 12 shows that the M_ELM-ConvNet achieved the highest average prediction accuracy of 99.24%. Thus, the proposed algorithm in this paper has strong noise suppression capability in the identification and classification of weak fault statuses.

In order to further verify the superiority of the proposed algorithm in computing time, the CNN model based on EBP was used as a comparison model to analyze the same sample data set with M_ELMConvNet. The results are shown in Figures 10 and 13. As can be seen from the figure, the calculation time of the algorithm increases linearly with the increase in the number of hidden units and the number of iterations. At the same time, the recognition accuracy of the algorithm gradually improves and tends to be stable. Considering the influence of the number of hidden units and the number of iterations on the recognition accuracy, the calculation time of 410 hidden units and 28 iterations was compared. One was 0.43 s, and the other was about 2000 s. The time difference is several orders of magnitude, which proved the superiority of the M_ELMConvNet algorithm in computational efficiency.

5. Conclusions and Further Works

In this paper, a new deep feature extraction and diagnosis method was proposed to improve the recognition accuracy and reduce computational complexity for weak failure signal of planetary bearing with large data volume. In M_ELM-ConvNet, ELM was embedded in the CNN model instead of convolution operation to avoid a repeated EBP operation process. After two processes of ELM feature dimensionality reduction and extraction, the amount of calculation was reduced and the prediction accuracy was improved. In addition, based on the parameter transfer theory, the model parameters extracted from the labeled training sample data are introduced into the unlabeled sample data training model to achieve prediction. The effectiveness and superiority are proven on experiment setup testing data. Moreover, analysis results show that the proposed model has advantages in recognition accuracy and operation speed compared with other methods.

The present work is mainly carried out in the case of sufficient sample data. However, in the actual operation of planetary bearings, the sample size of analysis data is unbalanced; that is, the trouble-free sample size is large, while the failure sample size is small. For failure data, such as in the early stage or in the case of large external noise, manual marking often leads to missed diagnosis or misdiagnosis. How to realize the self-supervised learning of unlabeled data and make it able to automatically extract data features and perform labeling is the work to be done in the future.

Data Availability

The data used to support the findings of this study are available from the corresponding author upon request.

Conflicts of Interest

The authors declare that they have no conflicts of interest.

References

[1] C. T. Yiakopoulos, K. C. Gryllias, and I. A. Antoniadis, "Rolling element bearing fault detection in industrial environments based on a K-means clustering approach," *Expert Systems with Applications*, vol. 38, no. 3, pp. 2888–2911, 2011.

[2] J. Xu, J. Zhang, T. Chen, and R. H. Liu, "A planet bearing fault case of wind turbine gearbox," *Advanced Materials Research*, vol. 953-954, pp. 472–477, 2014.

[3] D. Zhao, S. Liu, D. Gu et al., "Enhanced data-driven fault diagnosis for machines with small and unbalanced data based on variational auto-encoder," *Measurement Science and Technology*, vol. 31, no. 3, article 035004, 2020.

[4] F. Jia, Y. Lei, J. Lin, X. Zhou, and N. Lu, "Deep neural networks: a promising tool for fault characteristic mining and intelligent diagnosis of rotating machinery with massive data," *Mechanical Systems and Signal Processing*, vol. 72-73, pp. 303–315, 2016.

[5] Q. Wang, C. Yang, H. Wan, D. Deng, and A. K. Nandi, "Bearing fault diagnosis based on optimized variational mode decomposition and 1D convolutional neural networks," *Measurement Science and Technology*, vol. 32, no. 10, article 104007, 2021.

[6] Y. Gao, X. Liu, and J. Xiang, "FEM simulation-based generative adversarial networks to detect bearing faults," *IEEE Transactions on Industrial Informatics*, vol. 16, no. 7, pp. 4961–4971, 2020.

[7] X. Y. Liu, H. Z. Huang, and J. W. Xiang, "A personalized diagnosis method to detect faults in gears using numerical simulation and extreme learning machine," *Knowledge-Based Systems*, vol. 195, article 105653, 2020.

[8] Z. H. An, X. X. Jiang, J. Cao, R. Yang, and X. G. Li, "Self-learning transferable neural network for intelligent fault diagnosis of rotating machinery with unlabeled and imbalanced data," *Knowledge-Based Systems*, vol. 230, article 107374, 2021.

[9] M. M.M. Islam and J. Kim, "Automated bearing fault diagnosis scheme using 2D representation of wavelet packet transform and deep convolutional neural network," *Computers in Industry*, vol. 106, pp. 142–153, 2019.

[10] X. L. Pei, X. Zheng, and J. L. Wu, "Intelligent bearing fault diagnosis based on Teager energy operator demodulation and multiscale compressed sensing deep autoencoder," *Measurement*, vol. 179, article 109452, 2021.

[11] D. D. Cheng, L. J. Liu, and Z. Yu, "CNN-based intelligent fault-tolerant control design for turbofan engines with actuator faults," *IEEE Access*, vol. 9, pp. 28122–28139, 2021.

[12] B. Zhao, X. Zhang, Z. Zhan, and Q. Wu, "A robust construction of normalized CNN for online intelligent condition monitoring of rolling bearings considering variable working conditions and sources," *Measurement*, vol. 174, article 108973, 2021.

[13] L. Fu, L. Zhang, and J. Tao, "An improved deep convolutional neural network with multiscale convolution kernels for fault diagnosis of rolling bearing," *Materials Science and Engineering*, vol. 1043, no. 5, article 052021, 2021.

[14] J. Zhao, S. Yang, Q. Li, Y. Liu, X. Gu, and W. Liu, "A new bearing fault diagnosis method based on signal-to-image mapping and convolutional neural network," *Measurement*, vol. 176, article 109088, 2021.

[15] Z. Chen, A. Mauricio, W. Li, and K. Gryllias, "A deep learning method for bearing fault diagnosis based on cyclic spectral coherence and convolutional neural networks," *Mechanical Systems and Signal Processing*, vol. 140, article 106683, 2020.

[16] Z. Ye and J. Yu, "Deep morphological convolutional network for feature learning of vibration signals and its applications to gearbox fault diagnosis," *Mechanical Systems and Signal Processing*, vol. 161, article 107984, 2021.

[17] G. Huang, G. B. Huang, S. Song, and K. You, "Trends in extreme learning machines: a review," *Neural Networks*, vol. 61, pp. 32–48, 2015.

[18] L. Kasun, H. Zhou, G. B. Huang, and M. V. Chi, "Representational learning with ELMs for big data," *IEEE Intelligent Systems*, vol. 6, pp. 31–34, 2013.

[19] J. Tang, C. Deng, and G. Huang, "Extreme learning machine for multilayer perceptron," *IEEE Transactions on Neural Network and Learning System*, vol. 27, no. 4, pp. 809–821, 2016.

[20] Z. Chen and W. Li, "Multisensor feature fusion for bearing fault diagnosis using sparse autoencoder and deep belief network," *IEEE Transactions on Instrumentation and Measurement*, vol. 66, no. 7, pp. 1693–1702, 2017.

[21] H. Shao, H. Jiang, X. Zhang, and M. Niu, "Rolling bearing fault diagnosis using an optimization deep belief network,"

Measurement Science and Technology, vol. 26, no. 11, article 115002, 2015.

[22] C. Che, H. Wang, Q. Fu, and X. Ni, "Intelligent fault prediction of rolling bearing based on gate recurrent unit and hybrid autoencoder," *Proceedings of the Institution of Mechanical Engineers, Part C: Journal of Mechanical Engineering Science*, vol. 235, no. 6, pp. 1106–1114, 2021.

[23] X. Fang, Y. Cai, Z. Cai, X. Jiang, and Z. Chen, "Sparse feature learning of hyperspectral imagery via multiobjective-based extreme learning machine," *Sensors*, vol. 20, no. 5, p. 1262, 2020.

[24] Y. Cai, X. Liu, W. Yu, H. Peng, and Z. Cai, "Extreme learning machine based on evolutionary multi-objective optimization," in *International Conference on Bio-Inspired Computing: Theories and Applications*, pp. 420–435, Springer Singapore, 2017.

[25] Y. Wu, Y. Zhang, X. Liu, Z. Cai, and Y. Cai, "A multiobjective optimization-based sparse extreme learning machine algorithm," *Neurocomputing*, vol. 317, pp. 88–100, 2018.

[26] L. L. C. Kasun, Y. Yang, G. B. Huang, and Z. Zhang, "Dimension reduction with extreme learning machine," *IEEE Transactions on Image Processing*, vol. 25, no. 8, pp. 3906–3918, 2016.

[27] X. B. Wang, X. Zhang, Z. Li, and J. Wu, "Ensemble extreme learning machines for compound-fault diagnosis of rotating machinery," *Knowledge-Based Systems*, vol. 188, article 105012, 2020.

[28] S. Pang, X. Yang, X. Zhang, and Y. Sun, "Fault diagnosis of rotating machinery components with deep ELM ensemble induced by real-valued output-based diversity metric," *Mechanical Systems and Signal Processing*, vol. 159, article 107821, 2021.

[29] G. Du, Q. Xu, and X. Yang, "Fault diagnosis of rotating machinery components using a deep kernel extreme learning machine under different working conditions," *Measurement Science and Technology*, vol. 31, no. 11, article 115901, 2020.

[30] K. Li, M. Xiong, F. Li, L. Su, and J. Wu, "A novel fault diagnosis algorithm for rotating machinery based on a sparsity and neighborhood preserving deep extreme learning machine," *Neurocomputing*, vol. 350, pp. 261–270, 2019.

[31] J. Ou, H. Li, G. Huang, and G. Yang, "Intelligent analysis of tool wear state using stacked denoising autoencoder with online sequential-extreme learning machine," *Measurement*, vol. 167, article 108153, 2021.

[32] Z. Chen, K. Gryllias, and W. Li, "Mechanical fault diagnosis using convolutional neural networks and extreme learning machine," *Mechanical Systems and Signal Processing*, vol. 133, article 106272, 2019.

[33] R. Yang, H. Li, C. Wang, and C. He, "Rolling element bearing weak feature extraction based on improved optimal frequency band determination," *Proceedings of the Institution of Mechanical Engineers, Part C: Journal of Mechanical Engineering Science*, vol. 203-210, pp. 1989–1996, 2018.

[34] L. Zhang, J. Li, and H. Lu, "Saliency detection via extreme learning machine," *Neurocomputing*, vol. 218, pp. 103–112, 2016.

Research Article

Mechanism of Spectral Distortion for Real-Time Crack Propagation on Aluminum Alloy Structure

Bo Jin [ID],[1] Cunbo Lu,[1] Feng Zhang,[1] and Weifang Zhang[2]

[1]*Information Science Academy China Electronics Technology Group Corporation, Building No. 4, 36 Sidaokou North Rd., Haidian Dist., Beijing 100086, China*
[2]*School of Reliability and Systems Engineering, Beihang University, 37 Xueyuan Rd., Haidian Dist., Beijing 100191, China*

Correspondence should be addressed to Bo Jin; 403115059@qq.com

This study investigates four characteristic damage mechanisms of fiber Bragg grating (FBG) sensors, with fatigue crack propagation in aluminum alloy. The multipeak wavelength distinguish algorithm was developed for FBG spectrum quantitative analysis. The results distinguish a subordinate peak skewing significantly, associated with strain patterns along the FBG, corresponding to various crack lengths. For parallel bonded direction grating, the subordinate peak skewing appears at the strain pattern transition region. This is located at the ratio 32%-34% of crack length lying in the crack tip. Meanwhile, the four damage characteristics correspond to subordinate peak skewing. When the strain is distributed along the grating, spectral distortion occurs. In this region, the cubic strain pattern determines the shorter wavelength location of subordinate peaks. This corresponds to the 15%-17% ratio of crack length lying in the grating, causing spectral oscillations.

1. Introduction

Aluminum alloy is extensively employed in aircraft construction, because the constructs will experience structural damage in long-term service. This involves mechanisms such as fatigue, material aging, corrosion, and cracking problems [1]. Furthermore, the structural damage can be identified synchronously in real-time monitoring of aluminum alloy crack propagation [2]. Fiber Bragg grating (FBG) sensors have been acknowledged and used in structural health monitoring (SHM). For example, this is implemented in the concrete structure of bridges, nuclear power stations, and large dams. This is due to the following specific benefits of FBG sensors which include erosion resistance, small size, and multiplexing [3]. It is deliberated to be one of the most hopeful sensors in observing the strain distribution near the crack tip for propagation prediction. However, it is a challenge to utilize the FBG sensors in crack propagation monitoring of aluminum alloy components.

Several researchers have made contributions on interpretations for mechanisms of spectral characteristics,

regarding the various damage pattern identifications of composite materials. Takeda et al. place FBG sensors near the delamination to correlate spectral intensity and spread with crack progression [4]. They observe that the delamination starts at the end of the sensor and grows parallel along the longitudinal axis. The related spectrum shifts and splits into two distinct peaks. Childs et al. [5] relate these two peaks to the strain levels along the grating ahead and behind the delamination. They attempt to correlate the intensity ratio of these peaks to the delamination length. Sante [6] embedded a chirped FBG sensor near the bond line of a GFRP single-lap joint and validated the relationship between the disbanded tip position and the wavelength of the shape change. In addition, Ramly et al. [7] undertook research on the monitoring composite delamination areas. These results describe two peaks at lower and higher wavelengths in the reflection spectra, corresponding to the various forms of strain distribution. This continues with an increment of the delaminated area.

The shapes of the reflected spectra depend on the strain gradients along the axial grating of the FBG sensors
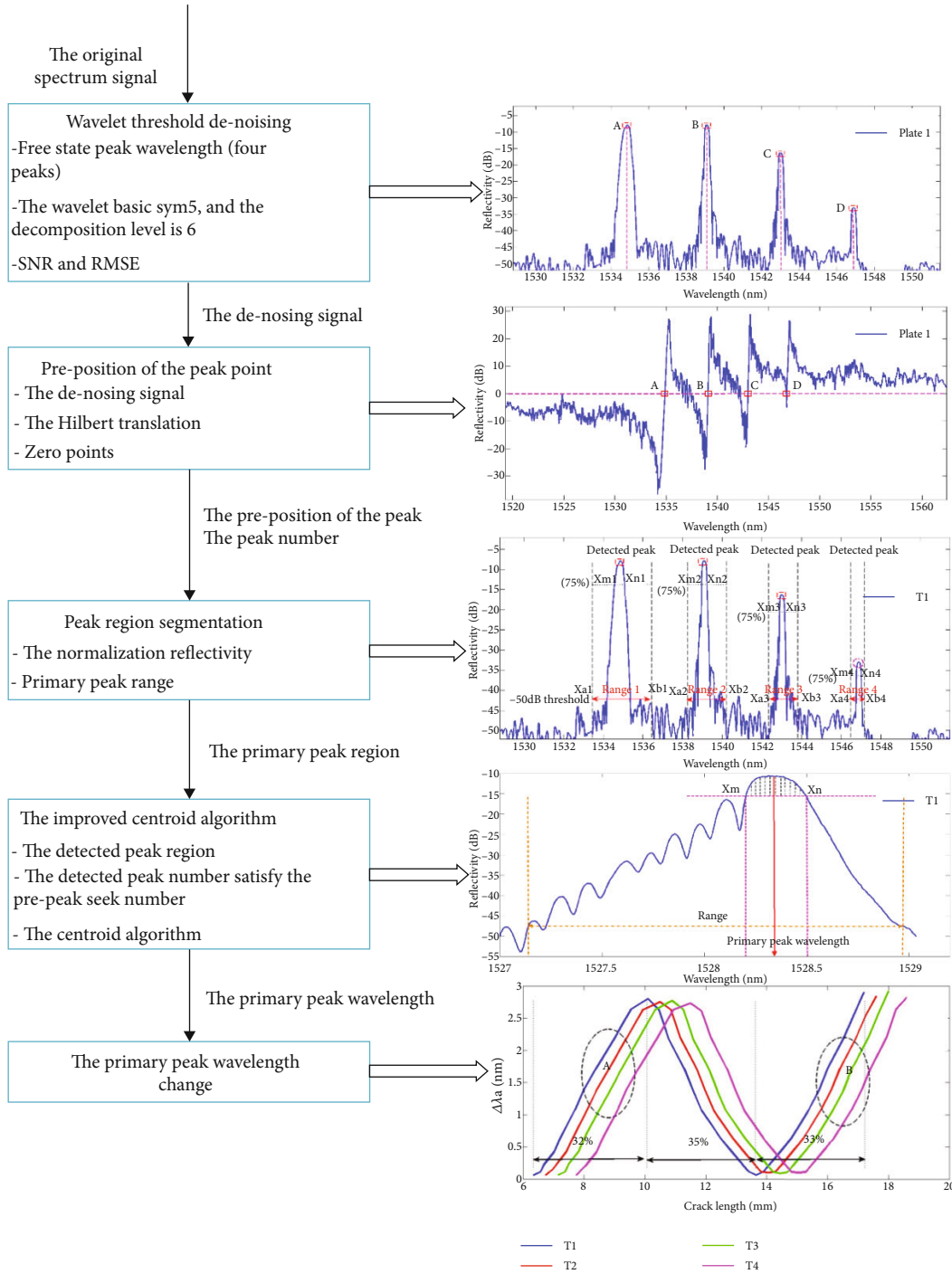
Figure 1: The diagram of the centroid peak shifting detection algorithm.

[8]. Thus, Rajabzadeh et al. [8] assume that the nonuniform strain distribution along the grating may be the main reason for spectrum distortion. In addition, numerical models are constructed to verify Rajabzadeh's statement. However, for real-time applications, the spectral distortion (or the subordinate peak appearance time) cannot be used as the determinate factor for crack length propagation. Our research suggests that the skewing of the subordinate peak corresponds to the crack propagation. In addition, Correia et al. [9] found that the turning of the subordinate peak is correlated with the ratio of effective sensing length to the actual bonded length. Also, the sensing grating regions can be divided into three sections called the effective interaction subregions. To analyze the comprehensive correlation of crack length with FBG spectral behavior, we will investigate four damage characteristics. This involves the primary wavelength variation, the number of subordinate peaks, the spectral bandwidth, and the subordinate wavelength skewing, in correspondence with the crack length.

2. Damage Characteristic Detection Algorithm

With the nonuniform strain sensing, the spectrum became asymmetric, broadened, and distorted; the traditional algorithm for extracting the FBG spectral central peak is difficult to realize the accurate wavelength value. In this paper, a multipeak wavelength distinguish algorithm is introduced.

It is necessary to denoise the spectrum signal, and the variation mode decomposition (VMD) combined with wavelet thresholding is developed. The subordinate wavelength data were extracted under the 3 dB bandwidth region, and the centroid algorithm is defined based on the damage spectrum. The diagram of the centroid peak shifting detection algorithm is shown in Figure 1.

2.1. VMD Wavelet Denoising Pretreatment Algorithm.

Traditionally, the variation mode decomposition (VMD) can sense multiple modes concurrently; under the same frequency [10], Li and Yao [11] introduced the band-limited intrinsic mode function (BLIMF) for signal acquisition. However, the algorithm lacks adaptability due to the fixed energy distribution of signal mode, corresponding to the determined decomposition layers. In this paper, a variation mode decomposition integrated with the wavelet threshold algorithm is produced. And the procedure of VMD wavelet denoising algorithm is as follows:

Step 1. The spectrum signal in the domain is decomposed by the VMD algorithm into band-limited intrinsic mode function (BLIMF) u_k in the frequency domain. And the optimal decomposition layers' number K is set to 6, and the corresponding optimal balance parameter α is set as 200.

Step 2. By soft thresholding the BLIMF value, the wavelet type is set to sym5 and the wavelet layer is set to 6 [12]. The improved soft threshold can be set as

$$\widehat{d_l} = \begin{cases} \text{sign} (d_i) \left(|d_i| - \dfrac{T_i}{\exp \left((|d_i|/T) - 1 \right)^2} \right), & |d_i| \geq T_i, \\ 0, & |d_i| < T_i, \end{cases} \tag{1}$$

where d_i represents the i_{th} improved threshold of the BLIMF. T_i represents each submodule threshold, and the solution formula is described as follows:

$$T = \frac{100\sigma \sqrt{2E_i \lg (N)}}{\lg (j + 1)}. \tag{2}$$

Here, mean square deviation σ is estimated by $\sigma = \text{median}(|c_i|: i = 1, 2 \cdots, N)/0.675$. The i_{th} BLIMF energy E_i is estimated as follows:

$$\widehat{E}_k = \frac{E_1^2}{\beta} \rho^{-k}, \quad k = 2, 3, 4 \cdots . \tag{3}$$

The shifting iteration process parameters β, ρ are set as 0.719 and 2.01 [13], respectively.

Step 2. The multidenoising is applied with various methods, such as the EMD with the detrend fluctuation analysis (EMD-DFA), EMD with the changed thresholding wavelet (EMD-changed wavelet), EMD-wavelet, and VMD-changed wavelet, as shown in Figure 2.

The VMD-changed wavelet method can efficiently preserve the detail signal without affecting the noise signal filtered.

2.2. The Multipeak Wavelength Distinguish Algorithm.

The deformed spectrum was split primarily for multipeak prepositioning, and secondarily the spectrum central wavelength was extracted segmentally. The detailed process is shown in Figure 3.

To extract the zero crossing points of the transformed signal, the denoised signal must be transformed by the Hilbert transform firstly. The Hilbert transform value equals the convolution integral between the signal $x(t)$ and $(\pi t)^{-1}$. The Hilbert transform $x(t)$ was denoted as

$$\widehat{x}(t) = H[x(t)] = x(t) * \frac{1}{\pi t}. \tag{4}$$

The denoising spectrum signal is shown in Figure 4(a), and the processed signal by the Hilbert transform is shown in Figure 4(b). To reduce the error of extracting extreme poles instead of zero crossing points, the peak slope and peak group-threshold method is proposed for the initial estimate of the primary peak area. The subsidiary peak recognition satisfy not only the value of zero crossing points under the Hilbert transform but also the peak threshold sharp increased 1 nm in slop shape, as shown in Figure 4(b). Meanwhile, to improve the accuracy of detection, the 3 dB threshold window function is defined in the preprocessing, as shown in Figure 4(c).

The intensity of $\widehat{x}(\lambda)$ has a sharp slop between the left and right pole points in Figure 4(b). Additionally, the intensity of $x(\lambda)$ in Figure 4(a) and $\widehat{x}(\lambda)$ in Figure 4(b) have the same fluctuating trend in the reflection area. The subsidiary peak number and the FWHM can be estimated.

Due to the advantage of high computation and precision, the centroid algorithm is applied to recognize the peak wavelength, as shown in Figure 5. The centroid algorithm produces a point corresponding to the geometric centroid of a spectrum, calculated by equation (5), where N is the size of the spectrum point vector, λ_i is the i_{th} point wavelength, and I_i is the i_{th} point reflectivity intensity.

$$\lambda_B = \frac{\sum_{i=1}^{N} \lambda_i I_i}{\sum_{i=1}^{N} I_i}. \tag{5}$$

3. Experiment Performance

To investigate the mechanisms of damage characteristics of different fatigue crack lengths, the employed specimens are bonded with FBG sensors. In the existing literature, the FBG sensors were embedded in composites for structural health monitoring. Ramakrishnan et al. [14] found that the

(a)

(b)
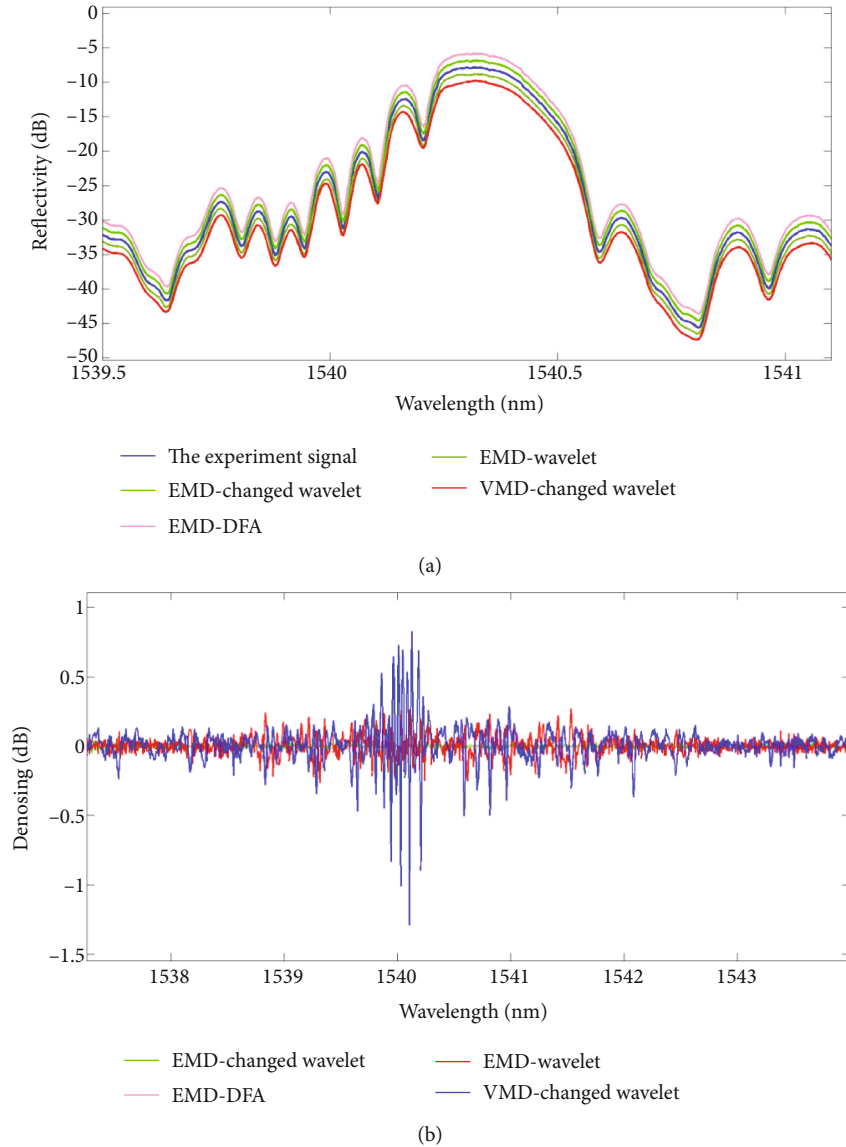
FIGURE 2: (a) The original spectrum signal. (b) The denoising signal by the proposed algorithm.

crack length was closely related to the delamination damage of composites, and the FBG sensors could sense the composite delamination. However, it is still a challenge for FBG to sense the crack damage of aluminum alloy. In this paper, the FBG sensors are adhered on the aluminum alloy plate, and the mechanism of damage characteristics corresponding to the crack propagation is studied. In this section, we evaluate the conduct for four proposed damage characteristics on FBG spectral experimental data. Therefore, an experiment in real-time crack propagation monitoring was performed with a high-resolution optical microscope SM125. In addition, the reflectance spectra were obtained and recorded with an optical spectral analyzer.

Strain field alternation caused changes in the full-spectral response that were detected and indicated that disband dependent nonlinear behavior of the structure appears in the dynamic spectral response. Jin et al. [15] found that the subordinate peak skewing corresponds closely to the crack length

and location. Meanwhile, further investigation on the subordinate peak skewed various with the ratio of crack length to the entire grating, which indicates that the first appeared time and the skewing of the subordinate peak are indicated by the crack location and length. Consequently, a real-time peak-seek algorithm for subordinate peak detection is applied, aided by the model carol method [16]. To calculate the peak width and subordinate peak location, the algorithm detects the maximum reflected optical power of each FBG.

3.1. Specimen. The objective system established in this paper is a plate made of aluminum alloy 7075-T6, with the dimensions of 300 mm × 100 mm × 2 mm, as shown in Figure 6. A 10 mm hole is in the center of the plate. To follow the crack tip with the FBG sensors, a 3 mm initial crack length is desired according to the standard. The specimen properties are shown in Table 1.

For strain sensing in various shape distributions along the grating, the FBG sensors with no covering layer are
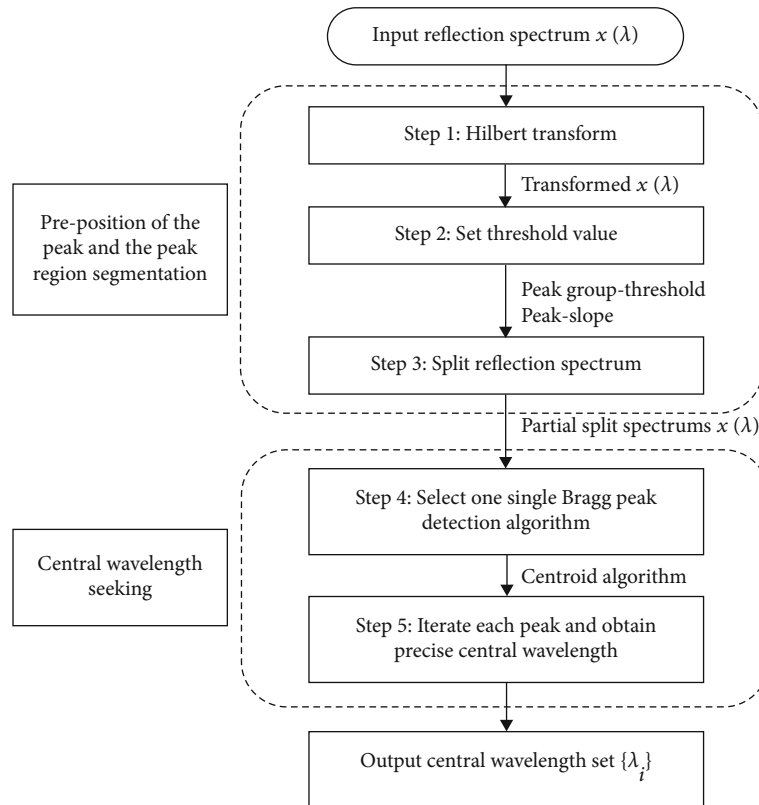
FIGURE 3: The diagram of multipeak central value diagnosis.

directly bonded in a horizontal plane onto the hole side in the 7075-T6 aluminum alloy specimen. This ensures a slow propagation of the crack into the sensing zone, and the FBG1 was placed 4 mm ahead of the initial crack tip with a 4 mm distance between FBG1 and FBG2. FBG parameters adopted in the experiment are as follows: grating length is 10.1 and 10.2 mm; bonded length is 11.3 and 11.4 mm; thickness of adhesive layer is about 0.3 mm; the liquid cyanoacrylate adhesive is used; and Young's modulus of the adhesive is 1.75 MPa.

3.2. Experiment Setup. A fatigue crack damage recognition test platform is developed, and FBG sensors are utilized to abstract the damage indicator. The overall view of the hole-edge crack experimental setup is composed of three main segments: fatigue loading equipment, optical modulation analyzer, and fatigue crack detection device (see Figure 7). Fatigue testing is undertaken using a hydraulic MTS machine with continuous fatigue loading along the axial direction. Constant amplitude loading spectra are used in this study, with a maximum loading set value of 65 MPa and a cycling frequency of 10 Hz. The FBG sensors were connected to an optical demodulator (SM125, Micro Optics Inc.), with high wavelength resolution. The reflected spectral data was recorded for real-time monitoring of crack propagation. Fatigue crack length was measured with an optical microscope, and crack tip propagation was observed with a Charge-Coupled Device (CCD) camera.

3.3. Mechanism of Damage Characteristics. The natural crack was initiated and propagated by submitting the plate

to a cyclical fatigue test. An FBG sensor was used to measure the strain distribution along the axial grating at different strain profiles, with the crack propagation. Data was obtained using the FBG sensing demodulation system throughout cyclic fatigue. Initially, the reflection spectra were symmetrical and developed a primary reflection spectrum. Subsequently, the peak simply moves backwards or forwards when the grating sensed a uniform strain profile. In this stage, its pitch changes accordingly with internal periodic modulation.

With the crack propagation, the spectral wavelength shifted gradually while the reflection spectrum showed a significant change in its shape. For example, Figure 8 shows when the subordinate peaks appear. In this period, FBG sensors have a gradual change in the grating period, which yield a characteristically broad and flat reflection spectrum. The subordinate peak skewing of the reflected spectra has a one-to-one correspondence with the proportion of crack length in the grating section. Meanwhile, the subordinate peak number changes with the fatigue crack propagation. During this process, the changing regularity of subordinate peak numbers closely relates to the proportion of crack length in the grating length. Noteworthy meaningful phenomena are that spectral distortion appears in the stage of ratio alternation. The distortion of the spectra is attributed to the eventually nonuniform distribution of strain along the grating.

Figure 8 shows the signal changes of the FBG sensors due to different crack lengths under cyclic crack propagation tests. The above-mentioned features would be applied to identify damage in real-time monitoring.

(a)

(b)

(c)
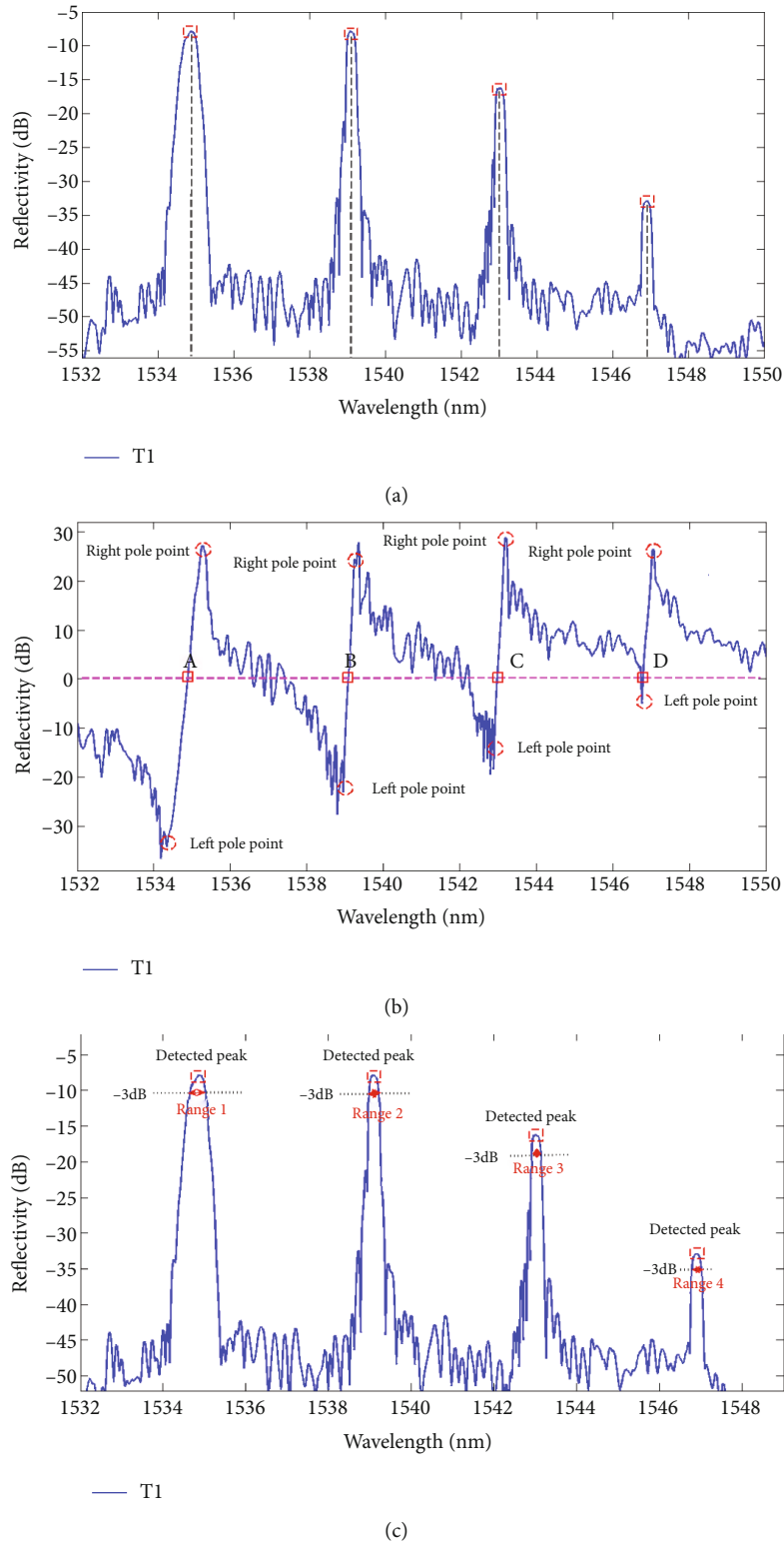
FIGURE 4: (a) The original spectrum. (b) The processed signal treatment by the Hilbert transform. (c) Peak diagnosis using the proposed algorithm.

3.3.1. The Primary Wavelength Variation. It is well understood that the primary wavelength corresponds to the average strain along the grating. When the grating senses compression/strain, the primary wavelength shifts towards shorter/ higher wavelength. Fernando et al. [17] illustrate the primary wavelength corresponding to the delamination with strain magnitude. According to Reference [18], the center wavelength increased linearly with the composite delamination damage.
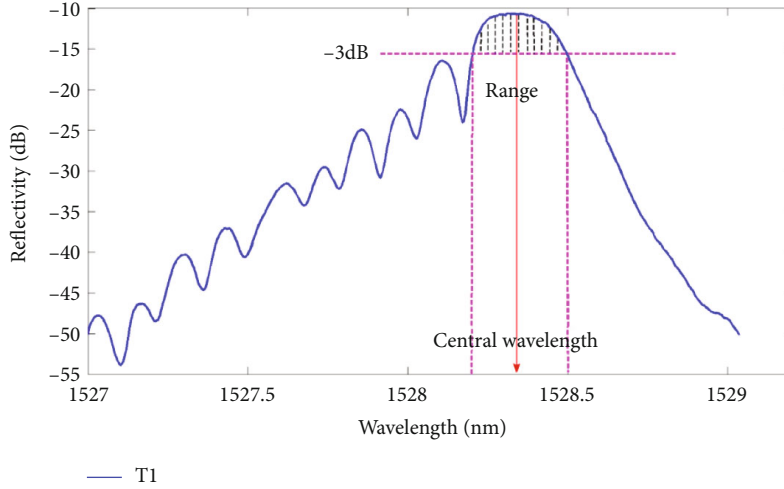
FIGURE 5: Schematic of the central wavelength detection by the centroid algorithm.
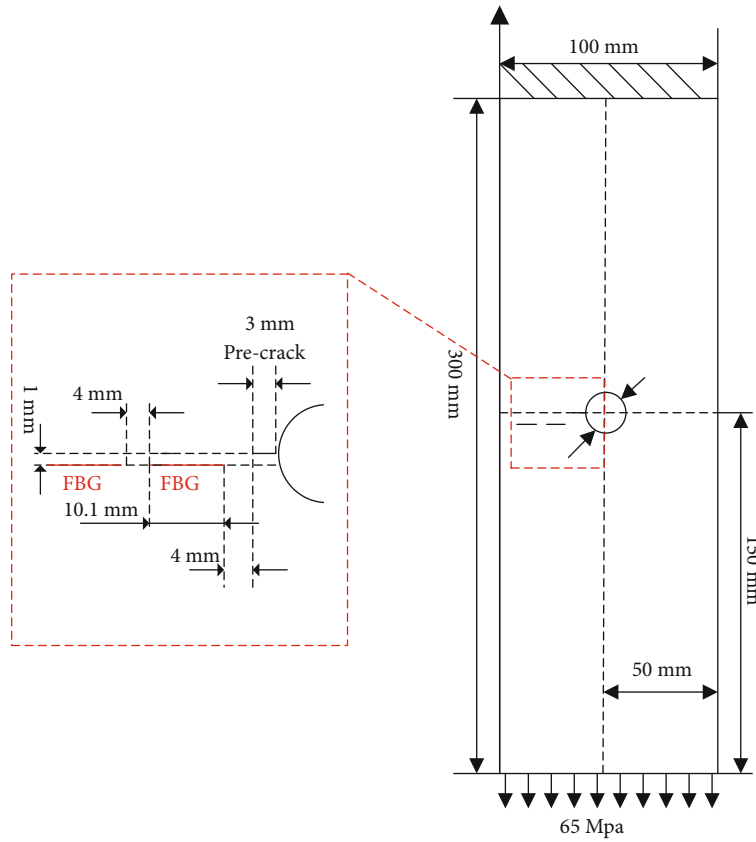
FIGURE 6: Schematic of the aluminum specimen.

TABLE 1: Mechanical properties of 7075-T6 aluminum alloy plates.

Material	Tensile strength (MPa)	Yield strength (MPa)	Poisson's ratio (MPa)	Elastic modulus (MPa)
AL7075-T6	572	503	0.33	73100

However, FBG sensors used for fatigue-induced damage monitoring were mainly bonded perpendicular to the external loading force. However, this research applies a force perpendicular to the fast axis of the fiber, and the crack propagation orientation is paralleled to the fast axis of the fiber. The experimental result shows that the reflection spectra were clearly narrow and symmetrical. Therefore, the primary reflection spectrum is only found at the initial state.
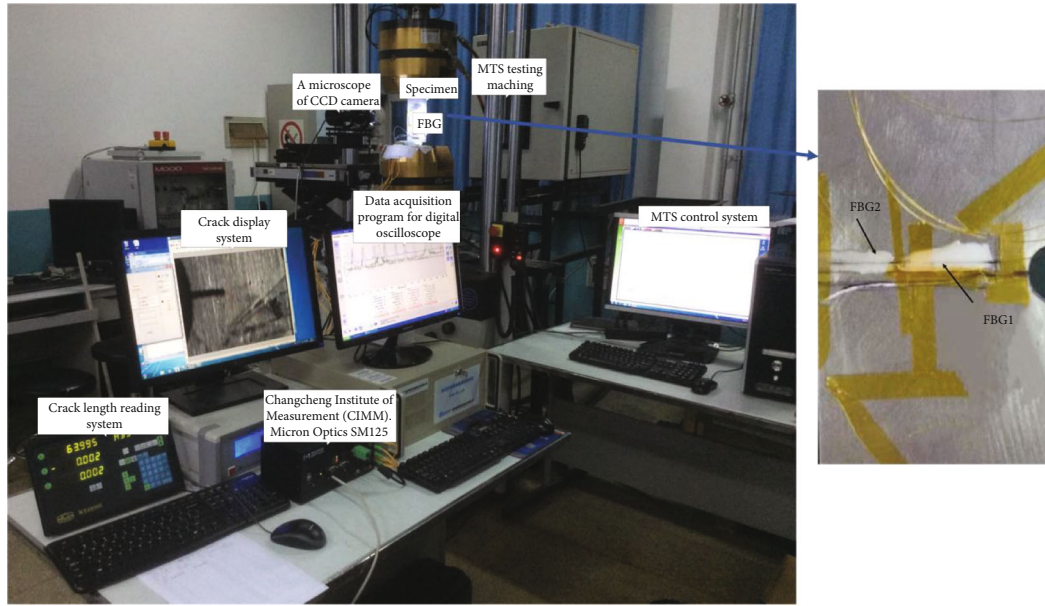
FIGURE 7: Experiment setup for the crack detection in aluminum structure.

Afterwards, the peak simply moves backwards or forwards when the grating sensed a uniform strain profile. In this stage, its pitch changes accordingly with internal periodic modulation. It was also observed that primary wavelength shift value was less than 0.1 nm during crack propagation. This is because there is a small offset between the center of the FBG and the intersection point between the FBG and neutral line.

With crack propagation, the nonuniform stain distribution is induced by the crack tip causing the reflection spectrum deformation. It should be noted here that the turning point coincides well within the ratio of crack length lying in the whole grating. At the ratio 32%-35% of crack tip located on the grating, the average strain value is distributed on the effective sensing. This value is relatively large, and the cubic strain pattern is distributed along the grating taking primary responsibility in spectral peak location decision. Thus, in regions A and B, the wavelength increased with crack propagation. When the ratio reaches about 36%-67%, the average strain value decreased and the quadratic strain pattern is distributed along the grating. Figure 9 shows the primary wavelength due to different crack lengths.

3.3.2. Spectral Bandwidth. The spectral bandwidth measurements are well represented by the average strain gradient along the FBG sensors. However, this does not yield an accurate measurement of the complexity of the strain field. Indeed, many researchers [19] found that the spectral bandwidth could respond to strain gradient. Hence, it had been applied for real-time in situ monitoring of composite material damage. Ussorio et al. [20] used the spectral bandwidth changes of distributed FBG sensors as indicators of matrix crack. Takeda et al. [21] estimated the composite delamination based on the quantitative change in the spectral bandwidth.

The spectral bandwidth indicator could be applied for both composites and metal materials. Jin et al. [22] have demonstrated that strain distributions along the grating creates localized resonances at different wavelengths by experimental studies. This provides a reason why the spectral distortion occurred. Meanwhile, the number of the subordinate peaks could significantly affect the spectrum bandwidth variation. Thus, spectral bandwidth would be used as an indicator for the hole-edge crack diagnosis. Spectral bandwidth represents the range of the induced strain values and thus the magnitude of the strain gradient along the grating. This research will utilize the full width at half maximum (FWHM). Accordingly, the spectral bandwidth is the most commonly used measurement of spectral distortion for FBG sensors [23].

Previous studies have demonstrated that the strain distribution along the grating is mainly due to the ratio of crack length lying in the grating with respect to the entire grating. Another observation could be made for spectral changes, due to crack propagation in which significant peak splitting occurs. However, it should be noted the total bandwidth increase may not be large in this period. The FWHM variation tendency shows gentle rise and decline in zones A and B, as shown in Figure 10. Meanwhile, the FWHM displays an obvious correlation with crack length until a crack saturation length was reached. The spectrum bandwidth was also directly related to strain distribution and has been previously applied [24]. This is because there is a small offset between the center of the FBG and the intersection point between the FBG and the neutral line.

It is known that the deformity of the reflection spectra is generally related to the strain distribution along the FBGs [25]. In fact, the distribution of strain patterns along the grating corresponds to crack propagation. The crack in the aluminum material can produce a strain concentration or gradient zone, which contains complex strain patterns. If
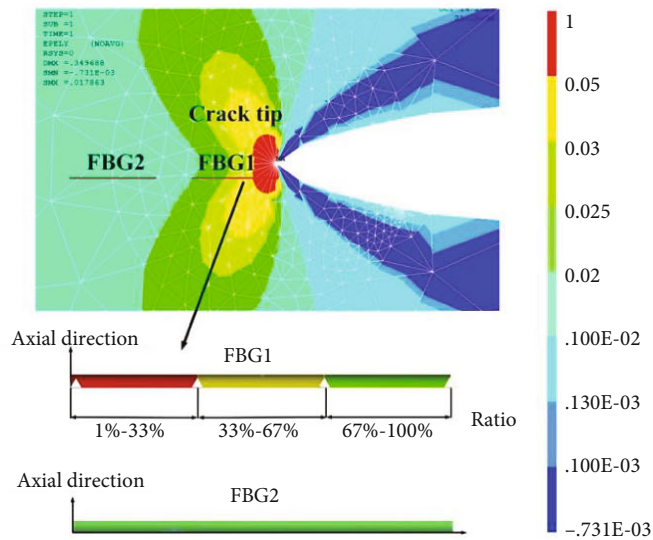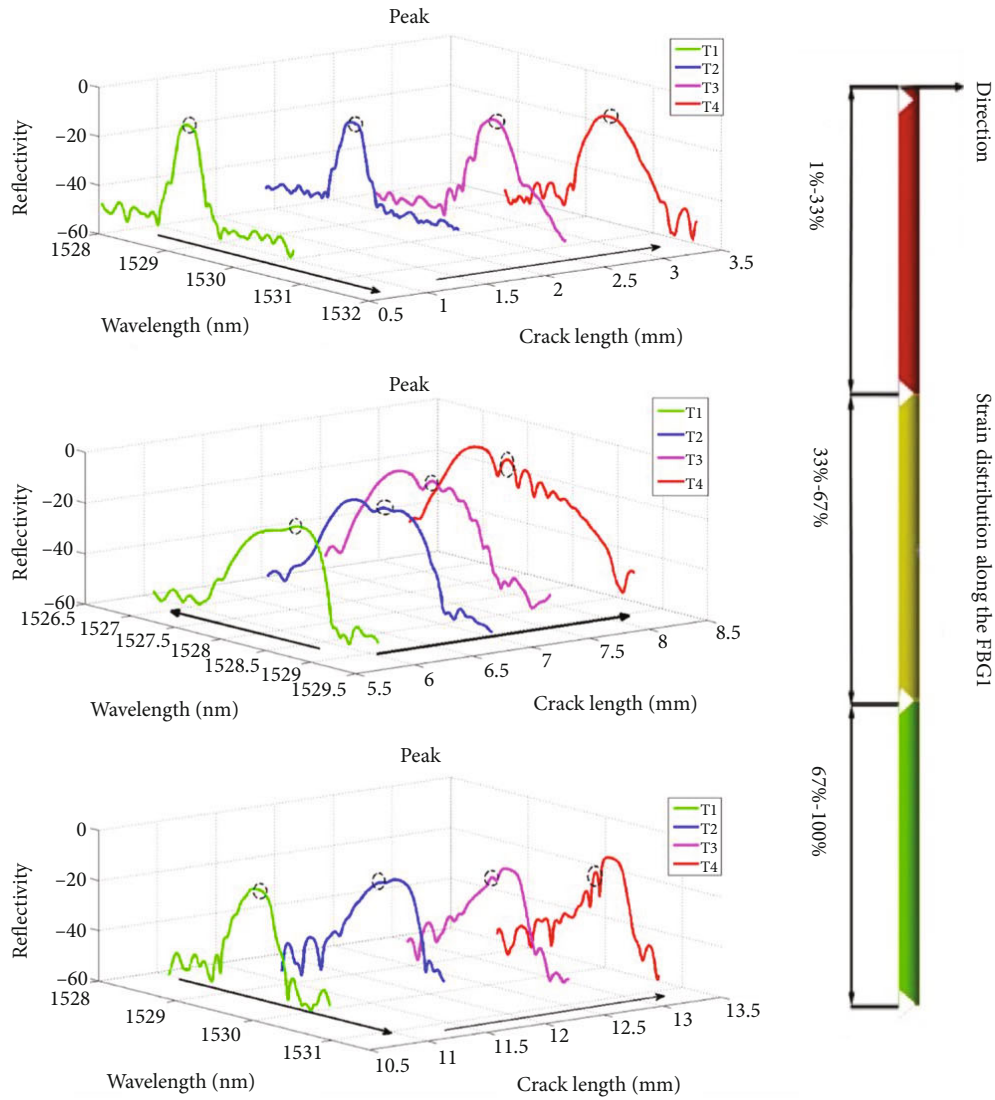
(a) Spectra of FBG1

FIGURE 8: Continued.
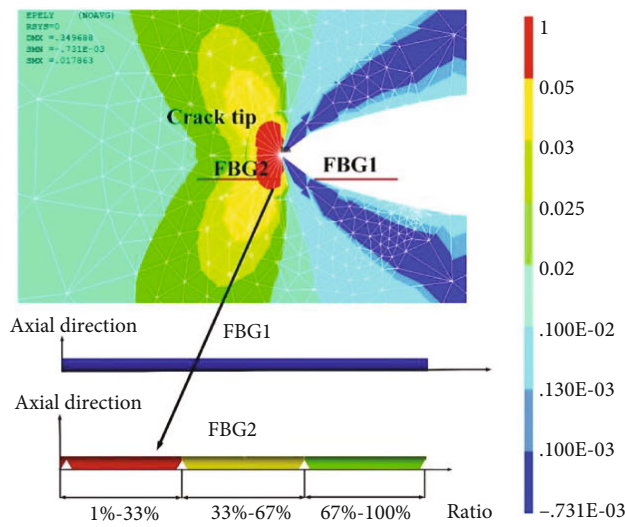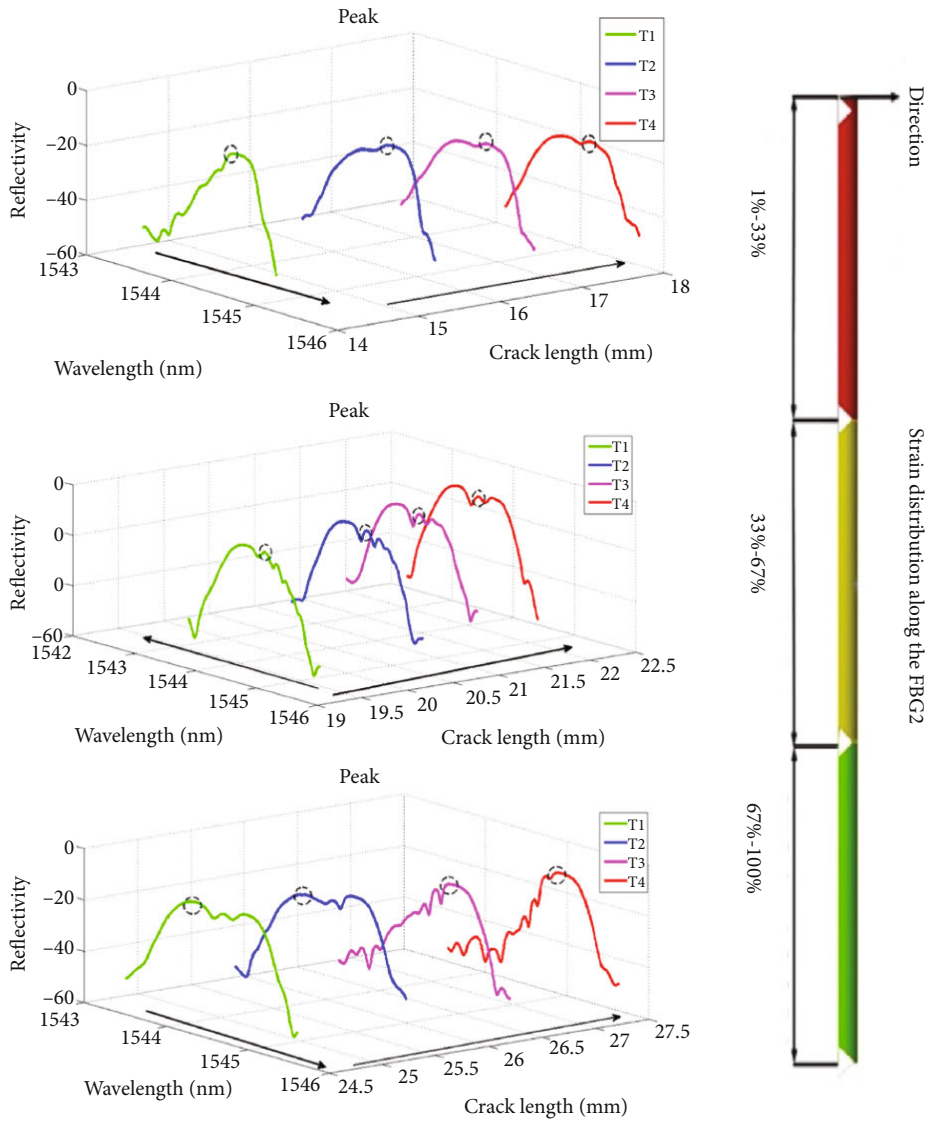
Figure 8: The corresponding spectra for different crack lengths.
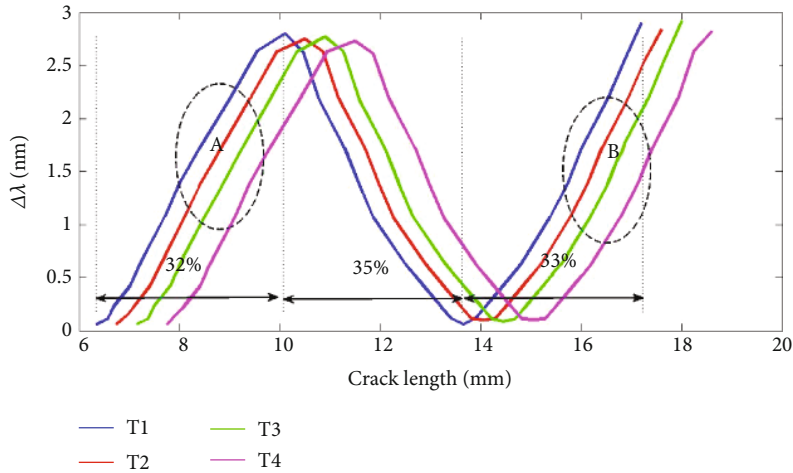
FIGURE 9: The primary wavelength variation vs. crack length.
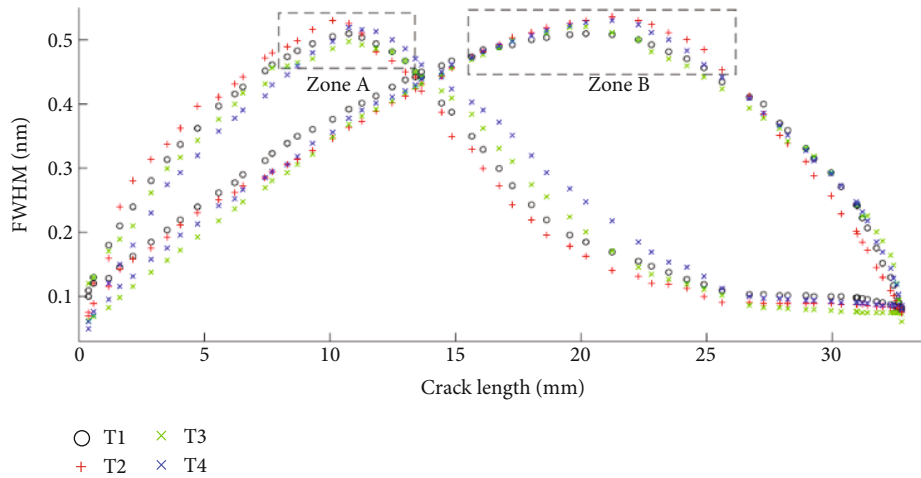
FIGURE 10: FWHM vs. crack length data for all four parallel plates.

different strain patterns are applied on the grating, the grating will suffer with the same nonuniform strain distribution pattern, causing a sensor response that is significantly more complicated relative to a uniform case [26]. The nonuniform strain along the grating will change the periodicity of the grating pattern. Hence, the grating pattern is modified from a uniform to a chirped configuration [27], as shown in Figure 10.

3.3.3. Number of Subordinate Peaks.
The crack in the aluminum material can produce a strain concentration, which contains complex strain patterns. The spectrum distortion corresponds to the strain pattern in the grating. Meanwhile, if the grating suffers with a similar nonuniform strain pattern, the sensor response is significantly more complicated compared to a uniform case [18]. This means that the spectral distortion relates to both the ratio of crack tip lying in the whole grating length and the location of the crack tip in the grating. The number of subordinate peaks is dependent on this ratio.

In this research, spectral datasets are collected by fixing four parallel specimens under cyclic fatigue tests. The reflected spectral data were normalized as for the spectral subordinate peak number method. Figure 11 displays a schematic diagram of the subordinate peak number counting. Although the high-order peaks had been filtered using the FBG sensing demodulation SM 125, the higher-order peaks imply no significant contribution to the crack propagation. Thus, the intensity of the reflection spectrum was normalized by the intensity of the highest component. The reflected spectrum data was selected with $\bar{r} \geq 0.5$ (i.e., full width at half maximum).

If the strain field is changing over a short effective segment of the whole grating length, the cubic strain pattern as the main form distributed along the grating. As only a discrete number of peaks are calculated, the relationship is not as smooth as the spectral primary wavelength measure.

At the 1%-67% ratio of the crack length lying in the whole grating, the number of the subordinate peaks shows an upward trend. This is especially important during the

(a) Primary peak seeking

(b) Threshold determination

(c) Nominalized reflectivity
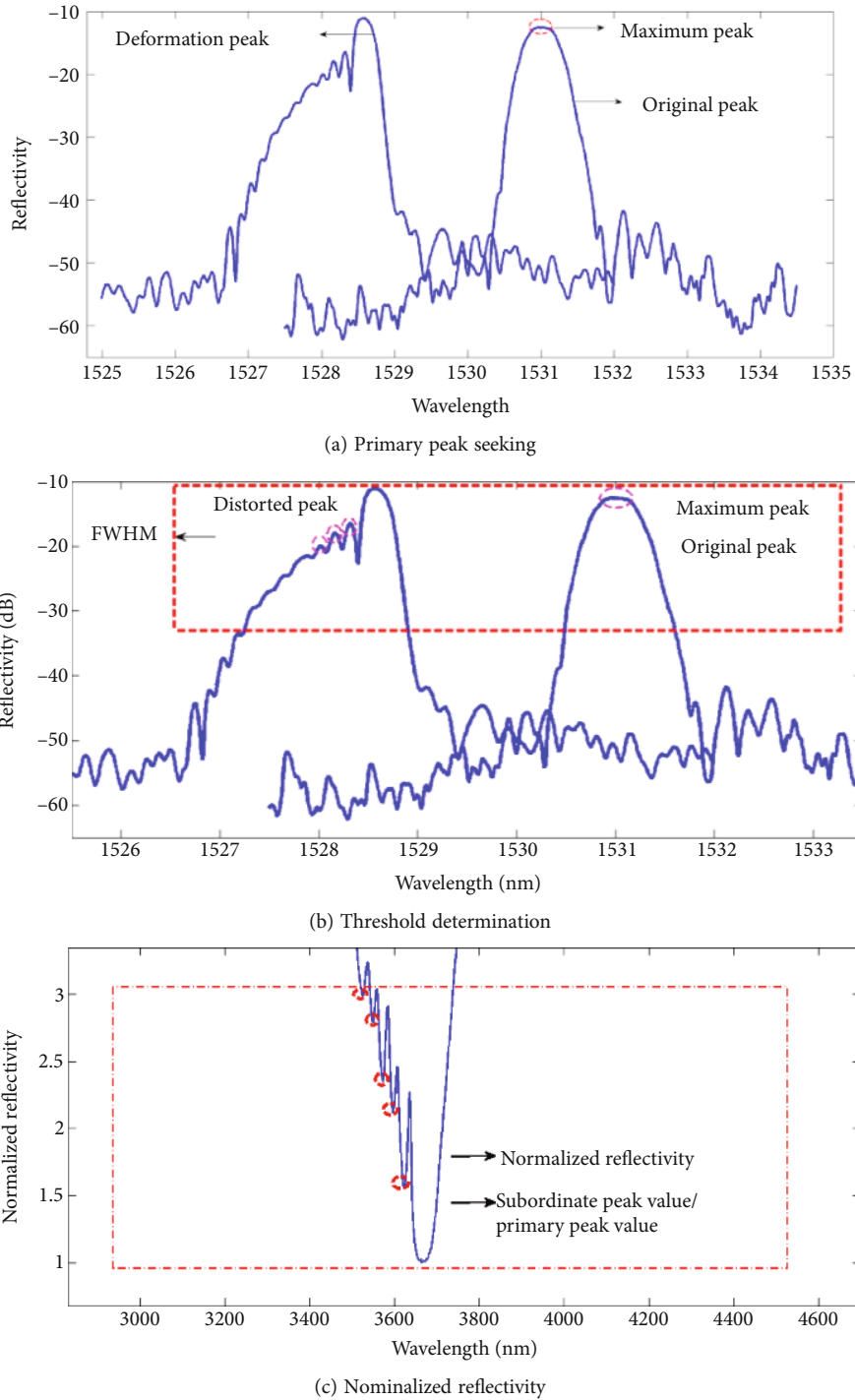
FIGURE 11: The schematic diagram of the subordinate peak number counting.

ratio of 1%-32%, where the subordinate peak number increased rapidly. The experimental spectral bandwidth is plotted for four parallel plates in Figure 12.

Thus, the number of subordinate peaks may be useful as an indicator of imminent failure of the aluminum material.

3.3.4. The Subordinate Wavelength Skewing. The location of subordinate peaks corresponds to the location of strain concentration on the FBG sensors. At the initial stage, about

15% ratio of crack length lying in the whole grating causes slitting of the spectra and distortion of the spectral shape. The subordinate peak appears at the shorter wavelength, and the wavelength only increased due to the strain value concentered on the short effective sensitive grating. Meanwhile, at about 32% ratio of the crack length lying in the whole grating, a similar trend of subordinate peak wavelength can be observed for crack propagation. As our previous research shows, this depends on the strain pattern

(a) FBG1

(b) FBG2
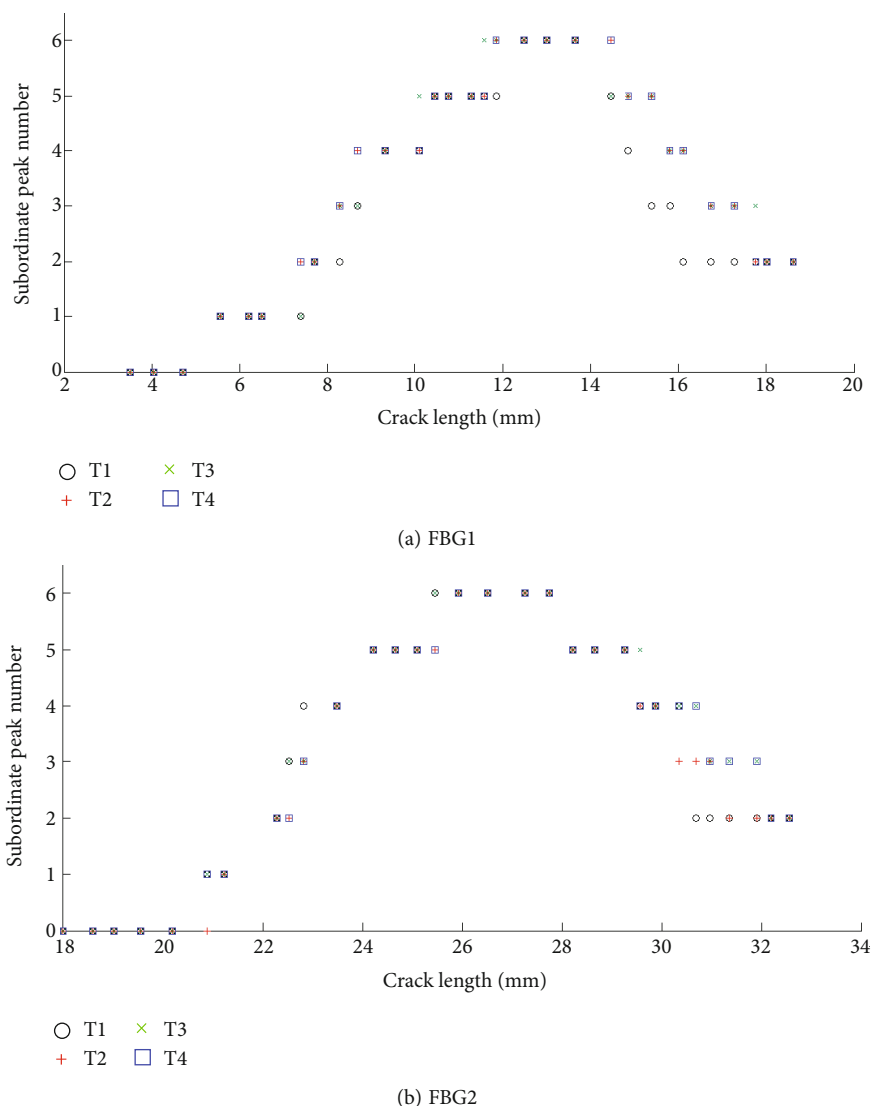
Figure 12: Number of subordinate peaks vs. crack length.

distribution along the grating. It must also include the different shapes of the strain distributions, for the analysis directly reflected the shape skewing of the subordinate peak.

Afterwards, the spectra become enlarged, and the subordinate peak skews at a longer wavelength and drifts to the same orientation. The nonuniform strain along the grating will change the periodicity of the grating pattern. In this way, the grating pattern is modified from a uniform to a chirped configuration [28]. Meanwhile, the subordinate peak wavelength shows a significant decline at the strain pattern transition region with the average strain decrease, as shown in zone A in Figure 13. Nevertheless, as the crack length increases, the strain pattern is distributed along the variable grating, and the widths of the measured spectra increased.

It is confirmed that oscillations of the spectrum can be related to the nonuniform strain distribution along the grating caused by cracks. Thus, they serve nonuniform strain patterns along the grating, and it is assumed to be the principal reason for the spectral oscillation [29]. Meanwhile, when the ratio reaches to about 67%, the subordinate peak

appears at a shorter wavelength, and the strain value distribution on the effective sensing region increased. Thus, the subordinate peak wavelength increased rapidly, as shown in zone B in Figure 13. The reflection spectra were even slit into several peaks at the ultimate break of the grating, at about 15% ratio of crack length lying in the whole grating.

To further explore the subordinate wavelength variation, the experimental data of four samples tested were analyzed, as shown in Figure 13.

4. Discussion

4.1. Subordinate Wavelength Skewing. When the compression strain is identified by the grating, the spectrum moves to a shorter wavelength. In contrast, when the tensile strain is detected by the grating, the spectrum moves to a longer wavelength [30]. The strain distribution around the crack tip is highly variable. It is worth mentioning that if the FBG was submitted to different strain patterns along the grating, different lower peaks will distort the reflected peak.
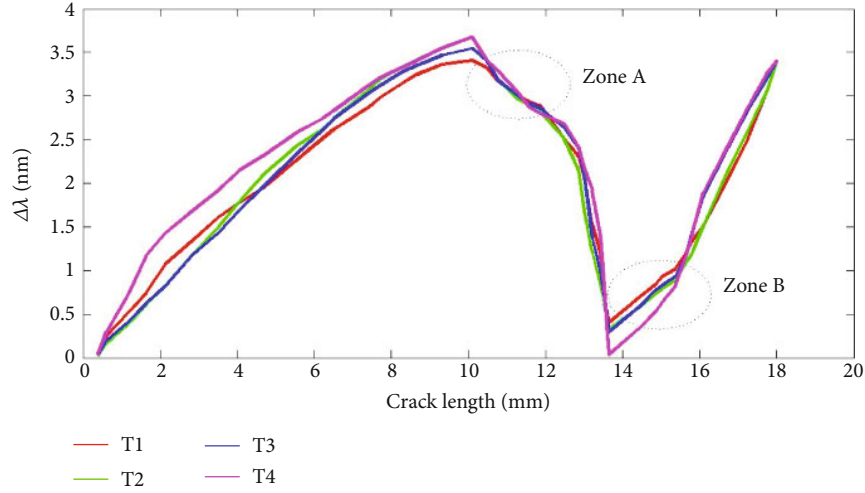
(a) FBG1
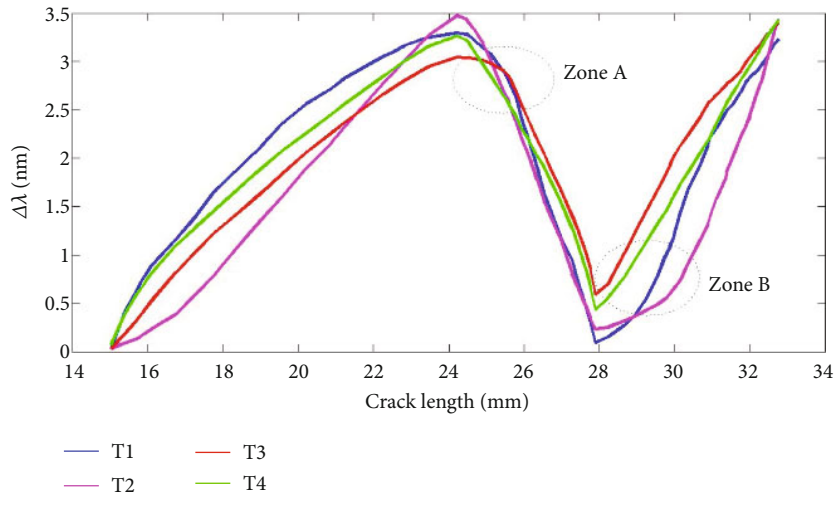
(b) FBG2

FIGURE 13: Subordinate peak skewing vs. crack length.

The slitting of the spectra occurred and the spectral shape becomes distorted. Meanwhile, the primary wavelength, FWHM, subordinate peak number, and subordinate wavelength skewing with the strain pattern change along the grating.

It is assumed that the subordinate peak location skewing corresponds to the change of the strain pattern along the grating, with respect to the crack propagation. This is especially true at the strain pattern transition region, which is located at the ratio 32-34% of crack length lying in the whole grating.

4.2. Spectral Distortion. Literature [31] shows that both elastic and plastic strains can be experienced in the grating. In combination with complex strain distributions around the crack tip, a serve strain distribution pattern could be sensed by the grating, such as linear, quadratic, and cubic strain distributions. The literature further reveals that the linear, quadratic, and cubic strain patterns along the grating determine the subordinate peak location.

Thus, it is assumed that the complex strain pattern perceived by the grating could be the chief reason of spectrum distortion, correlating with the ratio of crack length lying in the whole grating.

5. Conclusion

To determine the characteristic damage variation of FBG sensors with the crack propagation, FBG shows significant changes in the strain due to damage in the specimen. The four characteristic parameters were abstracted by analyzing experimental data. This was followed by the correlation of damage characteristics with crack length and investigated with the four damage characteristics, namely, the primary wavelength, the subordinate peak number, the FWHM, and the subordinate wavelength skewing.

During crack propagation, the subordinate peak skewed with the strain pattern transition region, with the ratio 32-34% of crack length lying in the grating length. Meanwhile, the FWHM, the primary wavelength, and the subordinate

peak number correspond to the subordinate peak skewing. Thus, it is confirmed that subordinate peak skewing can be applied as an effective indicator to evaluate the crack propagation for the aluminum.

Furthermore, the FBG-based demodulation method can be used as an interesting and alternative technique for real-time detection of transverse cracks in aluminum.

Data Availability

The processed data required to reproduce these findings cannot be shared at this time as the data also forms part of an ongoing study.

Conflicts of Interest

The authors declare no competing interests.

Authors' Contributions

Bo Jin and Cunbo Lu conceived the key idea and designed the experiments. Feng Zhang provided the academic support and checked the manuscript. Weifang Zhang performed the experiment and contributed to optical measurement tools. All authors made contributions to writing and revising the manuscript.

References

[1] G. C. Kahandawa, J. Epaarachchi, H. Wang, and K. T. Lau, "Use of FBG sensors for SHM in aerospace structures," *Photonic Sensors*, vol. 2, no. 3, pp. 203–214, 2012.

[2] J. P. Ou, "Some recent advance of intelligent monitoring system for civil infrastructures in mainland China," in *Proceedings of the First International Conference on Structural Health Monitoring and Intelligent Infrastructures*, pp. 131–144, Tokyo, Japan, 2003.

[3] D. Kinet, P. Mégret, K. W. Goossen, L. Qiu, D. Heider, and C. Caucheteur, "Fiber Bragg grating sensors toward structural health monitoring in composite materials: challenges and solutions," *Sensors*, vol. 14, no. 4, pp. 7394–7419, 2014.

[4] N. Takeda, Y. Okabe, and T. Mizutani, "Damage detection in composites using optical fibre sensors," *Proceedings of the Institution of Mechanical Engineers Part G Journal of Aerospace Engineering*, vol. 221, no. 4, pp. 497–508, 2007.

[5] P. Childs, A. C. L. Wong, W. Terry, and G. D. Peng, "Measurement of crack formation in concrete using embedded optical fibre sensors and differential strain analysis," *Measurement Science and Technology*, vol. 19, no. 6, article 065301, 2008.

[6] Sante and R. Di, "Fibre optic sensors for structural health monitoring of aircraft composite structures: recent advances and applications," *Sensors*, vol. 15, no. 8, pp. 18666–18713, 2015.

[7] R. Ramly, W. Kuntjoro, and M. K. Abd Rahman, "Embedded FBG sensor in aircraft smart composite materials for structural monitoring," *Applied Mechanics & Materials*, vol. 393, no. 393, pp. 311–316, 2013.

[8] A. Rajabzadeh, R. M. Groves, R. C. Hendriks, and R. Heusdens, "Modelling non-uniform strain distributions in aerospace composites using fibre Bragg gratings," in *25th International Conference on Optical Fiber Sensors*, Jeju, Korea, 2017.

[9] R. Correia, E. Chehura, S. W. James, and R. P. Tatam, "A pressure sensor based upon the transverse loading of a sub-section of an optical fibre Bragg grating," *Measurement Science & Technology*, vol. 18, no. 10, pp. 3103–3110, 2007.

[10] M. A. Soto, J. A. Ramírez, and L. Thévenaz, "Optimizing image denoising for long-range Brillouin distributed fiber sensing," *Journal of Lightwave Technology*, vol. 36, no. 4, pp. 1168–1177, 2018.

[11] M. Li and J. Yao, "All-fiber temporal photonic fractional Hilbert transformer based on a directly designed fiber Bragg grating," *Optics Letters*, vol. 35, no. 2, p. 223, 2010.

[12] Y. Chen, X. Yang, H. L. Liu, K. Yang, and Y. L. Zhang, "Processing FBG sensing signals with exponent modified Gaussian curve fitting peak detection method," *Spectroscopy and Spectral Analysis*, vol. 36, no. 5, pp. 1526–1531, 2016.

[13] S. Jiao, W. Shi, and L. Qian, "Self-adaptive partial discharge denoising based on variational mode decomposition and wavelet packet transform," in *2017 Chinese Automation Congress (CAC)*, Jinan, China, 2017.

[14] M. Ramakrishnan, G. Rajan, Y. Semenova, and G. Farrell, "Overview of fiber optic sensor technologies for strain/temperature sensing applications in composite materials," *Sensors*, vol. 16, no. 1, 2016.

[15] B. Jin, W. Zhang, F. Ren, M. Zhang, W. Dai, and Y. Wang, "Mechanism of subordinate peak skewing of FBG sensor during cracks propagation monitoring on aluminum alloy structure," *Journal of Sensors*, vol. 2017, Article ID 2857693, 7 pages, 2017.

[16] L. J. Cai, Z. Y. Li, Z. H. Tang, W. Meng, and Q. Liu, "A novel peak-seek algorithm used in FBG sensor demodulation system for vibration monitoring," *Applied Mechanics & Materials*, vol. 160, pp. 135–139, 2012.

[17] C. Fernando, A. Bernier, S. Banerjee, G. G. Kahandawa, and J. Eppaarchchi, "An investigation of the use of embedded FBG sensors to measure temperature and strain inside a concrete beam during the curing period and strain measurements under operational loading," *Procedia Engineering*, vol. 188, pp. 393–399, 2017.

[18] M. Kreuzer, "Strain measurement with fiber Bragg grating sensors," HBM, 2006.

[19] S. Takeda, Y. Okabe, and N. Takeda, "Monitoring of delamination growth in CFRP laminates using chirped FBG sensors," *Journal of Intelligent Material Systems and Structures*, vol. 19, no. 4, pp. 437–444, 2008.

[20] M. Ussorio, H. Wang, S. L. Ogin et al., "Modifications to FBG sensor spectra due to matrix cracking in a GFRP composite," *Construction and Building Materials*, vol. 20, no. 1–2, pp. 111–118, 2006.

[21] N. Takeda, Y. Okabe, J. Kuwahara, S. Kojima, and T. Ogisu, "Development of smart composite structures with small-diameter fiber Bragg grating sensors for damage detection: quantitative evaluation of delamination length in CFRP laminates using lamb wave sensing," *Composites Science and Technology*, vol. 65, no. 15–16, pp. 2575–2587, 2005.

[22] B. Jin, W. Zhang, M. Zhang, F. Ren, W. Dai, and Y. Wang, "Investigation on characteristic variation of the FBG spectrum with crack propagation in aluminum plate structures," *Materials*, vol. 10, no. 6, p. 588, 2017.

[23] K. Peters, P. Pattis, J. Botsis, and P. Giaccari, "Experimental verification of response of embedded optical fiber Bragg grating sensors in non-homogeneous strain fields," *Optics and Lasers in Engineering*, vol. 33, no. 2, pp. 107–119, 2000.

[24] G. Guo, D. A. Hackney, M. Pankow, and K. Peters, "Interrogation of a spectral profile division multiplexed FBG sensor network using a modified particle swarm optimization method," *Measurement Science & Technology*, vol. 28, no. 5, Article ID 055204, 2017.

[25] K. Peters, M. Studer, J. Botsis, A. Iocco, H. Limberger, and R. Salathé, "Embedded optical fiber Bragg grating sensor in a non-uniform strain field: measurements and simulations," *Experimental Mechanics*, vol. 41, no. 1, pp. 19–28, 2001.

[26] Y. Okabe, S. Yashiro, T. Kosaka, and N. Takeda, "Detection of transverse cracks in CFRP composites using embedded fiber Bragg grating sensors," *Smart Materials & Structures*, vol. 9, no. 6, pp. 832–838, 2000.

[27] K. J. Peters, M. Studer, J. Botsis, A. Iocco, H. G. Limberger, and R.-P. Salathe, "Measurement of stress concentrations using embedded optical fiber Bragg grating sensors," in *1999 Symposium on Smart Structures and Materials. International Society for Optics and Photonics*, Newport Beach, CA, United States, 1999.

[28] A. Othonos, "Fiber bragg gratings," *The Review of Scientific Instruments*, vol. 68, no. 12, pp. 4309–4341, 1997.

[29] S. Cięszczyk and P. Kisała, "Inverse problem of determining periodic surface profile oscillation defects of steel materials with a fiber Bragg grating sensor," *Applied Optics*, vol. 55, no. 6, pp. 1412–1420, 2016.

[30] J. F. Botero-Cadavid, J. D. Causado-Buelvas, and P. Torres, "Spectral properties of locally pressed fiber Bragg gratings written in polarization maintaining fibers," American Institute of Physics, 2008.

[31] J. Zhou, Z. Zhou, and D. Zhang, "Study on strain transfer characteristics of fiber Bragg grating sensors," *Journal of Intelligent Material Systems and Structures*, vol. 21, no. 11, pp. 1117–1122, 2010.

Research Article

Health Monitoring Framework for Weather Radar Based on Long Short-Term Memory Network with a Real Case Study

Wei Li,[1] **Dalin Wang** ,[2,3] **Wei Zhou,**[1] **Yimeng Wang,**[1] **and Chao Shen**[1]

[1]*Meteorological Observation Center, China Meteorological Administration, Beijing 100081, China*
[2]*Department of Industrial Engineering, Tsinghua University, Beijing 100084, China*
[3]*Jiaxing Healthier, Automation Co., Ltd., Jiaxing 314000, China*

Correspondence should be addressed to Dalin Wang; wangdl20@mails.tsinghua.edu.cn

The health management of weather radar plays a key role in achieving timely and accurate weather forecasting. The current practice mainly exploits a fixed threshold prespecified for some monitoring parameters for fault detection. This causes abundant false alarms due to the evolving working environments, increasing complexity of the modern weather radar, and the ignorance of the dependencies among monitoring parameters. To address the above issues, we propose a deep learning-based health monitoring framework for weather radar. First, we develop a two-stage approach for problem formulation that address issues of fault scarcity and abundant false fault alarms in processing the databases of monitoring data, fault alarm record, and maintenance records. The temporal evolution of weather radar under healthy conditions is represented by a long short-term memory network (LSTM) model. As such, any anomaly can be identified according to the deviation between the LSTM-based prediction and the actual measurement. Then, construct a health indicator based on the portion of the occurrence of deviation beyond a user-specified threshold within a time window. The proposed framework is demonstrated by a real case study for the Chinese S-band weather radar (CINRAD-SA). The results validate the effectiveness of the proposed framework in providing early fault warnings.

1. Introduction

A weather radar is a type of radar used to find precipitation, calculate its motion and intensity, and estimate the precipitation type [1]. Typically, a weather radar consists of five main subsystems including signal processor, transmitter, antenna, receiver, and control/communication processor. The data is sent to the data centre and is essential for timely and accurate weather forecasting. Modern weather radar has become more advanced with higher levels of digitization and integration, which poses challenges to maintaining its operational efficiency [2]. There is a need for proactive maintenance programs to monitor and manage the health condition of weather radar in a cost-effective manner. In the current practice, a fault alarm scheme is implemented by setting a predefined threshold for some state parameters, which often causes a large number of false alarms mainly due to the evolving working environments and the weakness of fixed threshold strategies [3].

The recent advances of machine learning provide powerful tools to explore the value of operational data in the health monitoring of weather radar. However, it is still at an infant stage for the meteorological community to use the data accumulated through the operating experience of weather radar [3–5]. Indeed, a wide range of methods has been applied in other industrial sectors that utilize data analytics to extract knowledge from historical data [6]. For instance, develop a knowledge-based system approach for sensor fault detection [7], diagnose the fault of rotating machinery based on decision tree and principal component analysis [8], monitor the condition of bridges based on a clustering approach [9], and identify contamination source using a sequential Bayesian approach [10].

Growing attention has been paid to deep learning techniques for end-to-end health management frameworks, because of their capability to handle large datasets and to automatically learn hidden features. Various deep learning

architectures and their variants are employed for fault detection, diagnosis, and prognostics such as feedforward neural network, convolutional neural network, recurrent neural network, and autoencoder [11]. For instance, develop a convolutional neural network-based model to detect wafer structural defect using wafer images [12], adopt a stacked autoencoder for the fault diagnosis of rotating machinery [13], and address the variable working conditions through deep transfer learning [14, 15]. Note that most current studies are developed using simulation or lab-testing datasets. There is still a gap for real field applications in aggregating data from various sources, which raises the challenges of data preparation [16]. The literature on deep learning applications in PHM is quite large and has received growing attention in a broad range of sectors. We refer the interested readers to the references in [17, 18] for a comprehensive review on this topic.

In this paper, we propose a deep learning-based health monitoring framework with real applications to Chinese S-band weather radar (CINRAD-SA). In particular, we develop a long short-term memory (LSTM) network-based predictive model to capture the temporal patterns of working conditions of weather radar. The multidimensional time-series data collected in the normal condition are used to train the LSTM network and hence obtain an LSTM network to represent the health state of weather radar. Given any future time instant, the anomaly can be identified based on the deviation between the actual measurement and the prediction provided by the LSTM. Once the degree of deviation goes beyond a user-specified threshold, the weather radar would be considered at a fault condition. Ultimately, the number of occurrences beyond the threshold within a time window would signify the severity of abnormalities, which is then used to construct the health indicator of the weather radar.

The effectiveness of our proposed framework is demonstrated using the operational data obtained at a radar station from 2019/01/01 to 2020/10/14. We discuss the issues in problem formulation and our solution based on a two-stage approach. Then, we validate the proposed framework by successfully showing an early warning of a severe fault that occurred on 2020/01/14. The results indicate the potential value of the proposed framework in support of practical maintenance planning.

The rest of this paper is organized as follows. Section 2 describes the background of recurrent neural networks and the data acquired through the operational experience of CINRAD-SA. Section 3 presents the proposed framework to predict and assess the health condition of weather radar. Section 4 demonstrates the proposed framework using a real case study. Section 5 presents the conclusions and discusses future research.

2. Background

2.1. Data Available in the Chinese S-Band Weather Radar.
There are three types of data collected through the operation of the CINRAD-SA: (1) the real-time monitoring data are multidimensional time series in form of floating-point and are collected based on the built-in sensors of the weather radar. There are typically hundreds of parameters for a weather radar; (2) fault alarm records are stored as a binary data format once some monitoring parameters go beyond a prespecified threshold value. Note that most of the alarm records are false alarm without the actual occurrence of fault; and (3) maintenance records contain the repair start and end times, the fault description, the replacement part, and the affiliated subsystem. The maintenance records can be used to locate the actual occurrence of a fault.

2.2. Long Short-Term Memory.
An LSTM is a type of recurrent neural network (RNN) that is specialized for sequential data such as time-series data, text stream, and audio clips. RNN can learn the sequential characteristics of data by formulating a looping mechanism through a stack of building units, called the cells. Specifically, a cell can memorize the information given the current input and then pass through the same cell sequentially to produce a single output for each step, namely, the hidden state. Then, feed this hidden state and new data input to the next step. This allows the cell in the next step to learn from the previous steps, to understand the sequential characteristics of the data.

As the simplest RNN, the vanilla RNN only has one hidden gate and is facing a common problem of gradient vanishing given long sequences of data. Hence, various cell designs lead to variants of RNN, such as gated recurrent unit and LSTM [11], among which the latter is the most commonly used. LSTM cell consists of three gates: forget, input, and output gates, the operations of which are shown in Figure 1. The previous hidden state H_{t-1} and the current data X_t are fed into the forget gate to remove the information that is not relevant to the previous cell. Then, update the cell state given the past hidden state and the current state using the input gate i_t and generate a new hidden state H_t using the output o_t based on the information of the updated cell C_t.

3. Proposed Health Monitoring Framework

This section presents the proposed framework as illustrated by the flowchart in Figure 2. There are two main parts including offline development and online deployment. The historical data would be prepared and preprocessed to be used for the LSTM-based predictive model development in the offline stage. Then, construct the health indicator of weather radar by leveraging the LSTM-based prediction and the online measurement. This results in a health monitoring framework that tracks the health condition of weather radar and provides early warning one health indicator. The details of each part are discussed in the following sections.

3.1. Problem Formulation.
We develop a two-stage approach to address the challenges involving problem formulation. There are two main challenges as follows:

   (i) The first challenge is data preparation to label the available monitoring data as either faulty or healthy conditions. Particularly, the monitoring data and
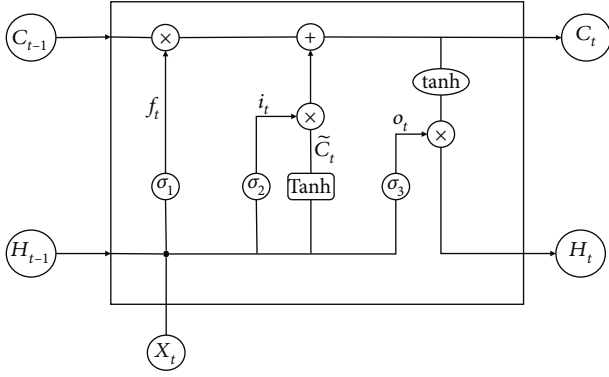
FIGURE 1: A diagram of the cell design of the long short-term memory (LSTM) network [19].

fault alarm records have the same timestamp. Ideally, the fault alarm records can be applied to annotate the radar condition. However, most of the fault alarm records are false alarms and cannot properly represent the actual radar condition and due to the methodological deficiency of the prefixed threshold strategy in the current practice. On the other hand, maintenance records represent the actual fault occurrence but have timestamps different from the real-monitoring data and fault alarm records

(ii) The second challenge is the limited amount of actual fault occurrence in the field. As such, it is not applicable to formulate a classification problem and directly use the binary state variable as the response variable indicating the radar state

Figure 3 illustrates a flowchart of the proposed two-stage approach. In the first stage, address the issue of abundant false alarms by synchronizing between fault alarm records and maintenance records. Specifically, we calibrate the fault alarm records by labelling the alarm records as 1 if their timestamp matches the maintenance records, otherwise 0. This results in the calibrated fault alarm records, which are representative of the actual radar faults. In the second stage, we intend to explore the association between the monitoring parameters and the calibrated fault alarm records. Then, formulate the health monitoring task as a regression problem. The response variable is set as the most relevant monitoring parameter and uses the other associated monitoring parameter as the explanatory variable. Overall, it is important for proper annotation of radar states and problem formulation so that assure the quality of data for model development and enable satisfactory predictive performance.

3.2. Predictive Model Development. Note that the working condition of weather radar is evolving continuously and pose challenges in learning predictive models with heterogeneity. Using the data of a large period would introduce much heterogeneity and hence compromise the predictive performance. Therefore, we recommend using the data two to three weeks before the time of interest for model training and learning to represent the latest working condition of

the weather radar. Suppose the condition of weather radar can be represented by multidimensional time-series data, a sliding window is firstly applied to segment the data into batches and reshape the data into the format (number of windows, window length, number of monitoring parameters). This produces the data vector corresponding to each LSTM cell as shown in Figure 4. Denote the training dataset as $D = \{x, y\}$, where x represents the multidimensional time-series data, and y represents the state parameter representing the health state of the weather radar. The network training aims to estimate the weights and bias parameters that characterize the predictive model. This is conducted by gradient-based optimization algorithms.

3.3. Health Indicator Construction. Suppose the LSTM-based predictive model is well trained and is then deployed online, given any time instant t, one can make a prediction $\widehat{y_{t+1}}$ for a newly arrived real-time monitoring data x_t within a time window length n, where $x_t = [x^{t-n+1}, \cdots, x^{t-1}, x^t]$. As shown in Equation (1). then calculate the deviation ρ_t between the prediction $\widehat{y_t}$ and the actual measurement y_t, where σ_t measures the dispersion under healthy conditions and is calculated based on the entire training dataset.

$$\rho_t = \log \left(\frac{(y_t - y_t \wedge)^2}{\sigma_t} \right). \tag{1}$$

Given a time instant, fault alarm would be triggered once its deviation ρ_t greater than a user-specified threshold $\rho_{\text{threshold}}$, which is set as 0.78 in this study. However, the likelihood of false alarms would be high due to the turbulence of the working condition. To alleviate the issue, a health indicator needs to be constructed by aggregating the features of deviation within a time duration. The key idea is that the number of occurrences beyond the threshold within a time duration can be considered as a precursor of the possibility or severity of abnormalities. Suppose the length of the time window for health indicator construction is m, we derive the health indicator as to the portion of occurrences less than the threshold in Equation (2). The health indicator can be used to track the health evolution of weather radar and provides references to support maintenance planning.

$$H_t = \frac{\sum_{j=1}^m I\left(\rho^{t-j+1} \le \rho_{\text{threshold}}\right)}{m}, \tag{2}$$

where H_t is the health indicator at time t, and $I(\bullet)$ is the indicator function, which equals 1 for deviation less than the threshold, and otherwise equals 0. The health indicator ranges from 0 to 1. The higher the health indicator, the better the performance of weather radar.

4. Case Study

This section demonstrates the real application of the proposed framework to monitor the health evolution of weather radar. Section 4.1 describes the problem formulation and model development. Section 4.2 presents the results and
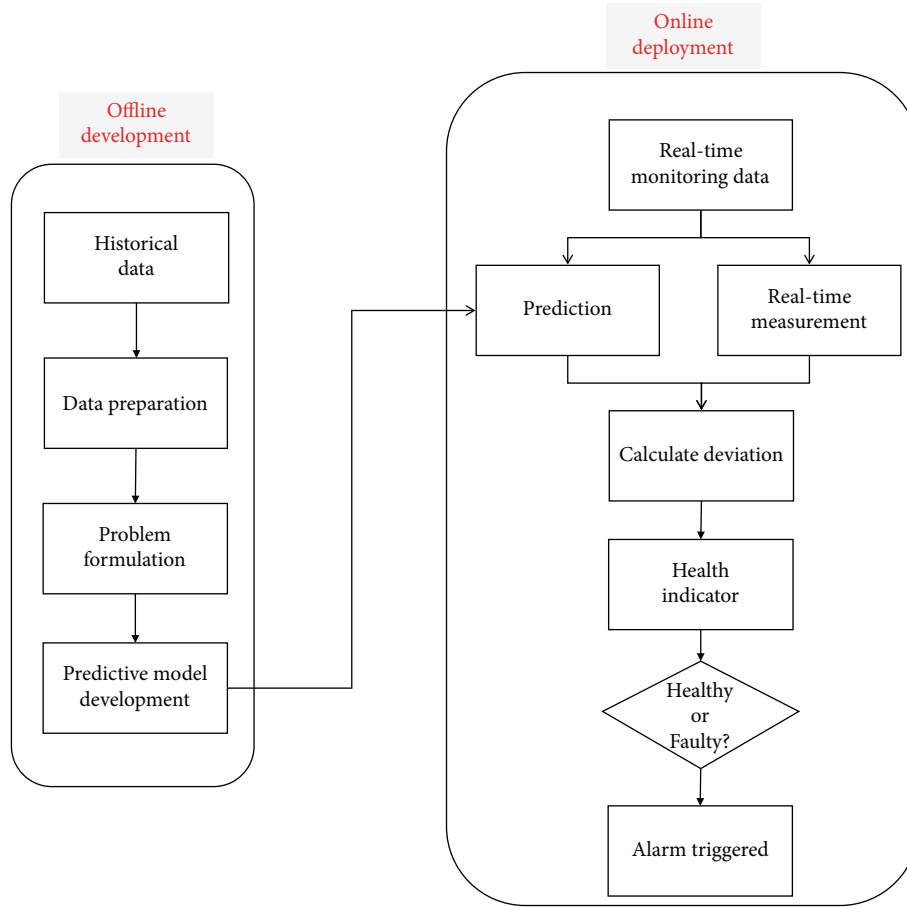
Figure 2: Flowchart of the proposed health monitoring framework for the weather radar.

discussions. The proposed framework was developed based on Python v3.6 and TensorFlow v1.5.0 using a desktop with Intel Core i7 9700 CPU@3.00GHz and 32 GB DDR4 RAM.

4.1. Problem Formulation and Model Development. For problem formulation, we apply the two-stage approach proposed in Section 3.1 to process the historical data as follows. (1) Use the maintenance records to calibrate the fault alarm records. Any fault alert records that happen within 6 minutes forward or backward of the maintenance records would be annotated as the actual faulty condition (1), otherwise healthy condition 0; (2) investigate the association between the monitoring parameters and the calibrated fault alarm records using the stepwise regression method [20]. We start with no monitoring parameter and test the addition of each monitoring parameter based on a linear regression model. The monitoring parameter is added if its inclusion can statistically significantly improve the model fit. Repeat this process until no parameter can further improve the model.

Indeed, the parameters considered important for fault detection might vary accordingly in different radar stations. This would detrimentally affect the stability of the prognostic model. Therefore, the feature selection is conducted using the historical data from 31 radar stations as summarized in Table 1. For instance, in the first radar station, we analyzed

the data collected between 1/1/2019 and 10/14/2020. The data contains 177814 examples with 139 monitoring parameters, each of which is collected every 6 minutes, 57625 fault alarm records, and 8 maintenance records. The number of false fault alarms is far greater than the actual number of faults when comparing the number of fault alarm records and the maintenance records. This highlights the limitation of the current practice using a predefined threshold as discussed in Section 3.1.

We proceed to identify the top monitoring parameters for each radar station, respectively, which account for 95% of the sum of the absolute value of the regression coefficient. Then, aggregate all the identified monitoring parameters. For the parameters shared in multiple stations, we sum up their regression coefficient in each station, namely, aggregated regression coefficient. The importance of each parameter can be further measured by the percentage of contribution to the total aggregated regression coefficient. As such, 38 monitoring parameters are identified as summarized in Table 2 in descending order. Expert judgment from the radar specialist is used as additional data for aiding feature selection. Accordingly, we screen out the parameters with an index within a range [24, 25] and [30, 38]. Finally, this results in 27 monitoring parameters in this study. This could help eliminate the parameter that is not important from a perspective of radar operation and also reduce the
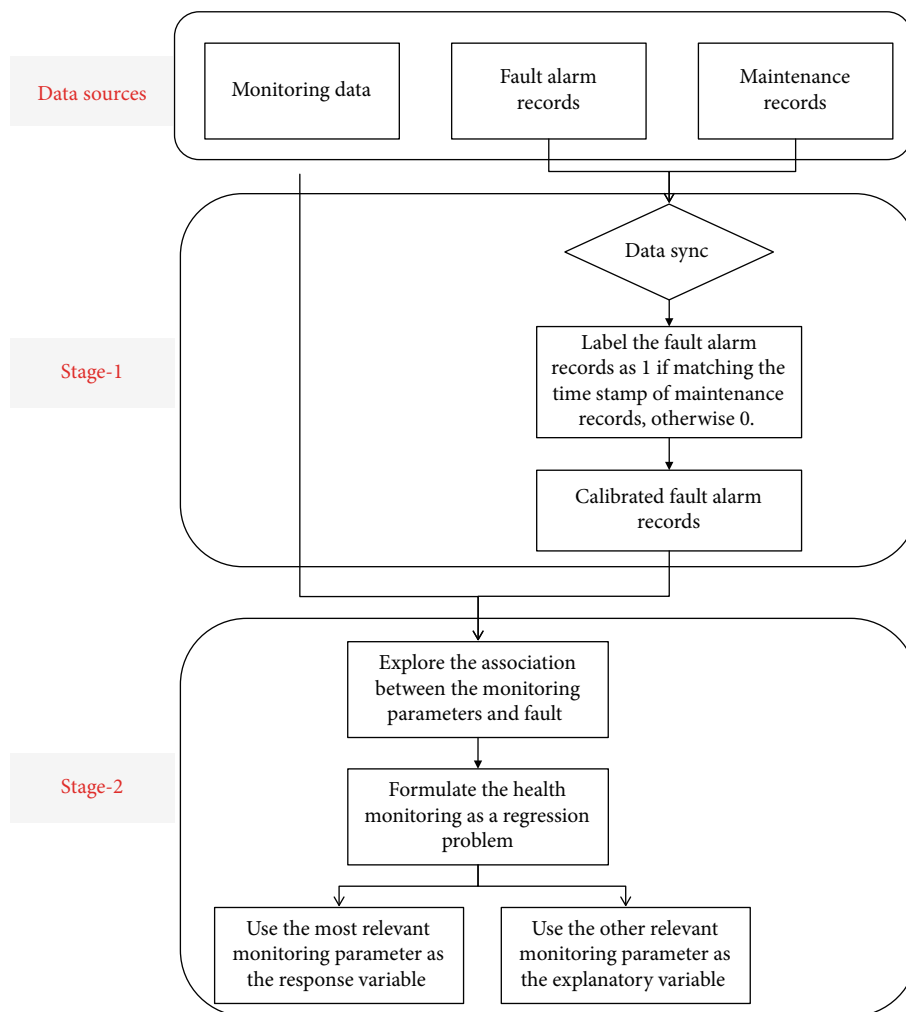
FIGURE 3: A two-stage approach for the problem formulation of the health monitoring of weather radar.
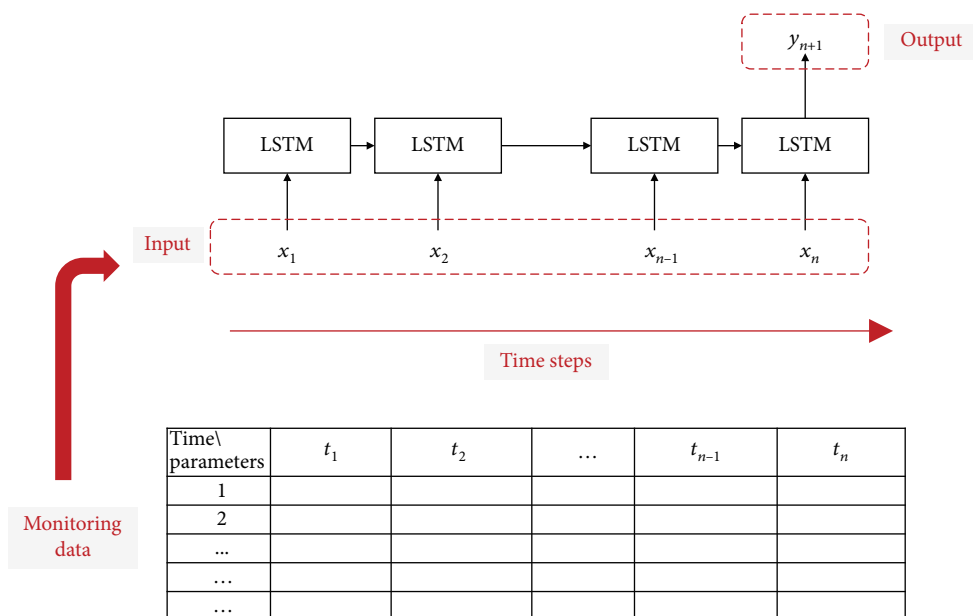
FIGURE 4: An illustration of the LSTM-based predictive model with a sliding window n and a prediction step 1.

Table 1: Summary of the historical dataset from 31 radar stations.

Index	Starting date	Ending date	Number of data	Number of fault alarms	Number of maintenance records
1	1/1/2019	10/14/2020	177814	57625	8
2	1/1/2016	12/31/2017	326441	1119	4
3	1/1/2016	12/31/2017	168695	1332	4
4	1/1/2016	12/31/2017	174460	168	4
5	1/1/2016	12/29/2017	150898	1168	3
6	1/1/2016	12/31/2017	360754	1673	3
7	1/1/2016	12/31/2017	224993	2783	2
8	1/1/2016	12/31/2017	293327	3647	2
9	1/1/2016	12/31/2017	180917	25	2
10	1/1/2016	12/31/2017	196358	3012	2
11	1/1/2016	12/31/2017	168769	3963	2
12	1/1/2016	12/31/2017	355831	1069	2
13	1/1/2016	12/31/2017	174854	1796	2
14	1/1/2016	12/31/2017	185265	1571	2
15	1/1/2016	12/31/2017	265552	1063	1
16	2/25/2016	12/31/2017	248989	4734	1
17	1/1/2016	12/5/2017	167021	1233	1
18	1/1/2016	12/31/2017	164983	635	1
19	1/1/2016	12/31/2017	181167	8682	1
20	1/1/2016	12/31/2017	314534	5571	1
21	1/1/2016	12/31/2017	174489	391	1
22	1/1/2016	12/31/2017	180082	2781	1
23	1/1/2016	12/31/2017	116269	2222	1
24	1/1/2016	12/31/2017	172160	136	1
25	5/23/2016	12/31/2017	143409	981	1
26	1/1/2016	12/31/2017	224820	4674	1
27	5/23/2016	12/31/2017	143994	119	1
28	1/1/2016	12/31/2017	187362	8693	1
29	1/1/2016	12/31/2017	437120	776	1
30	1/1/2016	12/31/2017	203572	4423	1
31	1/1/2016	12/31/2017	140639	3316	1

dimensionality of the data to facilitate the following mode development.

The parameter of ANT_AVG_PWR has the strongest relationship with a regression coefficient far greater than that of the other monitoring parameters. Therefore, the parameter of ANT_AVG_PWR is set as the response variable to represent the radar state, referred to as the state parameter in the following discussions. The other monitoring parameters constitute a 27-dimensional feature matrix describing the operating condition of weather radar and are used as the explanatory variables in the predictive model.

To demonstrate the proposed framework, we examine that whether the proposed framework can provide an early warning of the occurrence of an actual fault on 2020/01/14. A detailed failure analysis report showed that the root cause is the inverse peak overcurrent resulting from a transmitter modulator failure. We adopt the data collected both before and after the fault occurrence that is from 2019/11/01 to 2020/01/02 for model development. Specifically, the radar worked under healthy conditions from 2019/11/01 to 2020/01/02, and hence the corresponding data is used as the training dataset with 15435 examples; use the data between 2020/01/03 and 2020/01/20 as the test dataset with 4022 examples in either faulty or health condition. The training and test datasets are standardized and are reshaped with a time window length of 15. The model architecture consists of an LSTM layer.

4.2. Results and Discussions. Figure 5 shows a comparison between the actual state parameter and the LSTM-based prediction in both training and testing phases, where the x-axis is the operational time of weather radar, and the y-axis is the state parameter. The prediction shows a good fit for the actual measurement in the training phase. A significant difference is observed between the prediction and actual measurement in the testing phase, which indicates the occurrence of a radar fault.

TABLE 2: The top monitoring parameters associated with the calibrated fault alarm records of weather radar based on the historical dataset from 31 radar stations.

Index	Monitoring parameters	Aggregated regression coefficient	Importance measure	Description
1	ANT_AVG_PWR	71.19	35.12%	Average power of horizontally oriented antennas
2	XMTR_AVG_PWR	35.28	17.41%	Average power of transmitter
3	ANT_PEAK_PWR	26.49	13.07%	Peak power of horizontally oriented antennas
4	XMTR_PEAK_PWR	14.88	7.34%	Peak power of transmitter
5	EXPECTED_REFL_AMP8	7.29	3.60%	Reflectivity expectation 8
6	MEASURED_RF8_AMP3	4.19	2.07%	KD calibration measurement 3
7	MEASURED_REFL_AMP7	4.02	1.98%	Reflectivity measurement 7
8	MEASURED_REFL_AMP2	3.9	1.92%	Reflectivity measurement 2
9	MEASURED_REFL_AMP8	3.56	1.76%	Reflectivity measurement 8
10	UNFILTERED_LIN_CHAN_PWR	3.2	1.58%	Power of the horizontal channel before filtering
11	ANT_PWR_MTR_ZERO	2.81	1.39%	Power zero-calibration of horizontally oriented antennas
12	MEASURED_RF8_AMP2	2.4	1.18%	KD calibration measurement 2
13	MEASURED_REFL_AMP3	2.2	1.09%	Reflectivity measurement 3
14	EXPECTED_REFL_AMP6	1.7	0.84%	Reflectivity expectation 6
15	EXPECTED_RF8_AMP3	1.52	0.75%	KD calibration expectation 3
16	MEASURED_RF8_AMP6	1.48	0.73%	KD calibration measurement 6
17	MEASURED_REFL_AMP1	1.45	0.72%	Reflectivity measurement 1
18	MEASURED_RF8_AMP4	1.43	0.71%	KD calibration measurement 4
19	FILTERED_LIN_CHAN_PWR	1.31	0.65%	Power of the horizontal channel filtered
20	MEASURED_REFL_AMP4	1.31	0.65%	Reflectivity measurement 4
21	MEASURED_RF8_AMP5	1.25	0.62%	KD calibration measurement 5
22	EXPECTED_RF8_AMP1	1.18	0.58%	KD calibration expectation 1
23	MEASURED_RF8_AMP1	1.16	0.57%	KD calibration measurement 1
24	EXPECTED_RF8_AMP4	1.1	0.54%	KD calibration expectation 4
25	IDU_TEST_DETECTIONS	1.1	0.54%	Number of interference detections
26	EXPECTED_REFL_AMP1	1.08	0.53%	Reflectivity expectation 1
27	MEASURED_REFL_AMP6	0.95	0.47%	Reflectivity measurement 6
28	XMTR_PWR_MTR_ZERO	0.85	0.42%	Power zero-calibration of transmitter
29	EXPECTED_REFL_AMP4	0.59	0.29%	Reflectivity expectation 4
30	EXPECTED_REFL_AMP5	0.49	0.24%	Reflectivity expectation 5
31	EXPECTED_RF8_AMP6	0.33	0.16%	KD calibration expectation 6
32	EXPECTED_RF8_AMP5	0.3	0.15%	KD calibration expectation 5
33	EXPECTED_REFL_AMP7	0.2	0.10%	Reflectivity expectation 7
34	POWER_METER_RATIO_DB	0.18	0.09%	The power ratio of transmitter to antenna
35	EXPECTED_REFL_AMP3	0.1	0.05%	Reflectivity expectation 3
36	RNLPLG	0.1	0.05%	Long pulse noise level
37	EXPECTED_REFL_AMP2	0.08	0.04%	Reflectivity expectation 2
38	MEASURED_REFL_AMP5	0.05	0.02%	Reflectivity measurement 6

We further calculate the deviation between the actual measurement and prediction according to Equation (1). Figure 6 displays the deviation's temporal evolution and distribution. In Figure 6(a), the deviation fluctuates in healthy conditions below the threshold value as illustrated by the red dotted line and then tends to increase rapidly once an anomaly happens. As expected, the distribution of the deviation is positively skewed in Figure 6(b). A bimodal distribution is observed and shows the existence of two different modes (i.e., healthy and faulty conditions) in the operational

FIGURE 5: A comparison between the actual state parameter and the LSTM-based prediction.
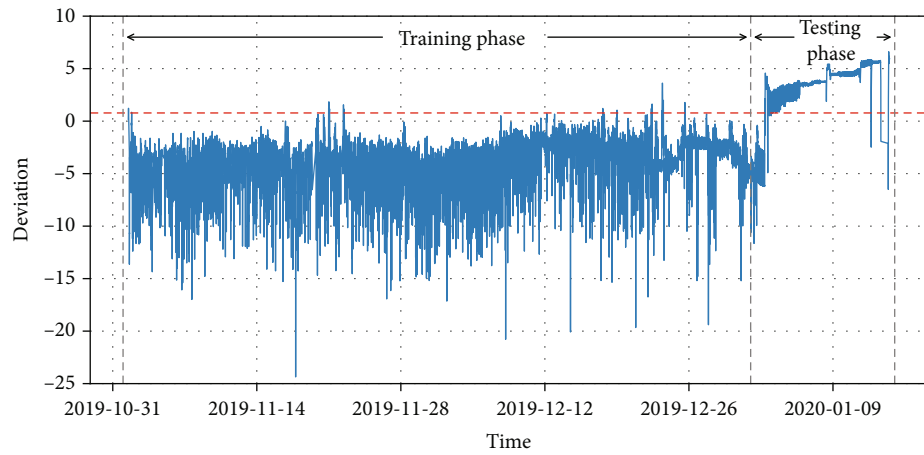
(a)
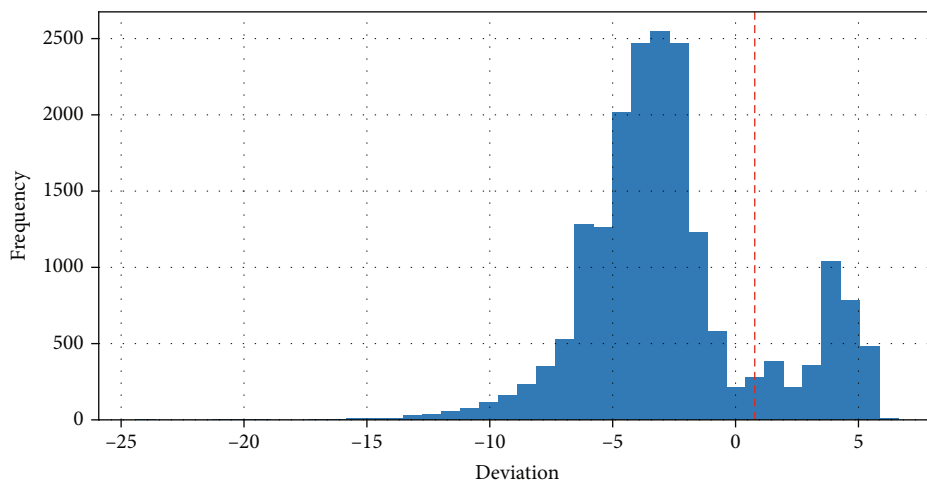
(b)

FIGURE 6: (a) Temporal evolution of the deviation between prediction and actual measurement. (b) Distribution of the deviation between prediction and actual measurement.
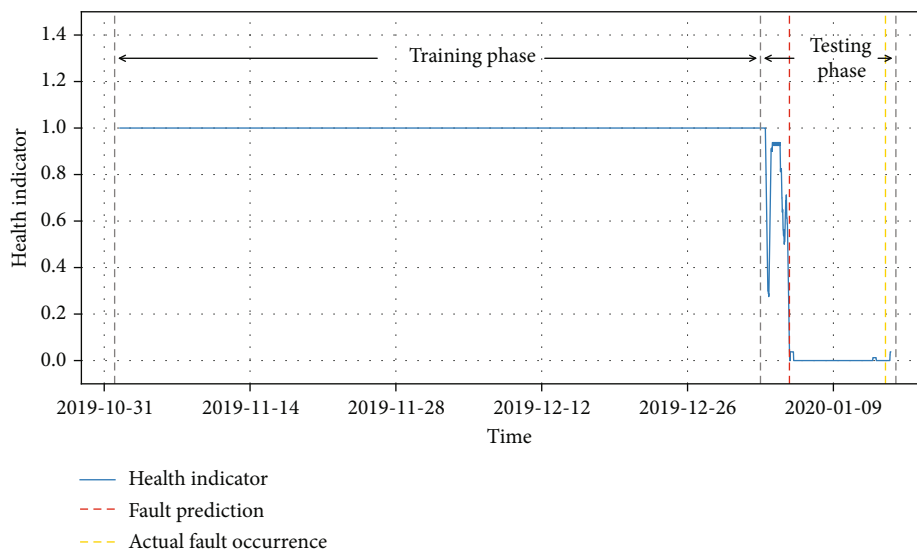
FIGURE 7: Temporal evolution of the health indicator based on the proposed health monitoring framework.

weather radar. Only a few occurrences beyond the threshold value of 0.78 and provide the basis to construct the health indicator.

The health indicator is derived by examining the deviation calculated within a duration of 80 measurements. This is equivalent to 8 hours since the measurement interval is 6 minutes. In other words, we determine the radar condition based on its overall performance within an 8-hour duration, to alleviate the impacts of the turbulence of working conditions. The resulting health indicator is illustrated in Figure 7, where the yellow line marks the time of actual fault occurrence and the red line marks the fault prediction given a threshold of health indicator as 0.05. Specifically, the time of fault prediction triggered is on 2020/01/04 at 17:15, which is nearly 10 days ahead of the actual fault occurrence on 2020/01/14. This would provide an early warning and hence avoid serious consequences and unscheduled downtime. Also, an early warning would provide sufficient time to order the repair or replacement parts as needed. Note that specifying the threshold of health indicators involves a trade-off between the operational economics and the risk of missed detections of actual faults. A higher threshold value leads to a lower risk of missed detection but raises operational costs.

5. Conclusions

In this paper, we developed a deep learning-based health monitoring framework based on the real-time monitoring parameters in weather radar. Specifically, we proposed a two-stage approach to address the issues of fault scarcity and abundant false fault alarm records in the current practice. Then, formulate the health monitoring framework as a regression problem based on the monitoring parameter relevant to actual radar fault. An LSTM model was developed to represent the temporal evolution of radar under healthy conditions. In doing so, any anomaly can be captured by the deviation between the actual measurement and the prediction provided by the LSTM. Ultimately, a health indicator of weather radar was constructed based on the portion of the occurrence of deviation beyond a user-specified threshold within a time window. The effectiveness of the proposed framework was validated by the data collected from 2019/01/01 to 2020/10/14. The results showed that the proposed framework successfully provided an early warning of the actual fault occurrence on 2020/01/14. Future work would be the development of maintenance planning based on the health monitoring framework and case studies using the monitoring data collected in other radar stations.

Data Availability

The data are not publicly available due to privacy restrictions.

Conflicts of Interest

The authors declare that there is no conflict of interest regarding the publication of this paper.

Acknowledgments

References

[1] P. Meischner, Ed., *Weather Radar: Principles and Advanced Applications*, Springer Science & Business Media, 2005.

[2] Y. Lyu, Z. Pang, C. Zhou, and P. Zhao, "Prognostics and health management technology for radar system," in *MATEC Web of Conferences (Vol. 309, p. 04009)*, EDP Sciences, 2020.

[3] W. Li, W. Zhou, Y. M. Wang, C. Shen, X. Zhang, and X. Li, "Meteorological radar fault diagnosis based on deep learning," in *2019 International Conference on Meteorology Observations (ICMO)*, pp. 1–4, ChengDu, China, 2019.

[4] H. Z. Cheng and X. F. Cheng, "A radar fault diagnosis expert system based on improved CBR," in *Applied Mechanics and Materials (Vol. 432, pp. 432-436)*, Trans Tech Publications Ltd., 2013.

[5] H. Yan, "Exploration and research on fault maintenance system of new generation weather radar," *Journal of Atmospheric Science Research*, vol. 2, no. 2, 2019.

[6] N. Khan, I. Yaqoob, I. A. T. Hashem et al., "Big data: survey, technologies, opportunities, and challenges," *The Scientific World Journal*, vol. 2014, 18 pages, 2014.

[7] J. C. da Silva, A. Saxena, E. Balaban, and K. Goebel, "A knowledge-based system approach for sensor fault modeling, detection and mitigation," *Expert Systems with Applications*, vol. 39, no. 12, pp. 10977–10989, 2012.

[8] W. Sun, J. Chen, and J. Li, "Decision tree and PCA-based fault diagnosis of rotating machinery," *Mechanical Systems and Signal Processing*, vol. 21, no. 3, pp. 1300–1317, 2007.

[9] A. Diez, N. L. D. Khoa, M. Makki Alamdari, Y. Wang, F. Chen, and P. Runcie, "A clustering approach for structural health monitoring on bridges," *Journal of Civil Structural Health Monitoring*, vol. 6, no. 3, pp. 429–445, 2016.

[10] C. Wang and S. Zhou, "Contamination source identification based on sequential Bayesian approach for water distribution network with stochastic demands," *IISE Transactions*, vol. 49, no. 9, pp. 899–910, 2017.

[11] I. Goodfellow, Y. Bengio, and A. Courville, *Deep Learning*, MIT Press, Cumberland, 2016.

[12] X. Chen, J. Chen, X. Han et al., "A light-weighted cnn model for wafer structural defect detection," *IEEE Access*, vol. 8, pp. 24006–24018, 2020.

[13] H. Shao, M. Xia, J. Wan, and C. De Silva, "Modified stacked auto-encoder using adaptive Morlet wavelet for intelligent fault diagnosis of rotating machinery," *IEEE/ASME Transactions on Mechatronics*, 2021.

[14] H. Shao, W. Li, M. Xia et al., "Fault diagnosis of a rotor-bearing system under variable rotating speeds using two-stage parameter transfer and infrared thermal images," *IEEE Transactions on Instrumentation and Measurement*, vol. 70, pp. 1–11, 2021.

[15] T. Han, C. Liu, R. Wu, and D. Jiang, "Deep transfer learning with limited data for machinery fault diagnosis," *Applied Soft Computing*, vol. 103, article 107150, 2021.

[16] J. Caceres, D. Gonzalez, T. Zhou, and E. L. Droguett, "A probabilistic Bayesian recurrent neural network for remaining useful life prognostics considering epistemic and aleatory uncertainties," *Structural Control and Health Monitoring*, vol. 28, no. 10, article e2811, 2021.

[17] R. Zhao, R. Yan, Z. Chen, K. Mao, P. Wang, and R. Gao, "Deep learning and its applications to machine health monitoring," *Mechanical Systems and Signal Processing*, vol. 115, pp. 213–237, 2019.

[18] F. Jia, Y. Lei, J. Lin, X. Zhou, and N. Lu, "Deep neural networks: a promising tool for fault characteristic mining and intelligent diagnosis of rotating machinery with massive data," *Mechanical Systems and Signal Processing*, vol. 72-73, pp. 303–315, 2016.

[19] H. D. Nguyen, K. P. Tran, S. Thomassey, and M. Hamad, "Forecasting and anomaly detection approaches using LSTM and LSTM autoencoder techniques with the applications in supply chain management," *International Journal of Information Management*, vol. 57, article 102282, 2021.

[20] C. K. Ing and T. L. Lai, "A stepwise regression method and consistent model selection for high-dimensional sparse linear models," *Statistica Sinica*, vol. 21, no. 4, pp. 1473–1513, 2011.

Hindawi

Research Article

Enhancing Interpretability of Data-Driven Fault Detection and Diagnosis Methodology with Maintainability Rules in Smart Building Management

Michael Yit Lin Chew iD **and Ke Yan** iD

Department of the Built Environment, National University of Singapore, Singapore 117566

Correspondence should be addressed to Ke Yan; yanke@nus.edu.sg

Data-driven fault detection and diagnosis (FDD) methods, referring to the newer generation of artificial intelligence (AI) empowered classification methods, such as data science analysis, big data, Internet of things (IoT), industry 4.0, etc., become increasingly important for facility management in the smart building design and smart city construction. While data-driven FDD methods nowadays outperform the majority of traditional FDD approaches, such as the physically based models and mathematically based models, in terms of both efficiency and accuracy, the interpretability of those methods does not grow significantly. Instead, according to the literature survey, the interpretability of the data-driven FDD methods becomes the main concern and creates barriers for those methods to be adopted in real-world industrial applications. In this study, we reviewed the existing data-driven FDD approaches for building mechanical & electrical engineering (M&E) services faults and discussed the interpretability of the modern data-driven FDD methods. Two data-driven FDD strategies integrating the expert reasoning of the faults were proposed. Lists of expert rules, knowledge of maintainability, international/local standards were concluded for various M&E services, including heating, ventilation air-conditioning (HVAC), plumbing, fire safety, electrical and elevator systems based on surveys of 110 buildings in Singapore. The surveyed results significantly enhance the interpretability of data-driven FDD methods for M&E services, potentially enhance the FDD performance in terms of accuracy and promote the data-driven FDD approaches to real-world facility management practices.

1. Introduction

1.1. Motivation. Aligning with the fast development of artificial intelligence (AI) technology, data-driven fault detection and diagnosis (FDD) plays an essential role in modern smart building maintenance and management systems [1]. However, while the data-driven FDD models are often viewed as black-box models, the interpretability of FDD models hinders the methods to be widely applied to real-world applications [2, 3]. Expert rules and standards are helpful for data-driven FDD methods to be adapted to real-world scenarios. The expert rules and standards not only increase the interpretability level of the data-driven FDD methods but also improve the FDD performance in terms of diagnosis accuracy rates. According to our literature survey, the rele-

vant expert knowledge is considered as a research gap in the field and is highly demanded to detect and diagnose possible faults in building equipment and services [4–6]. In this study, we are interested to concretize the expert knowledge, using maintainability rules and standards for FDD, both regionally and globally, of different building mechanical & electrical engineering (M&E) services, including HVAC systems, plumbing & sanitary, fire safety, electrical and elevators & escalators systems, and their critical components.

1.2. Background. Building fault detection and diagnosis (FDD) methods automatically recognize potential and existing building facility faults based on existing standards, expert knowledge and sensor information, which are important techniques ensuring the safety, efficiency and quality

services of building infrastructure and development [7, 8]. According to the different approaches replying to different types of evident information, FDD methods are categorized into data-driven FDD, physical model based FDD and mathematical model based FDD methods [9]. Data-driven FDD builds computational models based on historical sensor data, while different types of building faults are recognized as classes [10]. A physical model based FDD understands the whole building system using physics-based models and usually requires a significant amount of prior knowledge for faults identifications [11, 12]. A mathematical model based FDD methods also requires prior physics knowledge to define a rule space for an inferencing method searching for the corresponding faults [13, 14].

Data-driven fault detection and diagnosis methods represent the next-generation facility management and maintenance techniques adopting modern AI techniques, such as sensor networks [15, 16], data analytics [17], big data [18, 19], machine learning (ML) [20, 21], cybernetic intelligence (CI) [22, 23] and Internet of things (IoT) [24, 25] and etc. For different building infrastructures, such as heating, ventilation air-conditioning (HVAC), plumbing, fire safety, electrical and elevator systems. In the era of big data, smart building and smart city, data-driven FDD usually serves as one of the most important applications utilizing big data and one of the hottest research topics in the fields of smart city and industry 4.0 [26–28].

Compared with traditional physical model based and mathematical model based methods, data-driven FDD methods are usually more efficient, robust and accurate in detecting and diagnosing various building faults, while the machine learning (ML) techniques, such as the neural networks, are constructed for predictive analysis. The ML techniques are generally much more efficient and effective than traditional PM-FDD, MM-FDD and manual classification methods. For example, for HVAC FDD, the existing works showed FDD accuracy rates over 99% for typical chiller faults and 93% for air handling unit (AHU) faults [29–32]. Traditional approaches, such as the sensitivity test, can only achieve accuracy rates close to 83% for chiller faults and around 80% for AHU faults [33–37]. The 10% to 15% improvement on different FDD approaches saves the energy wasted in buildings significantly, enhances the overall building performance and maintains a sustainable environment for building infrastructure maintenance.

However, the interpretability of the data-driven FDD method has always been the problem for data-driven FDD methods and hinders the data-driven FDD techniques to be widely adopted in real-world applications. While the prediction accuracy and efficiency of the data-driven FDD methods improved significantly in recent years, the internal structures of the AI approaches become more complex, resulting in more challenges for model interpretation [38–41]. The data-driven FDD models were also tentatively called black-box models in many existing publications [42–44], which we believe is not accurate. Many data-driven FDD models are indeed interpretable. For example, Yan et al. [45] presented a decision tree model for FDD of air handling units (AHUs). The decision tree structure is interpretable with if-else rules. However, the if-else rules were not easily recognizable for experts deriving standards for AHU maintenance.

It is evident that the expert knowledge, experience, rules, ISO standards and maintenance guidelines are valuable information and can deeply influence the performance of data-driven FDD methods. Zhao et al. [46] demonstrated that the additional expert knowledge inputs can greatly enhance a Bayesian belief network (BBN) data-driven FDD model's performance by increasing the FDD accuracy for various chiller faults. Li et al. [47] improved [46] by integrated expert knowledge into a diagnostic Bayesian network (DBN) for AHU fault FDD. The reasonings of the AHU FDD were plotted by local casual graphs. The main shortcoming of the works [46, 47] is that the expert knowledge inputs were generally generated based on the authors' hypotheses.

1.3. Approach. In this study, we reviewed the recent publications on data-driven FDD for building mechanical & electrical engineering (M&E) services, including HVAC, plumbing, fire safety, electrical and elevator systems. Different M&E faults were surveyed over 110 buildings in Singapore, including commercial, hotels, industrial, institutional, clinical and residential buildings, for all three stages of infrastructure management life-cycles, in all design, construction and management stages. The expert knowledge of M&E FDD is converted into maintainability rules and international/local standards in Singapore. It is evident that the conveyed maintainability rules greatly enhance the interpretability of the data-driven FDD approach and potentially improve the diagnosis accuracy.

We propose two data-driven FDD methods integrating the maintainability rules for general facility management in buildings, particularly focusing on FDD. The two specific data-driven FDD methods integrating maintainability rules are 1. data-driven expert rules for decision making in smart building facility FDD; and 2. maintainability rules as inputs for data-driven FDD systems. The actual implementations of the two proposed approaches were omitted, while there were existing implementations such as [46, 47]. The main aim of this study is to specify the expert knowledge pool of M&E FDD using maintainability rules shown in Section 4. The specification greatly enhances the interpretability of the existing M&E FDD methods.

1.4. Contributions. The current work involves the following contributions to the state-of-art.

(i) Extending the existing data-driven FDD from HVAC systems to the infrastructure of the whole building. The majority of the existing work of data-driven FDD integrating expert knowledge, e.g., maintainability rules, focuses on HVAC FDD. In this study, we extend the above-mentioned data-driven FDD framework to the whole building system. The targeted facilities include almost all M&E services for smart building design

(ii) Identifying expert rules and standards for various M&E faults in buildings. A total of 110 buildings in Singapore, including commercial, hotels, industrial, institutional, clinical and residential buildings were surveyed, over all three stages of infrastructure management life-cycles, in all design, construction and management stages, collecting necessary FDD information based on experts' knowledge and international/local standards in Singapore. In this way, typical faults for the major M&E equipment are surveyed with detailed experts' rules and standards stated in tables. This main contribution impacts the literature for data-driven FDD approaches targeting building M&E services significantly

(iii) Enhancing the interpretability of the existing data-driven FDD methods for building infrastructure faults. The interpretability of the data-driven FDD methods has been a bottleneck problem for a long time. The surveyed expert rules and standards bridge the gap between theoretical FDD strategy and real-world practices. The interpretability enhancement greatly improves the practicality of the data-driven methods in Industry 4.0 [48] and Construction 4.0 [49].

(iv) Potentially improving the diagnosis accuracy of the existing data-driven FDD methods for building infrastructure faults. According to the literature study, such as the works of [46, 47], expert knowledge, e.g., the maintainability rules enhance the FDD performance significantly in terms of accuracy. The diagnosis accuracy improvements are justified by various publications [46, 47, 50–52].

2. Literature Review for Interpretability Study of the Existing M&E Services FDD Methods

Intelligent facilities management is one of the important topics for smart city design, smart building maintenance system development, Industry 4.0 and Construction 4.0. Techniques based on AI and data-driven approaches attract increasing attention from various perspectives. Besides the effectiveness and robustness of the data-driven approaches for data-driven FDD, the shortcomings and issues, such as the interpretability of the data-driven model and the efficiency for data-driven FDD algorithms, were raised in recent years.

Yan et al. [45] introduced a decision tree induction (DTI) based FDD method for detecting and diagnosing AHU faults. The proposed method is data-driven, and interpretable with a post-pruned binary tree structure. The main concern of [45] is that the derived rules do not explicitly map to expert reasoning available in the HVAC system design. Most of the DTI rules were still unreadable from the perspective of HVAC engineers. Mulumba et al. [50] worked on a Kalman filter-based FDD reasonings for AHU faults. The method works for various AHU faults and is also considered a data-driven approach. The shortcoming is again

that the Kalman filter rules do not map correspondingly to HVAC experts. Srinivasan et al. [51] showed the importance of explainable AI (XAI) for chiller fault detection systems to gain human trust. Li et al. [52] developed an explainable one-dimensional convolutional neural networks (CNN)-based fault diagnosis method for building HVAC systems.

Besides the interpretability study of FDD for HVAC systems, there are existing data-driven FDD approaches proposed for other M&E service systems. Kumar et al. [53] developed a deep learning detecting defects in sewerage systems. The deep learning structure relies on the CNN for object detection in images. The image processing technology using CNN is more interpretable using expert knowledge compared to other ML techniques. Gonzalez-Jimenez et al. [54] surveyed the existing fault diagnostic methods to examine faults for electric drives and revisited the general workflow using ML techniques for electric drive FDD. The main drawback of the data-driven FDD method as concluded in [54] is the lack of interpretability and the lack of explanations for specific phenomena in every particular electric drive. Gavan et al. [55] proposed to integrate expert rules and data-driven FDD methods to develop a positive energy building in France. The project has a nice workflow chart utilizing expert rules for building data analysis and FDD practices. However, it is an ongoing project and the performance of the proposed workflow is yet to be verified.

All the above-surveyed existing works showed that there are already quite many efforts on integrating expert rules and reasonings into the existing data-driven FDD methods to enhance the interpretability of the methods as well as improve the FDD performance on the classification accuracy for building maintenance problems. However, there still exist gaps between expert rules and data-driven methods, such as neural networks. The gap is mainly from the reasoning of AI and the ordinary reasoning of human beings. The most appropriate matching and fitting using the expert rules with the modern data-driven FDD methods remain unknown and desired further explorations, such as the current study. The current study expands the scope of the FDD methods and greatly enhances the applicable area of data-driven FDD methods in building services.

3. Integrating the Maintainability Rules into Data-Driven FDD for M&E Services

Two types of data-driven FDD strategies are available in general for the concept of next-generation AI-technology integrated smart buildings for facility management and maintenance. The first strategy is named post-caution maintenance. This strategy is widely adopted for modern buildings when expert knowledge of precautions is lacking. Without sufficient rules and guidance in the stages of design and construction, the only option left is monitoring the facilities regularly using physical, mathematical or AI-driven models and detecting potential errors with frequent data analysis. The expert knowledge and rules are added as an additional layer of the ML model for performance enhancement. Existing examples of post-caution maintenance include [46, 47].

TABLE 1: Normative References/Standards referred to for Mechanical and Electrical Systems.

Normative references/standards referred to for mechanical and electrical systems	
AHRI 260	Sound rating of ducted air moving and conditioning equipment
ANSI/ASHRAE 188-2018	Legionellosis: Risk management for building water systems
ANSI/ASHRAE/ACCA standard 180-2018	Standard practice for inspection and maintenance of commercial building HVAC systems
ANSI/ASHRAE/IES standard 90.1-2016	Energy standard for buildings except low- rise residential buildings
ANSI/ASHRAE/IES/USGBC standard 189.1-2014	Standard for the Design of High- Performance Green Buildings
AS 1668.2-2012	The use of ventilation and airconditioning in buildings — Mechanical ventilation in buildings
AS 1735.1 : 2016	Lifts, escalators and moving walks. General requirements
AS 2293 SET:2005	Emergency escape lighting and exit signs set
AS HB 197 : 1999	An introductory guide to the slip resistance of pedestrian surface materials
AS/NZS 2293.2 : 2019	Emergency escape lighting and exit signs for buildings inspection and maintenance
AS/NZS 4663 : 2004	Slip resistance measurement of existing pedestrian surfaces
ASHRAE guideline 12-2020	Managing the risk of Legionellosis associated with building water systems
ASME A17.1/CSA B44:2019	Safety code for elevators and escalators
ASME A17.3 : 2020	Safety code for existing elevators and escalators
ASME A17.6 : 2017	Standard for elevator suspension, compensation, and governor systems
BS 1363-4 : 2016	13 A plugs, socket-outlets, adaptors and connection units. Specification for 13 A fused connection units switched and unswitched
BS 5266-1 : 2016	Emergency lighting. Code of practice for the emergency lighting of premises
BS 5306-3 : 2017	Fire extinguishing installations and equipment on premises. Commissioning and maintenance of portable fire extinguishers. Code of practice
BS 5306-8 : 2012	Fire extinguishing installations and equipment on premises. Selection and positioning of portable fire extinguishers. Code of practice
BS 5306-9 : 2015	Fire extinguishing installations and equipment on premises. Recharging of portable fire extinguishers. Code of practice
BS 5655-11 : 2005	Lifts and service lifts. Code of practice for the undertaking of modifications to existing electric lifts
BS 5655-6 : 2011	Lifts and service lifts. Code of practice for the selection, installation and location of new lifts
BS 5839-1 : 2017	Fire detection and fire alarm systems for buildings. Code of practice for design, installation, commissioning and maintenance of systems in non-domestic premises
BS 5839-3 : 1988	Fire detection and alarm systems for buildings. Specification for automatic release mechanisms for certain fire protection equipment
BS 5839-6 : 2019	Fire detection and fire alarm systems for buildings. Code of practice for the design, installation, commissioning and maintenance of fire detection and fire alarm systems in domestic premises
BS 5839-9 : 2011	Fire detection and fire alarm systems for buildings. Code of practice for the design, installation, commissioning and maintenance of emergency voice communication systems
BS 5908-1 : 2012	Fire and explosion precautions at premises handling flammable gases, liquids and dusts. Code of practice for precautions against fire and explosion in chemical plants, chemical storage and similar premises
BS 6391 : 2009	Specification for non-percolating lay flat delivery hoses and hose assemblies for fire-fighting purposes
BS 6423 : 2014	Code of practice for maintenance of low-voltage switchgear and control gear
BS 6626 : 2010	Maintenance of electrical switchgear and control gear for voltages above 1 kV and up to and including 36 kV. Code of practice
BS 7255 : 2012	Code of practice for safe working on lifts
BS 7291-1 : 2010	Thermoplastics pipe and fitting systems for hot and cold water for domestic purpos-es and heating installations in buildings. General requirements
BS 7430 : 2011 + A1 : 2015	Code of practice for protective earthing of electrical installations

Table 1: Continued.

Normative references/standards referred to for mechanical and electrical systems	
BS 7671 : 2018	Requirements for electrical installations. IET wiring regulations
BS 7698-7 : 1996, ISO 8528-7 : 1994	Reciprocating internal combustion engine driven alternating current generating sets. Technical declarations for specification and design
BS 8486-1 : 2007 + A1 : 2011	Examination and test of new lifts before putting into service. Specification for means of determining compliance with BS EN 81. Electric lifts
BS 8512 : 2008	Electric cables. Code of practice for the storage, handling, installation and disposal of cables on wooden drums
BS 8554 : 2015	Code of practice for the sampling and monitoring of hot and cold water services in buildings
BS 8558 : 2015	Guide to the design, installation, testing and maintenance of services supplying water for domestic use within buildings and their curtilages. Complementary guidance to BS EN 806
BS 8899 : 2016	Improvement of fire-fighting and evacuation provisions in existing lifts. Code of practice
BS 9990 : 2015	Non automatic fire-fighting systems in buildings. Code of practice
BS EN 1004 : 2020	Mobile access and working towers made of prefabricated elements. Materials, dimensions, design loads, safety and performance requirements
BS EN 10088-2 : 2014	Stainless steels. Technical delivery conditions for sheet/plate and strip of corro-Sion resisting steels for general purposes
BS EN 1057 : 2006 + A1 : 2010	Copper and copper alloys. Seamless, round copper tubes for water and gas in sanitary and heating applications
BS EN 115-1 : 2008 + A1:2017	Safety of escalators and moving walks. Construction and installation
BS EN 13015 : 2001 + A1:2008	Maintenance for lifts and escalators. Rules for maintenance instructions
BS EN 13121-3 : 2016	GRP tanks and vessels for use above ground. Design and workmanship
BS EN 1402 : 2009	Rubber and plastics hoses and hose assemblies. Hydrostatic testing
BS EN 1567 : 1999	Building valves. Water pressure reducing valves and combination water reducing valves. Requirements and tests.
BS EN 16767 : 2016	Industrial valves. Steel and cast iron check valves
BS EN 1796 : 2013	Plastics piping systems for water supply with or without pressure. Glass-reinforced thermosetting plastics (GRP) based on unsaturated polyester resin (UP)
BS EN 1838 : 2013	Lighting applications. Emergency lighting
BS EN 1947 : 2014	Fire-fighting hoses. Semi-rigid delivery hoses and hose assemblies for pumps and vehicles
BS EN 1982 : 2017	Copper and copper alloys. Ingots and castings
BS EN 1992-1-1 : 2004 + A1 : 2014	Eurocode 2: Design of concrete structures. General rules and rules for buildings
BS EN 3 series	Portable fire extinguishers
BS EN 50172 : 2004, BS 5266-8 : 2004	Emergency escape lighting systems
BS EN 545 : 2010	Ductile iron pipes, fittings, accessories and their joints for water pipe- lines. Requirements and test methods
BS EN 598 : 2007 + A1 : 2009	Ductile iron pipes, fittings, accessories and their joints for sewerage applications. Requirements and test methods
BS EN 61009-2-1 : 1995	Specification for residual current operated circuit-breakers with integral overcur-rent protection for household and similar uses (RCBOs). Applicability of the general rules to RCBOs functionally independent of line voltage
BS EN 62305-1 : 2011	Protection against lightning. General principles
BS EN 694 : 2014	Fire-fighting hoses. Semi-rigid hoses for fixed systems
BS EN 805 : 2000	Water supply. Requirements for systems and components outside buildings
BS EN 806-5 : 2012	Specifications for installations inside buildings conveying water for human consumption. Operation and maintenance
BS EN 81-20 : 2020	Safety rules for the construction and installation of lifts. Lifts for the transport of persons and goods. Passenger and goods passenger lifts
BS EN 81-50 : 2020	Safety rules for the construction and installation of lifts. Examinations and tests. Design rules, calculations, examinations and tests of lift components

TABLE 1: Continued.

Normative references/standards referred to for mechanical and electrical systems	
BS EN ISO 16841 : 2014	Steel wire ropes. Pulling eyes for rope installation. Types and minimum re-quirements
BS EN ISO 21003-2 : 2008 + A1 : 2011	Multilayer piping systems for hot and cold water installations in-side buildings. Pipes
BS EN ISO 21003-3 : 2008	Multilayer piping systems for hot and cold water installations inside build-ings. Fittings
BS EN ISO 21003-5 : 2008	Multilayer piping systems for hot and cold water installations inside build-ings. Fitness for purpose of the system
BS ISO 10916 : 2014	Calculation of the impact of daylight utilization on the net and final energy de-mand for lighting
BS ISO 18738 : 2012	Measurement of lift ride quality. Lift (elevators)
BS ISO 18738-2 : 2012	Measurement of ride quality — Part 2: Escalators and moving walks
CSA Z412-2000 (R2016)	Guideline on office ergonomics
IEC 60079: 2021	Explosive atmosphere standards
IEC 61009-1 : 2010 + AMD1 : 2012 + AMD2:2013 CSV (Consolidated version)	Residual current operated circuit-breakers with integral overcurrent protection for household and similar uses (RCBOs) — Part 1: General rules
IEC 62305-3 : 2010	Protection against lightning — Part 3: Physical damage to structures and life hazard
IEC 62305-4 : 2010	Protection against lightning — Part 4: Electrical and electronic systems within struc-tures
ISO 10816-3 : 2009	Mechanical vibration — Evaluation of machine vibration by measurements on non-rotating parts — Part 3: Industrial machines with nominal power above 15 kW and nominal speeds be-tween 120 r/min and 15 000 r/min when measured in situ
ISO 12242 : 2012	Measurement of fluid flow in closed conduits — Ultrasonic transit- time meters for liquid
IISO 13612-1 : 2014	Heating and cooling systems in buildings — Method for calculation of the system performance and system design for heat pump systems — Part 1: Design and dimensioning
ISO 1452-1 : 2009	Plastics piping systems for water supply and for buried and aboveground drainage and sewerage under pressure – Unplaticized poly(vinyl chloride)(PVC-U) – Part 1: General
ISO 14798 : 2009	Lifts (elevators), escalators and moving walks — Risk assessment and reduction methodology
ISO 16814 : 2008	Building environment design — Indoor air quality — Methods of expressing the quality of indoor air for human occupancy
ISO 2017-1 : 2005	Mechanical vibration and shock — Resilient mounting systems — Part 1: Technical information to be exchanged for the application of isolation systems
ISO 2230 : 2002	Rubber products — Guidelines for storage
IISO 2408 : 2017	Steel wire ropes for general purposes — Minimum requirements
ISO 25745-1 : 2012	Energy performance of lifts, escalators and moving walks — Part 1: Energy measurement and verification
ISO 25745-2 : 2015	Energy performance of lifts, escalators and moving walks — Part 2: Energy calcula-tion and classification for lifts (elevators)
ISO 25745-3 : 2015	Energy performance of lifts, escalators and moving walks — Part 3: Energy calculation and classification of escalators and moving walks
ISO 29463-1 : 2011	High-efficiency filters and filter media for removing particles in air — Part 1: Classi-fication, performance testing and marking
ISO 29463-5 : 2011	High-efficiency filters and filter media for removing particles in air — Part 5: Test method for filter elements
ISO 3864-1 : 2011	Graphical symbols — Safety colours and safety signs — Part 1: Design principles for safety signs and safety markings
ISO 4344 : 2004	Steel wire ropes for lifts — Minimum requirements
ISO 5149-1 : 2014/Amd 1 : 2015	Refrigerating systems and heat pumps - safety and environmental requirements - part 1: Definitions, classification and selection criteria AMENDMENT 1: Correction of QLAV, QLMV
ISO 6182 series	Fire protection - automatic sprinkler systems
ISO 7240 series	Fire detection and alarm systems
ISO 7465 : 2007	Passenger lifts and service lifts — Guide rails for lift cars and counter- weights - T-type

Table 1: Continued.

Normative references/standards referred to for mechanical and electrical systems	
ISO 8995-1 : 2002/Cor 1 : 2005	Lighting of work places — Part 1: Indoor
ISO9996:1996	Mechanical vibration and shock — Disturbance to human activity and performance -classification
IISO/CD 8100-30 : 2019	Lifts for the transport of persons and goods - part 30: Class I, II, III and VI lifts installation
ISO/DIS 22559-1 : 2014	Safety requirements for lifts (elevators) - part 1: Global essential safety requirements (GESRs)
ISO/DTS 8100-21 : 2018	Lifts for the transport of persons and goods - part 21: Global safety parameters (GSPs) meeting the global essential safety requirements (GESRs)
ISO/FDIS 13253 : 2017	Ducted air-conditioners and air-to-air heat pumps - testing and rating for performance
ISO/NP TR 16765 : 2003	Comparison of worldwide safety standards on lifts for firefighters
ISO/PRF 7165 : 2017	Firefighting - portable fire extinguishers - performance and construction
ISO/TR 11071-2 : 2006	Comparison of worldwide lift safety standards -part 2: Hydraulic lifts (elevators)
ISO/TR 25743 : 2010	Lifts (elevators) - study of the use of lifts for evacuation during an emergency
JIS A 4302 : 2006	Inspection standard of elevator, escalator and dumbwaiter
JIS A 4422 : 2020	Toilet seat with shower unit
NFPA 10 : 2013	Standard for portable fire extinguishers
NFPA 101 – 2018	Life safety code
NFPA 110 - 2019	Standard for emergency and standby power systems
NFPA 13 - 2019	Standard for the installation of sprinkler systems
NFPA 14 – 2016	Standard for the installation of standpipe and hose systems
NFPA 25 – 2017	Standard for the inspection, testing, and maintenance of water-based fire protection systems
NFPA 72 – 2019	National Fire Alarm and signaling code
NFPA 780 – 2020	Standard for the installation of lightning protection systems
NFPA 80 – 2019	Standard for fire doors and other opening protectives
SS 141 : 2013	Specification for unplasticised PVC pipe for cold water services and industrial uses
SS 245 : 2014	Specification for glass reinforced polyester sectional water tanks
SS 332 : 2018	Specification for fire doors
SS 375-1 : 2015	Suitability of non-metallic products for use in contact with water intended for human consumption with regard to their effect on the quality of the water - part 1: Specification
SS 403 : 2013	Specification for 13A fused connection units switched and unswitched
SS 480 : 2016	Residual current operated circuit-breakers with integral overcurrent protec- tion for house-hold and similar uses (RCBOs) - general rules
SS 485 : 2011	Specification for slip resistance classification of pedestrian surface materials
SS 508-3 : 2013	Graphical symbols — Safety colours and safety signs — Design princi- ples for graphical symbols for use in safety signs
SS 514 : 2016	Code of practice for office ergonomics
SS 530 : 2014	Code of practice for energy efficiency standard for building services and equipment
SS 531-1 : 2006 (2019)	Code of practice for lighting of work places — Indoor
SS 532 : 2016	Code of practice for the storage of flammable liquids
SS 535 : 2018	Code of practice for installation, operation, maintenance, performance and construction requirements of mains failure standby generating systems
SS 538 : 2008	Code of practice for maintenance of electrical equipment of electrical installations
SS 546 : 2009	Code of practice for emergency voice communication systems in buildings
SS 550 : 2020	Code of practice for installation, operation and maintenance of electric passenger and goods lifts
SS 551 : 2009	Code of practice for earthing
SS 553 : 2016	Code of practice for air-conditioning and mechanical ventilation in buildings
SS 554 : 2016	Code of practice for indoor air quality for air-conditioned buildings
SS 555-1 : 2018	Code of practice for protection against lightning — Part 1: General principles

TABLE 1: Continued.

Normative references/standards referred to for mechanical and electrical systems	
SS 555-3 : 2018	Code of practice for protection against lightning — Part 3: Physical damage to structures and life hazard
SS 555-4 : 2018	Code of practice for protection against lightning — Part 4: Electrical and electronic systems within structures
SS 563-1 : 2010 (2017)	Code of practice for the design, installation and maintenance of emergency lighting and power supply systems in buildings — Part 1: Emergency lighting
SS 563-2 : 2010 (2017)	Code of practice for the design, installation and maintenance of emer- gency lighting and power supply systems in buildings — Part 2: Installation requirements and maintenance procedures
SS 564-1 : 2020	Green data centres - part 1: Energy and environmental management systems
SS 564-2 : 2020	Singapore standard for green data centres — Part 2: Guidance for energy and environmental management systems
SS 575 : 2012	Code of practice for fire hydrant, rising mains and hose reel systems
SS 578 : 2019	Code of practice for use and maintenance of portable fire extinguishers
SS 591 : 2013	Code of practice for long term measurement of central chilled water system energy efficiency
SS 626 : 2017	Code of practice for design, installation and maintenance of escalators and moving walks
SS CP 10 : 2005	Code of practice for the installation and servicing of electrical fire alarm systems
SS CP 48 : 2005	Code of practice for water services
SS CP 5 : 1998	Code of practice for electrical installations
SS CP 52 : 2004	Code of practice for automatic fire sprinkler system
SS CP 82 : 1999	Code of practice for waterproofing of reinforced concrete buildings
SS CP 99 : 2003	Code of practice for industrial noise control
SS EN 3–7 : 2012 (2020))	Portable fire extinguishers — Characteristics, performance requirements and test methods
SS IEC 60598-1 : 2016	Luminaires — Part 1: General requirements and tests
SS ISO 22301 : 2020	Security and resilience - business continuity management systems — Requirements
SS ISO 22313 : 2020	Security and Resilience - Business continuity management systems — Guidance on the use of ISO 22301
V DI 4707 : 2007	Lifts energy efficiency
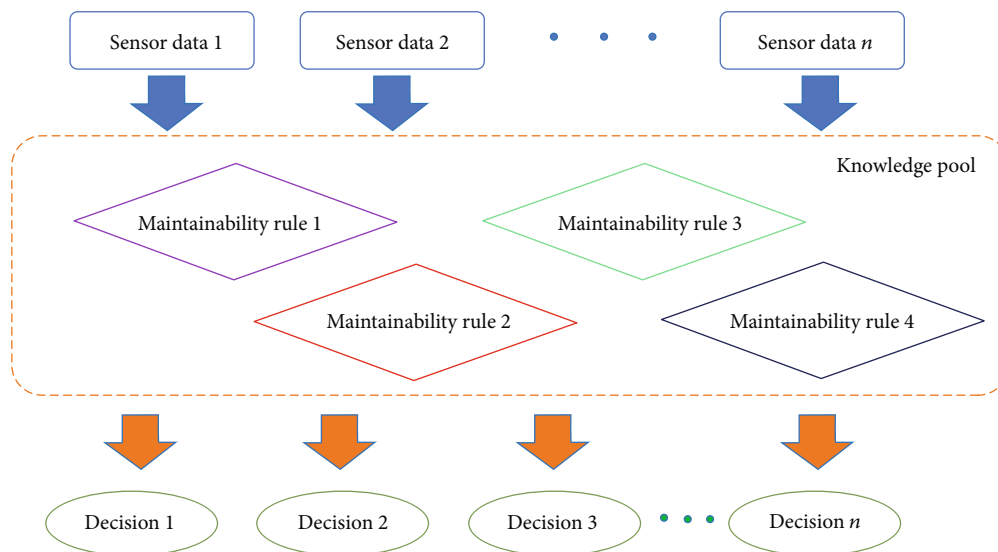
FIGURE 1: Knowledge-based system for precaution maintenance that constructs the knowledge pool using maintainability rules.

Table 2: Elevators & Escalators - Escalator.

Problem	Design	Construction	Maintenance
Escalator and passenger conveyor related maintainability issues Accumulation of debris within the escalator interior Footwear getting stuck between steps Good practice: Escalator cordoned off during maintenance operations to prevent unauthorised access	Ensure that the landing area of escalators and passenger conveyors have a surface that provides a secure foothold for a minimum distance of 0.85 m (measured from the root of the comb teeth) in accordance with AS 1735.1 or equivalent. Ensure that the escalator and its surroundings have sufficient and adequate illumination. The supporting structure for escalators and passenger conveyors should be designed in accordance with BS EN 115-1, SS 626 or equivalent. Comply with the safety code for elevator design and construction in accordance with ASME A17.1/CSA B44, ISO 8100-20, BS 8899 or equivalent. Incorporate anti-climbing, anti-sliding, access restriction and deflecting devices to maintain safe operation in accordance with SS 626 or equivalent.	Installation of escalators should be guided by the relevant standards and codes for safety and reliability in accordance with BS EN 115-1, SS 626 or equivalent. All machinery should be mounted securely and be defect free (e.g., should not have any oil leakage). To ensure safe operation without issues due to corrosion and wear and tear, all escalator components should be of durable and reliable make. All signs, inscriptions and notices should be made of durable materials in accordance with BS EN 115-1, SS 626 or equivalent.	Ensure proper housekeeping of escalator to keep it clean and free of debris. Building owner/operator need to conduct monthly maintenance of escalators (including maintenance of safety switches, sensors, emergency stops, and handrails) in accordance with SS 626, BS EN 115-1 or equivalent. The annual inspection and testing should be performed by an independent authorised examiner (AE). Bar access to the escalator or passenger conveyor with suitable devices and notices/signage displaying "no access/no entry" during maintenance, repair works, or inspections, in accordance with BS EN 115-1, SS 626 or equivalent. Adopt the inspection criteria for safety of escalators in accordance with JIS A 4302. Refer to procedure for ride quality measurements of escalators and moving walks in accordance with BS ISO 18738-2 or equivalent.

The second type of the data-driven FDD strategy is to involve the expert knowledge in the FDD monitoring of the entire life-cycle of all facilities, or precaution maintenance. With the experts in the fields of, e.g., project management, construction, interior design and quantity survey, relevant regional and global standards, such as SS, BS, ISO, EN, AS and ASTM (Table 1) can be adopted in the precaution of potential risks in the early stage of the FDD. However, there are generally gaps between those standards and the real-world maintenance strategy, i.e., lacking clear guidance of different maintenance rules for different elements of the M&E system. The main contribution of this study is providing systematic and comprehensive maintainability rules for all kinds of M&E elements.

In this section, we demonstrate two data-driven FDD strategies with the maintainability rules for precaution and post-caution maintenance, which apply the maintainability rules as the inputs and the knowledge pool, respectively. These two strategies serve as examples of the usage of the maintainability rules listed in the Tables in Section 4.

3.1. Knowledge-Based Rule System Integrated Data-Driven FDD for M&E Faults. A knowledge-based system is a fundamental AI system that makes decisions purely based on rules. A traditional knowledge-based system comprises a large set of if-else rules that builds a decision tree and processes FDD queries efficiently. A semantic of a typical knowledge-based FDD system is shown in Figure 1. The collected sensor data is evaluated by maintainability rules. The evaluation results lead to the various maintenance decisions following a tree-alike structure.

For example, following the escalator maintainability rules stated in Table 2: 'The landing area of escalators and
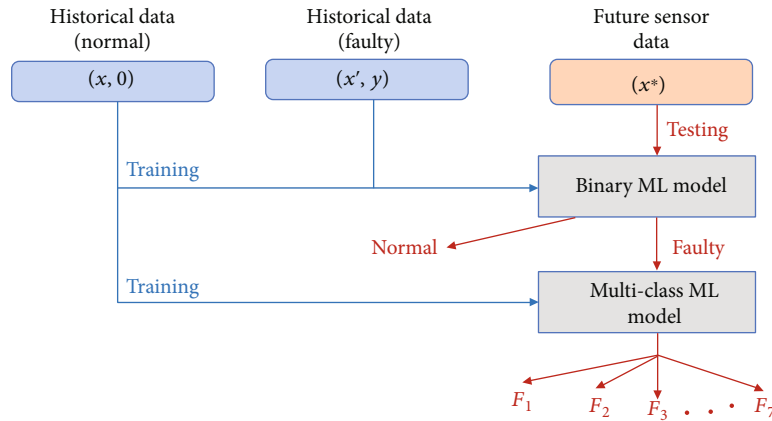
FIGURE 2: A typical FDD framework uses machine learning (ML) models to classify sensor data.
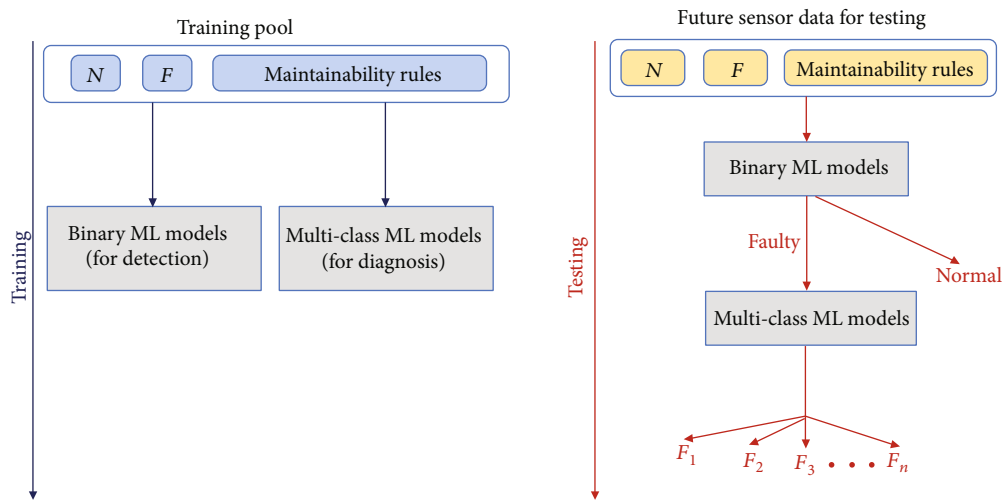
FIGURE 3: The improved FDD framework with maintainability for facility management.
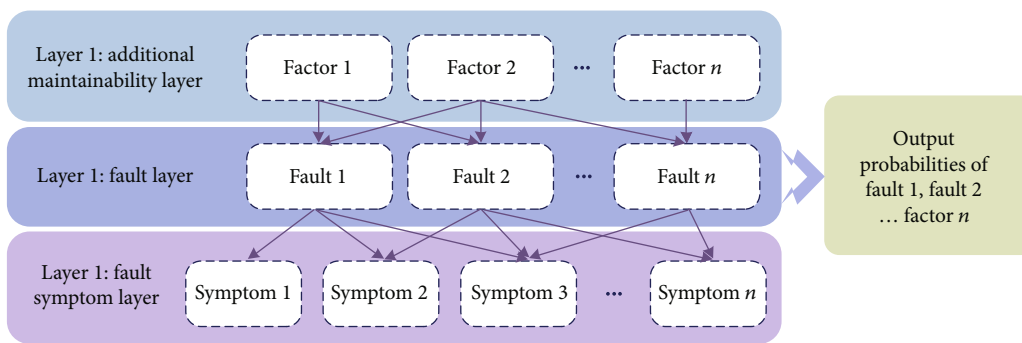
FIGURE 4: The three-layer Bayesian Belief Network integrating maintainability rules as an additional layer.

passenger conveyors should have a surface that provides a secure foothold for a minimum distance of 0.85 m (measured from the root of the comb teeth)', the measurement data collected from the sensor can be easily evaluated as 'satisfactory' or 'unsatisfactory'. Different evaluation results will arrive to different decisions for automated maintenance.

A knowledge-based FDD system integrating traditional data-driven FDD framework treats the knowledge pool

(Figure 1) as an expert system [9, 56]., where if-else rules are derived from maintainability rules. Following the existing rule-based system structures proposed in the related fields, such as [45, 57, 58], decisions for labeling various faults can be reached. The accuracy and performance of such FDD systems depend on the precision and reasonings of the rules. Compared with the existing rule-based systems, the maintainability rules proposed in this study are more precise

Table 3: HVAC System - Chiller Plant.

Problem	Design	Construction	Maintenance
Chiller frequently unloading (stop-start); compressor not starting	Conform to the minimum requirements for air-conditioning equipment efficiency in accordance with SS 530: 2014, ANSI/ASHRAE/IES standard 90.1 or equivalent. Specify proper placement for installation of temperature sensors/probes to capture realistic average temperatures of spaces. Conform to the safety and environmental requirements for refrigeration systems in accordance with ISO 5149-1 or equivalent.	For applications with high dynamic load conditions of a facility, install and commission chillers with variable speed drive (VSD) compressors. Ensure that schematics and maintenance regime of refrigerant leak detection system is handed over to maintenance personnel upon completion.	Set up appropriate cut-in and cut-out temperatures in chiller to avoid frequent unloading. Inspect evaporator tubes for excessive oil, dirt or frost; check operating condition of expansion valve; check condenser tubes for air, dirt, scale, and sludge, and clean/purge if necessary. Check condenser water supply and cooling tower efficiency. Inspect overload relay, and the condition of high- pressure and low- pressure cut-outs. Carry out monthly inspection on refrigerant level to avoid low pressure cut-outs of chiller in accordance with ANSI/ASHRAE/ACCA standard 180 or equivalent.
Rust stain			
Leaking condenser pipes Insufficient cooling/slow cooling	Design chiller plants for recommended cooling Demand with provisions for future expansions guided by SS 553, SS554, AS1668.2, ISO16814 or equivalent. Comply with air conditioning plant optimisation strategies (e.g. high-efficiency chillers, aggressive condenser water reset, medium temperature chilled water loop, chilled water VFD pumping, etc.) in accordance with SS564-1 or equivalent. Use refrigerants with zero ozone depleting potential (ODP) or global warming potential (GWP) of less than 100 [7]. Recommend installation of leak detection system in critical areas of plant rooms.	Cary out proper commissioning of chiller plant and set reasonable points. Perform post-installation monitoring of the installed instrument's performance through the BMS (building automation system) or EMS (energy measurement system). Document as-built drawings (including concealed services) for building user phase. Prepare and handover maintenance checklists for service and repair of each instrument during commissioning. Refer to measures for recommended monitoring procedures for chiller efficiency in accordance with SS 591 or equivalent.	Inspect temperature controllers and thermostatic control valve for any malfunctions and then reset. Perform routine inspection of condenser pipes. Carry out cleaning and servicing (de-scaling) if/when necessary. Routinely inspect insulation for any damaged/worn-out layers. Daily logging of chiller system to ensure system operates at optimum conditions. Any deviation from the intended chiller operation or alarms need to be attended promptly. Perform annual shutdown or overhauling in accordance with manufacturer's guidelines (ANSI/ASHRAE/ACCA standard 180).
Scale in condenser pipes			
No insulation for chilled water pipe			

Table 3: Continued.

Problem	Design	Construction	Maintenance
Leakage of refrigerant Chilled water pipe and condenser pipe leakage and condensation 	Adopt the pump system design calculation and recommend outputs in accordance with ISO 13612-1 or equivalent. Specify the use of unplasticized PVC pipes for cold water services/industrial use as in accordance with SS 141 or equivalent. Provide flow meters for chilled/condenser water loops.	Ensure proper workmanship during pipe installation and testing, especially at joints. Perform proper insulation of chilled water pipes to avoid condensation. Use primary-only variable flow chilled water pumping systems in accordance with SS 564-1 or equivalent.	Cary out quarterly check for pitting noise in pumps. Avoid harsh cleaning methods that may damage pipes or cause the thinning of pipes. Prepare maintenance checklist for flow meters (ultrasonic and full-bore magnetic in-line types) in accordance with SS 591, ISO 12242 or equivalent.
Leaking motor valve 			

TABLE 4: HVAC System - Cooling Towers.

Problem	Design	Construction	Maintenance
Biological fouling of cooling tower	Provide a suitable cooling tower design to prevent dirt accumulation and stagnation. Minimise tower fan power and size of towers for close approach in accordance with SS 564-1 or equivalent. Provide automatic chemical dosing system to ensure acess hatches, level indicators mixers, pump etc. can be easily reached by personnel for maintenance and operation.	Prepare and submit an operation and maintenance (O&M) manual. For the chemical dosing system after the successful commissioning of the system. Install equipment to routinely observe chemical tank levels and the tank condition of the automated dosing system. During installation, ensure that access hatches, level indicators, mixers, pumps, etc. can be easily reached by personnel for maintenance in the operation phase.	Perform frequent overall visual inspection and cooling tower sequencing. Clean tower fill, basin and drift eliminators. Conduct weekly check on fan motor; clean screen; make up water float and water sampling. Carry out monthly check of motor supports, fan blades, motor alignment. Check on condition of bearings and motor, as well as for nozzle clogging, annually. Clean cooling tower at least once a year. Perform monthly checks for legionnaire, scaling and corrosion in/of the condenser system. Disinfect and manually de-sludge cooling towers if required. Monitor water usage in cooling towers and review the efficiency. Ensure optimum scheduling of temporary shutdown and standby of cooling towers. Discharge used water from cooling owners into a sewerage system.
Foaming in cooling tower basin	Provide adequate reach to all parts of the cooling tower for cleaning so as to prevent bacterial growth.		
Scale and dirt build-up in fouled fills	Specify locally green certified cooling tower water treatment system [8], but not limited to automated non-dispersant, non-chemical treatment etc. as it will minimise the downstream maintenance issues. The automated system with the capability of checking of the conductivity and other recommended parameters can be also linked to the building management system (BMS).		
Water efficiency	Consider collection of condensates for re-use. Take into consideration the cycles of concentration of the cooling owner used in order to reduce blow-down frequencies. Avoid uncontrolled water losses due to drift, splash, overflow etc.	Ensure proper installation of float operated inlet valve to reduce frequencies of overflow. Link cooling towers in order to maintain water balance. Consider using solenoid operated inlet valves for cooling towers.	
Legionella outbreak	Avoid redundant pipework, bends, and loops for cooling system design. Allow easy access to all parts of the system for maintenance [9]. Minimise drift by enclosing cooling tower pond. Take the wind direction/distribution and the surrounding environment into account when designing the cooling system. Use non-corrosive, chemical-resistant, non-porous, smooth, opaque (to block sunlight) material to inhibit growth and proliferation of microorganisms.	Perform proper commissioning to ensure safe operation of cooling towers. Develop cooling tower maintenance manual including cleaning/water treatment/decontamination procedures and handover during commissioning. Ensure system is clear of dirt/debris/organic matter and clean before operation. It is presupposed that the control of legionella bacteria in cooling towers is in compliance with applicable statutory and regulatory requirements.	Cooling tower's water temperature should be monitored since elevated temperatures and moisture at air-water surfaces provide ideal conditions that may serve as a nutrient source for legionella growth. The chemical concentration limits of cooling tower effluents should be checked and in compliance with the relevant local standard. If cooling tower is not in use, it should be kept drained and dry. If not in use for more than 5 days, it should be drained, cleaned and disinfected before operating. Regular testing for legionella bacteria should be carried out and get water samples from the cooling tower pond in
Outbreak on air-water surfaces of cooling tower	Design of cooling towers must be capable for preventing dirt accumulation and water stagnation.		

TABLE 4: Continued.

Problem	Design	Construction	Maintenance
	Accommodate suitable and efficient water treatment methods in the system's design.		accordance with ASHRAE 12-2000, ANSI/ASHRAE ASHRAE 188 or equivalent.

Cooling tower air intake blocked by organic matter

Testing the water for legionella

TABLE 5: HVAC System - Air Handling Unit (AHU).
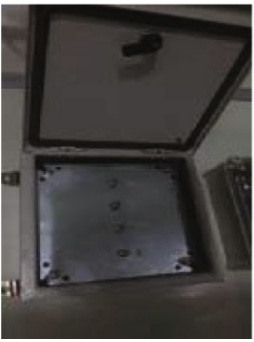
Problem	Design	Construction	Maintenance
Air distribution system efficiency	The design of an AHU system must take into consideration energy efficiency and maintainability when selecting the system and its components. Design AHU in accordance with ANSI/ASHRAE/IES standard 90.1/SS 553 or equivalent. Fan power limitation requirements in mechanical ventilation systems to comply with SS 553, AS 1668.2 or equivalent. Specify minimum performance for air-conditioning equipment (including test procedure) in accordance with SS 530, ANSI/ASHRAE/IES standard 90.1 or equivalent. Propose a biological film application on cooling coil.	It is presupposed that the installation (and subsequent operation) of the AHU is in compliance with statutory and regulatory requirements. For the vibration control of fan systems, refer to CP 99 for the installation/commissioning in accordance with ISO 9996 or equivalent. Install/integrate AHU system components (e.g. VFD, control dampers/actuators) off-site to ensure quality installation.	Clean dirt from impeller, fan scroll and blower blade, washable filters, filter frames and AHU frame slot. Clean cooling coil face with water. Flush with chemical cleaner, but avoid over dosage. Chemical wash should be carried out followed by thorough cleaning with water. Check for any dents on the coil fins. Comb/replace as needed. Clean off any hardened and dirty grease or grime from fan and motor shaft and lubricate properly. Do not use AHU rooms for storage and avoid housing installations that are not associated with the air-conditioning system, in accordance with SS 553, AS 1668.2 or equivalent.
Broken fan belt			
Blue/grey formicary corrosion on Al-cu cooling coil			
Noisy operation and excessive vibration	Careful design is necessary to reduce vibration disturbances caused by impact force. Conform to noise control and elimination guidelines. Use principles of vibration control in determining noise control measures in accordance with SS CP 99, AHRI 260, ISO 9996 or equivalent.	Use acoustic silencers, shock isolators, machine enclosures and partition walls to reduce noise disturbances. Use vibration isolators/mounting of equipment to minimise transmission of vibration from machine to load-bearing structure of the building in accordance with ANSI/AHRI Standard 260, CP 99, ISO 9996 or equivalent. Recommend installing vibration monitoring equipment for AHU to assist in predictive maintenance.	Inspection should be carried out to determine noise levels (ANSI/AHRI standard 260). Inspect chiller plant with maintenance experts if abnormal sound occurs. Isolation/mounting systems should be provided to reduce mechanical vibration and shock in accordance with ISO 2017-1 or equivalent. Vibration from bearings, and sliding and rolling friction could be reduced by maintaining minimum clearances and proper lubrication in accordance with CP 99, ANSI/AHRI Standard 260 or equivalent. Regular monitoring of AHU fan vibration should be carried out and compare with the vibration readings specified in ISO 10816-3 or equivalent.
Noisy fan motor			
Good practice: Install a connection box on AHU for vibration monitoring			

TABLE 6: HVAC System - Air Distribution and Terminal Systems.

Problem	Design	Construction	Maintenance
Dirty and mouldy ductwork Mould growth in duct	Conform to the design requirements for air duct systems, including for fittings and accessories, in accordance with SS 553 or equivalent (where consideration is given to air velocities in ducts, materials and construction method, etc.). Fulfil the compliance requirements of thermal insulation for pipework. Comply with the ductwork seal requirements. Ensure that rigid ducts are manufactured from steel, aluminium, glass-fibre or mineral wool, or other approved materials. Conform to the minimum duct insulation R-values for cooling supply/return ducts in accordance with SS 553, AS 1668.2 or equivalent.	Adopt the construction and installation requirements for air duct systems and their fittings and accessories. Ensure that the ducts or duct linings (where glass fibre or mineral wool is exposed to the air stream) are suitably protected to prevent fibre erosion. The ducts should be sturdily supported - provide metal hangers and brackets for supporting ducts. Guarantee that the inner surfaces of the ducts for supply and return air are smooth and resistant to abrasion in order to reduce dust accumulation in accordance with SS 553, AS 1668.2 or equivalent.	Carry out noise and air loss check when necessary. Perform testing and rating of performance of ducted air-conditioners (ventilation, exhaust and leakage air flow) in accordance with ISO/FDIS 13253. Carry out yearly check of ducting insulation. Perform duct leakage test as per industry requirements in accordance with SS 553, AS 1668.2 or equivalent.
Damper inside AHU collecting condensation, leading to biological growth Filter media choked at the air terminal Choked filter Bent aluminium fin	Provide locations for intake and return air terminals. Adopt the minimum standard air filter requirements with regard to the use of air filters for cleaning outdoor air so that no unfiltered air can enter the air handling system. Follow the recommended use of secondary air filter of 80% dust spot efficiency in accordance with SS 553, AS 1668.2 or equivalent. Use of locally green certified energy efficient air filters (SGBP) if space provision is adequate [8]. Provide sufficient access space for easy cleaning and replacement of filters. Provide a display system for temperature and relative humidity at each floor and at each tenanted area.	Carry out an alternate efficiency test method for filters in accordance with ISO 29463-5 or equivalent. Perform a one-time vet airflow test during commissioning and keep proper record of the report to ensure the cooling capacity is adequate in accordance with design load and applicable statutory and regulatory requirements, and that the noise level is within the desired level in accordance with applicable statutory and regulatory noise pollution standards.	Monitor air pressure and pressure drop across the filter and replace filter when needed. If filter is heavily dented, the filter should be replaced. Carry out leakage test to test filter for local penetration in accordance with ISO 29463-1. Carry out monthly check and observe the dust accumulation level in ducts or grilles.

TABLE 7: Plumbing & Sanitary Systems - General Pumping.

Problem	Design	Construction	Maintenance
Water supply — General defects	Adopt the pipe sizing requirements based on hydraulic design and pump performance. Provide allowance for head loss, and frictional loss due to internal roughness, loss at fittings, turbidity, surge and pumping facility. Do not oversize piping as slow flow will cause stagnation. Specify standard fittings such as tees, elbows, etc. in accordance with BS 7291-1, BS EN 598, BS EN 545 or equivalent.	The installation of water fittings should comply with the requirements as stipulated in SS 636 pr BS 8558. It is presupposed that it is also in compliance with applicable statutory and regulatory requirements. Fittings that are fabricated by welding together segmented pieces are not recommended. Avoid haphazard pipe laying. It is presupposed that all water tanks, pipes and fittings are in compliance with applicable statuary and regulatory requirements.	Perform thorough investigation to check compliance with SS 636 and BS8554. Monthly inspection of water flow rate and pressure should be carried out, and position and functioning of valves. Maintenance inspections of the pipe installation should be carried out and identify/rectify physical defects such as broken pipe braces, dents, or leaks in accordance with BS 8558, BS EN 806-5 or equivalent.

Leaky joint wetting the floor

Ceiling damaged by pipe leakage due to haphazard pipe laying

Leaky joints in inaccessible areas

Problem	Design	Construction	Maintenance
	Sufficient distance (>400 mm) should be maintained from structure or other services running parallel to each other, for easy maintenance and to avoid interference or damage. Pipes should be of adequate strength and durability, and adequately supported in accordance with BS 8558, SS 636 or equivalent.	Ensure that the pipes and fittings are stored and installed in accordance with manufacturer's instructions. Prevent any interior contamination. If contamination occurs, clean before installation. Take special care when joining two dissimilar materials.	Perform routine monitoring of piping system and check for any possible water seepage through the building fabric in accordance with BS 8558 : 2, BS EN 806-5 or equivalent. Repair the pipe joints properly using the correct jointing method. Tighten valve stems by replacing/fitting any missing gasket/washer.

Leaking pipe above ceiling

Leaky water pipes in the ceiling

TABLE 8: Plumbing & Sanitary Systems - Water Supply System.

Problem	Design	Construction	Maintenance
Corrosion and scaling of pipe/valve Scaling in pipe Corrosion of pipe flange	Specify materials that are resistant to corrosion and non-reactive to the conveyed water and surrounding ground in a cadence with BS EN 545, BS EN 598 or equivalent, and that do not impart any taste or toxicity to the water in accordance with BS EN 1796, SS 375-1 or equivalent. Use of single material for the entire system is preferable for easy connection/jointing. Specify pipe system material that does not react with the pumped medium.	Pipe penetrations and joints should strictly comply with manufacturer's instructions. Jointing material should not enter pipe. Caulking at penetration sleeve should be made watertight. Proper installation should be fulfilled while ensuring that the protective coating is not lost/ damaged during installation in accordance with BS 8558, SS 636 or equivalent.	Carry out quarterly chemical and bacteriological analysis of water used [10]. Perform monthly check of water supply for visual signs of leakage, scaling and corrosion of pipes, joints, valves, taps and mixers. Increase frequency of inspection for damp or polluted areas in accordance with BS 8554 or equivalent. Carry out monthly inspections and clean off/ remove any rust or scale. Re-paint parts in a timely manner if needed in accordance with BS EN 806-5 or equivalent.
Damaged piping Burst outdoor pipe Damaged outdoor pipes	Pipework design should consider factors such as the choice of material, rate of flow, accessibility, protection against damage, corrosion, avoidance of airlocks, water hammers, noise transmission, unsightly arrangements, vibration and expansion of fluid, stress and strains, etc. in accordance with BS EN 1057, BS EN ISO 21003-2, BS EN ISO 21003-3, BS EN ISO 21003-5 or equivalent. Provide adequate longitudinal support to pipe installations below ground to cater for loads and traffic vibration.	For underground pipe laying, fully compact bedding prior to installation and maintain the correct depth of trench, gradient, width and bottom condition. Properly align pipe work and use suitable joints. Ensure careful backfilling at an adequate depth for underground pipe laying. Completed sections should be tested for defects using leakage tests and should be rectified by the contractor as required. Maintain proper water pressure in piping system to avoid bursting from over pressurisation.	Carry out thorough cleaning and disinfection of service pipes on a monthly basis, and clean the main pipes semi-annually. If required, removal of blockage with manual cleaning method (e.g., plunger, drain rod, spring auger) should be performed. Carry out chemical de-scaling quarterly (care should be taken so that it does not harm the pipes or jointing by giving consideration to chemical type or contact time). Perform maintenance schedule to check for clogged outlets in accordance with BS 8558, SS 636 [11]. Isolate all leaks and faulty water pipes and fittings first to prevent water wastage before they are being repaired by a licensed plumber. All repairs should be done as soon as possible.

TABLE 8: Continued.

Problem	Design	Construction	Maintenance
Corroded galvanised piping Water hammer Cast iron pipe cracked by water hammer Thrust bearing of a submersible pump ruined by water hammer	Avoid water hammers (water pipe banging) in pipework design in accordance with JIS A 4422, BS EN 1057 or equivalent. Design airlocks and low supply pressure to minimise turbulent flow. Evaluate the required strength of valves and tightness of body and in between the inlet and outlet chamber in accordance with BS EN 1567 or equivalent.	Note that a water hammer may arise when the electric valves on appliances or single control valves are shut off fast. Although all noises due to water flow and pipe expansion cannot be removed, the contractor is responsible for fastening the pipes properly and commissioning valves/actuators to minimise the water hammer. Install check valve to control the creation of a vacuum in discharge pipe in accordance with BS EN 16767, BS EN 545 or equivalent.	Monthly pressure test should be carried out by operating pump for min. 1 hr with 125 m head or 150% of working pressure (whichever is greater) and check for any individual leakage or overall leakage. Semi-annual pressure test should be carried out for sewage pumps. Additional bracing or anchor block support at bends and branches should be provided in order to withstand the hydraulic thrust.

TABLE 8: Continued.

Problem	Design	Construction	Maintenance
Excessive vibration	Ensure that pumps are properly sized to meet the required pressure. Head loss, frictional loss and loss at bends should also be considered. Sewage pumps should be able to handle long and fibrous material. If required, pre-treatment (e.g., crushing) is provided. Specify variable speed drives (VSD) that are able to handle both maximum and variable demand. Ensure that the pump is mounted on an isolation bed (e.g., 150 mm insulated padding) and that no site adjustment in height or position should be done.	The installation of pumps should be adopted in accordance with manufacturer's instructions. Ensure proper construction of isolation beds and installation/mounting of equipment. Special attention should be given for tightness of joints, and alignment of bearings and pipes. Testing and commissioning of the auto and manual interchange of duty and standby pumps should be carried out.	Lubricate pump parts with oil or grease in accordance with manufacturer's instructions. Carry out routine checks, clean motor starter and all heavy current contacts, and replace worn parts. Visually check for any damage or missing parts (screw, nuts, strainer, etc.). Ensure that after installation, pump is tested with power on mode for any unusual vibration, noise, leakage or burnt smell.
Insufficient vibration damping causing wear-out of parts			
Dented pump impeller			
Sensor self-closing delayed-action basin taps	To specify the display contact numbers of maintenance staff so that users can report any faulty, leakages or damaged taps to them for immediate rectification.	To ensure the display contact numbers of maintenance staff so that users can report any faulty, leakages or damaged taps to them for immediate rectification.	Carry out routine checks to ensure that sensor self-closing delayed-action tap can function properly and when the tap is activated, the water is automatically cut-off after a pre-set period of time. The tap should automatically stop functioning during power failure in accordance with SS 448.
Self-closing delayed-action basin taps	To specify the display contact numbers of maintenance staff so that users can report any faulty, leakages or damaged taps to them for immediate rectification.	To ensure the display contact numbers of maintenance staff so that users can report any faulty, leakages or damaged taps to them for immediate rectification.	Carry out routine checks to ensure that self-closing delayed-action tap can function properly and that the water is automatically cut-off after a pre-set time in accordance with SS448.
Dual-flush low-capacity flushing cisterns	To specify the display contact numbers of maintenance staff so that users can report any faulty, leakages or damaged taps to them for immediate rectification.	To ensure the display contact numbers of maintenance staff so that users can report any faulty, leakages or damaged taps to them for immediate rectification.	Ensure that flushing cistern can function properly in accordance with SS574 and check for signs of leakage, defect or damage (including any leakage, defect or damage at the outlet and inlet valves).
Sensor urinal flush valves	To specify the display contact numbers of maintenance staff so that users can report any faulty, leakages or damaged taps to them for immediate rectification.	To ensure the display contact numbers of maintenance staff so that users can report any faulty, leakages or damaged taps to them for immediate rectification.	Carry out routine checks to ensure that sensor urinal flush valves can function properly and discharge the flush volumes not exceeding those specified in SS 636.
Sensor WC flush valves	To specify the display contact numbers of maintenance staff so that users can report any faulty, leakages or damaged taps to them for immediate rectification.	To ensure the display contact numbers of maintenance staff so that users can report any faulty, leakages or damaged taps to them for immediate rectification.	Carry out routine checks to ensure that sensor WC flush valves can function properly and discharge the flush volumes not exceeding 4.5 L per flush as specified in SS 636.

Table 9: Plumbing & Sanitary Systems - Water Tank.

Problem	Design	Construction	Maintenance
Unauthorised/poor accessibility Lack of safety cover and security lock in water tank Good practice; make provisions for access to water tank(s) for maintenance and/or inspection Leakage from water tank Corrosion of bolts and subsequent	Provide a permanent climbing ladder for easy inspection and cleaning of interior. If the ladder rises a vertical distance of more than three metres, then additional fall prevention measures should be considered such as install a safety cage [12, 13]. Provide a minimum of 600 mm space, all around the sides of the tank with at least 1.2 m space from the top of the tank to the ceiling for maintenance, repair and inspection purposes. Install minimum possible number of openings to each compartment; each opening should be fitted with a cover/trapdoor. Sanitary pipes should not be placed above potable water storage tank. Backwash water from swimming pool filter system backwash holding tank should be discharged into a sewerage system. Provide corrosion- resistant, mosquito-proof netting for overflow pipe/vent. Design a series of tanks instead of one large tank, to meet demand for isolation during maintenance, for ease of access.	Ensure there is adequate access space to and around the tank. Edge protection e.g., guardrail should be provided to prevent personnel from falling from open sides of the tank [12, 13]. Ensure that the tanks are not compartmentalised, so as to avoid the shutting off of the whole supply during cleaning (inconveniencing building users). For the purpose of safety and security, provide a lock to water tank, so that only authorised personnel can access it. Ensure that the access is easy and safe, and for authorised persons only. Comply with all security measures in accordance with SS 636 or equivalent.	Carry out general housekeeping within and around the tank room to remove any obstructions to maintenance access. Perform monthly cleaning of wash-out pipes to ensure proper flushing out of the water. Remove sand and dirt deposits in cisterns and tanks. Remove rust stains and repaint affected parts as recommended. Prevent dirt, dust, insects, birds, etc. from entering the tank. Carry out thorough cleaning and disinfection of tank interiors semi-annually.
	Ensure the proper design detailing of pipe penetrations at the tank to avoid leakage. Avoid cracks in concrete tanks; ensure water-tightness, through proper structural design. Specify appropriate water stops and sealants where pipes penetrate the structure. Maintain a minimum air gap above maximum water level in accordance with SS 245, BS EN 13121-3 or equivalent.	Construct the tank body in accordance with specifications (additive, coating, and lining), and render as a monolithic and watertight container. Maintain the exact size and positions of installed devices in accordance with SS 245, BS EN 13121-3 or equivalent. Commission tank by testing for water-tightness; check for any leakage, seepage, and water loss. Ensure that all components are functioning well.	Inspect drainage lines and basin. Carry out routine checks for rusting of metal tanks and apply anti-corrosive paint/coatings where necessary. Perform routine checks on float valve and liquid level indicator for damages to avoid potential overflow.

TABLE 9: Continued.

Problem	Design	Construction	Maintenance
leaking Of GRP tank Corroded water tank body	The body of the water tank should be made of watertight and corrosion-resistant material, such as reinforced or pre-stressed concrete, steel, and glass fibre reinforced plastics in accordance with SS 245, BS EN 13121-3 or equivalent.	Structure of water tank should be constructed with adequate strength and be free from any deformation. Refer to BS EN 10088-2 for standards for a Stainless-Steel Sectional Water Storage Tank (Minimum Grade 316).	Ensure that the parts (e.g., pipes/strainer) and fittings (e.g. ball float, valves) are corrosion-resistant and can be replaced over time. Perform timely re-application of coatings to avoid peeling and delamination of coat
Corroded tank body Corroded and damaged water tank Corroded water tank	Surface treatments, waterproof coating, or lining coating should be specified to resist water seepage and weathering. Ensure that such finishes do not affect the stored water's quality of hygiene in accordance with BS 8558, SS 636 or equivalent.	The water storage tank's installation should be certified by a professional engineer to ensure that it is structurally sound with regard to hydrostatic pressures, deflection and leakage. Use disinfectant to clean water tanks in accordance with BS EN 805 or equivalent. Once disinfectant has been sprayed on inner surfaces and pipes for the designated period, it should be thoroughly cleaned/removed.	(for steel tanks), and water seepage (for concrete tanks). Use disinfectant to clean water tanks in accordance with BS EN 805 or equivalent. Once disinfectant has been sprayed on inner surfaces and pipes for the designated period, it should be thoroughly cleaned/removed.

TABLE 9: Continued.

Problem	Design	Construction	Maintenance
Overflow of water	Decision on the size(s) of the tanks should be made based on water demand, supply, probability of pump failure, time needed for repairs, ratio of peak hours to average flow rate, provision of alternative supply or storage, etc. in accordance with BS 8558, SS 636 or equivalent.	Ensure that the tank is capable of handling various loads (as applicable) without showing cracks, stress or deformation in accordance with SS 245, BS EN 13121-3 or equivalent.	Carry out monthly inspections to check the operation of float valve or any other effective device for controlling the inflow of water. All valves should be periodically operated to ensure that the working parts are moving freely in accordance with BS 8558, SS 636 or equivalent. Inspect condition of overflow warning alarm for the water tank. Inspect the condition of warning alarm which indicates when water levels fall below 50 mm from the invert level of the pipes.
Overflow of water as seen from underneath a tank			
Potable water tanks			Cleaning and disinfection of potable water tanks should be adopted in accordance with SS 636 or equivalent.

TABLE 10: Fire Safety - Fire Extinguishers.

Problem	Design	Construction	Maintenance
Poor discharge of portable fire extinguisher Low pressure indicated in the fire extinguisher. This often leads to poor or no discharge Extinguishing cone missing Fire extinguishers not kept properly and not secured	The locations and number of portable fire extinguishers are to be based on the maximum travel route in accordance with SS EN 3 Series, BS 5306-8, ISO 7165 or equivalent. Access to or visibility of extinguishers should be unobstructed. Extinguishers should be visible along an escape route (preferably near room exits, along corridors and staircases, in lobbies, and on landing). The extinguishers' body and the parts should be of approved quality to prevent rusting, early damage or deterioration in accordance with BS EN 3 series).	Ensure the proper positioning (designated location, hung properly with label facing out) of fire extinguishers. For installation of small fire extinguishers (≤4 kg), hang on the wall with hanger or bracket such that the handle is about 1.5 m from floor. Hangers should be securely fixed. For installation of heavier fire extinguishers (≥4 kg), ensure carrying handle is about 1 m from floor and the arrangement will not hurt the person carrying it. Parts should be attached in accordance with manufacturer's instruction.	Conduct regular servicing to confirm required working condition. (Refer to the recommended schedules for maintenance in accordance with BS 5306-3 or equivalent. Conduct monthly inspection to ensure that the pressure gauge is in operative range and check for any sign of corrosion of the body of the extinguisher. Adopt the recharging frequency in accordance with the type of extinguisher. Adopt charging, testing and maintenance of fire extinguishers in accordance with SS 578 specifications or equivalent. Extinguishers should be recharged with the same agent only. No mixing or cross contamination allowed and no overfilling in accordance with BS 5306-9, NFPA 10 or equivalent.

Table 10: Continued.

Problem	Design	Construction	Maintenance
Fire door malfunctioning Self-closing closer Exit door obstructed by stacking of material	Fire door should be selected in terms of stability, integrity, insulation and installed in accordance with SS 332, NFPA 80 or equivalent and in compliance with applicable statutory and regulatory requirements. Modifications to fire doors are not allowed unless in accordance with SS 332 or supported by assessment report from an accredited testing laboratory.	Fix fire door in accordance with manufacturer recommendation. Fire door should be the same make and model as the tested prototype. Door frames installed during wall construction should be thoroughly grouted in cavity as deeply as possible with corrosion-proof anchor. Screws for attachment should be driven properly, and not hammered or placed in other positions in accordance with SS 332, NPFA 80 or equivalent. Ensure proper workmanship to avoid damaging/jamming/sagging door (e.g, tilted hinge).	Inspect fire doors at least once a year, to ensure that self-closing mechanism functions as intended at all times. Check for and remove any door stoppers, or materials stacked near or by the fire exit door. Remove any obstructions. Check integrity of door leaf and frame for superficial damage, structural damage and excessive bowing or deformation. Inspect hinges, latches, door closer, bolts and pull handle weekly. Automatic release mechanisms should be tested in accordance with BS 5839-3 or equivalent. Ensure that egress is unobstructed in case of emergency evacuation in accordance with evacuation plan and NFPA 101 or equivalent.

TABLE 11: Fire Safety - Fire Detection.

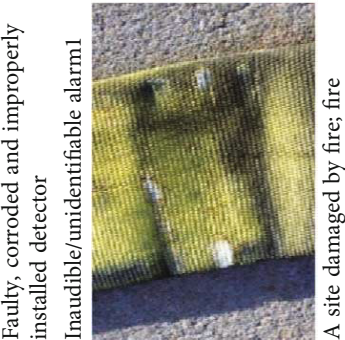| Problem	Design	Construction	Maintenance
Faulty fire alarm panel Fire alarm system fault indicated in fire alarm panel. A faulty fire panel can cause fire incidents to go unmonitored	Design system to accommodate false alarm management in accordance with SS 645 (formerly CP 10) and applicable statutory and regulatory requirements [14]. Maintain the alarm system in accordance with manufacturer's recommendations. The provision of alarm verification feature (AVF) and its functional requirement is covered under SS 645, subject to final approval from the relevant regulatory body to use it. Locate fire alarm panel in corrosion resistant cabinet without any exposure to excessive dampness. Fire panel connectivity should be independent and compatible with the building automation system (BAS). Specify red wiring for fire alarm system. Segregate from other ELV cables to remove electromagnetic interference. Use alarm verification features to reduce incidence of false alarms.	Identify circumstances that can lead to a high rate of false alarms and inform both the designer and user. Check to ensure acceptable levels of false alarms during commissioning in accordance with SS 645, BS 5839-1, BS 5839-6 or equivalent. Install neatly and protect with sleeve in accordance with manufacturer's requirements (care to be taken in concealed spaces). For the protection of joints in junction box, refer to minimum joint requirements.	Conduct regular testing and inspection of fire alarm panel in accordance with SS 645, BS 5839-1, BS 5839-6 or equivalent. Conduct daily check to ensure normal operation, and to record and rectify any faults. Perform weekly tests to check battery and voltage conditions. Conduct monthly simulation of zonal fire and fault conditions. Clean fire alarm panel for proper operation and visibility (NFPA 72). Keep fire panels safe and secure from unauthorised tampering.
Control panel displaying fault message and indicating that detectors are offline			
Faulty manual call point	Designate locations of manual call points along all exit routes and at final exits in accordance with BS 5839-1, BS 5839-6 or equivalent. Manual call points should be located in such a way that a person should not have to travel more than 45 m along an escape route to reach a manual call point, when the layout of the building is known. Each manual call point should be positioned 1.4 m (+/-200 mm) from floor level in accordance with BS 5839-1 or equivalent.	Ensure that manual call points are securely mounted and properly aligned in accordance with SS645 (formerly CP 10) or equivalent. Upon installation, test the system (e.g., three-second response test for manual call point, battery removal test, etc.) in accordance with BS 5839-1, BS 5839-6 or equivalent.	Conduct monthly test of manual call points on all alarm zones to ensure each part is functional, and especially check whether the remote auxiliary facilities are initiated or not. Monitor power supply and faulty wiring of call points and other elements of the fire detection system.
Dirty manual call point at an institutional building			

TABLE 11: Continued.

Problem	Design	Construction	Maintenance
Damaged manual call point. Faulty fire detector Dirty and damaged fire detector	Adopt the fire detection system requirements and applicable statutory and regulatory requirements [14] and in accordance with SS 615, ISO 7240 series, BS 5839-1, BS 5839-6 or equivalent. Ensure detectors are accessible for maintenance and replacement. Implement the selection of heat, smoke, and flame types based on requirements on-location. For decisions regarding the number of fire detectors, and their location and spacing design requirements, refer to SS 575, BS 9990 or equivalent.	Ensure the proper fitting of each fire detector, to avoid misalignment or damage caused by shock. Ensure quality workmanship so as to avoid detector obstruction and or detector being covered by paint. Remove paint, dust or any foreign material that can affect its function from detector.	Practice proper housekeeping to maintain cleanliness and avoid obstructions (especially at poorly accessible points). Inspect fire detectors weekly, and conduct monthly fire alarm simulations from a randomly selected detector to check the entire system. Perform annual test of 20% of all detectors; all detectors will be inspected over a five-year period in accordance with SS 645, BS 5839-1, BS 5839-6 or equivalent.
Faulty, corroded and improperly installed detector. Inaudible/unidentifiable alarm1 A site damaged by fire; fire	Design fire alarm system (e.g., location, type and number of alarms) in accordance with SS 645, BS 5839-1 or equivalent and emergency voice communication system in accordance with SS 546, BS 5839-9 or equivalent. Select alarm sound that is distinguishable from general clutter. Use a visual alarm with excessive background noise. Propose incident communication facilities in accordance with SS ISO	Establish, implement and maintain procedures for warning and communication (e.g., life safety); and set incident communication procedures in accordance with SS ISO 22313 or equivalent. Link lifts with audible warnings and emergency detection system and BMS, for emergency evacuation in accordance with ISO/TR 25743 or equivalent. Installation and cabling of fire alarm devices	Inspect alarms for defects (e.g., loose or blocked gong bolt, damaged or corroded alarm, alarm spoilt by temperature fluctuations, etc.). Conduct annual check of all installed speakers, amplifiers, and connecting appliances (including cables) and keep records. Conduct routine check of fire alarm panel indicator bulb operation and battery according with NFPA 72 or equivalent.

Table 11: Continued.

Problem	Design	Construction	Maintenance
propagated due to alarm system's failure to signal in time	22313 or equivalent and determine internal/external communication needs (e.g., through PA system integrated with iBMS) in accordance with SS ISO 22301 or equivalent.	should be done in such a manner where in the event of a fault, at least one sounder located within the vicinity of the control and indicating panel will remain in operation in accordance with BS 5839-1 or equivalent.	Perform real time monitoring and management of system performance.
Malfunctioning or damaged backup power/lighting	Design emergency power supply systems in buildings in accordance with SS 563-2 or equivalent; and emergency lighting fixtures in accordance with SS 563-1, BS 5266-1, BS EN 50172, BS 5266-8, AS/NZS 2293 SET or equivalent. Building emergency generator supply should be able to back up the emergency voice communication system in accordance with SS 546, BS 5839-9 or equivalent. Consider the use of a standby generator solely to provide power to emergency lighting systems, or in addition, to meet requirements other than those directly associated with emergency lighting.	Requirements for the installation of emergency power supply systems in buildings should be adopted in accordance with SS 563-2, BS EN 1838, BS 5266-1 or equivalent. Individual luminaires should be mounted to avoid glare and if possible, should be positioned at least 2 m above floor level (measured from floor to the underside of the luminaires). The horizontal illuminance on the Centre line of any exit cannot be less than 0.5 lux. A fuel supply should be readily available to ensure that emergency lighting operates continuously for the rated period following the failure of normal power supply in accordance with SS 563-2 or equivalent.	Ensure the maintenance of emergency power supply systems in buildings. Conduct a monthly manual test of emergency lights and replace batteries or lamps as soon as a fault is detected in accordance with SS 563-2, AS/NZS 2293.2/AMDT 3 or equivalent. Conduct monthly fire simulation test. Simulate failure of main power supply and test the efficiency of the standby battery. Ensure visual and audible fault signals are activated once the battery is disconnected.
Damaged exit signage; may interfere with egress during evacuation			
Good practice: Regularly test emergency exit signs to ensure that they are in working order			

TABLE 12: Fire Safety - Fire Hydrant System.

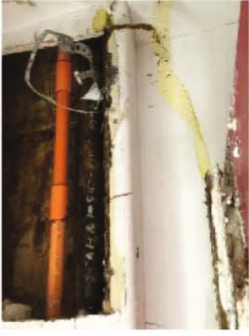| Problem	Design	Construction	Maintenance
Fire hose damaged (cut kink, leak, missing part, abrasion) Haphazard winding Damaged hose reel cabinet Damaged hose reel Damaged fire hose coupling	Ensure that the fire hose reel is suitable for the particular use of the facility in question, and that it is in accordance with BS EN 694, BS EN 1947 or equivalent. Adopt the technical quality acceptance for fire hoses in accordance with BS 6391. Fulfil cabinet specification (Size and mounting) in accordance with standard guidelines. Follow the distribution and number of fire hose reel cabinets in accordance with SS 575, BS 9990, NFPA 14 or equivalent. Adopt authority's stipulated requirements if water supply is taken directly from authority's water main. Ensure that access to or visibility of fire hose is not obstructed. Use maintenance-free fireproof material for the fire hose cabinet. The location should allow for 180° opening of cabinet door. The wall mounted type is only allowed in riser main shaft.	Protect hose reels from mechanical damages. The reel should be mounted overhead, but the nozzle retainer, hose guide and inlet valve must be kept at 900 mm above finished floor level in accordance with BS 9990, SS 575, NFPA 14 or equivalent. During commissioning, flush out the hose to remove harmful matter. Conduct flush out test to remove any kink or knot and to ensure that all valves and nozzles are operational. Ensure that reel brackets are firmly fixed, so that the hose can be used properly.	Perform proper housekeeping and avoid mishandling. Check for corrosion/leakage (of drum) once a month and ensure that hose, nozzle, stopcock, hinges, break glass device and cabinet are in acceptable working condition. Lubricate as required. Conduct monthly water flow pressure test and annual hydrostatic test in accordance with BS EN 1402 to check for defects or leaks, especially if the hose has been exposed to chemical or severe stress. During the test, the hose is completely run out and subjected to operational pressure. After the test, it should be dried and properly secured with a Velcro strap. Ensure that fire hose is stored in a cool, dry place in accordance with ISO 2230 or equivalent.

TABLE 12: Continued.
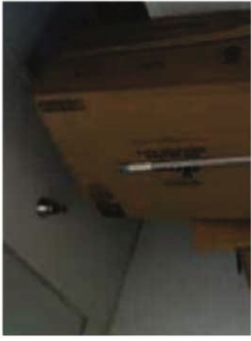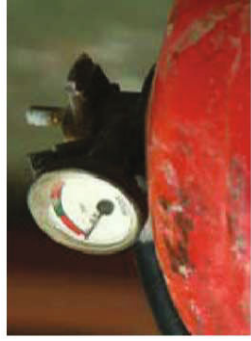
Problem	Design	Construction	Maintenance
Accessibility problems (difficulty in accessing fire hydrant)	For the location and number of fire hydrants, refer to the applicable statutory and regulatory requirements [14]. Adopt the positioning of breeching inlets as close as possible to rising main/hydrant in accordance with BS 9990, SS 575, NFPA 14 or equivalent.	Installation should be secure and safe, with special consideration given for potential sources of damage. Connections and position of valves should be guided by specifications. Risers must be securely anchored before any pressure or flow test is performed.	Perform proper daily housekeeping practices at hydrant points to remove obstructions (debris, stacked material) that impede accessibility. Ensure that the storage tanks are accessible for maintenance. Ensure that the valve pit is accessible for inspection and cleaning.
Inaccessible hydrant points due to positioning	Ensure that the locations are accessible, with no obstructions from parking, loading bays, landscaping, building elements, etc. Provide protection to hydrants from mechanical damage. Specify easily visible/identifiable signage and colour in accordance with SS 508-3, ISO 3864-1 or equivalent.	Hydrants should be made operable immediately after completion and should be tested to protect the construction site. Mounting height of hydrant and breeching inlet should be strictly maintained during installation in accordance with BS 9990, SS 575, NFPA 14 or equivalent.	Conduct semi-annual check for rust, dirt, or foreign material on valves, or other operating parts; as well as clean, paint and lubricate as required. Ensure that additional building elements, landscaping, etc. (during building operation and maintenance phase) do not impede accessibility to hydrant points in accordance with BS 9990 or equivalent.
Improper housekeeping practices, and storing of combustible material in wet riser			
Faulty fire hydrant point (damaged, jammed, leaky)	Materials that are strong and rust-proof (e.g. gunmetal parts) should be specified for the construction of hydrant pillar, in accordance with BS EN 1982 or equivalent. The rising main and other pipework are in compliance with applicable statuary and regulatory requirements. Pit covers on roadways should be able to withstand vehicular load in accordance with BS 9990, SS 575, NFPA 14 or equivalent.	Ensure the proper installation of all components (parts-stem, cap, plug, thread, etc.) without damaging them. Lubricate and paint for additional protection. Tighten outlet properly after commissioning and testing.	Conduct weekly check of isolating valves to ensure that they are kept locked in open position daily and that breeching inlets are functioning in accordance with NFPA 25 or equivalent. Conduct monthly checks for any leakage, blockage or corrosion, and for workable line pressure. Perform thorough inspection of booster pump and associated systems semi-annually. Ensure that a thorough inspection of the hydrants is annually performed by a competent professional.
Damaged hydrant			

Table 12: Continued.

Problem	Design	Construction	Maintenance
Damaged and unusable breaching valves			

TABLE 13: Fire Safety - Sprinkler System.

Problem	Design	Construction	Maintenance
Faulty/compromised sprinkler system Leaky sprinkler pipe Obstructed sprinkler Corroded and faulty sprinkler	Sprinkler design requirements should consider hydraulic principles and parameters such as hazard class, discharge density, and AMAO (assumed maximum area of operation) in accordance with CP 52, ISO 6182 series, NFPA 13 or equivalent. The usual requirement is 75 L/min for 2.5 m wide area. Rust resistant material should be specified to avoid corrosion, pitting and scaling. Potential obstructions should be considered during planning stage.	Installation and testing of sprinkler system, its associated controls, fire pumps and water supply should be guided by CP 52, NFPA 13 or equivalent. Mounting should be carried out in accordance with manufacturer's instructions. To adopt general guidelines in accordance with NFPA 13 or equivalent. Sprinkler system should be carefully installed to maintain correct orientation without hindrance by supports. Spare sprinklers and sprinkler spanner should be maintained after installation for future needs.	Conduct quarterly visual inspection of all sprinklers for any leakage, damages or grease/dirt in spray nozzle and replace as necessary. Conduct annual inspection of pipes and hangers for corrosion and mechanical damage (clean, paint or replace as necessary). Clean quarterly and remove any obstruction affecting efficient discharge from sprinklers. Check for any sign of corrosion or deposit of dirt, paint or foreign material in accordance with NFPA 13 or equivalent. Practice good housekeeping to avoid stacking of material leading to obstruction of sprinklers.

TABLE 14: Electrical Systems – Switchgear.
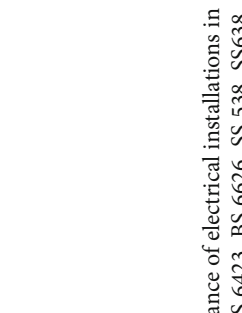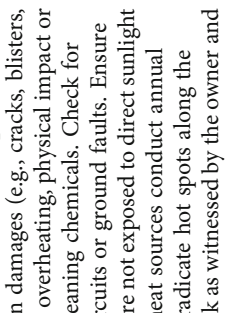
Problem	Design	Construction	Maintenance
Unsafe switchboard/electrical power distribution Water seepage in electrical closet Thermal image of an overheated circuit breaker Burnt cable	Adopt the requirements of electrical installations in accordance with BS 7671, SS 638 (formerly SS CP 5), NFPA 70 [15] or equivalent; including the location and number of power points. Ensure switchboards have adequate space and access for operation and maintenance. Specify suitable switch closets with regard to moisture exposure conditions. Refer to the definition of types and functionality of RCCBs (residual current circuit breakers, and specifications for RCBOs (residual current operated circuit breaker with overcurrent protection) in accordance with SS 480, type tested to IEC 61439, IEC 61009-1, BS EN 61009-2-1 or equivalent. Provide sub-metering system with remote measurement capability and link to BMS/EMS to track energy consumption data trends. Do not place sanitary pipes above electrical transformer/switchgear. Consider having arc chute design for switchboards with rating 200 A and above for protection and safety of personnel against explosion. Install fault management system to provide historical data trends for ease of troubleshooting and maintenance in the event of constant or random tripping to earth leakage. For minimal electrical shutdown to replace faulty breakers, consider having the plug-in breakers/ units building low voltage boards.	Adopt the guidelines for construction and compliance inspection of electrical connections and earthing in accordance with BS 1363-4, SS 403 or equivalent. Refer to BS 8512 for storage, handling and installation of power cables on wooden drums. Install sub-metering system with remote measurement capability and link to BMS/ EMS to track energy consumption data trends. Ensure all accessible metal parts of connection units are in electrical contact with the earthing terminal(s) in accordance with BS 1363-4, SS 403 or equivalent.	Adopt the maintenance of electrical installations in accordance with BS 6423, BS 6626, SS 538, SS638 (formerly CP5), NFPA 70B or equivalent. Check for insulation damages (e.g., cracks, blisters, warping) caused by overheating, physical impact or by spillage of cleaning chemicals. Check for potential short circuits or ground faults. Ensure that switchboards are not exposed to direct sunlight or alternative heat sources conduct annual shutdown to eradicate hot spots along the distribution network as witnessed by the owner and certified by a licensed electrical worker (LEW). Provide necessary warning notices/labels at switchboards (e.g., shock hazard warnings).

Table 15: Electrical Systems - Standby Generator.

Problem	Design	Construction	Maintenance
Standby power generator issues Failed connecting rod of diesel generator (Photo credit: Juarez et al., 2016) Burnt fuse Storage of combustible material in generator house Charging batteries of generator	Design mains failure standby power generation system in accordance with code requirements. Provide sufficient headroom (>2600 mm) in generator rooms for maintenance tasks - i.e., sufficient height to enable any portion of the generating set or equipment to be raised freely for dismantling — in accordance with SS 535, BS 7698-7, ISO 8528-7, NFPA 110 or equivalent. Adopt the general guidelines for earthing of generator sets and substations in accordance with BS 7430, SS 551 or equivalent. For daily diesel service tank package and tank storage (i.e., safety and suitability of design, emergency provisions, and minimisation of vapour hazard), refer to SS 532, BS 5908-1 or equivalent.	Adopt requirements for the construction, installation and testing of generator systems for buildings. Provide sufficient access and clear passage for construction and maintenance. Allotted spaces should be of sufficient strength or suitably strutted to support the loads in accordance with SS 535, BS 7698-7, ISO 8528-7, NFPA 110 or equivalent. Install indoor fuel tank with a level indicator that can be easily accessed for observation. List and mark electrical wiring and equipment located near/within hazardous zones (i.e., day tank) (as defined by NFPA 70 or IEC 60079 SER) for installation in an appropriate manner in accordance with SS 532, BS 5908-1 or equivalent.	Practice proper housekeeping and avoid stacking and storing of combustible materials in the generator house. Maintain records of preventive maintenance activities in a secure manner. Conduct general inspections daily and check on fuel, lubrication and cooling systems. Perform a monthly running of the generator on no load for half an hour. Check battery charger, starting batteries and drive belt tension. Adhere to the requirements for operation and maintenance of standby generator systems for buildings. Once a year, run load test on the generator and check to ensure that emergency supply can support all essential emergency services in accordance with SS 535, BS 7698-7, ISO 8528-7, NFPA 110 or equivalent.

TABLE 16: Electrical Systems - Artificial Lighting.

Problem	Design	Construction	Maintenance
Faulty/compromised artificial lighting and control system Discoloured outdoor lighting cover Corroded metal conduit	Ensure that lighting design will improve energy and sustainability objectives of the building, a centralised lighting control system should be specified to allow easy monitoring; or automate the system with a proper control strategy. Ensure the following: (a) The lighting control is readily accessible (b) Lamp efficacies and ballast energy performance should meet the latest minimal energy performance standard (MEPS) (c) Lighting power density is calculated for the building and, that it meets the lighting power budget in SS 530 (see also ANSI/ASHRAE/IES standard 90.1) Calculate daylighting in accordance with BS ISO 10916 or equivalent.	Adopt the recommended illumination levels for office areas and task activities in accordance with SS 514, CSA Z412-2000 (R2016), ISO 8995-1 or equivalent. Adopt the specifications for luminaires, for general requirements and tests in accordance with SS IEC 60598-1 or equivalent. Note that accordance with ISO 8995-1, SS 531-1 or equivalent, maintained illuminance depends on the maintenance characteristics of the lamp, the luminaire, the environment and maintenance programme. Separate control display and ornamental lighting.	Routine checking should be carried out of adequate lighting levels and maintain adequate lux for appropriate activities in accordance with users' needs and statutory guidelines in accordance with CSA Z412-2000 (R2016), ISO 8995-1, SS 531-1, SS 514 or equivalent. Lamp surfaces should be dusted off and cleaned. Regular inspection of light fittings should be carried out and replaced if burnt-out. Consider group re-lamping if lamps in the same batch are failing. Routine check on transformers and drivers of luminaires should be carried out. Exterior lights for corrosion, torn cables, compromised watertight seals and discolouration should be checked, remedial action should be taken where needed.

Table 17: Electrical Systems - Lightning Protection System (LPS) and Earthing.

Problem	Design	Construction	Maintenance
Lightning protection system (LPS) defects (corroded/exposed parts) Unsecured clamp/joint Corroded conductor	Adopt the protection measures to reduce risk of damage by lightning (e.g., injury to living beings, physical damage and failure of electrical and electronic systems) in accordance with SS 555-1, BS EN 62305-1, NFPA 780 or equivalent. Provide external lightning protection system (LPS) to intercept direct lightning flashes to the structure. Adopt the design considerations for system earthing, including selection of type of earthing system to be used. Material selection and minimum dimensions (for earth- electrodes to resist corrosion) should be guided by SS 551, BS 7430 or equivalent. Provide lightning electromagnetic impulse protection measures (LEMP) in accordance with SS 555-4, IEC 62305-4 or equivalent.	Construct and install air-termination system and LPS in accordance with IEC 62305-3, SS 555-3 or equivalent. Installation to be performed by certified LPS installers. Choose electrode locations that avoid the drainage of fertiliser and other materials into the area. Top soil should not be mixed with the backfill around an electrode. Use compatible metals for the electrode system or protect it by adopting cathodic protection in accordance with BS 7430, SS 551 or equivalent, to avoid hazards to adjacent ground systems.	A thorough check should be performed on surge arrestors and the earthing system once a year, together with the annual shutdown. Monthly inspection should be conducted by a Licensed Electrical Worker (LEW). Such inspection should cover internal LPS to avoid occurrence of dangerous sparking within the structure caused by lightning current flowing in the external LPS or other conductive parts of structure in accordance with IEC 62305-3, SS 555-3 or equivalent.

Table 18: Elevators & Escalators – General.

Problem	Design	Construction	Maintenance
Compromised/poor condition of elevator machine room	Adopt the local codes, and consider elevator system performance in accordance with SS 550, CIBSE Guide D, BS 5655-6, BS 5655-11, BS EN 81-20 or equivalent. Provide ease of access to the elevator machine room with outward opening door (minimum clear opening of 0.6 m ×1.8 m) and permanent safe access for personnel and heavy equipment. Equip machine room with electric lighting with a minimum illuminance of 200 Lux at floor level. Also provide switched socket-outlets in accordance with BS 5655-6, BS 5655-11, BS EN 81-20, SS 550 or equivalent. Provide good ventilation to the machine room (natural or mechanical). For natural ventilation, a 20% opening of the floor area is recommended to achieve cross-flow.	Consider provision for mechanical ventilation when the ambient temperature of the room exceeds 32°C in accordance with BS 5655-6, BS 5655-11, BS EN 81-20, SS 550 or equivalent. Properly commission elevator prior to operation in accordance with BS EN 81-20 or equivalent. Lift machine and drive should be securely mounted. All movable parts, the gear box, and joints should be sufficiently lubricated [16].	Regular inspection of room condition and practice proper housekeeping should be carried out. The room should not be used as storage; remove all non-elevator related materials from the machine room. Adequate lighting should be provided in the elevator machine room to allow workers to conduct maintenance works safely and efficiently [17]. Machine room should be ventilated to ensure the temperature difference measured at any point within 1000 mm of machinery and associated equipment does not exceed 38°C in accordance with BS 5655-6, BS 5655-11, BS 7255, BS EN 13015, SS 550 or equivalent.
Leaking ceiling of the machine room			
Good practice: Installing a cooling system in the machine room to prevent excessive heat in equipment			
Poorly-maintained elevator pit	Ensure proper waterproofing design of elevator pit in accordance with BS 5655-6, BS 5655-11, BS EN 81-20, SS 550 or equivalent. Specify corrosion resistant material and components in elevator system to minimise damage by presence of water or excessive moisture.	Test waterproofing of elevator pit before installation of elevator equipment in accordance with BS 5655-6, BS 5655-11, BS EN 8120, SS 550 or equivalent. Avoid any damage to waterproofing membrane during elevator installation.	The pit areas should always remain dry. If there is any presence of water, the source of water should be identified and eliminated. Routine inspection of the elevator pit should be carried out for water seepage due to faulty waterproofing membrane.
Leaking elevator pit			

TABLE 18: Continued.

Problem	Design	Construction	Maintenance
Lift lobbies with poor accessibility for the disabled Good practice: Design a wheelchair accessible lift lobby (photo shows an example from a residential building)	Encourage through or two-end entries for lift lobbies; or provide added space for dead-end lobbies to ensure the better distribution of waiting passengers in accordance with BS 5655-6, BS 5655-11, BS EN 81-20, SS 550 or equivalent. Provide rain covers for lift lobbies in residential buildings for protection from torrential rains.	Construct lift lobby pedestrian flooring in accordance with recommended minimum pendulum ratings specified in SS 485, HB 197, AS/NZS 4663 or equivalent.	Practice proper housekeeping to keep the lift lobbies clean and clear of dirt and avoid any obstruction or stacking to accommodate easy egress and ingress. Carry out routine inspection of lift call buttons and indicator displays; check that they are in acceptable working condition.

TABLE 19: Elevators & Escalators – Common Faults.

Problem	Design	Construction	Maintenance
Inaccurate elevator car levelling with the landing Elevator car is not levelled with the landing floor	The design guidelines for permanently installed electric lifts should be adopted in accordance with SS 550, CIBSE guide D, BS 5655-6, BS 5655-11, BS EN 81-20 or equivalent. The stopping accuracy of the elevator car against the landing floor should be ±10 mm. Global standards on lift safety in accordance with ISO/TR 11071-2 (i.e., assumption of safe operation assured to 125% of rated load, assuring reliability of electric safety devices, mechanical devices built and maintained in accordance with good practice) should be collated.	The guidelines for construction and installation of permanently installed electric lifts should be implemented in accordance with SS 550, BS 5655-6, BS 5655-11, BS EN 81-20 or equivalent. The safety rules for construction to be guided in accordance with BS EN 81-50 or equivalent. Every lift should be provided with a capacity plate located in a conspicuous place inside the car, indicating the rated load in kilograms and, in the case of passenger lifts, the maximum number of passengers to be carried in accordance with BS 5655-6, BS 5655-11, BS EN 81-20, SS 550 or equivalent.	Upgrade the control system, braking, and motor types. A micro-processor controller will electronically monitor and control motor rotation to ensure that the elevator car accurately stops at floor level. Review levelling of car to ensure the value is acceptable by standards to avoid risk of passengers tripping and falling (e.g., wheelchair users). Permit to operate (PTO) to be displayed in the lifts. Measure ride quality of elevators in accordance with BS ISO 18738.
Poor levelling can cause trip hazard Faulty door operation The elevator inner doors failed to	The gap for the elevator car doorway should not exceed 12 mm, and the clearance between elevator car door panels should be less than 10 mm. The elevator car should not make any movement if the car doors and landing doors are not properly closed and locked. Durable materials for the doors and more durable materials for their frames (e.g. metals) should be used in accordance with BS 5655-6, BS 5655-11, BS EN 81-20, SS 550 or equivalent.	Elevator car and landing doors should be tested to withstand an impact that is similar to the impact when a person collides with the door at running speed in accordance with BS EN 81-20 or equivalent. The main guiding elements of door should operate as intended. Doors should include retainers to keep the door panels in place in accordance with BS EN 81-20 or equivalent. Partially-closed door should open (if button controlling door opening is pressed); while the	Inspect elevator door and guides, shoes, and tracks. It should not show any permanent deformation or elastic deformation not greater than 15 mm (when force of >300 N is applied to 5 cm2 area at centre of door panels at a right angle) in accordance with BS 5655-6, BS 5655-11, BS 7255, BS EN 13015, SS 550 or equivalent. Review the service call frequency for the door. Increased service calls signify the need to upgrade/replace door operators.

Table 19: Continued.

Problem	Design	Construction	Maintenance
close completely during operation (Photo credit: Ben Tng, 2016)		door should remain open when the door open button is pressed.	
Jammed elevator doors do not close completely			

Table 20: Elevators & Escalators - Elevator Safety.

Problem	Design	Construction	Maintenance
Compromised safety and reliability Dirt and rust in machine Corroded guide rail	Specify electronic components for elevator system reliability in accordance with BS 5655-6, BS 5655-11, BS EN 81-20, SS 550 or equivalent. Ensure compliance to global essential safety requirements (GESRs) for lifts and local safety standards in accordance with ISO/DTS 8100-21. Design lift to ensure all lift parts do not affect safe operation under reasonable levels of depreciation.	Map out safety checks for lifts and classify them in accordance with safety and comfort requirements. Safety gear should be able to stop/hold lift car and counterweight within allowable distance in accordance with SS 550, BS 5655-6 or equivalent. Ensure proper installation and commissioning of emergency battery operated power supply (EBOPS) of lift car, braking system, call buttons, load alarm, safety switches functions, safety logic, emergency lighting and supply, etc..	Conduct conformance test for electronic components of lift machines which are susceptible to damage from high temperatures that may impair reliability in accordance with ISO/TR 25743 or equivalent. Conduct monthly safety- levelling of the car and landing. Follow the mandatory incident reporting procedure in the case of an accident/incident.
Faulty suspension ropes due to overloading Elevator suspension ropes severely damaged	Adopt the design requirements for rated loading capacity in accordance with SS 550, BS 5655-6, BS 5655-11, BS EN 81-20 or equivalent. Provide a lift monitoring system to enable remote tracking of lift breakdown. Refer to the guidelines for lift installation in accordance with ISO 8100-30, ISO 7465, ISO 14798, ISO/TR 16765 or equivalent. Consider designing separate service and passenger lifts. Specify durable materials for service lift floor and walls to withstand rough usage.	Overload weighing device should be provided and should activate an alarm when the load in the car exceeds the rated capacity in accordance with BS 5655-6, BS 5655-11, BS EN 81-20, SS 550 or equivalent. Suspension ropes should be installed in accordance with ISO 2408, BS EN ISO 16841 or equivalent. Ensure that they are properly and equally tensioned. If rope is damaged during installation, even if it passed tests prior to elevator service, the damaged rope should be replaced with a new rope, instead of just replacing the strands, in accordance with ASME A17.6 or equivalent. Lift capacity rate should be located at a noticeable position in the elevator car. It should indicate the rated load in kilograms and state the maximum number of passengers.	Periodic maintenance should be done by a BCA registered lift contractor at intervals not exceeding one month. An annual inspection and system test should be done by an independent Authorised Examiner (AE). Adopt the guidelines for the operation and maintenance of permanently installed electric lifts in accordance with SS 550, BS 5655-6, BS 5655-11, BS 7255, BS EN 13015 or equivalent. Annual test of safety equipment without load should be conducted. A full load test should be conducted every 5 years. Sufficiently lubricate ropes frequently to avoid abrasive wear between and within the strands. Ensure the timely replacement of ropes if they are permanently kinked, bent, or deformed in accordance with criteria set out in ASME A17.6 or equivalent. Lift ropes shall be tested against requirements

Table 20: Continued.

Problem	Design	Construction	Maintenance
Condition of (broken) ropes in addition to presence of rouge indicate ropes need to be replaced			of ISO 4344 or equivalent for signs of excessive wear and tear.
Broken suspension ropes Failure to activate overspeed governor	The governor ropes should be made from iron, steel, monel, metal, phosphor bronze Or stainless steel in accordance with ASME A17.3 or equivalent. The governor rope's diameter should be at least 6 mm in accordance with BS 5655-6, BS 5655-11, BS EN 81-20, SS 550 or equivalent. The electrical and mechanical tripping speeds should be guided by the requirements in	For safety code for the construction and installation of the overspeed governor, refer to BS EN 81-50 or equivalent. For the type of examination for overspeed governors, refer to BS EN 81-50 or equivalent, which requires a minimum of 2 tests conducted with 0,9 – 1,0 gn acceleration to check the strength of the overspeed governor. Adopt BS EN 81-50 for tests of tripping by breakage of suspension means.	Inspect the general condition of the speed governor, governor rope and diameter, tripping mechanism and governor switch and governor data plate with no power. Inspect overspeed governor under normal running conditions with power on in accordance with BS 5655-6, BS 5655-11, BS 7255, BS EN 13015, SS 550 or equivalent. Ensure that the governor rope shows no sign of

TABLE 20: Continued.

Problem	Design	Construction	Maintenance
	accordance with SS 550, BS 5655-6, BS 5655-11, BS EN 81-20 or equivalent.	Ensure that overspeed governor functions are commissioned as intended, for safety under all operating conditions.	excessive wear and tear, in accordance with the requirements in ISO 4344 or equivalent.

Example of a typical overspeed governor (photo credit: Jones, I. G. et al., 2013)

Table 21: Elevators & Escalators - Energy Efficiency.

Problem	Design	Construction	Maintenance
Inefficient energy performance Good practice: Application of LED lighting fittings in an elevator car. Good practice: Use of stainless-steel finishing to maximise illumination in car (by reflecting light). Also results in a more durable elevator car.	Select and design lift equipment that will cater to expected traffic needs with energy efficiency, as attained by proper equipment management in accordance with BS 5655-6, BS 5655-11, BS EN 81-20, SS 550 or equivalent. Adopt the energy calculation and classification for lifts in accordance with ISO 25745-2 or equivalent. For the minimum energy efficiency requirements, refer to SS 530 or equivalent. For the planning of energy efficiency of lifts and escalators, refer to VDI 4707 or equivalent.	Fulfil energy performance and verification of lifts in accordance with ISO 25745-1. Install luminaires which adhere to the maximum lighting power density for lift lobbies; i.e., 7 W/m^2. Install equipment to measure energy consumption on installed equipment of lifts with reference to ISO 257545 series (refer also to SS 530 or equivalent).	Adopt the measurements of energy consumption. Implement the energy calculations and classification of escalators and moving walks in accordance with ISO 25745-3 or equivalent. Conduct regular maintenance of the equipment to ensure moving parts are sufficiently lubricated and to identify early signs of wear and tear for timely corrective action and efficient equipment usage. Perform timely modernisation to enhance performance/energy efficiency in accordance with BS 5655-6, BS 5655-11, BS 7255, BS EN 13015, SS 550 or equivalent.
Poor/compromised lighting Burnt out elevator car lighting bulb.	Lift car should be provided with permanently fixed electric lights (no less than two lighting fittings per car to be provided). Ensure lighting intensity of at least 50 lux at floor level in accordance with BS 5655-6, BS 5655-11, BS EN 81-20, SS 550 or equivalent.	Install emergency luminaires in lift cars in accordance with SS 550, BS 5655-6, BS 5655-11, BS EN 81-20 or equivalent. Use energy efficient lighting with sensors during installation for energy efficiency.	Ensure that luminaires are protected to prevent injury of passengers from breakage; and to prevent access to live parts by passengers in accordance with BS 5655-6, BS 5655-11, BS 7255, BS EN 13015, SS 550 or equivalent.

and reasonable, consequently providing better results in terms of diagnostic accuracy.

3.2. Maintainability Rules as Inputs for Data-Driven FDD Systems. Data-driven FDD applied machine learning techniques to sensor data and performs automated classification with a pre-defined training process on the collected data. A typical data-driven FDD process is shown in Figure 2, where historical data containing both normal operational and faulty conditional data is received by the machine learning (ML) models. Two particular ML models are trained. The binary ML model handles the fault detection for facilities management, which classifies the future sensor data into normal or faulty classes. The multi-class ML model handles the fault diagnosis part, which classifies the faulty sensor data into different types of faults.

Traditional FDD methods, as shown in Figure 2, assume completely no background knowledge of the maintainability of the facilities. The maintainability rules that we proposed in this study provide a great opportunity to improve the existing FDD approaches. The simplest way of extending the current FDD framework with the maintainability rules is to treat them as inputs for the ML models. We formalize the proposed extension of the existing FDD framework in Figure 3.

In Figure 3, the traditional FDD framework has been improved by adding maintainability rules as inputs for both training and testing phases. Since ML models, in general, do not require background knowledge for classifications, the maintainability rules are served as additional inputs for both training and testing of the ML models. The maintainability rules have the potentials of enhancing the interpretation capability of the ML models as well as the prediction performance.

A concrete example of the proposed framework shown in Figure 3 is the three-layer Bayesian Belief Network (BBN) adapting the maintainability rules as an additional layer for FDD. The three-layer BBN is a three-layer neural network, calculating the probabilities of label assignment based on evidence and conditional probability. The details of the BBN construction can be found in [46, 47]. The internal structure of the BBN is illustrated in Figure 4, where expert knowledge is interpreted using maintainability rules as introduced in the Introduction Section (Section 1) and Section 4. For prediction probabilities calculated by neural networks, the maintainability rules provide evidence that influence the probability calculation. Therefore, the FDD accuracy will be improved significantly.

4. Maintainability Rules Study for Facility Management in M&E Services

In this section, we summarize the maintainability rules following the expert knowledge of typical components in M&E services, namely, HVAC system, plumbing and sanitary system, fire safety, electrical system and elevator & escalator system collected through survey and interview results over 110 buildings in Singapore, including commercial, hotels, industrial, institutional, clinical and residential build-

ings. The maintainability rules summarize the preventive checklist based on expert knowledge as well as standards regionally or globally in all design, construction and operational stages of buildings. The maintainability rules are useful serving as the knowledge pool for the post-caution FDD approach or as the additional maintainability layer for a precaution FDD approach, as explained in Section 3.

The maintainability rules for the chiller plant, the cooling tower, the air handling unit (AHU) and the air distribution, terminal system of the HVAC system are summarized in Tables 3–6, respectively. The maintainability guidance for general pumping issues, the water supply system and the water tank of the plumbing and sanitary system ae summarized in Tables 7–9, respectively. The maintainability issues for the fire detection, the fire hydrant system, the sprinkler system and the fire extinguishers of the fire safety (Table 10) are listed in Tables 11–13, respectively. The maintainability rules for the switchgear, the standby generator, the artificial lighting, the lightning protection system (LPS) and earthing are summarized in Tables 14–17, respectively. The general rules for the elevators and escalators, common faults for the elevators and escalators, the elevator safety, energy efficiency for the elevators and escalators and the maintenance for escalators, in general, are summarized in Tables 18–21, respectively.

The details of the regional (Singapore-based) and global standards, such as SS, BS, ISO, EN, AS and ASTM, are listed in Table 1.

5. Conclusions, Limitation & Future Works

Maintainability rules for M&E systems based on the survey and interview results of 110 buildings including commercial, hotels, industrial, institutional, healthcare and residential buildings are summarized. The maintainability rules are useful to be integrated into the existing data-driven FDD approaches for 1) an extension of the existing FDD algorithm to all M&E facilities in buildings, 2) enhancing the interpretability of the existing AI models and 3) improving the performances of the AI models. In Section 3, we demonstrate two data-driven FDD strategies integrating the maintainability rules, including 1) data-driven expert rules for decision making in smart building facility FDD; and 2) maintainability rules as inputs for data-driven FDD systems.

Based on the literature study, the surveyed maintainability rules will greatly enhance the interpretability of the existing data-driven FDD methods for M&E services and consequently promote the FDD methods to other building facilities and to other industrial areas, such as the Industry 4.0 evolution solutions. Furthermore, existing works show that the expert knowledge potentially improves the data-driven FDD results by adding the rules to the machine learning models, such as the decision trees.

The limitation of this study includes not showing the actual implementation of the maintainability rules integrated FDD framework, which we believe is a repetitive work to the existing publications. The main contribution of this study is first, to further extend the existing studies and concretize the maintainability rules that are used in existing

interpretable data-driven FDD methods based on expert knowledge and existing standards. The second main contribution is to extend the existing FDD methods to a broader scope of facility management.

Future study of this work includes the experiments on the accuracy and efficiency improvement on existing BMS system adding the maintainability rules for additional supports as well as a wider the scope of applications for maintainability rules in smart city design.

Data Availability

The research data used in this study is confidential and only accessible internally for employees of National University of Singapore.

Conflicts of Interest

The authors declare no conflict of interest.

Authors' Contributions

Conceptualization, M.Y.L.C.; methodology, M.Y.L.C.; investigation, M.Y.L.C.; resources, M.Y.L.C.; data curation, K.Y.; writing—original draft preparation, M.Y.L.C.& K.Y.; writing—review and editing, M.Y.L.C.& K.Y.; visualization, M.Y.L.C.& K.Y.; supervision, M.Y.L.C.; project administration, M.Y.L.C.; funding acquisition, K.Y.

Acknowledgments

References

[1] A. Dexter and J. Pakanen, Eds., "Demonstrating automated fault detection and diagnosis methods in real buildings," in *Technical Research Centre of Finland (VTT)*, Finland, 2001.

[2] H. C. Peitsman and V. E. Bakker, *Application of Black-Box Models to HVAC Systems for Fault Detection*, vol. No. CONF-960254-, American Society of Heating, Refrigerating and Air-Conditioning Engineers, Inc., Atlanta, GA (United States), 1996.

[3] D. Jacob, S. Dietz, S. Komhard, C. Neumann, and S. Herkel, "Black-box models for fault detection and performance monitoring of buildings," *Journal of Building Performance Simulation*, vol. 3, no. 1, pp. 53–62, 2010.

[4] Y. Zhao, T. Li, X. Zhang, and C. Zhang, "Artificial intelligence-based fault detection and diagnosis methods for building energy systems: advantages, challenges and the future," *Renewable and Sustainable Energy Reviews*, vol. 109, pp. 85–101, 2019.

[5] X. Dai and Z. Gao, "From model, signal to knowledge: a data-driven perspective of fault detection and diagnosis," *IEEE Transactions on Industrial Informatics*, vol. 9, no. 4, pp. 2226–2238, 2013.

[6] M. Galagedarage Don and F. Khan, "Dynamic process fault detection and diagnosis based on a combined approach of hidden Markov and Bayesian network model," *Chemical Engineering Science*, vol. 201, pp. 82–96, 2019.

[7] M. S. Mirnaghi and F. Haghighat, "Fault detection and diagnosis of large-scale HVAC systems in buildings using data-driven methods: a comprehensive review," *Energy and Buildings*, vol. 229, article 110492, 2020.

[8] Z. Shi and W. O'Brien, "Development and implementation of automated fault detection and diagnostics for building systems: a review," *Automation in Construction*, vol. 104, pp. 215–229, 2019.

[9] S. Katipamula and M. R. Brambley, "Review Article: Methods for Fault Detection, Diagnostics, and Prognostics for Building Systems—A Review, Part I," *Hvac&R Research*, vol. 11, no. 1, pp. 3–25, 2005.

[10] K. Yan, W. Shen, T. Mulumba, and A. Afshari, "ARX model based fault detection and diagnosis for chillers using support vector machines," *Energy and Buildings*, vol. 81, pp. 287–295, 2014.

[11] A. Chong and K. P. Lam, "Uncertainty analysis and parameter estimation of HVAC systems in building energy models," in *Proceedings of the 14th IBPSA building simulation conference*, vol. 1no. 1.4, p. 3, Hyderabad, India, 2015.

[12] A. Chong and K. Menberg, "Guidelines for the Bayesian calibration of building energy models," *Energy and Buildings*, vol. 174, pp. 527–547, 2018.

[13] W. Kim and S. Katipamula, "A review of fault detection and diagnostics methods for building systems," *Science and Technology for the Built Environment*, vol. 24, no. 1, pp. 3–21, 2018.

[14] G. Hackmann, W. Guo, G. Yan, Z. Sun, C. Lu, and S. Dyke, "Cyber-physical codesign of distributed structural health monitoring with wireless sensor networks," *IEEE Transactions on Parallel and Distributed Systems*, vol. 25, no. 1, pp. 63–72, 2014.

[15] Y. Cao, X. Zhou, and K. Yan, "Deep Learning Neural Network Model for Tunnel Ground Surface Settlement Prediction Based on Sensor Data," *Mathematical Problems in Engineering*, vol. 2021, Article ID 9488892, 14 pages, 2021.

[16] H. Kramer, G. Lin, C. Curtin, E. Crowe, and J. Granderson, "Building analytics and monitoring-based commissioning: industry practice, costs, and savings," *Energy Efficiency*, vol. 13, no. 3, pp. 537–549, 2020.

[17] Y. Shu, L. Ming, F. Cheng, Z. Zhang, and J. Zhao, "Abnormal situation management: challenges and opportunities in the big data era," *Computers & Chemical Engineering*, vol. 91, pp. 104–113, 2016.

[18] S. Lazarova-Molnar, H. R. Shaker, and N. Mohamed, "Fault detection and diagnosis for smart buildings: state of the art, trends and challenges," in *2016 3rd MEC international conference on big data and Smart City (ICBDSC)*, pp. 1–7, Muscat, Oman, 2016, March.

[19] C. Yang, W. Shen, Q. Chen, and B. Gunay, "A practical solution for HVAC prognostics: failure mode and effects analysis in building maintenance," *Journal of Building Engineering*, vol. 15, pp. 26–32, 2018.

[20] K. Yan, "Chiller Fault Detection and Diagnosis with Anomaly Detective Generative Adversarial Network," *Building and Environment*, vol. 201, article 107982, 2021.

[21] Z. Chen, "Facilities intelligence and evaluation: a multi-criteria assessment approach," *Energy and Buildings*, vol. 42, no. 5, pp. 728–734, 2010.

[22] K. Yan, L. Liu, Y. Xiang, and Q. Jin, "Guest editorial: AI and machine learning solution cyber intelligence technologies: new methodologies and applications," *IEEE Transactions on Industrial Informatics*, vol. 16, no. 10, pp. 6626–6631, 2020.

[23] R. Shohet, M. S. Kandil, Y. Wang, and J. J. McArthur, "Fault detection for non-condensing boilers using simulated building automation system sensor data," *Advanced Engineering Informatics*, vol. 46, article 101176, 2020.

[24] S. A. Gbadamosi, G. P. Hancke, and A. M. Abu-Mahfouz, "Building upon NB-IoT networks: a roadmap towards 5G new radio networks," *IEEE Access*, vol. 8, pp. 188641–188672, 2020.

[25] M. Dey, S. P. Rana, and S. Dudley, "A case study based approach for remote fault detection using multi-level machine learning in a smart building," *Smart Cities*, vol. 3, no. 2, pp. 401–419, 2020.

[26] M. Dey, S. P. Rana, and S. Dudley, "Smart building creation in large scale HVAC environments through automated fault detection and diagnosis," *Future Generation Computer Systems*, vol. 108, pp. 950–966, 2020.

[27] N. Mohamed, J. Al-Jaroodi, and S. Lazarova-Molnar, "Industry 4.0: Opportunities for Enhancing Energy Efficiency in Smart Factories," in *2019 IEEE International Systems Conference (SysCon)*, pp. 1–7, Orlando, Florida, USA, 2019.

[28] T. Mulumba, A. Afshari, K. Yan, W. Shen, and L. K. Norford, "Robust model-based fault diagnosis for air handling units," *Energy and Buildings*, vol. 86, pp. 698–707, 2015.

[29] K. Yan, Z. Ji, H. Lu, J. Huang, W. Shen, and Y. Xue, "Fast and accurate classification of time series data using extended ELM: application in fault diagnosis of air handling units," *IEEE Transactions on Systems, Man, and Cybernetics: Systems*, vol. 49, no. 7, pp. 1349–1356, 2017.

[30] K. Yan, Z. Ji, and W. Shen, "Online fault detection methods for chillers combining extended kalman filter and recursive one-class SVM," *Neurocomputing*, vol. 228, pp. 205–212, 2017.

[31] K. Yan, L. Ma, Y. Dai, W. Shen, Z. Ji, and D. Xie, "Selection des fonctions sequentielles et sensibles aux couts pour la detection et le diagnostic des defaillances du refroidisseur," *International Journal of Refrigeration*, vol. 86, pp. 401–409, 2018.

[32] S. Bendapudi and J. E. Braun, "A Review of Literature on Dynamic Models of Vapor Compression Equipment. Final report for ASHRAE RP-1043," in *American Society of Heating, Refrigerating and Air-Conditioning Engineers*, Atlanta, 2002.

[33] J. M. House, H. Vaezi-Nejad, and J. M. Whitcomb, "An expert rule set for fault detection in air-handling units/discussion," *ASHRAE Transactions*, vol. 107, p. 858, 2001.

[34] W. Y. Lee, J. M. House, C. Park, and G. E. Kelly, "Fault diagnosis of an air-handling unit using artificial neural networks," *Transactions-American society of heating refrigerating and air conditioning engineers*, vol. 102, pp. 540–549, 1996.

[35] S. Li, J. Wen, X. Zhou, and C. J. Klaassen, "Development and validation of a dynamic air handling unit model, part 2," *ASHRAE Transactions*, vol. 116, no. 1, pp. 57–73, 2010.

[36] S. Pourarian, J. Wen, D. Veronica, A. Pertzborn, X. Zhou, and R. Liu, "A tool for evaluating fault detection and diagnostic methods for fan coil units," *Energy and Buildings*, vol. 136, pp. 151–160, 2017.

[37] C. Zhong, K. Yan, Y. Dai, N. Jin, and B. Lou, "Energy efficiency solutions for buildings: automated fault diagnosis of air handling units using generative adversarial networks," *Energies*, vol. 12, no. 3, p. 527, 2019.

[38] A. Ragab, M. El-Koujok, B. Poulin, M. Amazouz, and S. Yacout, "Fault diagnosis in industrial chemical processes using interpretable patterns based on logical analysis of data," *Expert Systems with Applications*, vol. 95, pp. 368–383, 2018.

[39] A. Ragab, M. El Koujok, H. Ghezzaz, M. Amazouz, M. S. Ouali, and S. Yacout, "Deep understanding in industrial processes by complementing human expertise with interpretable patterns of machine learning," *Expert Systems with Applications*, vol. 122, pp. 388–405, 2019.

[40] J. Liu, G. Li, B. Liu, K. Li, and H. Chen, "Knowledge discovery of data-driven-based fault diagnostics for building energy systems: a case study of the building variable refrigerant flow system," *Energy*, vol. 174, pp. 873–885, 2019.

[41] B. Butzin, F. Golatowski, and D. Timmermann, "A Survey on Information Modeling and Ontologies in Building Automation," in *IECON 2017-43rd Annual Conference of the IEEE Industrial Electronics Society*, pp. 8615–8621, Beijing, China, 2017.

[42] A. Kroll, "Grey-box models: concepts and application," *New frontiers in computational intelligence and its applications*, vol. 57, pp. 42–51, 2000.

[43] H. Yoshida and S. Kumar, "Development of ARX model based off-line FDD technique for energy efficient buildings," *Renewable Energy*, vol. 22, no. 1-3, pp. 53–59, 2001.

[44] A. Costa, M. M. Keane, J. I. Torrens, and E. Corry, "Building operation and energy performance: monitoring, analysis and optimisation toolkit," *Applied Energy*, vol. 101, pp. 310–316, 2013.

[45] R. Yan, Z. Ma, Y. Zhao, and G. Kokogiannakis, "A decision tree based data-driven diagnostic strategy for air handling units," *Energy and Buildings*, vol. 133, pp. 37–45, 2016.

[46] Y. Zhao, F. Xiao, and S. Wang, "An intelligent chiller fault detection and diagnosis methodology using Bayesian belief network," *Energy and Buildings*, vol. 57, pp. 278–288, 2013.

[47] T. Li, Y. Zhao, C. Zhang, J. Luo, and X. Zhang, "A knowledge-guided and data-driven method for building HVAC systems fault diagnosis," *Building and Environment*, vol. 198, article 107850, 2021.

[48] S. Vaidya, P. Ambad, and S. Bhosle, "Industry 4.0 - A Glimpse," *Procedia manufacturing*, vol. 20, pp. 233–238, 2018.

[49] E. Forcael, I. Ferrari, A. Opazo-Vega, and J. A. Pulido-Arcas, "Construction 4.0: a literature review," *Sustainability*, vol. 12, no. 22, p. 9755, 2020.

[50] T. Mulumba, A. Afshari, and L. Friedrich, "Kalman filter-based fault detection and diagnosis for air handling units," in *Proceedings of the 15th International Refrigeration and Air Conditioning Conference*, West Lafayette, Indiana, USA, 2014.

[51] S. Srinivasan, P. Arjunan, B. Jin, A. L. Sangiovanni-Vincentelli, Z. Sultan, and K. Poolla, "Explainable AI for chiller fault-detection systems: gaining human trust," *Computer*, vol. 54, no. 10, pp. 60–68, 2021.

[52] G. Li, Q. Yao, C. Fan et al., "An explainable one-dimensional convolutional neural networks based fault diagnosis method for building heating, ventilation and air conditioning systems," *Building and Environment*, vol. 203, article 108057, 2021.

[53] S. S. Kumar, D. Abraham, and M. Rosenthal, "Leveraging Visualization Techniques to Develop Improved Deep Neural Network Architecture for Sewer Defect Identification," in *Construction Research Congress 2020: Infrastructure Systems and Sustainability*, pp. 827–835, American Society of Civil Engineers, Reston, VA, 2020.

[54] D. Gonzalez-Jimenez, J. del-Olmo, J. Poza, F. Garramiola, and P. Madina, "Data-driven fault diagnosis for electric drives: a review," *Sensors*, vol. 21, no. 12, p. 4024, 2021.

[55] V. Gavan, A. Perehinec, S. Agapoff, and S. Derouineau, "Rule based Fault Detection & Diagnosis for high performance buildings: application to a positive energy building in France," in *12th REHVA World Congress-CLIMA 2016*, Aalborg, Denmark, 2016.

[56] T. M. Rossi and J. E. Braun, "A statistical, rule-based fault detection and diagnostic method for vapor compression air conditioners," *Hvac&R Research*, vol. 3, no. 1, pp. 19–37, 1997.

[57] F. Arévalo, C. Tito, M. R. Diprasetya, and A. Schwung, "Fault Detection Assessment Using an Extended FMEA and a Rule-Based Expert System," in *2019 IEEE 17th International Conference on Industrial Informatics (INDIN)*, vol. 1, pp. 740–745, Helsinki-Espoo, Finland, 2019.

[58] S. Frank, G. Lin, X. Jin, R. Singla, A. Farthing, and J. Granderson, "A performance evaluation framework for building fault detection and diagnosis algorithms," *Energy and Buildings*, vol. 192, pp. 84–92, 2019.

Research Article

Zero-Correlation Linear Cryptanalysis on SPARX-64

Dawei Zhou,[1] Huaifeng Chen [ID],[2,3] Rui Zong,[4] and Ningning Song[2,3]

[1]*Department of Information Security, Naval University of Engineering, Wuhan, China*
[2]*The 6th Research Institute of China Electronics Corporation, Beijing, China*
[3]*National Engineering Laboratory for Industrial Control System Information Security Technology, China*
[4]*Verification & Validation Technology co., Ltd, Shenzhen, China*

Correspondence should be addressed to Huaifeng Chen; chenhf@ncse.com.cn

SPARX is a family of ARX-based block ciphers designed according to the long-trail strategy, which has 32-bit ARX-based SBoxes and has provable bounds against single-differential and single-linear cryptanalysis. Since its proposation, some third-party cryptanalysis methods have been presented. As far as we know, the best attacks against SPARX-64 covered 16 (out of 24) rounds. In this paper, we propose zero-correlation linear attacks on SPARX-64. At first, we construct some new zero-correlation linear distinguishers covering 14-round and 15-round SPARX-64. Then, 15,16,17 and 18-round versions can be attacked using multidimensional or multiple zero-correlation linear attack models, under DKP(distinct known plaintexts) settings. These are the best attacks against SPARX-64 up to now, regarding to the number of attacked rounds. Finally, we transform the zero-correlation distinguishers into integral ones using existing methods, which are also longer than the ones proposed by the designers.

1. Introduction

SPARX [1], introduced by Dinu et al. at ASIACRYPT'16, is the first ARX based family of block ciphers with the aim of providing provable security against single-trail differential and linear cryptanalysis. To achieve this target, the designers developed the long trail strategy which is different from the well-studied wide trail strategy [2] used in the design of AES. The long trail strategy advocates the use of large and comparatively expensive SBoxes in conjunction with cheaper and weaker linear layers. All the instances of SPARX, (SPARX-64/128, SPARX-128/128 and SPARX-128/128) use three or four rounds of SPECK [3] with subkeys as the big SBox, which can be specified using three simple operations: addition modulo 2^{16} ($\boxplus$), 16-bit rotations ($\lll 2$ and $\ggg 7$) and 16-bit Xor ($\oplus$).

There have been some cryptanalysis results on the family of SPARX. The designers gave the provable bounds on the probability of differential characteristic and the bias of linear trail. There is no differential or linear trail with significant probability for 5 (or more) steps. Also, they made integral

attacks with the help of Todo's division property [4]. For SPARX-64/128, the attack covers 15 rounds and recovers the key in time 2^{101} using 2^{37} chosen plaintexts. Morever, the integral attacks cover 22-round SPARX-128/128 and 24-round SPARX-128/256. Then Abdelkhalek et al. [5] attacked 16-round SPARX64-128 using impossible differential attack, with the help of one 13-round distinguisher and the dependencies between the subkeys. Later, Tolba et al. [6] proposed multidimensional zero-correlation linear attacks on up to 25 rounds of SPARX-128/256 and 22 rounds of SPARX-128/128. Recently, Ankele and List [7] presented chosen-ciphertext differential attacks on 16-round SPARX-64/128. Previous attack results on SPARX-64/128 are compared in Table 1.

There is no zero-correlation cryptanalysis results on SPARX-64/128 from the literatures and we focus on this method in this paper. Zero-correlation [8] is one powerful tool in the cryptanalysis of block ciphers. Similar to that the impossible differential distinguisher uses a differential with probability zero, the zero-correlation distinguisher uses a linear hull with correlation zero. Then this technique

#rounds	Attack types	Data	Time	Ref.
15	Integral	2^{37}CP	$2^{101.0}$	[1]
15	Impossible differential	$2^{51.0}$CP	$2^{94.1}$	[5]
16	Impossible differential	$2^{61.5}$KP	$2^{94.0}$	[5]
16	Truncated differential	2^{32}CC	2^{93}	[7]
16	Rectangle	$2^{59.6}$CC	2^{122}	[7]
16	Yoyo	2^{64}CP	2^{126}	[7]
15	Multidimensional zero-correlation	$2^{58.6}$DKP	2^{106}	Sect. 4.1
16	Multidimensional zero-correlation	$2^{62.5}$DKP	2^{101}	Sect. 4.2
17	Zero-correlation	$2^{63.6}$DKP	2^{127}	Sect. 5.1
18	Zero-correlation	$2^{63.6}$DKP	$2^{127.2}$	Sect. 5.2

∗ CP: Chosen Plaintext; KP: Known Plaintext; ∗ CC: Chosen Ciphertext; DKP: Distinct Known Plaintext. ∗ In KP settings, the samples are obtained randomly while in DKP settings there is a restriction that the plaintext-ciphertext samples are non-repeating.

develops a lot and some new models have been proposed, such as the multiple zero-correlation linear cryptanalysis [9], the multidimensional zero-correlation linear cryptanalysis [10] and some improved versions [11, 12]. In particular, Sun et al. [12] removed the approximation from the χ^2-distribution to the normal distribution during the construction of multiple and multidimensional zero-correlation linear attack (MPZC and MDZC) models, which released the restriction on the number 'ℓ' of zero-correlation linear hulls, i.e., 'ℓ' should be large enough. The new models were called χ^2-MPZC and χ^2-MDZC.

To improve the time complexity of linear attacks using *algorithm 2*, FFT technique was proposed in [13]. When the target bit for the linear distinguisher is a function of $x \oplus k$ where x, k are both n-bit values, the time can be improved from $2^{2 \cdot n}$ to $3 \cdot n \cdot 2^n$ simple calculations.

Our Contributions. We evaluate the security of SPARX-64/128 using the zero-correlation cryptanalysis in this paper:

(1) We find some new zero-correlation distinguishers. By extending the existing simple zero-correlation distinguisher proposed in [6], we construct several multidimensional zero-correlation distinguishers covering 14-round SPARX-64. Morever, with careful selection of the input mask, we can extend some distinguishers by one more round and get three 15-round zero-correlation distinguishers. These are the longest zero-correlation linear distinguishers of SPARX-64 as we know

(2) Using the new zero-correlation distinguishers, we make zero-correlation linear attacks with the help of multiple/multidimensional zero-correlation linear cryptanalysis model in [12]. The multidimensional zero-correlation attack covers 15-round and 16-round using 14-round distinguishers. Then the zero-correlation attack with one single 15-round linear hull covers 17-round. What's more, with the help of FFT technique, we also can attack 18-round

SPARX-64. These are the best attacks from the view of number of rounds attacked

(3) Also, we transform the zero-correlation linear distinguishers into integral distinguishers. As a result, we can get some 14-round and 15-round integral distinguishers with balanced properties. The balanced property means that the numbers of each value in the output sets are equal for the integral distinguisher, while the zero-sum property means the Xor-sum is zero

Outline. First, we describe the target block cipher SPARX-64/128 and the zero-correlation linear attack models in Sect.2. In Sect.3, we show how to construct the 14-round and 15-round zero-correlation linear distinguishers for SPARX-64. Then we give the multidimensional zero-correlation and multiple zero-correlation linear cryptanalysis against SPARX in Sect.4 and 5. Sect.6 describes some new integral distinguishers and finally, Sect.7 concludes this paper.

2. Preliminaries

2.1. Notations. The following symbols and notations are used throughout this paper:

(i) ⊞: addition modulo 2^{16}

(ii) ⊕: bit-wise Xor

(iii) ⋘: 16-bit rotation to the left

(iv) ⋙: 16-bit rotation to the right

(v) ‖: concatenation of two bit strings

(vi) x_L: left half (16-bit) of the word x (32-bit).

(vii) x_R: right half (16-bit) of the word x (32-bit).

(viii) SPECKEY-3R: three rounds of SPECKEY

(ix) K^{2i}, K^{2i+1}: the subkeys used in the left and, respectively, right SPECKEY-3R of the i-th step of SPARX-64. Each has three 32-bit words $K^{*,1}$, $K^{*,2}$, $K^{*,3}$, used in three rounds of SPECKEY-3R, respectively

(x) $1_b^x(0_b^x, ?_b^x)$: x-bit of '1'('0','?').'?' is one undetermined bit

(xi) $x[i]$: the i-th bit of bit string x. $x[0]$ is the least significant bit

(xii) $x[j \sim i]$: the concatenation of $x[j], x[j-1], \cdots, x[i]$, $j > i$

2.2. Brief Description of SPARX-64/128.

SPARX-64/128 is the lightest instance of the SPARX family. It operates on two 32-bit words and uses a 128-bit key. There are 8 steps and 3 rounds per step. A high level view of SPARX-64/128 and the general structure of a step is shown in Figure 1. Both branches have non-linear operations SPECKEY-3R, which means three rounds of SPECKEY, involving three 32-bit subkeys. SPECKEY splits the state into two 16-bit branches and xor the left and right half key bits, i.e., $K_L^{i,j}$ and $K_R^{i,j}$, in each branch before the non-linear operations. The linear layer $\mathscr{L}$ operates 32-bit value as follows,

$$\mathscr{L}(x) = x_L \oplus ((x_L \oplus x_R) \lll 8) \| x_R \oplus ((x_L \oplus x_R) \lll 8). \quad (1)$$

In the i-th step of SPARX-64, six 32-bit subkeys $K^{2i,1}$, $K^{2i,2}$, $K^{2i,3}$, $K^{2i+1,1}$, $K^{2i+1,2}$, $K^{2i+1,3}$ are involved. In particular, $K^{2i,1}$, $K^{2i,2}$, $K^{2i,3}$ are used in the left SPECKEY-3R and $K^{2i+1,1}$, $K^{2i+1,2}$, $K^{2i+1,3}$ are used in the right SPECKEY-3R.

The 128-bit permutation used in the key schedule is simple, which is shown in Algorithm 1. For more details, please refer to [1].

2.3. χ^2 – Multiple/Multidimensional Zero-Correlation Cryptanalysis.

We start this section with the introduction of MPZC and MDZC models. Suppose that there are N plaintext-ciphertext samples and ℓ zero-correlation linear approximations for an n-bit block cipher. For the i-th approximation, the adversary counts the samples which make the linear approximation hold and gets the corresponding counter T_i. Under the model of MPZC cryptanalysis, the adversary evaluates the following statistic:

$$T^{MP} = N \sum_{i=1}^{\ell} \left(2 \frac{T_i}{N} - 1 \right)^2. \quad (2)$$

For MDZC model, the ℓ zero-correlation linear approximations form a linear space (considering the zero vector in) with dimension m and then $\ell = 2^m - 1$. For each plaintext-ciphertext sample, the adversary evaluates the m base linear approximation and obtains an m-bit value z. By iterating all N samples, the adversary would get a counter vector $V[z]$ with $z = 0, 1, \cdots, 2^m - 1$. The statistic used in MDZC is:

$$T^{MD} = \sum_{z=0}^{2^m - 1} \frac{(V[z] - N2^{-m})^2}{N2^{-m}}. \quad (3)$$

To estimate the data complexity and success probability, researchers [14] considered two sampling models, i.e., KP and DKP. In KP settings, the samples are obtained randomly while in DKP settings there is a restriction that the plaintext-ciphertext samples are non-repeating. In [14], Blondeau and Nyberg proved T^{MP} and T^{MD} followed the same distribution when the same sampling method are applied. They gave the estimation method of data complexity under these two sampling models for MPZC and MDZC. Later, Sun et al. proposed the χ^2-MPZC and MDZC, in which they use the χ^2-distributions to model the statistics [12], instead of the normal distributions.

Considering two types of errors:

(i) *Type-1 error*: made by wrongfully discarding the cipher (false negative) and suppose the probability is α_0. This is related to the success probability P_S and $P_S = 1 - \alpha_0$

(ii) *Type-2 error*: made by wrongfully accepting a randomly chosen permutation as the cipher (false positive) and suppose the probability is α_1. This is related to the time complexity T_S of the exhaustive search phase and $T_S = 2^k \cdot \alpha_1$ where k is the length of the main key

Then the χ^2-MPZC and MDZC evaluate the data complexity as follows.where $\chi_{1-\alpha_0}^{(l)}$ and $\chi_{\alpha_1}^{(l)}$ are the respective quantiles of the χ^2-distribution with l degrees of freedom evaluated on the points $1 - \alpha_0$ and α_1.In the attacks, the threshold value to distinguisher the cipher and randomly chosen permutation is calculated as $\tau = \chi_{1-\alpha_0}^{(l)}$.

Theorem 1. in ([12])

Suppose that the linear approximations involved satisfy the hypotheses in [14]. The number N^{KP} of KPs requires in a MPZC or MDZC linear attack is

$$N^{KP} \approx \frac{2^n \left(\chi_{1-\alpha_0}^{(l)} - \chi_{\alpha_1}^{(l)} \right)}{\chi_{\alpha_1}^{(l)}}, \quad (4)$$

and the number N^{DKP} of DKPs required in a MPZC or MDZC linear attack is

$$N^{DKP} \approx \frac{2^n \left(\chi_{1-\alpha_0}^{(l)} - \chi_{\alpha_1}^{(l)} \right)}{\chi_{1-\alpha_0}^{(l)}}, \quad (5)$$
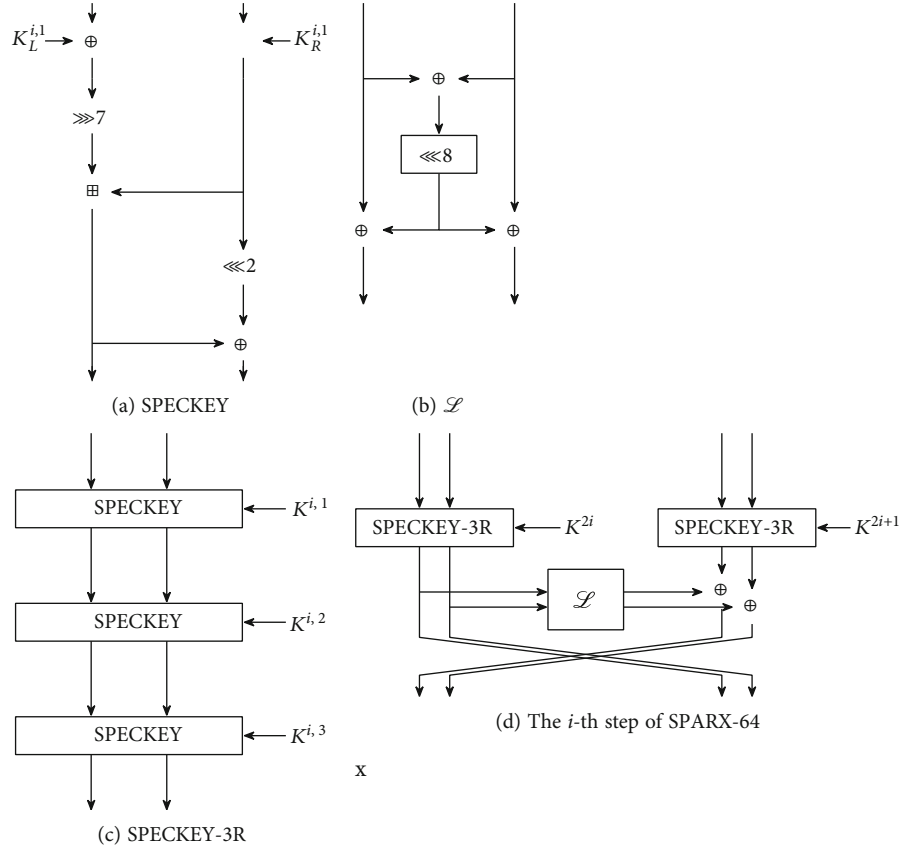
Figure 1: (a) The SPECKEY function; (b) The linear layer $\mathscr{L}$; (c) SPECKEY-3R; (d) The i-th step of SPARX-64.
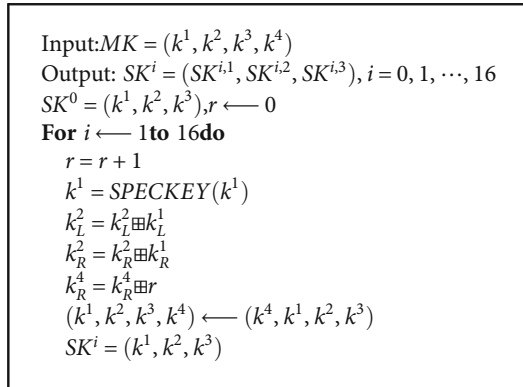
Algorithm 1: Key schedule of SPARX-64/128

3. Zero-Correlation Linear Hulls of SPARX-64

The 12-round zero-correlation linear hull of SPARX-64 proposed in [6] is shown in Figure 2, which is $(\alpha, 0) \longrightarrow (0, \beta)$, $\alpha \neq 0, \beta \neq 0$. α_1, α_2 are linear masks derived from the input mask α, while β_1, β_2 are linear masks derived from the output mask β. The contradiction appears in the second linear permutation $\mathscr{L}$, where the corresponding input mask is zero while the output mask is non-zero value $\alpha_2 (= \beta_2)$. This distinguisher is like the 5-round zero-correlation linear hull of Feistel structure [8] with bijected F functions, which only takes advantage of the properties of the structures. In the fol-
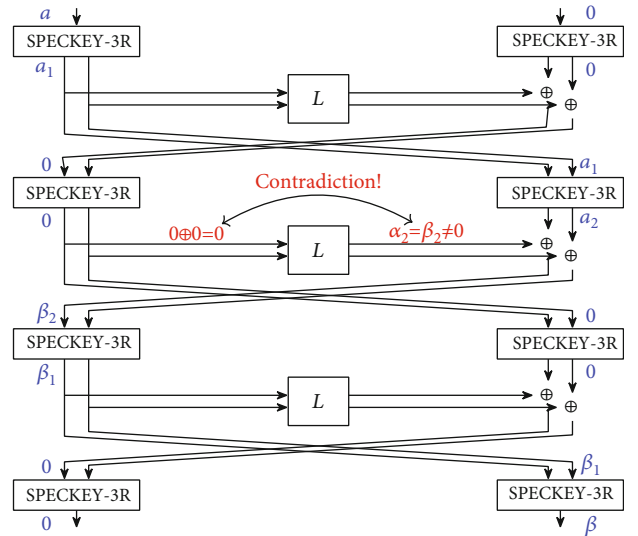
Figure 2: 12-Round Zero Correlation Linear Hull of SPARX64.

lowing subsections, we will study the detailed property of linear mask's propogation in SPECKEY and construct longer zero-correlation linear hulls.

Since there are only Xor ($\oplus$), Modulo Addition ($\boxplus$), Branch ($\vdash$) and Rotation ($\lll$ or $\ggg$), we review how the linear masks propogate through these operations. Let x, y, z be values and $\Gamma_x, \Gamma_y, \Gamma_z$ be the corresponding masks.

TABLE 2: Linear Masks' Relations among Some Simple Operations.

Operation	Values' relation	Masks' relation
$\oplus$	$z = x \oplus y$	$\Gamma_x = \Gamma_y = \Gamma_z$
$\vdash$	$y = x, z = x$	$\Gamma_x \oplus \Gamma_y \oplus \Gamma_z = 0.$
$\lll$	$y = x \lll i$	$\Gamma_y = \Gamma_x \lll i$
$\ggg$	$y = x \ggg i$	$\Gamma_y = \Gamma_x \ggg i$
$\boxplus$	$z = x \boxplus y$	$MSB^1(\Gamma_x) = MSB^1(\Gamma_y) = MSB^1(\Gamma_z)$

Suppose the position of the first bit '1' from the MSB is $MSB^1(x)$ for x. Then the masks' relations are shown in Table 2.

Only the Modulo Addition ('$\boxplus$') is non-linear and the corresponding correlation may be not one. However, when $\Gamma_x = \Gamma_y = \Gamma_z = 0x0000$ or $\Gamma_x = \Gamma_y = \Gamma_z = 0x0001$, the correlation at '$\boxplus$' is equal to 1.

3.1. Expand the Linear Hull with Input Mask $(\alpha, 0)$ Backward with Correlation One. In fact, by limiting the values of α and β, we can expand the number of rounds of zero-correlation linear hull. The main idea is to make the input mask (or output mask) go back (or forward) one more round with correlation one. The only non-linear operation in one SPECK round is'$\boxplus$', so we hope the corresponding input mask or output mask of'$\boxplus$' is $0x0000$ or $0x0001$, which leads to linear approximations with correlation one.

For the case of input mask α, we expect that Γ_1, Γ_2 be $0x0001$ or $0x0000$, where Γ_1, Γ_2 are the output masks of the '$\boxplus$' in Figure 3. It's easy to know that $\Gamma_2 = \alpha_L \oplus \alpha_R$ and $\Gamma_1 = (L^T\alpha)_L \oplus (L^T\alpha)_R$ where L^T is the transform of the linear layer. So we can get the following four equations:

$$(1)\begin{cases} \alpha_L \oplus \alpha_R = 0x0000 \\ (L^T\alpha)_L \oplus (L^T\alpha)_R = 0x0000 \end{cases} (2)\begin{cases} \alpha_L \oplus \alpha_R = 0x0000 \\ (L^T\alpha)_L \oplus (L^T\alpha)_R = 0x0001 \end{cases}$$

$$(3)\begin{cases} \alpha_L \oplus \alpha_R = 0x0001 \\ (L^T\alpha)_L \oplus (L^T\alpha)_R = 0x0000 \end{cases} (4)\begin{cases} \alpha_L \oplus \alpha_R = 0x0001 \\ (L^T\alpha)_L \oplus (L^T\alpha)_R = 0x0001 \end{cases}$$
(6)

According to $L^T\alpha = ((L^T\alpha)_L, (L^T\alpha)_R) = (\alpha_L \oplus (\alpha_L \oplus \alpha_R)_{\ggg 8}, \alpha_R \oplus (\alpha_L \oplus \alpha_R)_{\ggg 8})$, we know that only the first and forth equations have possible solutions.

(i) Equation Equation (4). holds when $\alpha_L = \alpha_R$

(ii) Equation Equation (7) holds when $\alpha_L = \alpha_R \oplus 0x0001$

We set the condition $\alpha_L = \alpha_R$ (See the left part of Figure 3) and then we can derive that the linear mask becomes

$$\left(\Gamma_1^{in1}, \Gamma_2^{in1}, \Gamma_3^{in1}, \Gamma_4^{in1}\right) = \left(0, (\alpha_R)_{\ggg 2}, 0, (\alpha_R)_{\ggg 2}\right) \quad (7)$$

after one decrypted round. In a further step, there is $\Gamma_3 = (\alpha_R \ggg 2) = \Gamma_4$. To expand one more round with correlation one, we hope the corresponding masks Γ_3, Γ_4 also be $0x0000$ or $0x0001$. Then we obtain the only non-zero solution

$\alpha_L = \alpha_R = 0x0004$. At last, we get the linear mask

$$\left(\Gamma_1^{in0}, \Gamma_2^{in0}, \Gamma_3^{in0}, \Gamma_4^{in0}\right) = (0x0080, 0x4001, 0x0080, 0x4001).$$
(8)

after two decrypted rounds.

Similarly, when the condition is $\alpha_L = \alpha_R \oplus 0x0001$ (See right part of Figure 3), we can derive that

$$\left(\Gamma_1^{in1}, \Gamma_2^{in1}, \Gamma_3^{in1}, \Gamma_4^{in1}\right) = \left(0x0080, (\alpha_R)_{\ggg 2} \oplus 0x0041, 0, (\alpha_R)_{\ggg 2} \oplus 0x0001\right)$$
(9)

Then there is $\Gamma_3 = (\alpha_R \ggg 2) \oplus 0x00c1, \Gamma_4 = (\alpha_R \ggg 2) \oplus 0x0081$. In this situation, there is no value of α satisfying $\Gamma_3, \Gamma_4 \in \{0x0000, 0x0001\}$ at the same time. This means that when $\alpha_L = \alpha_R \oplus 0x0001$, we can only expand the linear hull backward one more round and can not expand the linear hull two more rounds backward with correlation one.

3.2. Expand the Linear Hull with Output Mask $(0, \beta)$ Forward with Correlation One. For the output linear mask $(0, \beta)$, we follow the similar method. See Figure 4. At first, we hope that the linear masks Γ_5, Γ_6 taking value $0x0000$ or $0x0001$. So we can list the following equations.

$$(1)\begin{cases} \beta_L \ggg 7 = 0x0000 \\ (L^T\beta)_L \ggg 7 = 0x0000 \end{cases} (2)\begin{cases} \beta_L \ggg 7 = 0x0000 \\ (L^T\beta)_L \ggg 7 = 0x0001 \end{cases}$$

$$(3)\begin{cases} \beta_L \ggg 7 = 0x0001 \\ (L^T\beta)_L \ggg 7 = 0x0000 \end{cases} (4)\begin{cases} \beta_L \ggg 7 = 0x0001 \\ (L^T\beta)_L \ggg 7 = 0x0001 \end{cases}$$
(10)

According to $L^T\beta = ((L^T\beta)_L, (L^T\beta)_R) = (\beta_L \oplus (\beta_L \oplus \beta_R)_{\ggg 8}, \beta_R \oplus (\beta_L \oplus \beta_R)_{\ggg 8})$, we know that only the solutions are as follows.

(i) Equation Equation (4). holds when $\beta_L = \beta_R = 0x0000$

(ii) Equation Equation (5) holds when $\beta_L = 0x0000, \beta_R = 0x8000$

(iii) Equation Equation (7) holds when $\beta_L = 0x0080, \beta_R = 0x8080$

(iv) Equation Equation (8) holds when $\beta_L = 0x0080, \beta_R = 0x0080$

Figure 4 gives the detailed propogation of output linear mask $(0, \beta)$ when $\beta_L = 0x0000, \beta_R = 0x8000$ or $\beta_L = 0x0080, \beta_R = 0x8080$. The output mask after one more round is

$$\left(\Gamma_1^{out0}, \Gamma_2^{out0}, \Gamma_3^{out0}, \Gamma_4^{out0}\right)$$
$$= (0x0002, 0x0002, 0x0207, 0x0206), \left(\Gamma_1^{out0}, \Gamma_2^{out0}, \Gamma_3^{out0}, \Gamma_4^{out0}\right)$$
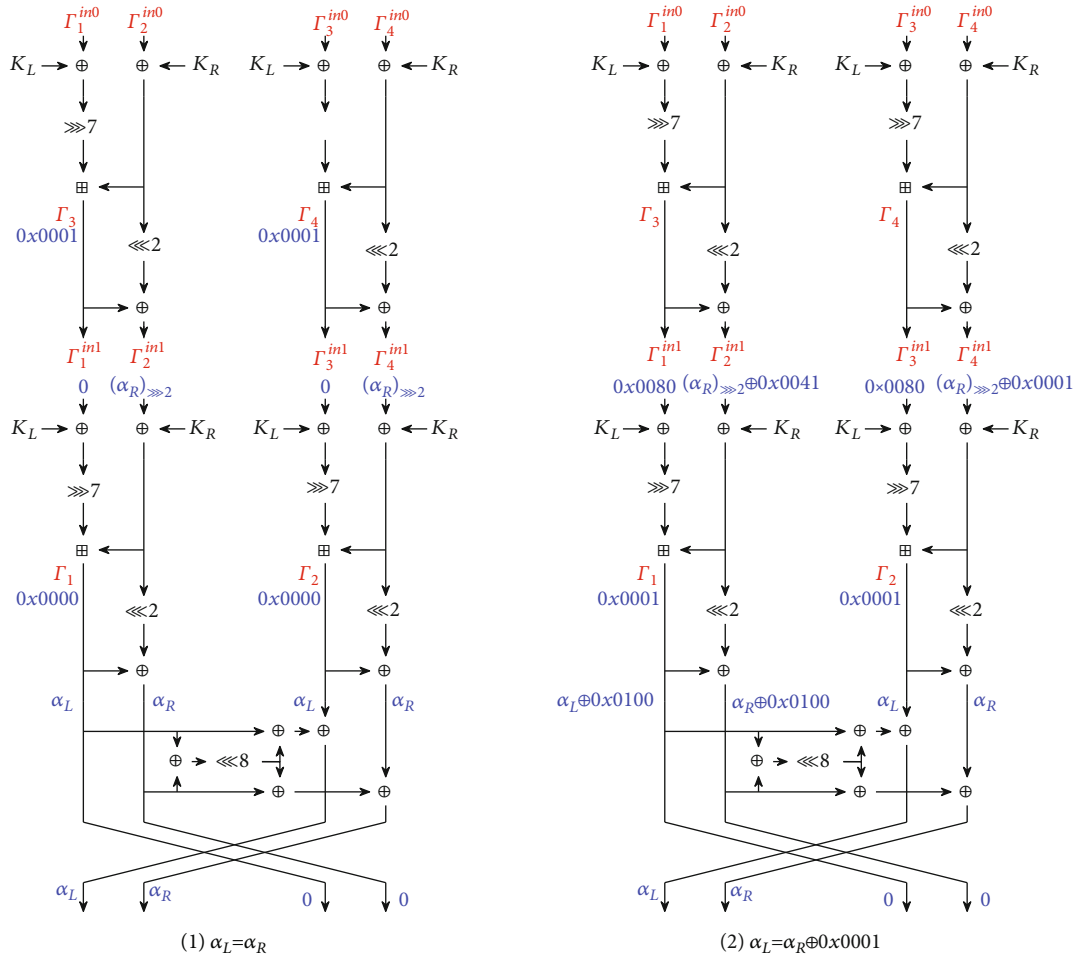$$= (0x0207, 0x0206, 0x0002, 0x0002),$$
(11)

FIGURE 3: Expand the input mask $(\alpha, 0)$ by two more rounds. Red signals represent the variable names and the blue are the corresponding values.
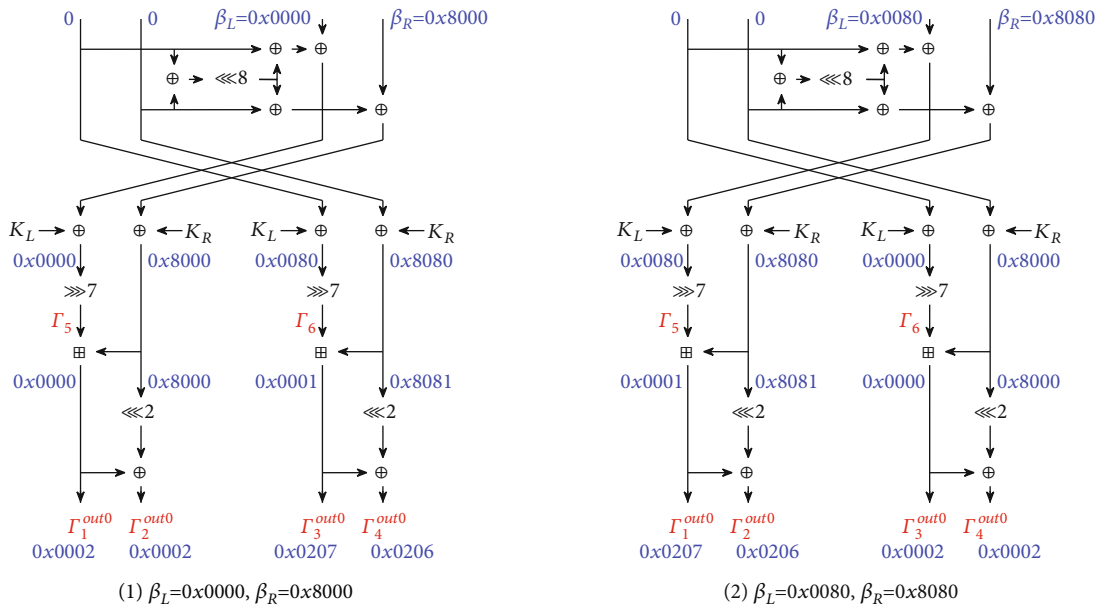

FIGURE 4: Expand the linear hull with output mask $(0, \beta)$ by one more round. Red signals represent the variable names and the blue are the corresponding values.

TABLE 3: Zero Correlation Linear Hulls of SPARX.

#R	Input mask(s)	Rounds covered	Output mask(s)
12	$(\alpha_L, \alpha_R, 0, 0)$	$\underbrace{\text{SPECKEY} - 3\text{R}}_{4\text{steps}}$	$(0, 0, \beta_L, \beta_R)$
14	$(0, \gamma, 0, \gamma),$ $(0, \gamma, 0, \gamma) \oplus$ $(0x0080, 0x0040, 0x0000, 0x0000)$	$\underbrace{\text{SPECKEY} - 1\text{R}, \text{SPECKEY} - 3\text{R}, \text{SPECKEY} - 1\text{R}}_{4\text{steps}}$	$(0x0207, 0x0206, 0x0002, 0x0002),$ $(0x0002, 0x0002, 0x0207, 0x0206),$ $(0x0205, 0x0204, 0x0205, 0x0204)$
15	$(0x0080, 0x4001, 0x0080, 0x4001)$	$\underbrace{\text{SPECKEY} - 2\text{R}, \text{SPECKEY} - 3\text{R}, \text{SPECKEY} - 1\text{R}}_{4\text{steps}}$	$(0x0207, 0x0206, 0x0002, 0x0002),$ $(0x0002, 0x0002, 0x0207, 0x0206),$ $(0x0205, 0x0204, 0x0205, 0x0204)$

γ: any 16-bit non-zero linear mask.

respectively. Otherwise, when $\beta_L = 0x0080$, $\beta_R = 0x0080$, there is

$$\left(\Gamma_1^{\text{out}0}, \Gamma_2^{\text{out}0}, \Gamma_3^{\text{out}0}, \Gamma_4^{\text{out}0}\right) = (0x0205, 0x0204, 0x0205, 0x0204). \tag{12}$$

We list the zero-correlation linear hulls in Table 3. $\#R$ denotes the number of rounds of the distinguishers.

4. Multidimensional Zero-Correlation Cryptanalysis of SPARX-64 Using 14-round Distinguishers

In this section, we give 15-round and 16-round multidimensional attacks with 14-round zero-correlation distinguishers in DKP sampling setting.

4.1. 15-Round Multidimensional Zero-Correlation Attack with One 14-round Distinguisher. Wu use one 14-round multidimensional zero-correlation distinguisher

$$(0, \gamma, 0, \gamma) \longrightarrow (0x0207, 0x0206, 0x0002, 0x0002) \tag{13}$$

to mount the attack. By adding one round at the top, the attack would cover 15 rounds. The symbols X_i, Y_i denote the corresponding states derived from the plaintexts or ciphertexts (See Figure 5). For enough plaintext-ciphertext samples, we need to guess the corresponding subkeys and get the numbers of all possible values of

$$[X_{1,1} \oplus X_{1,3}, (0x0207, 0x0206, 0x0002, 0x0002) \cdot Y_1]. \tag{14}$$

Since the MSB of $X_{1,1}$, *i.e.*, $X_{1,1}[15]$, is linear with $K_L^{2i,2}[15]$ and $K_R^{2i,2}[15]$, in the attack there is no need guessing these two key bits. For simplicity, we can set them as 0. Similarly, we can also set $K_L^{2i+1,2}[15]$ and $K_R^{2i+1,2}[15]$ as constant values. So in the round before the distinguisher, the keys need to be guessed are $k_1 = (K_L^{2i,2}[14 \sim 0], K_R^{2i,2}[14 \sim 0])$ and $k_2 = (K_L^{2i+1,2}[14 \sim 0], K_R^{2i+1,2}[14 \sim 0])$. Since Y_1 is linear with
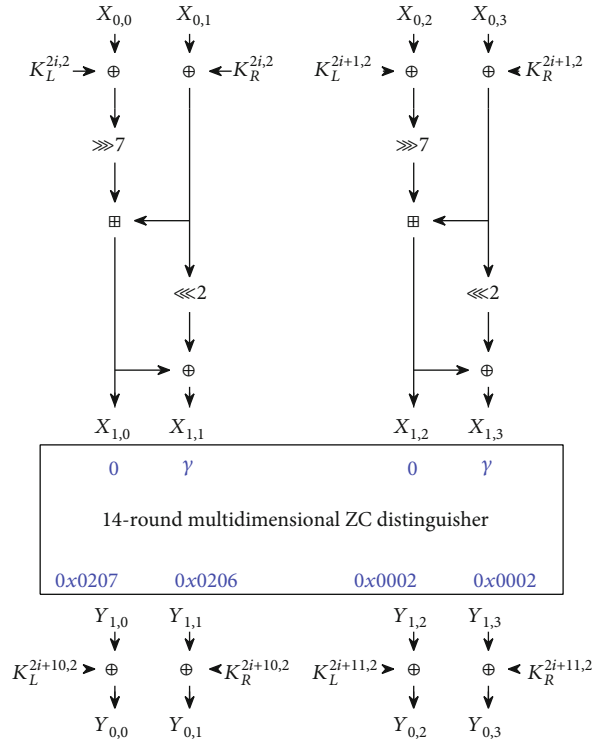
FIGURE 5: 15-Round Multidimensional Zero Correlation Linear Cryptanalysis on SPARX64.

$K^{2i+10,2}$ and $K^{2i+11,2}$, no key bits need to be guessed in the backward rounds.

Suppose the number of samples in the attack is N, the attack procedure is as follows.

(i) Step 1. For N values of $[X_0, Y_0]$, suppose $K^{2i+10,2}$, $K^{2i+11,2} = 0$, then $Y_0 = Y_1$. We can compute

$$t_{\text{out}} = (0x0207, 0x0206, 0x0002, 0x0002) \cdot Y_0. \tag{15}$$

We get N values of $[X_0, t_{\text{out}}]$.

(ii) Step 2. Guess 30 valid bits of k_1, encrypt $X_{0,0}, X_{0,1}$ by one round and we can get $X_{1,1}$. Store the numbers of $[X_{1,1}, X_{0,2}, X_{0,3}, t_{out}]$.

(iii) Step 3. Guess 30 valid bits of k_2, encrypt $X_{0,2}, X_{0,3}$ by one round and we can get $X_{1,3}$. Store the numbers of $[X_{1,1} \oplus X_{1,3}, t_{out}]$.

(iv) Step 4. For each guessed key, compute the statistic value used in the multidimensional zero-correlation attack, *i.e.*,

$$T = \sum_{X_{1,1}\oplus X_{1,3}, t_{out}} \frac{(V[X_{1,1} \oplus X_{1,3}, t_{out}] - N \cdot 2^{-m})^2}{N \cdot 2^{-m}}, \quad (16)$$

where $m = 17$. When T is smaller than the threshhold value τ, the key is supposed to be a right key candidate and can then be checked using two plaintext-ciphertext pairs.

By setting $\alpha_0 = 2^{-2.7}$ and $\alpha_1 = 2^{-23}$, we can compute that the data complexity $N \approx 2^{58.616}$ and threshold $\tau = 131593$. The first three steps need

$$N \cdot \frac{1}{15} + \left(N \cdot 2^{30} + 2^{49} \cdot 2^{30+30}\right) \cdot \frac{1}{15} \cdot \frac{1}{2} \approx 2^{105} \quad (17)$$

encryptions. The last step needs $2^{128} \cdot \alpha_1 = 2^{105}$ times encryption. So the total time complexity is about 2^{106} encryptions.

4.2. 16-Round Multidimensional Zero-Correlation Attack with One 14-round Distinguisher. We can append one more round at the bottom to attack 16 rounds (See Figure 6). To control the time complexity, we use part of the above distinguisher. In detail, we only consider the input mask with form $\gamma = (0^{16-t} *^t)$, which means the distinguisher has dimension $t + 1$. So $k_1 = (K_L^{2i,2}[t-2 \sim 0], K_R^{2i,2}[t-2 \sim 0], K_L^{2i+1,2}[t-2 \sim 0], K_R^{2i+1,2}[t-2 \sim 0])$ need to be guessed.

For the ouput mask $(0x0207, 0x0206, 0x0002, 0x0002)$, we expand it by one round. The mask pattern at Y_0 would become $(0^2 1?^{13}, 0^2 1?^{11} 0^2, 0^3 1?^{12}, 0^3 1?^{10} 0^2)_b$. Only the nonlinear key bits need to be guessed for the last round, which means we only consider $k_2 = (K_L^{2i+10,3}[12 \sim 0], K_R^{2i+10,3}[12 \sim 2])$, $k_3 = (K_L^{2i+11,3}[11 \sim 0], K_L^{2i+11,3}[11 \sim 2])$.

The attack proceudere is as follows.

(1) For N values of $[X_0, Y_0]$, compress Y_0 by one round and get $Y_{st1} = (Y_{0,0}[13 \sim 0], Y_{0,1}[13 \sim 2])$ and $Y_{st2} = (Y_{0,2}[12 \sim 0], Y_{0,3}[12 \sim 2])$.

(2) Guess $4t - 4$ bits of k_1, encrypt X_0 by one round and get $X_{1,1} \oplus X_{1,3}$. Store the numbers of $[X_{1,1} \oplus X_{1,3}, Y_{st1}, Y_{st2}]$.

(3) Guess 24 valid bits of k_2, decrypt Y_{st1} by one round and we can get $\beta_1 = (0x0207, 0x0206) \cdot (Y_{2,0}, Y_{2,1})$. Store the numbers of $[X_{1,1} \oplus X_{1,3}, \beta_1, Y_{st2}]$.
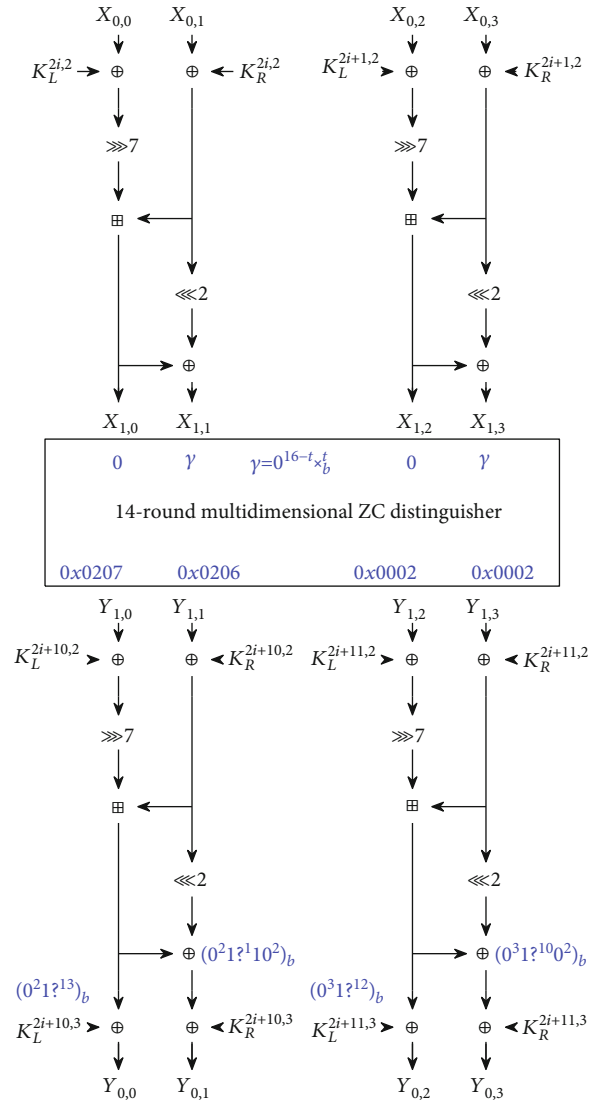
FIGURE 6: 16-Round Multidimensional Zero Correlation Linear Cryptanalysis on SPARX64.

(4) Guess 22 valid bits of k_3, decrypt Y_{st2} by one round and we can get $\beta_{out} = \beta_1 \oplus (0x0002, 0x0002) \cdot (Y_{2,2}, Y_{2,3})$. Store the numbers of $[X_{1,1} \oplus X_{1,3}, \beta_{out}]$.

(5) For each guessed key, compute the statistic value used in the multidimensional zero-correlation attack, *i.e.*,

$$T = \sum_{X_{1,1}\oplus X_{1,3}, \beta_{out}} \frac{(V[X_{1,1} \oplus X_{1,3}, \beta_{out}] - N \cdot 2^{-m})^2}{N \cdot 2^{-m}}, \quad (18)$$

where $m = t + 1$. When T is smaller than the threshhold value τ, the key is supposed to be a right key candidate and can then be checked using two plaintext-ciphertext pairs.

By setting $t = 8$, $\alpha_0 = 2^{-2.7}$ and $\alpha_1 = 2^{-28}$, we can compute that the data complexity $N \approx 2^{62.531}$ and threshold $\tau = 543$.

The first four steps need

$$N \cdot \frac{1}{16} + N \cdot 2^{4t-4} \cdot \frac{1}{16} + 2^{4t-4} \cdot \left(2^{54} \cdot 2^{24} + 2^{31} \cdot 2^{24+22}\right) \cdot \frac{1}{16} \cdot \frac{1}{2} \approx 2^{100} \tag{19}$$

encryptions. The last step needs $2^{128} \cdot \alpha_1 = 2^{100}$ times encryption. So the total time complexity is about 2^{101} encryptions.

5. Zero-Correlation Cryptanalysis of SPARX-64 Using 15-round Distinguisher

In this section, we give 17-round and 18-round attacks with 15-round zero-correlation distinguisher in DKP sampling setting. Notice that there is only one single zero-correlation linear hull. However, we also can use the multiple zero-correlation linear attack model to estimate the data complexity, as shown in [12].

5.1. 17-Round Zero-Correlation Attack with One 15-round Distinguisher. We use the 15-round zero-correlation distinguisher

$$(0x0080, 0x4001, 0x0080, 0x4001) \longrightarrow (0x0207, 0x0206, 0x0002, 0x0002) \tag{20}$$

to attack 17-round SPARX64/128.

We add one round at the top and one round at the bottom to make the attack which is similar to the 16-round attack, except that the distinguisher here is 15-round (See Figure 7). The key bits involved in this attack are $k_1 = (K_L^{2i,1}[15 \sim 7, 4 \sim 0], K_R^{2i,1}[13 \sim 0], K_L^{2i+1,1}[15 \sim 7, 4 \sim 0], K_R^{2i+1,1}[13 \sim 0])$ and $k_2 = (K_L^{2i+10,3}[12 \sim 0], K_R^{2i+10,3}[12 \sim 2]), k_3 = (K_L^{2i+11,3}[11 \sim 0], K_L^{2i+11,3}[11 \sim 2])$.

The attack procedure is as follows.

(1) For N values of $[X_0, Y_0]$, compress Y_0 by one round and get $Y_{st1} = (Y_{0,0}[13 \sim 0], Y_{0,1}[13 \sim 2])$ and $Y_{st2} = (Y_{0,2}[12 \sim 0], Y_{0,3}[12 \sim 2])$.

(2) Guess 56 bits of k_1, encrypt X_0 by one round and get $\beta_0 = (0x0080, 0x4001, 0x0080, 0x4001) \cdot X_1$. Calculate the numbers of $[Y_{st1}, Y_{st2}]$ according to the sign of β_0 (+1 if $\beta_0 = 0$, −1 if $\beta_0 = 1$).

(3) Guess 24 valid bits of k_2, decrypt Y_{st1} by one round and we can get $\beta_1 = (0x0207, 0x0206) \cdot (Y_{2,0}, Y_{2,1})$. Calculate the numbers of $[Y_{st2}]$ according to the sign of β_1

(4) Guess 22 valid bits of k_3, decrypt Y'_{st2} by one round and we can get $\beta_2 = (0x0002, 0x0002) \cdot (Y_{2,2}, Y_{2,3})$. Calculate the final counter C according to the sign of β_2

(5) For each guessed key, compute the statistic value used in the multiple zero-correlation attack, *i.e.,*
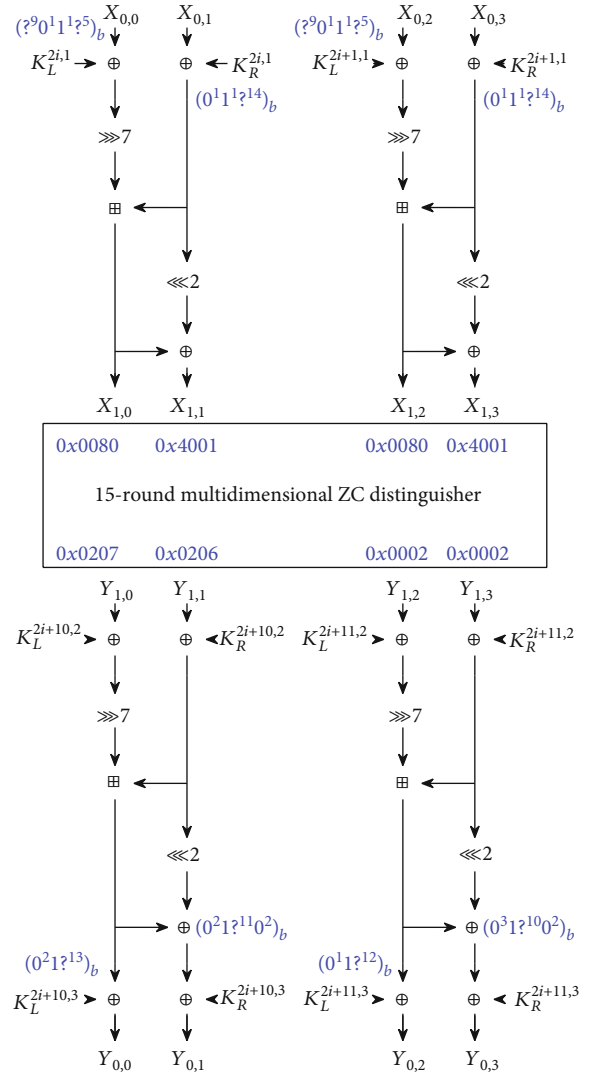
Figure 7: 17-Round Multidimensional Zero Correlation Linear Cryptanalysis on SPARX64.

$$T = N \left(\frac{C}{N}\right)^2. \tag{21}$$

When T is smaller than the threshhold value τ, the key is supposed to be a right key candidate and can then be checked using two plaintext-ciphertext pairs.

By setting $\alpha_0 = 2^{-2.7}$ and $\alpha_1 = 2^{-1}$, we can compute that the data complexity $N \approx 2^{63.634}$ and threshold $\tau = 2$. The first four steps need

$$N \cdot \frac{1}{17} + N \cdot 2^{56} \cdot \frac{1}{17} + 2^{56} \cdot \left(2^{46} \cdot 2^{24} + 2^{22} \cdot 2^{24+22}\right) \cdot \frac{1}{17} \cdot \frac{1}{2} \approx 2^{121.15} \tag{22}$$

encryptions. The last step needs $2^{128} \cdot \alpha_1 = 2^{127}$ times encryption. So the total time complexity is $T \approx 2^{127}$ encryptions.

TABLE 4: Integral Distinguishers of SPARX.

#R	Input sets($(x_0, x_1, x_2, x_3) \in \mathcal{S}$)	Rounds covered(f)	Active bit(s)($(y_0, y_1, y_2, y_3) \in f(\mathcal{S})$)
12	(C_0, C_1, A_0, A_1)	$\underbrace{\text{SPECKEY} - 3R}_{\text{4steps}}$	$(*, *, A_3, A_4)$
14	$(A_0, A_1, A_2, A_1 \oplus C)$	$\left(\text{SPEKEY} - 1R, \underbrace{\text{SPECKEY} - 3R}_{\text{4steps}}, \text{SPECKEY} - 1R \right)$	$(0x0207 \cdot y_0) \oplus (0x0206 \cdot y_1) \oplus$ $(0x0002 \cdot y_2) \oplus (0x0002 \cdot y_3)$
15	$(0x0080 \cdot x_0) \oplus (0x4001 \cdot x_1) \oplus$ $(0x0080 \cdot x_2) \oplus (0x4001 \cdot x_3) = \text{'}0\text{'}$ $(\text{or} = \text{'}1\text{'})$	$\left(\text{SPECKEY} - 2R, \underbrace{\text{SPECKEY} - 3R}_{\text{4steps}}, \text{SPECKEY} - 1R \right)$	$(0x0207 \cdot y_0) \oplus (0x0206 \cdot y_1) \oplus$ $(0x0002 \cdot y_2) \oplus (0x0002 \cdot y_3)$

5.2. 18-Round Zero-Correlation Attack with One 15-round Distinguisher. By adding one more round before the 17-round attack, we can extend the attack to 18 rounds. The key bits involved in the first round are $K^{2i-2,3}$ and $K^{2i-1,3}$. According to the key schedule, we know that

$$K^{2i-2,3} = K^{2i,1}, K^{2i-1,3} = K^{2i+1,1}. \tag{23}$$

Let P, Y_0 be the plaintext-ciphertext pair. The attack proceudere is as follows.

(1) For N values of $[P, Y_0]$, guess 64 bits of $K^{2i-2,3}$, $K^{2i-1,3}$ and encrypt P by two rounds and get

$$\beta_0 = (0x0080, 0x4001, 0x0080, 0x4001) \cdot X_1 \oplus Y_{0,0}[13] \oplus Y_{0,1}[13] \oplus Y_{0,2}[12] \oplus Y_{0,3}[12]. \tag{24}$$

Calculate the numbers of $[Y']$ according to the value of β_0 (+1 if $\beta_0 = 0$, −1 if $\beta_0 = 1$), where

$$Y' = (Y_{0,0}[12 \sim 0], Y_{0,1}[12 \sim 2], Y_{0,2}[11 \sim 0], Y_{0,3}[11 \sim 2]). \tag{25}$$

(2) It's clear that the target bit, *i.e.*, is a function of $Y' \oplus k$, where $k = (K_L^{2i+10,3}[12 \sim 0], K_R^{2i+10,3}[12 \sim 2], K_L^{2i+11,3}[11 \sim 0], K_L^{2i+11,3}[11 \sim 2])$. So the target counter C can be computed using FFT techniques for all possible keys

(3) For each guessed key, compute the statistic value used in the multiple zero-correlation attack, *i.e.*,

$$T = N \left(\frac{C}{N} \right)^2. \tag{26}$$

When T is smaller than the threshhold value τ, the key is

supposed to be a right key candidate and can then be checked using two plaintext-ciphertext pairs.

By setting $\alpha_0 = 2^{-2.7}$ and $\alpha_1 = 2^{-1}$, we can compute that the data complexity $N \approx 2^{63.634}$ and threshold $\tau = 2$. The first step needs $N \cdot 2^{64} \cdot 2/18 = 2^{124.464}$ encryptions. The second step needs $2^{64} \cdot 3 \cdot 46 \cdot 2^{46} = 2^{117.109}$ simple calculations. The last step needs $2^{128} \cdot \alpha_1 = 2^{127}$ times encryption. So the total time complexity is $T \approx 2^{127.2}$ encryptions.

6. Integral Distinguishers on SPARX

Zero-correlation linear distinguishers can be transformed into integral distinguishers according to the known results in [10, 15]. Theorem 6 describes the result given in [15].

Theorem 2. *(Corollary 4, [15])*
Let $F : F_2^n \longrightarrow F_2^n$ be a function on F_2^n, and let A be a subspace of F_2^n and $b \in F_2^n \setminus \{0\}$. Suppose that $A \longrightarrow b$ is a zero correlation linear hull of F, then for any $\lambda \in F_2^n$, $b \cdot F(x \oplus \lambda)$ is balanced on $A^{\perp}$.

As a result, we can transform the linear hulls in Table 3 to some integral distinguishers. Partial integral distinguisher are geven in Table 4.

Suppose the state of SPARX64/128 is represented as ($x_0, x_{1,2}, x_3$) where x_i is a 16-bit word. The 12-round integral distinguisher means if we set the value at x_0 and x_1 to consts and let the value at x_2, x_3 take all possible values, the values at x_2, x_3 after 4 steps (minus the last linear layer) will take all possible values. This is the same with that proposed in [1].

The 14-round distinguisher means that when letting the values at x_0, x_1, x_2 take all possible values and setting $x_3 = x_1$, after one SPECKEY round, four full steps and one SPECKEY round, the one bit result of $(0x0207 \cdot y_0) \oplus (0x0206 \cdot y_1) \oplus (0x0002 \cdot y_2) \oplus (0x0002 \cdot y_3)$ will be active, where (y_0, y_1, y_2, y_3) means the value after 14-round encryption. We can expand this distinguisher one more round forward with probability 1 to get one 15-round distinguisher. The input set has 2^{63} elements (x_0, x_1, x_2, x_3) which satisfy $(0x0080 \cdot x_0) \oplus (0x4001 \cdot x_1) \oplus (0x0080 \cdot x_2) \oplus (0x4001 \cdot x_3) = \text{'}0\text{'} (\text{or} = \text{'}1\text{'})$.

7. Conclusion

We have given zero-correlation cryptanalysis results against SPARX-64/128 in this paper. 14 and 15-round zero-correlation linear distinguishers have been proposed, which are the longest distinguishers as far as we know. Then, with the help of χ^2-MTZD and MPZC models, we have given 15, 16, 17 and 18-round key recovery attacks of SPARX-64/128 with post-whitening key. Our attacks cover the most rounds, while the existing attack on SPARX-64/128 covers 16 rounds. Also, we have transformed the new zero-correlation linear distinguishers into integral distinguishers. The longest one is 15-round, which is three rounds longer than the existing 12-round zero-correlation distinguisher.

Data Availability

The data used to support the findings of this study are included within the article

Conflicts of Interest

The authors declare that there are no conflicts of interest regarding the publication of this paper.

References

[1] D. Dinu, L. Perrin, A. Udovenko, V. Velichkov, J. Großschädl, and A. Biryukov, "Design strategies for arx with provable bounds: Sparx and lax," in *Advances in Cryptology – ASIA-CRYPT 2016*, J. H. Cheon and T. Takagi, Eds., pp. 484–513, Springer Berlin Heidelberg, Berlin, Heidelberg, 2016.

[2] J. Daemen and V. Rijmen, "Aes and the wide trail design strategy," in *Advances in Cryptology | EUROCRYPT 2002*, L. R. Knudsen, Ed., pp. 108-109, Springer Berlin Heidelberg, Berlin, Heidelberg, 2002.

[3] R. Beaulieu, D. Shors, J. Smith, S. Treatman-Clark, B. Weeks, and L. Wingers, *The simon and speck families of lightweight block ciphers*, Cryptology ePrint Archive, Report 2013, 2013, https://eprint.iacr.org/2013/404.

[4] Y. Todo, "Structural evaluation by generalized integral property," in *Advances in Cryptology – EUROCRYPT 2015*, I. E. Oswald and M. Fischlin, Eds., pp. 287–314, Springer Berlin Heidelberg, Berlin, Heidelberg, 2015.

[5] A. Abdelkhalek, M. Tolba, and A. M. Youssef, "Impossible differential attack on reduced round sparx-64/128," in *Progress in Cryptology – AFRICACRYPT 2017*, M. Joye and A. Nitaj, Eds., pp. 135–146, Springer International Publishing, Cham, 2017.

[6] M. Tolba, A. Abdelkhalek, and A. M. Youssef, "Multidimensional zerocorrelation linear cryptanalysis of reduced round sparx-128," in *Selected Areas in Cryptography – SAC 2017*, C. Adams and J. Camenisch, Eds., pp. 423–441, Springer International Publishing, Cham, 2018.

[7] R. Ankele and E. List, "Di_erential cryptanalysis of round-reduced sparx-64/128," in *applied cryptography and network security*, B. Preneel and F. Vercauteren, Eds., pp. 459–475, Springer International Publishing, Cham, 2018.

[8] A. Bogdanov and V. Rijmen, "Linear hulls with correlation zero and linear cryptanalysis of block ciphers," *Designs, Codes and Cryptography*, vol. 70, no. 3, pp. 369–383, 2014.

[9] A. Bogdanov and M. Wang, "Zero correlation linear cryptanalysis with reduced data complexity," in *Fast Software Encryption*, A. Canteaut, Ed., pp. 29–48, Springer Berlin Heidelberg, Berlin, Heidelberg, 2012.

[10] A. Bogdanov, G. Leander, K. Nyberg, and M. Wang, "Integral and multidimensional linear distinguishers with correlation zero," in *Advances in Cryptology – ASIACRYPT 2012*, X. Wang and K. Sako, Eds., pp. 244–261, Springer Berlin Heidelberg, Berlin, Heidelberg, 2012.

[11] H. Chen, T. Cui, and MeiqinWang, "Improving algorithm 2 in multidimensional (zero-correlation) linear cryptanalysis using χ^2-method," *Designs, Codes and Cryptography*, vol. 81, no. 3, pp. 523–540, 2016.

[12] L. Sun, H. Chen, and M. Wang, "Zero-correlation attacks: statistical models independent of the number of approximations," *Designs, Codes and Cryptography*, vol. 86, no. 9, pp. 1923–1945, 2018.

[13] C. Baudoin, F. X. Standaert, and J.-J. Quisquater, "Improving the time complexity of matsui's linear cryptanalysis," in *Information Security and Cryptology - ICISC 2007*, K.-H. Nam and G. Rhee, Eds., pp. 77–88, Springer Berlin Heidelberg, Berlin, Heidelberg, 2007.

[14] C. Blondeau and K. Nyberg, "Joint data and key distribution of simple, multiple, and multidimensional linear cryptanalysis test statistic and its impact to data complexity," *Designs, Codes and Cryptography*, vol. 82, no. 1-2, pp. 319–349, 2017.

[15] B. Sun, Z. Liu, V. Rijmen et al., "Links among impossible differential, integral and zero correlation linear cryptanalysis," in *Advances in Cryptology–CRYPTO 2015*, R. Gennaro and M. Robshaw, Eds., vol. 14, pp. 95–115, Springer Berlin Heidelberg, Berlin, Heidelberg, 2015.

Research Article

Tensor Transfer Learning for Intelligence Fault Diagnosis of Bearing with Semisupervised Partial Label Learning

Chaofan Hu,[1,2] **Zhichao Zhou,**[1] **Biao Wang,**[1] **WeiGuang Zheng** [ORCID]**,**[1,3,4] **and Shuilong He** [ORCID][1]

[1]*School of Mechanical and Electrical Engineering, Guilin 541004, China*
[2]*ShenZhen KeAnDa Electronic Technology Co. Ltd., Shenzhen 518038, China*
[3]*School of Mechanical and Automotive Engineering, Guangxi University of Science and Technology, Liuzhou 545616, China*
[4]*Commercial Vehicle Technology Center, Dong Feng Liuzhou Automobile Co., Ltd., Liuzhou 545005, China*

Correspondence should be addressed to WeiGuang Zheng; weiguang.zheng@foxmail.com

A new tensor transfer approach is proposed for rotating machinery intelligent fault diagnosis with semisupervised partial label learning in this paper. Firstly, the vibration signals are constructed as a three-way tensor via trial, condition, and channel. Secondly, for adapting the source and target domains tensor representations directly, without vectorization, the domain adaptation (DA) approach named tensor-aligned invariant subspace learning (TAISL) is first proposed for tensor representation when testing and training data are drawn from different distribution. Then, semisupervised partial label learning (SSPLL) is first introduced for tackling a problem that it is hard to label a large number of instances and there exists much data left to be unlabeled. Ultimately, the proposed method is used to identify faults. The effectiveness and feasibility of the proposed method has been thoroughly validated by transfer fault experiments. The experimental results show that the presented technique can achieve better performance.

1. Introduction

Fault diagnosis is a key process to ensure a reliable and cost-effective performance of engineered system research. Downtime caused by failures of components such as bearing faults directly reflects on the economic viability of large systems [1–4]. Therefore, for maintaining reliability and operational safety, fault detection has attracted a lot of attention [5].

In recent years, the fault classification method has been very successful for bearing based on an assumption, which is that candidate label sets are provided for all training examples [6]. Based on this assumption, lots of effort are taken on traditional intelligent fault diagnosis approaches. Liu et al. [7] proposed a personalized diagnosis method to detect faults in a bearing based on acceleration sensors and an finite element method (FEM) simulation driving SVM. A novel supervised sparse feature extraction method is proposed for rotating machine fault diagnosis in [8]. Reference [9] proposed a novel fault diagnosis method based on local-global deep neural network algorithm. A deep learning

model named renewable fusion fault diagnosis network is proposed for updating automatically as the collected fault data increases in [10]. Nowadays, various fault diagnosis methods have enriched fields of fault diagnosis. Some novel intelligent fault diagnosis techniques [11–14] are also promoted for fault diagnosis. It can be found that these approaches are applicable to vector data only. Aside from this, some tensor-based diagnosis techniques become prosperity in the fields of fault diagnosis, especially in the age of big data [5, 15, 16].

Although the researches above realized nice performance, they may suffer the two drawbacks as follows: (1) Through the literature review, it can be seen that an important assumption in these intelligent fault diagnosis methods is that the labeled training and unlabeled testing data come from the same distribution [17]. However, assumption fails by two main reasons [18]. Firstly, labeled fault signal are hard to be obtained from some equipments. Secondly, an intelligent fault diagnosis algorithm trained with labeled data possibly fails in classifying unlabeled data when the labeled

and unlabeled data are subject to different machines. Thus, distribution discrepancy exists between source and target domains, which causes important classification performance degenerates [17]. In order to handle with the domain distribution problem, DA techniques have been developed [19].

DA method establishes knowledge cross-domain transfer from source to target-domains via studying a domain-invariant feature subspace [17]. DA techniques have been successfully developed and applied in [20, 21]. Reference [22] proposed a defect identification method of wind turbine blades based on defect semantic features with transfer feature extractor. Reference [23] presented a novel domain adaptation model based on geodesic flow kernel (GFK) and strengthened feature extraction and Z-score normalization. Aside from this, reference [24] proposed a feature-based transfer neural network to identify the health states of motor bearings and gearbox bearings. A transferable convolutional neural network (CNN) [25] is proposed for intelligent fault diagnosis of rotary machinery.

Nevertheless, it can be seen that the existing diagnosis technique of transfer learning with DA approaches focus on the vector data. Therefore, the approaches are used to establish high-dimensional data; the data must be vectorized. Aside from this, vectorization always leads to high computational complexity and so on.

For addressing these issues, a new method is used for tensor data representation. The idea of the proposed method is that an invariant tensor subspace is used for adapting the tensor representations [17].

Different from the vector subspace, the tensor subspace concludes a set of subspaces characterizing each mode separately [21]. The proposed technique realizes mode-wise partial adaptation for reducing the dimensionality issue. Therefore, a joint optimization problem is formulated by seeking such a tensor subspace and learning the alignment matrices [17]. The issue is optimized via an alternating minimization method. In cross-domain visual recognition, the TAISL has achieved great success. However, there is no reports about TAISL for rotating machinery fault classification in available references.

(2) Through the literature review, it can be also seen that existing methods often assumes that each training example is associated with a ground-truth label. Nevertheless, one can only get access to a candidate label set associated with each training example among which only one label is valid in many practical applications [6]. Therefore, partial label learning (PLL) has been proposed for dealing with this kind of training examples in [26]. The PLL has attracted increasing research attention, so extensive PLL methods have been proposed in references [27, 28]. However, there is no reports about PLL for rotating machinery fault classification in available literatures.

A basic assumption is that all the candidate label sets are provided for training sample in the previous researches on PLL. Nevertheless, in practical applications, such assumption is difficult to hold [6]. A fault can be labeled by a candidate label set, but there still exist many faults that have actually no label information for them.

In this work, it is clear that neither PLL nor semisupervised learning (SSL) can address the issue concerned. For instance, although some examples could be very helpful, large numbers of unlabeled instances are ignored via PLL. The SSL assumes that the ground-truth single-label is accessible to each labeled training example, which is not the case in our situation.

A new method named SSPLL is introduced into the field of bearing fault diagnosis. It is critical that the candidate label sets of partial label instances are disambiguated and the dataset distribution information of unlabeled examples is used simultaneously. Particularly, the candidate label sets of partial label instances are disambiguated by an iterative label propagation step from partial label to unlabeled examples and the iterative label propagation procedure is used to distribute valid labels to unlabeled examples in proposed algorithm. Thus, a new approach is proposed for classification of bearing faults with semisupervised partial label learning based on tensor representation. The main highlights of the proposed method are generalized as follows:

(1) To deal with domain shift issue in tensor space, a novel DA method is proposed for bearing fault diagnosis based on tensor representation

(2) To adapt the source domain and target domain based on tensor representation, the tensor transfer learning is introduced

(3) To tackle a problem that it is hard to label a large number of instances and there exists much data left to be unlabeled, a new method named SSPLL is introduced to deal with this issue in intelligent fault diagnosis field

(4) To realize the process of labeling information propagation from the source domain to the target domain, a weighted graph is established in this paper

(5) To assist the iterative label propagation step, establishing four normalized weight matrix corresponding to the four phases in the label propagation step separately in this work

The remainder of this paper is structured as follows: in Section 2, the basic theory of the proposed method is described. The explored method are illustrated in Section 3. The developed method is validated in Section 4. In Section 5, the conclusions are drawn.

2. The Basic Theory of the Proposed Method

In this section, the theory of semisupervised partial label learning is introduced. $\mathcal{Y} \in \mathbb{R}^t$ denotes the d-dimensional example space and $\mathcal{X} = x_1, x_2, \cdots x_2$ represents the label space with n category labels in the raw PLL. Officially, $\mathscr{C} = (y_j, H_j) \| 1 \le j \le m$ means the partial label training set, where $y_j \in \mathcal{Y}$ denotes a d-dimensional signature vector $(y_{i1}, y_{i2}, \cdots y_{it}$ and $H_j \in \mathcal{Y}$ means the associated candidate label set. Basing on a critical assumption about PLL, the real label y_j for $\mathbf{x_j}$ is concealed in its candidate label set $(y_j \subseteq S_j)$ and thus is incapable of being attained by the learning method [6].
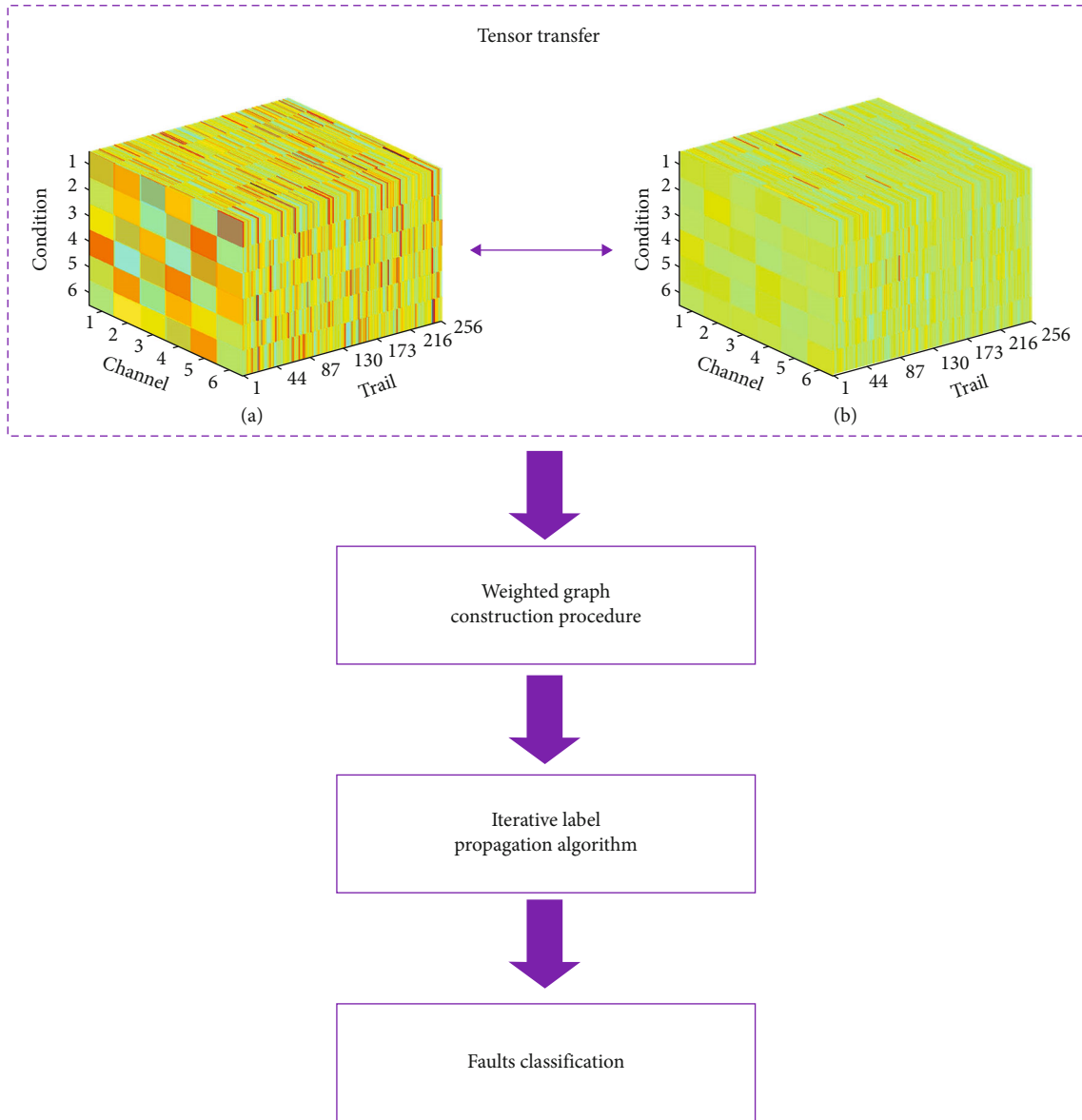
Figure 1: Framework of the proposed technique.

The training set contains partial label instances $\mathscr{D}_p = (x_j, S_j) \| 1 \le j \le m$ and unlabeled examples $\mathscr{D}_u = x_j \| 1 \le j \le m$ in the SSPLL. According to semisupervised partial label training set $\mathscr{C} = \mathscr{D}_p \cup \mathscr{D}_u$, a recognizing model $f : \mathscr{Y} \longrightarrow \mathscr{X}$ is induced from $\mathscr{C}$ by SSPLL, f predicts its label. Please refer to [5, 15, 16] for a basic theory of the proposed method.

3. The Proposed Method

Framework of the proposed technique is shown in Figure 1.

3.1. TAISL. Please refer to literature [29] for a detailed discussion of the TAISL. The domain adaptation and shift based on tensor representation are illustrated in Figure 2.

3.2. A Scheme. The adapt domains problem is tackled by introducing an invariant subspace between the source $\mathscr{S}$ and the target domains $\mathscr{T}$.

SSPLL is difficult that the learning approach is needed to disambiguate the candidate label sets of partial label instances and exploit the distribution information of unlabeled data simultaneously. A simple scheme is proposed for disambiguating the candidate label sets of partial label training instances. For example, the effective single-label is found from a candidate label set. Therefore, an easy SSL issue is introduced to replace previous problem. This new problem can be tackled by learning a method.

The step of label set disambiguation and unlabeled data exploitation are completely separated in the technique above. The disambiguation accuracy are incapable of being improved via unlabeled examples. For solving this key

Figure 2: Illustrations for domain adaptation and shift based on tensor representation.

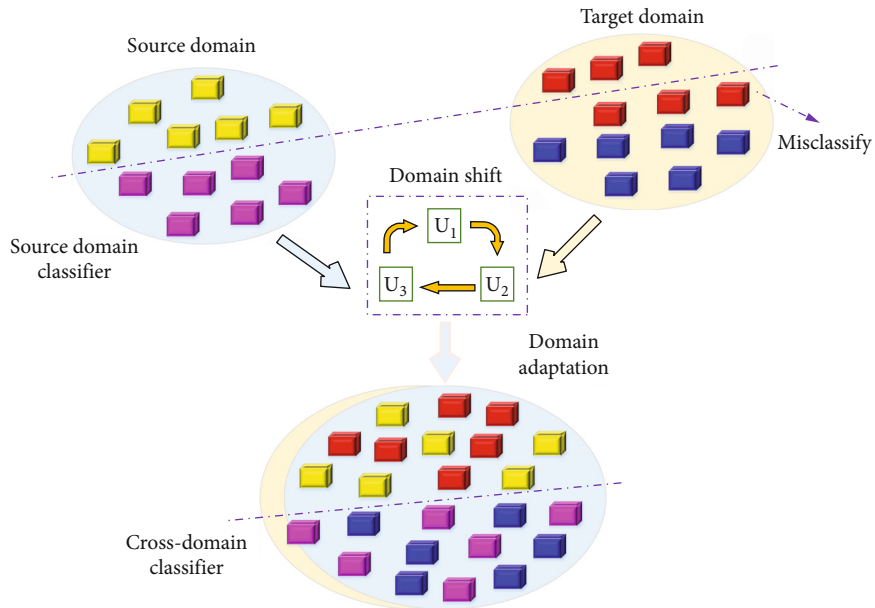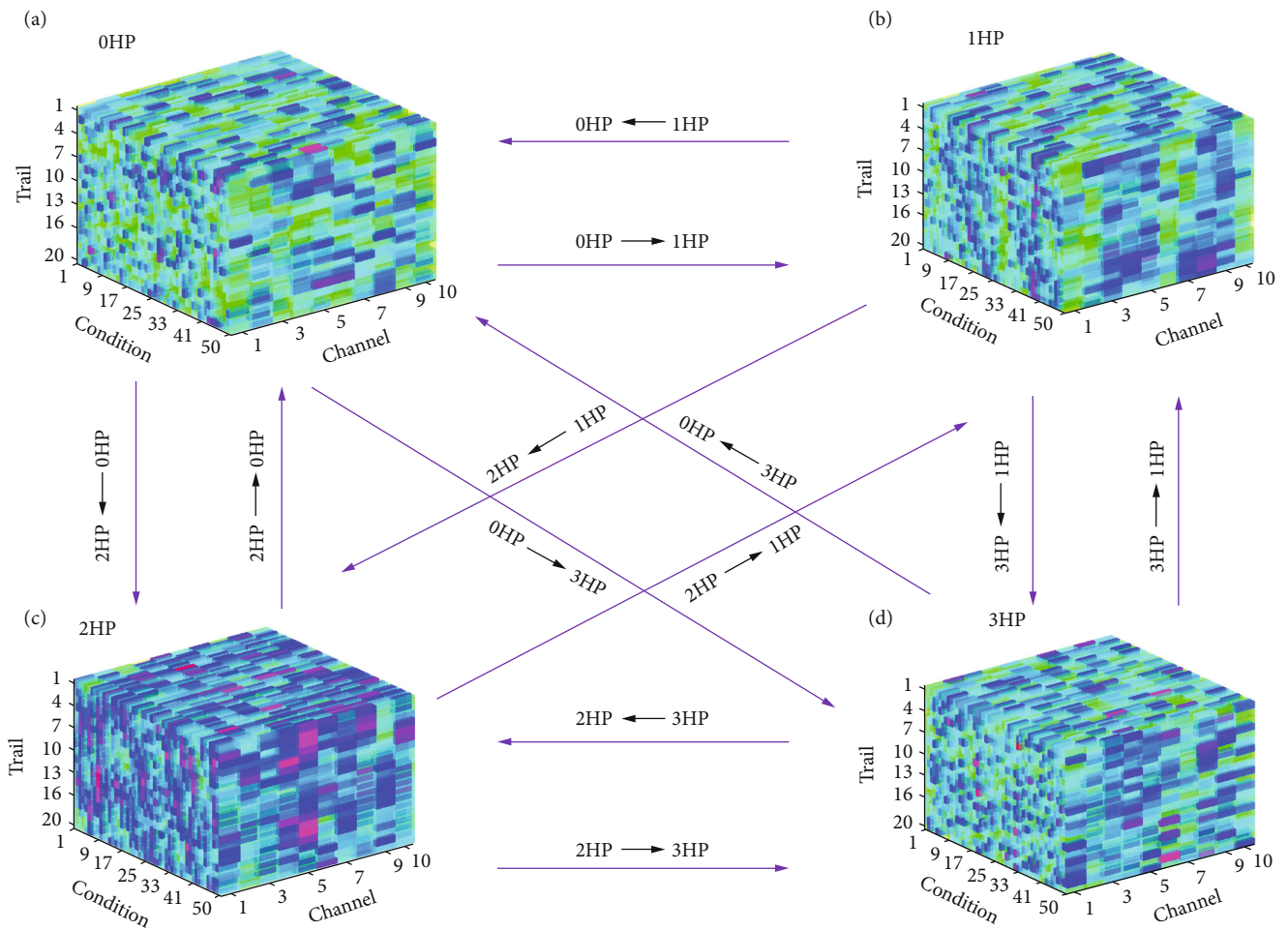Figure 3: The 12 transfer fault experiments of four loads: (a) 0 HP, (b) 1HP, (c) 2HP, and (d) 3HP.
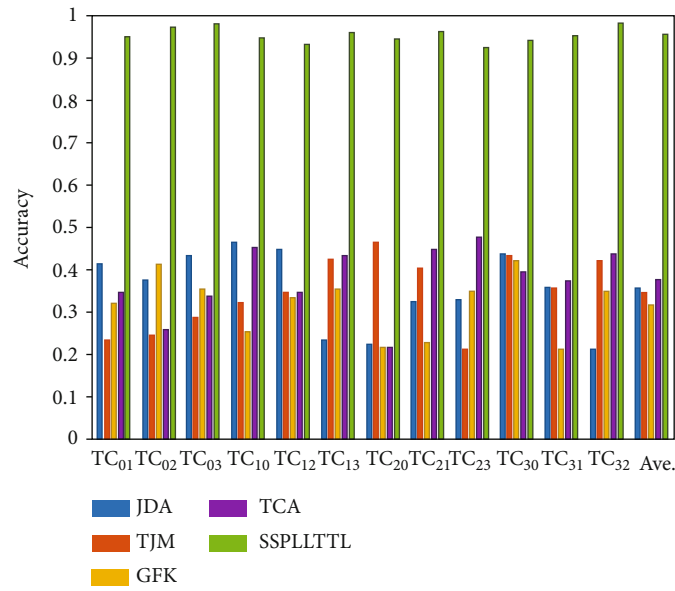
(a)
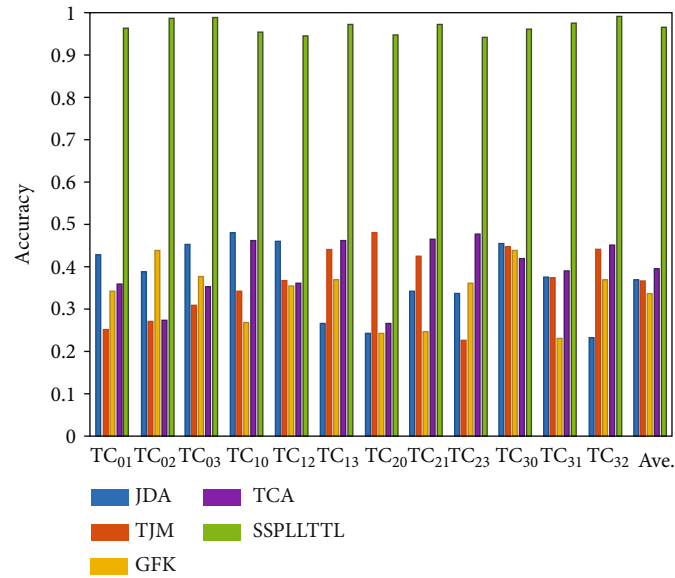
(b)

FIGURE 4: Continued.
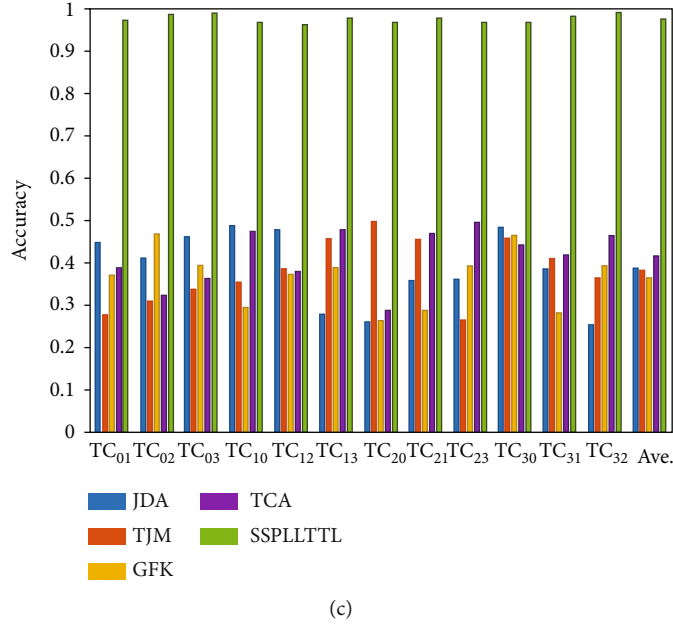
(c)
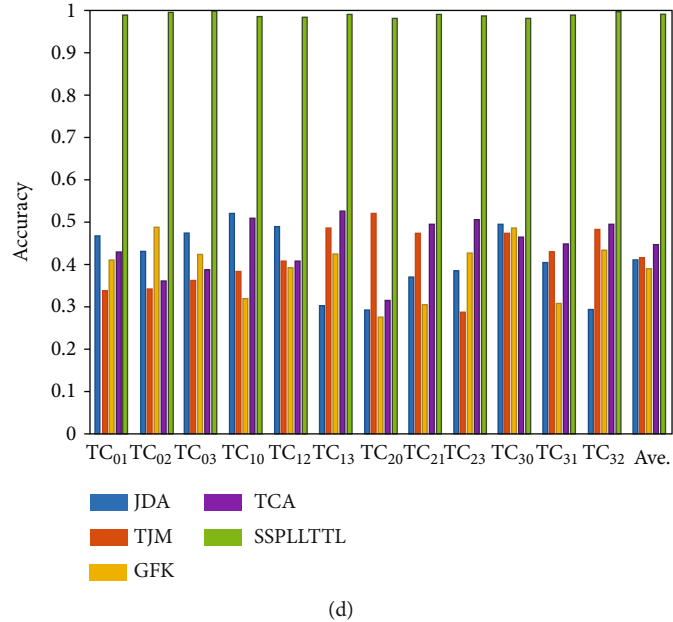
(d)

Figure 4: The partial label examples are obtained in the whole training instance by randomly sampling: (a) $p = 0.1$, (b) $p = 0.2$, (c) $p = 0.3$, and (d) $p = 0.4$.

limitation, an iterative label propagation algorithm is proposed for putting partial label instances and unlabeled examples into a structure in the presented the SSPLL technique.

3.3. *Weighted Graph Construction Procedure.* For achieving the process of labeling information propagation between the source domain set $\mathcal{S} = y_j \| 1 \leq i \leq s$ and the target domain set $\mathcal{T} y_j \| 1 \leq j \leq t$, a weighted graph [6] $\mathbf{G} = (\mathbf{O}, \mathbf{P}, \mathbf{K})$ is established over $\mathcal{S}$ and $\mathcal{T}$, while vertex set $\mathbf{O}$ represents the examples of source training set and vertex set $\mathbf{P}$ means the examples of target training set. Edge set $\mathbf{K}$ consists of the directed edges $\mathbf{O}$ and $\mathbf{P}$. For each example y_j in the target training set, its k-nearest neighbors $\mathcal{N}(y_j)$ in the source

training set are recognized. Thus, the edges of graph $\mathbf{G}$ are set as $\mathbf{K} = x_i ; x_j \| x_j \in \mathcal{N}(x_j) ; 1 \leq j \leq t$.

According to the graph $\mathbf{G}$ established above, a $t \times s$ weight matrix $\mathbf{W} = [w_{(i,j)}]_{(t \times s)}$ is able to be specified, where $w_{(j,i)} \gg 0$ if $(x_i, x_j) \in E$ and $w_{(j,i)} = 0$ otherwise. In this paper, for capturing the little influences between examples, the weight calculation approach is proposed for applying in the IPAL method [27], which selects the weights by addressing a new optimization issue:

$$\min_{\mathcal{W}_j} \left\| \mathbf{x}_j - \sum_{a=1}^{k} W_{j,i_a} \cdot x_{i_a} \right\| \text{s.t.} W_{j,i_a} \gg 0, i_a \in \mathcal{N}(x_j) ; 1 \leq a \leq t. \quad (1)$$

From Equation (1), a linear least square issue is fitted to optimize the weight vector, which can be found simply via a quadratic programming solver. Then, the row $\mathbf{W} = \mathbf{D}^{(-1)}\mathbf{W}$ is utilized to normalize weight matrix $\mathbf{W}$. Here, $\mathbf{D} = \text{diag}[d_1, d_2, \hat{a}]$ is a diagonal matrix with $d_j = \sum_{(i=1)}^{s} w_{(j,i)}$.

3.4. Iterative Label Propagation Algorithm. Four normalized weight matrices are established for facilitating the iterative label propagation step in the label propagation step separately. Particularly, $\mathbf{H} = \text{WGC}(\mathscr{C}_p, \mathscr{C}_u, k)$ is utilized for the label propagation from source domain set $\mathscr{C}_p$ to target domain set $\mathscr{C}_u$. $\mathbf{J} = \text{WGC}(\mathscr{C}_p, \mathscr{C}_p, k)$ is proposed for the label propagation from $\mathscr{C}_p$ to itself. $\mathbf{V} = WGC(\mathscr{C}_u, \mathscr{C}_u, k)$ is utilized for the label propagation from $\mathscr{C}_u$ to itself. $\mathbf{L} = WGC(\mathscr{C}_u, \mathscr{C}_p, k)$ is constructed for the label propagation from $\mathscr{C}_u$ to $\mathscr{C}_p$. Detailed description of the algorithm is illustrated in reference [6].

4. Experimental Validation

In this work, to prove the proposed method, the compared methods is introduced. These approaches contains: GFK [30] (geodesic flow kernel), TJM [31] (transfer joint matching), JDA [32] (joint distribution adaptation), and TCA [33] (transfer component analysis).

4.1. Dataset. By Case Western Reserve University [34] and Guilin University of Electronic Technology, the datasets are acquired. The used data were obtained by the 0 HP, 1 HP, 2 HP, and 3 HP. The four fault classes concludes outer race fault (OF), inner race fault (IF), ball fault (BF), and normal (N). Therefore, 12 transfer fault experiments have been used to validate the proposed method in this section in Figure 3. In addition, the three faults' diameters were 0.007, 0.014, and 0.021 inches, respectively. Therefore, ten conditions under four loads are used to demonstrate the performance of the proposed method. Parameters applied by the proposed method are set as $k = 10$, $\alpha = 0.70$, $\beta = 0.25$, $r = 0.7$, and $T = 100$. They are described as follows.

In this section, the proposed method is proved in 12 transfer experiments, which contains TC_{01}, TC_{02}, TC_{03}, TC_{10}, TC_{12}, TC_{13}, TC_{20}, TC_{21}, TC_{23}, TC_{30}, TC_{31}, and TC_{32}. The TC_{01} represents the 0 HP in the source domain and 1 HP in the target domain. The labeled samples are acquired in each transfer task of the source domain, and the unlabeled samples are acquired in each transfer task of the target domain.

4.1.1. Transfer Fault Identify Results in CWRU Dataset. The labeled examples are obtained in the source domain, and the unlabeled samples are acquired in target domain. The partial label samples are obtained in the whole training instance by randomly sampling $p \in 0.10, 0.20, 0.30, 0.40$. The experimental results are presented in Figure 4. As is illustrated in Figure 4, the results of five transfer fault detection experiments are shown. The transfer results of the proposed method are also compared with four approaches. According to the comparison results, it can be seen that the proposed
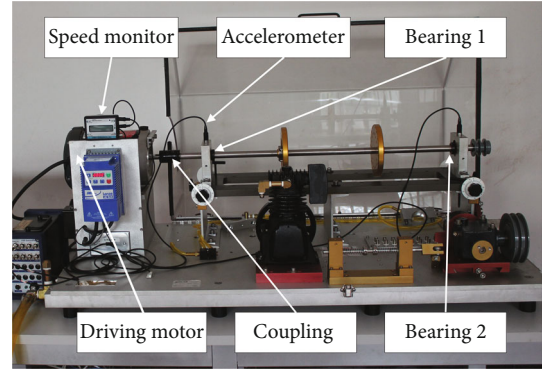
FIGURE 5: Machinery Fault Simulator test rig.

approach obtains the highest testing accuracy in the 12 transfer tasks among these four methods.

From Figure 4(a), the average testing accuracy of the proposed method is 95.6%, which is the highest one among these four methods. Due to be unsuitable to deal with tensor data, the average testing accuracy of JDA reaches 35.7%, which is smaller than the accuracy obtained by the proposed method. The average testing accuracy of TJM reaches 34.7% and the accuracy of GFK is 31.8%. Because they cannot extract high-level signatures from tensor samples of the target-domain, these two techniques realize poorer testing accuracies than the proposed method. In terms of TCA, its average accuracy reaches 37.8%, which is smaller than the testing accuracy realized by the proposed method.

When $p = 0.20$, the experimental results are presented in Figure 4(b). From Figure 4(b), the average testing accuracy of the proposed method is 96.8%, which is the highest one among these four methods. Due to be unsuitable to deal with tensor data, the average accuracy of JDA is 37.3%. The average testing accuracy of TJM reaches 36.8% and the accuracy of GFK is 33.9%. In terms of TCA, its average accuracy reaches 39.7%.

When $p = 0.30$, the experimental results are presented in Figure 4(c). From Figure 4(c), the average testing accuracy of the proposed method is 97.9%, which is the highest one among these four methods. Due to be unsuitable to deal with tensor data, the average accuracy of JDA is 39.2%. The testing accuracy of TJM is 38.4%, and the accuracy of GFK is 36.8%. In terms of TCA, its average accuracy reaches 41.8%.

The experimental results are presented in Figure 4(d) when $p = 0.40$. From Figure 4(d), the average testing accuracy of the proposed method is 98.9%, which is the highest one among these four methods. Due to being unsuitable to deal with tensor data, the average testing accuracy of JDA reaches 41.4%. The average testing accuracy of TJM reaches 41.9%, and the accuracy of GFK is 39.4%. In terms of TCA, its average accuracy reaches 44.8%.

According to the experimental results, the presented technique can correctly and accurately classify the 12 transfer tasks in the target domain. The results clearly show that TRSSPLL technology can identify fault categories more accurately and effectively than other methods.

4.1.2. Transfer Fault Identify Results in GUET Dataset. In this section, the data is acquired by Guilin University of

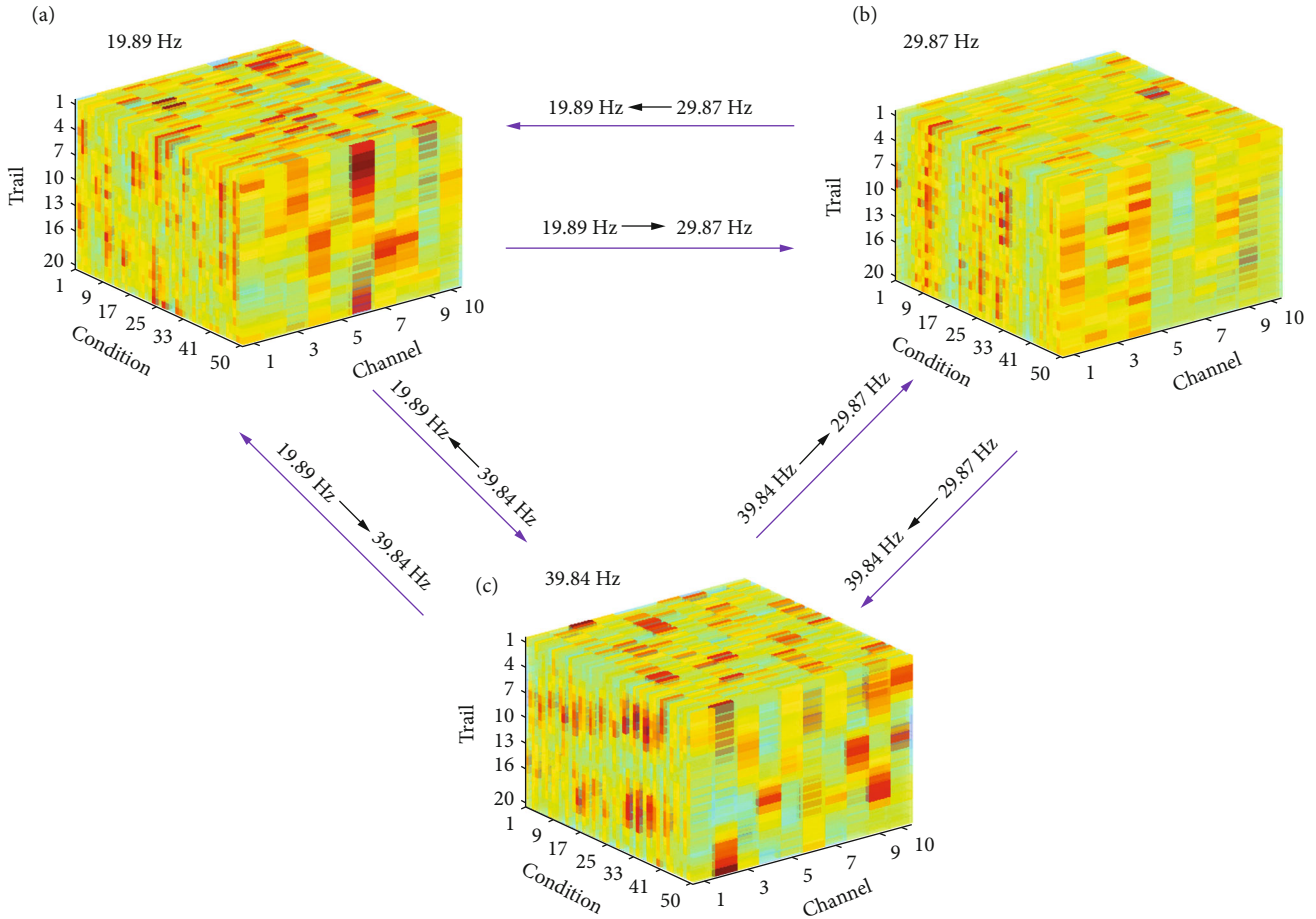FIGURE 6: The 6 transfer fault experiments of three rotating frequency schemes: (a) 19.89 Hz, (b) 29.87 Hz, and (c) 39.84 Hz.

Electronic Technology (GUET) for validating the presented technique. Figure 5 contains outer race fault (OF), ball fault (BF), inner race fault (IF), and normal (N). Used transfer data were obtained with three rotating frequency 19.89 Hz, 29.87 Hz, and 39.84 Hz. Therefore, four gear conditions under three rotating frequency schemes are established to validate performance of the proposed method in Figure 6. The DA transfer task of TC_{12} is selected in this work. The partial label examples are obtained in the whole training instance by randomly sampling $p \in 0.10, 0.20, 0.30, 0.40$.

The experimental results are showed in Figure 7. Compared with the other approaches, the presented approach can realize the best result. This further demonstates effectiveness and superiority of the proposed method. In addition, transfer diagnosis tasks can benefit from DA algorithms. The GUET data demonstrate the performance of the presented approach.

When $p = 0.10$, the results of the six cross-domain fault detection methods are shown in Figure 7(a). From Figure 7(a), it can be seen that the average test accuracy of the proposed algorithm reaches 96.4%, which is the highest of the five methods. The average test accuracy of JDA, TJM, GFK, and TCA reached 35.7%, 43%, 49%, and 44.2%, respectively.

When $p = 0.20$, the results of the six cross-domain fault detection methods are shown in Figure 7(b). It can be seen

that the average test accuracy of the proposed algorithm reaches 97.9%, which is the highest of the five methods. The average test accuracy of JDA, TJM, GFK, and TCA reached 37.5%, 45%, 507%, and 46.4%, respectively.

When $p = 0.30$, the results of the six transfer fault diagnosis methods are shown in Figure 7(c). The average accuracy of proposed algorithm is 98.6%, which is the highest of the five methods. The average test accuracy of JDA, TJM, GFK, and TCA reached 39.5%, 47.4%, 52.8%, and 48.6%, respectively.

When $p = 0.40$, the results of the six cross-domain fault detection methods are shown in Figure 7(d). The average test accuracy of the proposed algorithm reaches 99.4%, which is the highest of the five methods. The average test accuracy of JDA, TJM, GFK, and TCA reached 41.6%, 49.3%, 54.6%, and 50.8%, respectively.

According to the experimental results, the presented approach can accurately identify the six transfer tasks in the target domain. The results clearly show that the proposed technology can identify fault categories more accurately and effectively than other methods.

The proposed method is validated by different experiment data. The purpose of this paper is to deal with tensor data in source and target domain. As for JDA, TJM, GFK, and TCA, they are traditional transfer algorithms. It is

(a)

(b)

(c)

(d)
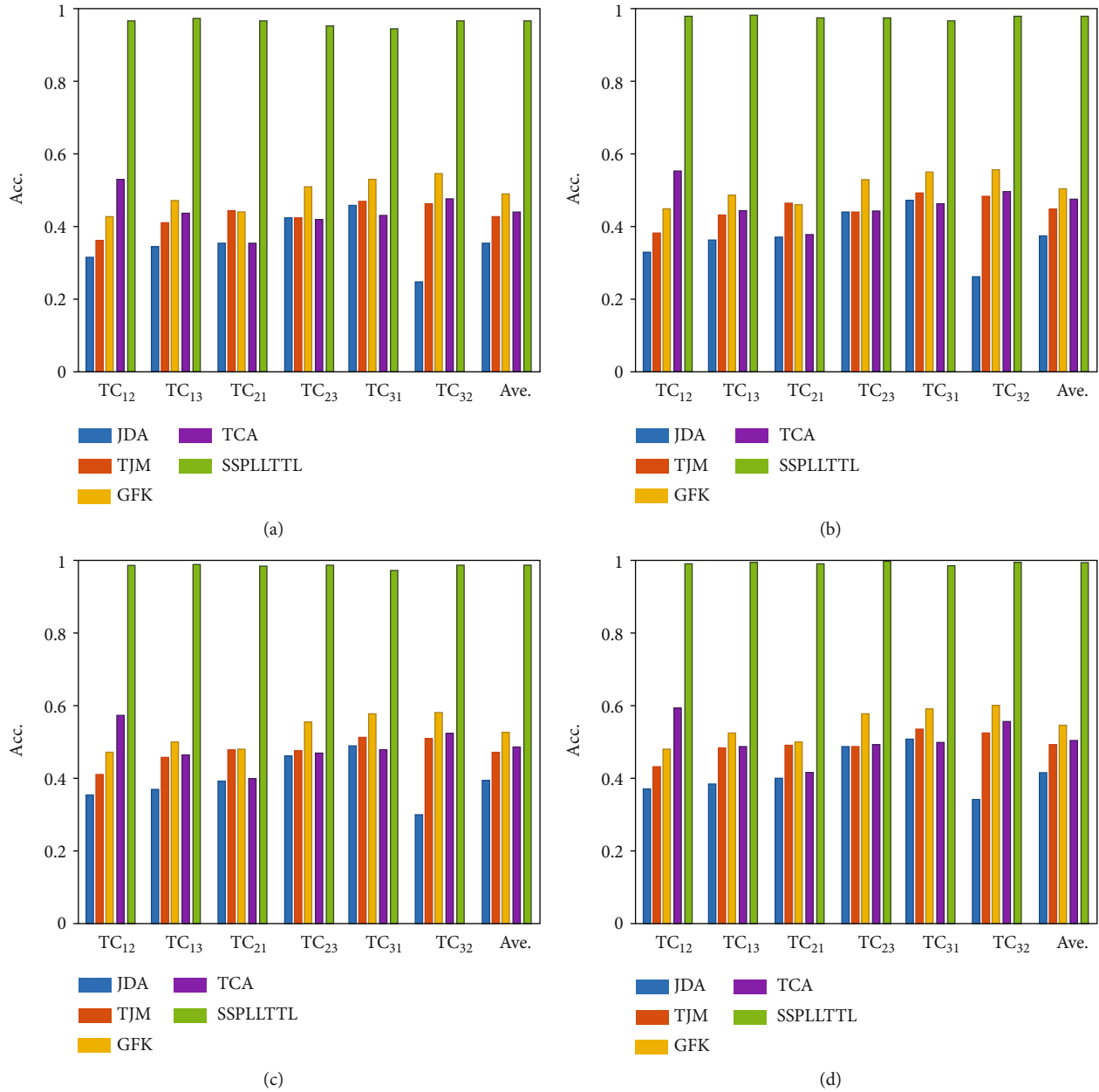
Figure 7: The partial label examples are obtained in the whole training instance by randomly sampling: (a) $p = 0.1$, (b) $p = 0.2$, (c) $p = 0.3$, and (d) $p = 0.4$.

undeniable that they have many advantages. They can only tackle vector-based data with cross-domain issue.

4.1.3. Comparisons with Related Works. General fault identify issues assume the training and testing data are obtained from the same machine. Various fault classification methods [35–38] have realized very high testing accuracy. However, these methods can not deal with the cross-domain fault diagnosis issue. For the transfer fault diagnosis issue, which the source and the target domains data are acquired for training model. In existing literature, the transfer fault diagnosis methods [17, 39] are proposed for tackling domain shift problems. Nevertheless, the proposed approach can

not handle with tensor data. Aside from this, the unlabeled data is not considered by these fault diagnosis techniques. Thus, for dealing with transfer, tensor data issues, and unlabeled data, a new tensor transfer approach is proposed for rotating machinery intelligent fault diagnosis with semi-supervised partial label learning in this paper.

In this paper, the data of training and testing are acquired in source and the target domains separately, so the transfer fault detection experiment is more difficult than existing cross-domain task. The testing accuracy has been realized 98.9% and 99.4% in two transfer tasks by the promoted technique, respectively. Therfore, according to consequences, the proposed method are competitive.

5. Conclusion

Since some information is hard to denote by vector arithmetic, thus, a new DA method based on tensor representation is first applied to adapt the source and target domains tensor data directly, without vectorization in the field of intelligent fault diagnosis. Then, SSPLL is proposed for training set consists of two kinds of weak supervision, i.e., partial label data and unlabeled data. An iterative label propagation method is introduced, which can process two kinds of weakly supervised data simultaneously by jointly propagating label between partial labeled and unlabeled instances and derive a good label assignment.

The employed approach realizes higher classification accuracy of bearing heath states compared with vector-based representation algorithms. Aside from this, the experimental results verify that the presented approach is superior to methods that only considering one kind of weak supervision. In future works, the model will be used to large-scale data, and weak supervision data will also be considered in dynamic environments. Then, a powerful invariant tensor subspace need to be learned in further research works.

Data Availability

The data used to support the findings of this study can be obtained through the first author's email.

Conflicts of Interest

The authors declare that they have no conflicts of interest.

Acknowledgments

References

[1] Z. He, H. Shao, Z. Ding, H. Jiang, and J. Cheng, "Modified deep auto-encoder driven by multi-source parameters for fault transfer prognosis of aero-engine," *IEEE Transactions on Industrial Electronics*, no. 99, 2021.

[2] Q. Zhu, B. Sun, Y. Zhou, W. Sun, and J. Xiang, "Sample augmentation for intelligent milling tool wear condition monitoring using numerical simulation and generative adversarial network," *IEEE Transactions on Instrumentation and Measurement*, vol. 70, pp. 1–10, 2021.

[3] Y. Zhou, B. Sun, W. Sun, and Z. Lei, "Tool wear condition monitoring based on a two-layer angle kernel extreme learning machine using sound sensor for milling process," *Journal of Intelligent Manufacturing*, 2020.

[4] Z. Lei, Y. Zhou, B. Sun, and W. Sun, "An intrinsic timescale decomposition-based kernel extreme learning machine method to detect tool wear conditions in the milling process," *The International Journal of Advanced Manufacturing Technology*, vol. 106, no. 3-4, pp. 1203–1212, 2020.

[5] C. Hu and Y. Wang, "Multidimensional denoising of rotating machine based on tensor factorization," *Mechanical Systems and Signal Processing*, vol. 122, pp. 273–289, 2019.

[6] Q. W. Wang, Y. F. Li, and Z. H. Zhou, "Partial label learning with unlabeled data," in *Proceedings of the 28th International Joint Conference on Artificial Intelligence*, pp. 3755–3761, Macao, China, 2019.

[7] X. Liu, H. Huang, and J. Xiang, "A personalized diagnosis method to detect faults in a bearing based on acceleration sensors and an fem simulation driving support vector machine," *Sensors*, vol. 20, no. 2, p. 420, 2020.

[8] W. Qian, S. Li, J. Wang, and Q. Wu, "A novel supervised sparse feature extraction method and its application on rotating machine fault diagnosis," *Neurocomputing*, vol. 320, pp. 129–140, 2018.

[9] X. Zhao and M. Jia, "A new local-global deep neural network and its application in rotating machinery fault diagnosis," *Neurocomputing*, vol. 366, pp. 215–233, 2019.

[10] K. Xu, S. Li, X. Jiang, Z. An, J. Wang, and T. Yu, "A renewable fusion fault diagnosis network for the variable speed conditions under unbalanced samples," *Neurocomputing*, vol. 379, pp. 12–29, 2020.

[11] H. Shao, M. Xia, J. Wan, and C. de Silva, "Modified stacked auto-encoder using adaptive Morlet wavelet for intelligent fault diagnosis of rotating machinery," *IEEE/ASME Transactions on Mechatronics*, no. 99, p. 1, 2021.

[12] X. Liu, H. Huang, and J. Xiang, "A personalized diagnosis method to detect faults in gears using numerical simulation and extreme learning machine," *Knowledge Based Systems*, vol. 195, article 105653, 2020.

[13] Y. Gao, X. Liu, and J. Xiang, "Fem simulation- based generative adversarial networks to detect bearing faults," *IEEE Transactions on Industrial Informatics*, vol. 16, no. 7, pp. 4961–4971, 2020.

[14] Z. He, H. Shao, J. Cheng, X. Zhao, and Y. Yang, "Support tensor machine with dynamic penalty factors and its application to the fault diagnosis of rotating machinery with unbalanced data," *Mechanical Systems and Signal Processing*, vol. 141, article 106441, 2020.

[15] C. Hu, Y. Wang, and T. Bai, "A tensor-based approach for Identification of multi-channel bearing compound faults," *IEEE Access*, vol. 7, pp. 38213–38223, 2019.

[16] C. Hu and Y. Wang, "Research on multi-channel signal denoising method for multiple faults diagnosis of rolling element bearings based on tensor factorization," *Journal of Mechanical Engineering*, no. 12, p. 7, 2019.

[17] X. Li, W. Zhang, and Q. Ding, "Cross-domain fault diagnosis of rolling element bearings using deep generative neural networks," *IEEE Transactions on Industrial Electronics*, vol. 66, no. 7, pp. 5525–5534, 2019.

[18] L. Guo, Y. Lei, S. Xing, T. Yan, and N. Li, "Deep convolutional transfer learning network: a new method for intelligent fault diagnosis of machines with unlabeled data," *IEEE Transactions on Industrial Electronics*, vol. 66, no. 9, pp. 7316–7325, 2019.

[19] H. Lu, L. Zhang, Z. Cao et al., "When unsupervised domain adaptation meets tensor representations," in *2017 IEEE*

International Conference on Computer Vision (ICCV), pp. 599–608, Venice, Italy, 2017.

[20] R. Aljundi, R. Emonet, D. Muselet, and M. Sebban, "Landmarks-based kernelized subspace alignment for unsupervised domain adaptation," in *Proceedings of the IEEE Conference on Computer Vision and Pattern Recognition*, pp. 56–63, Boston, MA, USA, 2015.

[21] B. Fernando, A. Habrard, M. Sebban, and T. Tuytelaars, "Unsupervised visual domain adaptation using subspace alignment," in *2013 IEEE International Conference on Computer Vision*, pp. 2960–2967, Sydney, NSW, Australia, 2013.

[22] Y. Yu, H. Cao, X. Yan, T. Wang, and S. S. Ge, "Defect identification of wind turbine blades based on defect semantic features with transfer feature extractor," *Neurocomputing*, vol. 376, pp. 1–9, 2020.

[23] Z. Zhang, H. Chen, S. Li, Z. An, and J. Wang, "A novel geodesic flow kernel based domain adaptation approach for intelligent fault diagnosis under varying working condition," *Neurocomputing*, vol. 376, pp. 54–64, 2020.

[24] B. Yang, Y. Lei, F. Jia, and S. Xing, "An intelligent fault diagnosis approach based on transfer learning from laboratory bearings to locomotive bearings," *Mechanical Systems and Signal Processing*, vol. 122, pp. 692–706, 2019.

[25] Z. Chen, K. Gryllias, and W. Li, "Intelligent fault diagnosis for rotary machinery using transferable convolutional neural network," *IEEE Transactions on Industrial Informatics*, vol. 16, no. 1, pp. 339–349, 2020.

[26] Y. C. Chen, V. M. Patel, R. Chellappa, and P. J. Phillips, "Ambiguously labeled learning using dictionaries," *IEEE Transactions on Information Forensics and Security*, vol. 9, no. 12, pp. 2076–2088, 2014.

[27] M. L. Zhang and F. Yu, "Solving the partial label learning problem: an instance-based approach," in *Twenty-Fourth International Joint Conference on Artificial Intelligence*, Buenos Aires, Argentina, 2015.

[28] C. Z. Tang and M. L. Zhang, "Confidence-rated discriminative partial label learning," in *Thirty-first AAAI Conference on artificial Intelligence*, San Francisco California USA, 2017.

[29] G. J. Hu Chaofan and W. Yanxue, "Cross-domain intelligent fault classification of bearings based on tensor-aligned invariant subspace learning and two-dimensional convolutional neural networks," *Knowledge-Based Systems*, 2020.

[30] B. Gong, Y. Shi, F. Sha, and K. Grauman, "Geodesic flow kernel for unsupervised domain adaptation," in *2012 IEEE Conference on Computer Vision and Pattern Recognition*, pp. 2066–2073, Providence, RI, USA, 2012.

[31] M. Long, J. Wang, G. Ding, J. Sun, and P. S. Yu, "Transfer joint matching for unsupervised domain adaptation," in *Proceedings of the IEEE conference on computer vision and pattern recognition*, pp. 1410–1417, Columbus, OH, USA, 2014.

[32] M. Long, J. Wang, G. Ding, J. Sun, and P. S. Yu, "Transfer feature learning with joint distribution adaptation," in *Proceedings of the IEEE international conference on computer vision*, pp. 2200–2207, Sydney, NSW, Australia, 2013.

[33] S. J. Pan, I. W. Tsang, J. T. Kwok, and Q. Yang, "Domain adaptation via transfer component analysis," *IEEE Transactions on Neural Networks*, vol. 22, no. 2, pp. 199–210, 2011.

[34] W. A. Smith and R. B. Randall, "Rolling element bearing diagnostics using the case western reserve university data: a benchmark study," *Mechanical Systems and Signal Processing*, vol. 64-65, pp. 100–131, 2015.

[35] Z. X. Hu, Y. Wang, M. F. Ge, and J. Liu, "Data-driven fault diagnosis method based on compressed sensing and improved multiscale network," *IEEE Transactions on Industrial Electronics*, vol. 67, no. 4, pp. 3216–3225, 2020.

[36] Y. Yang, H. Zheng, Y. Li, M. Xu, and Y. Chen, "A fault diagnosis scheme for rotating machinery using hierarchical symbolic analysis and convolutional neural network," *ISA Transactions*, vol. 91, pp. 235–252, 2019.

[37] J. Liang, Y. Zhang, J.-H. Zhong, and H. Yang, "A novel multi-segment feature fusion based fault classification approach for rotating machinery," *Mechanical Systems and Signal Processing*, vol. 122, pp. 19–41, 2019.

[38] X. Yan and M. Jia, "Intelligent fault diagnosis of rotating machinery using improved multiscale dispersion entropy and mrmr feature selection," *Knowledge-Based Systems*, vol. 163, pp. 450–471, 2019.

[39] H. Zheng, R. Wang, J. Yin, Y. Li, H. Lu, and M. Xu, "A new intelligent fault identification method based on transfer locality preserving projection for actual diagnosis scenario of rotating machinery," *Mechanical Systems and Signal Processing*, vol. 135, article 106344, 2020.

Research Article

Comprehensive Evaluation Model of Bearing Transportation Protection Effect of Bogie Traction Motor under Data Imbalance

Yi Liu,[1,2,3] **Qi Chang,**[1] **Jiaxin Luo,**[1] **LinLi,**[3] **Junfeng Man,**[1] **FenWei,**[4] **Qinlin Chen,**[4] **and Yiping Shen** [iD][4]

[1]*School of Computer Science, Hunan University of Technology, Zhuzhou, 412000 Hunan, China*
[2]*CRRC Zhuzhou Electric Locomotive Co., LTD., Zhuzhou, 412000 Hunan, China*
[3]*National Innovation Center of Advanced Rail Transit Equipment, Zhuzhou, 412000 Hunan, China*
[4]*Hunan Key Laboratory of Mechanical Equipment Health Maintenance, Hunan University of Science and Technology, Xiangtan, 411201 Hunan, China*

Correspondence should be addressed to Yiping Shen; yiping1011@163.com

Under different transportation protection, the sample data of bogie traction motor bearings of urban rail vehicles are seriously unbalanced, and the fault diagnosis ability and generalization effect are poor, which makes it difficult to evaluate the protection effect of bearings effectively. In this paper, a multimeasure hybrid evaluation model based on compressed sensing is proposed to evaluate the effect of bearing transportation protection under data imbalance. Firstly, bearing vibration signals under different transport protection conditions were compressed and sampled, and the original high-Witt collection in time domain, frequency domain, and time-frequency domain was extracted. Then, a multimeasure mixed feature evaluation model of correlation, distance, and signal was constructed, and the optimal multimeasure combination strategy was optimized by using comprehensive sensitivity score evaluation index. Finally, an evaluation model of bearing protection effect based on unified feature index was constructed by using the best feature subset evaluated, and the unified indicator was quantified to characterize the protection effect of different protection states. The experimental results show that the model can effectively evaluate bearings under different transport protection.

1. Introduction

As an important part of the walking part of urban rail transit vehicles, the bogie plays the role of motion orientation, bearing, and vibration reduction and is also the ultimate executor of traction and braking and plays an important role in the safe driving of the train [1]. At the present stage, the bogies put into use in China are mainly based on welding. Due to the characteristics of the welding process itself, the weld position of the bogies is easy to transmit residual stress and deformation will have influence, and the traction and driving device of the vehicle will be directly related to the quality of force transmission, and whether the structure is safety and reliable will directly affect the operation safety of

the train [2]. Traction motor is the key part of urban rail vehicle driving device, its operation state will directly affect the train performance and transportation efficiency, including rolling bearing which is one of the most widely used parts of traction motor, and the relevant research results show that the most prone to failure parts of traction motor is rolling bearing; bearing damage accounts for about 44% of traction motor failure [3]. Therefore, ensuring the quality of the bogie traction motor bearing is one of the important factors to ensure the safe, stable, and comfortable operation of the urban rail vehicles. Urban rail vehicles are often transported to the owner's site [4]. If the bearings are not protected during transportation, pseudocloth marks will occur due to the road turbulence, abnormal bearing sound during

site operation, and eventually mass replacement, which seriously affects the manufacturer's product quality of the bearing and causes serious hidden dangers to the safe operation of urban rail trains.

The protection effect assessment of the traction motor bearing of urban rail vehicles under different transportation protection has two main difficulties:

(1) In the signal collection of the urban rail vehicle steering gear traction motor bearing, there is a serious data imbalance phenomenon. The main reasons of this phenomenon are as follows. (a) With the vehicle running speed and the complex environment, the data flow accelerates, and the amount of state data increases. Due to the development and deterioration of the equipment state, the shortening of the monitoring period will also lead to the increase of the state data volume. (b) The bearing produces vibration signals containing impact attenuation components under different transportation protection, all of which have obvious nonlinear behavior, which eventually leads to the spectral bandwidth of the signal, excessive number of data collection, and massive data bring great pressure on data transmission, storage, and processing. (c) Under the actual working condition, the number of bearing fault signal samples is generally far less than the normal state signal. In conclusion, the mentioned factors will cause unbalanced bearing dataset

(2) The fault diagnosis ability of the bearing is poor, and the protective effect assessment is difficult to be effectively evaluated. The reasons of this phenomenon are as follows: the complex rotating mechanical structure and bad operating environment make the fault mode usually show strong complexity [5], and the "underlearning" problem of fault feature sensitivity in the widely used single measure evaluation model and the common feature parameter extraction of different analysis fields can only state the information of mechanical equipment characterized by vibration signal be described from different angles. The above situation causes the failure to obtain the status information in the bearing fault diagnosis, so as not to provide an accurate data basis for the pattern recognition and then affect the subsequent classification performance and effect assessment

2. Related Research Work

The application object of previous research is generally limited to the error data with similar distribution under constant and stable conditions. Unfortunately, this restriction has little effect in real-life scenarios. The working conditions are complex and changeable, which makes it difficult to extract effective fault diagnosis representation in practical application by previous deep representation learning methods [6, 7]. To solve the serious data imbalance of bearing vibration signal under continuous high sampling, this

paper adopts compression sensing (compressive sensing (CS)) theory also called compression sampling theory. A compressed sensing theory proposed by Donoho et al. [8–10], whose signal compression theory breaks through the Nyquist limit, can achieve less measurement compression sampling and complete high probability accurate reconstruction. Although the observation data is reduced, it contains enough original signal information for signal recovery to realize the "compression sampling" of the signal. The concept of this theory can be described as follows: for a collected time-domain target signal, as long as the signal is compression on a certain sparse transformation basis, a linear measurement matrix unrelated to the sparse transformation base and select an appropriate reconstruction algorithm to accurately reconstruct the signal based on the low-dimensional compression measurement. Currently, compressed sensing hotspots focus on three key problems: sparse representation, signal observation, and signal reconstruction [11, 12]. Early studies performed limited sampling studies using the compressibility of signals and sampled continuous signals using a fixed structural basis function at twice the information rate rather than twice the sampling frequency [13]. The notion of the uncertainty principles of sparse representation is first proposed by Donoho et al. [14]. Based on this result, El Ad and Bruckstein [15] further discuss the uniqueness of the sparse representation and prove the boundary conditions for the exact sparse reconstruction. Tropp [16] proposed more general conditions, unifying the reconstruction conditions for the sparse representation problem of the l_0 and l_1 norm constraints. Candes et al. [16] propose the exact reconstruction principle that further demonstrates the uniqueness of the sparse representation problem and discuss the stability, robustness, and the extension of the algorithm. Baraniuk et al. [17, 18] proposed that constrained isometries provide a theoretical basis for the observation matrix design and signal reconstruction. In recent years, CS has made some progress in image compression, face recognition, radar imaging, communication, and other fields [19], but at present, the research in the field of mechanical equipment fault diagnosis is still widely involved, and little research is applied in the field of urban rail vehicles.

The fault feature sensitivity "underlearning" problem in the single measure evaluation model and the feature parameter characterization information extracted by different single analysis domain often have significant undercompleteness. It is not difficult to find that extracting the multidomain multifeature parameter is a necessary guarantee to comprehensively describe the equipment fault state mode. Meanwhile, the feature weighted has rich feature sensitivity information to the original feature set with eigenweights without losing any feature parameter, giving the weighted feature set with better category discrimination ability. According to the principle of feature weighting, the calculation of its weight coefficient is closely related to various types of feature evaluation criteria, from which various characteristic weighting methods based on typical characteristic evaluation measures or their improved versions are born, for example, fault feature weighting based on compensation distance evaluation technology [20], nuclear space distance

measure [21], feature weighted scheme based on entropy, mean variance and mutual information, feature weighted based on joint Laplacian score, and feature weighting based on Fisher linear discrimination analysis. Moreover, Sáez et al. [22] proposed a novel feature weighted scheme based on interpolation method and Kolmogorov-Smirnov parametric statistical test for the performance improvement limited to noise-containing, redundancy, and weak correlation features; Ismail and Frigui [23] proposed a robust unsupervised learning algorithm for finite generalized Dirichlet hybrid model for realizing fuzzy clustering and feature weighted of noise-containing high-dimensional data. Similar to the selection of the optimal feature subset in feature selection, the determination of feature-weighted weight coefficient can be treated as a class of combinatorial optimization problems, so various evolutionary algorithms (including taboo search, harmonic search, and multiobjective optimization algorithm) [24] have been introduced into the construction of feature-weighted framework. However, most of the existing weight coefficient calculation methods based on feature evaluation criterion learn the sensitivity of features from a single measure such as distance, information, and correlation, which often causes poor learning results of fault feature sensitivity, which is not conducive to the improvement of feature clustering and classification performance. Based on the research of scholars, this paper proposes a multimeasure mixed evaluation model for accurate and comprehensive evaluation of bearings.

This paper studies the bogie traction motor bearing in urban rail vehicles and evaluates the reasonable bearing transportation protective measures during road transportation. A multimeasure hybrid evaluation model based on compression perception is proposed and applied to the transportation protection example of Ningbo Line 3 bearings, to verify the feasibility and technical advantages of the proposed method, evaluate the best protection measures to reduce the failure rate of bearings, provide theoretical basis and technical reference for the characterization of the transportation protection effect of urban rail vehicles, and then provide certain guarantee for the safe operation of urban rail vehicles. The overall technical route for evaluating the protection effect of urban rail vehicle bogie traction motor bearings under different transportation protection is shown in Figure 1.

3. Compression Sampling of Bearing Vibration Signal in the Field of Rail Transit

The status data of the mechanical equipment can reflect the real-time operation state of the equipment, which is an important basis for obtaining the changing trend of the equipment status and analyzing the root cause of the equipment failure. In the fault diagnosis of rail transit field, status data is an indispensable and important resource related to the operation, monitoring, and management of urban rail vehicles. In order to accurately grasp the health state of the equipment, it is the urgent problem to solve the imbalance of bearing dataset. Compression sensing theory provides new ideas for signal acquisition, analysis, and feature extrac-

tion, which is currently rarely involved in fault diagnosis in the field of rail transit. Compact data is used to obtain compressed data and deal with the storage of massive data, analyze compressed data from compressed data, reduce analysis and calculation links, save computational resources, and improve the efficiency of monitoring and diagnosis. The application of compression sensing theory to the signal sampling of equipment in rail vehicles provides an effective solution to the problem of data imbalance and its application in the storage, transmission, and analysis of urban rail vehicle equipment data. CS first performs the sparse transformation processing of the original signal and then measures the sparse data with the observation matrix, obtains the observation value far lower than the original signal dimension, and then restores the signal reconstruction algorithm of the compression perception theory framework to obtain the reconstruction signal with very little error with the original signal. The specific process is shown in Figure 2.

CS has been widely studied in many areas, but relatively little in the field of mechanical troubleshooting. This paper uses CS technology for the vibration signal of vehicle key components in the field of urban rail transit. In the whole evaluation process of the traction motor bearing of urban rail vehicle bogie, the processing process of compression sensing from the processing process of bearing vibration signal is mainly divided into two parts: one, acquisition and compression of signal; two, data reconstruction and analysis. The processing process of the bearing signal of the traction motor is shown in Figure 3.

3.1. Sparse Representation of the Signals in the Compressed Sampling. Sparse representation of signal in perception observation problem: compressed perception theory is the inverse problem of sparse representation theory, whose theory foundation implies the basis of signal sparsity. Shown in Figure 4 is a schematic diagram of sparse representation theory. The sparse representation of the signal is to transform the signal to a particular sparse space, yielding a small value of most of the transformation coefficients, namely, the resulting transformation coefficients are sparse or approximately sparse. Finding a base or compact frame Ψ makes the signal x sparse on Ψ and finding the transform coefficients: $S = \Psi X$ where S is an equivalent or approximated sparse representation of X. The choice of transform basis Ψ can be some kind of basis that has been widely used, such as wavelet base, Fourier base, and local Fourier base. In addition, a compact framework can be used to make a sparse representation of signals such as curve waves and contour waves, two classes of transform bases with better directivity [25]. The prerequisite for compressed sensing is that the signal must be sparingly sparse. For most signals, it is usually not sparse, but it is always able to find the appropriate base for the sparse transformation of the signal.

3.2. Selection of the Observation Matrix in the Compressed Sampling. Main content of the signal observation research: how to design the $M \times N$-dimensional observation matrix Φ, unrelated to the sparse basis to ensure that after the signal x decreases from N dimension length to M dimension, the
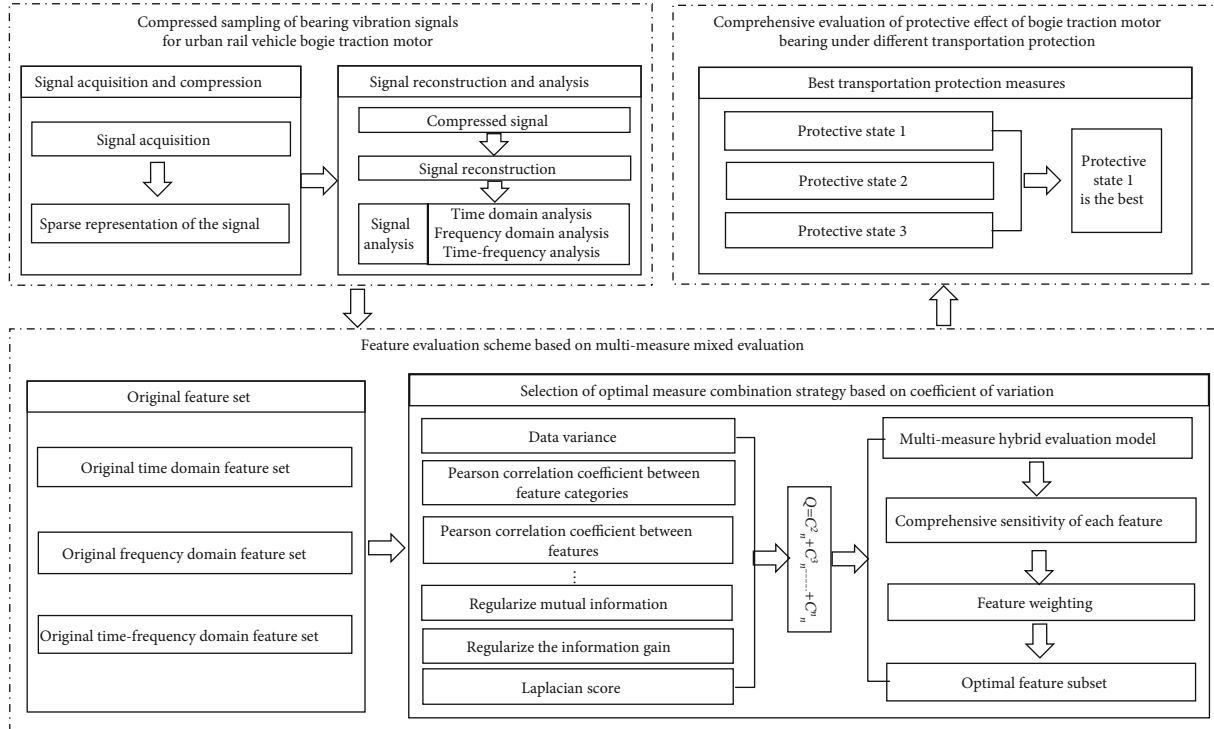
Figure 1: Technical schematic diagram of a multimeasure mixed evaluation model based on compression sensing.
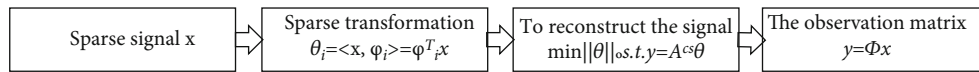
Figure 2: Compression perception flowchart.
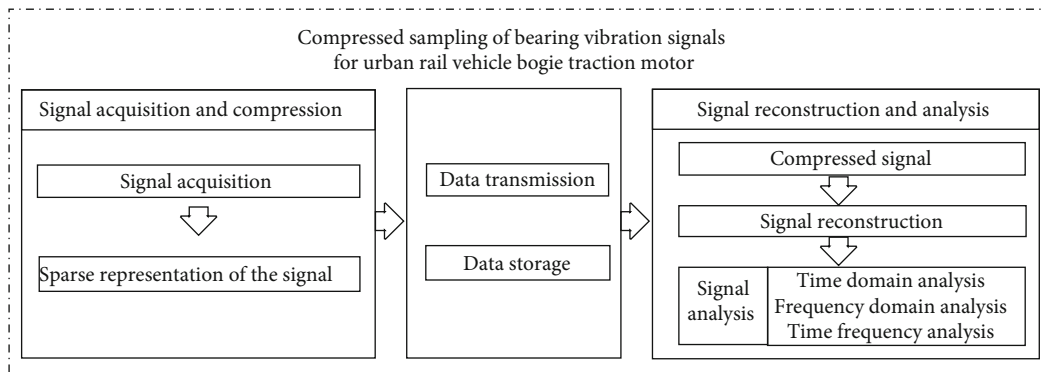
Figure 3: Signal processing process based on compression sensing for urban rail vehicle bearing.

main information is still not lost, and the original signal x can be recovered from the dimension-dimensional signal y. The core of signal observation: to study sampling protocols that can effectively extract useful information in the original signal and to obtain as few sampling points as possible. The need x to design a stable $m \times n$ dimensional observation matrix Φ is required to obtain the S set $Y = \Phi S = \Phi \Psi^T X$. This process can also be represented as a signal x for non-adaptive observations via matrix A^{cs}: $Y = A^{CS}X$ (where $A^{CS} = \Phi \Psi^T$ is called the CS information operator). The concern

is the selection of the observation matrix Φ, which needs to guarantee that the important information is not broken when the sparse vector S drops from n dimension to m dimension. In compressed sensing theory, an important criterion for judging whether a matrix can become a measurement matrix is limited isometric property (RIP). For example, for the k sparse vector $S \in R^N$, when it satisfies formula (1), the measurement matrix Φ satisfies the RIP. Most random matrices satisfy RIP, such as Gaussian and Bernoulli stochastic measurements [17].
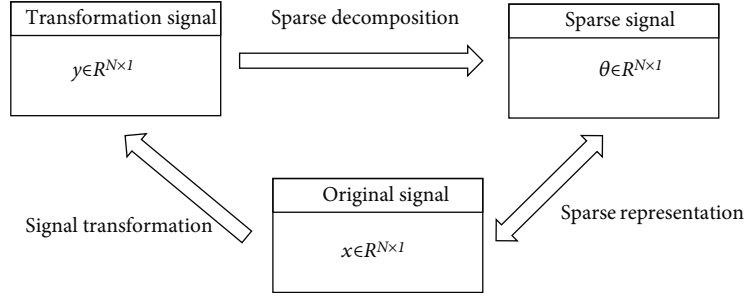
FIGURE 4: Sparse representation of theoretical diagram.

$$(1 - \varepsilon)\|S\|_2 \leq \|\Phi S\| \leq (1 + \varepsilon)\|S\|_2. \tag{1}$$

3.3. Design of the Reconstruction Algorithm in the Compression Sampling. The reconstructed recovery signal mainly solves the owed problem under a given sparse constraint and recovers the original signal with high probability from partially sampled data. The reconstruction of signals refers to the reconstruction of the original signal $y \in R^{M \times 1}$ from the dimension reduction signal $x \in R^{N \times 1}$. The key problem is how to design efficient, robust, and stable reconstruction algorithms. At the present stage, the CS reconstruction algorithm can be roughly divided into four categories: the first class: greedy iterative algorithm, aiming for the combinatorial optimization problem, which mainly take the link between signal and atomic dictionary as a more effective or nonzero way to measure atoms (coefficients). The fundamental principle is to find the support set of sparse vectors in an iterative way and to reconstruct the signal using a constrained support least squares estimation. The second class: convex optimization algorithm or optimization approximation methods, which find approximations of the signal by transforming nonconvex problems into convex problem solutions. The third kind of algorithm: based on the reconstruction algorithm proposed by the Bayesian framework, this algorithm takes into account the signal temporal correlation, especially when the signal has a strong temporal correlation, which can provide superior reconstruction accuracy than other reconstruction algorithms. Class 4: other algorithms: these methods support rapid signal sampling and reconstruction by packet testing, such as Fourier sampling, chain tracking, and Heavy Hitters on Steroids (HHS) tracking.

4. Evaluation Model Based on Multimeasure Mixed Evaluation Based on Compression Sensing

4.1. Compression Sensing of the Bearing Vibration Signal of the Bogie Traction Motor. The observation matrix dimension required to reconstruct the signal in the compressed sensing theory process is independent of the data sampling rate and the maximum frequency of the signal and is only directly related to the sparsity. To achieve compression sampling, the necessary sparsity processing of the signal is necessary to obtain the sparse signal in a specific space. In real life, the signal data is mostly nonsparse and requires some spatial

transformation methods. In this paper, we analyze the sparse representation performance of bearings using three common discrete cosine transform (DCT) [17], discrete Fourier transform (DFT) [22], and discrete wavelet transform (DWT) [26]. In order to intuitively analyze the sparse performance from the perspective of the quantization indicators, 2% of the threshold ε, data x peak value is first set as the threshold interval. That is, $\varepsilon = 2\%|\max(x_i - \min(x_i))|$, assumes the data points between data values as $[-\varepsilon, \varepsilon]$ to 0, and then exhausters the number of nonzero elements in N_0 data points in x, defines the sparse ratio $\eta_{2\%}$, $\eta_{2\%} = N_0/N$, where N_0 represents the number of data with numerical nonzero, the less sparse than $\eta_{2\%}$, the better the sparse ability of the signal. The generalized orthogonal matching tracking algorithm (GOMP) is chosen as the reconstruction algorithm, enter the observation matrix $\Phi^{P \times l}$, probational measurements obtained from the observation matrix $y^{p \times l}$, sparsity degree k, select the number of atoms S, $(S \leq K \& S \leq p/K)$ the output is the reconstructed signal $\hat{x}$. GOMP algorithm training procedure: first initialize the residual value of $r_0 = y$, index set $\Gamma_0 = \varnothing$, number of changes $k = 1$ (line 1); continuous search for S matching atoms, $k = k + 1$, search out the S atoms with the largest residual product change its corresponding index value added, $P = P_S||\langle r_{k-1}, \Phi_{PS}\rangle| = \max_M|\langle r_{k-1}, \Phi_j\rangle||, i \in [1, S], \Gamma_K = \Gamma_{K-1} \cup P$ (lines 2-7); update the candidate support set as well as the residual and correlation coefficients. The corresponding support set Φ_{Γ_K} is obtained using the updated candidate atomic index set Γ_K. Calculate the updated residual and correlation coefficients, $\hat{x}_{T_K} = \Phi_{\Gamma_K}^+ y, r_k = y - \Phi_{\Gamma_K} \hat{x}_{\Gamma_k}$. If the iterative stop condition meets $k < \min(K, p/S)$, the iterative process returns to step 2; otherwise, the iteration stops with the reconstruction signal $\hat{x} = x_{\Gamma_k}$, specifically, as shown in Algorithm 1.

4.2. Failure Characteristic Extraction of Bearing Vibration Signal of Bogie Traction Motor. With the failure of a part of the bogie or part of the bogie, the time domain waveform of the bogie state signal and the corresponding spectrum are different from the normal state, so it is considered that the characteristic parameters of the signal time domain and frequency domain distribution information are feasible to reveal the occurrence of the bogie failure. In addition, considering that the bearing is a rotating machine, the fault signal has low signal-to-noise ratio, nonlinear, and

1: **Initialize**: residual value $r_0 = y$, index set $\Gamma_0 = \varnothing$, number of changes $k = 1$
2: **for** k training iterations **do**
3:   **for** k_d iterations **do**
4:       Search for S matching atoms continuously
5:       The S atoms with the largest inner product of residuals are searched and added with their corresponding index value
6:       $P = P_S||\langle r_{k-1}, \Phi_{PS} \rangle| = \max_M |\langle r_{k-1}, \Phi_j \rangle||, i \in [1, S]$
7:       $\Gamma_K = \Gamma_{K-1} \cup P$
8:   **end for**
9:   **for** k_p iterations **do**
10:       update Φ_j, r_j, Γ_j
11:       The updated candidate atomic index set is used to obtain the corresponding support set, and the updated residuals and correlation coefficients are calculated.
12:       $\widehat{x}_{T_K} = \Phi_{\Gamma_K}^+ y, r_k = y - \Phi_{\Gamma_K} \widehat{x}_{\Gamma_k}$
13:   **if** $k < \min (K, p/S)$
14:   **return**
15:   **else**
16:       $\widehat{x} = x_{\Gamma_k}$
17: **end for**

ALGORITHM 1: GOMP training process.

nonstationary characteristics, and the characteristics of the time-frequency analysis methods (such as short-frequency Fourier transform, wavelet transform, and EMD) have higher fault state information ability than the time domain and frequency domain characteristic parameters. In order to obtain the bearing fault state information as fully as possible, the experiment selects 10 time domain and 5 frequency domain and 10 time-frequency domain energy and Lempel-Ziv frequency domain parameters. The selected time domain feature parameters form the original time domain feature set, $(T_1, T_2, \cdots, T_{10})$ (respectively: peak, mean, variance, harmonic average, margin index, cliff index, wavedness index, pulse index, peak index, and deviation index). The frequency domain characteristic parameters form the original frequency domain characteristic sets $(F_1, F_2, \cdots, F_5)$ (respectively: mean frequency, center of gravity frequency, root mean square frequency, standard difference frequency, and cliff frequency). Time-frequency characteristic parameters are based on the adaptive decomposition of the original fault signal using EMD. Energy features $\text{IMF} = [\text{IMF}_1, \text{IMF}_2, \cdots, \text{IMF}_5]$ extract the first five eigenmode components containing useful information and Lempel-Ziv complexity features $L = [L_1, L_2, \cdots, L_5]$.

4.3. Comprehensive Characteristic Index of Bearing Vibration Signal Based on Multimeasure Mixed Evaluation Model. The extraction of multicategory fault characteristic parameters is usually regarded as the basic guarantee for accurate fault diagnosis. However, if it is applied improperly, it is difficult to improve the fault diagnosis accuracy, because the sensitivity of the characteristic parameters is different. If the original Gavett collection is directly used as the input of the subsequent classifier, the advantage of sensitive characteristics on fault classification cannot be outstanding, and the correlation between nonsensitive characteristics will weaken the classification effect and improve the fault diagnosis accuracy. Characteristic evaluation just provides an effective solution

for the above problems. On the basis of certain evaluation criteria, the sensitivity of each characteristic parameter is learned, and the original characteristic set is filtered or weighted according to the learning results, which thus plays the purpose of improving the characteristic clustering and classification performance. Most of the widely used feature weighted methods use the weight coefficient (weight coefficient) as the core content [22] and screen the features and weighting of high Vite solicitation based on a single sensitivity evaluation model. At present, the feature evaluation model uses more distance, consistency, information, correlation measures, etc. [26] Common distance measures are pasteurized distance, Euclidean distance, and Marchhedean distance; information measure mainly includes mutual information and information gain; consistency measure is the main indicator; correlation measure includes Pearson (Pearson) correlation coefficient [27], minimum square regression error, probability error, Fisher score, Laplacian score, linear classification and analysis, and high calculation efficiency. The above single measurement feature evaluation methods can screen deredundancy features from a specific perspective, but their limitations are strong, which cannot be comprehensive screening features and fully reflect the protection information. The existing feature-weighted methods are realizing the learning and weighted processing of feature sensitivity based on a feature evaluation model of a single measure, ignoring the complementary effect of the multimeasure evaluation model and the composite gain effect on high-dimensional feature screening. Therefore, the experimental mixed measure feature evaluation model is composed of a random combination of n typical feature evaluation models in each single measure index benchmark, and the specific implementation process is shown in Figure 5. Different measure combination mixed strategies form $Q = C_n^2 + C_n^3 + \cdots C_n^n$ and then select the optimal measure combination strategy with the maximum variation coefficient. Secondly, the multimeasure optimal mixed
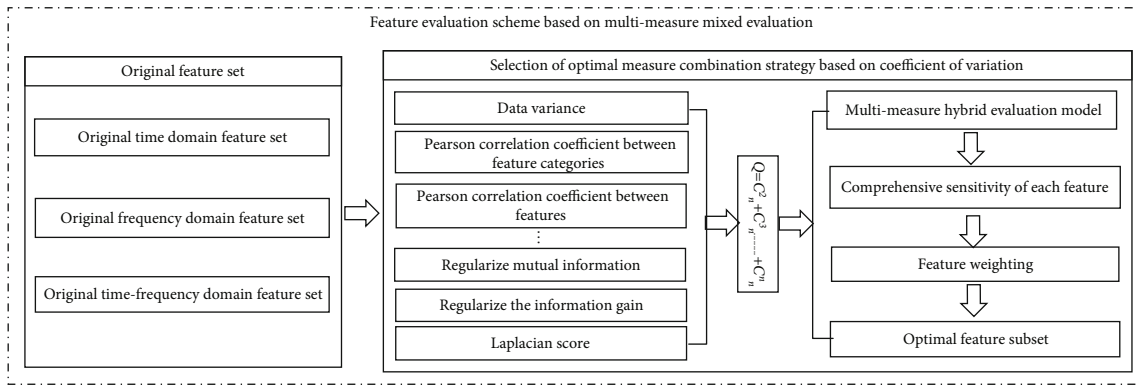
FIGURE 5: An evaluation model based on multimeasure mixing.

(a) The screw on the nondrive end is top dead

(b) The drive end is fixed by the strap

FIGURE 6: Protection status 1 setting.

evaluation model is calculated as the combined feature weight and the original eigenvalue. The detailed flow is shown in Figure 5.

Ten common feature evaluation models are selected as alternative subevaluation models for the mixed measure strategy model. It includes information measurement, correlation measure, and distance measure feature evaluation model. Due to the large number of mixed measure models with random free combination of different single measures, a large operational workload and too cumbersome mixed measurement strategy will produce a preferred comparison analysis process. Considering that the sensitivity of each single measure to the high-Witt solicitation varies, different feature subset dimensions remain when feature-weighted and filtered, cases where a measure removes only less nonsensitive features. The feature subsets are still too redundant, and it may even be difficult to select more sensitive features to form feature subsets for classification. Thus, initial screening and filtering of the submodel constituting the mixed measure model are required. A single measurement feature evaluation model with good sensitivity discrimination is retained. Avoid the difficulty of learning the poor compre-

hensive performance of a large number of mixed measure combination strategy sensitivity, resulting in the optimization process. Therefore, a preliminary selection of a single measure feature evaluation model before a mixed combination of a single measure feature evaluation model is done, and several single measure feature evaluation models with outstanding sensitivity are selected for the subsequent random mixing strategy and then the principle of the largest discrete coefficient of the mixed measure sensitivity and the largest cliff to select the best measure combination strategy.

Starting from ten common single measure feature evaluation models, the sensitivity score of time domain, frequency domain, and time-frequency domain of three different protective states of bogie is obtained of ten single measure models. It is found that different measures have different sensitivity to the feature set, some single measures are very sensitive to the feature set, and it is almost impossible to get a reduced subset of good features. Some single measures have good sensitivity learning effect to the feature set, high sensitivity features are more prominent, and nonsensitivity features are weakened, making the feature sensitivity differentiation more obvious. This section preliminarily selects
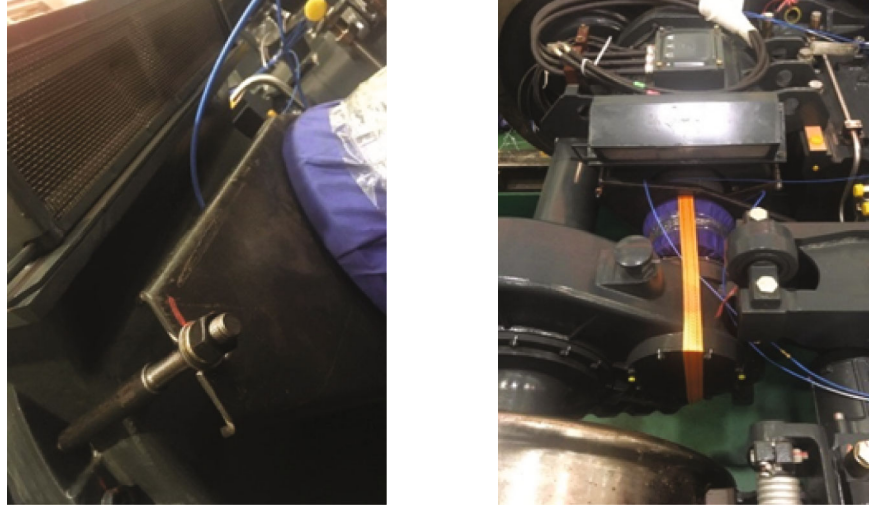
(a) Drive end decoupling pressure plate plus tie rod protection   (b) Drive end decoupling coupling fixing belt

FIGURE 7: Protection status 2 setting.
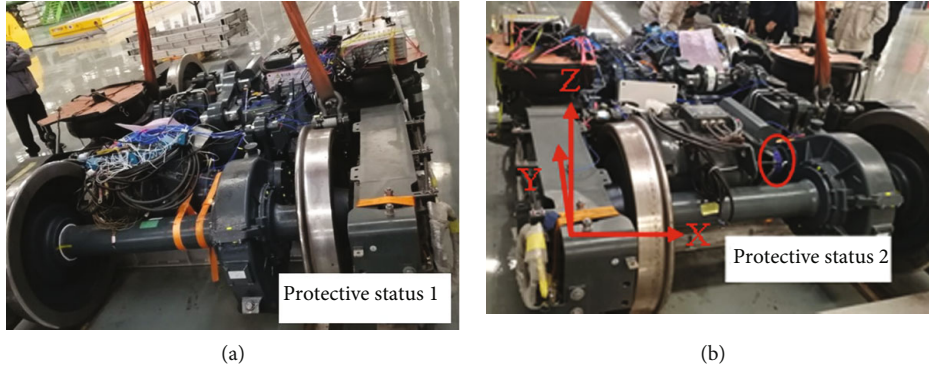
(a)   (b)

FIGURE 8: Overall layout of the protection scheme.

TABLE 1: Summary of protection status of motor bearings.

Protective status	Drive end	Nondrive end	Fixed binding of transmission end	Back and forth
1	Undecoupled	Screw top is dead	Longitudinal with the wheel axis	Go/return
2	Decoupled	Screw top is dead	Unfastened	Go
3	Undecoupled	The screw is not dead	Unfastened	Return

ten single measure evaluation models and is selected as the submodel of the subsequent mixed measure feature evaluation model. Because the dimension of each measure is inconsistent, but the dimension of the feature on each single measure is comparable, a uniformly defined threshold $\sigma^i = (\sum_l^j \lambda_j^i)/j$, λ_j^i is the type j feature sensitivity score of a single measure which is set for each single measure. If the sensitivity score of more than 10 characteristics of a single measure is greater than the mean value σ^i, the sensitivity score learning effect of the single measure is poor, and if the single measure is abandoned, the submodel for the subsequent evaluation model of mixed measurement characteristics is retained. Secondly, construct a mixed measure feature sensitivity learning model with cumulative effect composed

of individual measures, whose mathematical expression is as follows:

$$w_j^H = \frac{w_j^1 \times w_j^2 \times \cdots \times w_j^p}{w_j^{p+1} \times w_j^{p+2} \times \cdots \times w_j^n}. \tag{2}$$

In the formula, w_j^H represents the comprehensive measure sensitivity value of the j feature of the sample feature set in the H hybrid strategy; $w_j^1, w_j^2, \cdots, w_j^n$, respectively, represents the $1, 2, 3, \cdots, n$ kind single measure sensitivity value result of a sensitivity learned j feature in the feature set of a single measure feature evaluation model of $w_j^1 \sim w_j^p$ which is a sensitivity learning value that is positively

(a) Sensor 1

(b) Sensor 2

(c) Sensor 3

(d) Sensor 4

(e) Sensor 5

(f) Sensor 6

(g) Sensor 7

(h) Sensor 8

FIGURE 9: Sensor measuring point layout.
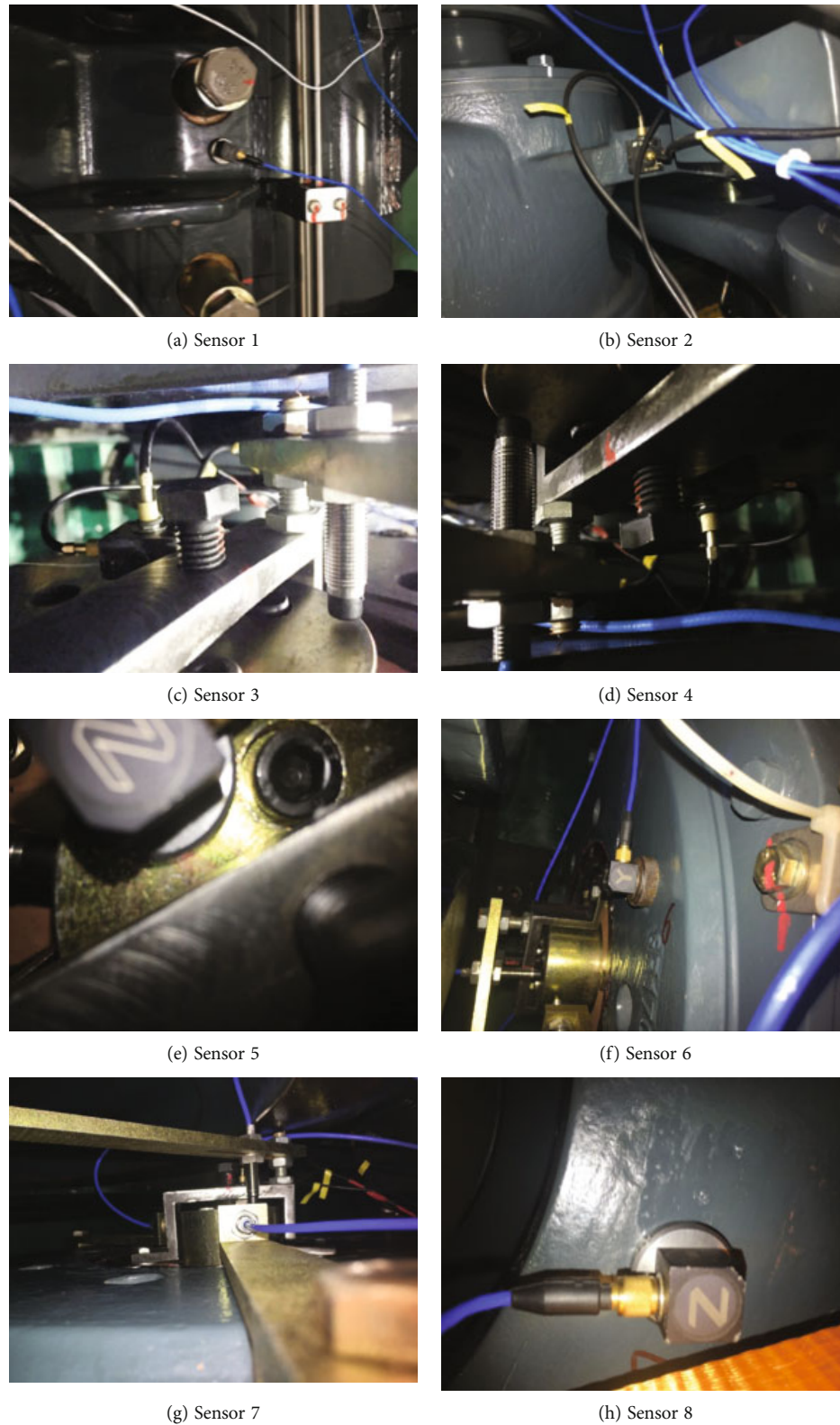
related with the characteristic sensitivity of the characteristic sensitivity of a single measurement evaluation model. $w_j^p \sim w_j^n$ is the sensitivity learning value of the first feature sensitivity score of the single measure evaluation model and the characteristic sensitivity of the single measurement model. Among them is $1 \le p \le n\,; 1 \le n \le 4$. In order to
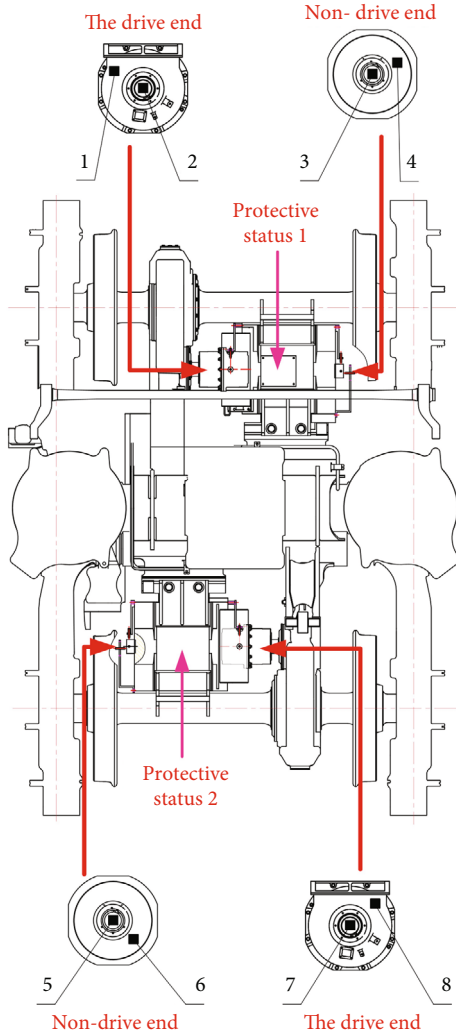
Figure 10: Schematic layout of sensor points on the bogie traction motor bearings.

Figure 11: Vibration signal of traction motor bearing.
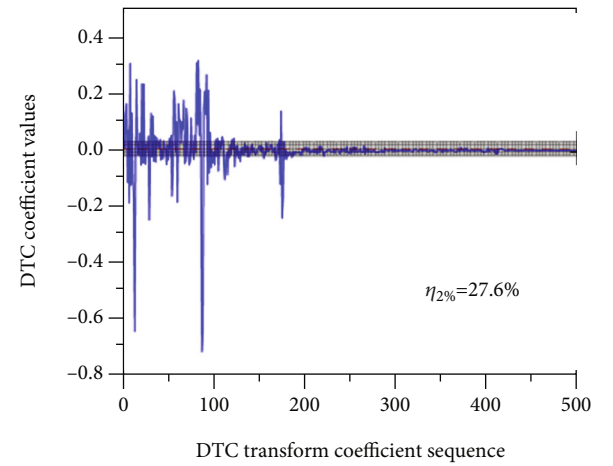
Figure 12: DCT sparse transformation.

avoid the diversity of sensitivity learning results of different single measure feature evaluation models, affecting the sensitivity learning of mixed measure evaluation models, the sensitivity score value w_j^i of each single measure model should be normalized. The formula for the normalization of the comprehensive measure sensitivity score w_j^i of the type j feature in the type i hybrid model is as follows:

$$\tilde{w}_j^i = 1 + 9\left(\frac{w_j^i - \min\left(w^i\right)}{\max\left(w^i\right) - \min\left(w^i\right)}\right). \quad (3)$$

After product mixing, the comprehensive measure sensitivity learning results w_j^i are obtained. The significance is to compare and evaluate the comprehensive measure sensitivity scores w_j^i obtained from the product effects of different scales under the same scale coefficient, which also makes the sensitivity of high-sensitivity features more prominent and weakens the effect on classification and

clustering in the nonsensitivity features. Thus, the clustering effect of the optimal feature subset is improved.

In order to evaluate the multimeasure mixed evaluation model after a single measure feature evaluation model, the multimeasure evaluation model for the multimeasure evaluation model with the maximum discrete coefficient and the maximum cliff and extract the sensitive feature subset of the best combination strategy for subsequent clustering and evaluation. The core idea is a dimensionless parameter index that reflects the degree of data discretization according to the discretization coefficient and cliff of the time series. The specific criterion of $\Psi_m = \sqrt{V_m \times K_m}$ is that the greater the cliff value K_m and the greater the discrete coefficient V_m of the mixed characteristic sensitivity score sequence, the higher the discrete degree of the characteristic data sequence and the greater the Ψ_m value. The reaction performance in the feature concentration is strengthening the feature sensitivity learning effect with high sensitivity and weakening the learning effect of nonsensitivity features. Make the high-sensitivity features stand out in the mixed measure strategy. Thus, it can be considered that the higher the cliff value of the eigenvalue and the greater the discrete

(a) Discrete Fourier sparse transform (real part)

(b) Discrete Fourier sparse transform (imaginary part)

FIGURE 13: DFT sparse transformation.

(a) Wavelength = 8

(b) Wavelength = 12

(c) Wavelength = 16

FIGURE 14: Discrete wavelet transform.

coefficient of the mixed characteristic sensitivity score value, the hybrid measure is best effective in sensitivity learning, and the more streamlined the subset of eigenvalue used for clustering classification. The formula for calculating the discrete coefficient of the comprehensive feature sensitivity score sequence defining V_m as the m kind mixed measure feature evaluation model is as follows:

$$V_m = \frac{S_m}{\bar{w}^{H-m}} = \frac{\sqrt{(1/(N-1))\sum_j^N \left(w_j^{H-m} - \bar{w}^{H-m}\right)^2}}{\bar{w}^{H-m}}. \quad (4)$$

In the formula, S_m is the standard difference in the sequence of mixed feature sensitivity scores of type and $\bar{w}^{H-m}$ is the mean of the mixed feature sensitivity score series of the m kind mixed measure feature evaluation model: $\bar{w}^{H-m} = (\sum_{j=1}^N (w_j^{H-m} - \bar{w}^{H-m}))/N$, N is the total number of features in the feature set, and w_j^{H-m} is the comprehensive sensitivity score of the j feature of different protective state features in the m kind mixed measure feature evaluation model. The formula defining the cliff value K_m of the m kind mixed measurement feature evaluation model is as follows:

$$K_m = \frac{E(x_m - \bar{x}_m)^4}{\sigma_m^4}. \quad (5)$$

In the formula, x_m, $\bar{x}_m$, and σ_m are the data series, mean, and standard difference of the mixed measure feature evaluation model of type m, respectively.

The specific criterion of $\Psi_m = \sqrt{V_m \times K_m}$ is based on the greater the cliff value K_m and the greater the discrete coefficient V_m of the mixed characteristic sensitivity score sequence, the higher the characteristic data sequence and the greater the Ψ_m value. The reaction performance in the feature concentration is strengthening the feature sensitivity learning effect with high sensitivity and weakening the learning effect of nonsensitivity features. Make the high sensitivity features stand out in the mixed measure strategy. Thus, it can be considered that the higher the cliff value of the e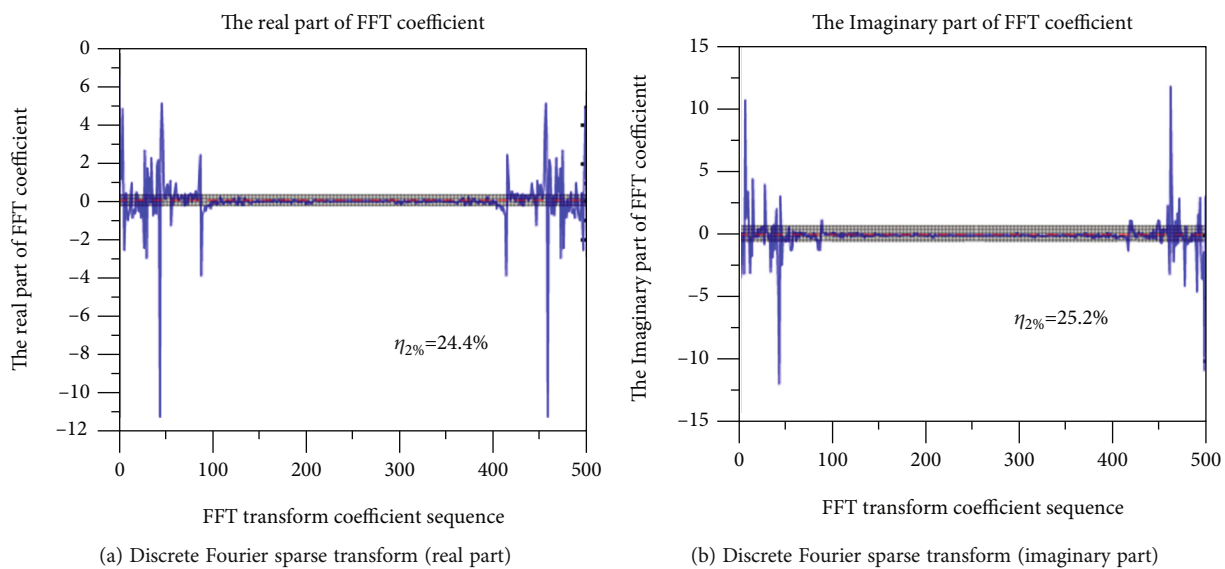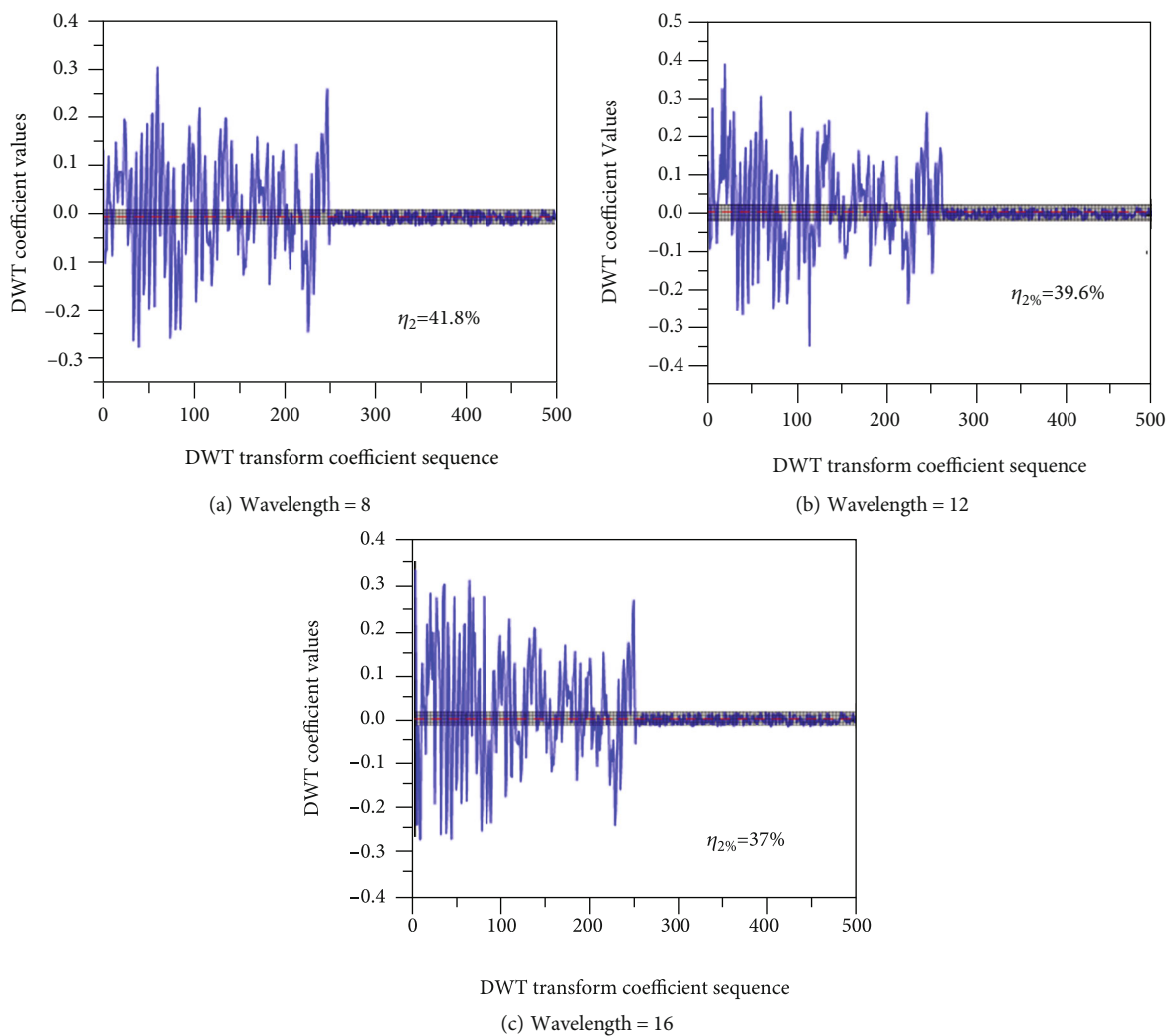igenvalue and the greater the discrete coefficient of the mixed characteristic sensitivity score value, the hybrid measure is best effective in sensitivity learning and the more streamlined the subset of eigenvalue used for clustering classification.

The traditional feature evaluation model with a single measure usually considers only from a single angle when extracting the optimal feature subset, which makes it difficult to evaluate the vibration signals in the whole time domain under different protection conditions. In order to better evaluate the protection effect of traction motor bearings under different protection conditions during transportation, this chapter proposes a multimeasure mixed evaluation model, which can extract multicategory and multimeasure characteristic parameters as feature sets. The novelty lies in that based on the feature index, sensitivity learning is carried out for the features in the multianalysis domain, a multimeasure mixed evaluation model is established based on the sin-
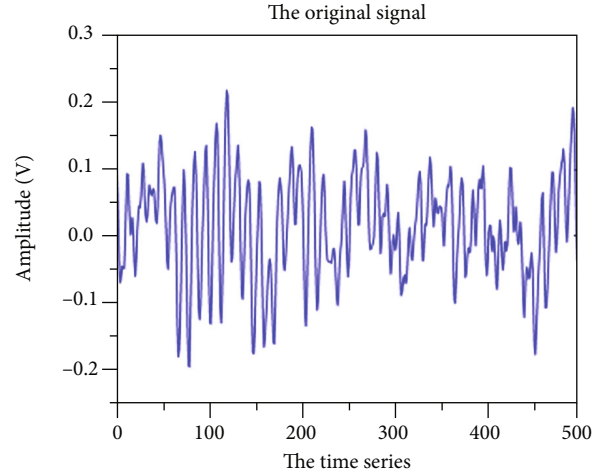
Figure 15: Original vibration signal.

gle measure feature evaluation feature index, and the optimal feature subset that is more conducive to evaluating the effects of different protection states is optimized by using the comprehensive feature evaluation index. Then, the unified feature index was established based on the optimal feature subset to comprehensively evaluate the protection effect under different protection conditions.

4.4. Build a Multimeasure Hybrid Evaluation Model Based on Compression Sensing. In this paper, based on the actual operating conditions of bogie traction motor bearings in urban rail vehicles, because the bearings are difficult to be effectively evaluated under different transportation protection, a multimeasure hybrid evaluation model based on compressive sensing is proposed. Firstly, vibration signals of traction motor bearing are sampled and compressed based on compressive sensing theory. Secondly, an optimal hybrid model feature evaluation framework with single measures such as distance, correlation, and information is constructed to learn feature sensitivity from the original feature set composed of time-frequency, frequency-domain, and frequency-domain feature parameters. At the same time, to design comprehensive features based on sensitivity score sequence variation coefficient of the multimeasure portfolio strategy optimization method and mixed with the optimal combination strategy measure corresponding comprehensive evaluation model to the original fault feature set sensitivity study and then the optimal comprehensive score of each feature sensitivity for each feature weights, build a new weighted feature set. Finally, the proposed feature sensitivity learning method is applied to the transportation of bogie traction motor bearings of Ningbo Line 3 urban rail vehicles, so as to verify the feasibility and technical advantages of the proposed new method. This method provides a technical basis for the difficulties existing in the traction motor bearings of transit sentence frame in the field of rail transit and provides a new idea for the data collection and reduction of vibration signals of bearings in the process of transportation, as well as reasonable transportation protection.

(a) Reconstruction signal based on DCT representation

(b) Reconstruction signal based on DFT representation

(c) Reconstruction signal based on DWT representation
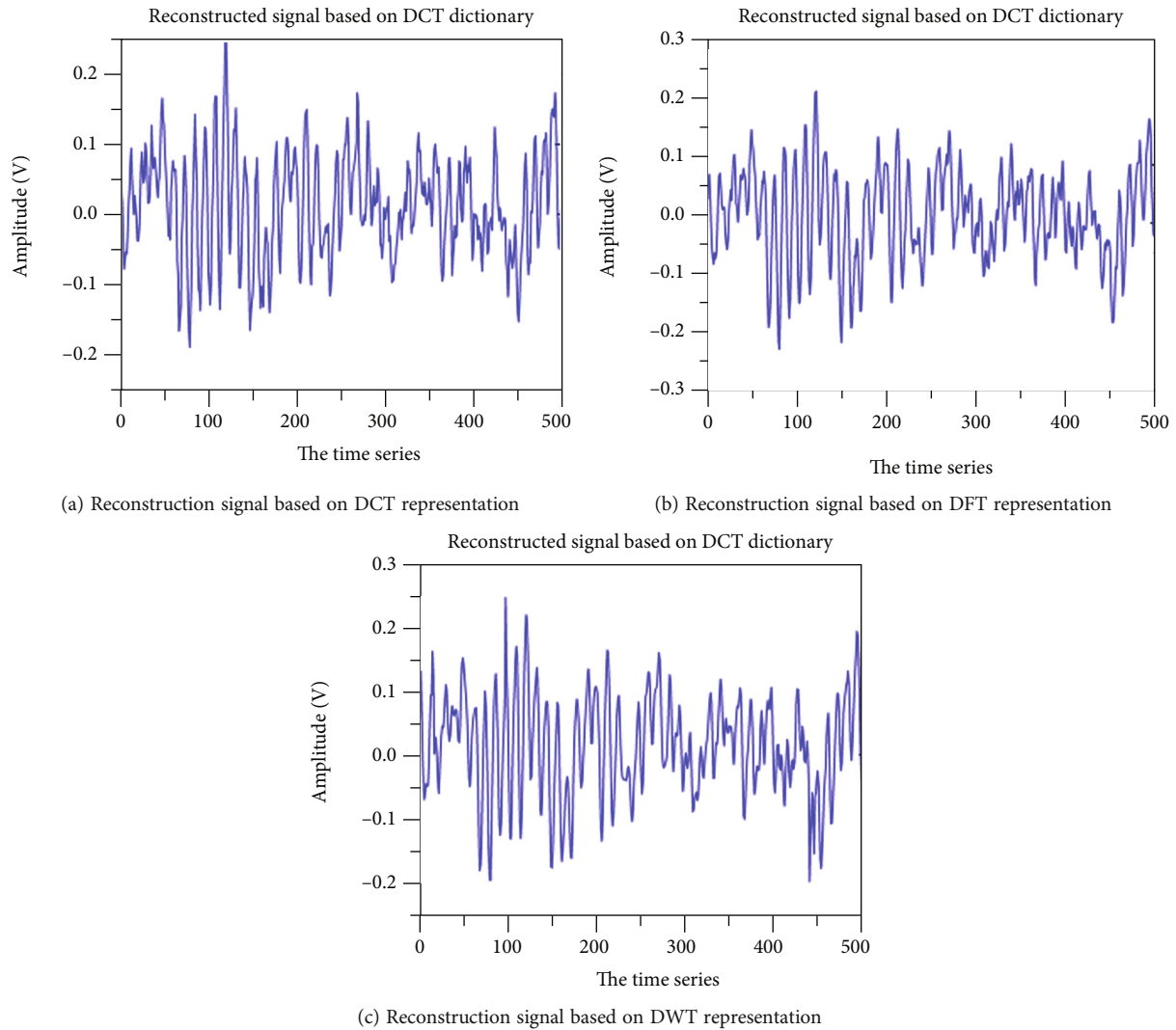
FIGURE 16: Comparison of reconstructed signals.

5. Experimental Analysis

5.1. Experimental Measurement

5.1.1. Three Protection States of Traction Motor Bearings.
The test object is the power bogie of Ningbo Line 3. The
bogie wheel pair is supported and fixed with iron shoes. In
the transportation process, the bogie two guided motors
adopt different protection methods to test the vibration
acceleration of bogie and motor bearings in Zhuzhou to
Ningbo section. In the process of road transportation, motor
bearings are protected as shown in Figure 6. Protection
status 1 and protection status 2 are used for the two motors,
respectively, during the departure, and protection status 1
remains unchanged while protection status 2 is changed to
protection status 3 during the return, so as to study the
protective effects of the three protection status on traction
motor bearings.

Figure 6 shows the defense mode in defense state 1,
Figure 7 shows the defense mode in defense state 2, and
Figure 8 shows the overall layout in defense state. In
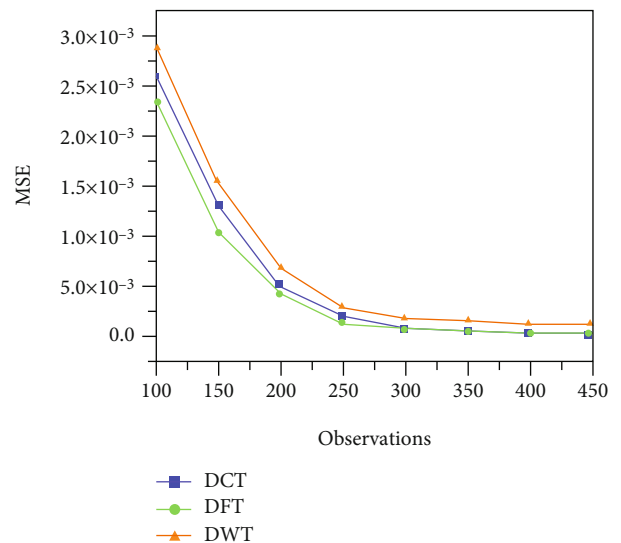
FIGURE 17: Mean square errors of reconstruction of different sparse
representation methods.
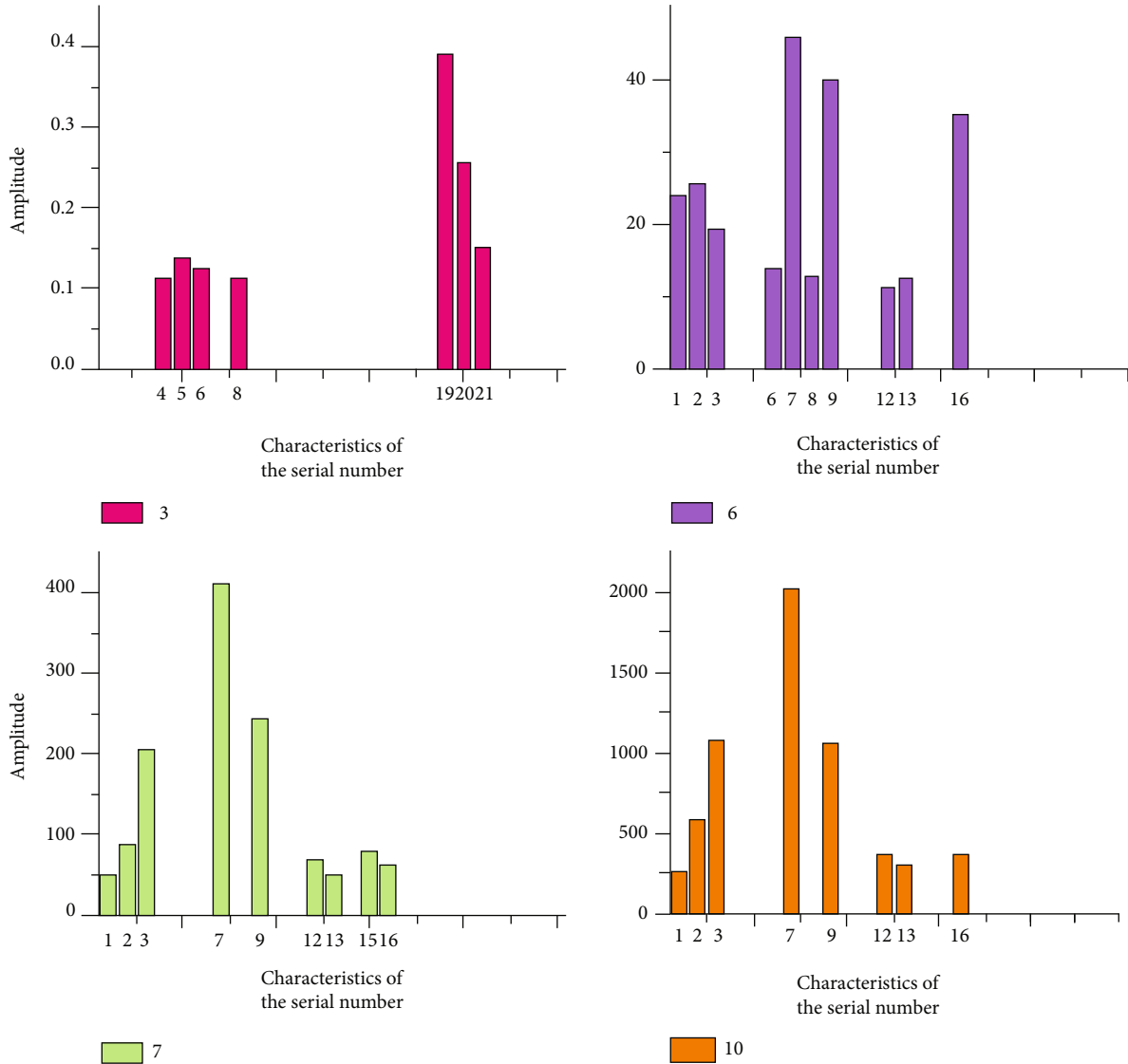
Figure 18: Preferred sensitivity score of a single measure sensitivity feature.

addition, the coordinate directions of the three-way acceleration sensor are defined. Since the vertical direction along the Z direction is most affected by road turbulence, the analysis of vertical vibration acceleration signal is mainly carried out. Table 1 shows three settings of the same protection state.

5.1.2. Measuring Point Arrangement of Traction Motor Bearing. A total of 8 acceleration sensors are arranged on the bogie, and the acceleration sensors at each measuring point are fixed by glue and magnetic suction seat. According to the designed sensor point position and sensor type, the sensor is arranged on the bogie traction motor. According to the position of the traction motor bearing in the bogie, in order to better collect the bearing vibration signal in the process of traction motor in the road, the arrangement of vibration sensor measuring points is shown in Figure 9. Figures 10(a)–10(h) correspond to sensors numbers 1-8.

5.2. Bearing Data Compression Perception. After the experimental test, the experimental data was up to 254 GB and was difficult for subsequent data analysis. This paper proposes a method to solve the problems of data mass and redundant data. Firstly, the vibration signal of a transport bearing is randomly selected to conduct compression sensing sparse representation analysis, and the DCT, DFT, and DWT transformation of the experimental signal are performed. In Figure 11, the sparse ratio of the original vibration signal is 91.4%. Figure 12 intuitively shows that the sparse ratio is 27.6% after the DCT transformation, and the sparsity of the vibration signal after the DCT transformation is higher than that of the original signal. Figure 13 is the result of the vibration signal after the DFT transformation, and the sparse ratio of the DFT coefficient is 24.4% and 25.2%, respectively, which is more prominent compared with the DCT transformation. Figure 14 shows that the sparsity of the vibration signal is well improved compared with the original signal. The sparse score of Daubechies wavelet

TABLE 2: Results of various evaluation parameters of characteristic sensitivity score of multimeasure mixed model.

Hybrid policy Group-up	A single type of measure included	Sensitivity learning score sequence standard difference S_m	Sensitivity scores learn the score sequence mean $\bar{w}^{H-m}$	Sensitivity scores learn the score sequence discrete coefficients V_m	Sensitivity scores learn the score sequence cliff values K_m	Comprehensive evaluation index of sensitivity score sequence Ψ_m
ω^{H-1}	3#, 6#	2.5450	3.5357	0.7198	3.2073	1.5194
ω^{H-2}	3#, 7#	2.1382	2.1456	0.9966	8.8875	2.9761
ω^{H-3}	3#, 10#	2.1179	2.2097	0.9585	8.7751	2.9001
ω^{H-4}	6#, 7#	1.9732	1.7685	1.1158	13.7512	3.9170
ω^{H-5}	6#, 10#	1.9489	1.7830	1.0931	14.1195	3.9286
ω^{H-6}	7#, 10#	1.8865	1.6264	1.1599	16.9705	4.4367
ω^{H-7}	3#, 6#, 7#	1.9730	1.7800	1.1085	13.6794	3.8940
ω^{H-8}	3#, 6#, 10#	1.9491	1.7938	1.0866	14.0398	3.9058
ω^{H-9}	3#, 7#, 10#	1.8903	1.6315	1.1587	16.7992	4.4119
ω^{H-10}	6#, 7#, 10#	1.8392	1.5276	1.2040	19.6013	4.8579
ω^{H-11}	3#, 6#, 7#, 10#	1.8387	1.5254	1.2054	19.6395	4.8655

lengths 8, 12, and 16 is 41.8%, 39.6%, and 37%, and the change of Daubechies wavelet length has little impact on the sparsity after the coefficient transformation.

Next, consider the influence of different sparse dictionary transformations on the compression effect of the bearing vibration signal, by setting three different sparse transformation dictionaries (DCT, DFT, and DWT), in which the Daubechies wavelet length of DWT is set to 16, selecting Gaussian random observation matrix and GOMP reconstruction algorithm. Using these three different sparse dictionaries to perform data compression measurement and reconstruct the experimental signal, we obtain the parameter indicators of the signal reconstruction performance of three different sparse dictionaries. Comparing Figures 15–17 shows that the signal reconstruction performance index of the base DFT is superior to that of DCT and DWT; in three different sparse transformation methods, DFT has better sparse performance and performance in data compression.

5.3. Quantitative Characterization of the Bearing Protection Effect Based on the Unified Characteristic Index. The original high-Witt collection including time domain features, frequency domain features, energy features based on EMD, and Lempel-Ziv complexity features of EMD is extracted. In order to further realize the dimensionality reduction of high-Witt collection and improve the performance of cluster classification, ten sensitivity scores as described above are learned, and the 3, 6, 7, and 10 single measure feature evaluation models are selected as the submodels of mixed multimeasure feature evaluation models according to the sensitivity learning results. They are intraclass and interclass integrated distance model, Pearson correlation coefficient model, Fisher score model, and Laplacian scoring model. The best sensitivity feature subset sensitivity score distribution under the four single measurement feature evaluation

indicators is shown in Figure 18. A hybrid measure feature evaluation model is constructed for the four preferred measure evaluation submodels. Since four random combinations into mixed measure models have 11 combination methods, the 11 mixed measure feature evaluation models learn the sensitivity, obtain the comprehensive sensitivity score sequence, and obtain the discrete coefficient, cliff value, and comprehensive evaluation index of the sensitivity learning results based on the comprehensive sensitivity score evaluation index Ψ_m. The results are shown in Table 2.

It can be seen from the table above that the discrete coefficient, cliff value, and comprehensive sensitivity score evaluation indicators of the mixed measure feature evaluation model after the random combination of four single measures are best performed when the 3, 6, 7, and 10 measures are fully combined. It can therefore be argued that the hybrid strategy exhibits outstanding performance in strengthening the sensitive features, weakening the nonsensitive features, and a subset of reduced optimal features. Features with large sensitivity scores are extracted as subfeatures of the subset of optimal feature subsets. Its feature number is 1, 2, 3, 7, 9, and 16.

To further verify that the extracted sensitivity scores perform well for the clustering effect of a subset of optimal features, principal component analysis (PCA [28]) of the best subsets of the optimal evaluation model is applied. To facilitate the application of PCA, visual analysis is performed. Figure 19 shows a visual analysis diagram of the first characteristic subset of the 3, 6, 7, and 10 single measure evaluation models. It can be seen that the best characteristic subset characteristics of the 3 and 6 single measures cannot be classified and clustered by data samples regardless of the serious travel overlap between the distance and different categories. The best characteristic subset corresponding to the 7 and 10 single measure evaluation models can cluster different protective state data samples effectively, but the distribution is scattered and the inner class range is large. From

(a) The best subcluster class effect of the third single measure

(b) The best subcluster class effect of the sixth single measure

(c) The best subcluster class effect of the 7 single measure

(d) Best subcluster class effect for the 10 single measure

(e) Clustering effect of the optimal characteristic subset with optimal multiple measures
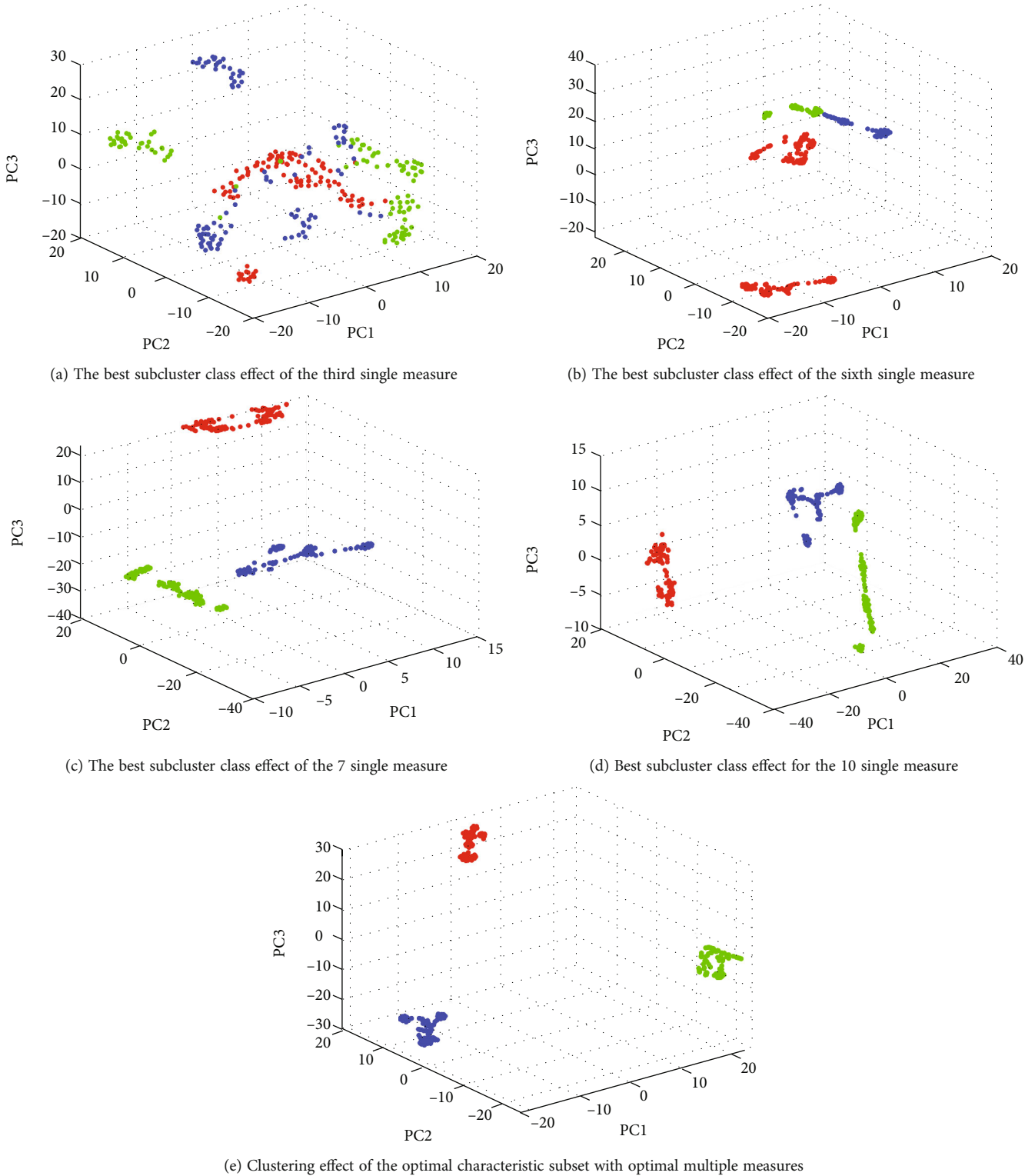
FIGURE 19: Cluster effect of the optimal subsets under different measures.

the perspective of interclass distance, the clustering effect is not prominent, and the optimal multimeasure mixed evaluation model is far better than the other four single measure subsets in classification clustering.

A Cartesian product is performed for the preferred optimal subfeature subset based on a multimeasure mixed eval-

uation model. The Cartesian product calculation expressions defining the unified feature metrics are

$$Q = \frac{v^1 \times v^2 \times \cdots \times v^p}{v^{p+1} \times v^{p+2} \times \cdots \times v^n}. \tag{6}$$
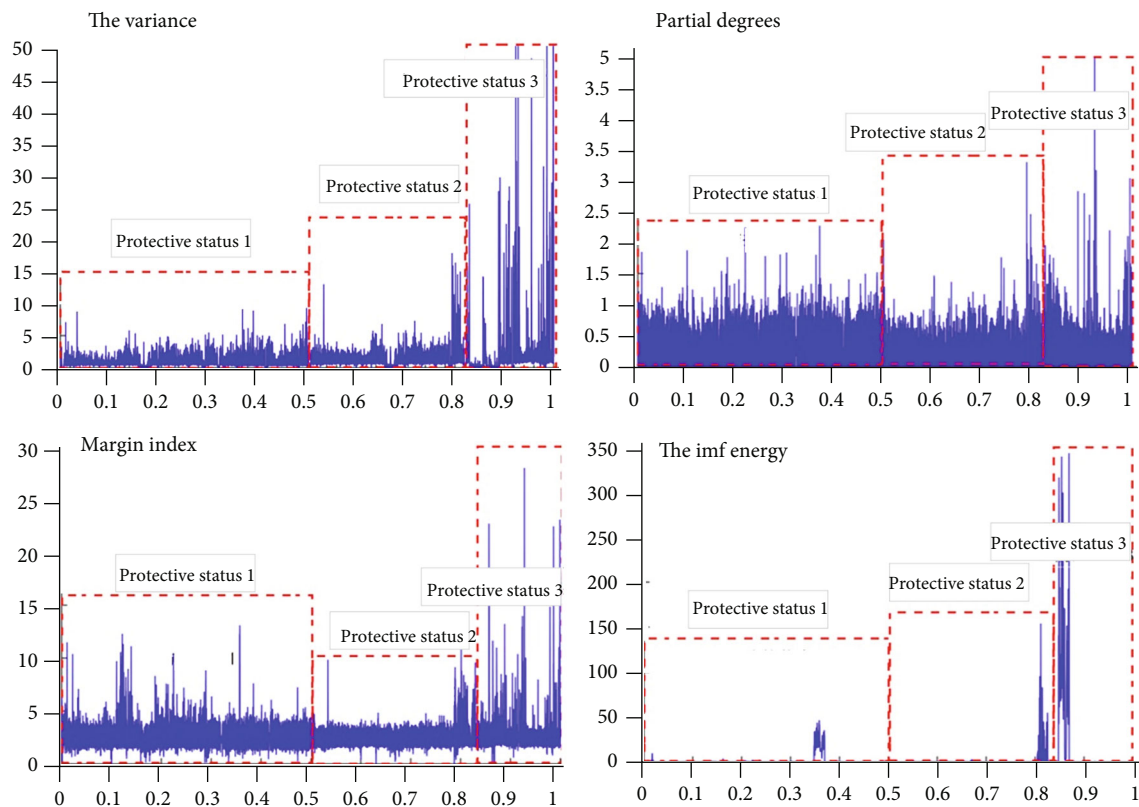
Figure 20: Part full time domain features.
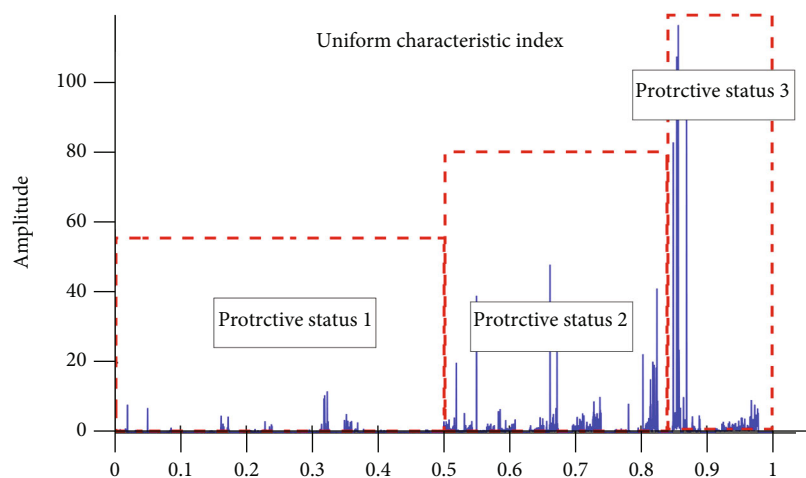
Figure 21: Comprehensive characteristic index.

In the formula, $v^1 \sim v^p$ protection is negative, and $v^{p+1} \sim v^n$ is the positive value with the protection effect, where Q is a unified feature indicator; $1 \le p \le n$, $1 \le n \le 6$. The characteristics of the characteristic subset are negatively related to the protection effect, that is, the greater the characteristics, the worse the protection effect, so the comprehensive characteristic indicators. And the larger the unified characteristic indicators, the worse the protection effect.

Figure 20 shows the distribution of different protective states in the time domain and the comprehensive evaluation from a single feature. Figure 21 is the comprehensive characteristic index of bogie bearing vibration signal after characteristic combination. The unified characteristic index based on the full time domain is the most significant in the protection state 3 (no protection) and the worst protection effect, while the unified characteristic index of protection state 1 is not significant; its peak is far less than the protection states

2 and 3, the best protection effect, and the protection effect of protection state 2 is secondary.

6. Conclusion

In this paper, the state characterization of bogie traction motor bearings under different transportation protection is studied, and the multimeasure hybrid characterization model based on compressive sensing theory is proposed, which is verified by the highway transportation example of Ningbo Line 3 urban rail vehicle bogie traction motor bearings. Experiment: when the protection state is undecoupled + the screw is not jacked (protection state 3), the bearing damage is the most serious. The second is when the protection state is decoupling + screw jacking (protection state 2). In the case that the protection state is undecoupled + binding + screw top (protection state 1), the bearing has almost no damage. That is, the protection effect is protection state 1 > protection state 2 > protection status 3.

Data Availability

The data and the Matlab programs used to support the findings of this study are available from the corresponding author upon request.

Conflicts of Interest

The authors declared no potential conflicts of interest with respect to the research, authorship, and/or publication of this article.

Authors' Contributions

The authors' contributions are as follows. Yi Liu was responsible for guiding conceptualization and methodology, criticism, and correction. Qi Chang was responsible for conceptualization, methodology, data curation, software, validation, investigation, and original draft. Jiaxin Luo was responsible for review and editing. Lin Li was responsible for investigation, providing test guidance, and review. Junfeng Man was responsible for review and editing. Wei Fen was responsible for investigation and review. Qilin Chen was responsible for software and review. Yiping Shen was responsible for guiding conceptualization, criticism, and correction.

Acknowledgments

References

[1] D. Chunmei, H. Minggao, and L. Meiqing, "Motor bearing protection for urban rail vehicle non-rail transportation," *Electric Locomotives & Mass Transit Vehicles J*, vol. 42, no. 2, pp. 62–64, 2019.

[2] E. J. Candes and T. Tao, "Near-optimal signal recovery from random projections: universal encoding strategies?," *IEEE Transactions on Information Theory*, vol. 52, no. 12, pp. 5406–5425, 2006.

[3] D. L. Donoho, "Compressed sensing," *IEEE Transactions on Information Theory*, vol. 52, no. 4, pp. 1289–1306, 2006.

[4] E. J. Candes, J. Romberg, and T. Tao, "Robust uncertainty principles: exact signal reconstruction from highly incomplete frequency information," *IEEE Transactions on Information Theory*, vol. 52, no. 2, pp. 489–509, 2006.

[5] Weifen, *Key Technology Research for Intelligent Fault Diagnosis of Rotating Mechanical Multi-Sensor Information Fusion*, Harbin University of Technology, China, 2018.

[6] D. Xiao, C. Qin, H. Yu, Y. Huang, and C. Liu, "Unsupervised deep representation learning for motor fault diagnosis by mutual information maximization," *Journal of Intelligent Manufacturing*, vol. 32, no. 2, pp. 377–391, 2021.

[7] J. Luo, J. Huang, and H. Li, "A case study of conditional deep convolutional generative adversarial networks in machine fault diagnosis," *Journal of Intelligent Manufacturing*, vol. 32, no. 2, pp. 407–425, 2021.

[8] Z.-C. Liao, X.-X. F. Bai, Y. Li, X.-C. Deng, and J. Sun, "Design, modeling, and verification of a test bench for braking simulation of 1/4 vehicle," *Proceedings of the Institution of Mechanical Engineers, Part D: Journal of Automobile Engineering*, vol. 234, no. 5, pp. 1425–1441, 2020.

[9] L. Qiang, Z. Shuo, and W. Yujun, "A dynamic response test rig of a full-scale rotor–journal bearing system," *Proceedings of the Institution of Mechanical Engineers*, vol. 233, no. 4, pp. 649–659, 2019.

[10] Y. He, K. Feng, M. Hu, and J. Cui, "An MCM-enhanced compressive sensing for weak fault feature extraction of rolling element bearings under variable speeds," *Shock and Vibration*, vol. 2020, 21 pages, 2020.

[11] J. Yang, X. Liao, X. Yuan et al., "Compressive sensing by learning a Gaussian mixture model from measurements," *IEEE Transactions on Image Processing*, vol. 24, no. 1, pp. 106–119, 2015.

[12] F. Krahmer, D. Needell, and R. Ward, "Compressive sensing with redundant dictionaries and structured measurements," *SIAM Journal on Mathematical Analysis*, vol. 47, no. 6, pp. 4606–4629, 2015.

[13] Q. H. Dai, "Research on compressed sensing," *Chinese Journal of Computers*, vol. 34, no. 3, pp. 425–434, 2011.

[14] D. L. Donoho and X. Huo, "Uncertainty principles and ideal atomic decomposition," *IEEE Transactions on Information Theory*, vol. 47, no. 7, pp. 2845–2862, 2011.

[15] M. El Ad and A. M. Bruckstein, "A generalized uncertainty principle and sparse representation in pairs of bases," *IEEE Transactions on Information Theory*, vol. 48, no. 9, pp. 2558–2567, 2002.

[16] J. A. Tropp, "Greed is good: algorithmic results for sparse approximation," *IEEE Transactions on Information Theory*, vol. 50, no. 10, pp. 2231–2242, 2004.

[17] R. Baraniuk, M. Davenport, R. DeVore, and M. Wakin, "A simple proof of the restricted isometry property for random matrices," *Constructive Approximation*, vol. 28, no. 3, pp. 253–263, 2008.

[18] E. J. Candès, "La propriete d'isometrie restreinte et ses consequences pour le compressed sensing," *Comptes Rendus Mathematique*, vol. 346, no. 9–10, pp. 589–592, 2008.

[19] L. Muyang and Y. Yuan, "Study on the rolling bearing fault signal extraction technology based on compression sensing," *Journal of Dalian Jiaotong University*, vol. 42, no. 3, pp. 21–26, 2021.

[20] Y. Lei, Z. He, Y. Zi, and X. Chen, "New clustering algorithm-based fault diagnosis using compensation distance evaluation technique," *Mechanical Systems and Signal Processing*, vol. 22, no. 2, pp. 419–435, 2008.

[21] S. Tang Baoping and Y. J. Zuqiang, "Fault diagnosis based on sensitive feature selection and manifold learning reduction," *Journal of Vibration and Shock*, vol. 33, no. 3, pp. 70–75, 2014.

[22] J. A. Sáez, J. Derrac, J. Luengo, and F. Herrera, "Statistical computation of feature weighting schemes through data estimation for nearest neighbor classifiers," *Pattern Recognition*, vol. 47, no. 12, pp. 3941–3948, 2014.

[23] M. Ismail and H. Frigui, "Unsupervised clustering and feature weighting based on generalized Dirichlet mixture modeling," *Information Sciences*, vol. 274, pp. 35–54, 2014.

[24] T. J. Yuen and R. Ramli, "Multi-objective optimization of all-wheel drive electric formula vehicle for performance and energy efficiency using evolutionary algorithms," *Proceedings of the Institution of Mechanical Engineers, Part D: Journal of Automobile Engineering*, vol. 234, no. 5, pp. 1472–1479, 2020.

[25] L. Shen, M. Caiwen, and L. Yan, "Review of compressed-sensing reconstruction algorithms," *Infrared and Laser Engineering*, vol. 42, no. S1, pp. 225–232, 2013.

[26] L. Zhang Fan and T. X. Jianguang, "Bearing troubleshooting based on compression sensing and multi-step feature learning," *Combined machine tool and automatic machining technology*, vol. 4, pp. 108–112, 2021.

[27] J. Xueling and D. Taihang, "Extraction of failure feature for electrical life prediction of AC contactor under mechanical vibration," *Instrument Journal*, vol. 40, no. 3, pp. 114–125, 2019.

[28] L. Jingzhang and W. Huang Xingshu, "Based on KPCA and improved K-means," *Journal of South China University of Technology (Natural Science Edition)*, vol. 48, no. 6, pp. 143–150, 2020.

Research Article

Bearing Fault Diagnosis under Variable Working Conditions Based on Deep Residual Shrinkage Networks and Transfer Learning

Xinyu Yang, Fulin Chi, Siyu Shao ![ORCID], and Qiang Zhang

Air and Missile Defense College, Air Force Engineering University, 710000 Xi'an, China

Correspondence should be addressed to Siyu Shao; cathygx.sy@gmail.com

Nowadays, deep learning has made great achievements in the field of rotating machinery fault diagnosis. But in the practical engineering scenarios, when facing a large number of unlabeled data and variable operating conditions, only using a deep learning algorithm may reduce the performance. In order to solve the above problem, this paper uses a method of combining transfer learning with deep learning. First, the deep shrinkage residual network is constructed by adding soft thresholds to extract the characteristics of bearing vibration data under noise redundancy. Then, the joint maximum mean deviation (JMMD) criterion and conditional domain adversarial (CDA) learning domain adapting network are used to align the source and target domains. At the same time, adding transferable semantic augmentation (TSA) regular items improves alignment performance between classes. Finally, the proposed model is verified by three experiments: variable load, variable speed, and variable noise, which overcomes the shortcomings of traditional deep learning and shallow transfer learning algorithms.

1. Introduction

With the development of modern industry toward intelligence, the health management mode of industrial equipment based on big data has become a hot research field. To achieve the goal of real-time monitoring of mechanical health and performance, it is increasingly important to speed up the establishment of a stable and reliable Prognostic and Health Management (PHM) [1]. In an industrial system, all working elements are in a relatively coupled working state, and any failure may affect the normal operation of the whole mechanical system. Since the measured signals are usually transient and dynamic, it is difficult to achieve early diagnosis of monitoring and failure by using the traditional time-frequency analysis method [2]. In order to ensure the highest possible uptime, the way of system maintenance should change to the way of real-time monitoring and predictive prevention [3]. To achieve these purposes, the intelligent fault diagnosis method has become an important research field in recent years.

The intelligent fault diagnosis method is developed on the basis of traditional machine learning and deep learning. Different from the traditional method of extracting fault feature signals manually, the intelligent fault diagnosis method does not require much prior knowledge about signal processing but directly extracts useful information from the vibration data collected and realizes early fault diagnosis in a data-driven way [4]. Among them, artificial neural network (ANN), support vector machine (SVM), deep neural network (DNN), and other models are the most widely used models for intelligent fault diagnosis [5, 6]. Merainani et al. [7] used a self-organizing feature map (SOM) neural network to identify and classify gearbox faults automatically and used a self-organizing and adaptive algorithm to identify gearbox early faults effectively. Lu et al. [8] used the stacked denoising autoencoder (SDA) for greedy layer-wise training and achieved higher accuracy than ANN and SVM in diagnosing signals containing ambient noise and fluctuating working conditions. In the development process of intelligent fault diagnosis, algorithms and data are always the

two most important cores. As the complexity of the system and the volume of data acquired increase, the cost of labeling data increases. When facing a large number of unlabeled data, it is difficult to guarantee an ideal accuracy simply by relying on the general deep learning network. At the same time, it is impossible for monitoring data to maintain the same spatial distribution throughout the survey period, considering the actual engineering conditions. The joint distribution of data changes with the change of mechanical speed, load, and noise. Therefore, in practical applications, the generalization performance based on intelligent fault diagnosis may be reduced.

Therefore, transfer learning as a new fault diagnosis tool solves the above problems well.Moreover, the theory of transfer learning has been continuously supplemented and perfected and has proved its applicability in various fields [9, 10]. The focus of transfer learning is how to solve new problems according to the knowledge that has been learned and reuse the learned knowledge through the similarity of the intrinsic characteristics of things [11]. Deep learning is superior in extracting the high-dimensional abstract features of data. It can map two groups of data with different distributions (source domain and target domain) into the same space. At this time, it can reduce the difference between features by transfer learning, which can not only accurately classify the source domain data but also achieve the purpose of domain adaptation. For some tasks with little difference in distribution, better results can be achieved in the target domain only by transferring the parameters of the pretrained network to the untrained network. However, in practice, the source and target domains have different feature spaces, but they can be aligned by minimizing the measurement differences between domains. Indicators for measuring the distribution differences between domains include KL divergence, maximum mean discrepancies (MMD), Wasserstein distance, and CORAL loss [12]. These indexes are added to the loss function, and then, the adaptive purpose is achieved through gradient descent. However, this shallow adaptive layer is still inadequate because it can only achieve the effect of domain adaptation globally, while overlapping confusion can occur in some domains with smaller discrimination. Deep transfer learning (DTL) based on deep network inherits the ability of the deep neural network to extract strong signal features. On the other hand, it overcomes the shortcomings of robustness and generalization of shallow transfer learning. Zheng et al. [13] summarized DTL into the following five methods: instance reweighting approach, feature transfer approach, classifier adaptation approach, deep learning-based approach, and adversarial-based approach. Han et al. [14] used the data of known working conditions to pretrain the CNN and realized the fault diagnosis under unknown working conditions based on CNN by fine-tuning the weight parameters. An et al. [15] used a multicore MMD domain adaptive framework to make the features of different domains approach each other in the reproducing kernel Hilbert space, which improved the stability and accuracy of the results. Wen et al. [16] used ResNet-50 combined with transfer learning to extract the characteristics of time domain fault signals

converted to RGB images and had achieved the most advanced results on the test dataset. These studies show the validity of deep transfer learning in the diagnosis of mechanical variable conditions, but there are still some problems that need further study: (1) Most transfer learning methods do not take into account the joint distribution between the classifier output labels and the input data but only the marginal distribution of the data. (2) The effect of the nonlinear feature extraction capability of the deep learning framework on domain adaptation was not discussed in the process of innovation of the transfer learning algorithm.

In view of the problems above, this paper conducts related research through the following ideas.

(1) Two modules are constructed to achieve domain adaptation for the source domain and target domain. On the one hand, using the joint distribution differences of input features and output labels, domain adaptations are made in feature extraction and classification layers by JMMD. On the other hand, cross-entropy was used between feature and prediction labels to conduct domain adversarial training to reduce domain drift. The two modules not only realize the maximum distinction between classes but also realize domain adaptation under multimode conditions. Meanwhile, transferable semantic augmentation (TSA) regular terms are added to the loss function to enhance the implicit characteristics of the source domain and improve the effect of domain adaptation

(2) A deep shrinkage residual network is constructed as the main network for feature extraction of one-dimensional vibration signals. By setting a soft threshold in the residual block, the noise in the original signal is suppressed, so that the fault characteristics can be better adapted in the mapping space, and the robustness of the whole algorithm framework is enhanced

(3) The datasets used in the experiment are the CWRU bearing dataset and the Canadian-Ottawa bearing dataset. The validity of the deep denoising domain adaptive network proposed in this paper is verified by the three scenarios of staged operation, continuous operation, and antinoise, and the most advanced results are obtained

2. Transfer Learning Method

2.1. Preliminaries. In transfer learning, "domain" and "task" are the two most important concepts. The domain and task are separately divided into the source domain, target domain, source task, and target task [11]. This paper intends to solve the problem of unsupervised domain adaptation where training data has labels and test data does not have labels. Formally, we denote $D_k^s = (x_i^{s,k}, y_i^{s,k})_{i=1}^k$ as labeled source domain data and $D^t = \{x_i^{t,k}\}_{i=1}^k$ as unlabeled target domain data, where x_i and y_i are, respectively, the ith

sample's features and the ith sample's labels. Among them, superscript s denotes the source domain, t denotes target domain, and K denotes the number of domains. Here also denotes a domain as $D = \{\mathcal{X}, P(X)\}$, where $\mathcal{X}$ is the d-dimensional feature space of the souce domain and target domain, and $P(X)$ is the marginal probability distribution, $X = \{x_1, x_2, \cdots, x_n\} \subset \mathcal{X}$. For a domain $D = \{\mathcal{X}, P(X)\}$, $T = \{\mathcal{Y}, P(Y|X)\}$ is used to represent a task of domain adaptation. Among them, $\mathcal{Y}$ is the label space and $P(Y|X)$ is the marginal probability distribution, that is, the marginal distribution relationship between feature vector X and label space $\mathcal{Y}$ under the mapping of prediction function $f(\cdot)$. In the network training period, only the source domain has label space, but the target domain does not have label space, so the training of prediction function $f(\cdot)$ can only rely on the source domain data. In the case of transfer, $D_s \neq D_t$ or $T_s \neq T_t$ is often present. Therefore, training the prediction function $f(\cdot)$ only through the source domain data will lead to limited generalization ability of the model. In order to achieve domain adaptation, it is necessary to integrate the differences between target domain data features and source domain data features into network training, so that the target domain data in the test set can be correctly mapped to its corresponding label space in the case of $P_s(X_s) \neq P_t(X_t)$.

2.2. JMMD and CDA. Borgwardt et al. [17] first proposed the maximum mean discrepancies (MMD) method to measure the difference between the two distributions in the statistical sense. Given the data characteristic distributions X_s and X_t of the source domain and target domain, MMD can be defined as follows:

$$\mathrm{MMD}_{\mathcal{H}}(X_s, X_t) = \left\| \frac{1}{n_S} \sum_{i=1}^{n_S} \phi(x_i^s) - \frac{1}{n_T} \sum_{j=1}^{n_T} \phi\left(x_j^T\right) \right\|_{\mathcal{H}}^2, \quad (1)$$

where $\mathcal{H}$ represents the reproducing kernel Hilbert space (RKHS), and the data is mapped from high-dimensional feature space to low-dimensional space through kernel function ϕ. In practical application, the domain adaptation of data through MMD under complex multimodal conditions is very limited, and the kernel parameters are difficult to optimize. Gretton et al. [18] proposed a convex combination of multiple cores for effective mapping estimation to achieve depth domain adaptation. However, when Multikernel MMD (MK-MMD) is used for depth domain adaptation, the feature can only be transferred at the top layer by deepening the number of network layers, and the transfer of label distribution $P(Y_S)$ and $Q(Y_t)$ still stays at the classification layer. In order to fully consider the joint distribution of feature space and label space in the field, Long et al. [19] proposed the joint maximum mean deviation (JMMD) method, which is defined as

$$\mathcal{L}_{\mathrm{JMMD}}(P, Q) = \left\| \mathbb{E}_P\left(\otimes_{l=1}^{|L|} \phi^l\left(z^{sl}\right) \right) - \mathbb{E}_Q\left(\otimes_{l=1}^{|L|} \phi^l\left(z^{tl}\right) \right) \right\|_{\otimes_{l=1}^{|L|}\mathcal{H}'}^2, \quad (2)$$

TABLE 1: Parameters of the GRL.

Layers	Parameters
Fc1	out_features = 2048
Dropout1	$P = 0.5$
Fc2	out_features = 1024
Dropout2	$P = 0.5$
Fc3	out_features = 2

where Z^{sl} represents the output of the activation function of the lth level network, $\otimes_{l=1}^{|L|} \phi^l(x^l) = \phi^1(x^1) \otimes \cdots \otimes \phi^{|L|}(x^{|L|})$. Compared with formula (1), JMMD calculates the mapping of each layer of feature space in tensor product Hilbert space when measuring distance. The feature samples are mapped to a fixed diameter hypersphere through the activation function, so that the samples with similar features gather more closely in the feature space; that is, the distance between classes is expanded and the distance between classes is reduced, so as to balance the training difficulty between different distributed data [20]. In order to enhance domain adaptation, this paper adopts the idea of the domain adversarial neural network for reference and forms a depth adversarial domain adaptation network by adding the gradient reversal layer (GRL) after the feature extraction layer. The structural parameters of GRL are the same as those in literature [21], which are all three fully connected layers. The specific parameters are shown in Table 1.

Unlike the MMD method that takes the space metric distance, adversarial-based domain training follows the idea of a game in the generative adversarial network, so that the source domain and the target domain can be aligned in the network training. The domain adversarial network is generally divided into feature extraction layer G_f, classification layer G_c, and domain identification layer G_d, and the parameters of each layer are represented by θ_f, θ_c, and θ_d, respectively. GRL is also called the domain discriminator. Its function is to maximize the classification loss between source domain and target domain and confuse target domain data with source domain data. The classifier in the network realizes the accurate classification of data by minimizing the classification loss. Different from the generative adversarial network, the domain adversarial network does not need a generator. In order to carry out adversarial training, we multiply the error of the gradient inversion layer by a negative parameter $-\lambda$, so that the network training objectives before and after the GRL layer are opposite, achieving adversarial training [22]. At the end of the adversarial training, it shows that the loss of the domain discriminator has reached the maximum, so the domain discriminator has aligned the source domain and the target domain to the greatest extent. However, domain adversarial training still has the same defect as MMD. It only calculates the marginal distribution of $P(X)$ and $Q(X)$ and ignores its joint distribution. Similar to JMMD, in order to solve the problem $P(X_s, Y_s) \neq Q(X_t, Y_t)$, it is necessary to consider the joint distribution of the sign extraction layer and classification layer.

The multidimensional and multifeature data in the feature layer and classification layer of the domain adversarial network are matrix operated by means of mean mapping $x \otimes y$. In the GRL layer, the source field label is set to 0, and the target field label is set to 1. In order to prevent the loss function value of individual samples from tending to infinity due to nontransfer, so that the domain adversarial training cannot converge effectively, before the training, the entropy criterion is applied to the label prediction probability corresponding to the feature [21]. The loss function formed by the above form is a conditional domain adversarial (CDA) loss function, which is defined as

$$w(H(p)) = 1 + e^{-H(p)}, \; H(p) = -\sum_{c=0}^{C-1} p_c \log p_c, \quad (3)$$

$$
\begin{aligned}
L_{\mathrm{CDA}}(\theta_f, \theta_d) = &-\frac{1}{n_s} w(H(p_i^s)) \sum_{i=1}^{n_s} \log\left[1 - D\left(F(x_i^s;\theta_f);\theta_d\right)\right] \\
&- \frac{1}{n_t} w(H(p_i^t)) \sum_{i=1}^{n_t} \log\left[D\left(F\left(x_j^t;\theta_f\right);\theta_d\right)\right].
\end{aligned}
\quad (4)
$$

2.3. Transferable Cross-Entropy Loss Learning. The methods of CDA and JMMD use the depth transferable features of the source domain and target domain to achieve domain adaptation. Therefore, superimposing the two in a transfer learning module can theoretically achieve the effect of complementary advantages, as JMMD not only reduces the difference of marginal distribution but also reduces the difference of joint distribution, and domain confrontation helps to reduce the phenomenon of domain drift in the process of domain adaptation. Transfer learning is widely applied in image recognition, and many transfer learning methods have achieved good results in the open dataset. However, compared with some image public datasets, the bearing fault signals also have the characteristics of high coupling, nonlinearity, and nonstationary. Therefore, in order to further enhance the domain adaptability of bearing fault diagnosis, we should make full use of the labeled samples in the source domain. As shown in Figure 1, Li et al. [23] proposed a transferable semantic augmentation (TSA) method to enhance the adaptability of the classifier by implicitly generating source features to target semantics.

For bearings of the same structure, the high-dimensional characteristics of vibration signals will migrate in all directions in the transfer learning, and the high-frequency characteristics induced by resonance will transfer along a certain direction of bearing frequency. Therefore, a quantitative measurement method is needed to highlight the direction that has the greatest impact on domain adaptation. Use μ_s and μ_t to represent the mean value of the feature space of the source domain and the target domain, respectively, and use $\Delta\mu^c = \mu_t^c - \mu_s^c$ to represent the difference of the mean value of a class c sample in the source domain and the target domain. The greater the difference, the greater the overall deviation, so the domain drift can be reduced by means of the value of $\Delta\mu^c$. However, the value of $\Delta\mu^c$ is rel-
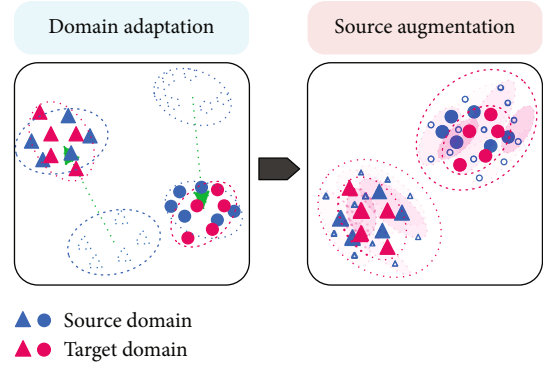

Figure 1: Illustration of TSA method.

atively extensive. In order to more accurately measure the distribution difference, it is also necessary to calculate the covariance $\sum_t^c$ in the target class and measure the difference of all offset directions of the target domain relative to the source domain at the highest level of the network. Finally, the multivariate distribution difference $N(\Delta\mu^c, \sum_t^c)$ is composed of interdomain mean difference $\Delta\mu^c$ and intratarget covariance $\sum_t^c$. It should be noted that the TSA method focuses on using the characteristics of the source domain to approach the target domain as much as possible. Here, the characteristics of the highest layer of the network refer to the output matrix $\mathbf{f}_{si} \sim N(\Delta\boldsymbol{\mu}^{y_{si}}, \boldsymbol{\Sigma}_t^{y_{si}})$ of the last full connection layer, which will be reflected in the following formula. In network training, the loss of transfer after M iterations is given by using cross-entropy:

$$\mathscr{L}_M = \frac{1}{n_s} \sum_{i=1}^{n_s} \mathbb{E}_{\tilde{\mathbf{f}}_{si}}\left[\log\left(\sum_{c=1}^C e^{\left(\mathbf{w}_c^\top - \mathbf{w}_{y_{si}}^\top\right)\tilde{\mathbf{f}}_{si} + \left(b_c - b_{y_{si}}\right)}\right)\right], \quad (5)$$

where $\mathbf{W}$ and b represent the weight matrix and offset vector of the last layer of the network and the full connection layer, respectively. Similarly, in order to improve the domain adaptability under unsupervised learning, it is necessary to use the joint distribution probability of label space and feature space. At this time, the target domain space lacks annotation, so we need to use the pseudolabel method and target features to form the mutual information value $\mathscr{L}_{M_I}$. Therefore, TSA is defined as follows:

$$\mathscr{L}_{\mathrm{TSA}} = \mathscr{L}_M + \beta\mathscr{L}_{MI}, \quad (6)$$

where β is an empirical parameter, and the value needs to be compared and explored in the experimental part [23]. The TSA loss function based on the interdomain characteristic mean deviation and class conditional covariance has less computation than the data generation antidomain adaptation, and its lightweight advantage can be embedded in other domain adaptation algorithms. Therefore, combined with the above domain adaptation methods, the loss function of unsupervised bearing fault transfer learning is constructed

as follows:

$$\mathscr{L}_{\text{LOSS}} = \mathscr{L}_{\text{JMMD}} + \mathscr{L}_{\text{CDA}} + \mathscr{L}_{\text{TSA}}. \tag{7}$$

In the process of domain adaptation, due to the random initialization of the network, the network parameters cannot reflect the real domain feature distribution in the initial stage, so the rich labels in the bearing source domain data are used for pretraining before transfer. After the set epoch, the classification layer can achieve better classification effect on the source domain and then start domain adaptation.

2.4. Deep Residual Shrinkage Networks. In the deep domain adaptation, the network backbone plays an important role in feature transfer. To some extent, the appropriate backbone network is more important than the advanced transfer algorithm [21]. In many experiments on domain adaptation, such as CNN [24], ResNet [25], VGG [26], and AE [27] show excellent feature extraction ability in the application of image transfer, semantic transfer, and signal transfer. However, there is no relevant research on which appropriate backbone network should be selected for specific transfer objects. The purpose of this paper is to carry out the transfer learning for bearing faults under complex and variable working conditions. It is hoped that the fault can be diagnosed early by the vibration data and labels collected from the bearings under unknown working conditions. Considering that in the process of actual vibration signal acquisition, the sensor collects not only the actual vibration signal of the tested bearing but also other noise signals, such as bearing vibration interference of other parts, noise interference of working environment, and noise interference of transmission parts. Suppressing noise interference is always a difficult and hot issue to extract weak signals of bearing early fault by signal processing methods [28]. Among them, various improved algorithms based on wavelet transform are widely used in bearing signal noise filtering, but the premise is to master the prior knowledge of the signal, and the design of the filter and the selection of wavelet parameters need continuous experiments to obtain the optimal value. In addition, the existence of noise will reduce the ability of the neural network to extract weak early fault feature signals and make the boundary of high-dimensional feature clusters blurred in clustering, so that the effect of domain adaptation becomes worse in the process of transfer. Therefore, in order to overcome the influence of noise on the domain adaptation of the bearing fault signal, a network layer similar to the filtering algorithm needs to be embedded in the backbone network to adaptively reduce the influence of noise on feature extraction. Zhao et al. [29] proposed adding a soft threshold to the residual network to automatically learn the noise threshold, reduce the noise interference, and realize the bearing fault diagnosis under high noise. Based on the deep residual shrinkage network, this paper will improve part of the network structure to build the backbone network in transfer learning.

2.4.1. Deep Residual Shrinkage Module. The residual shrinkage module is the basic unit of the deep residual shrinkage

⊗ Element-wise multiplication
⊘ Soft thresholding
⊕ Element-wise summation
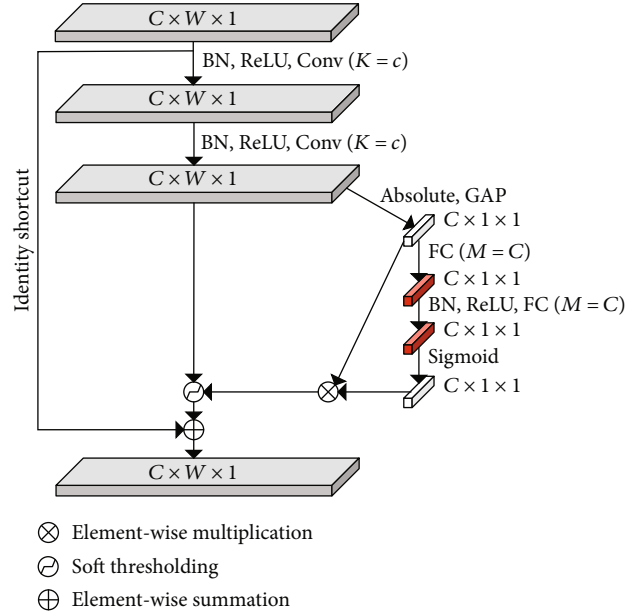
FIGURE 2: A building unit entitled RSBU-CW.
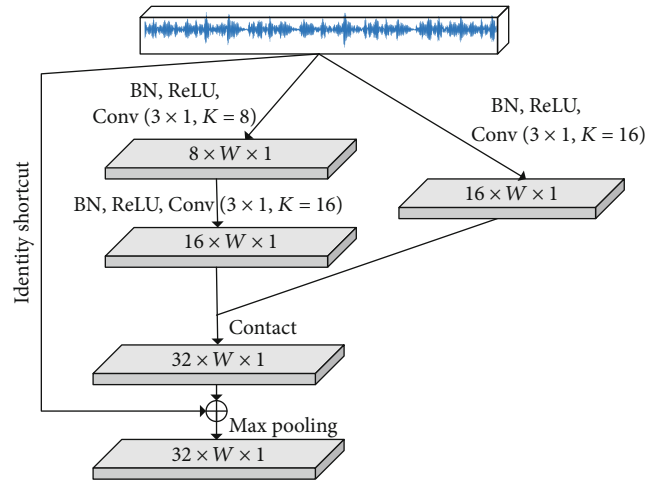
FIGURE 3: A building unit of improved pooling layer.

network, which embodies the idea of an attention mechanism: by eliminating the data features with a low contribution ratio, the important features are more prominent in the overall data features. Although this approach may eliminate the features conducive to transfer learning, it will remain in the network through the identity mapping in the residual module, but its proportion will be reduced after the transfer of the module. A residual shrinkage building unit with channel-wise thresholds (RSBU-CW) is shown in Figure 2.

C and W, respectively, represent the width and channel of the feature. Each channel of RSBU-CW has an independent threshold. The features are reduced to a one-dimensional vector through absolute value and global average pooling, and then, the one-dimensional vector is transmitted to the fully connected network with two-layer FC. Each channel can have an independent threshold by making

FIGURE 4: Domain transfer network based on deep residual shrinkage residual module.

TABLE 2: The description of class labels of CWRU.

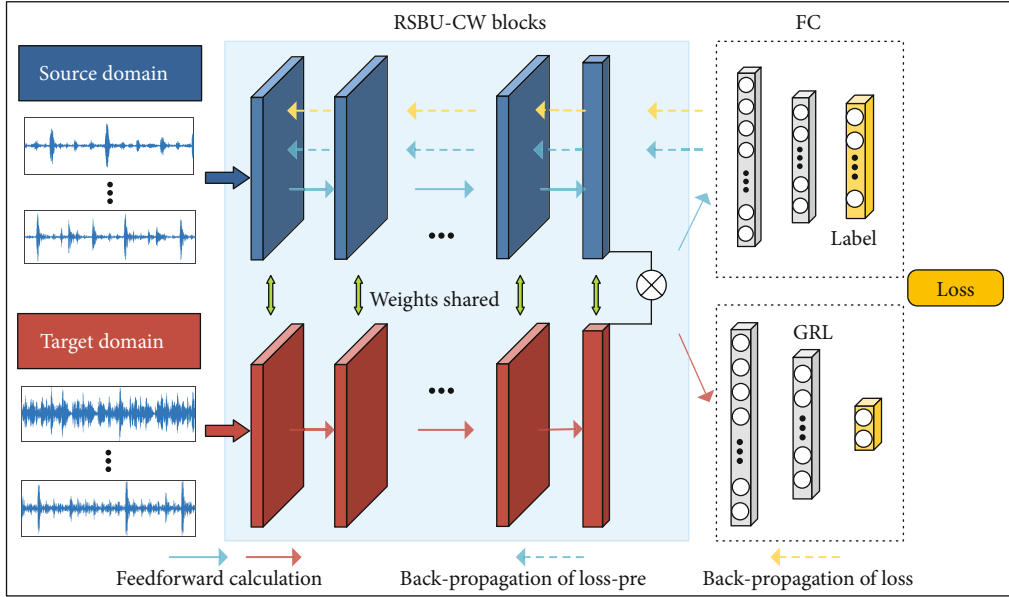| Task	Speed (rpm)	Fault location	Fault size (mils)	Class label
		OF	7	1
		OF	14	2
		OF	21	3
		BF	7	4
0/1	1797/1772	BF	14	5
2/3	1750/1730	BF	21	6
		IF	7	7
		IF	14	8
		IF	21	9
		NA	0	10

TABLE 3: The description of time-varying speed dataset.

Task	Speed-varying conditions	Fault location	Class label
0	Increasing speed	Healthy	1
1	Decreasing speed		
2	Increasing then decreasing speed	Inner race fault	2
3	Decreasing then increasing speed	Outer race fault	3

the number of neurons in the second layer consistent with the number of channels of the input feature map. The threshold τ_c can be defined as

$$\tau_c = \sigma_c \cdot \text{average} \left| \mathbf{X}_{i,j,c} \right|, \tag{8}$$

where σ_c is the parameter of the cth layer scaled to $(0, 1)$ and

i, j, and c are the indexes of width, height, and channel of the feature map X. In the network iterative training, the threshold of each channel will change with time. When the feature is in the range of $[-\tau_c, -\tau_c]$, the channel threshold will be set to 0, and those features $\mathbf{X}$ far from 0 will approach 0.

2.4.2. Improved Pooling Layer Based on Inception Module. The inception module is proposed to solve the problem of performance saturation and light weight when the number of layers of the google net network is deepened. From inception-V1 to V4, the model is constantly improved and the performance is also continuously improved. The main idea of inception is to transform large convolution blocks into small convolution blocks through series and stacking. Because the collected bearing data is one-dimensional vibration data, convolution pooling needs to be carried out before being transmitted to RSBU-CW. If the traditional large convolution block 7×1 is adopted, it will not be suitable for fault diagnosis of large bearing data in industry. In order to ensure the effect of feature extraction and reduce the volume of network calculation, for the one-dimensional time-domain input signal of bearing, an improved data pooling layer is shown in Figure 3.

The improved data pooling layer in the figure adopts 3 small convolution layers instead of 7×1 convolution layers. The number of channels is set to 8, 16, and 16, respectively, and the residual connection structure is added. Finally, the extracted data feature information is output through the maximum pooling layer.

2.4.3. Residual Block-Based Dilated Convolution. Dilated convolution has the same convolution operation as ordinary convolution, but dilated convolution uses a specific step to read data in a jumping way, which can obtain a larger receptive field while keeping the parameters unchanged, so that each convolution output contains more information. Therefore, this paper replaces the ordinary convolution in RSBU-
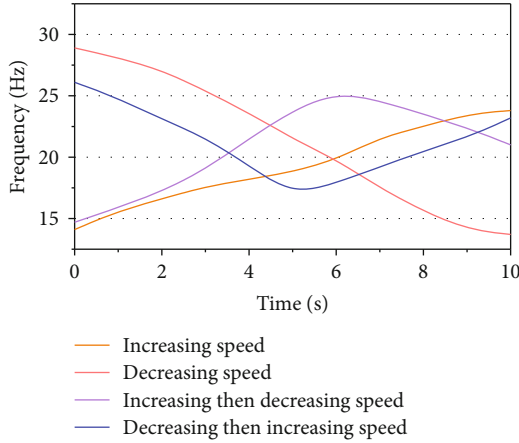
Figure 5: The change of frequency under time-varying rotational speed conditions.
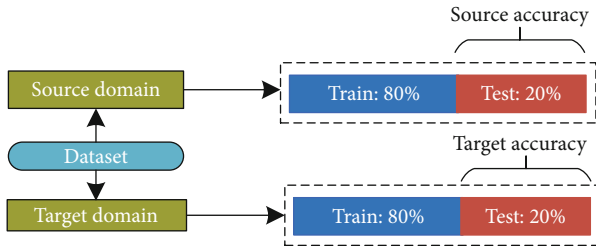

Figure 6: Division of input data.

CW with dilated convolution and increases the receptive field by setting the dilated rate. It is assumed that the kernel width of ordinary convolution is w. When the dilated convolution with dilated rate d is introduced, the width of the dilated convolution kernel becomes $w + (w-1)(d-1)$. And one-dimensional convolution is used; the height of the convolution kernel is always 1. Dilated convolution improves the sparsity of bearing signal characteristics, but at the same time, in order to ensure the continuity of vibration signal after convolution operation, the dilated rate should not be set too large. It is verified by relevant experiments that the bearing fault accuracy is higher when the dilated rate $d = 2$ is adopted. At this time, the receptive field obtained by the 3×3 convolution kernel in RSBU-CW is equivalent to the receptive field brought by the 5×5 convolution kernel.

2.5. Framework of Network Training. As shown in Figure 4, it is the network training framework proposed in this paper. Aiming at the problem of the generalization ability of traditional deep learning for bearing fault diagnosis under variable conditions, a domain transfer training network based on the deep residual shrinkage residual module is proposed. The whole network is composed of a backbone network using the RSBU-CW module and deep domain transfer algorithm. In order to improve the effect of domain transfer, the loss function consists of explicit JMMD loss and CDA loss and implicit TSA loss. The network is pretrained through the bearing vibration data with known labels in the source domain. After updating the network parameters, the unlabeled target domain data are transferred to accelerate the speed of the domain adaptation.

3. Experimental Results

In this section, two open-source bearing datasets will be used to verify the effectiveness of the proposed method in bearing fault diagnosis. The main framework is written by Python. All experiments were run on a computer equipped with i7-9300h CPU and NVIDIA GeForce GTX 1050 GPU.

3.1. Datasets

3.1.1. Case Western Reserve University (CWRU) Dataset. The CWRU [30] bearing dataset is an open-source dataset of the Case Western Reserve University Laboratory which is widely used in the research of bearing fault diagnosis. In the experiment, the amplitude data of SKF6205 motor bearing are collected by the acceleration sensors installed at the motor driving end and fan end. The data consists of normal bearing operation data and fault bearing operation data. The fault location and damage size are different. Detailed data description is shown in Table 2.

The bearing transfer tasks are {0, 1, 2, 3}, corresponding to four different speeds, respectively. The load of the bearing is also different at each speed. At a certain constant speed, it is divided into 10 data types. The locations of bearing faults are inner fault (IF), ball fault (BF), and outer fault (OF), where NA represents normal bearing.

3.1.2. University of Ottawa Bearing Dataset. The dataset is collected from the University of Ottawa laboratory [31]. Each sample of this dataset is collected under time-varying rotational speed conditions, which is different from the CWRU dataset. Detailed data description is shown in Table 3.

The collection time of each sample is 10 s in total, and the sampling frequency is 200 kHz. During the sampling time, the running speed of the bearing will change, which can be divided into four types: acceleration, deceleration, acceleration before deceleration, and deceleration before acceleration. As shown in Figure 5, the changes of bearing operating speed under four operating conditions are shown, respectively, and the speed is represented by bearing rotation frequency. The bearing health status is divided into three conditions: normal, inner ring fault, and outer ring fault. Among them, the transfer task $0 \longrightarrow 1$ indicates that the source domain is the fault data under the accelerated running condition, and the target domain is under the condition of bearing deceleration.

3.2. Implementation Details

3.2.1. Division of Input Data. The two datasets are slightly different in sample balance. Among them, the number of samples under normal working conditions of the CWRU dataset is more than that under other working conditions, while the sample number of Ottawa bearing data is well balanced. This experiment does not deal with the sample balance but makes the number of samples in each source
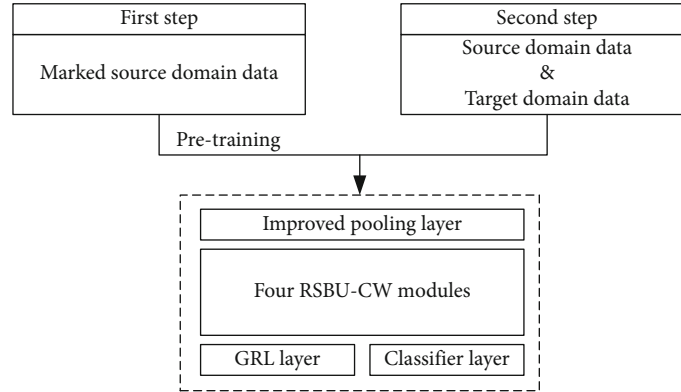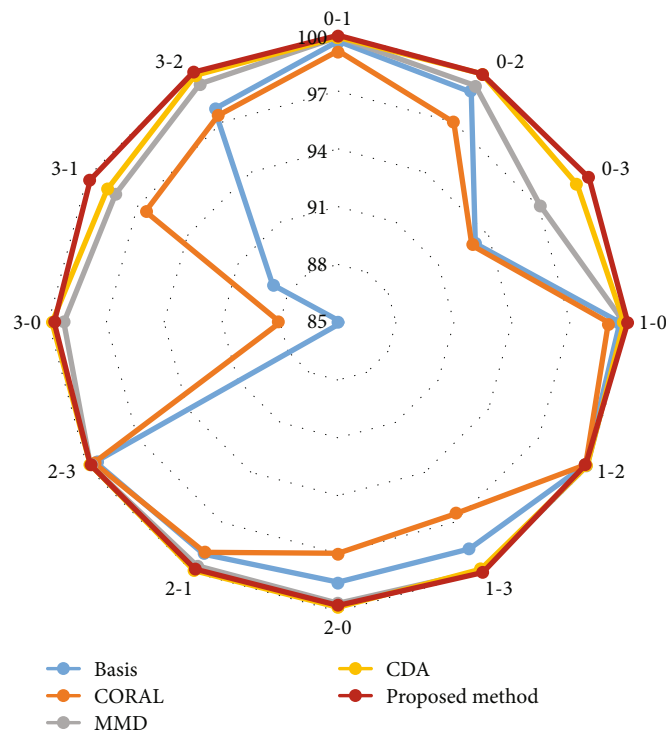
FIGURE 7: Training method.

FIGURE 8: Comparison of accuracy of five methods under CWRU dataset.

domain and target domain the same. When segmenting the bearing timing vibration signal, the method of enhanced data will not be used, because the enhanced data may overlap the training data and test data in a certain period of time, resulting in unreliable test accuracy. As shown in Figure 6, it is a schematic diagram of the division of source domain and target domain samples. Among them, the training sets of source domain samples and target domain samples account for 80%, and the test sets account for 20%. Considering the difference in sampling frequency between the two datasets, 1024 and 8192 are taken as the sample length of the CWRU dataset and Ottawa dataset, respectively.

3.2.2. Training Method. After the reasonable division of samples, the data of the source domain and target domain are sent to the network for training. The one-dimensional bear-

ing vibration data sample first passes through the improved pooling layer proposed in this paper, then passes through four RSBU-CW modules, and finally calculates the domain adaptive loss value through the GRL layer and classifier layer. In network training, the updating of parameters is divided into two stages. As shown in Figure 7, the first is the pretraining process using the marked source domain data, in which the target domain data does not participate in the training process. In the second stage, the source domain and target domain data are sent to the network at the same time for domain adaptation, and the loss value of domain adaptation is used for back propagation. Among them, 50 epochs are set for pretraining nodes and 200 epochs are set for domain adaptation nodes. The gradient descent algorithm adopts Adam, the momentum value is set to 0.9, and the batch size is 64.
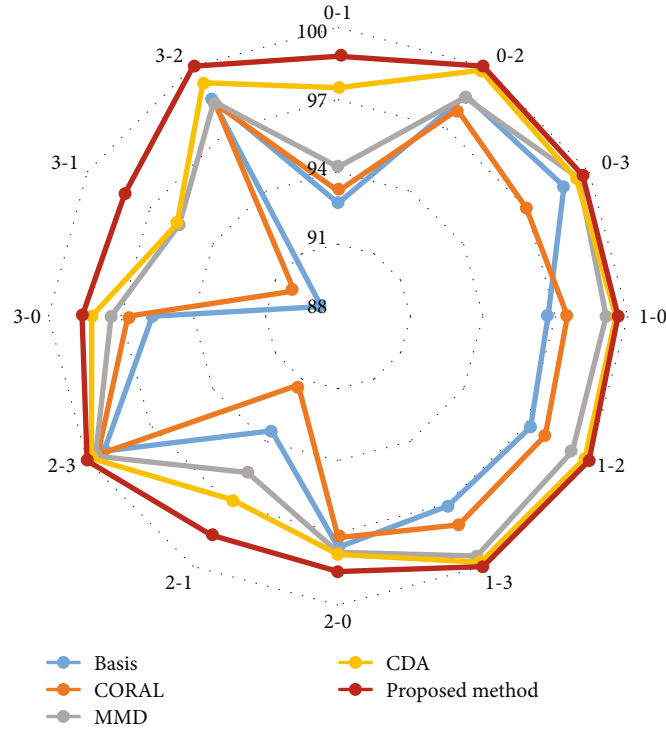
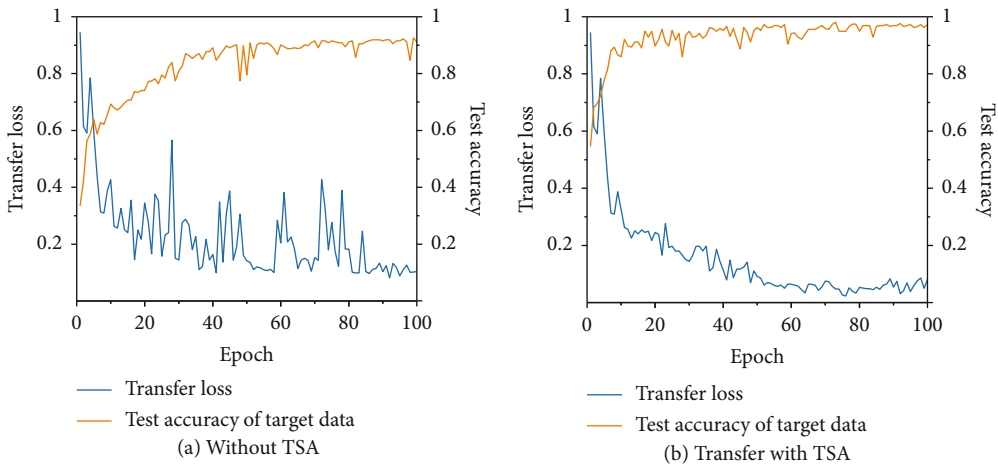Figure 9: Comparison of accuracy of five methods under Ottawa dataset.

Figure 10: Effect of TSA regular term on transfer loss and test accuracy of target data.

3.3. Evaluation Results.

In this paper, two open-source datasets are used to verify the effectiveness of the proposed model for bearing fault diagnosis under variable working conditions. In order to fit the industrial application scenario, the applicability of the model under high noise will also be discussed, and the results will be represented by visual charts.

3.3.1. Results of Models.

As shown in Figures 8 and 9, the test accuracy of two datasets under five methods is shown, respectively. The five methods are Basis, CORAL, MMD, CDA, and the method proposed in this paper. Among them,

Basis means that it does not use any domain adaptation method and only uses the network trained by the source domain data to test the test set of the target domain directly. The other three methods are common domain adaptation methods. In order to ensure the reliability of the results, 10 experiments were carried out for each method, and the average value of the test results of the last epoch was taken as the final result.

It can be seen from the figure that in addition to the CORAL method, adopting other domain adaptation methods can greatly improve the accuracy of fault diagnosis under variable working conditions; especially when the
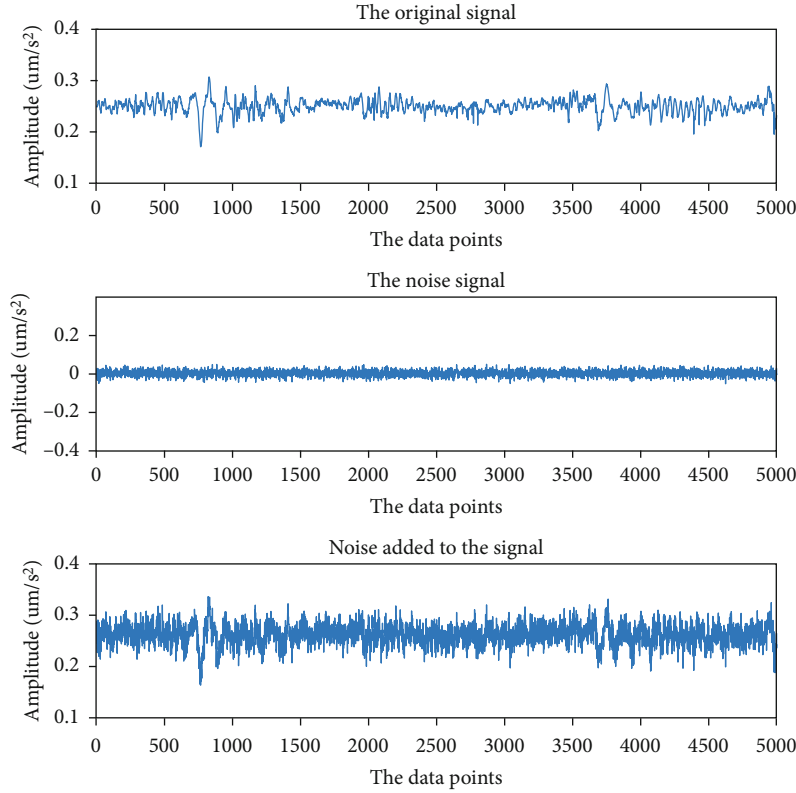
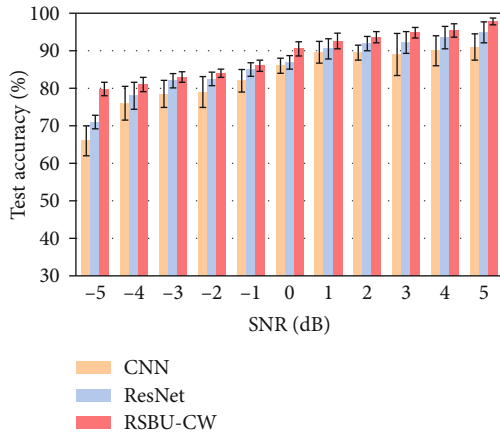FIGURE 11: Schematic diagram of adding Gaussian white noise to the signal.

FIGURE 12: Fault diagnosis accuracy of test dataset under Gaussian noise.

TABLE 4: The time cost of three backbone networks.

Backbone network	SNR (dB)	Training time (s)
CNN	-5 dB	1256 s
ResNet	-5 dB	1302 s
RSBU-CW	-5 dB	1109 s
CNN	5 dB	1145 s
ResNet	5 dB	1204 s
RSBU-CW	5 dB	1003 s

working conditions are greatly different, the more obvious the migration effect is. For example, for the mutual migration under the two working conditions $\{0, 3\}$ in Figure 8, the lifting effect is the most obvious under the domain adaptation method. For CWRU datasets, although the proposed method does not have much chance for improvement, the overall accuracy is still slightly higher than other methods. This is closely related to the dataset itself, because the faults of the CWRU dataset are artificially set, and the fault characteristics are obvious. In addition, the migration of the CWRU dataset is mainly the transfer under different loads, and the bearing data is measured under a uniform speed condition. In comparison, the working condition of the Ottawa dataset is more complex, and the speed difference between the migrated datasets is more obvious. The change of speed will lead to the change of fault characteristics, so the accuracy of Figure 9 is lower than that of Figure 8 as a whole. On the whole, the proposed method combines the advantages of domain confrontation migration and joint distribution migration. By embedding TSA loss, it solves the problem of domain drift in the traditional domain adaptation methods and enhances the adaptability of the classifier.

In order to further illustrate the influence of adding the TSA regular term on the training convergence results, Figure 10 draws the loss curve and test accuracy before and after adding the TSA regular term. The transfer task of the curve shown in the figure is (0, 1) in the Ottawa dataset.

It can be clearly seen that after adding the TSA regular term, the fluctuation of the transfer loss decline curve is
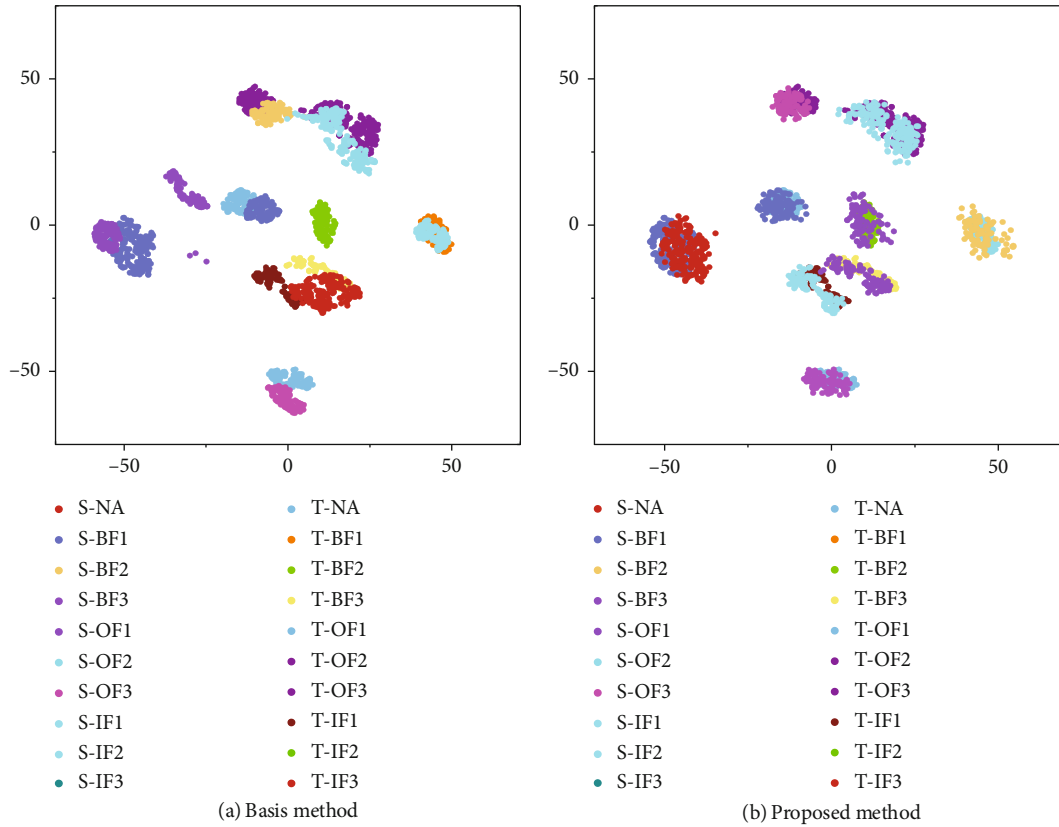
FIGURE 13: Network visualization of CWRU dataset transfer task 3 ⟶ 1.

improved, and the accuracy is significantly improved after 10 epochs. This is because before adding the TSA regular term, the domain migration method based on confrontation will cause the fluctuation of loss value, which will affect the accuracy of the test set. TSA can implicitly strengthen the migration of data features from the source domain to the target domain, enhance the ability of the classifier to adapt to the domain, and reduce the fluctuation of classification effect caused by adversarial domain training.

3.3.2. Robustness of Backbone Network. Backbone networks also have a great impact on domain adaptation. In order to fairly compare the effects of transfer learning, comparative experiments need to be carried out under the same backbone network, so the discussion of backbone networks has been ignored. In this paper, we choose a deep residual shrinkage network with antinoise effect, one is because of the need for industrial actual conditions, two is to suppress the effect of noise on domain migration. The actual measured bearing vibration signals contain rich noise signals, which can cause redundancy in data-intensive places, and denoising will help domain migration. As shown in Figure 11, in order to simulate the actual working environment, Gaussian white noise is added to the target in the experiment.

The experimental object is Ottawa bearing data. Three different network structures CNN, ResNet, and RSBU-CW are adopted to carry out the experiment according to the set domain migration task. The noise intensity is −5 dB ~ 5

dB, 10 experiments are carried out for each migration diagnosis task, and finally, the average value is taken as the result. As shown in Figure 12, the fault diagnosis accuracy of the test set in Gaussian noise is the average of all migration tasks. Among them, CNN and ResNet adopt convolution blocks of the same size as RSBU-CW. From the final results, it can be seen that the domain migration diagnosis effect of RSBU-CW in high noise environment is better than that of traditional CNN and ResNet and can maintain strong robustness. This is because the backbone network adopts the soft threshold as the shrinkage function, which effectively suppresses the redundant noise features in the bearing fault features, so as to give full play to the effect of the domain adaptation method. Although the introduction of a soft threshold will increase the amount of calculation of the network, higher fault diagnosis accuracy under variable working conditions of bearing is obtained. In order to further compare the influence of soft threshold on model complexity, Table 4 compares the training time of the three models under the noise intensity of -5 dB and 5 dB, respectively. It can be seen that the improvement of the data pooling layer in this paper has offset the influence brought by the introduction of a soft threshold algorithm to a certain extent.

3.3.3. Network Visualization. Figures 13 and 14 are the network visualization results embedded in the full connection layer using *t*-distributed stochastic neighbor embedding (t-SNE), where *S* represents the source domain sample, *T* represents the target domain sample, and *S*-Na represents the
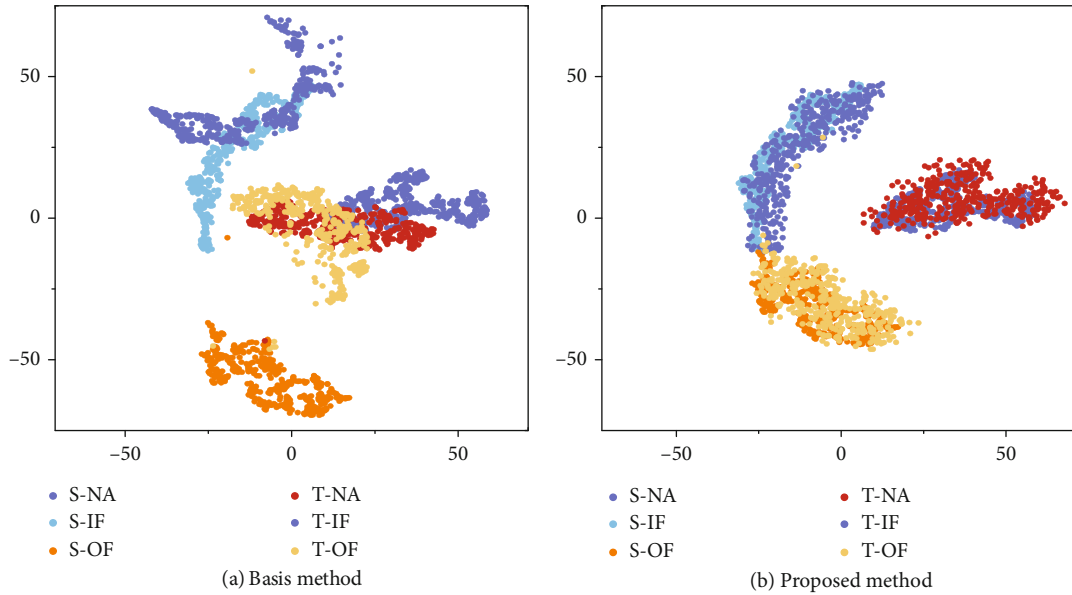
FIGURE 14: Network visualization of Ottawa dataset transfer task 3 ⟶ 1.

normal sample in the source domain. It can be seen from the clustering results that when no domain adaptation method is used, classes in the same domain can be effectively distinguished, but classes with the same source domain and target domain cannot get the correct mapping relationship, and a large number of overlapping regions can be found in the graph. Under the framework proposed in this paper, the same category between source and target domains is aligned well. Therefore, both the accuracy of domain adaptation and the results of network visualization prove the effectiveness of the network framework in this paper.

4. Conclusion

Based on the deep residual shrinkage network, this paper uses the combination of conditional domain adversarial domain adaptation and joint distribution domain adaptation to solve the problems of low fault diagnosis accuracy, weak antinoise performance, and weak generalization ability caused by load change and noise interference in the actual operating environment of rolling bearing. According to the experiments on two open-source datasets, the conclusions are as follows:

(1) The transfer method proposed in this paper integrates the advantages of adversarial domain transfer and joint distributed transfer. At the same time, by adding the TSA regular term, it effectively solves the problem of domain drift under unsupervised domain adaptation. Compared with other traditional preadaptation methods, the accuracy is increased. At the same time, it improves the performance of transfer between different fields and expands the application scope of intelligent fault diagnosis. It provides a new idea to solve the problem of facing a large number of unmarked data in bearing fault diagnosis

(2) Adding a soft threshold in the backbone network improves the robustness of the whole network framework. At the same time, in the antinoise experiment, the performance of the deep residual shrinkage network using a soft threshold is about 3% and 6% higher than that of the traditional CNN and ResNet networks, respectively, which realizes the antinoise function of bearing fault diagnosis in industry. In addition, by improving the pooling layer based on the concept module, the feature information in the original data is effectively extracted, so that this method can transfer the feature information in the data efficiently

(3) The two datasets, respectively, contain the variable load and variable speed operation of the bearing. From the diagnosis accuracy of the final test set, the greater the change difference between the source domain and the target domain, the more difficult the transfer. However, the dataset collection used in this paper is carried out in the ideal experimental environment, and there is still a gap with the actual industrial production environment. Therefore, it is still a challenge to carry out early fault prediction on the bearing data without labels under complex variable working conditions. At the same time, there is a lack of relevant comparative experiments on the setting of network training parameters in this paper. In the next research, it will be combined with other intelligent algorithms for relevant optimization

Data Availability

The data used to support the findings of this study are available from the Case Western Reserve University Bearing Data Center Website (https://csegroups.case.edu/bearingdatacenter/pages/welcome-case-western-reserve-university-bearing-data-center-website).

Conflicts of Interest

We declare that we do not have any commercial or associative interest that represents a conflict of interest in connection with the work submitted.

References

[1] J. Lee, F. J. Wu, and W. Y. Zhao, "Prognostics and health management design for rotary machinery systems– reviews, methodology and applications," *Mechanical Systems and Signal Processing*, vol. 42, no. 1-2, pp. 314–334, 2014.

[2] Z. W. Gao, C. Cecati, and S. X. Ding, "A survey of fault diagnosis and fault-tolerant techniques-part I: fault diagnosis with model-based and signal-based approaches," *IEEE Transactions on Industrial Electronics*, vol. 62, no. 6, pp. 3757–3767, 2015.

[3] Z. He, H. Shao, Z. Ding, H. Jiang, and J. Cheng, "Modified deep auto-encoder driven by multi-source parameters for fault transfer prognosis of aero-engine," *IEEE Transactions on Industrial Electronics*, vol. 69, no. 1, pp. 845–855, 2022.

[4] X. W. Dai and Z. W. Gao, "From model, signal to knowledge: a data-driven perspective of fault detection and diagnosis," *IEEE Transactions on Industrial Informatics*, vol. 9, no. 4, pp. 2226–2238, 2013.

[5] S. Zhang, S. Zhang, B. Wang, and T. G. Habetler, "Deep learning algorithms for bearing fault diagnostics—a comprehensive review," *Access*, vol. 8, pp. 29857–29881, 2020.

[6] X. Li, Y. Yang, H. Shao, X. Zhong, J. Cheng, and J. Cheng, "Symplectic weighted sparse support matrix machine for gear fault diagnosis," *Measurement*, vol. 168, p. 108392, 2021.

[7] B. Merainani, C. Rahmoune, and D. Benazzouz, "A novel gearbox fault feature extraction and classification using Hilbert empirical wavelet transform, singular value decomposition, and SOM neural network," *Journal of Vibration and Control*, vol. 24, no. 12, pp. 2512–2531, 2018.

[8] C. Lu, Z. Y. Wang, W. L. Qin, and J. Ma, "Fault diagnosis of rotary machinery components using a stacked denoising autoencoder-based health state identification," *Signal Processing*, vol. 130, pp. 377–388, 2017.

[9] S. J. Pan, I. W. Tsang, and J. T. Kwok, "Domain adaptation via transfer component analysis," *IEEE Transactions on Neural Networks*, vol. 22, no. 2, pp. 199–210, 2011.

[10] H. C. Shin, H. R. Roth, and M. C. Gao, "Deep convolutional neural networks for computer-aided detection: CNN architectures, dataset characteristics and transfer learning," *IEEE Transactions on Medical Imaging*, vol. 35, no. 5, pp. 1285–1298, 2016.

[11] S. J. Pan and Q. A. Yang, "A survey on transfer learning," *IEEE Transactions on Knowledge and Data Engineering*, vol. 22, no. 10, pp. 1345–1359, 2010.

[12] X. Li and W. Zhang, "Deep learning-based partial domain adaptation method on intelligent machinery fault diagnostics," *IEEE Transactions on Industrial Electronics*, vol. 68, no. 5, pp. 4351–4361, 2021.

[13] H. Zheng, R. Wang, Y. Yang et al., "Cross-domain fault diagnosis using knowledge transfer strategy: a review," *Access*, vol. 7, pp. 129260–129290, 2019.

[14] T. Han, C. Liu, and W. Yang, "Learning transferable features in deep convolutional neural networks for diagnosing unseen machine conditions," *ISA Transactions*, vol. 93, pp. 341–353, 2019.

[15] Z. An, S. Li, J. Wang, Y. Xin, and K. Xu, "Generalization of deep neural network for bearing fault diagnosis under different working conditions using multiple kernel method," *Neurocomputing*, vol. 352, pp. 42–53, 2019.

[16] L. Wen, X. Y. Li, and L. Gao, "A transfer convolutional neural network for fault diagnosis based on ResNet-50," *Neural Computing and Applications*, vol. 32, no. 10, pp. 6111–6124, 2020.

[17] K. M. Borgwardt, A. Gretton, M. J. Rasch, H. P. Kriegel, B. Schölkopf, and A. J. Smola, "Integrating structured biological data by kernel maximum mean discrepancy," *Bioinformatics*, vol. 22, no. 14, pp. e49–e57, 2006.

[18] A. Gretton, D. Sejdinovic, H. Strathmann et al., "Optimal kernel choice for large-scale two-sample tests," *Advances in Neural Information Processing Systems*, pp. 1205–1213, 2012.

[19] M. Long, H. Zhu, J. Wang, and M. I. Jordan, "Deep transfer learning with joint adaptation networks," *International Conference on Machine Learning*, pp. 2208–2217, 2017.

[20] J. Yosinski, J. Clune, Y. Bengio, and H. Lipson, "How transferable are features in deep neural networks?," 2014, https://arxiv.org/abs/1411.1792.

[21] Z. Zhao, Q. Zhang, X. Yu et al., "Unsupervised deep transfer learning for intelligent fault diagnosis: an open source and comparative study," 2019, https://arxiv.org/abs/1912.12528.

[22] Y. Ganin, E. Ustinova, H. Ajakan et al., "Domain-adversarial training of neural networks," *The journal of machine learning research*, vol. 17, no. 1, p. 2096, 2016.

[23] S. Li, M. Xie, K. Gong, C. H. Liu, Y. Wang, and W. Li, "Transferable semantic augmentation for domain adaptation," *Proceedings of the IEEE/CVF Conference on Computer Vision and Pattern Recognition*, pp. 11516–11525, 2021.

[24] W. P. Wang, Z. R. Wang, Z. F. Zhou et al., "Anomaly detection of industrial control systems based on transfer learning," *Tsinghua Science and Technology*, vol. 26, no. 6, pp. 821–832, 2021.

[25] A. Alhudhaif, K. Polat, and O. Karaman, "Determination of COVID-19 pneumonia based on generalized convolutional neural network model from chest X-ray images," vol. 180, Expert Systems with Applications, Oct, 2021, 180.

[26] E. Jangam, A. A. D. Barreto, and C. S. R. Annavarapu, "Automatic detection of COVID-19 from chest CT scan and chest X-rays images using deep learning, transfer learning and stacking," *Applied Intelligence*, pp. 1–17, 2021.

[27] X. Liu, Z. M. Cao, and Z. J. Zhang, "Short-term predictions of multiple wind turbine power outputs based on deep neural networks with transfer learning," *Energy*, vol. 217, p. 119356, 2021.

[28] A. Rai and S. H. Upadhyay, "A review on signal processing techniques utilized in the fault diagnosis of rolling element bearings," *Tribology International*, vol. 96, pp. 289–306, 2016.

[29] M. Zhao, S. Zhong, X. Fu, B. Tang, and M. Pecht, "Deep residual shrinkage networks for fault diagnosis," *IEEE Transactions on Industrial Informatics*, vol. 16, no. 7, pp. 4681–4690, 2020.

[30] "Case Western Reserve University," http://csegroups.case.edu/bearingdatacenter/home.

[31] H. Huang and N. Baddour, "Bearing vibration data collected under time-varying rotational speed conditions," *Data in Brief*, vol. 21, pp. 1745–1749, 2018.

Research Article

Bow and Stern Control Surface's Effectiveness and Influence on Supercavity

Ping Wei [ORCID],[1] **Wenrong Yan,**[1,2] **Shoufa Wang,**[1] **and Xin Yu**[1]

[1]*College of Weaponry Engineering, Naval University of Engineering, Wuhan 430033, China*
[2]*Xi'an Modern Chemistry Research Institute, Xi'an 710065, China*

Correspondence should be addressed to Ping Wei; pingwei501@126.com

The numerical model of supercavitating flow field was established based on multiphase model, cavitation model, and turbulence model. The model was employed to simulate the supercavitation flow for the supercavitating vehicle with two types of control surfaces: bow rudder and stern rudder. The influence of both control surfaces on the supercavity shape and rudder effectiveness is compared under the different rudder angles (0-12°), and the effectiveness and the influences on supercavities of bow rudder and stern rudder were explored according to the numerical research results. From the research results, the following conclusions can be drawn: (1) the bow rudders have stable rudder effectiveness and available rudder angle, and the bow rudders also have significant influence on supercavities' shape. (2) By contrast with the bow rudder, stern rudders' effectiveness is difficult to predict accurately, and the phenomenon of stalling will occur when stern rudders' rudder angle exceeds 6°; however, there is almost no influence of stern rudders on supercavities. (3) The bow and stern rudders joint control mode must take the influence on supercavities' shape and the accuracy of control force's forecasting into account at the same time. The research is helpful to the optimizing of superhigh-speed vehicles and the design of control modes.

1. Introduction

With the aid of a powerful propulsion device, the ultrahigh-speed underwater vehicle can achieve a superhigh speed of more than 200 kn in underwater [1], because it relies on the unique hydrodynamic layout mode to achieve a substantial reduction in the drag of the vehicle by wrapping most of the body in the supercavity. However, due to the existence of supercavitation, the hydrodynamic characteristics and the response characteristics of the control system displayed for the ultrahigh-speed vehicle are very different from those of the conventional underwater vehicle. Therefore, the optimization of the hydrodynamic layout and the navigation control mode are the research focus and difficulty and are also current research hotspots [2, 3]. The supercavitating vehicle mainly adopts the stern rudder control mode, the bow rudder control mode, and the joint control mode of the bow and stern control mode, and the precise prediction of rudder effect and supercavity shape is the key to the research of supercavitation navigation control technology [3, 4].

The supercavitation vehicle obtains greater control power by increasing the wetted area of the rudder blade, which can change the rudder effect characteristics and the cavitation shape because of the interaction between the rudder blade and the cavitation. Ignoring the deformation of supercavity and representing the rudder effect with the wetted area of the theoretical rudder blade, Wang et al. [5] used a wedge-shaped stern rudder as the control surface and studied the dynamic modeling and control problems. Li et al. [6] proposed a hydrodynamic layout mode using bow rudder control and studied the strong manoeuver control technology of supercavitating vehicles through ballistic simulation, but this study did not consider the effect of the hydroplaning of the body because of the main body cavitation deformation caused by the bow rudder. Dzieiski and Kurdila [7] proposed a hydrodynamic prediction method for wedge-shaped rudder blades coupled with cavitation and studied the control technology of supercavitating vehicle with the proposed method. Kuklinski [8] used experimental methods to study the formation and development of cavitation in disc

cavitator, conical cavitator, star-shaped cavitator, and cone-shaped cavitator with bow rudder and also carried quantitative analysis of the influence of multiple supercavitation morphology.

According to publicly published documents, the control force of ultrahigh-speed vehicle mainly comes from the hydrodynamic force of the bow rudder or the stern rudder. The navigation control is mainly based on theoretical cavitation to estimate the rudder effect according to the wetted area. Accurate prediction of the control force of supercavitating vehicle is very important for the optimization of hydrodynamic layout and navigation control research. To the best of our knowledge, there is no report on the study of the interaction between supercavitation and rudder. Both the bow rudder and the stern rudder cause the deformation of the main body cavitation, and the change of the cavitation shape also affects the rudder efficiency. In this paper, numerical simulation is used to study the rudder effect of the bow and stern rudder and the corresponding influence on the supercavitation shape of the main body. The prediction method of the rudder effect and the cavitation shape of the supercavitation vehicle is proposed to demonstrate the bow and stern rudder, and the pros and cons of the control mode are also discussed. The research results of this paper can provide references for the optimization of supercavitation hydrodynamic layout and the research of navigation control technology.

2. Numerical Model and Empirical Formula

For the study of supercavitation flow, the model test of low-speed variation has many limitations, and the process of high-speed cavitation test is difficult to control, and the results are difficult to observe. A large number of verification tests show that the numerical method simulates supercavitation flow with good performance [9, 10]. Based on the numerical methods and meshing strategies introduced in the literature, numerical models were established for the ultrahigh-speed aircraft with bow rudder and stern rudder control modes, respectively, and the rudder effect of the control surface and its influence on the supercavitation shape were also studied.

2.1. Description of the Problem. The control force of the bow and tail rudders is derived from the fluid power of the rudder blades for a supercavitating vehicle, and the puncture of the rudder blades will inevitably affect the cavitation shape nearby and afterwards. The cavitation deformation near the rudder blade will change the wetted area of the rudder blade, which in turn changes the rudder effect.

According to the position of the control surface, the supercavitating vehicle mainly adopts three control modes: the bow rudder mode, the stern rudder mode, and the joint control mode of the bow and stern rudder. The stern rudder mode relies on the rudder blade to pierce the cavitation to generate control force, which is difficult to accurately predict the rudder effect; the bow rudder mode uses the rudder blades installed on the cavitator to control navigation, and the rudder effect is stable, and the working distance is large,

which has a greater impact on the main body cavitation; the joint control mode of the bow and stern rudder is a new type of hydrodynamic layout mode, with the rudder piece of a smaller size, which combines the characteristics of the bow rudder mode and the stern rudder mode.

In this paper, numerical models were established for supercavitating vehicle with different hydrodynamic layout modes, and the rudder efficiency of the bow rudder and stern rudder and their influence on the supercavitation shape were studied, respectively. The bow and stern rudders adopt the classic "cross" layout pattern. The tail rudder is installed at the end of the cylindrical section of the vehicle, and the bow rudder is arranged on the conical cavitator. The layout of the bow and stern rudder is shown in Figure 1.

Both the bow rudder and the stern rudder use 24° wedge-shaped rudder blades. The rudder blades and the dimensions of the stern rudder model refer to a supercavitating underwater vehicle that adopts the stern rudder control mode. The diameter of the disc cavitator is 24 mm, the chord length is 20.18 mm, and the spread length is 44 mm. According to the principle of approximate equal resistance, the cavitation and tail rudder dimensions of the bow and rudder control mode are designed, which uses a 90° cone-shaped cavitation with a bottom diameter of 84 mm, a bow rudder chord length of 13.6 mm, and a bow rudder maximum elongation of 26.1 mm, and rudder area is 301 mm^2. Considering that the actual rudder effect of the stern rudder is related to the high speed of cavitation puncture, the effective area of the rudder blade is small, and the action distance of the rudder force of the stern rudder is longer, so the area of the bow rudder is only 20% of the area of the stern rudder.

2.2. Governing Equation. The governing equations involved in the numerical simulation of supercavitation flow include gas-liquid two-phase continuity equations, momentum equations, and turbulence equations. According to literature [11], the research content of this paper belongs to the homogeneous flow problem, and the mixture multiphase flow model can be used. The cavitation problem can be considered by the mass transfer between the phases described by the Schnerr and Sauer model. The turbulence simulation adopts realizable k-e turbulence model, which is robust and suitable for solving complex flow problems. The near-wall processing method in turbulence simulation can use scaled wall functions.

2.3. Model Processing and Meshing. This paper mainly studies the hydrodynamic characteristics of rudder blades under supercavitation conditions when rudder blades exist. In order to simplify the calculation process, the bow rudder model establishes the geometric model of the conical cavitation and the wedge-shaped rudder blades, without considering the rear body of the aircraft. The stern rudder model needs to consider the puncture of the stern rudder to the cavitation; therefore, a complete geometric model of the supercavitating vehicle is established, including the disc cavitator, the nose cone section, the cylindrical section, the stern rudder, and the tail nozzle. On the basis of the bow rudder and tail rudder models, the rudder blades are
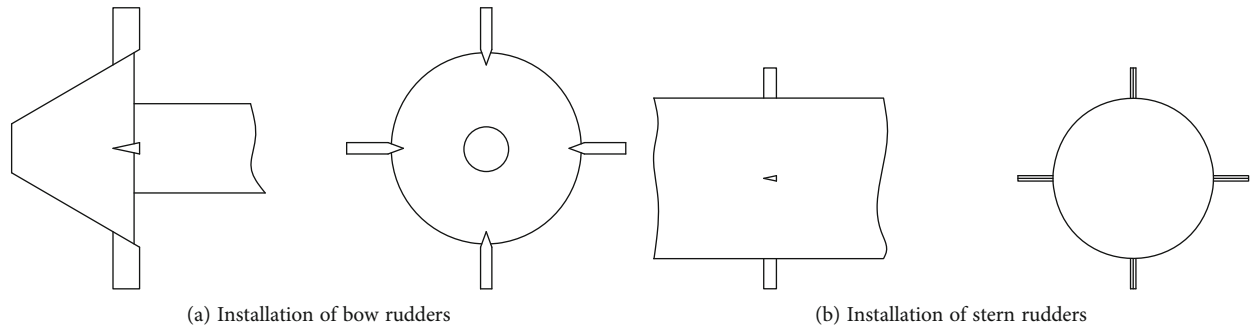
(a) Installation of bow rudders

(b) Installation of stern rudders

FIGURE 1: Local modes of the bow rudder and stern rudder: (a) the bow rudder; (b) the stern rudder.

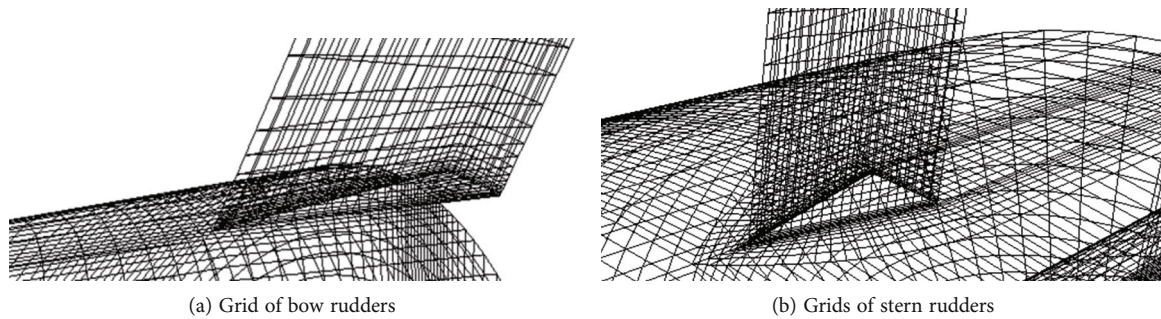(a) Grid of bow rudders

(b) Grids of stern rudders

FIGURE 2: Grid distribution near the rudder blades. (a) The bow rudder model; (b) the stern rudder model.

removed, and the model without appendage is established. By comparing the numerical simulation results with or without rudder blades, the influences of the bow rudder and stern rudder on the cavitation shape are studied, respectively.

For the numerical simulation of supercavitating flow involving the capture of phase transition and two-phase interface, a reasonable choice of the calculation domain scale during modeling can reduce the influence of boundary conditions on the calculation results. The diameter of the calculation domain is 35 times the maximum cross-sectional diameter of the theoretical cavity. The distance between the entrance of the calculation domain and the cavitator is 1 times the full length of the theoretical cavitation, and the distance between the outlet of the calculation domain and the cavitator is 2 times the full length of the theoretical cavitation.

According to the established geometric models of the bow and stern rudders, the GAMBIT software is used to divide the structured grid, and a boundary layer to the near wall is added, and the near wall grids are optimized to accurately simulate turbulence based on the turbulence model's requirements for $y+$. The wake area around the rudder blades and behind the rudder blades is divided into sufficiently fine grids to accurately capture cavitation bubbles. The grid independence test is carried to ensure that the numerical simulation results of the cavitation shape and fluid dynamics without the influence of the grid distribution.

According to the above-mentioned model simplification method and grid division principle, the geometric model of the rudder angle of $0°{\sim}12°$ is established, and the grid is

divided at $1°$ intervals, for the bow rudder and the stern rudder, respectively. The number of grid elements of the bow rudder model is 1.8 million, while the number of grid units in the stern rudder model is 2.2 million. The unattached models for reference with the bow rudder and stern rudder models are relatively simple, with a grid size of 0.9 million and 1.2 million, respectively. Taking the $0°$ working condition as an example, the grid distribution of the bow rudder and stern rudder models near the rudder blades is shown in Figures 2(a) and 2(b), respectively.

2.4. Boundary Condition Setting. The calculation domain uses a velocity inlet with free stream velocity of 100 m/s. The calculation domain uses a pressure outlet with an absolute pressure of 118540 Pa. The natural cavitation model is used to simulate the generation and development of supercavitation with a cavitation pressure of 3540 Pa. The calculation domain is surrounded by sliding walls, ignoring shear to weaken the influence of the wall on the flow field.

3. Numerical Simulation Study of Bow and Stern Rudder Models

According to the established bow rudder and stern rudder models, numerical simulation studies were carried out, respectively, and the hydrodynamic characteristics of the rudder blades and the influence of the rudder blades on the cavitation shape were obtained.

3.1. Layout of the Bow Rudder Mode. According to the numerical results of the $0{\sim}12°$ rudder angle, the

(a) Supercavity produced by cavitator with bow rudders (wholly)   (b) Supercavity produced by cavitator with bow rudders (partly)
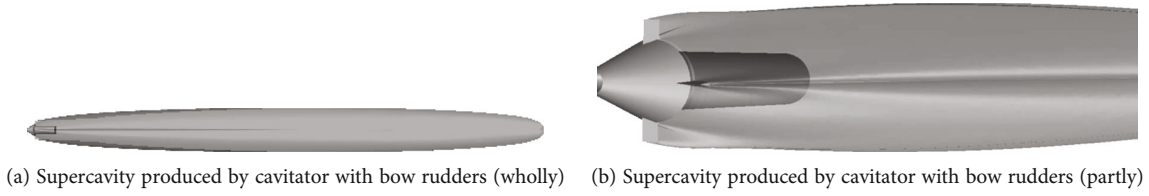
Figure 3: Supercavitating shape when the rudder angle of the bow and rudder is 0°. (a) The overall cavitation morphology; (b) the initial cavitation morphology.

hydrodynamic characteristics of the bow rudder are counted, and the rudder effect characteristics of the bow rudder are obtained. Compared with the model excluding the bow rudder, the influence of the bow rudder on the major supercavity shape is obtained, by analyzing the deformation of the supercavity.

3.1.1. The Influence of Bow Rudder on Supercavitation Morphology.

The bow rudder changes the inherent shape of the rotating body of the cavitator, resulting in a change in the shape of the supercavitation. Literature [12] pointed out that during the motion of supercavitating vehicle, the body would inevitably appear water skiing and be subjected to greater "hydroplaning," so the change of cavitation shape will ultimately affect the motion characteristics of the vehicle. In order to study the influence of the bow rudder on the supercavitation, according to the numerical simulation results of the bow rudder model, the supercavity shape is characterized by the iso-surface of the 50% gas volume fraction.

Considering that both the bow rudder and the rudder angle will have a significant impact on the supercavitation morphology, in order to highlight the focus of this research, only the 0° rudder angle condition is taken as an example to analyze the influence of the bow rudder on the supercavitation morphology. The shape of the supercavitation, when the bow rudder angle is 0°, is shown in Figure 3. The overall cavitation morphology is shown in Figure 3(a), and the initial cavitation morphology is shown in Figure 3(b). The numerical simulation results shown in Figure 3 are similar to the supercavity morphological characteristics obtained by the water tunnel test of the star-shaped cavitation in the literature [8].

Figure 3(a) shows that the supercavity generated by the bow rudder model is ellipsoid-like overall, and the maximum cross-sectional diameter of the bubble is in the middle position. The bow rudder cavitation has a great impact on the previous part of the main cavity. Figure 3(b) shows that four tail cavities are pulled out by the bow rudder, which significantly changes the morphology of the forepart of the supercavity. With the development of the main cavity, the tail cavities gradually merge with the main cavity.

The bow rudder model adopts the "cross-rudder" layout mode, which makes the cavitation profile of the cross-section of the rudder blade different from other section. According to the numerical simulation results, the cavitation axial section contour lines are extracted, and the cavitation contour lines through the axial section of the rudder blade and the axial section between the two rudder blades are, respectively, extracted for the bow rudder model. The two sections are vertical section (section 1) and 45° oblique section (section 2), which are reflected in the axial view of the bow rudder model in Figure 1. The comparison between the different cross-sectional contour lines of the supercavitation of the bow rudder model and the cavitation longitudinal profile of the no bow rudder model is shown in Figure 4.

Figure 4 shows that under the same flow conditions, the geometric dimensions of the supercavitation generated by the bow rudder model are larger than the supercavitation generated by the single cavitation model, in which the axial length is 7.7% larger. The cavitation profile of section 1 is affected by the bow rudder, and the symmetry of the cavitation bubble is destroyed, and the section with the largest radial dimension moves backward. The radial dimension of section 2 is larger than that of section 1, and the profile of the cavitation is still elliptical. With the development of cavitation, the difference between section 1 and section 2 gradually decreases.

In order to study the influence of the bow rudder on the cavitation development process, according to the numerical simulation results, the cavitation contours of the cross-sections at different axial positions with the distances of $0.1 Lm$, $0.3L m$, $0.5 Lm$, and $0.7 Lm$ from the cavitation are extracted and compared. The comparison of the cavitation contour lines corresponding to different axial positions is shown in Figure 5.

Figure 5 shows that the bow rudder has a significant effect on the shape of supercavitation and will change the original circular cross-section of the cavity. The rudder blade changes the position of the cavitation seriously, and the cavitation depression caused by the bow rudder disappears after the middle section.

3.1.2. The Hydrodynamic Characteristics of the Bow Rudder.

The wetness of the bow rudder is not affected by the supercavitation of the main body; therefore, the rudder effect is stable during the steering process, and the control force is only related to the rudder angle. The hydrodynamic force of the bow rudder includes the resistance in the same direction as the incoming flow and the lift perpendicular to the incoming flow. In order to facilitate the analysis, the hydrodynamics of the bow rudder are dimensionless, and the reference quantities are the incoming flow velocity, the density of water, and the wetted area of the rudder blades (the wetted area of the rudder blades is defined as the area of the longitudinal section of the wetted part). The hydrodynamic characteristics of the bow rudder after the nondimensionalization are shown in Figure 6.
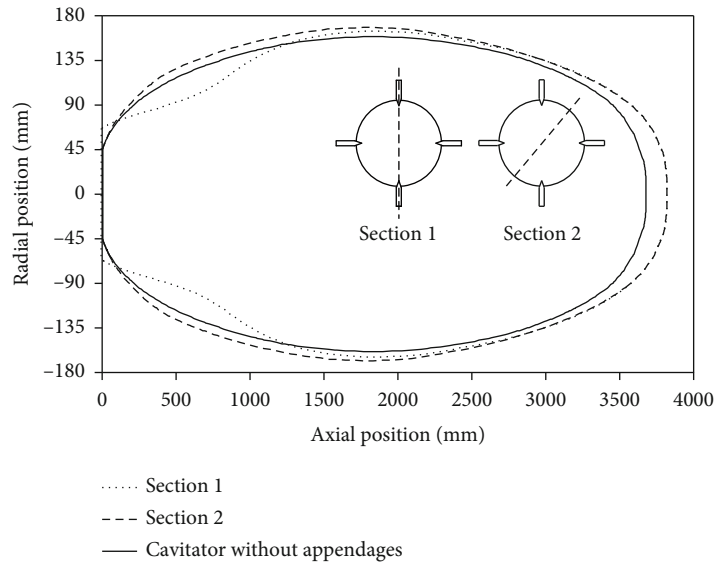
FIGURE 4: Contrast of axial section contour lines of supercavitation of the bow rudder model.
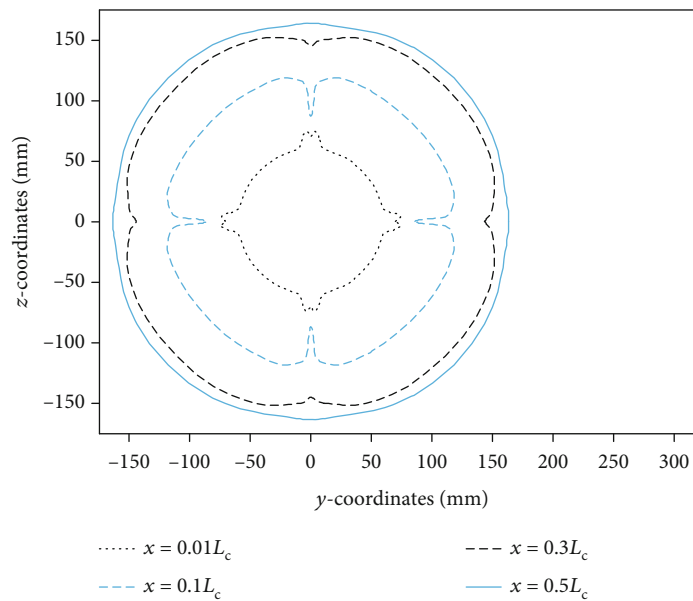

FIGURE 5: Contrast of supercavity transverse section contour lines of the bow rudder model.

Figure 6 shows that the lift coefficient of the bow rudder is positively correlated with the rudder angle. The linearity is good in the range of 0~10°, and it is nonlinear in the range of 10~12°, and the lift derivative gradually decreases. With the increase of the rudder angle, the drag coefficient of the bow rudder is almost unchanged within the range of 0~5°, and it increases significantly in the range of 6~12°. The drag coefficient of 12° rudder angle is about 80% higher than that of 0° rudder angle. The bow rudder reaches the maximum lift-to-drag ratio of 2.4 at 10° rudder angle.

3.2. Layout of the Stern Rudder Mode. According to the numerical simulation results of the stern rudder model with a rudder angle of 0~12°, the hydrodynamic characteristics of the stern rudder are counted to obtain the rudder effect characteristics of the stern rudder. Compared with the model excluding the stern rudder, the influence of the stern rudder on the major supercavity shape is obtained, by analyzing the deformation of the supercavity.

3.2.1. The Influence of Stern Rudder on Supercavitation Morphology. According to the numerical simulation results, the supercavitation of the stern rudder model and the unattached vehicle model is compared, and the influence of the stern rudder on the main body supercavitation is analyzed. The stern rudder is located at the tail of the cylindrical section of the supercavitation vehicle, and the shape of the main body's cavitation tail is mainly determined by the drainage
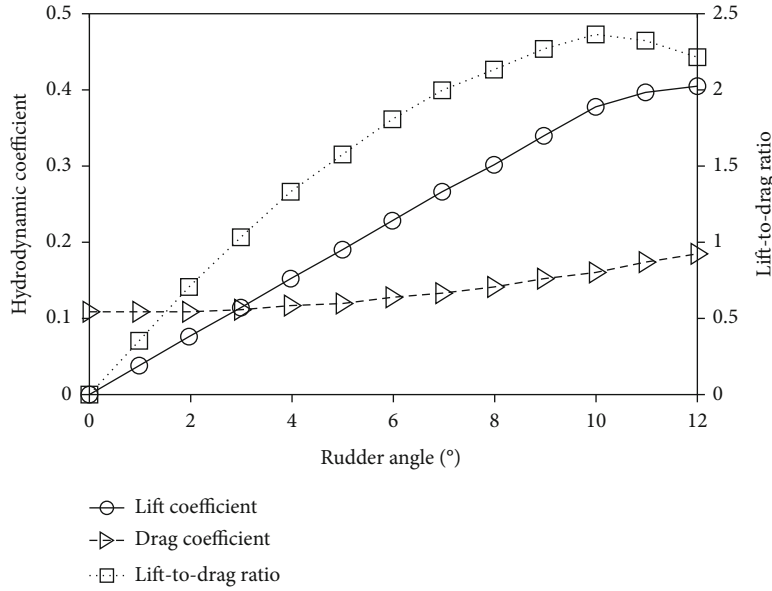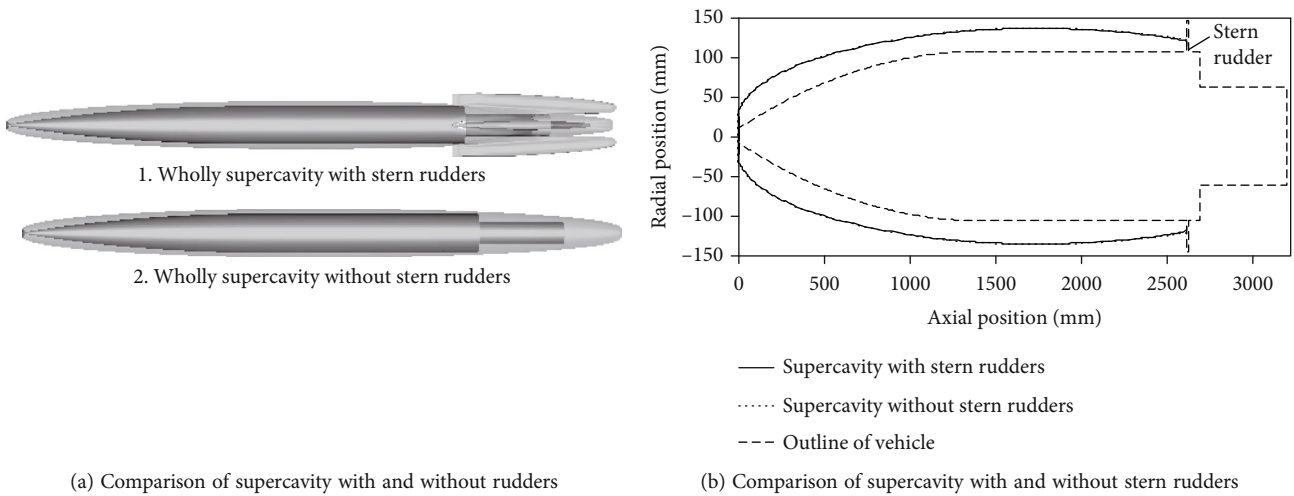
Figure 6: The hydrodynamic characteristics of the bow rudder.

(a) Comparison of supercavity with and without rudders

(b) Comparison of supercavity with and without stern rudders

Figure 7: The influence of stern rudder on supercavitation morphology.

of the engine nozzle for actual vehicle. Therefore, the main concern is the influence of the stern rudder on its previous supercavitation morphology. The main cavitation comparison of the stern rudder model and the unattached model is shown in Figure 7(a). The supercavitation contour line obtained by comparing the stern rudder with and without the stern rudder is shown in Figure 7(b).

Figure 7(a) shows that the stern rudder model and the unattached vehicle model have the same shape and size of the supercavitation. Figure 7(b) shows that the supercavitation contour lines obtained from the stern rudder model with and without the stern rudder model almost coincide before the rudder blade, which indicates that the stern rudder does not affect the shape of the supercavitation in front of the rudder.

The stern rudder punctures the main body cavitation, and the high pressure area of the rudder surface causes the cavitation near the rudder blade to dent, which makes the actual wet condition of the stern rudder change significantly. Studying the influence of the stern rudder on the cavitation shape near the rudder blade is helpful to predict the effective wetting area of the rudder blade, and then accurately predict the rudder effect. The comparison between the numerical simulation results and the experimental results of the supercavity deformation of the main body caused by the stern rudder is shown in Figure 8(a). The intersections of cavitation with stern flat rudder and stern straight rudder are shown in Figure 8(b). Figure 8(a) is a water tunnel test result of low-velocity ventilated supercavity. It is different from the numerical simulation conditions and

(a) Cavitation depression
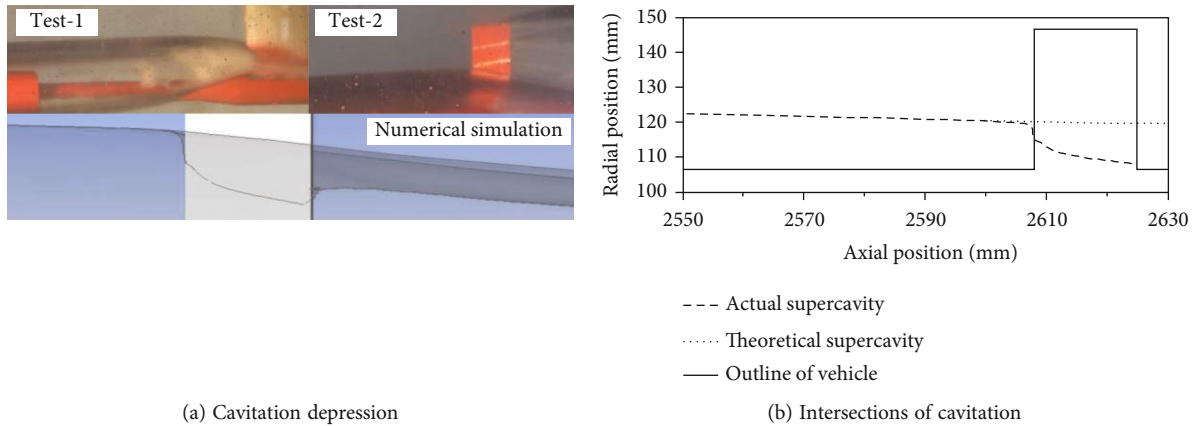
(b) Intersections of cavitation

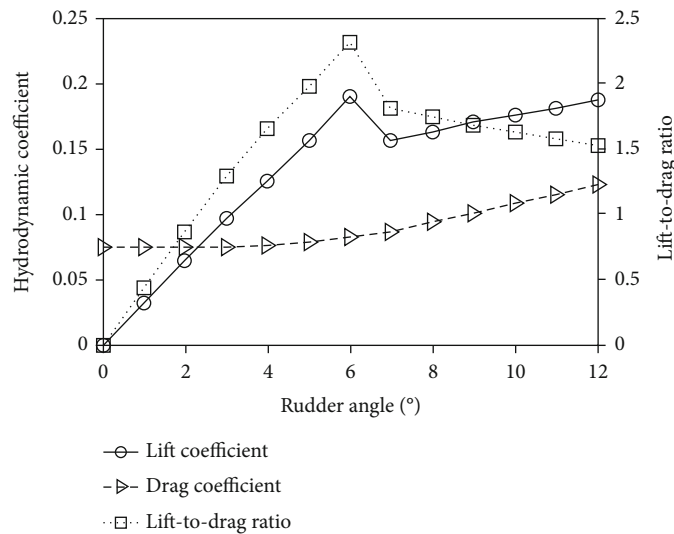FIGURE 8: Actual wetting of the rudder under cavitation puncture.

FIGURE 9: The hydrodynamic characteristics of the stern rudder under puncture cavitation.

shows that the stern rudder can cause the cavitation of the main body.

As shown in Figure 8(a), both the numerical simulation and water tunnel test results show that the rudder blade piercing the cavitation will cause supercavity deformation. Figure 8(b) shows that, when the angle of attack of the vehicle and the rudder angle of the stern rudder are both 0°, the actual wetted area of the stern rudder is 800 mm^2, which is 246 mm^2 larger than the theoretical wetted area. Therefore, the prediction of the rudder efficiency of the stern rudder should consider the supercavity deformation. There is a big difference between the rudder efficiency based on the theoretical cavitation shape and the actual situation.

3.2.2. The Hydrodynamic Characteristics of the Bow Rudder. The rudder effect of the stern rudder is directly related to the wetted area of the rudder blade, and the control force is not only related to the rudder angle but also affected by the actual wetted condition of the rudder blade. According to

the numerical simulation results, the hydrodynamic force received by the stern rudder is counted, and the rudder effect of the stern rudder under the condition of cavitation puncture is studied. The analysis method of the stern rudder hydrodynamic characteristics and the dimensionless process referred to the bow rudder model are also studied. The hydrodynamic characteristic curve of the stern rudder is shown in Figure 9.

Figure 9 shows the stern rudder lift characteristics show two different stages when supercavitation is punctured. The lift coefficient in the range of 0~6° has good linearity with respect to the rudder angle, and the lift coefficient of the rudder blade decreases abruptly at a rudder angle of 7°, even stalling occurs. The lift coefficient is still positively related to the rudder angle within the range of 7~12°, but it is only equivalent to the lift level at the rudder angle of 5~6°. The drag coefficient of the stern rudder in the range of 0~5° rudder angle does not change much, and it increases significantly with the increase of the rudder angle in the range of 5-12°.

The drag coefficient of the rudder angle of 12° increases by 60% relative to 5°.

4. Discussions

Figures 3–5 show the supercavitation generation and development of the bow rudder model, indicating that the bow rudder has a significant influence on the supercavitation morphology. The cross-sectional profile of the bubble is no longer circular, and the symmetry of the bubble is affected. Figures 7 and 8 show the generation and development of supercavitation in the stern rudder model, indicating that the stern rudder has little effect on the main cavitation and does not affect the shape and size of the cavitation in front of the rudder, but only causes local depression of the supercavity near the rudder blade.

Figures 6 and 9 show the hydrodynamic characteristics of the bow rudder model and the stern rudder blade, respectively. The lift coefficient of the bow rudder continues to increase with the increase of the rudder angle in the range of 0-12°. The lift coefficient of the stern rudder increases with the increase of the rudder angle in the range of 0-6°. The lift coefficient of the blade drops suddenly when the rudder angle is 7°. Although the lift coefficient in the range of 7-12° is positively correlated with the rudder angle, the value is only equivalent to the lift level at 5-6°. The maximum lift coefficient of the bow rudder is 0.41, while the stern rudder is only 0.19. Taking the effective wetted area of the rudder blade as a reference value, the lift derivative of the bow rudder is greater than that of the stern rudder. In addition, considering that the distance from the cavitation of the conventional supercavitation vehicle to the center of gravity is about twice the distance from the stern rudder to the center of gravity, therefore, the bow rudder control mode has better maneuverability.

In summary, the bow rudder model has good hydrodynamic characteristics, stable rudder efficiency, and large usable rudder angles. Thus, the bow rudder of the same size can provide greater control force and torque for the aircraft, but it has a greater impact on the cavitation shape, which will affect the prediction accuracy of the hydroplaning of the hull. The influence of the stern rudder model on the previous supercavitation shape of the rudder blade is negligible, but its effective wetting length is affected by the relative position between the vehicle and the supercavitation. In addition, the cavitation near the rudder blade also significantly affects the effective wetting area of the rudder blade, which brings difficulties to the hydrodynamic prediction of the stern rudder.

Based on the above analysis, the advantages and disadvantages of the supercavitating vehicle bow and stern rudder control modes are complementary. Reducing the elongation of the bow rudder reasonably weakens the influence of its multicavitation morphology, and reducing the chord length of the stern rudder can weaken the influence of the main cavitation on the rudder effect. Therefore, a large aspect ratio bow rudder and a small aspect ratio stern rudder are used to implement joint control of the supercavitation vehicle, which can simultaneously take into account the supercavitation shape and control force.

5. Conclusions

In this paper, a numerical model is established for the supercavitating vehicle in the bow and rudder control mode, and the numerical simulation is carried out for the 0~12° rudder angle. According to the numerical simulation results, the influence law of supercavitation shape and its hydrodynamic characteristics of the bow and stern rudder are studied. The following conclusions can be drawn:

(1) In the bow rudder control mode, the rudder blades have good hydrodynamic characteristics, stable rudder effect, and large available rudder angles, which can provide greater control force and torque. The bow rudder has a greater influence on the supercavity morphology, and the cross-sectional profile of the cavity before the midsection is significantly changed

(2) In the stern rudder control mode, the rudder blade has almost no effect on the cavitation shape in front of the rudder. The wetted length of the rudder blade is determined by the relative position relationship between the aircraft and the cavitation, and the actual rudder effect is related to the attitude and supercavitation morphology of the aircraft. The control force of the stern rudder is difficult to predict accurately

(3) The advantages and disadvantages of the bow rudder control mode and the stern rudder control mode are complementary. The use of a small aspect ratio bow rudder and a large aspect ratio stern rudder to implement joint control of the aircraft can simultaneously take into account the supercavitation shape and control force

The research in this paper can provide a reference for the optimization of the hydrodynamic layout of the supercavitating vehicle and the design of the control model.

Data Availability

The data used to support the findings of this study are available from the corresponding author upon request.

Conflicts of Interest

The authors declare that there is no conflict of interest regarding the publication of this paper.

References

[1] L. Kai, L. Dai-Jin, D. Jian-Jun, W. Yu-Cai, and Z. Yu-Wen, "Motion control model of supercavitating vehicle considering time-delay effect of supercavitation," *Journal of Traffic and Transportation Engineering*, vol. 10, no. 3, pp. 41–45, 2010.

[2] M. A. Hassouneh, V. Nguyen, B. Balachandran, and E. H. Abed, "Stability analysis and control of supercavitating

vehicles with advection delay," *Journal of Computational and Nonlinear Dynamics*, vol. 8, no. 2, p. 21003, 2013.

[3] L. Kai, L. Dai-Jin, Q. Kan, D. Jian-Jun, and W. Yu-Cai, "Hydrodynamic layout of strongly maneuvering underwater supercavitating vehicle," *Journal of Traffic and Transportation Engineering*, vol. 10, no. 4, pp. 45–57, 2010.

[4] V. Nguyen, *Dynamics and Control of Non-smooth Systems with Applications to Supercavitating Vehicles*, University of Maryland, College Park, 2011.

[5] J. H. Wang, Y. J. Wei, K. P. Yu, C. Wang, W. H. Huang, and R. Lu, "Modeling and control of underwater supercavitating vehicle based on memory effect of cavity," *Zhendong yu Chongji(Journal of Vibration and Shock)*, vol. 29, no. 8, pp. 160–163, 2010.

[6] D. Li, K. Luo, C. Huang, J. Dang, and Y. Zhang, "Dynamics model and control of high-speed supercavitating vehicles incorporated with time-delay," *International Journal of Non-linear Sciences and Numerical Simulation*, vol. 15, no. 3-4, pp. 221–230, 2014.

[7] J. Dzielski and A. Kurdila, "A benchmark control problem for supercavitating vehicles and an initial investigation of solutions," *Journal of Vibration and Control*, vol. 9, no. 7, pp. 791–804, 2003.

[8] R. Kuklinski, "Experimental studies in the control of cavitating bodies," in *AIAA guidance, navigation, and control conference and exhibit*, 2006.

[9] J.-L. Reboud, O. Coutier-Delgosha, B. Pouffary, and R. Fortes-Patella, "Fifth international symposium on cavitation," in *Numerical Simulation of Unsteady Cavitating Flows: Some Applications and Open Problems*, Osaka, Japan, 2003.

[10] Z. Guang, Y. Kaiping, Z. Jingjun, and L. Zhenwang, "Numerical research on hydrodynamic characteristics of supercavitating vehicle in the turning motion," *Chinese Journal of Applied Mechanics*, vol. 3, pp. 278–283, 2012.

[11] K.-p. Yu, G. Zhang, J.-j. Zhou, W. Zou, and Z.-w. Li, "Numerical study of the pitching motions of supercavitating vehicles," *Journal of Hydrodynamics*, vol. 24, no. 6, pp. 951–958, 2012.

[12] A. D. Vasin and E. V. Paryshev, "Immersion of a cylinder in a fluid through a cylindrical free surface," *Fluid Dynamics*, vol. 36, no. 2, pp. 169–177, 2001.

Research Article

An Adaptive Operational Modal Analysis Method Using Encoder LSTM with Random Decrement Technique

Min Qin [1], **Huaihai Chen** [1], **Ronghui Zheng** [1], **and Tianci Gao** [2]

[1]*State Key Laboratory of Mechanics and Control of Mechanical Structures, College of Aerospace Engineering, Nanjing University of Aeronautics and Astronautics, Nanjing 210016, China*
[2]*Flight Test Center of COMAC, Shanghai 200120, China*

Correspondence should be addressed to Huaihai Chen; chhnuaa@nuaa.edu.cn

A new parameter identification method under non-white noise excitation using transformer encoder and long short-term memory networks (LSTMs) is proposed in the paper. In this work, the random decrement technique (RDT) processing of the data is equivalent to eliminating the noise of the raw data. In general, the addition of the gate in LSTM allows the network to selectively store data, which avoids gradient disappearance and gradient explosion to a certain extent. It is worthwhile mentioning that the encoder can learn the essence of data, which reduces the burden for the LSTM. More specifically, establish as simple LSTM structure as possible to learn the data of this essence to achieve the best training effect. Finally, the proposed method is used for simulation and experimental verification, and the results show that the method has the advantages of high recognition accuracy, strong anti-noise ability, and fast convergence rate. Specially, the results indicated appropriate accuracy proposed by deep learning combined with traditional method for parameter identification as well as proper performance of the proposed method.

1. Introduction

Operational modal analysis only needs to measure the vibration response data of the structure, and there is no need to measure the input excitation, which saves the measure cost. In addition, the modal parameters can be directly applied to the on-line health monitoring and damage diagnosis of the structure. What is more, for some complex and large structures, such as aerospace vehicles, offshore platforms, and bridges, it is difficult to measure the excitation under the actual working conditions, so it is of great engineering significance to identify the modal parameters directly from the time-domain response signals of the structure [1–4]. Conventional modal analysis methods usually assume that the excitation of the structure is white noise, but in fact, in the working state of the structure, the ambient excitation is mostly non-white noise. Therefore, the research on structural modal parameter identification under non-white noise excitation is beneficial to the further development of structural dynamic analysis technology, so as to be better applied to engineering.

The RDT was a time-domain method to identify modal parameters proposed by Cole [5]. Subsequently, Ibrahim extended the RDT method to the field of multichannel signals and formed Ibrahim time-domain method, which was successfully applied to modal parameter identification of spacecraft model structure [6]. The RDT was originally applied to linear single degree of freedom systems with constant damping ratios, which was later used to extract aerodynamic damping from random crosswind responses [7]. Moreover, Kordestani et al. have proposed a two-stage time-domain output-only damage detection method with a new energy-based damage index [8]. As mentioned earlier, the RDT is used for monitoring and determining structural performance, being able to predict damage and handle the occurrence of sudden failures during operation of the structure. In brief, the RDT is considered as a unique nondestructive testing method, which is widely used in aerospace, civil engineering, and mechanical engineering [9]. In addition, other time-domain methods, such as natural excitation technique (NExT), eigensystem realization algorithm (ERA), and

stochastic subspace identification (SSI), have also been applied in engineering [10–15]. In general, the time-domain methods use the measured response signal to identify the modal parameters of the system directly without Fourier transform, which reduces the data transformation error, but the anti-noise ability is poor.

On the contrary, deep learning methods demonstrate more attractive advantages in the anti-noise interference and can be used in damage assessment, health monitoring, modal identification, and so on [16, 17]. Hopfield invented a single-layer feedback neural network Hopfield network to solve combinatorial optimization problems, which is the prototype of the earliest RNN [18]. Nevertheless, given the abundant literature for RNN, it is noticeable that the conventional RNNs usually suffer from a dilemma between the long-range dependence and gradient vanishing. As a remedy, Hochreiter and Schmidhuber proposed the LSTM [19], which greatly alleviated the problem of the early RNN training by using gating unit and memory mechanism. Subsequently, Gers et al. [20] introduced the forgetting gate mechanism on the basis of literature [19], so that the LSTM can reset its own state. Specifically, Greff et al. [21] reviewed the development of the LSTM, compared and analyzed the abilities of eight LSTM variants in speech recognition, handwriting recognition, and chord music modeling, and proved that forgetting gate and output activation function are the key components of the LSTM. It is fair to assert that the neural network represents the most successful identification technology used in the modeling of dynamic system, and it has a unique advantage in antinoise interference; scholars began to study the parameter identification method based on neural network, aiming at better application in practical engineering [22, 23]. Many attempts have already started in this field, such as Xu and Wang who proposed a RNN-based approach for modal parameter identification of structure-unknown systems [24]. Then, the work [25] presented a structural identification method based on RNN and autoregressive and moving average (ARMA) model. Zhang et al. studied the modal parameter identification based on neural network with ARMA [26]. RNNs have unique advantages in processing time series data, and the time-domain method for modal parameter identification based on RNNs has great development potential.

Generally speaking, the limitation of the conventional OMA methods on input-type greatly reduces the adaptability of this method in practical engineering application. However, using the advantages of traditional methods and neural networks to establish a new method is worth studying. For this purpose, an adaptive operational modal analysis method using encoder LSTM with RDT is proposed in this paper. Initially, the data is processed by RDT, so that the recognition accuracy is the highest on the premise of simplifying the model as much as possible. In the second step, with the addition of encoder, LSTM can be regarded as a decoder in autoencoder. Then, establish the simplest network structure as possible to achieve the best performance. Finally, the results indicated appropriate accuracy proposed by encoder LSTM for parameter identification as well as proper performance of the proposed method. The rest of this paper is

organized as follows. The RDT and the architecture of LSTM are described in Section 2. The proposed method and its simulation are described in Section 3. Experimental verification is described in Section 4. Finally, conclusions are given in Section 5.

2. Background

2.1. RDT. RDT extracts the free attenuation vibration response from the response of ambient excitation by means of average and mathematical statistics [5–7]. In a linear multidegree of freedom system, the forced vibration response of a measuring point under arbitrary excitation can be expressed as

$$y(t) = y(0)D(t) + \dot{y}(0)V(t) + \int_0^t m(t-\tau)u(\tau)d\tau, \quad (1)$$

where $D(t)$ is the free vibration response of the system with an initial displacement of 1 and an initial speed 0; $V(t)$ is the free vibration response of the system with initial displacement 0 and initial velocity 1; $y(0)$ and $\dot{y}(0)$ are the initial displacement and initial velocity of the system vibration, respectively; $m(t)$ is the unit impulse response function of the system; $u(t)$ is external excitation.

Selecting the appropriate constant A to intercept the random vibration response of a structure in situ $y(t)$, and a series of different intersection times t_i ($i = 1, 2, \cdots, N$) are obtained. The response from time ti can be expressed as

$$y(t - t_i) = y(t_i)D(t - t_i) + \dot{y}(t_i)V(t - t_i) + \int_{t_i}^t m(t-\tau)u(\tau)d\tau. \quad (2)$$

Since the $u(t)$ is stable, the starting point of time does not affect randomness. The $y(t - t_i)$ time series starting point t_i is moved to the origin of coordinates, and the corresponding subsample function can be expressed as

$$x_i(t) = AD(t) + \dot{y}(t_i)V(t) + \int_0^t m(t-\tau)u(\tau)d\tau. \quad (3)$$

Take the statistical average of $x_i(t)$

$$x(t) = \frac{1}{N}\sum_{i=1}^N x_i(t) \approx E\left[AD(t) + \dot{y}(t_i)V(t) + \int_0^t m(t-\tau)u(\tau)d\tau\right]$$
$$\approx AD(t) + E[\dot{y}(t_i)]V(t) + \int_0^t m(t-\tau)E[u(\tau)]d\tau. \quad (4)$$

The excitation $u(t)$ is random vibration with the mean value of 0, and the system vibration response $y(t)$ and $\dot{y}(t)$ are also stationary random vibration with mean value of 0.

$$\begin{cases} E[u(t)] = 0, \\ E[\dot{y}(t_i)] = 0, \end{cases} \quad (5)$$

$$x(t) \approx AD(t). \tag{6}$$

After RDT processing, the free vibration response with initial displacement A and initial velocity 0 is obtained [5–9]. RDT has the characteristics of simplicity and clear physical meaning, so it is used in the preprocessing part of the dataset.

2.2. LSTM. RNN is very effective for data with sequence characteristics, and it can mine temporal information in data [16]. However, due to the problems of gradient vanishing and gradient exploding, the training of RNN is very difficult and its application is very limited. Compared with RNN, LSTM has gating unit and memory mechanism and can selectively store information, so it solves the problems of gradient disappearance and gradient explosion.

In the LSTM, for each element in the input sequence, each layer computes the following function:

$$i_t = \sigma\left(W_{ii}x_t + b_{ii} + W_{hi}h_{t-1} + b_{hi}\right), \tag{7}$$

$$f_t = \sigma\left(W_{if}x_t + b_{if} + W_{hf}h_{t-1} + b_{hf}\right), \tag{8}$$

$$g_t = \tanh\left(W_{ig}x_t + b_{ig} + W_{hg}h_{t-1} + b_{hg}\right), \tag{9}$$

$$o_t = \sigma\left(W_{io}x_t + b_{io} + W_{ho}h_{t-1} + b_{ho}\right), \tag{10}$$

$$c_t = f_t \odot c_{t-1} + i_t \odot g_t, \tag{11}$$

$$h_t = o_t \odot \tanh\left(c_t\right), \tag{12}$$

$$\tanh\left(x\right) = \frac{e^x - e^{-x}}{e^x + e^{-x}}, \tag{13}$$

where h_t is the hidden state at time t, c_t is the cell state, x_t is the input, h_{t-1} is the hidden state of the layer at time $t-1$ or the initial hidden state at time 0, and i_t, f_t, g_t, and o_t are the input, forget, cell, and output gates, respectively. σ is the sigmoid function, and $\odot$ is the Hadamard product.

The method of Adam (adaptive moment estimation) [27] is used to optimize, which has the advantages of simple implementation, high efficiency, less memory consumption, and suitable for large gradient noise problems. The loss function is mean square error (MSE) as follows.

$$\text{Loss} = \frac{1}{2M}\sum_{i=1}^{M}(y_i - yy_i)^2, \tag{14}$$

where M is the total number of samples, y_i is the actual output value, and yy_i is the predicted output value.

3. The Proposed Method

Generally speaking, the rocket works in stages during launch, and the length is changing. Therefore, it is necessary to study the dynamic characteristics of beams with varying length. A cantilever beam with different length is taken as an example to verify the proposed method. The flowchart of the proposed method is shown in Figure 1.

3.1. Dataset Processing. Here, the cantilever beams with 11 different lengths are used for numerical simulation. Furthermore, each beam is divided into 10 elements (as shown in Figure 2 and Table 1). The modal damping ratios of the cantilever beam are set to 0.01. The lengths of these beams are 0.75 m, 0.755 m, 0.76 m, 0.765 m, 0.77 m, 0.775 m, 0.78 m, 0.785 m, 0.79 m, 0.795 m, and 0.80 m. The beam is excited by uncorrelated white noise input, and the outputs are acceleration responses.

The construction of dataset is the first and foremost step of network training. Before going into the model, data preprocessing is particularly important. The acceleration response signal preprocessed by RDT and analytical solution are regarded as the input and output data of the network, respectively. More specifically, the dataset is composed of 11000 samples, and each sample is a two-dimensional matrix. The ratio of training and testing data is 8 : 2.

$$\mathbf{I}(t) = \text{RDT}[y(t)], \tag{15}$$

where $\text{RDT}[\cdot]$ denotes the RDT, as described in Section 2.1.

3.2. The Encoder LSTM Model. Transformer encoder layer is made up of self-attention and feedforward network. The encoder can get the essence of the raw data, and then, we only need to create a small neural network to learn the essence of the data, which not only reduces the burden of the neural network but also achieves good results. The dataset is written into $\mathbf{g} = [g_1, g_2, \cdots, g_t, \cdots]$ after being processed by the transformer encoder layer.

Then, $\mathbf{g}$ is substituted into the LSTM layer for calculation.

$$\mathbf{L} = \text{LSTM}(\mathbf{g}), \tag{16}$$

where $\text{LSTM}[\cdot]$ denotes the LSTM network calculation, which is detailed in Section 2.2.

Finally, in the full connection layer,

$$\mathbf{Y}_i = \text{PReLU}(\mathbf{L}_i W_i + B_i), \tag{17}$$

where $\mathbf{L}$ and $\mathbf{Y}$ are input and output data, respectively. The PReLU function is selected in the fully connected layer, which is characterized by fast convergence and simple gradient calculation,

$$\text{PReLU}(x) = \begin{cases} x & x \geq 0, \\ ax & \text{otherwise.} \end{cases} \tag{18}$$

In brief, the proposed encoder and LSTM model are consist of the transformer encoder layer, the LSTM layers, and the fully connected layer (Figure 1). For convenience, we use E, L, and F to represent the transformer encoder layer, the LSTM layer, and the fully connected layer, respectively. When given data, the model first uses the transformer encoder layer E1 to learn features, where the number of expected features in the input is 512, and the number of heads in the multihead attention models is 8. Then, the features in E1 are inputted into the
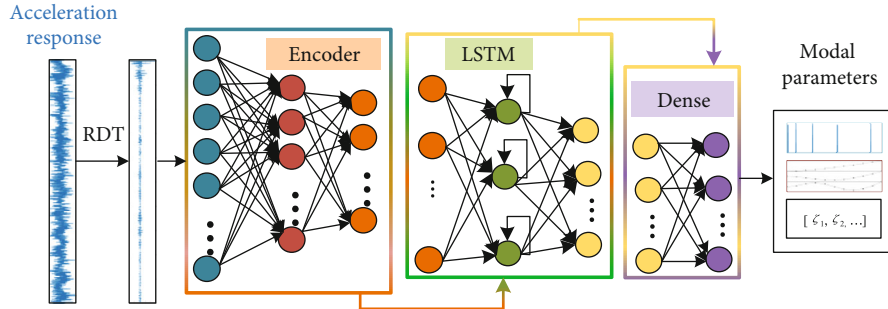
FIGURE 1: Flowchart of the proposed method.
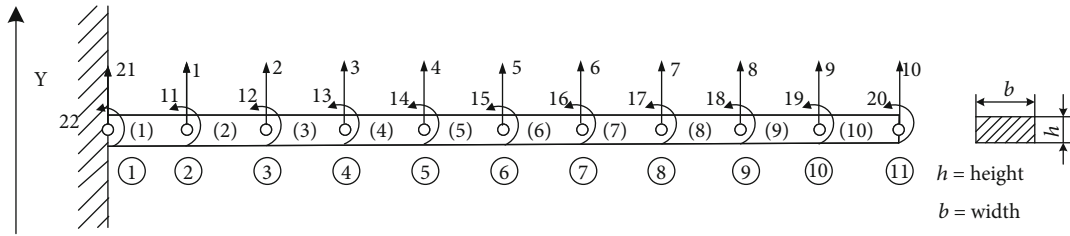
FIGURE 2: The structure diagram of the simulation example.

TABLE 1: The experimental and physical parameters of the 11 beams.

Physical parameters				Experimental parameters	
Section height (m)	Width (m)	Elastic modulus (Pa)	Mass density (kg/m³)	Spectral lines	Analysis frequency band (Hz)
0.012	0.06	7.1×10^{10}	2770	1600	1000
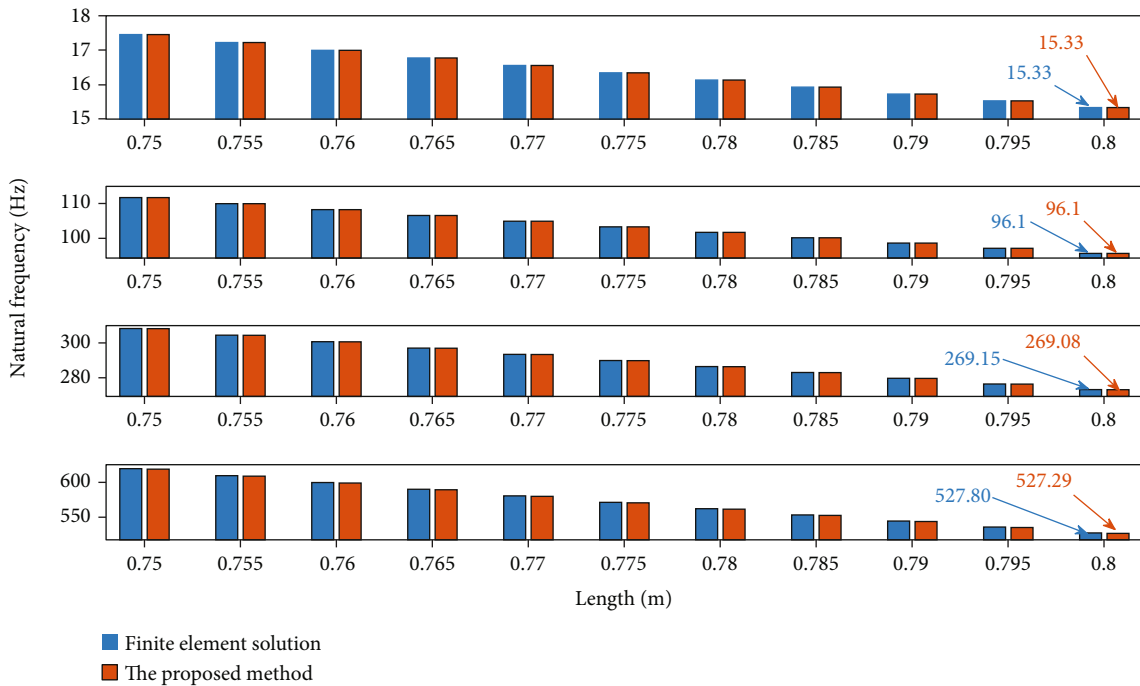
FIGURE 3: The natural frequencies of the simulation example.

layer L2 for deep learning through LSTMs. In the LSTMs, the number of expected features in the input is 512, the number of features in the hidden state is 256, and the number of recurrent layers is 3. Finally, the result is obtained after the calculation of the FC3. The network training process uses loss function to iterate until convergence.

FIGURE 4: The modal shapes of the simulation example.

FIGURE 5: Loss functions with different SNRs.

3.3. Results. Here, the encoder LSTM was established by repeatedly training with the iteration steps as 100 and the learning rate as 0.001. It is widely known tha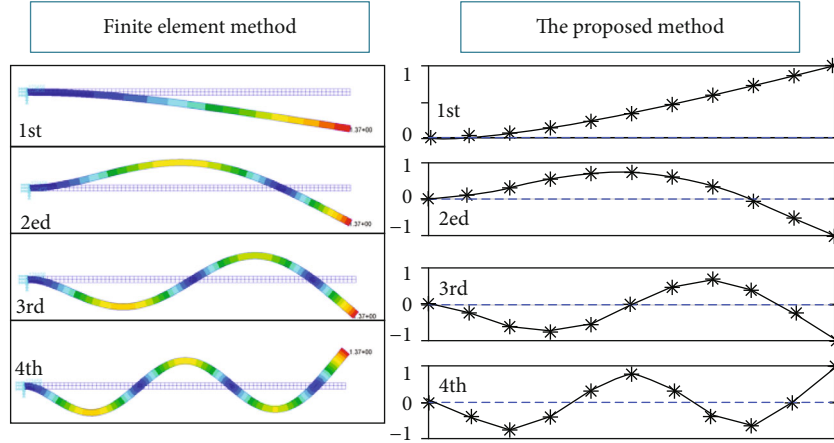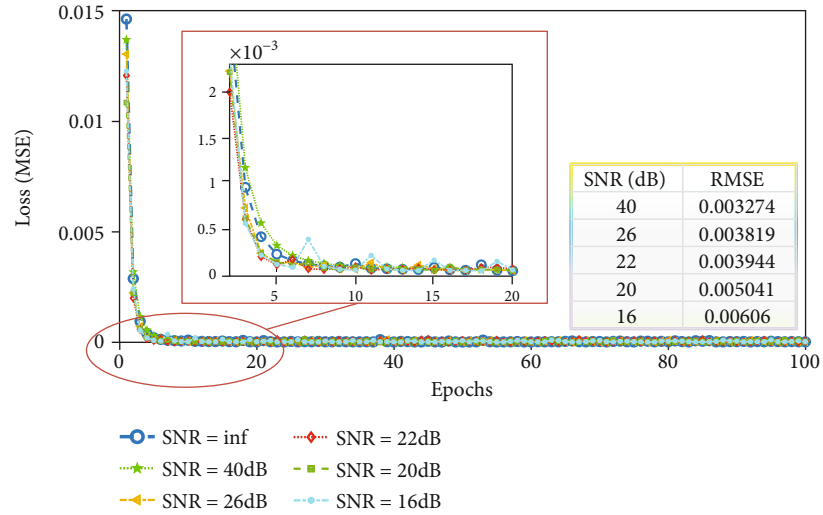t the finite element method can be directly used to solve the modal parameters of beam [28, 29]. And the natural frequency equation can be determined by the vibration differential equation [30] and boundary conditions, and then, the natural frequencies of the beam can be obtained. What is more, the analytical solution is taken as the output of the network and compared with the finite element solution (as shown in Figures 3 and 4).

Additionally, the beam with length = 0.8 m is taken as an example to illustrate. It is generally known that signal to noise ratio (SNR) [31] is a common index to evaluate the strength of noise in a signal. When the signal contains more noise, the value of SNR is smaller. P_{signal} is the power of the effective signal in the signal, and P_{noise} is the power of the noise in the signal. So in order to test the antinoise ability of the proposed method, noise with different SNR is added to the response data of the beam. Then, the data is preprocessed to establish a dataset. Finally, the dataset is substituted into the model for training and tested.

$$Error = \frac{Estimate\ value\text{-}reference\ value}{Reference\ value} \times 100\%, \quad (19)$$

$$SNR = 10\ \lg \left(\frac{P_{signal}}{P_{noise}} \right). \quad (20)$$

The MSE of the first 10 steps is greatly reduced, and it is close to the optimal value in the 20th step, reaching 10^{-5} orders of magnitude in the 50th step and the 100th step, which indicates that the proposed method has the advantage of fast convergence (as shown in Figure 5). In addition, the results of the beam under different SNRs are the same, which indicate that the proposed method has strong anti-noise performance.

4. Experimental Verification

4.1. Dataset Processing. A slender aluminum beam (as shown in Figure 6) is selected as the experimental specimen. The shaker table provides a base excitation along the Y direction. The sixth acceleration sensor measures the excitation signal, including white noise and non-white noise
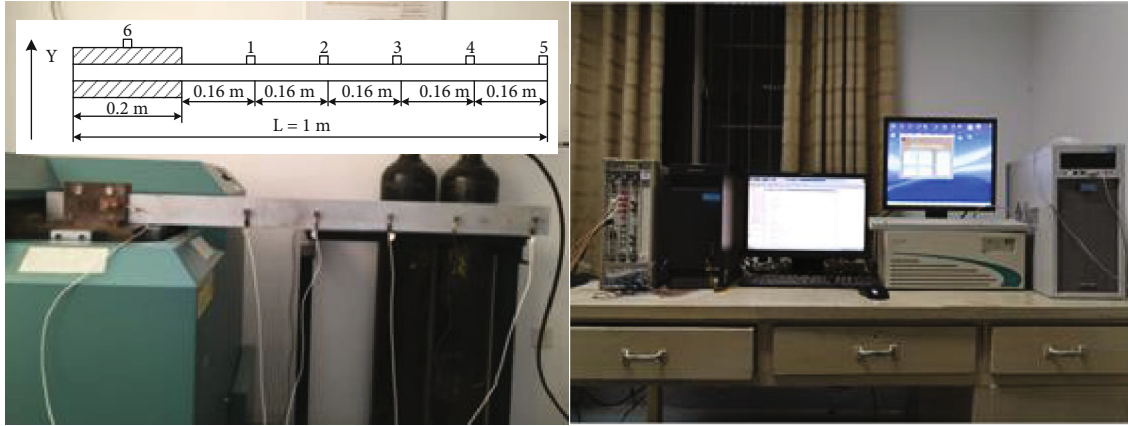
FIGURE 6: Experimental system.

TABLE 2: Experimental and physical parameters of the experimental example.

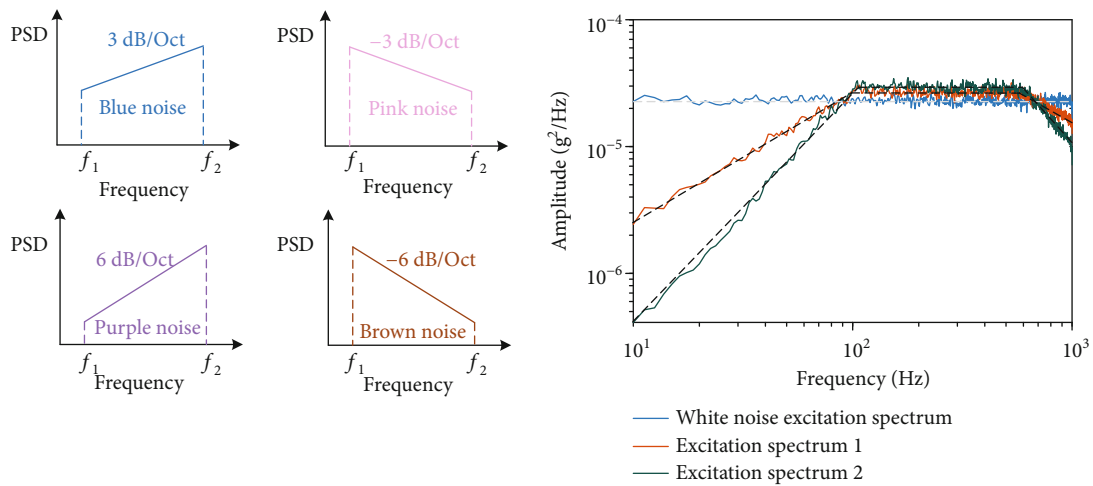| Physical parameters					Experimental parameters		
Length (m)	Section height (m)	Width (m)	Elastic modulus (Pa)	Mass density (kg/m³)	Spectral lines	Analysis frequency band (Hz)	Sampling frequency (Hz)
1	0.012	0.06	7.1×10^{10}	2770	800	1000	2560

FIGURE 7: Four typical non-white noises and excitation spectrums.

excitations, and other sensors measure the response signals. The settings are shown in Table 2. The acquisition equipment is the Agilent VXI plus and play system. Sensors are the sensory organs of various mechanical and electronic devices. Without sensors to capture and convert the original information accurately and reliably, all measurement and control cannot be realized [32, 33]. The sensor type is PCB 333B32 SN 25222.

The conventional OMA method usually assumes that the excitation of the structure is a uniform spectrum excitation. However, in the operational state of structures, such as the flight of aerospace, the passing of bridge, the wind load, or the earth pulsation action of high-rise structure, the ambient excitation is mostly nonuniform. All these states will restrict and affect the application and accuracy of the conventional

OMA method. Therefore, the modal analysis must be conducted under the nonuniform excitation spectrum. Traditionally, the four typical non-white noises correspond to blue noise, pink noise, purple noise, and brown noise. In order to make a more comprehensive study of different non-white noise excitation, the excitation spectra of four typical colored noise and white noise are mixed to excite the structure. Here, two typical trapezoidal spectra ambient excitations are used to excite the beam, and the vibration environment of the trapezoidal spectrum base excitation is controlled by the shaker table controller. Excitation spectrum 1 can be regarded as a combination of blue noise, narrow band white noise, and pink noise. Excitation spectrum 2 can be regarded as the combination of purple noise, narrow band white noise, and brown noise. More specifically, the
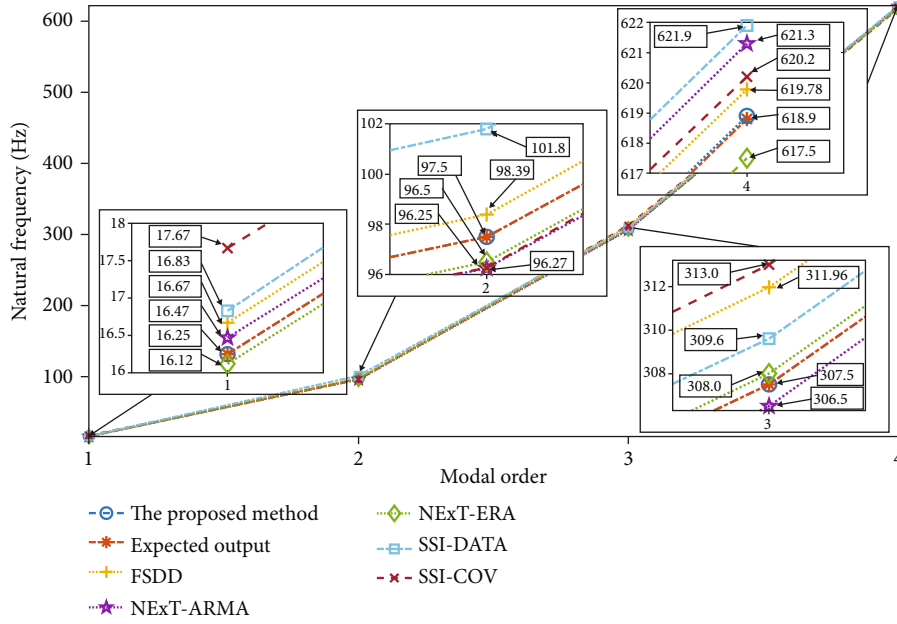
FIGURE 8: The natural frequencies of the experimental example.
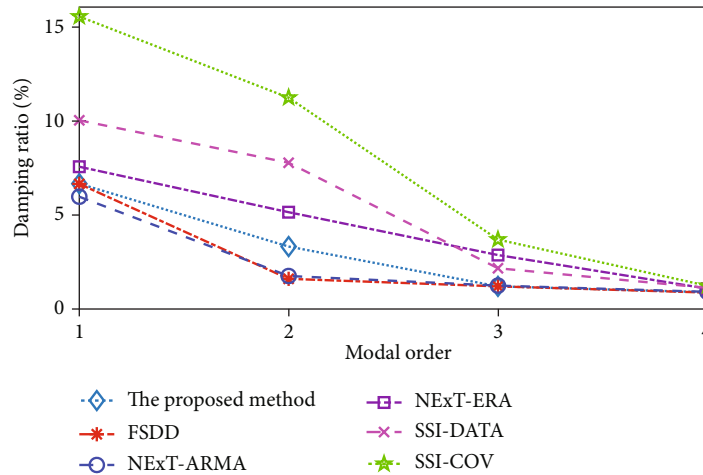
FIGURE 9: The damping ratios of the experimental example.

spectrums inflection frequency are 10, 100, 600, and 1000 Hz, respectively (as shown in Figure 7).

The acceleration response signals generated under the excitation of the white noise excitation spectrum, the excitation spectrum 1, and the excitation spectrum 2 are denoted as data 1, data 2, and data 3, respectively. Under laboratory conditions, the method of using the simultaneously measured excitation and response signals of the structure to obtain the transfer rate function of the system for parameter identification is called experimental modal analysis method (the results obtained by this method are referred to as expected output). The acceleration response signals preprocessed by RDT are still used as the input of the network, but the difference is that the output data of the network are the results of experimental modal analysis.

4.2. Model Training and Results. Under the laboratory conditions described in Section 4.1, NExT-ERA, NExT-ARMA, Data-Driven SSI (SSI-DATA) [34], Covariance-Driven SSI (SSI-COV) [35], frequency and spatial domain decomposition (FSDD) [36], and other methods are used to identify the modal parameters of the data 1, and the results are compared with the proposed method. Obviously, the natural frequencies identified by the proposed method are consistent with the expected output, so the recognition accuracy of the proposed method is higher than other methods (as shown in Figure 8). The damping is greatly affected by the external noise, and the recognition results of the proposed method are similar to NExT-ARMA method and FSDD method (as shown in Figure 9). The modal shape is consistent with the actual situation (as shown in Figure 10). Mode is the natural
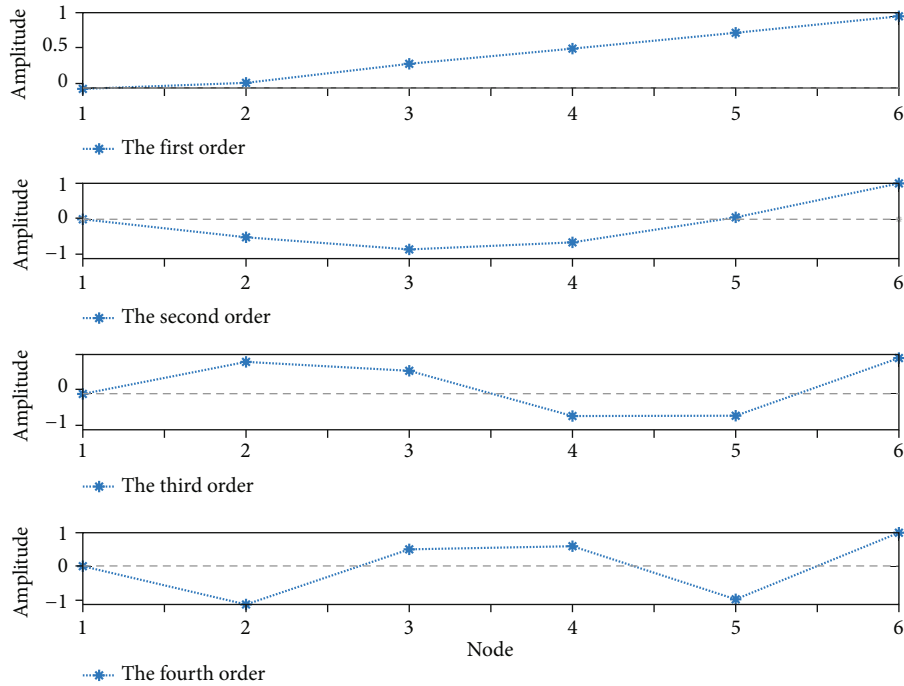
Figure 10: The modal shapes of the experimental example.

Data 2
Data 3
Computed criterion
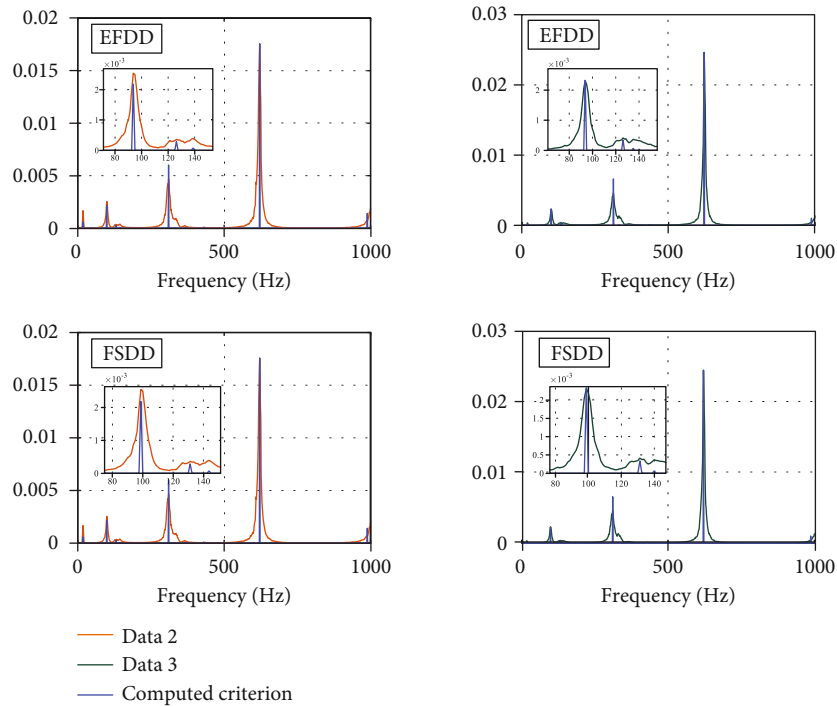
Figure 11: Modal parameters under non-white noise excitation.

vibration characteristic of the structure. Each mode has a specific natural frequency, damping ratio, and modal shape, so the modal parameters of the structure will not change due to different excitations. Nevertheless, taking EFDD and FSDD as examples, there are modal leakages and false modes in parameter identification of the data 2 and the data 3 (as shown in Figure 11), and the results are inconsistent with

the data 1, thereby suggesting that the conventional OMA method is not suitable for non-white noise excitation.

In order to test the performance of the proposed method, different network structures are used to train and test the same data, and the data includes data 1, data 2, and data 3. More specifically, Model 1 means that the data is not processed by RDT, but directly trained by RNN.
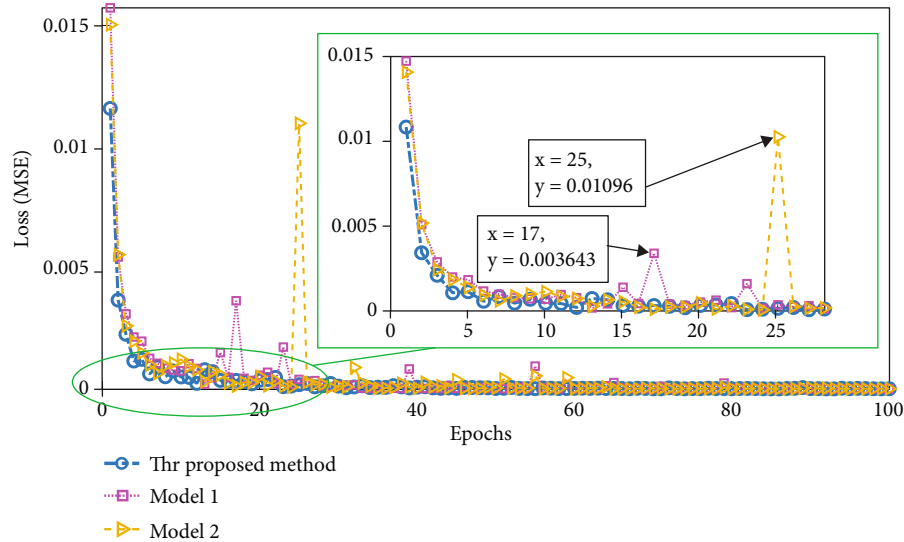
FIGURE 12: Loss functions with different models.

Model 2 means that the data is not processed by RDT but directly trained by the encoder LSTM.

Obviously, Model 1 has obvious bulge in step 17, and Model 2 has obvious bulge in step 25, which indicates that these network training effects are not good (as shown in Figure 12). Fortunately, the loss function of the proposed method is smooth, and the results are consistent with Figure 8, which shows that the network training effect is good and the modal parameter identification accuracy of the data is high. As well in the loss function of the proposed method, the MSE of the first 10 steps is greatly reduced, and it is close to the optimal value in the 20 steps, reaching 10^{-5} orders of magnitude in the 50th step and the 100th step, which shows that the proposed method has a fast convergence rate. As mentioned earlier, the proposed method has strong generalization ability.

5. Conclusion

An adaptive operational modal analysis method using transformer encoder and LSTM is proposed and has been applied to extract the mode from the acceleration response of cantilever beam model. Simulation and experimental results show that the proposed method has the advantages of strong antinoise ability, fast convergence, and high accuracy, which provides a new method for the application of modal analysis in engineering.

(a) In the simulation, the proposed method is used to identify the response data with noise of different SNR, and the results are the same, which proves that the method has strong anti-noise ability.

(b) In the experiment, different treatment methods are used for the beam, and the recognition results show that the proposed method is the best. Furthermore, in the loss function of the proposed, the first 10 steps decay rapidly and approach the optimal value at 20

steps, and the MSE of the 50th and 100th steps is in the order of 10^{-5}, which shows that the proposed method has a fast convergence rate.

(c) In the experiment, compared with other conventional methods, the proposed method has higher recognition accuracy for the data 1. In addition, the result of the data recognition by the proposed method is consistent with that of the data 1, and the convergence speed is fast, which shows that the method has strong generalization ability.

Data Availability

The data used to support the findings of this study are available from the corresponding author upon request.

Conflicts of Interest

The authors declared no potential conflicts of interest with respect to the research, authorship, and/or publication of this article.

Acknowledgments

References

[1] C. Wang, H. Huang, X. Lai, and J. Chen, "A new online operational modal analysis method for vibration control for linear time-varying structure," *Applied Sciences*, vol. 10, no. 1, p. 48, 2020.

[2] W. H. Fu, C. Wang, and J. W. Chen, "Operational modal analysis for vibration control following moving window locality preserving projections for linear slow-time-varying structures," *Applied Sciences*, vol. 11, no. 2, p. 791, 2021.

[3] M. J. Whelan, M. V. Gangone, K. D. Janoyan, and R. Jha, "Operational modal analysis of a multi-span skew bridge using real-time wireless sensor networks," *Journal of Vibration and Control*, vol. 17, no. 13, pp. 1952–1963, 2011.

[4] X. Dong, J. Lian, H. Wang, T. Yu, and Y. Zhao, "Structural vibration monitoring and operational modal analysis of offshore wind turbine structure," *Ocean Engineering*, vol. 150, pp. 280–297, 2018.

[5] Q. Wen, X. G. Hua, Z. Q. Chen, H. W. Niu, and X. Y. Wang, "AMD-based random decrement technique for modal identification of structures with close modes," *Journal of Aerospace Engineering*, vol. 31, no. 5, p. 04018057, 2018.

[6] S. R. Ibrahim, "Random decrement technique for modal identification of structures," *Journal of Spacecraft and Rockets*, vol. 14, no. 11, pp. 696–700, 1977.

[7] W. Hao and Q. S. Yang, "Applicability of random decrement technique in extracting aerodynamic damping of crosswind-excited tall buildings," *Journal of Building Engineering*, vol. 38, article 102248, 2021.

[8] H. Kordestani, C. W. Zhang, and M. Shadabfar, "Beam damage detection under a moving load using random decrement technique and Savitzky–Golay filter," *Sensors*, vol. 20, no. 1, pp. 243–258, 2020.

[9] R. Morsy, H. Marzouk, X. Gu, and A. Elshafey, "Use of the random decrement technique for nondestructive detection of damage to beams," *Materials and Structures*, vol. 49, no. 11, pp. 4719–4727, 2016.

[10] J. M. Seppanen, J. Turunen, M. Koivisto, N. Kishor, and L. C. Haarla, "Modal analysis of power systems through natural excitation technique," *IEEE Transactions on Power Systems*, vol. 29, no. 4, pp. 1642–1652, 2014.

[11] J. N. Juang and R. S. Pappa, "An eigensystem realization algorithm for modal parameter identification and model reduction," *Journal of Guidance Control and Dynamics*, vol. 8, no. 5, pp. 620–627, 1985.

[12] M. Chang and S. N. Pakzad, "Modified natural excitation technique for stochastic modal identification," *Journal of Structural Engineering*, vol. 139, no. 10, pp. 1753–1762, 2013.

[13] H. Y. Cui, W. Q. Peng, X. Xu, and M. Hong, "A damage identification method for a thin plate structure based on PVDF sensors and strain mode," *Proceedings of the Institution of Mechanical Engineers, Part C: Journal of Mechanical Engineering Science*, vol. 233, no. 14, pp. 4881–4895, 2019.

[14] B. Peeters and G. D. Roeck, "Reference-based stochastic subspace identification for output-only modal analysis," *Mechanical Systems and Signal Processing*, vol. 13, no. 6, pp. 855–878, 1999.

[15] Y. Zhou, X. Jiang, M. Zhang, J. Zhang, H. Sun, and X. Li, "Modal parameters identification of bridge by improved stochastic subspace identification method with Grubbs criterion," *Measurement and Control*, vol. 54, no. 3-4, pp. 457–464, 2021.

[16] H. Shi, M. H. Xu, and R. Li, "Deep learning for household load forecasting-a novel pooling deep RNN," *IEEE Transactions on Smart Grid*, vol. 9, no. 5, pp. 5271–5280, 2018.

[17] X. Y. Long, S. K. Zhao, C. Jiang, W. P. Li, and C. H. Liu, "Deep learning-based planar crack damage evaluation using convolutional neural networks," *Engineering Fracture Mechanics*, vol. 246, article 107604, 2021.

[18] J. Hopfield, "Neural networks and physical systems with emergent collective computational abilities," *Proceedings of the National Academy of Sciences of the United States of America*, vol. 79, no. 8, pp. 2554–2558, 1982.

[19] S. Hochreiter and J. Schmidhuber, "Long short-term memory," *Neural Computation*, vol. 9, no. 8, pp. 1735–1780, 1997.

[20] F. A. Gers, J. Schmidhuber, and F. A. Cummins, "Learning to forget: continual prediction with LSTM," *Neural Computation*, vol. 12, no. 10, pp. 2451–2471, 2000.

[21] K. Greff, R. K. Srivastava, J. Koutník, B. R. Steunebrink, and J. Schmidhuber, "LSTM: a search space odyssey," *IEEE Transactions on Neural Networks and Learning Systems*, vol. 28, no. 10, pp. 2222–2232, 2017.

[22] C. K. Qi, F. Gao, H. X. Li, and L. Deng, "A neural network-based distributed parameter model identification approach for microcantilever," *Proceedings of the Institution of Mechanical Engineers, Part C: Journal of Mechanical Engineering Science*, vol. 230, no. 20, pp. 3663–3676, 2015.

[23] A. K. Pravin, A. S. Dhoble, and P. M. Padole, "Deep neural network-based wind speed forecasting and fatigue analysis of a large composite wind turbine blade," *Proceedings of the Institution of Mechanical Engineers, Part C: Journal of Mechanical Engineering Science*, vol. 233, no. 8, pp. 2794–2812, 2019.

[24] J. Xu, Q. C. Meng, D. M. Zhou, and Y. Ge, "A modal parameters identification method based on recurrent neural networks," in *Proceedings of International Conference on Machine Learning and Cybernetics*, Shanghai, China, August 2004.

[25] J. Xu and X. L. Wang, "A structural identification method based on recurrent neural network and auto-regressive and moving average model," *Applied Mechanics and Materials*, vol. 256-259, no. 1, pp. 2261–2265, 2013.

[26] J. Zhang, T. Sato, S. Iai, and T. Hutchinson, "A pattern recognition technique for structural identification using observed vibration signals: linear case studies," *Engineering Structures*, vol. 30, no. 5, pp. 1439–1446, 2007.

[27] D. Kingma and J. Ba, *Adam: A Method for Stochastic Optimization*, Computer Science, 2014.

[28] Z. R. Jiang, K. R. Shi, D. W. N. Wang, K. R. Shi, J. Cai, and S. T. Wang, "Nonlinear finite element analysis of beam string structure," *Advanced Materials Research*, vol. 163-167, pp. 2124–2130, 2011.

[29] Y. Vetyukov, "Non-material finite element modelling of large vibrations of axially moving strings and beams," *Journal of Sound and Vibration*, vol. 414, no. 3, pp. 299–317, 2018.

[30] S. Çatal, "Solution of free vibration equations of beam on elastic soil by using differential transform method," *Applied Mathematical Modelling*, vol. 32, no. 9, pp. 1744–1757, 2008.

[31] J. Obuchowski, A. Wylomanska, and R. Zimroz, "Two-stage data driven filtering for local damage detection in presence of time varying signal to noise ratio," *Vibration Engineering and Technology of Machinery*, vol. 23, pp. 401–410, 2015.

[32] H. D. Shao, J. Lin, L. W. Zhang, D. Galar, and U. Kumar, "A novel approach of multisensory fusion to collaborative fault diagnosis in maintenance," *Information Fusion*, vol. 74, pp. 65–76, 2021.

[33] X. Li, Y. Yang, H. Shao, X. Zhong, J. Cheng, and J. Cheng, "Symplectic weighted sparse support matrix machine for gear fault diagnosis," *Measurement*, vol. 168, article 108392, 2021.

[34] J. F. Xin, S. Hu, and H. Li, "Experimental modal analysis of jacket-type platforms using data-driven stochastic subspace identification method," in *Proceedings of the ASME 2012 31st*

International Conference on Ocean, Offshore and Arctic Engineering, Rio de Janeiro, Brazil, July, 2012.

[35] L. Bonekemper, M. Wiemann, and P. Kraemer, "Automated set-up parameter estimation and result evaluation for SSI-Cov-OMA," *Vibroengineering PROCEDIA*, vol. 34, pp. 43–49, 2020.

[36] T. Wang, O. Celik, F. N. Catbas, and L. M. Zhang, "A frequency and spatial domain decomposition method for operational strain modal analysis and its application," *Engineering Structures*, vol. 114, no. 1, pp. 104–112, 2016.

Research Article

Detection and Early Warning of Toxic Gases Based on Semiconductor Wireless Sensors

Lin Feng,[1] Jian Wang [ID],[1] Ye Chen,[1] and Chao Ding[2]

[1]*State Key Laboratory of Fire Science, University of Science and Technology of China, Hefei 230026, China*
[2]*School of Environment and Energy Engineering, Anhui Jianzhu University, Hefei 230601, China*

Correspondence should be addressed to Jian Wang; wangj@ustc.edu.cn

This paper studies a semiconductor wireless sensor system, which is composed of a semiconductor wireless sensor sampling circuit, gas-sensitive signal alarm and wireless transmitting circuit, and wireless radio frequency signal receiving circuit. The system is suitable for wireless monitoring of hydrogen fluoride gas in chemical plants. The hydrogen fluoride gas sensor is designed, integrated, and classified according to the polarity and size of the sensor output signal. The signal processing circuit of the sensor output signal is made with an integrated design. This paper developed a simulation experimental system for the wireless monitoring network characteristics of toxic hydrogen fluoride gas and completed the monitoring system's sensor characteristic calibration and accuracy comparison simulation experiment, the communication distance test experiment of the communication system, and the research experiment on the influence of environmental humidity on the sensor characteristics of the monitoring system. In terms of software, the workflow of network nodes has been optimized. Since the structure of the wireless sensor network is not exactly the same in different application fields, the toxic gas monitoring system based on wireless sensor networks must focus on extending the network's life cycle. Without affecting the normal operation of the system, distributed compressed sensing can greatly extend the service life of the system. Therefore, this subject combines the compressed sensing technology developed in recent years with the air monitoring system for the processing of transmission data, in order to achieve the purpose of further reducing the energy consumption of the system. The simulation experiment demonstrated that the lmF neural network combined with gas sensor array technology can realize qualitative identification, quantitative analysis of single gas, and quantitative analysis of mixed combustible gas. The research work in this area also provides a new way to further combine the miniature hydrogen fluoride gas sensor unit with sensor technology, integrate the hydrogen fluoride gas sensor unit and the electronic tag, and expand the wireless application of the gas sensor.

1. Introduction

Toxic chemical leaks caused by chemical plant explosion accidents, forest fires, etc. could result in severe damage to human beings and be disastrous for the environment. With the development of science and technology, gas monitoring technology has been further developed, and various real-time and continuous detection equipment has appeared [1–3]. The increasing attention to hydrogen fluoride leak requires the expansion of the scope of the monitoring environment. It is difficult for a single monitoring point to cover these monitoring environments and monitor the measured environment in real time, so a preliminary environmental monitoring network has

emerged [4]. Based on the wired system, data of each monitoring point are transmitted to the central control platform to realize online monitoring. It is very important to monitor the toxic gas dispersion and improve the capabilities of disaster response. And to understand the changing trend of toxic and harmful hydrogen fluoride gas content in the environment, we provide very important data and basis for environmental monitoring such as industrial environment and people's living environment [5–7].

For the measurement of toxic gases, commonly used methods mainly include analytical chemistry methods, semiconductor gas-sensitive detection methods, contact combustion detection methods, spectral analysis methods,

electrochemical methods, etc. [8–10]. Among them, the electrochemical measurement method has a fast response speed, can realize online detection, and has good anti-interference to nonmeasured hydrogen fluoride gas, and the produced probe has a small volume and is easy to integrate. Therefore, the system studied in this paper adopts the electrochemical measurement method. Regarding the deficiencies of the above-mentioned equipment, how to realize economic, intelligent, and large-scale layout of monitoring points and realize the networked environmental monitoring has become a hot topic of research [11]. With the development of wireless communication technology, it is possible to solve these problems. At present, the gas detection equipment available on the market is only developed for single gas detection, and they transmit data through wires. If it is necessary to detect a variety of gases, the integration of these gas detection equipment will be very large. Moreover, for the monitoring environment where a large number of monitoring points need to be arranged, the wire transmission data layout is very troublesome and costly [12].

In response to this reality, based on the technology of sensors, wireless communication and wireless sensor networks, and other system-related technologies, this article has carried out a more detailed study on the toxic gas monitoring system and proposed a set of toxic gas monitoring systems based on the wireless sensor network. This paper proposes two design methods of gas sensor signal sampling circuits that individually sample the key points of the hydrogen fluoride gas state. The sampling output signal of the circuit jumps only when the specific hydrogen fluoride gas concentration in the environment to be measured reaches the prewarning concentration value. The control unit alarms by identifying the change in the output signal of the gas sensor sampling circuit. We integrate the design of wireless communication nodes and hydrogen fluoride gas sensors to realize wireless node communication for sensor data transmission and control command transmission and establish a central computer control platform to realize the selection of monitoring points and sensors and the automatic processing of measurement signals. A reasonable gas sensor conditioning circuit is designed in the article. In terms of software, the workflow of network nodes is optimized. The characteristic of the sampling circuit is that it can identify the status information of the hydrogen fluoride gas without continuous data collection and data analysis for the hydrogen fluoride gas sensor, and the detection speed is fast; at the same time, the circuit structure is simple, the components are few, and the cost is low, which is convenient for the hydrogen fluoride gas sensor. The gas sensor sampling circuit is integrated with various wireless sensor systems such as electronic tags.

2. Related Works

When a single sensor cannot make a good selection of hydrogen fluoride gas, it is necessary to use an array of hydrogen fluoride gas sensors to solve the problem of identifying the type of hydrogen fluoride gas. The increase in system power consumption brought about by a considerable number of sensors makes its application conditions very harsh, which greatly limits the application range of sensor arrays. Therefore, reducing power consumption has become one of the important core tasks of hydrogen fluoride gas sensor research [13].

Nikolic et al. [14] pioneered a semiconductor hydrogen fluoride gas sensor based on a microhotplate heating structure. The microhotplate of the sensor adopts a "sandwich" structure; that is, the upper and lower layers are made of SiO_2, and the middle layer is made of Si_3N_4. By etching the silicon substrate at the lower part of the microhotplate, the heat dissipation path of the microhotplate is reduced, and the power required to reach the predetermined operating temperature can be reduced. After experimental calculations, a power consumption of about 100 mW can ensure that the microhotplate is heated to 300°C. It can be seen that the application of MEMS technology in the sensor field has greatly reduced the power consumption of the microhotplate hydrogen fluoride gas sensor. Manes et al. [15] designed for the first time a microhotplate hydrogen fluoride gas sensor made of a CMOS compatible process. This initiative has laid a solid foundation for the realization of a highly integrated hydrogen fluoride gas sensor. The microhotplate is mainly composed of a SiO_2 dielectric film for electrical and thermal isolation, a suspended dielectric film supported by four arms, and a polysilicon heater. The microhotplate can be heated to above 300°C in just a few milliseconds, and the power consumption is less than 50 mW, so it has a good practical application prospect. Jo and Khan [16] combined multiplexers and differential readout circuits with integrated gas sensors and successfully developed a 4×4 tin dioxide integrated hydrogen fluoride gas sensor array. The microhotplate adopts a classic bridge structure, and its platinum snake-shaped heating circuit is embedded in a multilayer composite dielectric film. The differential readout circuit in the array can distinguish the resistance value of the gas-sensitive membrane within the range of 20 M. When the operating temperature is 300°C, its power consumption is only 16 mW.

Kim et al. [17] developed a CMOS compatible process microhotplate hydrogen fluoride gas sensor. In this sensor, metal tungsten is used as the heating resistance wire. At the same time, taking into account the reduction of heat dissipation of the microhotplate, the front body silicon corrosion suspension technology is adopted. The sensor can be heated to 300°C within 8 ms, and power consumption is only 19 mW and has a good response to 50 ppm ethanol hydrogen fluoride gas. In order to reduce power consumption, Zhang et al. [18] designed an optimized heating structure for the heating part of the semiconductor gas sensor. The heating structure only needs about 2 mW of power consumption to maintain the temperature at about 300°C. At the same time, the research group designed a pulse heating mode for the optimized heating structure and reduced the power consumption of the sensor heating part to about 350 μW. The system is based on WSN technology. In the event of a fire, we report to relevant personnel in time [19]. Based on WSN and GSM technology, some scholars have designed a set of data based on a solar power supply

and wireless sensor network hydrogen fluoride gas monitoring system and home security alarm system. This system could play an important role in antitheft and combustible hydrogen fluoride gas leakage and fire protection monitoring when a dangerous situation occurs. It sends an alarm message to the homeowner's mobile phone to ensure the safety of the family [20]. Some researchers have designed a water quality monitoring system, which is also based on WSN technology. The pH value, pollution level, temperature, and turbidity of water can be monitored, so that the environmental protection department can provide real-time guidance for industries such as industry, plantation, and aquaculture that depend on local water quality conditions [21–23].

3. The Detection and Early Warning Model Construction of Poisonous Gases Based on Semiconductor Wireless Sensors

3.1. Levels of Semiconductor Wireless Sensor Networks.
The hydrogen fluoride gas wireless monitoring network is mainly composed of monitoring nodes that can detect hydrogen fluoride gas and a central control platform that can receive data from various monitoring points and send monitoring commands. The monitoring node is an important part of the system, which includes the hydrogen fluoride gas sensor module, sensor working circuit, signal processing circuit, and wireless module. Figure 1 shows the semiconductor wireless sensor network topology.

Its working principle is as follows. The central control platform is initialized, and a wireless network is constructed. After each monitoring point joins the wireless network, the central control platform sends a monitoring command. After the monitoring point receives the command, the hydrogen fluoride gas sensor starts to collect gas concentration information. After the output signal is processed by the signal conditioning circuit, the data is sent to the corresponding wireless module, and the wireless module sends the data to the central control platform. The machine of the central control platform processes the received data and displays the concentration of various hydrogen fluoride gases in real time.

$$\alpha = (i, j, k) = (i(1), i(2); j(1), j(2); k(1), k(2)), \quad i, j, k \in Z. \tag{1}$$

The working circuit of the hydrogen fluoride gas sensor is to make each sensor work normally, which converts the current signal output by the sensor into a voltage signal. The signal conditioning circuit is classified according to the polarity and size of the output signal of the sensor, and the output signal of the sensor of the same type is amplified to prepare it for entering the single-chip microcomputer. The wireless network communication system is to realize the wireless data transmission from the monitoring point to the central control platform. The computer central control platform is to realize the intelligent control of monitoring

points and automatic processing of measurement signals.

$$\begin{cases} u(x, y) = \bar{u}(x, y), \\ v(x, y) = \bar{v}(x, y), \end{cases} \quad \bar{x}, \bar{y} \in S(\bar{u}). \tag{2}$$

A semiconductor element made of metal oxide or metal semiconductor oxide material is put into the gas to be measured and interacts with hydrogen fluoride gas to produce surface adsorption or reaction, which causes the characteristic change of the resistive element to measure the concentration of hydrogen fluoride gas. We put the sensor into the measured hydrogen fluoride gas, and the resistance value of the sensor will change with the concentration of hydrogen fluoride gas. It has the advantages of high sensitivity, convenient operation, small size, low cost, and short response time and recovery time.

$$\begin{cases} \phi(i, 1) = \dfrac{[\phi^+(i) + \phi^-(i)]}{2}, \\ \phi(i, 2) = \dfrac{[\phi^+(i) - \phi^-(i)]}{2}. \end{cases} \tag{3}$$

The high molecular hydrogen fluoride gas wireless sensor mainly uses its resistance, material surface acoustic wave propagation speed, frequency, material weight, and other physical properties to change with the specific gas encountered to realize gas detection.

$$\min TV(u) - \text{s.t.} |f - u(i, j)|_t^2 = \sigma^2. \tag{4}$$

According to the different gas-sensing characteristics of the materials used, this type of sensor can be divided into polymer resistance gas sensors, concentration electric gas sensors, surface acoustic wave gas sensors, and quartz vibrator gas sensors. The surface acoustic wave gas sensor is based on the speed or frequency of the sound wave propagating on the surface of the material, which changes as the gas-sensitive material absorbs the gas. The gas concentration can be detected by measuring the speed or frequency of the sound wave.

$$\widehat{s} = \frac{1}{(k(1) \times k(2))} \times \sum_{i=0}^{k1} \sum_{j=0}^{k2} s(i, j) \times p(x, t). \tag{5}$$

The nonresistive semiconductor hydrogen fluoride gas sensor uses some physical benefits and device characteristics to detect hydrogen fluoride gas, for example, the volt-ampere characteristic of the Schottky diode and the change characteristic of threshold voltage of the semiconductor field effect tube, the gas sensor made by using these two characteristics, and its current or voltage changes with the content of hydrogen fluoride gas. This type of sensor is mainly used to detect hydrogen fluoride gas.

3.2. Distribution of Early Warning Circuit Nodes.
The wireless communication node is mainly composed of a processor module, a wireless communication module, and an energy
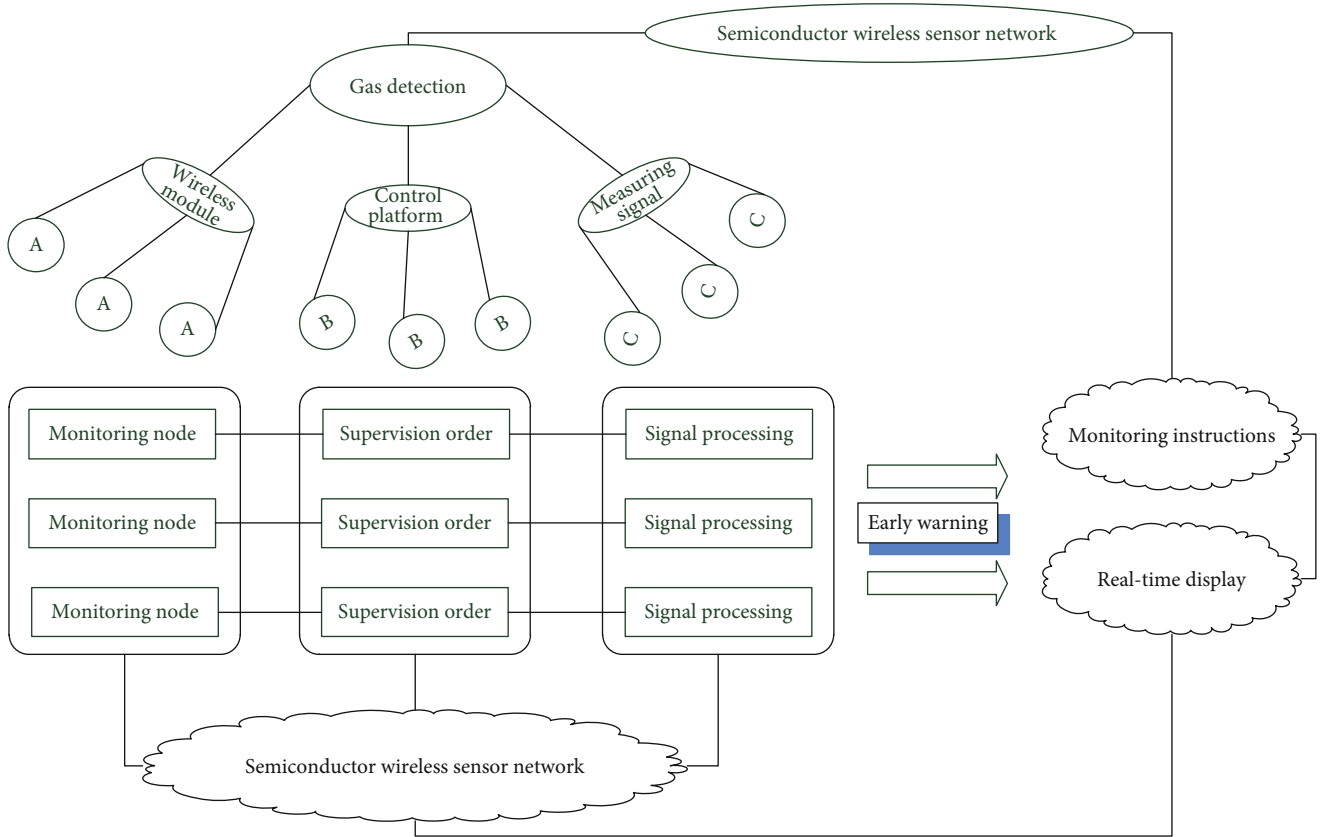
Error! No bookmark name given.

FIGURE 1: Semiconductor wireless sensor network topology.

supply module. In the entire system, the sensor is the main device that collects the type and concentration of hydrogen fluoride gas. It is one of the cores of the entire system, and its choice directly determines the entire system's recognition ability, recognition range, service life, and so on.

$$E(f(x)) = \frac{\sum_{i=1}^{n} w(t) \times f(x(t))}{\sum_{i=1}^{n} w(t)},$$

$$\frac{f(x)p(x \mid t)dx - 1}{n \times \int f(x)p(t \mid x)p(x)dx} = 0$$

(6)

In our system, a variety of different hydrogen fluoride gas sensors are needed. Choosing a suitable sensor combination plays a vital role in improving the performance of the entire system, and the semiconductor gas-sensing detection method is to put a resistive element made of metal oxide or metal semiconductor oxide material into the hydrogen fluoride gas to be measured and interact with the hydrogen fluoride gas to produce surface adsorption or reaction, causing the conductance of the resistive element rate or surface potential change to measure the hydrogen fluoride gas concentration. Table 1 shows the node description of the early warning circuit. Since it is necessary to amplify the sensor signal, if interference is introduced, it is easy to overwhelm the sensor signal or affect the quality of the sensor signal.

TABLE 1: Node description of the early warning circuit.

Node number	Response power (mW)	Working frequency (kHz)
1	7.15	100
2	9.03	110
3	5.97	105
4	5.62	97
5	7.14	104

Therefore, an operational amplifier with high common-mode rejection ratio, low temperature drift, and low offset voltage must be selected. Considering the power consumption factor, the selected amplifier must also be a low-power amplifier.

The processor module is responsible for controlling the operation of the entire sensor node, such as data storage, data A/D conversion, and processing the data collected by itself and data sent by other nodes; the wireless communication module is used to receive and send wireless signals, and the wireless sensor network terminal node performs wireless communication, which mainly includes two parts: radio frequency and baseband. The former provides the air interface for data communication, and the latter mainly provides the physical channel and data packet of the link. The energy

supply module provides the energy required for the operation of the sensor nodes, usually using microbatteries. When there is no toxic hydrogen fluoride gas in the environment or monitoring is not required, the toxic hydrogen fluoride gas wireless monitoring network sends control commands to the monitoring node through the central control platform, so that it turns off the sensor's power supply and stops the sensor from working. The use of multihop transmission here is based on the consideration of communication range or energy saving. The energy value and communication distance of the sink node are slightly stronger than those of the sensor node. It is a bridge between the sensor monitoring area and the external network. Due to the many monitoring points, the intelligent control of the opening and closing of the sensor greatly reduces the power consumption of the entire system. Considering that system monitoring is used not only in large-scale areas but also for some places where the monitoring range is small and does not require wireless data transmission, we consider adding system assistance design. In terms of wired transmission, if the signal is sent in the form of voltage, the signal is transmitted from the sending point to the receiving point through a long transmission line. The voltage signal will form a voltage drop through the output impedance of the sending circuit, the resistance of the transmission line, and other resistances, which is likely to cause the transmission of the signal. If the signal is sent in the form of current, the current provided by the sending circuit is always the desired current regardless of the transmission line resistance and other resistances, and the signal anti-interference ability is greatly improved.

3.3. Hydrogen Fluoride Gas Detection Based on Semiconductor Sensors.

Resistive semiconductor gas-sensing materials have a gas-sensing effect. When a special gas is adsorbed on the surface, the resistivity of the gas-sensitive material will change. Gas-sensitive resistors are made of metal oxide semiconductor materials. Through doping, the selectivity of hydrogen fluoride gas can be increased, and the gas sensitivity can be improved by setting the appropriate working temperature and improving the preparation process. Therefore, the gas sensor is designed by using the impedance characteristics of the metal oxide semiconductor gas sensor. To stabilize the output of v_{out}, we propose to control the gas. The sensitive resistance transducer is combined with the CMOS inverter, so that the high and low levels that fluctuate in a certain range can be converted into stable digital output signals 0 and 1. The gas-sensitive recognition analog recognition unit can be converted to a digital circuit. Therefore, the circuit can be effectively integrated into the storage unit and the control unit, and it is possible to realize the identification, storage, and control of the hydrogen fluoride gas signal. Table 2 shows the design of the hydrogen fluoride gas detection parameter.

The resistance R_x can be designed into a microarray structure, and the array resistances $R_1, R_2 \cdots R_x$ can be designed with different reference resistance values. According to actual use requirements, if you need to test the gas state of different hydrogen fluoride gas concentration points, you can choose different requirements through the digital

TABLE 2: Parameter design of hydrogen fluoride gas detection.

Gas index	Upper limit of concentration (%)	Lower limit of concentration (%)	Proportion
1	1.17	0.65	0.54
2	2.11	0.88	1.21
3	1.89	1.13	0.87
4	1.76	1.31	1.03

control switch. As the reference point, it can be designed into a gas sensor array structure to realize the monitoring of discrete monitoring points for hydrogen fluoride gas. In the low-level phase of the clock, the master-level transmission gate T_2 is turned on, and the gas-sensitive input signal is directly transmitted to the master-level latch output terminal QM. During this period, the slave-level is in the maintenance state, and the bistable circuit feedback maintains its original state. During the rising edge of the clock, the master stage stops sampling the input and the slave stage starts sampling. In the high state of the clock, the slave stage samples the output (QM) of the master stage, and the master stage is in the maintenance state. Since QM remains unchanged during the high level of the clock, the output Q only samples the input gas-sensing signal per cycle once. After the class A gas sensor amplifier is turned on, due to the power consumption of the tertiary tube being very high, after receiving an effective alarm signal, before processing the alarm information, the input voltage of the tertiary tube can be temporarily turned off through the digital switch. In this way, the tertiary tube is cut off and the alarm stops. This design is more flexible and can detect the return characteristics of the hydrogen fluoride gas sensor. If the requirements are not met, the gas-sensitive resistor can be replaced. The inverter has infinite input impedance and low input loss. Through a multistage inverter cascade, the output state can be amplified step by step. By monitoring the final output voltage change, the change of the gas state can be monitored. In addition, this circuit has lower power consumption than class A gas sensors and is more suitable for the power consumption requirements of wireless gas sensor systems.

3.4. Model Parameter Weight Optimization.

In the star-shaped network topology, all terminal monitoring points communicate directly with the central control platform, and there is no need for a network router in the middle. This kind of network topology is only suitable for the monitoring environment less than the maximum communication distance of two nodes. When the monitoring environment is greater than this distance, the central control platform cannot receive the data of each monitoring point. The mesh topology is different from the star topology. It can act as a router in the mesh topology, forwarding data and various control commands. As long as they are within the communication distance of each node, the central control platform can communicate with network routers. This kind of network is very complex, each node needs to maintain a large amount of information, and there is no fixed path in data transmission; the optimal path must be selected according

to the situation, and the construction is very difficult. When the potential is close to and the bias voltage is 0, the bottom current and noise are the smallest. When the sensor detects low-concentration gas, since the response current is small, it is desirable that the bottom current and bias current are as small as possible, so the bias voltage is grounded. The clustered network topology is an upgraded version of the star network topology. This network topology is composed of multiple star topology structures. In the clustered network topology, the data and command transmission paths are clear, and the functions of each wireless communication node in the network are clear. Compared with the mesh topology, the structure is simpler. Compared with the star network topology, it can realize the functions of network routing to forward data and control commands, which greatly increases the coverage area of the network. Figure 2 shows the topology of the semiconductor wireless sensor circuit.

First, the sensor nodes are deployed in the monitoring area (sensor field), usually by manual deployment or aircraft dissemination or even by means of rockets. Obviously, this kind of deployment has strong randomness, and the number of sensor nodes deployed each time is relatively large. Secondly, when the sensor nodes deployed in the monitoring area are successfully awakened, they form a network in a self-organizing manner and transfer data to the nodes through multihop relays. Finally, the data in the entire area is transmitted to the remote-control center for centralized processing by means of the convergence node link. At the same time, the user's query request can be sent to the sensor network. The sensitive element and the conversion element constitute the basic part of the sensor, and they, respectively, complete the two basic functions of detection and conversion. It is worth noting that not all sensors can be clearly divided into two parts: sensitive components and conversion components, such as semiconductor gas or temperature sensors, thermocouples, piezoelectric crystals, and optoelectronic devices.

4. Application and Analysis of the Detection and Early Warning Model of Toxic Gases Based on Semiconductor Wireless Sensors

4.1. Wireless Sensor Data Processing. The working process of the poisonous gas monitoring system based on the wireless sensor network is as follows: the sensor nodes arranged in the monitoring area will collect the data about the poisonous gas to the gateway node through the multihop ad hoc network, and the gateway node will collect the data to the gateway node. The data is transmitted to the Internet network through the GPRS network, and then, the monitoring center realizes real-time monitoring through the Internet network. Figure 3 shows the fan-shaped distribution of wireless sensor modules. The model of the GPRS module selected by this system is ZHD121AX GPRS DTU, which is the most important product of the ZZHD1X series of DTUs. It can enable non-IP system equipment to easily connect to the GPRS network and the Internet through the serial port. The GPRS

module is embedded with a TCP/IP protocol stack and adopts a general RS232/RS485/TTL interface. At the same time, the interactive interface of the GPRS module is easy to operate.

The node needs to be connected to the router when it is working, and the router is connected to the computer. At this time, the node and the computer are in the same local area network, and the data can be uploaded to the LabVIEW platform. The NB-IoT node introduces the Internet of thi5ngs card provided by National Telecom. This is connected to a radio frequency antenna to upload data to the developer platform through the NB-IoT network. Before each communication is completed, the gateway node will send a message requesting sleep to the data relay. After the data relay communicates with the upper computer, it will set up the entire network according to the requirements of the upper computer. The response of the sensor will still increase after it is removed from the test chamber. Under normal circumstances, when the sensor is removed from the gas to be measured, the response of the sensor will immediately begin to decrease because the reactant that produces the response does not exist. In the wireless data transmission part of the transformer online monitoring system, the coordinator node is connected to many terminal nodes, and the parameter data information collected by the terminal nodes is transmitted to the monitoring terminal, so that the coordinator node plays the role of the center, and many terminal nodes are connected to it, so the matrix use of the keyboard is necessary.

4.2. The Hardware Simulation Design of the Detection System. This section will simulate the actual sensing data in the WSN-based toxic gas monitoring system. The simulation data uses the buffer voltage data in the environmental monitoring data project. 100 nodes simultaneously detect the buffer voltage, and the buffer voltage changes over time. The amplitude changes slowly, and the geographical locations of the nodes are relatively close, so there is a correlation between these perception data. Now, we suppose that there are multiple signal groups, the number of signals contained in each signal group is $J = (1, 5, 10, 40)$, the length of each signal is $N = 50$, and the sparsity is $K = 5$. Since the difference between the data perceived by 100 nodes at the same time is small, it can be assumed that it is sparse in the Fourier domain. The connection method of the microhotplate hydrogen fluoride gas sensor in the two nodes is as described in the text. The series resistance R is 510 k. To prevent the wireless signal from being shielded, the node is placed in a paper box, and 40 ppm hydrogen fluoride gas and 60 ppm hydrogen fluoride gas are, respectively, introduced. We set an alarm when the hydrogen fluoride gas concentration is greater than 55 ppm. Figure 4 shows the line graph of the hydrogen fluoride concentration detected by wireless sensing. The test data was extracted on the LabVIEW platform and the National Internet of Things development platform, and the results are as follows.

As the concentration of hydrogen fluoride gas increases, the gas-sensitive resistance decreases, which will cause the gas-sensitive voltage signal to rise. It can be seen that the
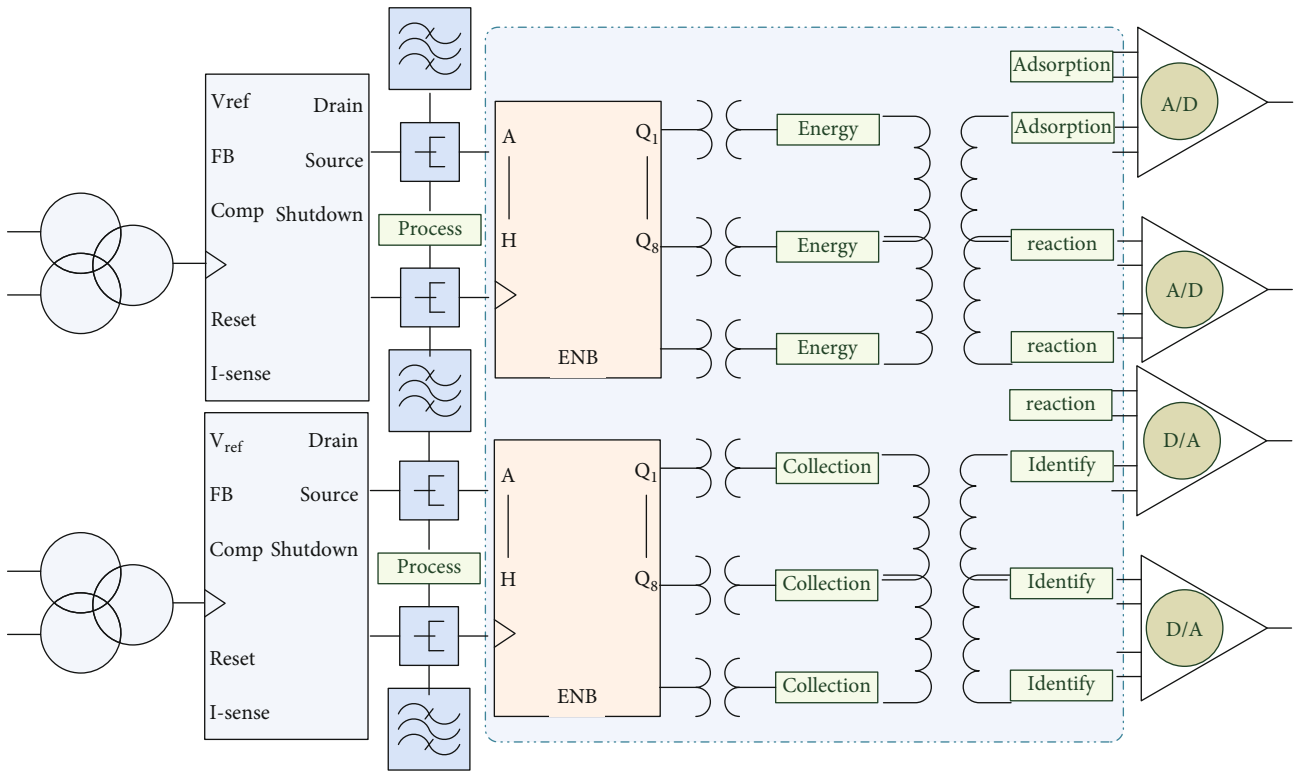
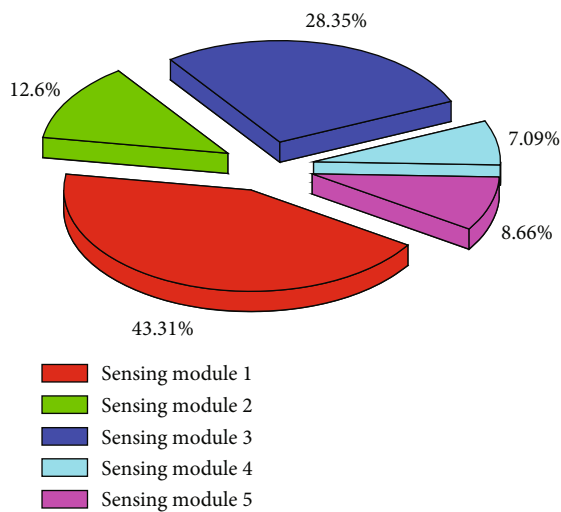FIGURE 2: Semiconductor wireless sensor circuit topology.

FIGURE 3: Fan-shaped distribution diagram of the proportion of wireless sensor modules.

gas-sensitive voltage signals collected by the two nodes are close to the same, increasing with the increase in the hydrogen fluoride gas concentration. At the same time, when the hydrogen fluoride gas concentration is greater than 55 ppm, the node immediately reports data and changes the reporting frequency to 1 min. When the hydrogen fluoride gas concentration is less than 55 ppm, the frequency of the node reporting data is changed to reporting data once every 10 minutes. Since TLC27C2L uses 5 V power supply and the power supply of the system is 12 V, it is necessary

to perform power conversion to obtain a 5 V voltage. The stability and accuracy of the op amp voltage directly affect the stability of the op amp and the stability of the output signal, so we must choose a high-precision power conversion chip and we must do a good job of anti-interference processing. According to these principles, we choose LM336. It is a precision 5 V shunt regulator diode integrated circuit. Since the high-speed reference has a short start-up time and remains in a low-power state when ADC conversion is not in progress, the use of a high-speed reference will result in lower overall power consumption. Based on the above points, the voltage reference selects the internal 1.65 V high-speed reference voltage. These IC voltage references can work like 5 V Zener diodes with a low temperature coefficient, with a dynamic impedance of 0.6, and the third terminal provided on the chip can easily fine-tune the reference voltage and temperature coefficient. The devices of this series are suitable for precision 5 V power supply and low voltage reference for a digital voltmeter, power supply, or operational amplifier.

From the above comparison, we can see that the power consumption of the processor and sensor module is lower and the power consumption of the communication module (sending, receiving, and idle) is higher. On the premise of not affecting the performance of the system, reducing the data transmission volume of the communication module can naturally reduce the time for the communication module to send and receive data, thereby achieving the goal of reducing the energy consumption of the communication module. Figure 5 shows the linear fit of the average energy consumption of the wireless sensor network. When the
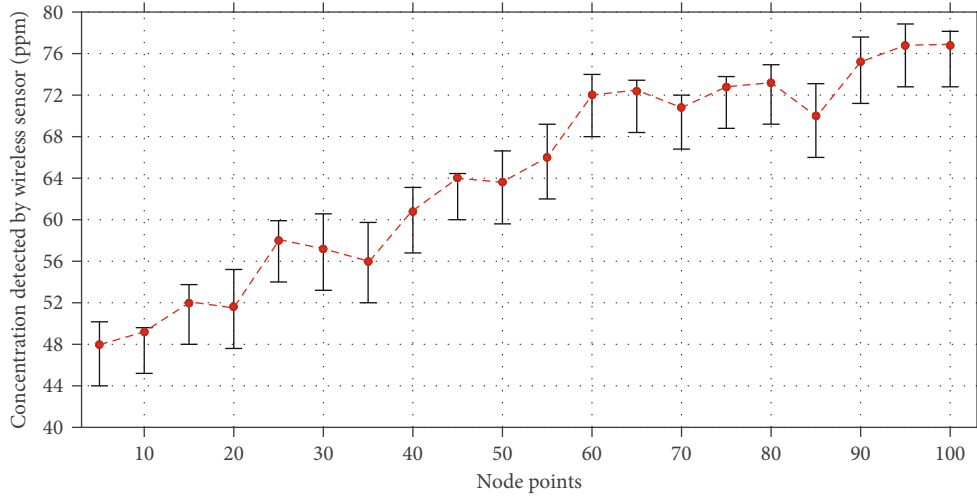
FIGURE 4: Line graph of hydrogen fluoride concentration detected by a wireless sensor.
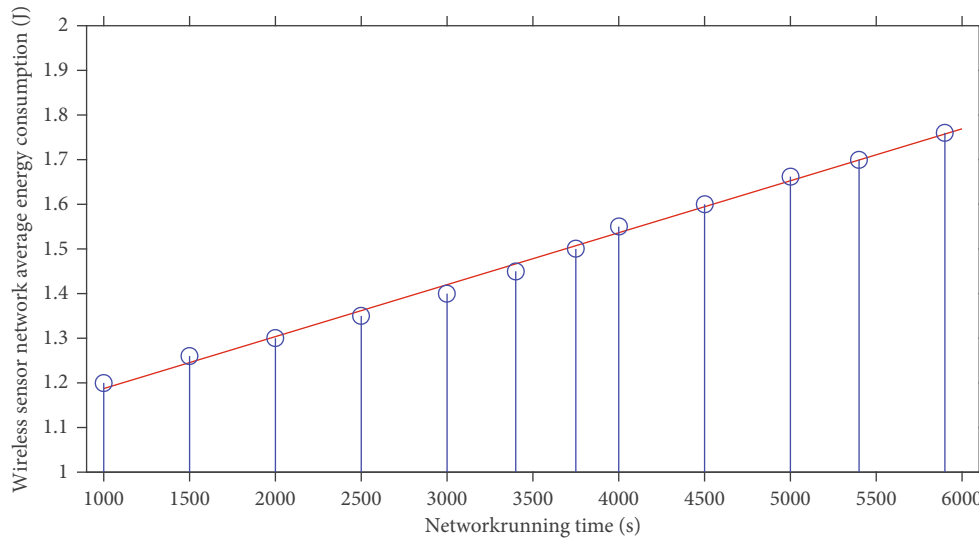

FIGURE 5: Linear fitting of average energy consumption of the wireless sensor network.

network runs for 1000 s, the average energy consumption of the nodes of the original algorithm is about 1.8 J, while the average energy consumption of the nodes of the algorithm in this paper is less than 1.6 J. At the same time, when the original algorithm runs for 1250 s, the nodes are almost exhausted, and the algorithm in this paper runs for about 2000 s before using up all the energy. Therefore, during the entire running time of the network, the average energy consumption of the algorithm nodes in this paper is significantly less than that of the original algorithm; that is, the algorithm in this paper has a better energy-saving effect than the original algorithm. Through simulation verification, in the data transmission of the toxic gas monitoring system based on the wireless sensor network, the superiority of compressed sensing and distributed compressed sensing is given. Without affecting the normal operation of the system, distributed compressed sensing can greatly extend the service life of the system.

4.3. Example Application and Analysis. The concentration of the hydrogen fluoride gas sample used in the simulation experiment in this section is limited to 40-4000 ppm, and the concentration interval is 20 ppm. Among them, 1200 samples are selected as the training samples of the wireless sensor network, and the remaining 131 samples are used as the test samples. Due to the large number of test samples, only 20 of the test result data are displayed here. Because the wireless module sends data at an interval of about 10 minutes, the length of the sent data is about 11 kbps and the wireless transmission rate is 16 Mbps. It only takes about milliseconds for the wireless module to send data once, so the average power consumption of the wireless module is approximately equal to its sleep power consumption. Figure 6 shows the data transmission rate comparison of the wireless sensor network. The sampling module only samples 5 times in the cycle, so the working time of the sampling module and impedance matching circuit cycle is about 50 μs. The pulse heating module is always working
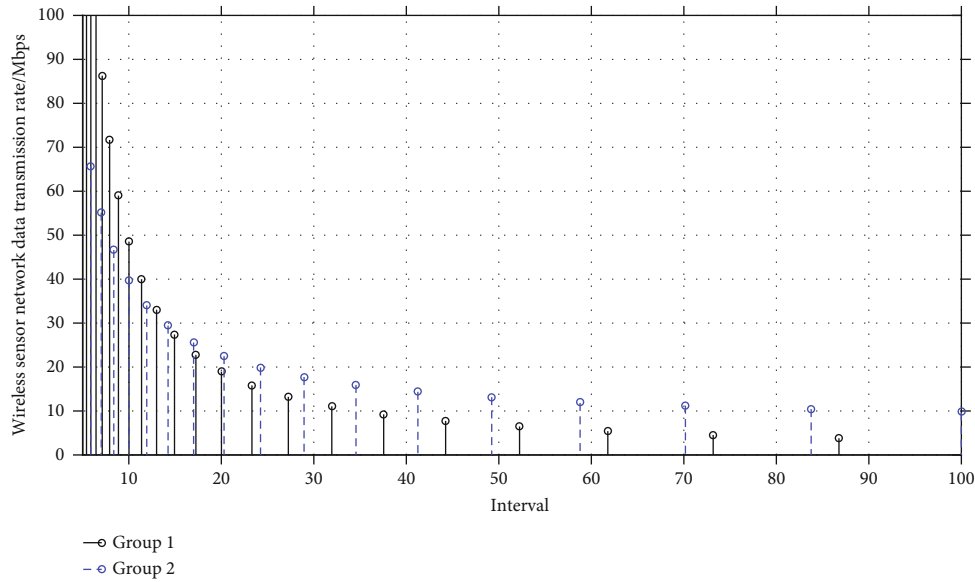
FIGURE 6: Comparison of the data transmission rate of the wireless sensor network.
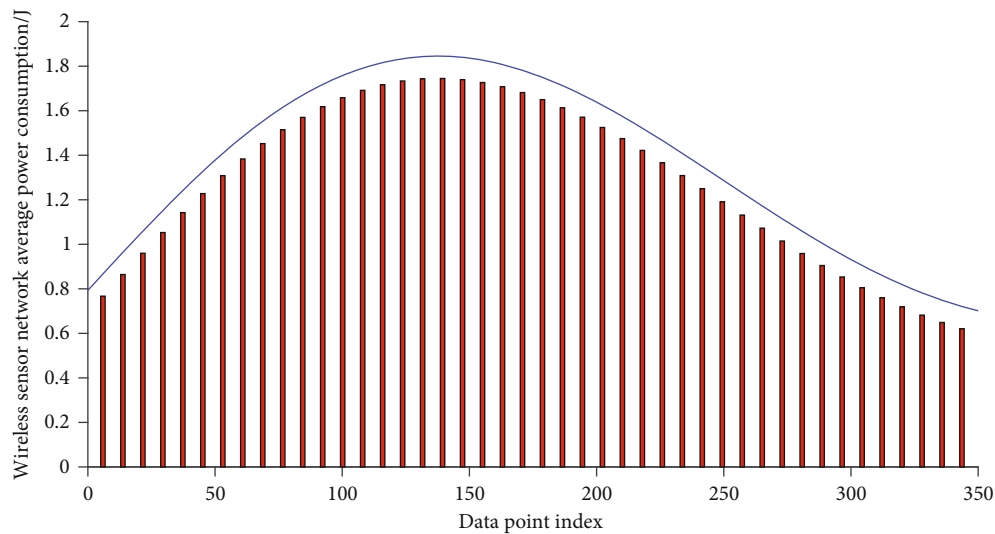

FIGURE 7: Bar graph of average power consumption of the wireless sensor network.

during the heating phase, so the working time in the cycle is 2 s. Each node is allocated to 5 subzones according to the set area number. In each zone, the nodes are randomly deployed, and the position will not be adjusted after deployment. The simulation time is 2500 s. Throughout the simulation process, the capacity consumed by each sensor node and the number of surviving nodes are recorded.

Compared with others, the CC3200 module, heating module, and sensor module consume the most power, because the CC3200 integrates a wireless module and consumes a lot of power. However, because the module has a very short working time in the node, the average power consumption is still relatively small. The total power consumption of the node is the sum of the average power consumption of each module, about 1.01 mW. Compared with ordinary Wi-Fi nodes (power consumption is about tens of milliwatts), it is reduced to about 1/20 of the original.

It can be seen that the power consumption of each module of the node designed with NB-IoT is very low, especially the wireless and processor modules. Relatively speaking, the average power consumption of the hydrogen fluoride gas sensor is the largest, followed by the heating module, and that of the power supply and wireless module is the lowest. Since multihop routing and forwarding are common methods of internal communication in wireless sensor networks, the connectivity of the network will affect the information exchange between sensor nodes, so it needs to be considered in the process of considering some coverage issues. Therefore, the power consumption of the hydrogen fluoride gas sensor and the heating module can be further reduced in the follow-up. Therefore, the wireless node developed in conjunction with NB-IoT is about 1/40 of the ordinary node. Figure 7 shows the histogram of the average power consumption of the wireless sensor network.

The experiment selected transformer partial discharge and hydrogen fluoride gas as monitoring parameters to construct an online monitoring model of a wireless sensor network. The normalized power spectrum content of the three frequency bands was selected as the first three variables of the input vector, and a tin dioxide semiconductor was also selected. The gas sensor measures the relative percentages of the seven faulty hydrogen fluoride gases of the transformer as the remaining seven variables of the input vector, so that there are ten input nodes in the network, and the output vector is selected as the fault code corresponding to the four fault types. Then, the trial-and-error method is used to determine that the number of nodes in the 30 hidden layers is reasonable, and the learning and training of the network are realized through learning samples. We can see that in the same running time, the number of surviving nodes using this algorithm is more than using the original algorithm. In the original algorithm, when the network runs for more than 1500 s, most of the nodes are dead, but with the algorithm in this paper, most of the nodes die when it runs for about 2250 s. Therefore, the survival rate of nodes using the algorithm in this paper is significantly higher than that in the original algorithm. The results show that both nodes can complete the functions of timed heating of sensors and data collection, wireless uploading, and network access. At the same time, when encountering hydrogen fluoride gas that exceeds the set threshold concentration, it can report data in time and light up the alarm.

5. Conclusion

For the monitoring of hydrogen fluoride gas in a large environment, monitoring points must be arranged at different locations to form a monitoring network. If we use wired data to transmit data, the cost is higher and the wiring is very troublesome. In some places, wired monitoring points may be difficult to achieve. In view of these shortcomings and the characteristics of wireless sensor networks, this paper needs to design a wireless monitoring network. This article realized the design of the wireless alarm module circuit composed of the gas sensor monitoring circuit and the wireless transmitting circuit, which completed the communication mode of the microcontroller and the radio frequency chip, as well as the design of the interface circuit and the power supply circuit. The key radio frequency parameters such as the working frequency band and transmit power of the radio frequency chip were selected. On the basis of compressed sensing theory, the distributed compressed sensing theory which has great advantages in signal group processing is further introduced. At the same time, this topic analyzes the energy consumption model of the node to prepare for the software energy consumption simulation. We use MATLAB software to verify the feasibility of these two algorithms in data transmission based on the wireless sensor network for the toxic gas monitoring system from the perspective of simulation. Using SILICON's WDS simulation software and IDE software, the RF parameters in the system and the microcontroller's register initialization parameters were set, and the program code was generated. In the end, this paper

designs the overall system of the semiconductor wireless sensor based on the above two gas sensor sampling circuits, the microcontroller, and the UHF radio frequency chip. The key parameters of the radio frequency circuit are tested on the demo board, and the radio frequency signal transmission distance can be greater than 10 m.

Data Availability

The data used to support the findings of this study are available from the corresponding author upon request.

Conflicts of Interest

We declare that there is no conflict of interest.

Acknowledgments

References

[1] P. V. M. Deshmukh, D. M. Adat, B. P. Ladgaonakar, and S. K. Tilekar, "Designing of an embedded system for wireless sensor network for hazardous gas leakage control for industrial application," *i-Manager's Journal on Embedded Systems*, vol. 6, no. 2, p. 175, 2018.

[2] W. Rahmaniar and A. Wicaksono, "Design and implementation of a mobile robot for carbon monoxide monitoring," *Journal of Robotics and Control (JRC)*, vol. 2, no. 1, pp. 4–6, 2021.

[3] M. F. Farooqui and A. Shamim, "3D inkjet printed disposable environmental monitoring wireless sensor node," in *International Microwave Symposium*, pp. 1379–1382, Honolulu, HI, USA, 2017.

[4] Y. Fan, X. Zhu, H. Sui, H. Sun, and Z. Wang, "Design and application of toxic and harmful gas monitoring system in fire fighting," *Sensors*, vol. 19, no. 2, p. 369, 2019.

[5] M. F. Farooqui, M. A. Karimi, K. N. Salama, and A. Shamim, "3D-printed disposable wireless sensors with integrated microelectronics for large area environmental monitoring," *Advanced Materials Technologies*, vol. 2, no. 8, article 1700051, 2017.

[6] S. Suryono, B. Surarso, R. Saputra, and S. Sudalma, "Real-time decision support system for carbon monoxide threat warning using online expert system," *Journal of Applied Engineering Science*, vol. 17, no. 1, pp. 18–25, 2019.

[7] F. Aliyu and T. Sheltami, "Development of an energy-harvesting toxic and combustible gas sensor for oil and gas industries," *Sensors and Actuators B: Chemical*, vol. 231, pp. 265–275, 2016.

[8] X. Qiu, Y. Wei, N. Li et al., "Development of an early warning fire detection system based on a laser spectroscopic carbon monoxide sensor using a 32-bit system-on-chip," *Infrared Physics & Technology*, vol. 96, pp. 44–51, 2019.

[9] S. Moorat, H. Pervaiz, F. Soomro, and M. M. Mughal, "Development of an Arduino based device for early detection of gas leakage in hospitals & industries," *University of Sindh Journal of Information and Communication Technology*, vol. 2, no. 1, pp. 68–72, 2018.

[10] A. Gazis and E. Katsiri, "Smart home IoT sensors: principles and applications-a review of low-cost and low-power solutions," *International Journal on Engineering Technologies and Informatics*, vol. 2, no. 1, pp. 19–23, 2021.

[11] F. Saeed, A. Paul, A. Rehman, W. Hong, and H. Seo, "IoT-based intelligent modeling of smart home environment for fire prevention and safety," *Journal of Sensor and Actuator Networks*, vol. 7, no. 1, p. 11, 2018.

[12] V. D. Ambeth Kumar, D. Elangovan, G. Gokul, J. Praveen Samuel, and V. D. Ashok Kumar, "Wireless sensing system for the welfare of sewer labourers," *Healthcare Technology Letters*, vol. 5, no. 4, pp. 107–112, 2018.

[13] C. K. Amuzuvi and P. K. Ashilevi, "Making the use and storage of liquefied petroleum gs safe by using electronic gas leakage detectors–opportunities and threats," *Ghana Journal of Technology*, vol. 1, no. 1, pp. 12–20, 2016.

[14] M. V. Nikolic, V. Milovanovic, Z. Z. Vasiljevic, and Z. Stamenkovic, "Semiconductor gas sensors: materials, technology, design, and application," *Sensors*, vol. 20, no. 22, p. 6694, 2020.

[15] G. Manes, G. Collodi, L. Gelpi et al., "Realtime gas emission monitoring at hazardous sites using a distributed point-source sensing infrastructure," *Sensors*, vol. 16, no. 1, p. 121, 2016.

[16] B. W. Jo and R. M. A. Khan, "An Internet of things system for underground mine air quality pollutant prediction based on azure machine learning," *Sensors*, vol. 18, no. 4, p. 930, 2018.

[17] D. Kim, S. J. Kim, and S. Kim, "Development of novel complementary metal-oxide semiconductor-based colorimetric sensors for rapid detection of industrially important gases," *Sensors and Actuators B: Chemical*, vol. 265, pp. 600–608, 2018.

[18] C. Zhang, Y. Fu, F. Deng, B. Wei, and X. Wu, "Methane gas density monitoring and predicting based on RFID sensor tag and CNN algorithm," *Electronics*, vol. 7, no. 5, p. 69, 2018.

[19] J. P. Devadhasan, D. Kim, D. Y. Lee, and S. Kim, "Smartphone coupled handheld array reader for real-time toxic gas detection," *Analytica Chimica Acta*, vol. 984, pp. 168–176, 2017.

[20] X. Chen, T. Wang, Y. Han et al., "Wearable NO_2 sensing and wireless application based on ZnS nanoparticles/nitrogen-doped reduced graphene oxide," *Sensors and Actuators B: Chemical*, vol. 345, article 130423, 2021.

[21] J. Palacín, D. Martínez, E. Clotet et al., "Application of an array of metal-oxide semiconductor gas sensors in an assistant personal robot for early gas leak detection," *Sensors*, vol. 19, no. 9, p. 1957, 2019.

[22] X. Gong, L. Duan, X. Chen, and J. Zhang, "When social network effect meets congestion effect in wireless networks: data usage equilibrium and optimal pricing," *IEEE Journal on Selected Areas in Communications*, vol. 35, no. 2, pp. 449–462, 2017.

[23] S. H. Jeong, B. Son, and J. H. Lee, "Asymptotic performance analysis of the MUSIC algorithm for direction-of-arrival estimation," *Applied Sciences*, vol. 10, no. 6, p. 2063, 2020.

Research Article

A Generalizable Sample Resolution Augmentation Method for Mechanical Fault Diagnosis Based on ESPCN

Zhenyun Chu [iD],[1] **Shanshan Ji** [iD],[1] **Jinrui Wang** [iD],[1] **Xiaoyu Wang** [iD],[1] **Zongzhen Zhang** [iD],[1] **Xuefeng Zhao** [iD],[2] **and Baokun Han** [iD][1]

[1]*College of Mechanical and Electronic Engineering, Shandong University of Science and Technology, Qingdao 266590, China*
[2]*Yantai Zhenghai Hi-Tech Co., Ltd., Yantai 264000, China*

Correspondence should be addressed to Shanshan Ji; jiss33@163.com and Jinrui Wang; wangjr33@163.com

Data augmentation has become a hot topic in the field of mechanical intelligent fault diagnosis. It can expand the limited training dataset by generating simulated samples, but there is still no effective method augmenting the resolution of low resolution sample. In this paper, a simple algorithm, namely, efficient subpixel convolutional neural network (ESPCN), is proposed to solve this deficiency. The ESPCN model performs the arrange operation on the raw low resolution data through the subpixel layer and outputs the result of four-channel multifeature maps. Then, the sample resolution is increased to four times compared with the raw low resolution sample. Finally, the generated high resolution dataset is employed to train the stacked autoencoders (SAE) for fault classification, and the raw high resolution dataset is used for testing. Two fault diagnosis cases with different sample dimensions and rotating speeds are set up to simulate the low resolution situation, and the experimental results verify the feasibility of the proposed algorithm.

1. Introduction

Mechanical fault diagnosis has entered the age of artificial intelligence as technology rapidly increases [1, 2]. Meanwhile, the development of intelligent fault diagnosis cannot be separated from the support of enough measured vibration signal. When a part of a rotating machine has a local defect, a pulse with a short duration will be generated, and the vibration signal will show the fault feature of amplitude modulation [3, 4]. The vibration signal measured from the surface of the machinery consists of many vibrating parts, such as the rotation of bearings and the meshing of gears [5]. Thus, vibration signal analysis is a useful technique for mechanical fault diagnosis.

However, the phenomenon of insufficient samples occurs frequently in practical application scenarios. Therefore, many researchers focus on using deep learning algorithms such as generative adversarial networks (GAN) [6] to increase the number of raw samples. Zhou et al. [7] proposed to use a scheme of global optimization to enhance the raw

GAN to generate more discriminative fault samples. Shao et al. [8] input fault time-domain data with different label types to GAN to generate 1D simulation signal samples and then input them to convolutional neural network (CNN) with raw signals to realize data augmentation and fault classification. Wang et al. [9] used conditional GAN (CGAN) to simulate effective fault features automatically from fault signal and realize data augmentation and selected stacked autoencoders (SAE) [10] for accurate fault classification.

Furthermore, the quality of data is also particularly important. The higher the sample resolution is, the easier to detecting the smallest change of the measured object is [11]. It is also the requirement for the establishment of digital twins. More data points collected per unit time facilitate analyzing the internal characteristics of the measured object and realizing the accurate diagnosis of the machinery [12–14]. Thus, high resolution samples are generally employed in the study of fault diagnosis [15, 16]. However, the aforementioned methods can only increase the volume of the dataset but cannot augment the sample resolution.

For a set of mechanical devices rotating at high speed, it is difficult to collect enough feature information by a signal collector with a low sampling frequency. So, the higher of the sample resolution is, the more conveniency to find the fault of the equipment, but the high resolution samples cannot be acquired due to the limitation of the signal acquisition equipment. In addition, research on resolution augmentation in fault diagnosis field is few and far between. By contrast, the resolution augmentation technology is a common tool to recreate high resolution image in the field of image processing [17]. Thus, it is worth considering to adopt resolution augmentation technology for the low resolution signal of the rotating machinery. Superresolution convolutional neural network (SRCNN) [18], superresolution generative adversarial network (SRGAN) [19], deep reconstruction classification networks (DRCN) [20], and efficient subpixel convolutional neural network (ESPCN) [21] are common resolution augmentation algorithms. For example, the low resolution image can be magnified to the shape of the target according to bi-3 interpolation of the SRCNN, and a CNN model is used to realize nonlinear mapping. Next, the low resolution image can be expanded and reconstructed by the upper sampling interpolation. In this paper, ESPCN is presented to augment the signal resolution of single sample. Furthermore, the accuracy of fault classification is tested by the SAE network to evaluate the performance of data augmentation. The contributions of this study can be summarized as follows:

(1) The proposed ESPCN model can learn features from a low resolution sample and enhance the sample resolution by four times compared to raw signal

(2) The generated high resolution dataset is employed to train the SAE model for fault classification and the raw high resolution dataset are used for testing

(3) Two experimental cases (different sample dimensions and rotating speeds) are set to simulate the low resolution situation and verify the effectiveness of the propose method

The remainder of this paper is structured as follows: Section 2 details theoretical backgrounds of ESPCN and SAE. In Section 3, the faut diagnosis framework based on ESPCN is described. Two diagnosis cases of gear and bearing datasets are set up in Section 4. Section 5 gives the conclusion.

2. Theoretical Background

2.1. ESPCN.
Figure 1 shows that a subpixel convolutional layer and several convolutional layers constitute the ESPCN network. The raw image serves as the input to the network, and the low resolution image with the same size is output through the l-channel convolutional neural network. Then, the subpixel convolution layer is adopted to sequentially arrange the low resolution hidden layer features sequentially into a group of high resolution images. The first l-1 channel of the convolutional neural network is as follows:

$$f_1(I_{\mathrm{LR}}; W_1; b_1) = j(W_1 \times I_{\mathrm{LR}} + b_1),$$
$$f_l(I_{\mathrm{LR}}; W_{1:l}; b_{1:l}) = j(W_l \times f_{l-1}(I_{\mathrm{LR}}) + b_l), \tag{1}$$

where W_l, b_l, and $l \in (1, L-1)$ are learnable weights and offsets, W_l is a 2D convolutional tensor with the shape of $n_{l-1} \times n_l \times k_l \times k_l$, where n_l is the feature number at layer l, k_l is the convolutional kernel number at layer l, and offset b_l is the vector with the length of n_l. After the convolutional network layer, the feature map of r^2 channel is obtained and then is sent to the subpixel convolution layer for sampling.

$$I_{\mathrm{SR}} = f_L(I_{\mathrm{LR}}) = \mathrm{PS}(W_L \times f_{L-1}(I_{\mathrm{LR}}) + b_L), \tag{2}$$

where PS is a periodic shuffling operator that rearranges the elements with shape $H \times W \times C \cdot r^2$ to shape $rH \times rW \times C$, and H and W are the height and width of the real-value tensor, respectively. I_{LR} and I_{SR} own C color channels. x and y denote the output pixel coordinates in the high resolution space. PS can sequentially arrange low resolution features into a group of high resolution image and can be defined as follows:

$$\mathrm{PS}(T)_{x,y,c} = T_{\lfloor x/r \rfloor, \lfloor y/r \rfloor, c \cdot r \cdot \mathrm{mod}\,(y/r) + c \cdot \mathrm{mod}\,(x/r)}, \tag{3}$$

where x and y are the output pixel coordinates in the high resolution space.

Pixel-wise mean squared error (MSE) of the reconstruction is used as the cost function to train the network, whose mathematical expression can be written as follows:

$$x(W_{1:L}, b_{1:L}) = \frac{1}{r^2 HW} \sum_{x=1}^{rH} \sum_{y=1}^{rW} \left(I_{\mathrm{HR}}^{x,y} - f_L^{x,y}(I_{\mathrm{LR}}) \right)^2, \tag{4}$$

where $I_{\mathrm{HR}}^n (n = 1 \cdots N)$ denotes the high resolution image examples, and $I_{\mathrm{LR}}^n (n = 1 \cdots N)$ denotes the resulting low resolution image examples.

2.2. Stacked Autoencoders.
Autoencoder (AE) [22] is adopted for feature extraction and sample reconstruction. As the composition of SAE, it has the feedforward neural network structure [23]. The basic architecture of AE consists of an encoder section and a decoder section. The encoder can compress the input data into latent space features, whereas the decoder reconstructs the input from the latent space representation.

Assuming $\{x_n\}_{n=1}^N$ is an unlabeled dataset where $x_n \in R^{m \times 1}$, the process of the encoder can be depicted as follows:

$$h_n = s_f(Wx_n + b), \tag{5}$$

where h_n is the hidden encoder vector mapped from x_n, s_f denotes activation function, b denotes bias vector, and W denotes the weight matrix.

g_θ' is the decoding function that maps h_n from the low-dimensional feature back into the high-dimensional feature. The process of the decoder can be defined as follows:
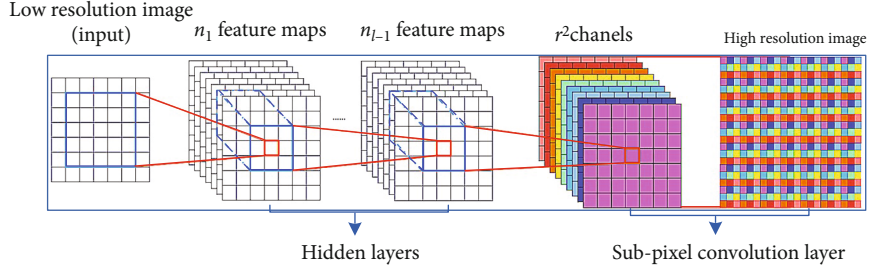
Figure 1: Structure of ESPCN.

$$\widehat{x}_n = s_g\left(W^T h_n + d\right), \tag{6}$$

where the activation function s_g is the same as s_f, and d and W^T are the bias vector and weight matrix, respectively.

MSE is adopted to minimize the reconstruction error:

$$\phi AE\left(\theta, \theta'\right) = \frac{1}{n} \sum_{n=1}^{N} L\left(x_n, g_{\theta'}\left(f_{\theta}(\widehat{x}_n)\right)\right), \tag{7}$$

where the parameter set of the AEs are $\theta = \{W, b\}$ and $\theta' = \{W^T, d\}$.

Figure 2 depicts that SAE to stack the autoencoder layer by layer to construct the DNN that is to take the hidden layer of the first AE as the input of the second AE. Feed forward layer-wise learning is employed for network training, softmax regression is adopted as classifier, and back propagation (BP) algorithm is used for weight updating and parameter fine-tuning.

3. Proposed Framework

Figure 3 shows the structure of the proposed ESPCN and SAE for signal resolution augmentation and fault classification. In the process of signal resolution augmentation, the hidden layers of ESPCN are expressed by the following:

$$\begin{aligned} f_1(X_{LR}\,;W_1) &= f(W_1 \times X_{LR}), \\ f_2(X_{LR}\,;W_2) &= f(W_2 \times f_1(X_{LR})), \\ f_3(X_{LR}\,;W_3) &= f(W_3 \times f_2(X_{LR})), \end{aligned} \tag{8}$$

where the first two layers own 64 and 32 channels, respectively [24]. Scaled exponential linear unit (SELU) [25] is selected as the activation function $\phi(\cdot)$, which makes the sample distribution automatically normalized to zero mean and unit variance, to ensure that the gradient does not explode or disappear during the network training. Then, the feature of low resolution sample is learned through the hidden layers, and the subpixel layer is adopted to realize the operation of resolution augmentation, which is composed of a fully connected layer and a periodic shuffling operator. The fully connected layer outputs r^2 ($r = 2$) channel feature maps with the same dimension of the input data, and then the generated data are obtained according to the following formula:

$$X_{SR} = f_3(X_{LR}) = PS(W_3 \times f_2(X_{LR})), \tag{9}$$

where X^{SR} is a high resolution sample generated by the proposed network, PS function is adopted to enhance the resolution by four times, and the form is able to be defined by the following:

$$PS(T)_{p,q} = T_{\lfloor p/r \rfloor \cdot \lfloor q/r \rfloor \cdot r \cdot \text{mod } (q/r) + \text{mod } (p/r)} \tag{10}$$

The final loss function we used is MSE which can measure the difference between the raw sample and the generated low resolution features as follows:

$$\xi(W_{1:L}, b_{1:L}) = \frac{1}{r^2 HW} \sum_{x=1}^{rH} \sum_{y=1}^{rW} \left(f_3^{x,y}(X_{LR}) - X_{LR}\right)^2. \tag{11}$$

In the process of fault classification, the generated high resolution dataset is input to the SAE directly for feature extraction and fault classification, so as to achieve model training. Then, the raw high resolution dataset is used for testing.

4. Experiment Results and Analysis

4.1. Case 1: Fault Diagnosis of Bearing under the Same Sampling Frequency

4.1.1. Data Description. Figure 4 shows that the bearing fault test rig from Shandong University of Science and Technology (SDUST) [3] is set to explore the performance of ESPCN in resolution augmentation. The platform contains electric motor, load disc, bearing seat, gearbox, and powder brake. The bearing type is N205EU cylindrical roller bearing. As shown in Figure 5, three fault types including inner race fault (IF), outer race fault (OF), and roller fault (RF) are introduced to the bearing. 800 (200×4) samples from 4 health states are extracted to form the required dataset. The motor bearing vibration signal is collected from the LMS data acquisition instrument, the type of the sensor is vibration acceleration sensor as show in Figure 4, and the sampling frequency is 25.6 kHz. The senor is installed on the surface of the bearing seat. Simultaneously, motor speed is set to 3000 r/min.

In this section, 600 is set as the dimension of a low resolution sample, and 300 Fourier coefficients are obtained after FFT. Then, 2400 is set as the dimension of a high
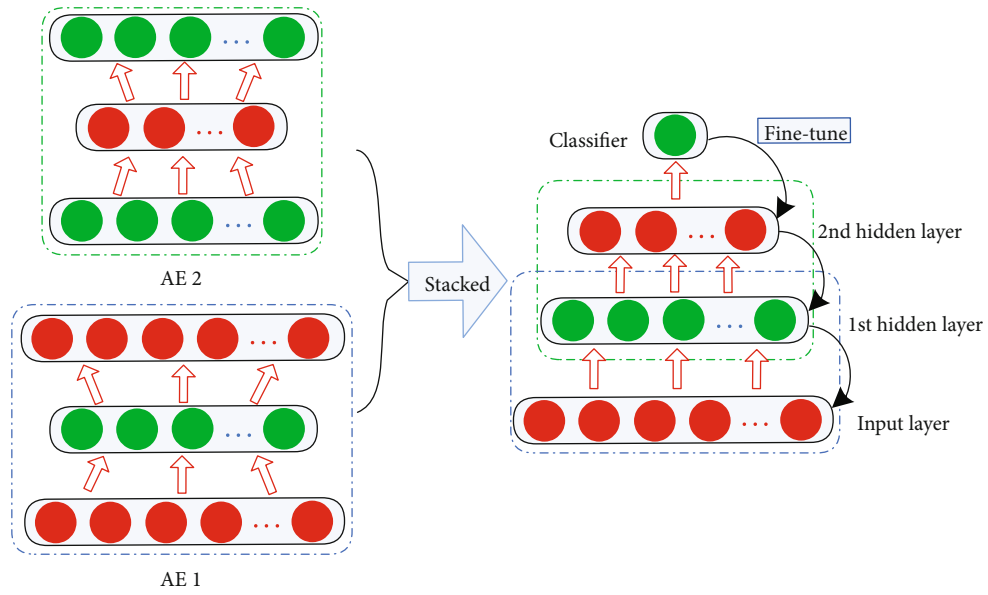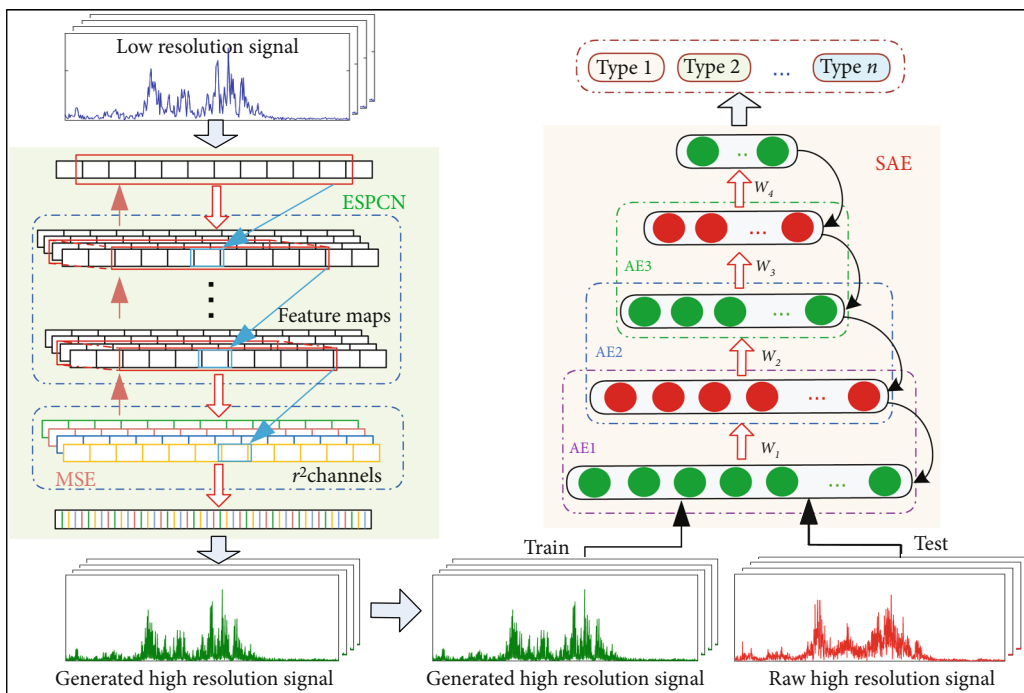
FIGURE 2: Structure of SAE.

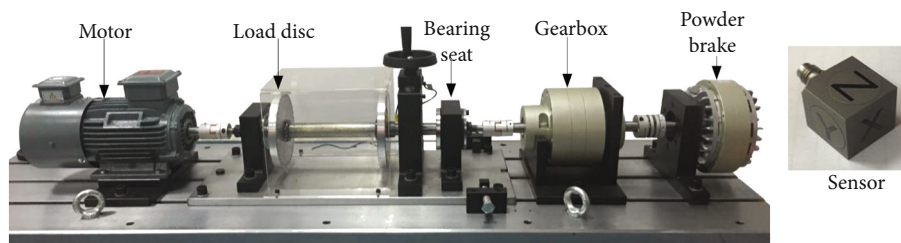FIGURE 3: Flow chart of the proposed method.
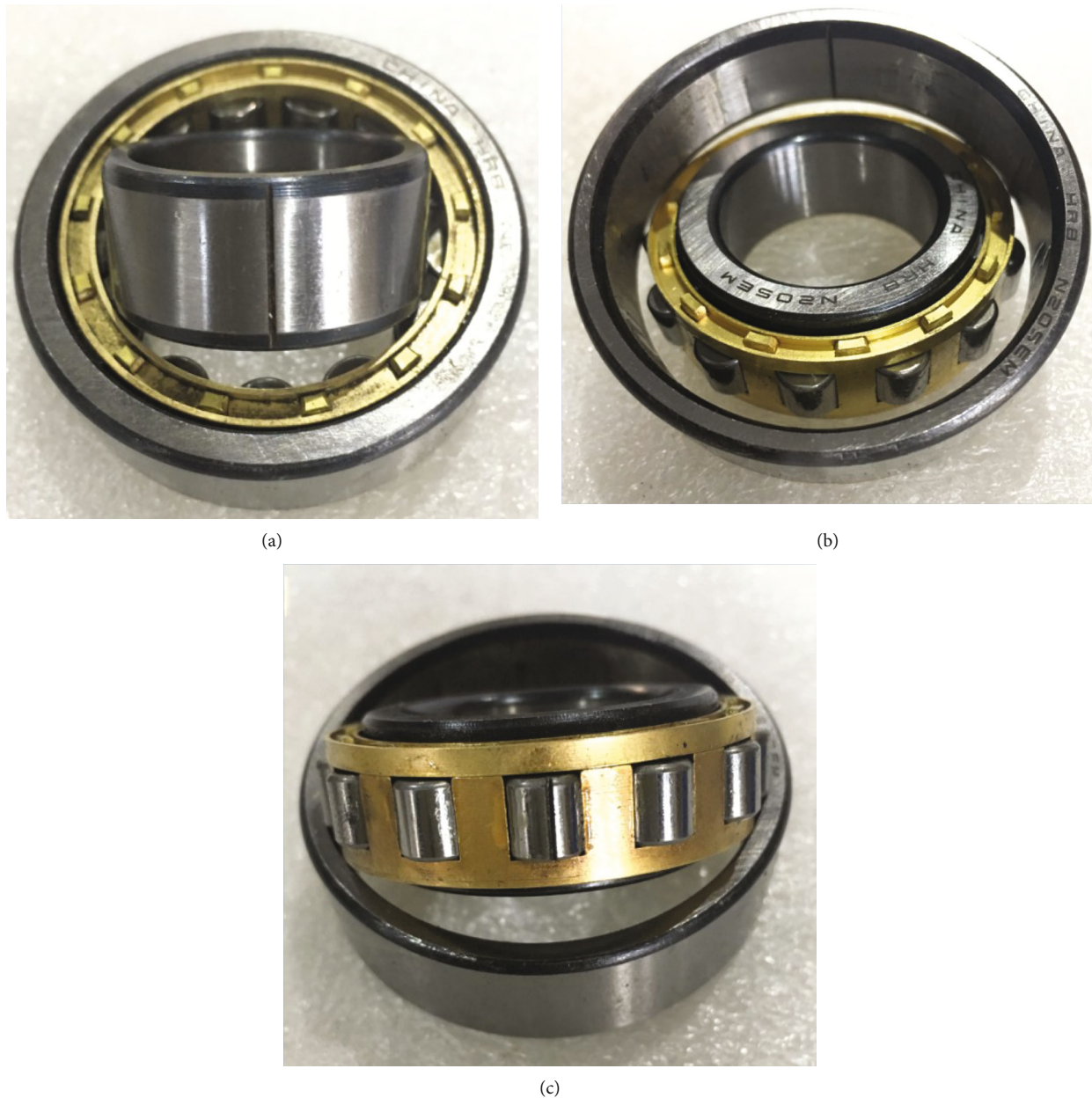

FIGURE 4: Bearing fault test rig.

(a)

(b)

(c)

FIGURE 5: Three fault modes of bearing: (a) IF, (b) OF, and (c) RF.

resolution sample, and 1200 Fourier coefficients are obtained. The parameters of ESPCN are set as follows: The epoch is set to 40, the batch size is 50, the learning rate is set to 0.1, and the SELU is selected as activation function. Furthermore, SAE is used to evaluate the performance of the sample generated by the ESPCN network, and the network parameters of each layer in SAE are [1200, 600, 200, 100, 4]. The output size at the output layer equals the number of the fault types. Softmax regression [26] is adopted at the classifier, and error back propagation [27] is used to fine-tune the model. Batch normalization (BN) [28] is applied before each hidden layer of the SAE. The raw low resolution dataset is input into the ESPCN network, and the generated high resolution dataset is used as the training set of the SAE. Finally, the raw high resolution dataset are used for testing.

4.1.2. Diagnosis Results. Figure 6 displays the spectra graphs of three data types (low resolution spectra, generated high resolution spectra, and raw high resolution spectra). Distinguish different fault types from th spectra graphs is difficult, and the classification network based on SAE must be used to extract features and distinguish fault types. On the one hand, the higher the sampling frequency is, the better the training effect of the SAE network, since the low resolution sample includes just one circle information of the bearing signal that contains much fewer features. On the other hand, the feature distribution of the generated high

(a) Low resolution spectra

(b) Spectra generated by ESPCN
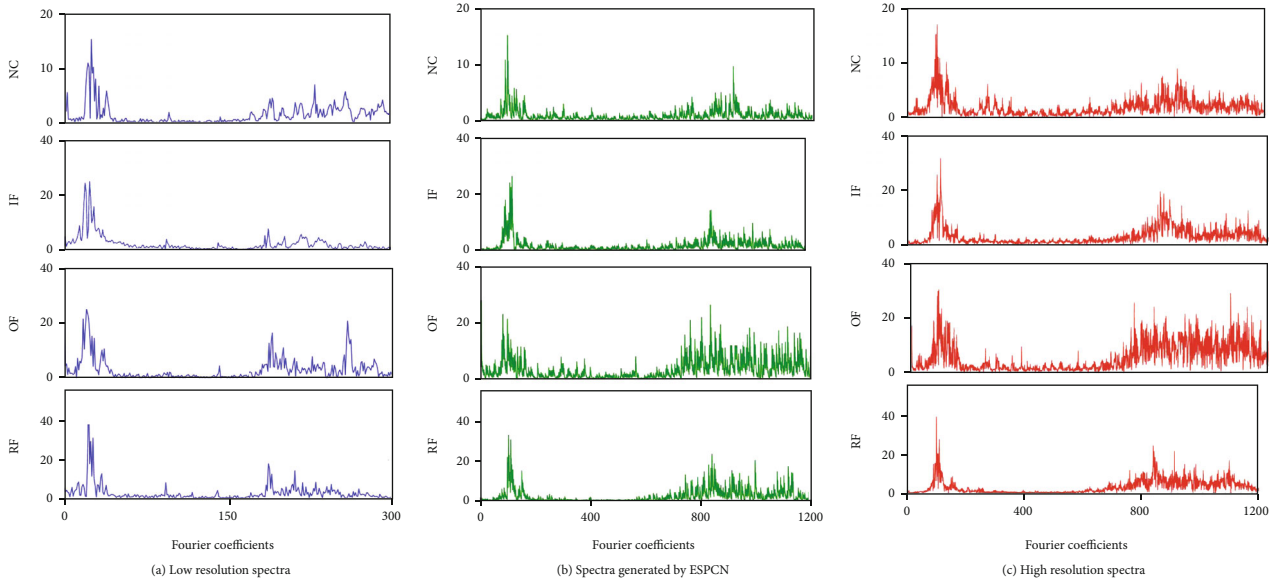
(c) High resolution spectra

FIGURE 6: Spectra comparison of three bearing data types. (a) Low resolution spectra. (b) Spectra generated by ESPCN. (c) High resolution spectra.

resolution sample is almost the similar to the raw high resolution sample, which owns the same feature dimension and frequency domain graphs.

For comparative analysis, two datasets (low/high resolution dataset) are employed for fault classification, respectively. The diagnosis results are shown in Figure 7. 15 trials are repeated for each experiment to reduce the effect of randomness. It can be seen that the result from the low resolution dataset is not well, and the testing accuracy is 95.76% with 0.25% standard deviation. In contrast, the data obtained by the ESPCN can achieve a higher average accuracy which is 98.76 ± 0.46%. Since ESPCN can enhance the resolution of low resolution dataset by 4 times, the sample owns much more effective features, which helps the classification network to identify samples with different health conditions. Besides, the high resolution data achieves the highest accuracy of 99.96 ± 0.06%, since the high resolution own the raw and abundant information of the fault type.

To map the learned high-dimensional feature vector of SAE into a 2D feature vector, t-distributed stochastic neighbor embedding (t-SNE) [29] is applied that can show the diagnosis effect of the three kinds of datasets. In Figure 8(a), the clustering result of the low resolution data is the worst, several samples are mixed with one another, and various levels of misclassification are observed between different fault types. In Figure 8(b), the classification result of the ESPCN is much better than that of the low resolution data, and almost all the samples under different health conditions are well separated. In addition, the clustering result of the high resolution dataset in Figure 8(c) is the best, and the same sample set displays much more compact aggregation. Moreover, the feature learning process of the ESPCN network is displayed in Figure 9. Figure 9(a) displays the learned features of 64 channels from the low resolution samples. Different colors in each channel represents the current feature strength. The features of these channels are

combined and extracted into one feature value, and then the feature map of Figure 9(b) is achieved. The differentiation of all the channels increases as the network layer increasing, and the learned features become more and more apparent. Finally, four-channel low-resolution simulation samples are obtained as shown in Figure 9(c).

4.2. Case 2: Fault Diagnosis of Bearing under Speed Fluctuation Condition. Figure 10 shows the gearbox fault test bench that contains electric motor, coupling, gearbox, and bearing seats. Figure 11 shows 10 different health conditions: normal condition (NC), sun wheel crack (WC), sun wheel pit (WP), sun wheel worn (WW), pinion crack (PC), pinion pit (PP), pinion worn (PW), and three compound fault types (WWPW, WPPC, and WPPW). The sampling frequency is 12.8 kHz, and the senor is installed on the surface of the gearbox. The rotating speed is controlled by a frequency converter as shown in Figure 10, and the speed varies between 700 r/min and 1500 r/min randomly. The sampling frequency is fixed; so, the sample resolution will become lower with the speed increasing, because the sample points per rotate will become much less and the collected feature information will also reduce.

The model parameters of ESPCN are the same as that in case 1. The low resolution and high resolution datasets have 200 samples, and each sample owns 600 and 2400 sample points, respectively. The structure of three gear samples is randomly displayed in Figures 12(a)–12(c). The collected signals of different fault categories exhibit different speed fluctuations in the time domain. Figure 12(d) shows the irregular rotation rate fluctuation curves of three fault categories vary from 700 to 1500 r/min. Figure 13 shows the spectra of three different data types. It is found that the low resolution spectra also have the least feature information in Figure 13(a). Figure 13(b) illustrates the spectra generated by the proposed method based on the low resolution data,

FIGURE 7: Classification results of three bearing datasets.

(a) Low resolution

(b) ESPCN

(c) High resolution
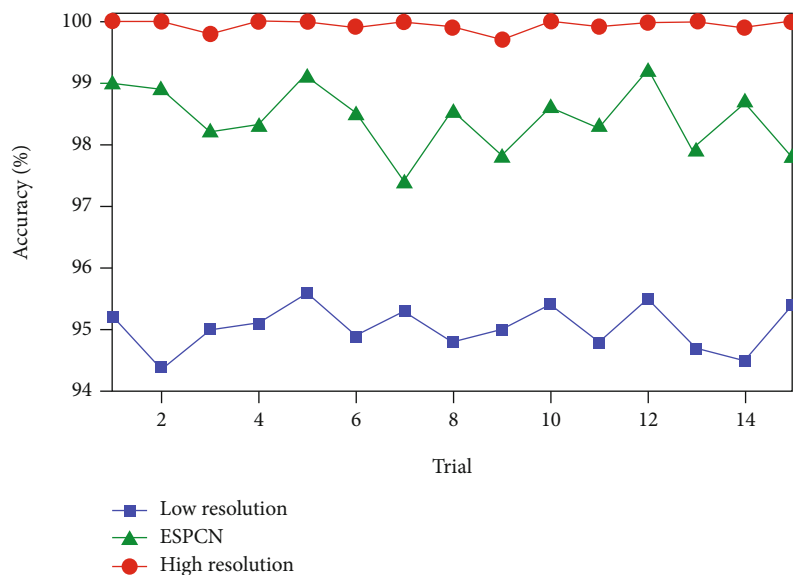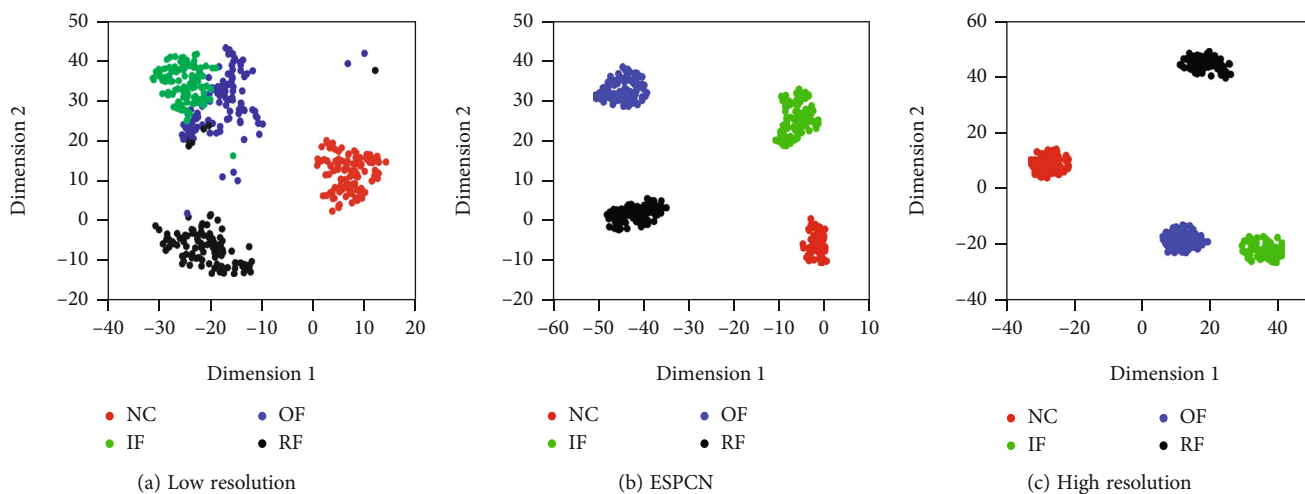
FIGURE 8: Visualization results of three bearing datasets.

(a) First fully connected layer

(b) Second fully connected layer

(c) Third fully connected layer

FIGURE 9: Feature visualization of different layers for bearing data in ESPCN.

FIGURE 10: Bench of gearbox fault.

(a) WC   (b) WP   (c) WW
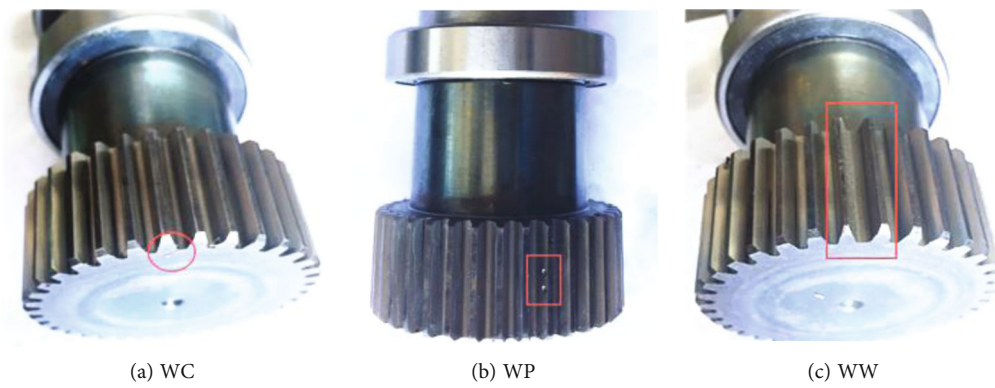
FIGURE 11: Fault feature diagrams of sun and planet wheels.
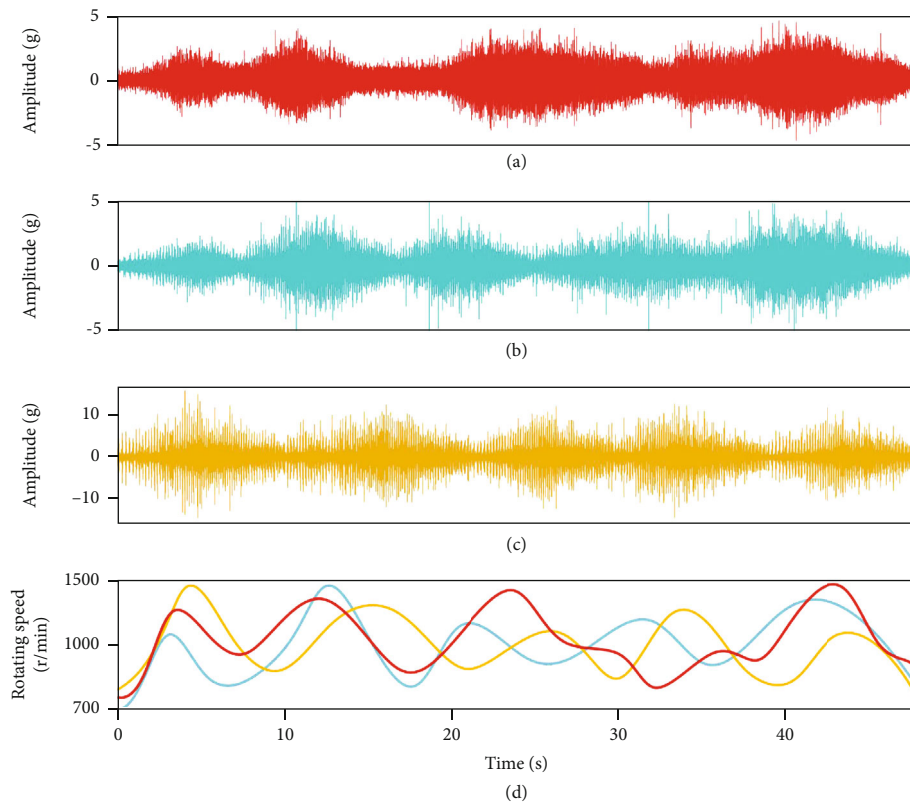
FIGURE 12: Speed fluctuation diagrams of three health states: (a) NC, (b) WW, (c) WWPW, and (d) Speed curves.
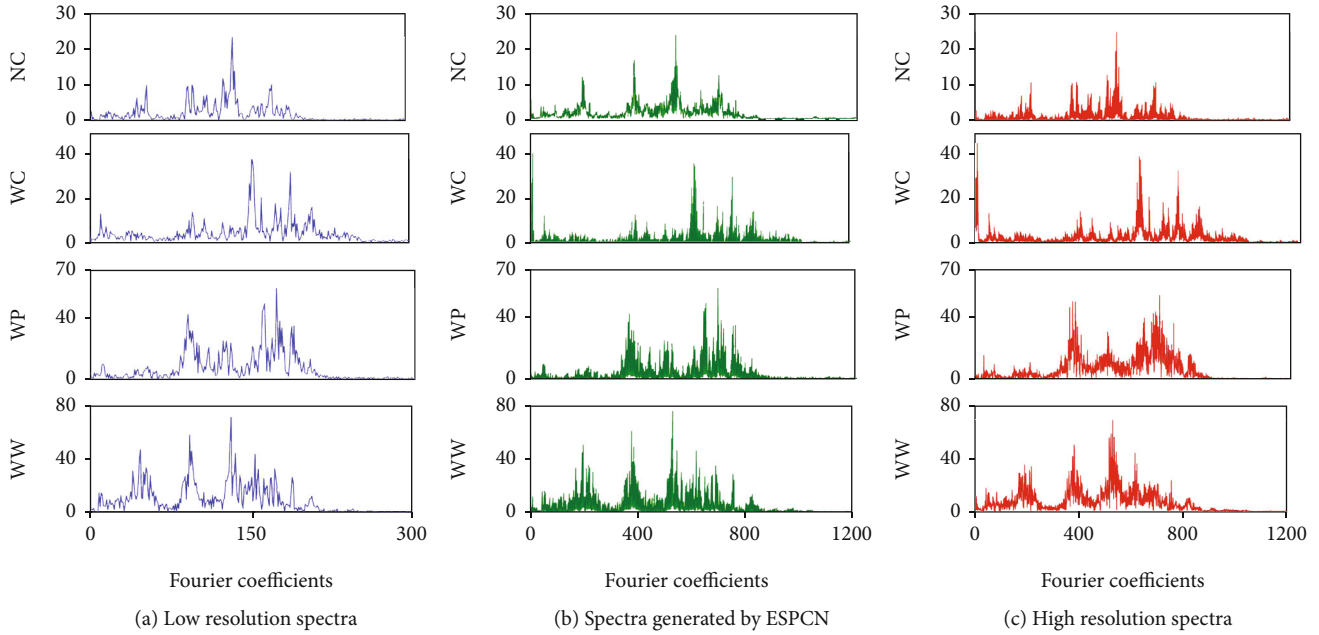
Figure 13: Spectra comparison of four data types. (a) Low resolution spectra. (b) Spectra generated by ESPCN. (c) High resolution spectra.
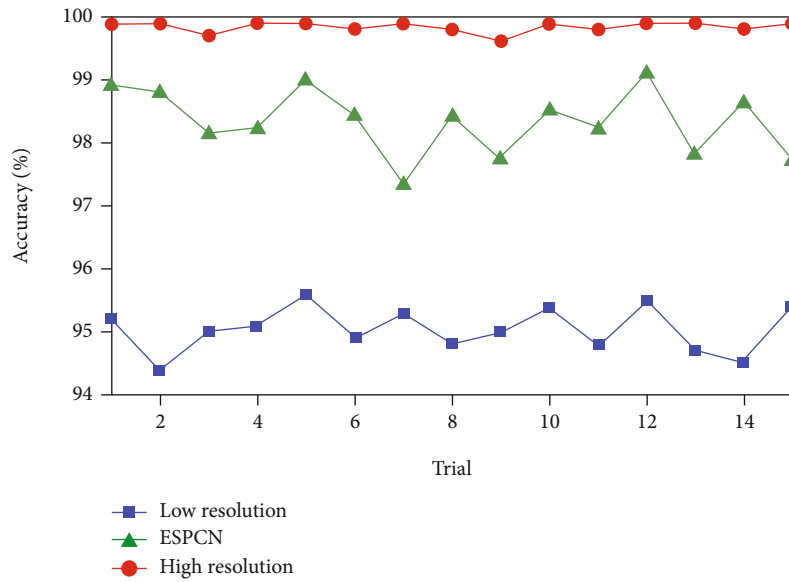
Figure 14: Testing accuracies of four data types.

and Figure 13(c) displays the raw high resolution spectra. It can be easy to see that the generated high resolution spectra also display the same feature trend as the raw high resolution spectra, which is much helpful for the accurate fault diagnosis of gearbox.

The diagnosis results of the above three data types are displayed in Figure 14. Undoubtedly, the high resolution dataset achieves the highest accuracy $99.53 \pm 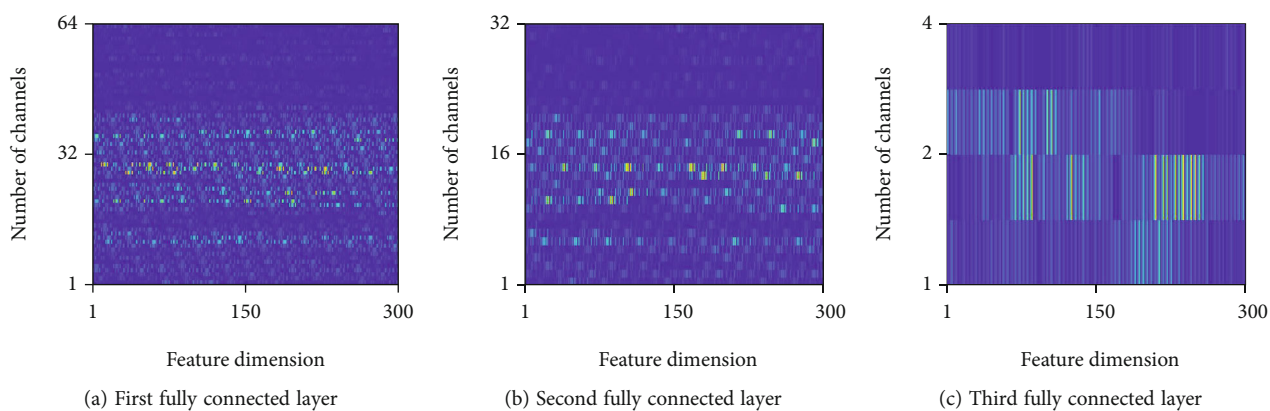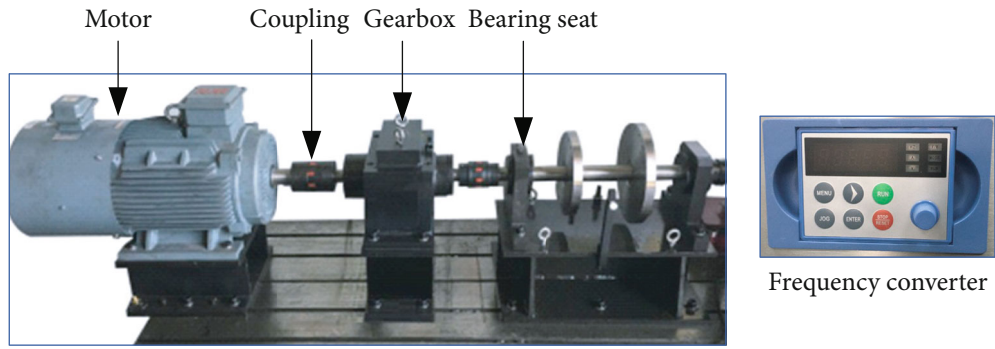0.23\%$. In comparison, the low resolution dataset obtains the lowest accuracy $94.56 \pm 0.45\%$. The diagnosis accuracy of the ESPCN

is lower than that of the high resolution dataset: the average accuracy is $98.23 \pm 0.67\%$. In addition, t-SNE is also adopted to display the visualization result of dimension reduction. Figure 15(a) shows that the dimension reduction samples of WC and WP are mixed with each other, and samples of all the types are also not clustered. Figure 15(b) shows that the cluster result of the ESPCN is better than those of the low resolution dataset. In addition, the high resolution dataset also performs the best, and all the samples under different health states are separated with each other.

(a) Low resolution   (b) ESPCN   (c) High resolution
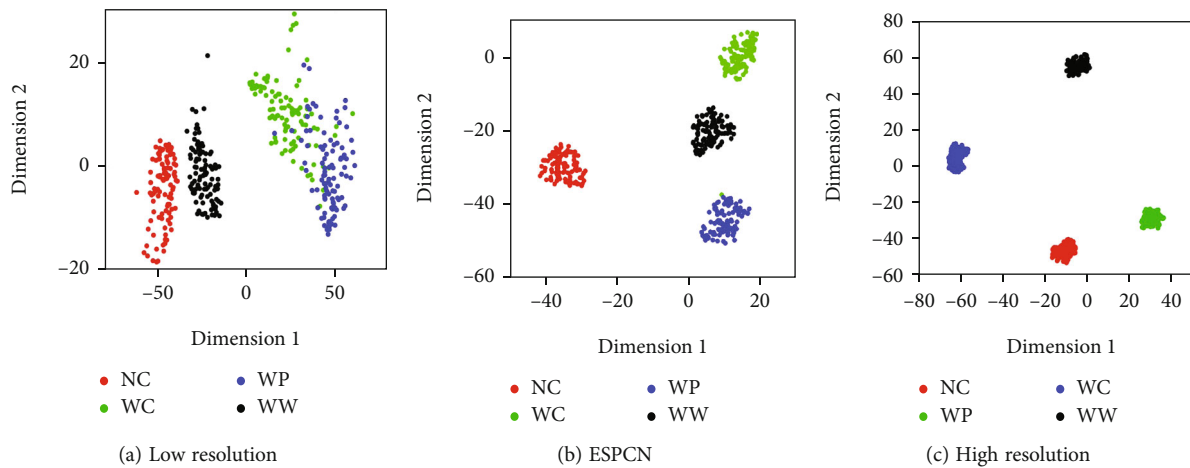
FIGURE 15: Visualization results of three gearbox datasets.

5. Conclusions

In this paper, a generalizable deep learning framework based on ESPCN is proposed to improve the resolution of bearing and gearbox signals. First, four-channel features are mapped from the low resolution sample. Then, the high resolution sample is output from the subpixel fully connected layer. Finally, the sample resolution is augmented by four times by using the ESPCN network. In the case studies, the classification results illustrate that the sample generated by the ESPCN model is effectiveness and can obtain a high diagnosis accuracy. Although the proposed method can improve the diagnosis accuracy of the low resolution dataset, the theoretical basis of the high resolution feature learning is not explicit. Moreover, it is interest to generate high resolution sample directly from the raw time domain signal. The authors will investigate this topic in future study.

Data Availability

The data used to support the findings of this study are available from the corresponding author upon request.

Conflicts of Interest

The authors declare that they have no conflicts of interest.

Acknowledgments

References

[1] H. Shao, J. Lin, L. Zhang, D. Galar, and U. Kumar, "A novel approach of multisensory fusion to collaborative fault diagnosis in maintenance," *Information Fusion*, vol. 74, pp. 65–76, 2021.

[2] B. Han, S. Ji, J. Wang, H. Bao, and X. Jiang, "An intelligent diagnosis framework for roller bearing fault under speed fluctuation condition," *Neurocomputing*, vol. 420, pp. 171–180, 2021.

[3] R. Islam, S. Khan, and J. Kim, "Discriminant feature distribution analysis-based hybrid feature selection for online bearing fault diagnosis in induction motors," *Journal of Sensors*, vol. 2016, Article ID 7145715, 16 pages, 2016.

[4] B. Han, X. Zhang, J. Wang, Z. An, S. Jia, and G. Zhang, "Hybrid distance-guided adversarial network for intelligent fault diagnosis under different working conditions," *Measurement*, vol. 176, article 109197, 2021.

[5] Z. Zhang, S. Li, J. Wang, Y. Xin, and Z. An, "General normalized sparse filtering: A novel unsupervised learning method for rotating machinery fault diagnosis," *Mechanical Systems and Signal Processing*, vol. 124, pp. 596–612, 2019.

[6] I. Goodfellow, J. Pouget-Abadie, M. Mirza et al., *Generative Adversarial Nets*, Advances in Neural Information Processing Systems, 2014.

[7] F. Zhou, S. Yang, H. Fujita, D. Chen, and C. Wen, "Deep learning fault diagnosis method based on global optimization GAN for unbalanced data," *Knowledge-Based Systems*, vol. 187, article 104837, 2020.

[8] S. Shao, P. Wang, and R. Yan, "Generative adversarial networks for data augmentation in machine fault diagnosis," *Computers in Industry*, vol. 106, pp. 85–93, 2019.

[9] J. Wang, B. Han, H. Bao, M. Wang, Z. Chu, and Y. Shen, "Data augment method for machine fault diagnosis using conditional generative adversarial networks," *Proceedings of the Institution of Mechanical Engineers Part D Journal of Automobile Engineering*, vol. 234, no. 12, article 095440702092325, pp. 2719–2727, 2020.

[10] Y. Bengio, "Learning deep architectures for AI," *Foundations & Trends in Machine Learning*, vol. 2, no. 1, pp. 1–127, 2009.

[11] X. Li, Y. Yang, H. Shao, X. Zhong, J. Cheng, and J. Cheng, "Symplectic weighted sparse support matrix machine for gear fault diagnosis," *Measurement*, vol. 168, article 108392, 2021.

[12] Z. Wang, X. He, B. Yang, and N. Li, "Subdomain adaptation transfer learning network for fault diagnosis of roller bearings," *IEEE Transactions on Industrial Electronics*, 2021.

[13] Z. Zhang, S. Li, J. Lu, J. Wang, and X. Jiang, "A novel intelligent fault diagnosis method based on fast intrinsic component filtering and pseudo-normalization," *Mechanical Systems and Signal Processing*, vol. 145, article 106923, 2020.

[14] Z. An, X. Jiang, J. Cao, R. Yang, and X. Li, "Self-learning transferable neural network for intelligent fault diagnosis of rotating machinery with unlabeled and imbalanced data," *Knowledge-Based Systems*, vol. 230, no. 27, article 107374, 2021.

[15] Y. Fan and G. Zheng, "Research of high-resolution vibration signal detection technique and application to mechanical fault diagnosis," *Mechanical Systems and Signal Processing*, vol. 21, no. 2, pp. 678–687, 2007.

[16] Z. Wang, J. Zhou, W. Du, Y. Lei, and J. Wang, "Bearing fault diagnosis method based on adaptive maximum cyclostationarity blind deconvolution," *Mechanical Systems and Signal Processing*, vol. 162, no. 5-8, p. 108018, 2022.

[17] J. Wang, S. Zhu, and Y. Gong, "Resolution enhancement based on learning the sparse association of image patches," *Pattern Recognition Letters*, vol. 31, no. 1, pp. 1–10, 2010.

[18] C. Ward, J. Harguess, B. Crabb, and S. Parameswaran, "Image quality assessment for determining efficacy and limitations of super-resolution convolutional neural network (SRCNN)," *In Proceedings of the Applications of Digital Image Processing XL*, vol. 10396, 2017.

[19] C. Ledig, L. Theis, F. Huszár et al., "Photo-realistic single image super-resolution using a generative adversarial network," in *In Proceedings of the Proceedings of the IEEE conference on computer vision and pattern recognition*, pp. 4681–4690, Los Alamitos, USA, 2017.

[20] J. Kim, J. Lee, and K. Lee, "Deeply-recursive convolutional network for image super-resolution," in *In Proceedings of the Proceedings of the IEEE conference on computer vision and pattern recognition*, pp. 1637–1645, Las Vegas, USA, 2016.

[21] W. Shi, J. Caballero, F. Huszár et al., "Real-time single image and video super-resolution using an efficient sub-pixel convolutional neural network," in *In Proceedings of the Proceedings of the IEEE conference on computer vision and pattern recognition*, pp. 1874–1883, Las Vegas, USA, 2016.

[22] F. Jia, Y. Lei, J. Lin, X. Zhou, and N. Lu, "Deep neural networks: a promising tool for fault characteristic mining and intelligent diagnosis of rotating machinery with massive data," *Mechanical Systems and Signal Processing*, vol. 72-73, pp. 303–315, 2016.

[23] X. Wu, Y. Zhang, C. Cheng, and Z. Peng, "A hybrid classification autoencoder for semi-supervised fault diagnosis in rotating machinery," *Mechanical Systems and Signal Processing*, vol. 149, article 107327, 2021.

[24] M. Xu, D. Wang, and X. Du, "A video frame resolution and frame rate amplification method with optical flow method and ESPCN model," in *In Proceedings of the Proceedings of the 2020 3rd International Conference on Image and Graphics Processing*, pp. 91–95, Rabat, Morocco, 2020.

[25] G. Klambauer, T. Unterthiner, A. Mayr, and S. Hochreiter, "Self-normalizing neural networks," in *Proceedings of the 31st international conference on neural information processing systems*, pp. 972–981, Long Beach, USA, 2017.

[26] B. Jain, "Warped softmax regression for time series classification," *Knowledge and Information Systems*, vol. 63, no. 3, pp. 589–619, 2021.

[27] D. Zhang, W. Li, X. Wu, and X. Lv, "Application of simulated annealing genetic algorithm optimized back propagation(BP) neural network in fault diagnosis," *International Journal of Modeling Simulation & Scientific Computing*, vol. 10, no. 4, pp. 1950024–1950049, 2019.

[28] S. Ioffe and C. Szegedy, "Batch normalization: Accelerating deep network training by reducing internal covariate shift," in *In Proceedings of the International conference on machine learning*, pp. 448–456, Lille, France, 2015.

[29] M. Van and G. Hinton, "Visualizing data using t-SNE," *Journal of Machine Learning Research*, vol. 85, no. 9, pp. 2579–2605, 2008.

Research Article

Composite Fault Diagnosis of Rolling Bearing Based on Optimized Wavelet Packet AR Spectrum Energy Entropy Combined with Adaptive No Velocity Term PSO-SOM-BPNN

Hongwei Fan [iD] **,[1,2] Yang Yan,[1] Xuhui Zhang,[1,2] Xiangang Cao,[1,2] and Jiateng Ma[1]**

[1]*School of Mechanical Engineering, Xi'an University of Science and Technology, Xi'an 710054, China*
[2]*Shaanxi Key Laboratory of Mine Electromechanical Equipment Intelligent Monitoring, Xi'an 710054, China*

Correspondence should be addressed to Hongwei Fan; hw_fan@xust.edu.cn

Aiming at the problem of low diagnosis efficiency and accuracy, due to noise and cross aliasing among various faults when diagnosing composite faults of rolling bearing under actual working conditions, a composite fault diagnosis method of rolling bearing based on optimized wavelet packet autoregressive (AR) spectral energy entropy and adaptive no velocity term particle swarm optimization-self organizing map-back propagation neural network (ANVTPSO-SOM-BPNN) is proposed. The energy entropy feature is extracted from the bearing vibration signal through wavelet packet AR spectrum, and SOM and BPNN are combined to form a series network. For PSO, the velocity term is discarded and the inertia weight and learning factor are adaptively adjusted. Finally, the Dempster-Shafer (D-S) evidence fusion diagnosis is carried out. To get closer to the application condition, the data are collected near and far away from the fault point for the composite fault diagnosis, which verifies the effectiveness of the proposed method.

1. Introduction

Rolling bearing is one of the most important components in rotating machinery. It plays an important role in supporting rotating shaft and reducing friction. Its working state is of great significance to the normal operation of the whole rotating machine [1–4]. In practical engineering, the fault often does not appear alone, and the probability of composite fault of the same bearing is also large. Composite faults are two or more faults that are interrelated and cross influenced at the same time [5]. And the vibration signals caused by different faults will interfere with each other and produce the coupling phenomenon, which makes the signal more complex and difficult to accurately diagnose faults. Therefore, the fault diagnosis of rolling bearing has the important practical value [6].

For the fault diagnosis of bearing, the feature extraction, neural network, and multi-information fusion are the research focuses. For the feature extraction, the wavelet packet decom-

position is a typical processing method of unsteady signal, which can process the signal more finely [7]. Tang and Deng [8] proposed a composite bearing fault feature separation method based on the improved harmonic wavelet packet decomposition to decompose the signal of intermediate frequency part and extract more effective signals. He et al. [9] applied the adaptive redundant multiwavelet packet to composite fault diagnosis of rotating machinery, proposed the normalized multifractal entropy as the evaluation criterion, adaptively constructed multiwavelet, and determined the fault sensitive frequency band by the relative energy ratio of characteristic frequency. Ma et al. [10] decomposed the composite fault signal using multiwavelet packet, reconstructed the signal with permutation entropy as the evaluation index, and finally demodulated and extracted the fault features using energy operator. For the fault diagnosis of rolling bearing, Abbasion et al. [11] preprocessed the vibration signal through wavelet analysis and then used support vector machine (SVM) to

diagnose the faults. Janssens et al. [12] applied the convolutional neural network (CNN) to multi fault diagnosis. Lv and Yao [13] used wavelet packet decomposition combined with back propagation neural network (BPNN) to diagnose the faults. Among them, BPNN is widely used for the fault diagnosis of rolling bearing due to its strong nonlinear mapping ability and high self-learning and adaptive ability [14]. However, the standard BPNN is easy to fall into the local optimal solution and relies too much on samples. According to the defects of BPNN, Huang et al. [15] used the global search ability of genetic algorithm to optimize BPNN. Gong et al. [16] combined the self-organizing map (SOM) with BPNN to obtain the better classification results and improve the convergence speed. Ju et al. [17] optimized the weight and threshold of BPNN through particle swarm optimization (PSO) and extracted the feature energy through wavelet packet, which improved the diagnosis efficiency and accuracy. The standard PSO also has its disadvantages, such as low convergence accuracy and easy to fall into local extremum. Wang and Wang [18] introduced the decline index and iteration threshold to improve the linear decline weight of the standard PSO and verified the advantages of improved PSO in search accuracy, convergence speed, and stability. Zhu and Xue [19] adaptively modified the learning factor to better balance the local and global search ability in view of the problem that the fixed value of learning factor in PSO affects the algorithm performance. Aiming at the signal fuzziness and uncertainty of composite fault, the diagnosis result is further improved by information fusion. Khazaee et al. [20] fused vibration and sound signals through Dempster-Shafer (D-S) evidence theory for fault diagnosis of gearbox and achieved ideal results. Feng and Pereira[21] applied the wavelet neural network and evidence theory to fault diagnosis of rotating machine and verified the effectiveness.

This paper proposes a new diagnosis method based on optimized wavelet packet AR spectral energy entropy to adaptive no velocity term PSO-SOM-BPNN (ANVTPSO-SOM-BPNN). In order to be closer to the real working conditions on site, data are collected near the fault points and far away from the fault points, respectively. The energy entropy characteristics of bearing vibration signals are extracted through wavelet packet AR spectrum. The basis function and decomposition layers of wavelet packet decomposition are optimally selected. SOM and BPNN are combined to form a series network, and PSO discards the velocity term and adaptively adjusts the inertia weight and learning factor. Finally, the proposed method is used to fuse the diagnosis results at two measuring points at D-S evidence decision level to improve the efficiency and accuracy in the composite fault diagnosis of rolling bearing.

2. Methodology

During the operation of rolling bearing, due to the interaction of inner ring, outer ring, and rolling element, it is easy to form overlapping composite faults. Among them, the fault features with weak energy may be submerged by the features with other strong energy or noise, which affects the accuracy of fault diagnosis. Therefore, at first, vibration accelerators are installed at two different measuring points to collect the vibration signals.

Secondly, two kinds of collected signal are preprocessed and then extract the signal features. And two kinds of extracted fault feature are diagnosed in the new method, to obtain two kinds of basic probability distribution. Finally, two probability distributions are fused by D-S evidence theory to achieve the purpose of fault diagnosis using multi-information fusion. The overall research idea of composite fault diagnosis of rolling bearing is shown in Figure 1.

2.1. Wavelet Packet AR Spectral Entropy Feature Extraction Method

2.1.1. Principle of Wavelet Packet Decomposition. Wavelet packet decomposition overcomes the defect that wavelet analysis only decomposes the low-frequency part of signal. It also decomposes the high-frequency part and improves time-frequency resolution. The specific algorithm is as follows.

Given scaling function $\phi(t)$ and wavelet basis function $\psi(t)$, two-scale equations are satisfied between them:

$$\begin{cases} \phi(t) = \sqrt{2} \sum_{k \in Z} h_k \phi(2t - k), \\ \psi(t) = \sqrt{2} \sum_{k \in Z} g_k \phi(2t - k), \end{cases} \quad (1)$$

where k is the time translation factor; h_k is the low-pass filter coefficient; and g_k is the high-pass filter coefficient.

The wavelet packet decomposition algorithm is

$$\begin{cases} d_l^{j,2n} = \sum_k a_{k-2l} d_k^{j+1,n}, \\ d_l^{j,2n+1} = \sum_k b_{k-2l} d_k^{j+1,n}, \end{cases} \quad (2)$$

where j is the number of wavelet packet decomposition layers; $d_l^{j,2n}$ is the low-frequency coefficient decomposed by layer j; and $d_l^{j,2n+1}$ is the high-frequency coefficient decomposed by layer j.

The wavelet packet reconstruction algorithm is

$$d_l^{j+1,n} = \sum_k \left(h_{l-2k} d_k^{j,2n} + g_{l-2k} d_k^{j,2n+1} \right), \quad (3)$$

where h_{l-2k} is the low-frequency coefficient reconstructed by wavelet packet and g_{l-2k} is the high-frequency coefficient reconstructed by wavelet packet.

2.1.2. AR Spectrum Estimation. Due to the complexity of composite fault signal of rolling bearing, it is difficult to obtain the accurate fault characteristics only by wavelet packet decomposition. Therefore, it needs to be further processed on the basis of wavelet packet decomposition. The basic idea of AR spectrum estimation is to establish an AR model for time series signal and then calculate the self-power spectrum of signal with model coefficients [22].
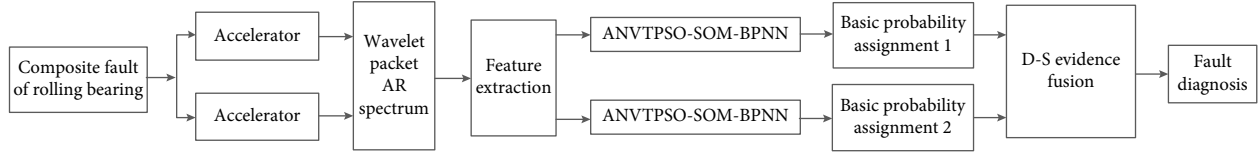
FIGURE 1: General research idea of rolling bearing composite fault diagnosis.

The general expression of AR model is

$$g(x) = s(x) - \sum_{i=1}^{R} a_i g(x - i), \qquad (4)$$

where $g(x)$ is autoregressive time series; $s(x)$ is finite band-width white noise with normal distribution with mean value of 0 and variance of σ_s^2; a_i is regression coefficient; and R is model order.

If equation (4) is regarded as the input/output equation of a system, $s(x)$ can be regarded as the white noise input of the system, and $g(x)$ is the response output of the system under the excitation of limited bandwidth white noise.

According to the definition of self-power spectrum and transfer function, the unilateral spectrum of signal can be expressed by the following formula:

$$G_y(f) = \frac{2T_s \sigma_s^2}{\left| 1 + \sum_{i=1}^{R} a_i e^{-i2\pi k T_s} \right|^2}, \qquad (5)$$

where $f \in [0, f_s/2.56]$; $T_s = 1/f_s$; and f_s is the sampling frequency.

2.1.3. Determination of Wavelet Packet Decomposition Levels.

The selection of decomposition levels not only affects the fault feature extraction but also determines the dimension of feature vector. When the number of decomposition layers is too small, the information of each frequency band cannot be completely decomposed, and the bearing feature information is not accurately extracted, which affects the accuracy of fault diagnosis. Although increasing the number of wavelet packet decomposition layers can analyze the fault signal more finely, the number of signals after decomposition increases. When the number of decomposition layers is too many, the dimension of feature vector is too large, which affects the efficiency of fault identification. Therefore, the number of wavelet packet decomposition layers must consider the characteristics of the signal itself. In this paper, the optimal number of decomposition layers is calculated by the following equation [23]:

$$J = \left\{ \max \left| j < \log_2 \frac{f_s}{4f_{sf}} \right. \right\}, \quad j \in Z, \qquad (6)$$

where J is the maximum number of layers; f_s is the sampling frequency; and f_{sf} is the signal frequency.

For the vibration signal of rolling bearing, especially the fault state signal, the frequency of useful signal is divided into two types: (1) rotation frequency and (2) fault frequency [24]. The wavelet packet decomposition aims to find fault features, so the signal frequency f_{sf} can be replaced by fault feature frequency [25].

2.1.4. Selection of Wavelet Packet Basis Function

(1) Information Entropy Principle. Information entropy is the measure of information disorder in information theory. The greater the entropy, the greater the disorder of information and the smaller the contribution of information. On the contrary, the smaller the entropy, the smaller the disorder of information and the greater the contribution of information. The working state of rolling bearing is often expressed in the form of vibration state. When rolling bearing fails, the vibration signal will change accordingly. Therefore, extracting information entropy from vibration signal in the time-frequency domain can reflect the vibration state of rolling bearing.

(2) Wavelet Packet Energy Entropy. The construction steps of wavelet packet energy entropy are as follows.

Step 1. The composite fault signal of rolling bearing is decomposed by wavelet packet. After the signal is decomposed in j layers, 2^j sub-signals are generated. The energy of the node n of layer j, the $S_{j,n}$, is expressed as

$$E_{j,n} = \sum_{q=1}^{Q} \left(S_{j,n}(q) \right)^2, \qquad (7)$$

where j is the number of wavelet packet decomposition layers; $n = 0, 1, \cdots, 2^j - 1$ is the node n of the layer j; and Q is the signal length.

Step 2. The total signal energy is expressed as

$$E_j = \sum_{n=0}^{2^j-1} E_{j,n}. \qquad (8)$$

Step 3. The proportion of energy of each node in the total energy is recorded as

$$p_{j,n} = \frac{E_{j,n}}{E_j}. \qquad (9)$$

Step 4. $p_{j,0}, p_{j,1}, \cdots, p_{j,2^j-1}$ is the energy distribution of each frequency band in layer j after the signal is decomposed by wavelet packet. According to Shannon's theorem, the wavelet packet energy entropy corresponding to each node is defined as

$$H_{j,n} = -p_{j,n} * \log p_{j,n}. \tag{10}$$

Step 5. The total energy entropy of the signal is expressed as

$$H_j = - \sum_{n=0}^{2^j-1} p_{j,n} * \log p_{j,n}. \tag{11}$$

(3) Selection of Wavelet Packet Basis Functions. In wavelet packet decomposition, the parts where the signal waveform is similar to the waveform of the selected wavelet packet basis function are enhanced and the rest are suppressed [26], so the greater the wavelet packet energy after decomposition. In information theory, the more regular the signal is, the higher the contribution value of information will be, and the smaller the energy entropy of wavelet packet will be. According to the principle of maximum ratio of total energy and total energy entropy of wavelet packet, the larger the ratio is, the more similar the selected wavelet packet basis function is to the original signal [27]. The ratio formula of total energy and total energy entropy of wavelet packet is

$$\sigma = \frac{E_j}{H_j}. \tag{12}$$

2.1.5. Construction of Wavelet Packet AR Spectral Entropy Eigenvector. The construction steps of wavelet packet AR spectral entropy eigenvector are as follows.

Step 1. The optimal wavelet basis is selected to decompose the collected vibration signals by j level wavelet packet decomposition and generate 2^j wavelet packet coefficients.

Step 2. According to the wavelet packet filter selected in the decomposition process, its dual filter is selected for reconstruction. When reconstructing a certain frequency band signal, set the wavelet packet coefficients of other frequency bands to zero to make the reconstructed signal only contain the time-domain waveform of the frequency band signal.

Step 3. The AR spectrum of each reconstructed signal is estimated to obtain the AR spectrum containing only specific frequency information.

Step 4. Calculate the energy entropy of wavelet packet AR spectrum band.

Step 5. The energy entropy of wavelet packet AR spectrum band is normalized, and the feature vector is constructed.

2.2. Fault Diagnosis Model of ANVTPSO-SOM-BPNN

2.2.1. SOM-BPNN Algorithm. BPNN is a multilayer feedforward neural network trained according to the error back propagation. It is a supervised learning network, which is trained on the premise of known expected output. SOM is an unsupervised, self-organizing, and visual network composed of fully connected neuron arrays. The two are connected in series

to form a combined SOM-BPNN model, which has both the advantages of SOM and BPNN. After the sample data enters SOM, the preliminary classification of samples is realized. The essence of training the secondary network is to add a dimension to the training sample vector and use it as the input of the secondary network. The newly added dimension is used to mark the classification results of the primary network, which can promote the training of the secondary network. Theoretically, it can effectively reduce the training time of the secondary network and make the whole combined network converge faster. As the primary network training, SOM does not need a large sample set, so SOM-BPNN also has the same characteristics. Therefore, the combination of two neural networks can achieve the complementary advantages, so as to improve the accuracy of fault diagnosis. The essence of SOM-BPNN is to add a competition layer in front of the hidden layer of BPNN, and its structure is shown in Figure 2.

The implementation process of SOM-BPNN is as follows.

Step 1. Construct the training samples, and normalize the input samples.

Step 2. Determine the number of layers and nodes of SOM and BPNN, respectively.

Step 3. Classify the input samples preliminarily with SOM.

Step 4. Add a dimension to the training sample vector according to the preliminary classification results of SOM, and use the new vector as the input of the secondary BPNN.

Step 5. Start training after the BPNN input layer of the secondary network receiving the new sample vector, until the model reaches the convergence requirement.

The combined network is the SOM-BPNN model which can classify the input sample set more accurately. The classification of test samples is realized by inputting the test sample set into the model.

2.2.2. ANVTPSO Algorithm. PSO is the search for the optimal solution through the cooperation among individuals in the group. In practice, a group of random particles is initialized, and in each iterative search process, the particles continuously update through the extreme (P_{ia}, P_{ga}) until the optimal solution is found within the set number of iterative steps. Among them, P_{ia} is the optimal solution found so far by the particle itself, which is the individual extreme value, and P_{ga} is the optimal solution found so far by the whole population, which is the global extreme value.

$$V_{ia}(t+1) = w(t)V_{ia}(t) + c_1 r_1(P_{ia}(t) - X_{ia}(t)) + c_2 r_2(P_{ga}(t) - X_{ia}(t)),$$
$$X_{ia}(t+1) = X_{ia}(t) + V_{ia}(t+1), \tag{13}$$

where $V_{ia}(t+1)$ and $X_{ia}(t+1)$ are the particle velocity and position of the i particle in the a dimension in the $t+1$ iteration, respectively; $w(t)$ is inertia weight; t is the number of
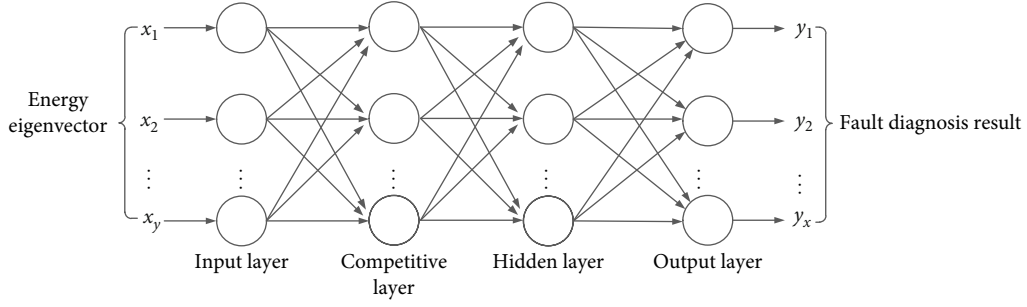
FIGURE 2: Topological structure of the SOM-BPNN model.

iterations; c_1 and c_2 are learning factors; and r_1 and r_2 are random numbers at $[0, 1]$.

In order to avoid the influence of randomly given initial velocity of particles on the convergence speed and accuracy, the velocity term of the standard PSO is abandoned [28], and the position is updated according to the following equation:

$$X_{ia}(t+1) = w(t)X_{ia}(t) + c_1 r_1 (P_{ia}(t) - X_{ia}(t)) + c_2 r_2 (P_{ga}(t) - X_{ia}(t)).$$
(14)

PSO has the disadvantages of easy premature convergence, low convergence accuracy, and low later iteration efficiency [29]. Inertia weight w regulates the searching ability of particles in solution space, and its value affects the optimization level of the algorithm. Meanwhile, because PSO has the evolutionary stages, different learning factors should be set in different stages. Based on this, this paper uses an adaptive method to modify the inertia weight, which changes with the change of particle objective function value [30], expressed by equation (15). Asynchronous nonlinear adaptive adjustment learning factor is adopted [31], which is expressed by equation (16).

$$w = \begin{cases} w_{\min} - \dfrac{(w_{\max} - w_{\min}) * (f - f_{\min})}{f_{\text{avg}} - f_{\min}}, & f \leq f_{\text{avg}}, \\ w_{\max}, & f > f_{\text{avg}}, \end{cases}$$
(15)

where $w_{\max}$ is the maximum inertia weight; $w_{\min}$ is the minimum inertia weight; f is the real-time objective function value of the particle; and f_{avg} and $f_{\min}$ are the average and minimum values of all current particles, respectively.

$$\begin{cases} c_1 = 2 + \dfrac{f - f_{\text{avg}}}{f_{\text{avg}} - f_{\min}}, \\ c_2 = 2 - \dfrac{f - f_{\text{avg}}}{f_{\text{avg}} - f_{\min}}, \end{cases}$$
(16)

where 2 is the initial value of learning factors c_1 and c_2.

2.2.3. ANVTPSO-SOM-BPNN Model. The preliminary classification of input samples is realized through SOM. According to the preliminary classification results, a dimension is added to the training sample vector, and the newly formed feature vector is used as the input of SOM-BPNN. However, the initial network connection weight and node threshold of

SOM-BPNN, like BPNN, are usually determined based on experience and are easy to fall into local optimal solution, which limits the convergence efficiency of the network. But PSO can search in a large space, and when it is used to optimize the threshold and weight of SOM-BPNN, it can avoid the above problems to a certain extent. Because the parameter setting of PSO has a great impact on the final result, this paper adopts an adaptive way to adjust the inertia weight and learning factor of PSO and round off its velocity term to avoid the influence of particle initial velocity on the convergence speed and solution accuracy, which is the new ANVTPSO algorithm, used for SOM-BPNN threshold and weight optimization, to improve the accuracy of fault diagnosis. ANVTPSO-SOM-BPNN diagnostic model is constructed, and the process is shown in Figure 3.

The process of ANVTPSO-SOM-BPNN algorithm is as follows.

Step 1. Set the input node, network competition layer, and other parameters in SOM, according to the characteristic data. Use the classification results obtained by SOM as the training sample vector, and add a dimension; then, form a new feature data set with the original feature data.

Step 2. Set the input node N, hidden layer node L, output node M, and other parameters according to the new feature data set. Clarify the structure of SOM-BPNN.

Step 3. Initialize PSO, calculate its search space dimension a, and set parameters such as population number and maximum iteration times $T_{\max}$.

Step 4. Use the characteristic data as the input of SOM-BPNN to calculate the fitness value of each particle. Fitness function takes the mean square error function MSE between the actual training output and the expected output.

Step 5. Calculate the initial individual optimal position P_{ia} and global optimal position P_{ga} of PSO.

Step 6. Discard the velocity term of PSO, update the position according to equation (14), update the inertia weight according to equation (15), and update the learning factor according to equation (16), so as to obtain the individual and global

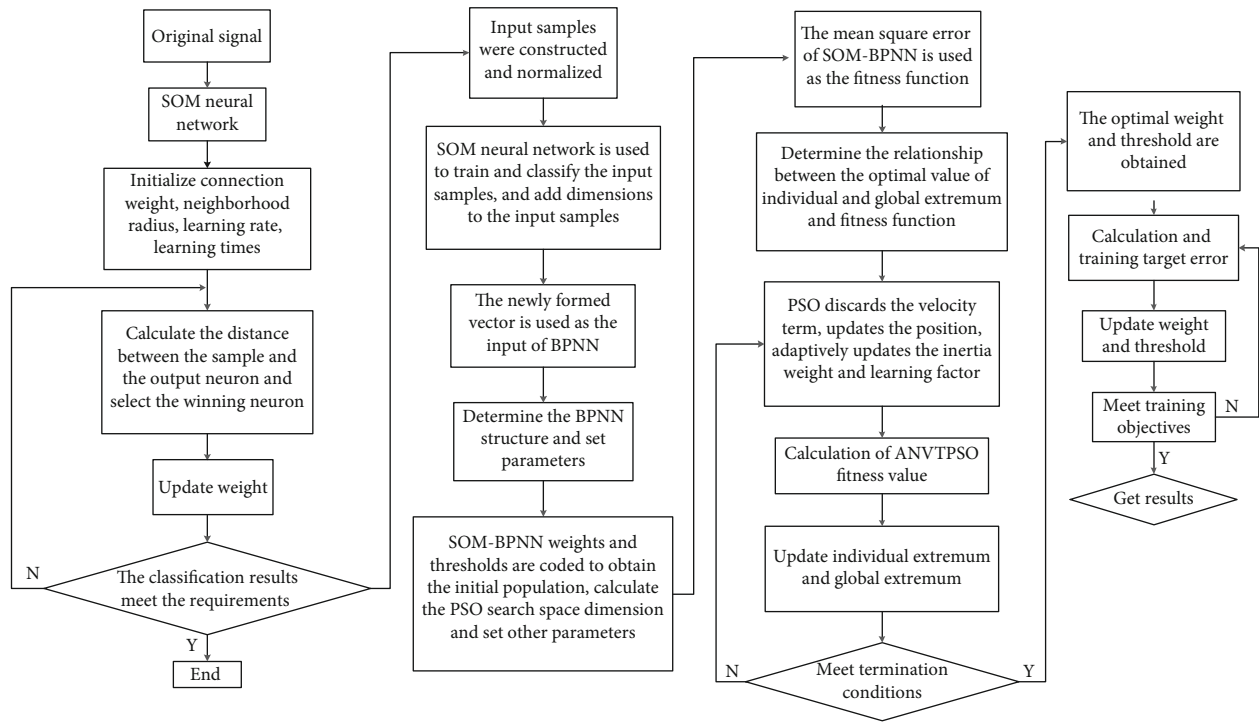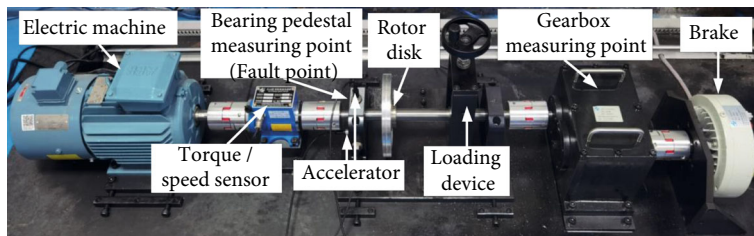FIGURE 3: Flow chart of ANVTPSO-SOM-BPNN algorithm.

FIGURE 4: Fault diagnosis comprehensive test platform.

(a)   (b)
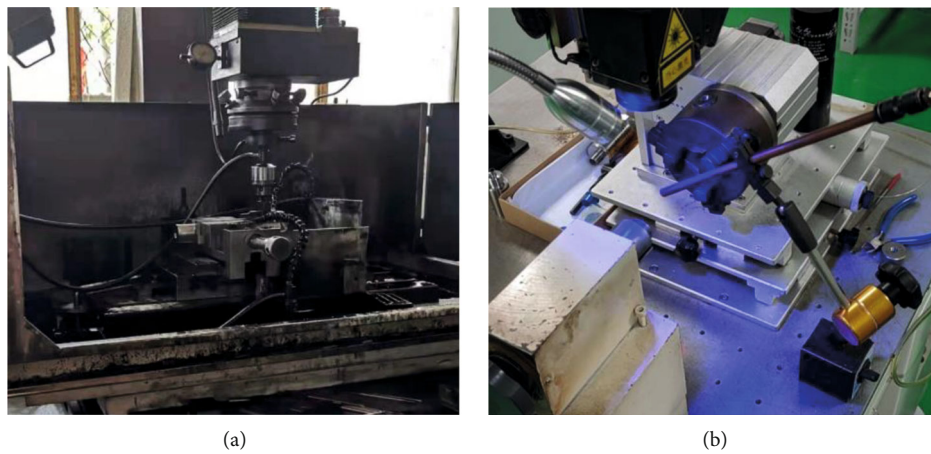
FIGURE 5: Fault machining equipment: (a) EDM; (b) laser welding machine.

(a)

(b)

(c)

FIGURE 6: Finished fault bearings: (a) inner ring and outer ring; (b) inner ring and rolling element; (c) outer ring and rolling element.

TABLE 1: Fault size of rolling bearing.

Bearing status	Fault size (mm)
Normal	0
Inner ring crack and outer ring crack	$2 * 1.5 * 0.5 + 2 * 1.5 * 0.5$
Inner ring crack and rolling element pitting	$2 * 1.5 * 0.5 + 1s$ (pit corrosion)
Outer ring crack and rolling element pitting	$2 * 1.5 * 0.5 + 1s$ (pit corrosion)

TABLE 2: Fault characteristic frequency of rolling bearing.

Fault location	Frequency (Hz)
Inner ring	162.23
Outer ring	107.77
Rolling element	71.33

optimal extreme value. And then, the PSO position is mapped to obtain the optimal weight and threshold.

Step 7. Bring the optimized weight and threshold into SOM-BPNN, and continue tuning until the training objectives are met.

2.3. D-S Evidence Theory

2.3.1. Principle of D-S Evidence Theory.
D-S evidence theory has good practicability, so it is widely used in the field of multisensor target recognition [32, 33]. Its main characteristics include the following: it satisfies the weaker conditions than Bayesian probability theory and has the ability to directly express "uncertainty" and "do not know" [34].

Definition 1. If Θ is a finite sample set and all propositions in the set are mutually exclusive, set Θ is called the identification framework. The power set of Θ is composed of all subsets and various combinations of identification framework Θ, noted as 2^{Θ}. Take Θ as the identification framework of

Table 3: Decomposition level of wavelet packet.

Fault location	Decomposition level
Inner ring	$J < 3.98$
Outer ring	$J < 4.57$
Rolling element	$J < 5.16$

proposition A. A assign the basic probability function m as $m(A)$ which is the mapping of set 2^{Θ} to $[0,1]$.

The function $m : 2^{\Theta} \longrightarrow [0, 1]$ satisfies the following conditions:

$$\begin{cases} m(\phi) = 0, \\ \sum_{A \subseteq \Theta} m(A) = 1, \end{cases} \tag{17}$$

where $0 \leq m(A) \leq 1$, A is called focal element, and $m(A)$ is the basic probability assignment of A, indicating the trust degree in A.

Definition 2. Mapping $Bel(A)$: $2^{\Theta} \longrightarrow [0, 1]$ is the confidence function defined on Θ, which reflects the exact trust degree of A. The expression is

$$Bel(A) = \sum_{B \subseteq A} m(B). \tag{18}$$

Mapping $PI(A)$: $2^{\Theta} \longrightarrow [0, 1]$ is a plausible function defined on Θ, which represents the degree of nonfalse trust in proposition A. It is also an uncertainty measure that seems to be possible for proposition A. The expression is

$$PI(A) = 1 - Bel(\bar{A}) \tag{19}$$

where $PI(A)$ and $Bel(A)$ represent the upper and lower limits of the function, respectively.

Definition 3. $[Bel(A), Pl(A)]$ is defined as the trust interval of proposition A. $[0, Bel(A)]$ represents the support evidence interval of proposition A. $[Pl(A), 1]$ represents the rejection evidence interval of proposition A.

Definition 4. D-S evidence theory synthesis rule: let m_1 and m_2 be the basic reliability distribution on the same identification framework Θ and meet the following conditions:

$$\sum_{A_i \cap A_j = \phi} m_1(A_i) m_2(A_j) < 1. \tag{20}$$

Then, the combined basic probability distribution function is

$$m(A) = \frac{\sum_{A_i \cap A_j = A} m_1(A_i) m_2(A_j)}{1 - \sum_{A_i \cap A_j = \phi} m_1(A_i) m_2(A_j)}. \tag{21}$$

2.3.2. Fault Diagnosis Based on D-S Evidence Fusion. The composite fault signals of rolling bearing obtained by multiple sensors are processed by wavelet packet AR spectral entropy, and the relevant eigenvalues are extracted. The composite fault diagnosis is carried out by using ANVTPSO-SOM-BPNN, and the output is used as evidence which is fused through D-S evidence theory to construct a new fault diagnosis model. The model makes full use of the advantages of D-S theory in dealing with uncertain problems and the powerful nonlinear processing ability of neural network and uses the self-learning ability of neural network to solve the problem that it is difficult to obtain the basic probability assignment in D-S theory. At the same time, if there is no noise, the target recognition will be easy, but in practice, the noise is inevitable. Therefore, using multiple sensors for recognition and fusing the recognition results of each sensor can improve the recognition rate.

The implementation process of the proposed diagnosis model based on D-S evidence fusion is as follows.

Step 1. Obtain the target feature vector. The collected composite fault signals of rolling bearing are extracted by wavelet packet AR spectral entropy.

Step 2. Input the target eigenvector into ANVTPSO-SOM-BPNN model.

Step 3. Normalize the diagnostic output of ANVTPSO-SOM-BPNN model, with a range of $[0, 1]$; calculate the error E_n between the actual output and the expected output of the diagnostic model, as shown in equation (22). The basic probability value of each focus element is shown in equation (23). The uncertainty degree $m(\theta)$ of the diagnostic model is shown in equation (24).

$$E_n = \frac{1}{2} * \sum (t_{ni} - y_{ni}), \tag{22}$$

where t_{ni} is the expected value of the output neuron and y_{ni} is the actual value of the output neuron.

$$m(A_i) = \frac{y(A_i)}{S_n}, \tag{23}$$

where $m(A_i)$ is the basic probability of each focal element; $y(A_i)$ is the diagnostic result; and $S_n = \sum_{i=1}^{n} y(A_i) + E_n$.

$$m(\theta) = 1 - \sum_{i=0}^{R} m(A_i). \tag{24}$$

Step 4. Obtain the final result by multi-information fusion with evidence combination rules.

3. Experiments

3.1. Experimental Data Collection. In order to verify the effect of the composite fault diagnosis method of rolling bearing based on ANVTPSO-SOM-BPNN combined with wavelet packet AR spectral entropy, the experimental test

TABLE 4: Ratio of total energy and total energy entropy of wavelet packet (radial mean value of direct fault point).

Type	sym8	db4	db5	db8	db10
Normal	0.7071	0.7075	0.7069	0.7072	0.7078
Inner ring and outer ring	0.8215	0.8218	0.8212	0.8216	0.8221
Inner ring and rolling element	0.8714	0.8710	0.8705	0.8715	0.8728
Outer ring and rolling element	1.0236	1.0220	1.0219	1.0237	1.0249

TABLE 5: Ratio of total energy and total energy entropy of wavelet packet (axial mean value of direct fault point).

Type	sym8	db4	db5	db8	db10
Normal	1.0148	1.0118	1.0122	1.0149	1.0156
Inner ring and outer ring	1.1893	1.1892	1.1886	1.1891	1.1896
Inner ring and rolling element	0.9888	0.9871	0.9872	0.9893	0.9903
Outer ring and rolling element	1.0543	1.0529	1.0528	1.0544	1.0553

TABLE 6: Ratio of total energy and total energy entropy of wavelet packet (radial mean value of gearbox).

Type	sym8	db4	db5	db8	db10
Normal	2.6329	2.6375	2.6346	2.6329	2.6332
Inner ring and outer ring	2.5379	2.5415	2.5385	2.5393	2.5401
Inner ring and rolling element	2.6280	2.6309	2.6279	2.6286	2.6282
Outer ring and rolling element	2.5099	2.5119	2.5096	2.5088	2.5097

TABLE 7: Ratio of total energy and total energy entropy of wavelet packet (axial mean value of gearbox).

Type	sym8	db4	db5	db8	db10
Normal	3.2479	3.2479	3.2456	3.2472	3.2497
Inner ring and outer ring	2.8983	2.8962	2.8951	2.8985	2.9004
Inner ring and rolling element	3.2146	3.2151	3.2128	3.2148	3.2167
Outer ring and rolling element	3.1967	3.1949	3.1932	3.1968	3.1991

TABLE 8: Parameters of ANSVTPSO-SOM-BPNN.

ANVTPSO parameters	Value	SOM parameters	Value	BPNN parameters	Value
Number of population particles x	20	Input node	9	Input node N	10
Spatial dimension a	199	Network competition layer	$6 * 6$	Hidden layer node L	13
Position X	[-1, 1]	Topological function	Hextop	Output node M	4
Learning factor c_1	Undetermined	Distance function	Linkdist	Maximum training times	1000
Learning factor c_2	Undetermined	Classification stage learning rate	0.9	Training objectives	10^{-8}
Inertia weight W_{max}	0.9	Classification stage learning step	1000	Learning rate	0.001
Inertia weight W_{min}	0.4	Learning rate in tuning phase	0.02	Hidden layer transfer function	Tansig
Maximum number of iterations T_{max}	20	Tuning phase domain distance	1	Output layer transfer function	Purelin

is carried out on the comprehensive experimental platform for fault diagnosis of mechanical transmission system, as shown in Figure 4. The test-bed consists of three-phase variable frequency motor, rotor bearing system, radial loading device, parallel shaft gearbox, and magnetic particle brake. The rolling bearing in the bearing pedestal on the left side of the rotor is selected as the tested object. The used bearing model is NSK6205, the number of rolling elements Z is 9, the diameter of rolling elements d is 7.94 mm, the pitch diameter D is 39.36 mm, and the contact angle α is 0°.

Set the motor speed at 1800 r/min and no load; install the composite fault part at the bearing seat as the fault source. Set the bearing pedestal and gearbox as two measuring points for vibration signal acquisition, and the vertical

TABLE 9: Comparison of bearing fault diagnosis results (radial direction of fault point).

Diagnostic method	Iteration steps	Diagnostic accuracy (%)
BPNN	12	100

TABLE 10: Comparison of bearing fault diagnosis results (axial direction of fault point).

Diagnostic method	Iteration steps	Diagnostic accuracy (%)
BPNN	135	97
ANVTPSO-SOM-BPNN	81	97

radial and axial direction corresponding to the measuring points adopt the accelerators with a sensitivity of 103 mV/g (g is gravity acceleration). When collecting the vibration signal of composite fault of rolling bearing, the sampling time is set as 1 s and the sampling rate is set as 10.24 kHz. A total of 300 groups of vibration acceleration signals are collected, including the normal, inner ring crack and outer ring crack, inner ring crack and rolling element pitting, and outer ring crack and rolling element pitting, and each type has 75 groups. The signal samples are divided into a training set and test set in 2 : 1.

The inner ring and outer ring are machined by using electrical discharge machine (EDM), and the rolling element has the 1 second pit corrosion by using TH-RFT300 high-speed laser welding machine. The fault machining equipment is shown in Figure 5. The finished fault bearings are shown in Figure 6. The fault size is shown in Table 1, and the fault characteristic frequency is shown in Table 2.

3.2. Experimental Data Analysis

3.2.1. Determining the Optimal Number of Wavelet Packet Decomposition Layers.
The purpose of wavelet packet decomposition is to find fault characteristics. Therefore, the signal frequency can be replaced by fault characteristic frequency. The number of decomposition layers can be calculated by equation (6), as shown in Table 3.

Table 3 shows that according to the characteristic frequencies of different fault parts of the bearing, the best values of wavelet packet decomposition layers are 3 to 5. Because the composite fault signal is more complex than a single fault case, in order to retain the useful information of four types of bearing vibration signals to the greatest extent, in the selection of unified decomposition layers, if the number of decomposition layers exceeds 3, the inner ring signal may be over decomposed, resulting in the loss of useful information in the composite fault. After comprehensive consideration, the number of wavelet packet decomposition layers in this paper is 3.

3.2.2. Determining the Optimal Wavelet Basis Function.
75 groups of 4 types of bearing data are selected, and the 5 types of wavelet bases sym8, db4, db5, db8, and db10 are decomposed in 3 layers by wavelet packet and calculated according

to formula (12) to obtain the ratio of wavelet packet total energy and total energy entropy corresponding to the 4 types of bearing data. In order to eliminate the uncertain influence caused by individual signals, the mean value of parameters under various states is calculated. The corresponding calculation results are shown in Tables 4–7.

It can be seen from Tables 4 and 5 that the ratio of total energy and total energy entropy of wavelet packet in 4 types of bearings in the measuring points of bearing pedestal (direct fault point) is db10, which is the largest in the data of radial and axial measuring points. According to the principle that the greater the ratio of total energy and total energy entropy of wavelet packet, the better the decomposition effect of wavelet packet, db10 is regarded as the optimal wavelet basis function of wavelet packet decomposition of 4 kinds of bearing signals in radial measuring points and axial measuring points of bearing pedestal. It can be seen from Tables 6 and 7 that the ratio of total energy of wavelet packet to total energy entropy of four types of bearings in the gearbox measuring points is db4 and db10, respectively, in the radial and axial data. Similarly, db4 and db10 are taken as the optimal wavelet basis function for wavelet packet decomposition of 4 types of bearing signals in the gearbox radial direction measuring points and axial measuring points.

3.3. Determination of the ANVTPSO-SOM-BPNN Parameters.
The parameters of ANVTPSO-SOM-BPNN are shown in Table 8, where the spatial dimension of particles a [35] and the selection of the optimal number of nodes L in the hidden layer are shown in equations (25) and (26), respectively.

$$a = N * L + L * M + L + M, \qquad (25)$$

$$L = \sqrt{(M + N)} + \varepsilon, \quad 0 < \varepsilon < 10. \qquad (26)$$

3.4. Result Analysis.
BPNN, SOM-BPNN, PSO-SOM-BPNN, and ANVTPSO-SOM-BPNN were used for the composite fault diagnosis of rolling bearing, respectively. The expected output of the state categories of the tested rolling bearing are normal (1 0 0 0), inner ring fault (0 1 0 0), outer ring fault (0 0 1 0), and rolling element fault (0 0 0 1).

In order to verify the advantages of the method proposed in this paper, at first, optimize the wavelet basis function and decomposition levels of wavelet packet AR spectrum energy entropy, extract the characteristics of energy entropy, and compare SOM-BPNN with standard BPNN to verify that the series network has more advantages in convergence speed than a single network. Second, the PSO-SOM-BPNN is compared with SOM-BPNN to verify the optimization effect of PSO on SOM-BPNN. Then, compare the above 3 schemes BPNN with ANVTPSO-SOM-BPNN, study the series advantages of both unsupervised learning network and supervised learning network, and verify the impact of improved PSO on fault diagnosis results. Finally, the collected multisensor data are used for fault diagnosis through the ANVTPSO-SOM-BPNN constructed in this paper, and the results are fused at the decision level through D-S evidence theory, so as to improve the final fault diagnosis rate.
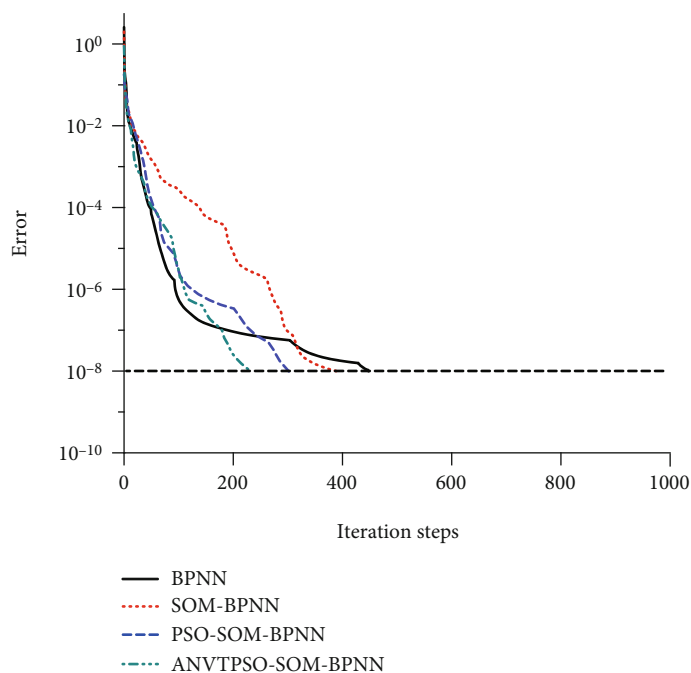
FIGURE 7: Error curves of four kinds of diagnosis models (gearbox radial direction).
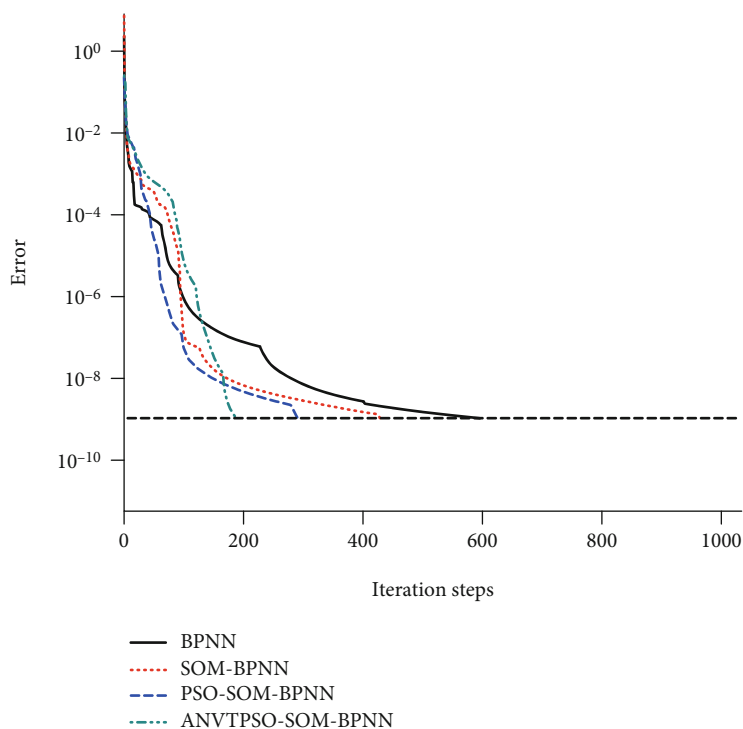

FIGURE 8: Error curves of four kinds of diagnosis models (gearbox axial direction).

Through fault diagnosis of vibration signals of radial measuring points and axial measuring points of bearing pedestal, the diagnosis results are shown in Tables 9 and 10, respectively.

As shown in Table 9, in the radial measuring points of the bearing pedestal, because they are close to the fault point, there is less noise interference, and the fault characteristics of the collected vibration signals are obvious. Therefore, the fault diagnosis using standard BPNN can reach 100%, and the number of iterative steps is only 12. Table 10 presents that in the axial measuring point, the standard BPNN used for fault diagnosis reach 97%, and the number of

TABLE 11: Comparison of bearing fault diagnosis results (gearbox radial direction).

Diagnostic method	Iteration steps	Diagnostic accuracy (%)
BPNN	448	82
SOM-BPNN	389	85
PSO-SOM-BPNN	302	87
ANVTPSO-SOM-BPNN	240	92

TABLE 12: Comparison of bearing fault diagnosis results (gearbox axial direction).

Diagnostic method	Iteration steps	Diagnostic accuracy (%)
BPNN	576	91
SOM-BPNN	415	93
PSO-SOM-BPNN	282	95
ANVTPSO-SOM-BPNN	182	96

iterative steps is 135. The ANVTPSO-SOM-BPNN method proposed in this paper is used for diagnosis, with an accuracy of 97%, which is the same as the diagnosis result of the standard BPNN, but the number of iterative steps is 81; compared with the former, it reduces 54 steps.

To sum up, the data collected at the measuring point of the bearing pedestal has less interference and obvious fault characteristics, so the basic diagnosis algorithm used in both radial and axial direction data has a high accuracy. However, in real working conditions, due to the influence of various on-site factors, it is impossible to install sensors to collect vibration signals close to the direct fault point. Therefore, the indirect gearbox measuring point is more universal in line with the actual working conditions.

Figures 7 and 8, respectively, demonstrate the mean square error of the four diagnostic methods of the radial measuring point and axial measuring point of gearbox with the number of training times. The comparison of diagnostic results of the composite fault of rolling bearing is shown in Tables 11 and 12.

Figure 7 indicates that BPNN, PSO-SOM-BPNN, and ANVTPSO-SOM-BPNN intersect near 50 steps and the error of ANVTPSO-SOM-BPNN is the smallest before the intersection. After the intersection, the BPNN always keeps the minimum error until the second intersection with ANVTPSO-SOM-BPNN near 200 steps. After the second intersection, ANVTPSO-SOM-BPNN converges faster. Before SOM-BPNN intersects with BPNN, SOM-BPNN error is always the largest, and it converges faster after the bifurcation point. From the details of the iterative process, the four methods all have fallen into the local minimum for a short time, resulting in the increase of the total iterative steps, but ANVTPSO-SOM-BPNN performs better than the other methods. Figure 8 displays that BPNN and SOM-BPNN intersect near 100 steps.

The error of BPNN before intersection is the smallest, but it is easier to fall into the local minimum than SOM-BPNN, and the convergence speed becomes slower and the total number of iterative steps increases after intersection. Before the intersection of PSO-SOM-BPNN and ANVTPSO-SOM-BPNN, the error is the smallest among the four methods, and the number of relative falling into the local minimum is the least. After the intersection, ANVTPSO-SOM-BPNN converges faster and takes the least iterative steps to reach the training target.

Above all, ANVTPSO-SOM-BPNN has the advantages of series connection of unsupervised learning network and supervised learning network. Combined with ANVTPSO, at the gearbox measuring points with more interference, it can reach the training target faster for both radial and axial vibration signal diagnosis, which proves that the proposed new method has an obvious optimization effect.

Tables 11 and 12 show the quantitative data of the four methods in the radial and axial measuring points of gearbox. Table 11 reveals that the diagnostic accuracy of SOM-BPNN is 3% higher than that of BPNN. Compared with SOM-BPNN, the diagnostic accuracy of PSO-SOM-BPNN is improved by 2%, and the number of iterative steps is reduced by 87. Table 12 suggests that the diagnostic accuracy of SOM-BPNN is 2% higher than that of BPNN. Compared with SOM-BPNN, the diagnostic accuracy of PSO-SOM-BPNN is improved by 2%, and the number of iterative steps is reduced by 133. In both radial and axial directions, the PSO learning factor in PSO-SOM-BPNN is taken as $c_1 = c_2 = 1.49445$ according to experience, while the ANVTPSO-SOM-BPNN adaptively adjusts the inertia weight and learning factor, so that the inertia weight is taken as $w = 0.9$ in the initial stage and $w = 0.4$ in the later stage, the radial learning factor is $c_1 = 1.4175$ and $c_2 = 2.5825$ in the later stage, and the axial learning factor is $c_1 = 1.6984$ and $c_2 = 2.3016$ in the later stage. As mentioned above, the axial learning factor of bearing pedestal is $c_1 = 1.5736$ and $c_2 = 2.4264$ in the later stage. Both the inertia weight and learning factor meet the needs of different stages of the algorithm through adaptation. After many tests, the accuracy of ANVTPSO-SOM-BPNN is higher than other methods, and the number of iterative steps also has great advantages. Table 11 presents that in the radial direction, the diagnostic accuracy reaches 92% at step 240. Table 12 shows that in the axial direction, the diagnostic accuracy reached 96% at step 182.

Tables 13 and 14 display the partial basic probability distribution values of the radial and axial measuring points of gearbox after the output results of the ANVTPSO-SOM-BPNN model are processed according to formula (22) and formula (23) and the uncertainty degree of the diagnostic model according to equation (24). Table 15 presents the partial basic probability distribution values and uncertainty degree of the two measuring points after D-S evidence fusion. Table 16 indicates that the diagnosis results of the newly proposed ANVTPSO-SOM-BPNN method in this paper at the radial and axial measuring points of gearbox are fused at the decision level, and the accuracy of fault diagnosis reaches 100%. The diagnostic accuracy after fusion was improved by 8% and 4% compared with the radial and axial ANVTPSO-SOM-BPNN in the gearbox, respectively. When

TABLE 13: Basic probability distribution value of ANVTPSO-SOM-BPNN (gearbox radial direction).

Type	$m_1(A_1)$	$m_1(A_2)$	$m_1(A_3)$	$m_1(A_4)$	$m_1(\theta)$
Normal	0.9373	0.0416	0.0200	0	0.0011
Inner ring and outer ring	0.0764	0.8403	0.0764	0	0.0069
Inner ring and rolling element	0.0212	0.0422	0.9354	0	0.0012
Outer ring and rolling element	0.0839	0	0.0840	0.8235	0.0086

TABLE 14: Basic probability distribution value of ANVTPSO-SOM-BPNN (gearbox axial direction).

Type	$m_2(A_1)$	$m_2(A_2)$	$m_2(A_3)$	$m_2(A_4)$	$m_2(\theta)$
Normal	0.7670	0	0.2050	0.0006	0.0274
Inner ring and outer ring	0	0.9994	0.0004	0.0002	0
Inner ring and rolling element	0.1051	0	0.8887	0	0.0062
Outer ring and rolling element	0.0000	0.0059	0.0117	0.9823	0.0001

TABLE 15: Basic probability distribution value after D-S evidence fusion.

Type	$m(A_1)$	$m(A_2)$	$m(A_3)$	$m(A_4)$	$m(\theta)$
Normal	0.9920	0.0015	0.0065	0	0
Inner ring and outer ring	0	1.0000	0	0	0
Inner ring and rolling element	0.0030	0.0003	0.9967	0	0
Outer ring and rolling element	0	0.0001	0.0013	0.9986	0

TABLE 16: D-S evidence fusion diagnosis results.

Diagnostic method	Diagnostic accuracy (%)
ANVTPSO-SOM-BPNN (radial & axial)	100

compared with the diagnostic accuracy of BPNN in the radial direction of the fault point, it also reaches 100%. And compared with the diagnostic accuracy of ANVTPSO-SOM-BPNN in the axial direction of the fault point, it is improved by 3%. In conclusion, it is proved that the method proposed in this paper can achieve high diagnosis accuracy even at the gearbox measuring point far away from the fault point.

4. Conclusions

(1) The method of wavelet packet AR spectrum energy entropy can effectively extract the composite fault feature components in the vibration signal of rolling bearing and can better eliminate interference and noise. The optimal selection of wavelet packet decomposition layers and basis function in wavelet packet AR spectrum energy entropy can avoid the external interference caused by blind selection

(2) The adaptive inertia weight and learning factor are introduced into the standard PSO algorithm to meet the needs of the algorithm for parameters in different stages, and the velocity term is discarded to avoid the influence of the initial particle velocity on the convergence speed and solution accuracy of the algorithm, which significantly improves the search speed and convergence accuracy of the algorithm compared with the conventional method

(3) Build ANVTPSO-SOM-BPNN diagnostic model. SOM-BPNN avoids the influence of the limitations of a single algorithm on the diagnosis results, so that the primary network can promote the training of the secondary network. Then ANVTPSO is used to optimize the threshold and weight of SOM-BPNN to avoid falling into the local optimal solution, so as to improve the diagnostic accuracy

(4) In the actual working condition, it is common for the same rolling bearing to coexist multiple faults, and the installation scheme of sensors also have a great impact on the accuracy of diagnosis. In this paper, both the data of fault point and far away from fault point are collected by multiple acceleration sensors, and the proposed method based on optimal wavelet packet AR spectrum energy entropy combined with ANVTPSO-SOM-BPNN is used for multi-information fusion diagnosis. By comparing the diagnosis results of two measuring points, it is found that even at the gearbox measuring point far away from the direct fault point, the diagnosis results can achieve high accuracy and effectively diagnose the composite fault of rolling bearing under noise

Data Availability

Conflicts of Interest

The authors declare that they have no known competing financial interests or personal relationships that could have appeared to influence the work reported in this paper.

Acknowledgments

References

[1] A. Gałęzia and K. Gryllias, "Application of the combined Teager-Kaiser envelope for bearing fault diagnosis," *Measurement*, vol. 182, article 109710, 2021.

[2] D. T. Hoang and H. J. Kang, "A survey on deep learning based bearing fault diagnosis," *Neurocomputing*, vol. 335, pp. 327–335, 2019.

[3] K. Yu, R. L. Tian, J. W. Tan, and H. Ma, "An adaptive sensitive frequency band selection method for empirical wavelet transform and its application in bearing fault diagnosis," *Measurement*, vol. 134, pp. 375–384, 2019.

[4] X. Li, Y. Yang, H. D. Shao, X. Zhong, J. Cheng, and J. Cheng, "Symplectic weighted sparse support matrix machine for gear fault diagnosis," *Measurement*, vol. 168, article 108392, 2021.

[5] D. D. Liu, W. D. Cheng, W. G. Wen, and G. T. Wan, "Composite fault diagnosis of rolling bearing based on envelope demodulation filter," *Journal of Central South University(natural science)*, vol. 49, no. 4, pp. 881–887, 2018.

[6] L. L. Cui, C. G. Wu, and N. Wu, "Composite fault diagnosis of rolling bearings based on EMD and ICA algorithm," *Journal of Beijing University of Technology*, vol. 40, no. 10, pp. 1459–1464, 2014.

[7] X. X. Zheng and M. N. Li, "Health state evaluation based on wavelet packet and pchmm for vulnerable components of wind turbines," *Acta Energiae Solaris Sinica*, vol. 40, no. 2, pp. 370–379, 2019.

[8] G. J. Tang and F. Y. Deng, "Compound fault features separation method of rolling element bearing based on improved harmonic wavelet packet decomposition," *Chinese Journal of Scientific Instrument*, vol. 36, no. 1, pp. 143–151, 2015.

[9] S. He, J. Chen, Z. Zhou, Y. Zi, Y. Wang, and X. Wang, "Multifractal entropy based adaptive multiwavelet construction and its application for mechanical compound-fault diagnosis," *Mechanical Systems and Signal Processing*, vol. 76-77, pp. 742–758, 2016.

[10] B. D. Ma, S. J. Hu, Y. F. Meng, B. Song, and T. Wu, "Rolling bearings compound fault diagnosis method based on multiwavelet packet and energy operator demodulating method," *Noise and Vibration Control*, vol. 38, no. 4, pp. 154–158, 2018.

[11] S. Abbasion, A. Rafsanjani, A. Farshidianfar, and N. Irani, "Rolling element bearings multi-fault classification based on the wavelet denoising and support vector machine," *Mechanical Systems & Signal Processing*, vol. 21, no. 7, pp. 2933–2945, 2007.

[12] O. Janssens, V. Slavkovikj, B. Vervisch et al., "Convolutional neural network based fault detection for rotating machinery," *Journal of Sound and Vibration*, vol. 377, pp. 331–345, 2016.

[13] N. Lv and P. X. Yao, "Fault diagnosis of rolling bearing based on BP neural network," *Coal Mine Machinery*, vol. 41, no. 8, pp. 172-173, 2020.

[14] J. M. Li, X. F. Yao, X. D. Wang, Q. W. Yu, and Y. G. Zhang, "Multiscale local features learning based on BP neural network for rolling bearing intelligent fault diagnosis," *Measurement*, vol. 153, 2020.

[15] W. C. Huang, L. J. Wang, J. W. Liu, and B. J. Chen, "Rolling bearings fault recognition based on multi feature fusion and GA-BP mode," *Machine Tool & Hydraulics*, vol. 49, no. 6, pp. 170–173, 2021.

[16] M. Gong, H. X. Pan, and H. L. Lan, "Diesel engine fault diagnosis based on combination of optimal wavelet packet and SOM-BP," *Coal Mine Machinery*, vol. 33, no. 10, pp. 278–280, 2012.

[17] C. Ju, C. Zhang, H. W. Fan, X. H. Zhang, Y. Q. Yang, and Y. Yan, "Rolling bearing fault diagnosis based on wavelet packet decomposition and PSO-BPNN," *Industry and Mine Automation*, vol. 46, no. 8, pp. 70–74, 2020.

[18] L. Wang and X. K. Wang, "Modified particle swarm optimizer using non-linear inertia weight," *Computer Engineering and Applications*, vol. 43, no. 4, pp. 47-48, 2007.

[19] Y. M. Zhu and P. X. Xue, "The research of PSO based on the adaptive changes of acceleration coefficients," *Journal of Shaanxi University of Science & Technology(Natural Science Edition)*, vol. 33, no. 4, pp. 172–177, 2015.

[20] M. Khazaee, H. Ahmadi, M. Omid, A. Moosavian, and M. Khazaee, "Classifier fusion of vibration and acoustic signals for fault diagnosis and classification of planetary gears based on Dempster-Shafer evidence theory," *Proceedings of the Institution of Mechanical Engineers, Part E: Journal of Process Mechanical Engineering*, vol. 228, no. 1, pp. 21–32, 2014.

[21] D. C. Feng and J. M. D. Pereira, "Study on information fusion based on wavelet neural network and evidence theory in fault diagnosis," in *2007 8th International Conference on Electronic Measurement and Instruments*, Xi'an, China, 2007IEEE Press.

[22] L. L. Zhang, Y. G. Zhao, Y. K. Xiao, S. D. Luo, H. Y. Liao, and Q. X. Pan, "Automobile transmission bearing fault feature extraction based on wavelet packet-auto regressive model spectrum," *Journal of Vibration, Measurement & Diagnosis*, vol. 31, no. 4, pp. 492–495, 2011.

[23] W. Q. Wang and S. Yang, "A method for choosing the wavelet decomposition level in structural fault analysis," *Structure & Environment Engineering*, vol. 36, no. 4, pp. 34–41, 2009.

[24] X. L. Liu, H. G. Liu, J. H. Yang, G. Litak, G. Cheng, and S. Han, "Improving the bearing fault diagnosis efficiency by the adaptive stochastic resonance in a new nonlinear system," *Mechanical Systems and Signal Processing*, vol. 96, pp. 58–76, 2017.

[25] M. Y. Liu, *Research of motor bearing fault diagnosis methods based on vibration signal [M.S. thesis]*, Harbin Institute of Technology, Harbin, China, 2016.

[26] M. L. Tian and X. L. Wang, "Wavelet analysis method applied in fault diagnosis of motor and selection of wavelet base," *Coal Mine Machinery*, vol. 28, no. 5, pp. 176–178, 2007.

[27] P. K. Kankar, S. C. Sharma, and S. P. Harsha, "Fault diagnosis of rolling element bearing using cyclic autocorrelation and wavelet transform," *Neurocomputing*, vol. 110, no. 8, pp. 9–17, 2013.

[28] W. Hu and Z. S. Li, "A simpler and more effective particle swarm optimization algorithm," *Journal of Software*, vol. 18, no. 4, pp. 861–868, 2007.

[29] X. Wei, N. Q. Shu, P. C. Cui, and B. Wu, "Power transformer fault integrated diagnosis based on improved PSO-BP neural networks and D-S evidential reasoning," *Automation of Electric Power Systems*, vol. 30, no. 7, pp. 46–50, 2006.

[30] Z. Wen and H. K. Sun, *MATLAB intelligent algorithm*, Tsinghua University Press, Beijing, China, 2017.

[31] Q. J. Tong, Q. Zhao, and M. Li, "Particle swarm optimization algorithm based on adaptive dynamic change," *Microelectronics & Computer*, vol. 36, no. 2, pp. 6–10, 2019.

[32] Y. B. Li, J. Chen, F. Ye, and D. D. Liu, "The improvement of DS evidence theory and its application in IR/MMW target recognition," *Journal of Sensors*, vol. 2016, no. 6, 2016.

[33] P. Wang, C. X. Shang, and Z. Z. Han, "Target identification based on evidence theory of improved basic probability assignment," in *Electronics, Communications and Networks IV*, pp. 1171–1175, London, U.K., 2015.

[34] S. Li, J. W. Tan, and K. Yu, "Composite fault diagnosis research of rolling bearing based on combination of neural network and improved D-S evidence theory," *Machine Tool & Hydraulics*, vol. 46, no. 1, pp. 153–157, 2018.

[35] J. Dong, W. W. Qin, Y. J. Li, Q. Q. Li, and L. W. Deng, "Fast multi-objective antenna design based on improved back propagation neural network surrogate model," *Journal of Electronics & Information Technology*, vol. 40, no. 11, pp. 2712–2719, 2018.